Comptes Rendus
de l'Académie des sciences

1878-1543 (electronic)

Chimie

Volume 25, Special Issue S1, 2022

Special issue / *Numéro spécial*

Microcrystalline pathologies: Clinical issues and nanochemistry / *Pathologies microcristallines : questions cliniques et nanochimie*

Guest editors / *Rédacteurs en chef invités*

Dominique Bazin, Michel Daudon, Vincent Frochot, Emmanuel Letavernier, Jean-Philippe Haymann

Académie des sciences — Paris

INSTITUT DE FRANCE
Académie des sciences

CENTRE MERSENNE

Comptes Rendus

Chimie

Objective of the journal

Comptes Rendus Chimie is a peer-reviewed electronic journal of international standing, covering all areas of the discipline. It publishes mainly special issues, but also original research articles, preliminary announcements, review articles, historical perspectives, pedagogical texts or conference proceedings, without length limit, in English or in French. Comptes Rendus Chimie is published according to a virtuous policy of diamond open access, free for authors (no publication fees) as well as for readers (immediate and permanent open access).

About the journal

All journal's information, including the text of published articles, which is fully open access, is available from the journal website at https://comptes-rendus.academie-sciences.fr/chimie/.

Author enquiries

For enquiries relating to the submission of articles, please visit this journal's homepage at https://comptes-rendus.academie-sciences.fr/chimie/.

Contact

Académie des sciences
23, quai de Conti, 75006 Paris, France
CR-Chimie@academie-sciences.fr

Comptes Rendus
Chimie
2022, 25, nº S1

Contents / *Sommaire*

Comptes Rendus
Chimie
2022, Vol. 25, Special Issue S1, p. 1-6
https://doi.org/10.5802/crchim.207

Microcrystalline pathologies: Clinical issues and nanochemistry / *Pathologies microcristallines : questions cliniques et nanochimie*

Guest editors

Rédacteurs invités

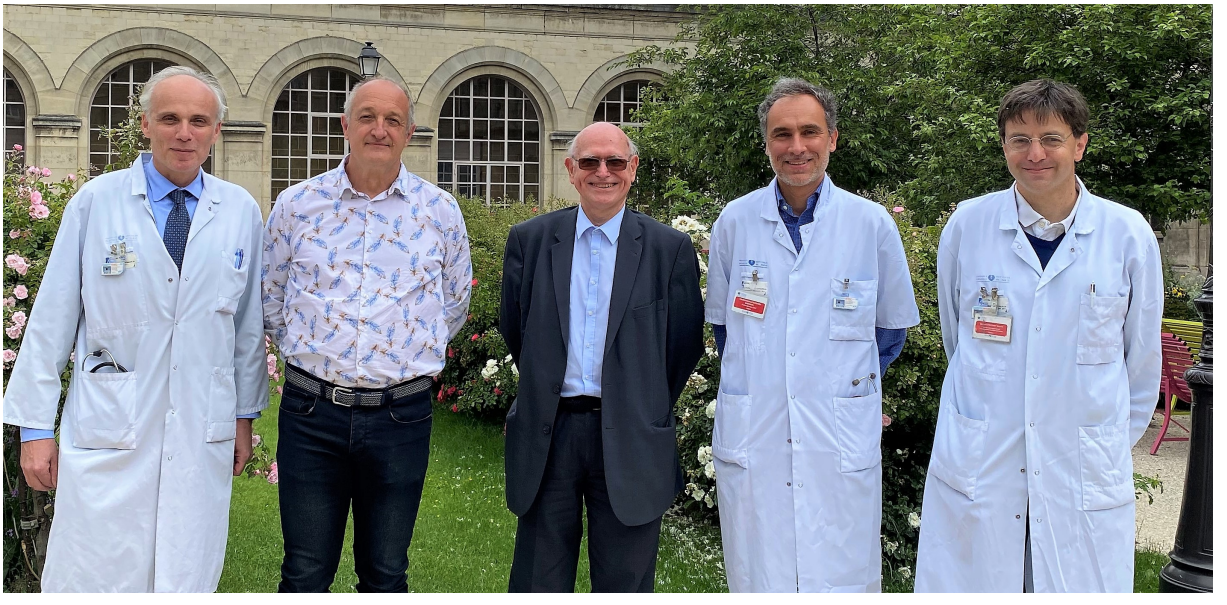

Jean-Philippe Haymann, Dominique Bazin, Michel Daudon, Emmanuel Letavernier, Vincent Frochot

Jean-Philippe Haymann, MD, PhD, is a nephrologist, full professor of physiology at Sorbonne University (Paris, France) and currently runs the metabolic and stone centre department of Tenon Hospital (AP-HP, Paris).

Jean-Philippe Haymann, néphrologue, professeur de physiologie à Sorbonne Université est actuellement chef du Service des Explorations Fonctionnelles Multidisciplinaires de l'Hôpital Tenon (AP-HP, Paris).

Dominique Bazin Research Director at the CNRS Institute of Physical Chemistry in Orsay (Île-de-France), studied solid state physics at the Université Paris XI, Orsay, where he obtained his 3ème Cycle thesis in 1985 on the characterization of nanometer scale metallic clusters. He was appointed CNRS researcher in 1985 in the solid state physics group at LURE (Laboratoire pour l'Utilisation du Rayonnement Electromagnétique) to develop in situ X-ray absorption spectroscopy (XAS) characterization of supported nanometer scale metallic clusters used in in various industrial processes such as reforming, Fischer–Tropsch synthesis or automotive afterburning. In 1991, he undertook a postdoctoral fellowship in Professor Dale Sayers' group in Raleigh at NCSU (North Carolina State University) for 14 months to develop AWAXS (Anomalous Wide Angle X-ray

Scattering) data analysis. He was appointed director at CNRS in 2001, and in 2004 moved to LPS (Laboratoire de Physique des Solides), Université Paris XI in Orsay, to develop the characterisation of pathological calcifications (PCs) such as kidney stones. To characterise the first steps in the pathogenesis process and to develop new diagnostic tools, several techniques including scanning electron microscopy, Fourier transform infrared spectroscopy, as well as techniques specific to synchrotron radiation such as XAS or micro X-Ray diffraction (μXRD) were applied. In 2012 he moved to LCMCP (Laboratoire de Chimie de la Matière Condensée de Paris) at the Collège de France to develop the application of soft chemistry concepts, developed by Prof. J. Livage, to advance understanding of PC physicochemistry. Finally in 2018 he moved to the Institute of Physical Chemistry at Université Paris Saclay to develop PC characterization using nanoIR spectroscopies such as AFMIR (a combination of atomic force microscopy and IR spectroscopy) and OPTIR (Optical PhotoThermal IR). His current research interests include the different kinds of PC occurring in kidney, prostate, breast, thyroid, and skin. Rationalising this diversity of origin is of primary importance in understanding details of the relevant pathogenic mechanisms and their relationship to either homogeneous or heterogeneous nucleation. All this research is underpinned by close collaboration with clinicians, resulting in several new medical diagnostic tools, for example in primary hyperoxaluria and kidney infection diseases.

Dominique Bazin est directeur de recherche au CNRS à l'Institut de Chimie Physique d'Orsay situé sur le campus de l'université Paris Saclay. Il a étudié la physique des solides à l'université Paris XI où il a passé sa thèse de troisième cycle en 1985. Le sujet de la thèse portait sur la caractérisation d'agrégats métalliques de dimension nanométrique. En 1985, il est nommé chargé de recherche au CNRS au laboratoire LURE (Laboratoire pour l'Utilisation du Rayonnement Electromagnétique) au sein du groupe de physique des solides pour développer la caractérisation in situ par spectroscopie d'absorption X d'agrégats métalliques supportés utilisés dans différents processus industriels comme le reformage, la synthèse Fischer–Tropsch ou la postcombustion automobile. En 1991, il effectue un stage postdoctoral de 14 mois dans le groupe du Prof. Dale Sayers à l'université d'état de Caroline du Nord à Raleigh pour développer l'analyse des diagrammes de diffraction anomale aux grands angles. Il a été nommé directeur de recherche CNRS en 2001 et en 2004 il est affecté au LPS (Laboratoire de Physique des Solides) à Orsay sur le campus de l'université Paris XI pour développer la caractérisation physicochimique de calcifications pathologiques (CP). Pour décrire les premières étapes de leur pathogénèse et pour définir de nouveaux outils de diagnostic médicaux, différentes techniques de caractérisation comme la microscopie électronique à balayage, la spectroscopie InfraRouge (IR) à transformée de Fourier ou des techniques spécifiques au rayonnement synchrotron comme la spectroscopie d'absorption X ou la microdiffraction sont mises en oeuvre. En 2012, il est affecté au LCMCP (Laboratoire de Chimie de la Matière Condensée de Paris) au collège de France pour projeter les concepts de chimie douce développés par le Prof. J. Livage dans le domaine des CP. Finalement, il est nommé en 2018 à l'institut de Chimie Physique sur le campus de l'université Paris Saclay pour développer la caractérisation des CP par les spectroscopies nanoIR que sont l'AFMIR (microscope à force atomique couplé à un laser IR) et OPTIR (une source de lumière visible couplée à un laser IR). Ses recherches actuelles portent sur différents types de CP présentes au niveau du rein, de la prostate, des glandes mammaires, de la thyroïde et de la peau. Prendre en compte cette ubiquité est primordial si l'on veut comprendre en détails les processus de pathogénèse de ces CP qui peuvent être associées à des processus de nucléation soit homogène soit hétérogène. Cette recherche effectuée en collaboration étroite avec des cliniciens a permis l'élaboration de nouveaux outils de diagnostics mis en oeuvre à l'hôpital. À titre d'exemple, certains concernent l'hyperoxalurie primaire et les infections urinaires.

Michel Daudon graduated as a pharmacist (with a minor in biology) from the University of Paris XI. In 1976, he began working on renal lithiasis pathologies in the CRISTAL Laboratory (Centre de Recherches et d'Information Scientifique et Technique Appliquées aux Lithiases), created by Dr. René Jean Réveillaud. He took over the management of that laboratory in 1986. He obtained a State Doctorate in Pharmaceutical Sciences in 1988 with the Thesis Prize of Biochemistry of the Paris XI University for his work entitled "Contribution of the physico-chemical analysis of stones and urinary crystals to the etio-pathogenesis of lithiasis disease: study of a model, calcium oxalate" where a new morpho-constitutional classification of urinary stones

and a calcium oxalate crystallization nomogram for the management and follow-up of patients are described. At the CRISTAL Laboratory, then in the Department of Biochemistry of the Necker Hospital, he developed the concept of morpho-constitutional analysis of calculi by optical examination of the structure of stones and sequential infrared analysis to determine the morphological type and the precise crystalline composition whose numerous and sometimes very specific relationships to the pathology have gradually been established and are now a very effective way to understand the aetiology of lithiasis pathologies. After passing the competitive examination to become a hospital practitioner in 1990, he joined the Biochemistry Department A of Professor Michel Bailly at Necker Hospital to develop the exploration of lithiasis pathologies based on the morphological and infrared analysis of stones, the study of crystalluria and the metabolic exploration of stone formers, in partnership with clinicians, and especially Professor Paul Jungers, nephrologist passionate about understanding the pathological processes responsible for kidney diseases including nephrolithiasis. From 1989 to 1996, he led the research team on renal crystalline pathologies within the INSERM U90 Unit led by Professor Tilman Drueke. In 2011, he joined the Laboratory of Multidisciplinary Functional Explorations of the Tenon Hospital, directed by Professor Laurent Baud and then by Professor Jean-Philippe Haymann, to develop this specialized activity oriented towards the physical analysis of urinary stones and crystals. He was attached to a research group on renal pathologies within the INSERM Unit UMRS 1155 of Tenon Hospital created by Professor Pierre Ronco. Since 1986, Michel Daudon has been responsible for Quality Controls on the Analysis of Stones and Urinary Crystals to which most laboratories trained in those techniques and in the diagnosis of lithiasis pathologies adhere. Co-founder in 2000 of the European Urolithiasis Society (EULIS), now part of the European Association of Urology, he participated in the establishment of collaborations between nephrologists and urologists in the field of lithiasis. In 2001, he created the University Diploma of Urolithiasis, initially issued by the Paris-XI University and then taken over by the Pierre and Marie Curie University, now integrated into Sorbonne Universities. In 2011, EULIS awarded him an award for his involvement in the study of stones and lithiasic pathologies and in 2014, the French Association of Urology awarded him the Félix Guyon Medal for all his activities in the field of lithiasis. In 2015, the acquisition of two Spotlight 400 infrared imagers as part of a research project funded by the Île-de-France made it possible to develop the diagnosis of crystalline pathologies by infrared identification of intratissular crystals on biopsies from kidneys, but also from other organs where crystals can be deposited. This has made it possible to make or correct many diagnoses and, in the case of renal pathologies, to stabilize or restore the deteriorating function of kidneys or grafts due to their invasion by crystals often linked to undiagnosed genetic diseases. A close collaboration with physicists, established thanks to Dominique Bazin over the past twenty years, has made it possible to carry out numerous research projects based on the use of physical analysis techniques, such as X-ray diffraction, X-ray fluorescence, scanning electron microscopy and techniques available on large instruments such as the SOLEIL synchrotron or the Saclay nuclear reactor. Those research projects allowed, thanks to the competence and involvement of many researchers such as Armel Le Bail, Paul Dumas, Christophe Sandt, Matthieu Réfrégiers, Solenn Réguer, Dominique Thiaudière, Stéphan Rouzière, Gilles André, Guy Matzen to name but a few, to establish or supplement by X-ray diffraction crystal structures of compounds involved in lithiasis, to show the role of bacteria in the development of certain stones whose composition did not orient towards that etiology, to establish that, for a given crystalline species, there was a relationship between the shape of the crystals, their mode of aggregation and the macroscopic morphology of the stone, therefore the pathology responsible, to measure the size of the nanocrystals engaged in the lithogenic process with differences according to the etiological context, or to specify the potential relationships between the presence of heavy metals and the crystalline phases identified in the stones. During his career, Michel Daudon has been the author or co-author of several hundred scientific articles and five books dedicated to urolithiasis or spectroscopic analysis techniques of calculi.

Michel Daudon est pharmacien de formation (option biologie), diplômé de l'Université Paris XI. Dès 1976, il a commencé à travailler sur les pathologies lithiasiques rénales dans le Laboratoire CRISTAL (Centre de Recherches et d'Information Scientifique et Technique Appliquées aux Lithiases, créé par le Docteur René Jean Réveillaud. Il a pris la direction de ce laboratoire en 1986 Il a obtenu un Doctorat d'État ès Sciences Pharmaceutiques en 1988 avec le prix de thèse de Biochimie de l'Université Paris XI pour son travail intitulé « Contribution de l'analyse

physico-chimique des calculs et des cristaux urinaires à l'étio-pathogénie de la maladie lithiasique : étude d'un modèle, l'oxalate de calcium » où sont décrits une nouvelle classification morpho-constitutionnelle des calculs urinaires et un nomogramme de cristallisation oxalocalcique pour la prise en charge et le suivi des patients. Au Laboratoire CRISTAL, puis dans le Service de Biochimie de l'Hôpital Necker, il a développé le concept d'analyse morpho-constitutionnelle des calculs par examen optique de la structure des calculs et analyse séquentielle infrarouge pour en déterminer le type morphologique et la composition cristalline précise dont les nombreuses et parfois très spécifiques relations à la pathologie ont peu à peu été établies et s'imposent aujourd'hui comme un moyen très efficace pour appréhender l'étiologie des pathologies lithiasiques. Après avoir réussi le concours de praticien hospitalier en 1990, il a été intégré à l'Hôpital Necker dans le Service de Biochimie A du Professeur Michel Bailly pour y développer une activité d'exploration des pathologies lithiasiques fondée sur l'analyse morphologique et infrarouge des calculs, l'étude de la cristallurie et l'exploration métabolique sanguine et urinaire des patients lithiasiques, en partenariat avec les cliniciens, et tout particulièrement le Professeur Paul Jungers, néphrologue passionné par la compréhension des processus pathologiques responsables des maladies rénales et notamment des lithiases. De 1989 à 1996, il a dirigé l'équipe de recherches sur les pathologies cristallines rénales au sein de l'Unité INSERM U90 dirigée par le Professeur Tilman Drueke. En 2011, il a rejoint le Laboratoire d'Explorations Fonctionnelles Multidisciplinaires de l'Hôpital Tenon, dirigé par le Professeur Laurent Baud puis par le Professeur Jean-Philippe Haymann, pour y développer cette activité spécialisée orientée vers l'analyse physique des calculs et des cristaux urinaires. Il a été rattaché à un groupe de recherches sur les pathologies rénales au sein de l'Unité INSERM UMRS 1155 de l'Hôpital Tenon créée par le Professeur Pierre Ronco. Depuis 1986, Michel Daudon est responsable des Contrôles de Qualité sur l'Analyse des Calculs et des cristaux urinaires auxquels adhèrent la plupart des laboratoires formés à ces techniques et au diagnostic des pathologies lithiasiques. Co-fondateur en 2000 de l'European Urolithiasis Society (EULIS), intégrée aujourd'hui à l'European Association of Urology, il a participé à la mise en place de collaborations entre néphrologues et urologues européens dans le domaine de la lithiase. En 2001, il a créé le Diplôme Universitaire de Lithiase Urinaire, délivré initialement par l'Université Paris-Sud et repris ensuite par l'Université Pierre et Marie Curie, intégrée aujourd'hui au sein de Sorbonne Universités. En 2011, l'EULIS lui a décerné un award pour son implication dans l'étude des calculs et des pathologies lithiasiques et en 2014, l'Association Française d'Urologie lui a décerné la médaille Félix Guyon pour l'ensemble de ses activités dans le domaine de la lithiase. En 2015, l'acquisition d'imageurs infrarouge dans le cadre d'un projet de recherche financé par l'Ile de France a permis de développer le diagnostic des pathologies cristallines par identification infrarouge des cristaux intratissulaires sur des biopsies rénales, mais aussi provenant d'autres organes où des cristaux peuvent se déposer. Cela a permis de faire ou de redresser de nombreux diagnostics et, dans le cas des pathologies rénales, de stabiliser ou de restaurer la fonction de reins ou de greffons en cours de détérioration à cause de leur envahissement par des cristaux souvent liés à des maladies génétiques non diagnostiquées. Une étroite collaboration avec les physiciens, établie grâce à Dominique Bazin depuis une vingtaine d'années, a permis de réaliser de nombreux travaux de recherche fondés sur l'utilisation de techniques physiques d'analyse, comme la diffraction des rayons X, la fluorescence X, la microscopie électronique à balayage et des techniques disponibles sur les grands instruments comme le synchrotron SOLEIL ou le réacteur nucléaire de Saclay. Ces travaux ont permis, grâce à la compétence et l'implication de nombreux chercheurs comme Armel Le Bail, Paul Dumas, Christophe Sandt, Matthieu Réfrégiers, Solenn Réguer, Dominique Thiaudière, Stéphan Rouzière, Gilles André, Guy Matzen… pour n'en citer que quelques-uns, d'établir ou de compléter par diffraction des rayons X des structures cristallines de composés impliqués dans les lithiases, de montrer le rôle de bactéries dans le développement de certains calculs dont la composition n'orientait pas vers cette étiologie, d'établir que, pour une espèce cristalline donnée, il existait une relation entre la forme des cristaux, leur mode d'agrégation et la morphologie macroscopique du calcul, donc la pathologie responsable, de mesurer la taille des nanocristaux engagés dans le processus lithogène avec des différences selon le contexte étiologique, ou encore de préciser les relations potentielles entre la présence de métaux lourds et les phases cristallines identifiées dans les calculs. Au cours de sa carrière, Michel Daudon a été l'auteur ou le co-auteur de plusieurs centaines d'articles scientifiques et de cinq livres dédiés à la lithiase urinaire ou aux techniques d'analyse spectroscopique des calculs.

Emmanuel Letavernier, born in 1975, is professor of physiology at Sorbonne University and nephrologist at Tenon Hospital, Paris, France. He obtained his MD in 2004 and his PhD in 2008. He was appointed assistant professor in 2011 and professor in 2014 at Sorbonne University. He first dedicated his research program to inflammatory processes involved in kidney disease and tissue repair. Since 2008, he has developed original research programs dedidacted to biomineralization and more specifically kidney stones and kidney tissue mineralization, with a bench to bedside approach mixing experimental murine models, collaboration with physicists and chemists and clinical studies. This approach allowed to file patents and to identify new compounds as potential treatments against kidney stones, decreasing urine oxalate excretion and leading to ongoing clinical trials. An important part of the research program is the identification of factors leading to the formation of Randall's plaque, the very first step of stone formation in the kidneys. Among these factors, pyrophosphate deficiency seems a relevant target, as evidenced by clinical and experimental models. He also studied murine models of cystinuria, hyperoxaluria and other genetic diseases and focuses his research on factors regulating uric acid renal excretion and on new mechanisms causative for infection-related stones. Another promising field of research is the identification of factors involved in vascular calcification induced by chronic kidney disease. Most of that research program is based upon international collaborations with physicists, chemists, biologists and physicians.

Emmanuel Letavernier, né en 1975, est professeur de physiologie à Sorbonne Université, néphrologue de formation et praticien hospitalier à l'hôpital Tenon à Paris (Assistance Publique des Hôpitaux de Paris). Il a obtenu sa thèse de médecine en 2004 et sa thèse de sciences en 2008. Il a été nommé MCU-PH en 2011 et PU-PH en 2014 à Sorbonne Université. Il a dédié ses travaux de recherche aux mécanismes impliqués dans l'inflammation et la réparation rénale puis depuis 2008 s'est intéressé aux processus de biominéralisation, notamment rénale et vasculaire. Il a développé une approche transversale combinant la mise au point de nouveaux modèles murins de maladie lithiasique, avec des travaux basés sur la caractérisation physicochimique des calcifications pathologiques et des études cliniques. Cette approche a permis de déposer des brevets et de lancer des études cliniques actuellement en cours sur de nouveaux composés permettant de réduire le risque de maladie lithiasique, notamment l'hyperoxalurie. Des travaux récents ont aussi mis en évidence le rôle clé du déficit en pyrophosphate dans le développement des calcifications rénales. Il s'intéresse actuellement aux processus de calcifications vasculaires, à l'homéostasie de l'acide urique et aux calcifications rénales induites par les bactéries. Cette recherche est possible grâce à des collaborations internationales avec des physiciens, des chimistes, des biologistes et de médecins.

Vincent Frochot, is a medical biologist, former intern and university hospital assistant at the Paris hospitals and the Pierre and Marie Curie Faculty of Medicine (Paris 6), graduated from the University of Paris V. In 2011 he obtained his University Thesis ("HNF-4a: a key player in the intestinal transfer of fatty acids") in the INSERM UMRS 872 unit of Professor Chambaz. From 2011, he started to work on renal lithiasis pathologies in the biochemistry laboratory of the Necker-Enfants malades hospital; in 2015, he joined the Laboratoire d'Explorations Fonctionnelles Multidisciplinaires of the Tenon Hospital, directed by Professor Laurent Baud and then by Professor Jean-Philippe Haymann, and where Doctor Michel Daudon works to develop this specialised activity oriented towards the physical analysis of urinary stones and crystals. He was attached to a research group on renal pathologies within the INSERM UMRS 1155 unit at the Tenon Hospital created by Professor Pierre Ronco. In 2015, the acquisition of infrared imagers within the framework of a research project financed by the Île-de-France region allowed the development of the diagnosis of crystalline pathologies by infrared identification of intra-tissue crystals on renal biopsies, but also from other organs where crystals can be deposited. This has made it possible to make or correct many diagnoses and, in the case of renal pathologies, to stabilise or restore the deteriorating function of kidneys or transplants due to their invasion by crystals often linked to undiagnosed genetic diseases.

Vincent Frochot est biologiste médical, ancien interne et assistant hospitalo-universitaire des hôpitaux de Paris et faculté de médecine Pierre et Marie Curie (Paris 6) diplômé de l'Université Paris V. En 2011 il obtient sa Thèse d'Université : « HNF-4a : un acteur clef du transfert intestinal des acides gras » dans l'unité INSERM

UMRS 872 du Professeur Chambaz. À partir de 2011, il a commencé à travailler sur les pathologies lithiasiques rénales dans le laboratoire de biochimie de l'hôpital Necker-Enfants malades ; en 2015, il a rejoint le Laboratoire d'Explorations Fonctionnelles Multidisciplinaires de l'Hôpital Tenon, dirigé par le Professeur Laurent Baud puis par le Professeur Jean-Philippe Haymann, et où le Docteur Michel Daudon exerce pour y développer cette activité spécialisée orientée vers l'analyse physique des calculs et des cristaux urinaires. Il a été rattaché à un groupe de recherches sur les pathologies rénales au sein de l'Unité INSERM UMRS 1155 de l'Hôpital Tenon créée par le Professeur Pierre Ronco. En 2015, l'acquisition d'imageurs infrarouge dans le cadre d'un projet de recherche financé par l'Île-de-France a permis de développer le diagnostic des pathologies cristallines par identification infrarouge des cristaux intra tissulaires sur des biopsies rénales, mais aussi provenant d'autres organes où des cristaux peuvent se déposer. Cela a permis de faire ou de redresser de nombreux diagnostics et, dans le cas des pathologies rénales, de stabiliser ou de restaurer la fonction de reins ou de greffons en cours de détérioration à cause de leur envahissement par des cristaux souvent liés à des maladies génétiques non diagnostiquées.

Comptes Rendus
Chimie
2022, Vol. 25, Special Issue S1, p. 7-9
https://doi.org/10.5802/crchim.215

Microcrystalline pathologies: Clinical issues and nanochemistry / *Pathologies microcristallines : questions cliniques et nanochimie*

Tribute to Paul Jungers (1932–2022)

Dominique Joly[a] **and Michel Daudon**[*, b]

[a] Necker Hospital, Paris, France
[b] Tenon Hospital, Paris, France
E-mails: dominique.joly@aphp.fr (D. Joly), daudonmichel24@gmail.com (M. Daudon)

Issue date: 1 September 2022

Originally from a modest family in Lorraine, he said that from a very young age he learned a culture of work and dignity.

"My vocation was inspired by the enthusiasm I had felt for Pasteur's brilliant discoveries, during natural science classes in the final years of high school. I was fascinated by the logic that demonstrated the inanity of the theory of spontaneous generation, and by the discovery of the principles of immunity and their application to vaccination. I admired Pasteur's willingness to devote his discoveries to the service of mankind and the courage it had required of him to take the risk of vaccinating, thereby defying all conventions and prohibitions... Pasteur represented for me a model of scientific requirement, and passion for caring, that corresponded to my aspirations; this confirmed my vocation to undertake medical studies."

Having graduated Major of the PCB of Nancy, he is admitted as a scholarship holder to the Cité Universitaire and begins his medical studies in Paris.

"During my first two outpatient internships in the surgical departments of the Necker Hospital, I took advantage of the proximity of Professor Hamburger's department to follow his wonderful weekly visit, where his scientific and humanistic approach to medicine influenced me deeply."

"It was my good fortune to be accepted as an intern from the outset, then as clinic head (1961–1970), and finally as an associate. I had the privilege of living through all the stages of the nephrology adventure, from the advent of medical resuscitation to the beginnings of acute renal failure treatment by the artificial kidney, chronic renal failure by periodic hemodialysis, and finally to the continuous improvements in the conservative treatment and prevention of chronic renal failure."

During his 40 years at Necker Hospital, Paul Jungers developed an eclectic research programme. He published numerous books and books' chapters and more than 300 publications in the most prestigious journals. His dynamism was contagious: it benefitted several generations of interns, clinic heads, doctors in the process of specialization, residents from all parts of the world, and doctors from associated dialysis centres: as soon as he spotted good will and expertise he initiated scientific collaborative work.

The common thread of this monumental labour? "To benefit patients without delay by applying cutting edge therapeutic advances as and when they are made." Most studies have led to tangible therapeutic applications. Among the main therapeutic topics addressed are:

* Corresponding author.

• Hepatitis B. Paul Jungers described the epidemiology of hepatitis B incidence in patients and caregivers in haemodialysis units, and coordinated the national randomized trial of an Institut Pasteur vaccine. Colleagues had to be convinced of the need for a prospective randomised trial, which by definition puts half of the participating subjects at risk of contamination without treatment. The national ethics committee convened on this occasion validated the principle of the trial, attracting unanimous support. From 1981, vaccination enabled the gradual eradication of hepatitis B in dialysis and resuscitation units, and its prevention in the general population.

• Treatment of severe forms of lupus nephropathy. In an evaluation (led by JF Bach) in 32 patients, supplementation of corticosteroids with cyclophosphamide significantly improved the remission rate of severe forms of lupus nephropathy.

• Pregnancy in lupus patients. Epidemiological studies, conducted with Maxime Dougados, François Tron, Frédéric Lioté and Pascal Houillier, established the conditions necessary for favourable foetal and maternal pregnancy outcomes in women with lupus nephropathy. Collaboration with the Necker Hospital endocrinology department defined the principles of hormonal contraception so as to avoid exacerbation of the disease.

• Pregnancy issues in women with nephropathy. Pregnancy was not recommended at the time in women with kidney disease. Considering that the aspiration of motherhood is legitimate for any woman, and that this (in effect) prohibition was not based on rigorous proof, Paul Jungers undertook an epidemiological study, with the help of Pascal Houillier and Dominique Forget, in more than a thousand patients, pregnant or not, with kidney diseases of all types. This study established the optimal conditions of planned pregnancy leading to successful live birth without exacerbating maternal nephropathy. In addition, a case-control study of 360 women with different types of primary glomerulonephritis demonstrated that pregnancy by itself does not increase the risk of progression to renal failure when kidney function is initially normal or close to normal. These studies, the findings from which have been universally confirmed and adopted, have enabled many women to fulfil their desire for motherhood.

• Treatment of chronic uremia by keto-analogues. From 1982 the possibility of slowing the progression of uremia by using a preparation of essential amino acids lacking their alpha-amino groups was investigated with Philippe Chauveau. This approach enabled a substantial delay in the initiation of replacement dialysis in many patients, an important objective at a time when the number of dialysis stations was still very inadequate. This nutritional approach, restrictive and difficult to comply with, was abandoned in France when sufficient dialysis stations became available, but was made available again a few years ago.

• Highlighting and contrasting the adverse consequences, in patients with chronic renal failure, of late initiation of dialysis management, with the benefits of early nephrological follow-up.

• Evaluation of the respective indications, for replacement dialysis or conservative treatment, and their consequences, in very elderly subjects with advanced renal failure.

• Highlighting, with Philippe Chauveau and Malik Touam, the atherogenic role of hyperhomocysteinemia in chronic renal failure, and the possibility of correcting it with oral folic acid (with the complementary benefit of enhancing erythropoiesis).

• Study of immune dysregulation induced by the uremic state, in particular highlighting the increase in the plasma level of pro-inflammatory cytokines (TNFα and IL-1β) and advanced oxidation proteins products (AOPP) responsible for oxidative stress contributing to atherogenesis, with Béatrice Descamps-Latscha and Lucienne Chatenoud.

• Epidemiological demonstration of a threefold higher incidence of atherothrombotic accidents in dialysis and predialysed renal insufficiency, characterizing accelerated atheroma, and analysis of risk factors for atheroma in uremics, leading to the concept of the importance of cardioprotection in these patients, with NK Man, Ziad Massy, Thao Nguyen-Khoa and Gérard London.

• Comprehensive epidemiological survey on the incidence of end-stage renal failure treated with replacement dialysis in Ile de France in 1998, which served as a pilot study for the development of the national “REIN” programme (Epidemiology and Information in Nephrology Network).

• Complete revision, with Michel Daudon, of the concepts around the exploration and medical treatment of urolithiasis, both in its common and severe hereditary forms, and development of new practical

rules adopted since by the entire uro-nephrological community. Paul Jungers was very early interested in the concept that among the common chemical compounds of kidney stones, namely calcium oxalate, calcium phosphate or uric acid, crystalline phases within the same chemical species were more important to take into account to understand the cause of the stones. He was always eager to understand the precise causes of lithiasic pathologies to propose the most suitable treatment for each patient. With regard to calcium oxalate, which is the most common chemical species of kidney stones, Paul Jungers was quickly convinced of the clinical interest of distinguishing between crystalline species and pathology and in particular of the privileged links between whewellite and urinary oxalate on the one hand and weddellite and urinary calcium on the other. He was a strong advocate of the morpho-constitutional analysis of urinary calculi by physical methods at a time when chemical analysis was still very widespread. Very attentive to detect as early as possible the causes of lithiasis, especially from genetic origin, likely to have deleterious consequences on kidney function, he has greatly contributed to raising awareness in the urological community of the importance of exploring lithiasic patients very early from the first stone manifestation. Thanks to his unwavering commitment, practices have gradually evolved for the benefit of patients. Paul Jungers also understood early on that two calculi of the same crystalline composition could have very different structural characteristics, therefore different morphologies that signed in an even more specific way the pathology involved in the lithiasic process. This approach has proven to be particularly effective for the early diagnosis of genetic pathologies such as primary hyperoxaluria or distal tubular acidosis or acquired diseases such as Sjögren syndrome. This relationship between precise (non-dietary) cause and stone morphology was then extended to other clinical contexts such as inflammatory bowel diseases, bariatric surgery or chronic diarrhoea sometimes responsible for very active lithogenic processes that can impair kidney function.

Paul Jungers was also a remarkable, passionate and captivating teacher. His didactic works on lithiasis, Chronic Kidney Disease, and dialysis, regularly republished and updated, have trained and continue to train generations of French-speaking nephrologists.

Respected and admired, but far from intimidating, Paul Jungers was very close to the nursing staff, as well as an empathetic clinician, truly listening to patients during his consultations and during hospitalizations. Ahead of his time, he understood the importance of comprehensive and not exclusively technical patient care for kidney disease.

"Starting from the principle that it is not only up to the patient to adapt to the treatment, but also for the treatment to adapt to the patient, it seemed essential to me to individually adapt therapeutic prescriptions to conditions of lifestyle and activity, family context, and patient age, and to pay the greatest attention to their morale and concerns. My greatest reward was to see many patients, who approached our consultation with reserved and anxious faces, leave with a smile, assured that all possible measures were implemented to delay the deadline for dialysis and allow them to lead as normal lives as possible."

An accomplished researcher, teacher and physician, Paul Jungers was a role model for many. Those who had the chance to work alongside him loved this enthusiastic man, teeming with ideas, insightful, tenacious, and upright and demanding certainly, but also warm, attentive and available.

In 2012, Paul Jungers received with emotion the Jean Hamburger Medal of the Society of Nephrology. These words bring together the French and French-speaking nephrology family to pay tribute to him.

Our thoughts are with his widow, Mrs. Suzanne Jungers, his children Mr. and Mrs. Olivier Jungers, Mr. and Mrs. Pierre-Yves Jungers, and his grandchildren, Pierre, Victoire, Bryan, Lara, and Nicolas.

Dominique Joly

Michel Daudon

Comptes Rendus
Chimie
2022, Vol. 25, Special Issue S1, p. 11-35
https://doi.org/10.5802/crchim.200

Foreword to microcrystalline pathologies: combining clinical activity and fundamental research at the nanoscale

Dominique Bazin *, [a, b], **Michel Daudon** [c, d, e], **Vincent Frochot** [c, d, e], **Jean-Philippe Haymann** [c, d, e] and **Emmanuel Letavernier** [c, d, e]

[a] Institut de Chimie Physique, UMR CNRS 8000, Bâtiment 350, Université Paris Saclay, 91405 Orsay cedex, France

[b] Laboratoire de physique des solides, UMR CNRS 8502, Bâtiment 510, Université Paris Saclay, 91405 Orsay cedex, France

[c] Sorbonne Université, UMR S 1155, Paris, France

[d] INSERM, UMR S 1155, Paris, France

[e] Explorations fonctionnelles multidisciplinaires, AP-HP, Hôpital Tenon, Paris, France

E-mails: dominique.bazin@universite-paris-saclay.fr (D. Bazin), daudonmichel24@gmail.com (M. Daudon), vincent.frochot@tnn.aphp.fr (V. Frochot), jean-philippe.haymann@tnn.aphp.fr (J.-P. Haymann), emmanuel.letavernier@tnn.aphp.fr (E. Letavernier)

Abstract. This contribution underlines the key role of physicochemical characterisation techniques in the area of medical research. The starting point centres on the Mid-InfraRed platform located at the Tenon hospital and dedicated to multidisciplinary functional investigations. In the last two decades, we have enhanced this platform by creating a network combining researchers from varied disciplines such as physicists, chemists, and clinicians. The resultant research dynamism is underscored by metrics such as 71 references in Pubmed and 129 in Web of Science, and the high impact of the journals in which we have published (New England Journal of Medicine, Kidney International, Chemical Review…). It is of paramount importance to disseminate these physicochemical techniques among young doctors, and to establish collaborations with appropriate private companies.

Keywords. Pathological calcification, Disease, Medical diagnostic, Nanochemistry, Physicochemistry.
Issue date: 1 September 2022

1. Introduction

Among crystalline pathologies, urinary lithiasis (from the Greek lithos,) was widespread in ancient populations [1,2]. In fact, crystalline pathologies [3–11] (Figure 1) can affect all human organs and encompass several major diseases such as cancer [12–19], cardiovascular [20–23], infection [24–31], genetic [32–37] and neurodegenerative disorders [38,39] and rheumatological diseases [40]. The pathogenesis of

* Corresponding author.

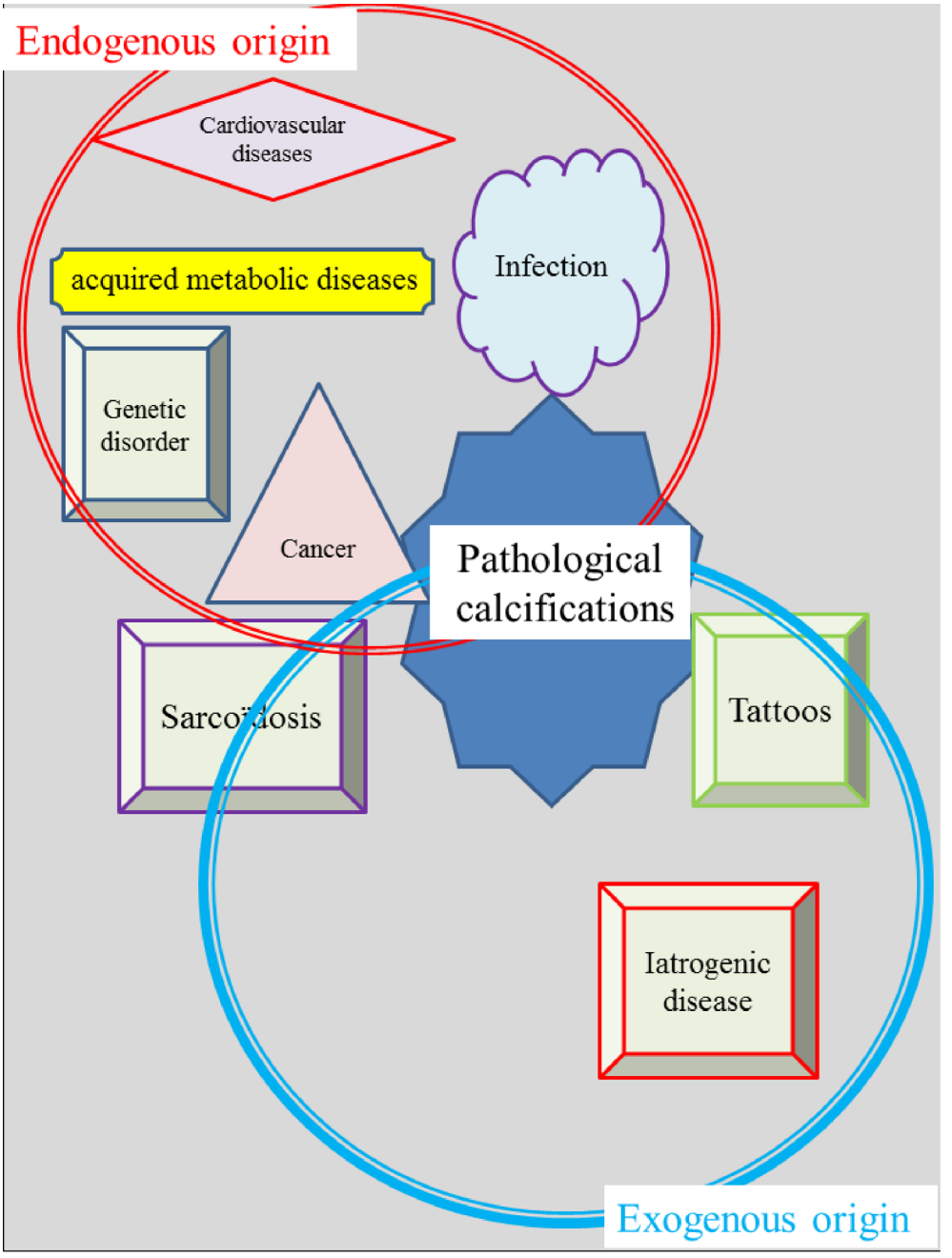

Figure 1. Schematic representation of crystalline pathologies; we can distinguish two different families according to the origin of the abnormal deposit.

calcifications can be observed in the case of new public health problems such as the one related to Zika virus, in which the presence of cerebral calcifications has been emphasized [41–43].

At this point, it is worth underlining that some of these pathologies are highly prevalent; urolithiasis affects 10% of the population [44] while the prevalence of osteoarthritis is approximately 10% in men

and 13% in women among adults 60 years of age or older [40].

The complexity of such research also arises from the multiple origins of the pathologies. Figure 1 gives a schematic representation of some crystalline pathologies. We distinguish the ones in which the abnormal deposits are generated inside the body with physiological participation, while in the second family it is the introduction of foreign chemical compounds which initiate the disease. For example, primary hyperoxaluria leads to the formation of calcium oxalate kidney stones from endogenous calcium and oxalate in the human body [45,46] while in some cases of sarcoidosis, it is the insertion of silica in the skin which induces the formation of cutaneous granuloma [47–54]. Note that in sarcoidosis the presence of calcium carbonate calcifications from endogenous calcium and carbonate has also been emphasised [53]. Recently, we have considered the case of tattoos [55] for which the number of organic and inorganic compounds inserted in the skin is huge [56, 57]. Iatrogenic disease is the third component leading to abnormal deposits of exogeneous origin that we have considered [58–66]. In fact, exogenous and endogenous factors often may be intertwined in a calcification process (for example, in the case of JJ stent encrustation, the foreign body promotes heterogeneous nucleation in patients with hypercalciuria and/or urinary tract infection). The endogenous as well as the exogenous origin of the pathological calcifications explains their broad chemical diversity.

What is the exact relationship between the calcification and the pathology? The answer is quite complex. Sometimes the calcification is classified as benign by the clinician, as in the case of breast calcifications composed of calcium oxalate dihydrate. Such type I microcalcifications are found only in benign cysts and are not associated with carcinoma or epithelial hyperplasia [67]. By contrast, breast calcifications made of calcium phosphate may be, but are not always, associated with tumor processes [67–69]. Regarding the urinary tract, there is evidence linking the formation of kidney stones containing struvite to urinary tract infection [70–74]. In contrast, the calcification processes of some bacteria induced by a serum calcification factor may be a component of the vertebrate immunological response against bacterial infections [75]. Finally, recent publications indicate that ectopic calcification is an active biological process and may induce a modification of cellular phenotype [76].

In this contribution, we would like to discuss and highlight the different kinds of research we have performed around the processes of biological mineralization and, more generally, on the presence of abnormal deposits in tissues. Some well-chosen examples will show that, despite a number of significant publications in this field, many experiments still remain to be performed to describe their pathogenesis precisely.

2. On the definition of crystalline pathologies

A classic definition of the chemical composition of abnormal deposits in the human body is “the accumulation of calcium salts in a tissue”. Such a definition is completely inadequate. In the kidney for instance many chemical compounds without calcium have been identified (Figure 2). Field Emission Scanning Electron Microscopy (FE-SEM) offers the opportunity to observe them at the submicrometer scale [77–80].

Figure 2 exemplifies some of them more precisely: dihydroxyadenine crystals (Figure 2A) related to the genetic disease adenine phosphoribosyltransferase (APRT) deficiency [81–86], uric acid (Figure 2B) as a consequence of metabolic syndrome and derangement of renal acid–base metabolism, resulting in a lower urine pH and an increased risk of uric acid stone disease [87–91], cystine (Figure 2C) accounting for 1–2% of all cases of urolithiasis [92–96] and related to cystinuria, an autosomal recessive disorder resulting in a transport defect of dibasic aminoacids through the tubular membrane of the nephron, and struvite (Figure 2D) considered as a marker of urinary tract infection by urea-splitting micro-organisms [25,70–74]. Furthermore, in examples of iatrogenic pathologies, several compounds corresponding to drugs and their metabolites have been reported [58–66].

Other compounds without calcium have been identified in other organs as well [97–102]. Among them, we can mention cholesterol in gall bladder [98,99], or monosodium urate causative for gout in joints [101,102]. Finally, some chemical compounds contain calcium but are amorphous, as in

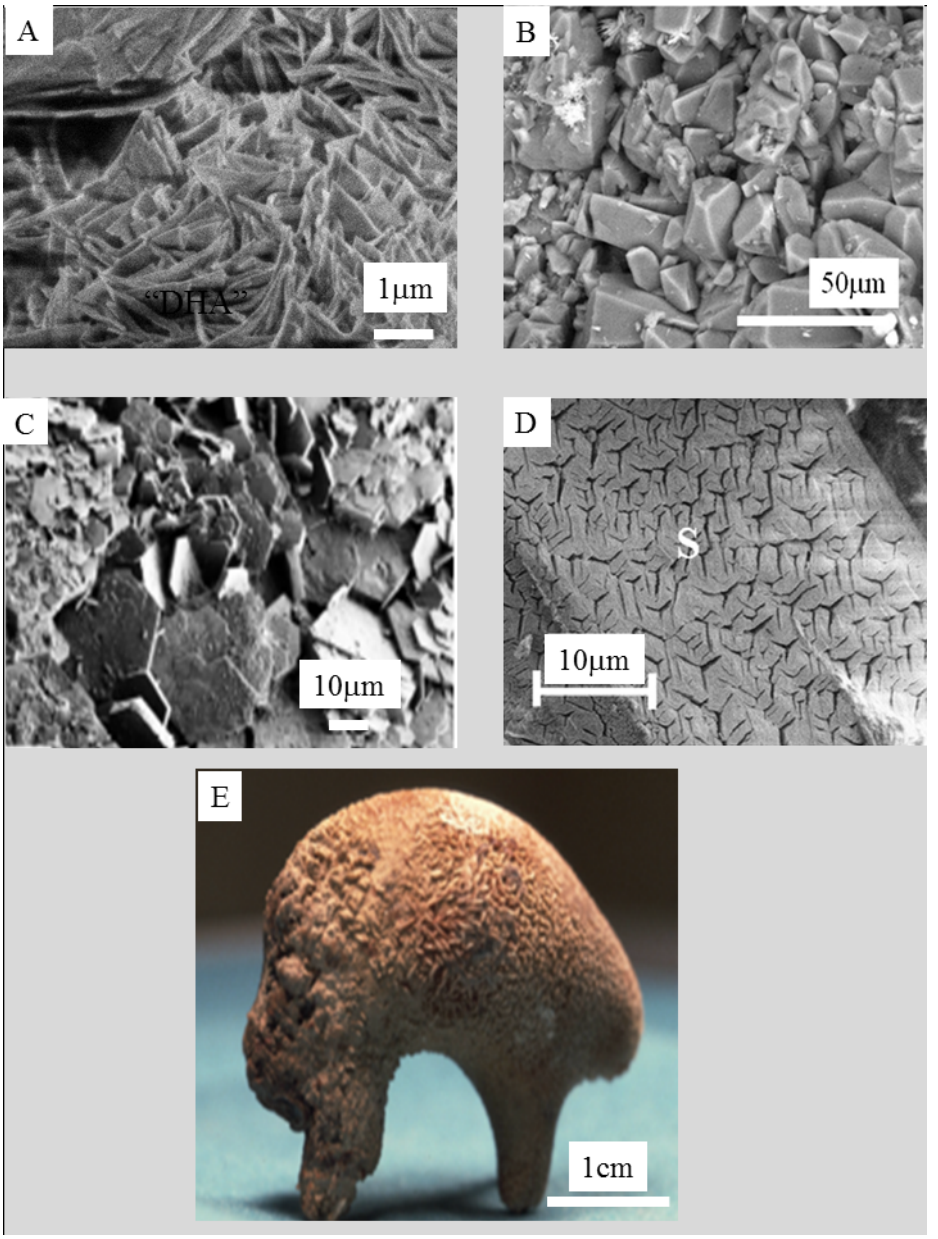

Figure 2. Examples of chemical compounds without calcium identified in the kidney. (A) 2,8-dihydroxyadenine (6-Amino-1H-purine-2,8(7H,9H)-dione, $C_5H_5N_5O_2$; (B) Uric acid (7,9-dihydro-1H-purine-2,6,8(3H)-trione, $C_5H_4N_4O_3$) (C) L-cystine (2-amino-3-(2-amino-2-carboxy-ethyl)disulfanyl-propanoic acid, L–$C_6H_{12}N_2O_4S_2$); (D) Struvite (Magnesium ammonium phosphate, $MgNH_4PO_4 \cdot 6H_2O$); (E) kidney stone containing a mixture of calcium oxalate monohydrate, calcium oxalate dihydrate and carbonated apatite.

the case of amorphous carbonated calcium phosphate which has been identified in different organs like breast [13,103], thyroid [104–106] and kidney [3,107]. "Crystalline pathology" is thus not really an appropriate definition and "pathologies related to abnormal deposits" may be a better one. However, it is a fact that numerous pathological deposits are composed of calcium salts. Today, as illustrated in Figure 2E, the majority of kidney stones is made of a mixture of calcium oxalates and calcium phosphates [108–110].

3. Characterization by physicochemical techniques

Chemical compounds may be present in abnormal deposits as different crystalline phases that may be related to different biological conditions [1–10]. Moreover, as well demonstrated for urinary stones [111–120], the morphological characteristics of these concretions may be a marker of specific pathological conditions regardless of the crystalline phase. Finally, a large diversity of molecules may be involved in crystalline pathologies. For example, more than 105 compounds have been identified in kidney stones [121] and more than 25 compounds have been identified by μFTIR spectroscopy in kidney biopsies [64,122,123].

Taking into account this broad chemical diversity of abnormal tissue deposits, conventional hospital staining procedures cannot be considered to precisely determine their chemical composition [124]. In fact, however, characterization by techniques such as FT-IR spectroscopy has been routinely used at the hospital for several decades for determination of kidney stone composition [125–129]. Figure 3 shows the four experimental devices routinely used at the "Service des Explorations Fonctionnelles" at the Tenon Hospital.

Using this platform, more than 85,000 kidney stones have been analysed by FTIR spectroscopy, as well as more than 2000 biological tissues, including more than 1600 kidney biopsies. Such investigations, involving several public or private analytical laboratories, are accepted by the French social security system. Surprisingly, this is discussed as being only a future reality in a recent article on the subject "is infrared spectroscopy ready for the clinic?" in a journal dedicated to analytical chemistry [130].

Figure 4 shows different techniques used in our research on predominantly human samples [131–135]. Some of them are "classics" i.e. Raman and Infra-Red spectroscopies [136–139], Second Harmonic Generation (SHG), Scanning and Transmission Electron Microscopy (SEM and TEM) [80,140–142], μX-ray fluorescence [143–147], μ X-ray diffraction [148–153] or Nuclear Magnetic Resonance (NMR) [154–159].

Other techniques, implemented in a synchrotron radiation centre [131–135], include X-ray absorption spectroscopy (Diffabs beamline) [160–165], μX-ray diffraction (Proxima and Cristal beamlines) [166, 167], nanotomography (Nanoscopium beamline) [168], and μ FTIR (SMIS beamline) [123]. We have also performed experiments on location at a nuclear research reactor [90,93,131,169,170], as well as at the European Synchrotron Radiation Facility [147]. All these physicochemical techniques complement the conventional ones implemented at the hospital such as histochemistry, staining and genetic analysis.

We may distinguish several stages in this research (Figure 5). The starting point (Figure 5A) is based on optical microscopic and FTIR spectroscopic observations, leading to a morphoconstitutional model [111–122].

From there, we proceed to micrometer scale characterization, including determination of trace elements in order to assess their role in the pathogenic process [134,135]. Currently we also use characterization techniques to describe the pathological calcifications at the nanometer scale. We are able to assess not only the morphology but also the chemistry of pathological calcifications either by determining the elements which constitute the abnormal deposit [141,142] or by an identification of specific chemical compounds at the nanometer scale [171, 172]. To achieve this, we have combined atomic force microscopy and IR lasers (AFMIR) [173,174], TEM integrated with electron energy loss spectromicroscopy [175], and synchrotron radiation-induced nano X-ray fluorescence [176].

We have already investigated biological samples from different organs and parts of the human body, namely kidney [177–183], prostate [184,185], breast [13,103], thyroid [104–106], cartilage [186–193], bone [194–197], tooth [198], pancreas [199], skin and hairs [53–55,147,165,168,200–203] and cardiovascular system [140,204,205]. We have also investigated cells [206], mice [207–210], and med-

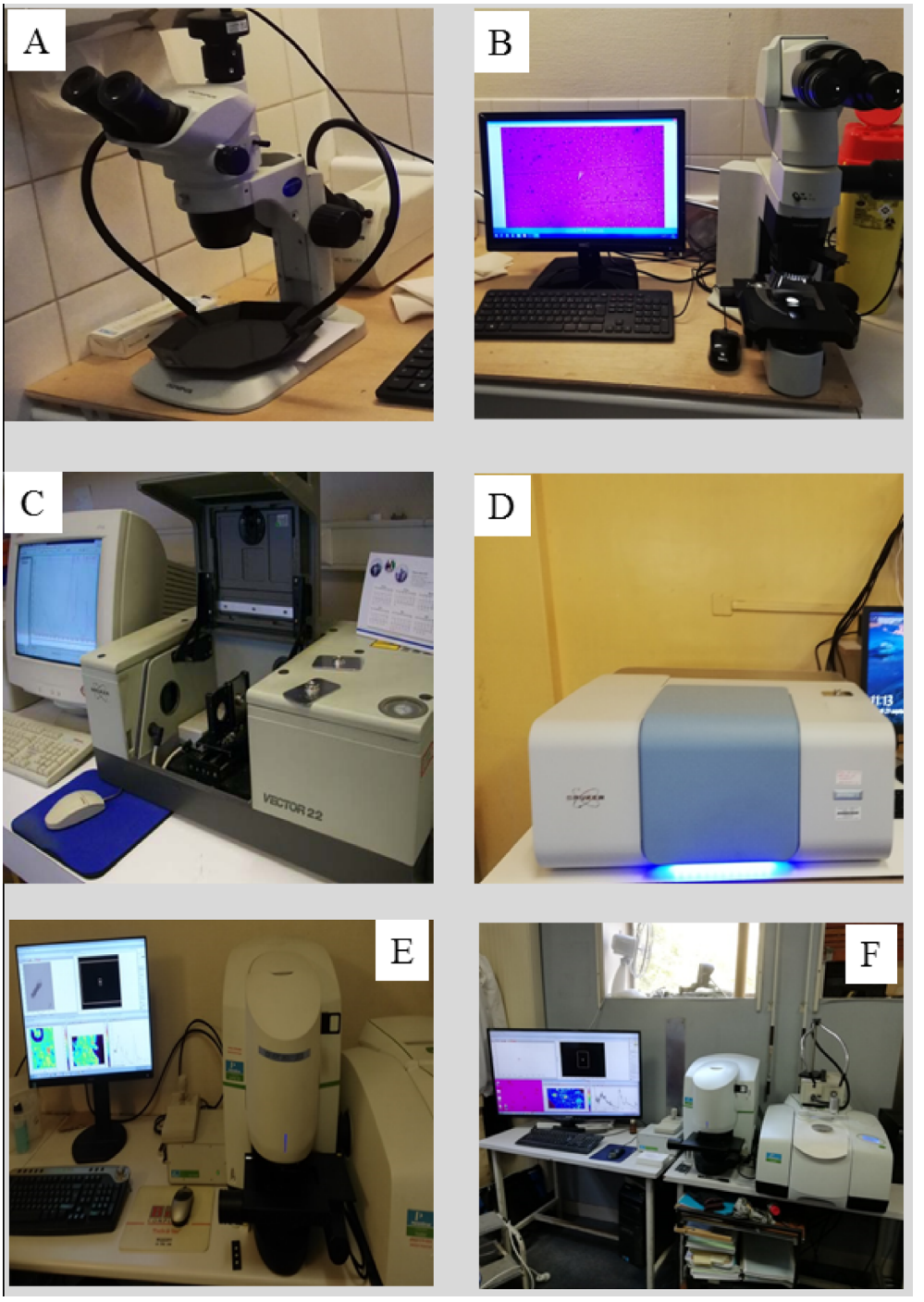

Figure 3. Experimental devices used at the service des explorations fonctionnelles at the Tenon Hospital. (A) Stereomicroscopy for morphological analysis of stones, (B) optical microscope with polarized light for examination of crystals in tissue, (C) and (D) Fourier transform infrared spectrometer Vector 22 (C) and Invenio (D) from Bruker Optics for identifying crystalline phases of stones, (E) and (F) μFTIR Spotlight 400 imager from Perkin–Elmer for identifying crystals observed in tissue biopsy slices.

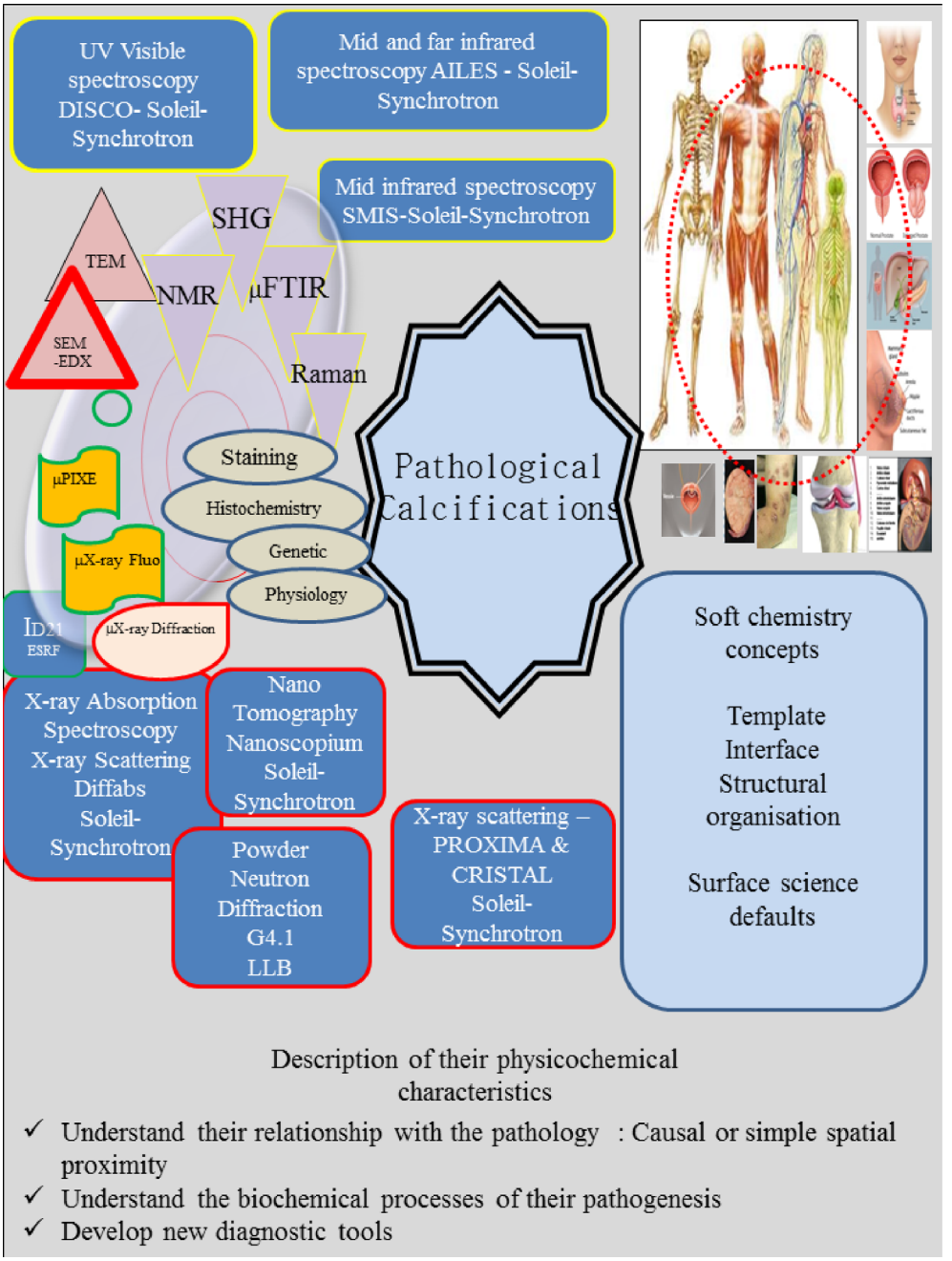

Figure 4. Schematic of our pathological calcification research axis. While some in-lab characterization techniques can be considered as diagnostic tools, access to those associated with large scale instruments is governed by committee which makes rapid clinical applications difficult.

ical devices [211,212], as well as chemical compounds identified in kidney stones synthesised using microfluidics [213]. Investigations of such diverse biological samples requires collaboration between physico-chemists and the medical community and leads smoothly to the establishment of efficient net-

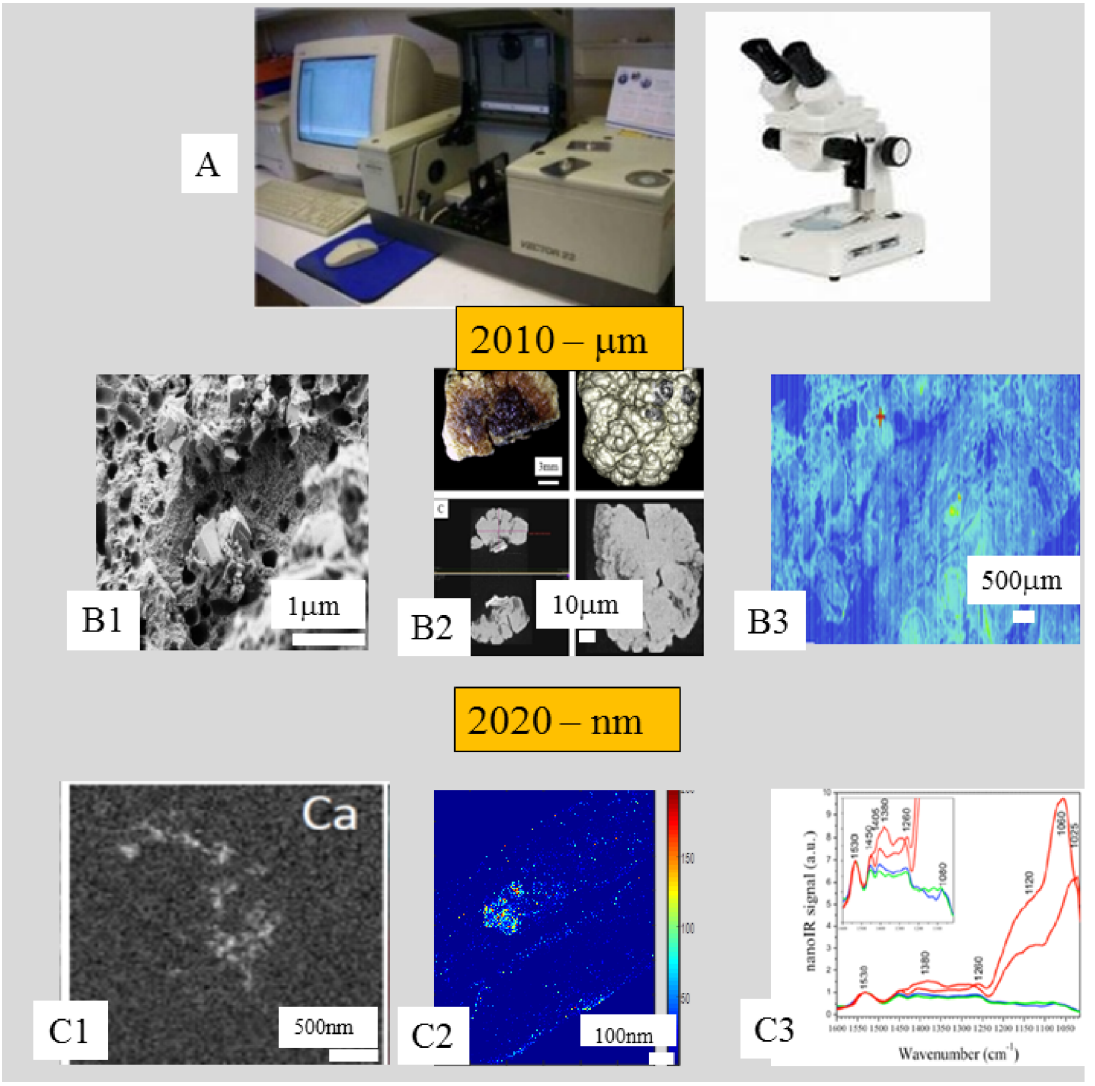

Figure 5. Different stages in pathological calcification characterization. (A) Morphoconstitutionnal analysis of kidney stones by optical microscopy and FTIR spectroscopy (B) Micrometer scale analysis, (B1) SEM imaging, (B2) 3D micrometer scale tomography, (B3) Chemical mapping via µFTIR spectroscopy, (C) Nanometer scale analysis, (C1) TEM observations, (C2) X-ray fluorescence mapping (data collected on the Synchrotron Soleil Nanoscopium beamline), (C3) Nanometer scale IR data collected in AFMIR configuration (Spatial resolution of 50 nm).

works. Regarding the analysis procedure, it is worth emphasizing that all these data are analysed taking into account the soft chemistry concepts introduced by Professor J. Livage (Collège de France), as well as those rooted in surface science (Figure 4).

Finally, we have recently complemented our research via theoretical Density Functional Theory (DFT) approaches [214–217], an efficient approach to predict and elucidate the crystallographic structure of compounds such as whitlockite [215] or calcium oxalate polyhydrates [216]. Particular effort has recently been devoted to modelling the interaction between proteins and calcification processes. For this purpose, we simplify interactions by modelling calcification components as nanometer scale metallic clusters and the proteins as simple diatomic

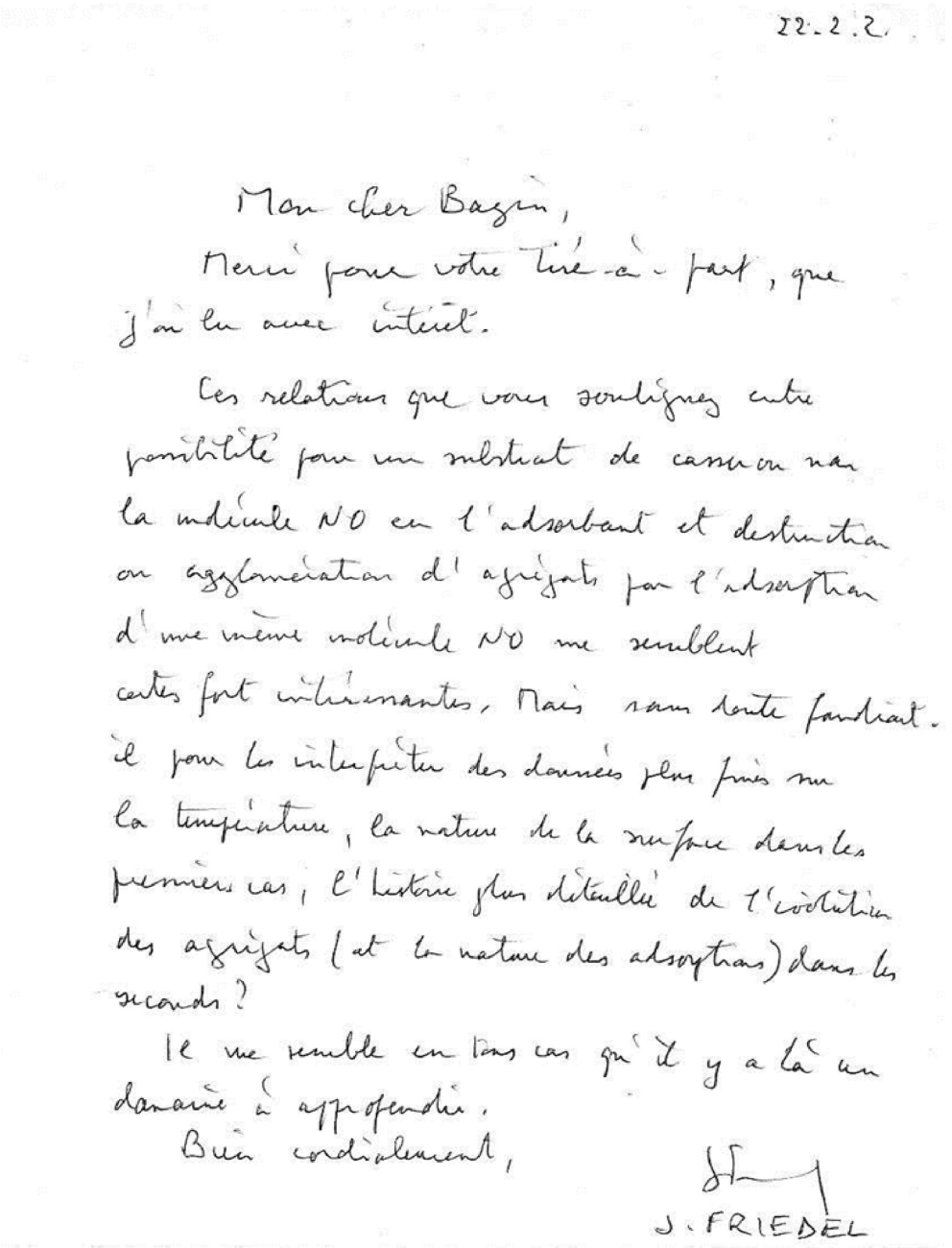

22.2.2.

Mon cher Bazin,

Merci pour votre tiré-à-part, que j'ai lu avec intérêt.

Les relations que vous soulignez entre possibilité pour un substrat de casser ou non la molécule NO en l'adsorbant et destruction ou agglomération d'agrégats par l'adsorption d'une même molécule NO me semblent certes fort intéressantes, mais sans doute faudrait-il pour les interpréter des données plus fines sur la température, la nature de la surface dans les premiers cas, l'histoire plus détaillée de l'évolution des agrégats (et la nature des adsorptifs) dans les seconds?

Il me semble en tous cas qu'il y a là un domaine à approfondir.

Bien cordialement,

J. FRIEDEL

Figure 6. Letter of J. Friedel regarding the interaction between NO and a nanometer scale metallic cluster.

molecules [218,219]. Even though this is a drastic simplification, the parameters which determine the differences between molecular, and dissociative, adsorption, such as temperature, the geometrical and the electronic nature of the surface, and the adsorption site are not well understood [220,221]. Figure 6 shows a letter from Professor J. Friedel supporting this hypothesis based on which such investigations have to be performed. Although simplified, much can be learnt from this system.

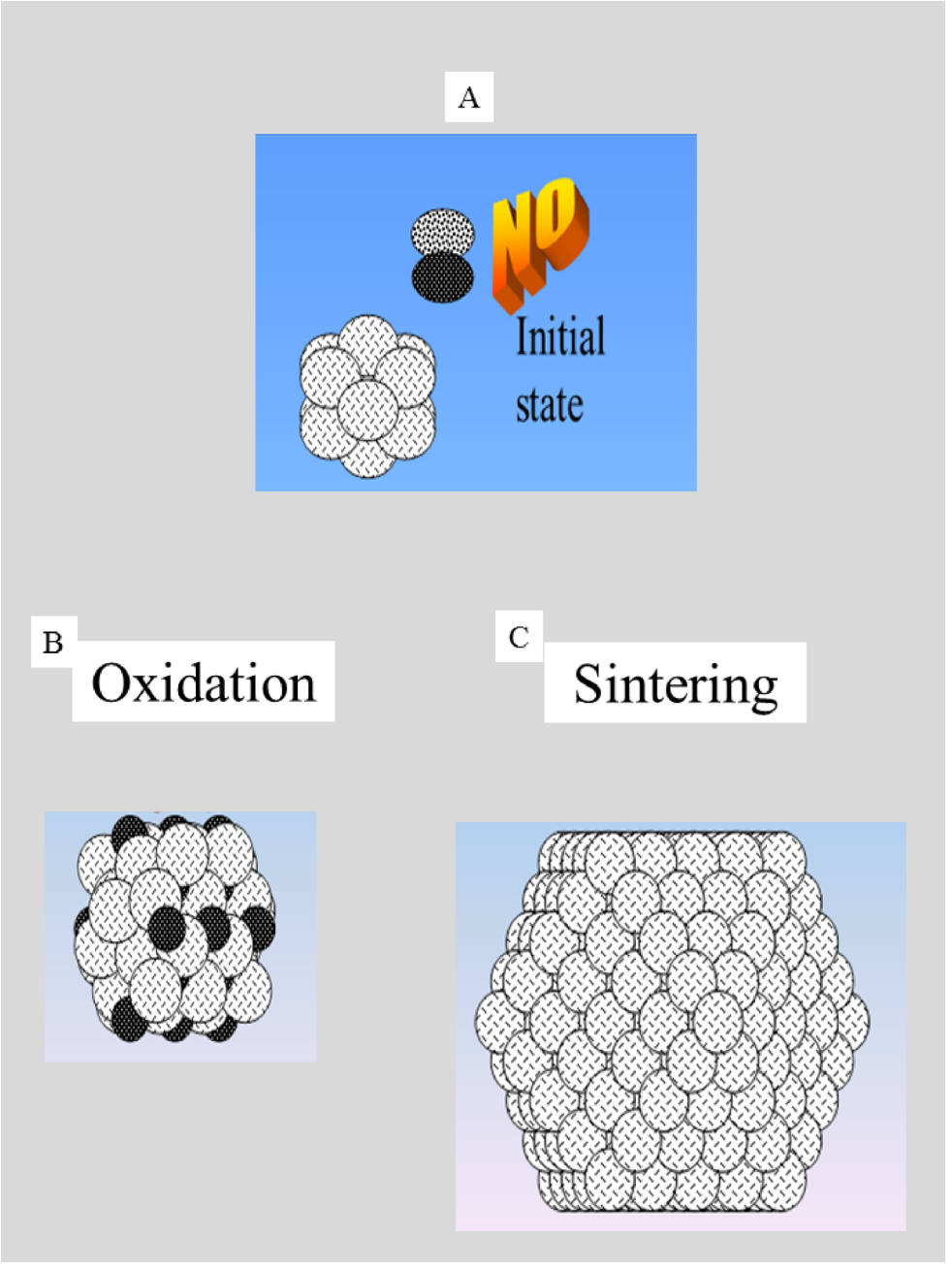

Figure 7. Some fundamental aspects of the adsorption process.

Figure 7 shows the initial state (nanometer scale metallic particle, and a NO molecule), and subsequent possibilities for mutual interaction [222–224].

Dissociative adsorption of NO on the metallic cluster leading to the formation of an oxide and the desorption of N_2 [225] is the first possibility. The second is physisorption of the NO on the metallic cluster, which can induce a significant growth of the

nanometer scale cluster [226,227]. What can we learn from these alternative possibilities? In the first case, we have a significant modification of the chemistry of the nanometer scale cluster (from metallic to an oxide) and a significant modification of the adsorbed molecule (dissociation process). Returning to our model in which the metallic cluster represents the calcification and the NO molecule the protein, it is clear that the final character of the calcifications, and by analogy with NO, the protein, can differ considerably from the initial. Such a fundamental approach is a necessary step in understanding precisely how molecules interact with nanocrystals and possibly modify their morphology [228–232].

As a preliminary conclusion, the characterization of pathological calcifications beyond observations initiated from routine clinical observations [111–122] and performed at the hospital (optical microscopy and μFTIR spectroscopy) has led to many significant breakthroughs based on more cutting edge physicochemical characterization techniques. A complete set of results provides more precise information about the relationship between calcification and disease, and the development of new diagnostic tools. All these data have been published in major medical and chemistry journals such as *New England Journal of Medicine* [35,36], *Chemical Review* [3], *ACS Nano* [142], *Arthritis Rheumatology* [186,187], *J. Am. Soc. Nephrol.* [62,207], *Kidney International* [233,234] and *JAMA* [200].

4. Diversity in the very first pathogenic stages

Recently, we have overviewed the various different mechanisms described for the nucleation of pathological calcifications [10]. Nephrolithiasis is generally the result of crystal formation, aggregation and retention in the kidney and is thus related to homogeneous nucleation (Figure 8) in supersaturated solutions [235–238]. Note that Randall's plaque [239, 240] plays a key role in the pathogenesis of kidney stones [241–244]. Kidney stones may also be initiated from tubular plugs which are a frequent finding in human distal tubules [244,245].

As illustrated in several publications, the nature of the deposit may differ according to the specific area of the organ where it was observed, underlining the close relationship to the local tissue physiology [3, 123]. In other pathological conditions like metabolic syndrome and/or diabetes mellitus, multiple supersaturations of both calcium oxalate and uric acid may favour crystallization of one species (for example uric acid) and only secondarily of the second (for example calcium oxalate), explaining why patients suffering these diseases may form mixed stones containing alternating layers of these two compounds. In other cases, the two crystalline species are closely mixed. Notably, uric acid stones also contain calcium oxalate in more than 63% of cases. These two chemical species can crystallize in urine and form aggregates by heterogeneous nucleation or by epitaxial processes [10]. About one third of urine samples containing uric acid crystals also contain those of calcium oxalate.

Heterogeneous nucleation is another mechanism involved in the formation of other pathological calcifications. DNA [246] and elastin [247] have been identified as organic scaffolds. The role of other proteins may be more complex. For example, Cerini *et al.* [248] have studied the promotion of calcium oxalate crystallization by albumin, with specific favouring of the dihydrate form. The authors conclude that due to rapid nucleation of small crystals, saturation levels fall, and thus albumin might be protective.

Thanks to nanometer scale structural descriptions, another mechanism, via extracellular matrix vesicles (MV) containing a high level of alkaline phosphatase, has been identified in the induction of de novo mineral deposition in cartilage, bone, and dentin [249]. The presence of MV in kidney [141,142, 250] as well as vascular smooth muscle [251] has also been reported.

5. Calcifications versus tissues—How calcifications may alter tissues?

In the case of Randall's plaque, we know that ectopic calcifications made of calcium phosphate apatite may pass through the tissue and appear at the surface of the papillary epithelium where they play a crucial role in the pathogenesis of kidney stones [239–244]. In fact, such major tissue alteration occurs in other pathological processes. In the case of epidermal necrolysis, i.e., Stevens Johnson syndrome and toxic epidermal necrolysis, atypical healing retardation with calcinosis cutis, may be explained by the presence of calcification. Lastly, a simple change

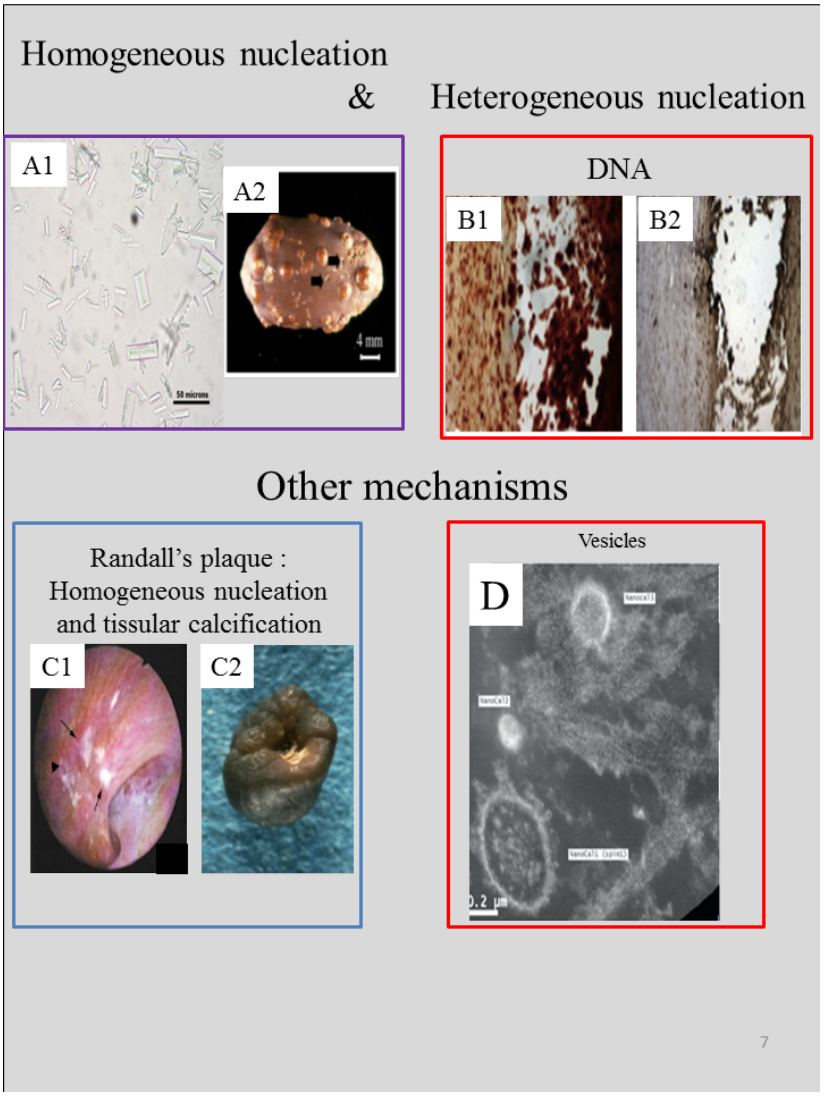

Figure 8. (a) Homogeneous nucleation. When the patient has a chronic high number of crystallites in urine (a1), a kidney stone is generated (a2). In the case of heterogeneous nucleation, part of the DNA may serve as a nucleus (b1) alizarine staining to reveal the calcification and (b2) immunostaining to visualise DNA). In the case of a Randall's plaque, crystallites generated through homogeneous nucleation are trapped by a calcification present on the tissue (white spots on c1) and a kidney stone with a RP is generated (white spots on c2). Finally, the presence of vesicles containing calcium salts (phosphate and/or carbonate) has been noted in the kidney (d).

in wall composition (medial calcium overload of elastic fibers) can decrease aortic elasticity. Elastocalcinosis can induce destruction of elastic fibers, leading to arterial stiffness, which has been associated with the development of left ventricular hypertrophy in a normotensive model [252].

Similar pathological processes may occur in other parts of the human body. For example, in breast cancer, Ductal carcinoma in situ (DCIS) is considered as a non-invasive or pre-invasive breast cancer and is associated with cast-type calcifications. It is possible that these pathological calcifications may break the

milk ducts leading to cancer cells spreading into surrounding breast tissue.

6. Presence of pathological calcification and loss of the renal function

An interesting clinical and physicochemical question is raised by the relationship between the presence of pathological kidney calcification and loss of renal function.

Are pathological calcifications responsible for renal dysfunction?

We can open the discussion with the case of kidney stones. The obstruction of one or both ureters prevents urine passing into the bladder and out of the body. If not treated rapidly, kidney damage may ensue, in severe cases leading to kidney failure, sepsis (life-threatening infection), or ultimately death. Such obstructions don't depend on the chemical phase of the stone.

Intratubular crystalline precipitation can also lead to acute renal insufficiency. For example, resultant blockage of urine flow can also be associated with the presence of plugs composed of apatite or other crystalline phases. These cases involve the collecting duct(s). Some genetic diseases such as APRT deficiency, a rare autosomal recessive disorder, may cause 2,8-dihydroxyadenine stones, and, secondarily, renal failure due to intratubular crystalline precipitation. Repeated obstruction of tubules and interstitial deposits by 2,8-dihydroxyadenine crystals may result in irreversible loss of kidney function [34,253,254] and sometimes end-stage renal failure [255–258]. Finally, several medications, notably acyclovir, sulfonamides, methotrexate, indinavir, and triamterene, are associated with the production of crystals that are insoluble in human urine [61–64,259].

This all raises a major question: Is it simply the obstruction which leads to renal insufficiency, or is it in fact tissue inflammation induced by the presence of crystals? Recent studies suggest the likelihood that inflammatory processes act together with obstruction to promote renal damage [86], a process which has been discussed in detail in 2,8-dihydroxyadenine nephropathy [86], and development of Randall's plaques [260].

Besides this, the presence of only very few crystallites in a biopsy may reveal a pathological condition. In a kidney biopsy in which only a single crystallite of calcium oxalate was observed, UV–visible spectroscopy experiments clearly showed a significant oxalate signal in numerous surrounding cells, suggesting that the presence of even one crystal is an indicator of local supersaturation. Thus it seems that this supersaturation leading to pathogenic crystals also significantly affects neighbouring cells.

7. A specific example: the effect of plant extracts on kidney stones

We should highlight the effects of plants in our urolithiasis research [261]. For example, we have used FE-SEM to assess the ability of plant extracts, namely *Arenaria ammophila* (leaves and stems), *Parietaria officinalis* (leaves, and flowers, studied separately), *Paronychia argentea* (flowers), to dissolve cystine stones in vitro. All these plants are widely claimed to treat or prevent urolithiasis [262] in traditional medicine.

Recently, we have also studied the effect of green tea infusions in hypercalciuric renal stone patients [263]. It is well known that excessive consumption of plants such as rhubarb containing high levels of oxalate may lead to significant quantities of calcium oxalate monohydrate in kidney tissues leading to a loss of kidney function [264,265]. By contrast, in the case of tea, an oxalate-rich plant, tea extracts, particularly of green tea, may have beneficial clinical effects due to the presence of antioxidant polyphenol compounds such as catechins. In our study, the data showed no evidence for increased stone risk factors or oxalate-dependent stones in daily green tea drinkers [266]. Also, it is worth emphasizing that other studies have been devoted to tea due to the presence of aluminium and other toxic elements in the leaves [267].

Finally it is noteworthy that absorption of large quantities of caffeine may lead, combined with other factors, to the formation of kidney stones; in a recent publication, 1-methyluric acid nephropathy has been identified in three kidney biopsies [268].

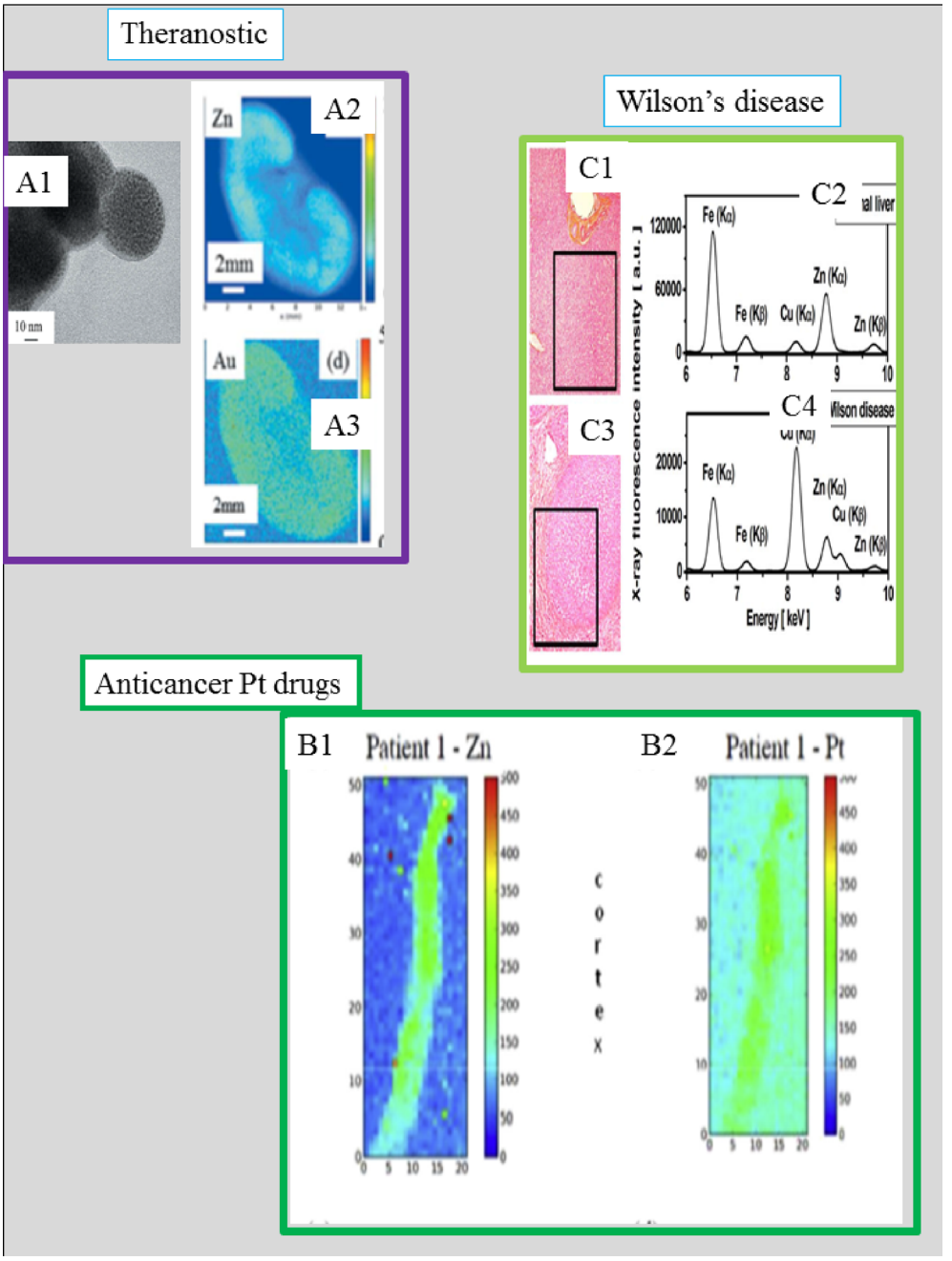

Figure 9. (a1) TEM image of the Au25(4ATP)18 cluster: Spatial repartition of different elements, namely Zn (a2) and Au (a3), obtained using the intensity of the corresponding X-ray fluorescence emission lines (QR-AuQDs exposed rat kidney embedded in paraffin) as contrast image (map: 13.7 mm × 19.3 mm, 30 μm resolution, 20 ms acquisition time). (b1) and (b2): Spatial repartition of Zn and Pt in a kidney biopsy collected on a patient treated with Pt anticancer drugs. (c1 to c4): Tissue sections of 5 μm thickness were stained with HES. Portal tract and centrilobular vein are present on the section of normal liver (patient #3) (upper image). WD liver (patient #46) exhibits nodules surrounded by fibrosis (lower image). Synchrotron radiation XRF spectra were acquired on the area delimited by the black squares. Representative XRF spectra acquired on tissue sections from normal liver and WD showing peaks characteristic of the composite elements.

8. Beyond pathological calcifications

Note that our research is not limited to pathological calcifications. We also participate in other research fields (Figure 9), namely the nephrotoxicity of Pt anticancer drugs [269,270], the vectorisation of drugs through "quantum rattle-gold quantum dots" (QR-AuQDs) [271], Wilson's disease (WD) which is a result of copper accumulation [272], urothelial carcinoma grades [273], and TiO_2 particles at hair surfaces [168]. In this research, we take advantage of our previous investigations using μX-ray fluorescence on trace elements in kidney stones and in tissues.

In the case of Pt anticancer drug nephrotoxicity [269,270], we have investigated mice as well as patients, the ultimate goal being to prove that such X-ray fluorescence measurements can find a place in clinical practice. Indeed, as we can see in Figures 8 b1 and 8 b2, it is possible to confirm the presence of platinum in patient kidney biopsy. Such data can form part of the patient clinical file and help the clinician to assess the loss of kidney function.

The first example concerns nanometer-scale systems developed recently for the treatment of various severe pathologies [274,275]. The characterization of such nanomaterials, which can contribute to both diagnosis and therapy, can be easily performed using synchrotron radiation-specific techniques [276–284], in order to determine their size [276–279], their morphology [280,281], the modification of their electronic state during the growth process [282,283], or the adsorption process of molecules at their surface [284,285]. Here, using a completely new technology, the "flyscan" mode, it was possible to assess the presence of QR-AuQDs in various rat organs [271]. Such observations constitute a significant breakthrough opportunity to test new nanomaterials with potential medical uses.

The last example focuses on Wilson's disease, also known as hepatolenticular degeneration, which is a severe disorder of copper homeostasis [272]. Several excellent physicochemistry based studies have been performed on liver [286,287]. As shown in Figure 8c, X-ray fluorescence is a more efficient technique than the classical staining currently used in the clinic to confirm the presence of copper.

9. Building a national and international network

The different selected examples discussed in this contribution show the complexity of pathological calcification research. The dynamism of our research is proven by some standard publication indicators, such as 135 results on Web of Science for 2119 citations, or 71 results on PubMed.

At the national level, our research involves collaborations among several hospitals, namely Tenon, Bichat, St Louis, Lariboisière, Rothschild, Ambroise Paré in the Paris area and other hospitals in various French regions (CHU of Lille, Toulouse, Nantes, CH of Pontoise…).

At the international level, numerous strong collaborations with research groups in different countries have been established and resulted in several publications. Among them we can cite Dr. A. Pozdzik (Department of Nephrology, Dialysis and Renal Transplantation, Brugmann Hospital, Université Libre de Bruxelles, Brussels, Belgium), Professor F. Tielens (Free University of Brussels, Belgium) , Professor J. C. Williams (Department of Anatomy and Cell Biology, Indiana University School of Medicine, Indianapolis, Indiana, USA) [287,288], Professor M. Duer and Dr. D. Reid (Department of Chemistry, University of Cambridge, Great Britain), Dr. F. Preitner (Mouse Metabolic Facility of the Cardiomet Center, University Hospital, Lausanne, Switzerland), Dr. J. Bertazzo (Department of Materials, South Kensington Campus, Imperial College, London, Great Britain), and Dr. X. Keller [289] (Zurich hospital, Switzerland).

10. Knowledge transfer

Our collaborations between physicists and physicians provides the opportunity for young doctors from different medical specialties (cardiology, dermatology, nephrology, otorhinolaryngology, rheumatology, urology) to receive training and insights in physicochemical characterization techniques and possibilities.

11. Perspectives on the synchrotron soleil upgrade (In collaboration with Dr. E. Boudelique, Dr. H. Colboc, Dr. E. Esteve)

As previously shown [290–292], synchrotron radiation plays a pivotal role in our research. Experiments have been performed on seven different beamlines at soleil (SMIS, AILES, DISCO, CRISTAL, PROXIMA, NANOSCOPIUM, DIFFABS), one on ESRF, and one on another large instrument, the LLB (G4.1), where we have used neutrons as a probe, in very diverse research related to urology, nephrology, rheumatology, and dermatology.

In this research, the role of the beamline scientists is clearly of major significance, and numerous fruitful discussions regarding the information yielded by each technique as well as sample preparation protocols have taken place. Thanks to the SMIS beamline, the first set of μFTIR experiments on 15 kidney biopsies served to initiate a research project which was accepted and funded by the CORDDIM, allowing a platform to be created consisting of two μFTIR imagers, on which more than 1600 human kidney biopsies have been performed. The technology allowing this transfer is of prime importance for the clinician.

Following various discussions around the upgrade of the synchrotron Soleil, we have defined some priorities for analysis of tissue at a very small scale. It is of primary importance to be able to precisely know the position of the micro or nano probe on the sample. For exemple, in the case of kidney, the nephron is constituted of different elements, namely the glomerulus, the proximal tubule, the loop of Henle, and the distal tubule, in each of which the biochemical environment (pH, calcium concentration, etc…) can be very different. Calcifications may also take place in the interstitium in the cortex and the medulla, and also in the papilla where we can find Randall's plaques. A comparison between the chemical composition of pathological calcifications and the normal physiological environment is clearly a key to understand the disease. In a perfect world, the kidney would be placed under the synchrotron beam in such a way that the clinician would be able to position the nanometer probe on a specific organ structure such as a glomerulus, or a proximal or distal tubule. We thus would like to have a functional optical device comparable to those in the hospital (magnification ×100), and be able to know the exact position of the beam on the sample via an optical laser. Also, it will be advantageous to automate rapid sample mounting and demounting, as is already done on various beamlines [293].

In terms of the acquisition procedure, it is of primary importance to define experimental parameters such the size of the map directly onto a touch-sensitive screen without prior knowledge of the software code. Moreover, it must be possible to perform experiments remotely [294].

It is very convenient for the clinician to carry out different experiments on the same sample. For example, on a beamline such Diffabs, it is possible to collect X-ray diffraction as well as X-ray absorption data on the same sample. In the case of cartilage this experimental configuration generates very valuable information from which trace elements and chemical composition of pathological calcifications can be deduced. Also, it would be advantageous if the sample support used for synchrotron experiments is compatible with other techniques such FE-SEM or μFTIR spectroscopy. This will require a significant effort to achieve, particularly for studies at the nanometer scale where new physical challenges will have to be solved.

Nanometer scale measurements may yield significant information regarding interaction between mineral and proteins or between mineral and cells. The first experiments performed on nanoscopium opens a major perspective on the 3D distribution of mineral as well as trace elements such Zn.

12. Conclusion

The quest for characterization techniques to generate significant information on microcrystalline pathologies for the clinician is constantly active. In Figure 10, we present a short list of selected results. The latest efforts towards this goal are related to the fact that these biological entities contain organic as well as inorganic compounds.

This prompted us to perform experiments on human biopsies using non-linear optical spectroscopy, namely Second Harmonic Generation (SHG), as well as fluorescence, in order to assess its potential on ectopic calcifications. Non-linear optical spectroscopy

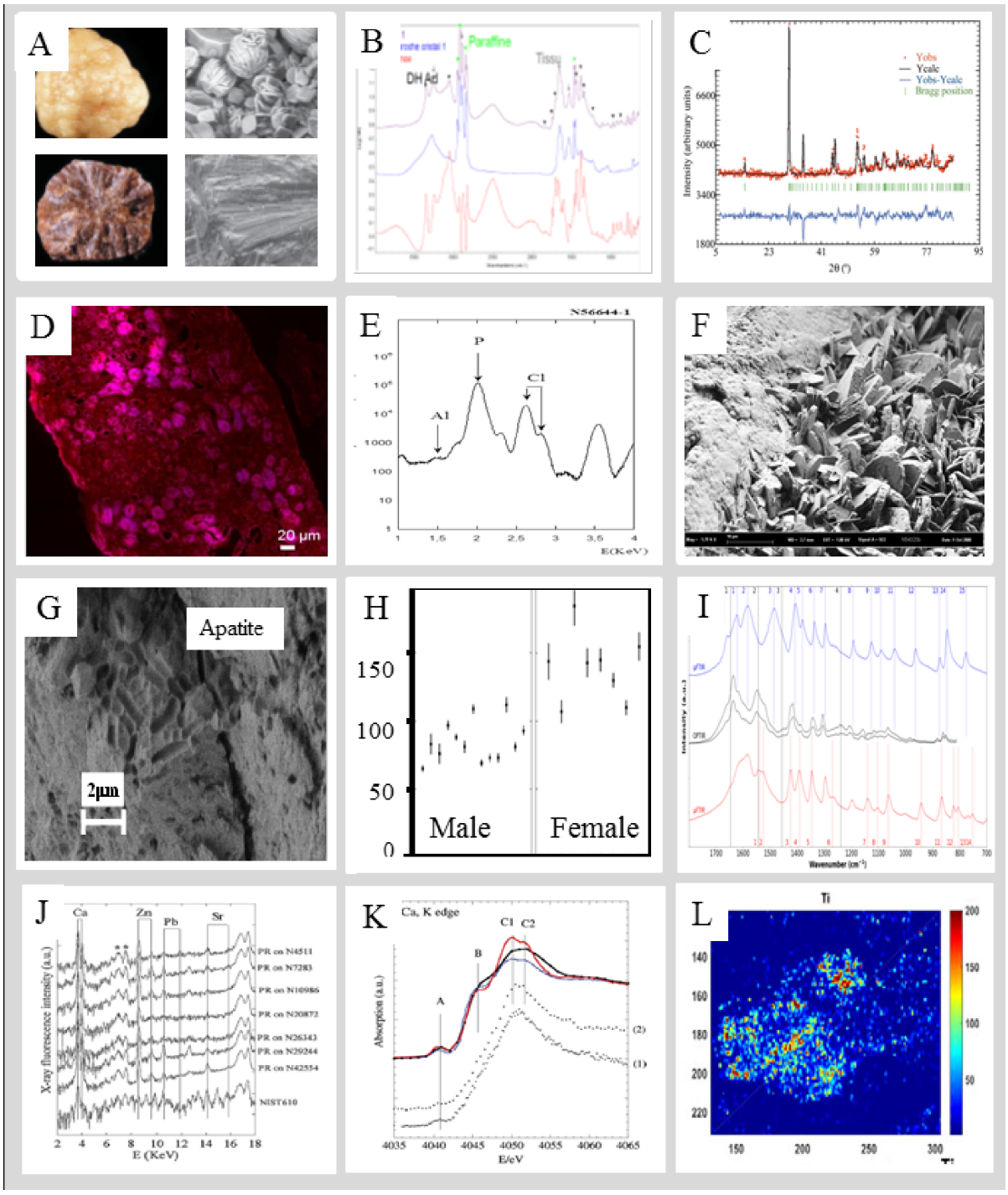

Figure 10. (A) SEM as a diagnostic tool for primary hyperoxaluria. (B) µFTIR spectroscopy on kidney tissue as a diagnostic tool, in a case of APRT deficiency. (C) Neutron scattering to assess a drug effect for the treatment of cystinuria. (D) NanoUV spectroscopy to assess the presence of oxalate in kidney tissue.

Figure 10. (**cont**.) (E) Micro X-ray fluorescence performed at ESRF indicating the presence of Al in kidney stone. (F) SEM illustrating the process of kidney stone growth on RP. (G) SEM as a diagnostic tool for urinary infection in the absence of clinical symptoms (H) Neutron scattering to define UA crystal size modifications which occur between metabolic syndrome and diabetes (I) NanoIR indicatinging the presence of cysteine in intracellular crystals. (J) X-ray fluorescence showing an abnormal quantity of Zn in RP, indicating an inflammatory process. (K) Xanes spectra collected at Ca K edge of RP (L) NanoX-ray fluorescence performed on Synchrotron Soleil indicating the presence of Ti on hair.

is a non-invasive technique which enables investigations of different biological tissues based on SHG spectroscopy [295–298]. Among the different indispensable laboratory techniques allowing characterization of nanometer scale materials [299] are NanoIR i.e. AFM-IR [171–174] as well as PTO-IR (Optical PhotoThermal IR) [300,301], which should lead to major breakthroughs in the coming years.

Conflicts of interest

Authors have no conflict of interest to declare.

Acknowledgments

It is a great honour to thank all the people who have played a significant role in building this interface between physics, chemistry and medicine: Dr. X. Carpentier (Nice Hospital), Dr. Ch. Chappard (Lariboisière Hospital), Professor P. Conort (La Pitié-Salpetrière Hospital), Dr. P. Dorfmüller (La Pitié-Salpetrière Hospital), Dr. E. Estève (Tenon Hospital), Professor D. Hannouche (Lariboisière Hospital), Professor P. Jungers (Necker Hospital), Professor B. Knebelman (Necker Hospital), Dr. E. A. Korng (Lariboisière Hospital), Professor F. Liote (Lariboisière Hospital), Dr. M. Livrozet (Tenon Hospital), Professor M. Mathonnet (Limoges Hospital), Professor P. Méria (Saint-Louis Hospital), Dr. C. Nguyen (Lariboisière Hospital), Dr. J. Rode (Tenon Hospital), Professor P. Ronco (Tenon Hospital), Dr. I. Tostivint (La Pitié-Salpetrière Hospital), Professor O. Traxer (Tenon Hospital) and Professor J. C. Williams (Department of Anatomy and Cell Biology, Indiana University School of Medicine, Indianapolis, Indiana, USA) for providing samples and useful discussions.

Also, regarding the physicochemistry, this research could not have been performed without the scientific advice of Dr. P.-A. Albouy (LPS), Dr. G. André (LLB), Dr. A. Bianchi (INSERM-U7561), Dr. P. Chevallier (LURE), Dr. A. Cousson (LLB), Dr. P. Dumas (SOLEIL Synchrotron), Professor M. Duer (Department of Chemistry, University of Cambridge, United kingdom), Dr. E. El Kaim (SOLEIL Synchrotron), Dr. B. Fayard (LPS-ESRF), Dr. E. Foy (Laboratoire Pierre-Süe), Dr. J.-L. Hazemann (ESRF), Dr. L. Hennet (CEMHTI), Dr. F. Jamme (SOLEIL Synchrotron), Dr. A. Lebail (Laboratoire des Fluorures), Dr. F. Lenaour (Hôpital Paul Brousse), Dr. O. Mathon (ESRF), Dr. K. Medjoubi (SOLEIL Synchrotron), Dr. G. Matzen (CEMHTI), Dr. C. Mocuta (SOLEIL Synchrotron), Dr. R. Papoular (CEA), Dr. P. Reboul, (UMR 7561), Dr. M. Réfrégiers (SOLEIL Synchrotron), Dr. S. Reguer (SOLEIL Synchrotron), Dr. D. Reid (Department of Chemistry, University of Cambridge), Dr. S. Rouzière (LPS), Dr. S. Kaščáková (Hôpital Paul Brousse), Dr. J.-P. Samama (SOLEIL Synchrotron), Dr. C. Sandt (SOLEIL Synchrotron), Dr. M. C. Schanne-Klain (LOB, Polytechnique), Dr. D. Reid (Department of chemistry, Cambridge University, United kingdom), Dr. A. Somogy (SOLEIL Synchrotron), Dr. D. Thiaudière (SOLEIL Synchrotron), Dr. E. Véron (CEMHTI) and Dr. R. Weil (LPS).

This work was supported by the Physics and Chemistry Institutes of CNRS and by contracts ANR-09-BLAN-0120-02, ANR-12-BS08-0022, ANR13JSV10010-01, convergence UPMC CVG1205, Labex Matisse, Labex Michem and CORDDIM-2013-COD130042. The authors are grateful to the SOLEIL Synchrotron Facility and the Leon Brillouin laboratory for beam time allocation.

References

[1] M. G. Baron, N. Benmoussa, D. Bazin, I. Abadie, M. Daudon, Ph. Charlier, *Urolithiasis*, 2019, **47**, 487-488.

[2] G. R. Colmont, D. Bazin, M. Daudon, *C. R. Chim.*, 2022, **25**, no. S1, 431-444.

[3] D. Bazin, M. Daudon, C. Combes, C. Rey, *Chem. Rev.*, 2012, **112**, 5092-5120.

[4] D. Bazin, M. Daudon, *J. Phys. D: Appl. Phys.*, 2012, **45**, article no. 383001.

[5] L. N. Poloni, M. D. Ward, *Chem. Mater.*, 2014, **26**, 477-495.

[6] D. Bazin, M. Daudon, *Ann. Biol. Clin.*, 2015, **73**, 517-534.

[7] S. R. Mulay, H.-J. Anders, *N. Engl. J. Med.*, 2016, **374**, 2465-2476.

[8] M. Li, J. Zhang, L. Wang, B. Wang, Ch. V. Putnis, *J. Phys. Chem. B*, 2018, **122**, 1580-1587.

[9] E. Tsolaki, S. Bertazzo, *Materials*, 2019, **12**, article no. 3126.

[10] D. Bazin, E. Letavernier, J. P. Haymann, V. Frochot, M. Daudon, *Ann. Biol. Clin.*, 2020, **78**, 349-362.

[11] L. N. Cossey, Z. Dvanajscak, Ch. P. Larsen, *Semin. Diagn. Pathol.*, 2020, **37**, 135-142.

[12] L. Frappart, M. Boudeulle, J. Boumendil, H. C. Lin, I. Martinon, C. Palayer, Y. Mallet-Guy, D. Raudrant, A. Bremond, Y. Rochet, J. Feroldi, *Human Pathol.*, 1984, **15**, 880-889.

[13] A. Ben Lakhdar, M. Daudon, M. C. Matthieu, A. Kellum, C. Balleyguier, D. Bazin, *C. R. Chim.*, 2016, **19**, 1610-1624.

[14] R. Scott, C. Kendall, N. Stone, K. Rogers, *Sci. Rep.*, 2017, **7**, article no. 136.

[15] D. A. Spak, J. S. Plaxco, L. Santiago, M. J. Dryden, B. E. Dogan, *Diagn. Interv. Imaging*, 2017, **98**, article no. 179.

[16] J. A. M. R. Kunitake, S. Choi, K. X. Nguyen, M. M. Lee, F. He, D. Sudilovsky, P. G. Morris, M. S. Jochelson, C. A. Hudis, D. A. Muller, P. Fratzl, C. Fischbach, A. Masi, L. A. Estroff, *J. Struct. Biol.*, 2018, **202**, 25-34.

[17] J. M. Richards, J. A. M. R. Kunitake, H. B. Hunt, A. N. Wnorowski, D. W. Lin, A. L. Boskey, E. Donnelly, L. A. Estroff, J. T. Butcher, *Acta Biomater.*, 2018, **71**, 24-36.

[18] S. De Santis, G. Sotgiu, A. Crescenzi, Ch. Taffon, A. C. Felici, M. Orsini, *J. Pharmacol. Biomed. Anal.*, 2020, **190**, article no. 113534.

[19] S. J. Magny, R. Shikhman, A. L. Keppke, "Breast imaging reporting and data system. [Updated 2020 September 5]", in *StatPearls Internet*, StatPearls Publishing, Treasure Island, FL, 2021, available from: https://www.ncbi.nlm.nih.gov/books/NBK459169/.

[20] A. Millan, P. Lanzer, V. Sorribas, *Front. Cell Dev. Biol.*, 2021, **9**, article no. 633465.

[21] P. Lanzer, M. Boehm, V. Sorribas, M. Thiriet, J. Janzen, Th. Zeller St., C. Hilaire, C. Shanahan, *Eur. Heart J.*, 2014, **35**, 1515-1525.

[22] A. P. Sage, Y. Tintut, L. L. Demer, *Nat. Rev. Cardiol.*, 2010, **7**, 528-536.

[23] E. R. Mohler 3rd, *Am. J. Cardiol.*, 2004, **94**, 1396-1402.

[24] M. Resnick, *Urol. Clin. North Am.*, 1981, **8**, 265-276.

[25] X. Carpentier, M. Daudon, O. Traxer, P. Jungers, A. Mazouyes, G. Matzen, E. Véron, D. Bazin, *Urology*, 2009, **73**, 968-975.

[26] J. Prywer, A. Torzewska, *Cryst. Res. Technol.*, 2010, **45**, 1283-1289.

[27] M. Daudon, P. Jungers, in *Urinary Tract Stone Disease* (N. P. Rao, G. M. Preminger, J. P. Kavanagh, eds.), Springer, London, 2011, 225-237.

[28] D. Bazin, G. André, R. Weil, G. Matzen, E. Véron, X. Carpentier, M. Daudon, *Urology*, 2012, **79**, 786-790.

[29] R. Flannigan, W. H. Choy, B. Chew, D. Lange, *Nat. Rev. Urol.*, 2014, **11**, 333-341.

[30] E. J. Espinosa-Ortiz, B. H. Eisner, D. Lange, R. Gerlach, *Nat. Rev. Urol.*, 2019, **16**, 35-53.

[31] M. Daudon, M. Petay, S. Vimont, A. Denizet, F. Tielens, J.-Ph. Haymann, E. Letavernier, V. Frochot, D. Bazin, *C. R. Chim.*, 2022, **25**, no. S1, 315-334.

[32] P. Cochat, G. Rumsby, *N. Engl. J. Med.*, 2013, **369**, 649-658.

[33] G. Bollee, M. Daudon, I. Ceballos-Picot, *World J. Clin. Urol.*, 2014, **3**, 218-226.

[34] G. Bollée, C. Dollinger, L. Boutaud, D. Guillemot, A. Bensman, J. Harambat, P. Deteix, M. Daudon, B. Knebelmann, I. Ceballos-Picot, *J. Am. Soc. Nephrol.*, 2010, **21**, 679-688.

[35] M. Daudon, P. Jungers, D. Bazin, *N. Engl. J. Med.*, 2008, **359**, 100-102.

[36] M. Daudon, P. Jungers, D. Bazin, *N. Engl. J. Med.*, 2009, **360**, 1680.

[37] A. Dessombz, E. Letavernier, J.-Ph. Haymann, D. Bazin, M. Daudon, *J. Urol.*, 2015, **193**, 1564-1569.

[38] J. R. M. Oliveira, M. F. Oliveira, *Sci. Rep.*, 2016, **6**, article no. 22961.

[39] A. A. Mufaddel, G. A. Al-Hassani, *Neurosciences (Riyadh)*, 2014, **19**, 171-177.

[40] E. R. Vina, C. Kent Kwoh, *Curr. Opin. Rheumatol.*, 2018, **30**, 160-167.

[41] P. Brasil, J. P. Pereira Jr., M. E. Moreira, R. M. Ribeiro Nogueira, L. Damasceno, M. Wakimoto, R. S. Rabello, S. G. Valderramos, U.-A. Halai, T. S. Salles, A. A. Zin, D. Horovitz, P. Daltro, M. Boechat, C. Raja Gabaglia, P. Carvalho de Sequeira, J. H. Pilotto, R. Medialdea-Carrera, D. Cotrim da Cunha, L. M. Abreu de Carvalho, M. Pone, A. Machado Siqueira, G. A. Calvet, A. E. Rodrigues Baião, E. S. Neves, P. R. Nassar de Carvalho, R. H. Hasue, P. B. Marschik, C. Einspieler, C. Janzen, J. D. Cherry, A. M. Bispo de Filippis, K. Nielsen-Saines, *N. Engl. J. Med.*, 2016, **375**, 2321-2334.

[42] S. Wu, Y. Zeng, A. Lerner, B. Gao, M. Law, *Front. Neurol.*, 2018, **9**, article no. 227.

[43] A. Ferreira da Silva, *Radiol. Bras.*, 2018, **51**, 270-271.

[44] M. Daudon, *Ann. Urol. (Paris)*, 2005, **39**, 209-231.

[45] P. Cochat, *Kidney Int.*, 1999, **55**, 2533-2547.

[46] E. Leumann, B. Hoppe, *J. Am. Soc. Nephrol.*, 2001, **12**, 1986-1993.

[47] R. P. Baughman, A. S. Teirstein, M. A. Judson, M. D. Rossman, H. Yeager Jr., E. A. Bresnitz, L. DePalo, G. Hunninghake, M. C. Iannuzzi, C. J. Johns, G. McLennan, D. R. Moller, L. S. Newman, D. L. Rabin, C. Rose, B. Rybicki, S. E. Weinberger, M. L. Terrin, G. L. Knatterud, R. Cherniak, *Am. J. Respir. Crit. Care Med.*, 2001, **164**, 1885-1889.

[48] A. Haimovic, M. Sanchez, M. A. Judson, S. Prystowsky, *J. Am. Acad. Dermatol.*, 2012, **66**, 699.e1-699.e18.

[49] G. Zissel, J. Müller-Quernheim, *Clin. Chest Med.*, 2008, **36**, 549-560.

[50] K. A. Wanat, M. Rosenbach, *Clin. Chest Med.*, 2015, **36**, 685-702.

[51] J. P. Callen, *Arch. Dermatol.*, 2001, **137**, 485-486.

[52] M. Catinon, C. Chemarin, F. Thivolet, M. Kambouchner, J.-F. Bernaudin, C. Cavalin, A.-M. Sfarghiu, F. Arbib, O. Freynet, N. Freymond, J.-F. Mornex, P.-A. Rosental, M. Vincent, D. Valeyre, Ch. Pison, *Eur. Respir. J.*, 2017, **50**, article no. PA3263.

[53] H. Colboc, D. Bazin, Ph. Moguelet, V. Frochot, R. Weil, E. Letavernier, Ch. Jouanneau, C. Frances, C. Bachmeyer, J.-F. Bernaudin, M. Daudon, *C. R. Chim.*, 2016, **19**, 1631-1641.

[54] H. Colboc, P. Moguelet, D. Bazin, C. Bachmeyer, V. Fro-

chot, R. Weil, E. Letavernier, C. Jouanneau, M. Daudon, J. F. Bernaudin, *J. Eur. Acad. Dermatol. Venereol.*, 2019, **33**, 198-203.

[55] H. Colboc, D. Bazin, P. Moguelet, S. Reguer, R. Amode, C. Jouanneau, I. Lucas, L. Deschamps, V. Descamps, N. Kluger, *J. Eur. Acad. Dermatol. Venereol.*, 2020, **34**, e313-e315.

[56] G. Forte, F. Petrucci, A. Cristaudo, B. Bocca, *Sci. Total Environ.*, 2009, **407**, 5997-6002.

[57] M. Arl, D. J. Nogueira, J. Sch. Köerich, N. M. Justino, D. S. Vicentini, W. G. Matias, *J. Hazard. Mater.*, 2019, **364**, 548-561.

[58] M. Daudon, M. F. Protat, R. J. Réveillaud, *Néphrologie*, 1982, **3**, 119-123.

[59] F. Sorgel, B. Ettinger, L. Z. Benet, *J. Urol.*, 1985, **134**, 871-873.

[60] M. A. Perazella, *Am. J. Med. Sci.*, 2003, **325**, 349-362.

[61] V. Frochot, D. Bazin, E. Letavernier, Ch. Jouanneau, J.-Ph. Haymann, M. Daudon, *C. R. Chim.*, 2016, **19**, 1565-1572.

[62] Y. Luque, K. Louis, C. Jouanneau, S. Placier, E. Esteve, D. Bazin, E. Rondeau, E. Letavernier, A. Wolfromm, C. Gosset, A. Boueilh, M. Burbach, P. Frère, M.-C. Verpont, S. Vandermeersch, D. Langui, M. Daudon, V. Frochot, L. Mesnard, *J. Am. Soc. Nephrol.*, 2017, **28**, 1723-1728.

[63] A.-L. Faucon, M. Daudon, V. Frochot, D. Bazin, B. Terris, V. Caudwell, *Kidney Int.*, 2018, **93**, 1251-1252.

[64] M. Daudon, V. Frochot, D. Bazin, P. Jungers, *Drugs*, 2018, **78**, 163-201.

[65] M. C. Morales-Alvarez, *Adv. Chronic Kidney Dis.*, 2020, **27**, 31-37.

[66] G. Chebion, E. Bugni, V. Gerin, M. Daudon, V. Castiglione, *C. R. Chim.*, 2022, **25**, no. S1, 295-306.

[67] T. Oyama, T. Sano, T. Hikino, Q. Xue, K. Iijima, T. Nakajima, F. Koerner, *Virchows Arch.*, 2002, **440**, 267-273.

[68] Y. V. Nalawade, *Indian J. Radiol. Imaging*, 2009, **19**, 282-286.

[69] S. S. Kang, E. Y. Ko, B.-K. Han, J. H. Shin, *Eur. J. Radiol.*, 2008, **67**, 285-291.

[70] D. P. Griffith, *Kidney Int.*, 1978, **13**, 372-382.

[71] F. Grases, A. Costa-Bauza, *Arch. Esp. Urol.*, 2021, **74**, 35-48.

[72] F. Meiouet, S. El Kabbaj, M. Daudon, *Prog. Urol.*, 2019, **29**, 173-182.

[73] M. Mirković, A. Dosen, S. Erić, P. Vulić, B. Matović, A. Rosić, *Microchem. J.*, 2020, **152**, article no. 104429.

[74] P. Das, G. Gupta, V. Velu, R. Awasthi, K. Dua, H. Malipeddi, *Biomed. Pharmacother.*, 2017, **96**, 361-370.

[75] C. K. Arellano, "The calcification of Staphylococcus aureus bacteria: a potential defense mechanism against infections", PhD Thesis, University of California, San Diego, USA, 2010.

[76] L. Hortells, S. Sur, C. St. Hilaire, *Front. Cardiovasc. Med.*, 2018, **5**, article no. 27.

[77] F. Brisset, M. Repoux, J. Ruste, F. Grillon, F. Robaut, *Microscopie électronique à balayage et Microanalyses*, EDP Sciences, Paris, 2009.

[78] S. Ghosh, S. Basu, S. Chakraborty, A. Mukherjee, *J. Appl. Crystallogr.*, 2009, **42**, 629-635.

[79] M. Kocademir, A. Baykal, M. Kumru, M. Lutfu Tahmaz, *Spectrochim. Acta A Mol. Biomol. Spectrosc.*, 2016, **160**, 1-7.

[80] D. Bazin, E. Bouderlique, M. Daudon, V. Frochot, J.-Ph. Haymann, E. Letavernier, F. Tielens, R. Weil, *C. R. Chim.*, 2022, **25**, no. S1, 37-60.

[81] Y. Hidaka, T. D. Palella, T. E. O'Toole, S. A. Tarlé, W. N. Kelley, *J. Clin. Invest.*, 1987, **80**, 1409-1415.

[82] G. Bollée, J. Harambat, A. Bensman, B. Knebelmann, M. Daudon, I. Ceballos-Picot, *Clin. J. Am. Soc. Nephrol.*, 2012, **7**, 1521-1527.

[83] I. Ceballos-Picot, J. L. Perignon, M. Hamet, M. Daudon, P. Kamoun, *Lancet*, 1992, **339**, 1050-1051.

[84] V. Edvardsson, R. Palsson, I. Olafsson, G. Hjaltadottir, T. Laxdal, *Am. J. Kidney Dis.*, 2001, **38**, 473-480.

[85] V. Orn Edvardsson, A. Sahota, R. Palsson, "Adenine phosphoribosyltransferase deficiency. 2012 August 30 [Updated 2019 September 26]", in *GeneReviews® [Internet]* (M. P. Adam, H. H. Ardinger, R. A. Pagon *et al.*, eds.), University of Washington, Seattle, Seattle, WA, 1993–2021.

[86] E. Bouderlique, E. Tang, J. Perez, H.-K. Ea, F. Renaudin, A. Coudert, S. Vandermeersch, D. Bazin, J.-Ph. Haymann, C. Saint-Jacques, V. Frochot, M. Daudon, E. Letavernier, *C. R. Chim.*, 2022, **25**, no. S1, 393-405.

[87] C. R. Powell, M. L. Stoller, B. E. Schwartz, C. Kane, D. L. Gentle, J. E. Bruce, S. W. Leslie, *Urology*, 2000, **55**, 825-830.

[88] C. Y. Pak, K. Sakhaee, R. D. Peterson, J. R. Poindexter, W. H. Frawley, *Kidney Int.*, 2001, **60**, 757-761.

[89] M. Daudon, O. Traxer, P. Conort, B. Lacour, P. Jungers, *J. Am. Soc. Nephrol.*, 2006, **17**, 2026-2033.

[90] M. Daudon, E. Letavernier, R. Weil, E. Véron, G. Matzen, G. André, D. Bazin, *C. R. Chim.*, 2016, **19**, 1527-1534.

[91] E. Letavernier, M. Flamant, C. Marsault, J.-Ph. Haymann, G. Müller, L. Villa, J. Cloutier, O. Traxer, M. Daudon, *C. R. Chim.*, 2022, **25**, no. S1, 307-314.

[92] E. Letavernier, O. Traxer, J.-P. Haymann, D. Bazin, M. Daudon, *Prog. Urol.—FMC*, 2012, **22**, F119-F123.

[93] D. Bazin, M. Daudon, G. André, R. Weil, E. Véron, G. Matzen, *J. Appl. Crystallogr.*, 2014, **47**, 719-725.

[94] M. Livrozet, S. Vandermeersch, L. Mesnard, E. Thioulouse, J. Jaubert, J.-J. Boffa, J.-Ph. Haymann, L. Baud, D. Bazin, M. Daudon, E. Letavernier, *PLoS One*, 2014, **9**, article no. e102700.

[95] J. P. Haymann, M. Livrozet, J. Rode, S. Doizi, O. Traxer, V. Frochot, E. Letavernier, D. Bazin, M. Daudon, *Prog. Urol.—FMC*, 2021, **31**, F1-F7.

[96] C. Prot-Bertoye, M. Daudon, I. Tostivint, M. P. Dousseaux, J. Defazio, O. Traxer, B. Knebelmann, M. Courbebaisse, *Néphrol. Thér.*, 2021, **17**, S100-S107.

[97] D. Bazin, J.-Ph. Haymann, E. Letavernier, J. Rode, M. Daudon, *Presse Med.*, 2014, **43**, 135-148.

[98] M. Daudon, D. Bazin, *J. Phys.: Conf. Ser.*, 2013, **425**, article no. 022006.

[99] Y. Chen, J. Kong, S. Wu, *Lab. Invest.*, 2015, **95**, 124-131.

[100] V. K. Singh, B. S. Jaswal, J. Sharma, P. K. Rai, *Biophys. Rev.*, 2020, **12**, 647-668.

[101] F. Renaudin, S. Sarda, L. Campillo-Gimenez, Ch. Séverac, Th. Léger, C. Charvillat, Ch. Rey, F. Lioté, J.-M. Camadro, H.-K. Ea, Ch. Combes, *J. Funct. Biomater.*, 2019, **10**, article no. 18.

[102] M. A. Martillo, L. Nazzal, D. B. Crittenden, *Curr. Rheumatol. Rep.*, 2014, **16**, article no. 400.

[103] M. Petay, M. Cherfan, A. Deniset, E. Bouderlique, S. Reguer, A. Dazzi, J. Mathurin, M. Daudon, V. Frochot, J.-Ph. Hay-

mann, E. Letavernier, D. Bazin, *C. R. Chim.*, 2022, **25**, no. S1, 553-576.
[104] M. Mathonnet, A. Dessombz, D. Bazin, R. Weil, F. Triponez, M. Pusztaszeri, M. Daudon, *C. R. Chim.*, 2016, **19**, 1672-1678.
[105] J. Guerlain, S. Perie, M. Lefevre, J. Perez, S. Vandermeersch, Ch. Jouanneau, L. Huguet, V. Frochot, E. Letavernier, R. Weil, S. Rouziere, D. Bazin, M. Daudon, J. P. Haymann, *PLoS One*, 2019, **14**, article no. e0224138.
[106] L. Henry, D. Bazin, C. Policar, J.-Ph. Haymann, M. Daudon, V. Frochot, M. Mathonnet, *C. R. Chim.*, 2022, **25**, no. S1, 503-515.
[107] V. Frochot, M. Daudon, *Int. J. Surgery*, 2016, **36**, 624-632.
[108] G. C. Curhan, *Urol. Clin. North Am.*, 2007, **34**, 287-293.
[109] M. Daudon, *EMC Urologie*, 2013, **6**, 1-13.
[110] Y. Liu, Y. Chen, B. Liao, D. Luo, K. Wang, H. Li, G. Zeng, *Asian J. Urol.*, 2018, **5**, 205-214.
[111] M. Daudon, C. A. Bader, P. Jungers, *Scanning Microsc.*, 1993, **7**, 1081-1104.
[112] M. Daudon, *Arch. Pédiatr.*, 2000, **7**, 855-865.
[113] M. Daudon, P. Jungers, *Nephron Physiol.*, 2004, **98**, 31-36.
[114] M. Daudon, P. Jungers, D. Bazin, *AIP Conf. Proc.*, 2008, **1049**, 199-215.
[115] M. Daudon, H. Bouzidi, D. Bazin, *Urol. Res.*, 2010, **38**, 459-467.
[116] M. Daudon, *Prog. Urol.—FMC*, 2012, **22**, F87-F93.
[117] M. Daudon, O. Traxer, P. Jungers, *Lithiase Urinaire*, 2e ed., Médecine-Sciences, Lavoisier, Paris, 2012, 672 pages.
[118] J. Cloutier, L. Villa, O. Traxer, M. Daudon, *World J. Urol.*, 2015, **33**, 157-169.
[119] M. Daudon, A. Dessombz, V. Frochot, E. Letavernier, J.-Ph. Haymann, P. Jungers, D. Bazin, *C. R. Chim.*, 2016, **19**, 1470-1491.
[120] J. C. Williams Jr., G. Gambaro, A. Rodgers, J. Asplin, O. Bonny, A. Costa-Bauzá, P. M. Ferraro, G. Fogazzi, D. G. Fuster, D. S. Goldfarb, F. Grases, I. P. Heilberg, D. Kok, E. Letavernier, G. Lippi, M. Marangella, A. Nouvenne, M. Petrarulo, R. Siener, H.-G. Tiselius, O. Traxer, A. Trinchieri, E. Croppi, W. G. Robertson, *Urolithiasis*, 2021, **49**, 1-16.
[121] M. Daudon, P. Jungers, "Stone composition and morphology: a window on etiology", in *Urolithiasis: Basic Science and Clinical Practice* (J. J. Talati, H. G. Tiselius, D. M. Albala, Z. Ye, eds.), Springer Verlag, London, 2012, 113-140.
[122] L. Estepa, M. Daudon, *Biospectroscopy*, 1997, **3**, 347-369.
[123] A. Dessombz, D. Bazin, P. Dumas, C. Sandt, J. Sule-Suso, M. Daudon, *PLoS One*, 2011, **6**, article no. e28007.
[124] L. F. Bonewald, S. E. Harris, J. Rosser, M. R. Dallas, S. Dallas, N. P. Camacho, B. Boyan, A. Boskey, *Calcif. Tissue Int.*, 2003, **72**, 537-547.
[125] L. Maurice-Estepa, P. Levillain, B. Lacour, M. Daudon, *Scand. J. Urol. Nephrol.*, 1999, **33**, 299-305.
[126] N. Quy Dao, M. Daudon, *Infrared and Raman Spectra of Calculi*, Elsevier, Paris, 1997.
[127] C. Türk, T. Knoll, A. Petrik *et al.*, *Guidelines on Urolithiasis*, European Association of Urology, Arnhem, The Netherlands, 2013.
[128] M. Daudon, D. Bazin, *C. R. Chim.*, 2016, **19**, 1416-1423.
[129] A. H. Khan, S. Imran, J. Talati, L. Jafri, *Investig. Clin. Urol.*, 2018, **59**, 32-37.
[130] D. Finlayson, Ch. Rinaldi, M. J. Baker, *Anal. Chem.*, 2019, **91**, 12117-12128.
[131] D. Bazin, M. Daudon, P. Chevallier, S. Rouzière, E. Elkaim, D. Thiaudiere, B. Fayard, E. Foy, P. A. Albouy, G. André, G. Matzen, E. Véron, *Ann. Biol. Clin. (Paris)*, 2006, **64**, 125-139.
[132] D. Bazin, M. Daudon, "Nouvelles Méthodes d'étude des calculs et plaques de Randall", in *Actualités néphrologiques Jean Hamburger* (P. Lesavre, T. Drüeke, C. Legendre, P. Niaudet, eds.), Flammarion–Médecine, Paris, 2010, 75-98.
[133] M. Daudon, D. Bazin, "New techniques to characterize kidney stones and Randall's plaque", in *Urolithiasis: Basic Science and Clinical Practice* (J. J. Talati, H. G. Tiselius, D. M. Albala, Z. Ye, eds.), Springer, Berlin, 2012, 683-707.
[134] D. Bazin, E. Letavernier, J.-P. Haymann, P. Méria, M. Daudon, *Prog. Urol.*, 2016, **26**, 608-618.
[135] D. Bazin, M. Daudon, *J. Spectrosc. Imaging*, 2019, **8**, article no. a16.
[136] M. Daudon, H. Jaeschke-Boyer, M. F. Protat, R. J. Réveillaud, *Actual. Chim.*, 1980, **4**, 25-29.
[137] M. Daudon, M. F. Protat, R. J. Réveillaud, H. Jaeschke-Boyer, *Fortsch. Urol. Nephrol.*, 1981, **17**, 311-321.
[138] I. T. Lucas, D. Bazin, M. Daudon, *C. R. Chim.*, 2022, **25**, no. S1, 83-103.
[139] S. Tamosaityte, M. Pucetaite, A. Zelvys, S. Varvuolyte, V. Hendrixson, V. Sablinskas, *C. R. Chim.*, 2022, **25**, no. S1, 73-82.
[140] P. Dorfmüller, D. Bazin, S. Aubert, R. Weil, F. Brisset, M. Daudon, F. Capron, I. Brochériou, *Cardiol. Res. Pract.*, 2010, **2010**, article no. 685926.
[141] C. Verrier, D. Bazin, L. Huguet, O. Stéphan, A. Gloter, M.-Ch. Verpont, V. Frochot, J.-Ph. Haymann, I. Brocheriou, O. Traxer, M. Daudon, E. Letavernier, *J. Urol.*, 2016, **196**, 1566-1574.
[142] C. Gay, E. Letavernier, M.-Ch. Verpont, M. Walls, D. Bazin, M. Daudon, N. Nassif, O. Stephan, M. de Fruto, *ACS Nano*, 2020, **14**, 1823-1836.
[143] D. Bazin, P. Chevallier, G. Matzen, P. Jungers, M. Daudon, *Urol. Res.*, 2007, **35**, 179-184.
[144] X. Carpentier, D. Bazin, Ch. Combes, A. Mazouyes, S. Rouzière, P.-A. Albouy, E. Foy, M. Daudon, *J. Trace Elem. Med. Biol.*, 2011, **25**, 160-165.
[145] B. Hannache, A. Boutefnouchet, D. Bazin, E. Foy, M. Daudon, *Prog. Urol.*, 2015, **25**, 22-26.
[146] S. Rouzière, D. Bazin, M. Daudon, *C. R. Chim.*, 2016, **19**, 1404-1415.
[147] D. Bazin, E. Foy, S. Reguer, S. Rouzière, B. Fayard, H. Colboc, J.-Ph. Haymann, M. Daudon, C. Mocuta, *C. R. Chim.*, 2022, **25**, no. S1, 165-188.
[148] A. Le Bail, *Mater. Sci. Forum*, 2001, **378**, 65-70.
[149] A. Le Bail, *Powder Diffr.*, 2004, **19**, 249-254.
[150] A. Le Bail, D. Bazin, M. Daudon, A. Brochot, V. Robbez-Masson, V. Maisonneuve, *Acta Crystallogr. B*, 2009, **65**, 350-354.
[151] M. Daudon, D. Bazin, K. Adil, A. Le Bail, *Acta Crystallogr. E*, 2011, **67**, article no. o1458.
[152] A. Le Bail, M. Daudon, D. Bazin, *Acta Crystallogr. C*, 2013, **69**, 734-737.
[153] D. Bazin, V. Frochot, J.-Ph. Haymann, E. Letavernier, M. Daudon, *C. R. Chim.*, 2022, **25**, no. S1, 133-147.

[154] M. Bak, J. K. Thomsen, H. J. Jakobsen, S. E. Petersen, T. E. Petersen, N. C. Nielsen, *J. Urol.*, 2000, **164**, 856-863.

[155] H. Colas, L. Bonhomme-Coury, C. Coelho Diogo, F. Tielens, Ch. Gervais, D. Bazin, D. Laurencin, M. E. Smith, J. V. Hanna, M. Daudon, Ch. Bonhomme, *Cryst. Eng. Commun.*, 2013, **15**, 8840-8847.

[156] A. Dessombz, G. Coulibaly, B. Kirakoya, R. W. Ouedraogo, A. Lengani, S. Rouzière, R. Weil, L. Picaut, Ch. Bonhomme, F. Babonneau, D. Bazin, M. Daudon, *C. R. Chim.*, 2016, **19**, 1573-1579.

[157] Y. Li, D. G. Reid, D. Bazin, M. Daudon, M. J. Duer, *C. R. Chim.*, 2016, **19**, 1665-1671.

[158] S. Shadbolt, G. E. Jackson, A. L. Rodgers, *NMR Biomed.*, 2019, **32**, article no. e4177.

[159] C. Leroy, L. Bonhomme-Coury, Ch. Gervais, F. Tielens, F. Babonneau, M. Daudon, D. Bazin, E. Letavernier, D. Laurencin, D. Iuga, J. V. Hanna, M. E. Smith, Ch. Bonhomme, *Magn. Reson.*, 2021, **2**, 1-13.

[160] D. E. Sayers, F. W. Lytle, E. A. Stern, *Adv. X-ray Anal.*, 1970, **13**, 248-271.

[161] E. A. Stern, D. E. Sayers, F. W. Lytle, *Phys. Rev. B*, 1975, **11**, 4836-4846.

[162] D. Bazin, X. Carpentier, I. Brocheriou, P. Dorfmuller, S. Aubert, Ch. Chappard, D. Thiaudière, S. Reguer, G. Waychunas, P. Jungers, M. Daudon, *Biochimie*, 2009, **91**, 1294-1300.

[163] D. Bazin, X. Carpentier, O. Traxer, D. Thiaudière, A. Somogyi, S. Reguer, G. Waychunas, P. Jungers, M. Daudon, *J. Synchrotron Radiat.*, 2008, **15**, 506-509.

[164] S. Reguer, C. Mocuta, D. Thiaudière, M. Daudon, D. Bazin, *C. R. Chim.*, 2016, **19**, 1424-1431.

[165] D. Bazin, S. Reguer, D. Vantelon, J.-Ph. Haymann, E. Letavernier, V. Frochot, M. Daudon, E. Esteve, H. Colboc, *C. R. Chim.*, 2022, **25**, no. S1, 189-208.

[166] D. Bazin, M. Daudon, E. Elkaim, A. Le Bail, L. Smrcok, *C. R. Chim.*, 2016, **19**, 1535-1541.

[167] D. Bazin, R. J. Papoular, E. Elkaim, R. Weil, D. Thiaudière, C. Pisapia, B. Ménez, N. S. Hwang, F. Tielens, M. Livrozet, E. Bouderlique, J.-Ph. Haymann, E. Letavernier, L. Hennet, V. Frochot, M. Daudon, *C. R. Chim.*, 2022, **25**, no. S1, 343-354.

[168] F. Brunet-Possenti, L. Deschamps, H. Colboc, A. Somogyi, K. Medjoubi, D. Bazin, V. Descamps, *J. Eur. Acad. Dermatol. Venereol.*, 2018, **32**, e442-e443.

[169] M. Daudon, D. Bazin, G. André, P. Jungers, A. Cousson, P. Chevallier, E. Véron, G. Matzen, *J. Appl. Crystallogr.*, 2009, **42**, 109-115.

[170] F. Damay, D. Bazin, M. Daudon, G. André, *C. R. Chim.*, 2016, **19**, 1432-1434.

[171] E. Esteve, Y. Luque, J. Waeytens, D. Bazin, L. Mesnard, Ch. Jouanneau, P. Ronco, A. Dazzi, M. Daudon, A. Deniset-Besseau, *Anal. Chem.*, 2020, **92**, 7388-7392.

[172] D. Bazin, M. Rabant, J. Mathurin, M. Petay, A. Deniset-Besseau, A. Dazzi, Y. Su, E. P. Hessou, F. Tielens, F. Borondics, M. Livrozet, E. Bouderlique, J.-Ph. Haymann, E. Letavernier, V. Frochot, M. Daudon, *C. R. Chim.*, 2022, **25**, no. S1, 489-502.

[173] A. Dazzi, C. B. Prater, *Chem. Rev.*, 2017, **17**, 5146-5173.

[174] J. Mathurin, A. Deniset-Besseau, D. Bazin, E. Dartois, M. Wagner, A. Dazzi, *J. Appl. Phys.*, 2022, **131**, article no. 010901.

[175] R. F. Egerton, M. Malac, *J. Electron Spectrosc. Relat. Phenom.*, 2005, **143**, 43-50.

[176] K. Medjoubi, G. Baranton, A. Somogyi, *Microsc. Microanal.*, 2018, **24**, 252-253.

[177] M. Daudon, O. Traxer, P. Jungers, D. Bazin, *AIP Conf. Proc.*, 2007, **900**, 26-34.

[178] M. Daudon, D. Bazin, E. Letavernier, *Urolithiasis*, 2015, **43**, 5-11.

[179] D. Bazin, C. Leroy, F. Tielens, Ch. Bonhomme, L. Bonhomme-Coury, F. Damay, D. Le Denmat, J. Sadoine, J. Rode, V. Frochot, E. Letavernier, J.-Ph. Haymann, M. Daudon, *C. R. Chim.*, 2016, **19**, 1492-1503.

[180] M. Daudon, E. Letavernier, V. Frochot, J.-Ph. Haymann, D. Bazin, P. Jungers, *C. R. Chim.*, 2016, **19**, 1504-1513.

[181] A. Lionet, M. Haeck, A. Garstka, V. Gnemmi, D. Bazin, E. Letavernier, J.-Ph. Haymann, Ch. Noel, M. Daudon, *C. R. Chim.*, 2016, **19**, 1542-1547.

[182] D. Bazin, D. Portehault, F. Tielens, J. Livage, Ch. Bonhomme, L. Bonhomme, J.-Ph. Haymann, A. Abou-Hassan, G. Laffite, V. Frochot, E. Letavernier, M. Daudon, *C. R. Chim.*, 2016, **19**, 1558-1564.

[183] V. Frochot, V. Castiglione, I. T. Lucas, J.-Ph. Haymann, E. Letavernier, D. Bazin, G. B. Fogazzi, M. Daudon, *Clin. Chim. Acta*, 2021, **515**, 1-4.

[184] A. Dessombz, P. Méria, D. Bazin, M. Daudon, *PLoS One*, 2012, **7**, article no. e51691.

[185] A. Dessombz, P. Méria, D. Bazin, E. Foy, S. Rouzière, R. Weil, M. Daudon, *Prog. Urol.*, 2011, **21**, 940-945.

[186] C. Nguyen, H.-K. Ea, D. Bazin, M. Daudon, F. Lioté, *Arthritis Rheum.*, 2010, **62**, 2829-2830.

[187] H.-K. Ea, C. Nguyen, D. Bazin, A. Bianchi, J. Guicheux, P. Reboul, M. Daudon, F. Lioté, *Arthritis Rheum.*, 2011, **63**, 10-18.

[188] C. Nguyen, H. K. Ea, D. Thiaudière, S. Reguer, D. Hannouche, M. Daudon, F. Lioté, D. Bazin, *J. Synchrotron Radiat.*, 2011, **18**, 475-480.

[189] H.-K. Ea, V. Chobaz, C. Nguyen, S. Nasi, P. van Lent, M. Daudon, A. Dessombz, D. Bazin, G. McCarthy, B. Jolles-Haeberli, A. Ives, D. Van Linthoudt, A. So, F. Lioté, N. Busso, *PLoS One*, 2013, **8**, article no. e57352.

[190] A. Dessombz, C. Nguyen, H.-K. Ea, S. Rouzière, E. Foy, D. Hannouche, S. Réguer, F.-E. Picca, D. Thiaudière, F. Lioté, M. Daudon, D. Bazin, *J. Trace Elem. Med. Biol.*, 2013, **27**, 326-333.

[191] Ch. Nguyen, D. Bazin, M. Daudon, A. Chatron-Colliet, D. Hannouche, A. Bianchi, D. Côme, A. So, N. Busso, F. Lioté, H.-K. Ea, *Arthritis Res. Ther.*, 2013, **15**, article no. R103.

[192] H.-K. Ea, A. Gauffenic, Q. D. Nguyen, N. G. Pham, O. Olivier, V. Frochot, D. Bazin, N. H. Le, C. Marty, A. Ostertag, M. Cohen-Solal, J.-D. Laredo, P. Richette, Th. Bardin, *Arthritis Rheumatol.*, 2021, **73**, 324-329.

[193] A. Gauffenic, D. Bazin, Ch. Combes, M. Daudon, H.-K. Ea, *C. R. Chim.*, 2022, **25**, no. S1, 517-534.

[194] D. Bazin, C. Chappard, C. Combes, X. Carpentier, S. Rouzière, G. André, G. Matzen, M. Allix, D. Thiaudière, S. Reguer, P. Jungers, M. Daudon, *Osteoporosis Int.*, 2009, **20**, 1065-1075.

[195] D. Bazin, M. Daudon, Ch. Chappard, J. J. Rehr, D. Thiaudière, S. Reguer, *J. Synchrotron Radiat.*, 2011, **18**, 912-918.

[196] D. Bazin, A. Dessombz, Ch. Nguyen, H. K. Ea, F. Lioté,

J. Rehr, Ch. Chappard, S. Rouzière, D. Thiaudière, S. Reguer, M. Daudon, *J. Synchrotron Radiat.*, 2014, **21**, 136-142.

[197] Ch. Chappard, G. André, M. Daudon, D. Bazin, *C. R. Chim.*, 2016, **19**, 1625-1630.

[198] C. Bardet, F. Courson, Y. Wu, M. Khaddam, B. Salmon, S. Ribes, J. Thumfart, P. M. Yamaguti, G. Y. Rochefort, M.-L. Figueres, T. Breiderhoff, A. GarciaCastaño, B. Vallée, D. Le Denmat, B. Baroukh, T. Guilbert, A. Schmitt, J.-M. Massé, D. Bazin, G. Lorenz, M. Morawietz, J. Hou, P. Carvalho-Lobato, M. C. Manzanares, J.-C. Fricain, D. Talmud, R. Demontis, F. Neves, D. Zenaty, A. Berdal, A. Kiesow, M. Petzold, S. Menashi, A. Linglart, A. C. Acevedo, R. Vargas-Poussou, D. Müller, P. Houillier, C. Chaussain, *J. Bone Miner. Res.*, 2016, **31**, 498-513.

[199] C. J. Cros, D. Bazin, A. Kellum, V. Rebours, M. Daudon, *C. R. Chim.*, 2016, **19**, 1642-1664.

[200] H. Colboc, Ph. Moguelet, D. Bazin, P. Carvalho, A.-S. Dillies, G. Chaby, H. Maillard, D. Kottler, E. Goujon, Ch. Jurus, M. Panaye, V. Frochot, E. Letavernier, M. Daudon, I. Lucas, R. Weil, Ph. Courville, J.-B. Monfort, F. Chasset, P. Senet, *J. Am. Med. Assc. Dermatol.*, 2019, **155**, 789-796.

[201] H. Colboc, J. Fontaine, D. Bazin, V. Frochot, E. Letavernier, M. Daudon, N. Laporte, S. Rouzière, M. Reby, A. Galezowski, Ch. Forasassi, S. Meaume, *J. Gerontol. A Biol. Sci. Med. Sci.*, 2022, **77**, 27-32.

[202] H. Colboc, Ph. Moguelet, E. Letavernier, V. Frochot, J.-F. Bernaudin, R. Weil, S. Rouzière, P. Seneth, C. Bachmeyeri, N. Laporte, I. Lucas, V. Descamps, R. Amodek, F. Brunet-Possentik, N. Kluger, L. Deschamps, A. Dubois, S. Reguer, A. Somogyi, K. Medjoubi, M. Refregiers, M. Daudon, D. Bazin, *C. R. Chim.*, 2022, **25**, no. S1, 445-476.

[203] H. Colboc, Th. Bettuzzi, M. Badrignans, D. Bazin, A. Boury, E. Letavernier, V. Frochot, E. Tang, Ph. Moguelet, N. Ortonne, N. de Prost, S. Ingen-Housz-Oro, *C. R. Chim.*, 2022, **25**, no. S1, 477-487.

[204] A. A. Pozdzik, P. Demetter, M. Tooulou, A. Hamade, J. Nortier, D. Bazin, M. Daudon, *J. Nanomed. Nanotechnol.*, 2015, **6**, article no. 1000342.

[205] E. Bouderlique, E. Tang, J. Zaworski, A. Coudert, D. Bazin, F. Borondics, J.-Ph. Haymann, G. Leftheriotis, L. Martin, M. Daudon, E. Letavernier, *Int. J. Mol. Sci.*, 2022, **23**, article no. 2302.

[206] L. Louvet, D. Bazin, J. Büchel, S. Steppan, J. Passlick-Deetjen, Z. A. Massy, *PLoS One*, 2015, **10**, article no. e0115342.

[207] F. Preitner, A. Laverriere, S. Metref, A. Da Costa, C. Roger, S. Rotman, D. Bazin, M. Daudon, Ch. Sandt, A. Dessombz, B. Thorens, *Am. J. Physiol. Renal Physiol.*, 2013, **305**, F786-F795.

[208] E. Letavernier, G. Kauffenstein, L. Huguet, N. Navasiolava, E. Bouderlique, E. Tang, L. Delaitre, D. Bazin, M. de Frutos, C. Gay, J. Perez, M. C. Verpont, J.-Ph. Haymann, V. Pomozi, J. Zoll, O. Le Saux, M. Daudon, G. Leftheriotis, L. Martin, *J. Am. Soc. Nephrol.*, 2018, **29**, 2337-2347.

[209] H. Bilbault, J. Perez, L. Huguet, S. Vandermeersch, S. Placier, N. Tabibzadeh, V. Frochot, E. Letavernier, D. Bazin, M. Daudon, J.-P. Haymann, *Sci. Rep.*, 2018, **8**, article no. 16319.

[210] E. Bouderlique, E. Tang, J. Perez, A. Coudert, D. Bazin, M.-Ch. Verpont, Ch. Duranton, I. Rubera, J.-Ph. Haymann, G. Leftheriotis, L. Martin, M. Daudon, E. Letavernier, *Am. J. Pathol.*, 2019, **189**, 2171-2180.

[211] C. Poulard, A. Dessombz, M. Daudon, D. Bazin, *C. R. Chim.*, 2016, **19**, 1597-1609.

[212] A. Nouaille, A. Descazeaud, F. Desgrandchamps, D. Bazin, M. Daudon, A. Masson Lecomte, P. Mongiat-Artus, P. Méria, *Prog. Urol.*, 2021, **31**, 348-356.

[213] G. Laffite, C. Leroy, C. Bonhomme, L. Bonhomme-Coury, E. Letavernier, M. Daudon, V. Frochot, J. P. Haymann, S. Rouzière, I. T. Lucas, D. Bazin, F. Babonneau, A. Abou-Hassan, *Lab. Chip*, 2016, **16**, 1157-1160.

[214] F. Tielens, J. Vekeman, D. Bazin, M. Daudon, *C. R. Chim.*, 2022, **25**, no. S1, 209-218.

[215] Th. Debroise, E. Colombo, G. Belletti, J. Vekeman, Y. Su, R. Papoular, N. S. Hwang, D. Bazin, M. Daudon, P. Quaino, F. Tielens, *Cryst. Growth Des.*, 2020, **20**, 2553-2561.

[216] I. Petit, G. D. Belletti, Th. Debroise, M. J. Llansola-Portoles, I. T. Lucas, C. Leroy, Ch. Bonhomme, L. Bonhomme-Coury, D. Bazin, M. Daudon, E. Letavernier, J. Ph. Haymann, V. Frochot, F. Babonneau, P. Quaino, F. Tielens, *ChemistrySelect*, 2018, **3**, 8801-8812.

[217] J. Vekeman, J. Torres, C. E. David, E. Van de Perre, K. M. Wissing, E. Letavernier, D. Bazin, M. Daudon, A. Pozdzik, F. Tielens, *Nanomaterials*, 2021, **11**, article no. 1763.

[218] D. Bazin, C. Mottet, G. Tréglia, J. Lynch, *Appl. Surf. Sci.*, 2000, **164**, 140-146.

[219] D. Bazin, C. Mottet, G. Tréglia, *Appl. Catal. A*, 2000, **200**, 47-54.

[220] D. Bazin, *Top. Catal.*, 2002, **18**, 79-84.

[221] D. Bazin, D. Sayers, J. Lynch, L. Guczi, G. Tréglia, C. Mottet, *Oil Gas Sci. Technol.—Rev. IFP*, 2006, **61**, 677-689.

[222] D. Bazin, *Macromol. Res.*, 2006, **14**, 230-234.

[223] D. Bazin, *C. R. Chim.*, 2014, **17**, 615-624.

[224] D. Bazin, J. Vekeman, Q. Wang, X. Deraet, F. De Proft, H. Guesmi, F. Tielens, *C. R. Chim.*, 2022, **25**, no. S3, Online first.

[225] T. Campbell, A. J. Dent, S. Diaz-Moreno, J. Evans, S. G. Fiddy, M. A. Newton, S. Turin, *Chem. Commun.*, 2002, **30**, 304-305.

[226] S. Schneider, D. Bazin, F. Garin, G. Maire, M. Capelle, G. Meunier, R. Noirot, *Appl. Catal.*, 1999, **189**, 139-145.

[227] S. Schneider, D. Bazin, G. Meunier, R. Noirot, M. Capelle, F. Garin, G. Maire, *Catal. Lett.*, 2001, **71**, 155-162.

[228] D. Bazin, F. Tielens, *Appl. Catal.*, 2015, **504**, 631-641.

[229] F. Tielens, D. Bazin, *C. R. Chim.*, 2018, **21**, 174-181.

[230] I. C. Oğuz, H. Guesmi, D. Bazin, F. Tielens, *J. Phys. Chem. C*, 2019, **123**, 20314-20318.

[231] N. Takagi, K. Ishimura, R. Fukuda, M. Ehara, S. Sakaki, *J. Phys. Chem. A*, 2019, **123**, 7021-7033.

[232] J. Vekeman, Q. Wang, X. Deraet, D. Bazin, F. De Proft, H. Guesmi, F. Tielens, *Chem. Phys. Chem.*, accepted.

[233] M. Livrozet, E. Esteve, M. Daudon, J. Zaworski, J.-Ph. Haymann, V. Frochot, J.-J. Boffa, D. Bazin, J.-F. Benoist, E. Letavernier, *Kidney Int.*, 2020, **97**, 1307-1308.

[234] E. Letavernier, C. Verrier, F. Goussard, J. Perez, L. Huguet, J.-Ph. Haymann, L. Baud, D. Bazin, M. Daudon, *Kidney Int.*, 2016, **90**, 809-817.

[235] M. Daudon, V. Frochot, D. Bazin, P. Jungers, *C. R. Chim.*, 2016, **19**, 1514-1526.

[236] J. M. Baumann, B. Affolter, *World J. Nephrol.*, 2014, **3**, 256-267.
[237] Ph. Jouvet, L. Priqueler, M.-F. Gagnadoux, D. Jan, A. Beringer, F. Lacaille, Y. Revillon, M. Broyer, M. Daudon, *Kidney Int.*, 1998, **53**, 1412-1416.
[238] G. B. Fogazzi, *Nephrol. Dial. Transplant.*, 1996, **11**, 379-387.
[239] A. Randall, *Ann. Surg.*, 1937, **105**, 1009-1027.
[240] A. Randall, *N. Engl. J. Med.*, 1936, **214**, 234-242.
[241] M. Daudon, O. Traxer, J. C. Williams, D. Bazin, "Randall's plaque", in *Urinary Tract Stone Disease* (N. P. Rao, G. M. Preminger, J. P. Kavangh, eds.), Springer, Berlin, ISBN 978-1-84800-361-3.
[242] E. Letavernier, D. Bazin, M. Daudon, *C. R. Chim.*, 2016, **19**, 1456-1460.
[243] D. Bazin, E. Letavernier, Ch. Jouanneau, P. Ronco, Ch. Sandt, P. Dumas, G. Matzen, E. Véron, J.-Ph. Haymann, O. Traxer, P. Conort, M. Daudon, *C. R. Chim.*, 2016, **19**, 1461-1469.
[244] E. Van de Perre, D. Bazin, V. Estrade, E. Bouderlique, K. M. Wissing, M. Daudon, E. Letavernier, *C. R. Chim.*, 2022, **25**, no. S1, 373-391.
[245] L. Huguet, M. Le Dudal, M. Livrozet, D. Bazin, V. Frochot, J. Perez, J. Ph. Haymann, I. Brocheriou, M. Daudon, E. Letavernier, *Urolithiasis*, 2018, **46**, 333-341.
[246] R. Coscas, M. Bensussan, M.-P. Jacob, L. Louedec, Z. Massy, J. Sadoine, M. Daudon, C. Chaussain, D. Bazin, J.-B. Michel, *Atherosclerosis*, 2017, **259**, 60-67.
[247] Z. Khavandga, H. Roman, J. Li, S. Lee, H. Vali, J. Brinckmann, E. C. Davis, M. Murshed, *J. Bone Miner. Res.*, 2014, **29**, 327-337.
[248] C. Cerini, S. Geider, B. Dussol, C. Hennequin, M. Daudon, S. Veesler, S. Nitsche, R. Boistelle, P. Berthézène, P. Dupuy, A. Vazi, Y. Berland, J.-Ch. Dagorn, J.-M. Verdier, *Kidney Int.*, 1999, **55**, 1776-1786.
[249] R. E. Wuthier, L. N. Y. Wu, G. R. Sauer, B. R. Genge, T. Yoshimori, Y. Ishikawa, *Bone Miner.*, 1992, **17**, 290-295.
[250] S. R. Khan, D. E. Rodriguez, L. B. Gower, M. Monga, *J. Urol.*, 2012, **187**, 1094-1100.
[251] N. X. Chen, K. D. O'Neil, S. M. Moe, *Kidney Int.*, 2018, **93**, 343-354.
[252] N. Niederhoffer, I. Lartaud-Idjouadiene, Ph. Giummelly, C. Duvivier, R. Peslin, J. Atkinson, *Hypertension*, 1997, **29**, 999-1006.
[253] L. Estépa-Maurice, C. Hennequin, C. Marfisi, C. Bader, B. Lacour, M. Daudon, *Am. J. Clin. Pathol.*, 1996, **105**, 576-582.
[254] N. Gopalakrishnan, D. Rajasekar, J. Dhanapriya, T. Dineshkumar, R. Sakthirajan, T. Balasubramaniyan, V. Murugesan, *Saudi J. Kidney Dis. Transplant.*, 2018, **29**, 462-465.
[255] D. Glicklich, H. E. Gruber, A. J. Matas, V. A. Tellis, G. Karwa, K. Finley, C. Salem, R. Soberman, J. E. Seegmiller, *Q. J. Med.*, 1988, **258**, 785-793.
[256] E.-R. Gagné, E. Deland, M. Daudon, L.-H. Noel, T. Nawar, *Am. J. Kidney Dis.*, 1994, **24**, 104-107.
[257] P. Stratta, G. B. Fogazzi, C. Canavese, A. Airoldi, R. Fenoglio, C. Bozzola, I. Ceballos-Picot, G. Bollée, M. Daudon, *Am. J. Kidney Dis.*, 2010, **56**, 585-590.
[258] S. A. George, S. Al-Rushaidan, I. Francis, M. R. N. Nampoory, *Exp. Clin. Transplant.*, 2017, **5**, 574-577.
[259] M. A. Perazella, *Am. J. Med.*, 1999, **106**, 459-465.
[260] S. R. Khan, *C. R. Chim.*, 2022, **25**, no. S1, 355-372.
[261] M. J. Macıa, E. Garcıa, P. J. Vidaurre, *J. Ethnopharmacol.*, 2005, **97**, 337-350.
[262] B. Hannache, D. Bazin, A. Boutefnouchet, M. Daudon, *Prog. Urol.*, 2012, **22**, 577-582.
[263] J. Rode, D. Bazin, A. Dessombz, Y. Benzerara, E. Letavernier, N. Tabibzadeh, A. Hoznek, M. Tligui, O. Traxer, M. Daudon, J.-Ph. Haymann, *Nutrients*, 2019, **11**, article no. 256.
[264] M. Albersmeyer, R. Hilge, A. Schröttle, M. Weiss, Th. Sitter, V. Vielhauer, *BMC Nephrol.*, 2012, **13**, article no. 141.
[265] D. Bazin, E. Letavernier, J.-Ph. Haymann, F. Tielens, A. Kellum, M. Daudon, *C. R. Chim.*, 2016, **19**, 1548-1557.
[266] S. B. Lotito, B. Frei, *Free Radic. Biol. Med.*, 2006, **41**, 1727-1746.
[267] H. P. Carr, E. Lombi, H. Kupper, S. P. McGrath, M. H. Wong, *Agron. Sustain. Dev.*, 2003, **23**, 705-710.
[268] J. Zaworski, E. Bouderlique, D. Anglicheau, J.-P. Duong Van Huyen, V. Gnemmi, J.-B. Gibier, Y. Neugebauer, J.-Ph. Haymann, D. Bazin, V. Frochot, M. Daudon, E. Letavernier, *Kidney Int. Rep.*, 2020, **5**, 737-741.
[269] E. Esteve, D. Bazin, C. Jouanneau, S. Rouzière, A. Bataille, A. Kellum, K. Provost, Ch. Mocuta, S. Reguer, P. Ronco, J. Rehr, J.-Ph. Haymann, E. Letavernier, A. Hertig, *C. R. Chim.*, 2016, **19**, 1580-1585.
[270] E. Esteve, D. Bazin, C. Jouanneau, S. Rouzière, A. Bataille, A. Kellum, K. Provost, Ch. Mocuta, S. Reguer, P. Ronco, J. Rehr, J.-Ph. Haymann, E. Letavernier, A. Hertig, *C. R. Chim.*, 2016, **19**, 1586-1596.
[271] E. Esteve, S. Reguer, C. Boissiere, C. Chanéac, G. Lugo, C. Jouanneau, C. Mocuta, D. Thiaudière, N. Leclercq, B. Leyh, J. F. Greisch, J. Berthault, M. Daudon, P. Ronco, D. Bazin, *J. Synchrotron Radiat.*, 2017, **24**, 991-999.
[272] S. Kaščáková, C. M. Kewish, S. Rouzière, F. Schmitt, R. Sobesky, J. Poupon, C. Sandt, B. Francou, A. Somogyi, D. Samuel, E. Jacquemin, A. Dubart-Kupperschmitt, T. H. Nguyen, D. Bazin, J.-C. DuclosVallée, C. Guettier, F. Le Naour, *J. Pathol. Clin. Res.*, 2016, **2**, 175-186.
[273] B. Pradère, F. Poulon, E. Compérat, I. Lucas, D. Bazin, S. Doizi, O. Cussenot, O. Traxer, D. Abi Haidar, *J. Biophoton.*, 2018, **11**, article no. e201800065.
[274] R. Oun, Y. E. Moussa, N. J. Wheate, *Dalton Trans.*, 2018, **47**, 6645-6653.
[275] Y. Min, J. M. Caster, M. J. Eblan, A. Z. Wang, *Chem. Rev.*, 2015, **115**, 11147-11190.
[276] D. Bazin, D. Sayers, J. Rehr, *J. Phys. Chem. B*, 1997, **101**, 11040-11050.
[277] D. Bazin, D. Sayers, J. J. Rehr, C. Mottet, *J. Phys. Chem.*, 1997, **101**, 5332-5336.
[278] D. Bazin, J. Rehr, *J. Phys. Chem. C*, 2011, **115**, 23233-23236.
[279] J. Moonen, J. Slot, L. Lefferts, D. Bazin, H. Dexpert, *Physica B*, 1995, **208**, 689-690.
[280] D. Bazin, L. Guczi, J. Lynch, *Appl. Catal. A*, 2002, **226**, 87-113.
[281] D. Bazin, J. Lynch, M. Ramos-Fernandez, *Oil Gas Sci. Technol.—Rev. IFP*, 2003, **58**, 667-683.
[282] D. Bazin, J. Rehr, *J. Phys. Chem. B*, 2003, **107**, 12398-12402.
[283] D. Bazin, H. Dexpert, J. Lynch, J. P. Bournonville, *J. Synchrotron Radiat.*, 1999, **6**, 465-467.
[284] D. Bazin, J. Rehr, *Catal. Lett.*, 2003, **87**, 85-90.
[285] R. Revel, D. Bazin, Ph. Parent, C. Laffon, *Catal. Lett.*, 2001, **74**, 189-192.

[286] Ch. Sandt, Ch. Peng, N. Trcera, F. Chiappini, A.-M. Flank, C. Guettier, P. Dumas, *Anal. Chem.*, 2012, **84**, 10260-10266.
[287] F. Le Naour, L. Gadea, M. Danulot, I. Yousef, E. Vibert, M. Wavelet, S. Kaščáková, D. Castaing, D. Samuel, P. Dumas, C. Guettier, *Gastroenterology*, 2015, **148**, 295-298.
[288] M. Daudon, P. Jungers, D. Bazin, J. C. Williams Jr., *Urolithiasis*, 2018, **46**, 459-470.
[289] E. X. Keller, V. De Coninck, M. Audouin, S. Doizi, D. Bazin, M. Daudon, O. Traxer, *J. Biophoton.*, 2019, **12**, article no. e201800227.
[290] D. Bazin, Ch. Jouanneau, S. Bertazzo, Ch. Sandt, A. Dessombz, M. Réfrégiers, P. Dumas, J. Frederick, J.-Ph. Haymann, E. Letavernier, P. Ronco, M. Daudon, *C. R. Chim.*, 2016, **19**, 1439-1454.
[291] D. Bazin, E. Letavernier, J.-Ph. Haymann, *C. R. Chim.*, 2016, **19**, 1395-1403.
[292] X. Carpentier, D. Bazin, P. Jungers, S. Reguer, D. Thiaudière, M. Daudon, *J. Synchrotron Radiat.*, 2010, **17**, 374-379.
[293] G. Snell, C. Cork, R. Nordmeyer, E. Cornell, G. Meigs, D. Yegian, J. Jaklevic, J. Jin, R. C. Stevens, Th. Earnest, *Structure*, 2004, **12**, 537-545.
[294] S. J. A. Figueroa, D. B. Beniz, J. C. Mauricio, J. R. Piton, S. A. Parry, G. Cibin, *J. Synchrotron Radiat.*, 2018, **25**, 953-959.
[295] P. J. Campagnola, A. C. Millard, M. Terasaki, P. E. Hoppe, C. J. Malone, W. A. Mohler, *Biophys. J.*, 2002, **82**, 493-508.
[296] A. Benoit, G. Latour, M.-C. Schanne-Klein, J.-M. Allain, *J. Mech. Behav. Biomed. Mater.*, 2016, **60**, 93-105.
[297] A. Nazac, S. Bancelin, B. Teig, B. H. Ibrahim, H. Fernandez, M.-C. Schanne-Klein, A. De Martino, *Microsc. Res. Tech.*, 2015, **78**, 723-730.
[298] S. Bancelin, C. Aimé, I. Gusachenko, L. Kowalczuk, G. Latour, T. Coradin, M.-C. Schanne-Klein, *Nat. Commun.*, 2014, **5**, article no. 4920.
[299] D. Bazin, *C. R. Chim.*, 2022, **25**, no. S3, Forthcoming.
[300] O. Klementieva, Ch. Sandt, I. Martinsson, M. Kansiz, G. K. Gouras, F. Borondics, *Adv. Sci.*, 2020, **7**, article no. 1903004.
[301] D. Bazin, E. Bouderlique, E. Tang, M. Daudon, J.-Ph. Haymann, V. Frochot, E. Letavernier, E. Van de Perre, J. C. Williams Jr., J. E. Lingeman, F. Borondics, *C. R. Chim.*, 2022, **25**, no. S1, 105-131.
[302] M. P. Linnes, A. E. Krambeck, L. Cornell, J. C. Williams Jr., M. Korinek, E. J. Bergstralh, X. Li, A. D. Rule, C. M. McCollough, T. J. Vrtiska, J. C. Lieske, *Kidney Int.*, 2013, **84**, 818-825.
[303] J. C. Williams, J. E. Lingeman, M. Daudon, D. Bazin, *C. R. Chim.*, 2022, **25**, no. S1, 61-72.

Comptes Rendus
Chimie
2022, Vol. 25, Special Issue S1, p. 37-60
https://doi.org/10.5802/crchim.101

Microcrystalline pathologies: Clinical issues and nanochemistry / *Pathologies microcristallines : questions cliniques et nanochimie*

Scanning electron microscopy—a powerful imaging technique for the clinician

Dominique Bazin [*, a, b], **Elise Bouderlique** [c, d, e], **Michel Daudon** [c, d, e], **Vincent Frochot** [c, d, e], **Jean-Philippe Haymann** [c, d, e], **Emmanuel Letavernier** [c, d, e], **Frederik Tielens** [f] **and Raphaël Weil** [a]

[a] Institut de Chimie Physique, UMR CNRS 8000, Bâtiment 350, Université Paris Saclay, 91405 Orsay cedex, France

[b] Laboratoire de physique des solides, UMR CNRS 8502, Bâtiment 510, Université Paris-Sud, 91405 Orsay cedex, France

[c] Sorbonne Universités, UPMC Univ Paris 06, UMR S 702, Paris, France

[d] INSERM, UMR S 702, Paris, France

[e] Explorations fonctionnelles multidisciplinaires, AP-HP, Hôpital Tenon, Paris, France

[f] General Chemistry (ALGC), Vrije Universiteit Brussel (Free University Brussels-VUB), Pleinlaan 2, 1050 Brussel, Belgium

E-mails: dominique.bazin@universite-paris-saclay.fr (D. Bazin), Eliseboud@aol.com (E. Bouderlique), michel.daudon@aphp.fr (M. Daudon), vincent.frochot@aphp.fr (V. Frochot), jean-Philippe.haymann@aphp.fr (J.-P. Haymann), emmanuel.letavernier@aphp.fr (E. Letavernier), frederik.tielens@vub.be (F. Tielens), raphael.weil@u-psud.fr (R. Weil)

Abstract. Since its first use several decades ago, scanning electron microscopy has been used in numerous investigations dedicated to biological systems. This contribution focuses on observations on pathological calcifications in order to review several major applications of primary importance to the clinician. Among these, we highlight such observations as medical diagnostic tools in pathologies arising from primary hyperoxaluria and urinary infections.

Keywords. Scanning electron microscopy, Pathological calcifications, Kidney stones, Breast calcifications, Breast cancer.

Published online: 9 August 2021, Issue date: 1 September 2022

1. Introduction

The history of the electron microscope dates back to the first third of the twentieth century when E. Ruska and M. Knoll, from the University of Berlin, created the first instrument in 1931 [1,2]. Basically, scanning electron microscopy (SEM) uses a finely focused beam of electrons in order to produce a resolution image of a sample [3]. In the case of biological samples, such an experimental setup allows imaging with a lateral resolution around 200 nm

* Corresponding author.

without sample preparation (magnification around 45,000).

Several investigations of structures related to kidney stones (KS) were performed as early as over 40 years ago [4–9]. Fujita *et al.* [5] showed that SEM precisely describes the three-dimensional architecture of the endothelial cell. As far as KS are concerned, Phaneuf-Mimeault and Tawashi [6] showed that the surface crystals have random axial orientations and that the gross configuration seems to be determined by the fibrous organic matrix.

Nowadays, SEM of pathological calcifications [10–12] is a very active research field. Typical recent publications include studies on kidney [13–24], salivary stones [25], breast [26–28], cardiovascular system [29, 30], cartilage [31,32], gallstones [33], prostatic stones [34,35], thyroid [36], liver [37], ileal [38], or medical devices [39]. These examples convincingly show that SEM is an essential laboratory tool that continues to provide new clues about the pathogenesis of these biological samples.

This success may be ascribed to the significant recent advances in the various components of a scanning electron microscope, namely the electron gun, optics, and detectors, enabling entirely new opportunities [3,40]. For instance, detection at low voltage (between 0.5 and 2 kV) without the usual surface carbon deposition leads to novel breakthroughs regarding pathological calcifications [41,42] as well as tissue alterations [43,44]. Additionally, biological samples used for nanometer scale observations are compatible with other techniques such as Fourier Transform Infra-Red (FTIR), Raman, and Nano-UV spectroscopies [45,46].

The aim of this survey is to use selected examples to illustrate different research applications of SEM. We show that a precise description of crystallite morphology and surface may be a basis for diagnosis or deciphering the biomechanism governing the genesis of concretions and ectopic calcifications [47,48]. We define "nanocrystals" and "crystallites" according to Van Meerssche and Feneau-Dupont, i.e., crystallites (measuring typically some tens of micrometers) are made of a collection of nanocrystals (measuring typically some hundreds of nanometers), to describe the structural hierarchy of pathological calcifications [49]. We will start by briefly recapitulating the underlying physics of SEM.

2. Basic SEM physics

The first component of a SEM is the electron gun [50]. Conventional electron guns use thermal energy to emit electrons from a cathode. The main disadvantage of this experimental device is related to the surface area of the source which emits electrons. Its dimension is rather large (10–30 μm) and the energy spread spans a few electron volts, because of the excess thermal energy supplied by heating. A new type of electron gun was developed in the late twentieth century. It is based on the tunneling, or Schottky effect, to produce electrons from a tip, in which case the source size is less than 10 nm, and the energy dispersion is now only a few tenths of an electron volt.

The second key element defining the properties of the SEM is constituted by a set of detectors. These depend on the fact that the electron beam focused over a surface (Figure 1) produces various kinds of electrons as well as photons [3], allowing the experimentalist to gather information regarding the surface topography and the elemental composition of the sample at the submicrometer scale [51].

Among these components, a backscatter electron detector (BSD) detects elastically scattered electrons, and takes advantages of the fact that higher atomic number atoms have a higher probability of producing an elastic collision because of their greater cross-sectional area [52]. Thus, brightness of the image obtained is directly proportional to atomic number, so backscatter electron (BSE) images provide an elegant way to distinguish different chemical phases at the sample surface. BSE detectors are typically located above the sample in the sample chamber.

The so called secondary electrons [53] are lower energy electrons emitted when a solid is irradiated with high energy electrons or other particles; two kinds of detectors, namely the conventional Everhart–Thornley type and in-lens detectors, are usually positioned in the sample chamber. The former produces images which are more dependent on the sample topography than the ones obtained by a BSE detector.

One of the key advantages of modern SEM instruments is their spatial resolution [51–54]. By using electrons instead of photons for imaging samples, SEM can achieve nanometer spatial resolution [55–57]. This ability depends on several factors such

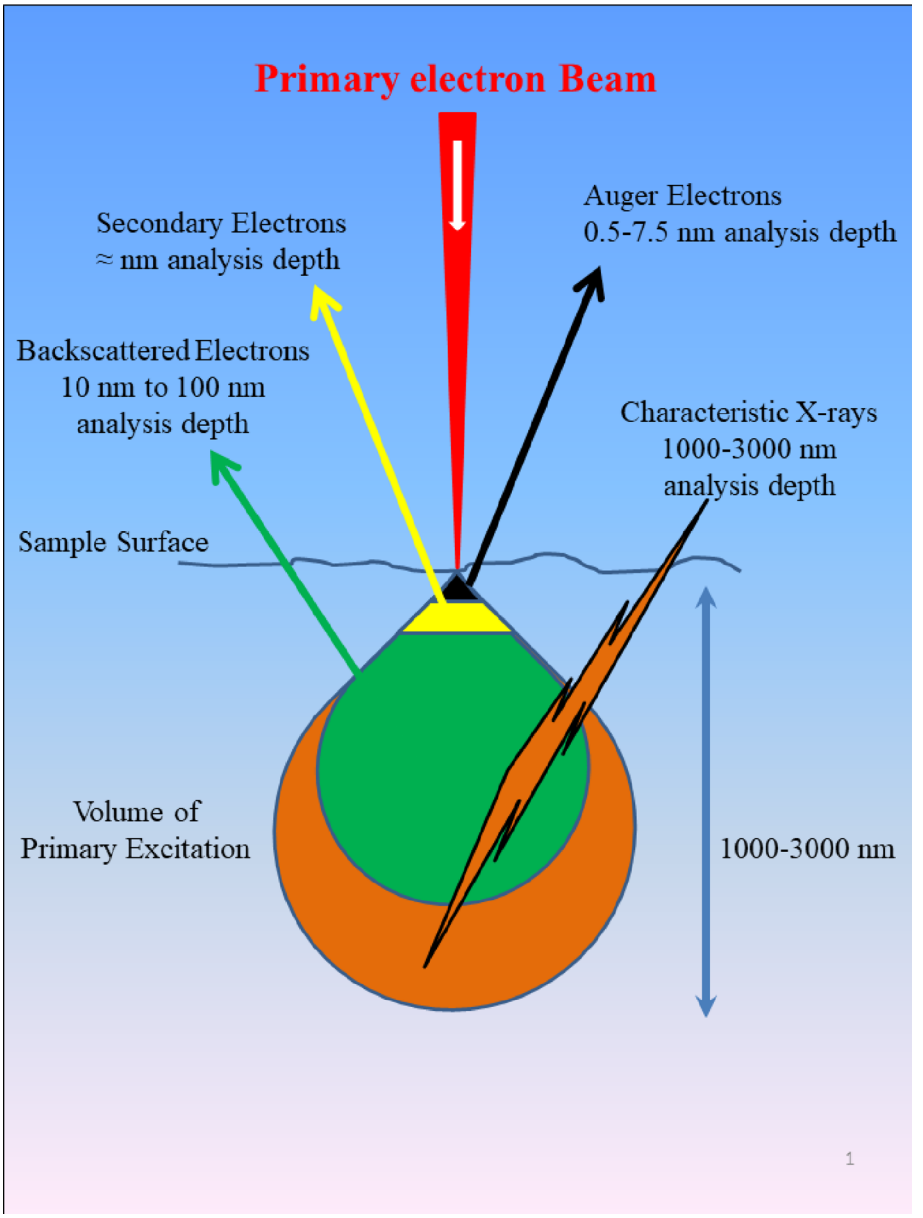

Figure 1. Schematic representation of the different kinds of particles i.e., electrons (backscattered electrons, secondary electrons, Auger electrons) and photons produced after the irradiation of matter by primary electrons. The analysis depth is given for the different particles.

as the electron spot size, which is determined by the way electrons are produced and focused, as well as the interaction volume of the electron beam with the sample. Even though they fall short of providing atomic resolution, some SEMs can typically achieve resolution between 1 and 20 nm. The distance from the final pole piece of the lens to the sample, called working distance, is about a few millimeters. To improve the resolution, working distance, source energy, and current density are crucial parameters.

3. Sample preparation

Visualizing biological samples with an electron microscope is not easy, mostly because of the intrinsic nature of the electron and matter interactions which defined the image formation. In order to be able to collect SEM images, biological samples have to be placed inside high vacuum. Such experimental conditions usually lead to a quite complex preparation protocol [58–60].

In the case of pathological calcifications, it is of primary importance to preserve the physicochemical integrity of the abnormal deposit. Such priority is associated to the relationship which exists between the physicochemistry of the calcification (i.e., the chemical composition and the crystal morphology) and the pathology which induced its formation [61–64]. In the case of KS, there is simply no preparation. The concretions are directly positioned under the electron beam. In our case, a field-effect "gun" microscope, namely a Zeiss SUPRA55-VP SEM, was used for the observation of microstructure. High-resolution observations were obtained by an Everhart–Thornley SE detector. To maintain the physicochemical integrity of the samples, measurements were taken without the usual deposits of carbon at the surface of the sample (Figure 2).

Regarding tissue embedded in paraffin, three to five micron slices are deposited on low-e microscope slides (MirrIR, Kevley Technologies, Tienta Sciences, Indianapolis). The paraffin was then chemically removed (xylene 100% during 30 min to 4 h) in order to improve the crystal detection under the microscope (Figure 2).

4. Crystal morphology

It is now well accepted that a relationship exists between crystallographic structure and morphology, exemplified by Jean Baptiste Louis Romé de l'Isle's discovery of the fact that the various shapes of crystals of the same natural or artificial substance are all intimately related to each other. More precisely, by measuring the angles between the faces of crystals, he established the fundamental principle that these angles are characteristic for a given substance. This discovery is known as the law of constant angles [65].

A second important relationship, the law of symmetry, established by Haüy [66], states that the edges, angles, and faces of a crystal form are related by symmetry. Thus, for example, when one face of an octahedron is modified by its combination with another form (for example by truncation), all other faces of the octahedron should be modified at this point in the same way.

In fact, according to the Gibbs–Curie–Wulff theorem [67], the equilibrium crystal form will be such as to minimize the total surface energy for a given volume. This equilibrium form is defined in vacuum. Unfortunately, the presence of other compounds can modify this equilibrium through adsorption processes. As recalled by Zhang [68], the shape of a crystal is governed by the relative growth rates of each of the crystal faces present. The most prominent face of a crystal is the slowest growing, while the smallest face is the fastest growing [69]. The interplay between thermodynamics and kinetics during the growth process makes predictions of the final geometry challenging [70].

5. SEM as diagnostic tool

Some authors have suggested SEM as a fundamental method for routine urinary stone identification, which also reveals additional detailed information unobtainable by other methods, such as the morphology, the size, and the elemental composition of crystallites present in kidney stones [18]. At this point, recall that more than one hundred chemical phases have been identified in kidney stones and more than 100 different etiologies may be involved in stone formation [61–64]. Moreover, some chemical phases, such as whewellite ($CaC_2O_4{\cdot}H_2O$) or weddellite ($CaC_2O_4{\cdot}2{\cdot}xH_2O$ (with x = 0–0.5) [71] may correspond to very different morphologies. According to the morphoconstitutional model [61–64,72], five different morphological aspects of whewellite stones, namely Ia, Ib, Ic, Id, and Ie, correspond to five different lithogenic conditions. Also, phase transformations such as the transition of weddellite to whewellite (for the oxalates) or brushite to apatite (for the phosphates) occur (Figure 3). Finally, it is not possible to evaluate the carbonation rate of apatite, an essential parameter related to infection [73], through SEM. Thus, due to this diversity of chemical phases, crystal morphology within a single chemical phase, as well as the possibility of phase transitions,

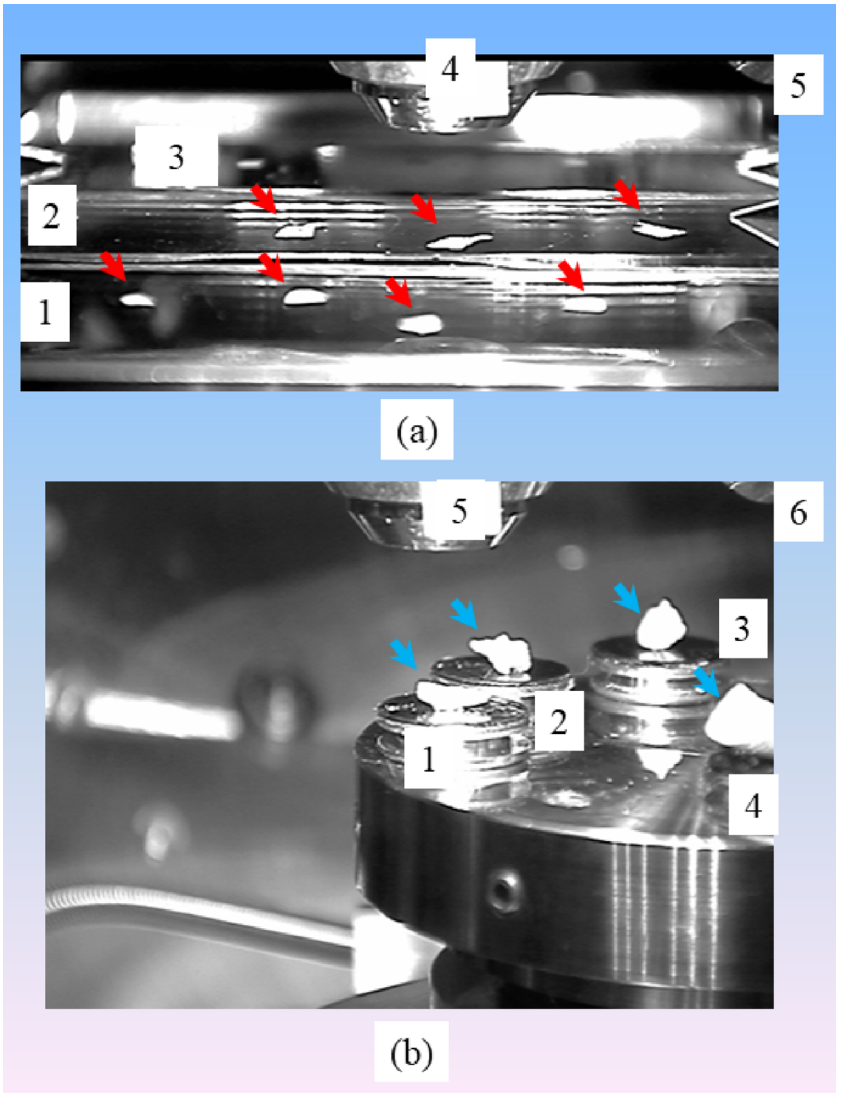

Figure 2. (a) Skin biopsies (red arrows) positioned on low-e microscope slides (1, 2, 3) (MirrIR, Kevley Technologies, Tienta Sciences, Indianapolis) compatible with Fourier transform Infrared Spectroscopy, an electron gun (4), an Everhart–Thornley SE detector (5). (b) Kidney stones (blue arrows) on their support (1 to 4), an electron gun (5), an Everhart–Thornley SE detector (6).

SEM cannot replace the gold standard FTIR spectroscopy [74–76].

Nevertheless, there are numerous exceptions where SEM provides detailed information at the micrometer scale, which can be of primary importance for the clinician (Figure 4).

For example, in the case of primary hyperoxaluria, the most severe lithogenetic disease, we have shown that the morphology of whewellite crystallites is distinctive (Figures 4a and b) from that observed in the case of dietary hyperoxaluria. Such direct examination constitutes a simple, rapid, and inexpensive tool that would suggest early diagnosis of primary hyperoxaluria type 1 [41,42]. Recall that multiple defective genes can underlie this disease so the genetic approach to diagnosis can be long and expensive. For calcium oxalate dihydrate, it has been established that the presence of dodecahedral crystallites

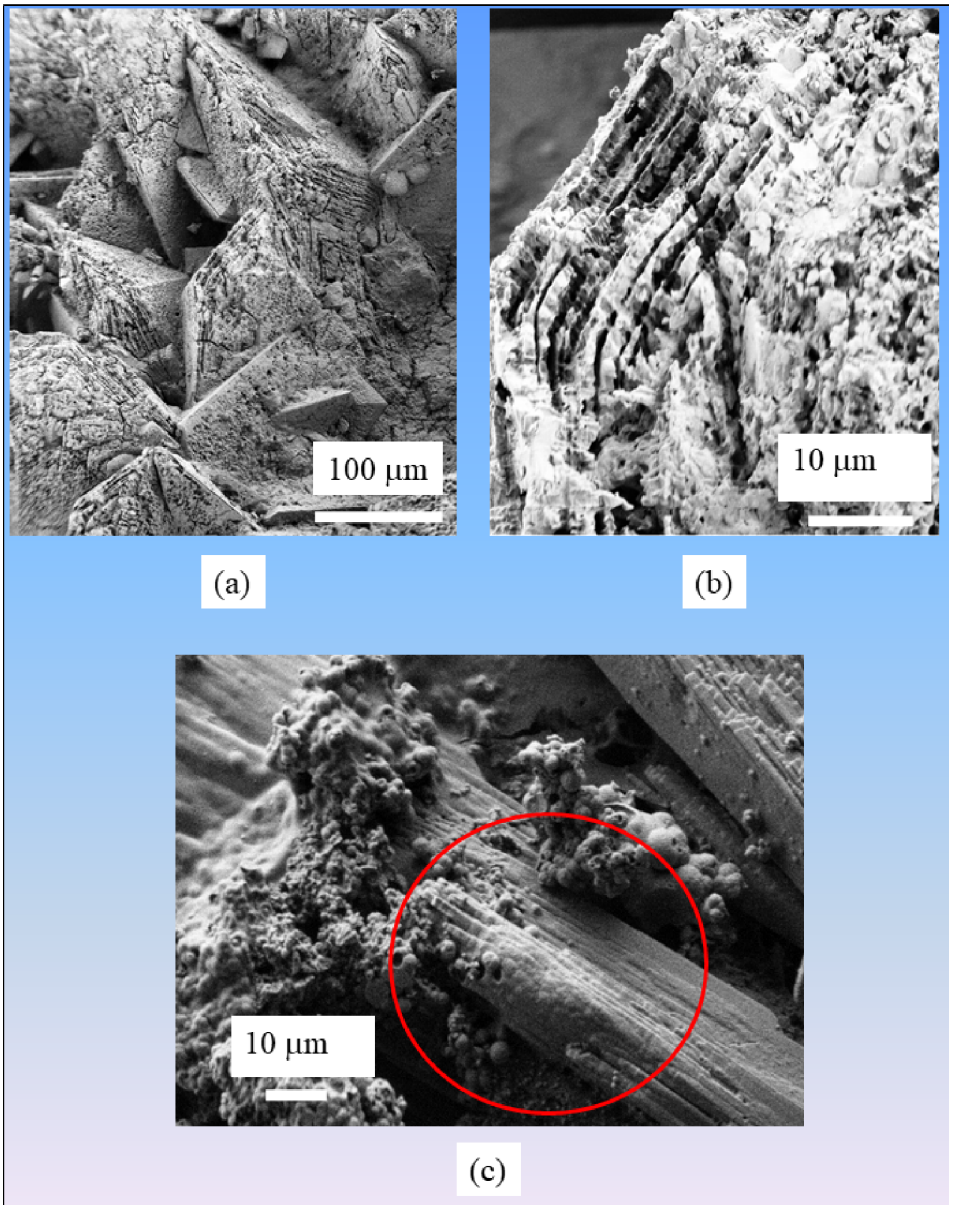

Figure 3. (a) SEM observation showing weddellite crystallites displaying their usual bipyramidal morphologies with alteration at their surface induced by a phase transition. (b) SEM observations showing the transition between acicular brushite and spherical apatite.

(i.e., bipyramidal with a thick zone between the two pyramids) is indicative of heavy hypercalciuria [77].

Another case where SEM makes a crucial contribution concerns kidney stones related to infection (Figure 4c). In patients with kidney stones without struvite, and with negative urine culture results, we have proposed SEM observations in order to confirm the possible presence of bacterial imprints [73,78]. Of note, due to the crystal size such bacterial imprints cannot be detected in struvite, except in the areas of the stone that contain apatite crystals.

Regarding the quantitative aspect, such approach occurs in the case of crystalluria when the number of crystallites is considered [77], but it is difficult to

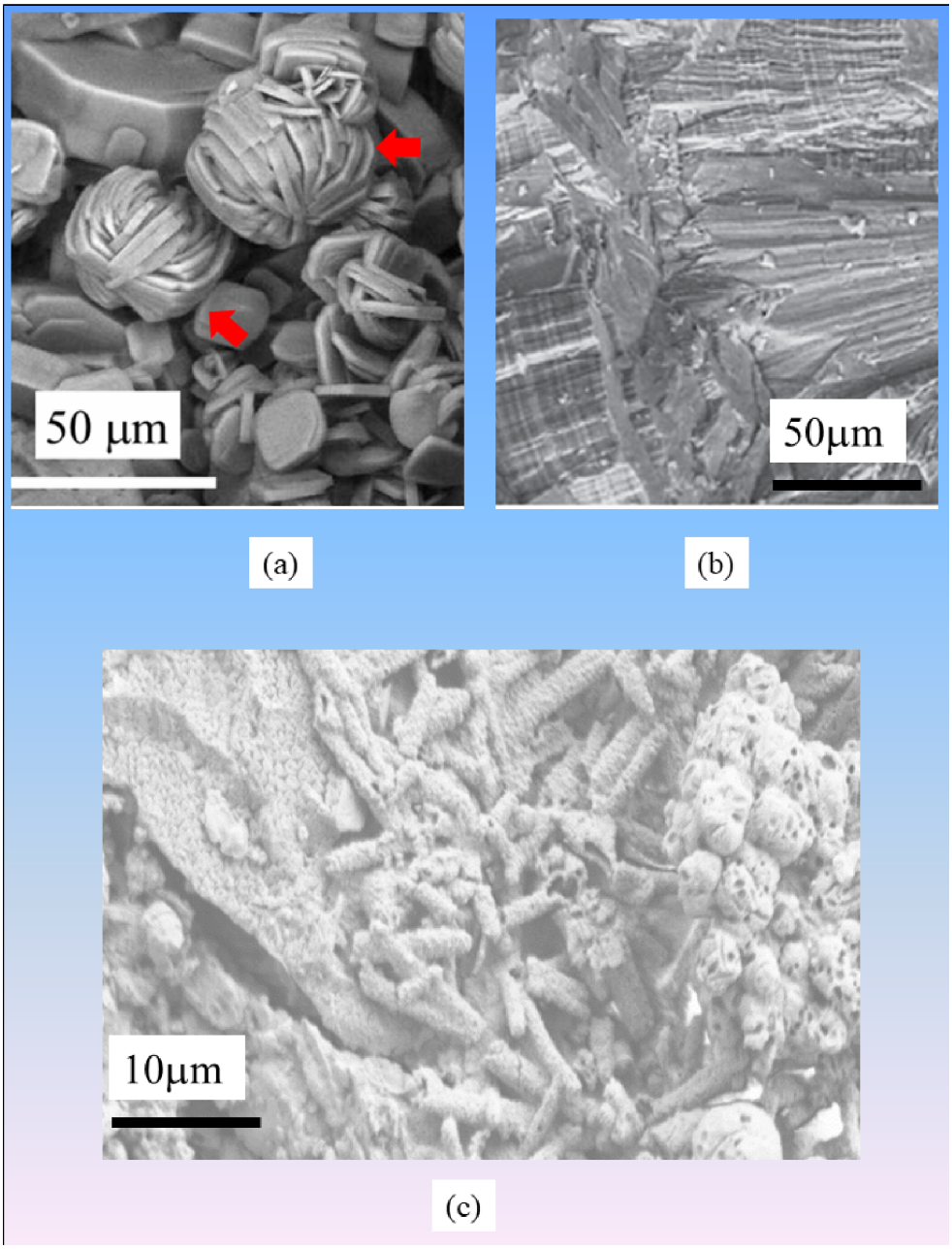

Figure 4. SEM observation of a kidney stone related to (a) genetic primary hyperoxaluria and (b) related to intermittent hyperoxaluria of dietary origin. (c) SEM observation of bacterial imprints and bacteria surrounded by calcifications.

have a similar approach in the case of SEM observations. In the case of kidney stones, only the surface is examined and a significant quantitative determination of the number of crystallites per unit surface needs numerous observations. From a clinical practice point of view, FTIR spectroscopy constitutes a cheaper and quicker method to obtain a quantitative information regarding the chemical composition

[69–71]. Nevertheless, in the near future, such determination through SEM observations of the surface of the kidney stone may be relevant with the help of machine learning [79].

6. Elucidating the pathogenesis of Randall's plaque

Randall's plaque represents a major issue in urology [80,81]. Several papers report evidence that Randall's plaque (RP) present at the tip of the renal papilla may initiate whewellite (Figure 5a) and more rarely weddellite stones [82–91]. Some of these investigations have been dedicated to the pathogenesis of this pathological calcification; recent data show clearly that vitamin D and calcium supplementation accelerates the formation of RP in a murine model [91].

Other publications report various RP chemical compositions. While calcium phosphate apatite (CA) as well as amorphous carbonated calcium phosphate (ACCP) are the major components of most RPs (Figure 5b) [92], other chemical phases such as whitlockite, brushite, and sodium hydrogen urate monohydrate (NaUr) [90] have been identified in about 5% of RP (Figure 5c). Such chemical diversity underlines the fact that several very different mechanisms may be related to the pathogenesis of RP.

Note that RP constituted by NaUr appeared to be sex dependent. NaUr-containing RP was found in 4.3% of stones from male patients and in only 0.6% of cases in female patients ($p < 0.00001$). This is consistent with the ratio observed in stones made of NaUr as the major component. Moreover, RP also exists on weddellite KS (Figure 5d), although the fact that weddellite crystals are very large may explain why RP is observed preferentially on whewellite KS.

A striking feature of RP composed of CA is related to their structure. As we can see in Figure 6, all the RP present on whewellite KS show the same morphology [93,94]. RP are made of a conglomeration of calcified tubules and vessels (vasa recta) reflecting the morphology of the tip of the papilla. Figure 6e shows a normal papilla where we can see the tubule exit orifices (yellow arrows).

Higher magnification observations are shown in Figure 7. Note the calcium phosphate cluster within one tubular lumen (Figure 7a, yellow arrow), while other tubules are empty with calcified walls (black arrow). Figure 7b shows that the walls of the tubules are constituted by an agglomeration of CA spheres [95–97]. Finally, in Figure 7c, a plug inside the tubule is visualized [98].

7. The process of kidney stone growth from RP

We now discuss the growth of a whewellite KS from RP. Only a few papers discuss this particular point [93,94,99,100]. According to Sethmann *et al.* [94], ions from CaP-supersaturated interstitial fluid may diffuse through porous RP into the urine, where a resulting local increase in whewellite supersaturation could trigger crystal nucleation and hence initiate stone formation (Figure 8).

At this point, we must emphasize that calcium oxalate crystallites are present in urine even in the case of healthy subjects (7% vs. 40% in stone formers) [101]. It is their high occurrence over time which is abnormal. In fact, in our case, we observe "classical" whewellite crystallites (Figure 6). Note that in some cases we found whewellite crystallites coated with calcium phosphate as well, which can be due to simple deposition of urinary calcium phosphate. In the pathogenesis model we have proposed, large randomly oriented whewellite crystals are trapped on a phase of CA crystals embedded in proteins acting as a "glue" [93]. This conjecture is clearly supported by Figure 8c. Thus, it seems that the hypothesis of epitaxy between Ca phosphate (RP) and Ca oxalate (KS) is not relevant in this case [100]. Note also that the surface of biological apatite is hydrated [102–104].

The surfaces exposed by the whewellite crystallites are those of the growing crystal in aqueous conditions. The crystal description can be found in our recent paper [70]. We can see (Figure 7) the (100), (12-1), and (010) surface of the crystallites, showing the different (12-1)/(010) surface ratios due to the growth process.

Theoretically some attempts have been performed to predict and understand oxalate polymorphism in the past [70,105]. A very pedagogical paper on the topic has been written by Millan [105]. Since that time the chemical computational tools have been evolved dramatically and we recently revisited this topic using quantum chemical DFT methods and molecular dynamic tools. Note that DFT offers the opportunity to assess adsorption of molecules and thus the reactivity as well as the morphology of small crystals [106–108].

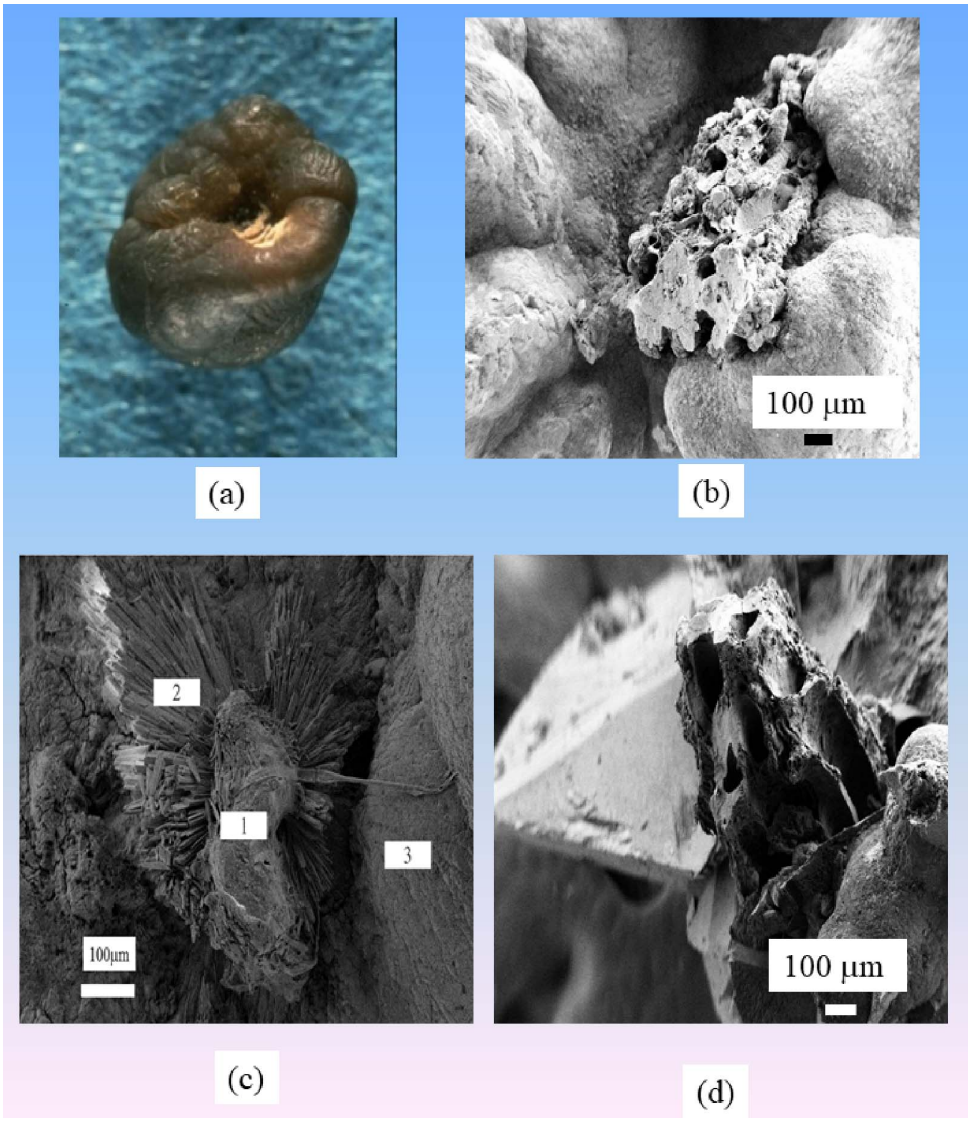

Figure 5. (a) RP made of CA positioned on a whewellite KS. (b) SEM observation of an RP made of CA. (c) SEM observation of an RP made of NaUr. Microscopic aspect of an RP (areas 1 and 2) composed of a mixture of NaUr needles and carbapatite attached to a whewellite calculus (area 3). NaUr needles of large dimension are visible on area 2. (d) RP on a weddellite KS. Note the large size of weddellite crystallites, which may explain why RP is rarely observed on weddellite stones.

In 2001, Millan [105] suggested carefully that, in his conclusion, not only the thermodynamics play a role in the expressed morphology but also the kinetics of the formation of the different surfaces. This result was clearly confirmed by us recently [70]. Moreover, we showed that the effect on the surface formation kinetics can be expressed by including a correction factor to the surface energies. This correction factor, which is purely mathematical, is expected to be related with the kinetics and can be related to the reactions taking place in a DFT-Molecular dynamics calculation on the growth of a specific sur-

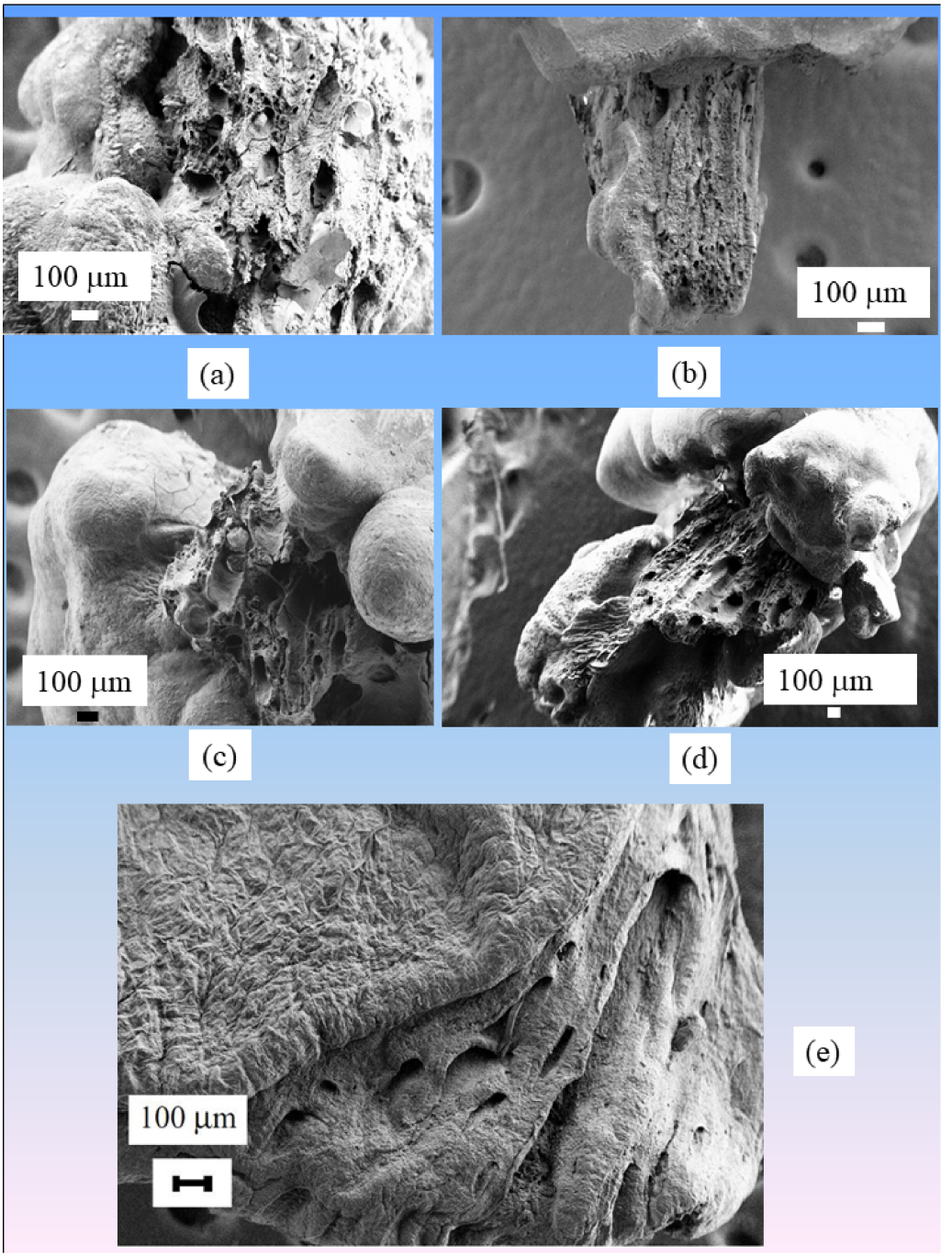

Figure 6. (a–d) SEM observations of RP made of CA. (e) Tip of the papilla with tubule exits labeled with yellow arrows.

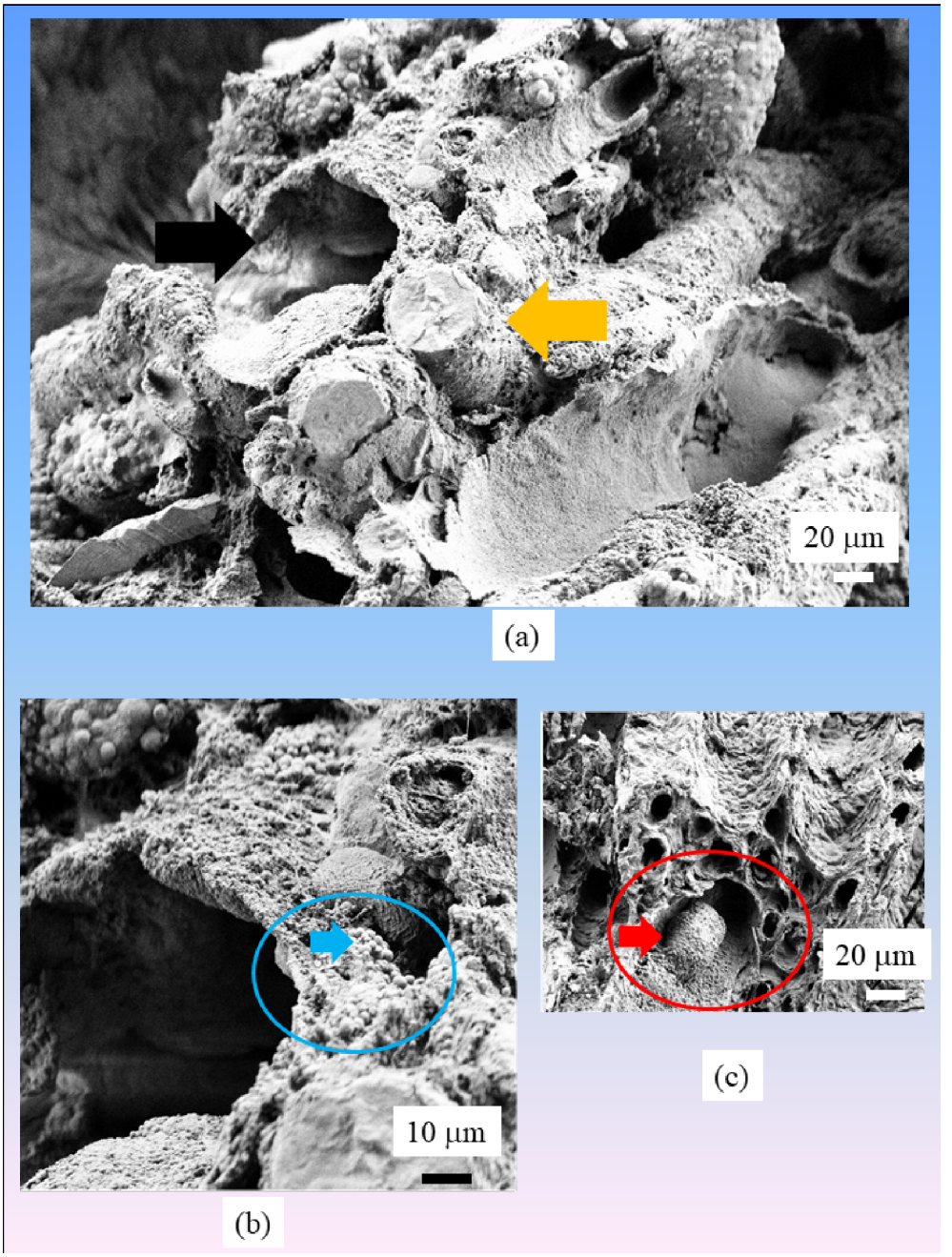

Figure 7. (a–c) SEM observations at high magnification of RP made of CA. (c) Tubular plug in mouse papilla.

face in aqueous conditions. The predictions on the effect of the kinetics on the whewellite morphology is shown in Figure 9, following the discussion reported in Ref. [70].

However, what is striking is the sintered aspect of the (12-1) and (010) surfaces, which is not seen in aqueous conditions. This might be ascribed to the presence of complexing agents such

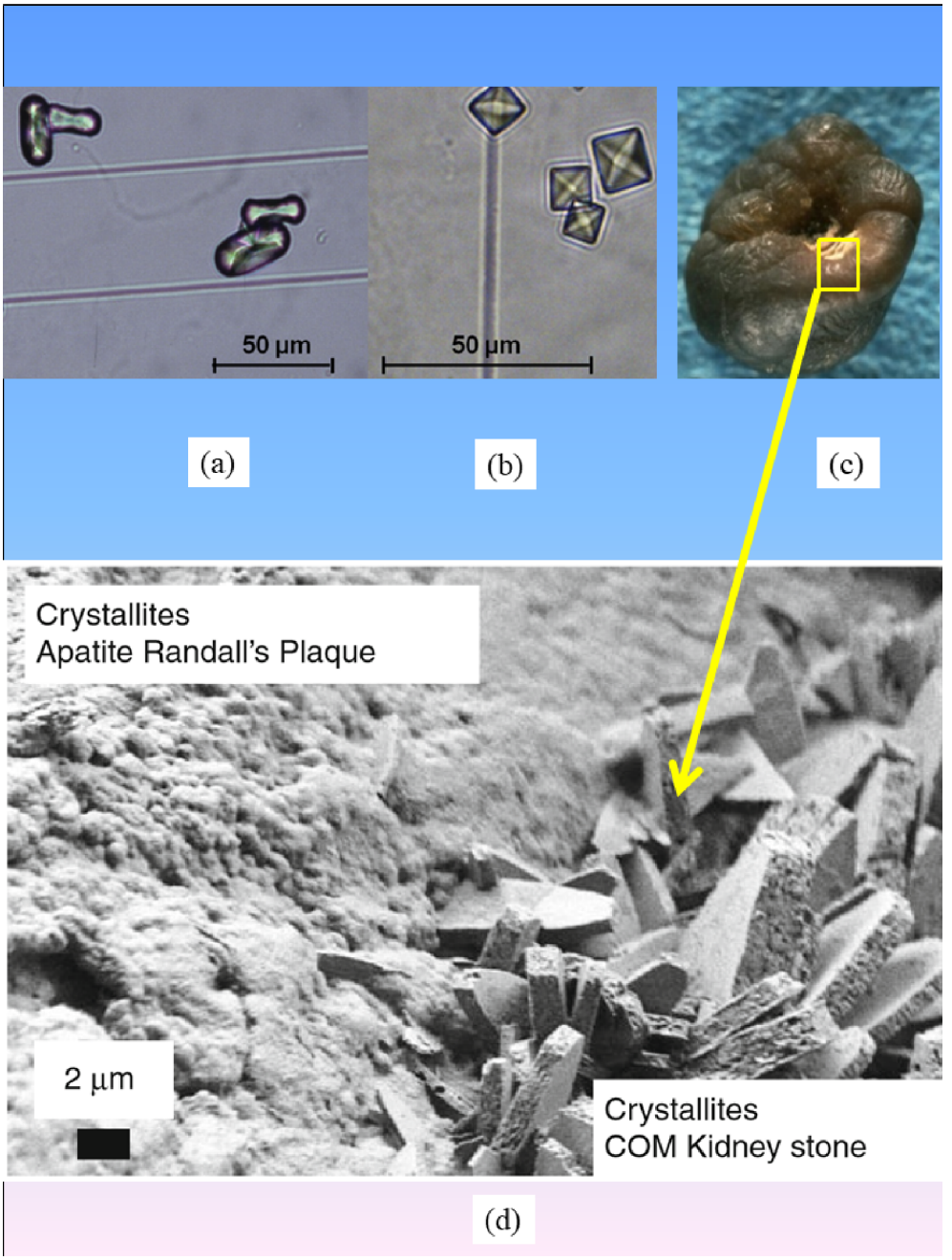

Figure 8. (a) Whewellite and (b) weddellite crystallites in urine. (c) Whewellite KS with RP, yellow square labels the interface between KS and RP. (d) SEM observations of the interface between RP and whewellite KS.

as citrate ion, which is known to modify the kinetics of weddellite polyhydrate nucleation and crystal growth. The sintering also exerts a relatively high impact on surface degradation, which parallels the catechin chelation effect on weddellite [70].

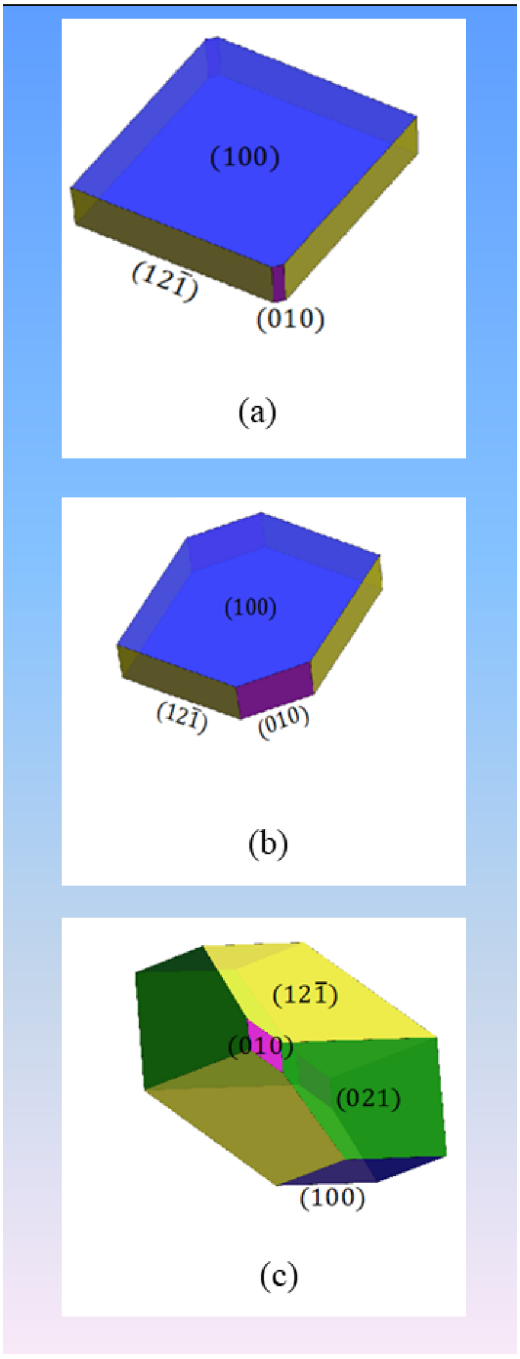

Figure 9. (a) Morphology prediction of COM crystal with the water molecules, without (001) face. (b) Same but with a surface energy correction of -0.1 J·m^{-2} on the (010) face. (c) Same but with energy corrections: -0.03 J·m^{-2} for (021) and (010) surface energies. (Figure adapted from [58].)

8. Elucidating the effect of drugs on kidney stones

In addition to primary hyperoxaluria, several other genetic abnormalities lead to kidney stone pathogenesis, such as inherited distal renal tubular acidosis leading to the formation of calcium phosphate stones with a specific morphology [109], or adenine phosphoribosyltransferase (APRT) deficiency which results in 2,8-dihydroxyadenine (DHA) crystals [110, 111]. Cystinuria, an autosomal recessive disorder, presents a similar picture, leading to stone formation in kidneys and accounting for 1–2% of all cases of urolithiasis. As underlined by Worcester *et al.* [112], cystinuria occupies a unique position among renal stone diseases due to a high recurrence rate. Also, the formation of cystine stones is frequently associated with progression toward chronic kidney disease and renal failure [113–117].

According to the classification of kidney stones [61–64], two distinctive morphologies named type Va (the most common one related to untreated patients) and type Vb (Figures 10a and b) exist. As we can see in Figure 10b, a diffuse concentric structure exists in the periphery of Vb stones with a core of unorganized agglomerates of cystine crystals. SEM shows large crystals displaying flat surfaces with well-defined corners and edges in Va cystine kidney stones (Figure 10c). When the patient follows a conventional treatment based on urine alkalization, significant erosion of the cystine crystal surface occurs (Figure 10d).

Among the results of our investigation [115], it is worth emphasizing that the surface state of cystine crystallites depends on the drug taken by the patient. In a patient treated with tiopronine (Figure 10e), we observed hexagonal holes which correspond to dissolved small cystine crystals, while large ones have lost their typical hexagonal shape. Such a surface state is very different from that observed in a patient treated with captopril (Figure 10e) in which numerous scattered holes, similar to wormholes in a stone, are observed.

9. Biopsy imaging

Scanning and transmission mode electron microscopy of biopsies has been performed for several decades [118–122]. In our investigations, we

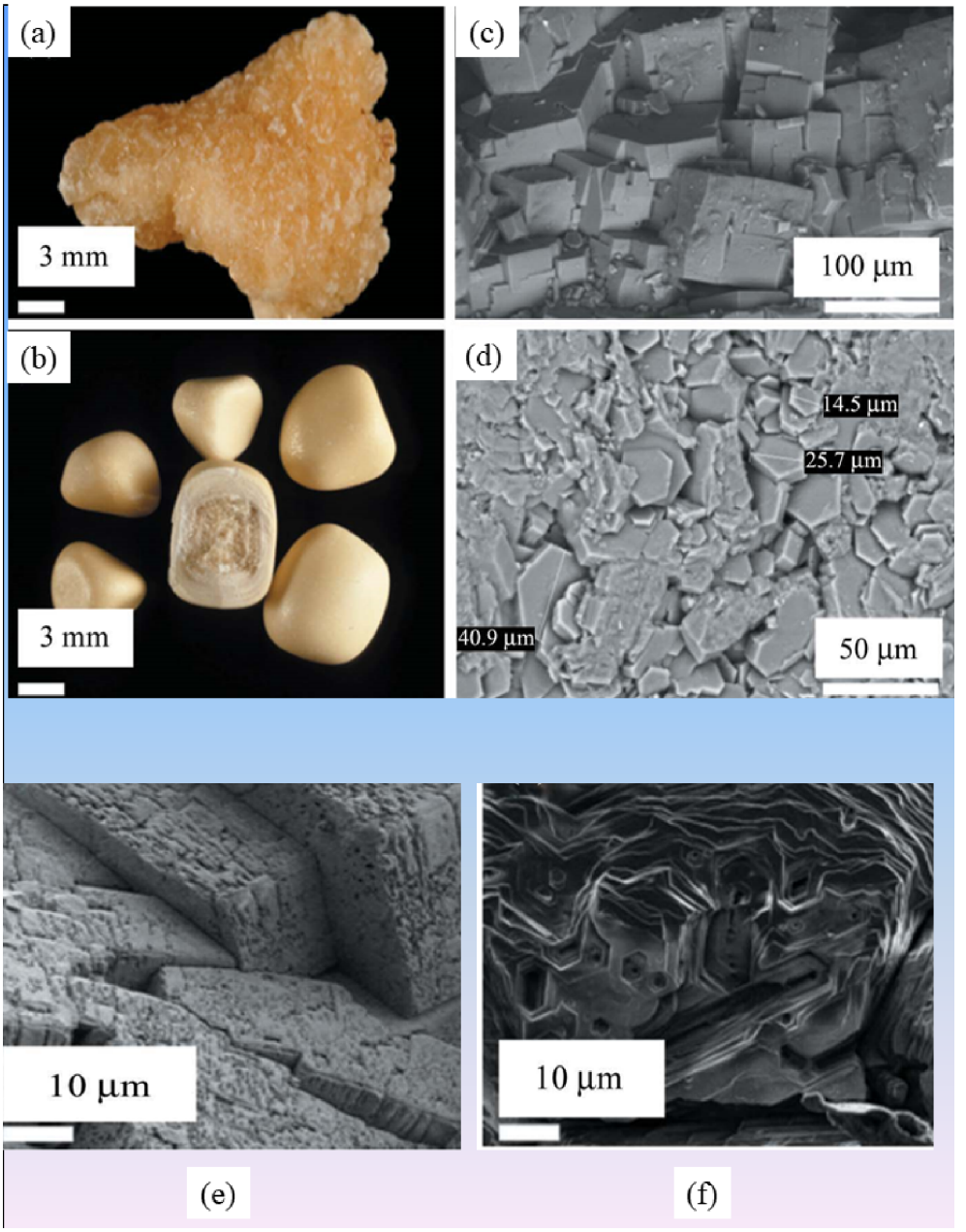

Figure 10. (a) Va cystine kidney stone. (b) Vb cystine kidney stones. (c) SEM image of a typical Va cystine kidney stone. (d) SEM image of a Vb kidney stone. (e) Example of impaired surface of cystine crystals displaying numerous scattered holes similar to wormholes in a stone from a patient treated with captopril. The bulk of the crystals is not affected by such a treatment. (f) Significant erosion of the surface of cystine crystals in a patient treated with tiopronine. Note the hexagonal holes which correspond to dissolved small cystine crystals. Large ones have lost their typical hexagonal shape.

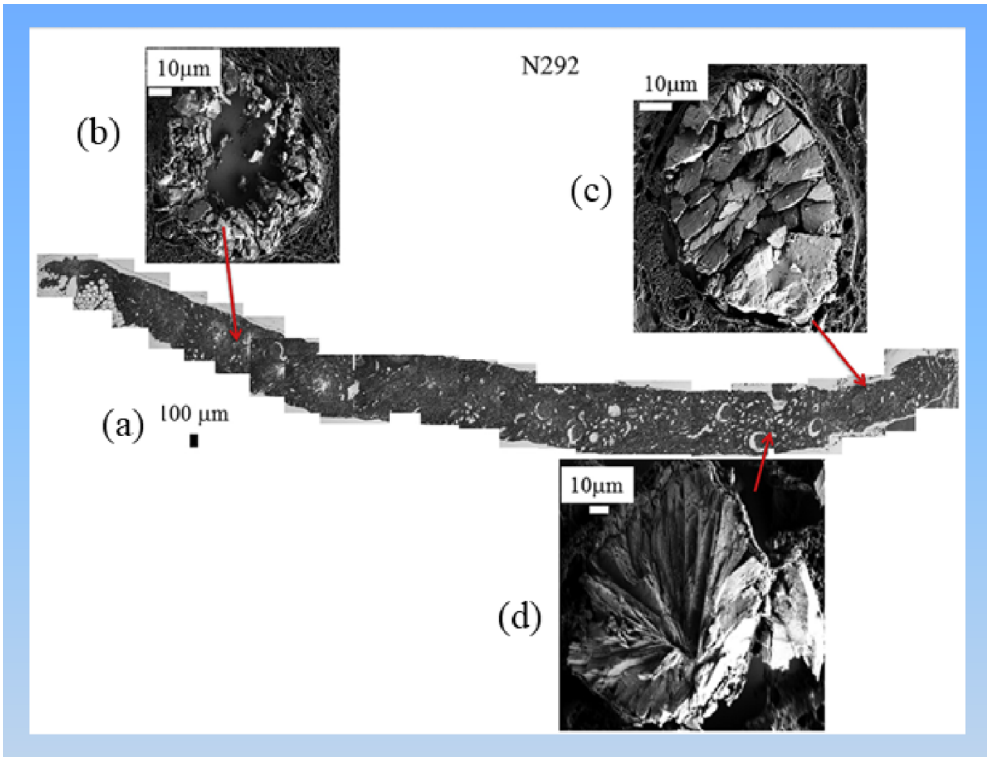

Figure 11. (a) Topology of the different abnormal deposits in kidney biopsy N292. Agglomeration of "large" crystallites is observed in the lumen of tubules (c) while agglomerations of "small" crystallites are located in the tubular cells (b). (d) Radial agglomeration of platelets.

have used FE-SEM on human biopsy tissue coming from various organs namely kidney [123–126], pancreas [127], skin [128–131], hairs [132], breast [26], thyroid [133,134], or arterial wall [135], but of course we must stress that such opportunities exist for cells and mice as well [136–140].

Localization and morphology are two key points which can be addressed through SEM observations on kidney biopsies (Figure 11a). For example, with respect to morphology, small (Figure 11b) and large (Figure 11c) crystallites as well as a radial agglomeration of platelets (Figure 11d) can be observed. Also, it is noteworthy that large crystallites are located in the lumen of tubules (Figure 11c) while "small" ones are in the tubular cells (Figure 11b). It is well known that the composition of the tubule fluid depends on the segment of the nephron. This modulation of the composition along the nephron in addition to various pathological conditions for hyperoxaluria may explain why various configurations can be observed by SEM.

In the case of breast, SEM offers the opportunity to define two different kinds of calcification, namely the well-known plaque easily detected by optical microscopy (Figure 12a), and micrometer and submicrometer spherical entities (Figures 12b and c). Finally, it was possible to relate these two families of calcifications. As we can see in Figure 12d, SEM provides structural evidence that micrometer scale plaques are the result of agglomeration of submicrometer scale spherical calcifications.

Observations at higher magnification underline diversity in the inner structure of the spherical entities (Figure 13), suggesting diversity in the nucleation/growing processes.

Finally, note that not all the spherical structures in tissues are always composed of CA (Figure 14). For instance, in skin calcium carbonate has been detected [128]. It is thus of primary importance to the clinician to precisely identify the chemical composition of spherical entities through either IR or Raman spectroscopies [74,76,141–143].

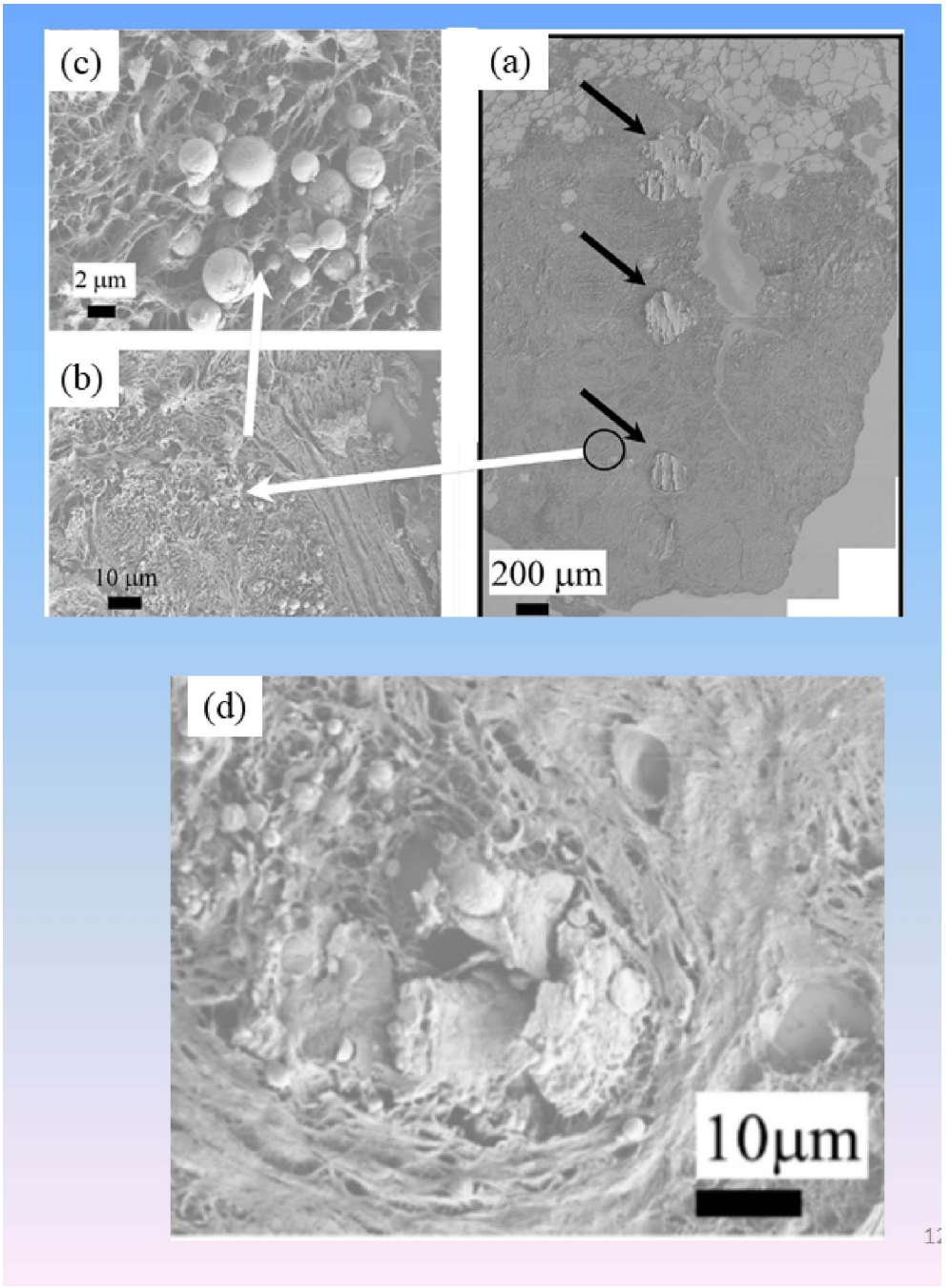

Figure 12. (a) FE-SEM observations of sample 13H2606 (Fibroadenoma) showing heavily mineralized deposits with very small entities invisible at this magnification. (b, c) Submicrometer scale spherules corresponding to the black circle of Figure 2a are visualized at higher magnifications. (d) SEM observations seem to show that "heavily" mineralized deposits are the result of the agglomeration of submicrometer scale spherules.

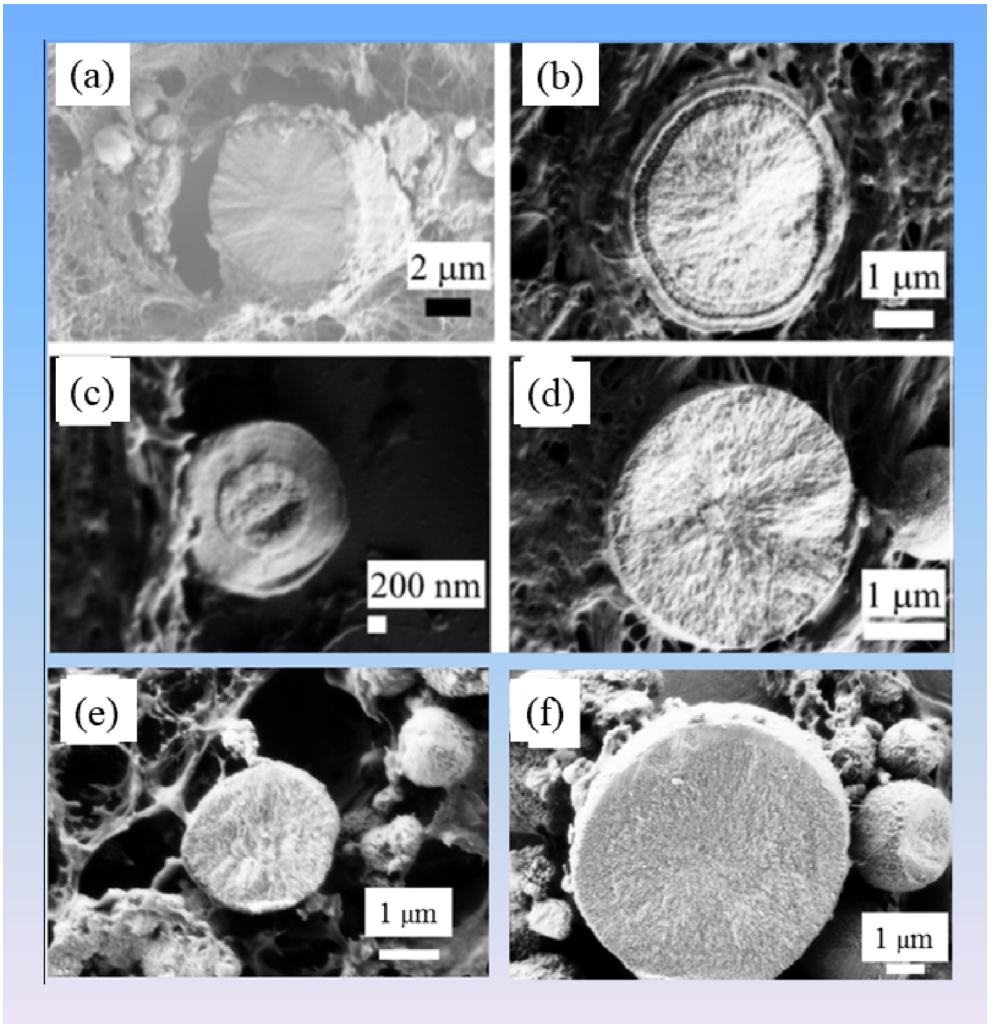

Figure 13. Different internal structures of CA sphericules present in breast (a–d: (a) radial structure; (b, c) concentric layers; (d) radial structure) and kidney (e, f: without structure).

10. Imaging of medical devices

Finally, we must underline that SEM plays an important role in the characterization of the surface of medical devices [39,144–147]. Recently, we have characterized the surface state and the elastic properties of a set of JJ stents [39] on which pathological calcifications were present (Figure 15). It was quite a surprise for the clinicians that black marks on the surface of JJ stents to help urologists during the operation, significantly alter the surface and may ultimately serve as nucleation centers. Note that ureteral replacement devices have also been studied [147].

11. Energy-dispersive X-ray spectroscopy

X-ray fluorescence induced by electron spectroscopy constitutes a powerful technique which allows elemental identification by measuring the number and energy of X-rays emitted from the biological sample after excitation with an electron beam. Even if the detection limit is more important than the one related to X-ray fluorescence induced by protons or photons [148,149], such spectroscopy can give very interesting information regarding the chemistry of pathological calcifications [18,150–153].

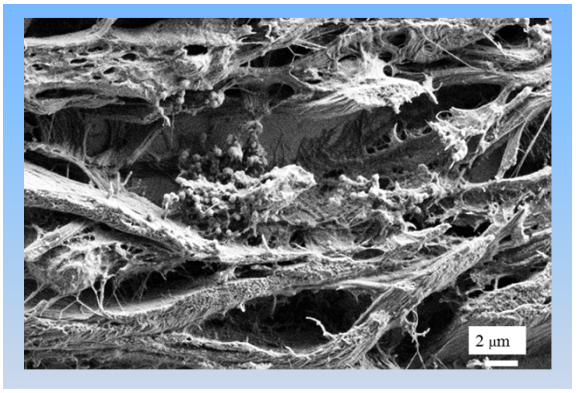

Figure 14. The sphericules present in the skin (for a patient affected by sarcoidosis) are made of calcium carbonate as shown by FTIR spectroscopy and energy dispersive X-ray measurements.

For example, Racek *et al.* [18] have selected a set of 30 samples covering the most common types of human kidney stones for an investigation through SEM coupled with energy-dispersive spectroscopy. After application of standardization, these authors show that it is possible to obtain a quantitative microanalysis with detection limits of 400 ppm (Mg, P, S, Cl, K, Ca), 500 ppm (Na), and 1200 ppm (F). Such spectroscopy can thus bring information regarding the presence of light elements such Mg or F, which are generally not discussed in the case of X-ray fluorescence experiments induced by photons [154–156].

Recently, we have investigated a set of kidney stones containing whitlockite in order to assess the relationship between this chemical compound and infection. Whitlockite is a calcium phosphate phase of crucial interest in several pathologies [157–161]. In order to confirm its presence in kidney stones, we have performed EDX measurements. On Figure 16, SEM observations allow us to underline the presence of pseudocubic crystallites with a trigonal geometry. EDX spectra shows contributions of some of the elements present in the Wk stoichiometric formula $Ca_9Mg(HPO_4)(PO_4)_6$, namely O, P, Mg, and Ca (Figure 16b).

12. Complementarity with other techniques

In our research dedicated to pathological calcifications, we have tried to take into account the hierarchical structure as well as the chemical diversity of such biological entities [10,11]. A precise identification of the organic [162] and inorganic parts [163] as well as of the trace elements [148,149] has thus to be performed. To attain this goal, in lab characterization techniques [163–165] as well as ones related to large scale instruments, such synchrotron radiation [166–172] or neutron [72,78,103,166,173,174] facilities are needed.

To describe the hierarchical structure, we have used optical, scanning electron as well as transmission electron (TEM) and scanning transmission electron microscopes (STEM) [89,91,92,175]. We have thus described these biological entities at the millimeter, micrometer, and nanometer scales. If the elementary composition can be given by EDX spec-

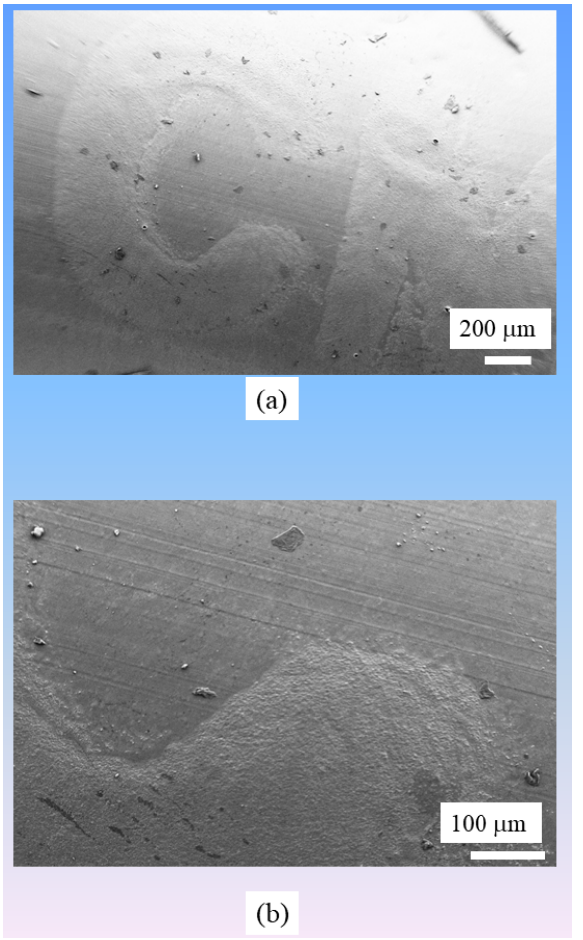

Figure 15. Alteration of the surface state of a JJ stent at black positioning marks.

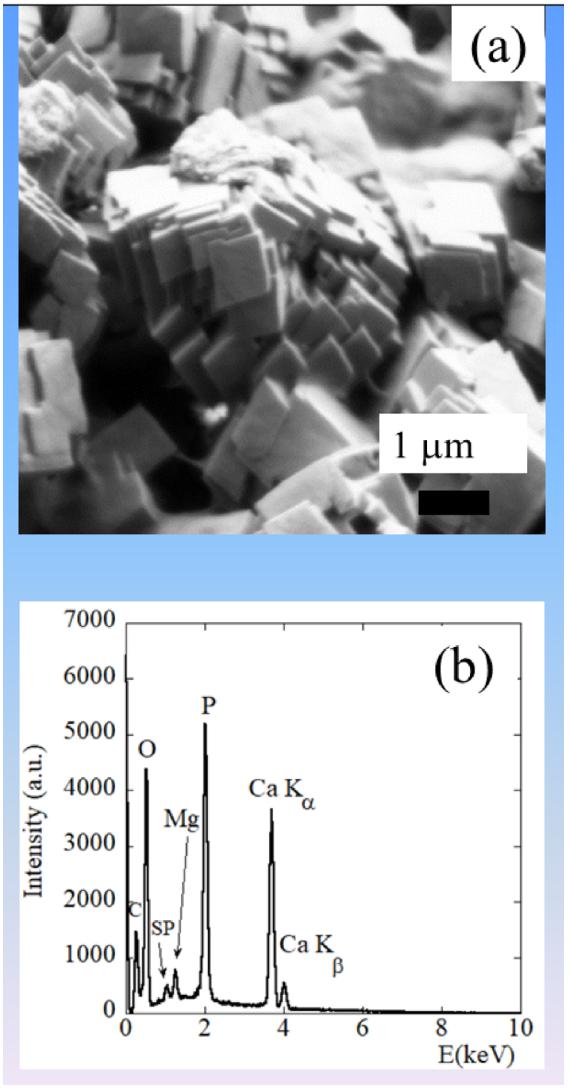

Figure 16. (a) Characteristic pseudocubic morphology of Wk as seen by FE-SEM and corresponding EDX spectrum, (b) in which the contributions of C (K_α = 0.277 keV), O (K_α = 0.525 keV), Mg (K_α = 1.253 keV), P (K_α = 2.014 keV), and Ca (K_α = 3.691 keV, K_β = 4.012 keV) are clear. Note the presence of a sum peak (SP) due to the coincidence of two O K_α photons.

troscopy at submicrometer scale, other X-ray fluorescence spectroscopy which are more sensitive but associated with less spatial resolution can give complementary information [176,177]. Regarding electron microscopy, electron energy-loss spectroscopy can be used to describe the local environment of elements and can be thus considered as a very exciting way to complete information given by EDX spectroscopy. Recent studies have proved that EELS can provide highly relevant information concerning the formation mechanisms of these entities [175,178–182].

Finally, X-ray absorption spectroscopy [183–185], which uses synchrotron radiation as a probe, offers major structural and electronic information regarding the local structure of materials of medical interest encompassing those without long range order such as Pt anticancer molecules [123,138,186] or nanometer scale particles [187–190]. In our case, we have used XAS to describe the local environment of trace elements present in different pathological calcifications [155,169,191–193], thus obtaining a more precise chemical description than the one obtained by EDX spectroscopy but quite similar to the ones gathered by EELS [175,178–182].

13. A major perspective: environmental SEM

Among the different major developments related to SEM, we have to underline the one published by Robinson [194,195], which has modified the vacuum system of a scanning electron microscope in order to be able to study hydrated specimens. According to this pioneer work, such modification has enabled the observation of biological specimens partially immersed in water at temperatures just above 0 °C with a spatial resolution of approximately 0.2 µm.

Thanks to several major improvements, environmental SEM now constitutes an indispensable tool for life and medical sciences [196–198]. Environmental SEM offers a unique opportunity to image wet and insulating materials such as bacteria biofilm [199–201]. At this point, it is worth to underline that special attention has to be paid to the protocol preparation in order to avoid effects of irradiation [202,203]. In some publications, the possibility to collect SEM images of live cells as well as live bacteria has been underlined and a recent publication has discussed this possibility [204].

Regarding urology, environmental SEM has been used to investigate the formation of biofilm on medical device [205,206]. Recently, Fernández-Delgado *et al.* [206] have used environment SEM to study the

pathogenesis of biofilm on the surface of urinary catheters induced by a human pathogen namely *Proteus mirabilis*. Their study shows, for the first time, the ability of clinical and environmental *P. mirabilis* strains to develop contrasting biofilms on chitin and stainless steel surfaces. In the case of pathological calcifications, environmental SEM may play an important role for a better understanding of the relationship between bacteria and struvite, for example [207].

14. Conclusion

The selected examples discussed clearly show that SEM constitutes a major tool used in many research fields encompassing medical diagnosis, the action of drugs on concretions (here KS), and the description of growth processes of pathological calcifications. Actually, SEM acts at the interfaces between medical diagnosis and research in addressing challenging issues. However, it is quite probable that SEM devices will soon be introduced into anatomical pathology laboratories. Moreover, combined with other characterization and modeling techniques, we can expect exploration and understanding the origin of calcifications at the atomic scale. This concerted approach will enable us to tackle the multi-scale challenge of linking medical diagnosis with the atomic structure of the pathology.

Acknowledgments

This work was supported by the Physics and Chemistry Institutes of Centre national de la recherche scientifique and by contracts ANR-09-BLAN-0120-02, ANR-12-BS080022, ANR-13-JSV-10010-01, convergence UPMC CVG1205, and CORDDIM-2013-COD130042.

References

[1] E. Ruska, "The development of the electron microscope and of Electron microscopy (Nobel Lecture)", *Angewandte Chemie International Edition in English*, 1987, **26**, no. 7, 595-605.

[2] A. Bogner, P. H. Jouneau, G. Thollet, D. Basset, C. Gauthier, *Micron*, 2007, **38**, 390-401.

[3] F. Brisset, M. Repoux, J. Ruste, F. Grillon, F. Robaut, *Microscopie Electronique à Balayage et Microanalyses*, EDP Sciences, 2009, ISBN: 978-2759823222.

[4] P. M. Andrews, K. R. Porter, *Am. J. Anat.*, 1974, **140**, 81-116.

[5] T. Fujita, J. Tokunaga, M. Edanaga, *Cell Tissue Res.*, 1976, **166**, 299-314.

[6] F. Phaneuf-Mimeault, R. Tawashi, *Eur. Urol.*, 1977, **3**, 171-175.

[7] S. R. Khan, R. L. Hackett, *J. Urol.*, 1986, **135**, 818-825.

[8] A. Oren, H. Husdan, P.-T. Cheng, R. Khanna, A. Pierratos, G. Digenis, D. Oreopoulos, *Kidney Int.*, 1984, **25**, 534-538.

[9] P. T. Cheng, K. P. H. Pritzker, J. Tausch, A. Pittaway, J. Millard, *Scanning Electron Microsc. III*, 1981, **1**, 163-168.

[10] D. Bazin, M. Daudon, C. Combes, C. Rey, *Chem. Rev.*, 2012, **112**, 5092-5120.

[11] D. Bazin, M. Daudon, *J. Phys. D: Appl. Phys.*, 2012, **45**, article no. 383001.

[12] D. Bazin, J.-P. Haymann, E. Letavernier, J. Rode, M. Daudon, *La Presse médicale*, 2014, **43**, 135-148.

[13] H. H. Chang, C. L. Cheng, P. J. Huang, S. Y. Lin, *Anal. Bioanal. Chem.*, 2014, **406**, 359-366.

[14] A. Lionet, M. Haeck, A. Garstka, V. Gnemmi, D. Bazin, E. Letavernier, J.-P. Haymann, C. Noel, M. Daudon, *C. R. Chim.*, 2016, **19**, 1542-1547.

[15] S. Pramanik, S. Ghosh, A. Roy, R. Mukherjee, A. K. Mukherjee, *Z. Kristallogr. Cryst. Mater.*, 2016, **231**, 97-105.

[16] A. Dessombz, G. Coulibaly, B. Kirakoya, R. W. Ouedraogo, A. Lengani, S. Rouzière, R. Weil, L. Picaut, C. Bonhomme, F. Babonneau, D. Bazin, M. Daudon, *C. R. Chim.*, 2016, **19**, 1573-1579.

[17] P. Chatterjee, A. Paramita, A. K. Chakraborty, *Spectrochim. Acta Part A*, 2018, **200**, 33-42.

[18] M. Racek, J. Racek, I. Hupáková, *Scand. J. Clin. Lab. Invest.*, 2019, **79**, 208-217.

[19] M. A. P. Manzoor, M. Mujeeburahiman, P.-D. Rekha, *Urolithiasis*, 2019, **47**, 137-148.

[20] E. X. Keller, V. de Coninck, M. Audouin, S. Doizi, D. Bazin, M. Daudon, O. Traxer, *J. Biophotonics*, 2019, **12**, article no. e201800227.

[21] M. G. Baron, N. Benmoussa, D. Bazin, I. Abadie, M. Daudon, P. Charlier, *Urolithiasis*, 2019, **47**, 487-488.

[22] M. Mirković, A. Dosena, S. Erić, P. Vulić, B. Matović, A. Rosić, *Microchem. J.*, 2020, **152**, article no. 104429.

[23] J. Zaworski, E. Bouderlique, D. Anglicheau, J.-P. Duong Van Huyen, V. Gnemmi, J.-B. Gibier, Y. Neugebauer, J.-P. Haymann, D. Bazin, V. Frochot, M. Daudon, E. Letavernier, *Kidney Int. Rep.*, 2020, **5**, 737-741.

[24] V. Frochot, V. Castiglione, I. Lucas, J.-P. Haymann, E. Letavernier, D. Bazin, G. Fogazzi, M. Daudon, *Clin. Chim. Acta*, 2020, **515**, 1-4.

[25] P. Nolasco, P. V. Coelho, C. Coelho, D. F. Angelo, J. R. Dias, N. M. Alves, A. Maurício, M. F. C. Pereira, A. P. Alves de Matos, R. C. Martins, P. A. Carvalho, *Microsc. Microanal.*, 2019, **25**, 151-163.

[26] A. Ben Lakhdar, M. Daudon, M. C. Matthieu, A. Kellum, C. Balleyguier, D. Bazin, *C. R. Chim.*, 2016, **19**, 1610-1624.

[27] R. Scott, C. Kendall, N. Stone, K. Rogers, *Sci. Rep.*, 2017, **7**, article no. 136.

[28] J. A. M. R. Kunitake, S. Choi, K. X. Nguyen, M. M. Lee, F. He, D. Sudilovsky, P. G. Morris, M. S. Jochelson, C. A. Hudis, D. A. Muller, P. Fratzl, C. Fischbach, A. Masic, L. A. Estroff, *J. Struct. Biol.*, 2018, **202**, 25-34.

[29] S. C. Curtze, M. Kratz, M. Steinert, S. Vogta, *Sci. Rep.*, 2016, **6**, article no. 23285.

[30] P. Dorfmüller, D. Bazin, S. Aubert, R. Weil, F. Brisset, M. Daudon, F. Capron, I. Brochériou, *Cardiol. Res. Pract.*, 2010, article no. 685926.

[31] C. Nguyen, D. Bazin, M. Daudon, A. Chatron-Colliet, D. Hannouche, A. Bianchi, D. Côme, A. So, N. Busso, F. Lioté, H.-K. Ea, *Arthritis Res. Ther.*, 2013, **15**, article no. R103.

[32] H.-K. Ea, C. Nguyen, D. Bazin, A. Bianchi, J. Guicheux, P. Reboul, M. Daudon, F. Lioté, *Arthritis Rheum.*, 2010, **63**, 10-18.

[33] H. A. Almarshad, S. M. Badawy, A. F. Alsharari, *Comb. Chem. High Throughput Screen.*, 2018, **21**, 495-500.

[34] A. Dessombz, P. Méria, D. Bazin, M. Daudon, *PLoS One*, 2012, **7**, article no. e51691.

[35] A. Dessombz, P. Méria, D. Bazin, E. Foy, S. Rouzière, R. Weil, M. Daudon, *Prog. Urol.*, 2011, **21**, 940-945.

[36] S. De Santis, G. Sotgiu, A. Crescenzi, C. Tafffon, A. Felici, M. Orsini, *J. Pharm. Biomed. Anal.*, 2020, **190**, article no. 113534.

[37] M. Olaya, S. Aldana, M. Maya, F. Gil, *J. Dev. Orig. Health Dis.*, 2017, **8**, 613-617.

[38] A.-L. Faucon, M. Daudon, V. Frochot, D. Bazin, B. Terris, V. Caudwell, *Kidney Int.*, 2018, **93**, 1251-1252.

[39] C. Poulard, A. Dessombz, M. Daudon, D. Bazin, *C. R. Chim.*, 2016, **19**, 1597-1604.

[40] D. Bazin, M. Daudon, *Ann. Biol. Clin.*, 2015, **73**, 517-534.

[41] M. Daudon, P. Jungers, D. Bazin, *N. Engl. J. Med.*, 2008, **359**, 100-102.

[42] M. Daudon, P. Jungers, D. Bazin, *N. Engl. J. Med.*, 2009, **360**, 1680.

[43] H. Miyazaki, H. Uozaki, A. Tojo, S. Hirashima, S. Inaga, K. Sakuma, Y. Morishita, M. Fukayama, *Pathol. Res. Pract.*, 2012, **208**, 503-509.

[44] C. Dittmayer, E. Volcker, I. Wacker, R. R. Schröder, S. Bachmann, *Kidney Int.*, 2018, **94**, 625-631.

[45] D. Bazin, C. Jouanneau, S. Bertazzo, C. Sandt, A. Dessombz, M. Réfrégiers, P. Dumas, J. Frederick, J.-P. Haymann, E. Letavernierg, P. Ronco, M. Daudon, *C. R. Chim.*, 2016, **19**, 1439-1450.

[46] E. Esteve, C. Jouanneau, E. Letavernier, P. Ronco, M. Daudon, D. Bazin, M. Réfrégiers, *Nephrol. Ther.*, 2015, **11**, 279.

[47] D. Bazin, E. Letavernier, J. P. Haymann, V. Frochot, M. Daudon, *Ann. Biol. Clin.*, 2020, **78**, 349-362.

[48] N. Vidavsky, J. A. M. R. Kunitake, L. A. Estroff, *Adv. Healthc. Mater.*, 2020, article no. e2001271.

[49] M. Van Meerssche, J. Feneau-Dupont, *Introduction à la Cristallographie et à la Chimie Structurale*, Vander, Louvain, 1973.

[50] T. Kogure, *Dev. Clay Sci.*, 2013, **5**, 275-317.

[51] R. F. Egerton, *Physical Principles of Electron Microscopy: An Introduction to TEM, SEM, and AEM*, Springer, New York, 2005, 202 pages.

[52] B. J. Griffin, *Scanning*, 2011, **33**, 162-173.

[53] D. A. Moncrieff, P. R. Barker, *Scanning*, 1978, **1**, 195-197.

[54] D. C. Joy, *Ultramicroscopy*, 1991, **37**, 216-233.

[55] K. de Haan, Z. S. Ballard, Y. Rivenson, Y. Wu, A. Ozcan, *Sci. Rep.*, 2019, **9**, article no. 12050.

[56] A. E. Vladár, M. T. Postek, B. Ming, *Microsc. Today*, 2009, **17**, 6-13.

[57] D. C. Joy, *AIP Conf. Proc.*, 2005, **788**, 535-542.

[58] S. P. Collins, R. K. Pope, R. W. Scheetz, R. I. Ray, P. A. Wagner, B. J. Little, *Microsc. Res. Tech.*, 1993, **25**, 398-405.

[59] S. E. Kirk, J. N. Skepper, A. M. Donald, *J. Microsc.*, 2009, **233**, 205-224.

[60] D. B. Peckys, J.-P. Baudoin, M. Eder, U. Werner, N. de Jonge, *Sci. Rep.*, 2013, **3**, article no. 2626.

[61] M. Daudon, C. A. Bader, P. Jungers, *Scanning Microsc.*, 1993, **7**, 1081-1104.

[62] M. Daudon, *Ann. Urol.*, 2005, **39**, 209-231.

[63] M. Daudon, P. Jungers, "Stone composition and morphology: a window on etiology", in *Urolithiasis: Basic Science and Clinical Practice* (J. J. Talati, H. G. Tiselius, D. M. Albala, Z. Ye, eds.), Springer, London, 2012, 113-140.

[64] M. Daudon, A. Dessombz, V. Frochot, E. Letavernier, J.-P. Haymann, P. Jungers, D. Bazin, *C. R. Chim.*, 2016, **19**, 1470-1491.

[65] J. N. Lalena, *Crystallogr. Rev.*, 2006, **12**, 125-180.

[66] H. Kubbinga, *Z. Kristallogr.*, 2012, **227**, 1-26.

[67] G. Wulff, *Z. Kristallogr.*, 1901, **34**, 449-530.

[68] Y. Zhang, *Trop. J. Pharm. Res.*, 2014, **13**, 829-834.

[69] J. C. Givand, R. W. Rousseau, P. J. Ludovice, *J. Cryst. Growth*, 1998, **194**, 228-238.

[70] T. Debroise, T. Sedzik, J. Vekeman, Y. Su, C. Bonhomme, F. Tielens, *Cryst. Growth Des.*, 2020, **20**, 3807-3815.

[71] I. Petit, G. D. Belletti, T. Debroise, M. Llansola, I. T. Lucas, C. Leroy, C. Bonhomme, L. Bonhomme-Coury, D. Bazin, M. Daudon, E. Letavernier, J. P. Haymann, V. Frochot, F. Babonneau, P. Quaino, F. Tielens, *ChemistrySelect*, 2018, **3**, 8801-8812.

[72] M. Daudon, D. Bazin, G. André, P. Jungers, A. Cousson, P. Chevallier, E. Véron, G. Matzen, *J. Appl. Cryst.*, 2009, **42**, 109-115.

[73] X. Carpentier, M. Daudon, O. Traxer, P. Jungers, A. Mazouyes, G. Matzen, E. Véron, D. Bazin, *Urology*, 2009, **73**, 968-975.

[74] L. Estepa, M. Daudon, *Biospectroscopy*, 1997, **3**, 347-369.

[75] M. L. Giannossi, *J. X-Ray Sci. Technol.*, 2015, **23**, 401-407.

[76] M. Daudon, D. Bazin, *C. R. Chim.*, 2016, **19**, 1416-1423.

[77] M. Daudon, V. Frochot, D. Bazin, P. Jungers, *C. R. Chim.*, 2016, **19**, 1514-1526.

[78] D. Bazin, G. André, R. Weil, G. Matzen, E. Véron, X. Carpentier, M. Daudon, *Urology*, 2012, **79**, 786-790.

[79] W. Lopes, G. N. F. Cruz, M. L. Rodrigues, M. H. Vainstein, L. Kmetzsch, C. C. Staats, M. H. Vainstein, A. Schrank, *Sci. Rep.*, 2020, **10**, article no. 2362.

[80] A. Randall, *N. Engl. J. Med.*, 1936, **214**, 234-237.

[81] A. Randall, *Ann. Surg.*, 1937, **105**, 1009-1027.

[82] A. P. Evan, J. E. Lingeman, F. L. Coe, J. H. Parks, S. B. Bledsoe, Y. Shao, A. J. Sommer, R. F. Paterson, R. L. Kuo, M. Grynpas, *J. Clin. Invest.*, 2003, **111**, 607-616.

[83] M. Daudon, O. Traxer, P. Jungers, D. Bazin, *AIP Conf. Proc.*, 2007, **900**, 26-34.

[84] X. Carpentier, D. Bazin, P. Jungers, S. Reguer, D. Thiaudière, M. Daudon, *J. Synchrotron Radiat.*, 2010, **17**, 374-379.

[85] M. Daudon, P. Jungers, D. Bazin, *AIP Conf. Proc.*, 2008, **1049**, 199-215.

[86] X. Carpentier, D. Bazin, C. Combes, A. Mazouyes, S. Rouzière, P.-A. Albouy, E. Foy, M. Daudon, *J. Trace Elem. Med. Biol.*, 2011, **25**, 160-165.

[87] M. Daudon, D. Bazin, E. Letavernier, *Urolithiasis*, 2015, **43**, 5-11.
[88] E. Letavernier, D. Bazin, M. Daudon, *C. R. Chim.*, 2016, **19**, 1456-1460.
[89] C. Verrier, D. Bazin, L. Huguet, O. Stéphan, A. Gloter, M.-C. Verpont, V. Frochot, J.-P. Haymann, I. Brocheriou, O. Traxer, M. Daudon, E. Letavernier, *J. Urol.*, 2016, **196**, 1566-1574.
[90] D. Bazin, E. Letavernier, C. Jouanneau, P. Ronco, C. Sandt, P. Dumas, G. Matzen, E. Véron, J.-P. Haymann, O. Traxe, P. Conort, M. Daudon, *C. R. Chim.*, 2016, **19**, 1461-1469.
[91] E. Letavernier, G. Kauffenstein, L. Huguet, N. Navasiolava, E. Bouderlique, E. Tang, L. Delaitre, D. Bazin, M. de Frutos, C. Gay, J. Perez, M. C. Verpont, J.-P. Haymann, V. Pomozi, J. Zoll, O. Le Saux, M. Daudon, G. Leftheriotis, L. Martin, *J. Am. Soc. Nephrol.*, 2018, **29**, 2337-2347.
[92] E. Bouderlique, E. Tang, J. Perez, A. Coudert, D. Bazin, M.-C. Verpont, C. Duranton, I. Rubera, J.-P. Haymann, G. Leftheriotis, L. Martin, M. Daudon, E. Letavernier, *Am. J. Pathol.*, 2019, **189**, 2171-2180.
[93] M. Daudon, O. Traxer, J. C. Williams, D. Bazin, "Randall's Plaque", in *Urinary Tract Stone Disease* (N. P. Rao, G. M. Preminger, J. P. Kavangh, eds.), Springer, New York, 2011, ISBN 978-1-84800-361-3.
[94] I. Sethmann, G. Wendt-Nordahl, T. Knoll, F. Enzmann, L. Simon, H.-J. Kleebe, *Urolithiasis*, 2017, **45**, 235-248.
[95] N. Çiftçioğlu, K. Vejdani, O. Lee, G. Mathew, K. M. Aho, E. O. Kajander, D. S. McKay, J. A. Jones, M. L. Stoller, *Int. J. Nanomed.*, 2008, **3**, 105-115.
[96] L. C. Delatte, J. L. R. Minon-Cifuentes, J. A. Medina, *J. Urol.*, 1985, **133**, 490-494.
[97] E. Pieras, A. Costa-Bauzá, M. Ramis, F. Grases, *Sci. World J.*, 2006, **6**, 2411-2419.
[98] L. Huguet, M. Le Dudal, M. Livrozet, D. Bazin, V. Frochot, J. Perez, J. P. Haymann, I. Brocheriou, M. Daudon, E. Letavernier, *Urolithiasis*, 2018, **46**, 333-341.
[99] A. P. Evan, F. L. Coe, J. E. Lingeman, Y. Shao, A. J. Sommer, S. B. Bledsoe, J. C. Anderson, E. M. Worecester, *Anat. Rec.*, 2007, **290**, 1315-1323.
[100] S. R. Khan, B. K. Canales, *Urolithiasis*, 2015, **43**, 109-123.
[101] H. V. Nguyen, M. Daudon, R. J. Réveillaud, P. Jungers, *Nephrologie*, 1987, **8**, 65-69.
[102] D. Eichert, C. Combes, C. Drouet, C. Rey, *Key Eng. Mater.*, 2005, **284–286**, 3-6.
[103] D. Bazin, C. Chappard, C. Combes, X. Carpentier, S. Rouzière, G. André, G. Matzen, M. Allix, D. Thiaudière, S. Reguer, P. Jungers, M. Daudon, *Osteoporos. Int.*, 2009, **20**, 1065-1075.
[104] C. Rey, C. Combes, C. Drouet, S. Cazalbou, D. Grossin, F. Brouillet, S. Sarda, *Progress in Crystal Growth and Characterization of Materials*, vol. 60, Elsevier, 2014, 63-73 pages.
[105] A. Millan, *Cryst. Growth Des.*, 2001, **1**, 245-254.
[106] D. Bazin, F. Tielens, *Appl. Catal.*, 2015, **504**, 631-641.
[107] F. Tielens, D. Bazin, *C. R. Chim.*, 2018, **21**, 174-181.
[108] I. C. Oguz, H. Guesmi, D. Bazin, F. Tielens, *J. Phys. Chem. C*, 2019, **123**, 20314-20318.
[109] A. Dessombz, E. Letavernier, J.-P. Haymann, D. Bazin, M. Daudon, *J. Urol.*, 2015, **193**, 1564-1569.
[110] G. Bollé, C. Dollinger, L. Boutaud, D. Guillemot, A. Bensman, J. Harambat, P. Deteix, M. Daudon, B. Knebelmann, I. Ceballos-Picot, *J. Am. Soc. Nephrol.*, 2010, **21**, 679-688.
[111] A. Dessombz, D. Bazin, P. Dumas, C. Sandt, J. Sule-Suso, M. Daudon, *PLoS One*, 2011, **6**, article no. e28007.
[112] E. M. Worcester, J. H. Parks, A. P. Evan, F. L. Coe, *J. Urol.*, 2006, **176**, 600-603.
[113] E. Letavernier, O. Traxer, J.-P. Haymann, D. Bazin, M. Daudon, *Prog. Urol. – FMC*, 2012, **22**, F119-F123.
[114] B. Hannache, D. Bazin, A. Boutefnouchet, M. Daudon, *Prog. Urol.*, 2012, **22**, 577-582.
[115] D. Bazin, M. Daudon, A. Gilles, R. Weil, E. Véron, G. Matzen, *J. Appl. Cryst.*, 2014, **47**, 719-725.
[116] M. Livrozet, S. Vandermeersch, L. Mesnard, E. Thioulouse, J. Jaubert, J.-J. Boffa, J.-P. Haymann, L. Baud, D. Bazin, M. Daudon, E. Letavernier, *PLoS One*, 2014, **9**, article no. e102700.
[117] J. P. Haymann, M. Livrozet, J. Rode, S. Doizi, O. Traxer, V. Frochot, E. Letavernier, D. Bazin, M. Daudon, *Prog. Urol. – FMC*, 2021, **31**, F1-F7.
[118] J. V. Johannessen, *Kidney Int.*, 1973, **3**, 46-50.
[119] Y. Collan, P. Hirsimäki, H. Aho, M. Wuorela, J. Sundström, R. Tertti, K. Metsärinne, *Ultrastruct. Pathol.*, 2005, **29**, 461-468.
[120] S. Conti, N. perico, R. Novelli, C. Carra, A. benigni, G. Remuzzi, *Sci. Rep.*, 2018, **8**, article no. 4909.
[121] W.-L. Ng, K. F. So, P. C. So, H. K. Ngai, *Pathology*, 1982, **14**, 299-302.
[122] H. Miyazaki, H. Uozakia, A. Tojo, S. Hirashima, S. Inaga, K. Sakuma, Y. Morishita, M. Fukayama, *Path. Res. Pract.*, 2012, **208**, 503-509.
[123] E. Esteve, D. Bazin, C. Jouanneau, S. Rouzière, A. Bataille, A. Kellum, K. Provost, C. Mocuta, S. Reguer, P. Ronco, J. Rehr, J.-P. Haymann, E. Letavernier, A. Hertig, *C. R. Chim.*, 2016, **19**, 1586-1589.
[124] D. Bazin, E. Letavernier, J.-P. Haymann, F. Tielens, A. Kellum, M. Daudon, *C. R. Chim.*, 2016, **19**, 1548-1557.
[125] V. Frochot, D. Bazin, E. Letavernier, C. Jouanneau, J.-P. Haymann, M. Daudon, *C. R. Chim.*, 2016, **19**, 1565-1572.
[126] M. Daudon, V. Frochot, D. Bazin, P. Jungers, *Drugs*, 2018, **78**, 163-201.
[127] J. Cros, D. Bazin, A. Kellum, V. Rebours, M. Daudon, *C. R. Chim.*, 2016, **19**, 1642-1655.
[128] H. Colboc, D. Bazin, P. Moguelet, V. Frochot, R. Weil, E. Letavernier, C. Jouanneau, C. Frances, C. Bachmeyer, J.-F. Bernaudin, M. Daudon, *C. R. Chim.*, 2016, **19**, 1631-1641.
[129] H. Colboc, P. Moguelet, D. Bazin, C. Bachmeyer, V. Frochot, R. Weil, E. Letavernier, C. Jouanneau, M. Daudon, J. F. Bernaudin, *J. Eur. Acad. Dermatol. Venereol.*, 2019, **33**, 198-203.
[130] H. Colboc, P. Moguelet, D. Bazin, P. Carvalho, A.-S. Dillies, G. Chaby, H. Maillard, D. Kottler, E. Goujon, C. Jurus, M. Panaye, V. Frochot, E. Letavernier, M. Daudon, I. Lucas, R. Weil, P. Courville, J.-B. Monfort, F. Chasset, P. Senet, *JAMA Dermatol.*, 2019, **155**, 789-796.
[131] H. Colboc, D. Bazin, P. Moguelet, S. Reguer, R. Amode, C. Jouanneau, I. Lucas, L. Deschamps, V. Descamps, N. Kluger, *J. Eur. Acad. Dermatol. Venereol.*, 2020, **34**, e313-e315.
[132] F. Brunet-Possenti, L. Deschamps, H. Colboc, A. Somogyi, K. Medjoubi, D. Bazin, V. Descamps, *J. Eur. Acad. Dermatol. Venereol.*, 2018, **32**, e442-e443.

[133] M. Mathonnet, A. Dessombz, D. Bazin, R. Weil, F. Triponez, M. Pusztaszeri, M. Daudon, *C. R. Chim.*, 2016, **19**, 1672-1678.
[134] J. Guerlain, S. Perie, M. Lefevre, J. Perez, S. Vandermeersch, C. Jouanneau, L. Huguet, V. Frochot, E. Letavernier, R. Weil, S. Rouzière, D. Bazin, M. Daudon, J. P. Haymann, *PLoS One*, 2019, **14**, article no. e0224138.
[135] R. Coscas, M. Bensussan, M.-P. Jacob, L. Louedec, Z. Massy, J. Sadoine, M. Daudon, C. Chaussain, D. Bazin, J.-B. Michel, *Atherosclerosis*, 2017, **259**, 60-67.
[136] F. Preitner, A. Laverriere, S. Metref, A. Da Costa, C. Roger, S. Rotman, D. Bazin, M. Daudon, C. Sandt, A. Dessombz, B. Thorens, *Am. J. Physiol. Renal Physiol.*, 2013, **305**, F786-F795.
[137] L. Louvet, D. Bazin, J. Büchel, S. Steppan, J. Passlick-Deetjen, Z. A. Massy, *PLoS One*, 2015, **10**, article no. e0115342.
[138] E. Esteve, D. Bazin, C. Jouanneau, S. Rouzière, A. Bataille, A. Kellum, K. Provost, C. Mocuta, S. Reguer, P. Ronco, J. Rehr, J.-P. Haymann, E. Letavernier, A. Hertig, *C. R. Chim.*, 2016, **19**, 1580-1585.
[139] C. Bardet, F. Courson, Y. Wu, M. Khaddam, B. Salmon, S. Ribes, J. Thumfart, P. M. Yamaguti, G. Y. Rochefort, M.-L. Figueres, T. Breiderhoff, A. Garcia Castaño, B. Vallée, D. Le Denmat, B. Baroukh, T. Guilbert, A. Schmitt, J.-M. Massé, D. Bazin, G. Lorenz, M. Morawietz, J. Hou, P. Carvalho-Lobato, M. C. Manzanares, J.-C. Fricain, D. Talmud, R. Demontis, F. Neves, D. Zenaty, A. Berdal, A. Kiesow, M. Petzold, S. Menashi, A. Linglart, A. C. Acevedo, R. Vargas-Poussou, D. Müller, P. Houillier, C. Chaussain, *J. Bone Miner. Res.*, 2016, **31**, 498-513.
[140] H. Bilbault, J. Perez, L. Huguet, S. Vandermeersch, S. Placier, N. Tabibzadeh, V. Frochot, E. Letavernier, D. Bazin, M. Daudon, J.-P. Haymann, *Sci. Rep.*, 2018, **8**, article no. 16319.
[141] M. Daudon, M. F. Protat, R. J. Reveillaud, H. Jaeschke-Boyerl, *Kidney Int.*, 1983, **23**, 842-850.
[142] L. Maurice-Estepa, P. Levillain, B. Lacour, M. Daudon, *Scand. J. Urol. Nephrol.*, 1999, **33**, 299-305.
[143] V. Castiglione, P.-Y. Sacré, E. Cavalier, P. Hubert, R. Gadisseur, E. Ziemons, *PLoS One*, 2018, **13**, article no. e0201460.
[144] B. A. Vanderbrink, A. R. Rastinehad, M. C. Ost, A. D. Smith, *J. Endourol.*, 2008, **22**, 905-912.
[145] W.-J. Fu, Z.-X. Wang, G. Li, F.-Z. Cui, Y. Zhang, X. Zhang, *Biomed. Mater.*, 2012, **7**, article no. 065002.
[146] C. Torrecilla, J. Fernández-Concha, J. R. Cansino, J. A. Mainez, J. H. Amón, S. Costas, O. Angerri, E. Emiliani, M. A. Arrabal Martín, M. A. Arrabal Polo, A. García, M. C. Reina, J. F. Sánchez, A. Budía, D. Pérez-Fentes, F. Grases, A. Costa-Bauzá, J. Cuñé, *BMC Urol.*, 2020, **20**, article no. 65.
[147] A. Nouaille, A. Descazeaud, F. Desgrandchamps, D. Bazin, M. Daudon, A. Masson Lecomte, P. Mongiat-Artus, P. Méria, *Prog. Urol.*, 2021, **31**, 348-356.
[148] M. Uo, T. Wada, T. Sugiyama, *Jpn. Dent. Sci. Rev.*, 2015, **51**, 2-9.
[149] S. Rouzière, D. Bazin, M. Daudon, *C. R. Chim.*, 2016, **19**, 1404-1415.
[150] V. Uvarov, I. Popov, N. Shapur, T. Abdin, O. N. Gofrit, D. Pode, M. Duvdevani, *Environ. Geochem. Health*, 2011, **33**, 613-622.
[151] M. S. Yalçın, M. Tek, *J. Appl. Spectrosc.*, 2019, **85**, 1050-1057.
[152] H. A. Walli, W. J. Abed Ali, *J. Phys.: Conf. Ser.*, 2019, **1294**, article no. 072003.
[153] K. Seevakan, *Malaya J. Mat.*, 2020, **8**, 1240-1242.
[154] D. Bazin, P. Chevallier, G. Matzen, P. Jungers, M. Daudon, *Urol. Res.*, 2007, **35**, 179-184.
[155] A. Dessombz, C. Nguyen, H.-K. Ea, S. Rouzière, E. Foy, D. Hannouche, S. Réguer, F.-E. Picca, D. Thiaudière, F. Lioté, M. Daudon, D. Bazin, *J. Trace Elem. Med. Biol.*, 2013, **27**, 326-333.
[156] B. Hannache, A. Boutefnouchet, D. Bazin, E. Foy, M. Daudon, *Prog. Urol.*, 2015, **25**, 22-26.
[157] J. Gervasoni, A. Primiano, P. M. Ferraro, A. Urbani, G. Gambaro, S. Persichilli, *J. Chem.*, 2018, **2018**, article no. 4621256.
[158] R. Lagier, C. A. Baud, *Pathol. Res. Pract.*, 2003, **199**, 329-335.
[159] D. Bazin, E. Letavernier, J.-P. Haymann, P. Méria, M. Daudon, *Prog. Urol.*, 2016, **26**, 608-618.
[160] D. Bazin, M. Daudon, *J. Spect. Imaging*, 2019, **8**, article no. a16.
[161] D. Bazin, E. Letavernier, J.-P. Haymann, *C. R. Chim.*, 2016, **19**, 1395-1403.
[162] Y. Li, D. G. Reid, D. Bazin, M. Daudon, M. J. Duer, *C. R. Chim.*, 2016, **19**, 1665-1671.
[163] M. Daudon, D. Bazin, "New techniques to characterize kidney stones And Randall's plaque", in *Urolithiasis: Basic Science and Clinical Practice* (J. J. Talati, H. G. Tiselius, D. M. Albala, Z. Ye, eds.), Springer, New York, 2012, 683-707.
[164] H. Colas, L. Bonhomme-Coury, C. Coelho Diogo, F. Tielens, C. Gervais, D. Bazin, D. Laurencin, M. E. Smith, J. V. Hanna, M. Daudon, C. Bonhomme, *Cryst. Eng. Comm.*, 2013, **15**, 8840-8847.
[165] D. Bazin, C. Leroy, F. Tielens, C. Bonhomme, L. Bonhomme-Coury, F. Damay, D. Le Denmat, J. Sadoine, J. Rode, V. Frochot, E. Letavernier, J.-P. Haymann, M. Daudon, *C. R. Chim.*, 2016, **19**, 1492-1503.
[166] D. Bazin, M. Daudon, P. Chevallier, S. Rouzière, E. Elkaim, D. Thiaudiere, B. Fayard, E. Foy, P. A. Albouy, G. André, G. Matzen, E. Véron, *Ann. Biol. Clin. (Paris)*, 2006, **64**, 125-139.
[167] D. Bazin, X. Carpentier, O. Traxer, D. Thiaudière, A. Somogyi, S. Reguer, G. Waychunas, P. Jungers, M. Daudon, *J. Synchrotron Radiat.*, 2008, **15**, 506-509.
[168] X. Carpentier, D. Bazin, P. Jungers, S. Reguer, D. Thiaudière, M. Daudon, *J. Synchrotron Radiat.*, 2010, **17**, 374-379.
[169] D. Bazin, M. Daudon, C. Chappard, J. J. Rehr, D. Thiaudière, S. Reguer, *J. Synchrotron Radiat.*, 2011, **18**, 912-918.
[170] M. Daudon, D. Bazin, *J. Phys.: Conf. Ser.*, 2013, **425**, article no. 022006.
[171] S. Reguer, C. Mocuta, D. Thiaudière, M. Daudon, D. Bazin, *C. R. Chim.*, 2016, **19**, 1424-1431.
[172] D. Bazin, M. Daudon, E. Elkaim, A. Le Bail, L. Smrcok, *C. R. Chim.*, 2016, **19**, 1535-1541.
[173] F. Damay, D. Bazin, M. Daudon, G. André, *C. R. Chim.*, 2016, **19**, 1432-1438.
[174] M. Daudon, E. Letavernier, R. Weil, E. Véron, G. Matzen, G. André, D. Bazin, *C. R. Chim.*, 2016, **19**, 1527-1534.
[175] C. Gay, E. Letavernier, M.-C. Verpont, M. Walls, D. Bazin, M. Daudon, N. Nassif, O. Stephan, M. de Fruto, *ACS Nano*, 2020, **14**, 1823-1836.
[176] E. Esteve, S. Reguer, C. Boissiere, C. Chanéac, G. Lugo,

C. Jouanneau, C. Mocuta, D. Thiaudière, N. Leclercq, B. Leyh, J. F. Greisch, J. Berthault, M. Daudon, P. Ronco, D. Bazin, *J. Synchrotron Radiat.*, 2017, **24**, 991-999.

[177] S. Kaščáková, C. M. Kewish, S. Rouzière, F. Schmitt, R. Sobesky, J. Poupon, C. Sandt, B. Francou, A. Somogyi, D. Samuel, E. Jacquemin, A. DubartKupperschmitt, T. H. Nguyen, D. Bazin, J.-C. DuclosVallée, C. Guettier, F. Le Naour, *J. Pathol. Clin. Res.*, 2016, **2**, 175-186.

[178] M. M. Kłosowski, R. J. Friederichs, R. Nichol, N. Antolin, R. Carzaniga, W. Windl, S. M. Best, S. J. Shefelbine, D. W. McComb, A. E. Porter, *Acta Biomater.*, 2015, **20**, 129-139.

[179] K. Nitiputri, Q. M. Ramasse, H. Autefage, C. M. McGilvery, S. Boonrungsiman, N. D. Evans, M. M. Stevens, A. E. Porter, *ACS Nano*, 2016, **10**, 6826-6835.

[180] S. Boonrungsiman, E. Gentleman, R. Carzaniga, N. D. Evans, D. W. McComb, A. E. Porter, M. M. Stevens, *Proc. Natl. Acad. Sci. USA*, 2012, **109**, 14170-14175.

[181] V. Srot, B. Bussmann, U. Salzberger, J. Deuschle, M. Watanabe, B. Pokorny, I. Jelenko Turinek, A. F. Mark, P. A. van Aken, *ACS Nano*, 2017, **11**, 239-248.

[182] V. Srot, U. G. K. Wegst, U. Salzberger, C. T. Koch, K. Hahn, P. Kopold, P. A. van Aken, *Micron*, 2013, **48**, 54-64.

[183] D. E. Sayers, E. A. Stern, F. W. Lytle, *Phys. Rev. Let.*, 1971, **27**, 1204-1207.

[184] F. W. Lytle, D. A. Sayers, E. A. Stern, *Phys. Rev. B*, 1975, **11**, 4825-4835.

[185] E. A. Stern, D. E. Sayers, F. W. Lytle, *Phys. Rev. B*, 1975, **11**, 4836-4846.

[186] R. Oun, Y. E. Moussa, N. J. Wheate, *Dalton Trans.*, 2018, **47**, 6645-6653.

[187] X. Yang, M. Yang, B. Pang, M. Vara, Y. Xia, *Chem. Rev.*, 2015, **115**, 10410-10488.

[188] D. Bazin, D. A. Sayers, J. J. Rehr, *J. Phys. Chem. B*, 1997, **101**, 11040-11050.

[189] D. Bazin, D. A. Sayers, J. J. Rehr, C. Mottet, *J. Phys. Chem. B*, 1997, **101**, 5332-5336.

[190] D. Bazin, J. J. Rehr, *J. Phys. Chem. B*, 2003, **107**, 12398-12402.

[191] D. Bazin, A. Dessombz, C. Nguyen, H. K. Ea, F. Lioté, J. Rehr, C. Chappard, S. Rouzière, D. Thiaudière, S. Reguer, M. Daudon, *J. Synchrotron Radiat.*, 2014, **21**, 136-142.

[192] C. Nguyen, H. K. Ea, D. Thiaudiere, S. Reguer, D. Hannouche, M. Daudon, F. Lioté, D. Bazin, *J. Synchrotron Radiat.*, 2011, **18**, 475-480.

[193] D. Bazin, X. Carpentier, I. Brocheriou, P. Dorfmuller, S. Aubert, C. Chappard, D. Thiaudière, S. Reguer, G. Waychunas, P. Jungers, M. Daudon, *Biochimie*, 2009, **91**, 1294-1300.

[194] V. N. Robinson, *J. Microsc.*, 1975, **103**, 71-77.

[195] V. N. Robinson, *Microsc. Today*, 1997, **5**, 14-15.

[196] P. Mestres, N. Putz, M. Laue, *Microsc. Microanal.*, 2003, **9**, 490-491.

[197] S. Thiberge, A. Nechushtan, D. Sprinzak, O. Gileadi, V. Behar, O. Zik, Y. Chowers, S. Michael, J. Schlessinger, E. Moses, *Proc. Natl. Acad. Sci. USA*, 2004, **101**, 3346-3351.

[198] S. Guthrie, "Exploration of the use of ESEM for the study of biological materials", PhD Thesis, University of Cambridge, UK, 2008.

[199] I. B. Beech, C. W. S. Cheung, D. B. Johnson, J. R. Smith, *Biofouling*, 1996, **10**, 65-77.

[200] J. H. Priester, A. M. Horst, L. C. Van De Werfhorst, J. L. Saleta, L. A. K. Mertes, P. A. Holden, *J. Microbiol. Methods*, 2007, **68**, 577-587.

[201] L. Bergmans, P. Moisiadis, B. Van Meerbeek, M. Quirynen, P. Lambrechts, *Int. Endod. J.*, 2005, **38**, 775-788.

[202] A. M. Donald, *Nat. Mater.*, 2003, **2**, 511-516.

[203] J. E. McGregor, L. T. L. Staniewicz, S. E. Guthrie Neé Kirk, A. M. Donald, *Methods Mol. Biol.*, 2013, **931**, 493-516.

[204] N. de Jonge, D. B. Peckys, *ACS Nano*, 2016, **10**, 9061-9063.

[205] A. Trinidad, A. Ibáñez, D. Gómez, J. R. García-Berrocal, R. Ramírez-Camacho, "Application of environmental scanning electron microscopy for study of biofilms in medical devices", in *Microscopy: Science, Technology, Applications and Education* (A. Méndez-Vilas, J. Díaz, eds.), Microscopy Book Series, Formatex Research Center, Badajoz, Spain, 2010, 204-210.

[206] M. Fernández-Delgado, Z. Duque, H. Rojas, P. Suárez, M. Contreras, M. A. García-Amado, C. Alciaturi, *Ann. Microbiol.*, 2015, **65**, 1401-1409.

[207] E. J. Espinosa-Ortiz, B. H. Eisner, D. Lange, R. Gerlach, *Nat. Rev. Urol.*, 2019, **16**, 35-53.

Comptes Rendus
Chimie
2022, Vol. 25, Special Issue S1, p. 61-72
https://doi.org/10.5802/crchim.89

Microcrystalline pathologies: Clinical issues and nanochemistry / *Pathologies microcristallines : questions cliniques et nanochimie*

Using micro computed tomographic imaging for analyzing kidney stones

James C. Williams Jr*, [a], James E. Lingeman [b], Michel Daudon [c, d] and Dominique Bazin [e]

[a] Department of Anatomy, Cell Biology & Physiology, Indiana University School of Medicine, Indianapolis, Indiana, USA

[b] Department of Urology, Indiana University School of Medicine, Indianapolis, Indiana, USA

[c] UMR S1155, INSERM/UPMC, 4 Rue de la Chine, 75970 Paris Cedex 20, France

[d] AP-HP, Hôpital Tenon, Explorations fonctionnelles multidisciplinaires, 4 Rue de la Chine, 75970 Paris Cedex 20, France

[e] Université Paris-Saclay, CNRS, Institut de Chimie Physique, 310 rue Michel Magat, 91400 Orsay, France

E-mails: jwillia3@iu.edu (J. C. Williams Jr), JLingeman@IUHealth.org (J. E. Lingeman), michel.daudon@tnn.aphp.fr (M. Daudon), dominique.bazin@universite-paris-saclay.fr (D. Bazin)

Abstract. Stone analysis is a critical part of the clinical characterization of urolithiasis. This article reviews the strengths and limitations of micro CT in the analysis of stones. Using micro CT alone in a series of 757 stone specimens, micro CT identified the 458 majority calcium oxalate specimens with a sensitivity of 99.6% and specificity of 95.3%. Micro CT alone was also successful in identifying majority apatite, brushite, uric acid, and struvite stones. For some minor minerals—such as apatite in calcium oxalate or calcium salts in uric acid stones—micro CT enables the detection of minute quantities well below 1%. The addition of a standard for calibrating X-ray attenuation values improves the ability of micro CT to identify common stone minerals. The three-dimensional nature of micro CT also allows for the visualization of surface features in stones, which is valuable for the study of stone formation.

Keywords. Calcium oxalate, Apatite, Uric acid, Struvite, Brushite.

Published online: 29 June 2021, Issue date: 1 September 2022

1. Introduction

Urinary stone analysis is an essential part of the diagnosis and treatment of stone diseases [1–3], but the laboratory methods used for stone analysis have remained largely unchanged for seventy years, involving the manual dissection of stones followed by molecular spectroscopy for mineral identification [4–6]. One technology that remains relatively novel in the field of stone analysis is micro computed tomographic imaging (micro CT) [7–9].

The method was first applied to kidney stones for

* Corresponding author.

study of the mechanisms of stone breakage by shock wave lithotripsy [10], and in those studies it became clear that micro CT could provide exquisite detail of the structure of urinary stones. It has now been applied to the analysis of urinary stones for over a decade [7,11], for different kinds of kidney stones including those of calcium oxalate [12–14], apatite [15], brushite [16], cystine [17], and uric acid [18].

Despite the extensive use of micro CT in imaging urinary stones, little has been published on how well micro CT performs, by itself, in identifying stone mineral. The purpose of the present paper is to introduce the technology to those unfamiliar with it, to present data on the accuracy of stone analyses done using micro CT alone, to propose a simple method for standardizing X-ray attenuation values to aid in identification of mineral type by micro CT, to describe the characteristics of different minerals as they appear by micro CT, and to show the potential of micro CT to accurately report the three-dimensional structure of stones.

2. Basics of micro CT imaging

The basic operation of a micro CT system is illustrated in Figure 1. The process is very much like the old "step-and-shoot" clinical CT systems [19], except that with micro CT the specimen itself is rotated and not the X-ray source/detector. The specimen is mounted in the path of a microfocus X-ray source and the shadow of the specimen is collected by a high-resolution X-ray camera. After one image is collected, the specimen is rotated slightly (e.g., 0.7°) and a new image collected. This is repeated until at least 180° of rotation is captured. The set of shadow images can then be converted to tomographic image slices using the Feldkamp method [20].

The size of specimens for micro CT is generally limited to a few centimeters in dimension, and to obtain the high-resolution characteristic of micro CT, the intensities of X-rays are high and the exposure times are relatively long (typically 15–30 min of continuous irradiation, which is generally inappropriate for living things, although for intermediate-resolution, it is possible to use micro CT in laboratory animals [21]).

3. Methods

This paper provides an overview of the method of micro CT, but also gives results of a study designed to test how well micro CT can analyze stones by itself. Most of the stones analyzed for the present paper were collected as part of an ongoing study of kidney stones, in which patients are consented for study under the Indiana University Internal Review Board (under guidelines from the United States Health and Human Services Office of Human Subjects protection). The rest of the stones were obtained as de-identified specimens, in large part as discards from a stone analysis laboratory (Beck Analytical, Greenwood, IN, USA), but also as de-identified specimens provided by other research groups for analysis. Each stone specimen was rinsed and dried at room temperature. It was then scanned using the Skyscan 1172 Micro CT system (Bruker, Kontich, Belgium), typically using 60 kVp, 0.5 mm Al filter, and 0.7° rotation step for final (cubic) voxel sizes of 2–12 μm. Stones were typically mounted in Styrofoam for scanning, as that material is remarkably X-ray lucent.

Following micro CT imaging, the minerals present were tentatively identified by a single investigator (JCW) using only photographs of the stones and the micro CT image stacks. Portions of each stone specimen were then dissected away and analyzed using conventional Fourier-transform infrared spectroscopy (FT-IR, using the KBr pellet method). If the results of the FT-IR analysis did not account for all the apparently different minerals seen by micro CT, more samples were run by FT-IR. The FT-IR results were used as ground truth for the mineral composition of each specimen, and the micro CT observations taken beforehand (i.e., blinded to the FT-IR) were graded as correct or incorrect.

Standardizing the X-ray attenuation values for micro CT with stones (e.g., establishing CT numbers as Hounsfield units) is extremely problematic because of the wide range of stone sizes scanned (over 4 orders of magnitude, from about 0.05 to over 1000 mm^3). In general, there is no way to correctly adjust beam hardening correction during image reconstruction to compensate for such dramatic variations in sample volume [22]. Additionally, we always maximize the magnification in the Skyscan 1172 micro CT system for each specimen to gain the best resolution possible. While it would be possible to

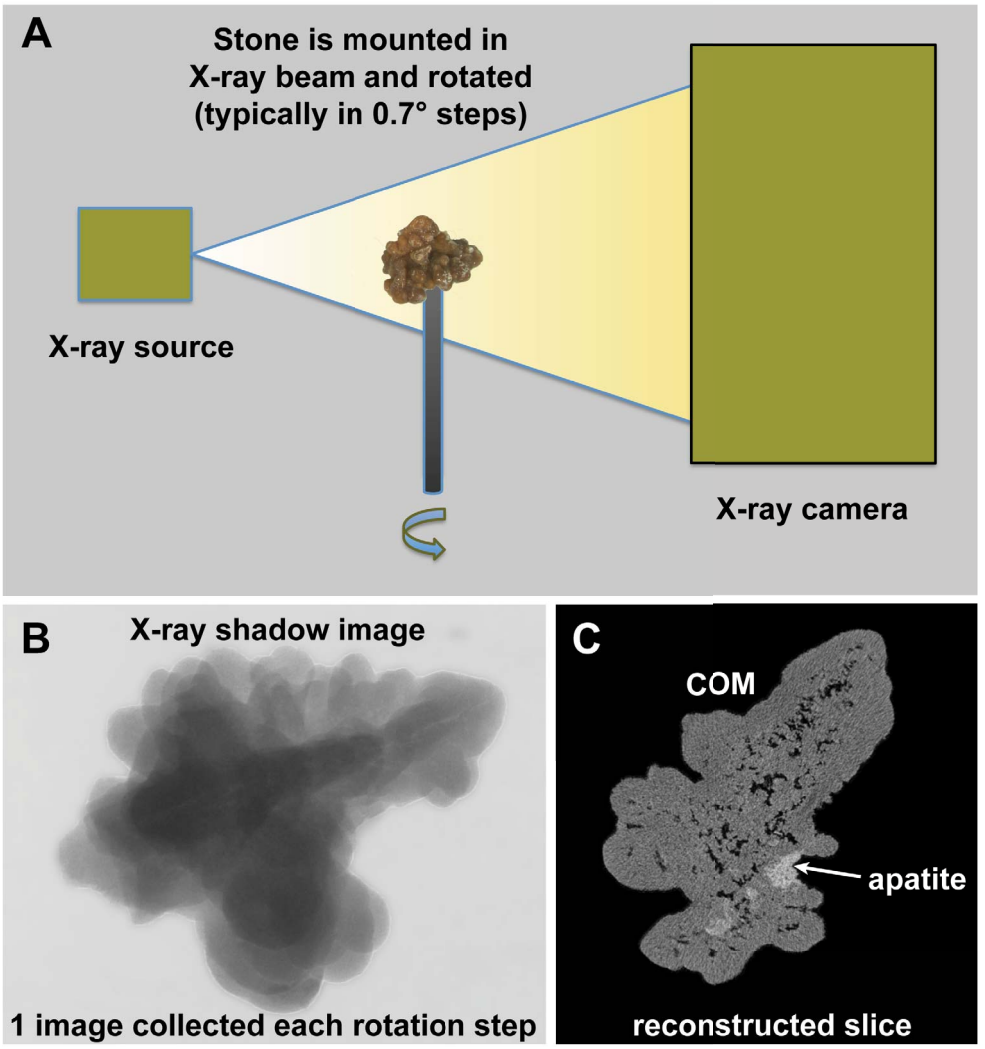

Figure 1. Basic scheme of micro CT. (A) The X-ray source shines a cone beam onto the specimen and the shadow of the specimen is captured using a high-resolution digital camera. The specimen is rotated in steps and a shadow image (B) collected at each step. The collection of rotation images is then processed mathematically to yield image slices (C). COM: calcium oxalate monohydrate.

run a comparably sized standard at each magnification used for imaging stone specimens, this would be terribly impractical. To overcome this difficulty, we recently have been including a stone standard with the micro CT scan of at least one sample within each patient specimen. The stone standard is composed of FT-IR-verified calcium oxalate monohydrate (COM) and uric acid and is about 2 mm in diameter (Figure 2). Inclusion of this standard has allowed standardization of apparent X-ray attenuation values within any scan. Apparent attenuation values were mapped to an arbitrary scale in which the attenuation of the uric acid standard portion was taken to be 4500 and that of COM was 17,500 (to match arbitrary CT numbers seen in an earlier study [8]).

Three-dimensional (3D) imaging of micro CT image stacks was done using the 3D Viewer plugin on ImageJ [24].

In displaying 3D surface renderings of stones, we have sometimes encountered individuals who mistakenly presume that such images are similar to scanning electron microscopy (SEM). To demonstrate

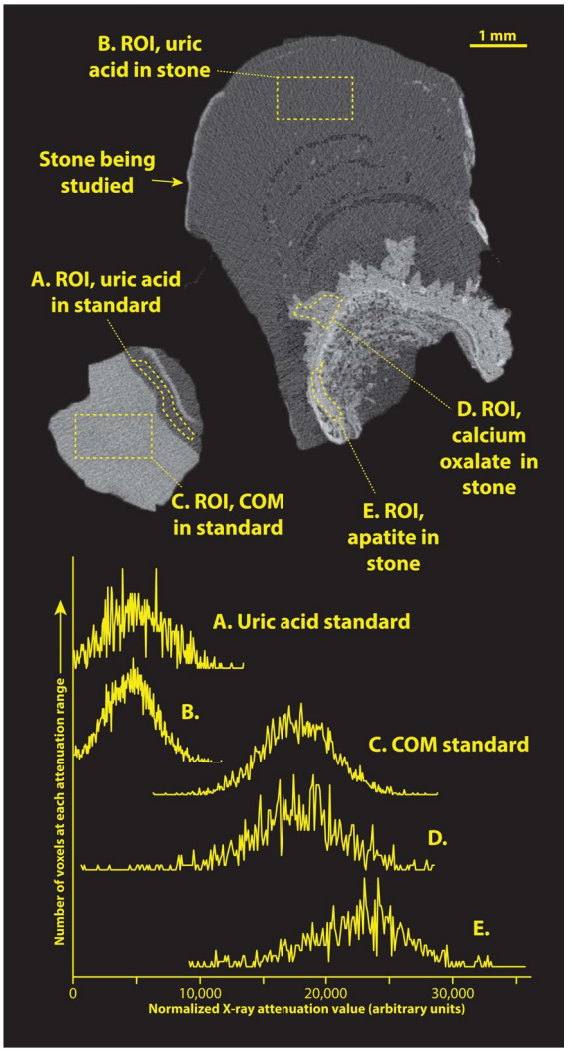

Figure 2. Example of a patient specimen scanned along with the COM/uric acid standard. Top shows image slice of micro CT of specimen, right, and standard, left. Regions-of-interest (ROI's) are shown as drawn within this image, and histograms of pixel values within each ROI are shown below. Note that the CT numbers from image slice have been transformed to match the arbitrary scale previously published [8]. For comparison, the actual linear attenuation coefficient (μ) of uric acid at this voltage is approximately 0.40/cm for uric acid stones, and 1.01/cm for COM [23].

the differences between these methods, some stones were also imaged using SEM, using a Zeiss SUPRA 55VP field emission-scanning electron microscope. In order to preserve the structural and the chemical integrities, the SEM observations were made at low voltage (1.4 keV) and without the usual deposits of carbon at the surface of the sample [25].

4. Results and discussion

Overall accuracies for mineral identifications using micro CT are shown in Table 1. The data show that micro CT by itself is relatively useful for analyzing stones, but that significant errors did occur. In particular, infrequent stone types were never correctly identified using micro CT alone. This was expected, as an absence of experience with a rare mineral precluded the chance of recognizing peculiar morphologies, even if they were present. For example, we have examined only a handful of specimens containing any whitlockite, and no consistent morphology of this mineral has been apparent by micro CT, but we cannot rule out the possibility that this mineral could be recognized using micro CT with more experience. A great many of the organic materials (all the urates, 1-methyl uric acid, dihydroxyadenine, matrix stone) had an X-ray attenuation value similar to that of uric acid, also without apparent uniqueness of morphology by micro CT.

The distribution of mineral types in this series reflects the fact that the stone specimens came primarily from a urology practice that receives a great many referrals for difficult stone cases. Thus it is that 7.7% of the specimens were majority brushite and 1.5% cystine stones, both of which are considerably higher proportions than seen in most studies [26]. Similarly, the proportion of calcium oxalate stones in this series was correspondingly low (60.5%).

Identification of apatite as the major mineral using micro CT alone was the most problematic of the common minerals, with a sensitivity of only 88.5% for 114 specimens. This is partly due to the remarkable variability in morphology of apatite stones [15], and the wide variation in X-ray attenuation of apatite mineral in stones (see more on this below). Early in the series, there were also a few instances of confusing densely packed brushite with COM,

Table 1. Overall accuracy of micro CT analysis used by itself to identify majority mineral among 757 urinary stone specimens

Major mineral	Number	Sensitivity (%)	Specificity (%)
Calcium oxalate	458	99.6	95.3
Apatite	114	88.5	99.2
Brushite	58	89.7	99.6
Uric acid	56	96.4	99.4
Struvite	49	93.9	99.6
Cystine	11	90.9	99.6
Ammonium acid urate	3	0	99.6
1-methyl uric acid	1	0	100
Sodium acid urate	1	0	100
Mixed urates	1	0	100
Calcium tartrate tetrahydrate	1	0	100
Dihydroxyadenine	1	0	100
Matrix stone	1	0	100
Octacalcium phosphate	1	0	100
Whitlockite	1	0	100

Sensitivity is calculated as the number of correct identifications divided by the total number of specimens of that majority mineral (as verified by spectroscopic analysis). Specificity is the proportion of specimens correctly identified as *not* being composed of that majority mineral; less than 100% specificity indicates that there was at least one specimen that was incorrectly identified as being composed of that majority mineral.

two forms which can appear with remarkably similar morphology by micro CT (also described more below). This confusion between COM and brushite has been largely eliminated in recent years by using an attenuation standard (Figure 2).

4.1. *Variation in attenuation values for stone mineral in micro CT*

Using a single mineral standard (composed of COM and uric acid, Figure 2) that was included with micro CT scans, the apparent attenuation values for a variety of minerals is shown in Figure 3. Note that even though the mineral in each of the regions tested was verified by FT-IR, the X-ray attenuation values varied within each mineral type. This presumably is due to variation in the density of mineral crystals within the stone matrix [27]. Nevertheless, these attenuation measurements have proved to be very useful in identifying mineral on micro CT scan. For example, a specimen that yields X-ray attenuation in the middle range (7000–12,000) can subsequently be identified by its visual appearance: If it consists of dull brown, polygonal crystals, it is likely to be calcium tartrate tetrahydrate [28]; if it consists of sparkling crystals, it is almost certainly cystine [5]; if the crystals are white, or the stone consists of rather coarse layers, the stone is probably composed of struvite [2]. Similarly, the higher attenuation of brushite than the COM in the standard has enabled more accurate identification of densely packed brushite stones and eliminated the confusion with COM that had sometimes occurred in the past.

4.2. *General appearance of calcium oxalate by micro CT*

Several micro CT images of COM and of calcium oxalate dihydrate (COD) have already been published [7,12,29], but the most common forms that we

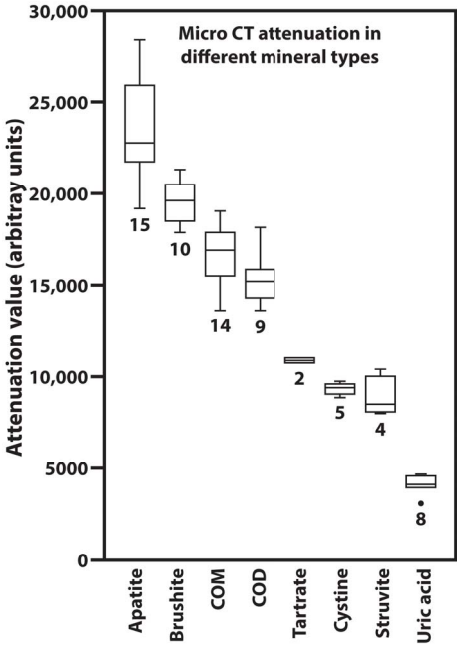

Figure 3. Variation in attenuation values for urinary stone minerals, all measured against the same standard of COM and uric acid (Figure 2). Numerals indicate the number of different specimens measured. Each measurement was done on a region of stone specimen that had been confirmed in its composition using infrared spectroscopy. Plots show boxes to indicate first and third quartiles, with the horizontal line indicating the median. Whiskers extend to the outermost point or to 1.5 times the interquartile distance (whichever is smaller). The outlier point (for uric acid) shows a specimen with an attenuation value more than 1.5 times the interquartile distance below the first quartile. COD: calcium oxalate dihydrate. Tartrate: calcium tartrate tetrahydrate.

have seen consist of tightly packed COM, of stones with obvious shapes of COD crystals some of which have been converted to COM [5], and others composed mainly of unconverted COD (Figure 4). Panel A shows a typical stone composed of tightly packed COM (type Ia [2]). By micro CT the COM appears as a rather homogeneous gray. Void regions are commonly seen in such stones, and the presence of any apatite is easily recognized [27]. In stones with less-tightly packed COM, the outlines of COM regions are sometimes suggestive of the characteristic polygons of COD crystals. Polygonal surface crystals were quite obvious in the stone shown in Figure 4B, where the crystal shapes are easy to see on the photograph of the stone surface. This stone was apparently formed initially as COD but with subsequent conversion of almost all of the COD to COM. Unconverted COD crystals are apparent in Figure 4C, along with the early stages of conversion to COM, which interestingly can occur from within the interior of the COD crystal [30].

4.3. *Apatite by micro CT*

Figure 5 shows some common morphologies of majority apatite stones. Apatite is the stone mineral with the highest effective atomic number [31], and so it commonly shows up in micro CT as the brightest (most X-ray attenuating) mineral, but it is also clear that apatite can be present in stones in some kind of low-density form. This is seen in the common layering morphology of apatite, with alternating bright and dark layers [15,32]. Extensive analysis of layered apatite stones (not containing calcium oxalate) using FT-IR has never revealed any mineral in the dark layers other than apatite. This is consistent with the description of type IVa stones with concentric layering by Daudon et al., who also found only apatite in this morphology of apatite stone [2]. Similarly, larger X-ray-dark regions within an apatite stone (as shown by the asterisk in Figure 5) always have shown in our experience only apatite by FT-IR. Thus it seems certain that apatite can deposit in stones in both an X-ray dense form and also with lower densities of mineral content (presumably suspended in organic material). Figure 5B shows a stone in which apatite layers alternate with COD (the IIa + IVa morphology, commonly occurring with hypercalciuria [33]). Panel C shows an apatite stone with a large, central region of lower X-ray attenuation and with a thin shell composed of COM.

4.4. *Brushite by micro CT*

Several micro CT images of brushite stones are already published [12,16,32,34], but the two primary morphologies seen by micro CT are shown in Figure 6. When the brushite in stones manifests as long,

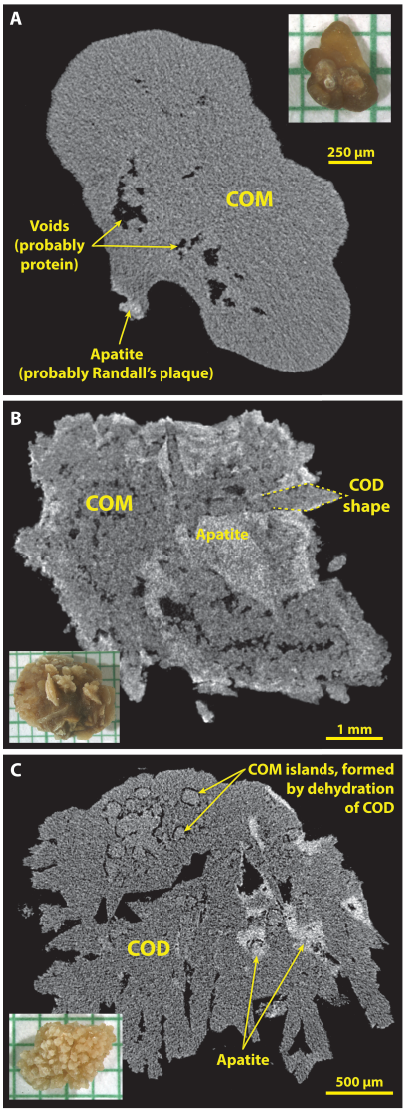

Figure 4. Typical morphologies of calcium oxalate stones as seen by micro CT. Insets show photographs of stones on mm paper. (A) Type Ia stone, probably on Randall's plaque, shows the rather homogeneous gray appearance of tightly packed COM. (B) Stone showing COD crystal shapes but in which the COD has been almost entirely converted to COM. (C) Stone composed mainly of COD, but showing the beginning stages of conversion to COM. In stones forming as COD crystals, it was common to see the interstices filled with apatite (panels B and C), as has been previously described [30].

radial crystals, it is quite distinctive and easy to recognize (Figure 6A). When brushite occurs with calcium oxalate, it is also easy to distinguish, as its X-ray attenuation is generally brighter than that of the oxalates, as shown in multiple examples in reference [16]. In contrast, we have often been fooled in the past by brushite stones in which the mineral is compact (Figure 6B), and this was the primary source of false positives for COM (Table 1). When a stone specimen is scanned with a standard containing COM, recognition of compact brushite stones by their X-ray attenuation has been straightforward.

4.5. *Uric acid by micro CT*

The accuracy of identifying uric acid stones solely by micro CT was good (Table 1), but undoubtedly the unique colors of these stones played some role in their being so easily recognized. For example, when one has a urinary stone that is orange in color, the subsequent discovery of it being composed of uric acid is not surprising. Nevertheless, the identification of uric acid by micro CT is still likely to be quite accurate without seeing the color of the stone, as its X-ray attenuation value is by far the lowest of the major minerals. As shown in Figure 7, if one adjusts the micro CT image so that the details of any calcium salts are visible, uric acid appears almost as dark as air.

As shown in Figure 7A, even rather pure uric acid stones almost always had inclusions of calcium salts, which most commonly were found to be COM (if the inclusions were large enough to analyze spectroscopically). Out of the 55 specimens containing majority uric acid, only 2 showed no inclusions of calcium salts by micro CT, but quite a few showed calcium salts as <1% of the total volume of the stone, a level that is not likely to be detected spectroscopically. In a larger series, about 12% of majority uric acid stones were found to be pure [26], but the macroscopic methods used for analysis in that series were unlikely to have detected the presence of calcium salts with volume <1% of the total [35]. The content of calcium salts in uric acid stones may have clinical consequences, as this is a likely cause for failure of dissolution therapy [36].

4.6. *Struvite by micro CT*

Recognition of struvite in urinary stones is relied upon as a clinical indicator of infection [37], but anal-

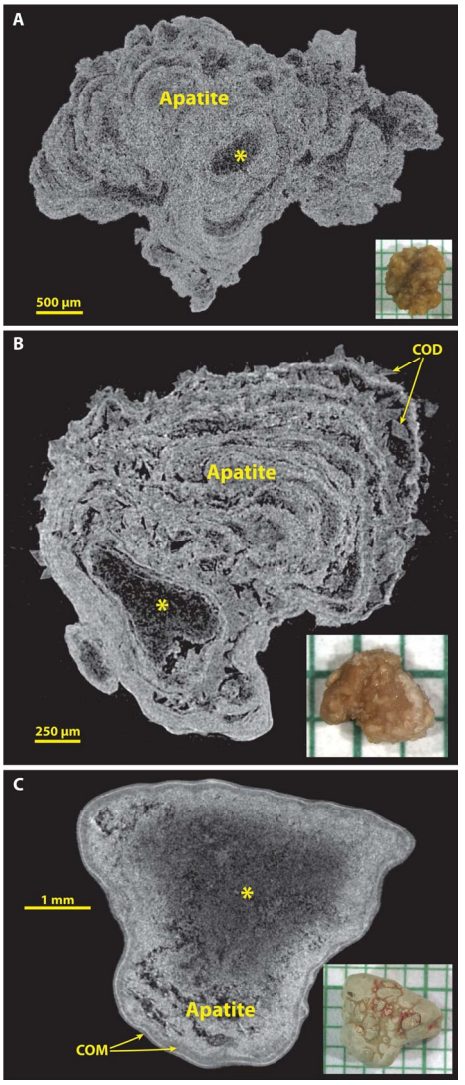

Figure 5. Apatite stones most commonly show alternation of X-ray-dense and more lucent layers, and often relatively large X-ray-lucent regions (*). Spectroscopic analysis of X-ray-lucent regions in apatite stones has always shown only apatite, but sometimes with an increase in the protein content of the material. (A) A typical apatite stone, pure by spectroscopic analysis. (B) An example of the IVa + IIa morphology, with COD crystals between apatite layers. (C) An apatite stone that has thin layers of COM at its surface.

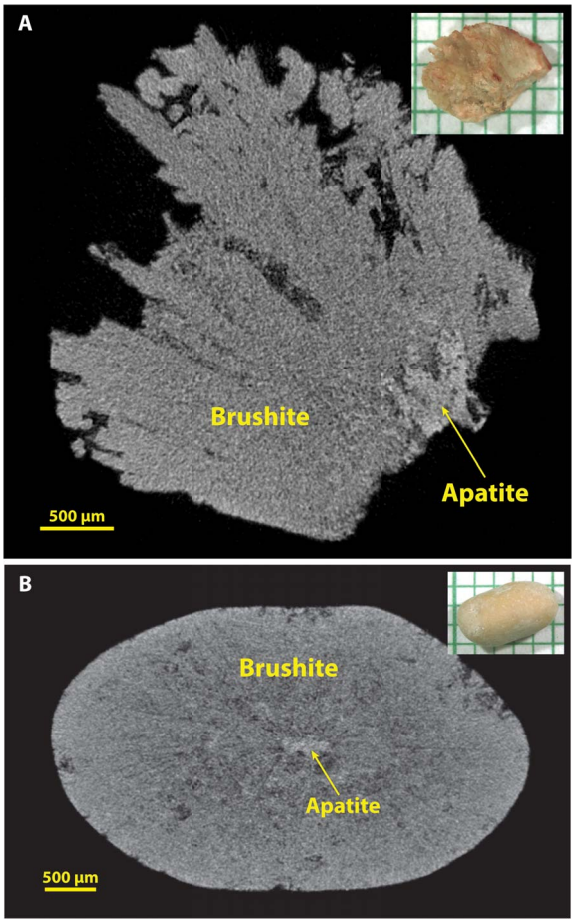

Figure 6. Brushite stones. (A) Brushite with radial crystals, which are quite distinctive by micro CT. (B) Brushite in a more compact form, which can be easily mistaken for COM by micro CT. Inclusion of a COM standard with the micro CT scan can make identification of brushite easier because brushite tends to have a higher X-ray attenuation than does COM (see Figure 3).

ysis of struvite by commercial laboratories has been shown to be the most problematic of all the major stone minerals [38]. Similarly, our recognition of struvite solely by micro CT has not been without error; in our series of stones shown in Table 1, there were 49 specimens with majority struvite and 3 of these were missed (along with another 3 specimens falsely identified as struvite). Failure to identify struvite as a minority mineral has been even more common in our specimen series, as infection stones commonly present with alternating layers of apatite and struvite [2]. When the apatite dominates by volume and the struvite layers are relatively thin, it is quite easy

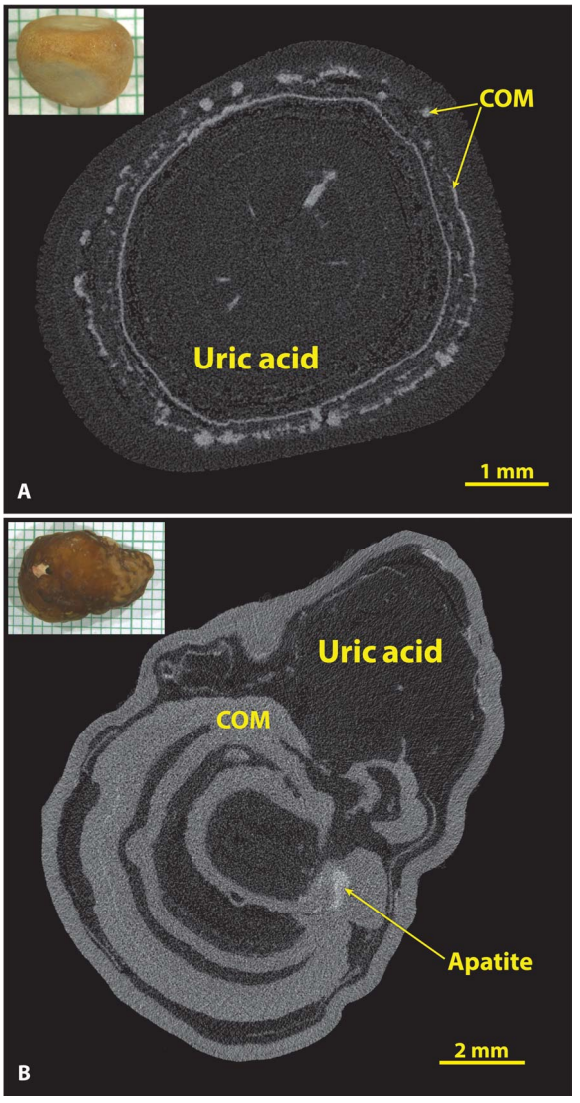

Figure 7. Uric acid in stones has the lowest X-ray attenuation values of the common stone minerals. (A) A typical uric acid stone, nearly pure (93% uric acid by volume). (B) A stone with alternating layers of uric acid and COM. In both (A) and (B) the uric acid was of the anhydrous form by spectroscopic analysis, but the dihydrate form of uric acid looks exactly the same by micro CT.

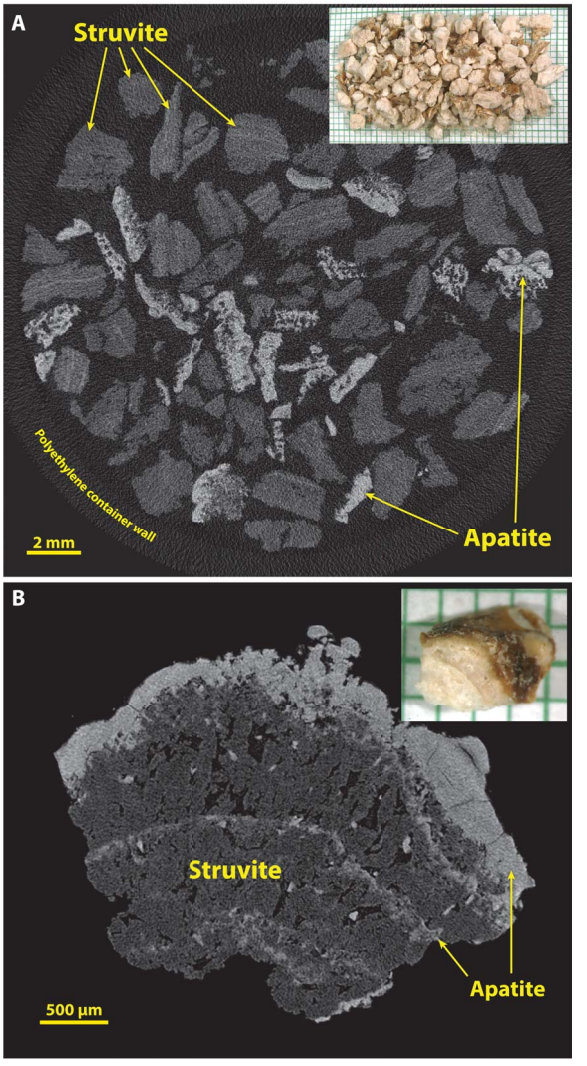

Figure 8. Struvite stones. Infection stones are commonly of large size, and thus usually appear for analysis as multiple fragments retrieved from a suction reservoir following endoscopy. (A) Multiple fragments from a large stone, scanned *en masse* in a plastic container. Note that the X-ray attenuation of struvite is rather low, but struvite stones commonly also contain apatite. (B) Higher resolution of a struvite stone fragment to show the typical microstructure of this type of stone.

to miss the minor content of struvite by micro CT. When the struvite layers are thicker, one can more easily recognize the middle-level of X-ray attenuation of the struvite (Figure 3) and identify that mineral properly.

In our experience, struvite is most commonly encountered in large stones, which for analysis often

consist merely of fragments that have been recovered from the saline suction reservoir, as shown in Figure 8A. In this setting, it is generally easy to recognize struvite fragments by their mid-range values for X-ray attenuation (Figure 3), invariably accompanied by fragments containing apatite. Figure 8A also illustrates the ability of micro CT to scan a large specimen of stone fragments at once. It should be noted, though, that the scanning of such a large specimen generally can be done only at lower values for image resolution, and usually with increased noise in the image. Some micro CT systems have the ability to scan such large specimens at high resolution, but the scan times are correspondingly long and the image files excessively large. An alternative is to scan collections of fragments at lower resolution and then select single fragments for scanning at higher resolution, as shown in Figure 8B, which shows coarse crystals of struvite sandwiched by apatite.

4.7. *3D surface renderings using micro CT*

Because the micro CT image stack is typically composed of cubic voxels, it is a straightforward process to carry out a surface rendering to reveal 3D structure. This method is especially powerful for small stones, which can be scanned at high resolution. Figure 9 shows such an example of very early growth of a COM stone onto a piece of Randall's plaque that was pulled from the tip of the renal papilla. The surface renderings (shown in panels A and C) show collecting duct lumens with great clarity. However, the mineralized tubules at the edge of the Randall's plaque (such as that indicated by the left arrowhead in the slice image shown in panel B) were not visualized by the surface rendering method, presumably because of unevenness in the X-ray attenuation of the apatite in Randall's plaque. Note that the photograph in Figure 9A does not show the collecting ducts so easily seen in the micro CT surface rendering. This is probably because the surface of the stone was covered with X-ray-lucent organic material (including epithelium covering the plaque and lining the lumens of the collecting ducts) that obscured the view in the photograph.

Surface rendering with micro CT cannot provide the surface detail visible using SEM, as shown in Figure 10. The surface rendering easily shows the region of Randall's plaque—which is also easily seen in the photograph—but with very little detail on the plaque. Because this stone was much larger than the calculus shown in Figure 9, it could not be scanned

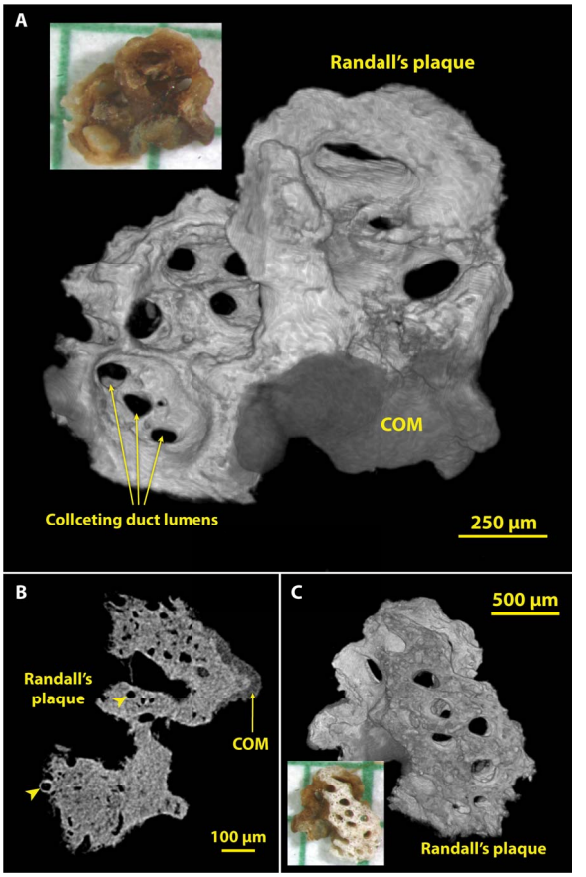

Figure 9. Using micro CT to visualize structures in three dimensions (3D). Shown are images of a small calculus that had been adherent to the renal papilla. The bulk of the "stone" was actually well-developed Randall's plaque, with a small region of COM overgrowth from the urine. (A) 3D surface rendering showing the side of the calculus that faced the urine. Lumens of collecting ducts (about 100–150 µm in diameter) through the mineralized plaque are obvious. (B) Micro CT slice through part of the calculus showing COM overgrowth and the lumens of thin limbs and vessels within the plaque region (arrowheads). (C) Surface rendering of the underside of the calculus. Micro CT scan of this calculus was high resolution (2.08 µm voxel size).

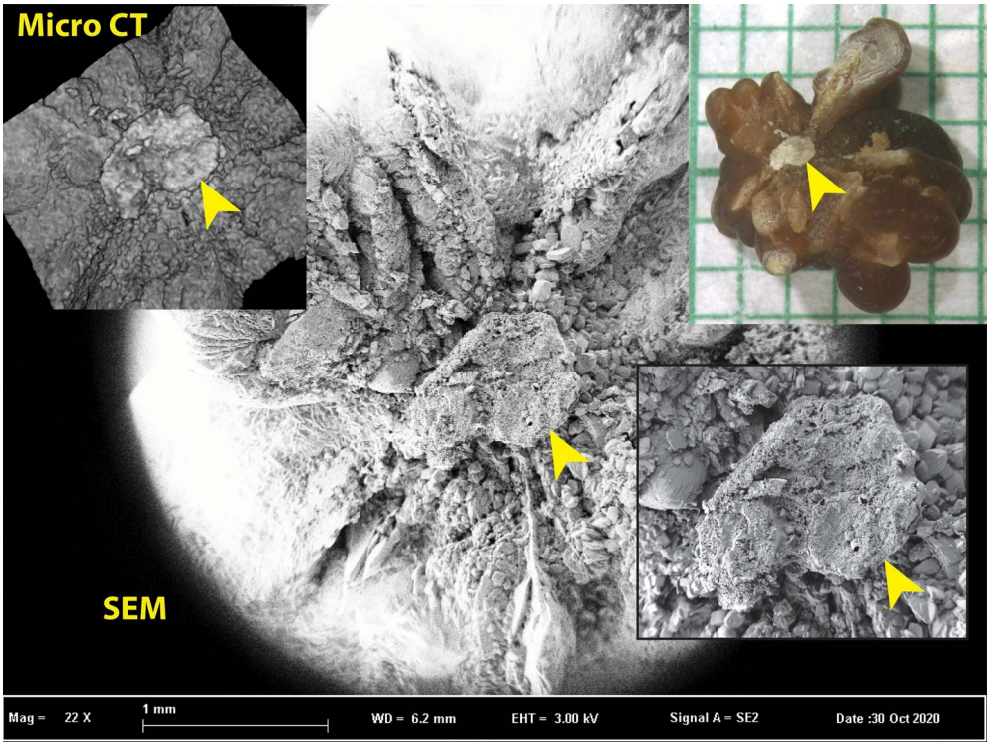

Figure 10. Comparison of the ability of micro CT to show surface features with the superior ability of scanning electron microscopy (SEM). Inset upper right shows stone with apparent Randall's plaque umbilication (arrowhead). Inset upper left shows micro CT surface rendering from an image stack (with 5.9 μm cubic voxels). The plaque region is recognizable in the micro CT surface rendering but is unable to show the detail apparent by SEM (background and inset lower right).

with as high a resolution, and so the quality of the 3D rendering is correspondingly lower. Surface details are seen much more clearly with SEM.

5. Conclusion

Micro CT is a powerful tool for visualizing urinary stones. The X-ray attenuation values of common stone minerals allow easy visualization of stone structure and mineral identification, especially if an attenuation standard is included with a specimen. However, micro CT alone cannot identify many rarer stone types, which still require spectroscopic analysis. The 3D rendering capabilities of micro CT provide insight into the structure of nascent stones, and thus this method has great value in the study of pathophysiological mechanisms of stone disease.

Acknowledgements

The work described here was all performed on micro CT systems obtained through shared instrumentation grants (NIH S10 RR023710 and NIH S10 OD016208). Stones came mainly from patients enrolled in NIH P01 DK056788, with additional support from NIH R01 DK124776. We thank Drs. Michael Borofsky, Marawan El Tayeb, Glenn Gerber, Jonathan Harper, Amy Krambeck, John Lieske, David Lifshitz, Marcelino Rivera, and James Smotherman for providing de-identified specimens, and Molly Jackson, Courtney Weiler, Tony Gardner, Josh Heiman, Blake Anderson, and Angela Sabo for help with stone and data analysis over the years.

References

[1] J. C. Williams Jr, G. Gambaro, A. Rodgers, J. Asplin, O. Bonny, A. Costa-Bauzá, P. M. Ferraro, G. Fogazzi, D. G. Fuster, D. S. Goldfarb *et al.*, *Urolithiasis*, 2021, **49**, 1-16.

[2] M. Daudon, C. A. Bader, P. Jungers, *Scanning Microsc.*, 1993, **7**, 1081-1106.

[3] M. Daudon, A. Dessombz, V. Frochot, E. Letavernier, J.-P. Haymann, P. Jungers, D. Bazin, *C. R. Chim.*, 2016, **19**, 1470-1491.

[4] E. L. Prien, C. Frondel, *J. Urol.*, 1947, **57**, 949-994.

[5] M. Daudon, J. C. Williams Jr, "Characteristics of human kidney stones", in *Kidney Stones* (F. Coe, E. M. Worcester, J. E. Lingeman, A. P. Evan, eds.), Jaypee Medical Publishers, London, UK, 2020, 77-97.

[6] M. Daudon, P. Jungers, D. Bazin, J. C. Williams Jr, *Urolithiasis*, 2018, **46**, 459-470.

[7] J. C. Williams Jr, J. A. McAteer, A. P. Evan, J. E. Lingeman, *Urol. Res.*, 2010, **38**, 477-484.

[8] C. A. Zarse, J. A. McAteer, A. J. Sommer, S. C. Kim, E. K. Hatt, J. E. Lingeman, A. P. Evan, J. C. Williams Jr, *BMC Urol.*, 2004, **4**, article no. 15.

[9] P. Ruegsegger, B. Koller, R. Muller, *Calcif. Tissue Int.*, 1996, **58**, 24-29.

[10] R. O. Cleveland, J. A. McAteer, R. Müller, *J. Acoust. Soc. Am.*, 2001, **110**, 1733-1736.

[11] D. Bazin, C. Leroy, F. Tielens, C. Bonhomme, L. Bonhomme-Coury, F. Damay, D. Le Denmat, J. Sadoine *et al.*, *C. R. Chim.*, 2016, **19**, 1492-1503.

[12] J. C. Williams Jr, E. Worcester, J. E. Lingeman, *Urolithiasis*, 2017, **45**, 19-25.

[13] C. A. Zarse, T. A. Hameed, M. E. Jackson, Y. A. Pishchalnikov, J. E. Lingeman, J. A. McAteer, J. C. Williams Jr, *Urol. Res.*, 2007, **35**, 201-206.

[14] B. R. Matlaga, A. D. Shore, T. Magnuson, J. M. Clark, R. Johns, M. A. Makary, *J. Urol.*, 2009, **181**, 2573-2577.

[15] R. Pramanik, J. R. Asplin, M. E. Jackson, J. C. Williams Jr, *Urol. Res.*, 2008, **36**, 251-258.

[16] J. C. Williams Jr, M. S. Borofsky, S. B. Bledsoe, A. P. Evan, F. L. Coe, E. M. Worcester, J. E. Lingeman, *J. Urol.*, 2018, **199**, 186-192.

[17] S. C. Kim, E. K. Hatt, J. E. Lingeman, R. B. Nadler, J. A. McAteer, J. C. Williams Jr, *J. Urol.*, 2005, **174**, 1468-1471.

[18] A. N. Primak, J. G. Fletcher, T. J. Vrtiska, O. P. Dzyubak, J. C. Lieske, M. E. Jackson, J. C. Williams, C. H. McCollough, *Acad. Radiol.*, 2007, **14**, 1441-1447.

[19] G. N. Hounsfield, *Br. J. Radiol.*, 1973, **46**, 1016-1022.

[20] L. A. Feldkamp, L. C. Davis, J. W. Kress, *J. Opt. Soc. Am. A*, 1984, **1**, 612-619.

[21] E. M. B. McNerny, D. T. Buening, M. W. Aref, N. X. Chen, S. M. Moe, M. R. Allen, *Bone*, 2019, **125**, 16-24.

[22] P. L. Salmon, X. Liu, *Open Access J. Sci. Technol.*, 2014, **2**, article no. 101142.

[23] H. D. Mitcheson, R. G. Zamenhof, M. S. Bankoff, E. L. Prien, *J. Urol.*, 1983, **130**, 814-819.

[24] J. Schindelin, I. Arganda-Carreras, E. Frise, V. Kaynig, M. Longair, T. Pietzsch, S. Preibisch, C. Rueden *et al.*, *Nat. Methods*, 2012, **9**, 676-682.

[25] D. Bazin, M. Daudon, *Ann. Biol. Clin. (Paris)*, 2015, **73**, 517-534.

[26] M. Daudon, R. Donsimoni, C. Hennequin, S. Fellahi, G. Le Moel, M. Paris, S. Troupel, B. Lacour, *Urol. Res.*, 1995, **23**, 319-326.

[27] S. Winfree, C. Weiler, S. B. Bledsoe, T. Gardner, A. J. Sommer, A. P. Evan, J. E. Lingeman, A. E. Krambeck, E. M. Worcester, T. M. El-Achkar, J. C. Williams Jr, *Urolithiasis*, 2021, **49**, 123-135.

[28] C. Kleinguetl, J. C. Williams Jr, J. C. Lieske, M. Daudon, M. E. Rivera, P. J. Jannetto, J. Bornhorst, D. Rokke, E. T. Bird, J. E. Lingeman, M. M. El Tayeb, *Urology*, 2019, **126**, 49-63.

[29] J. C. Williams Jr, J. E. Lingeman, F. L. Coe, E. M. Worcester, A. P. Evan, *Urolithiasis*, 2015, **43**, 13-17.

[30] G. Schubert, G. Brien, *Int. Urol. Nephrol.*, 1981, **13**, 249-260.

[31] M. Qu, J. C. Ramirez-Giraldo, S. Leng, J. C. Williams, T. J. Vrtiska, J. C. Lieske, C. H. McCollough, *Am. J. Roentgenol.*, 2011, **196**, 1279-1287.

[32] A. P. Evan, J. E. Lingeman, E. M. Worcester, A. J. Sommer, C. L. Phillips, J. C. Williams Jr, F. L. Coe, *Anat. Rec.*, 2014, **297**, 731-748.

[33] M. Daudon, *Rev. Med. Suisse Romande*, 2004, **124**, 445-453.

[34] M. S. Makki, S. Winfree, J. E. Lingeman, F. A. Witzmann, E. M. Worcester, A. E. Krambeck, F. L. Coe, A. P. Evan *et al.*, *Kidney Int. Rep.*, 2020, **5**, 663-677.

[35] S. S. Pollack, G. L. Carlson, *Am. J. Clin. Pathol.*, 1969, **52**, 656-660.

[36] C. Reichard, B. C. Gill, C. Sarkissian, S. De, M. Monga, *Urology*, 2015, **85**, 296-298.

[37] D. P. Griffith, *Kidney Int.*, 1978, **13**, 372-382.

[38] A. E. Krambeck, N. F. Khan, M. E. Jackson, J. E. Lingeman, J. A. McAteer, J. C. Williams Jr, *J. Urol.*, 2010, **184**, 1543-1549.

Comptes Rendus
Chimie
2022, Vol. 25, Special Issue S1, p. 73-82
https://doi.org/10.5802/crchim.121

Microcrystalline pathologies: Clinical issues and nanochemistry / *Pathologies microcristallines : questions cliniques et nanochimie*

Raman spectroscopy as a non-destructive tool to determine the chemical composition of urinary sediments

Sandra Tamosaityte [a], Milda Pucetaite [a, b], Arunas Zelvys [c], Sonata Varvuolyte [c], Vaiva Hendrixson [c] and Valdas Sablinskas [*, a]

[a] Faculty of Physics, Vilnius University, Sauletekio al. 9, LT-10222 Vilnius, Lithuania

[b] Department of Biology, Lund University, Sölvegatan 37, 22362 Lund, Sweden

[c] Faculty of Medicine, Vilnius University, M.K. Ciurlionio g. 21, LT-03101, Vilnius, Lithuania

E-mails: s.tamosaityte@gmail.com (S. Tamosaityte), milda.pucetaite@gmail.com (M. Pucetaite), arunas.zelvys@santa.lt (A. Zelvys), sonata.varvuolyte@mf.vu.lt (S. Varvuolyte), vaiva.hendrixson@mf.vu.lt (V. Hendrixson), valdas.sablinskas@ff.vu.lt (V. Sablinskas)

Abstract. Urolithiasis is a common disease worldwide, but its causes are still not well understood. In many cases, crystalluria provides an early indication of urinary stone formation, and characterisation of the urinary deposits could help doctors to take early preventative measures to stop their further growth. Nowadays, the gold standard for the analysis of urinary deposits is optical microscopy, but the morphology-based information it provides can often be unreliable and incomplete, particularly for deposits with no defined crystalline structure. In response to the need of a more attested method, we used Raman spectroscopy to determine the chemical composition of urinary deposits and urinary stones of 15 patients with urolithiasis in order to find out whether direct correlation between the composition of the corresponding stones and the deposits exists. We found that the main chemical compounds typically constituting urinary stones also form the deposits and that their composition correlates in eleven out of fifteen cases. However, brushite deposits that we found in two cases did not result in brushite, but mixed calcium oxalate monohydrate and phosphate stones. Overall, Raman spectroscopy is an informative and reliable method that can be used for analysis of urinary sediments for early diagnosis of urinary stone formation.

Keywords. Urolithiasis, Crystalluria, Urinary stones, Urinary sediments, Raman scattering, Spectroscopy.

Published online: 28 September 2021, Issue date: 1 September 2022

* Corresponding author.

1. Introduction

Urinary stone disease is a common condition, and its prevalence is increasing worldwide. Current incidence varies among different countries from 1% to 20% and can constitute major costs for health care systems as well as significantly decrease the quality of life for people with the disease [1,2]. Early diagnosis could aid in prescribing treatment that prevents urinary stone growth and avoid more expensive and, in severe cases, invasive stone removal procedures [3].

Urinary stone formation processes are believed to be caused by urinary saturation with typical urinary stone forming materials such as calcium oxalate, uric acid, various urates, calcium phosphates, amorphous phosphates, and magnesium ammonium phosphate hexahydrate (struvite). This leads to formation of urinary deposits (or sediments) that are indicative of urolithiasis [4–6]. Less commonly, urinary deposits can also be constituted from cystine [7], various lipids [8], and metabolites of some drugs [9,10] that contribute to the stone formation processes. Qualitative chemical analysis of chemical composition of urinary sediments plays an important role in taking early preventive measures to stop urinary stones from forming or growing [4,6,11]. Such analysis is usually challenging because of their small size, brittleness and inhomogeneity [12]. Optical microscopy is currently considered the gold standard for this purpose, and it is the only method used in clinical practice [10,13]. Visual morphology-based inspection of urinary sediments is, however, not precise enough, since it is based on the examination of the shapes of sediments and cannot be reliable when the structure of these sediments is atypical or amorphous or consists of multiple components.

Alternative methods to optical microscopy are still in high demand in the medical field for qualitative and quantitative chemical analysis of urinary deposits. The chemical composition of urinary stones is routinely analysed using vibrational spectroscopy [12,14–20], X-ray diffraction [19,21], and scanning electron microscopy with element distribution analysis (SEM-EDAX) [22]. For urinary sediments, SEM-EDAX experiments have also been carried out, but information about the chemical composition of the sample provided by such experiments are not accurate enough [23]. More reliable results have been obtained by means of infrared (IR) microspectroscopy, but the quality of the results is very dependent on the size of the sediment under study, which is also limited to approximately 10 μm [12,24,25]. In addition, IR spectra of urinary deposits can be significantly affected by Mie scattering, which seriously obstructs analysis [24]. Finally, larger crystals cannot be measured in the transmission mode of the IR microscope without additional sample preparation, and the specular reflection signal that could be used instead suffers from spectral distortions that are difficult to correct for [14]. Raman spectroscopy is a method complementary to IR microspectroscopy, but it offers higher spatial resolution, meaning that smaller samples can be analysed [25,26]. It also allows the challenges posed by analyzing Mie scattering or reflectance IR spectra to be overcome. The main disadvantage of the method, fluorescence that can overwhelm the Raman scattering signal, can be suppressed or even eliminated by using a Fourier transform (FT) Raman spectrometer that employs a near-IR (NIR) laser for excitation of Raman scattering.

In Raman spectroscopy experiments [27], a monochromatic light source, usually a laser, is employed to excite the molecules of a sample. Fluorescence that interferes with the Raman signal originates when a molecule is excited to higher electronic energy states. It happens when the energy of the laser photons exceeds the gap between the electronic energy levels of the molecule. This is especially critical issue for “real life” samples the molecular compounds of which might not possess electronic transition in the visible spectral region but very often are contaminated with fluorescent impurities such as various pigments. Such impurities cannot always be removed from the sample, as is the case for urinary sediments [28,29]. Using lasers of longer wavelength reduces the probability of such electronic excitation and, in turn, occurrence of fluorescence. Since over the past decades NIR laser sources have become widely available, their implementation in Raman spectroscopy experiments has been gaining popularity in various fields, especially in biology and medicine [30]. It has been used in a few case studies for identification of unrecognized crystals in the urine of patients suffering from gout [31] and psoriatic arthritis [32]. It has also been recently shown that a dispersive Raman spectroscopy system using

785 nm excitation can be useful for the identification of small urinary crystals in patients with urolithiasis [33,34]. Automatic analysis of single-component deposits has also proven to be possible [33]. In this work, we specifically examined the potential of FT–Raman spectroscopy with 1064 nm laser excitation to explore the chemical composition of urinary sediments. This approach can further improve the sensitivity for identifying such sediments by reducing fluorescence background. Importantly, we investigated the chemical composition of urinary stones from the same patients with urolithiasis to determine whether direct correlation between the composition of the corresponding stones and the deposits exists.

2. Material and methods

For the duration of one year of the project described here, urine samples of every patient with acute uronephrolithiasis hospitalised at the Urology Centre of Vilnius University Santaros Clinics were collected—fifteen in total. The samples were investigated with NIR Raman spectroscopy. The chemical composition of the urinary stones removed from the same patients was also checked by means of FTIR spectroscopy. For the stones, this bulk analysis technique allows better identification of overall composition than Raman spectroscopy, which yields information on micrometer-sized areas that are analysed.

Urine samples were centrifuged in order to separate the urinary crystals. The precipitates were filtered on Whatman ashless grade 542 filters for 24 h at room temperature to remove the remaining liquid. All particles larger than 2.7 μm in diameter remained on the surface of the filter, but only the larger ones (typically >100 μm in size) were collected with the aid of a small needle. Those particles were transferred to the surface of a silver mirror, a typical substrate in spectroscopic analysis that does not produce any Raman signal of its own [35]. This procedure is suitable to collect single crystallites for Raman spectroscopic analysis. The use of artificially synthesised magnetic nanoparticles which adhere to the crystallites in urine solution has been shown to provide possibility to automatically detect, hold and release them for Raman analysis [33], which provides potential for fast identification of many urinary deposits in the future.

Spectra were recorded with a MultiRAM (Bruker Optik GmbH, Ettlingen, Germany) FT–Raman spectrometer equipped with microscope stage and a gold-plated mirror objective (focal length 33 mm) which yields the diameter of the focused laser beam on the sample equal to 100 μm. Samples were excited with a Nd:YAG laser having a wavelength of 1064 nm to produce Raman scattered radiation, which was collected by a liquid-nitrogen–cooled Ge diode detector. The spectra were collected at a resolution of 5 cm^{-1}. Depending on the size and morphology of the urinary deposits, 200 to 170,000 scans were acquired and averaged for a single resultant spectrum. Also, the power of the excitation laser was varied between 5 and 600 mW in order to avoid thermal damage caused by focused NIR laser radiation in the samples more sensitive to heating. The effects of heating in such samples were observed in the spectra as a broad band of black-body radiation in the wavenumber region above 2500 cm^{-1}. Reference spectra of pure chemical compounds (Sigma Aldrich) typically constituting urinary sediments were recorded for the qualitative evaluation of the spectra allowing us to identify all constituents in the analysed deposits with high chemical sensitivity. Spectral analysis was performed on raw spectra with no pre-processing procedures applied. Optical images of the urinary crystals were recorded using the visible mode of the same instrument, which includes a visible light source and a CCD camera for this purpose.

For the FTIR studies, the urinary stones were ground with an agate mortar, mixed with IR-transparent KBr powder (ratio 1:100) and pressed into a pellet using a hydraulic press. The KBr pellets were analysed with a Vertex 70 IR spectrometer (Bruker Optik GmbH, Ettlingen, Germany) equipped with a liquid nitrogen cool mercury cadmium telluride (MCT) detector. The spectra were recorded with 4 cm^{-1} spectral resolution. One hundred twenty-eight (128) interferograms were obtained, averaged, and converted into a resulting spectrum using the three-term Blackman–Harris apodization function and a zero-filling factor of 2. The spectra were analysed by comparing them with pure chemical component reference spectra recorded in the same way.

3. Results

The chemical composition of the urinary sediments of fifteen patients suffering from urolithiasis was

investigated by means of Raman spectroscopy. The characteristic Raman spectra and optical images of the sediments are shown in Figures 1–4. In the spectra that are presented in the figures, the spectral region varies depending on the valuable spectral information of interest. The most characteristic spectral bands are also indicated in the spectra. Although the samples in some cases also contained cells, all the analysed deposits yielded clear signal of the constituting minerals. This could be explained by the fact that the Raman scattering cross-section of minerals is typically much higher while also predominantly containing spectral bands in lower wavenumber region compared to organic compounds constituting cells.

Analysis of the Raman spectra of urinary sediments confirmed that the main urinary stone forming materials were present at elevated concentrations in the urine of patients with urolithiasis: (i) calcium oxalate monohydrate $CaC_2O_4{\cdot}H_2O$ (n = 5, 33%); (ii) urates: uric acid $C_5H_4N_4O_3$, uric acid dihydrate $C_5H_4N_4O_3{\cdot}2H_2O$, and ammonium acid urate $C_5H_7N_5O_3$ (n = 4, 27%); (iii) brushite $CaHPO_4{\cdot}2H_2O$ (n = 4, 27%); (iv) struvite $(NH_4)MgPO_4{\cdot}6H_2O$ (n = 1, 7%). Those were single-component sediments. One of the urinary deposits was composed of three different components: calcium oxalate monohydrate, hydroxyapatite, and calcite. We did not find crystals of calcium oxalate dehydrate nor the rare compounds, such as N-acetylsulfametoxazole or other drugs, in any of the analysed sediments. Since Raman spectra of sediment constituting materials are distinct, this likely due to the small size of the sample set limited by the duration of the project and the low prevalence of acute neprolithiasis patients in Lithuania, and not due to limitations of the technique.

Table 1 summarizes the 15 cases of the chemical composition of urinary sediments and chemical composition of urinary stones from the same patients. At least one molecular compound was the same among samples coming from the same patient. However, oxalate stones were always accompanied by phosphatic additives, amorphous phosphates and hydroxyapatite being the most common. The phosphates were not found in corresponding urinary sediments. Instead, brushite and struvite were found in five urinary sediment samples. Particularly in the case of brushite sediments, low correlation was observed with the composition of corresponding urinary stones, which were constituted from amorphous phosphates, hydroxyapatite and calcium oxalate instead. Different urates were found in the urinary sediments, but the urinary stones of all those patients were composed of uric acid anhydrous. In this case, we still consider that the chemical composition of urinary deposits correlates since uric acid dihydrate and ammonium acid urate are less stable forms of urates and can recrystallize into uric acid anhydrous under decrease in urine pH [36,37].

4. Discussion

Urine saturation with some specific chemical elements—usually oxalates, phosphates, ammonium ions, and magnesium—is a primary and required factor for increased risk of urinary stone formation [38]. Nevertheless, initial crystallisation resulting in 10–12 μm single urinary crystals does not necessarily lead to the formation of a urinary stones and is common for healthy people [39,40]. Precipitation of significant amounts of crystals and/or suitable conditions in the urinary tract is, however, very likely to lead to the aggregation of small crystals typically bound by a protein matrix. Such sediments, which are made of small crystals or are mixed with an organic matrix, are larger and usually have an obscure morphology [40]. In addition, some aggregates can consist of several chemical compounds. Urinary stone formation is much more frequent in patients with larger size crystals and aggregates in their urine [41]. Particular attention should be paid when investigating the chemical composition of such larger crystals and aggregates. Here we used a FT–Raman spectrometer that allowed us analysing urinary crystals and aggregates approximately 100 μm in size. However, even smaller sediments as small as 1 μm could and should in the future be analysed using the method by employing objectives of higher magnification and numerical aperture for tighter focusing of laser radiation.

Optical microscopy, which is nowadays used in laboratory medicine, is unable to recognize large single or multi-chemical aggregates because of their unusual morphology [10,13,41]. The crystals having the most clinical significance are often left unidentified or incorrectly identified during routine urinalysis.

FT–Raman spectroscopy proved to be a suitable method to determine the exact molecular compounds of urinary sediments independent of their

Table 1. Presence of chemical components in urinary sediments and urinary stones among 15 patients suffering from urinary stone disease

Chemical composition of urinary sediments	Chemical composition of urinary stones	Number of cases
Calcium oxalate monohydrate	Calcium oxalate monohydrate + amorphous phosphates	3
Calcium oxalate monohydrate	Calcium oxalate monohydrate + hydroxyapatite	2
Uric acid anhydrous	Uric acid anhydrous	1
Uric acid dihydrate	Uric acid anhydrous	2
Ammonium acid urate	Uric acid anhydrous	1
Brushite	Calcium oxalate monohydrate + amorphous phosphates	3
Brushite	Calcium oxalate monohydrate + hydroxyapatite	1
Struvite	Struvite	1
Calcium oxalate monohydrate + calcite + hydroxyapatite	Struvite + hydroxyapatite + calcium oxalate monohydrate	1

morphology. Figures 1 and 2 illustrate cases when both typical and atypical crystals of brushite and struvite were found in samples. Brushite tends to form crystals shaped as long prisms with one sharp end and combine into spiky star-like formations as shown in the upper image of Figure 1. The bottom image, however, reveals morphologically indescribable sediment. Raman spectra were found to be the same for both and the sediments were identified as brushite. A very similar situation was encountered for atypical sediments and sediments having a defined morphology, both corresponding to struvite when investigated by means of Raman scattering spectroscopy.

It turned out to be challenging to record Raman spectrum of high quality in terms of signal-to-noise ratio for deposits of calcium oxalate, which were heated when exposed to the laser radiation and subsequently thermally damaged. The heating could be caused by a typically brown colour of the larger calcium oxalate crystals suggesting presence of pigments or other types of organic contaminants, which increase the absorption of the laser radiation and makes them more susceptible to heating. Therefore, the power of the laser had to be low and the number of spectra averaged had to be increased substantially to achieve a signal-to-noise ratio sufficient for spectral analysis. This in turn increased the time required for the experiment. Importantly, Raman spectroscopy allows one to distinguish different hydrates of calcium oxalate, which can be indicative of the different aetiology of the urinary stone and provide important information for subsequent treatment [20]. The most intense spectral bands of calcium oxalate monohydrate are a doublet at 1490 cm^{-1} and 1463 cm^{-1} assigned to symmetrical ν_s (COO^-) stretch vibrations. On the other hand, calcium oxalate dihydrate yields only one spectral band in this spectral region near 1477 cm^{-1} [16]. The Raman spectrum in Figure 3 clearly shows the urinary sediment to be calcium oxalate monohydrate. It is not possible to obtain such information from the optical image, since the large, likely aggregated deposit does not appear in the typical shape of calcium oxalate crystals.

Raman spectra are also useful for distinguishing various types of urates. Uric acid anhydrous and uric acid dihydrate are the most common urates constituting urinary stones and urinary sediments. Uric acid monohydrate is also reported as a possible constituent [42]. Of note, both hydrates are rarely found in urinary stones, with the hydration possibly lost during stone growth. We have, however, discerned the presence of uric acid dihydrate in urinary deposits. An example of the atypical morphological structure of a uric acid dihydrate urinary deposit is shown in Figure 4 together with the Raman spectrum of the deposit. Uric acid anhydrous and ammonium acid urate were also identified as constituents of urinary sediments in this work. The varying intensities and Raman shifts of the spectral bands related to the in-plane bending motions of purine rings can be used as spectral markers for recognition of various urates.

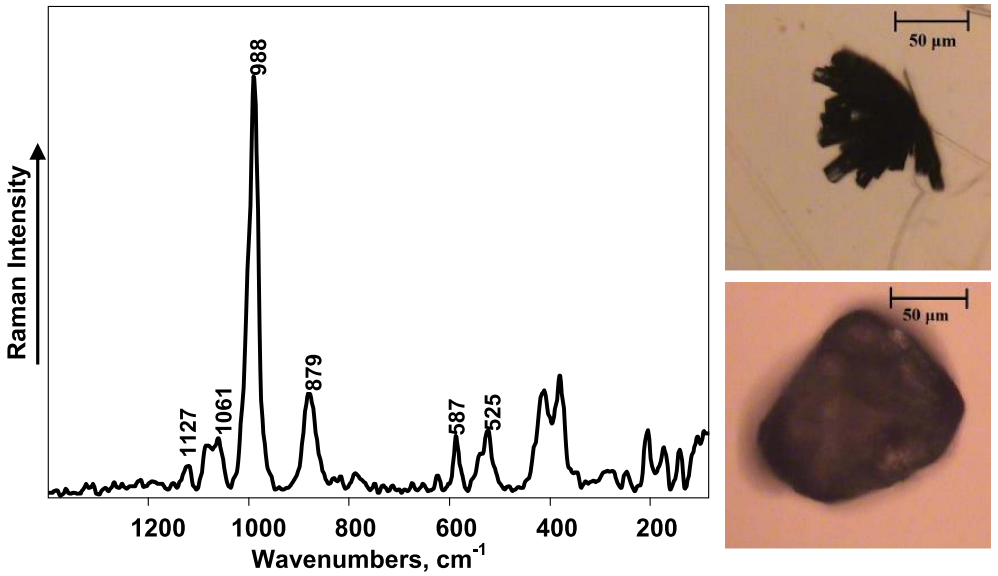

Figure 1. FT–Raman spectrum of brushite urinary sediments (laser power: 180 mW, number of averaged spectra: 2000) (left) and optical images of typical (top) and atypical (bottom) urinary deposits composed of brushite.

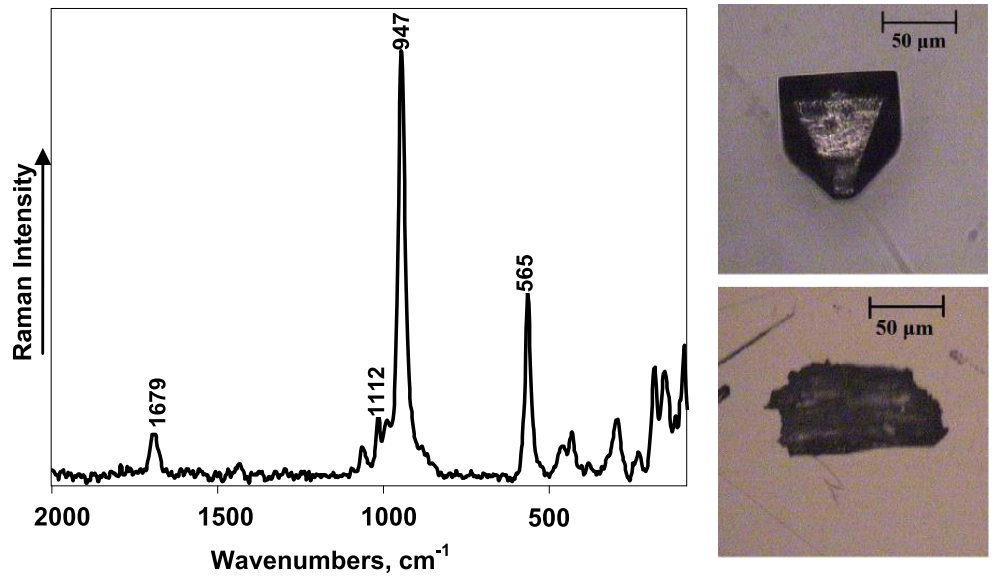

Figure 2. FT–Raman spectrum of struvite urinary sediments (laser power: 180 mW, number of averaged spectra: 2000) (left) and optical images of typical (top) and atypical (bottom) urinary deposits composed of struvite.

FT–Raman scattering spectroscopy proved to be a reliable method to determine the chemical composition of multi-component urinary sediments. As can be seen from the optical image of the urinary deposit in Figure 5, it has irregular morphology and no crystal structure, which makes it very difficult

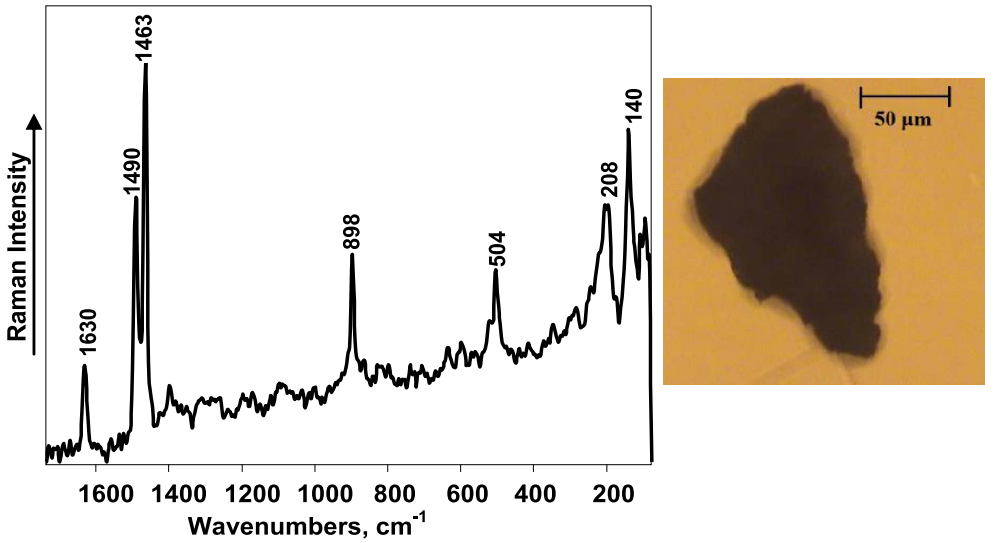

Figure 3. FT–Raman spectrum (laser power: 9 mW, number of averaged spectra: 170,000) (left) and optical image (right) of calcium oxalate monohydrate urinary sediment.

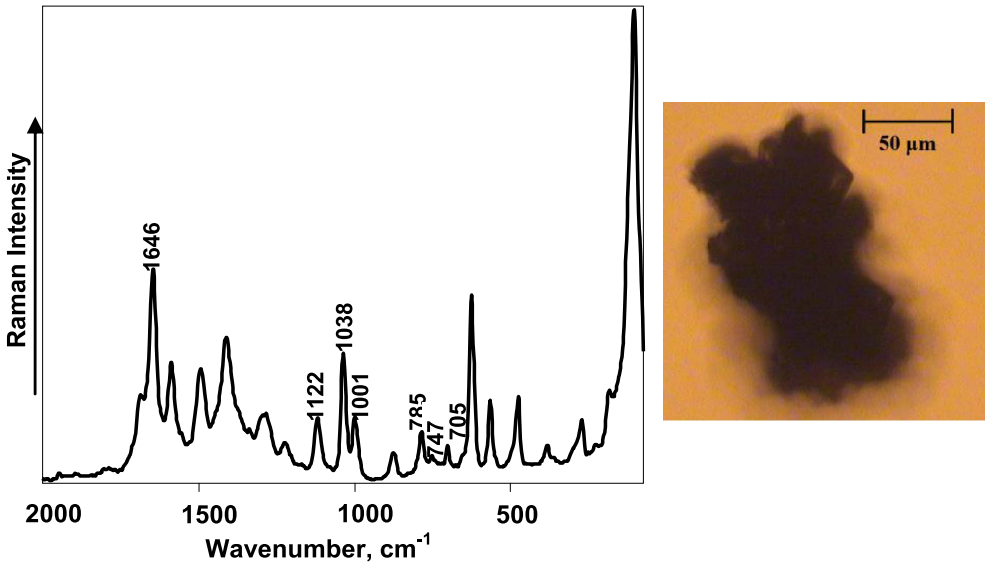

Figure 4. FT–Raman spectrum (laser power: 80 mW, number of averaged spectra: 20,000) (left) and optical image (right) of uric acid urinary sediment.

to determine its chemical composition. On the contrary, the Raman spectrum of this deposit indicates the three different chemical compounds: calcium oxalate monohydrate, hydroxyapatite, and calcite. The most intensive spectral band, which is at 1085 cm^{-1} and is characteristic of the vibrations of the CO_3^{2-} group, and the one at 280 cm^{-1} represent $CaCO_3$ (calcite) in the sample [43]. A spectral band at 960 cm^{-1} characteristic of hydroxyapatite can also be observed. All other spectral bands in the Raman spectrum of this urinary deposit are assigned to calcium oxalate monohydrate.

The close similarity of the chemical composition of urinary sediments of patients with the same

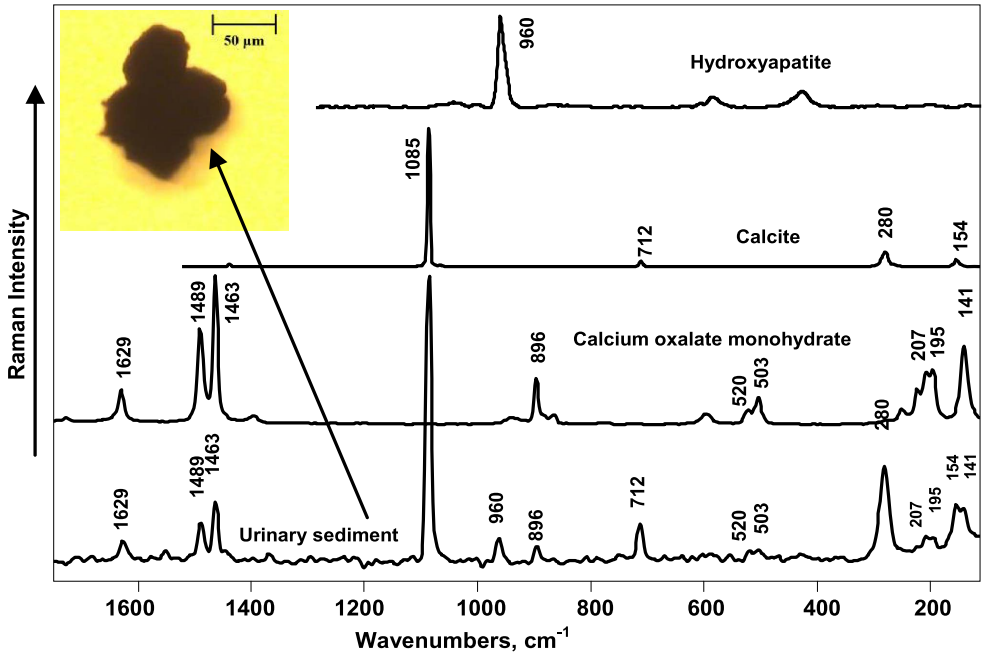

Figure 5. Optical image of urinary deposit (top left corner), Raman spectra of the deposit (bottom), and reference chemical compounds indicating calcium oxalate monohydrate, calcite, and hydroxyapatite Raman spectra.

urinary stone disease indicates that saturation of urine with specific chemical elements can result in urinary stone formation. For patients in the risk group, such as those with increased possibility of recurrence or with a family history of urinary stones, the exact evaluation of the chemical components in urinary sediments could be crucial for prevention purposes.

The differences between the chemical composition of urinary sediments and urinary stones can also provide valuable information concerning the processes of urinary stone formation. In our study, uric acid urinary stones were composed of uric acid anhydrous, but the urinary deposits of the same patients were also found to be uric acid dihydrate or ammonium acid urate. This suggests the occurrence of dehydration and ion separation processes at the time of stone formation.

The most significant differences were found in the patients having urinary sediments of brushite and stones having a mixture of calcium oxalate monohydrate with amorphous phosphates or with hydroxyapatite. Brushite and amorphous phosphates, as well as calcium oxalate, are formed in high calcium concentrations. Hydroxyapatite can occur via phase transformation from brushite [44]. Thus, the existence of brushite in urine can suggest the existence of hypercalciuria and formation of calcium oxalate-phosphate stones. On the other hand, as a constituent in multicomponent urinary stones, pure brushite occurrence varies from less than 1% to about 20% according to various authors [12,45], and in general it is considered a rare component [16]. For single component calcium oxalate stones, only calcium oxalate urinary sediments were found.

In this work we provide pilot evidence for the correlation between the chemical composition of urinary sediments and stones, but more patients need to be included in the study for the results to be statistically reliable. We show that FT–Raman spectroscopy is suitable for reliably identifying urinary deposits larger than 100 μm in size with no significant influence of fluorescence as observed in previous studies [31,33]. The long spectral acquisition time is the main limiting factor for the method to be used in a routine way in clinical practice. This can be alleviated in the future by using high magnification and numerical aperture objectives (which would also result in

ability to analyse samples as small as 1 μm) or applying mathematical noise reduction procedures for low signal-to-noise spectra [46–48].

Urinary stones are usually diagnosed in an already late stage of their formation, e.g., only when the patient starts feeling pain. Regular tests of urinary sediments to determine its exact chemical composition could be key to early prevention of urinary stone disease. In this work, Raman spectroscopy proved to be informative for the chemical identification of both typical and atypical urinary crystals and crystal clusters. Although this is a pilot study and more patient cases need to be investigated for the results to be statistically reliable, spectral analysis of the deposits could help in prescribing the appropriate preventive measures, such as diet and lifestyle changes, for people at risk of urinary stones. In addition, distinguishing chemical compounds of even the smallest chemical differences can be of high value in determining the causes and conditions of the initial formation and growth processes of urinary stones.

5. Conclusions

FT–Raman spectroscopy is an effective and very sensitive method to determine the chemical composition of urinary sediments no matter their morphological structure and is especially useful for the investigation of unusual crystals and amorphous clusters, which cannot be identified by optical microscopy widely used in standard medical practice. Use of 1064 nm NIR laser for excitation of Raman scattering ensures suppression of fluorescence background common in biological samples. In contrast to optical microscopy, the method does not rely on the skills of laboratory personnel since the Raman spectra provides direct chemical information at molecular level. We found correlation between the chemical composition of urinary stones and urinary sediments, which suggests that the examination of the sediments by FT–Raman spectroscopy can be considered a relevant approach for early diagnosis of urinary stone formation and determination of appropriate action to prevent this process.

References

[1] Y. Liu, Y. Chen, B. Liao, D. Luo, K. Wang, H. Li, G. Zeng, *Asian J. Urol.*, 2018, **5**, 205-214.

[2] I. Sorokin, C. Mamoulakis, K. Miyazawa, A. Rodgers, J. Talati, Y. Lotan, *World J. Urol.*, 2017, **35**, 1301-1320.

[3] O. A. Raheem, Y. S. Khandwala, R. L. Sur, K. R. Ghani, J. D. Denstedt, *Eur. Urol. Focus*, 2017, **3**, 18-26.

[4] S. R. Khan, M. S. Pearle, W. G. Robertson, G. Gambaro, B. K. Canales, S. Doizi, O. Traxer, H.-G. Tiselius, *Nat. Rev. Dis. Primers*, 2016, **2**, 1-23.

[5] T. Alelign, B. Petros, *Adv. Urol.*, 2018, **2018**, article no. e3068365.

[6] V. Frochot, M. Daudon, *Int. J. Surg.*, 2016, **36**, 624-632.

[7] C. Martins Maria, A. Meyers Anthony, A. Whalley Natalie, L. Rodgers Allen, *J. Urol.*, 2002, **167**, 317-321.

[8] S. R. Khan, P. A. Glenton, *Brit. J. Urol.*, 1996, **77**, 506-511.

[9] G. B. Fogazzi, *Nephrol. Dial. Transplant.*, 1996, **11**, 379-387.

[10] C. Cavanaugh, M. A. Perazella, *Am. J. Kidney Dis.*, 2019, **73**, 258-272.

[11] M. Daudon, V. Frochot, *Clin. Chem. Lab. Med. (CCLM)*, 2015, **53**, s1479-s1487.

[12] L. Estepa, M. Daudon, *Biospectroscopy*, 1997, **3**, 347-369.

[13] M. E. Baños-Laredo, C. A. Núñez-Álvarez, *J. Cabiedes Reumatol. Clín. (Engl. Ed.)*, 2010, **6**, 268-272.

[14] M. Pucetaite, V. Hendrixson, A. Zelvys, F. Jankevicius, R. Tyla, J. Ceponkus, V. Sablinskas, *J. Mol. Struct.*, 2013, **1031**, 38-42.

[15] M. Pucetaite, S. Tamosaityte, R. Galli, V. Sablinskas, G. Steiner, *J. Raman Spectrosc.*, 2017, **48**, 22-29.

[16] P. Carmona, J. Bellanato, E. Escolar, *Biospectroscopy*, 1997, **3**, 331-346.

[17] A. H. Khan, S. Imran, J. Talati, L. Jafri, *Investig. Clin. Urol.*, 2018, **59**, 32-37.

[18] X. Cui, Z. Zhao, G. Zhang, S. Chen, Y. Zhao, J. Lu, *Biomed. Opt. Express*, 2018, **9**, 4175-4183.

[19] V. K. Singh, P. K. Rai, *Biophys. Rev.*, 2014, **6**, 291-310.

[20] M. Daudon, A. Dessombz, V. Frochot, E. Letavernier, J.-P. Haymann, P. Jungers, D. Bazin, *C. R. Chim.*, 2016, **19**, 1470-1491.

[21] P. A. Bhatt, P. Paul, *J. Chem. Sci.*, 2008, **120**, 267-273.

[22] Y. M. Fazil Marickar, P. R. Lekshmi, L. Varma, P. Koshy, *Urol. Res.*, 2009, **37**, 271-276.

[23] Y. M. Fazil Marickar, P. R. Lekshmi, L. Varma, P. Koshy, *Urol. Res.*, 2009, **37**, 277-282.

[24] S. Tamosaityte, E. Baltakyte, D. Blazevic, M. Pucetaite, J. Ceponkus, V. Hendrixson, S. Varvuolyte, V. Sablinskas, in *Proc. of SPIE*, vol. 8798, SPIE, 2013.

[25] M. Daudon, M. F. Protat, R. J. Reveillaud, H. Jaeschke-Boyer, *Kidney Int.*, 1983, **23**, 842-850.

[26] V. Castiglione, P.-Y. Sacré, E. Cavalier, P. Hubert, R. Gadisseur, E. Ziemons, *PLoS ONE*, 2018, **13**, article no. e0201460.

[27] A. Kudelski, *Talanta*, 2008, **76**, 1-8.

[28] J. A. T. Poloni, M. A. Perazella, E. Keitel, C. A. Marroni, S. B. Leite, L. N. Rotta, *CN*, 2019, **92**, 141-150.

[29] J. Berüter, J.-P. Colombo, U. P. Schlunegger, *Eur. J. Biochem.*, 1975, **56**, 239-244.

[30] C. Krafft, *Anal. Bioanal. Chem.*, 2004, **378**, 60-62.

[31] Z.-T. Chen, C.-H. Wang, H. K. Chiang, in *Proc. of SPIE*, vol. 11359, SPIE, 2020.

[32] V. Frochot, V. Castiglione, I. T. Lucas, J.-P. Haymann, E. Letavernier, D. Bazin, G. B. Fogazzi, M. Daudon, *Clin. Chim. Acta*, 2021, **515**, 1-4.

[33] P.-A. Lo, Y.-H. Huang, Y.-C. Chiu, L.-C. Huang, J.-L. Bai, S.-H.

Wu, C.-C. Huang, H. K. Chiang, *J. Raman Spectrosc.*, 2019, **50**, 34-40.

[34] C.-H. Wang, J.-X. Zeng, P.-C. Chen, H.-H. K. Chiang, in *Future Trends in Biomedical and Health Informatics and Cybersecurity in Medical Devices* (K.-P. Lin, R. Magjarevic, P. de Carvalho, eds.), Springer International Publishing, Cham, 2020, 122-128.

[35] L. Cui, H. J. Butler, P. L. Martin-Hirsch, F. L. Martin, *Anal. Methods*, 2016, **8**, 481-487.

[36] M. Cameron, N. M. Maalouf, J. Poindexter, B. Adams-Huet, K. Sakhaee, O. W. Moe, *Kidney Int.*, 2012, **81**, 1123-1130.

[37] Z. Wang, L. Königsberger, E. Königsberger, *Monatsh Chem.*, 2018, **149**, 327-332.

[38] A. P. Evan, *Pediatr. Nephrol.*, 2010, **25**, 831-841.

[39] M. Daudon, C. Hennequin, G. Boujelben, B. Lacour, P. Jungers, *Kidney Int.*, 2005, **67**, 1934-1943.

[40] B.-S. Gui, R. Xie, X.-Q. Yao, M.-R. Li, J.-M. Ouyang, *Bioinorg. Chem. Appl.*, 2009, **2009**, article no. e925297.

[41] Y. M. Fazil Marickar, A. Salim, *Urol. Res.*, 2009, **37**, 359-368.

[42] G. Schubert, G. Reck, H. Jancke, W. Kraus, C. Patzelt, *Urol. Res.*, 2005, **33**, 231-238.

[43] J. Urmos, S. K. Sharma, F. T. Mackenzie, *Am. Mineral.*, 1991, **76**, 641-646.

[44] A. Hesse, D. Heimbach, *World J. Urol.*, 1999, **17**, 308-315.

[45] L. Benramdane, M. Bouatia, M. O. B. Idrissi, M. Draoui, *Spectrosc. Lett.*, 2008, **41**, 72-80.

[46] S. J. Barton, T. E. Ward, B. M. Hennelly, *Anal. Methods*, 2018, **10**, 3759-3769.

[47] H. Chen, W. Xu, N. Broderick, J. Han, *J. Raman Spectrosc.*, 2018, **49**, 1529-1539.

[48] X. Y. Zhao, G. Y. Liu, Y. T. Sui, M. Xu, L. Tong, *Spectrochim. Acta A: Mol. Biomol. Spectrosc.*, 2021, **250**, article no. 119374.

Comptes Rendus
Chimie
2022, Vol. 25, Special Issue S1, p. 83-103
https://doi.org/10.5802/crchim.110

Microcrystalline pathologies: Clinical issues and nanochemistry / *Pathologies microcristallines : questions cliniques et nanochimie*

Raman opportunities in the field of pathological calcifications

Ivan T. Lucas *, [a], **Dominique Bazin** [b, c] and **Michel Daudon** [d, e, f]

[a] Laboratoire LISE UMR 8235 CNRS-SU, Sorbonne Université, Paris, France
URL: https://www.lise.upmc.fr/en/user/31

[b] Université Paris-Saclay, CNRS, Institut de Chimie Physique, 91405 Orsay cedex, France

[c] Université Paris-Saclay, CNRS, Laboratoire de Physique des Solides, 91405, Orsay, France
URL: https://www.equipes.lps.u-psud.fr/Bazin/

[d] Sorbonne Université, UPMC Univ Paris 06, UMR S 1155, Paris, France

[e] INSERM, UMR S 1155, Paris, France

[f] Explorations fonctionnelles multidisciplinaires, AP-HP, Hôpital Tenon, Paris, France

E-mails: ivan.lucas@sorbonne-universite.fr (I. T. Lucas), dominique.bazin@universite-paris-saclay.fr (D. Bazin), daudonmichel24@gmail.com (M. Daudon)

Abstract. The aim of this contribution is to present to the community the very unique diagnostic capabilities of Raman spectroscopy in the context of pathological calcifications. By offering the clinician the opportunity to determine within seconds the chemical composition of micron-sized crystallites, possibly *in vivo*, Raman analyses find no equivalent among the large set of analytical tools available. After a brief recap of some peculiar aspects of this spectrometry and a presentation of the latest instrumental developments, this review gathers the most recent literature on the use of Raman to diagnose various lithiases or microcrystalline pathologies.

Keywords. Raman, Medical application, Lithiasis, Breast, Kidney, *In vivo*.
Published online: 17 September 2021, Issue date: 1 September 2022

1. Introduction

First described in 1928 by Raman and Krishnan [1] from which it gets its name and predicted theoretically by Smekal in 1923 [2], Raman spectroscopy is an optical spectroscopy which allows the vibrational signatures of probed compounds to be extracted from the scattered light upon illumination of a sample with a monochromatic excitation source (ultraviolet, visible or infrared laser Raman probe) [3,4]. Raman spectroscopy constitutes a powerful non-destructive and label-free technique widely used for chemical analysis (solid, liquid, gas) that when combined with

* Corresponding author.

optical microscopy can provide chemical information at the sub-micrometer scale [5,6].

As diagnostic tool in medicine, Raman spectroscopy was first applied to stone analysis in the early eighties [7,8]. Then, it has been applied to complex biological samples, such as fluids [9,10], cells [11,12], minerals as physiological [13–15] and pathological calcifications [16–18] and tissues [19]. Such versatility explains the numerous applications of Raman spectroscopy in different specialties of medicine [20–22], among which are nephrology [23–30], rheumatology [31–33], hematology [34–36], gastroenterology [37,38] or endocrinology [39,40]. Note that *in vivo* Raman experiments are also envisaged and proofs of concepts have already been demonstrated in a few domains of applications [41–44].

The aim of this publication is to gather and present striking results related to pathological calcifications [16,17,45–51] and to introduce the most recent developments of Raman spectroscopy, opening new opportunities in this field of research. After a brief presentation of the underlying theoretical concepts associated with Raman spectroscopy and Raman instrumentation, the performance of the technique will be discussed relatively to the ones of mid-infrared vibrational spectroscopy also largely used in medicine. Then, a literature review focusing on pathological calcifications and featuring the most recent works will be presented.

2. Some important aspects regarding Raman spectroscopy

2.1. *Notion of Raman shift*

A Raman spectrum depicts the optical transitions between the various rotational–vibrational energy states of molecules, or crystallites and therefore gives access to the precise characterization of a material chemical composition [52,53]. Raman spectra represent on the x-axis either the wavelength (λ: nm) or the energy (ν: wavenumber in inverse centimeter cm^{-1}) associated with the optical transitions and on the y-axis their probability of occurrence (number of counts associated with the number of Raman photons reaching the photosensitive detector). Note that as Raman spectroscopy does not rely on light absorption but on inelastic light scattering, which is of higher or lower energy than the incident laser light, the energy of the transition on the abscissa, displayed as *Raman shift,* is calculated from the difference between the energy of the Raman laser probe ν_0 and the energy of the scattered light ν_i:

$$\text{Raman shift } (cm^{-1}): \nu_0 - \nu_i = \left(\frac{1}{\lambda_0} - \frac{1}{\lambda_i}\right) \times 10^7. \quad (1)$$

2.2. *Vibration modes in Raman and IR spectroscopy*

The "*Raman active*" energy transitions observed on Raman spectra originate from a change in the polarizability of a molecular entity, i.e. the distortion of its electron cloud upon interaction with the incident light (strong oscillating electromagnetic field in the UV, visible, infrared energy domain). These transitions differ from the ones observed in IR spectroscopy based on the variation of the dipolar moment of the molecular entity. Both can be predicted from the symmetry of the molecular entity using mathematical symmetry operations (group theory). From a microscopic point of view, the energy transitions correspond to specific molecular distortions or vibration modes (+ rotation) of molecular bounds (as-symmetrical stretching: ν, bending: δ, rocking: ρ, wagging: π, ω and twisting: τ) triggered upon interaction with photons. Molecules with multiple elements of symmetry can show vibrational modes active both in Raman and in IR spectroscopies. For instance vibration modes and therefore energy transitions associated with specific chemical functional groups like P–O stretching of phosphate PO_4^{3-}, C–O stretching of carbonate CO_3^{2-}, S–O stretching of sulfate SO_4^{2-} groups in organic or inorganic compounds, C–H and C–C stretching or bending in carbohydrate compounds, can be observed both in Raman and IR spectra and around similar energy values. Note however that polarized bonds like C–O, O–H produce strong intensity IR bands (large net dipole moment due to charge motion) but are weaker Raman scatterers since bond length changes consequent on vibrational motion only result in small additional polarization effects. Conversely more neutral bonds (C–C, C=C) are strong Raman scatterers (large changes in polarizability upon atom motions) but produce weaker intensity IR bands (small variation of dipole moment).

2.3. *Notion of "virtual" state*

In the framework of quantum mechanics, a molecular entity can be described as a sum of discrete accessible energy states upon interaction with photons. Depending on the energy of the incoming radiofrequency perturbation (UV–Vis, infrared), the molecular entities in their initial state will be promoted (excited) to various higher energy states (new ro–vibrational state in the same or different electronic state). As Raman spectroscopy can use energetic probes (UV or Vis), molecular entities can be, under specific conditions, promoted to a superior electronic excited state (Resonance Raman processes,) or in most common cases to a so-called "*virtual*" state (associated with distorted electron clouds), of which the very existence or physical meaning is still under debate in the community.

2.4. *Stokes vs anti-Stokes, right or left?*

Upon relaxation from the excited state, the molecular entity is downgraded to a lower energy state while emitting a Raman photon scattered statistically in all possible directions of space [54,55]. The emitted photon can originate from a relaxation to an energy state higher than the initial state and is therefore of lower energy than the incident photon ("*Stokes*" photons associated with energy loss) or can be associated with a relaxation to a lower energy state than the initial one ("*anti-Stokes*" photons associated with energy gain). A same vibration mode will therefore produce both *Stokes* and "*anti-Stokes*" photons as depicted in Figures 1a and b. The Raman shifts (ν_0–ν_{Stokes}) and (ν_0–$\nu_{\text{anti-Stokes}}$) are the same in magnitude but of opposite sign and therefore appear on Raman spectra on each side of the Raman probe energy used as the zero energy reference. Raman peaks (bands) associated with Stokes and anti-Stokes photons correspond respectively to positive and negative Raman shifts energy (right and left sides of the spectrum respectively). Note that depending on the nature of laser line rejection filters used (long pass: "*edge*" filters or stop band: "*notch*" filters), either only *Stokes* or both *Stokes* and *anti-Stokes* parts of the spectrum can be exploitable as illustrated in Figure 1b. Different energy ranges are covered by the spectrometer (CCD detector/grating) depending on the Raman probe used as also shown in Figure 1b.

The intensity of the Raman bands associated with a specific vibration mode of the molecular entity is directly proportional to the probability of occurrence of the associated optical transition. This intensity will therefore increase with the number of irradiated entities (concentration in the volume of the sample irradiated) and with the number of incident photons (laser power per surface unit and time of exposure). Note that Raman bands have a characteristic Lorentzian shape (not Gaussian due to the vibrational population relaxation process) and can therefore be easily distinguished from artifacts on spectra (sharp peaks—"glitch"—due for instance to gamma rays hitting randomly the detector). As at room temperature, the population of molecular entities in energy states higher than the ground state is statistically low (Boltzmann distribution), *anti-Stokes* Raman bands are of lower intensity (zero at zero Kelvin) than the *Stokes* bands (see Figure 1b) and are therefore not exploited in most cases (except in Coherent *anti-Stokes* Raman Spectroscopy: CARS).

2.5. *Raman efficiency*

The Raman process giving rise to inelastically scattered photons (*Stokes* and *anti-Stokes*) is extremely inefficient (1 Raman photon ν_S or $\nu_{A\text{-}S}$ for 10^7 incident/elastically scattered photon ν_0. This efficiency strongly depends on the nature of the compounds analyzed by Raman spectroscopy. Compounds with high "cross-section" for Raman scattering like carbonaceous materials have such high intensity Raman signature than even a single layer of carbon atoms (graphene) and can be easily detected. Most of the other compounds give weak intensity Raman signatures even under strong laser irradiation, which explains why IR spectroscopy was preferred for decades [56]. The cross-section for scattering (elastic and inelastic) depends on the excitation wavelength to the inverse fourth power [57]:

$$\text{Raman intensity} \propto \frac{1}{\lambda_{\text{Exc}}^4}. \tag{2}$$

The Raman signal intensity of a sample illuminated at 248 nm is therefore of two orders of magnitude higher than when using a 785 nm laser line as seen in Figure 2.

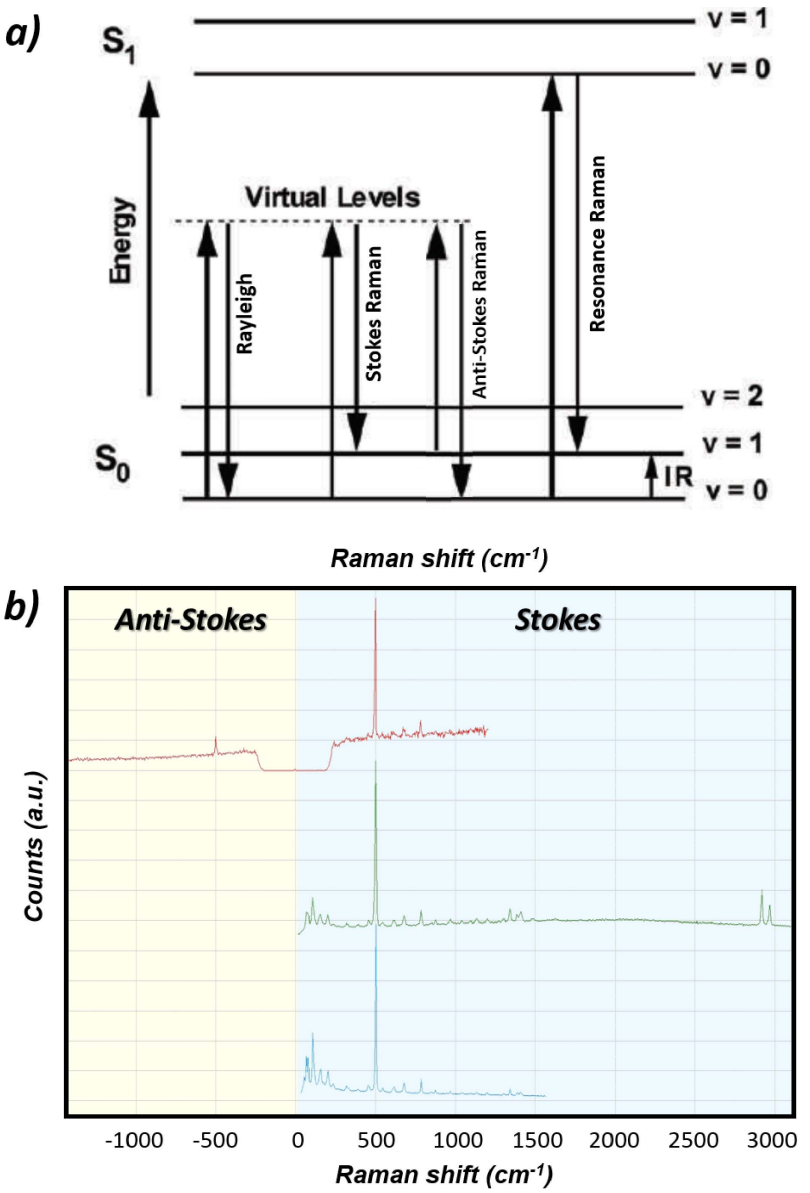

Figure 1. (a) Origin of the optical transitions behind elastic *Rayleigh* scattering, inelastic *Stokes and anti-Stokes Raman* scattering and *Resonance Raman* scattering. The difference in energy between the incident photons and the Raman photons (Raman shift) corresponds to the difference in energy of the different vibrational states otherwise accessible by InfraRed spectroscopy. (b) Raman spectra of cystine powder using various Raman probes 633 nm (red spectrum), 532 nm (green spectrum) and 785 nm (blue spectrum). The laser line rejection filter "band-stop notch" used in combination with the 633 nm Raman probe explains the discontinuity of the spectrum around 0 cm^{-1} (zero intensity) and the possibility to observe both *anti-Stokes* and *Stokes* main Raman bands of cystine (±500 cm^{-1}). The long-pass rejection filter used for 532 and 785 nm Raman probes allows detection of *Stokes* bands only but at low energy at as close as 50 cm^{-1} to the laser line. Note also, the different energy ranges covered by the spectrometer (CCD detector/grating) at 785 nm and 532 nm (~1500 cm^{-1} *vs* ~3000 cm^{-1} on our equipment).

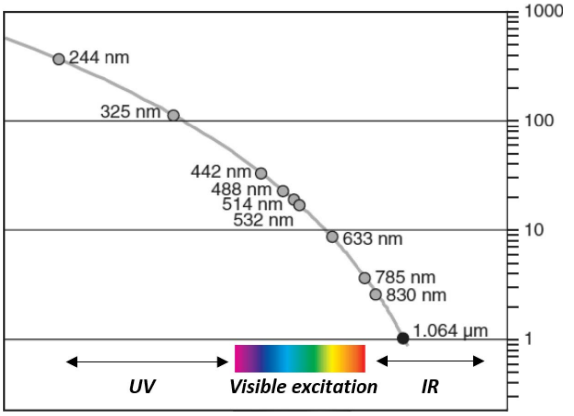

Figure 2. Influence of the laser source (Raman probe) used for Raman signal excitation on the scattering signal intensity: close to three orders of magnitude in Rayleigh and Raman intensities can be observed between deep UV (244 nm) and IR (1064 nm) excitations.

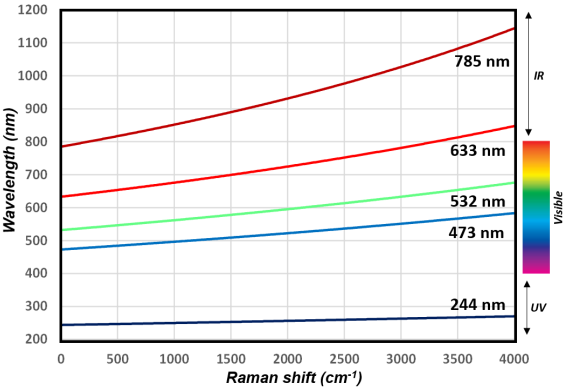

Figure 3. Relation between the wavelength of *Stokes* Raman scattered photons and their Raman shift expressed as $(\nu_0 - \nu_S)$, as a function of the laser excitation/Raman probe (see (1), with ν_0 the energy of the laser excitation and ν_S the energy of the scattered photons). The narrow wavelength range associated with a typical vibrational spectrum of 4000 cm^{-1} (30 nm for 244 nm excitation, ~200 nm for 633 nm excitation) explains, for instance, the high lateral resolution of Raman imaging on the whole spectral range (4000 cm^{-1}) contrary to infrared spectroscopy for which the wavelength range is typically 2.5–25 µm. As a result of the different energy ranges at 785 nm and 532 nm illustrated in Figure 1b (~1500 cm^{-1} *vs* ~3000 cm^{-1} on our equipment), the spectral resolution with 785 nm Raman probe is nearly twice that with 532 nm.

2.6. *Some characteristics of Raman spectra*

A typical Raman spectrum which covers the energy range 0–4000 cm^{-1} (from metal oxides M–O vibrational modes at low wavenumbers to O–H stretching modes at high wavenumbers) corresponds to a short range of wavelength λ (nm), e.g. 30 nm apart from the laser line in deep UV (244 nm) *vs* ~200 nm for a 633 nm laser line as illustrated on Figure 3. This has important implications on the lateral resolution of the analysis (see below). Moreover, because of the non-linearity between the wavelength associated with a specific transition and the calculated Raman shift, the characteristics of the excitation wavelength, of the spectrometer (diffraction grating, focal distance) and of the detector size affect considerably the achievable spectral range in cm^{-1} (decreases when λ_{exc} increases) and therefore the spectral resolutions (increases with λ_{exc}) as illustrated in Figure 1b.

2.7. *Confocal Raman microscopy*

Raman spectroscopy can be coupled to optical microscopy and piezo stages offering high resolution compositional mapping capabilities (see setup in Figure 4). The lateral (in the *XY* sample plane) resolution achievable, i.e. the ability to distinguish two surface objects as separate entities, is diffraction limited (Abbe, 1873) and can be defined according to the Abbe, Rayleigh (1896) or Sparrow criteria as roughly half of the wavelength of illumination:

$$\text{Abbe resolution}_{x,y} = \frac{\lambda_{exc}}{2\text{NA}} \sim \frac{\lambda_{exc}}{2} \qquad (3)$$

with NA the numerical aperture of the objective defined as $n \cdot \sin(\theta)$ with n the refractive index and θ the half-angle of collection. This lateral resolution in Raman microscopy is much lower than with IR microscopy, i.e. (sub) micrometric (1 µm at 785 nm, 0.336 µm at 248 nm excitation with a 0.90NA/100x objective). Note that for Raman spectroscopy, the spatial resolution is nearly constant along the spectrum as a typical Raman spectrum (4000 cm^{-1}) is

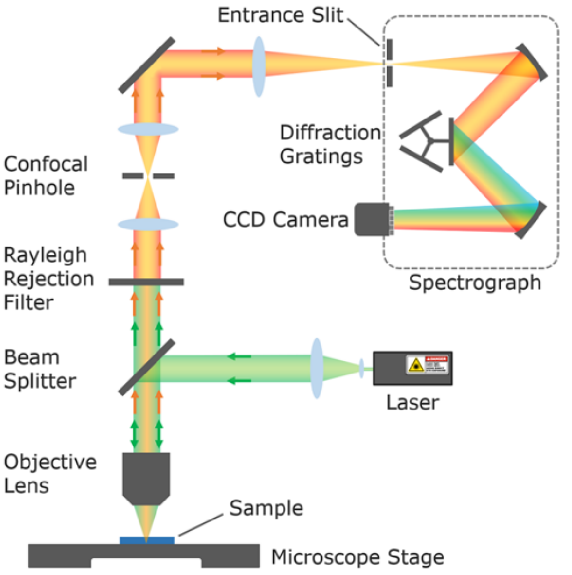

Figure 4. Design of a dispersive Raman confocal microscope (Image: Edinburgh Instruments) equipped with one or several monochromatic laser sources (Raman probe) with cleaning filters to narrow their spectral emission (bandpass filters and intensity attenuation filters not represented here), a rejection filter to suppress the dominant *Rayleigh* scattering (green beam), a confocal pinhole to selectively collect photons originating only from the sample focal plane (orange beam), a diffraction grating to spread the Raman photons of different energy (optical transition of the various molecular entities in the sample) on the detector (CCD camera).

contained within 30–200 nm depending on the excitation wavelength as mentioned earlier, this is not the case of IR spectroscopy using broadband sources like glowbars [58,59]. The range of the mid-infrared domain is typically between 4000 cm^{-1} and 400 cm^{-1} or between 2.5 μm and 25 μm. The spatial resolution varies thus along the spectrum between around 1–10 μm.

By placing a pinhole aperture (e.g. 2 × 2 blades perpendicular to one another) at the entrance of the spectrometer, it is possible to block the photons which do not originate from the focal plane on the sample (before and after), the so-called confocal Raman microscopy. By selecting objectives with low field depth (high NA objectives with large collection angle) and minimizing the pinhole size, the penetration depth of the analysis (depth resolution along the Z axis of the sample) can be reduced and the lateral resolution increased. Also the contribution of signal originating from the medium between the sample and the objective (atmosphere or liquid) can be minimized. Note that in such confocal configuration, the sensitivity of the analysis (Raman intensity) critically depends on the accuracy of the Raman probe focalization on the sample (and of the optical alignment). Proper focalization of the Raman probe can be difficult to achieve on rough and inhomogeneous samples, compromising the quality of compositional mapping. The depth resolution (Z axis) defined by Abbe is significantly lower than the lateral resolution, in the order of 1–2 μm depending on the wavelength of illumination:

$$\text{Abbe resolution}_z = \frac{2\lambda_{\text{exc}}}{\text{NA}^2}. \tag{4}$$

With the development of laser sources with very narrow excitation, photosensitive detectors with high quantum efficiency (PMT, CCD) and high quality optical elements (mirrors, beams separators, filters and gratings), the possibility to couple Raman spectroscopy with highly resolved confocal optical microscopy and to work on high water-content samples (no water absorption using non-infrared laser sources), Raman spectroscopy/microscopy use has been booming in the last twenty years in the academic and industrial communities.

Such high depth resolution which allows the extraction of Raman signature at different focal planes is interesting for optical sectioning of samples. By combining XY translation stages with submicrometer step resolution and Z motion of the objective lens, three-dimensional (3D) sectioning of samples can be obtained. In medicine for instance, numerous studies have been led on skin because *in vivo* confocal Raman spectroscopy constitutes a non-invasive optical method resolution which allows

the skin morphology to be visualized and (subsurface) structures in the skin to be targeted [59]. Without dissection, it is also possible to separate Raman signal originating from the inner layer of skin, namely the dermis, from the Raman signal coming from the outer layer, namely the epidermis, the axial resolution being of a few microns. Several studies dedicated to skin have explored vitiligo [59–61], atopic and psoriatic skin [62], basal cell carcinoma [63] or psoriasis inflammatory disease [64].

2.8. *Fluorescence: the Ramanist's enemy*

As mentioned earlier, Raman spectroscopy can use energetic probes (UV or Vis) and excited molecular entities can therefore be promoted to a superior electronic state. Under such condition, relaxation can also occur through fluorescence emission, giving rise to bell-shaped background on the *Stokes* spectral side only of the Raman spectra, as the fluorescence photons are of lower energy than the excitation source. For samples with strong auto-fluorescence (case of many biological samples with protein matrix), the Raman signatures can be dominated or even totally masked by the fluorescence background, resulting in their impossible detection and analysis as illustrated in Figure 5.

A first alternative is to use deep UV light sources (<250 nm), for which the emission of fluorescence does not interfere with the Raman signal detection, given that at such low wavelength, the two signals are well separated. As mentioned earlier, a typical Raman spectrum (4000 cm^{-1}) in deep UV indeed occurs within only 30 nm apart from the laser line. The main disadvantages of UV illumination for bio-sample characterization are the dominating Raman signal from DNA related to the Raman resonant purine and pyrimidine bases of DNA at excitation wavelengths shorter than 300 nm, and the possible sample damages under such energetic beam (photo/thermal degradation).

A second alternative is to use near-infrared light sources (from 700 nm up to 1064 nm) which induce less sample damages, minimize fluorescence signal as fewer systems absorb in NIR as compared to the ones in visible, but with a price to pay, the dramatic loss of sensitivity (lower Raman efficiency and lower sensitivity of detector in the NIR region). With confocal Raman microscope, the depth of analysis, and therefore the fluorescence signal level, can be reduced by maximizing the confocality of the analysis.

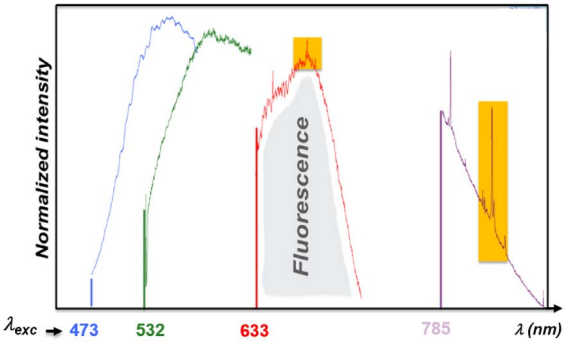

Figure 5. Influence of the laser source (Raman probe) used for Raman signal excitation on the background signal intensity (fluorescence): the Raman band of a Whewellite kidney stone (highlighted in orange) can be clearly observed with near-infrared laser sources (785 nm) while for blue and green excitations the Raman signal is totally screened by the strong fluorescence signal of the sample [65].

Note that, rough and inhomogeneous (bio)samples can give rise to large backgrounds on Raman spectra, which are not only attributed to auto-fluorescence but also to photons entering the spectrometer in a non-collimated way (stray light possibly due to scattering effect of both the laser source and of the Raman signal [66]).

3. New developments related to Raman spectroscopy

As mentioned earlier, one main limitation associated with Raman spectroscopy is its lack of sensitivity, especially with Raman probes close to the near-infrared. The progress in the fundamental understanding of the Raman process and of its enhancement together with major instrumental technical developments have allowed significant increase of Raman spectroscopy sensitivity and diagnosis capabilities [67].

3.1. *Dispersive Raman versus Fourier-transform Raman*

One main strength of Raman spectroscopy lies in the fact that the chemical signature is contained in

the scattered light (all the inelastic photons associated with the different molecular vibrations) collected upon irradiation with a monochromatic laser source. This means that the Raman spectrum (Raman intensity *vs* wavelength) can be reconstructed by dispersing the scattered light on a photodetector (e.g. a photomultiplier tube: PMT) using a rotating diffraction grating. Even better the Raman spectrum can be obtained instantly by dispersing the scattered light directly on the multiple photosensors of a Charge Coupled Device (CCD) detector, provided that the Raman signal is intense enough.

This contrasts with IR spectroscopy which uses a broadband excitation source (glowbar) and a signal interferometric detection. In such detection scheme, constructive and destructive interferences of the signal originating from the sample with a reference signal (the excitation source) are generated and modulated by controlling the optical path-length difference between the two signals (moving mirror). The resulting interferogram can be mathematically treated using a Fourier transform to extract the transmitted (or reflected) light intensity at each wavelength of excitation (FTIR). This detection method is extremely sensitive but requires relatively long signal collection times (signal accumulation at each mirror displacement step). Fourier-transform Raman spectroscopy also exists with 1064 nm excitation sources, allowing the collection of fluorescence-free Raman spectra for most of the compounds identified in abnormal deposits as published by Quy Dao and Daudon [68]. However this powerful solution requires long acquisition time to compensate for the very low scattering efficiency at such high wavelength and cannot be implemented on samples with high water content. FT-Raman has since been eclipsed by dispersive Raman system using near-infrared laser source (e.g. 785 nm) and detectors with better sensitivity in the near-IR region. In a recent publication, Yang *et al.* [69] have studied the laser wavelength dependence of background fluorescence in Raman spectroscopic analysis of synovial fluid from symptomatic joints. They show that both samples coming from asymptomatic and symptomatic patients had significant levels of fluorescence at excitation wavelengths below 700 nm, while experiments performed at 785 nm demonstrate sufficient sensitivity to identify crystals isolated from the synovial fluid.

> *Many biological samples show, upon illumination with visible laser light sources, strong auto-fluorescence background which tend to dominate/screen their Raman signature. FT-Raman using a monochromatic infrared laser source (1064 nm) has long been the technical solution to circumvent this problem, but is now overthrown by dispersive Raman systems (confocal microscopes) equipped with near-infrared monochromatic light sources (785 or 830 nm).*

3.2. *How to amplify the Raman signal?*

Since the discovery in the *1970s* of the properties of metal nanostructures upon illumination to amplify the Raman scattering intensity of objects in close proximity, a whole field of study named "enhanced Raman spectroscopy" (ERS) has opened up. Upon irradiation, the free electrons of the nanostructured metal oscillate at once (plasmon resonance) creating locally a strong enhancement of the electromagnetic field (EMF) and thereby of the incident and scattered light [5,70]. As the Raman intensity depends on the EMF intensity at the power two, a power four can be expected for the Raman signal enhancement ($I_{\text{Raman}} \propto |\text{EMF}|^2 \times |\text{EMF}|^2$). As plasmon absorption at a given wavelength relates directly to the band structure of the metal (and to its color), plasmon resonance and Raman signal enhancement can be observed on aluminum nanostructures upon UV irradiation (also 785 nm although this phenomenon is not currently explained), and upon visible illumination on silver, gold and copper [60]. The size and shape of the metal nanostructures determine the excitation wavelength giving rise to plasmon resonance and signal enhancement ranging from one to three orders of magnitude [71]. Materials to be analyzed can be deposited on a SERS active substrate (surface-enhanced Raman spectroscopy), alternatively colloidal gold nanoparticles coated or not with shells of insulating layers (SiO_2, Al_2O_3: Shell Isolated Nanoparticles Raman Enhanced Spectroscopy SHINERS). Core–shell nanoparticles have been applied on biological systems, for instance Xu's

group utilized SHINERS technique to obtain fingerprint information and investigate the type II microcalcifications in breast tissues [72,73]. They obtained a series of Raman and SHINERS spectra and detected in tissues Type II microcalcifications using statistical data processing (Multivariate analyses like Principal Component Analysis: PCA). This is the first report of SHINERS used in the diagnosis of breast cancer cells. Since this pioneering work, different reviews dedicated to the use of SERS and SHINERS for investigations in medicine have been published [74–76].

Another offshoot of ERS called Tip-Enhanced Raman Spectroscopy (TERS) uses Au or Ag tapered tips as scanning probes brought in close contact with the surface of interest [77,78]. Illumination of the tip apex with a laser through a high-NA objective, generates localized surface plasmons (the so-called hotspot) creating a very strong EMF enhancement at the tip–sample junction and thereby a strong enhancement of the Raman signal of the objects below the tip. Note that the lateral resolution offered by TERS can reach upto a few nanometers in the ambient [79] whatever the chosen excitation wavelength, explaining its designation by nanoRaman; this overcoming of the diffraction limit barrier constitutes a major breakthrough as compared to classical micro-Raman experiments [80–82]. Although TERS was developed by the early 2000s, it remained at the conceptual stage for almost a decade, primarily because of the poor reproducibility in the manufacturing of TERS-active probes. TERS is currently booming and has already found numerous applications as the significant decrease in the spatial (lateral and depth) resolution offers new analytical opportunities, like nanoscale chemical analysis or imaging of biological species and structures without the need of chemical labeling. A few recent reviews have been dedicated to the topic [83–90] reporting TERS analysis of nucleic acids (DNA, RNA) with direct sequencing [91], peptides and proteins, lipids and viruses, bacteria and cell membranes. The group of Lagugne-Labarthet [92] also studied the adsorption of phosphoprotein osteopontin (OPN) on calcium oxalate monohydrate (COM). They found preferential adsorption of OPN on certain COM crystal facets at the origin of inhibition of crystal growth, confirming previous work of Sheng *et al.* [93] based on SEM and AFM imaging methodology.

> *Raman signal enhancement techniques (SERS) introduced in the early 1970s have been largely used for the characterization of biological sample. An offshoot using nanoparticles (SHINERS) as signal amplifiers shows great promise for in vivo analyses. Its counterpart, TERS using metal nanoprobes, displays high sensitivity and provides chemical imaging with nanoscale lateral resolution, offering a new opportunity to localize pathological calcifications inside specific organites of cells.*

In *resonant Raman*, by tuning the laser excitation to match an electronic transition of the molecular entity under scrutiny (see Figure 1), a coupling between electronic and vibrational transition occurs, leading to a strong enhancement of the Raman scattering (Resonance Raman: RR), up to 10^6 times. As visible excitation usually triggers strong fluorescence background especially for biological samples, UV or deep UV is proposed as an alternative. Resonant enhancement associated with TERS analysis enabled, for instance, the detection of cytochrome C in mitochondria [94].

3.3. *Fluorescence rejection in time-resolved Raman*

In order to investigate reaction mechanisms by capturing the chemical signature of short life time intermediates (radicals, excited states), time-resolved Raman spectroscopies, covering Femtosecond stimulated Raman (FSRS), Kerr-Gated Raman, Coherent-anti-Stokes Raman (CARS), have been developed [95]. The experimental setup combines pumps and probes spectroscopy (which involves two ultrafast laser beams, a pump beam to initialize the Raman transitions and a probe beam to stimulate the Raman transition) with highly efficient spectrometers, and highly sensitive high speed multichannel detectors. Such experimental configuration allows fluorescence-free Raman spectra to be collected with acquisition time ranging between microsecond to picosecond. The pioneering work of Weisberg and co-workers [96] was reported in 1976 and today time-resolved Raman spectroscopy constitutes a mature technique leading to numerous publications, most

of them in physics. Note that ultrafast Raman spectroscopic techniques can be combined with the use of plasmonic substrates or scanning probes [97].

3.4. *Raman implementation in vivo*

Several technical solutions have been proposed to extract Raman signatures *in vivo*, including Transmission Raman (TRS) which is possible as Raman does not rely on photon absorption and as the light can spread randomly through thick samples. Spatially offset Raman spectroscopy (SORS) developed by Matousek *et al.* [98] as early as 2005 introduces a spatial separation between the laser excitation and Raman collection (note that TR can be seen as an extreme case of SORS: transmission SORS). SORS relies on the fact that deep penetrating photons tend to migrate laterally, away from the illumination source, while scattered photons (Raman) are less likely to do so when reaching the surface of the sample. TRS and SORS enable analyses through thick and turbid materials (containers, packaging) up to 5 cm in the absence of photon absorption with applications in security, food safety, pharmaceutics and medicine including transcutaneous analysis (diagnosis of osteoporosis, possible bone regrowth monitoring and breast cancer through the detection and distinction of benign or malignant microcalcifications) [99]. SORS can be implemented using optical fibers for both illumination and Raman signal collection. To maximize the collection efficiency and control the offset distance, optical fibers constituted of a central illumination fiber surrounded by multiple collection fibers (or inversely: inverted SORS) organized as a ring at a given offset distance from the central illumination point are often used. Implementation of SORS can be coupled to the use of SERS active gold nanoparticles in targeted tissues (SESORS).

The development of fiber optical Raman probes is crucial for clinical *in vivo* applications, their association with standard medical endoscopes for instance holds great promise for *intra-operative* medical diagnosis (lung, brain, digestive and urinary systems, breast cancer, cardiovascular diseases) [100]. The implementation of fiber-optic Raman probe is complex as silica-based optical fibers (core and cladding) generate a strong Raman signal which can screen the Raman signal of the sample. Excitation and signal detection/collections path are then usually separated enabling specific filtration at the distal fiber end, i.e. a narrow-band/short-pass filter to suppress the silica signal background on the excitation fiber and a long-pass filter at the collection entrance to avoid reentry of the laser light into the fiber. Addition of filters usually comes at a high price. Focusing lens can also be added to the design. The design (diameter) of the resulting probe mostly depends on the application, fiber bundle diameters as small as 1 mm in catheters have been reported to be developed to fit into the endoscopic channels of cystoscopes, colonoscopes; fiber optical Raman probes must in any case withstand repeated sterilization processes. Note that the association of endoscopic Raman probes and of SERS-active nanoparticles (120 nm diameter) functionalized with tumor-target contrast agents has been envisaged for the endoscopic detection of small polyps and flat lesions in the colon [101] with no clinical application up to date.

4. Selected applications of Raman spectroscopy

In the following paragraphs a selection of investigations performed on pathological calcifications developed in breast [102–113], kidney [114–139], gallbladder [140–149], prostate [150–161], skin [162–168], testicular microlithiasis [169–178], atherosclerosis [179–196] and cartilage [197–200] are presented. Each section is associated with different organs and the related pathologies are preceded with some medical notions presented succinctly. The limitations and advantages of Raman spectroscopy are also discussed.

4.1. *Breast calcifications*

Breast cancer is the most common cancer in Europe [102]. It develops in breast tissues, in which it can be distinguished in the lobules or glands for milk production and ducts that connect the lobules to the nipple. Two types of breast calcifications have been described [103]. The first one composed of calcium oxalate dihydrate is always related to benign conditions [104]. In fact, calcium oxalate dihydrate is not stable and a phase transition may occur, leading to the formation of calcium oxalate monohydrate [105]. Note that such a chemical phase has not been reported in the literature to the best of our knowledge. The second one is composed of carbonated calcium

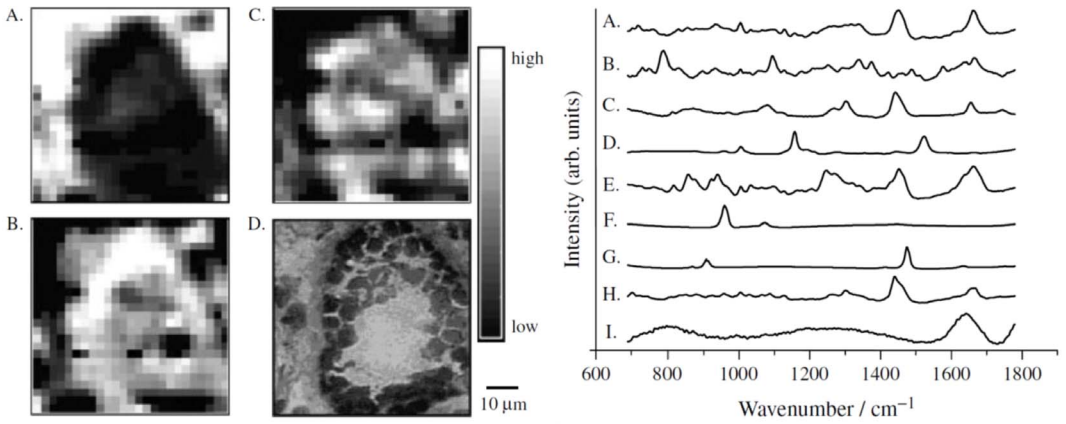

Figure 6. Left—MicroRaman mapping images of normal breast duct (A–C) with corresponding serial stained section (D). Each image reveals the contribution of a specific morphological element to the region under scrutiny (A) collagen; (B) cell cytoplasm; (C) cell nucleus. They have been produced by ordinary least-squares fitting of each data point in the image with the reference spectra presented to the right. Right—Reference spectra used in the morphological model of the breast: (A) cell cytoplasm; (B) cell nucleus; (C) fat; (D) β-carotene; (E) collagen; (F) calcium hydroxyapatite; (G) calcium oxalate; (H) cholesterol-like; (I) water. Reprint from Shafer-Peltier *et al.* [104].

phosphate apatite (or CA) and may be related to either benign or malignant conditions.

An example of Raman maps of a normal breast duct built by fitting of each image pixels with reference Raman spectra of different cell components is shown in Figure 6. The resulting images which the contrast depends on the different component abundance but also on their respective Raman cross-section correlate well with the tissue architecture.

Several works on breast calcifications also point out other chemical phases namely amorphous carbonated calcium phosphate [106] and whitlockite [107]. Recently, Vanna *et al.* [108] have suggested that the presence of whitlockite is a marker of benignity in benign breast microcalcifications. This is in contradiction with the work of Kunitake *et al.* [109] which reveals the presence of CA and spheroidal whitlockite particles in invasive cancer within a matrix containing spectroscopic signatures of collagen, non-collagen proteins, cholesterol, carotenoids, and DNA. It seems that the relationship between whitlockite and the severity of breast cancer is quite complex. As underlined by Scott *et al.* [110], the proportion of magnesium whitlockite increases from benign *in situ* carcinoma to invasive cancer. Finally, Tsolaki *et al.* [111] have recently established a strong correlation between the presence of whitlockite particles and the occurrence of malignant tumor by applying nanoanalytical methods to healthy, benign and malignant tumors' breast tissue biopsies from patients.

The level of carbonate in apatite is another parameter which can be assessed through Raman spectroscopy [112,113]. Baker *et al.* [113] report significant correlations between the carbonate composition level of microcalcification mainly composed of CA and pathology grades namely benign, *in situ* carcinoma and invasive carcinoma. We have also estimated the carbonate content of CA calcifications through μFTIR spectroscopy [106]. Thanks to the micrometer size of the probe, the data show that the chemical compositions as well as the carbonate level are very inhomogeneous in the case of ductal carcinoma *in situ*. More precisely, through a precise analysis of the FTIR spectrum, we established that the proportion of amorphous carbonated calcium phosphate as well as the carbonation rate vary from the center to the edge of a large (almost 1 mm) calcification.

4.2. *Kidney stones and kidney biopsies*

Raman spectroscopy has long been used to determine the chemical composition of kidney stones.

Almost forty years ago, Daudon *et al.* [114] published a study which discussed the advantages and the limitations of this spectroscopy. These authors underlined the fact that Raman, at the opposite of FTIR spectroscopy, allows the characterization of micron-sized crystals. Since that pioneering work, and thanks to the development of commercial Raman microscope setups, many scholars have studied kidney stones by Raman spectroscopy [114–127]. One example is given in Figure 7. Also, several researchers have shown that it is possible now to predict Raman vibrations from the crystallographic structure [128,129], therefore easing the interpretation of Raman signatures.

Among the different investigations dedicated to kidney stones, Carmona *et al.* [116] have extended the application of Raman spectroscopy of human kidney stones to urinary calculi from canine, feline, and equine animal species. More recently, Cui *et al.* [126] have collected 135 kidney stones and used these data to test a variety of machine learning models to establish a kidney stone classification. At this point, we must recall that the chemical composition is not the only parameter to establish a significant link with the etiology. The morphology of the calculi at the macrometer and micrometer scale is also of relevant importance [130–133]. The formation of calcium oxalate monohydrate KS can be related for instance to either a severe genetic disease, namely primary hyperoxaluria or a dietary disorder [134,135].

Regarding the comparison between μFTIR and Raman spectroscopy, Chang *et al.* [124] underline the possibility to analyze the stone composition extracted from urine spectroscopy analysis. This experimental configuration developed by Chang offers the opportunity to characterize micrometer scale stones in urine through Raman spectroscopy. More recently, Frochot *et al.* revealed the presence of several calcium carbonate polymorphs, including the rare vaterite form, in urine sediments of patients [18] following vegetable-rich diets (see Figure 8).

Finally, we would like to emphasize that Raman spectroscopy can be applied to kidney biopsies and soft tissue biopsies in general [136–139]. Lloyd *et al.* [136] have for instance considered a severe pathology, namely calciphylaxis, generally seen in patients with kidney failure and which induces the pathogenesis of calcifications in different soft tissues. Their analysis of Raman spectra show that abnormal deposits present in tissues were consistently made of CA. From an experimental point of view [139], we have tried to develop specific supports for kidney biopsy on which a set of characterization techniques namely Raman, μFTIR spectroscopies as well as scanning electron microscopy and UV spectroscopy can be implemented.

4.3. *Gallstones*

Most of the papers dedicated to gallstones focus on their chemical composition. Zheng *et al.* [140] consider three parts, namely the surface of the stone, the subsurface interior, and the center of the stone. Analysis of the Raman spectra shows that these three parts contain bilirubin and that cholesterol was present only at the outer surface of the stone. Some authors underline the presence of other chemical compounds. In the publication of Iordanidis *et al.* [141] and of Stringer *et al.* [142], the presence of calcium carbonate has been also pointed out. Finally, other calcium salts namely calcium bilirubinate as well as calcium palmitate have been detected by Kaufman *et al.* [143].

Regarding the formation of gallstone, as noticed by Bouchier [144] overproduction of cholesterol by the liver is the major metabolic precedent of cholesterol gallstones. Such overproduction of cholesterol is related to obesity, drugs, or other factors. The role of bacteria in the formation of gallstones has been discussed since about forty years [145–147]. Beta-glucuronidase of bacteria are responsible for the formation of calcium bilirubinate stones through the hydrolysis of bilirubin glucuronide to free bilirubin, which is insoluble in water [148]. Note that Hazrah *et al.* [149] underline the fact that gallstones from most patients contain live bacteria with the potential to cause infective complications. These data strongly suggest that several mechanisms may be involved in stone formation and that, as reported for kidney stones, an accurate identification of crystalline phases is needed to help the physician identify the cause for the formation of these stones.

4.4. *Prostate tissue and prostatic stones*

The main type of surgery for prostate cancer is a radical prostatectomy [150]. Such surgical procedure leads to the observation of prostatic calculi which

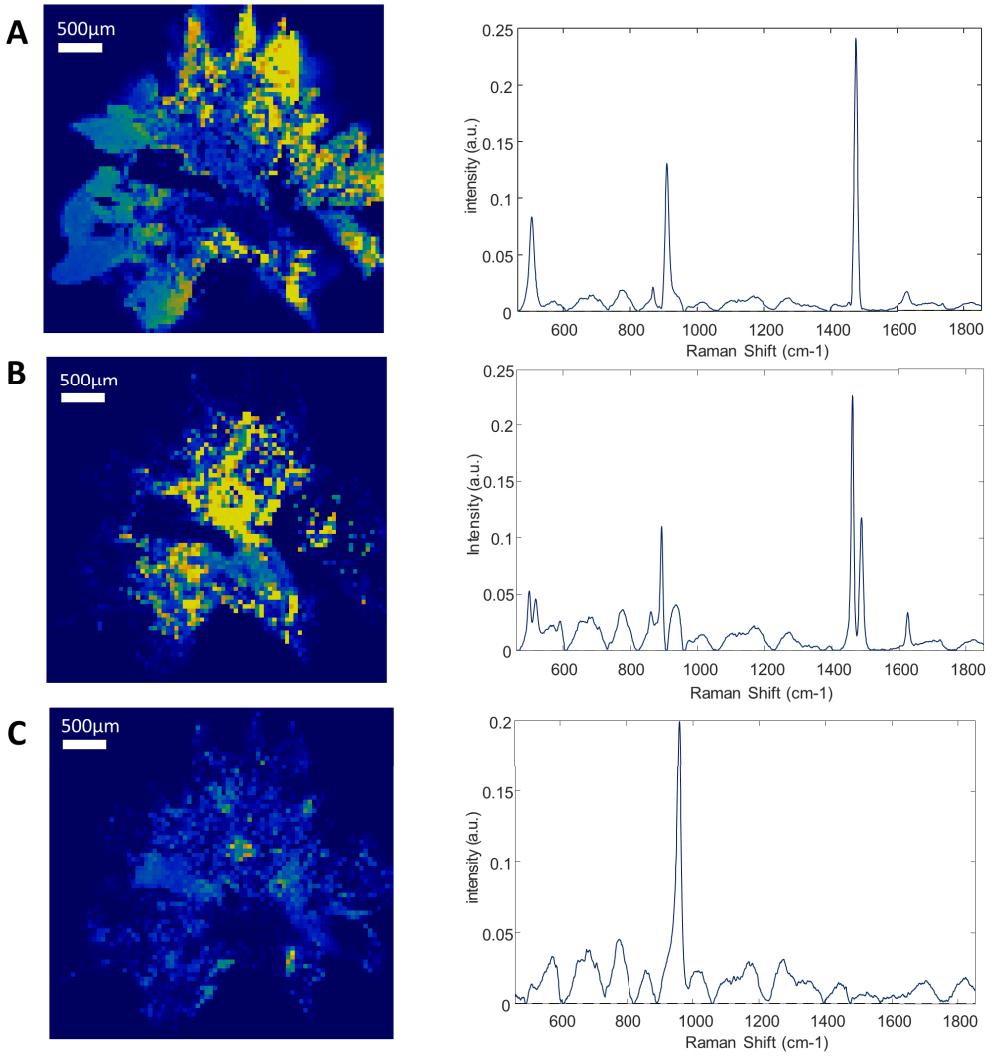

Figure 7. Composition mapping of sliced and milled kidney stone—Left: Raman intensity mapping (step size: 50 µm) of (A) calcium oxalate dihydrate (COD: single Raman band at 1475 cm^{-1}), (B) calcium oxalate monohydrate (COM: double Raman band at 1461 and 1487 cm^{-1}) and (C) apatite (964 cm^{-1}) and their corresponding Raman spectra (right), revealing COD within the peripheral spikes of the stone and COM within its center. The yellow to dark blue scale represents respectively the high density of a given component or its absence. Reprint from Castiglione *et al.* [125].

are a very common finding. Almost 99% of surgically removed prostates contain stones which often occur in middle-aged and old men without causing any specific symptoms. These concretions are generally considered clinically insignificant and therefore, only a few papers have investigated these calcifications [151–155]. Sfanos *et al.* [151] have identified several chemical compounds in prostatic calculi namely calcium phosphate, CA and calcium oxalate monohydrate. Dessombz *et al.* [152,153] have also underlined the presence of brushite ($CaHPO_4{\cdot}2H_2O$), amorphous carbonated calcium phosphate, calcium oxalate dihydrate, octacalcium phosphate pentahydrate ($Ca_8H_2(PO_4)_6{\cdot}5H_2O$) and whitlockite. Recently, Hsu *et al.* [154] have proposed a portable fiber-optic Raman spectroscope for fast chemical analysis of prostatic stones. Such experimental device has identified the different chemical phases previously

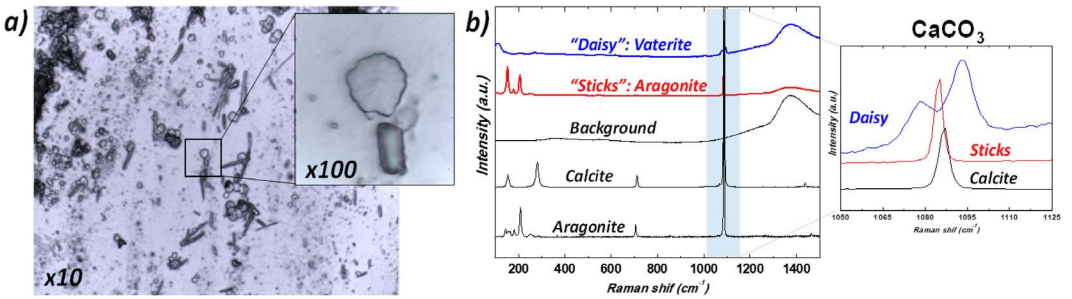

Figure 8. Crystalluria—(a) Optical micrograph (magnification ×100) of urinary sediments, (b) typical Raman spectra of the different variants of calcium carbonate crystals vaterite (daisy-like crystals) and aragonite (sticks and needles) found in urine of patients. A possible association with a diet rich in vegetables has been hypothesized for some subjects whose urine contained daisy-like crystals. Reprint from Frochot *et al.* [18].

reported. Moreover, Kontoyannis *et al.* [155] have used Raman spectroscopy to identify the chemical compounds present on prostatic stent.

Another research field based on Raman spectroscopy which is very exciting is related to the diagnosis of prostate cancer [156–160]. For example, it is worthwhile to underline the work of Chen *et al.* [161]. In that publication, the authors use SERS to point out prostate cancer in patients through the detection of a prostate-specific antigen level of 4–10 ng/mL present in blood serum. Such procedure avoids the biopsy prostate operation.

4.5. *Skin*

As we have seen previously, Raman spectroscopy offers the possibility to determine *in vivo* the chemical composition of specific area. This peculiar property has been used in numerous investigations for very different purposes like the penetration of drugs into the skin to the study of skin cancer [162–165].

Like for other soft tissues, the Raman spectrum of skin is dominated by the vibrational bands of its structural proteins, amino acids and lipids [166]. Such Raman spectra thus contain numerous bands related to the different molecular groups present in skin. For example, in the stratum corneum, we can quote cysteine, tryptophan, hydroxyproline, phenylalanine, etc. It is thus possible to extract from the analysis of Raman spectrum different chemical modifications of the skin. Changes in diseased tissue are driven by changes in cellular biochemistry. For example, the results gathered by Santos *et al.* [167] show that the Raman bands between 2840 and 2930 cm^{-1} have increased intensity for melanoma when compared to benign melanocytic lesions, suggesting an increase in lipid content in melanoma.

Another health problem regarding skin is related to tattoos. Several investigations through Raman spectroscopy have been performed [168–171]. Yakes *et al.* [168] have created a spectral library of the pigments for each laser wavelength. Such library is proposed to help the identification of all the pigments made by the different manufacturers. Indeed, Darvin *et al.* [169] have identified through Raman spectroscopy tattoo ink pigments *in vivo* and their depth dependence in human tattooed skin confirming their presence in the papillary and reticular dermis. Such approach is of primary importance because different pathologies are linked to skin tattoos, such as allergic reactions [170] and cancer (keratoacanthoma) [171]. In our work, we underlined the presence of the same red azo pigment (*PR170*) in all three keratoacanthoma cases, consistently associated with metal oxide. Generation of primary aromatic amines from azo pigments such as *PR170* in humans as the consequence of enzymatic activity, thermal decomposition, or photodegradation after UV light exposure is suspected to be at the origin of the observed cancers [171].

4.6. *Testicular microlithiasis*

During ultrasonographic investigation of the testis, it is possible to detect the presence of multiple

tiny calcifications. Such testicular microlithiasis (TM) appears as 1- to 3-mm-sized multiple foci within the parenchyma of the testis [172–174]. In a recent epidemiological study, Peterson *et al.* [175] indicate that testicular microlithiasis occurs in more than 5% of healthy young men. The conclusion of their study indicates that testicular microlithiasis is a common finding in asymptomatic men that may not be related to testicular cancer.

According to Renshaw [176], two types of calcifications exist consisting either of amorphous calcific debris or laminated calcifications. Regarding the chemical characterization of such abnormal deposits, we can quote the work of Smith *et al.* [177]. These authors have evaluated the use of percutaneous testicular sperm aspiration in the assessment of azoospermia and its association with seminiferous tubule microliths. To obtain the chemical composition of the microliths, X-ray diffraction experiments have been performed. The position of the diffraction peaks is in line with those corresponding of hydroxyapatite. Unfortunately, the width of the diffraction peaks was not measured. Such a parameter may give information regarding the size and the morphology of the chemical crystal phase.

More recently, De Jong *et al.* [178] have characterized microliths found in different types of benign and malignant gonadal pathologies through Raman spectroscopy. The precise analysis of the data underlines in the chemical composition the presence of calcium phosphate apatite. Also, these authors have noticed the presence of glycogen surrounding the microliths located in each testicular sample adjacent to testicular germ cell tumors and carcinoma *in situ* as well as gonadoblastoma.

4.7. *Atherosclerosis*

Cardiovascular disease is now a leading cause of disability and premature mortality globally [179]. Atherosclerosis constitutes the main pathological process of most cardiovascular diseases. As underlined by Hong [180], atherosclerosis can be observed in young people, remain latent and asymptomatic for long periods and then may progress into its advanced stages. The fact that patients with unstable plaques are at great risk for a sudden heart attack (i.e. myocardial infarction) when a plaque suddenly ruptures has motivated numerous investigations (see for example [181–183]).

Regarding the plaque evolution, three states can be distinguished [184] namely fibrolipid plaques, calcified and ossified plaques, and vulnerable atherosclerotic plaques. These authors have observed a clear correlation between the Raman spectra of plaques in the aortic tunica intimal wall of a human corpse and three states of plaque evolution. More precisely, in the case of highly calcified deposits on the atherosclerotic plaques and ossified lesion, they have measured a sharp peak at 964 cm^{-1} in the Raman spectra which corresponds to the totally symmetric ν_1 stretch of PO_4^{3-} engaged in CA. In Figure 9, Buschman *et al.* [185] show clearly that it is possible to discriminate different elements of coronary artery morphologic structures with Raman spectroscopy.

Several publications have already identified this chemical compound in atherosclerotic plaques [186–190]. Generally, this compound coexists with its amorphous precursor, amorphous calcium phosphate hydroxyapatite and it is worth mentioning that the totally symmetric ν_1 stretch constitutes an interesting indicator of the degree of crystallinity. At 955 cm^{-1}, this structure is associated with an amorphous highly carbonated bone. At 963 cm^{-1} it corresponds to a more ordered non-carbonated phase [191,192]. Other chemical phases have been identified namely, whitlockite, calcium carbonate, calcium oxalate (in coronary artery calcification in dialysis patients) [193], calcium phosphate and calcium pyrophosphate ($Ca_2P_2O_7$) [194].

Using FTIR spectroscopy, Coscas *et al.* [195] have demonstrated that free DNA could be involved in arterial calcification formation by precipitating calcium phosphate apatite crystals in the vessel wall. Moreover, bundles of faceted microrods inserted into the surface of the vessel have been found at the outset of the calcification formation as suggested by Dorfmüller *et al.* [196].

4.8. *Cartilage*

Regarding cartilage, several investigations attest to the accuracy of Raman spectroscopic imaging measurements to gather information regarding the spatial distribution of biochemical components in a biological tissue [18,197,198]. Among them, Albro *et al.* [197] as well as Bergholt *et al.* [198] show that

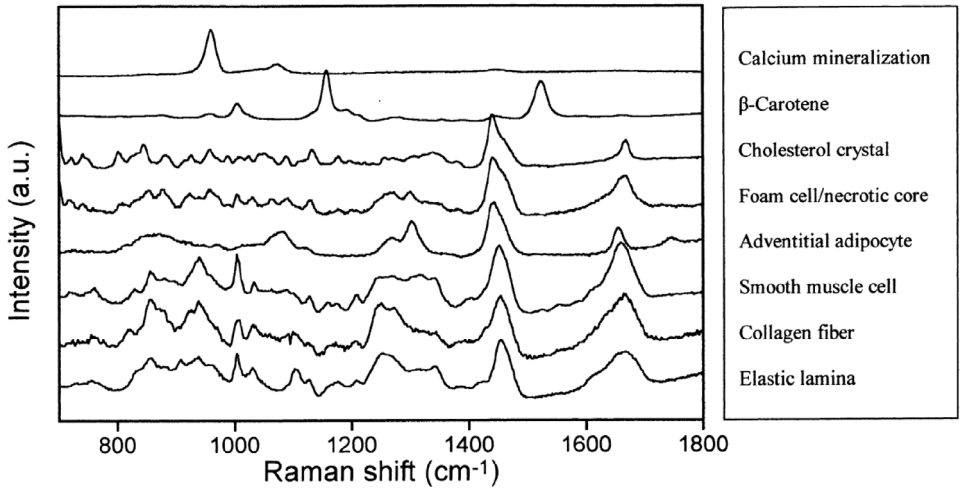

Figure 9. Raman spectra of morphologic structures commonly observed in human atherosclerotic coronary artery used as references to assess lesions, plaque instability and disease progression, possibly *in vivo* using fiber-optic probes. Reprint from Buschman *et al.* [185].

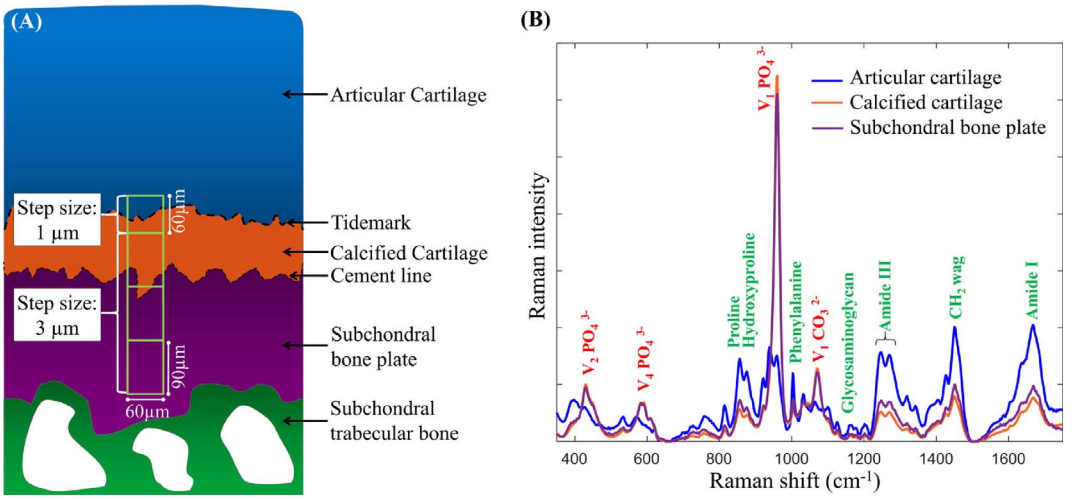

Figure 10. (A) A schematic representation of the human osteochondral junction highlighting the different regions where multiple Raman microspectroscopic measurements for statistical processing (Principal Component Analysis: PCA) have been made. The measurement step size for the first region (60 μm × 60 μm) where the tidemark is located is 1 μm, a step size of 3 μm was used for all other regions (each region: 60 μm × 90 μm). (B) Mean baseline-corrected vector-normalized Raman spectra (reproduced with 10 principal components) from the deep articular cartilage, calcified cartilage and subchondral bone plate, respectively. The major mineral compounds phosphate and carbonate are annotated with red labels, and the organic counterparts with green labels. Reprinted from Gupta *et al.* [20].

Raman spectroscopic imaging can be used to assess the degree of heterogeneities in engineered tissues and their depth dependence. Such information is of prime importance to assess the success of tissue growth strategies. Regarding pathological calcifications, Gupta *et al.* [20] have analyzed the spatial composition of mineralized osteochondral tissues, i.e. calcified cartilage (CC) and subchondral bone plate

(SBP) from unfixed, hydrated specimens. Figure 10 shows that the size of the probe allows a detailed description of the biochemistry related to the tidemark. Among their results, these authors clearly show that in early osteoarthritis, the mineralization tends to increase, and the mineral contains fewer carbonate substitutions.

Another interesting point on cartilage which has been investigated by Fields *et al.* [199] concerns the high temperature behavior of collagen and collagenous tissue, which is important for surgical procedures and biomaterials. Their Raman experiments reveal the presence of bound water within the collagen component of connective tissue even after freeze-drying and its role in denaturation that is accompanied by or perhaps preceded with breakdown of the primary polypeptide structure. Finally, Shaikh *et al.* [200] underlines the fact that Raman spectroscopy is able to provide biochemical details regarding potential for scoring the severity of cartilage lesions, which could be useful in determining the optimal treatment strategy during cartilage repair surgery.

5. Conclusion

Although Raman spectroscopy is still scarcely used in the medical community, all the examples shown in this review, taken mostly from recent literature, clearly demonstrate that Raman spectroscopy is a unique diagnostic tool which gives valuable information to the clinician in various medical specialties encompassing breast cancer, nephrology, cardiology and dermatology without much difficulties in implementation. With the development of fiber optical probes integrating spectroscopic analysis (Raman but also fluorescence multimodal probes) in addition to classical imaging and treatment (i.e. laser lithotripsy), great diagnostic perspectives can be anticipated per-operating or *in vivo*.

Acknowledgments

This work was supported by the Physics and Chemistry Institutes of Centre National de la Recherche Scientifique and by contracts ANR-09-BLAN-0120-02, ANR-12-BS080022, ANR-13-JSV-10010-01, convergence UPMC CVG1205 and CORDDIM-2013-COD130042.

References

[1] C. V. Raman, K. S. Krishnan, *Nature*, 1928, **121**, 501-502.
[2] A. Smekal, *Naturwissenschaften*, 1923, **11**, 873-875.
[3] E. Smith, G. Dent, *Modern Raman Spectroscopy: A Practical Approach*, Wiley, Chichester, UK, 2005.
[4] D. A. Long, *The Raman Effect: A Unified Treatment of the Theory of Raman Scattering by Molecules*, Wiley, Chichester, UK, 2002.
[5] R. L. McCreery, *Chemical Analysis, Vol. 157: Raman Spectroscopy for Chemical Analysis*, Wiley, New York, 2000.
[6] R. Aroca, *Surface-Enhanced Vibrational Spectroscopy*, Wiley Chichester, UK, 2006.
[7] M. Daudon, H. Jaeschke-Boyer, M. F. Protat, R. J. Réveillaud, *Actual. Chim.*, 1980, **4**, 25-29.
[8] M. Daudon, M. F. Protat, R. J. Réveillaud, H. Jaeschke-Boyer, *Kidney Int.*, 1983, **6**, 842-850.
[9] A. Bonifacio, S. Cervo, V. Sergo, *Anal. Bioanal. Chem.*, 2015, **407**, 8265-8277.
[10] I. Maitra, C. L. M. Morais, K. M. G. Lima, K. M. Ashton, R. S. Date, F. L. Martin, *J. Biophotonics*, 2020, **13**, article no. e201960132.
[11] R. Smith, K. L. Wright, L. Ashton, *Analyst*, 2016, **141**, 3590-3600.
[12] J. M. Surmacki, B. J. Woodhams, A. Haslehurst, B. A. J. Ponder, S. E. Bohndiek, *Sci. Rep.*, 2018, **8**, article no. 12604.
[13] M. T. Kirchner, H. G. M. Edwards, D. Lucy, A. M. Pollard, *J. Raman Spectrosc.*, 1997, **28**, 171-178.
[14] D. Bazin, C. Chappard, C. Combes, X. Carpentier, S. Rouzière, G. André, G. Matzen, M. Allix, D. Thiaudière, S. Reguer, P. Jungers, M. Daudon, *Osteoporos. Int.*, 2009, **20**, 1065-1075.
[15] G. S. Mandair, M. D. Morrisa, *Bonekey Rep.*, 2015, **4**, 1-8.
[16] D. Bazin, M. Daudon, C. Combes, C. Rey, *Chem. Rev.*, 2012, **112**, 5092-5120.
[17] D. Bazin, E. Letavernier, J.-P. Haymann, V. Frochot, M. Daudon, *Ann. Biol. Clin.*, 2020, **78**, 349-362.
[18] V. Frochot, V. Castiglione, I. T. Lucas, J.-P. Haymann, E. Letavernier, D. Bazin, G. B. Fogazzi, M. Daudon, *Clin. Chim. Acta*, 2021, **515**, 1-4.
[19] S. M. Ali, F. Bonnier, A. Tfayli, H. Lambkin, K. Flynn, V. McDonagh, C. Healy, T. C. Lee, F. M. Lyng, H. J. Byrne, *J. Biomed. Opt.*, 2013, **18**, article no. 061202.
[20] S. D. Gupta, M. A. J. Finnilä, S. S. Karhula, S. Kauppinen, A. Joukainen, H. Kröger, R. K. Korhonen, A. Thambyah, L. Rieppo, S. Saarakkala, *Acta Biomater.*, 2020, **106**, 145-155.
[21] K. Kong, C. Kendall, N. Stone, I. Notingher, *Adv. Drug Deliv. Rev.*, 2015, **89**, 121-134.
[22] W. Petrich, *Appl. Spectrosc. Rev.*, 2001, **36**, 181-237.
[23] V. Vuiblet, T. T. Nguyen, A. Wynckel, M. Fere, L. Van-Gulick, V. Untereiner, P. Birembaut, P. Rieu, O. Piot, *Analyst*, 2015, **140**, 7382-7390.
[24] C. J. Sperati, C. Zhang, M. Delsante, R. Gupta, S. Bagnasco, I. Barman, *Kidney Int. Rep.*, 2018, **3**, 997-1003.
[25] J. Fleureau, K. Bensalah, D. Rolland, O. Lavastre, N. Rioux-Leclercq, F. Guillé, J.-J. Patard, L. Senhadji, R. de Crevoisier, *Expert Syst. Appl.*, 2011, **38**, 14301-14306.
[26] A. A. Lykina, D. N. Artemyev, V. I. Kukushkin, I. A. Bratchenko, N. S. Aleksandrov, V. P. Zakharov, *J. Phys.: Conf. Ser.*, 2018, **1096**, article no. 012116.

[27] A. Kai-chingHau, T. H. Kwan, P. Kam-tao Li, *J. Am. Soc. Nephrol.*, 2009, **20**, 245-250.
[28] R. S. Senger, M. Sullivan, A. Gouldin, S. Lundgren, K. Merrifield, C. Steen, E. Baker, T. Vu, B. Agnor, G. Martinez, H. Coogan, W. Carswell, V. Kavuru, L. Karageorge, D. Dev, P. Du, A. Sklar, J. Pirkle Jr, S. Guelich, G. Orlando, J. L. Robertson, *PLoS One*, 2020, **15**, article no. e0227281.
[29] V. R. Kodati, G. E. Tomasi, J. L. Turumin, A. T. Tu, *Appl. Spectrosc.*, 1990, **44**, 1134-1136.
[30] P. Crow, J. Uff, J. Farmer, M. Wright, N. Stone, *BJU Int.*, 2004, **93**, 1232-1236.
[31] S. Hoey, D. H. Brown, A. A. McConnell, W. E. Smith, M. Marabani, R. D. Sturrock, *J. Inorg. Biochem.*, 1988, **34**, 189-199.
[32] A. Abhishek, D. J. Curran, F. Bilwani, A. C. Jones, M. R. Towler, M. Doherty, *Rheumatology*, 2016, **55**, 379-380.
[33] C. D. Hosu, V. Moisoiu, A. Stefancu, E. Antonescu, L. F. Leopold, N. Leopold, D. Fodor, *Lasers Med. Sci.*, 2019, **34**, 827-834.
[34] S. Managò, C. Valente, P. Mirabelli, D. Circolo, F. Basile, D. Corda, A. C. De Luca, *Sci. Rep.*, 2016, **6**, article no. 24821.
[35] C. G. Atkins, K. Buckley, M. W. Blades, R. F. B. Turner, *Appl. Spectrosc.*, 2017, **71**, 767-793.
[36] R. Gautam, J.-Y. Oh, M. B. Marques, R. A. Dluhy, R. P. Patel, *Lab. Med.*, 2018, **49**, 298-310.
[37] N. Sharma, N. Takeshita, K. Yu Ho, *Clin. Endosc.*, 2016, **49**, 404-407.
[38] K. Lee, O. Y. Lee, Y. I. Kwon, S. Won, O. W. Kwon, Y. W. Joo, H. L. Lee, D. W. Jun, B. C. Yoon, H. S. Choi, J. S. Hahm, *Gastroenterology*, 2011, **140**, S-765.
[39] U. Parlatan, M. T. Inanc, B. Y. Ozgor, E. Oral, E. Bastu, M. B. Unlu, G. Basar, *Sci. Rep.*, 2019, **9**, article no. 19795.
[40] E. Guevara, J. C. Torres-Galván, M. G. Ramírez-Elías, C. Luevano-Contreras, F. Javier González, *Biomed. Opt. Express*, 2018, **9**, 4998-5010.
[41] T. D. Hong, D. Phat, P. Plaza, M. Daudon, N. Q. Dao, *Clin. Chem.*, 1992, **38**, 292-298.
[42] P. J. Caspers, H. A. Bruining, G. J. Puppels, G. W. Lucassen, E. A. Carter, *J. Invest. Dermatol.*, 2001, **116**, 434-442.
[43] A. Quatela, L. Miloudi, A. Tfayli, A. Baillet-Guffroy, *Skin Pharmaco Physiol.*, 2016, **29**, 102-109.
[44] C. A. Téllez, T. O. Mendes, L. Dos Santos, M. G. P. Silva, L. Pereira, P. Fávero, P. Singh, A. A. Martin, *Vib. Spectrosc.*, 2019, **100**, 40-47.
[45] D. Bazin, M. Daudon, P. Chevallier, S. Rouzière, E. Elkaim, D. Thiaudière, B. Fayard, E. Foy, P. A. Albouy, G. André, G. Matzen, E. Véron, *Ann. Biol. Clin. (Paris)*, 2006, **64**, 125-139.
[46] D. Bazin, M. Daudon, *J. Phys. D: Appl. Phys.*, 2012, **45**, article no. 383001.
[47] M. Daudon, D. Bazin, *J. Phys.: Conf. Ser.*, 2013, **425**, article no. 022006.
[48] D. Bazin, M. Daudon, *Ann. Biol. Clin.*, 2015, **73**, 517-534.
[49] D. Bazin, E. Letavernier, J.-P. Haymann, *C. R. Chim.*, 2016, **19**, 1395-1403.
[50] E. Tsolaki, S. Bertazzo, *Materials*, 2019, **12**, article no. 3126.
[51] M. Li, J. Zhang, L. Wang, B. Wang, C. V. Putnis, *J. Phys. Chem.*, 2018, **B 122**, 1580-1587.
[52] Z. Xu, Z. He, Y. Song, X. Fu, M. Rommel, X. Luo, A. Hartmaier, J. Zhang, F. Fang, *Micromachines (Basel)*, 2018, **9**, article no. 361.
[53] R. S. Das, Y. K. Agrawal, *Vib. Spectrosc.*, 2011, **57**, 163-176.
[54] S. F. Parker, *Spectrochim. Acta A: Mol. Spectrosc.*, 1994, **50**, 1841-1856.
[55] T. H. Kauffmann, N. Kokanyan, M. Fontana, *J. Raman Spectrosc.*, 2019, **50**, 418-424.
[56] L. Miller, P. Dumas, *Biochim. Biophys. Acta*, 2006, **1758**, 846-857.
[57] R. Singh, *Phys. Perspect.*, 2002, **4**, 399-420.
[58] M. Daudon, D. Bazin, *C. R. Chim.*, 2016, **19**, 1416-1423.
[59] P. J. Caspers, G. W. Lucassen, G. J. Puppels, *J. Biophys.*, 2003, **85**, 572-580.
[60] K. U. Schallreuter, J. Moore, J. M. Wood, W. D. Beazley, D. C. Gaze, D. J. Tobin, H. S. Marshall, A. Panske, E. Panzig, N. A. Hibberts, *J. Investig. Dermatol. Symp. Proc.*, 1999, **4**, 91-96.
[61] J. N. Anker, W. P. Hall, O. Lyandres, N. C. Shah, J. Zhao, R. P. Van Duyne, *Nat. Mater.*, 2008, **7**, 442-453.
[62] J. Wohlrab, A. Vollmann, S. Wartewig, W. C. Marsch, R. Neubert, *Biopolymers*, 2001, **62**, 141-146.
[63] A. Nijssen, T. C. Bakker Schut, F. Heule, P. J. Caspers, D. P. Hayes, M. H. Neumann, G. J. Puppels, *J. Invest. Dermatol.*, 2002, **119**, 64-69.
[64] J. Schleusener, S. Guo, M. E. Darvin, G. Thiede, O. Chernavskaia, F. Knorr, J. Lademann, J. Popp, T. W. Bocklitz, *Biomed. Opt. Express*, 2021, **12**, 1123-1135.
[65] B. Pradere, I. Lucas, D. Abi Haidar, D. Bazin, S. Doizi, M. Daudon, O. Traxer, *Progr. Urol.*, 2017, **27**, 749-749.
[66] F. Bonnier, S. M. Ali, P. Knief, H. Lambkin, K. Flynn, V. McDonagh, C. Healy, T. C. Lee, F. M. Lyng, H. J. Byrn, *Vib. Spectrosc.*, 2012, **61**, 124-132.
[67] R. R. Jones, D. C. Hooper, L. Zhang, D. Wolverson, V. K. Valev, *Nanoscale Res. Lett.*, 2019, **14**, article no. 231.
[68] N. Quy Dao, M. Daudon, *Infrared and Raman Spectra of Calculi*, Elsevier, Paris, 1997.
[69] S. Yang, B. Li, M. N. Slipchenko, A. Akkus, N. G. Singer, Y. N. Yeni, O. Akkusa, *J. Raman Spectrosc.*, 2013, **44**, 1089-1095.
[70] H. Wang, D. W. Brandl, P. Nordlander, N. J. Halas, *Acc. Chem. Res.*, 2007, **40**, 53-62.
[71] Z. Q. Tian, B. Ren, J. F. Li, Z. L. Yang, *ChemComm.*, 2007, 3514-3534.
[72] C. Zheng, W. Shao, S. K. Paidi, B. Han, T. Fu, D. Wu, L. R. Bi, W. Q. Xu, Z. M. Fan, I. Barman, *Nanoscale*, 2015, **7**, 16960-16968.
[73] H. Zhang, B. Han, C. Zheng, Y. Du, L. Liang, W. Xu, Z. Fan, *Cancer Res.*, 2015, **75**, article no. P2-05-15.
[74] W. Xie, S. Schlücker, *Phys. Chem. Chem. Phys.*, 2013, **15**, 5329-5344.
[75] R. Weiss, M. Palatinszky, M. Wagner, R. Niessner, M. Elsner, M. Seidel, N. P. Ivleva, *Analyst*, 2019, **144**, 943-953.
[76] J. Krajczewski, A. Kudelski, *Front. Chem.*, 2019, **7**, article no. 410.
[77] R. M. Stöckle, Y. D. Suh, V. Deckert, R. Zenobi, *Chem. Phys. Lett.*, 2000, **3**, 131-136.
[78] M. S. Anderson, *Appl. Phys. Lett.*, 2000, **76**, 3130-3132.
[79] T. Deckert-Gaudig, V. Deckert, *Phys. Chem. Chem. Phys.*, 2010, **12**, 12040-12049.
[80] E. Abbe, *Arch. Mikroskop. Anat.*, 1873, **9**, 413-468.
[81] L. Rayleigh, *J. R. Microsc. Soc.*, 1903, **23**, 474-482.

[82] G. L. Carr, *Rev. Sci. Instrum.*, 2001, **72**, article no. 1613.
[83] S. Bonhommeau, S. Lecomte, *ChemPhysChem*, 2018, **19**, 8-18.
[84] R. Meyer, X. Yao, V. Deckert, *Trends Analyt. Chem.*, 2018, **102**, 250-258.
[85] G. Kolhatkar, J. Plathier, A. Ruediger, *J. Mater. Chem. C*, 2018, **6**, 1307-1319.
[86] N. Kumar, B. M. Weckhuysen, A. J. Wain, A. J. Pollard, *Nat. Protoc.*, 2019, **14**, 1169-1193.
[87] L. Gao, H. Zhao, T. Li, P. Huo, D. Chen, B. Liu, *Int. J. Mol. Sci.*, 2018, **19**, article no. 1193.
[88] K. Olschewski, E. Kammer, S. Stokel, T. Bocklitz, T. Deckert-Gaudig, R. Zell, D. Cialla-May, K. Weber, V. Deckert, J. Popp, *Nanoscale*, 2015, **7**, 4545-4552.
[89] L. Gao, H. Zhao, T. Li, P. Huo, D. Chen, B. Liu, *Int. J. Mol. Sci.*, 2018, **19**, 1193-1209.
[90] X. Wang, *Curr. Opin. Biotechnol.*, 2020, **64**, 218-229.
[91] Z. He, Z. Han, M. Kizer, R. J. Linhardt, X. Wang, A. M. Sinyukov, J. Wang, V. Deckert, A. V. Sokolov, J. Hu, M. O. Scully, *J. Am. Chem. Soc.*, 2019, **141**, 753-757.
[92] N. Kazemi-Zanjani, H. Chen, H. A. Goldberg, G. K. Hunter, B. Grohe, F. Lagugné-Labarthet, *J. Am. Chem. Soc.*, 2012, **134**, 17076-17082.
[93] X. Sheng, T. Jung, J. A. Wesson, M. D. Ward, *Proc. Natl. Acad. Sci. USA*, 2005, **102**, 267-272.
[94] R. Böhme, M. Mkandawire, U. Krause-Buchholz, P. Rösch, G. Rödel, J. Popp, V. Deckert, *ChemComm.*, 2011, **47**, 11453-11455.
[95] S. K. Sahoo, S. Umapathy, A. W. Parker, *Appl. Spectrosc.*, 2011, **65**, 1087-1115.
[96] P. Pagsberg, R. Wilbrandt, K. B. Hansen, K. V. Weisberg, *Chem. Phys. Lett.*, 1976, **39**, 538-541.
[97] N. L. Gruenke, M. F. Cardinal, M. O. McAnally, R. R. Frontiera, G. C. Schatza, R. P. Van Duyne, *Chem. Soc. Rev.*, 2016, **45**, 2263-2290.
[98] P. Matousek, L. P. Clark, E. R. C. Draper, M. D. Morris, A. E. Goodship, N. Everall, M. Towrie, W. F. Finney, A. W. Parker, *Appl. Spectrosc.*, 2005, **59**, 393-400.
[99] F. Nicolson, M. F. Kircher, N. Stone, P. Matousek, *Chem. Soc. Rev.*, 2021, **50**, 556-568.
[100] E. Cordero, I. Latka, C. Matthäus, I. W. Schie, J. Popp, *J. Biomed. Opt.*, 2018, **23**, article no. 071210.
[101] E. Garai, S. Sensarn, C. L. Zavaleta, N. O. Loewke, S. Rogalla, M. J. Mandella, S. A. Felt, S. Friedland, J. T. C. Liu, S. S. Gambhir, C. H. Contag, *PLoS One*, 2015, **10**, article no. e0123185.
[102] L. Iacoviello, M. Bonaccio, G. de Gaetano, M. B. Donati, *Semin. Cancer Biol.*, 2021, **72**, 4-10.
[103] T. Oyama, T. Sano, T. Hikino, Q. Xue, K. Iijima, T. Nakajima, F. Koerner, *Virchows Arch.*, 2002, **440**, 267-273.
[104] K. E. Shafer-Peltier, A. S. Haka, M. Fitzmaurice, J. Crowe, J. Myles, R. R. Dasari, M. S. Feld, *J. Raman Spectrosc.*, 2002, **33**, 552-563.
[105] D. Bazin, C. Leroy, F. Tielens, C. Bonhomme, L. Bonhomme-Coury, F. Damay, D. Le Denmat, J. Sadoine, J. Rode, V. Frochot, E. Letavernier, J.-P. Haymann, M. Daudon, *C. R. Chim.*, 2016, **19**, 1492-1503.
[106] A. Ben Lakhdar, M. Daudon, M.-C. Mathieu, A. Kellum, C. Balleyguier, D. Bazin, *C. R. Chim.*, 2016, **19**, 1610-1624.
[107] R. Scott, C. Kendall, N. Stone, K. Rogers, *Sci. Rep.*, 2017, **7**, article no. 136.
[108] R. Vanna, C. Morasso, B. Marcinnò, F. Piccotti, E. Torti, D. Altamura, S. Albasini, M. Agozzino, L. Villani, L. Sorrentino, O. Bunk, F. Leporati, C. Giannini, F. Corsi, *Cancer Res.*, 2020, **80**, 1762-1772.
[109] J. A. M. R. Kunitake, S. Choi, K. X. Nguyen, M. M. Lee, F. He, D. Sudilovsky, P. G. Morris, M. S. Jochelson, C. A. Hudis, D. A. Muller, P. Fratzl, C. Fischbach, A. Masic, L. A. Estroff, *J. Struct. Biol.*, 2018, **202**, 25-34.
[110] R. Scott, N. Stone, C. Kendall, K. Geraki, K. Rogers, *NPJ Breast Cancer*, 2016, **2**, article no. 16029.
[111] E. Tsolaki, W. Doran, J. Overbeck, L. Magnani, A. Olivo, I. K. Herrmann, S. Bertazzo, bioRxiv, 2021.
[112] R. Sathyavathi, A. Saha, J. S. Soares, N. Spegazzini, S. McGee, R. R. Dasari, M. Fitzmaurice, I. Barman, *Sci. Rep.*, 2015, **5**, article no. 9907.
[113] R. Baker, K. D. Rogers, N. Shepherd, N. Stone, *Br. J. Cancer*, 2010, **103**, 1034-1039.
[114] M. Daudon, M. F. Protat, R. J. Reveillaud, H. Jaeschke-Boyer, *Kidney Int.*, 1983, **23**, 842-850.
[115] C. G. Kontoyannis, N. C. Bouropoulos, P. G. Koutsoukos, *Appl. Spectrosc.*, 1997, **51**, 64-67.
[116] P. Carmona, J. Bellanato, E. Escolar, *Biospectroscopy*, 1997, **3**, 331-346.
[117] C. Paluszkiewicz, M. Gałka, W. Kwiatek, A. Parczewski, S. Walas, *Biospectroscopy*, 1997, **3**, 403-407.
[118] K. Safaa, H. Khalil, A. A. Mohamead, *J. Appl. Sci. Res.*, 2007, **5**, 387-391.
[119] T. N. Moroz, N. A. Palchik, A. V. Dar'in, *Nucl. Instrum. Methods Phys. Res.*, 2009, **A 603**, 141-145.
[120] J. R. Guerra-López, J. A. Güida, C. O. DellaVédova, *Urol. Res.*, 2010, **38**, 383-390.
[121] R. Selvaraju, A. Raja, G. Thiruppathi, *Spectrochim. Acta A*, 2013, **114**, 650-657.
[122] J. Tonannavar, G. Deshpande, J. Yenagi, S. B. Patil, N. A. Patil, B. G. Mulimani, *Spectrochim. Acta A*, 2016, **154**, 20-26.
[123] C. Conti, M. Casati, C. Colombo, M. Realini, L. Brambilla, G. Zerbi, *Spectrochim. Acta A*, 2014, **128**, 413-419.
[124] C. C. Chang, Y. Chiu, *Urol. Sci.*, 2017, **28**, 19-22.
[125] V. Castiglione, P.-Y. Sacré, E. Cavalier, P. Hubert, R. Gadisseur, E. Ziemons, *PLoS One*, 2018, **13**, article no. e0201460.
[126] X. Cui, Z. Zhao, G. Zhang, S. Chen, Y. Zhao, J. Lu, *Biomed. Opt. Express*, 2018, **9**, 4175-4183.
[127] P.-A. Lo, Y.-H. Huang, Y.-C. Chiu, L.-C. Huang, J.-L. Bai, S.-H. Wu, C.-C. Huang, H. K. Chiang, *Raman Spectrosc.*, 2019, **50**, 34-40.
[128] S. Z. Fairchild, C. F. Bradshaw, W. Su, S. K. Guharay, *Appl. Spectrosc.*, 2009, **63**, 733-741.
[129] I. Petit, G. D. Belletti, T. Debroise, M. J. Llansola-Portoles, I. T. Lucas, C. Leroy, C. Bonhomme, L. Bonhomme-Coury, D. Bazin, M. Daudon, E. Letavernier, J. P. Haymann, V. Frochot, F. Babonneau, P. Quaino, F. Tielens, *ChemistrySelect*, 2018, **3**, 8801-8812.
[130] M. Daudon, C. A. Bader, P. Jungers, *Scanning Microsc.*, 1993, **7**, 1081-1104.
[131] M. Daudon, *Arch. Pédiatr.*, 2000, **7**, 855-865.
[132] M. Daudon, V. Frochot, D. Bazin, P. Jungers, *C. R. Chim.*, 2016, **19**, 1514-1526.

[133] M. Daudon, P. Jungers, D. Bazin, J. C. Williams Jr, *Urolithiasis*, 2018, **46**, 459-470.
[134] M. Daudon, P. Jungers, D. Bazin, *New Engl. J. Med.*, 2008, **359**, 100-102.
[135] M. Daudon, D. Bazin, G. André, P. Jungers, A. Cousson, P. Chevallier, E. Véron, G. Matzen, *J. Appl. Crystallogr.*, 2009, **42**, 109-115.
[136] W. R. Lloyd, S. Agarwal, S. U. Nigwekar, K. Esmonde-White, S. Loder, S. Fagan, J. Goverman, B. R. Olsen, D. Jumlongras, M. D. Morris, B. Levi, *J. Biomed. Opt.*, 2015, **20**, article no. 080501.
[137] Y. Liu, Z. Du, J. Zhang, H. Jiang, *Oncotarget*, 2017, **8**, 36012-36019.
[138] V. Vuiblet, M. Fere, E. Bankole, A. Wynckel, C. Gobinet, P. Birembaut, O. Piot, P. Rieu, *Sci. Rep.*, 2016, **6**, article no. 33045.
[139] D. Bazin, C. Jouanneau, S. Bertazzo, C. Sandt, A. Dessombz, M. Réfrégiers, P. Dumas, J. Frederick, J.-P. Haymann, E. Letavernier, P. Ronco, M. Daudon, *C. R. Chim.*, 2016, **19**, 1439-1450.
[140] S. Zheng, A. T. Tu, *Appl. Spectrosc.*, 1986, **40**, 1099-1103.
[141] A. Iordanidis, J. Garcia-Guinea, C. Giousef, A. Angelopoulos, M. Doulgerakis, L. Papadopoulou, *Spectrosc. Lett.*, 2013, **46**, 301-306.
[142] M. D. Stringer, R. D. Soloway, D. R. Taylor, K. Riyad, G. Toogood, *J. Pediatr. Surg.*, 2007, **42**, 1677-1682.
[143] H. S. Kaufman, T. H. Magnuson, H. A. Pitt, P. Frasca, K. D. Lillemoe, *Hepatology*, 1994, **19**, 1124-1132.
[144] I. A. Bouchier, *Keio J. Med.*, 1992, **41**, 1-5.
[145] T. Maki, T. Matsushiro, N. Suzuki, *Am. J. Surg.*, 1982, **144**, 302-305.
[146] F. Cetta, *Ann. Surg.*, 1991, **213**, 315-326.
[147] L. Vitetta, S. P. Best, A. Sali, *Med. Hypotheses*, 2000, **55**, 502-506.
[148] M. Tabata, F. Nakayama, *Prog. Clin. Biol. Res.*, 1984, **152**, 163-174.
[149] P. Hazrah, K. T. H. Oahn, M. Tewari, A. K. Pandey, K. Kumar, T. M. Mohapatra, H. S. Shukla, *HPB (Oxford)*, 2004, **6**, 28-32.
[150] J. S. Hyun, *World J. Men's Health*, 2018, **36**, 15-21.
[151] K. S. Sfanos, B. A. Wilson, A. M. De Marzo, W. B. Isaacs, *Proc. Natl. Acad. Sci. USA*, 2009, **106**, 3443-3448.
[152] A. Dessombz, P. Méria, D. Bazin, E. Foy, S. Rouzière, R. Weil, M. Daudon, *Prog. Urol.*, 2011, **21**, 940-945.
[153] A. Dessombz, P. Méria, D. Bazin, M. Daudon, *PLoS One*, 2012, **7**, article no. e51691.
[154] T. H. S. Hsu, S.-Y. Lin, *Biomed. Spectrosc. Imaging*, 2014, **3**, 161-178.
[155] C. G. Kontoyannis, N. Bouropoulos, N. Bouropoulos, H. H. Dauaher, N. V. Vagenas, *Appl. Spectrosc.*, 2000, **54**, 225-229.
[156] P. Crow, N. Stone, C. A. Kendall, J. S. Uff, J. A. M. Farmer, H. Barr, M. P. J. Wright, *Br. J. Cancer*, 2003, **89**, 106-108.
[157] S. Devpura, J. S. Thakur, F. H. Sarkar, W. A. Sakr, V. M. Naik, R. Naika, *Vib. Spectrosc.*, 2010, **53**, 227-232.
[158] F. L. Magalhães, A. M. C. Machado, E. Paulino, S. K. Sahoo, A. M. de Paula, A. M. Garcia, I. Barman, J. S. Soares, M. Mamede, *J. Biomed. Opt.*, 2018, **23**, article no. 121613.
[159] K. Aubertin, J. Desroches, M. Jermyn, V. Q. Trinh, F. Saad, D. Trudel, F. Leblond, *Biomed. Opt. Express*, 2018, **9**, 4294-4305.
[160] A.-A. Grosset, F. Dallaire, T. Nguyen, M. Birlea, J. Wong, F. Daoust, N. Roy, A. Kougioumoutzakis, F. Azzi, K. Aubertin, S. Kadoury, M. Latour, R. Albadine, S. Prendeville, P. Boutros, M. Fraser, R. G. Bristow, T. van der Kwast, M. Orain, H. Brisson, N. Benzerdjeb, H. Hovington, A. Bergeron, Y. Fradet, B. Têtu, F. Saad, F. Leblond, D. Trudel, *PLoS Med.*, 2001, **17**, article no. e1003281.
[161] N. Chen, M. Rong, X. Shao, H. Zhang, S. Liu, B. Dong, W. Xue, T. Wang, T. Li, J. Pan, *Int. J. Nanomedicine*, 2017, **12**, 5399-5407.
[162] E. Brauchle, S. Noor, E. Holtorf, C. Garbe, K. Schenke-Layland, C. Busch, *Clin. Exp. Dermatol.*, 2014, **39**, 636-645.
[163] S. Laing, S. Bielfeldt, K.-P. Wilhelm, J. Obst, *Skin Res. Technol.*, 2019, **25**, 578-586.
[164] N. Jung, B. Vukosavljevic, M. Windbergs, "Raman spectroscopy in skin research and dermal drug delivery", in *Confocal Raman Microscopy* (J. Toporski, T. Dieing, O. Hollricher, eds.), Springer Series in Surface Sciences, vol. 66, Springer, Cham, Switzerland, 2018, 421-448.
[165] A. Sharma, S. Sharma, A. Zarrow, R. A. Schwartz, W. C. Lambert, *Indian J. Dermatol.*, 2016, **61**, 1-8.
[166] G. Pezzotti, M. Boffelli, D. Miyamori, T. Uemura, Y. Marunaka, W. Zhu, H. Ikegaya, *J. Biomed. Opt.*, 2015, **20**, article no. 065008.
[167] I. P. Santos, P. J. Caspers, T. C. Bakker Schut, R. van Doorn, V. NoordhoekHegt, S. Koljenović, G. J. Puppels, *Anal. Chem.*, 2016, **88**, 7683-7688.
[168] B. J. Yakes, T. J. Michael, M. Perez-Gonzalez, B. P. Harp, *J. Raman Spectrosc.*, 2017, **48**, 736-743.
[169] M. E. Darvin, J. Schleusener, F. Parenz, O. Seidel, C. Krafft, J. Popp, J. Lademann, *Analyst*, 2018, **143**, 4990-4999.
[170] K. H. Carlsen, M. Køcks, M. Sepehri, *J. Serup Skin Res. Technol.*, 2016, **22**, 460-469.
[171] H. Colboc, D. Bazin, P. Moguelet, S. Reguer, R. Amode, C. Jouanneau, I. Lucas, L. Deschamps, V. Descamps, N. Kluger, *J. Eur. Acad. Dermatol. Venereol.*, 2020, **34**, article no. e313.
[172] B. L. Parra, D. D. Venable, E. Gonzalez, J. A. Eastham, *Urology*, 1996, **48**, 797-799.
[173] N. J. van Casteren, L. H. J. Looijenga, G. R. Dohle, *Int. J. Androl.*, 2009, **32**, 279-287.
[174] G. C. Parenti, U. De Giorgi, E. Gaddoni, V. Conteduca, S. Zago, P. Campioni, M. Giganti, F. Albarell, *Andrology*, 2014, **3**, article no. 1000115.
[175] A. C. Peterson, J. M. Bauman, D. E. Light, L. P. McMann, R. A. Costbile, *J. Urol.*, 2001, **166**, 2061-2064.
[176] A. A. Renshaw, *J. Urol.*, 1998, **160**, 1625-1628.
[177] G. D. Smith, I. Steele, R. B. Barnes, L. A. Levine, *Fertil. Steril.*, 1999, **72**, 467-471.
[178] B. W. D. De Jong, C. A. De Gouveia Brazao, H. Stoop, K. P. Wolffenbuttel, J. W. Oosterhuis, G. J. Puppels, R. F. A. Weber, L. H. J. Looijenga, D. J. Kok, *Urology*, 2004, **171**, 92-96.
[179] P. Song, Z. Fang, H. Wang, Y. Cai, K. Rahimi, Y. Zhu, F. G. R. Fowkes, F. J. I. Fowkes, I. Rudan, *Lancet Glob. Health*, 2020, **8**, article no. e721.
[180] Y. M. Hong, *Korean Circ. J.*, 2010, **40**, 1-9.
[181] G. V. Nogueira, L. Silveira, A. A. Martin, R. A. Zângaro, M. T. T. Pacheco, M. C. Chavantes, C. A. Pasqualucci, *J. Biomed. Opt. Raman Spectrosc.*, 2005, **10**, article no. 031117.

[182] R. Rocha, L. Silveira Jr, A. B. Villaverde, C. A. Pasqualucci, M. S. Costa, A. Brugnera Jr, M. T. Pacheco, *Photomed. Laser Surg.*, 2007, **25**, 482-486.

[183] M. B. Peres, L. Silveira Jr, R. A. Zângaro, M. T. Pacheco, C. A. Pasqualucci, *Lasers Med. Sci.*, 2011, **26**, 645-655.

[184] C.-H. Liu, S. Boydston-White, A. Weisberg, W. Wang, L. A. Sordillo, A. Perotte, V. P. Tomaselli, P. P. Sordillo, Z. Pei, L. Shi, R. R. Alfano, *J. Biomed. Opt.*, 2016, **21**, article no. 127006.

[185] H. P. Buschmann, J. T. Motz, G. Deinum, T. J. Romer, M. Fitzmaurice, J. R. Kramer, A. Van der Larrse, A. V. Bruschke, M. S. Feld, *Cardiovasc. Pathol.*, 2001, **10**, 59-68.

[186] A. Y. F. You, M. S. Bergholt, J.-P. St-Pierre, W. Kit-Anan, I. J. Pence, A. H. Chester, M. H. Yacoub, S. Bertazzo, M. M. Stevens, *Sci. Adv.*, 2017, **3**, article no. e1701156.

[187] P. Lanzer, M. Boehm, V. Sorribas, M. Thiriet, J. Janzen, T. Zeller, C. St. Hilaire, C. Shanahan, *Eur. Heart J.*, 2014, **35**, 1515-1525.

[188] R. Z. LeGeros, *Z. Kardiol.*, 2001, **90**, 116-124.

[189] S. Agarwal, S. Bertazzo, *C. R. Chim.*, 2016, **19**, 1605-1609.

[190] S. Sarig, T. A. Weiss, I. Katz, F. Kahana, R. Azoury, E. Okon, H. S. Kruth, *Lab. Invest.*, 1994, **71**, 782-787.

[191] M. D. Morris, A. Carden, R. M. Rajachar, D. H. Kohn, *Proc. SPIE*, 2002, **4614**, 47-54.

[192] G. Penel, G. Leroy, C. Rey, C. Bres, *Calcif. Tissue Int.*, 1998, **63**, 475-481.

[193] Y. Nishizawa, C. Higuchi, T. Nakaoka, H. Omori, T. Ogawa, H. Sakura, K. Nitta, *Ther. Apher. Dial.*, 2018, **22**, 365-370.

[194] J. S. Lee, J. D. Morrisett, C.-H. Tung, *Atherosclerosis*, 2012, **224**, 340-347.

[195] R. Coscas, M. Bensussan, M.-P. Jacob, L. Louedec, Z. Massy, J. Sadoine, M. Daudon, C. Chaussain, D. Bazin, J.-B. Michel, *Atherosclerosis*, 2017, **259**, 60-67.

[196] P. Dorfmüller, D. Bazin, S. Aubert, R. Weil, F. Brisset, M. Daudon, F. Capron, I. Brochériou, *Cardiol. Res. Pract.*, 2010, article no. 685926.

[197] M. B. Albro, M. S. Bergholt, J. P. St-Pierre, A. VinalsGuitart, H. M. Zlotnick, E. G. Evita, M. M. Stevens, *NPJ Regen. Med.*, 2018, **3**, article no. 3.

[198] M. S. Bergholt, J.-P. St-Pierre, G. S. Offeddu, P. A. Parmar, M. B. Albro, J. L. Puetzer, M. L. Oyen, M. M. Stevens, *ACS Cent. Sci.*, 2016, **2**, 885-895.

[199] M. Fields, N. Spencer, J. Dudhia, P. F. McMillan, *Biopolymers*, 2017, **107**, article no. e23017.

[200] R. Shaikh, E. Nippolainen, V. Virtanen, J. Torniainen, L. Rieppo, S. Saarakkala, I. O. Afara, J. Töyräs, *J. Raman Spectrosc.*, 2021, 1-9.

Comptes Rendus
Chimie
2022, Vol. 25, Special Issue S1, p. 105-131
https://doi.org/10.5802/crchim.196

Microcrystalline pathologies: Clinical issues and nanochemistry / *Pathologies microcristallines : questions cliniques et nanochimie*

Using mid infrared to perform investigations beyond the diffraction limits of microcristalline pathologies: advantages and limitation of Optical PhotoThermal IR spectroscopy

Dominique Bazin[*, a, b], **Elise Bouderlique**[c, d], **Ellie Tang**[c, d], **Michel Daudon**[c, d, e], **Jean-Philippe Haymann**[c, d, e], **Vincent Frochot**[c, d, e], **Emmanuel Letavernier**[c, d, e], **Els Van de Perre**[f], **James C. Williams Jr.**[g], **James E. Lingeman**[h] **and Ferenc Borondics**[i]

[a] Institut de Chimie Physique, UMR CNRS 8000, Bâtiment 350, Université Paris Saclay, 91405 Orsay cedex, France

[b] Laboratoire de Physique des Solides, UMR CNRS 8502, Bâtiment 510, Université Paris-Sud, 91405 Orsay cedex, France

[c] Sorbonne Universités, UPMC Univ Paris 06, UMR S 702, Paris, France

[d] INSERM, UMR S 1155, Paris, France

[e] Explorations fonctionnelles multidisciplinaires, AP-HP, Hôpital Tenon, Paris, France

[f] Vrije Universiteit Brussel (VUB), Universitair Ziekenhuis Brussel (UZ Brussel), Nephrology Department, Brussels, Belgium

[g] Department of Anatomy, Cell Biology & Physiology, Indiana University School of Medicine, Indianapolis, Indiana, USA

[h] Department of Urology, Indiana University School of Medicine, Indianapolis, Indiana, USA

[i] Synchrotron SOLEIL, L'Orme des Merisiers, Saint-Aubin, BP 48, 91192 Gif-sur-Yvette, France

E-mails: dominique.bazin@universite-paris-saclay.fr (D. Bazin), elise.bouderlique@inserm.fr (E. Bouderlique), Ellieyali.tang@hotmail.com (E. Tang), daudonmichel24@gmail.com (M. Daudon), Jean-philippe.haymann@aphp.fr (J.-P. Haymann), vincent.frochot@aphp.fr (V. Frochot), emmanuel.letavernier@aphp.fr (E. Letavernier), Els.VandePerre@uzbrussel.be (E. Van de Perre), jwillia3@iu.edu (J. C. Williams, Jr.), JLingeman@IUHealth.org (J. E. Lingeman), ferenc.borondics@synchrotron-soleil.fr (F. Borondics)

[*] Corresponding author.

Abstract. Understanding the physico-chemistry related to cristalline pathologies constitutes a challenge in several medical specialities such as nephrology, dermatology or oncology. Regarding nephrology, the chemical diversity of concretions such as kidney stones calls for characterization techniques to determine the chemical composition of concretions. The starting point of this contribution is given by Fourier Transform InfraRed (FTIR) spectroscopy which is routinely used at the hospital to determine the chemical composition of kidney stones as well as ectopic calcifications present in kidney biopsy. For kidney stones, the quantity of sample is sufficient to perform a significant analysis through classical FTIR. For ectopic calcifications, μFTIR can be inefficient in the case of μcalcification in the tissue when their size is less than 10 μm. For such samples, Optical PhotoThermal IR (OPT-IR) spectroscopy may constitute a way to overcome this experimental difficulty through the acquisition of IR spectrum with a spatial resolution close to 500 nm.

To illustrate such opportunity, we first compare the IR spectrum acquired with a classical experimental set-up related to classical IR spectroscopy to IR spectrum collected with a OPT-IR one for different compounds namely calcium oxalate monohydrate, calcium oxalate dehydrate, calcium phosphate apatite and magnesium ammonium phosphate hexahydrate. Such comparison helps us to assess specificity of OPT-IR. Then, we consider several pathological calcifications associated to hyperoxaluria, adenine phosphoribosyltransferase (APRT) deficiency or the presence of Randall's plaque. We will see that the nanometer spatial resolution constitutes a major advantage versus a micrometre one. Also, in the case of Randall's plaque, we show that OPT-IR can determine the chemical composition of microscopic concretion without any kind of preparation. Such experimental fact is clearly a major advantage. Finally, we also extended this first investigation in nephrology by considering breast calcifications. In that case, if the number of chemical phases is quite low compared to the number of chemical phases identified in ectopic calcifications present in kidney (four instead of 24), the challenge is related to the possibility to distinguish between the different calcium phosphate namely amorphous carbonated calcium phosphate, CA and whitlockite.

The complete set of data indicates the limitations and the advantages of OPT-IR spectroscopy.

Keywords. PhotoThermal IR spectroscopy, Pathological calcifications, Randall's plaque, Kidney stones, Breast calcifications, Kidney biopsy.

Published online: 27 July 2022, Issue date: 1 September 2022

1. Introduction

An analysis of the medical literature indicates clearly an ubiquity of microcrystalline pathologies [1–7] in human which encompass several major diseases such as cancer [8–10], cardiovascular [11–13], infection [14–19] as well as genetic [20–26] disorders. It should be kept in mind that abnormal deposits in human tissues may have endogenous as well as exogenous origin [27–29].

Among the different microcristalline pathologies [1–7], urolithiasis is probably the most popular. Epidemiological surveys of urolithiasis have shown that in economically developed countries the prevalence rate ranged between 4% and 20% [30–33]. As noticed by Trinchieri [34], in the latter part of the 20th century prevalence and incidence of upper urinary tract stones were still increasing in Western countries probably resulting from improvements in clinical-diagnostic procedures and changes in nutritional and environmental factors.

In the service des explorations fonctionnelles of the Tenon hospital, 3000 kidney stones are analyzed each year following the morpho-constitutional stone analysis described four decades ago [35–41]. In short, the standardized protocol comprises two steps:

- First, a stereomicroscope (magnification ×10–40) is used to examine the surface and section of the calculus, with the identification of the nucleus (or core) and to observe the inner organization. For each stone, the size, the form, the color, the aspect (smooth, rough or spiky) of the surface, the presence of a papillary imprint (umbilication), the presence of Randall's plaque, the aspect of the section (well organized with concentric layers and/or radiating organization, or poorly organized and loose structure) and location and aspect of the nucleus is considered.
- Second, an analysis is performed by Fourier Transform InfraRed (FTIR) [42–45] of a sample of each part of the calculus (nucleus, mid-section and surface), whenever allowed by the size of the stone, and in all cases, the determination of the global proportion of com-

ponents in a powdered sample of the whole stone [46–49].

Such physicochemical information leads to a medical diagnosis for the clinician. For kidney stones, the amount of samples is sufficient to perform classical FTIR experiments. Also, other parameters have to be considered such as the price of the apparatus as well as the facility to handle experiments. All these points lead to the fact that for kidney stones, it is not necessary to use micro and nano IR spectroscopies.

The challenge lies in the identification of chemical compounds present in pathological microcrystalline deposits (PMCD). It is of clinical importance to accurately identify crystals found in the tissue as soon as possible. Figure 1 presents a typical set of data which can be obtained through classical μFTIR spectroscopy. Here, FTIR hyperspectral images were recorded with a Spectrum Spotlight 400 FTIR imaging system (Perkin Elmer Life Sciences, France), with a spectral resolution of 8 cm^{-1}. Each spectral image, covering the biopsy, consisted of about 30,000 spectra. A precise identification of PMCD is straightforward through the position of characteristic IR absorption bands.

The two primary features due to proteins (Figure 1c), are the amide I (1600–1700 cm^{-1}) and amide II (1500–1560 cm^{-1}) bands, which arise primarily from the C–O and C–N stretching vibrations of the peptide bond, respectively [14]. Apart from these contributions, IR absorption bands of calcium oxalate monohydrate (COM) positioned at 780 cm^{-1} (black arrow in Figure 1c) or at 1314 cm^{-1} (red arrow in Figure 1c) may be selected to obtain the spatial distribution of COM crystallites within the biopsy.

One drawback is that IR spectroscopy needs a data bank in which spectra of chemical compounds are gathered to compare them to the IR spectra collected from the sample [50]. In the case of the presence of a chemical compound with unknown crystallographic structure in the chemical composition of an abnormal deposit, X-ray scattering constitutes a more valuable technique [51–53].

In most clinical cases, μFTIR spectroscopy is able to characterize microcristals present in kidney biopsies [49,54]. Such measurements are also performed at Tenon hospital. Let's just recall that at the Tenon Hospital, more than 85,000 kidney stones have been analysed by FTIR spectroscopy, as well as more than 2000 biological tissues, including more than 1600 kidney biopsies [4,54,55].

Unfortunately, one limitation of μFTIR lies in its lateral spatial resolution. The diffraction of the long mid-IR wavelengths (2.5 μm–25 μm) limits the lateral resolution of IR microscopy to several micrometers [56,57]. More precisely, this lateral resolution R_L is given by the relationship:

$$R_L = 0.61\lambda / n\mathrm{NA}$$

where λ is the wavelength, n is the index of refraction of the surrounding media (1 for air), and NA is the numerical aperture of the microscope objective. The most commonly used microscope focusing element is a reflective Cassegrain objective, which is commercially available and features numerical apertures (NA) up to ~0.7 [58]. The above formula indicates that the lateral resolution varies along the IR spectrum from 25 μm (at 400 cm^{-1}) to 2.5 μm (at 4000 cm^{-1}). Even if the lateral resolution can be improved by a factor of four by using germanium attenuated total reflection objectives it is insufficient to reach the nanoscale range [59,60].

Using mid IR as a diagnostic tool at the hospital [35–41] or to assess more deeply the biochemical parameters responsible to the genesis of PMCD [6] led us to consider techniques able to characterize nanometer scale PMCD. For the clinician, an early characterization of a disease is a key factor to efficiently treat the patient with specific drugs [19,20].

At least two possibilities exist to perform IR spectroscopy beyond the diffraction limit i.e., to bridge the resolving power gap between the micrometer and nanometer ranges. The first one is a combination of atomic force microscopes (AFM) and IR spectroscopy (AFM-IR) [61,62]. The second one is the Optical PhotoThermal IR (OPT-IR) spectroscopy [63]. The first one has been already applied in the case of abnormal deposit of a widely prescribed antibiotic, vancomycin [64], in kidney tissue [65]. The complete set of experiments including μFTIR as well as AFM-IR spectroscopies has given valuable information regarding the exact nature of vancomycin-associated nephrotoxicity [64–66] and of PMCD in the case of cystinosis [25].

In this contribution, we assess the advantages and limitations of OPT-IR spectroscopy for chemical investigation of PMCD in different kinds of human

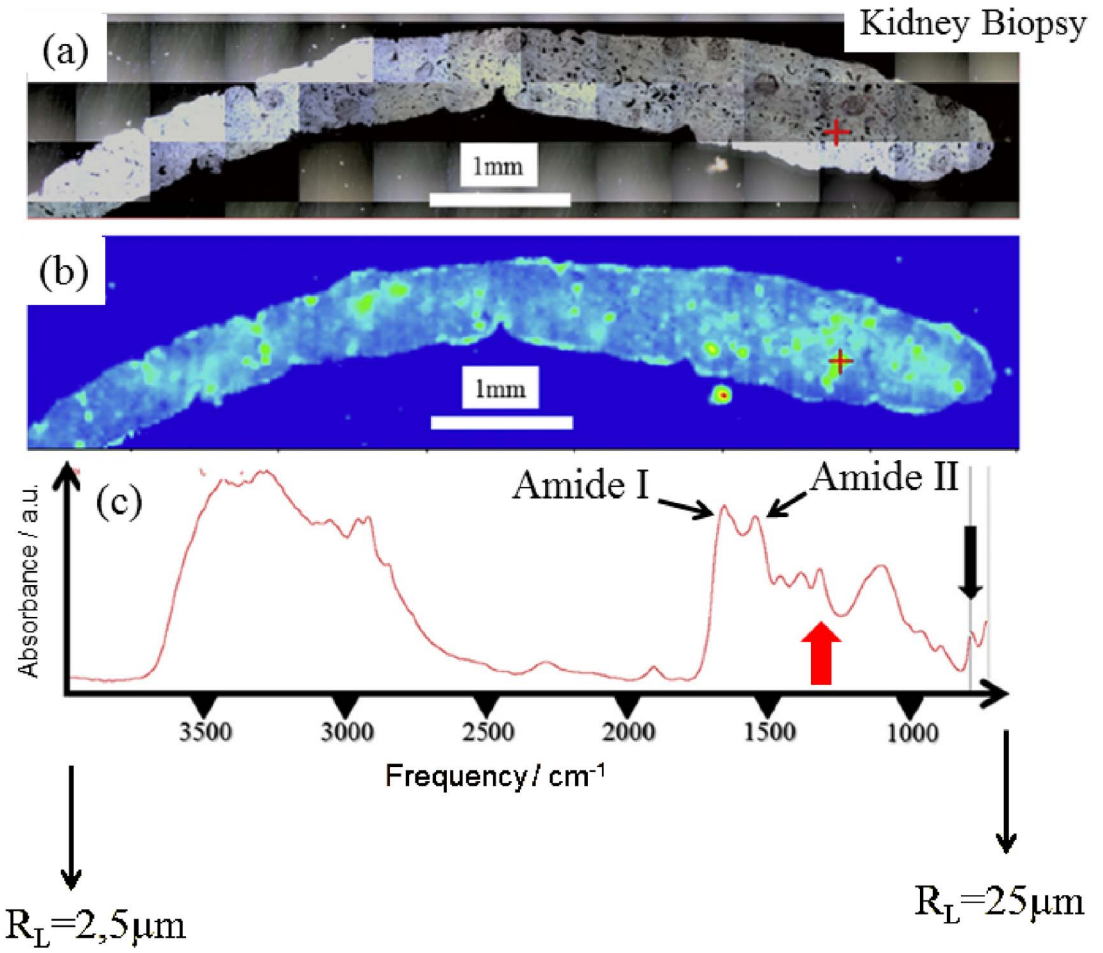

Figure 1. Biopsy from a graft kidney in a patient suffering from primary hyperoxaluria (B274). (a) Optical photography, and (b) spatial distribution of calcium oxalate monohydrate (COM) deposits in the biopsy as given by the intensity of the infrared spectrum (c) at 780 cm^{-1}. The red cross in (b) represents the biopsy point analyzed in (c) by µFTIR. We have indicated the lateral resolution (R_L) at the beginning and the end of the IR spectrum.

tissues, mostly in kidney and also in breast. In the case of kidney biopsies, we used kidney stones as reference compounds. In the case on breast biopsies, we show that other organs can be considered and that for breast tissues we assess the discrimination through OPT-IR experiments between different calcium phosphate namely amorphous carbonated calcium phosphate (ACCP), calcium phosphate apatite (CA) and whitlockite (Wk) which constitutes a key point for medical diagnostic. The ultimate goal is to evaluate if OPT-IR offers a better balance between chemical specificity and spatial resolution than µFTIR [56,57], Raman [67–69] for the identification of nanoPMCD.

2. Methods

The very first photothermal deflection experiments were published three and four decades ago [63, 70]. Basically, such an experiment is based on a pump-probe architecture using two laser sources, one for mid-infrared excitation (the pump) and the other one for measuring the photothermal effect (the probe). These two lasers are collinearly combined by a dichroic mirror. Such architecture is associated

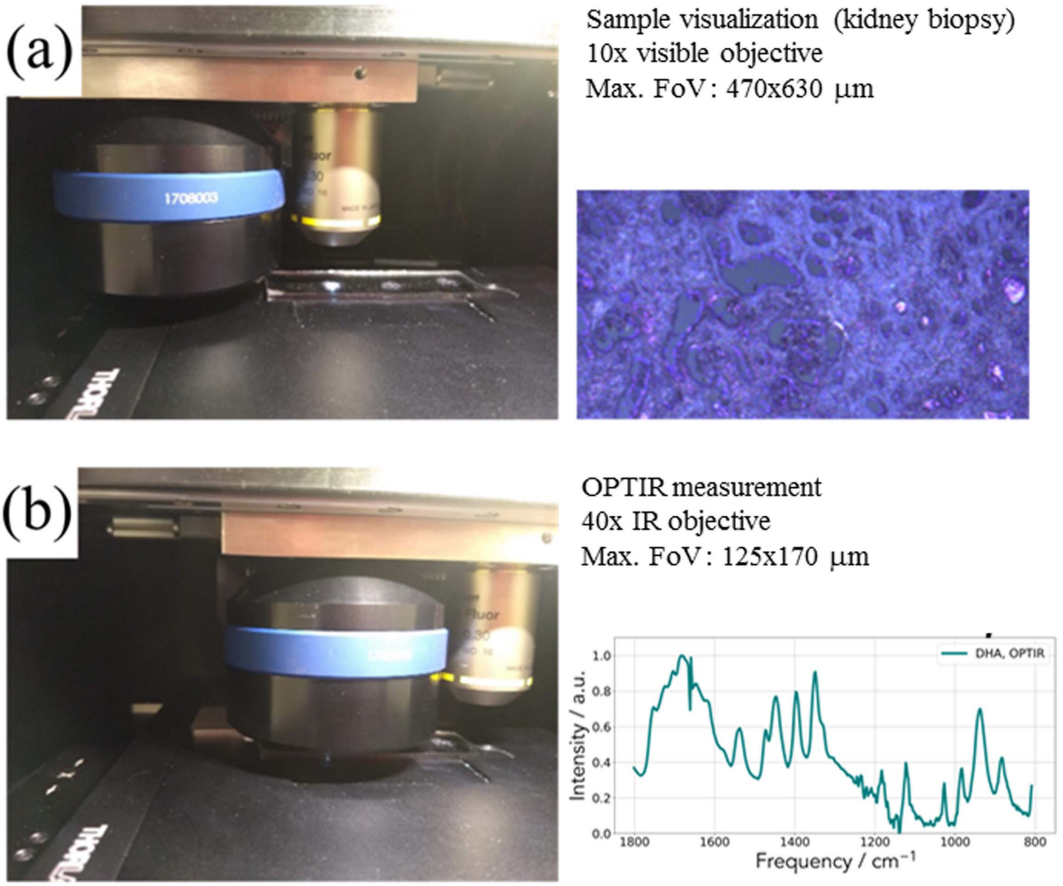

Figure 2. Experimental set up used for the characterization of pathological deposits. (a) Sample visualization with an optical microscope. (b) Schwarzschild objective for the acquisition of the IR spectrum.

with a better spatial resolution through a (visible) optical probe beam that can be focused much smaller than the IR beam. While, as previously mentioned, the lateral resolution of IR microscopy is equal to several micrometers, the lateral resolution of an OPT-IR microscope is around with 500 nm [71].

Another major advantage is that an OPT-IR microscope is a non-contact technique. It offers thus the opportunity to investigate thick samples (even several centimeters) i.e., surfaces without the contact limitations of an ATR (attenuated total reflection) device. This is of primary importance because the presence of pathological deposits in tissue constitutes a significant difficulty to obtain very thin samples. In this contribution, we have made the choice to collect OPT-IR on samples which have been previously studied by µFTIR and Field emission Scanning Electron Microscopy coupled with energy-dispersive X-ray analysis (FE-SEM-EDX) [72]. We have already shown that the possibility to perform different experiments on the same sample led to more significant information for the clinician [54,73,74]. Note that regarding the samples, ethical approval was obtained by the ethical committee of Tenon Hospital for this study. Each sample was only named by a study number, without indication of the name of the patient or potential identification data.

In the case of our experiments (Figure 2), OPT-IR measurements (spectra and images) were acquired on the mIRage™ Infrared Microscope (Photothermal Spectroscopy Corp., Santa Barbara, CA, USA). Spectra were performed in reflection mode, 2 cm^{-1} spectral data point spacing, through a 40×, 0.78 NA, 8 mm working distance Schwarzschild objective. The pump

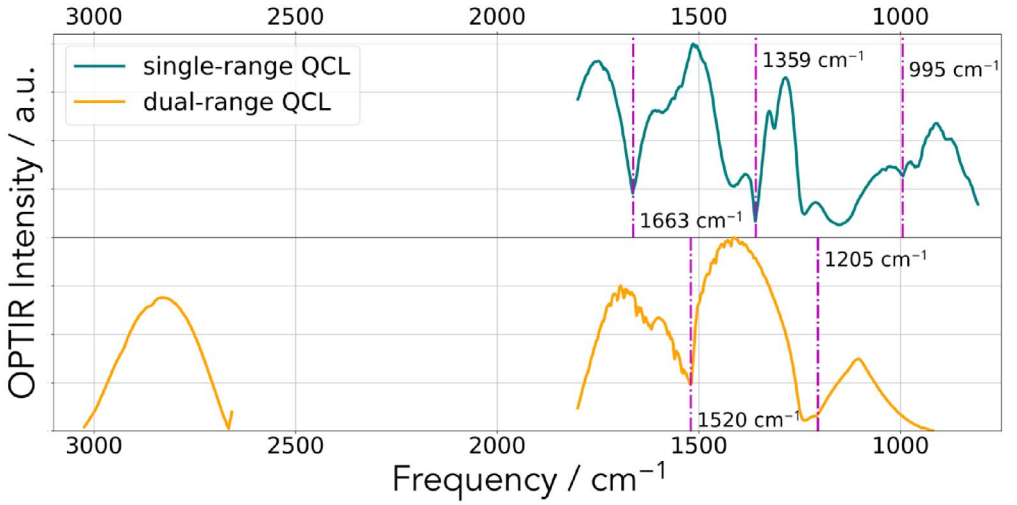

Figure 3. Typical IR spectrum corresponding of the incident beam. Dashed magenta lines show the laser stage transition frequencies.

IR sources were two pulsed, tunable four-stage Quantum Cascade Laser (QCL) devices, scanning from 800 to 1900 cm^{-1} or 920–3050 cm^{-1} (with a gap between 1800–2600 cm^{-1}). Regarding the probe, we used a CW 532 nm visible variable power laser.

Our biological samples were placed either on a CaF_2 substrate or on low-e reflective microscope slides (MirrIR, Kevley Technologies, Tienta Sciences, Indianapolis). In our case, we have not remove artifacts potentially arising due to imperfect switching between neighboring QCL laser stage (Figure 3). We used the open-source Quasar software (https://quasar.codes) and the Orange Spectroscopy toolbox for multivariate statistical analysis [75]. To generate data of high signal-to-noise ratio, 20–50 spectra were collected. In Figure 2, we can see a typical IR spectrum corresponding to the DHA compound. Two configurations have been used (Figure 3). In the first configuration, the transitions between the different IR sources are clearly visible and are positioned at 1663 cm^{-1}, 1359 cm^{-1} and 995 cm^{-1}. In the second configuration, the transitions between the different IR sources are clearly visible and are positioned at 1520 cm^{-1} and 1205 cm^{-1} (Figure 3).

Regarding classical FTIR spectroscopy [46,47], each kidney stone was analyzed in absorbance mode on a Bruker Vector 22 spectrometer by accumulation of 32 spectra between 4000 and 400 cm^{-1}, with resolution 4 cm^{-1} and time acquisition 1 s/spectrum. For

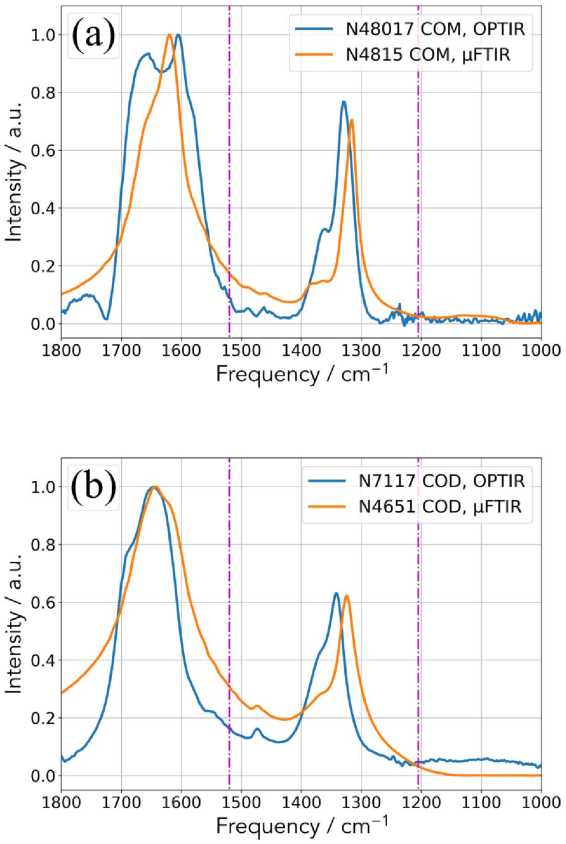

Figure 4. Comparison between the two experimental set up (OPT-IR and µFTIR) for two COM kidney stones (N48017 and N4815) (a) and two COD kidney stones (N7117 and N4651) (b).

the biopsy, FTIR hyperspectral images were recorded with a Spectrum Spotlight 400 FTIR imaging system (Perkin Elmer Life Sciences, France).

3. Results and discussion

Thanks to the opportunity offered by a commercial experimental set up device, numerous kinds of samples have been already investigated through OPT-IR spectroscopy encompassing submicrometer atmospheric particles [76], polymers [77], fragments from a historical painting [78] or nanocomposites [79]. Several exciting research works have also been published on biological samples [80–89]. Among them we can quote the possibility to discriminate different types of lung cells on histopathology glass slides [80], to determine relevant molecular structures directly in neurons [81] as well as the orientation of collagen in tendon [82].

In all these publications, the OPT-IR technique provides an elegant non-contact way to chemically identify different kind of compounds with higher spatial resolution than conventional IR microscopes, while maintaining the advantages of an optical microscope-based platform. We would like to show different microcrystalline pathologies on which OPT-IR can bring valuable information to the clinician. To attain this goal, it is of primary importance to compare the IR spectrum acquired with a classical experimental set-up related to classical IR spectroscopy to IR spectrum collected with a OPT-IR one for different compounds namely calcium oxalate monohydrate, calcium oxalate dehydrate, calcium phosphate apatite and magnesium ammonium phosphate hexahydrate.

3.1. *Biological reference compounds collected at the nanometer scale*

In Figures 4 and 5, we have selected a set of reference compounds corresponding to different chemical phases identified in kidney stones and compared their IR spectra obtained with two experimental set up, namely μFTIR and OPT-IR configurations. In figure 5, we can see that some differences exist between μFTIR and OPT-IR for calcium oxalate monohydrate (COM) [89–91] (Figure 4a) and dihydrate (Figure 4b) [92] mainly due to the transition between the laser stages. In both cases, around 1200 cm^{-1}, the incident IR signals by the mIRage™ experimental set up are quite noisy in line with weak intensity of the IR laser in this part of the spectra.

Regarding calcium oxalate monohydrate (Figure 4a), the assignment of the most intense IR bands (1618 cm^{-1}, 1312 cm^{-1}, 782 cm^{-1}, 667 cm^{-1}, 514 cm^{-1}) is well known [89–91]. More precisely, high absorbance at 1618 and 1312 cm^{-1} belong to C=O and C–O, respectively. Regarding calcium oxalate dehydrated (COD) (Figure 4b), the most intense vibrations are shifted at 1643 cm^{-1} and 1325 cm^{-1} [91,92].

Regarding the phosphate salts (Figure 5), we have considered two biological reference compounds: calcium phosphate apatite (CA) [93–96] and struvite (magnesium ammonium phosphate hexahydrate, MAP) [16,18].

Clearly, some differences exist which may have different origins. The first one is related to the fact that μFTIR gives an average chemical composition (the quantity sample is around μg) while OPT-IR gives a local chemical composition (the size of the probe spot is 500 nm). Actually, biological samples have never made of only one component and always they contain at least some proportions of matrix compounds such as proteins. In addition, kidney stones are made of two or more crystalline species in more than 93% of cases. It is thus possible to collect an IR spectrum dominated by proteins with the OPT-IR experimental setup with a sample for which the chemical composition given by μFTIR is 99% COM and 1% proteins. Finally, the presence of amorphous calcium phosphate which is associated to a shoulder in the absorption band positioned at 1030 cm^{-1} FTIR spectra has to be considered.

Moreover, a chemical analysis based on IR lasers at the nanometer scale still constitutes a challenge. For example, Mathurin *et al.* [97] shows experimental data which reveal significant differences in the agreement between AFM-IR and conventional FTIR data, depending on the studied mineral. More precisely, the spectra recorded in AFM-IR and FTIR microscopy are very similar in the case of the smectite (Figure 6a). But if they consider AFM-IR and FTIR spectra collected for forsterite single crystal, some band positions as well as some band ratios are drastically different (Figure 6b).

The origin of such huge spectral differences observed in the case of the forsterite crystal is multi-

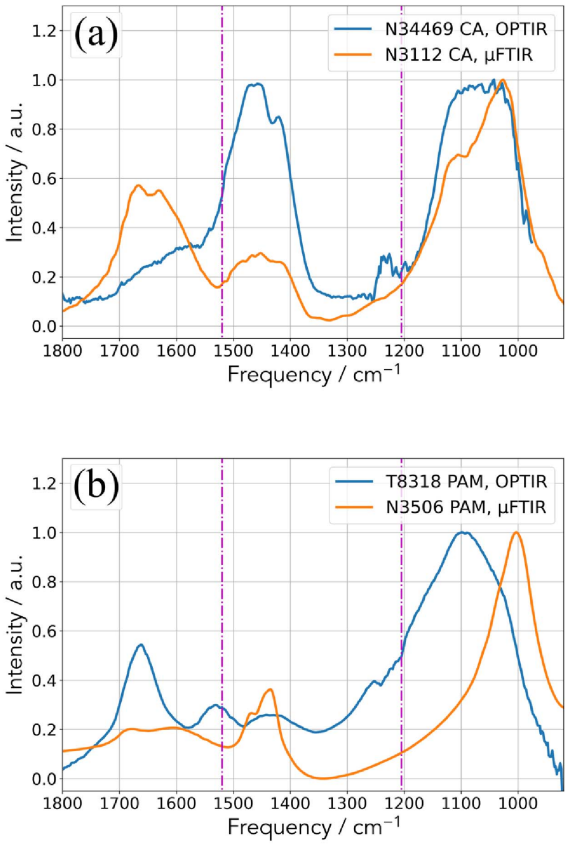

Figure 5. Comparison between the two experimental set up (OPT-IR and µFTIR) for (a) two CA kidney stones and (b) two MAP kidney stones.

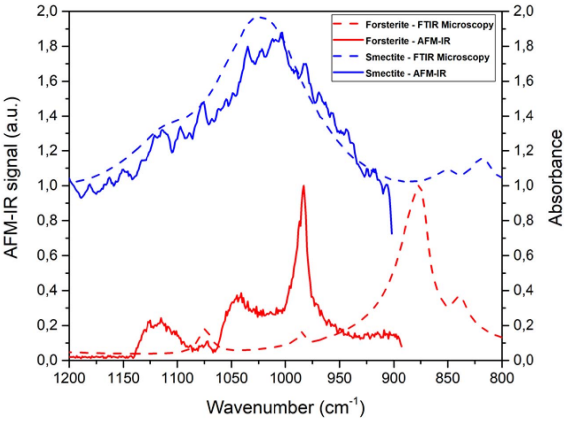

Figure 6. Comparison of the FTIR microscopy spectrum (dashed line) and the AFM-IR spectrum (line) obtained on smectite powder (blue) and on forsterite polished sections (red). Both AFM-IR spectra are obtained in contact mode with top-down illumination and gold coated tip.

ple. Crystal orientation, the optical behavior of the sample as well as geometry of the experiments may have significant effects on the IR spectrum. Also, scattering processes of laser with wavelengths close to the dimensions of the crystals may have to be considered.

3.2. *Hyperoxaluria and calcium oxalate monohydrate ectopic calcifications*

As noticed recently by Alelign and Petros [98], despite considerable improvements in the development of new therapies, the incidence of urolithiasis increases worldwide affecting 12% of the world population at some stage in their lifetime. Calcium-based stones are predominant renal stones comprising about 80% of all urinary calculi [99]. Such high prevalence explains the fact that several studies have been dedicated to the crystallography and the chemistry of calcium oxalate compounds [100–104].

Crystalline calcium oxalate exists in three hydrated forms known as monoclinic whewellite (monohydrate, COM) [89,91], tetragonal weddellite (dihydrate, COD), [91,105,106] and triclinic caoxite (trihydrate, COT) [91]. Recently, amorphous calcium oxalate has been synthetized [107,108]. This compound constitutes a transition step during the chemical transition between COD and COM, the last one being the more stable [109,110]. Regarding their prevalence, COM is the most frequent, while COD is about two to three times less common [111]. The trihydrate form is rarely observed [112]. Another significant clinical difference between COM and COD comes from the fact that in clinical practice COM is related to hyperoxaluria states while COD is associated to hypercalciuria ones [113,114].

Regarding the presence of ectopic calcification made of calcium oxalate, as usual [4,49,115], we start by observations through a FE-SEM-EDX microscope (Figures 7a–c). In this contribution, we have used a Zeiss SUPRA 55VP FE-SEM. To preserve the structural and the chemical integrities, All the SEM observations are made at low voltage (1.4 keV) and with-

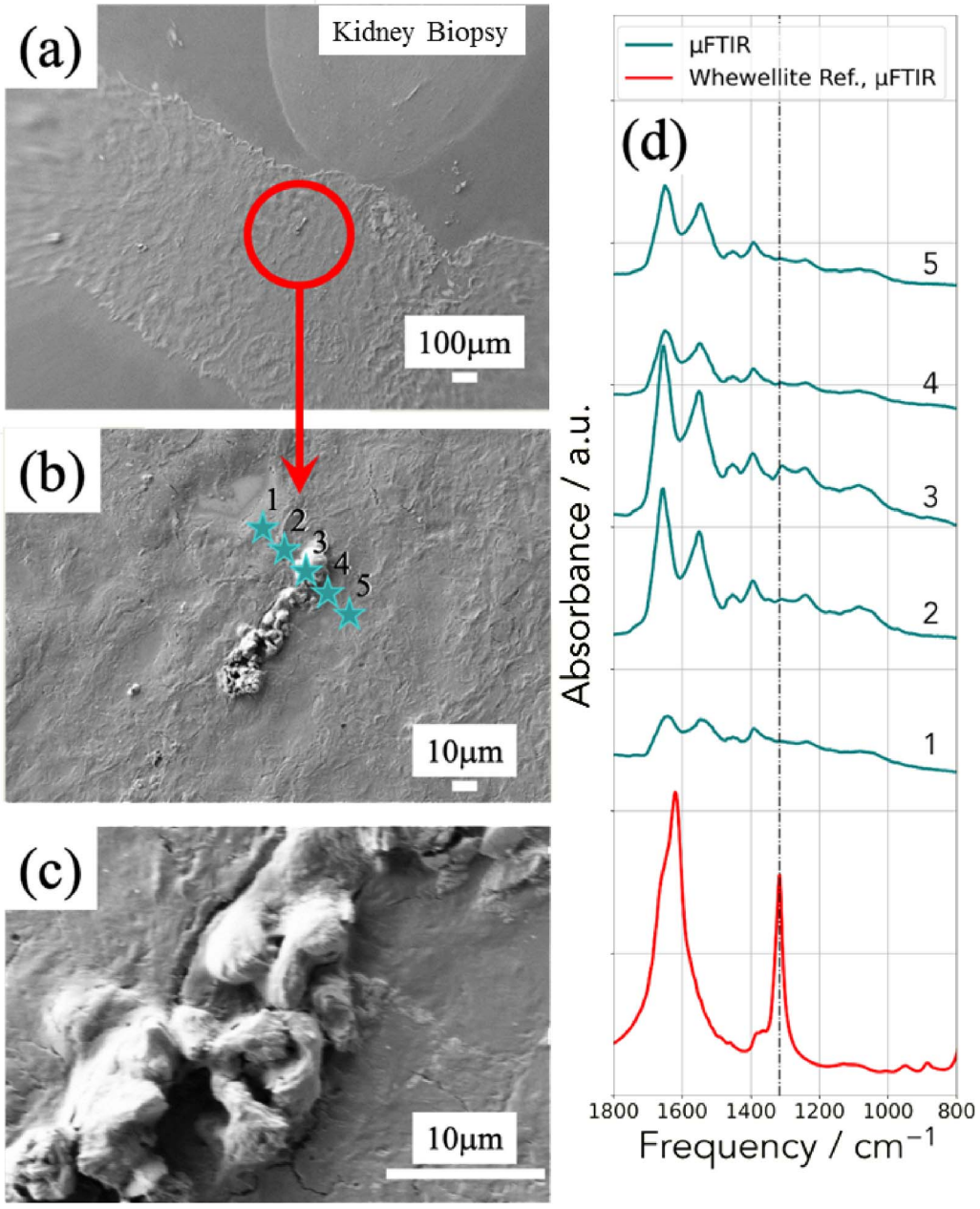

Figure 7. (a–c) Scanning electron microscopy at different magnifications of ectopic calcification present in a kidney biopsy. (d) FTIR spectra collected for the different locations of the IR beam as indicated in (b).

out the usual deposits of carbon at the surface of the sample. Such observations allow us to localize precisely the PMCD in the kidney biopsy. In Figure 7d, we can see IR spectra collected on different points of interest (POI) defined in Figure 8b.

As discussed previously, due to the micrometer spatial resolution of the FTIR spectrometer, we can observe the two bands amide I and II associated to the tissue even if the probe is positioned on the calcification (location 3 in Figure 8b). As it is generally the case, their relative intensities are not always the same. This is due to the preparation proto-

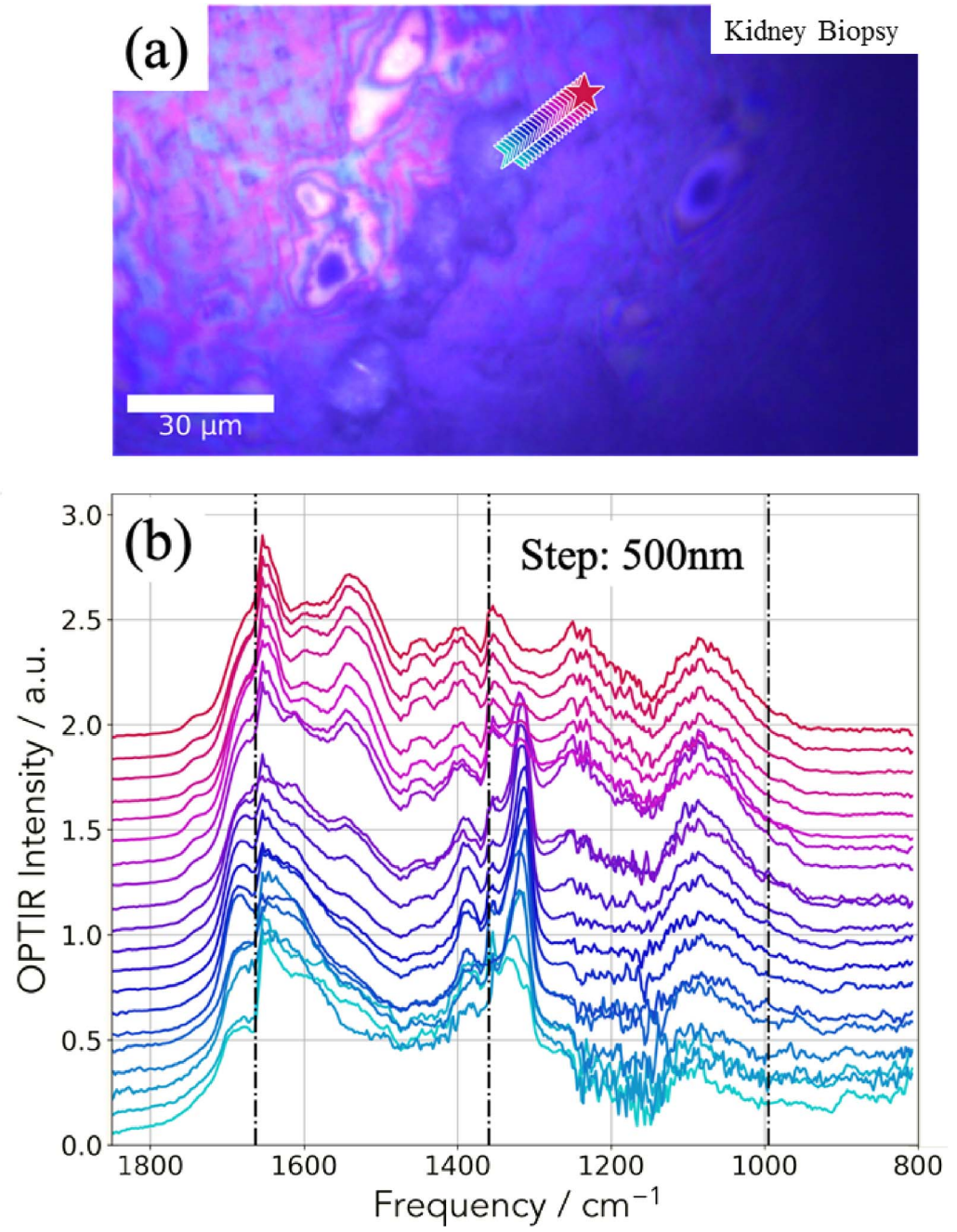

Figure 8. (a) Optical image collected by the OPT-IR microscope. (b) 20 OPT-IR spectra collected along the line defined in (a).

col which is optimized to preserve the physicochemical integrity of the ectopic calcification. Regarding the chemical composition of the ectopic calcifications, the presence of IR bands at 1315 cm^{-1} clearly indicates the presence of calcium oxalate monohydrate (its spectrum has been plotted at the bottom of Figure 7d).

The IR spectra collected by the mIRage™ experimental set up are presented in Figure 8b, each spectrum corresponding to a star shown in Figure 8a.

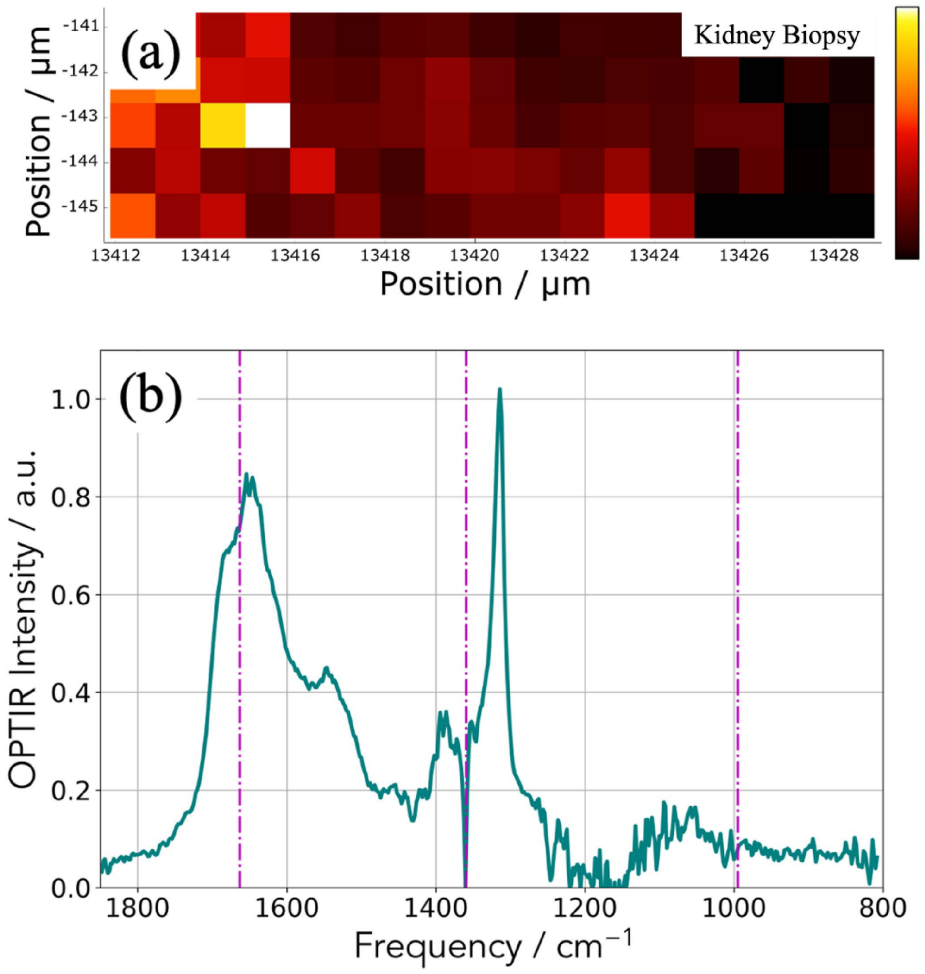

Figure 9. (a) Spatial distribution of the integrated 1302–1327 cm^{-1} IR absorption band specific to COM. (b) OPT-IR spectrum from the highest intensity (white) pixel of (a). Spectra were smoothed with a 5-point Savitzky–Golay filter and normalized to the integral between 1600–1850 cm^{-1}.

As we have observed through µFTIR spectroscopy, the relative intensity between the amide I and II are not the usual ones. An additional explanation of this observation comes from the transition between the two IR laser stages which is positioned on the amide I band. For this sample, thanks to the high spatial resolution, we have collected an IR spectrum every 500 nm (Figure 8b). The observation of a sudden modification of IR spectra when the probe move on the ectopic calcification indicates that the spatial resolution of the mIRage experimental set up is effectively around 500 nm. Note that the intensity ratio of the two bands of COM (1315 and 1618 cm^{-1}) may be not always the same due to the fact the two lasers used here are polarized. Also note the variation of the position of the band at 1315 cm^{-1} which may be due to the same reason.

In Figure 9, another way to collect IR data is shown. We select an absorption band of the OPT-IR spectrum (Figure 9b) which corresponds here for calcium oxalate monohydrate (Figure 8a) and we have plotted the maximum of this absorption band versus its position to obtain the spatial repartition of COM with a lateral resolution of 500 nm (Figure 9a).

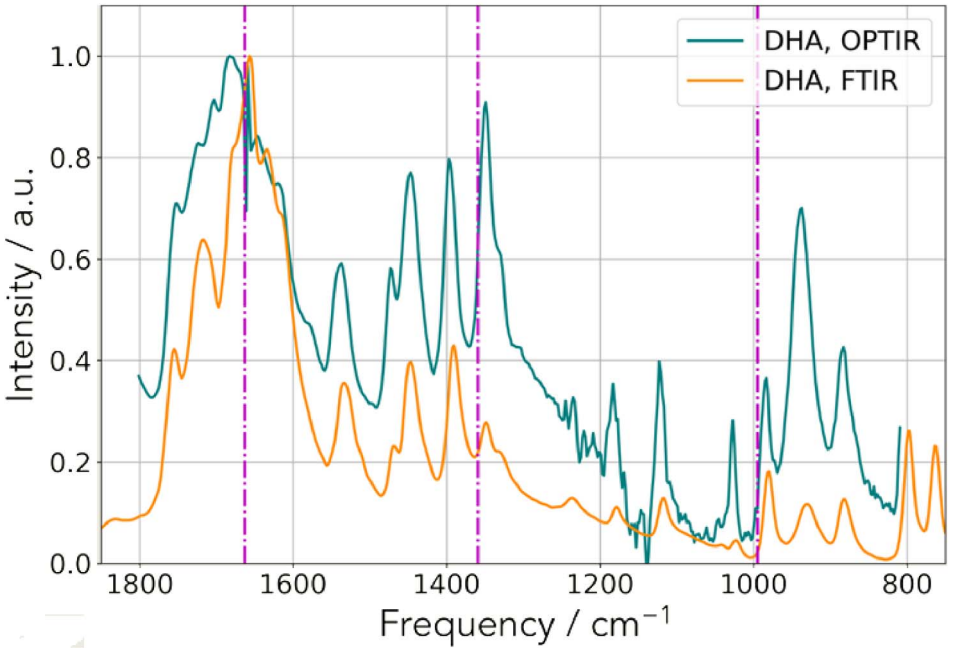

Figure 10. Comparison between techniques. IR spectrum collected on a classical FTIR device (orange) and an OPT-IR spectrum acquired on the mIRage™ experimental set up (teal).

3.3. *The adenine phosphoribosyltransferase (APRT) deficiency*

Among the genetic diseases which induce the formation of ectopic mineralizations in kidney we can quote adenine phosphoribosyltransferase (APRT) deficiency which is a rare autosomal recessive disorder. This genetic disease induces the formation of 2,8-dihydroxyadenine (DHA) stones and renal failure secondary to intratubular crystalline precipitation [24,116,117]. Different ways exist to establish the medical diagnosis including the identification of typical DHA crystals in urine or renal biopsy, a genetic investigation as well as the measurement of APRT activity in erythrocytes. As underlined by Bollée *et al.* [117], early diagnosis of the disease is critical because patients may develop renal failure [118–120] that may be efficiently prevented by allopurinol, a xanthine oxydase inhibitor. We have already demonstrated that μFTIR spectroscopy constitutes an elegant way to perform an early diagnosis of this genetic disease [121].

We performed IR experiments using an OPT-IR experimental set up. For that purpose, we start by considering a kidney stone made of DHA and by collecting IR spectra. As we can see in Figure 10, the spectral correspondence and excellent signal to noise ratio allows the clinician to recognize the IR spectrum of DHA crystals [24,55,121].

After obtaining these results, we inspected a mouse (as an animal model for this pathology) as well as a human biopsy. Regarding the human biopsy, SEM observations allowed us to localize abnormal deposits (Figure 11). μFTIR spectra were collected (Figure 12) clearly show the presence of DHA crystals.

On this human biopsy, mIRage experiments have been also performed and we can see in Figure 12, these IR spectra clearly underline the presence of DHA crystals. One interesting point is that the amide I and II bands are not always visible. It seems that with a probe of 500 nm IR spectra on DHA crystals alone can be collected. As for the previous sample, it is possible to build the spatial distribution of DHA crystals from one selected IR band through its intensity (Figure 13).

Figure 14 shows the potential of OPT-IR in hyperspectral measurements through an example of hierarchical cluster analysis. Here, we have calculated the Euclidean distances of individual spectra and used

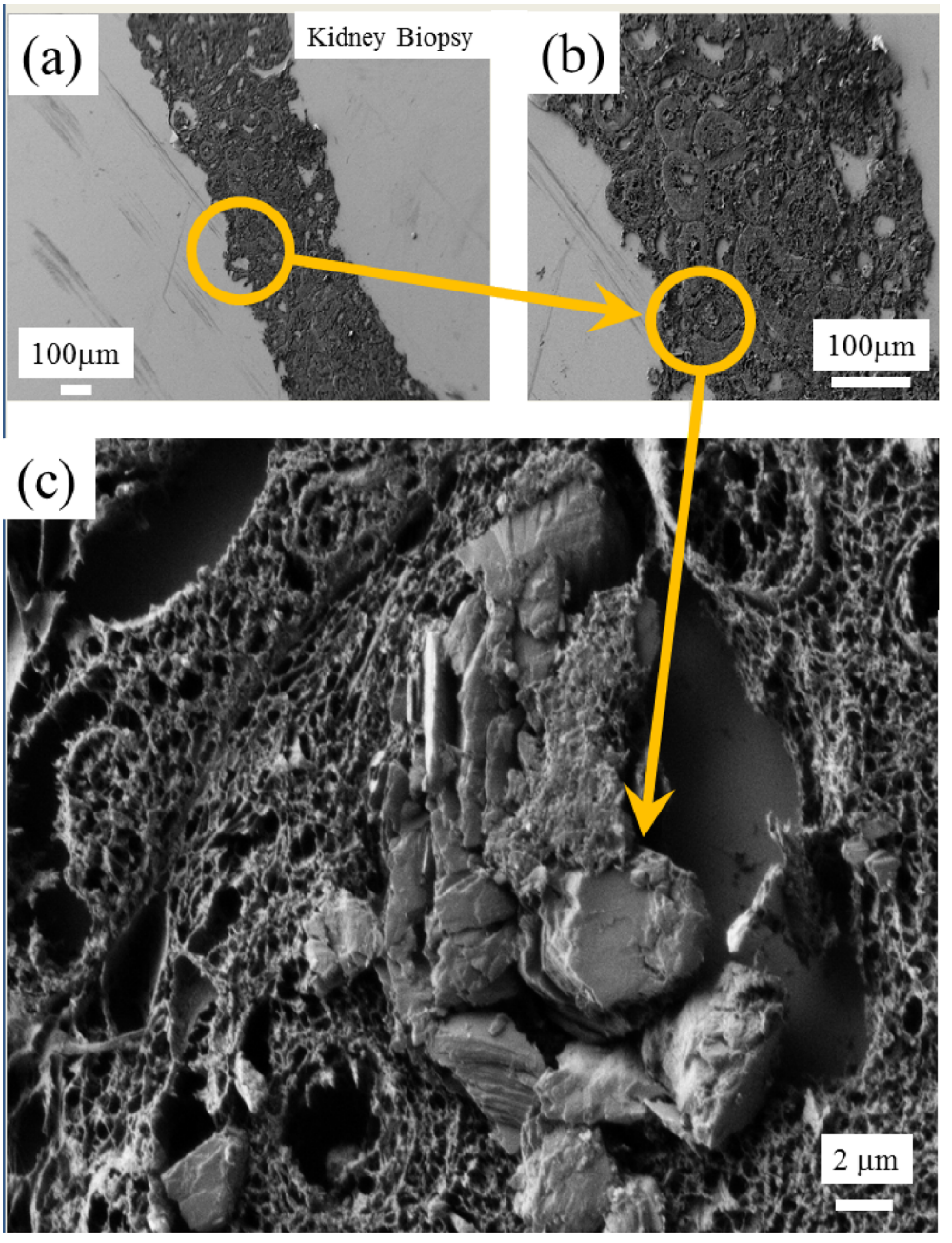

Figure 11. SEM images of DHA deposit at different magnifications present in a human kidney biopsy.

the Ward linkage to determine cluster distances. Plotting the spatial distribution of the Euclidean distance of each spectrum from the average spectrum (Figure 14a) highlights a high-intensity area in the middle of the map. The result of HCA is shown in Figure 14b, where the top two clusters are highlighted in red and blue. By calculating the cluster averages for each cluster, we can clearly identify the DHA rich area different from the average spectrum of the surrounding tissue (Figure 14c).

Regarding the mouse kidney, we used the 500 nm probe to underline the possible presence of DHA

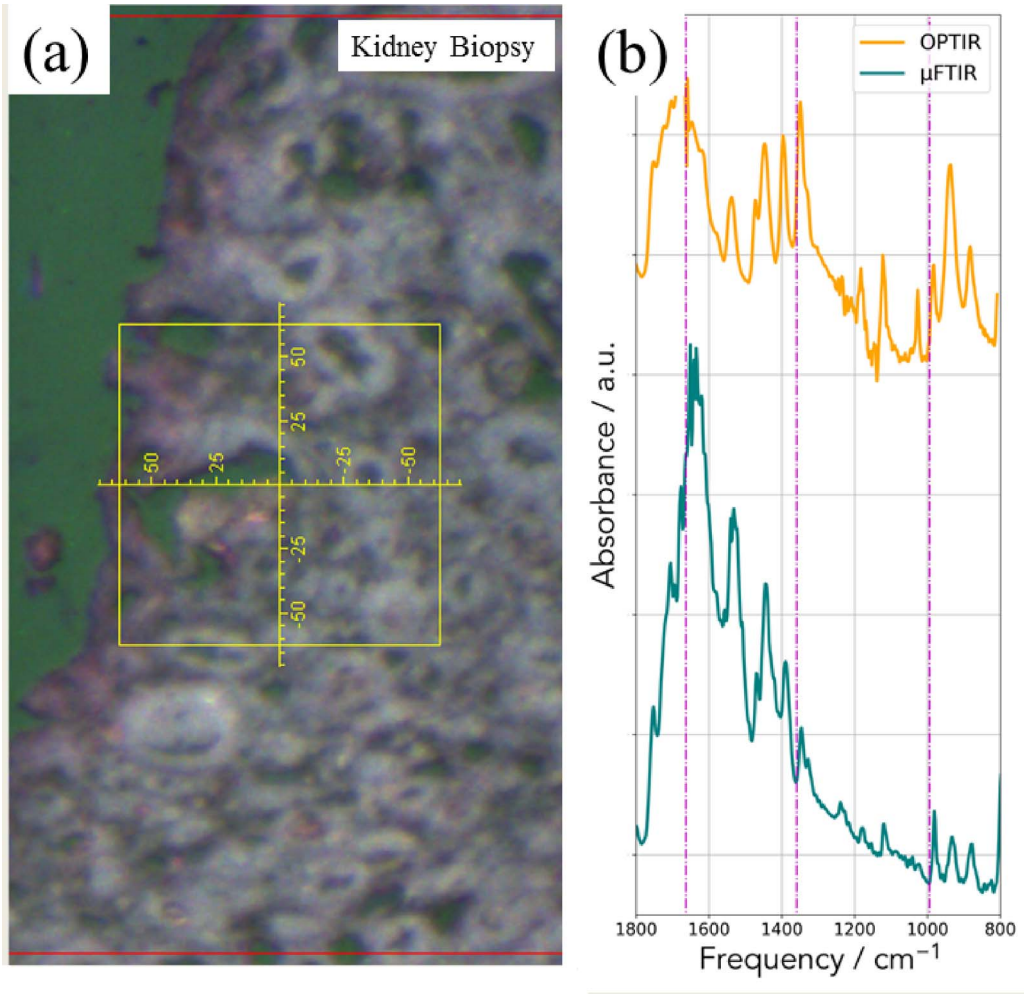

Figure 12. (a) Optical photography. (b) IR spectra (with the µFTIR and the OPT-IR experimental set up) showing the presence of DHA crystals.

crystals. In Figure 15a, we selected two areas of interest (Figures 15b and c). For each area, we collected IR spectra using the mIRage™ experimental set up (Figures 16 and 17). One simple way to analyze the IR data can be performed by considering the 1000–800 cm^{-1} region where DHA has quite intense IR absorption bands.

The different IR spectra collected with the mIRage™ experimental set up show significant differences with the IR spectra corresponding to DHA. Thus, DHA seems to be absent (Figures 16 and 17).

3.4. *Giving major information through nondestructive techniques*

With the help of OPT-IR nanospectroscopy and SEM-EDX, it is possible to gather information regarding the chemistry and the topology of kidney stones without any kind of preparation. In a recent paper, we have also combined micro computed tomographic imaging (micro CT) and SEM-EDX [122]. Micro CT is a powerful tool for visualizing urinary stones allowing easy visualization of stone structure and mineral identification, especially if an attenuation standard is included with a specimen [122–126]. Regarding micro CT, experiments were conducted using the

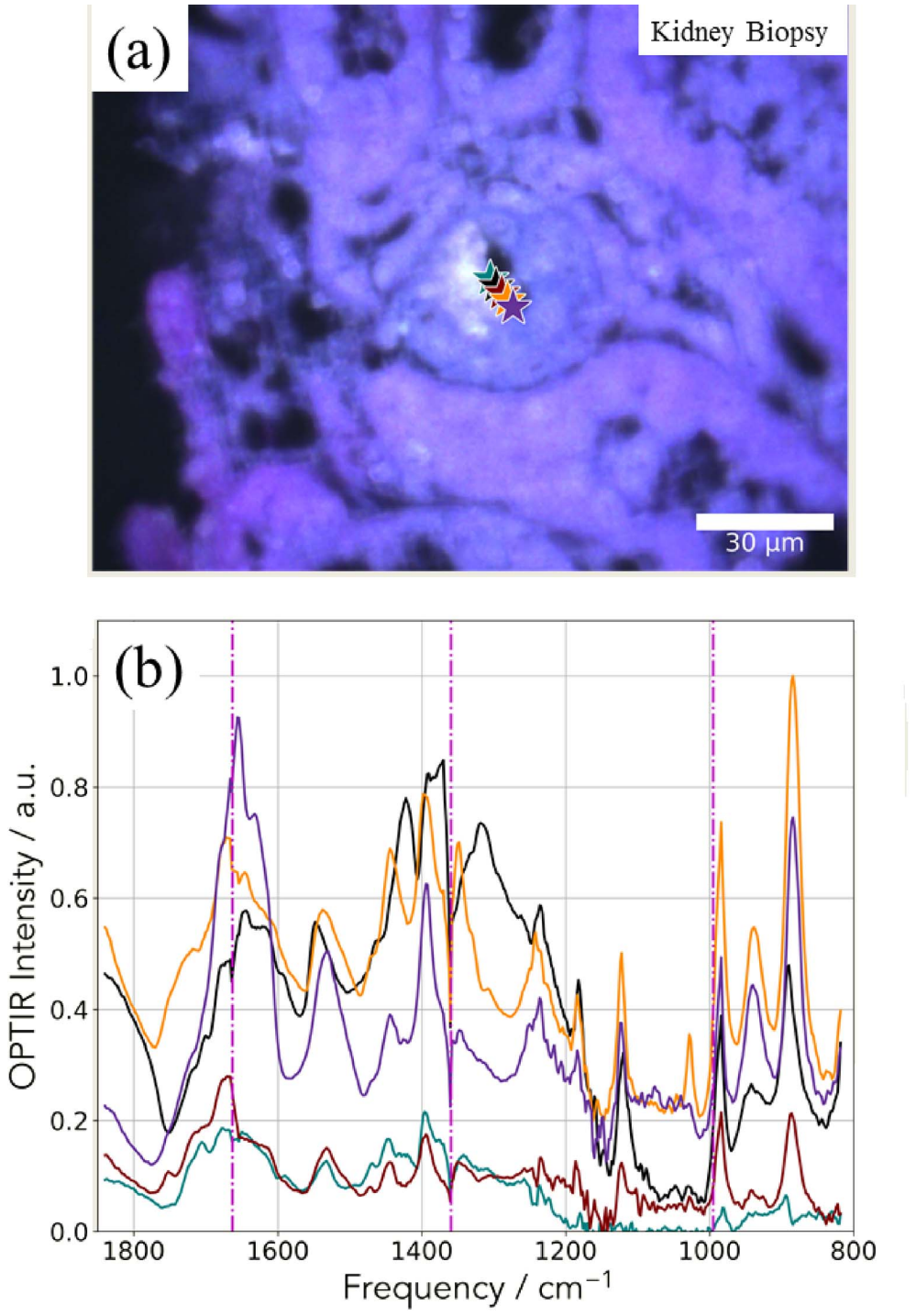

Figure 13. (a) Optical image; (b) OPT-IR spectra showing the presence of DHA deposits in a human kidney biopsy.

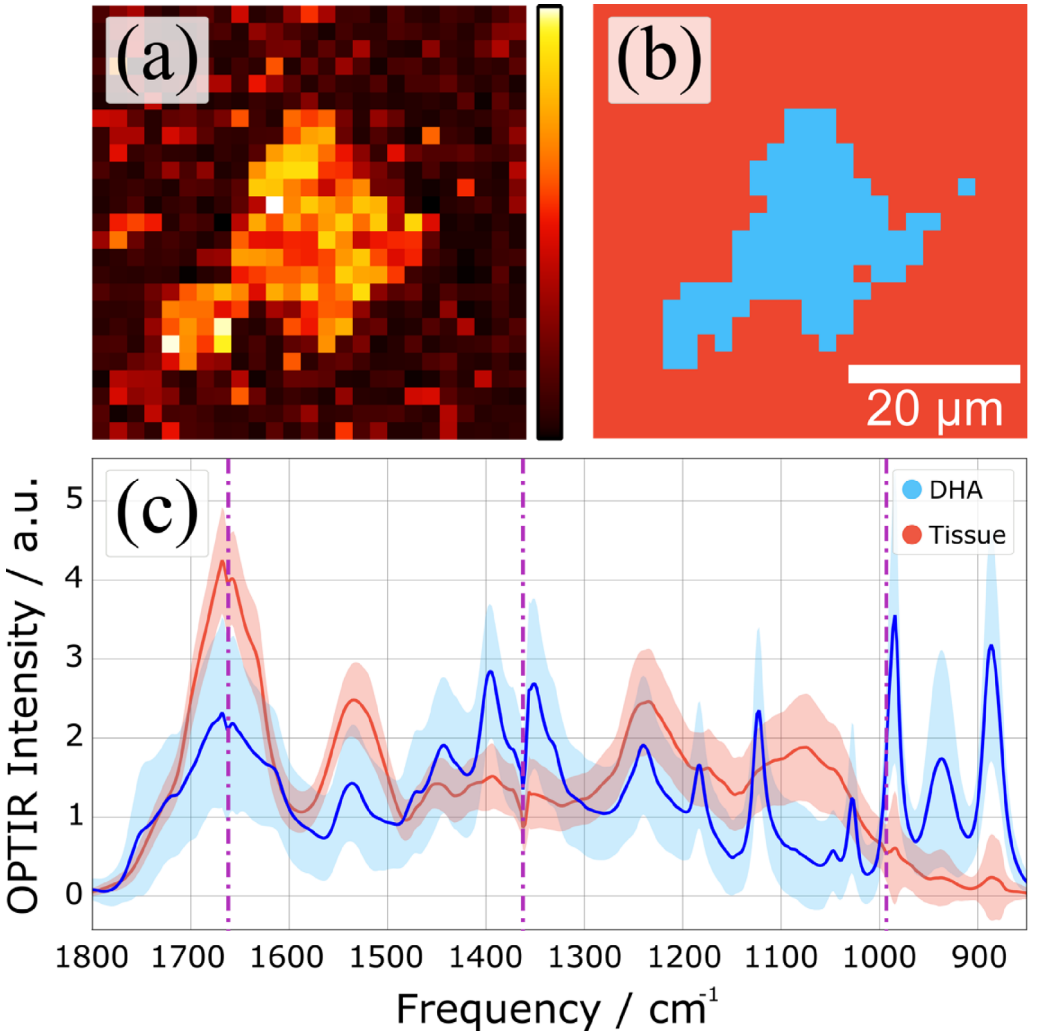

Figure 14. Hierarchical cluster analysis (HCA) of a hyperspectral dataset. (a) Spatial distribution of the Euclidean distance from the average spectrum. (b) Spatial distribution of two clusters identified by HCA. (c) Cluster averages and their standard deviation.

Skyscan 1172 Micro CT system (Bruker, Kontich, Belgium), typically using 60 kVp, 0.5 mm Al filter, and 0.7° rotation step for final (cubic) voxel sizes of 2–12 µm. Stones were typically mounted in Styrofoam for scanning, as that material is remarkably X-ray lucent [122].

We have considered here two kidney stones. The first one was collected as part of an ongoing study of kidney stones, in which patients are consented for study under the Indiana University Internal Review Board (under guidelines from the United States Health and Human Services Office of Human Subjects protection). That stone was mainly composed of COD. The second one comes from Tenon Hospital. It was mainly composed of COM. These two kidney stones are made of calcium oxalate, and, at their surface, a white deposit exists named Randall's plaque [127–132]. The formation mechanism of Randall's plaque, which remains incompletely understood, has been addressed in many publications during the last two decades [133–143]. As underlined by Van de Perre *et al.* [143], optical microscopy of eliminated kidney stones grown on Randall's plaque typically reveals a papillary umbilication, the imprint of the previous papillary attachment, which can be found as an irregular depression, while some stones

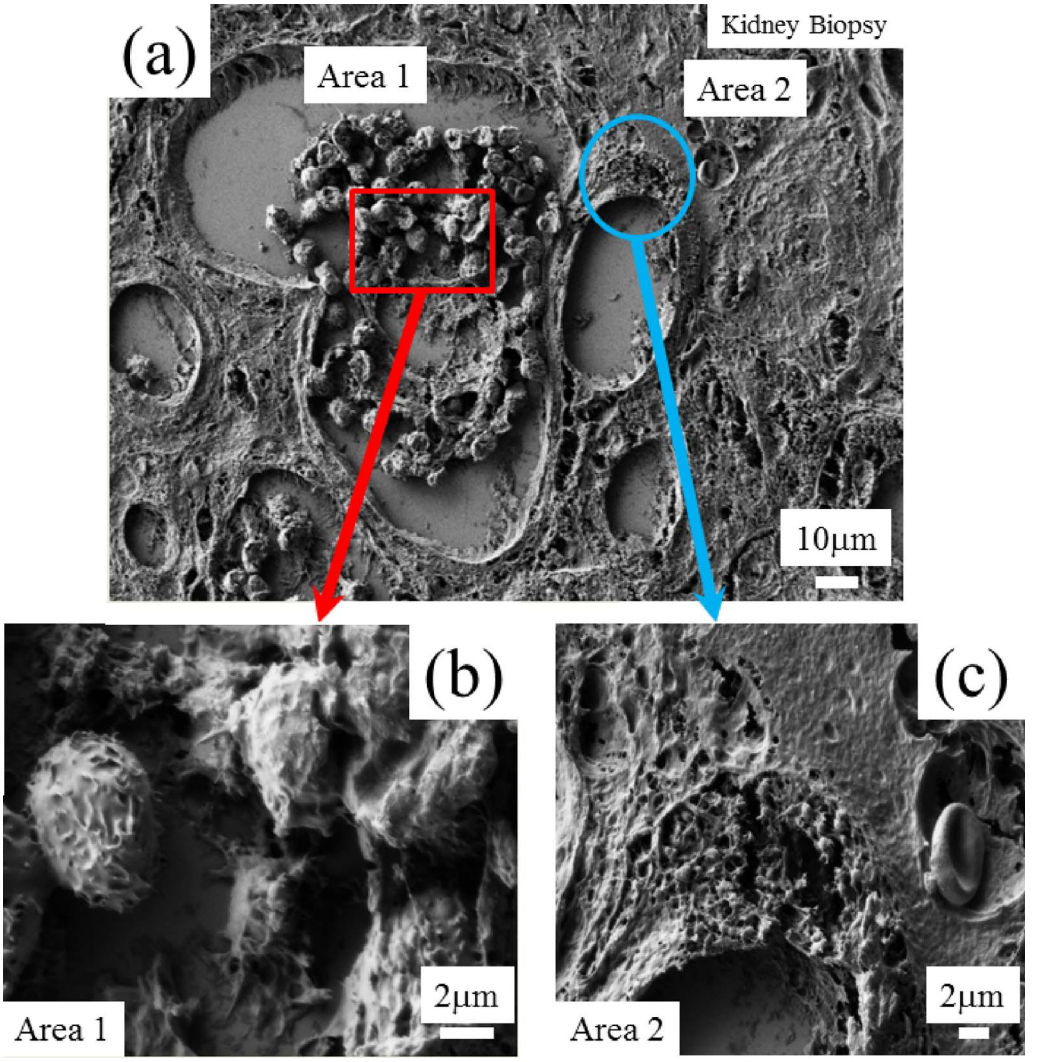

Figure 15. Scanning electron microscopy at different magnifications to select areas of interest for the mouse kidney (b) and (c).

can display plaque remnants at the umbilication as well.

In Figure 18, we can see images of the two kidney stones corresponding to SEM (Figures 18a and b) observations and micro CT (Figure 18c) for the first one (KRP 453) and SEM (Figures 18d and e) observations for the second one (86396). On SEM as well as on the micro CT scans we can see clearly the two chemical phases of the kidney stones i.e. calcium oxalate crystals and calcium phosphate apatite of the RP. The chemical analysis as given by OPT-IR spectroscopy performed for the two samples shows clearly that the Randall's plaque was made of calcium phosphate apatite (Figure 19), a result in line with previous publications [133–144].

4. Another pathological calcifications: the case of breast cancer

As underlined previously, microcrystalline pathologies affect all the Human organs and among them the presence of calcifications in breast is of primary importance due to its possible link to cancer. Breast cancer is a worldwide public health problem and

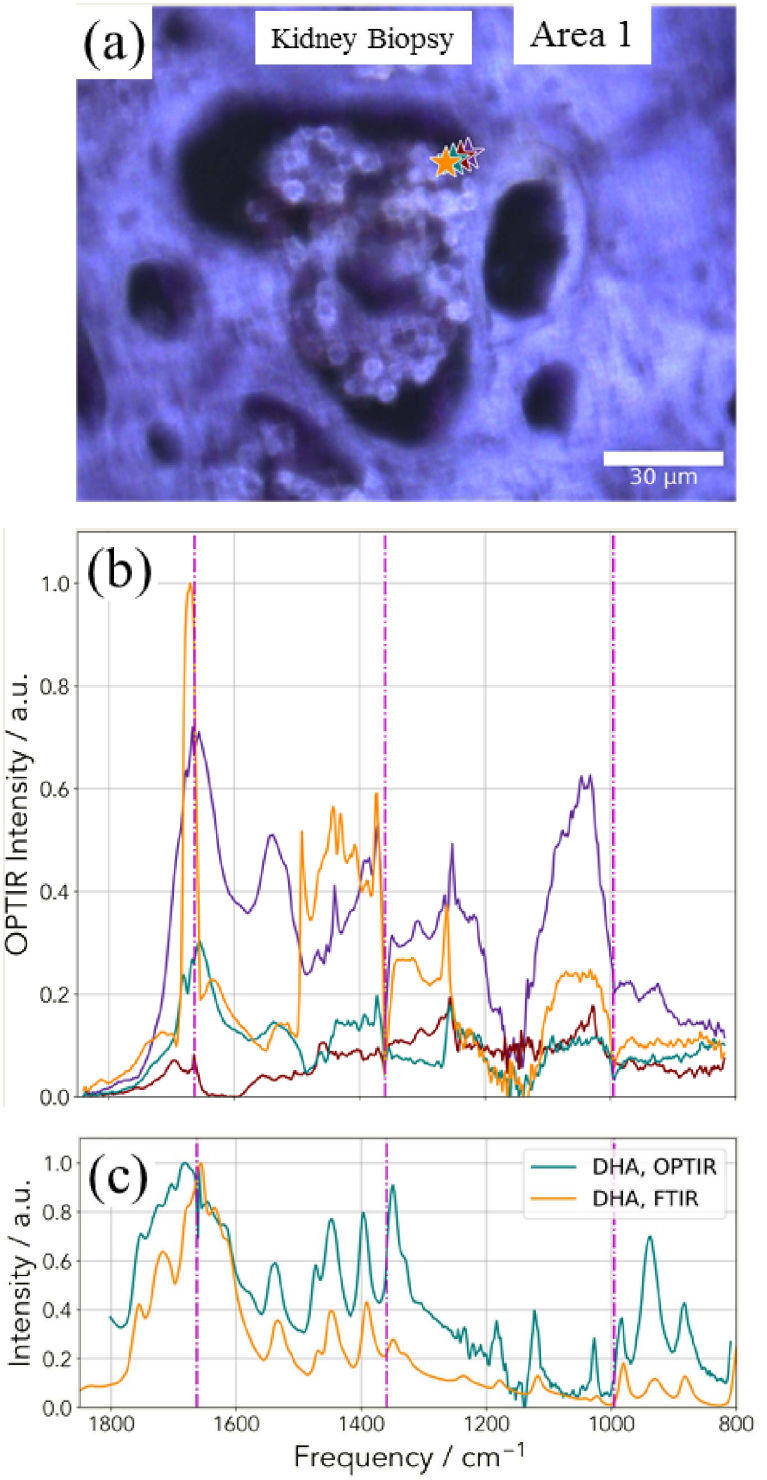

Figure 16. (a) Optical image corresponding to the deposit identified through SEM (Figure 15) and (b) OPT-IR spectra corresponding to the different points of interest (stars in a). (c) OPT-IR and FTIR spectra of DHA reference compound.

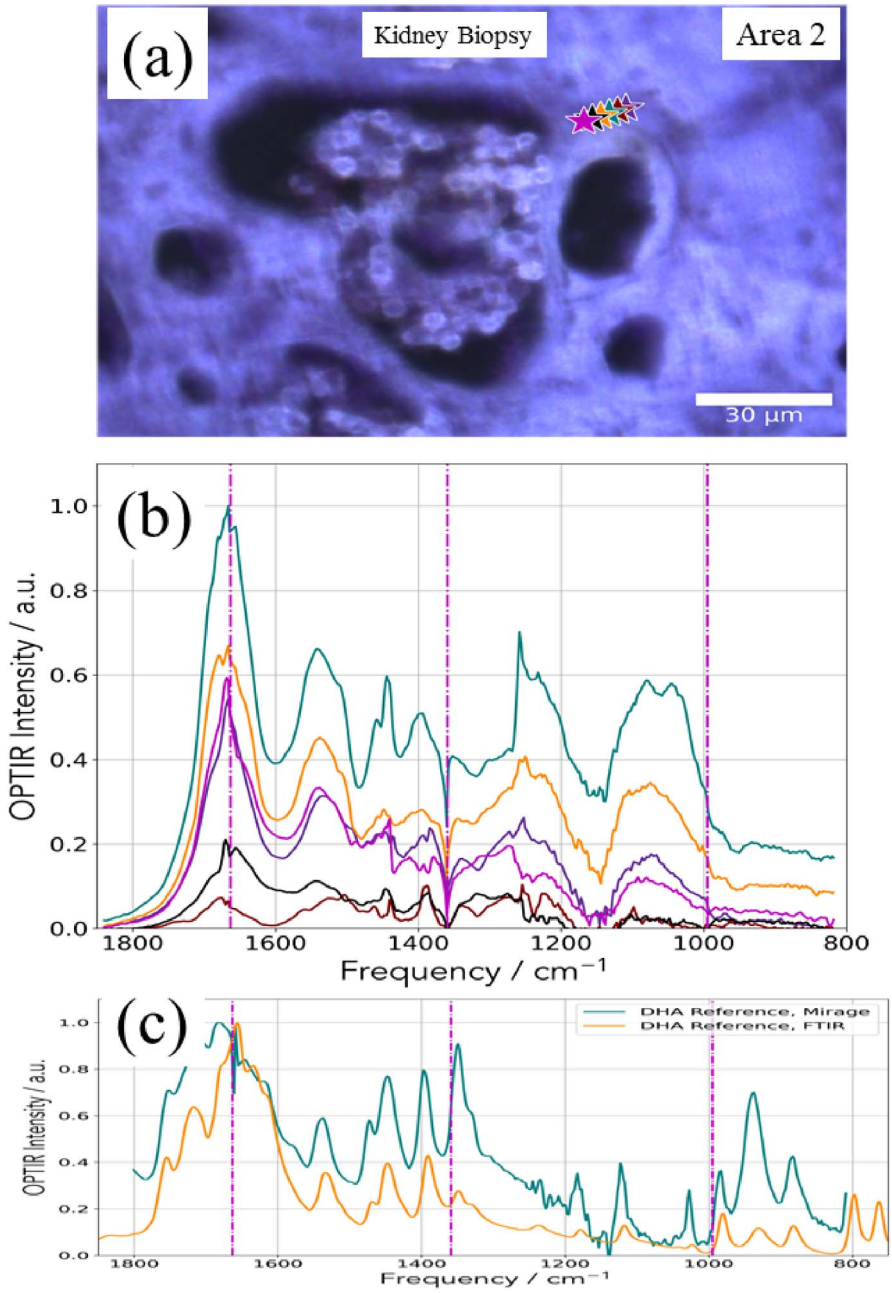

Figure 17. (a) Optical image corresponding to the deposit identified through SEM (Figure 15) and (b) OPT-IR spectra corresponding to the different points of interest (stars in a). (c) OPT-IR and FTIR spectra of DHA reference compound.

is the most common cause of cancer deaths, accounting for approximately 16% of cancer deaths in adult women [145]. Breast microcalcifications (BMC) which appear as white spots or flecks on a mammogram are related to calcifications in which the diameter is less than 1 mm [146–152]. At this point, it is worth to mention that the current spatial resolution mammographs without magnification ranged between 100 and 200 µm [149].

In a recent publication, we have underlined that

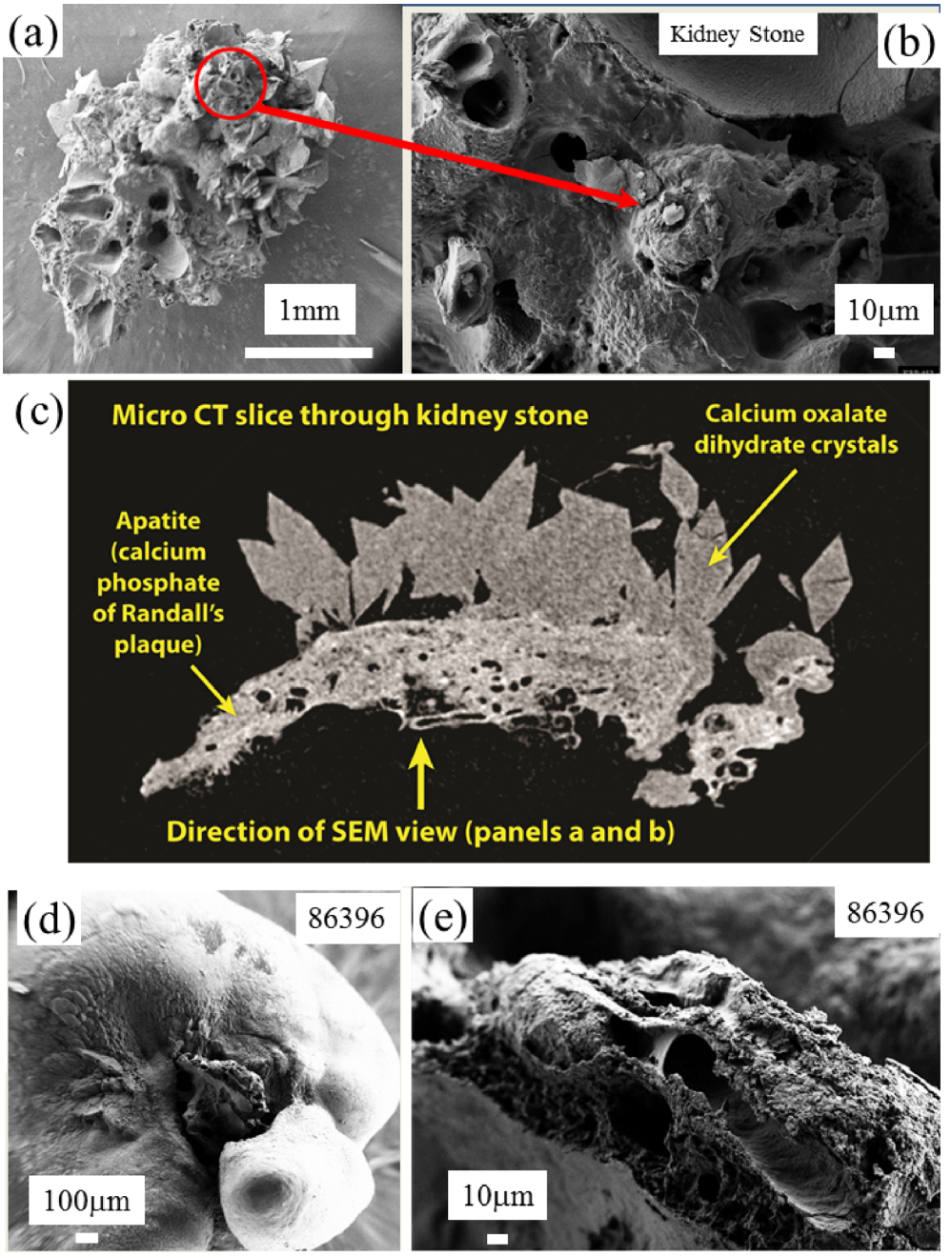

Figure 18. (a,b) SEM images of a RP at the top of a kidney stone. (c) CT tomography of the KRP 453 stone. (d,e) SEM images of a RP at the top of the kidney stone 86396.

microcalcifications as seen through usual mammography are made of nanometer scale breast calcifications made of spherical entities [8]. Such structural characteristic leads to the fact that the determination of the chemical composition of such nanometer scale entities cannot be performed through classical µFTIR spectroscopy. This is due to the chemical diversity of BMC in which different chemical phases

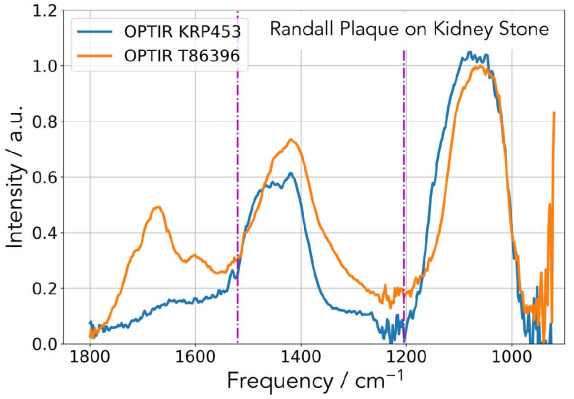

Figure 19. OPT-IR spectrum of the RP for the two samples giving the same chemical composition namely a mixing of ACCP and CA compounds.

namely calcium oxalate dihydrate [153], amorphous and nanometer scale crystals of calcium phosphate apatite with different levels of carbonatation [8,154–157] as well as whitlockite (Wk) [158–161] have been identified. For BMC, the number of chemical phases is thus quite low compared to the number of chemical phases identified in ectopic calcifications present in kidney (four instead of 24) [4,55]. It is also worth to underline the importance of micro and nano spectroscopies which are able to point out the variation of the level of carbonatation from the core to the surface of a BMC [8].

In Figure 20, we show SEM observations of microcalcification displaying a typical morphology related to Wk (different from the one observed in kidney stones [19]). Due to the small size of this abnormal deposit, it is quite difficult to obtain an IR spectrum with a sufficient signal to noise ratio with a classical μFTIR experimental device.

In Figure 21, we can see clearly than the OPT-IR nanospectroscopy is able to collect a significant IR spectrum which underlines the presence of whitlockite in the chemical composition of this abnormal deposit present in breast biopsy. OPT-IR nanospectroscopy seems to underline the presence of a calcium phosphate compound but it is quite difficult to say that this signal corresponds to Wk.

On Figure 22, the FTIR spectra of calcium phosphate identified in PMCD have been plotted. As we can see, it is details on the absorption bands (shoulders and shift) which are the keys to distinguish between Wk, ACCP and CA. Considering all the IR spectra we have collected through OPT-IR, it seems that such discrimination between all the calcium phosphate compounds is quite difficult.

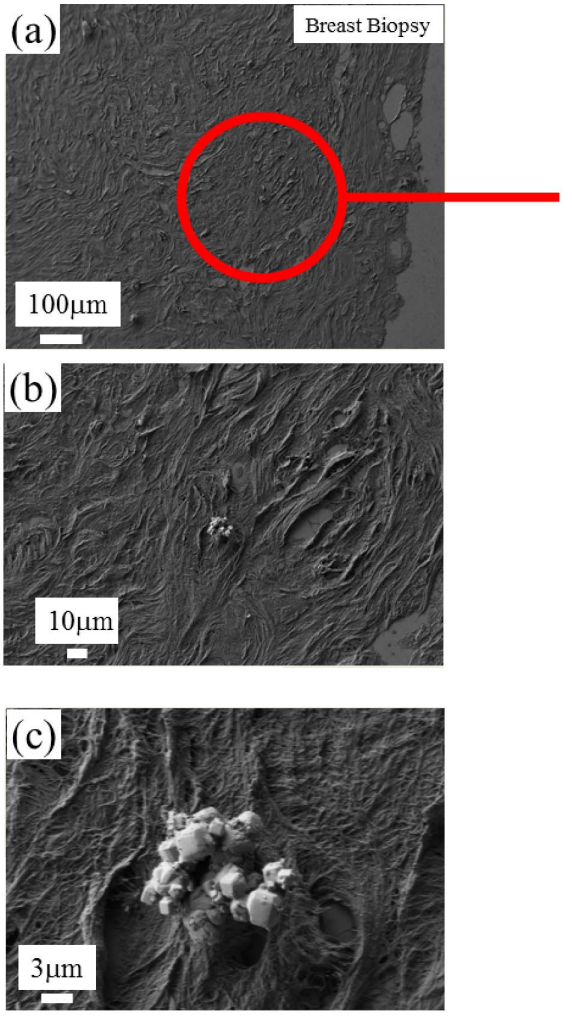

Figure 20. SEM images of an agglomeration of Wk crystals present in a breast biopsy.

5. Conclusion

It is well accepted in the medical community that conventional IR spectroscopy constitutes the golden standard to obtain a precise chemical composition of kidney stones. The emergence of IR spectroscopy associated to spatial resolution below one micrometer constitutes an incredible opportunity to describe

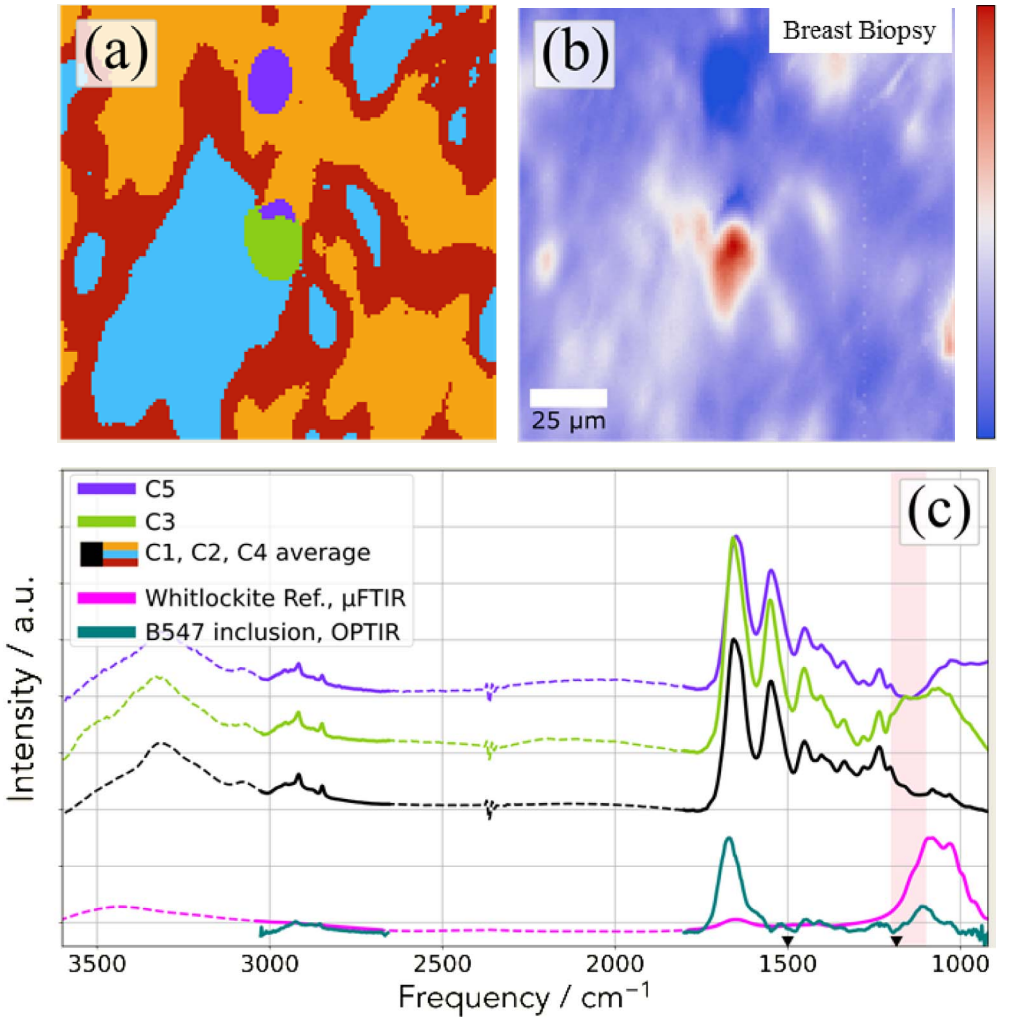

Figure 21. FTIR imaging of the deposit identified through SEM (Figure 20). (a) k-means cluster map of the observed area, the colors are related to the cluster defined on (c). (b) Distribution of the integral value between 1100–1200 cm^{-1} highlighted in red in the bottom panel (c) Cluster averages based on (a). Here C1, C2, and C4 clusters were merged (shown in black) as they belong to the surrounding tissue. Data were collected with an Agilent imaging set up. An OPT-IR spectrum collected from the sample inclusion of B547 and µFTIR spectra recorded on a reference sample are shown in teal and magenta colors, respectively. The regions accessible with the dual-band QCL are plotted with continuous and the parts not covered by the laser with dashed line.

chemical heterogeneity or interface of complex biological samples.

In this contribution we have considered different chemical phases which have been identified in pathological concretions and tissue crystalline deposits. The comparison between IR spectra collected with conventional IR spectroscopy and IR spectra collected at the nanometer scale through OPT-IR may show significant discrepancies depending on which chemical phase is investigated. Such differences exist for other spectroscopies such as AFM-IR or Raman spectroscopy and may have different origins.

In the case of pathologies related to cystine and DHA crystals, the signal to noise ratio is excellent and thus characterization at the nanometer scale

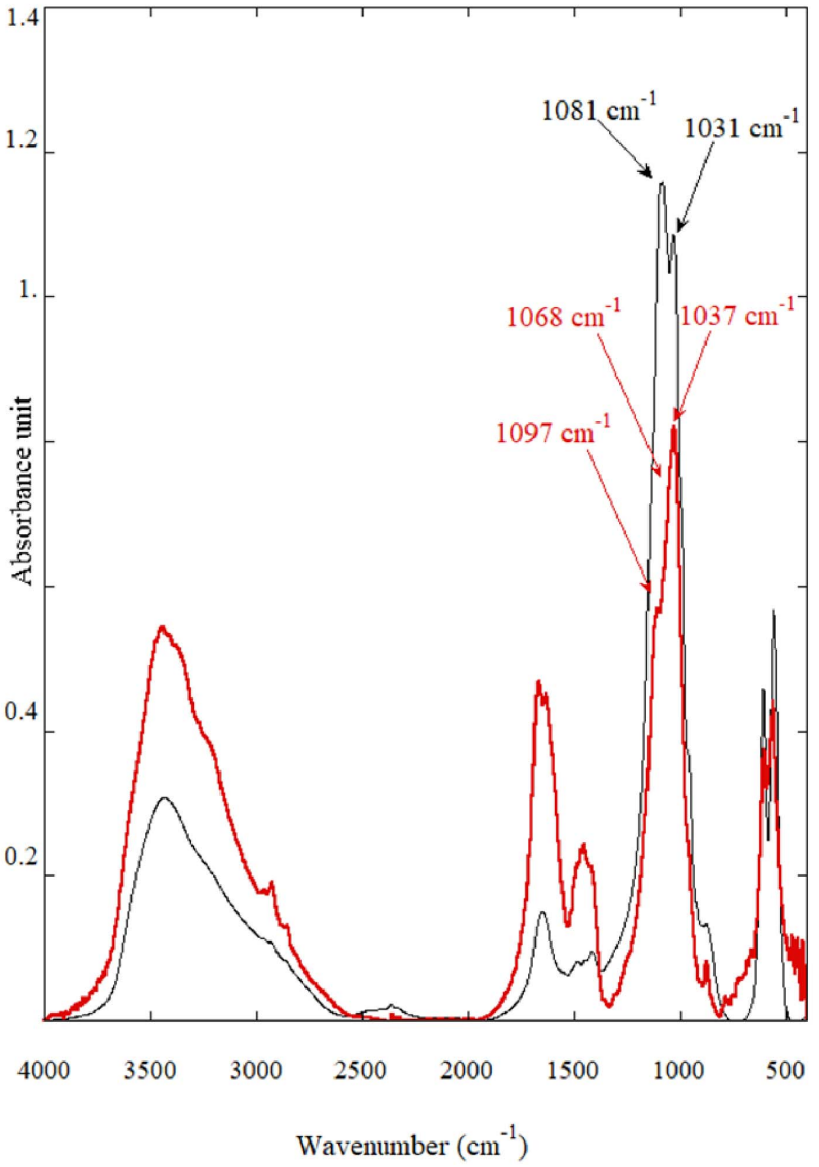

Figure 22. Classical FTIR spectra of calcium phosphate compounds identified in PMCD namely Wk (in black) with the splitting at 1081 and 1031 cm^{-1} and of a mixing of ACCP and CA (in red) with the shoulders at 1097 cm^{-1} (corresponding to CA) and 1068 cm^{-1} (corresponding to ACCP).

through IR spectroscopy can be considered for organic compounds. For the other chemical phases, namely minerals with broad IR absorption bands, such characterization seems to be more difficult. Let's recall also that a shift (a few cm^{-1}) of IR bands for calcium oxalate may be associated to the presence of both COD and COM (underlining that the patient suffers from hyperoxaluria (linked to the presence of COM) and hypercalciuria (linked to the presence of COD). One problem comes from the possibility to distinguish between different calcium phosphate compounds which is clearly a limitation in the case of breast calcification.

Complementary experiments are ongoing to clearly define the origin of the discrepancy which can exist for different chemical phases identified

in pathological calcifications between conventional μFTIR and OPT-IR spectroscopy.

Conflicts of interest

Authors have no conflict of interest to declare.

References

[1] D. Bazin, M. Daudon, C. Combes, C. Rey, *Chem. Rev.*, 2012, **112**, 5092-5120.

[2] D. Bazin, M. Daudon, *J. Phys. D: Appl. Phys.*, 2012, **45**, article no. 383001.

[3] L. N. Poloni, M. D. Ward, *Chem. Mater.*, 2014, **26**, 477-495.

[4] D. Bazin, M. Daudon, *Ann. Biol. Clin.*, 2015, **73**, 517-534.

[5] E. Tsolaki, S. Bertazzo, *Materials*, 2019, **12**, article no. 3126.

[6] D. Bazin, E. Letavernier, J. P. Haymann, V. Frochot, M. Daudon, *Ann. Biol. Clin.*, 2020, **78**, 349-362.

[7] D. Bazin, M. Daudon, V. Frochot, J.-Ph. Haymann, E. Letavernier, *C. R. Chim.*, 2022, **25**, no. S1, 133-147.

[8] A. Ben Lakhdar, M. Daudon, M. C. Matthieu, A. Kellum, C. Balleyguier, D. Bazin, *C. R. Chim.*, 2016, **19**, 1610-1624.

[9] R. Scott, C. Kendall, N. Stone, K. Rogers, *Sci. Rep.*, 2017, **7**, article no. 136.

[10] J. A. M. R. Kunitake, S. Choi, K. X. Nguyen, M. M. Lee, F. He, D. Sudilovsky, P. G. Morris, M. S. Jochelson, C. A. Hudis, D. A. Muller, P. Fratzl, C. Fischbach, A. Masi, L. A. Estroff, *J. Struct. Biol.*, 2018, **202**, 25-34.

[11] P. Dorfmüller, D. Bazin, S. Aubert, R. Weil, F. Brisset, M. Daudon, F. Capron, I. Brocheriou, *Cardiol. Res. Pract.*, 2010, **2010**, article no. 685926.

[12] R. Coscas, M. Bensussan, M.-P. Jacob, L. Louedec, Z. Massy, J. Sadoine, M. Daudon, C. Chaussain, D. Bazin, J.-B. Michel, *Atherosclerosis*, 2017, **259**, 60-67.

[13] A. P. Sage, Y. Tintut, L. L. Demer, *Nat. Rev. Cardiol.*, 2010, **7**, 528-536.

[14] X. Carpentier, M. Daudon, O. Traxer, P. Jungers, A. Mazouyes, G. Matzen, E. Véron, D. Bazin, *Urology*, 2009, **73**, 968-975.

[15] D. Bazin, G. André, R. Weil, G. Matzen, E. Véron, X. Carpentier, M. Daudon, *Urology*, 2012, **79**, 786-790.

[16] R. Flannigan, W. H. Choy, B. Chew, D. Lange, *Nat. Rev. Urol.*, 2014, **11**, 333-341.

[17] E. J. Espinosa-Ortiz, B. H. Eisner, D. Lange, R. Gerlach, *Nat. Rev. Urol.*, 2019, **16**, 35-53.

[18] M. Daudon, M. Petay, S. Vimont, A. Denizet, F. Tielens, J.-Ph. Haymann, E. Letavernier, V. Frochot, D. Bazin, *C. R. Chim.*, 2022, **25**, no. S1, 315-334.

[19] D. Bazin, R. J. Papoular, E. Elkaim, R. Weil, D. Thiaudière, C. Pisapia, B. Ménez, N. S. Hwang, F. Tielens, M. Livrozet, E. Bouderlique, J.-Ph. Haymann, E. Letavernier, L. Hennet, V. Frochot, M. Daudon, *C. R. Chim.*, 2022, **25**, no. S1, 343-354.

[20] P. Cochat, G. Rumsby, *New Engl. J. Med.*, 2013, **369**, 649-658.

[21] M. Daudon, P. Jungers, D. Bazin, *New Engl. J. Med.*, 2008, **359**, 100-102.

[22] A. Dessombz, E. Letavernier, J.-Ph. Haymann, D. Bazin, M. Daudon, *J. Urol.*, 2015, **193**, 1564-1569.

[23] J. R. M. Oliveira, M. F. Oliveira, *Sci. Rep.*, 2016, **6**, article no. 22961.

[24] E. Bouderlique, E. Tang, J. Perez, H.-K. Ea, F. Renaudin, A. Coudert, S. Vandermeersch, D. Bazin, J.-Ph. Haymann, C. Saint-Jacques, V. Frochot, M. Daudon, E. Letavernier, *C. R. Chim.*, 2022, **25**, no. S1, 393-405.

[25] D. Bazin, M. Rabant, J. Mathurin, M. Petay, A. Deniset-Besseau, A. Dazzi, Y. Su, E. P. Hessou, F. Tielens, F. Borondics, M. Livrozet, E. Bouderlique, J.-Ph. Haymann, E. Letavernier, V. Frochot, M. Daudon, *C. R. Chim.*, 2022, **25**, no. S1, 489-502.

[26] F. Meiouet, S. El Kabbaj, M. Daudon, *C. R. Chim.*, 2022, **25**, no. S1, 281-293.

[27] H. Colboc, Ph. Moguelet, E. Letavernier, V. Frochot, J.-F. Bernaudin, R. Weil, S. Rouzière, P. Seneth, C. Bachmeyeri, N. Laporte, I. Lucas, V. Descamps, R. Amodek, F. Brunet-Possentik, N. Kluger, L. Deschamps, A. Dubois, S. Reguer, A. Somogyi, K. Medjoubi, M. Refregiers, M. Daudon, D. Bazin, *C. R. Chim.*, 2022, **25**, no. S1, 445-476.

[28] G. Chebion, E. Bugni, V. Gerin, M. Daudon, V. Castiglione, *C. R. Chim.*, 2022, **25**, no. S1, 295-306.

[29] M. Daudon, V. Frochot, D. Bazin, P. Jungers, *Drugs*, 2018, **78**, 163-201.

[30] A. Trinchieri, *Arch. Ital. Urol. Androl.*, 1996, **68**, 203-250.

[31] M. Daudon, B. Knebelmann, *Rev. Prat.*, 2011, **61**, 372-378.

[32] I. Sorokin, C. Mamoulakis, K. Miyazawa, A. Rodgers, J. Talati, Y. Lotan, *World J. Urol.*, 2017, **35**, 1301-1320.

[33] Y. Liu, Y. Chen, B. Liao, D. Luo, K. Wang, H. Li, G. Zeng, *Asian J. Urol.*, 2018, **5**, 205-214.

[34] A. Trinchieri, *Clin. Cases Miner. Bone Metab.*, 2008, **5**, 101-106.

[35] M. Daudon, C. A. Bader, P. Jungers, *Scanning Microsc.*, 1993, **7**, 1081-1104.

[36] M. Daudon, *Arch. Pédiatr.*, 2000, **7**, 855-865.

[37] M. Daudon, P. Jungers, *Nephron Physiol.*, 2004, **98**, 31-36.

[38] M. Daudon, P. Jungers, D. Bazin, *AIP Conf. Proc.*, 2008, **1049**, 199-215.

[39] M. Daudon, H. Bouzidi, D. Bazin, *Urol. Res.*, 2010, **38**, 459-467.

[40] M. Daudon, A. Dessombz, V. Frochot, E. Letavernier, J.-Ph. Haymann, P. Jungers, D. Bazin, *C. R. Chim.*, 2016, **19**, 1470-1491.

[41] J. C. Williams Jr., G. Gambaro, A. Rodgers, J. Asplin, O. Bonny, A. Costa-Bauzá, P. M. Ferraro, G. Fogazzi, D. G. Fuster, D. S. Goldfarb, F. Grases, I. P. Heilberg, D. Kok, E. Letavernier, G. Lippi, M. Marangella, A. Nouvenne, M. Petrarulo, R. Siener, H.-G. Tiselius, O. Traxer, A. Trinchieri, E. Croppi, W. G. Robertson, *Urolithiasis*, 2021, **49**, 1-16.

[42] G. Herzberg, *Molecular Spectra and Molecular Structure. Vol. 2: Infrared and Raman Spectra of Polyatomic Molecules*, Van Nostrand, Reinhold, New York, 1945.

[43] H. Humecki, *Practical Applications of Infrared Microspectroscopy*, Marcel Dekker, Inc., New York, 1995.

[44] D. C. Fernandez, R. Bhargava, S. M. Hewitt, I. W. Levin, *Nat. Biotechnol.*, 2005, **23**, 469-474.

[45] L. M. Miller, P. Dumas, *Biochim. Biophys. Acta – Biomembr.*, 2006, **1758**, 846-857.

[46] L. Maurice-Estepa, P. Levillain, B. Lacour, M. Daudon, *Scand. J. Urol. Nephrol.*, 1999, **33**, 299-305.

[47] L. Estepa, M. Daudon, *Biospectroscopy*, 1997, **3**, 347-369.

[48] M. Daudon, D. Bazin, *C. R. Chim.*, 2016, **19**, 1416-1423.

[49] D. Bazin, E. Letavernier, J.-Ph. Haymann, F. Tielens, A. Kellum, M. Daudon, *C. R. Chim.*, 2016, **19**, 1548-1557.
[50] D. Nguyen Quy, M. Daudon, *Infrared et Raman Spectra of Calculi*, Elsevier, Paris, 1997.
[51] M. Daudon, D. Bazin, K. Adil, A. Le Bail, *Acta Crystallogr. E*, 2011, **67**, article no. o1458.
[52] A. Le Bail, D. Bazin, M. Daudon, A. Brochot, V. Robbez-Masson, V. Maisonneuve, *Acta Crystallogr. B*, 2009, **65**, 350-354.
[53] D. Bazin, M. Daudon, E. Elkaim, A. Le Bail, L. Smrcok, *C. R. Chim.*, 2016, **19**, 1535-1541.
[54] D. Bazin, Ch. Jouanneau, S. Bertazzo, Ch. Sandt, A. Dessombz, M. Réfrégiers, P. Dumas, J. Frederick, J.-Ph. Haymann, E. Letavernier, P. Ronco, M. Daudon, *C. R. Chim.*, 2016, **19**, 1439-1455.
[55] A. Dessombz, D. Bazin, P. Dumas, C. Sandt, J. Sule-Suso, M. Daudon, *PLoS One*, 2011, **6**, article no. e28007.
[56] C. Petibois, M. Piccinini, M. C. Guidi, A. Marcelli, *J. Synchrotron Radiat.*, 2010, **17**, 1-11.
[57] M. J. Nasse, M. J. Walsh, E. C. Mattson, R. Reininger, A. Kajdacsy-Balla, V. Macias, R. Bhargava, C. J. Hirschmugl, *Nat. Methods*, 2011, **8**, 413-416.
[58] A. M. Hanninen, R. C. Prince, R. Ramos, M. V. Plikus, E. O. Potma, *Biomed. Opt. Express*, 2018, **9**, 4807-4817.
[59] A. Centrone, *Annu. Rev. Anal. Chem.*, 2015, **8**, 101-126.
[60] G. L. Carr, *Rev. Sci. Instrum.*, 2001, **72**, article no. 1613.
[61] A. Dazzi, F. Glotin, R. Carminati, *J. Appl. Phys.*, 2010, **107**, article no. 124519.
[62] A. Dazzi, C. B. Prater, *Chem. Rev.*, 2017, **17**, 5146-5173.
[63] D. Fournier, F. Lepoutre, A. Boccara, *J. Phys.*, 1983, **44**, 479-482.
[64] Y. Luque, K. Louis, C. Jouanneau, S. Placier, E. Esteve, D. Bazin, E. Rondeau, E. Letavernier, A. Wolfromm, C. Gosset, A. Boueilh, M. Burbach, P. Frère, M.-C. Verpont, S. Vandermeersch, D. Langui, M. Daudon, V. Frochot, L. Mesnard, *J. Am. Soc. Nephrol.*, 2017, **28**, 1723-1728.
[65] E. Esteve, Y. Luque, J. Waeytens, D. Bazin, L. Mesnard, Ch. Jouanneau, P. Ronco, A. Dazzi, M. Daudon, A. Deniset-Besseau, *Anal. Chem.*, 2020, **92**, 7388-7392.
[66] E. Esteve, "Applications des outils physicochimiques à la physiologie et physiopathologie rénale", PhD Thesis, Sorbonne University, Paris, France, 2021.
[67] V. Castiglione, P.-Y. Sacré, E. Cavalier, P. Hubert, R. Gadisseur, E. Ziemons, *PLoS One*, 2018, **13**, article no. e0201460.
[68] I. Lucas, D. Bazin, M. Daudon, *C. R. Chim.*, 2022, **25**, no. S1, 83-103.
[69] S. Tamosaityte, M. Pucetaite, A. Zelvys, S. Varvuolyte, V. Hendrixson, V. Sablinskas, *C. R. Chim.*, 2022, **25**, no. S1, 73-82.
[70] M. Harada, K. Iwamoto, T. Kitamori, T. Sawada, *Anal. Chem.*, 1993, **65**, 2938-2940.
[71] M. Kansiz, C. Prater, E. Dillon, M. Lo, J. Anderson, C. Marcott, A. Demissie, Y. Chen, G. Kunkel, *Microsc. Today*, 2020, **28**, 26-36.
[72] D. Bazin, E. Bouderlique, M. Daudon, V. Frochot, J.-Ph. Haymann, E. Letavernier, F. Tielens, R. Weil, *C. R. Chim.*, 2022, **25**, no. S1, 37-60.
[73] D. Bazin, M. Daudon, *J. Spectral Imaging*, 2019, **8**, article no. a16.
[74] M. Daudon, D. Bazin, "New techniques to characterize kidney stones and Randall's plaque", in *Urolithiasis: Basic Science and Clinical Practice* (J. J. Talati, H. G. Tiselius, D. M. Albala, Z. Ye, eds.), Springer, Berlin, 2012, 683-707.
[75] M. Toplak, S. T. Read, C. Sandt, F. Borondics, *Cells*, 2021, **10**, article no. 2300.
[76] N. E. Olson, Y. Xiao, Z. Lei, A. P. Ault, *Anal. Chem.*, 2020, **92**, 9932-9939.
[77] N. Baden, H. Kobayashi, N. Urayama, *Int. J. Polym. Anal. Character.*, 2020, **25**, 1-7.
[78] V. Beltran, A. Marchetti, G. Nuyts, M. Leeuwestein, Ch. Sandt, F. Borondics, K. De Wael, *Angew. Chem. Int. Ed. Eng.*, 2021, **60**, 22753-22760.
[79] A. J. Wang, E. P. Dillon, S. Maharjan, K.-S. Liao, B. P. McElhenny, T. Tong, S. Chen, J. Bao, S. A. Curran, *Adv. Mater. Interfaces*, 2021, **8**, article no. 2001720.
[80] M. Kansiz, L. M. Dowling, I. Yousef, O. Guaitella, F. Borondics, J. Sulé-Suso, *Anal. Chem.*, 2021, **93**, 11081-11088.
[81] N. Gustavsson, A. Paulus, I. Martinsson, A. Engdahl, K. Medjoubi, K. Klementiev, A. Somogyi, T. Deierborg, F. Borondics, G. K. Gouras, O. Klementieva, *Light: Sci. Appl.*, 2021, **10**, article no. 151.
[82] G. Bakir, B. E. Girouard, R. Wiens, S. Mastel, E. Dillon, M. Kansiz, K. M. Gough, *Molecules*, 2020, **25**, article no. 4295.
[83] C. Lima, H. Muhamadali, Y. Xu, M. Kansiz, R. Goodacre, *Anal. Chem.*, 2021, **93**, 3082-3088.
[84] A. Spadea, J. Denbigh, M. J. Lawrence, M. Kansiz, P. Gardner, *Anal. Chem.*, 2021, **93**, 3938-3950.
[85] P. Zhao, Y. Zhao, L. Cui, Y. Tian, Z. Zhang, Q. Zhu, W. Zhao, *Sci. Total Environ.*, 2021, **775**, article no. 145846.
[86] D. Khanal, J. Zhang, W.-R. Ke, M. M. Banaszak Holl, H.-K. Chan, *Anal. Chem.*, 2020, **92**, 8323-8332.
[87] D. Zhang, C. Li, C. Zhang, M. N. Slipchenko, G. Eakins, J.-X. Cheng, *Sci. Adv.*, 2016, **2**, article no. e1600521.
[88] O. Klementieva, Ch. Sandt, I. Martinsson, M. Kansiz, G. K. Gouras, F. Borodics, *Adv. Sci.*, 2020, **7**, article no. 1903004.
[89] T. Echigo, M. Kimata, A. Kyono, M. Shimizu, T. Hatta, *Mineral. Mag.*, 2005, **69**, 77-88.
[90] M. Daudon, D. Bazin, G. Andre, P. Jungers, A. Cousson, P. Chevallier, E. Véron, G. Matzen, *J. Appl. Crystallogr.*, 2009, **42**, 109-115.
[91] I. Petit, G. D. Belletti, Th. Debroise, M. J. Llansola-Portoles, I. T. Lucas, C. Leroy, Ch. Bonhomme, L. Bonhomme-Coury, D. Bazin, M. Daudon, E. Letavernier, J. Ph. Haymann, V. Frochot, F. Babonneau, P. Quaino, F. Tielens, *Chemistry Select*, 2018, **3**, 8801-8812.
[92] C. Conti, L. Brambilla, Ch. Colombo, D. Dellasega, G. Diego Gatta, M. Realini, G. Zerbi, *Phys. Chem. Chem. Phys.*, 2010, **12**, 14560-14566.
[93] Q. Liu, S. Huang, J. P. Matinlinna, Zh. Chen, H. Pan, *BioMed Res. Int.*, 2013, **2013**, article no. 929748.
[94] Ch. Combes, S. Cazalbou, Ch. Rey, *Minerals*, 2016, **6**, 1-25.
[95] D. Bazin, C. Chappard, C. Combes, X. Carpentier, S. Rouzière, G. André, G. Matzen, M. Allix, D. Thiaudière, S. Reguer, P. Jungers, M. Daudon, *Osteoporos. Int.*, 2009, **20**, 1065-1075.
[96] X. Carpentier, D. Bazin, P. Jungers, S. Reguer, D. Thiaudière, M. Daudon, *J. Synchrotron. Radiat.*, 2010, **17**, 374-379.
[97] J. Mathurin, A. Deniset-Besseau, D. Bazin, E. Dartois, M. Wagner, A. Dazzi, *J. Appl. Phys.*, 2022, **131**, article no. 010901.

[98] T. Alelign, B. Petros, *Adv. Urol.*, 2018, **2018**, article no. 3068365.
[99] F. L. Coe, A. Evan, E. Worcester, *J. Clin. Investig.*, 2005, **115**, 2598-2608.
[100] A. Guerra, A. Ticinesi, F. Allegri, S. Pinelli, R. Aloe, T. Meschi, *Urolithiasis*, 2020, **48**, 271-279.
[101] T. Debroise, T. Sedzik, J. Vekeman, Y. Y. Su, Ch. Bonhomme, F. Tielens, *Cryst. Growth Design*, 2020, **20**, 3807-3815.
[102] M. Shepelenko, Y. Feldman, L. Leiserowitz, L. Kronik, *Cryst. Growth Design*, 2020, **20**, 858-865.
[103] A. V. Kustov, A. I. Strelnikov, *Urol. J.*, 2018, **15**, 87-91.
[104] W. Zhao, N. Sharma, F. Jones, P. Raiteri, J. D. Gale, R. Demichelis, *Cryst. Growth Design*, 2016, **16**, 5954-5965.
[105] A. Frey-Wyssling, *Am. J. Bot.*, 1981, **68**, 130-141.
[106] A. Thomas, E. Rosseeva, O. Hochrein, W. Carillo-Cabrera, P. Simon, P. Duchstein, D. Zahn, R. Kniep, *Chem. Eur. J.*, 2012, **18**, 4000-4009.
[107] A. Gehl, M. Dietzsch, M. Mondeshki, S. Bach, T. Häger, B. Barton, U. Kolb, W. Tremel, *Chem. Eur. J.*, 2015, **21**, 18192-18201.
[108] M. Hajira, R. Grafb, W. Tremel, *Chem. Commun.*, 2014, **50**, 6534-6536.
[109] D. Bazin, C. Leroy, F. Tielens, Ch. Bonhomme, L. Bonhomme-Coury, F. Damay, D. Le Denmat, J. Sadoine, J. Rode, V. Frochot, E. Letavernier, J.-Ph. Haymann, M. Daudon, *C. R. Chim.*, 2016, **19**, 1492-1503.
[110] M. Daudon, E. Letavernier, V. Frochot, J.-Ph. Haymann, D. Bazin, P. Jungers, *C. R. Chim.*, 2016, **19**, 1504-1513.
[111] M. Daudon, *Ann. Urol.*, 2005, **39**, 209-231.
[112] R. C. Walton, J. P. Kavanagh, B. R. Heywood, P. N. Rao, *J. Cryst. Growth*, 2005, **284**, 517-529.
[113] M. Daudon, C. A. Bader, P. Jungers, *Scanning Microsc.*, 1993, **7**, 1081-1104.
[114] M. Daudon, P. Junger, D. Bazin, *New Engl. J. Med.*, 2008, **359**, 100-102.
[115] A. Lionet, M. Haeck, A. Garstka, V. Gnemmi, D. Bazin, E. Letavernier, J.-Ph. Haymann, Ch. Noel, M. Daudon, *C. R. Chim.*, 2016, **19**, 1542-1547.
[116] P. Cartier, M. Hamet, *Clin. Chim. Acta*, 1968, **20**, 205-214.
[117] G. Bollée, C. Dollinger, L. Boutaud, D. Guillemot, A. Bensman, J. Harambat, P. Deteix, M. Daudon, B. Knebelmann, I. Ceballos-Picot, *J. Am. Soc. Nephrol.*, 2010, **21**, 679-688.
[118] B. Benedetto, R. Madden, A. Kurbanov, G. Braden, J. Freeman, G. S. Lipkowitz, *Am. J. Kidney Dis.*, 2001, **37**, E37.1-E37.4.
[119] K. H. Fye, A. Sahota, D. C. Hancock, A. B. Gelb, J. Chen, J. W. Sparks, R. K. Sibley, J. A. Tischfield, *Arch. Internat. Med.*, 1993, **153**, 767-770.
[120] D. Glicklich, H. E. Gruber, A. J. Matas, V. A. Tellis, G. Karwa, K. Finley, C. Salem, R. Soberman, J. Seegmiller, *Q. J. Med.*, 1988, **68**, 785-793.
[121] L. Estepa-Maurice, C. Hennequin, C. Marfisi, C. Bader, B. Lacour, M. Daudon, *Am. J. Clin. Pathol.*, 1996, **105**, 576-582.
[122] J. C. Williams Jr, J. E. Lingeman, M. Daudon, D. Bazin, *C. R. Chim.*, 2022, **25**, no. S1, 61-72.
[123] P. Ruegsegger, B. Koller, R. Muller, *Calcif. Tissue Int.*, 1996, **58**, 24-29.
[124] C. A. Zarse, J. A. McAteer, A. J. Sommer, S. C. Kim, E. K. Hatt, J. E. Lingeman, A. P. Evan, J. C. Williams Jr, *BMC Urol.*, 2004, **4**, article no. 15.
[125] J. C. Williams Jr, J. A. McAteer, A. P. Evan, J. E. Lingeman, *Urol. Res.*, 2010, **38**, 477-484.
[126] J. Harper, J. Lingeman, R. Sweet, I. Metzler, P. Sunaryo, J. C. Williams, A. Maxwell, J. Thiel, B. Cunitz, B. Dunmire, M. Bailey, M. D. Sorensen, *J. Urol.*, 2022, **207**, 1067-1076.
[127] A. Randall, *Ann. Surg.*, 1937, **105**, 1009-1027.
[128] M. Daudon, O. Traxer, P. Jungers, D. Bazin, *AIP Conf. Proc.*, 2007, **900**, 26-34.
[129] M. Daudon, P. Jungers, D. Bazin, *AIP Conf. Proc.*, 2008, **1049**, 199-215.
[130] M. Daudon, O. Traxer, J. C. Williams, D. Bazin, "Randall's plaques", in *Urinary Tract Stone Disease*, Springer, Berlin, 2010.
[131] M. Daudon, D. Bazin, E. Letavernier, *Urolithiasis*, 2015, **43**, 5-11.
[132] E. Letavernier, D. Bazin, M. Daudon, *C. R. Chim.*, 2016, **19**, 1456-1460.
[133] S. Ohman, L. Larsson, *Med. Hypotheses*, 1992, **39**, 360-363.
[134] A. Evan, J. Lingeman, F. L. Coe, E. Worcester, *Kidney Int.*, 2006, **69**, 1313-1318.
[135] M. Daudon, D. Bazin, *J. Phys.: Conf. Ser.*, 2013, **425**, article no. 022006.
[136] E. Letavernier, S. Vandermeersch, O. Traxer, M. Tligui, L. Baud, P. Ronco, J.-Ph. Haymann, M. Daudon, *Medicine (Baltimore)*, 2015, **94**, article no. e566.
[137] D. Bazin, E. Letavernier, Ch. Jouanneau, P. Ronco, Ch. Sandt, P. Dumas, G. Matzen, E. Véron, J.-Ph. Haymann, O. Traxer, P. Conort, M. Daudon, *C. R. Chim.*, 2016, **19**, 1461-1469.
[138] C. Verrier, D. Bazin, L. Huguet, O. Stéphan, A. Gloter, M.-Ch. Verpont, V. Frochot, J.-Ph. Haymann, I. Brocheriou, O. Traxer, M. Daudon, E. Letavernier, *J. Urol.*, 2016, **196**, 1566-1574.
[139] E. Letavernier, G. Kauffenstein, L. Huguet, N. Navasiolava, E. Bouderlique, E. Tang, L. Delaitre, D. Bazin, M. de Frutos, C. Gay, J. Perez, M. C. Verpont, J.-Ph. Haymann, V. Pomozi, J. Zoll, O. Le Saux, M. Daudon, G. Leftheriotis, L. Martin, *J. Am. Soc. Nephrol.*, 2018, **29**, 2337-2347.
[140] C. Gay, E. Letavernier, M.-Ch. Verpont, M. Walls, D. Bazin, M. Daudon, N. Nassif, O. Stephan, M. de Frutos, *ACS Nano*, 2020, **14**, 1823-1836.
[141] S. R. Khan, B. K. Canales, P. R. Dominguez-Gutierrez, *Nat. Rev. Nephrol.*, 2021, **17**, 417-433.
[142] S. R. Khan, *C. R. Chim.*, 2022, **25**, no. S1, 355-372.
[143] E. Van de Perre, D. Bazin, V. Estrade, E. Bouderlique, K. M. Wissing, M. Daudon, E. Letavernier, *C. R. Chim.*, 2022, **25**, no. S1, 373-391.
[144] X. Carpentier, D. Bazin, Ch. Combes, A. Mazouyes, S. Rouzière, P.-A. Albouy, E. Foy, M. Daudon, *J. Trace Elem. Med. Biol.*, 2011, **25**, 160-165.
[145] R. F. Cox, M. P. Morgan, *Bone*, 2013, **53**, 437-445.
[146] Y. V. Nalawade, *Indian J. Radiol. Imaging*, 2009, **19**, 282-286.
[147] M. P. Morgan, M. M. Cooke, G. M. McCarthy, *J. Mammary Gland Biol. Neoplasia*, 2005, **10**, 181-187.
[148] S. O'Grady, M. P. Morgan, *BBA - Rev. Cancer*, 2018, **1869**, 310-320.
[149] P. Henrot, A. Leroux, C. Barlier, P. Génin, *Diagn. Interv. Imaging*, 2014, **95**, 141-152.

[150] K. S. Shin, M. Laohajaratsang, S. Men, B. Figueroa, S. M. Dintzis, D. Fu, *Theranostics*, 2020, **10**, 5865-5878.
[151] M. Petay, M. Cherfan, E. Bouderlique, S. Reguer, J. Mathurin, A. Dazzi, M. l'Heronde, M. Daudon, E. Letavernier, A. Deniset-Besseau, D. Bazin, *C. R. Chim.*, 2022, **25**, no. S1, 553-576.
[152] S. Gosling, D. Calabrese, J. Nallala, Ch. Greenwood, S. Pinder, L. King, J. Marks, D. Pinto, Th. Lynch, I. D. Lyburn, E. S. Hwang, Grand Challenge PRECISION Consortium, K. Rogers, N. Stone, *Analyst*, 2022, **147**, 1641-1654.
[153] M. J. Radi, *Arch. Pathol. Lab. Med.*, 1989, **113**, 1367-1369.
[154] C. Tornos, E. Silva, A. El-Naggar, K. P. Pritzker, *Am. J. Surg. Pathol.*, 1990, **14**, 961-968.
[155] L. D. Truong, J. Cartwright, L. Alpert, *Mod. Pathol.*, 1992, **5**, 146-152.
[156] H. Poggi, H. C. W. Skinner, J. J. Ague, D. Carter, *Am. Mineral.*, 1998, **83**, 1122-1126.
[157] R. Baker, K. D. Rogers, N. Shepherd, N. Stone, *Br. J. Cancer*, 2010, **103**, 1034-1039.
[158] O. Hassler, *Cancer*, 1969, **23**, 1103-1109.
[159] S. Gosling, R. Scott, C. Greenwood, P. Bouzy, J. Nallala, I. D. Lyburn, N. Stone, K. Rogers, *J. Mammary Gland Biol. Neoplasia*, 2019, **334**, 333-342.
[160] E. Tsolaki, W. Doran, L. Magnani, A. Olivo, I. K. Herrmann, S. Bertazzo, 2021, bioRxiv preprint, https://doi.org/10.1101/2020.04.29.067660.
[161] R. Vanna, C. Morasso, B. Marcinnò, F. Piccotti, E. Torti, D. Altamura, S. Albasini, M. Agozzino, L. Villani, L. Sorrentino, O. Bunk, F. Leporati, C. Giannini, F. Cors, *Cancer Res.*, 2020, **80**, 1762-1772.

Comptes Rendus
Chimie
2022, Vol. 25, Special Issue S1, p. 133-147
https://doi.org/10.5802/crchim.96

Microcrystalline pathologies: Clinical issues and nanochemistry / *Pathologies microcristallines : questions cliniques et nanochimie*

Crystal size in μcrystalline pathologies and its clinical implication

Dominique Bazin [*, a], **Vincent Frochot** [b, c], **Jean-Philippe Haymann** [b, c], **Emmanuel Letavernier** [b, c] **and Michel Daudon** [b, c]

[a] Université Paris-Saclay, CNRS, Institut de Chimie Physique, 91405 Orsay cedex, France

[b] AP-HP, Hôpital Tenon, Service des explorations fonctionnelles, 75020 Paris, France

[c] Unité INSERM UMR S 1155, UPMC, Hôpital Tenon, 75020 Paris, France

E-mails: dominique.bazin@universite-paris-saclay.fr (D. Bazin), vincent.frochot@aphp.fr (V. Frochot), Jean-Philippe.haymann@aphp.fr (J.-P. Haymann), emmanuel.letavernier@aphp.fr (E. Letavernier), michel.daudon@aphp.fr (M. Daudon)

Abstract. Chemical composition is not the only information establishing a significant link between kidney stones and the pathology which induces urolithiasis. Structural parameters such as morphology and crystal and crystallite size are also of primary importance. In this contribution, we would like to assess the relationship of crystal size of different chemical phases with the pathology underlying such calcifications. Based on literature as well as on some of our measurements, we will appreciate the value of this structural parameter for different crystalline species in various clinical or biological conditions and in helping the clinician, especially to understand why bacterial imprints in infection-related stones are only visible in calcium phosphate apatite deposits.

Keywords. Lithiasis, X-ray diffraction, Infection, Bacteria, Imprints.
Published online: 28 July 2021, Issue date: 1 September 2022

1. Introduction

Microcrystalline pathology is an exciting research field [1–10] in which most investigations have been performed on the mineral component of the biological deposits induced by the pathology. With respect to urolithiasis, the morphoconstitutional model defines the morphology of the kidney stones as one of the key parameters to establish a link between the kidney stone and the pathology which has induced it [11–18].

For several years, we have been describing the morphology and the size of the crystallites and nanocrystals which constitute the kidney stone (KS). From a physicochemical point of view, we used the terms "nanocrystals" and "crystallites" according to Van Meerssche and Feneau-Dupont [19] in order to define the structural hierarchy of these mineral concretions. Crystallites (measuring typically some tens of micrometers) are made of a collection of crystals (measuring typically some hundreds of nanometers).

* Corresponding author.

At the mesoscopic scale, the morphology and size of crystallites can be determined by scanning electron microscopy (SEM) [6,20,21], while at the nanometric scale, the size of crystals is determined by X-ray scattering [22–24], powder neutron diffraction (PND) [25,26], X-ray absorption spectroscopy [27–31] or by transmission electron microscopy [32–36].

In this contribution, we would like to review the crystal size of the principal chemical compounds identified in kidney stones namely calcium oxalate, calcium phosphate, uric acid, struvite, and cystine. This structural parameter is of primary importance in the case of pathological calcifications. For example, it is related to their toxicity [37–39]. The cooperative effects of Na^+ and citrates on the dissolution of calcium oxalate crystals can be also be discussed in terms of this structural parameter [40].

We have selected papers which have focussed on measurement of crystal size and discuss the implication of this structural parameter in medical research.

2. Determination of crystal size

Numerous excellent publications and books have been dedicated to X-ray scattering [22–24,41–44]. Scattering occurs whenever electromagnetic radiation interacts with matters. As underlined by Woolfson [41], X-ray scattering can be thought of as due to the absorption of incident radiation with subsequent re-emission. Such re-emission consists of two components. One has the same wavelength (equivalent to energy) as the incident radiation and is called Thomson scattering. The second one has a longer wavelength (or a lower energy) than that of the incident radiation with a difference of wavelength depending on the angle of scatter. Here, we will focus on the Thomson scattering.

In the case of a crystal, the scattered radiation from each atom is coherent with respect to that from all others (Figure 1).

The Debye scattering equation elegantly relates the scattering intensity to the geometry of the crystal [45–52].

$$I(q) = \sum_i \sum_j f_i(q) f_j(q) \sin(qR_{ij})/qR_{ij}$$

In this equation, $I(q)$ is the angle dependent intensity (q is the momentum transfer, i.e. $q = 4\pi \sin\theta/\lambda$) from Thomson scattering, the sums

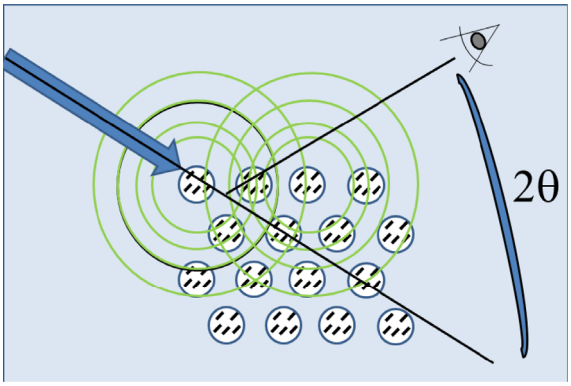

Figure 1. As pointed out by Cassetta [42], when the electromagnetic wave (blue arrow) interacts with atomic electrons, a secondary wave (with the same wavelength) is scattered in all directions by the atom itself (green circles). The secondary waves produced by the three-dimensional regular array of atoms give rise to interference phenomena which can be destructive or constructive depending on the disposition of the atoms relative to the incident radiation. At the angle of 2θ, constructive interference X-ray scattering peaks are observed.

over i and j are over all the atoms, R_{ij} is the distance between the atoms i and j, and f_i and f_j are the angle dependent atomic scattering factors. This equation neglects thermal disorder as well as Compton scattering, as a first approximation. A significant point relevant to this equation is the fact that the scattering factors, which take into account the interaction between X-rays and matter, have been tabulated by Sasaki [53] and that R_{ij} can be obtained easily from a structural model of the crystal [54–64].

Figure 2 shows the use of the Debye scattering equation to calculate the scattering intensity corresponding to face centered cubic (fcc) nanometer-scale platinum clusters of different sizes (represented by different numbers, N, of atoms).

For a cluster containing 13 atoms, the scattering peaks are very broad, exemplifying the fact that X-ray scattering is best suited for materials with long range order. Furthermore the figure also shows that the scattering peak width depends significantly on the size of the cluster.

For a nanometer-scale cluster with a “spherical”

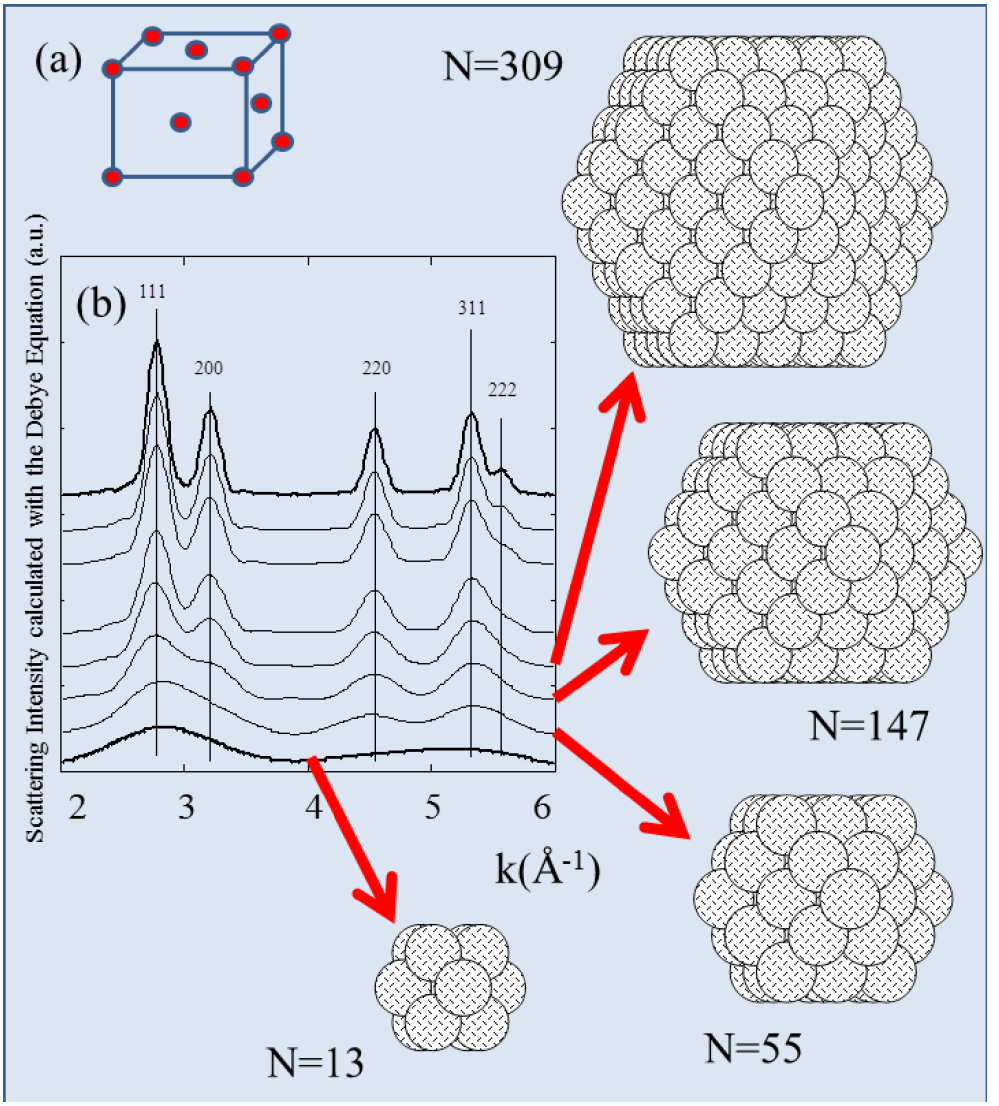

Figure 2. (a) Simple scheme for a fcc arrangement of atoms. (b) Diffraction diagram calculated for fcc nanometer-scale clusters of *N* platinum atoms.

morphology the amplitude of all the intensities are equivalent (Figure 2). This is not the case for asymmetric structures such as nanotubes (Figure 3). X-ray diffraction is thus very sensitive to the size and the morphology of nanometer-scale clusters, especially for monodisperse population.

Miranda and Sasaki [65] pointed out that the Scherrer or Debye–Scherrer equation [66,67] can be used to obtain nanocrystal size (D) from X-ray powder diffraction measurements by a simple relationship between D, the full width at half-maximum (Θ) of the diffraction peak, the Bragg angle (θ_B) and the wavelength of the radiation (λ) [68]. k is a dimensionless number of the order of unity [69], known as the Scherrer constant, after Scherrer [66] who first used this method of estimating crystallite sizes.

$$\Theta \approx k\lambda / D\cos(\theta_B)$$

This equation assumes that the incoming scattered radiation does not interact with other atoms ("kinematical" or "geometrical" theory of X-ray diffraction). Bear in mind that the Scherrer

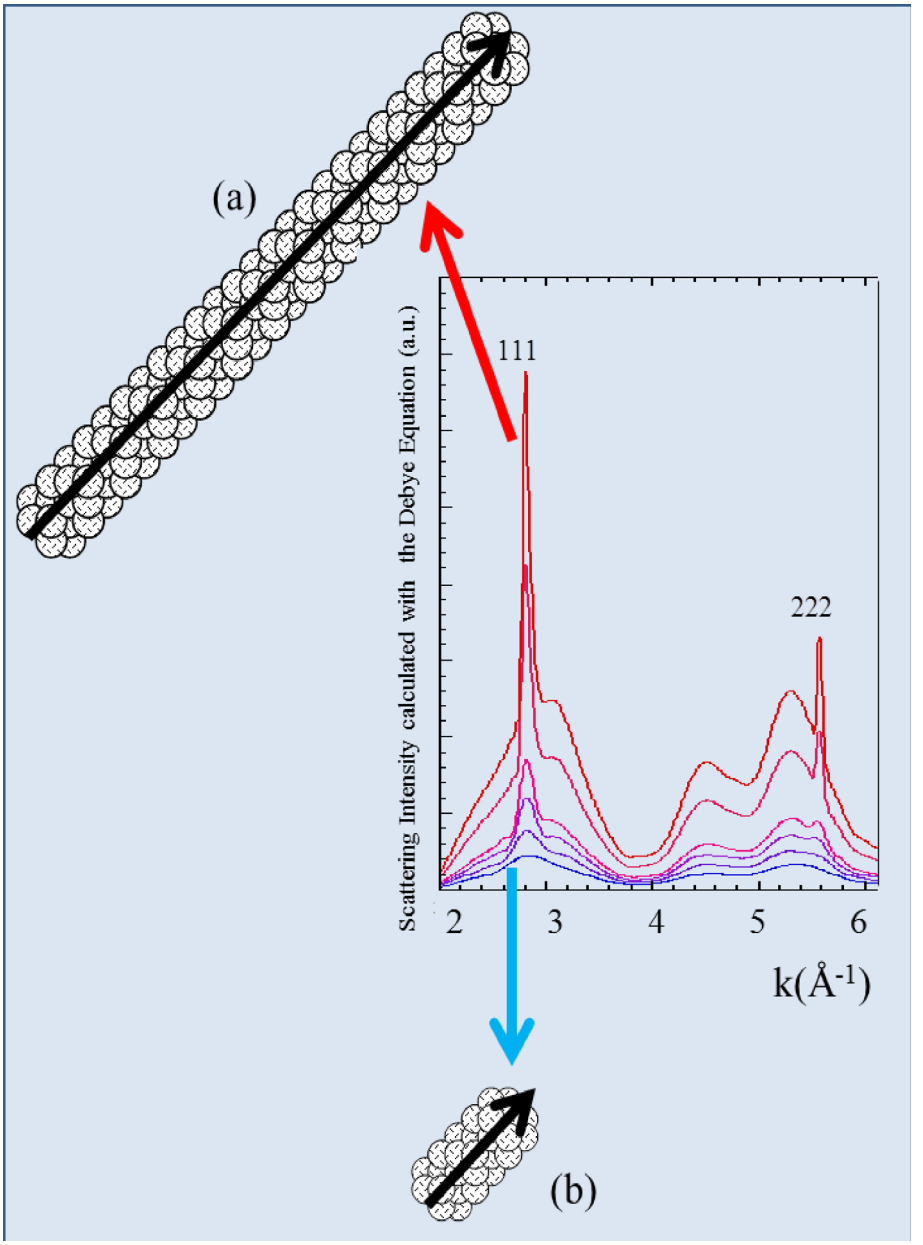

Figure 3. The diffraction peaks of a nanotube display different widths (a) and (b). The 111 direction which corresponds to the long axis of the nanotube is associated with the sharpest diffraction peak.

equation does not take into account the type or scattering power of the atoms, the crystal symmetry, or the reflection used. Despite all the simplifications, the size of nanometer crystals yielded is very similar to those obtained by other techniques. Londoño-Restrepo *et al.* [70] have measured the nanocrystal sizes obtained by the analysis of X-ray scattering diagrams using Scherrer's equation and the analysis of images by High Resolution Transmission Electron Microscopy. The nanocrystal sizes for raw samples obtained by both methods are mutually consistent, which confirms that Scherrer's

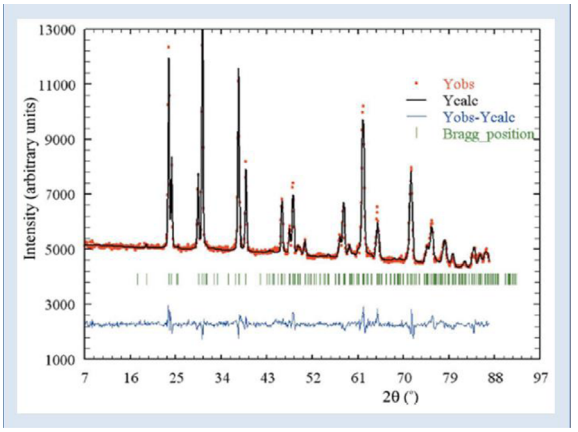

Figure 4. Final refinement, with experimental (circles), calculated (dashes), and difference PND patterns of the sample T11283. Tick marks below the profiles indicate the peak positions of allowed Bragg reflections for whewellite [71].

equation is an excellent tool to determine the size for nanocrystals. There is also excellent agreement between theoretical calculations of the scattering intensity by nanometer-scale clusters using the Debye equation [45–52] and the Scherrer law.

3. The case of calcium oxalate monohydrate KS

According to the morphoconstitutional model [11–18], five main subtypes, namely Ia, Ib, Ic, Id and Ie of calcium oxalate monohydrate kidney stones exist. All have been investigated by SEM and Neutron Diffraction or Powder Neutron Diffraction (PND) [71]. Neutrons are electrically neutral and interact only weakly with matter, and thus have a penetration depth of several centimeters [72]. In Figure 4, we show the final refinement, with experimental (circles), calculated (dashes), and difference PND patterns of the sample N11283. The mean sizes of the nanocrystals in these five subtypes (range 75–125 nm) were 107 nm (Ia), 80 nm (Ib), 110 nm (Ic), 90 nm (Ic) and 105 nm (Ie). These values are consistent with the investigation of Uvarov *et al.* [73]. If the crystal sizes are similar but the subtypes are different, the structural characteristics of the crystallites differ considerably [74]. Figure 5 shows the distinctive morphology of the calcium oxalate form crystallites for Ia (a), Ic (b) and Ie (c).

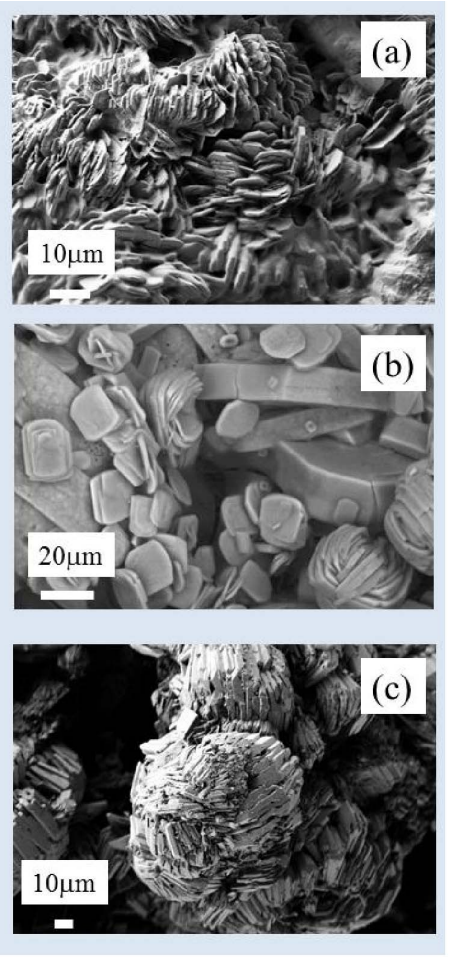

Figure 5. Peculiar morphology for COM crystallites in the case of Ia (a), Ic (b) and Ie (c) subtype (hyperoxaluria).

4. The case of calcium oxalate dihydrate (COD) crystals

Calcium oxalate crystals found in urine samples of stone formers range from 0.5 to 85 μm in size. Indeed, crystal size seems to be related to urine biochemistry. As shown in Figure 6, we found that among 5427 urine samples containing COD crystals, the mean size of the crystals is slightly increasing according to the calcium oxalate molar product (pCaOx). By contrast, the maximal size measured for COD crystals in urine is tenfold higher when pCaOx increased from 2.28 to 4.26 $(mmol/l)^2$.

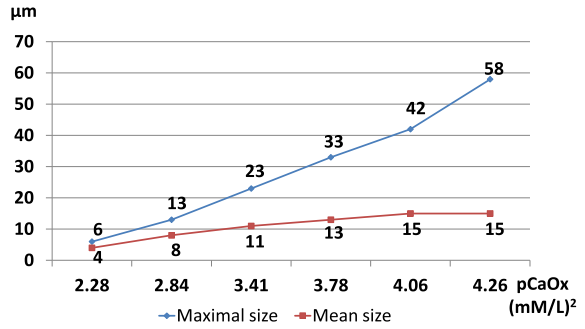

Figure 6. Size of calcium oxalate dihydrate crystals found in urine according to the calcium oxalate molar product.

5. The case of calcium phosphate apatite KS

Calcium phosphate in the form of carbapatite (CA) is a very common crystalline phase in urinary stones. Taking into account a large data bank including 50,000 stones acquired over the past three decades, CA has been identified by selective infrared analysis in 80% of all stones in both sexes, in most cases as a minor component [75]. It is worth underlining that despite its low proportion, CA is often clinically relevant as an initiating phase of the lithogenic process, as observed in stones developed from a Randall's plaque [76–81].

XRD as well as PND experiments have been performed on CA typical of physiological (bones) as well as pathological (Randall's plaque) calcifications [85–87]. Moreover, using atomic force microscopy, Eppell *et al.* [82] have obtained direct three-dimensional visual evidence of the size and shape of native protein-free mineralites isolated from mature bovine bone. Data analysis show that approximately 98% of the crystals are less than 2 nm thick displaying a plate-like habit. In Figure 7, the authors contrast the thicknesses (a), the widths (b), and the lengths (c), of the small mineralites.

These structural characteristics are consistent with our PND (Figure 8) and XRD experiments (Figure 9). Figure 8 illustrates several kinds of samples [83]. High temperature calcinated stoichiometric synthetic hydroxyapatites are characterized by a neutron diffraction diagram with sharp diffraction peaks because the size of the crystal is typically around a few micrometers (see Figure 2 for rationalization). In the case of synthetic nanocrystalline

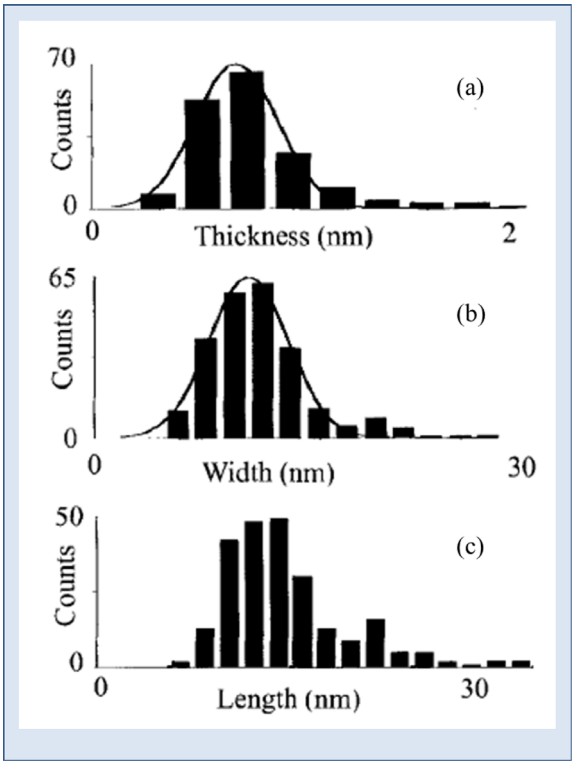

Figure 7. Histograms of AFM assessed dimensions of small protein-free mineralites from bone. The dimensions were normally distributed: best-fit Gaussians were superimposed on each histogram: (a) thicknesses (b) widths (c) lengths [82].

apatites, the diffraction peak widths are more significant because the size of the crystals is around several nanometers, except the 002 diffraction peak which indicates the anisotropy of the platelet-like nanocrystals of all these compounds. Finally, PND diagrams of physiological apatites are very similar to those of synthetic nanocrystalline apatites [88–91].

At the micrometer scale, SEM shows that the plate-like crystals are agglomerated and appear as spherical structures (Figure 9).

6. The case of struvite KS

Struvite (magnesium ammonium phosphate hexahydrate) stones form as a result of UTI (Urinary Tract Infection) by urease-producing pathogens and are thus often referred to as infection stones [92–96]. As pointed out by Flannigan *et al.* [93], struvite

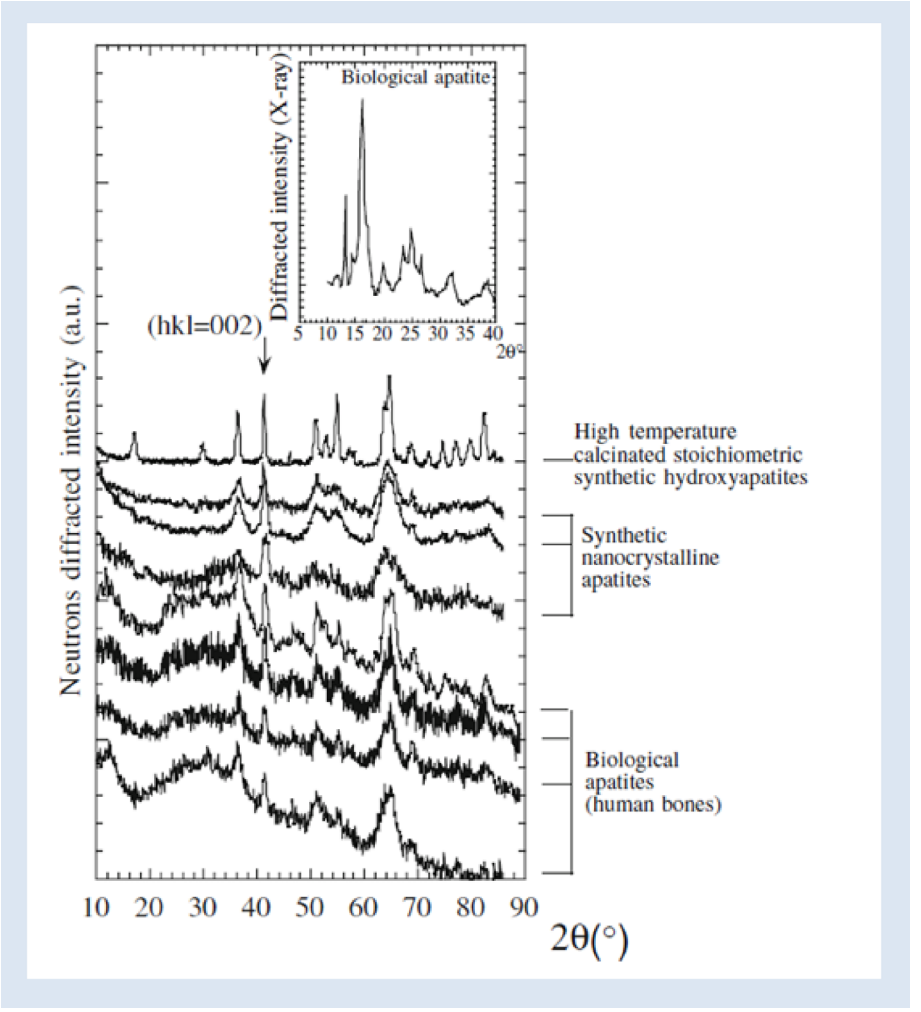

Figure 8. Neutron diffractograms of three families of apatite: high temperature calcinated synthetic apatite, room-temperature synthetic apatites and biological apatites (bones). The insert shows a corresponding X-ray diffractogram [83].

stone formation is exclusively associated with both gram-positive and gram-negative urease-producing species.

To explain the absence of bacterial imprints at the surface of struvite crystallites [84,97], PND experiments have been performed. As Figure 10 shows, the diffraction peaks of the struvite stone (stone T33776) are significantly sharper than those of nanocrystalline CA (stone T21934), indicating that the size of struvite crystals is much more significant than that of CA crystals. The data analysis indicates a struvite crystal mean size of 250 nm±25 nm, close to the maximum value that can be measured with our devices.

Note that, at the micrometer scale, struvite crystallites (Figure 11) display a typical specific 3-branch star surface morphology, in agreement with previous studies [98–100].

7. The case of whitlockite KS

Among phosphates, the species most frequently associated with infection are whitlockite [101,102], especially in women, and struvite in both male and female patients ($p < 0.0001$ vs. calcium oxalates in both sexes). Moreover calcium phosphate stones containing more than 30% whitlockite are associated with UTI in 81% of cases.

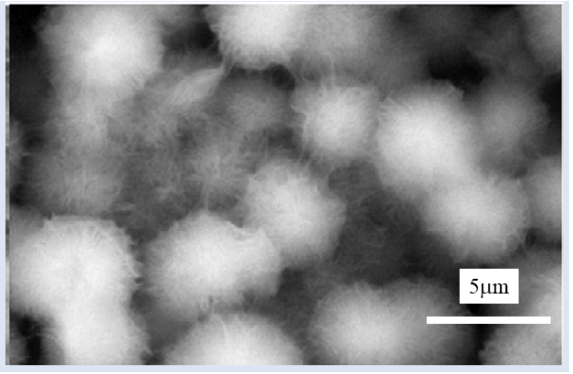

Figure 9. SEM of spherical CA entities in a kidney stone.

Recently, we have performed a set of X-ray scattering experiments using synchrotron radiation as a probe on the CRISTAL beamline of the Soleil synchrotron [103]. Thanks to recent advances [104,105] it was possible to perform a complete Rietveld analysis to obtain crystal sizes of whitlockite in different kidney stones [106]. The results are summarized in Table 1.

The average is around 185 nm, a much more significant value than reported for CA but quite similar to those of other chemical phases.

At the micrometer scale, whitlockite pseudo cubic crystallites are observed by SEM, a morphology consistent with their crystallographic structure [106,107].

8. The case of uric acid KS

As observed by Kenny and Goldfarb [108], with the proportion of obese Americans increasing and the association of obesity with low urine pH, uric acid nephrolithiasis is of paramount importance to the nephrologist, rheumatologist, and internist. Regarding prevalence, roughly 10% of stones in the United States are uric acid [109]. Between 1996 and 2007, a significant increase in the incidence of kidney stones in the pediatric population has been observed and such increases seem to be linked to the concomitant rise in obesity [110,111].

In a recent investigation, we have considered uric acid anhydrous (UAA) kidney stones and have measured their crystal size by neutron diffraction (Figure 13) [112].

Table 1. Whitlockite crystal size for different kidney stones as measured by synchrotron XRD

Kidney stone	Crystal size
T32616	290 nm ± 10 nm
T38952	90 nm ± 10 nm
T43068	30 nm ± 10 nm
T43736	250 nm ± 10 nm
T45449	330 nm ± 10 nm
T51263	330 nm ± 10 nm
T52975	130 nm ± 10 nm
T55785	190 nm ± 10 nm
T74647	90 nm ± 10 nm
T74808	120 nm ± 10 nm

This structural parameter was significantly different between male and female patients (84.7 ± 5.3 nm vs. 140.2 ± 6.7 nm, $p = 0.000003$). One of the striking points of this investigation is the fact that when type 2 diabetes develops, this structural difference between male and female vanished (76.1 ± 3.9 nm vs. 78.8 ± 4.2 nm, not significant).

Finally, on Figure 14, we can see a specific structure corresponding to the phase conversion between the two uric acid species (from dihydrate to anhydrous). Such observation is in line with the publication of Grases *et al.* [114] which has described the composition and structure of a set of uric acid stones and considers in vitro investigation of the crystallization behavior of uric acid.

9. The case of cystine KS

Cystinuria, an inheritable autosomal recessive disorder of amino acid transport, affects the epithelial cells of the renal tubules as well as the gastrointestinal tract [115–117]. This genetic pathology is characterized by abnormal concentrations of cystine and the other dibasic amino acids in the urine, leading to the formation of cystine renal stones because of the low solubility of cystine in urine [118,119]. It is the most frequent genetic cause of stone formation. Although two genes have been identified as causing this disease (SLC3A1 and SLC7A9), other unknown genes may also be involved in cystinuria [120,121].

The goal of the neutron scattering experiments (Figure 15) we have performed on cystine kidney

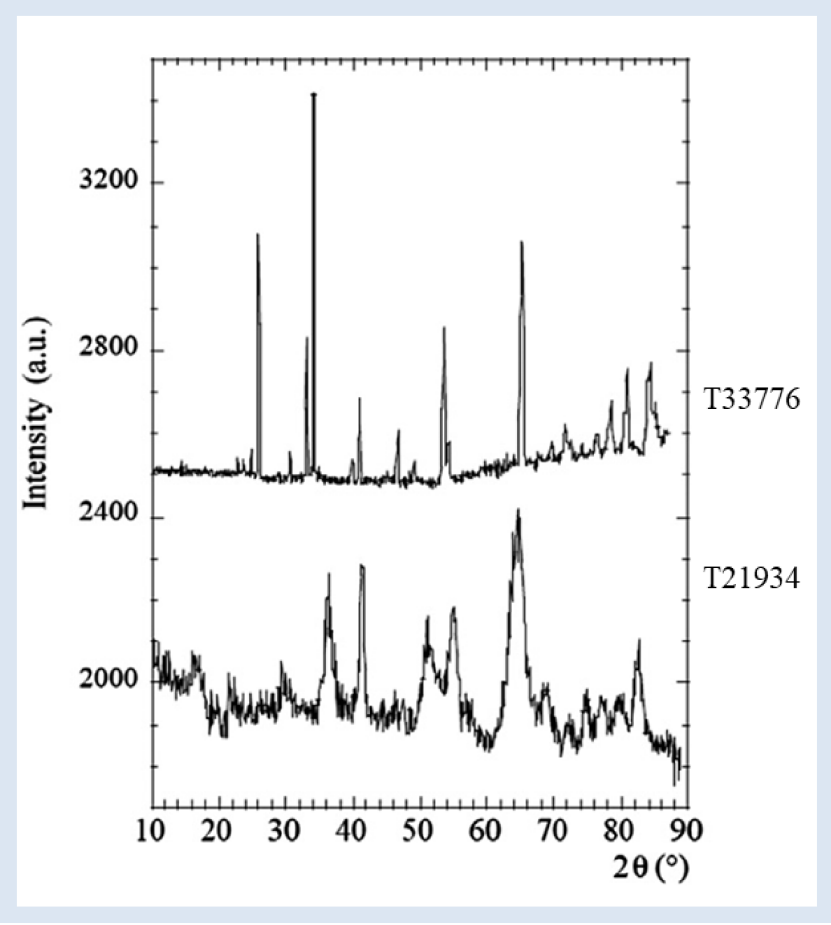

Figure 10. Neutron diffraction diagrams [84] collected for selected samples (T33776: struvite stone, T21934: calcium carbonated apatite stone).

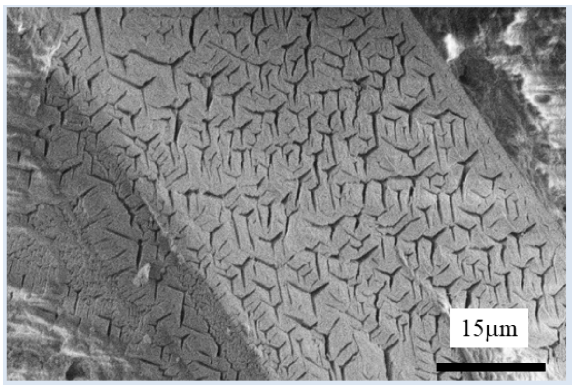

Figure 11. Typical morphologic features of struvite crystallites. Note the absence of bacterial imprints [84].

Figure 12. SEM images of whitlockite crystallites.

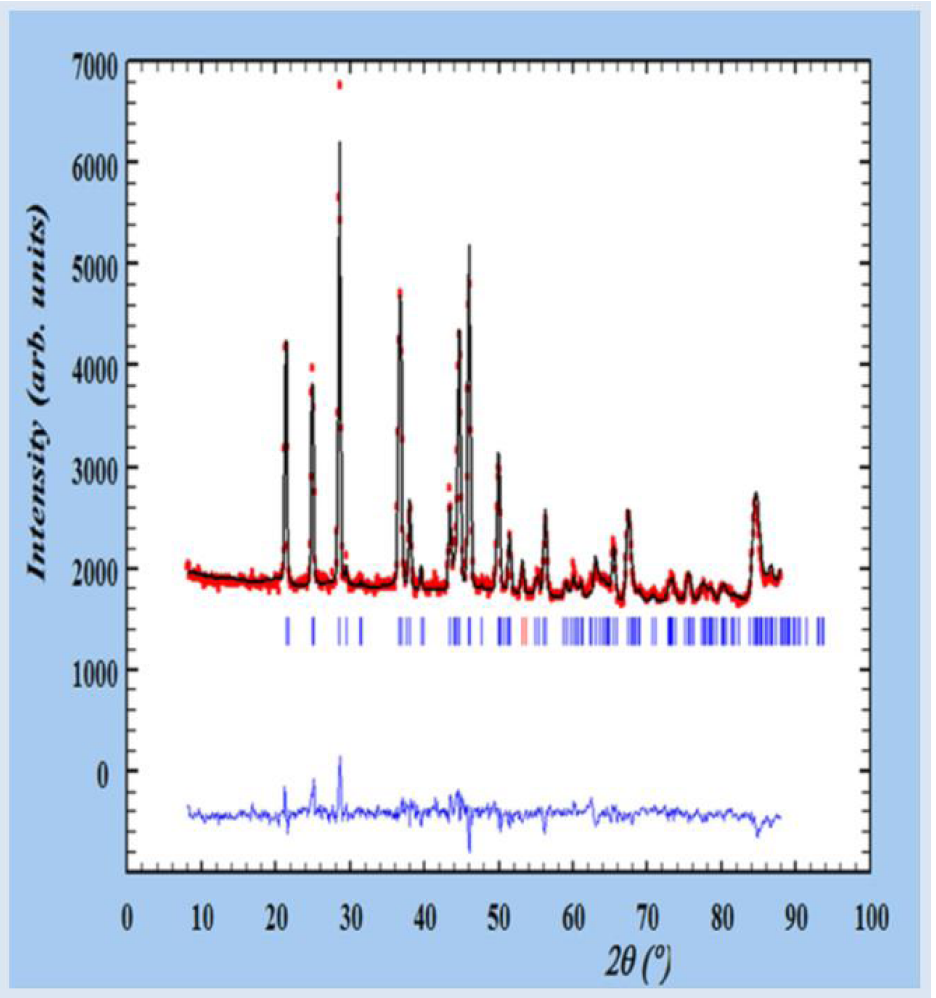

Figure 13. Final refinement, with experimental (red points), calculated (black line) and their difference (blue line), obtained for the kidney stone T40161. Tick marks below the profiles indicate the peak positions of allowed Bragg reflections for UAA [112].

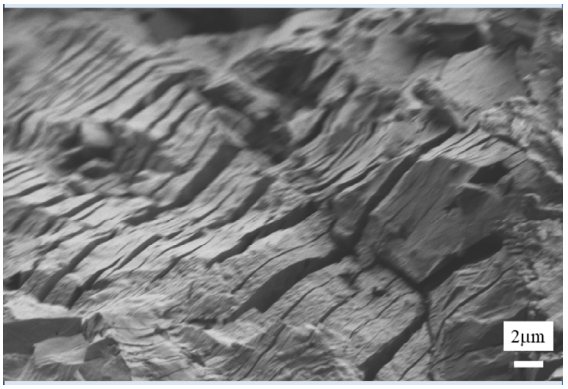

Figure 14. SEM images of uric acid kidney stones.

stones was to determine if medical treatment significantly modifies the size of cystine crystals [113]. The neutron data indicate clearly that treatment based on alkalinization by sodium bicarbonate significantly reduces the size of cystine crystals, from about 200 nm to about 120 nm. Moreover, as Figure 16 shows, alkalinization significantly modifies cystine crystallite morphology.

10. Discussion

The crystal structural characteristics of pathological calcifications constitute a key medical parameter for e.g. their toxicity [122]. For example, Sun *et al.* [38]

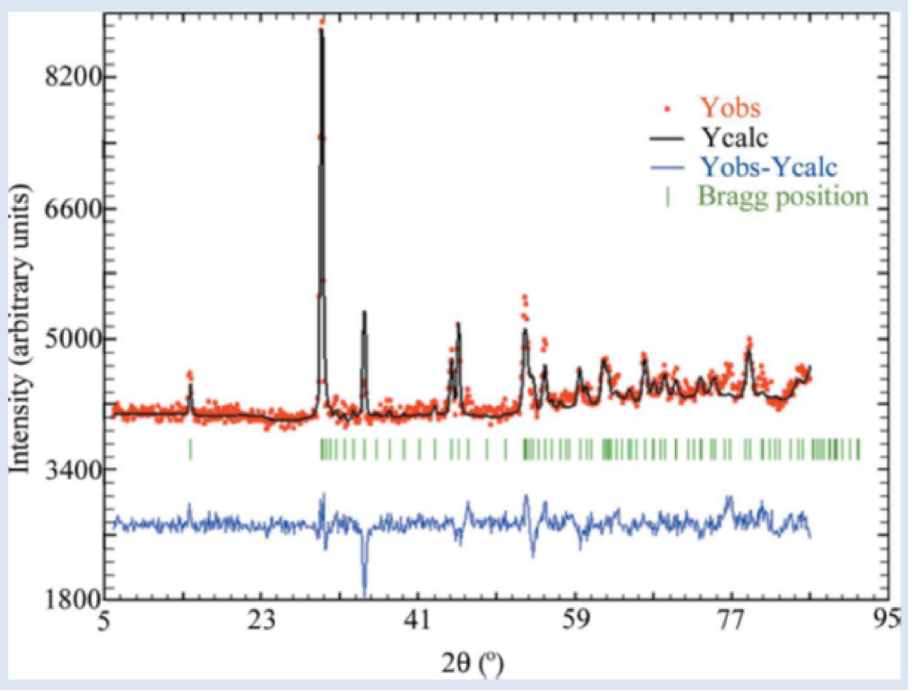

Figure 15. Typical observed (Y_{obs} in red), calculated (Y_{calc} in black), and difference, profiles (Y_{obs}–Y_{calc} in blue) of the PND diagram of a cystine kidney stone. Tick marks (Bragg position in green) below the profiles indicate the peak positions of allowed Bragg reflections for cystine [113].

have demonstrated that crystal shapes and aggregation states are crucial factors affecting crystal toxicity in renal epithelial cells. In a previous study, the same group [37] also showed that nano-sized COM and COD crystals induced much greater cell death (sum of apoptosis and necrosis) than micron-sized crystals. With respect to hydroxyapatite (HAP), a recent investigation shows that nanoscale HAP-40 nm and HAP-70 nm were more toxic to HK-2 cells than the micron-sized HAP-1 μm [123]. Note that for HAP, the crystal morphology is also a major structural parameter in regard to inflammation process [124]. Crystal structural parameters can also be related to physiological parameters or developmental processes. For example, Leventouri *et al.* [125] have noted that the crystallinity of dental hydroxyapatite decreases with tooth age. Also, it is worth emphasizing that enamel crystallinity also exerts effects on mammalian and vertebrate dental evolution [126]. Finally, the importance of the size and morphology of crystal in perturbation of biological tissues has been noted for other chemical phases including calcium pyrophosphate [127] and monosodium urate [128].

The various results we have presented show clearly that the crystal size associated with the different solid chemical phases identified in urine i.e. calcium oxalate monohydrate (COM or whewellite), struvite, whitlockite, uric acid and cystine is around 100 nm while the crystal size of calcium phosphate apatite is generally around 30 nm. Such results are consistent with previous publications showing the same differences between crystal sizes of calcium phosphate apatite, and other chemical phases [47,129]. For example, Uvarov *et al.* [73] highlight that weddellite crystal size was always greater than that of whewellite when they were simultaneously present, while brushite exhibits the largest crystallites of all.

From a physicochemical point of view, the comparison between the size measured by XRD via the Scherrer law, and the SEM observations, presents an opportunity to discuss the difference between the size of a crystal as measured by SEM observations and what is in fact measured by the Scherrer law i.e. the coherently scattering domain size. For example, in the cases of whitlockite (Figure 12)

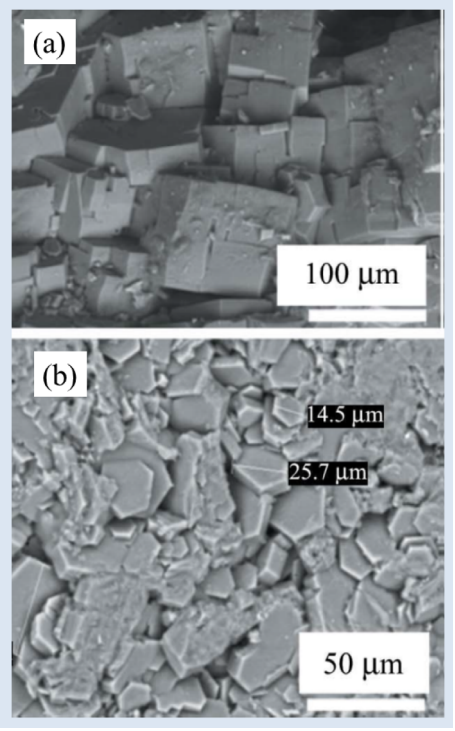

Figure 16. (a) SEM image of a typical Va cystine kidney stone made of large crystals exhibiting flat surfaces with well-defined corners and edges. The stone was removed from the kidney of an untreated patient. (b) SEM image of a Vb kidney stone [113].

and cystine (Figure 16a), well-defined edges and surfaces are clearly visible, giving the impression that micrometer-scale crystals are visualized and not crystallites. In fact, for these chemical phases, the difference between the coherently scattering domain size on a hundreds of nanometer scale, and the size of crystallites, indicates the presence of numerous structural defects which induce loss of long range order.

From a clinical point of view, we have mentioned that the crystal size is a key parameter in understanding interactions with cells. Differences in crystal size between calcium phosphate apatite and the other chemical phases is also of primary importance in understanding the localization of bacterial imprints, structural features which have been observed at the surface of concretions arising in various organs. Several papers have discussed the presence of bacterial imprints at the surface of kidney stones [84,97, 130,131], in prostatic stones [132,133], and of concretions in the bile duct [134]. In the case of prostate and kidney, the bacterial imprints were observed at the surface of the calcium phosphate apatite components of the concretions. None were observed at the surface of struvite crystallites although struvite is clearly related to urinary tract infection. To explain this apparent contradiction, we use the analogy of a man walking on a beach [84]. If the beach is sandy he leaves footprints, but not if the beach is stony. Bacterial imprints may thus appear in the small calcium carbonated apatite nanocrystals rather than in the large struvite ones. As shown for uric acid, COD or cystine, the size of either nanocrystals or of crystallites may be relevant to correlate biological crystals and biochemistry or medical treatment or pathological conditions.

11. Conclusion

Using examples from literature we have highlighted crystals and crystallite structural parameters of chemical phases identified in kidney stones by SEM and interpretation of XRD or PND diagrams. All reports point to the fact that the crystal size of most of the relevant chemical phases, namely calcium oxalate monohydrate (COM or whewellite), calcium oxalate dihydrate (COD or weddelite), brushite, struvite, whitlockite, uric acid, and cystine, is around 100 nm, whereas that of calcium phosphate apatite is predominantly around 30 nm.

These explain why bacterial imprints are only observed at the surface of calcium phosphate apatite kidney stones. Even though struvite is strongly associated with infection [135], its large crystal size can explain why bacterial imprints cannot form and be observed on the surface of struvite crystallites. Many of these observations around crystal size have clinical applications. SEM findings can thus help identify bacterial influences and better define urolithiasis etiology in patients generating kidney stones from which struvite is absent, and who give negative urine culture results and no evidence of fever.

Acknowledgments

This work was supported by the Physics and Chemistry Institutes of CNRS and by contracts ANR-09-BLAN-0120-02, ANR-12-BS08-0022,

ANR13JSV10010-01, convergence UPMC CVG1205, Labex Matisse, Labex Michem and CORDDIM-2013-COD130042. The authors are grateful to the SOLEIL Synchrotron Facility and the Leon Brillouin laboratory for beam time allocation.

References

[1] D. Bazin, M. Daudon, C. Combes, C. Rey, *Chem. Rev.*, 2012, **112**, 5092-5120.

[2] D. Bazin, M. Daudon, *J. Phys. D: Appl. Phys.*, 2012, **45**, article no. 383001.

[3] M. Daudon, D. Bazin, *J. Phys.: Conf. Ser.*, 2013, **425**, article no. 022006.

[4] L. N. Poloni, M. D. Ward, *Chem. Mater.*, 2014, **26**, 477-495.

[5] D. Bazin, J.-P. Haymann, E. Letavernier, J. Rode, M. Daudon, *Presse Med.*, 2014, **43**, 135-148.

[6] D. Bazin, M. Daudon, *Ann. Biol. Clin.*, 2015, **73**, 517-534.

[7] D. Bazin, E. Letavernier, J.-P. Haymann, P. Méria, M. Daudon, *Prog. Urol.*, 2016, **26**, 608-618.

[8] E. Tsolaki, S. Bertazzo, *Materials*, 2019, **12**, article no. 3126.

[9] D. Bazin, E. Letavernier, J. P. Haymann, V. Frochot, M. Daudon, *Ann. Biol. Clin.*, 2020, **78**, 349-362.

[10] N. Vidavsky, J. A. M. R. Kunitake, L. A. Estroff, *Adv. Healthc. Mater.*, 2020, article no. e2001271.

[11] M. Daudon, C. A. Bader, P. Jungers, *Scanning Microsc.*, 1993, **7**, 1081-1104.

[12] M. Daudon, *Arch. Pédiatr.*, 2000, **7**, 855-865.

[13] M. Daudon, P. Jungers, D. Bazin, *AIP Conf. Proc.*, 2008, **1049**, 199-215.

[14] V. Frochot, M. Daudon, *Int. J. Surg.*, 2016, **36**, 624-632.

[15] M. Daudon, *Prog. Urol.—FMC*, 2012, **22**, F87-F93.

[16] M. Daudon, O. Traxer, P. Jungers, *Lithiase Urinaire*, 2nd ed., Médecine-Sciences, Lavoisier, Paris, 2012, 672 pages.

[17] J. Cloutier, L. Villa, O. Traxer, M. Daudon, *World J. Urol.*, 2015, **33**, 157-169.

[18] M. Daudon, A. Dessombz, V. Frochot, E. Letavernier, J.-P. Haymann, P. Jungers, D. Bazin, *C. R. Chim.*, 2016, **19**, 1470-1491.

[19] M. Van Meerssche, J. Feneau-Dupont, *Introduction à la cristallographie Et à la chimie structurale*, Ed. Vander, Louvain, 1973.

[20] F. Brisset, M. Repoux, J. Ruste, F. Grillon, F. Robaut, *Microscopie Electronique à Balayage et Microanalyses*, EDP Sciences, 2009, ISBN: 978-2-7598-0082-7.

[21] M. Daudon, D. Bazin, "New techniques to characterize kidney stones and Randall's plaque", in *Urolithiasis: Basic Science and Clinical Practice* (J. J. Talati, H. G. Tiselius, D. M. Albala, Z. Ye, eds.), Springer, New York, 2012, 683-707.

[22] A. Guinier, *X-ray Diffraction in Crystals, Imperfect Crystals and Amorphous Bodies*, W.H. Freeman & Co., San Francisco, 1963.

[23] A. Guinier, *Théorie et technique de la radiocristallographie*, Dunod, Paris, 1964.

[24] A. Le Bail, H. Duroy, J. L. Fourquet, *Math. Res. Bull.*, 1988, **23**, 447-452.

[25] V. K. Pecharsky, P. Y. Zavalij, *Fundamentals of Powder Diffraction and Structural Characterization of Materials*, Springer-Verlag, New York, 2005.

[26] C. Kumar (ed.), *X-ray and Neutron Techniques for Nanomaterials Characterization*, Springer, Berlin, Heidelberg, 2016.

[27] D. E. Sayers, F. W. Lytle, E. A. Stern, *Adv. X-ray Anal.*, 1970, **13**, 248-271.

[28] E. A. Stern, D. E. Sayers, F. W. Lytle, *Phys. Rev. B*, 1975, **11**, 4836-4846.

[29] D. C. Bazin, D. A. Sayers, *Jpn. J. Appl. Phys.*, 1993, **32**, 249-251.

[30] D. C. Bazin, D. A. Sayers, *Jpn. J. Appl. Phys.*, 1993, **32**, 252-254.

[31] J. Moonen, J. Slot, L. Lefferts, D. Bazin, H. Dexpert, *Physica B*, 1995, **208**, 689-690.

[32] K. Nitiputri, Q. M. Ramasse, H. Autefage, C. M. McGilvery, S. Boonrungsiman, N. D. Evans, M. M. Stevens, A. E. Porter, *ACS Nano*, 2016, **10**, 6826-6835.

[33] C. Verrier, D. Bazin, L. Huguet, O. Stéphan, A. Gloter, M.-C. Verpont, V. Frochot, J.-P. Haymann, I. Brocheriou, O. Traxer, M. Daudon, E. Letavernier, *J. Urol.*, 2016, **196**, 1566-1574.

[34] C. Bardet, F. Courson, Y. Wu, M. Khaddam, B. Salmon, S. Ribes, J. Thumfart, P. M. Yamaguti, G. Y. Rochefort, M.-L. Figueres, T. Breiderhoff, A. GarciaCastaño, B. Vallée, D. Le Denmat, B. Baroukh, T. Guilbert, A. Schmitt, J.-M. Massé, D. Bazin, G. Lorenz, M. Morawietz, J. Hou, P. Carvalho-Lobato, M. C. Manzanares, J.-C. Fricain, D. Talmud, R. Demontis, F. Neves, D. Zenaty, A. Berdal, A. Kiesow, M. Petzold, S. Menashi, A. Linglart, A. C. Acevedo, R. Vargas-Poussou, D. Müller, P. Houillier, C. Chaussain, *J. Bone Miner. Res.*, 2016, **31**, 498-513.

[35] E. Bouderlique, E. Tang, J. Perez, A. Coudert, D. Bazin, M.-C. Verpont, C. Duranton, I. Rubera, J.-P. Haymann, G. Leftheriotis, L. Martin, M. Daudon, E. Letavernier, *Am. J. Pathol.*, 2019, **189**, 2171-2180.

[36] C. Gay, E. Letavernier, M.-C. Verpont, M. Walls, D. Bazin, M. Daudon, N. Nassif, O. Stephan, M. de Fruto, *ACS Nano*, 2020, **14**, 1823-1836.

[37] X.-Y. Sun, J.-M. Ouyang, W.-Y. Zhu, Y.-B. Li, Q.-Z. Gan, *J. Mater. Chem. B*, 2015, **3**, 1864-1878.

[38] X.-Y. Sun, Q.-Z. Gan, J.-M. Ouyang, *Cell Death Discov.*, 2015, **1**, article no. 15055.

[39] X.-Y. Sun, M. Xu, J.-M. Ouyang, *ACS Omega*, 2017, **2**, 6039-6052.

[40] M. Shanthil, K. Sandeep, P. K. Sajith, *Phys. Chem. Chem. Phys.*, 2020, **22**, 4788-4792.

[41] M. M. Woolfson, *An Introduction to X-ray Crystallography*, Cambridge Press, Cambridge, 1970.

[42] A. Cassetta, "X-ray diffraction (XRD)", in *Encyclopedia of Membranes* (E. Drioli, L. Giorno, eds.), Springer, Berlin, Heidelberg, 2014.

[43] B. E. Warren, *X-ray Diffraction*, Dover, New York, 1990.

[44] H. M. Rietveld, *J. Appl. Crystallogr.*, 1969, **2**, 65-71.

[45] P. J. W. Debye, *Ann. Phys.*, 1913, **348**, 49-92.

[46] P. J. W. Debye, *Ann. Phys.*, 1915, **351**, 809-823.

[47] A. Cervellino, C. Giannini, A. Guagliardi, *J. Appl. Crystallogr.*, 2003, **36**, 1148-1158.

[48] S. J. L. Billinge, I. Levin, *Science*, 2007, **316**, 561-565.

[49] L. Gelisio, P. Scardi, *Acta Crystallogr. A*, 2016, **72**, 608-620.

[50] P. Scardi, S. J. L. Billinge, R. Neder, A. Cervellino, *Acta Crystallogr. A*, 2016, **72**, 589-590.

[51] A. S. Vorokh, *Nanosyst. Phys. Chem. Math.*, 2018, **9**, 364-369.
[52] A. E. Ross, D. G. McCulloch, D. R. McKenzie, *Acta Crystallogr. A*, 2020, **76**, 468-473.
[53] S. Sasaki, *KEK Report 83-82*, National Laboratory for High Energy Physics, Tsukuba, Japan, 1983.
[54] D. Bazin, D. A. Sayers, J. J. Rehr, *J. Phys. Chem. B*, 1997, **101**, 11040-11050.
[55] D. Bazin, L. Guczi, J. Lynch, *Appl. Catal.*, 2002, **226**, 87-113.
[56] B. Ingham, *Crystallogr. Rev.*, 2015, **21**, 229-303.
[57] A. Cervellino, R. Frison, F. Bertolotti, A. Guagliardi, *J. Appl. Crystallogr.*, 2015, **48**, 2026-2032.
[58] F. Ferri, F. Bertolotti, A. Guagliardi, N. Masciocchi, *Sci. Rep.*, 2020, **10**, article no. 12759.
[59] D. Bazin, R. Revel, *J. Synchrotron Radiat.*, 1999, **6**, 483-485.
[60] R. Revel, D. Bazin, E. Elkaim, Y. Kihn, H. Dexpert, *J. Phys. Chem. B*, 2000, **104**, 9828-9835.
[61] D. Bazin, J. Lynch, M. Ramos-Fernandez, *Oil Gas Sci. Technol.—Rev. IFP*, 2003, **58**, 667-683.
[62] O. Ducreux, B. Rebours, J. Lynch, M. Roy-Auberger, D. Bazin, *Oil Gas Sci.Technol.—Rev. IFP*, 2009, **64**, 49-62.
[63] A. O. Bokuniaeva, A. S. Vorokh, *J. Phys.: Conf. Ser.*, 2019, **1410**, article no. 012057.
[64] F. Bertolotti, A. Vivani, D. Moscheni, F. Ferri, A. Cervellino, N. Masciocchi, A. Guagliardi, *Nanomaterials*, 2020, **10**, article no. 743.
[65] M. A. R. Miranda, J. M. Sasaki, *Acta Crystallogr. A*, 2018, **74**, 54-65.
[66] P. Scherrer, *Achr. Ges. Wiss. Göttingen*, 1918, **1**, 98-100.
[67] U. Holzwarth, N. Gibson, *Nat. Nanotechnol.*, 2011, **6**, 534.
[68] A. L. Patterson, *Phys. Rev.*, 1939, **56**, 978-982.
[69] J. I. Langford, A. J. C. Wilson, *J. Appl. Crystallogr.*, 1978, **11**, 102-113.
[70] S. M. Londoño-Restrepo, R. Jeronimo-Cruz, B. M. Millán-Malo, E. M. Rivera-Muñoz, M. E. Rodriguez-García, *Sci. Rep.*, 2019, **9**, article no. 5915.
[71] D. Bazin, M. Daudon, G. André, R. Weil, E. Véron, G. Matzen, *J. Appl. Crysallogr.*, 2014, **47**, 719-725.
[72] F. Damay, D. Bazin, M. Daudon, G. André, *C. R. Chim.*, 2016, **19**, 1432-1438.
[73] V. Uvarov, I. Popov, N. Shapur, T. Abdin, O. N. Gofrit, D. Pode, M. Duvdevani, *Environ. Geochem. Health*, 2011, **33**, 613-622.
[74] M. Daudon, P. Jungers, D. Bazin, *New Engl. J. Med.*, 2008, **359**, 100-102.
[75] M. Daudon, H. Bouzidi, D. Bazin, *Urol. Res.*, 2010, **38**, 459-467.
[76] A. Randall, *Ann. Surg.*, 1937, **105**, 1009-1027.
[77] M. Daudon, O. Traxer, P. Jungers, D. Bazin, *AIP Conf. Proc.*, 2007, **900**, 26-34.
[78] M. Daudon, O. Traxer, J. C. Williams, D. Bazin, "Randall's Plaque", in *Urinary Tract Stone Disease* (N. P. Rao, G. M. Preminger, J. P. Kavangh, eds.), Springer, New York, 2011, ISBN 978-1-84800-361-3.
[79] E. Letavernier, D. Bazin, M. Daudon, *C. R. Chim.*, 2016, **19**, 1456-1460.
[80] D. Bazin, E. Letavernier, C. Jouanneau, P. Ronco, C. Sandt, P. Dumas, G. Matzen, E. Véron, J.-P. Haymann, O. Traxe, P. Conort, M. Daudon, *C. R. Chim.*, 2016, **19**, 1461-1469.
[81] E. Letavernier, G. Kauffenstein, L. Huguet, N. Navasiolava, E. Bouderlique, E. Tang, L. Delaitre, D. Bazin, M. de Frutos, C. Gay, J. Perez, M. C. Verpont, J.-P. Haymann, V. Pomozi, J. Zoll, O. Le Saux, M. Daudon, G. Leftheriotis, L. Martin, *J. Am. Soc. Nephrol.*, 2018, **29**, 2337-2347.
[82] S. J. Eppell, W. Tong, J. L. Katz, L. Kuhn, M. J. Glimcher, *J. Orthop. Res.*, 2001, **19**, 1027-1034.
[83] D. Bazin, C. Chappard, C. Combes, X. Carpentier, S. Rouzière, G. André, G. Matzen, M. Allix, D. Thiaudière, S. Reguer, P. Jungers, M. Daudon, *Osteoporos. Int.*, 2009, **20**, 1065-1075.
[84] D. Bazin, G. André, R. Weil, G. Matzen, E. Véron, X. Carpentier, M. Daudon, *Urology*, 2012, **79**, 786-790.
[85] X. Carpentier, D. Bazin, C. Combes, A. Mazouyes, S. Rouzière, P.-A. Albouy, E. Foy, M. Daudon, *J. Trace Elem. Med. Biol.*, 2011, **25**, 160-165.
[86] U. Vetter, E. D. Eanes, J. B. Kopp, J. D. Termine, P. Gehron Robey, *Calcif. Tissue Int.*, 1991, **49**, 248-250.
[87] G. E. Bacon, A. E. Goodship, *J. Appl. Crystallogr.*, 2007, **40**, 349-353.
[88] S. Cazalbou, C. Combes, D. Eichert, C. Rey, M. J. Glimcher, *J. Bone Miner. Metab.*, 2004, **22**, 310-317.
[89] S. Cazalbou, D. Eichert, C. Drouet, C. Combes, C. Rey, *C. R. Palevol*, 2004, **3**, 563-572.
[90] C. Rey, C. Combes, C. Drouet, H. Sfihi, A. Barroug, *Mat. Sci. Eng. C*, 2007, **27**, 198-205.
[91] C. Drouet, C. Rey, in *Nanostructured Biomaterials for Regenerative Medicine* (V. Guarino, M. Iafisco, S. Spriano, eds.), Woodhead Publishing Series in Biomaterials, Elsevier, 2020.
[92] R. J. Reveillaud, M. Daudon, "Struvite stones analysis by infrared spectrophotometry in adults and children", in *Urolithiasis and Related Clinical Research* (P. O. Schwille, L. H. Smith, W. G. Robertson, W. Vahlensieck, eds.), Springer, Boston, MA, 1985.
[93] R. Flannigan, W. H. Choy, B. Chew, D. Lange, *Nat. Rev. Urol.*, 2014, **11**, 333-341.
[94] M. Daudon, P. Jungers, D. Bazin, J. C. Williams Jr., *Urolithiasis*, 2018, **46**, 459-470.
[95] M. A. P. Manzoor, B. Singh, A. K. Agrawal, A. B. Arun, M. Mujeeburahiman, P. D. Rekha, *PLoS One*, 2018, **13**, article no. e0202306.
[96] J. C. Williams Jr., A. J. Sacks, K. Englert, R. Deal, T. L. Farmer, M. E. Jackson, J. E. Lingeman, J. A. McAteer, *J. Endourol.*, 2012, **26**, 726-731.
[97] X. Carpentier, M. Daudon, O. Traxer, P. Jungers, A. Mazouyes, G. Matzen, E. Véron, D. Bazin, *Urology*, 2009, **73**, 968-975.
[98] A. N. Kofina, P. G. Koutsoukos, *Cryst. Growth Des.*, 2005, **5**, 489-496.
[99] J. Prywer, A. Torzewska, *Cryst. Growth Des.*, 2009, **9**, 3538-3543.
[100] J. Prywer, A. Torzewska, *Cryst. Res. Technol.*, 2010, **45**, 1283-1289.
[101] L. Maurice-Estepa, P. Levillain, B. Lacour, M. Daudon, *Scand. J. Urol. Nephrol.*, 1999, **88**, 299-305.
[102] F. A. Shah, *Acta Biomater.*, 2021, **125**, 72-82.
[103] D. Bazin, M. Daudon, E. Elkaim, A. Le Bail, L. Smrcok, *C. R. Chim.*, 2016, **19**, 1535-1541.
[104] S. Amirthalingam, A. Ramesh, S. S. Lee, N. S. Hwang, R. Jayakumar, *ACS Appl. Bio Mater.*, 2018, **1**, 1037-1046.
[105] T. Debroise, E. Colombo, G. Belletti, J. Vekeman, Y. Su, R. Papoular, N. S. Hwang, D. Bazin, M. Daudon, P. Quaino, F. Tielens, *Cryst. Growth Des.*, 2020, **20**, 2553-2561.

[106] D. Bazin, R. J. Papoular, E. Elkaim, R. Weil, D. Thiaudière, C. Pisapia, B. Ménez, N. S. Hwang, F. Tielens, M. Livrozet, E. Bouderlique, J.-P. Haymann, E. Letavernier, L. Hennet, V. Frochot, M. Daudon, *C. R. Chim.*, 2022, **25**, no. S1, 343-354.
[107] C. Frondel, *Am. Mineral.*, 1941, **26**, 145-152.
[108] J.-E. S. Kenny, D. S. Goldfarb, *Curr. Rheumatol. Rep.*, 2010, **12**, 125-129.
[109] N. S. Mandel, G. S. Mandel, *J. Urol.*, 1989, **142**, 1516-1521.
[110] L. Durner, A. Bourdoumis, N. Buchholz, *C. R. Chim.*, 2016, **19**, 1451-1455.
[111] D. J. Sas, *J. Pediatr.*, 2010, **157**, 132-137.
[112] M. Daudon, E. Letavernier, R. Weil, E. Véron, G. Matzen, G. André, D. Bazin, *C. R. Chim.*, 2016, **19**, 1527-1534.
[113] D. Bazin, M. Daudon, G. André, R. Weil, E. Véron, G. Matzen, *J. Appl. Crystallogr.*, 2014, **47**, 719-725.
[114] F. Grases, A. L. Villacampa, A. Costa Bauza, O. Sohnel, *Scanning Microsc.*, 1999, **13**, 223-234.
[115] A. Trinchieri, G. Dormia, E. Montanari, G. Zanetti, *Arch. Ital. Urol. Androl.*, 2004, **76**, 129-134.
[116] L. Dello Strologo, G. Rizzoni, *Acta Paediatr. Suppl.*, 2006, **95**, 31-33.
[117] A. Sahota, J. A. Tischfield, D. S. Goldfarb, M. D. Ward, L. Hu, *Urolithiasis*, 2019, **47**, 57-66.
[118] E. Letavernier, O. Traxer, J.-P. Haymann, D. Bazin, M. Daudon, *Prog. Urol.—FMC*, 2012, **22**, F119-F123.
[119] J. P. Haymann, M. Livrozet, J. Rode, S. Doizi, O. Traxer, V. Frochot, E. Letavernier, D. Bazin, M. Daudon, *Prog. Urol.—FMC*, 2021, **31**, F1-F7.
[120] L. Feliubadaló, M. L. Arbonés, S. Mañas, J. Chillarón, J. Visa, M. Rodés, F. Rousaud, A. Zorzano, M. Palacín, V. Nunes, *Hum. Mol. Genet.*, 2003, **12**, 2097-2108.
[121] M. Livrozet, S. Vandermeersch, L. Mesnard, E. Thioulouse, J. Jaubert, J.-J. Boffa, J.-P. Haymann, L. Baud, D. Bazin, M. Daudon, E. Letavernier, *PLoS ONE*, 2014, **9**, article no. e102700.
[122] S. R. Khan, *Urol. Res.*, 1995, **23**, 71-79.
[123] X.-Y. Sun, J.-Y. Chen, C.-Y. Rao, J.-M. Ouyang, *Int. J. Nanomedicine*, 2020, **15**, 5043-5060.
[124] F. Lebre, R. Sridharan, M. J. Sawkins, D. J. Kelly, F. J. O'Brien, C. Lavelle, *Sci. Rep.*, 2017, **7**, article no. 2922.
[125] T. Leventouri, A. Antonakos, A. Kyriacou, R. Venturelli, E. Liarokapis, V. Perdikatsis, *Int. J. Biomater.*, 2009, **2009**, article no. 698547.
[126] A. Kallistová, R. Skála, M. Šlouf, P. Čejchan, I. Matulková, I. Horáček, *Sci. Rep.*, 2018, **8**, article no. 5544.
[127] A. Swan, B. Heywood, B. Chapman, H. Seward, P. Dieppe, *Ann. Rheum. Dis.*, 1995, **54**, 825-830.
[128] M. A. Martillo, L. Nazzal, D. B. Crittenden, *Curr. Rheumatol. Rep.*, 2014, **16**, 400-408.
[129] P. Chatterjee, A. Chakraborty, A. K. Mukherjee, *Spectrochim. Acta Part A*, 2018, **200**, 33-42.
[130] L. Cifuentes Delatte, M. Santos, *Eur. Urol.*, 1977, **3**, 96-99.
[131] K. M. Englert, J. A. McAteer, J. E. Lingeman, J. C. Williams Jr, *Urolithiasis*, 2013, **41**, 389-394.
[132] A. Dessombz, P. Méria, D. Bazin, M. Daudon, *PLoS One*, 2012, **7**, article no. e51691.
[133] A. Dessombz, P. Méria, D. Bazin, E. Foy, S. Rouzière, R. Weil, M. Daudon, *Prog. Urol.*, 2011, **21**, 940-945.
[134] J. W. C. Leung, J. Y. Sung, J. W. Costerton, *J. Clin. Microbiol.*, 1989, **27**, 915-921.
[135] E. J. Espinosa-Ortiz, B. H. Eisner, D. Lange, R. Gerlach, *Nat. Rev. Urol.*, 2019, **16**, 35-53.

Comptes Rendus
Chimie
2022, Vol. 25, Special Issue S1, p. 149-163
https://doi.org/10.5802/crchim.154

Microcrystalline pathologies: Clinical issues and nanochemistry / *Pathologies microcristallines : questions cliniques et nanochimie*

Peculiar opportunities given by XPS spectroscopy for the clinician

Flavio Siro Brigiano [a], **Dominique Bazin** *, [b, c] **and Frederik Tielens** *, [a]

[a] General Chemistry (ALGC) – Materials Modelling Group, Vrije Universiteit Brussel (Free University Brussels-VUB), Pleinlaan 2, 1050 Brussel, Belgium

[b] Université Paris-Saclay, CNRS, Institut de Chimie Physique, 91405 Orsay cedex, France

[c] Université Paris-Saclay, CNRS, Laboratoire de Physique des Solides, 91405, Orsay, France

E-mails: Flavio.Siro.Brigiano@vub.be (F. S. Brigiano), dominique.bazin@universite-paris-saclay.fr (D. Bazin), frederik.tielens@vub.be (F. Tielens)

Abstract. X-ray Photoelectron Spectroscopy (XPS) constitutes an elegant way to describe the chemical characteristics of the surface of biological materials. It is thus a unique approach to decipher the interaction between biological materials and tissues. In the case of medical implants, it is thus possible to understand its biocompatibility as well as its integration in the body which can be wanted in the case of prothesis or avoided in the case of JJ-stents. More precisely, XPS can bring valuable information of the interaction between physiological calcification (here bone) and the prosthesis as well as the interaction between pathological calcifications (lithiasis) and the JJ-stent. This mini overview is dedicated to two communities, the physical chemists and the clinicians. In the first part of this overview, after an introduction on the basic principles of XPS, we focus on the theoretical techniques adopted for the computation of XPS spectra of materials.

The second part, dedicated to clinicians, describes the use of XPS for the characterization of biological materials. We report which kind of chemical information can be gained by this surface-sensitive technique and how this information has a relevant impact on medical applications.

Through different examples, we show that XPS is a strong and very useful tool, and thus receiving a crucial place in medical research.

Keywords. XPS, Pathological calcification, Medicine, Prothesis, Biomaterials.
Published online: 16 February 2022, Issue date: 1 September 2022

1. Introduction

In 1887, the discovery of the photoelectric effect by Hertz [1] gives the basis of the X-ray Photoelectron Spectroscopy (XPS) or electron spectroscopy for chemical analysis (ESCA). The first use of XPS to investigate surface properties was made by Siegbahn in the mid-1960s [2] and led to numerous breakthroughs in physics [3,4] as well as in nanochemistry later on [5,6]. Now, XPS spectroscopy has become a relatively simple and increasingly routinary

* Corresponding authors.

technique for the compositional and chemical state analysis of surfaces [7,8].

In medicine, XPS spectroscopy brings valuable information in different specialities. On the surface of biomaterials, XPS spectroscopy is able to give an identification and a quantification of possible contaminants [9]. XPS spectroscopy may also describe the covalent attachment of adhesive peptides used to enhance osteoblast adhesion on titanium implants and prostheses [10]. Lastly, it is worth to underline that pathological [11–13] as well as physiological calcifications and biologically interesting phases [14–22] have been investigated through XPS spectroscopy to characterize either the very first steps of their pathogenesis [23,24] or the process of bone formation.

The aim of this publication is to present recent results obtained in the field of biomaterials and pathological calcifications by means of XPS spectroscopy, and to discuss the perspectives of the method. To attain this goal, we will start by a brief (more details can be found in different excellent books or reviews [25–29]) description on the basic principles of XPS, followed by a presentation of the computational techniques available nowadays for the calculations of theoretical XPS spectra of materials. The second part, namely XPS for the clinician, is dedicated to the medical community. Through different examples, we try to show that XPS is a strong and very useful tool which has a crucial place in medical research.

2. Basic elements of XPS spectroscopy

Like other characterization techniques namely X-ray diffraction or X-ray fluorescence [30–33], XPS uses X-ray photons as a probe. While X-ray diffraction and X-ray fluorescence involves incident photons of high energy and the detection of photons, XPS spectroscopy uses low-energy (~1.5 keV) X-rays and is based on the detection of photoelectrons emitted from the sample [6–10]. It is the measurement of the kinetic energy of these photoelectrons emitted from the surface which yields information on the electronic states of atoms present at the surface.

E_k, the kinetic energy of the emitted photoelectron is given by the Einstein equation: $E_k = h\nu - E_B - \varphi_s$ where E_B is the binding energy of an electron in its initial state in the atom, $h\nu$ is the energy of the X-ray photon and φ_s is the work function of the sample. From the known $h\nu$ and the measured

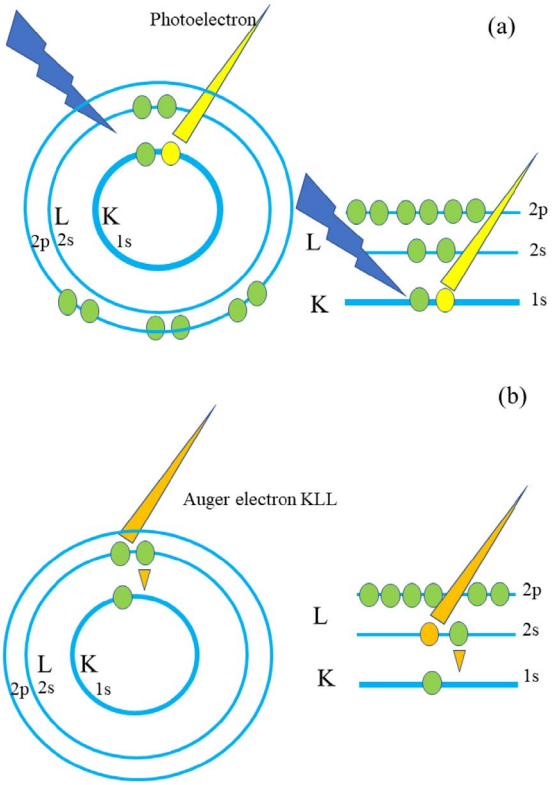

Figure 1. Schematic representation related to the different steps of the photoelectron and Auger electrons emission.

E_k, the binding energy of the element E_B is obtained. It is worth to notice that in a XPS spectra, a second family of electrons coming from the surface, Auger electrons [7,34–37], gives rise to additional peaks. The emission of Auger electrons happens after the photoabsorption and the emission of the photoelectron which created a vacancy. An electron from a higher energy (corresponding to an electronic transition between 2s and 1s state on Figure 1b) releases energy able to expulse an electron (2s on Figure 1b). Such an Auger electron is emitted with a kinetic energy that is independent of the X-ray energy.

From an experimental point of view, XPS spectroscopy can be considered as in lab experiment. Clinicians have to consider this technique through intimate collaboration with p7hysical chemists in order to0 discuss the preparation procedure of the sample taking into account4pc working under vacuum and the nature of the surface. Shard [38] have discussed different points that should be considered

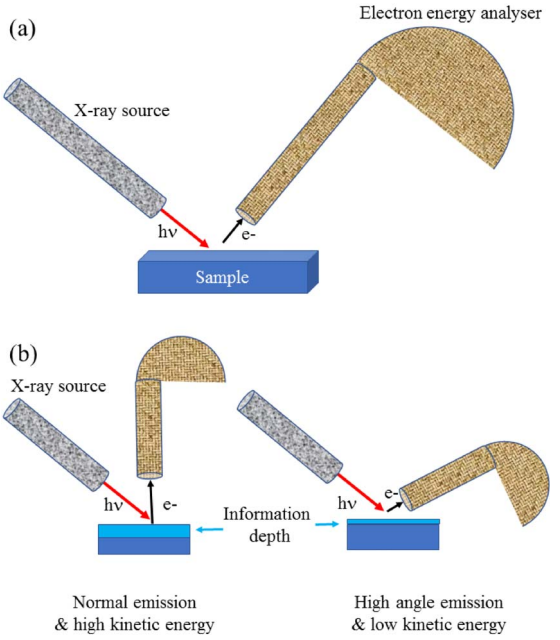

Figure 2. (a) Schematic view of the photoelectron spectrometer with a hemispherical electron energy analyzer. (b) By changing the geometry, it is possible to modulate the thickness of the sample which is analyzed.

to obtain reliable and meaningful information from quantitative XPS encompassing the necessity for reference data as well as a consistent and methodical method for the separation of inelastic background from peaks. In a classical XPS experiment (Figure 2), the incident monochromatic photons beam is given by aluminum ($h\nu$ = 1486.6 eV) or magnesium ($h\nu$ = 1253.6 eV) K_α.

As pointed out by Vohrer *et al.* [39], experimental developments lead to micro or small spot-XPS systems with near-micron spatial resolution. The analysis of the photoelectron energy implies that the sample is placed in a vacuum chamber, under the best vacuum conditions achievable, typically $\sim 10^{-10}$ torr. Regarding the detection, the binding energies of electrons detected are measured in electron-volts (eV) with an accuracy of ±0.1 eV. The most common type is the electrostatic hemispherical analyzer consisting of two concentric hemispheres [40]. Note that it is possible to modulate the thickness of the sample which is analyzed through a modification of the experimental conditions.

One of the major advantages of XPS spectroscopy comes from the fact that this spectroscopy provides information on almost all the elements in the Periodic Table (except hydrogen and helium). At this point, it is worth to underline that while X-ray fluorescence is limited to the identification and the quantification of elements present in the sample [31,32, 41,42], high resolution scans of the XPS peaks can differentiated elements of the same kind but with different states and environments.

Another major advantage comes from the fact that photoelectrons are emitted from the very top surface (1–10 nm) of any solid surface. Such advantage can be easily understood from the following equation which gives the probability, p, that a photoelectron escapes from the sample without losing energy. In this equation, $\lambda_e(E)$ is defined as the photoelectron inelastic mean free path and θ the angle between the incident beam and the normal of the surface

$$p = -z/\exp(\lambda_e(E)\cos\theta)$$

$\lambda_e(E)$ corresponds to the average distance between collisions in which an emerging photoelectron loses energy. If a photoelectron loses kinetic energy in a collision, the information regarding the chemical information of the sample is loss. The information of a XPS spectrum is thus given by photoelectron corresponding to $\lambda_e(E)$ equal typically to 2–5 nm, the other photoelectron contributes to the background.

3. Computational tools for the computation of XPS spectra: first principles calculations

In this paragraph we summarize the fundamental physics behind XPS, illustrated with some theoretical calculations and studies used in the interpretation and prediction of experimental XPS data. After having introduced the theoretical formalism, we provide an overview on the techniques for the computation of theoretical XPS spectra that can provide a full rationalization of XPS experiments on biological materials.

The use of theoretical chemistry computational tools to help in the characterization of biological materials timidly but firmly starting to become the state-of-the-art [43,44]. Theoretical chemistry which is already omni-present in materials science and which is expected to break open the limits of materials design known up till now will continue to

obtain a dominating position thanks to the evolution of the computing power and algorithms. Artificial intelligence, machine learning, neural network calculations etc. are the tools that will enable to solve the complex calculations behind the fundamental laws of physics at the level of the atom and electrons of matter.

Today, we are not yet at this point but this revolution in scientific working protocols is slowly arriving at its aim. The theoretical chemistry-based computations applied on systems of interest by the clinician are still scarce, but some methods can be used already. Especially, on biological mineralisation samples some work has been performed [45–48].

Typically, structural parameters such as unit cell parameters and atomic coordinates are optimized, but also spectroscopic data (IR and Raman spectra) can be simulated [49,50]. These simulated data are then a very valuable source of data for comparison with experimental data for the interpretation of the spectra. The models itself provide a molecular picture of the material. Diffraction (X-ray, neutron and electron) patterns are also available thanks to the structural optimisations [51].

However, other spectroscopies, such as XPS are less calculated in general. Some studies are dedicated on the calculation strategies, and/or applied to some specific families of materials. In what follows we would like to give an overview on the methods used in materials modelling science and provide some applications of them, which hopefully will inspire the modelling community to apply XPS on materials of biological interest.

XPS spectroscopy has been widely employed in the field of heterogeneous catalysis since its capability in probing changes in the local bonding environments of atoms at the boundaries between solid surfaces and other media along a reaction process e.g. adsorption and surface reconstruction phenomena [52–54]. The complexity of the surface chemistry, characterized by a broad spectra of surfaces sites each one with a specific interaction with the substrates and molecules, makes the interpretation of XPS experimental spectra often not straightforward and univocal. Computational approaches able to assign the different components of the XPS spectra to groups of atoms with specific chemical environments are therefore mandatory for the full rationalization of XPS experiments.

The binding energy BE of a given electronic level can be expressed as the energy difference between the initial N electron non-ionized state and the $N-1$ electron final ionized state:

$$\mathrm{BE} = E^{n-1}(\mathrm{final}) - E^{n}(\mathrm{initial}).$$

The BE can be calculated with different degrees of approximation. When the electronic density is considered frozen, not free to relax in response to the ionization of the system, the BE can be expressed as the negative value of the orbital energy $-\varepsilon_i$ (Koopmans

theorem) from which the electr8on is removed. This is known as Frozen Orbital (FO) approach. In the FO approach the BE is calculated as the7 difference between the neutral ground state HF (Hartree–Fock) energy and the ionized system HF energy obtained by the HF orbitals of the neutral system.

Absolute BEs cannot be predicted by density functional theory (DFT) calculations since the Koopmans theorem does not hold for Kohn and Sham (KS) orbitals, as recently shown by Pueyo Bellafont *et al.* [55]. Conversely, DFT calculations in the FO approach have been shown to reflect the experimental trends in Core level binding energy shifts (ΔBEs) for a series of gas phase molecules [55]. The BEs and ΔBEs calculated by the FO approach mainly provide information on the chemical bonding features of the initial neutral ground state (initial state effect), since the relaxation of the electronic orbitals is not taken into account in the final ionized system.

More accurate estimations of the BEs can be obtained by considering the energy difference between the final ionized state and the initial neutral ground state, taking into account the electron density relaxation in response to the electron hole. This approach is known as ΔSCF.

The calculations of gas phase molecules BEs based on DFT and HF in the ΔSCF scheme, have been shown to reproduce absolute experimental BEs with a good degree of accuracy [56–58]. However, this could be due to cancellation of errors arising from the neglect of relativistic effects, the poor description of correlation energies and incompleteness of the basis set. In this regard Pueyo Bellafont *et al.* [59] have directly taken into account relativistic effect in the calculations of 1S core level BEs of N, F, C and

B atoms belonging to 68 gas phase molecules with different functional groups. HF and DFT calculations (TPSS functional) in the ΔSCF scheme have been performed. The calculated BEs result to be underestimated with respect to the experimental values of 0.11 (HF) and 0.05 eV (TPPS).

An alternative promising method for the computing of gas phase molecules BEs is represented by the GW quasi particle approach [60]. In this approach the HF equations are generalized in terms of Greens functions (G), which poles correspond to the ionization potentials and electronic affinities. In this framework based on ab initio calculations, the ionization potentials and electronic affinities are connected to the dielectric function and self-energy of the system. In the GW method the response of the electron density to the core hole is described by a perturbative approach where the system self-energy is expanded in a Taylor series of the dynamically screened Coulomb interaction (W).

In the past, the GW approach has been successfully applied for the computation of valence electron ionization energies in solid and gas phase molecules. More recently, the use of the GW approach has been also extended to the calculations of core electrons BEs of gas phase molecules [61,62]. In this regard the work of Goltze *et al.* [61] applies a partial self-consistent GW scheme for the computation of 1s core level BEs of 68 molecular systems. This work points out how the use of GGA functionals (currently used for the calculation of valence electrons BEs) for the initialization of Green functions and the Coulomb interaction are not enough for an accurate computation of core electrons BEs. By contrast the use of Hybrid functionals with high percentage of exact exchange and the inclusion of relativistic effects provides accurate BEs that agree within 0.3 and 0.2 eV with experiments. The main advantage of the GW methods with respect ΔSCF ones lies in the direct computation of ionization potential and electron affinities from the quasi-particle energy of respectively occupied and not occupied electronic levels.

We now move our attention to the methods developed for the computation of BEs and ΔBEs of periodic systems. In the last two decades the astonishing increasing in the computational power has led surface science to pass from a cluster to a periodic approach for the modelling of surfaces. In the past, computational works modelling the adsorption process on oxides and metal surfaces by the clusters approach have provided useful information into the nature of the interaction between the adsorbate and the surfaces [63,64]. However, the small size of the clusters leads to edge effects due to dangling atoms and possible wrong stoichiometry. These issues can be overcome by correctly coordinating the dangling atoms by other atoms, leading, however, to possible new unwanted effects on the computed BE and ΔBEs. Periodic systems are used in order to avoid these effects.

This has led to the conceiving of new approaches for the computation of ΔBEs of atoms on large periodic surfaces. The difficulties in computing XPS spectra on large periodic models arise from two main reasons:

(1) The ionization of one core electron in a given surface atom leads to a charged periodic cell. The coulomb repulsion between the periodically repeated infinite unit cells could introduce artefacts in the calculated values core level BEs and ΔBEs.
(2) Generally, Periodic codes (VASP [65–69], CP2K [70]) are not "full electron", the core electrons are not explicitly treated. The effect of the atomic core electrons on the valence electron density is modelled by Pseudo Potentials.

In order to overcome such limitations different approaches have been proposed in the literature for the calculation of XPS spectra of periodic models in a ΔSCF scheme. In their pioneering work Pehlke and Scheffler *et al.* [71] calculate core level shift of clean (001) Ga and Si surfaces for excited atoms located at different distance from the surface. The authors generate Hamann–Schluter Chiang pseudo potentials for respectively the neutral and the ionized Si and Ge atoms (with 2p and 3d core holes). The comparison between the excited and the initial ground states revealed a higher screening at the surface with respect to the bulk.

More recently Ljumberg *et al.* [72] has implemented XPS calculations for periodic and non-periodic systems on the GPAW code, based on DFT and the projector-augmented wave (PAW) method [69,73]. Interestingly the authors find variations up to 10 eV in the BEs when adopting closed and open shell calculations in the test case of H_2O

molecule. It follows that the use of spin polarized calculation is necessary for this approach. Curiously, as pointed out in the recent review of Vines *et al.* [74], negligible differences are instead found between spin and not spin-polarized calculations when adopting the "full electron" cluster approach [64]. The calculation of XPS energies (ΔBEs) by the PAW approach of CO molecule adsorbed on Ni(100) surface has provided an error of around 2 eV with respect to the experimental value [64].

The implementation of core level ΔBEs calculations on periodic systems with PAW based approach and their successful combination with in-situ XPS experiments has led to an increasing number of innovative studies on the characterization of the adsorption and the reactivity of small organic species at metal and metal oxide surfaces. For instance, PAW based approaches have been successfully applied for the computation of XPS energies of: (i) CO molecule adsorbed on Ni(100), Fe(100) and Rh(111) surfaces [72,75,76], (ii) sulphur oxidation on Palladium [77,78], (iii) aspartic acid and methyl Acetoacetate adsorbed on Ni(100) [79,80] and (iv) small molecular species on copper oxide surfaces [81]. We also highlight the work of Trinh *et al.* [81], where a synergistic approach of experimental XPS and DFT calculations is proposed in order to determine the Hubbard terms (U term) for adsorbate/intermediate species on transition metal oxide surfaces.

As a drawback, the periodic ΔSCF calculations imply the use of approaches in order to prevent the spurious core electron holes' interaction between the replica of the final system ($N-1$ electron), that would lead to Coulomb divergence. The introduction of a uniform background opposite charge [82] and the addition of electrons in the conduction band [76,83] of the final systems have been the two main approaches adopted to circumvent such problem. However, the addition of fictitious counter charges in the final system can introduce spurious effects in the calculated values of core level BEs and ΔBEs [84].

In this regard Ozaki *et al.* [85] have proposed a new approach based on DFT calculations, where a penalty function is used in order to model the electron core hole and the spurious interaction between the replica is removed using the Coulomb cut-off method. Another interesting methodology is the one of Lischner *et al.* [86,87] where absolute core electrons BEs are calculated by DFT-based all-electrons ΔSCF calculations. In these works, core-level binding energies for a series of adsorbates on Cu(111) surfaces are computed. In a first step the adsorbate structures are optimized on a periodic slab model of the Cu(111) surface. Then, a cluster of 88 Cu atoms is extracted from the slab and the core BEs are calculated using the all-electron ΔSCF. These calculations have led to accurate absolute BEs with a mean unsigned error of 0.08 eV and 0.13 eV for respectively the M06 and PBE functional.

An alternative approach for an accurate prediction of periodic systems ΔBEs is represented by the Janak–Slater (JS) transition state method [88,89]. This approach considers half occupation of the core level (CL) rather than a full core-hole as in other ΔSCF approaches. This is done in order to minimize the fictitious repulsion between the replicas. Recent studies have reported the JS to provide ΔBEs of gas phase molecules and periodic surfaces [82,83] in good agreement with experiments, when adopting a PAW description of the atomic cores (implemented on VASP).

Beyond ΔSCF approaches, the XPS spectra of periodic systems have also been computed by GW methods [90,91]. We find of particular interest the work Zhu *et al.* [90] where an implementation based on crystalline Gaussian Basis set for the computation of core-electrons BEs on periodic systems in the GW scheme, is presented. Also, in this case the use of hybrid functionals with a high percentage of exact exchange results to be mandatory for the computation of accurate core electrons BEs.

The GW method presents the main advantage with respect to the ΔSCF approaches to not need considering the final ionized system for the computation of BEs in periodic systems. This avoids possible spurious effects arising from the core-holes interaction between the replicas.

4. XPS for the clinician, some more simple considerations

In this section, we briefly describe some of the studies on the characterization by XPS spectroscopy of materials with biological and medical interest.

The objective is to provide to the reader an idea of which chemical information can be gained by XPS experiments on these materials and which is their

impact on application in the fields of medicine and biology.

In particular we focus on the two major elements which play a pivotal role in medicine namely titanium and calcium. Titanium is a material widely used in the medical field for orthopedic prosthesis and implant dentistry [92,93] while calcium is an element at the core of the research performed on pathological and physiological calcifications as well as bioactive biominerals for orthopedic applications [11,12,94–96].

Different investigations have been dedicated to describing precisely the chemical and physical nature of the TiO_2 oxide layer in order to understand why freshly cut titanium seems to be more active in cell adhesion than titanium aged 4 weeks or more [97,98]. Titanium dioxide may have an amorphous state and eleven polymorphic phases [99]. Thermodynamically, Rutile [100,101] is the more stable phase, while anatase and brookite are metastable. These two last polymorphs will be transformed into rutile at higher temperature. As underlined by Peng *et al.* [102], a competition process occurs between the osteoblasts and pathogens introduced during surgery, on the surface of prostheses. Such competition has motivated numerous investigations on this major research subject with different characterization techniques [103,104].

As underlined in the publication of Roy *et al.* [105], XPS spectroscopy gives major information on the surface. The authors have considered two commercially available Osteoplant Base™ and Rapid™ titanium dental implants. On Figure 3a, we can see that like XRF spectroscopy, different elements can be identified. More precisely, the XPS spectrum is dominated by photoelectron peaks, corresponding to electrons originating in the 1s orbitals of the C, N, O and F or in the 2s or 2p orbitals of Ti and Al atoms in the sample surface. The intensity of the XPS spectra depends on the concentration of the element present. Moreover, peaks corresponding to the Auger process are visible (C_{KLL}, Ti_{LMM}, O_{KLL}…). The third component of a XPS spectrum is related to the background which comes from electrons excited by the X-ray Bremsstrahlung radiation at low binding energy as well as from inelastically scattered photoelectrons at higher binding energy.

But XPS spectroscopy gives more information. As we can see on Figure 3b, XPS spectroscopy is able through a deconvolution process to distinguish the different oxidation states of Ti namely Ti^{4+}, Ti^{2+} and Ti^0. Basically, the spin–orbit splitting (splitting between $Ti2p_{3/2}$ and $Ti2p_{1/2}$) is approximately the same for Ti^{4+}, Ti^{2+} and Ti^0). Regarding the chemical shift between Ti^0 and Ti^{4+}, the charge withdrawn leads to a 2p orbital relaxation to higher binding energy.

In their study, Roy *et al.* [105] demonstrate clearly through XPS spectroscopy that UVC irradiation was able to reverse biological ageing of titanium by greatly reducing the amount of carbon contamination present on the implant surface by up to 4 times, while the topography of the surface was not affected.

Note that information can be obtained also through the O2p peak (Figure 4). As reported by Song *et al.* [106], two large peaks could be measured located at 529.4 and 530.7 eV. These peaks can be assigned to TiO_2 and TiOH respectively [107].

Calcium is another key element in medicine. The chemistry of Calcium orthophosphate is quite complex and encompasses in medicine amorphous and nanocrystals compounds [108–110]. Demri and Muester [111] have measured the 2p XPS photoemission lines of different compounds containing calcium compounds (Figure 5). The contributions of the $Ca2p_{3/2}$ and $Ca2p_{1/2}$ can be distinguished for each compound. The position of the most intense $Ca2p_{3/2}$ peak is found to be strongly dependent on the local chemical environment of the Ca atom.

The CaO and $CaCO_3$ peaks are found located around 346.5 eV, while the calcium atoms bounded to phosphate groups are located at about 347 eV. For the compounds characterized by bonds with high ionic character (sulphates, nitrates, etc.), the $Ca2p_{3/2}$ peak is found shifted at higher binding energy. Such measurements illustrate the high sensitivity of XPS spectroscopy to the structure and chemical nature of the environment experienced by Ca, an element which plays a major role in medicine.

5. Selected examples related to medicine

Several papers [112,113] have underlined the different instrumentation and methodology advances that have enhanced the ability to study organic and biological systems through XPS spectroscopy. Among the biological systems and biomaterials which can be investigated through XPS spectroscopy, we can

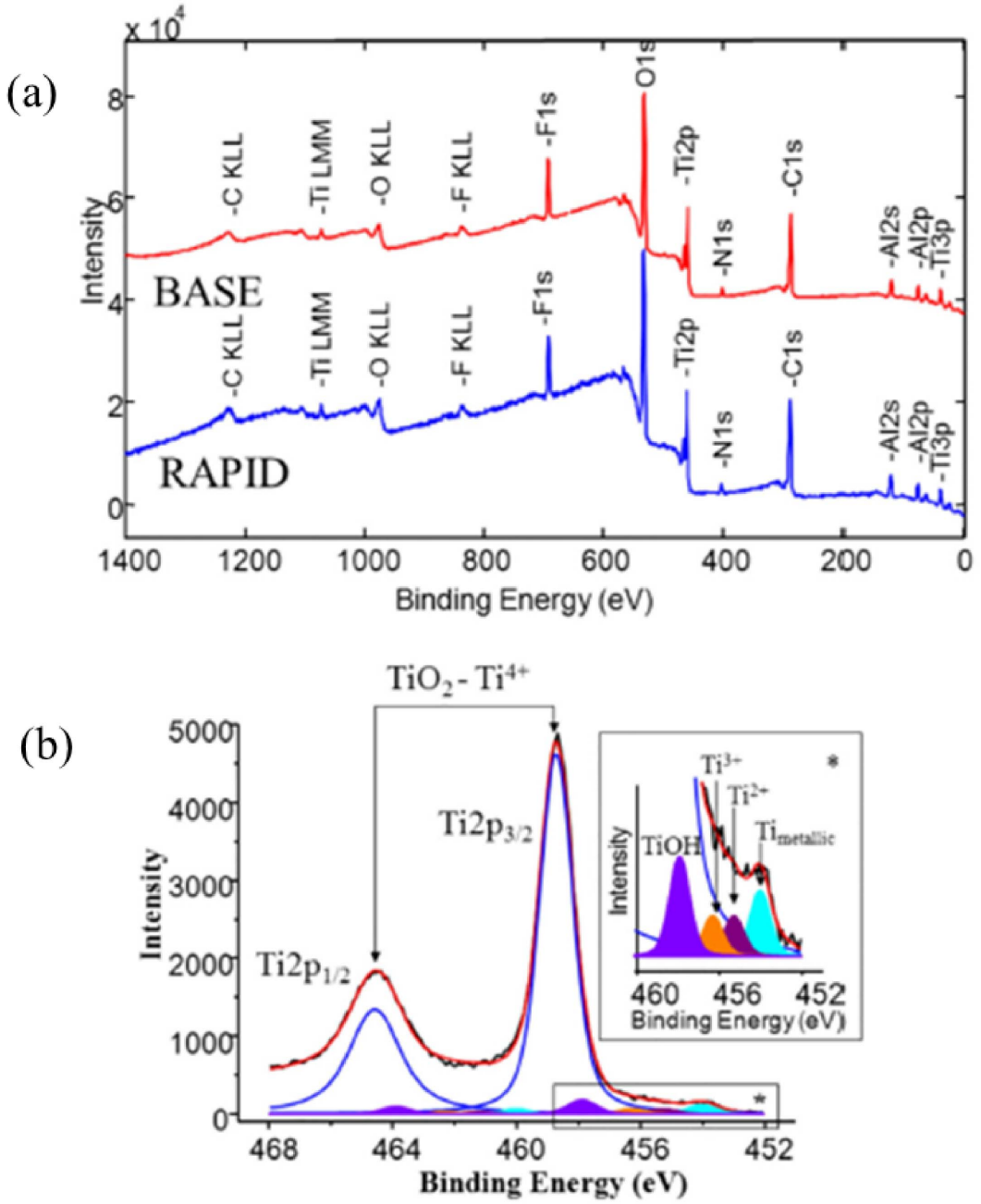

Figure 3. (a) The XPS survey spectra obtained for two samples the BASE (red) and RAPID (blue) implants as received. On both surfaces Ti, O, C, Al and F were detectable. (b) High resolution XPS spectrum of the Ti2p core line for RAPID implant. The shape of the 2p doublet was fitted by to five sub-doublets. The doublet with the highest intensity corresponded to TiO_2 component. The enlarged region presented the $Ti2p_{3/2}$ peaks corresponded to hydrated water Ti–OH, various oxidation states and metallic state of titanium (Roy *et al.* [105]).

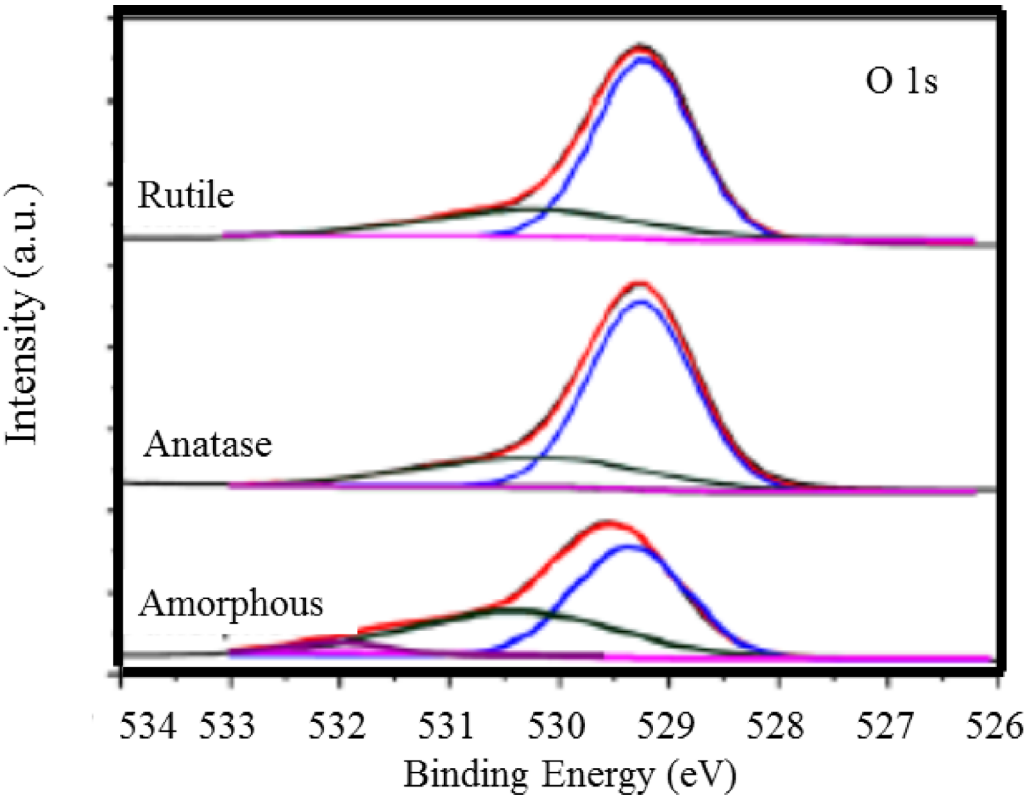

Figure 4. XPS core level spectra for O1s of TiO_2 samples as prepared and annealed at 450 °C and 700 °C (Song *et al.* [106]).

quote bacteria [114,115], Human cells [116,117], dental implants [118–120], intraocular lens [121,122] or physiological as well as pathological calcifications such as (not only human ones) [123–125], teeth [126–128], vascular calcifications [13,129] or kidney stones [130].

5.1. *XPS studies of implants*

5.1.1. *Multicomponents implants*

Regarding their chemical structure, implants may be composed of several elements. Titanium and its alloys are widely used in dental implants and hip-prostheses due to their excellent biocompatibility [131]. The characterization of their surface is clearly of primary importance to understand the relationship between the implant and physiological calcifications namely bones or teeth. For example, using XPS, it is possible to determine quantitatively the surface hydroxyl concentration, which results of the dissociation of a water molecule at the surface, on low specific surface area metal oxides such as TiO_2 and Fe_2O_3 [132,133]. Similar approach can be performed to characterize the surface of tetragonal stabilized ZrO_2 with the addition of 3 mol% Y_2O_3 dental implants [134]. For such implants which contain several elements, XPS can give the Y/Zr atomic ratio. As underlined by Zinelis *et al.* [134], a high value of this parameter may indicate yttria segregation. Recently, Su *et al.* [135] provide a brief summary of state-of-art of surface biofunctionalization on implantable metals by CaP coatings.

With XPS, it is also possible to describe the modifications of the surface induced by a chemical treatment. Takadama *et al.* [136] show through XPS study that a NaOH and treatments of a Ti–6Al–4V alloy produce an Al and V free amorphous sodium titanate surface layer on the surface. Note that a chemical treatment of the surface may also modify significantly its topology. Kang *et al.* [119] have observed that the electrochemical oxidation process for

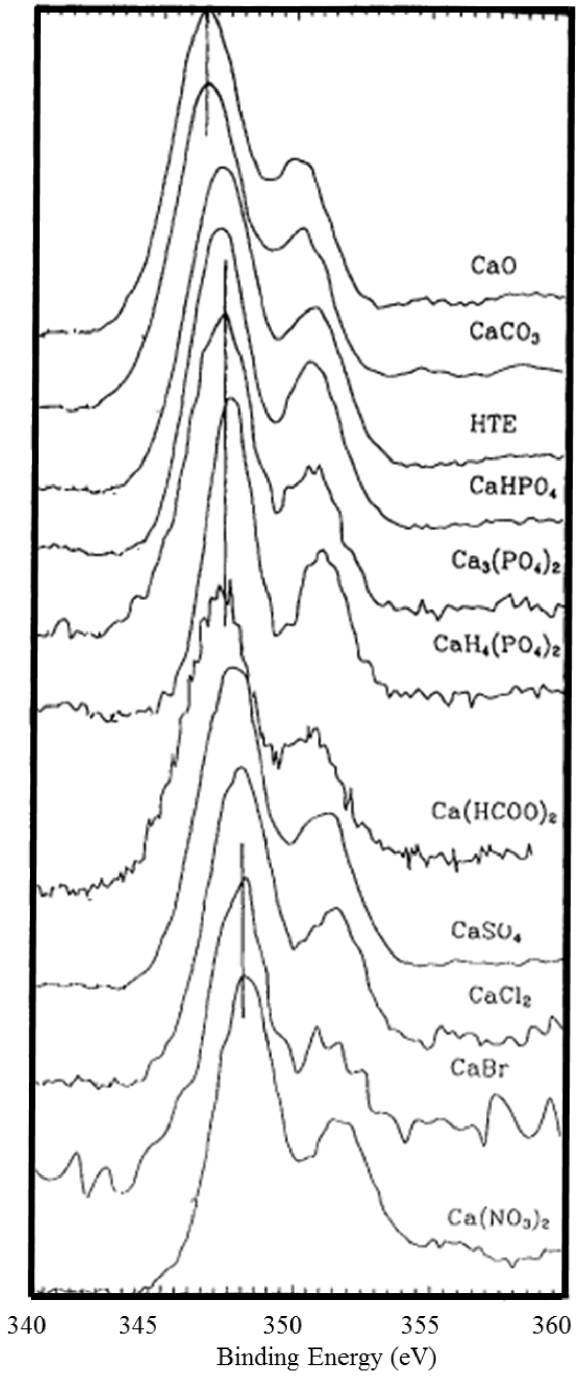

Figure 5. Ca2p spectra taken for different compounds (Demri and Muester [111]).

Ti implants produces microporous surface (pore size: 0.5–3.0 μm) and modify surface chemistry due to incorporation of anions of the used electrolyte. Regarding commercially pure titanium, Korotin *et al.* [137] have characterized through XPS such compound before and after chemical treatment (in 1% HF, 1 min and in 40% HF, 1 min). These authors found that acid treatment reduces the content of hydrocarbons increasing the surface energy and biocompatibility (through an increase of the oxygen concentration on the surface) of Ti-implants.

Then, on top of TiO_2 surface, zinc oxide nanoparticles can be used as a coating material to inhibit bacterial adhesion and promote osteoblast growth [138]. Recently, Chang *et al.* [139] have proposed a reliable method by considering the peak shift of Zn2p in XPS to inspect the ZnO matrix, rather than O1s. Finally, coating based on calcium phosphate apatite could significantly improve the biological performances of metallic implants [140,141]. As underlined by Lu *et al.* [142] hydroxyapatite is closed to the mineral part of bones and teeth and display a spontaneous interfacial osteointegration when implanted. In their investigation, these authors show that the Ca/P and O/Ca XPS peak ratios provide identification of the CaP phase(s) present in the surface and establish their mole fractions. More precisely, the relative intensity of shake-up satellite II related to O(1s) decreases in the following order: β-TCP (Tricalcium phosphate) > HAP (Hydroxyapatite) > OCP (Octacalcium phosphate) > DCP (dibasic calcium phosphate) > DCPD (dibasic calcium phosphate dihydrate) > MCP (monobasic calcium Phosphate).

Finally, Combes *et al.* [143] have investigated the nucleation and growth of dicalcium phosphate dihydrate ($CaHPO_4{\cdot}2H_2O$) on titanium powder at 37 °C and pH 5.5. Combining XPS and IR experiments, these authors observed that at the earliest stage of contact with the supersaturated solution, the oxidized titanium surface exhibited an increase of the xylation rate associated with calcium and phosphate uptake. Also, there are direct evidence that the first calcium phosphate layer exhibits the IR characteristics of amorphous calcium phosphate. It is at the end of the induction period that the formation of DCPD crystals was observed.

5.1.2. *Toxicity of implants*

For such biomaterials, investigations of their surface may be relevant to control their physicochemical structural characteristics and also to assess toxicity problems such as the ones related to the release

of TiO_2 particles which may also compromise bone-forming cell functions [138]. Recently, Kim *et al.* [144] have presented a general review of titanium toxicity pointing for example the accumulation of metal debris such as titanium, aluminum, and vanadium found in the bone marrow of some patients or the presence of inflammatory cells around titanium particles in peri-implantitis biopsies.

Oje and Ogwu [145] have underlined the presence of a non-stoichiometric oxide phase. Such conclusion is based on the measurement of the $Cr2p_{3/2}$ spectrum which display peaks at binding energy positions of approximately 575.25, 576.40 and 578.46 eV. In line with the publication of Ogwu *et al.* [146], the peak at approximately 575.25 eV indicates a non-stoichiometric oxide phase between metallic chromium at 574.9 eV and the Cr_2O_3 peak located at 576.40 eV.

5.2. *XPS studies of pathological and physiological calcifications*

The deposit of calcium phosphate at the surface of biomedical implants may be a major problem. It is the case for explanted intraocular lens [147], JJ-stents [148,149] or heart valves [150].

Bian *et al.* [151] have studied the degradation behaviors and in-vivo biocompatibility of a rare earth- and aluminum-free magnesium-based stent. The XPS data give the elementary composition at the surface through the detection of the contribution coming from Mg, O, Ca, P, C and minor Na. The possible presence of calcium phosphate hydroxyapatite on the surface is based on the measurements of Ca2p peak at 350.90 eV, along with P2p peak at 133.36 eV and O1s peak at 531.17 eV [152]. Simon *et al.* [121] have combined XPS and Ar^+ ion sputtering in order to investigate elemental depth profiles, as the sample can be analyzed layer by layer on the nanometric scale. As noticed by these authors, this is the first investigation on explanted intraocular lenses using XPS depth profiling in order to examine the inside of the opacifying deposits.

Regarding pathological calcifications, XPS offers the opportunity to study the adsorption of molecules or cations at the surface of chemical compounds which have been identified in pathological calcifications. Also, Gourgas *et al.* [13] used a set of characterization techniques including XPS spectroscopy to understand how pathological calcification is initiated on the vascular extracellular matrix. In their conclusion, the authors show that an interdisciplinary approach combining animal models and materials science can provide insights into the mechanism of vascular calcification in line with previous publications [11,12]. In their investigation, Gourgas *et al.* [13] have used XPS spectroscopy to underline the presence of CaP calcifications in on aorta sections. In this work, the authors used XPS to identify mineral phases present in calcified arteries from mouse models. Using XPS, they showed that the amount of calcium phosphate minerals is significantly increasing with time. Also, they observed a significant increase in the average Ca/P ratios overtime which showing the conversion of precursor phases into crystalline apatite phases. Overall, this work shows that mineral deposition in medial arterial calcification starts with precipitation of precursor phases (amorphous calcium phosphate and OCP) and further transformation to hydroxyapatite and carbonated hydroxyapatite.

Finally, XPS spectroscopy offers the opportunity to characterize physiological calcifications such as bones [124] or teeth [108]. The analysis of their surface may give major information regarding the presence of trace elements at their surface [153], the thickness of adsorbed mouth rinse components on dental enamel [154] or the adsorption process of drugs [124]. Zhao *et al.* [124] have investigated the effects of Sr-incorporation on scaffold physicochemical and mechanical properties, bioactivity, cytotoxicity, and bone formation rate. In the XPS spectra, two major peaks for Sr were measured with binding energies of 269.13 eV ($Sr3p_{3/2}$) and 133.52 eV ($Sr3d_{5/2}$). The incorporation of Sr increased the Ca element binding energy, with the $Ca2p_{3/2}$ peak increasing from 347.08 eV to 348.24 eV.

6. Conclusions

In this short overview we considered the use of XPS characterization methods in the field of clinical sciences. Some elements regarding the theoretical formalism in particular with respect to first principles calculations are given, followed by some practical and experimental information regarding XPS. Two

families of mineralization systems are discussed towards their XPS properties: mineralization originating from implants and from physiological pathological origin. Concerning the most studied family of both mentioned some more details are given on multicomponent implants, their toxicity, and their calcifications.

It is a timely work since it was noticed that XPS is becoming of interest in the analysis of biological mineralization applications, and that the experimental methodologies are available. Theoretical quantum chemical-based calculations have been performed so far on different solid systems and on surfaces in particular, but much less on biological mineral systems. However, it is clear that from the works published in the literature the computational methods are ready to be used on biological mineral systems and they are not only restricted to inorganic materials and heterogenous catalysts. In conclusion our message would be that a bright future of XPS is expected in the field of clinical sciences.

Conflicts of interest

Authors have no conflict of interest to declare.

Acknowledgement

FT wishes to acknowledge the VUB for support, among other through a Strategic Research Program awarded to his group.

References

[1] H. Hertz, *Ann. Phys.*, 1887, **31**, 983-1000.
[2] K. Siegbahn, *Et. Al., Nova Acta Regiae Soc. Sci., Ser. IV*, 1967, **20**, 1-282.
[3] C. R. Brundle, G. Conti, P. Mack, *J. Electron Spectr. Relat. Phenom.*, 2012, **178–179**, 433-448.
[4] R. Escamilla, E. Carvajal, M. Cruz-Irisson, F. Morales, L. Huerta, E. Verdin, *J. Mater. Sci.*, 2016, **51**, 6411-6418.
[5] O. Sublemontier, C. Nicolas, D. Aureau, M. Patanen, H. Kintz, X. Liu, M.-A. Gaveau, J.-L. Le Garrec, E. Robert, F.-A. Barreda, A. Etcheberry, C. Reynaud, J. B. Mitchell, C. Miron, *J. Phys. Chem. Lett.*, 2014, **5**, 3399-3403.
[6] L. Nguyen, P. P. Tao, H. Liu, M. Al-Hada, M. Amati, H. Sezen, L. Gregoratti, Y. Tang, S. D. House, F. F. Tao, *Langmuir*, 2018, **34**, 9606-9616.
[7] M. P. Seah, *Surf. Interface Anal.*, 1980, **2**, 222-239.
[8] P. M. Dietrich, S. Bahr, T. Yamamoto, M. Meyer, A. Thissen, *J. Electron Spectr. Relat. Phenom.*, 2019, **231**, 118-126.
[9] R. W. Paynter, M. W. King, R. G. Guidoin, T. Rao, *Int. J. Artif. Organs*, 1989, **12**, 189-194.
[10] G. Iucci, M. Dettin, C. Battocchio, R. Gambaretto, C. Dibello, G. Polzonetti, *Mater. Sci. Eng. C*, 2007, **27**, 1201-1206.
[11] D. Bazin, M. Daudon, C. Combes, C. Rey, *Chem. Rev.*, 2012, **112**, 5092-5120.
[12] D. Bazin, M. Daudon, *J. Phys. D: Appl. Phys.*, 2012, **45**, article no. 383001.
[13] O. Gourgas, J. Marulanda, P. Zhang, M. Murshed, M. Cerruti, *Arterioscler. Thromb. Vasc. Biol.*, 2018, **38**, 363-372.
[14] E. Leitao, M. A. Barbosa, K. de Groot, *J. Mater. Sci. Mater. Med.*, 1997, **8**, 423-426.
[15] C. Battistoni, M. P. Casaletto, G. M. Ingo, S. Kaciulis, G. Mattogno, L. Pandolfi, *Surf. Interface Anal.*, 2000, **29**, 773-781.
[16] C. Viornery, Y. Chevolot, D. Léonard, B.-O. Aronsson, P. Péchy, H. J. Mathieu, P. Descouts, M. Grätzel, *Langmuir*, 2002, **18**, 2582-2589.
[17] M. P. Casaletto, S. Kaciulis, G. Mattogno, A. Mezzi, L. Ambrosio, F. Branda, *Surf. Interface Anal.*, 2002, **34**, 45-49.
[18] F. Barrère, A. Lebugle, C. A. van Blitterswijk, K. de Groot, P. Layrolle, C. Rey, *J. Mater. Sci. Mater. Med.*, 2003, **14**, 419-425.
[19] G. M. Ingo, S. Kaciulis, A. Mezzi, T. Valente, G. Gusmano, *Surf. Interface Anal.*, 2004, **36**, 1147-1150.
[20] Z. Mladenovic, A. Sahlin-Platt, Å. Bengtsson, M. Ransjö, A. Shchukarev, *Surf. Interface Anal.*, 2010, **42**, 452-456.
[21] Z. Ren, Y. Wang, S. Ma, S. Duan, X. Yang, P. Gao, X. Zhang, Q. Cai, *ACS Appl. Mater. Interfaces*, 2015, **7**, 19006-19015.
[22] J. M. Andronowski, A. Z. Mundorff, R. A. Davis, E. W. Price, *J. Anal. At. Spectrom.*, 2019, **34**, 2074-2082.
[23] D. Bazin, E. Letavernier, J. P. Haymann, V. Frochot, M. Daudon, *Ann. Biol. Clin.*, 2020, **78**, 349-362.
[24] N. Vidavsky, J. A. M. R. Kunitake, L. A. Estroff, *Adv. Healthcare Mater.*, 2020, article no. 2001271.
[25] C. S. Fadley, *J. Electr. Spectr. Relat. Phenom.*, 2010, **178–179**, 2-32.
[26] P. S. Bagus, E. S. Ilton, C. J. Nelin, *Surf. Sci. Rep.*, 2013, **68**, 273-304.
[27] C. R. Brundle, B. V. Crist, *J. Vac. Sci. Technol. A*, 2020, **38**, article no. 041001.
[28] J. C. Fuggle, E. Umbach, D. Menzel, K. Wandelt, C. R. Brundle, *Solid State Commun.*, 1978, **27**, 65-69.
[29] A. Jablonski, *J. Electr. Spectr. Relat. Phenom.*, 2013, **189**, 81-95.
[30] S. Reguer, C. Mocuta, D. Thiaudière, M. Daudon, D. Bazin, *C. R. Chim.*, 2016, **19**, 1424-1431.
[31] S. Rouzière, D. Bazin, M. Daudon, *C. R. Chim.*, 2016, **19**, 1404-1415.
[32] D. Bazin, E. Foy, S. Reguer, S. Rouzière, B. Fayard, H. Colboc, J.-P. Haymann, M. Daudon, C. Mocuta, *C. R. Chim.*, 2022, **25**, no. S1, 164-188.
[33] D. Bazin, V. Frochot, J.-P. Haymann, E. Letavernier, M. Daudon, *C. R. Chim.*, 2022, **25**, no. S1, 133-147.
[34] D. S. You, H. M. Li, Z. J. Ding, *J. Electron Spectr. Relat. Phenom.*, 2018, **222**, 156-161.
[35] M. Xu, D. Fujita, J. Gao, N. Hanagata, *ACS Nano*, 2010, **4**, 2937-2945.
[36] P. Sutter, E. Sutter, *APL Mater.*, 2014, **2**, article no. 092502.
[37] P. H. Holloway, *J. Vac. Sci. Technol.*, 1975, **12**, 1418-1422.

[38] A. G. Shard, *J. Vac. Sci. Technol. A*, 2020, **38**, article no. 041201.
[39] U. Vohrer, C. Blomfield, S. Page, A. Roberts, *Appl. Surf. Sci.*, 2005, **52**, 61-65.
[40] G. Greczynski, L. Hultman, *Prog. Mater. Sci.*, 2020, **107**, article no. 100591.
[41] M. Quintin, *J. Phys. IV*, 1996, **C4**, C599-C609.
[42] R. Jenkins, *Anal. Chem.*, 1984, **56**, 1099A-1106A.
[43] M. M. Millard, "Surface characterization of biological materials by X-ray photoelectron spectroscopy", in *Contemporary Topics in Analytical and Clinical Chemistry* (D. M. Hercules, G. M. Hieftje, L. R. Snyder, M. A. Evenson, eds.), Springer, Boston, 1978.
[44] P. S. Vanzillotta, G. A. Soares, I. N. Bastos, R. A. Simão, N. K. Kuromoto, *Mater. Res.*, 2004, **7**, 437-444.
[45] J. A. L. Rabone, N. H. de Leeuw, *Phys. Chem. Minerals*, 2007, **34**, 495-506.
[46] G. Ulian, D. Moro, G. Valdrè, *Biomolecules*, 2021, **11**, article no. 728.
[47] Y. Tang, H. F. Chappell, M. T. Dove, R. J. Reeder, Y. J. Lee, *Biomaterials*, 2009, **30**, 2864-2872.
[48] F. Tielens, J. Vekeman, D. Bazin, M. Daudon, *C. R. Chim.*, 2022, **25**, no. S1, 209-218.
[49] I. Petit, G. D. Belletti, T. Debroise, M. J. Llansola-Portoles, I. T. Lucas, C. Leroy, C. Bonhomme, L. Bonhomme-Coury, D. Bazin, M. Daudon, E. Letavernier, J. P. Haymann, V. Frochot, F. Babonneau, P. Quaino, F. Tielens, *Chem. Select*, 2018, **3**, article no. 8801.
[50] T. Debroise, E. Colombo, G. Belletti, J. Vekeman, Y. Su, R. Papoular, N. S. Hwang, D. Bazin, M. Daudon, P. Quaino, F. Tielens, *Cryst. Growth Des.*, 2020, **20**, 2553-2561.
[51] D. Bazin, C. Leroy, F. Tielens, C. Bonhomme, L. Bonhomme-Coury, F. Damay, D. Le Denmat, J. Sadoine, J. Rode, V. Frochot, E. Letavernier, J.-P. Haymann, M. Daudon, *C. R. Chim.*, 2016, **19**, 1492-1503.
[52] Y. Lykhach, T. Staudt, M. P. A. Lorenz, R. Streber, A. Bayer, H. P. Steinrück, J. Libuda, *Chem. Phys. Chem.*, 2010, **11**, 1496-1504.
[53] M. Happel, N. Luckas, F. Vines, M. Sobota, M. Laurin, A. Görling, J. Libuda, *J. Phys. Chem. C*, 2011, **115**, 479-491.
[54] I. Niedermaier, C. Kolbeck, N. Taccardi, P. S. Schulz, J. Li, T. Drewello, P. Wasserscheid, H. P. Steinrück, F. Maier, *Chem. Phys. Chem.*, 2012, **13**, 1725-1735.
[55] N. Pueyo Bellafont, F. Illas, P. S. Bagus, *Phys. Chem. Chem. Phys.*, 2015, **17**, 4015-4019.
[56] N. Pueyo Bellafont, P. S. Bagus, F. Illas, *J. Chem. Phys.*, 2015, **142**, article no. 214102.
[57] G. Cavigliasso, D. P. Chong, *J. Chem. Phys.*, 1999, **111**, article no. 9485.
[58] Y. Takahata, A. dos Santos Marques, R. Custodio, *J. Mol. Struct.: Theochem.*, 2010, **959**, 106-112.
[59] N. Pueyo Bellafont, F. Viñes, F. Illas, *J. Chem. Theor. Comput.*, 2016, **12**, 324-331.
[60] L. Hedin, *Phys. Rev.*, 1965, **139**, A796-A823.
[61] D. Golze, L. Keller, P. Rinke, *J. Phys. Chem. Lett.*, 2020, **11**, 1840-1847.
[62] M. J. Van Setten, R. Costa, F. Vines, F. Illas, *J. Chem. Theor. Comput.*, 2018, **14**, 877-883.
[63] P. S. Bagus, F. Illas, G. Pacchioni, F. Parmigiani, *JESRA*, 1999, **100**, 215-236.
[64] P. S. Bagus, E. S. Ilton, C. J. Nelin, *Surf. Sci. Rep.*, 2013, **68**, 273-304.
[65] G. Kresse, J. Hafner, *Phys. Rev. B*, 1993, **47**, 558-561.
[66] G. Kresse, J. Hafner, *Phys. Rev. B*, 1994, **49**, 14251-14269.
[67] G. Kresse, J. Furthmaller, *Comput. Mater. Sci.*, 1996, **6**, 15-50.
[68] G. Kresse, J. Hafner, *J. Phys. Condens. Matter*, 1994, **6**, article no. 8245.
[69] G. Kresse, D. Joubert, *Phys. Rev.*, 1999, **59**, 1758-1775.
[70] T. D. Kühne, M. Iannuzzi, M. Del Ben, V. V. Rybkin, P. Seewald, F. Stein, J. Hutter, *J. Chem. Phys.*, 2020, **152**, article no. 194103.
[71] E. Pehlke, M. Scheffler, *Phys. Rev. Lett.*, 1993, **71**, 2338-2341.
[72] M. P. Ljungberg, J. J. Mortensen, L. G. M. Pettersson, *JESRA*, 2011, **184**, 427-435.
[73] P. E. Blöchl, *Phys. Rev. B*, 1994, **50**, 17953-17979.
[74] F. Viñes, C. Sousa, F. Illas, *Phys. Chem. Chem. Phys.*, 2018, **20**, 8403-8410.
[75] J. Gladh, H. Öberg, J. Li, M. P. Ljungberg, A. Matsuda, H. Ogasawara, H. Öström, *J. Chem. Phys.*, 2012, **136**, article no. 034702.
[76] L. Köhler, G. Kresse, *Phys. Rev. B*, 2004, **70**, article no. 165405.
[77] K. Gotterbarm, N. Luckas, O. Höfert, M. P. Lorenz, R. Streber, C. Papp, A. Görling, *J. Chem. Phys.*, 2012, **136**, article no. 094702.
[78] R. C. Salvarezza, P. Carro, *Phys. Chem. Chem. Phys.*, 2015, **17**, 24349-24355.
[79] W. Quevedo, J. Ontaneda, A. Large, J. M. Seymour, R. A. Bennett, R. Grau-Crespo, G. Held, *Langmuir*, 2020, **36**, 9399-9411.
[80] P. Tsaousis, J. Ontaneda, L. Bignardi, R. A. Bennett, R. Grau-Crespo, G. Held, *J. Phys. Chem. C*, 2018, **122**, 6186-6194.
[81] Q. T. Trinh, K. Bhola, P. N. Amaniampong, F. Jérôme, S. H. Mushrif, *J. Phys. Chem. C*, 2018, **122**, 22397-22406.
[82] N. Pueyo Bellafont, F. Viñes, W. Hieringer, F. J. Illas, *Comput. Chem.*, 2017, **38**, 518-522.
[83] N. García-Romeral, M. Keyhanian, A. Morales-García, F. Illas, *Nanoscale Adv.*, 2021, **3**, 2793-2801.
[84] P. S. Bagus, C. J. Nelin, X. Zhao, S. V. Levchenko, E. Davis, X. Weng, F. Spath, C. Papp, H. Kuhlenbeck, H.-J. Freund, *Phys. Rev. B: Condens. Matter Mater. Phys.*, 2019, **100**, article no. 115419.
[85] T. Ozaki, C.-C. Lee, *Phys. Rev. Lett.*, 2017, **118**, article no. 026401.
[86] J. M. Kahk, J. Lischner, *Phys. Chem. Chem. Phys*, 2018, **20**, 30403-30411.
[87] J. M. Kahk, J. Lischner, *Phys. Rev. Mater.*, 2019, **3**, article no. 100801.
[88] J. F. Janak, *Phys. Rev. B: Condens. Matter Mater. Phys.*, 1978, **18**, 7165-7168.
[89] J. C. Slater, *Adv. Quantum Chem.*, 1972, **6**, 1-92.
[90] T. Zhu, G. K. L. Chan, *J. Chem. Theor. Comput.*, 2021, **17**, 727-741.
[91] J. M. Kahk, G. S. Michelitsch, R. J. Maurer, K. Reuter, J. Lischner, *J. Phys. Chem. Lett.*, 2021, **12**, 9353-9359.
[92] S. Cometa, M. A. Bonifacio, A. M. Ferreira, P. Gentile, E. De Giglio, *Materials*, 2020, **13**, article no. 705.
[93] S. Kaciulis, G. Mattogno, A. Napoli, E. Bemporad, F. Ferrari,

A. Montenero, G. Gnappi, *J. Electron Spectr. Relat. Phenom.*, 1998, **95**, 61-69.
[94] C. Combes, S. Cazalbou, C. Rey, *Minerals*, 2016, **6**, article no. 34.
[95] C. Rey, C. Combes, C. Drouet, H. Sfihi, A. Barroug, *Mater. Sci. Eng. C*, 2007, **27**, 198-205.
[96] D. Bazin, C. Chappard, C. Combes, X. Carpentier, S. Rouzière, G. André, G. Matzen, M. Allix, D. Thiaudière, S. Reguer, P. Jungers, M. Daudon, *Osteoporosis Int.*, 2009, **20**, 1065-1075.
[97] W. Att, N. Hori, M. Takeuchi, J. Ouyang, Y. Yang, M. Anpo, T. Ogawa, *Biomaterials*, 2009, **30**, 5352-5363.
[98] M. Roy, W. Hędzelek, *J. Stomatol. (Czas. Stomatol.)*, 2014, **67**, 682-691.
[99] H. Sutrisno, S. Sunarto, *Indo. J. Chem.*, 2010, **10**, 143-148.
[100] S. C. Abrahams, J. L. Bernstein, *J. Chem. Phys.*, 1971, **55**, article no. 3206.
[101] R. J. Swope, J. R. Smyth, A. C. Larson, *Am. Mineral.*, 1995, **80**, 448-453.
[102] Z. Peng, J. Ni, K. Zheng, Y. Shen, X. Wang, G. He, S. Jin, T. Tang, *Int. J. Nanomed.*, 2013, **8**, 3093-3105.
[103] K. Das, S. Bose, A. Bandyopadhyay, *J. Biomed. Mater. Res. A*, 2009, **90**, 225-237.
[104] E. Gongadze, D. Kabaso, S. Bauer, J. Park, P. Schmuki, A. Iglič, *Mini. Rev. Med. Chem.*, 2013, **13**, 194-200.
[105] M. Roy, A. Pompella, J. Kubacki, J. Szade, R. A. Roy, W. Hedzelek, *PLoS One*, 2016, **11**, article no. e0157481.
[106] Y. Y. Song, H. Hildebrand, P. Schmuki, *Surf. Sci.*, 2010, **604**, 346-353.
[107] T. D. Sargeant, M. S. Rao, C. Y. Koh, S. I. Stupp, *Biomaterials*, 2008, **29**, 1085-1098.
[108] J. C. Elliot, "Studies in inorganic chemistry 18", in *Structure and Chemistry of the Apatites and other Calcium Orthophosphates*, Elsevier Science, Amsterdam, 1994, 53-62.
[109] L. Wang, G. H. Nancollas, *Chem. Rev.*, 2008, **108**, 4628-4669.
[110] C. Combes, C. Rey, *Acta Biomater.*, 2010, **6**, 3362-3378.
[111] B. Demri, D. Muester, *J. Mater. Process. Technol.*, 1995, **55**, 311-314.
[112] B. D. Ratner, D. G. Castner, *Colloids Surf. B*, 1994, **2**, 333-346.
[113] D. R. Baer, M. H. Engelhard, *J. Electron Spectr. Relat. Phenom.*, 2010, **178–179**, 415-432.
[114] H. C. van der Mei, J. de Vries, H. J. Busscher, *Surf. Sci. Rep.*, 2000, **39**, 1-24.
[115] F. Ahimou, C. J. P. Boonaert, Y. Adriaensen, P. Jacques, P. Thonart, M. Paquot, P. G. Rouxhet, *J. Colloid Interface Sci.*, 2007, **309**, 49-55.
[116] A. Skallberg, C. Brommesson, K. Uvdal, *Biointerphases*, 2017, **12**, article no. 02C408.
[117] P. B. Dengis, P. G. Rouxhet, *J. Microbiol. Methods*, 1996, **26**, 171-183.
[118] W. H. Lee, C. Y. Hyun, *Appl. Surf. Sci.*, 2006, **252**, 4250-4256.
[119] B.-S. Kang, Y.-T. Sul, S.-J. Oh, H.-J. Lee, T. Albrektsson, *Acta Biomater.*, 2009, **5**, 2222-2229.
[120] N. Arroyo-Lamas, I. Arteagoitia, U. Ugalde, *Int. J. Mol. Sci.*, 2021, **22**, article no. 2597.
[121] V. Simon, T. Radu, A. Vulpoi, C. Rosca, D. Eniu, *Appl. Surf. Sci.*, 2015, **325**, 124-131.
[122] R. Wang, J. Xia, J. Tang, D. Liu, S. Zhu, S. Wen, Q. Lin, *J. Ocul. Pharmacol. Ther.*, 2021, **37**, 172-180.
[123] H. Nakada, Y. Numata, T. Sakae, H. Kimura-Suda, Y. Tanimoto, H. Saeki, M. Teranishi, T. Kato, R. Z. LeGeros, *J. Hard Tissue Biol.*, 2010, **19**, 101-110.
[124] Y. Zhao, D. Guo, S. Hou, H. Zhong, J. Yan, C. Zhang, Y. Zhou, *PLoS One*, 2013, **8**, article no. e69339.
[125] T. G. Avval, S. C. Chapman, V. Carver, P. Dietrich, A. Thißen, M. R. Linford, *Surf. Sci. Spectra*, 2021, **28**, article no. 014002.
[126] J. F. Perdok, H. C. Van Der Mei, H. J. Busscher, M. J. Genet, P. G. Rouxhet, *J. Clin. Dent. Fall*, 1990, **2**, 43-47.
[127] D. Shah, T. Roychowdhury, S. Bahr, P. Dietrich, M. Meyer, A. Thißen, M. R. Linford, *Surf. Sci. Spectra*, 2019, **26**, article no. 014016.
[128] C. M. Zamudio-Ortega, R. Contreras-Bulnes, R. J. Scougall-Vilchis, R. A. Morales-Luckie, O. F. Olea-Mejía, L. E. Rodríguez-Vilchis, *Eur. J. Paediatr. Dent.*, 2014, **15**, 275-280.
[129] A. Parashar, O. Gourgas, K. Lau, J. Li, L. Muiznieks, S. Sharpe, E. Davis, M. Cerruti, M. Murshed, *J. Struct. Biol.*, 2021, **213**, article no. 107637.
[130] T. Roychowdhury, S. Bahr, P. Dietrich, M. Meyer, A. Thißen, M. R. Linford, *Surf. Sci. Spectra*, 2019, **26**, article no. 014017.
[131] A. T. Sidambe, *Mater. (Basel)*, 2014, **7**, 8168-8188.
[132] G. W. Simmons, B. C. Beard, *J. Phys. Chem.*, 1987, **91**, 1143-1148.
[133] B. Erdem, R. A. Hunsicker, G. W. Simmons, E. D. Sudol, V. L. Dimonie, M. S. El-Aasser, *Langmuir*, 2001, **17**, 2664-2669.
[134] S. Zinelis, A. Thomas, K. Syres, N. Silikas, G. Eliades, *Dent. Mater.*, 2010, **26**, 295-305.
[135] Y. Su, I. Cockerill, Y. Zheng, L. Tang, Y.-X. Qin, D. Zhu, *Bioactive Materials*, 2019, **4**, 196-206.
[136] H. Takadama, H. M. Kim, T. Kokubo, T. Nakamura, *Sci. Technol. Adv. Mater.*, 2001, **2**, 389-396.
[137] D. M. Korotin, S. Bartkowski, E. Z. Kurmaev, M. Meumann, E. B. Yakushina, R. Z. Valiev, S. O. Cholakh, *J. Biomater. Nanobiotechnol.*, 2012, **3**, 87-91.
[138] W. Souza, S. G. Piperni, P. Laviola, A. L. Rossi, M. I. D. Rossi, B. S. Archanjo, P. E. Leite, M. H. Fernandes, L. A. Rocha, J. M. Granjeiro, A. R. Ribeiro, *Sci. Rep.*, 2019, **9**, article no. 9309.
[139] F.-M. Chang, S. Brahma, J.-H. Huang, Z.-Z. Wu, K.-Y. Lo, *Sci. Rep.*, 2019, **9**, article no. 905.
[140] S. V. Dorozhkin, *Acta Biomater.*, 2014, **7**, 2919-2934.
[141] S. Shadanbaz, G. J. Dias, *Acta Biomater.*, 2012, **1**, 20-30.
[142] H. B. Lu, C. T. Campbell, D. J. Graham, B. D. Ratner, *Anal. Chem.*, 2000, **72**, 2886-2894.
[143] C. Combes, C. Rey, M. Freche, *Colloids Surf. B*, 1998, **11**, 15-27.
[144] K. T. Kim, M. Y. Eo, T. T. H. Nguyen, S. M. Kim, *Int J. Implant Dent.*, 2019, **5**, article no. 10.
[145] A. M. Oje, A. A. Ogwu, *R. Soc. Open Sci.*, 2017, **4**, article no. 170218.
[146] A. A. Ogwu, A. M. Oje, J. Kavanagh, *Mater. Res. Express*, 2016, **3**, article no. 045401.
[147] M. Rahimi, A. Azimi, M. Hosseinzadeh, *J. Ophthalmic Vis. Res.*, 2018, **13**, 195-199.
[148] C. Poulard, A. Dessombz, M. Daudon, D. Bazin, *C. R. Chim.*, 2016, **19**, 1597-1604.
[149] C. Torrecilla, J. Fernández-Concha, J. R. Cansino, J. A. Mainez, J. H. Amón, S. Costas, O. Angerri, E. Emiliani, M. A. Arrabal Martín, M. A. Arrabal Polo, A. García, M. C. Reina, J. F. Sánchez, A. Budía, D. Pérez-Fentes, F. Grases, A. Costa-Bauzá, J. Cuñé, *BMC Urol.*, 2020, **20**, article no. 65.

[150] P. R. Cipriano, M. E. Billingham, P. E. Oyer, L. M. Kutsche, E. B. Stinson, *Circulation*, 1982, **66**, 1100-1104.
[151] D. Bian, X. Zhou, J. Liu, W. Li, D. Shen, Y. Zheng, W. Gu, J. Jiang, M. Li, X. Chu, L. Ma, X. Wang, Y. Zhang, S. Leeflang, J. Zhou, *Acta Biomater.*, 2012, **124**, 382-397.
[152] B. Demri, D. Muster, *J. Mater. Process. Technol.*, 1995, **55**, 311-314.
[153] A. E. Nelson, N. K. S. Hildebrand, P. W. Major, *Surf. Sci. Spectra*, 2002, **9**, 250-259.
[154] H. J. Busscher, H. C. van der Mei, M. J. Genet, J. F. Perdok, P. G. Rouxhet, *Surf. Interface Anal.*, 1990, **15**, 344-346.

Comptes Rendus
Chimie
2022, Vol. 25, Special Issue S1, p. 165-188
https://doi.org/10.5802/crchim.103

Microcrystalline pathologies: Clinical issues and nanochemistry / *Pathologies microcristallines : questions cliniques et nanochimie*

The crucial contribution of X-ray fluorescence spectroscopy in medicine

L'apport incontournable de la spectroscopie de fluorescence X en médecine

Dominique Bazin [*, a, b], **Eddy Foy** [c], **Solenn Reguer** [d], **Stéphan Rouzière** [b], **Barbara Fayard** [e], **Hester Colboc** [f], **Jean-Philippe Haymann** [g, h, i], **Michel Daudon** [g, h, i] **and Cristian Mocuta** [d]

[a] Université Paris-Saclay, CNRS, Institut de Chimie Physique, 91405 Orsay cedex, France

[b] Université Paris-Saclay, CNRS, Laboratoire de Physique des Solides, 91405, Orsay, France

[c] Université Paris-Saclay, CEA, CNRS, NIMBE-LAPA, 91191 Gif-sur-Yvette, France

[d] Synchrotron SOLEIL, L'Orme des Merisiers, Saint-Aubin, BP 48, 91192 Gif-sur-Yvette, France

[e] European Synchrotron Radiation Facility, 71, avenue des Martyrs CS 40220, 38043 Grenoble Cedex 9, France

[f] Sorbonne Université, AP-HP, Hôpital Rothschild, Service Plaies et Cicatrisation, Paris, France

[g] Sorbonne Universités, UPMC Univ Paris 06, UMR S 702, Paris, France

[h] INSERM, UMR S 702, Paris, France

[i] Explorations fonctionnelles multidisciplinaires, AP-HP, Hôpital Tenon, Paris, France

E-mails: dominique.bazin@universite-paris-saclay.fr (D. Bazin), eddy.foy@cea.fr (E. Foy), solenn.reguer@synchrotron-soleil.fr (S. Reguer), stephan.rouziere@u-psud.fr (S. Rouzière), barbara.fayard@novitom.com (B. Fayard), hester.colboc@aphp.fr (H. Colboc), jean-Philippe.haymann@aphp.fr (J.-P. Haymann), michel.daudon@aphp.fr (M. Daudon), cristian.mocuta@synchrotron-soleil.fr (C. Mocuta)

[*] Corresponding author.

Abstract. This contribution tries to indicate to the clinician what kind of information can be investigated through X-ray fluorescence, what kind of information can be extracted from this spectroscopy and finally how it competes with other tools described in previous publications such as Fourier Transform Infrared or Raman spectroscopy, X-ray Absorption Near Edge Structure spectroscopy and X-ray diffraction. To attain this goal, several examples based on X-ray fluorescence experiments performed on biological samples namely concretions, medical devices, biological fluids as well as tissues are presented.

Résumé. Cette contribution vise à sensibiliser le clinicien sur l'utilisation de la spectroscopie de fluorescence X en précisant le type d'échantillon pouvant être étudié et les informations exploitables. De plus, la complémentarité avec d'autres techniques analytiques présentées dans des publications précédentes, telles que les spectroscopies vibrationnelles (spectroscopie infrarouge à transformée de Fourier et Raman), la spectroscopie d'absorption des rayons X et la diffraction des rayons X est discutée. Différents résultats de mesures par spectroscopie de fluorescence X effectués sur des échantillons biologiques de différentes natures (concrétions, dispositifs médicaux, fluides et tissus biologiques) sont présentés.

Keywords. X-ray fluorescence spectroscopy, Medicine, Biological samples, Concretions, Tissues, Biological fluids.

Mots-clés. Spectroscopie de fluorescence X, Médecine, Échantillons biologiques, Concrétions, Tissus, Fluides biologiques.

Published online: 17 August 2021, Issue date: 1 September 2022

1. Introduction

In addition to the precise theoretical and experimental description of X-ray fluorescence (XRF) spectroscopy previously made [1–7], the present review is nonetheless important in order to show the clinician the kind of sample that can be investigated using XRF, the kind of information that can be derived from these analyses and how it competes with other analytical tools [8–13].

For example, while vibrational spectroscopies such as Infrared spectroscopy used routinely at the hospital [14–16] give accurate determination of the chemical composition of kidney stones, these vibrational techniques are unable to assess the presence of trace elements in these concretions [17–19] or to determine the presence of a compound for which the crystallographic structure has not been established [20–22]. It is for example the case of calcium tartrate tetrahydrate [23,24].

Highlighting the presence or the absence of some elements in biological tissues may be of great interest in medicine in the sense that it can help in diagnosis [25–32]. Indeed, the presence of lead may indicate a diagnosis of saturnism [33] while accumulation of copper may be related to Wilson's disease [34]. Finally, the role of magnesium, zinc, copper, and manganese ions on the kinetics of crystal growth of calcium oxalate has been discussed [17,35]. Some elements may play some role in the very first steps of the pathogenesis of calcification [36–38].

The appeal of X-ray based analysis for pathological calcification lies in several major advantages such as precious samples or which exist in very low quantity. First of all, it is a non-invasive technique, to the best of our knowledge material changes are not observed (no phase transition) during the experiment, even when using synchrotron radiation as a source. In most cases, the biological samples can be investigated directly, no preparation is required, with little or no pre-treatment. The sensitivity of XRF is excellent (some times less than μg/g) because in most cases, the aim is to detect heavy elements in a matrix which contains mainly light elements such as C, N and O: this configuration is quite positive with regard to this technique as shown in the following scientific cases. In addition, the acquisition time is quite short, and evaluation times vary from few seconds up to few minutes depending on the classical laboratory instrument used, down to few milliseconds when using brilliant synchrotron source. All these benefits imply that the presence or absence of numerous potential elements can be validated in a few minutes in the most basic form of the technique, including measurement and data processing.

First, the present contribution describes briefly the complementary techniques, which are able to detect trace elements (in addition to XRF), and this description includes their advantages and drawbacks. Then, some key points regarding XRF spectroscopy

Table 1. Methods for trace element analysis

	Analytical methods
Destructive analysis	AAS (atomic absorption spectroscopy)
	ICP-AES (inductively coupled plasma-atomic emission spectroscopy)
	ICP-MS (inductively coupled plasma-mass spectroscopy)
Semi-destructive	LA-ICP-MS (laser abrasion-ICP-MS)
	SIMS (secondary ion mass spectroscopy)
Non-destructive	EDS (energy dispersive X-ray spectroscopy) or WDS (wavelength dispersive X-ray spectroscopy)
	XRF
	NAA (neutron activation analysis)
	PIXE (particle induced X-ray emission spectroscopy)

will be underlined. Finally, while the previous review paper focused on the contribution of XRF to pathological calcification studies [39], the present one highlights recent results obtained on various kinds of biological samples.

2. Some notions regarding different techniques for the detection of trace elements

In a recent review, Uo *et al.* [40] have defined three families namely destructive, semi-destructive and non-destructive, for the techniques dedicated to the detection of trace elements (Table 1).

As noticed by the authors, the first three ones, namely AAS, ICP-AES and ICP-MS are quite popular for trace element analysis. In the case of AAS [41], the number of elements detected is quite low even if some recent experimental developments allow the measurements for a significant number of elements. For example, Rello *et al.* [42] measured Mo and Ti levels in a dried urine spot using solid sampling high resolution continuum source graphite furnace AAS. Unfortunately, the destructive nature of these methods is a strong inconvenience in the case of kidney biopsy. For such biological samples, it is of major importance to localize the calcification: is it present in the glomerulus or in the proximal or distal tubule?

When considering non-destructive techniques, their availability must also be considered. Indeed, regarding PIXE analysis, a source of protons is needed and to date there are only two experimental setups existing in France [43]. Furthermore, the set of non-destructive techniques (Table 2) displays very different sensitivities [40]. Clearly, the limit of detection of SEM–EDS seems to be quite high. Nevertheless, because the dimension of the probe is very small, the presence of trace elements in submicrometer particles can be underlined. The localization of trace elements versus an alteration of the tissue such a tumor can be important to establish a medical diagnosis. One efficient way to be able to decipher the role of trace elements is to detect them with a non-destructive technique which has a great sensitivity and then be able to localize the abnormal deposit accurately in the biological tissue. Such an approach calls for classical XRF spectroscopy and in a second step, to perform such experiments using the synchrotron radiation as a source. In the latter case, the spatial resolution may be optimized at different scales from millimeters through micrometers down to nanometers.

3. Some basic features regarding XRF

XRF relies on the emission of characteristic secondary X-rays emitted from specific atoms after irradiation of the materials by high energy X-ray beam [44–47]. The first commercial XRF spectrometer was developed in the 1950s [48]. Since then, XRF has attracted increasing consideration in numerous research areas [49].

The physical principle of the XRF is illustrated in Figure 1. The excitation of core electrons (present on the K or L shell) of the sample by an X-ray photon

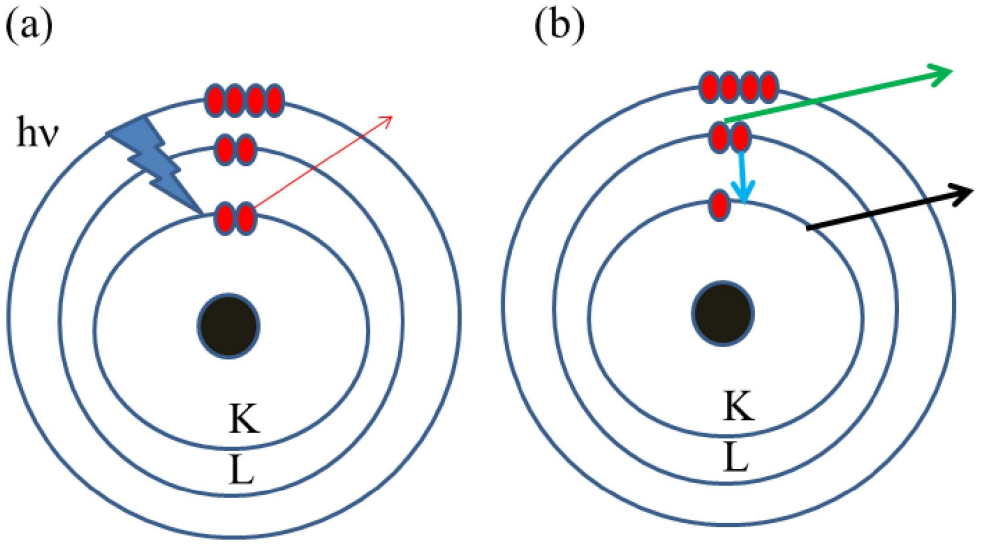

Figure 1. Basic physics related to XRF spectroscopy. The incident X-ray photon (a) creates a hole following the ejection (red arrow) of a 1s electron. (b) Such a hole disappears after an electronic transition (blue arrow) which induces the emission of an Auger electron or an X-ray photon (green arrow), called the fluorescent radiation (black arrow).

Table 2. Methods for trace element analysis

Technique	Excitation source	Sample preparation	Measurements conditions	Limit of detection (ppm)	Spatial resolution (μm)
PIXE	Protons	Dehydrated	High vacuum	1–10	1–3
EDS	Electrons	Dehydrated	High vacuum	≈5000	≈0.1
XRF	In lab X-rays	None	Ambient pressure	≈50	30–50
XRF	Synchrotron radiation	None	Ambient pressure	≈1	≈0.01

leads at the atomic scale to the ejection of an electron called photoelectron (Figure 1a). The formation of a core hole leads to electronic transition which induces the emission of a photon or an Auger electron (Figure 1b). One of the key points of XRF relies on the fact that the energy of the emitted photon is specific to the photo-excited atom [50–52] (Figure 2, Table 3).

4. Data analysis process procedures

4.1. *Experimental facility setup*

Nowadays, laboratory XRF setups benefit from up-to-date instrumental developments enabling the detection of trace elements with the highest efficiency (Figure 3). Typical XRF setup includes (i) an X-ray generator with a Cu or Mo anticathode, for example, producing high energy radiation (8.04 keV for Cu anticathode and 17.48 keV for Mo anticathode) allowing the detection of most of the elements of the periodic table, (ii) a multilayer mirror optics focusing a monochromatic beam onto the sample and (iii) a SDD (Silicon Drift Detector) energy dispersive detector (see Figure 3). Further, measurements may also be carried out at a micrometric scale by using microbeams with size down to 20 μm in diameter [53]. The XRF setup, using a sealed tube X-ray source, represents a highly compact instrument which can easily be transported in a hospital.

Over the past several years, commercial XRF devices have been developed (see for example the review by Bosco Ref. [54]) and used essentially to de-

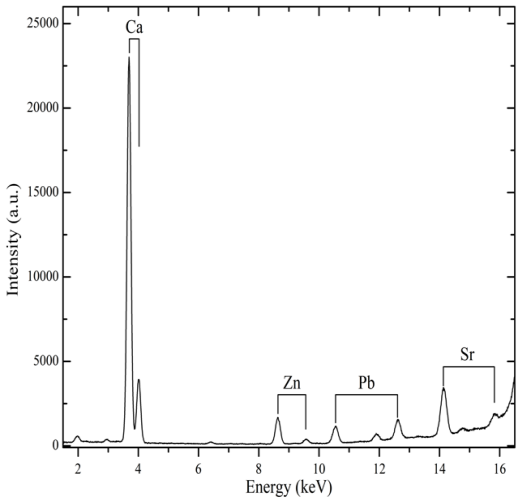

Figure 2. XRF spectrum collected for a biological apatite (bone) linked to a pathological calcification showing the contributions of Ca (K_α = 3.69 keV, K_β = 4.01 keV), Zn (K_α = 8.64 keV, K_β = 9.57 keV), Pb (L_α = 10.55 keV, L_β = 12.61 keV) and Sr (K_α = 14.16 keV, K_β = 15.84 keV).

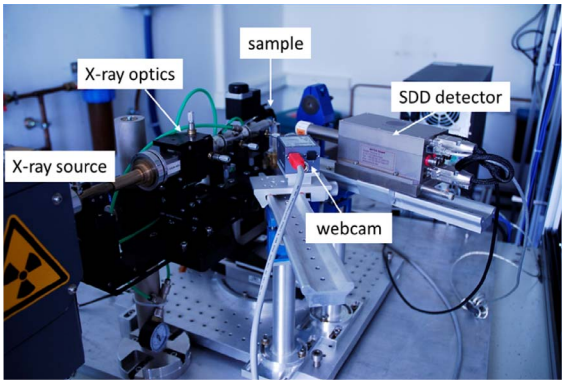

Figure 3. Laboratory XRF setup at Laboratoire de Physique des Solides (Orsay, France).

tect health problems in people working in the mining and construction industry [55]. Even if their sensitivity is less than thta of the laboratory experimental setup, commercial XRF devices offer the opportunity to gather information "at home" regarding the presence of different heavy elements such as Pb in bone [56], Zn in human toenail clipping [57] and human nail [58], Cr [59] and Fe [60] in skin, Zr in

Table 3. Characteristic X-ray emission (keV) for selected elements identified in biological samples

Atomic number	Element	Characteristic X-ray emission line (keV)			
		$K_{\alpha 1}$	$K_{\alpha 2}$	K_β	$L_{\alpha 1}$
3	Li	0.05			
6	C	0.27			
7	N	0.39			
8	O	0.52			
9	F	0.67			
11	Na	1.04	1.04	1.07	
12	Mg	1.25	1.25	1.30	
15	P	2.013	2.01	2.14	
16	S	2.30	2.30	2.46	
17	Cl	2.62	2.62	2.81	
18	Ar	2.95	2.95	3.19	
19	K	3.31	3.31	3.58	
20	Ca	3.69	3.68	4.01	
22	Ti	4.51	5.50	4.93	
24	Cr	5.41	5.40	5.94	
25	Mn	5.90	5.89	6.49	
26	Fe	6.40	6.39	7.05	
29	Cu	8.04	8.02	8.90	
30	Zn	8.63	8.61	9.57	
33	As	10.54	10.50	11.72	
78	Pt				9.44
82	Pb				10.55
83	Bi				10.83

dental restorative resin materials [61], tooth abnormalities (pulp stones) [62–64], the determination of Fe in blood [65] or the presence of Pu (Plutonium) for workers decommissioning the Fukushima Daiichi nuclear power plant [66].

Practically a portable XRF setup (Figure 4) can be used for solid metals and alloys, ores and soils [67]. Using a gold anode X-Ray generator, under 50 kV high voltage excitation, it offers a powerful source and highly sensitive measurements. Thus the detection limit is lowered for high Z elements and investigation of low Z elements such as Mg, Al, Si and P can be achieved via He purge between the detector and the sample (Figure 4). The spot size is also tuneable

Figure 4. Portable X-ray instrument on its portable test stand at the NIMBE-LAPA laboratory (Saclay, France).

from a larger spot of 8 mm diameter to a smaller spot of 3 mm diameter. Furthermore, thanks to a CCD camera, the visualization and location of the areas of interest on the sample is possible. Finally, by connecting the portable XRF with a simple USB cable to a computer, all the data and spectra are fetched from the instrument using a dedicated software for advanced analysis of the results.

Also noteworthy is the recent development of portable XRF devices that allow assessing the presence of Pu in biological fluids [68–70]. As underlined by Izumoto *et al.* [68], fast on-site detection of Pu is usually performed by analysis of α-particles emitted from the adhesive tape peeled off the wound. These authors have developed a new strategy based on XRF where blood is deposited on filter paper. With that experimental procedure using lead as a model for Pu, the XRF signal is proportional to the Pb concentration in blood. With a measurement time of 30 s, these authors estimate the minimum detection limit of Pb in blood collected by filter paper to be 2.4 ppm.

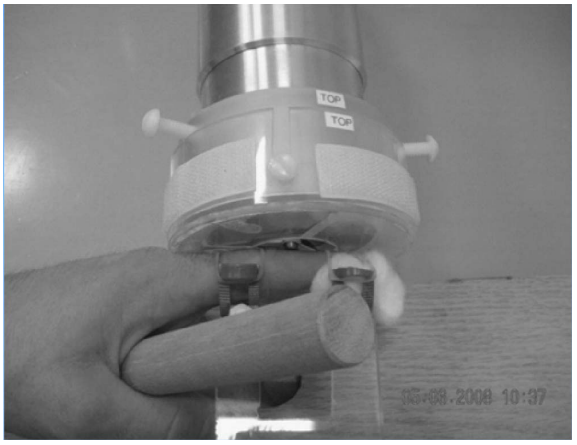

Figure 5. Experimental setup able to measure the content of Sr in human finger through in vivo XRF measurement.

4.2. *In vivo investigations based on XRF measurements*

At the hospital, in vivo XRF on human tissue can be also considered. Among the early in vivo XRF experiments, the publication of Pavoni *et al.* [71] discussed the feasibility of in vivo XRF study of the thyroid following stable I (iodine) administration. In vivo XRF analysis of Hg (mercury) in kidney, liver, thyroid, blood and urine has been recently investigated [72, 73]. The mean kidney Hg concentration was 24 μg/g in the exposed workers, and 1 μg/g in the controls. A statistically significant correlation between Hg in the kidney and in urine was found. Also, the Hg levels in liver and thyroid in the exposed workers were below the detection limit.

In the case of the work of Moise *et al.* [74], XRF spectra were collected on the finger and on the ankle bone sites, representing primarily cortical and trabecular bone, respectively (Figure 5). The acquisition time being 30 min, these publications underline the possibility of monitoring and measuring bone Sr (strontium) levels over time.

4.3. *XRF using Synchrotron Radiation as a source*

The major advantages of using synchrotron sources to do XRF measurements are now discussed [39,75–78]. While the brightness of a conventional X-ray tube is around 10^{10} photons/s·mrad^2·mm^2, the corresponding value of synchrotron radiation sources is

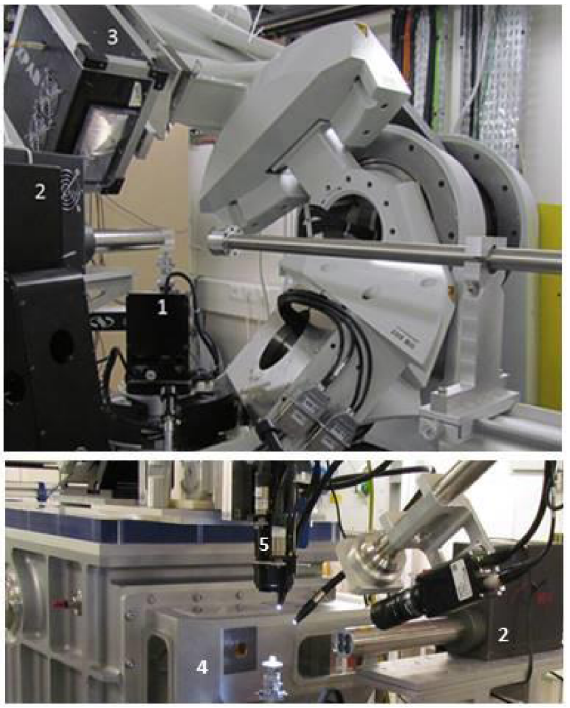

Figure 6. Experimental setup at DiffAbs beamline, SOLEIL synchrotron (St Aubin, France), for (a) standard (300 μm) and (b) microbeam (10 μm) modes. 1: sample holder with translation tables, 2: XRF detector (4 elements SDD), 3:2 dimensions detector for X-ray diffraction (XPAD 3.2) 4: vacuum chamber containing Kirkpatrick–Baez optics, 5: Camera microscope.

between 10^{15} and 10^{20}. The sensitivity of XRF is thus much better when the experiments (Figure 6) are performed on such a large scale instrument [79]. In addition, in the case of synchrotron radiation sources the beam can be focused down to the micrometer or even nanometer scale allowing local analyses [80,81].

Numerous works have been published on the basis of the subcellular beam size. Among them, a study established the concentration profiles of Fe, Cu, Zn, Br, Sr and Pb in different parts of a tooth in order to discuss the possible influence of diet [82]. It is also possible to acquire 2D maps [83]. In a recent review, Gherase and Fleming [84] present numerous investigations using spatial resolution several micrometers to reveal the distribution of trace elements (<a few μg/g). As underlined by these authors, current research effort is aimed not only at measuring the abnormal elemental distributions associated with various diseases, but also at indicating or discovering possible biological mechanisms that could explain such observations.

Nowadays, there is the possibility to gather information on the spatial distribution of trace elements inside cells [85]. For example, Ortega *et al.* [86] have developed an original experimental setup which allows aquisition of XRF images with a 90 nm spatial resolution. Such an experimental device leads to important medical results like the accumulation of iron in dopamine neurovesicles. Several major breakthroughs have been achieved using such nanometer spatial resolution [87–89]. Note that such unique characteristics lead to the conception and the realization of beamline dedicated to medicine (see for example Refs. [90–94]).

4.4. *Data processing and analysis*

After the energy calibration of the XRF detector, the very first step of the data processing, which leads to the determination of the spatial distribution of the different elements is given by a fitting procedure of the fluorescence lines for each XRF spectrum. This allows to identify and evaluate the contribution of each element semi-quantitatively. In some cases, the contribution to the measured signal of two elements can be quite close and/or (partially) superimposed and a deconvolution process has to be performed, like in the case of the energy related to Au L_α and Zn K_β fluorescence emission (Figure 7, from Ref. [95]).

If mapping with XRF contrasts are realized (see e.g., Section 5), visual correlations between the chemical species and their presence in particular regions of the sample can be sometimes noted, but they can also be the result of a subjective view. A more thorough quantitative and statistical analysis is thus expected to support (or not) the visual impression, but also to give more precise information regarding the chemical species identified in the XRF spectra, and to quantify as well the degree of correlation (i.e. any statistical pattern or relationships or even dependence between the datasets). Correlations are useful quantities to be examined, since they can potentially indicate a predictive relationship to be exploited.

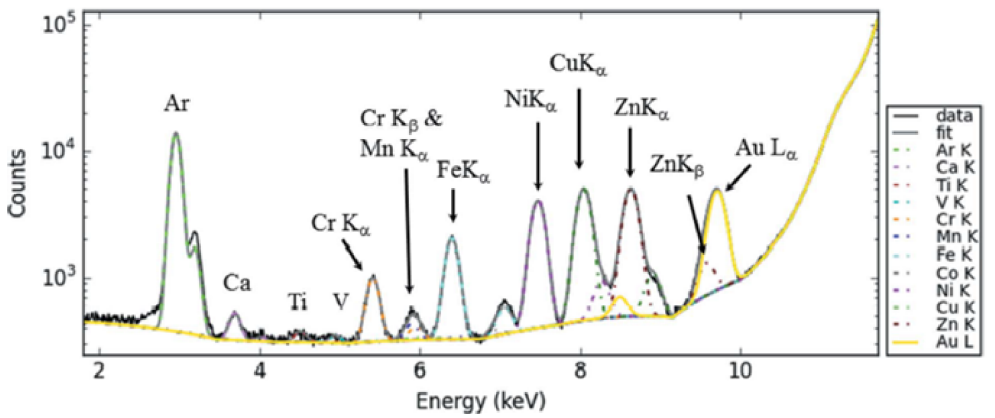

Figure 7. Typical XRF spectrum collected for a biological sample with the contribution of Ca (K_α at 3.691 keV, K_β at 4.012 keV), Fe (K_α at 6.404 keV, K_β at 7.058 keV), Zn (K_α at 8.638 keV, K_β at 9.572 keV). Special attention has been devoted to distinguish, by peak deconvolution, the respective contributions of Zn (K_α = 9.572 keV) and Au (L_α = 9.713 keV) between 9 and 10 keV.

Nevertheless, one has to be particularly cautious in drawing conclusions, and several issues have to be carefully considered:

- the smaller the size of the available dataset, the more likely is it to observe a correlation that might not be real and not observable if the same set can be extended. Thus, with small datasets (or small parts of them), correlations can be unreliable.
- presence of single unusual points in the datasets (outlier) can make the computed correlation coefficients highly misleading.
- a correlation between two variables is not a sufficient condition to establish such a causal relationship relating these variables, in either direction.

As previously shown [95–98], the XRF contrasted maps can be analyzed using Intensity Correlation Analysis methods in order to highlight possible correlations related to the presence of the different chemical elements in a sample. Other correlation coefficients can be used as well, but they will not be discussed here. The reader can also refer to the detailed work of Dunn *et al.* [98] and references therein.

Let us briefly describe some correlation approaches [99–104], considering the case of two XRF contrasted images (labeled in the following as image 1 and image 2) of the same lateral size and resolution (same number of points), obtained on the very same sample region, but showing the distribution of two different chemical elements. $X_{i,j}$ and $Y_{i,j}$ are the intensity of the pixel of coordinates (i, j) for the two images, respectively.

(A) In a first step, scatter plots can be used. If one expects that the dataset of image 2 ($Y_{i,j}$) is somehow dependent of the one in image 1 ($X_{i,j}$), plotting them as a scatter plot (using Y and X axis respectively) allows drawing some conclusions: (i) a positive correlation between X and Y variables is found if the obtained pattern exhibits a positive slope (from lower left to upper right of the graph, i.e. the Y variable tends to increase when the X variable is increasing); (ii) a negative correlation is found if the above mentioned trend is opposite; (iii) no correlation generally translates into no trends noticed in the scattered plots. Possibly, the result can be fitted (but no "universal" model exists) and the degree of correlation can thus be quantified by the parameters of the fit and their comparison between similar datasets.

(B) The Pearson colocalization coefficient for two variables is defined as the ratio of the covariance of the two variables by the product

of their standard deviation:

$$r_p = \frac{\sum(X_{i,j} - X_{\text{ave}})(Y_{i,j} - Y_{\text{ave}})}{\sqrt{\sum(X_{i,j} - X_{\text{ave}})^2 \sum(Y_{i,j} - Y_{\text{ave}})^2}}$$

with the summations being performed over the entire considered dataset/image, i.e., all the pixels of coordinates (i, j), and X_{ave} and Y_{ave} denoting the average intensity for the two images, respectively.

The obtained parameter representing the correlation of the intensity distribution in the two images is thus independent of their brightness. With this definition, r_p parameter takes values from -1 to $+1$. A value of r_p close to 1 means that the images are strongly correlated or there is a good colocalization of the signal in the two images (brighter areas in image 1 correspond to brighter areas in image 2). $r_p \approx 0$ is a signature of no correlation of the two images. As also pointed out above, we should note in this case that finding a value close to 0 for the r_p parameter does not necessarily imply that the respective variables (X and Y) are independent. In the particular case of r_p close to -1, the images are negatively correlated (or excluded), having reversed contrast: image 2 is the negative of image 1, or brighter areas in image 1 correspond to darker areas in image 2 and vice versa.

In practice, for the datasets, and in order to reduce errors for real sample images, the Pearson colocalization coefficient should be calculated on the investigated object only. The background is excluded from the calculations (masked out by setting it to a non-physical negative value, for example) the above summations are performed only inside the sample (for the pixels of coordinates (i, j) for which $X_{i,j} > 0$ and $Y_{i,j} > 0$).

The interpretation of the results based only on the Pearson coefficient might give rise to controversy: the results are rather sensitive to noise and are reliable only for high correlation (which is not always the case in experiments).

(C) In order to push this analysis further, other coefficients and correlation maps can be calculated. Pearson correlation coefficient is a symmetric quantity, which can be a limitation in the interpretation of the results. To overcome this issue, the Manders' (colocalization) coefficients M12 and M21 allow to know, for M12, how well the intense pixels in image 1, which are above a certain intensity threshold, colocalizes with intense pixels in image 2 (i.e. the probability to find bright pixels, above a certain threshold value, in image 2 only at the positions of intense pixels in image 1) and vice versa for M21. When using this approach, a threshold for the XRF signal needs to be used to calculate M12 and M21 [84]; for each image, it was set to half of the average signal, average calculated over the whole image.

Denoting the threshold values of X and Y images by τ_x and τ_y respectively (their values can be 0 as well), this can be written as:

$$M12 = \frac{\sum(X_{i,\text{coloc}})}{\sum(X_i)} \quad \text{with } X_{i,\text{coloc}} = X_i \text{ if } Y_i > \tau_y \text{ and } X_{i,\text{coloc}} = 0 \text{ otherwise}$$

$$M21 = \frac{\sum(Y_{i,\text{coloc}})}{\sum(Y_i)} \quad \text{with } Y_{i,\text{coloc}} = Y_i \text{ if } X_i > \tau_x \text{ and } Y_{i,\text{coloc}} = 0 \text{ otherwise.}$$

The last two approaches mentioned above (Pearson and Manders coefficients) are not equivalent, and give complementary information. Also, note that the Manders coefficients are not necessarily symmetric. For example, it might be that a great part (or all) of the intense pixels of image 1 corresponds to intense pixels in image 2 (M12 $\sim$ 1), but the opposite might not be true: regions of the bright signal in the second image might not have any correspondence to image 1 (M21 $\ll$ 1). An example is shown in Section 6.6.

All the correlation/colocalization approaches might have advantages and drawbacks—none of them should *a priori* be considered better than the other. A careful examination is always needed and the choice of one approach over the other largely depends on the particular sample, datasets available and the question(s) to be addressed. A tentative workflow to guide the researcher in identifying and applying the proper (or better) technique can be found in [98].

5. Sample preparation

The characterization of trace elements present in biological samples is not easy. Some problems may come from washing process which may change significantly the location of diffusible trace elements. Forty years ago, Stika *et al.* [105] underlined the necessity of low temperature preparative procedures for diffusible ion localization using the ion microscope. Using conventional fixation procedures, these authors have observed significant ion loss and redistribution which exceeded the 1 μm lateral resolution. More recently, Porcaro *et al.* [106] distinguished two major bias that can be encountered under X-rays. First is the modification of the native chemical species during sample processing, and second the alteration of chemical species during XAS analysis, due to beam irradiation damage. Following the publication of Bacquart *et al.* [107] the use of cryogenic conditions for sampling followed by the storage in an inert atmosphere all along the analytical process is highly advocated to preserve the initial chemical species. Keeping the sample at low temperature also during the analysis offers the supplementary advantage to limit the irradiation damage and to reduce the element loss that is induced by intense beam irradiation, especially when a focused beam is used. For our experiments, biological tissue were embedded in paraffin, three to five microns slices were deposited on low-e microscope slides (MirrIR, Kevley Technologies, Tienta Sciences, Indianapolis). The paraffin was then chemically removed (xylene 100% for 30 min to 4 h) in order to improve the crystal detection under the microscope. Note that as underlined by Pushie *et al.* [4], the possibility for altered chemical speciation, elemental redistribution, leaching, or contamination from the long list of reagents or preparation steps used in paraffin and methacrylate embedding processes should always be considered.

6. Scientific cases

6.1. *Biomarker in biological fluids*

Several kinds of biological fluids namely blood [108–110], amniotic fluid [111], urine [112], semen [113], saliva [114], sweat [115] can be investigated by XRF. As noticed by Langstraat *et al.* [116], human blood can be analyzed using XRF through the presence of elements K, Cl and Fe. In the case of semen, the significant elements are K, Cl and Zn. For saliva, the element K can be underlined, and finally urine and sweat contain K, Cl and Ca [117].

For the clinician, a major question is related to the selection of the best non-invasive biomarker to perform XRF experiments. To identify the best human biomarkers for Sb exposure, Ye *et al.* [118] have analyzed 480 environmental samples from an active Sb mining area in Hunan, China. For this study, they consider urine, saliva, hair and nails, the drinking water being the more important contribution (85–100% of the average daily dose—ADD). The authors found a positive correlation between ADD and Sb content in hair ($p = 0.02$), but not in urine ($p = 0.051$), saliva ($p = 0.52$) or nails ($p = 0.85$), suggesting that hair is the best non-invasive biomarker.

Finally, XRF may bring valuable information to the sports medicine physician. In a recent study, Jablan *et al.* [119] explored the impact of endurance exercise on urinary level of trace elements such as Ca, P, K, Na, Se, Zn, Mn, Cu, Fe and Co using the bench top Total Reflection XRF (TXRF) spectrometer. The results underline that the level of Co increased tenfold after the race. Such observation/conclusion is in line with the fact that Co helps assimilation of Fe and hemoglobin synthesis inducing erythropoiesis, and consequently enhances endurance [120].

6.2. *Highlighting heavy elements in drugs*

It is known that several drugs contain heavy elements in their chemical composition [121,122], as Pt, Cu and Sr cited in the following examples. As underlined by Johnstone *et al.* [123], since the discovery of cisplatin by Rosenberg in 1960 [124], Pt-based drugs became a mainstay of cancer therapy. More precisely, approximately half of all patients undergoing chemotherapeutic treatment receive a Pt drug namely cisplatin (cis-[Pt(II) $(NH_3)_2Cl_2$]), carboplatin and oxaliplatin [125]. Recently, some authors demonstrated that inhibition of dengue virus serotype 2 in Vero cells can be obtained with [Cu(2,4,5-triphenyl-1H-imidazole) $2(H_2O)_2]\cdot Cl_2$ [126]. Sr-based drugs increase bone mass in postmenopausal osteoporosis patients and reduce fracture risk [127–131].

In a recent study, Esteve *et al.* [96,97] have shown that it is possible to detect Zn and Pt in kidney biopsy

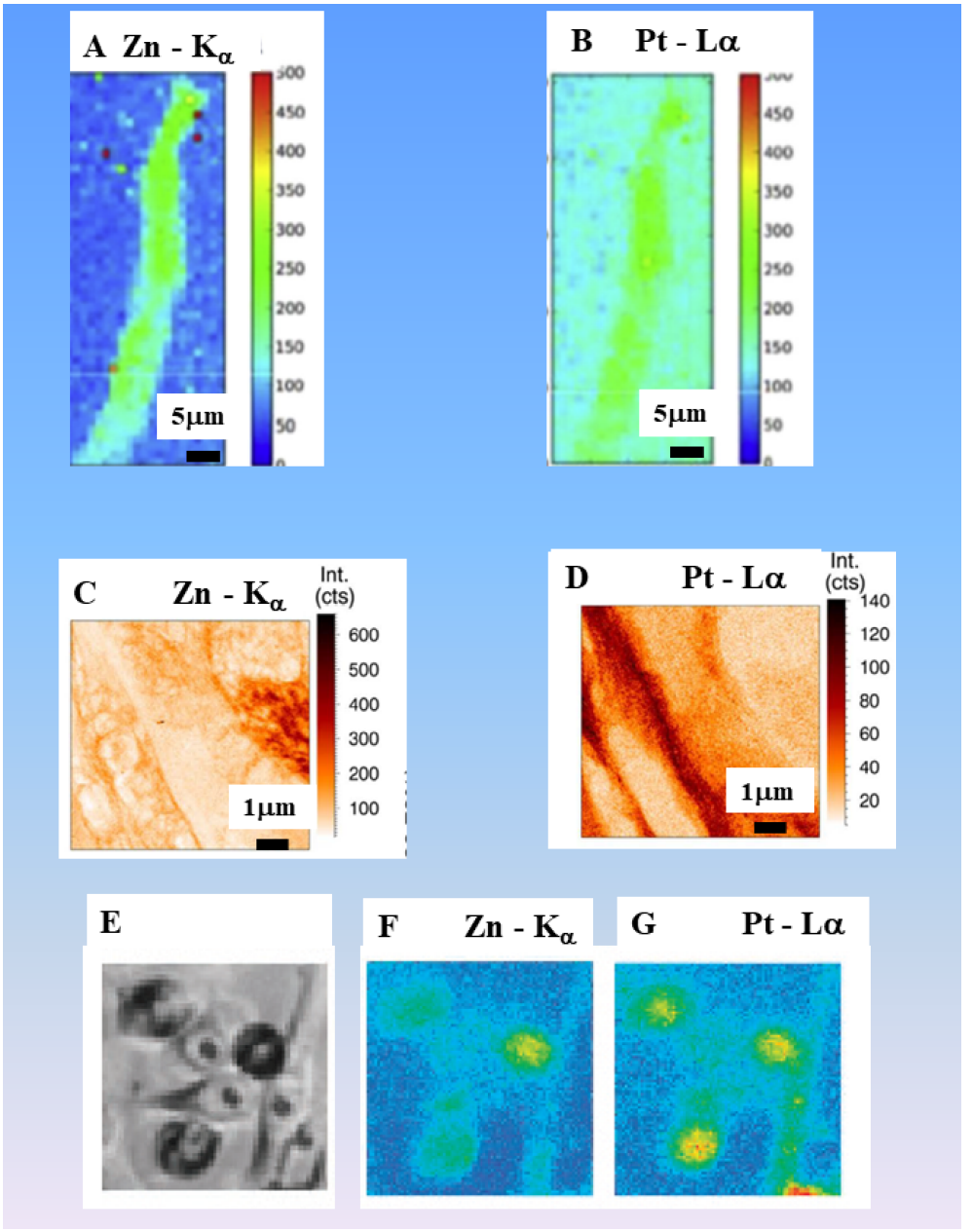

Figure 8. (a, b) Zn and Pt XRF maps collected in the case of a human kidney biopsy (from Ref. [97]); (c, d) Zn and Pt XRF maps collected in the case of female mice (from Ref. [132]). Scanned area 16 × 16 µm, beam dimensions 50 × 50 nm^2, 50 nm step size, measurement time 0.1 s per point, primary beam energy 17.5 keV; (e–g) (from Ref. [133]) cell morphologies obtained by Nomarski are shown at x100 magnification, each field of view is equivalent to an area of 70 × 70 µm, Zn and Pt maps obtained using SXFM.

of patients (Figures 8a, b). In one case, the detection of Pt was made six days after the last oxaliplatin injection, while for the second case, the biopsy was performed more than 15 days after the first drug injection and several dialysis. Using nano-XRF spectroscopy, Laforce *et al.* [132] examined the Pt

Table 4. Disorders due to an accumulation of Mn, Cu, or Fe and causing neurotoxicity, OMIM is for Online Mendelian Inheritance in Man

Disorders	Transition metal	Inheritance	Gene	OMIM	Gene function	Symptoms
Hypermanganesemia with dystonia 1	Mn	Autosomal recessive	*SLC30A10*	613280	Manganese transporter	Dystonia, cock-walk gait Parkinsonism
Wilson's disease	Cu	Autosomal recessive	*ATP7B*	277900	Copper transporter	Dysarthria, dysphagia, tremor, dystonic rigidity
Acaeruloplasminaemia, Cerebellar ataxia, Hypoceruloplasminemia	Fe	Autosomal recessive	*CP*	604290	Ferroxidase	Chorea, ataxia, dystonia, Parkinsonism, Diabetes mellitus

distribution in ovarian tissues. The measurements proved that Pt resides predominantly outsides the cancer cells in the stroma of the tissue (Figures 8c, d). Figures 8e–g, report some images from the paper of Shimura *et al.* [133]. Scanning XRF microscopy (SXFM) allows to map intracellular elements after treatment with cis-diamminedichloroplatinum(II) (CDDP), a Pt-based anticancer agent. A precise analysis of several spatial repartitions regarding Pt and Zn, reveals that the average Pt content of CDDP-resistant cells was 2.6 times less than that of sensitive cells, and the Zn content was inversely correlated with the intracellular Pt content.

This approach can be extended to drugs without heavy elements but with advanced materials, namely mesoporous silica [134] or gold nanostructures [135], that are able to enhance treatment. In such design for the drug, XRF also gives the possibility to localize the drug through gold quantum dots precisely inside the organ [95] or in a cell [136]. Finally, it is clear that such an approach can help the clinician to establish a heavy metal intoxication diagnosis and to understand more deeply the toxicity mechanism [137].

6.3. *Diseases related to a metal dysregulation*

As underlined by Umair and Alfadhel [138], genetic disorders associated with metal metabolism constitute a vast group of disorders [139], mostly resulting from defects in the proteins/enzymes involved in nutrient metabolism and energy production. Table 4 gives some physiological details regarding several genetic disorders [139]. Such genetic disorders may lead to accumulation of heavy elements. For example, the accumulation of Fe [140], Mn [141], Cu [142], Se [143] or Zn [144] in brain induces severe neurodegeneration. XRF was used to investigate several diseases related to a metal dysregulation. Among them Menkes disease [145,146] is linked to a Cu deficiency and Wilson disease [147] is related to an accumulation of Cu in tissues.

In the first case and to estimate the standard therapy, Kinebuchi *et al.* [148] have evaluated the Cu distribution at subcellular level of resolution in the treated classic Menkes disease patients through XRF. A careful analysis of the data indicates that a standard therapy supplies almost enough Cu for patient tissues but passes through the tissues to venous and lymph systems. Regarding Wilson's disease, different studies were performed through XRF [34,149] or through LA-ICP-MS [150] to determine the Cu concentration in tissues. A recent study clearly showed that XRF is more sensitive than staining procedure used routinely at the hospital [34]: a laboratory-based XRF spectrometer is sufficient to reveal the excess of Cu in tissues.

6.4. *Diseases related to the adsorption of toxic elements*

Recently, different investigations have underlined a high content of nephrotoxic elements such as Al [151–153] and Mn [154] in green tea leaves. While

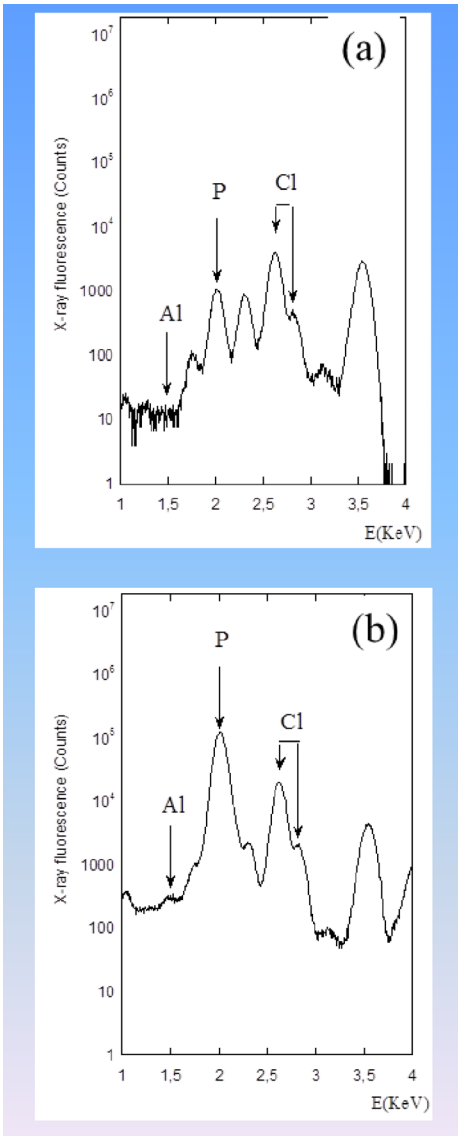

Figure 9. Typical XRF spectrum collected for a kidney stone showing clearly the contributions of Al ($K_\alpha \approx K_\beta = 1.487$ keV). Contributions coming from other elements such P ($K_\alpha = 2.01$ keV, $K_\beta = 2.14$ keV) or Cl ($K_\alpha = 2.62$ keV, $K_\beta = 2.81$ keV) can be also identified.

daily intakes of Al present in food were estimated as 2 ± 6 ng for children and 9 ± 14 ng for adults [154], several studies reported that in some of the tea infusions, toxic metals exceed the maximum permissible limits stipulated by different countries [155]. For example, levels of Al stipulated were 0.06–16.82 mg·L^{-1}. Moreover, among the different human diseases related to Al [156], it seems that Alzheimer's disease is associated with the presence of Al [157,158] and thus the high Al content in tea is a matter of concern.

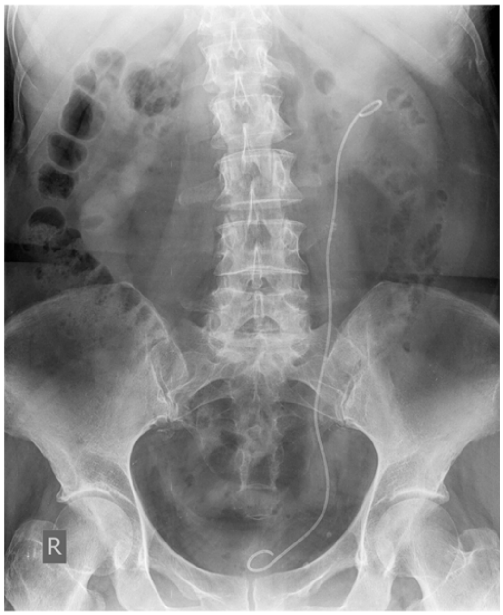

Figure 10. Correctly positioned double J stent. References: Clinical center "Dr Dragisa Misovic-Dedinje"—Belgrade/RS.

XRF measurements performed on kidney stones reveal some Al contribution (Figure 9). Works are in progress to establish a correlation with the consumption of tea [159,160]. Note that tea leaves contain calcium oxalate and that calcium oxalate (monohydrate and dehydrate) have been identified in kidney stones [161].

6.5. *Heavy elements in medical devices*

Medical devices may contain heavy elements and their possible release constitutes a real health problem [162]. Orthopedic implants [163,164], JJ stents [165–167] or dental implants [168,169] contain heavy elements. Regarding orthopedic implants, several investigations have underlined the presence of oxide particles containing Cr [170–172] in tissues around retrieved metal on metal implants. Considering JJ stents are made of polymeric biomaterials, in

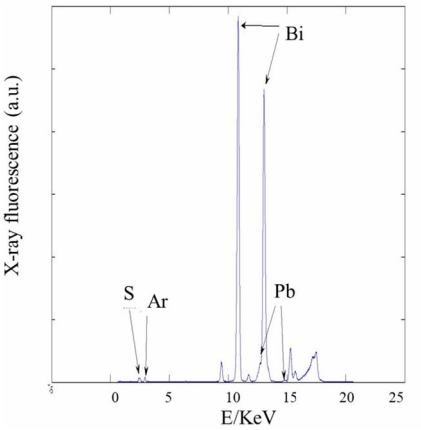

Figure 11. Presence of Bi and S in a JJ stent underlined by XRF.

order to verify the location of this medical device in the urinary system through X-ray radiography (Figure 10), heavy elements namely Ba [173], Bi, Ta or W may be added [174]. The release of such elements may lead to pathologies and it is thus crucial to determine their nature, which can easily be done by XRF measurements (Figure 11).

In order to investigate the possible release of Fe and Cr from orthopedic implants, Ektessabi *et al.* [175] have performed XRF experiments. The complete set of data showed that some elements of the implant namely Ti, Fe and Cr are present in the prosthesis. Similar results regarding the contamination by metallic elements released from joint prostheses were obtained by PIXE [176].

6.6. *The case of tattoos*

Tattooing has gained tremendous popularity in Western countries where approximately 10% of the populations have at least one tattoo. In fact, the tattoo prevalence overseas and in Europe is even higher, especially among the youth, for whom it is up to 15–25% according to the country [177]. The presence of different metals including Ti, Fe, Cr or Zn have been identified in the chemical composition of tattoo's ink [178]. Those elements, injected into the dermis, remain lifelong in the skin [179]. Moreover, recent data show that these inks contain metals incorporated in nano- and submicron particles [180]. Such chemical and structural characteristics of the inks used for tattoos may explain why, as reported by Kluger [181], many complications are related to tattoos encompassing ink allergy, benign or malignant tumors. It is thus of primary importance to determine the chemical nature of organic and inorganic elements within tattoo inks and the spatial distributions of these elements within the skin reactions to tattoos. XRF experiments were performed to attain these goals, such spectroscopy being able to determine and localize the heavy elements versus some specific structures of the tissue [182–186].

In a recent study, a set of tattooed patients suffering from skin cancer was considered [187]. Indeed, several types of carcinogenic compounds were identified in tattoo inks, including primary aromatic amines (PAA), cleavage products of organic azocolorants. An analysis of the medical literature indicates a possible association between skin cancers including cases of keratoacanthoma (KA) and the use of red inks [188].

The clinical and histopathological data from three patients diagnosed with tattoo associated KA indicate that they have developed KA on red ink within several weeks following the tattoo setup procedure. Histopathological data indicate the presence of intradermal red pigments, located in the direct periphery of the tumoral mass. XRF maps acquired on the different biopsies revealed elemental distribution and it was able to discuss more deeply the relationship between KA and the chemical composition/distribution of tattoo ink. Observation through an optical microscope (Figure 12a), shows mainly pink and black inks in the superficial and deep dermis.

In order to illustrate the quantitative results that can be obtained from the XRF contrast maps obtained on the biopsies and collected on the DiffAbs beamline (SOLEIL Synchrotron), they are analyzed using the above detailed approaches (see Section 4.4). The analysis can be, of course, performed on the full dataset (XY map) or regions of it. Figure 12 (b to e) shows XY raster maps with XRF contrast corresponding to various elements.

The correlation analysis was performed for all the possible resulting combinations of the situations mentioned above (more than four elements, for full image and three ROIs), but we will give in the following as a detailed example, two situations: correlations of XRF maps with Ti–Fe and Ti–Zn contrasts only for

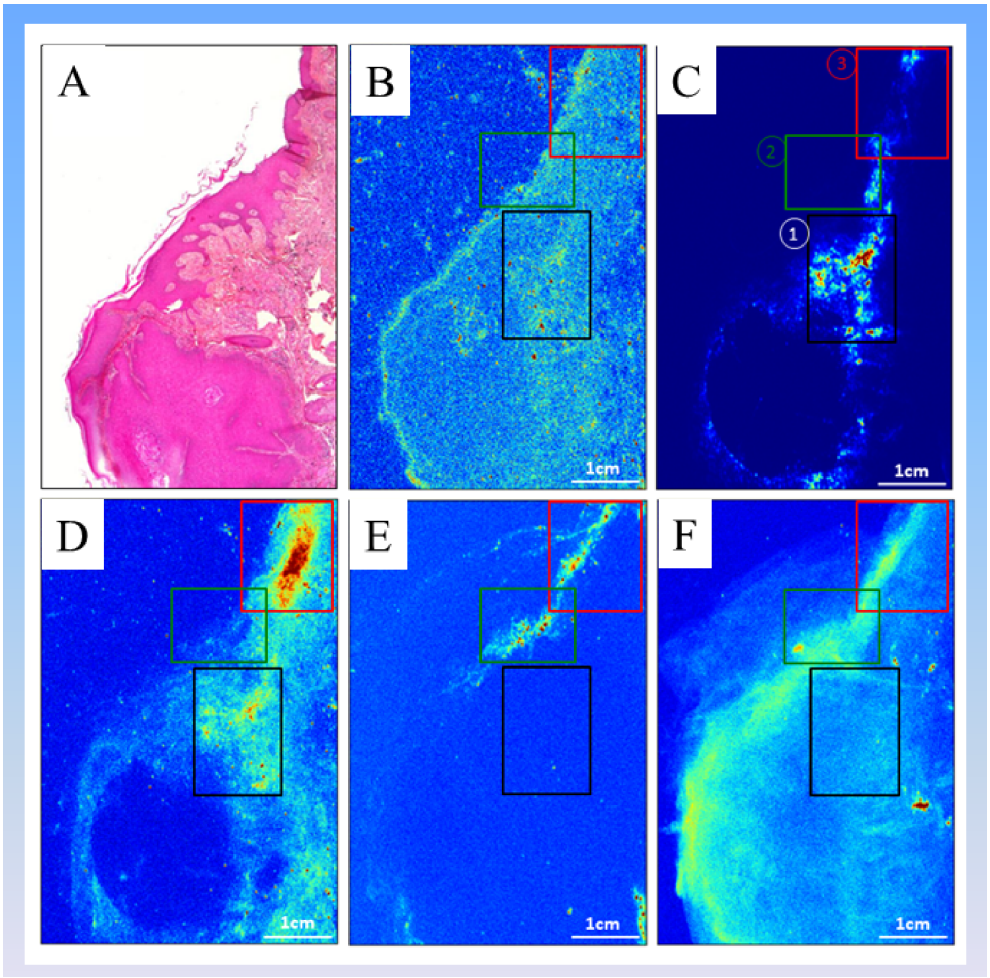

Figure 12. (a) HES (Hematoxylin Erythrosine Saffron)-stained image obtained using ×25 magnification. Raster maps with XRF contrast corresponding to (b) Ca (intensity with a maximum equal to 20), (c) Ti (intensity with a maximum equal to 1000), (d) Fe (intensity with a maximum equal to 60), (e) Cu (intensity with a maximum equal to 200) and (f) Zn (intensity with a maximum equal to 140) respectively. Three regions of interest (ROIs) are also highlighted, and will be used in the following for the analysis. The color scale is linear (from blue to red), and spans from 0 to the above reported maximum value for each map.

ROI no. 1 (cf. Figure 12). The results are shown in Figure 13 (a and b panels respectively).

For the Ti–Fe XRF maps (Figure 13a), the scatter plot shows a positive correlation, which is confirmed by a positive Pearson coefficient. Visual examination of the XRF maps also show that the same areas of the ROI seem to exhibit both Ti and Fe signal. Nevertheless, it is the use of the Manders coefficients which allow quantifying the co-existence of the Ti and Fe in this region: with a value of M12 = M(Ti–Fe) = 0.89, the probability to find Fe at each point where Ti is present is rather large (almost 90%). The inverse situation is slightly less favorable: the probability to find Ti at each point where Fe is present is slightly smaller, amounting to only ~60%. Such a result is difficult to argue by simple visual examination of the data, if no mathematical quantification is performed.

It is a little bit more complex to interpret the Ti–Zn XRF maps (Figure 13b), if one uses only scatter plot and Pearson coefficient. The scatter plot does

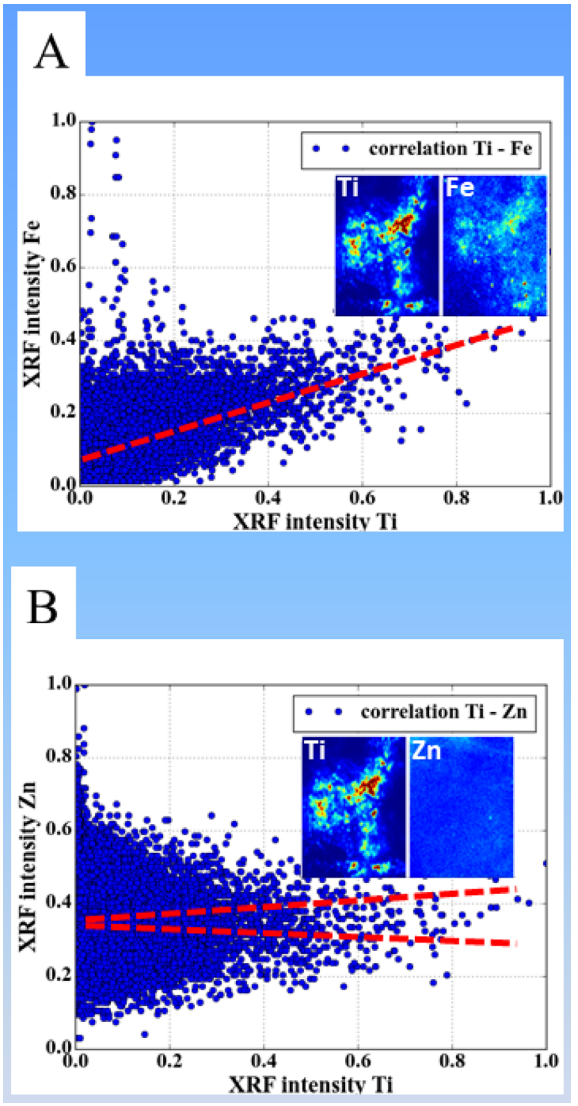

Figure 13. Analysis performed for ROI no. 1/XRF maps with (a) Ti–Fe and (b) Ti–Zn contrasts. The scatter plots are shown, with the dotted lines being guides for the eye; the insets show the respective zooms on the used ROIs of the XRF maps. The calculated Pearson (P) and Manders (M) coefficients are (a) P(Ti–Fe) = 0.51, M(Ti–Fe) = 0.89, M(Fe-Ti) = 0.59 and (b) P(Ti–Zn) = −0.11, M(Ti–Zn) = 0.98, M(Zn–Ti) = 0.53 (see also Tables 5 and 6).

not really allow to conclude a positive or negative correlation, while the slightly negative Pearson coefficient (−0.11) would suggest that the presence of the two chemical species is slightly anti-correlated in the considered ROI. A careful examination of the XRF maps and noting that the Zn signal seems to be approximately uniformly distributed in the considered ROI is confirmed by the calculated Manders coefficients: M(Ti–Zn) amounts almost unity, showing that in any sample point (in ROI no.1) where Ti is present, Zn is also detected. The reverse is not anymore true; M(Zn–Ti) is of about 50%. Considering that Zn is present over the whole ROI no.1 area, this corresponds to a presence of the Ti in only approximately half of this region of the sample.

Tables 5 and 6 below show the obtained results (Pearson and Manders coefficients) for the different chemical element combinations and different considered ROIs. The first chemical element (el.1) is reported on the first (leftmost) column, and the second one (el.2) on the first (topmost) row.

The values of the Manders coefficients M(X–Zn) (X = Ca, Ti, Fe, Cu) are typically larger than 80% (with exception in the case of X = Cu/full image, but still with a significantly large value of 68%). This result implies that whatever the chemical element X is, when detected on the XRF maps or ROIs, the Zn is systematically present as well. This is somehow expected and in full agreement with the observed rather uniform distribution of Zn over major part of the XRF map (or at least the regions where the other elements are present), as it can be visually detected in Figures 12 and 13. It is only in the case of X = Cu (and full image) that probably there are some areas of the sample where the presence of the Cu is not correlated with the one of the Zn.

Another interesting case to be discussed is the correlation of Ti and Fe. The large values (about 80 to 90%) for Manders coefficient M(Ti–Fe) indicates that the presence of Ti is systematically accompanied by the presence of Fe. The reverse is not true, and, depending on the chosen area to be investigated, in regions with detected Fe, the Ti can also be detected/correlated with probabilities ranging from 25 to 60%.

Another case which might be worthwhile to be noticed: Cu–Fe, with M(Cu–Fe) ~60% and M(Fe–Cu) ~30%. It shows that in areas with detected Cu, the probability to find Fe is rather high (60%), but the reverse (finding Cu in Fe rich areas) is much less probable (30%).

Table 5. Calculated Pearson coefficients for different pairs of chemical elements (el.1, el.2)

el.1\el.2	Ca	Ti	Fe	Cu	Zn
Ca		☒ = 0.07	☒ = 0.04	☒ = 0.07	☒ = 0.05
	xxx	① = 0.11	① = 0.05	① = 0.03	① = 0.02
	xxx	② = 0.03	② = 0.11	② = 0.07	② = 0.23
		③ = 0.01	③ = 0.07	③ = 0.05	③ = 0.05
Ti			☒ = 0.16	☒ = −0.00	☒ = 0.01
	xxx	xxx	① = 0.51	① = 0.04	① = −0.11
	xxx	xxx	② = 0.47	② = −0.11	② = −0.16
			③ = 0.10	③ = 0.16	③ = 0.13
Fe				☒ = 0.07	☒ = 0.03
	xxx	xxx	xxx	① = −0.01	① = −0.01
	xxx	xxx	xxx	② = 0.05	② = 0.16
				③ = −0.09	③ = 0.05
Cu					☒ = 0.08
	xxx	xxx	xxx	xxx	① = 0.04
	xxx	xxx	xxx	xxx	② = 0.30
					③ = 0.35
Zn	xxx	xxx	xxx	xxx	xxx
	xxx	xxx	xxx	xxx	xxx

☒ = Full image, ① = ROI1, ② = ROI2, ③ = ROI3. The values of the coefficients are colored according to the following color map: black [<0.0]; blue [0.0–0.1]; green [0.1–0.2]; orange [0.2–0.3]; red [>0.3].

From a medical point of view, these spatial correlations between heavy elements can be related to at least three different aspects. The first one is related to the mixing of pigments which is made to obtain the color of the tattoos. For example, orange or light red is a mix between red (iron oxide) and white (TiO_2 or ZnO) [180]. A second aspect is linked to the fact that a heavy element can trigger inflammation process in the skin, leading to the co-location of exogenous heavy metal (TiO_2 for example) present in the ink and Zn, an element of metalloproteins which are engaged in cutaneous inflammation [189]. Finally, inflamed tissues are usually associated to increased blood vascularization. There is hence a possibility to have a superposition of exogenous heavy metals and the accumulation of blood which contains iron. To explore those three aspects, we have to know if iron and zinc have an endogenous or an exogenous origin. Such information is not available by XRF but could be by X-ray absorption spectroscopy [190–192].

In the case of Ti, its exogenous origin is obvious. TiO_2 was associated with a low toxicity particle but this view changed after The International Agency for Research on Cancer (IARC) indicated that TiO_2 is possibly carcinogenic to humans [193]. Here, XRF data have detected a significant presence of TiO_2 around the tumor, and underlining a possible cancerogen effect of this metal [187].

Zhang *et al.* [194] have compared regular TiO_2 particles (including fine nano-TiO_2 and microsize nano-TiO_2) and nano-TiO_2 particles and showed that nano-TiO_2 particles have a stronger catalytic activity. Quite recently, Xue *et al.* [195] explored the cytotoxicity and oxidative stress induced by nano-TiO_2 under UVA irradiation with different crystal forms (anatase, rutile and anatase/rutile) and sizes (4 to 60 nm) in human keratinocyte HaCaT cells. Their results indicated that anatase and amorphous forms of nano-TiO_2 showed higher cytotoxicity than the rutile form. More precisely, nano-TiO_2 could induce the

Table 6. Calculated Manders coefficients for different pairs of chemical elements (el.1, el.2)

el.1\el.2	Ca	Ti	Fe	Cu	Zn
Ca		☒ = 0.227	☒ = 0.566	☒ = 0.221	☒ = 0.815
	xxx	① = 0.563	① = 0.817	① = 0.181	① = 0.985
	xxx	② = 0.163	② = 0.600	② = 0.351	② = 0.868
		③ = 0.321	③ = 0.691	③ = 0.335	③ = 0.848
Ti	☒ = 0.701		☒ = 0.786	☒ = 0.167	☒ = 0.978
	① = 0.595	xxx	① = 0.889	① = 0.184	① = 0.983
	② = 0.695	xxx	② = 0.982	② = 0.209	② = 0.898
	③ = 0.705		③ = 0.940	③ = 0.331	③ = 0.965
Fe	☒ = 0.622	☒ = 0.306		☒ = 0.213	☒ = 0.887
	① = 0.562	① = 0.593	xxx	① = 0.179	① = 0.986
	② = 0.632	② = 0.243	xxx	② = 0.376	② = 0.918
	③ = 0.667	③ = 0.414		③ = 0.250	③ = 0.925
Cu	☒ = 0.492	☒ = 0.165	☒ = 0.431		☒ = 0.684
	① = 0.541	① = 0.541	① = 0.776	xxx	① = 0.986
	② = 0.548	② = 0.095	② = 0.557	xxx	② = 0.942
	③ = 0.584	③ = 0.351	③ = 0.634		③ = 0.842
Zn	☒ = 0.577	☒ = 0.233	☒ = 0.557	☒ = 0.212	
	① = 0.545	① = 0.530	① = 0.793	① = 0.183	xxx
	② = 0.526	② = 0.135	② = 0.528	② = 0.392	xxx
	③ = 0.675	③ = 0.350	③ = 0.763	③ = 0.303	

☒ = Full image, ① = ROI1, ② = ROI2, ③ = ROI3. The values of the coefficients are colored according to the following color map: black [0.0–0.2]; blue [0.2–0.4]; green [0.4–0.6]; orange [0.6–0.8]; red [0.8–1.0].

generation of reactive oxygen species ROS and damage HaCaT cells under UVA irradiation. Under irradiation, it is well known that TiO_2 may generate a significant quantity of ROS which play important roles in the modulation of cell survival, cell death, differentiation, cell signaling, and inflammation-related factor production [196]. Finally, Ross *et al.* [197] have underlined another aspect regarding the relationship between TiO_2 and tattoo showing that TiO_2 is over-represented in tattoos that respond poorly to laser treatment.

7. Synergy with other physicochemical techniques

While XRF and other techniques (see part 2: AAS, ICP-AES, ICP-MS…) reveal the nature and concentration of the heavy elements present in biological samples, it can be interesting to the clinician to know in which chemical phases these heavy elements reside.

To attain this goal, different complementary techniques can be selected. The first ones are classic in-lab techniques. Among them, Raman plays a key role. For example, in the case where Ti is revealed in skin tattoos, it allows to distinguish between two Ti oxide polymorphs namely rutile and anatase [198, 199]. The Raman spectra clearly pointed out the presence of the rutile polymorph for a patient who presented a keratoacanthoma (Skin cancer) [187]. Such complementary information can be obtained with Raman spectroscopy for other elements such Zn [200] or Fe [201]. It is worthwhile to underline that in the case of Fe, Mossbauer spectroscopy constitutes a powerful technique to discriminate between

all the different Fe oxides [202,203] and that spectroscopy may be associated with a spatial resolution of ~10–20 μm [204].

Complementary structural information is available through X-ray Absorption Near Edge Structure (XANES) spectroscopy to determine the structure around elements previously detected by XRF [190, 191,205]. When Cr is detected, it is of primary importance to know the oxidation state of this element. While Cr(III) serves as a nutritional supplement, and may play a role in glucose and lipid metabolism, Cr(VI) is very toxic inducing a wide variety of injuries in cells, such as DNA damage [206]. Through XANES spectroscopy, Ortega *et al.* [207] have shown that soluble Cr(VI) compounds are fully reduced to Cr(III) in cells. XANES spectroscopy can bring complementary valuable information also in the case of nanometer scale metallic particles [208–211], a nanomaterial which have numerous applications in medicine [212–214].

X-ray diffraction (XRD) can also be used to reveal the long range structure of compounds [215–221]. Among the different investigations which are based on the association between XRD and XRF spectroscopy [222–226], we can quote the determination of the chemical composition of microcalcification, present in cartilage, which was obtained using XRD on selected points corresponding to high concentration of Ca as defined by XRF spectroscopy [227].

8. Conclusion

The scientific cases presented above, regarding the opportunities of XRF in medicine, show clearly that XRF now plays a key role in establishing a diagnosis or in understanding deeply the interaction between heavy elements and human tissues at the subcellular level. Even if the sensitivity of such a technique is higher when synchrotron radiation is used as a source [228], this technique can be used in hospitals, using portable instrument or laboratory setup, giving almost in real time the nature and the concentration of the different elements present, even at trace levels.

Acknowledgments

This work was supported by the Physics and Chemistry Institutes of CNRS and by contracts ANR-09-BLAN-0120-02, ANR-12-BS08-0022, ANR13JSV10010-01, convergence UPMC CVG1205, Labex Matisse, Labex Michem and CORDDIM-2013-COD130042. The authors are grateful to the SOLEIL Synchrotron Facility and ESRF for beam time allocation and would like to very much thank the support groups and beamline teams of SOLEIL and ESRF for their help during experiments.

References

[1] G. Sagnac, *Thèse, seconde partie : Rayons secondaires dérivés des rayons de Röntgen*, Faculté des sciences de Paris, 1900.
[2] P. Wobrauschek, *X-ray Spectrom.*, 2007, **36**, 289-300.
[3] M. West, A. T. Ellis, P. J. Potts, C. Streli, C. Vanhoof, D. Wegrzynek, P. Wobrauschek, *J. Anal. At. Spectrom.*, 2013, **28**, 1544-1590.
[4] M. J. Pushie, I. J. Pickering, M. Korbas, M. J. Hackett, G. N. George, *Chem. Rev.*, 2014, **114**, 8499-8541.
[5] R. Zhang, L. Li, Y. Sultanbawa, Z. P. Xu, *Am. J. Nucl. Med. Mol. Imaging*, 2018, **8**, 169-188.
[6] T. D. T. Oyedotun, *Geol. Ecol. Landsc.*, 2018, **2**, 148-154.
[7] G. N. George, I. J. Pickering, in *European Biophysical Societies Encyclopedia of Biophysics* (G. Roberts, A. Watts, eds.), Springer, Berlin, Heidelberg, 2018.
[8] E. V. Yusenko, K. V. Yusenko, I. V. Korolkov, A. A. Shubin, F. P. Kapsargin, A. A. Efremov, M. V. Yusenko, *Cent. Eur. J. Chem.*, 2013, **11**, 2107-2119.
[9] V. K. Singh, B. S. Jaswal, J. Sharma, P. K. Rai, *Biophys. Rev.*, 2020, **12**, 647-668.
[10] M. Daudon, D. Bazin, "Application of Physical Methods to Kidney Stones and Randall's. Plaque Characterization", in *Urolithiasis: Basic Science and Clinical Practice*, Springer-Verlag, London, 2012, 683-707.
[11] M. Daudon, D. Bazin, *J. Phys.: Conf. Ser.*, 2013, **425**, article no. 022006.
[12] D. Bazin, C. Jouanneau, S. Bertazzo, C. Sandt, A. Dessombz, M. Réfrégiers, P. Dumas, J. Frederick, J.-P. Haymann, E. Letavernier, P. Ronco, M. Daudon, *C. R. Chim.*, 2016, **19**, 1439-1450.
[13] F. Damay, D. Bazin, M. Daudon, G. André, *C. R. Chim.*, 2016, **19**, 1432-1438.
[14] L. Estepa-Maurice, C. Hennequin, C. Marfisi, C. Bader, B. Lacour, M. Daudon, *Am. J. Clin. Pathol.*, 1996, **105**, 576-582.
[15] D. Bazin, M. Daudon, *Ann. Biol. Clin.*, 2015, **73**, 517-534.
[16] M. Daudon, D. Bazin, *C. R. Chim.*, 2016, **19**, 1416-1423.
[17] D. Bazin, P. Chevallier, G. Matzen, P. Jungers, M. Daudon, *Urol. Res.*, 2007, **35**, 179-184.
[18] B. Hannache, A. Boutefnouchet, D. Bazin, M. Daudon, E. Foy, S. Rouzière, A. Dahdouh, *Prog. Urol.*, 2015, **25**, 22-26.
[19] D. Bazin, M. Daudon, C. Combes, C. Rey, *Chem. Rev.*, 2012, **112**, 5092-5120.
[20] M. Daudon, D. Bazin, K. Adil, A. Le Bail, *Acta Crystallogr.*, 2011, **E67**, o1458.
[21] A. Le Bail, M. Daudon, D. Bazin, *Acta Crystallogr.*, 2013, **C69**, 734-737.
[22] D. Bazin, M. Daudon, E. Elkaim, A. Le Bail, L. Smrcok, *C. R. Chim.*, 2016, **19**, 1535-1541.

[23] A. Le Bail, D. Bazin, M. Daudon, A. Brochot, V. Robbez-Masson, V. Maisonneuve, *Acta Crystallogr.*, 2009, **B65**, 350-354.
[24] C. Kleinguet, J. C. Williams Jr, J. C. Lieske, M. Daudon, M. E. Rivera, P. J. Jannetto, J. Bornhorst, D. Rokke, E. T. Bird, J. E. Lingeman, M. M. El Tayeb, *Urology*, 2019, **126**, 49-53.
[25] K. Geraki, M. J. Farquharson, *Radiat. Phys. Chem.*, 2001, **61**, 603-605.
[26] M. P. Lue-Meru, E. Gimenez, E. A. Hernández-Caraballo, A. Rojas, E. D. Greaves, *Spectrochim. Acta B: At. Spectrosc.*, 2001, **56**, 2195-2201.
[27] L. Finney, S. Mandava, L. Ursos, W. Zhang, D. Rodi, S. Vogt, D. Legnini, J. Maser, F. Ikpatt, O. I. Olopade, D. Glesne, *Proc. Natl. Acad. Sci. USA*, 2007, **104**, 2247-2252.
[28] J. Börjesson, S. Mattsson, *Powder Diffr.*, 2007, **22**, 130-137.
[29] M. Piacenti da Silva, O. L. A. Domingues Zucchi, A. Ribeiro-Silva, M. E. Poletti, *Spectrochim. Acta B: At. Spectrosc.*, 2009, **64**, 587-592.
[30] J. Kuta, J. Machát, D. Benová, R. Červenka, T. Kořistková, *Cent. Eur. J. Chem.*, 2012, **10**, 1475-1483.
[31] V. K. Singh, P. K. Rai, *Biophys. Rev.*, 2014, **6**, 291-310.
[32] J. Kuta, S. Smetanová, D. Benová, T. Kořistková, J. Machát, *Environ. Geochem. Health*, 2016, **38**, 133-143.
[33] A. J. Specht, Y. Lin, M. Weisskopf, C. Yan, H. Hu, J. Xu, L. H. Nie, *Biomarkers*, 2016, **21**, 347-352.
[34] S. Kascakova, C. M. Kewish, S. Rouzière, F. Schmitt, R. Sobesky, J. Poupon, C. Sandt, B. Francou, A. Somogyi, D. Samuel, E. Jacquemin, A. Dubart-Kupperschmitt, T. Huy Nguyen, D. Bazin, J.-C. Duclos-Vallée, C. Guettier, F. Le Naour, *J. Path.: Clin. Res.*, 2016, **2**, 175-186.
[35] F. Grases, C. Genestar, A. Mill, *J. Crystallogr. Growth*, 1989, **94**, 507-515.
[36] E. Tsolaki, S. Bertazzo, *Materials*, 2019, **12**, article no. 3126.
[37] D. Bazin, E. Letavernier, J. P. Haymann, V. Frochot, M. Daudon, *Ann. Biol. Clin.*, 2020, **78**, 349-362.
[38] N. Vidavsky, J. A. M. R. Kunitake, L. A. Estroff, *Adv. Healthc. Mater.*, 2020, article no. e2001271.
[39] S. Rouzière, D. Bazin, M. Daudon, *C. R. Chim.*, 2016, **19**, 1404-1415.
[40] M. Uo, T. Wada, T. Sugiyama, *Jpn. Dent. Sci. Rev.*, 2015, **51**, 2-9.
[41] S. L. C. Ferreira, M. A. Bezerra, A. S. Santos, W. N. L. Dos Santos, C. G. Novaes, O. M. C. de Oliveira, M. L. Oliveira, R. L. Garcia, *Trends Anal. Chem.*, 2018, **100**, 1-6.
[42] L. Rello, A. C. Lapena, M. Aramendia, M. A. Belarra, M. Resano, *Spectrochim. Acta*, 2013, **B81**, 11-19.
[43] J. C. Dran, J. Salomon, T. Calligaro, P. Walter, *Nucl. Instrum. Methods B*, 2004, **7**, 219-220.
[44] D. Bazin, M. Daudon, P. Chevallier, S. Rouzière, E. Elkaim, D. Thiaudière, B. Fayard, E. Foy, P. A. Albouy, G. André, G. Matzen, E. Véron, *Ann. Biol. Clin.*, 2006, **64**, 125-139.
[45] Z. W. Chen, W. M. Gibson, H. Huang, *X-Ray Opt. Instrum.*, 2008, article no. 318171.
[46] D. Bazin, E. Letavernier, J.-P. Haymann, P. Méria, M. Daudon, *Prog. Urol.*, 2016, **26**, 608-618.
[47] D. Bazin, J.-P. Haymann, E. Letavernier, J. Rode, M. Daudon, *Presse Méd.*, 2014, **43**, 135-148.
[48] M. Taylor, R. Bytheway, B. K. Tanner, M. Watanabe, G. Isoyama, C. Spielmann, "X-Ray sources", in *X-Ray Spectrometry: Recent Technological Advances*, John Wiley & Sons, Ltd., Hoboken, NJ, USA, 2004, 13-62.
[49] M. West, A. T. Ellis, P. J. Potts, C. Streli, C. Vanhoof, D. Wegrzynek, P. Wobrauschek, *J. Anal. At. Spectrom.*, 2011, **26**, 1919-1963.
[50] H. Chen, M. M. Rogalski, J. N. Anker, *Phys. Chem. Chem. Phys.*, 2012, **14**, 13469-13486.
[51] C. J. Fahrni, *Curr. Opin. Chem. Biol.*, 2007, **11**, 121-127.
[52] M. S. del Rio, A. Brunetti, B. Golosio, A. Somogyi, A. Simionovici, "XRAYLIB tables (X-ray fluorescence cross-section)", Calculations using XRAYLIB 2.3 November 14, 2003, http://ftp.esrf.fr/pub/scisoft/xraylib/xraylib_tables_v2.3.pdf.
[53] S. Rouzière, E. Jourdanneau, B. Kasmi, P. Joly, D. Petermann, P. A. Albouy, *J. Appl. Crystallogr.*, 2010, **43**, 1131-1133.
[54] G. L. Bosco, *Trends Anal. Chem.*, 2013, **45**, 121-134.
[55] B. Lemiere, *J. Geochem. Explor.*, 2018, **188**, 350-363.
[56] A. J. Specht, M. Weisskopf, L. H. Nie, *J. Biomakers*, 2014, article no. 398032.
[57] D. E. B. Fleming, S. L. Crook, C. T. Evans, M. N. Nader, M. Atia, J. M. T. Hicks, E. Sweeney, C. R. McFarlane, J. S. Kim, E. Keltie, A. Adisesh, *J. Trace Elem. Med. Biol.*, 2020, **62**, article no. 126603.
[58] D. E. B. Fleming, S. R. Bennett, C. J. Frederickson, *J. Trace Elem. Med. Biol.*, 2018, **50**, 609-614.
[59] F. S. M. Afzal, A. Al-Ebraheem, D. R. Chettle, E. D. Desouza, M. J. Farquharson, J. M. O'Meara, A. Pidruczny, B. C. Wainman, F. E. McNeill, *NIM B*, 2018, **433**, 1-9.
[60] E. Dao, M. P. Zeller, B. C. Wainman, M. J. Farquharson, *J. Trace Elem. Med. Biol.*, 2018, **50**, 305-311.
[61] M. A. Bush, R. G. Miller, J. Prutsman-Pfeiffer, P. J. Bush, *J. Forensic Sci.*, 2007, **52**, 157-165.
[62] F. Berès, J. Isaac, L. Mouton, S. Rouzière, A. Berdal, S. Simon, A. Dessombz, *J. Endod. J. Elsevier*, 2016, **42**, 432-438.
[63] G. Lignon, F. Beres, M. Quentric, S. Rouzière, R. Weil, M. De La Dure-Molla, A. Naveau, R. Kozyraki, A. Dessombz, A. Berdal, *Front. Physiol.*, 2017, **8**, article no. 267.
[64] F. Berès, G. Lignon, S. Rouzière, C. Mauprivez, S. Simon, A. Berdal, A. Dessombz, *Connect. Tissue Res.*, 2018, **59**, 46-51.
[65] C. B. Zamboni, S. Metairon, L. Kovacs, D. V. Macedo, M. A. Rizzutto, *J. Radioanal. Nucl. Chem.*, 2016, **307**, 1641-1643.
[66] H. Yoshii, K. Yanagihara, H. Imaseki, T. Hamano, H. Yamanishi, M. Inagaki, Y. Sakai, N. Sugiura, O. Kurihara, K. Sakai, *PLoS ONE*, 2014, **9**, article no. e101966.
[67] F. Téreygeol, A. Arles, E. Foy, N. Florsch, M. Llubes, *Archeo-Sciences*, 2010, **34**, 243-252.
[68] Y. Izumoto, T. Matsuyama, M. Mizuhira, H. Imaseki, T. Hamano, Y. Sakai, Y. Oguri, H. Yoshii, *J. Radiol. Prot.*, 2018, **38**, 1384-1392.
[69] Y. Izumoto, K. Fukutsu, K. Takamura, Y. Sakai, Y. Oguri, H. Yoshii, *J. Radiol. Prot.*, 2020, **40**, 692-703.
[70] S. L. Sugarman, W. M. Findley, R. E. Toohey, N. Dainiak, *Health Phys.*, 2018, **115**, 57-64.
[71] P. Pavoni, L. Raganella, S. Di Luzio, G. Izzo, A. Magrini, "Feasibility of in vivo XRF dynamic study of the thyroid following stable iodine administration", in *X-ray Fluorescent Scanning of the Thyroid. Developments in Nuclear Medicine* (M. H. Jonckheer, F. Deconinck, eds.), vol. 3, Springer, Dordrecht, 1983.

[72] J. Börjesson, L. Barregård, G. Sällsten, A. Schütz, R. Jonson, M. Alpsten, S. Mattsson, *Phys. Med. Biol.*, 1995, **40**, 413-426.
[73] J. M. O'Meara, J. Börjesson, D. R. Chettle, *Appl. Radiat. Isot.*, 2000, **53**, 639-646.
[74] H. Moise, J. D. Adachi, D. R. Chettle, A. Pejović-Milić, *Bone*, 2012, **51**, 93-97.
[75] J. B. Pelka, *Acta Phys. Pol. A*, 2008, **114**, 309-329.
[76] D. Bazin, M. Daudon, *J. Phys. D Appl. Phys.*, 2012, **45**, article no. 383001.
[77] D. Bazin, M. Daudon, *J. Spect. Imaging*, 2019, **8**, article no. a16.
[78] P. Suortti, W. Thomlinson, *Phys. Med. Biol.*, 2003, **48**, article no. R1-35.
[79] D. Eichert, L. Gregoratti, B. Kaulich, A. Marcello, P. Melpignano, L. Quaroni, M. Kiskinova, *Anal. Bioanal. Chem.*, 2007, **389**, 1121-1132.
[80] A. Sakdinawat, D. Attwood, *Nat. Photonics*, 2010, **4**, 840-848.
[81] H. Rarback, D. Shu, S. C. Feng, H. Ade, J. Kirz, I. McNulty, *Rev. Sci. Instrum.*, 1988, **59**, 52-59.
[82] M. L. Carvalho, C. Casaca, J. P. Marques, T. Pinheiro, A. S. Cunha, *X-ray Spectrom.*, 2001, **30**, 190-193.
[83] L. J. Bauer, H. A. Mustafa, P. Zaslansky, I. Mantouvalou, *Acta Biomater.*, 2020, **109**, 142-152.
[84] M. R. Gherase, D. E. B. Fleming, *Crystals*, 2020, **10**, article no. 12.
[85] J. E. Penner-Hahn, "Technologies for detecting metals in single cells", in *Metallomics and the Cell. Metal Ions in Life Sciences* (L. Banci, ed.), vol. 12, Springer, Dordrecht, 2013.
[86] R. Ortega, P. Cloetens, G. Devès, A. Carmona, S. Bohic, *PLoS ONE*, 2007, **2**, article no. e925.
[87] E. Kosior, S. Bohic, H. Suhonen, R. Ortega, G. Devès, A. Carmona, F. Marchid, J.-F. Guillet, P. Cloetens, *J. Struct. Biol.*, 2012, **177**, 239-247.
[88] R. Ortega, C. Bresson, A. Fraysse, C. Sandre, G. Devès, C. Gombert, M. Tabarant, P. Bleuet, H. Seznec, A. Simionovici, P. Moretto, C. Moulin, *Toxicol. Lett.*, 2009, **188**, 26-32.
[89] S. Bohic, D. Hare, A. Daoust, P. Cloetens, E. L. Barbier, "Spatially resolved imaging methods to probe metals in the brain: from subcellular to organ level", in *Metal Ions in Neurological Systems* (W. Linert, H. Kozlowski, eds.), Springer, Vienna, 2012.
[90] M. Krisch, A. Bravin, "ID17 - Biomedical Beamline on ESRF facility", https://www.esrf.eu/UsersAndScience/Experiments/CBS/ID17.
[91] H. Elleaume, S. Fiedler, F. Estève, B. Bertrand, A. M. Charvet, P. Berkvens, G. Berruyer, T. Brochard, G. Le Duc, C. Nemoz, R. Rénier, P. Suortti, W. Thomlinson, J. F. Le Bas, *Phys. Med. Biol.*, 2000, **45**, article no. L39.
[92] M. Torikoshi, T. Tsunoo, M. Endo, K. Noda, M. Kumada, S. Yamada, F. Soga, K. Hyodo, *J. Biomed. Opt.*, 2001, **6**, 371-377.
[93] P. Suortti, W. Thomlinson, *Phys. Med. Biol.*, 2003, **48**, R1-R35.
[94] C. Hall, R. Lewis, *Phil. Trans. R. Soc. A*, 2019, **377**, article no. 20180240.
[95] E. Esteve, S. Reguer, C. Boissiere, C. Chanéac, G. Lugo, C. Jouanneau, C. Mocuta, D. Thiaudière, N. Leclercq, B. Leyh, J. F. Greisch, J. Berthault, M. Daudon, P. Ronco, D. Bazin, *J. Synchrotron Radiat.*, 2017, **24**, 991-999.
[96] E. Esteve, D. Bazin, C. Jouanneau, S. Rouzière, A. Bataille, A. Kellum, K. Provost, C. Mocuta, S. Reguer, P. Ronco, J. Rehr, J.-P. Haymann, E. Letavernier, A. Hertig, *C. R. Chim.*, 2016, **19**, 1580-1585.
[97] E. Esteve, D. Bazin, C. Jouanneau, S. Rouzière, A. Bataille, A. Kellum, K. Provost, C. Mocuta, S. Reguer, P. Ronco, J. Rehr, J.-P. Haymann, E. Letavernier, A. Hertig, *C. R. Chim.*, 2016, **19**, 1586-1589.
[98] K. W. Dunn, M. M. Kamocka, J. H. McDonald, *Am. J. Physiol. Cell Physiol.*, 2011, **300**, C723-C742.
[99] Q. Li, A. Lau, T. J. Morris, L. Guo, C. B. Fordyce, E. F. Stanley, *J. Neurosci.*, 2004, **24**, 4070-4081.
[100] S. Bolte, F. P. Cordelie, *Res. J. Microsc.*, 2006, **224**, 213-232.
[101] E. E. M. Manders, F. J. Verbeek, J. A. Aten, *J. Microsc.*, 2003, **169**, 375-382.
[102] J. L. Rodgers, W. A. Nicewander, *Am. Stat.*, 1988, **42**, 59-66.
[103] A. G. Asuero, A. Sayago, A. G. González, *Crit. Rev. Anal. Chem.*, 2007, **36**, 41-59.
[104] S. M. Webb, *Amer. Inst. Phys. Conf. Proc.*, 2011, article no. 1365196.
[105] K. M. Stika, K. L. Bielat, G. H. Morrison, *J. Microsc.*, 1980, **118**, 409-420.
[106] F. Porcaro, S. Roudeau, A. Carmona, R. Ortega, *Trends Anal. Chem.*, 2018, **104**, 22-41.
[107] T. Bacquart, G. Devès, A. Carmona, R. Tucoulou, S. Bohic, R. Ortega, *Anal. Chem.*, 2007, **79**, 7353-7359.
[108] E. D. Greaves, L. M. Marco Parra, A. Rojas, L. Sajo-Bohus, *X-ray Spectrom.*, 2000, **29**, 349-353.
[109] R. Ayala, E. Alvarez, P. Wobrauschek, *Spectrochim. Acta B*, 1991, **46**, 1429-1432.
[110] Y. Izumoto, T. Matsuyama, M. Mizuhira, H. Imaseki, T. Hamano, Y. Sakai, Y. Oguri, H. Yoshii, *J. Radiol. Prot.*, 2018, **38**, 1384-1392.
[111] E. D. Greaves, J. Meitin, L. Sajo-Bohus, C. Castelli, J. Liendo, C. Borberg, *Adv. X-ray Chem. Anal. (Japan)*, 1995, **26**, 47-52.
[112] J. Börjesson, L. Barregård, G. Sällsten, A. Schütz, R. Jonson, M. Alpsten, S. Mattsson, *Phys. Med. Biol.*, 1995, **40**, 413-426.
[113] U. Majewska, P. Łyżwa, A. Kubala-Kukuś, D. Banaś, J. Wudarczyk-Moćko, I. Stabrawa, S. Góźdź, *Spectrochim. Acta B*, 2018, **147**, 121-125.
[114] L. Pascolo, L. Zupin, A. Gianoncelli, E. Giolo, S. Luppi, M. Martinelli, D. De Rocco, S. Sala, S. Crovella, G. Ricci, *Nuclear Inst. Methods Phys. Res. B*, 2019, **459**, 120-124.
[115] D. Maia, A. C. Andrello, I. J. Vitorino, C. Appoloni, *X-ray Spectrom.*, 2016, **45**, 220-224.
[116] K. Langstraat, A. Knijnenberg, G. Edelman, L. Van de Merwe, A. van Loon, J. Dik, A. Van Asten, *Sci. Rep.*, 2017, **7**, article no. 15056.
[117] L. M. Marco, E. A. Hernandez-Caraballo, *Spectrochim. Acta B*, 2004, **59**, 1077-1090.
[118] L. Ye, S. Qiu, X. Li, Y. Jiang, C. Jing, *Sci. Total Environ.*, 2018, **640–641**, 1-8.
[119] J. Jablan, S. Inic, H. Stosnach, M. O. Hadziabdic, L. Vujic, A.-M. Domijan, *J. Trace Elem. Med. Biol.*, 2017, **41**, 54-59.
[120] I. P. Zaitseva, A. A. Skalny, A. A. Tinkov, E. S. Berezkina, A. R. Grabeklis, A. V. Skalny, *Biol. Trace Elem. Res.*, 2015, **163**, 58-66.
[121] J. Börjesson, M. Alpsten, S. Huang, R. Jonson, S. Mattsson, C. Thornberg, "In vivo X-ray fluorescence analysis

with applications to platinum, gold and mercury in man—experiments, improvements, and patient measurements", in *Human Body Composition. Basic Life Sciences* (K. J. Ellis, J. D. Eastman, eds.), vol. 60, Springer, Boston, MA, 1993.
[122] M. Frezza, S. Hindo, D. Chen, A. Davenport, S. Schmitt, D. Tomco, Q. P. Dou, *Curr. Pharm. Des.*, 2010, **16**, 1813-1825.
[123] T. C. Johnstone, G. Y. Park, S. J. Lippard, *Anticancer Res.*, 2014, **34**, 471-476.
[124] B. Rosenberg, L. Van Camp, T. Krigas, *Nature*, 1965, **205**, 698-699.
[125] M. Galanski, M. A. Jakupec, B. K. Keppler, *Curr. Med. Chem.*, 2005, **12**, 2075-2094.
[126] T. H. Sucipto, F. Martak, *Infect. Dis. Rep.*, 2020, **12**, article no. 8744.
[127] P. J. Meunier, C. Roux, E. Seeman, S. Ortolani, J. E. Badurski, T. D. Spector, J. Cannata, A. Balogh, E. Lemmel, S. Pors-Nielsen, R. Rizzoli, H. K. Genant, J. Reginster, *N. Engl. J. Med.*, 2004, **350**, 459-468.
[128] D. Bazin, M. Daudon, C. Chappard, J. J. Rehr, D. Thiaudière, S. Reguer, *J. Synchrotron Radiat.*, 2011, **18**, 912-918.
[129] D. Bazin, A. Dessombz, C. Nguyen, H. K. Ea, F. Lioté, J. Rehr, C. Chappard, S. Rouzière, D. Thiaudière, S. Reguer, M. Daudon, *J. Synchrotron Radiat.*, 2014, **21**, 136-142.
[130] Y. Sekine, R. Motokawa, N. Kozai, T. Ohnuki, D. Datsumura, T. Tsuji, R. Kawasaki, K. Akiyoshi, *Sci. Rep.*, 2017, **7**, article no. 2064.
[131] W. Querido, A. L. Rossi, M. Farina, *Micron*, 2016, **80**, 122-134.
[132] B. Laforce, C. Carlier, B. Vekemans, J. Villanova, R. Tucoulou, W. Ceelen, L. Vincze, *Sci. Rep.*, 2016, **6**, article no. 29999.
[133] M. Shimura, A. Saito, S. Matsuyama, T. Sakuma, Y. Terui, K. Ueno, H. Yumoto, K. Yamauchi, K. Yamamura, H. Mimura, Y. Sano, M. Yabashi, K. Tamasaku, K. Nishio, Y. Nishino, K. Endo, K. Hatake, Y. Mori, Y. Ishizaka, T. Ishikawa, *Cancer Res.*, 2005, **65**, 4998-5002.
[134] I. I. Slowing, B. G. Trewyn, S. Giri, V. S.-Y. Lin, *Adv. Funct. Mater.*, 2007, **17**, 1225-1236.
[135] X. Yang, M. Yang, B. Pang, M. Vara, Y. Xia, *Chem. Rev.*, 2015, **115**, 10410-10488.
[136] S. Corezzi, L. Urbanelli, P. Cloetens, C. Emiliani, L. Helfen, S. Bohic, F. Elise, D. Fioretto, *Anal. Biochem.*, 2009, **388**, 33-39.
[137] R. Oun, Y. E. Moussa, N. J. Wheate, *Dalton Trans.*, 2018, **47**, 6645-6653.
[138] M. Umair, M. Alfadhel, *Cells*, 2019, **8**, article no. 1598.
[139] C. R. Ferreira, W. A. Gahl, *Transl. Sci. Rare Dis.*, 2017, **18**, 101-139.
[140] M. C. Kruer, *Int. Rev. Neurobiol.*, 2013, **110**, 165-194.
[141] P. Chen, J. Bornhorst, M. Aschner, *Front Biosci.*, 2018, **23**, 1655-1679.
[142] T. Litwin, K. Dzieżyc, M. Karliński, G. Ghabik, W. Czepiel, A. Członkowska, *J. Neurol. Sci.*, 2015, **355**, 162-167.
[143] M. A. Reeves, P. R. Hoffmann, *Cell Mol. Life Sci.*, 2009, **66**, 2457-2478.
[144] Y. Perez, Z. Shorer, K. Liani-Leibson, P. Chabosseau, R. Kadir, M. Volodarsky, D. Halperin, S. Barber-Zucker, H. Shalev, R. Schreiber, L. Gradstein, E. Gurevich, R. Zarivach, G. A. Rutter, D. Landau, O. S. Birk, *Brain*, 2017, **140**, 928-939.
[145] H. Kodama, C. Fujisawa, W. Bhadhprasit, *Curr. Drug Metab.*, 2012, **13**, 237-250.
[146] P. D. Bie, P. Muller, C. Wijmenga, L. W. J. Klomp, *J. Med. Genet.*, 2007, **44**, 673-688.
[147] T. Y. Tao, J. D. Gitlin, *Hepatology*, 2003, **37**, 1241-1247.
[148] M. Kinebuchi, A. Matsuura, T. Kiyono, Y. Nomura, S. Kimura, *Sci. Rep.*, 2016, **6**, article no. 33247.
[149] O. Hachmöller, A. G. Buzanich, M. Aichler, M. Radtke, D. Dietrich, K. Schwamborn, L. Lutz, M. Werner, M. Sperling, A. Walch, U. Karst, *Metallomics*, 2016, **8**, 648-653.
[150] S. Weiskirchen, P. Kim, R. Weiskirchen, *Ann. Transl. Med.*, 2019, **7**, S72-S76.
[151] T. P. Flaten, *Coord. Chem. Rev.*, 2002, **228**, 385-395.
[152] B. Kralj, I. Krizaj, P. Bukovec, S. Slejko, R. Milacic, *Anal. Bioanal. Chem.*, 2005, **383**, 467-475.
[153] Z. Xie, Z. Chen, W. Sun, X. Guo, B. Yin, J. Wang, *Chin. Geogr. Sci.*, 2007, **17**, 376-382.
[154] Y. Ozdemir, S. Gucer, *Food Chem.*, 1998, **61**, 679-689.
[155] J. E. T. Pennington, *Food Addit. Contam.*, 1988, **5**, 161-232.
[156] T. Karak, R. M. Bhagat, *Food Res. Int.*, 2010, **43**, 2234-2252.
[157] G. Crisponi, V. M. Nurchi, G. Faa, M. Remelli, *Monatsh. Chem.*, 2011, **142**, 331-340.
[158] D. R. C. McLachlan, *Environmentrics*, 1995, **6**, 233-275.
[159] J. Y. Ruan, M. H. Wong, *Environ. Geochem. Health*, 2001, **23**, 53-63.
[160] M. H. Wong, K. F. Fung, H. P. Carr, *Toxicol. Lett.*, 2003, **137**, 111-120.
[161] J. Rode, D. Bazin, A. Dessombz, Y. Benzerara, E. Letavernier, N. Tabibzadeh, A. Hoznek, M. Tligui, O. Traxer, M. Daudon, J.-P. Haymann, *Nutrients*, 2019, **11**, article no. 256.
[162] H. Matusiewicz, *Acta Biomater.*, 2014, **10**, 2379-2403.
[163] W. Z. W. Teo, P. C. Schalock, *Dermatol. Ther. (Heidelb)*, 2017, **7**, 53-64.
[164] T. Kim, C. Wang See, X. Li, D. Zhu, *Eng. Regen.*, 2020, **1**, 6-18.
[165] M. Jafary-Zadeh, G. P. Kumar, P. S. Branicio, M. Seifi, J. J. Lewandowski, F. Cui, *J. Funct. Biomater.*, 2018, **9**, article no. 19.
[166] C. Poulard, A. Dessombz, M. Daudon, D. Bazin, *C. R. Chim.*, 2016, **19**, 1597-1604.
[167] A. Nouaille, A. Descazeaud, F. Desgrandchamps, D. Bazin, M. Daudon, A. Masson Lecomte, P. Mongiat-Artus, P. Meria, *Prog. Urol.*, 2021, **31**, 348-356.
[168] J. Přikrylová, J. Procházková, Š. Podzimek, *BioMed. Res. Int.*, 2019, article no. 2519205.
[169] R. Poljak-Guberina, D. Knezović-Zlatarić, M. Katunarić, *Acta Stomat. Croat.*, 2002, 447-450.
[170] I. Catelas, J. B. Medley, P. A. Campbell, O. L. Huk, J. D. Bobyn, *J. Biomed. Mater. Res. B. Appl. Biomater.*, 2004, **70**, 167-178.
[171] I. Catelas, P. A. Campbell, J. D. Bobyn, J. B. Medley, O. L. Huk, *Proc. Inst. Mech. Eng. H.*, 2006, **220**, 195-208.
[172] A. E. Goode, J. M. Perkins, A. Sandison, C. Karunakaran, H. Cheng, D. Wall, J. A. Skinner, A. J. Hart, A. E. Porter, D. W. McComb, M. P. Ryan, *Chem. Commun.*, 2012, **48**, 8335-8337.
[173] X. Wang, H. Shan, J. Wang, Y. Hou, J. Ding, Q. Chen, J. Guan, C. Wang, X. Chen, *Int. J. Nanomed.*, 2015, **10**, 3055-3064.
[174] J. L. Pariente, L. Bordenave, R. Bareille, C. Ohayon-Courtes, C. Baquey, M. Le Guillou, *Biomaterials*, 1999, **20**, 523-527.
[175] A. Ektessabi, S. Shikine, N. Kitamura, M. Rokkum, C. Johansson, *X-Ray Spectrom.*, 2001, **30**, 44-48.
[176] E. Chassot, J. L. Irigaray, S. Terver, G. Vanneuville, *Med. Eng. Phys.*, 2004, **26**, 193-199.

[177] N. Kluger, *Curr. Probl. Dermatol.*, 2015, **48**, 6-20.
[178] L. Rubio, E. Guerra, C. Garcia-Jares, M. Lores, *Anal. Chim. Acta*, 2019, **1079**, 59-72.
[179] M. Arl, D. J. Nogueira, J. S. Köerich, N. M. Justino, D. S. Vicentini, W. G. Matia, *J. Hazardous Mater.*, 2019, **364**, 548-561.
[180] B. Battistini, F. Petrucci, I. De Angelis, C. M. Failla, B. Bocca, *Chemosphere*, 2020, **245**, article no. 125667.
[181] N. Kluger, *Presse Méd.*, 2020, **49**, article no. 104055.
[182] I. Schreiver, B. Hesse, C. Seim, H. Castillo-Michel, J. Villanova, P. Laux, N. Dreiack, R. Penning, R. Tucoulou, M. Cotte, A. Luch, *Sci. Rep.*, 2017, **7**, article no. 11395.
[183] I. Schreiver, B. Hesse, C. Seim, H. Castillo-Michel, L. Anklamm, J. Villanova, N. Dreiack, A. Lagrange, R. Penning, C. De Cuyper, R. Tucoulou, W. Bäumler, M. Cotte, A. Luch, *Part. Fibre Toxicol.*, 2019, **16**, article no. 33.
[184] P. E. Galavis, N. J. Sanfilippo, I. J. Das, *PLoS ONE*, 2019, **14**, article no. e0220030.
[185] G. Riffo, C. Ramírez-Lama, L. Bennun, *J. Cosmet. Dermatol. Sci. Appl.*, 2020, **10**, 33-53.
[186] M. Manso, S. Pessanha, M. Guerra, U. Reinholz, C. Afonso, M. Radtke, H. Lourenço, M. L. Carvalho, A. G. Buzanich, *Biol. Trace Elem. Res.*, 2019, **187**, 596-601.
[187] H. Colboc, D. Bazin, P. Moguelet, S. Reguer, R. Amode, C. Jouanneau, I. Lucas, L. Deschamps, V. Descamps, N. Kluger, *J. Eur. Acad. Dermatol. Venereol.*, 2020, **34**, e313-e315.
[188] P. Laux, T. Tralau, J. Tentschert, A. Blume, S. Al Dahouk, W. Bäumler, E. Bernstein, B. Bocca, A. Alimonti, H. Colebrook, C. de Cuyper, L. Dähne, U. Hauri, P. C. Howard, P. Janssen, L. Katz, B. Klitzman, N. Kluger, L. Krutak, T. Platzek, V. Scott-Lang, J. Serup, W. Teubner, I. Schreiver, E. Wilkniß, A. Luch, *Lancet*, 2016, **387**, 395-402.
[189] A. S. Prasad, *J. Trace Elem. Med. Biol.*, 2014, **28**, 364-371.
[190] D. E. Sayers, F. W. Lytle, E. A. Stern, *Adv. X-ray Anal.*, 1970, **13**, 248-271.
[191] E. A. Stern, D. E. Sayers, F. W. Lytle, *Phys. Rev. B*, 1975, **11**, 4836-4846.
[192] D. Bazin, X. Carpentier, I. Brocheriou, P. Dorfmuller, S. Aubert, C. Chappard, D. Thiaudière, S. Reguer, G. Waychunas, P. Jungers, M. Daudon, *Biochimie*, 2009, **91**, 1294-1300.
[193] R. Baan, K. Straif, Y. Grosse, B. Secretan, F. El Ghissassi, V. Cogliano, On behalf of the WHO International Agency for Research on Cancer Monograph Working Group, *Carbon Black, Titanium Dioxide, and Talc*, IARC Monographs on the Evaluation of Carcinogenic Risks to Humans, vol. 93, International Agency for Research on Cancer, Lyon, France, 2010, ISBN-13, 978-92-832-1293-5.
[194] X. Zhang, W. Li, Z. Yang, *Arch. Toxicol.*, 2015, **89**, 2207-22017.
[195] C. Xue, J. Wu, F. Lan, W. Liu, X. Yang, F. Zeng, H. Xu, *J. Nanosci. Nanotechnol.*, 2010, **10**, 8500-8507.
[196] A. A. Dayem, M. K. Hossain, S. B. Lee, K. Kim, S. K. Saha, G.-M. Yang, H. Y. Choi, S.-G. Cho, *Int. J. Mol. Sci.*, 2017, **18**, article no. 120.
[197] E. V. Ross, S. Yashar, N. Michaud, R. Fitzpatrick, R. Geronemus, W. D. Tope, R. R. Anderson, *Arch. Dermatol.*, 2001, **137**, 33-37.
[198] O. Frank, M. Zukalova, B. Laskova, J. Kürti, J. Koltai, L. Kavan, *Phys. Chem. Chem. Phys.*, 2012, **14**, 14567-14572.
[199] B. J. Yakes, T. J. Michael, M. Perez-Gonzalez, B. P. Harp, *J. Raman Spectrosc.*, 2017, **48**, 736-743.
[200] R. Zhang, P.-G. Yin, N. Wang, L. Guo, *Solid State Sci.*, 2009, **11**, 865-869.
[201] Q. Han, L. Xu, C. Wang, H. Zhang, *J. Phys. Chem. C*, 2007, **111**, 5034-5038.
[202] R. Zboril, M. Mashlan, D. Petridis, *Chem. Mater.*, 2002, **14**, 969-982.
[203] M. I. Oshtrakh, M. V. Ushakov, V. Šepelák, V. A. Semionkin, P. C. Morais, *Spectrochim. Acta A: Mol. Biomol. Spectrosc.*, 2016, **152**, 666-679.
[204] R. Blukis, R. Rüffer, A. I. Chumakov, R. J. Harrison, *Meteorit. Planet. Sci.*, 2017, **52**, 925-936.
[205] J. J. Rehr, A. L. Ankudinov, *Coord. Chem. Rev.*, 2005, **249**, 131-140.
[206] H. Sun, J. Brocato, M. Costa, *Curr. Environ. Health Rep.*, 2015, **2**, 295-303.
[207] R. Ortega, B. Fayard, M. Salomé, G. Devès, J. Susini, *Chem. Res. Toxicol.*, 2005, **18**, 1512-1519.
[208] D. Bazin, D. Sayers, J. Rehr, *J. Phys. Chem.*, 1997, **B101**, 11040-11050.
[209] D. Bazin, D. Sayers, J. J. Rehr, C. Mottet, *J. Phys. Chem.*, 1997, **101**, 5332-5336.
[210] D. Bazin, J. Rehr, *J. Phys. Chem. C*, 2011, **115**, 23233-23236.
[211] J. Moonen, J. Slot, L. Lefferts, D. Bazin, H. Dexpert, *Physica B*, 1995, **208**, 689-690.
[212] S. K. Murthy, *Int. J. Nanomed.*, 2007, **2**, 129-141.
[213] E. H. Chang, J. B. Harford, M. A. W. Eaton, P. M. Boisseau, A. Dube, R. Hayeshi, H. Swai, D. S. Lee, *Biochem. Biophys. Res. Commun.*, 2015, **468**, 511-517.
[214] G. Chen, I. Roy, C. Yang, P. N. Prasad, *Chem. Rev.*, 2016, **116**, 2826-2885.
[215] A. Guinier, *X-ray Diffraction in Crystals, Imperfect Crystals and Amorphous Bodies*, Dunod, Paris, 1956.
[216] A. Guinier, "X-ray diffraction in Crystals", in *Imperfect Crystals and Amorphous Bodies*, W. H. Freeman & Co., San Francisco, 1963.
[217] A. Guinier, *Théorie et technique de la radiocristallographie*, Dunod, Paris, 1964.
[218] A. Le Bail, H. Duroy, J. L. Fourquet, *Math. Res. Bull.*, 1988, **23**, 447-452.
[219] V. K. Pecharsky, P. Y. Zavalij, *Fundamentals of Powder Diffraction and Structural Characterization of Materials*, Springer-Verlag, New York, 2005.
[220] C. Kumar (ed.), *X-ray and Neutron Techniques for Nanomaterials Characterization*, Springer, Berlin, Heidelberg, 2016.
[221] D. Bazin, C. Chappard, C. Combes, X. Carpentier, S. Rouzière, G. André, G. Matzen, M. Allix, D. Thiaudière, S. Reguer, P. Jungers, M. Daudon, *Osteoporos. Int.*, 2009, **20**, 1065-1075.
[222] D. Szabo, "Removal of calcifications from distal canals of mandibular molars with the gentlewave™ system", PhD Thesis, The University of Western Ontario, University of British Columbia, USA, 2003.
[223] X. Carpentier, D. Bazin, C. Combes, A. Mazouyes, S. Rouzière, P.-A. Albouy, E. Foy, M. Daudon, *J. Trace Elem. Med. Biol.*, 2011, **25**, 160-165.
[224] G. Schlieper, A. Aretz, S. C. Verberckmoes, T. Krüger, G. J. Behets, R. Ghadimi, T. E. Weirich, D. Rohrmann, S. Langer, J. H. Tordoir, K. Amann, R. Westenfeld, V. M. Brandenburg,

P. C. D'Haese, J. Mayer, M. Ketteler, M. D. McKee, J. Floege, *JASN*, 2010, **21**, 689-696.

[225] S. D. Blaschko, J. Miller, T. Chi, L. Flechner, S. Fakra, A. Kahn, P. Kapahi, M. L. Stoller, *J. Urol.*, 2013, **189**, 726-734.

[226] A. Dessombz, G. Coulibaly, B. Kirakoya, R. W. Ouedraogo, A. Lengani, S. Rouzière, R. Weil, L. Picaut, C. Bonhomme, F. Babonneau, D. Bazin, M. Daudon, *C. R. Chim.*, 2016, **19**, 1573-1579.

[227] A. Dessombz, C. Nguyen, H.-K. Ea, S. Rouzière, E. Foy, D. Hannouche, S. Réguer, F.-E. Picca, D. Thiaudière, F. Lioté, M. Daudon, D. Bazin, *J. Trace Elem. Med. Biol.*, 2013, **27**, 326-333.

[228] S. Reguer, C. Mocuta, D. Thiaudière, M. Daudon, D. Bazin, *C. R. Chim.*, 2016, **19**, 1424-1431.

Comptes Rendus
Chimie
2022, Vol. 25, Special Issue S1, p. 189-208
https://doi.org/10.5802/crchim.129

Microcrystalline pathologies: Clinical issues and nanochemistry / *Pathologies microcristallines : questions cliniques et nanochimie*

XANES spectroscopy for the clinician

Dominique Bazin [*, a, b], **Solenn Reguer** [c], **Delphine Vantelon** [c], **Jean-Philippe Haymann** [d, e, f], **Emmanuel Letavernier** [d, e, f], **Vincent Frochot** [d, e, f], **Michel Daudon** [d, e, f], **Emmanuel Esteve** [g, h] **and Hester Colboc** [i]

[a] Université Paris-Saclay, CNRS, Institut de Chimie Physique, 91405 Orsay cedex, France

[b] Université Paris-Saclay, CNRS, Laboratoire de Physique des Solides, 91405, Orsay, France

[c] Synchrotron SOLEIL, L'Orme des Merisiers, Saint-Aubin, BP 48, 91192 Gif-sur-Yvette, France

[d] Sorbonne Universités, UPMC Univ Paris 06, UMR S 702, Paris, France

[e] INSERM, UMR S 702, Paris, France

[f] Explorations fonctionnelles multidisciplinaires, AP-HP, Hôpital Tenon, Paris, France

[g] Sorbonne Université, UPMC Paris 06, Institut National de la Santé et de la Recherche Médicale, Unité Mixte de Recherche S 1155, F-75020 Paris, France

[h] AP-HP, Hôpital Tenon, Department of Nephrology and Dialysis, Paris, France

[i] Sorbonne Université, AP-HP, Hôpital Rothschild, Service Plaies et Cicatrisation, Paris, France

E-mails: dominique.bazin@universite-paris-saclay.fr (D. Bazin), solenn.reguer@synchrotron-soleil.fr (S. Reguer), delphine.vantelon@synchrotron-soleil.fr (D. Vantelon), jean-Philippe.haymann@aphp.fr (J.-P. Haymann), emmanuel.letavernier@aphp.fr (E. Letavernier), vincent.frochot@aphp.fr (V. Frochot), daudonmichel24@gmail.com (M. Daudon), emmanuel.esteve@aphp.fr (E. Esteve), hester.colboc@aphp.fr (H. Colboc)

Abstract. XANES spectroscopy, which uses synchrotron radiation as a probe, offers substantial information about the local structure of biological samples, encompassing those without long range order such as Pt anticancer molecules, and nanometre scale or amorphous particles of calcium phosphate. Its subcellular spatial resolution, as well as its capacity to operate at room temperatures and pressures represent major advantages for medical research. Moreover, paraffin embedded biopsy samples can be analysed without any further preparation, Key publications which illustrate these capacities are presented.

Keywords. XANES, Medicine, Calcium, Platinum, Drug.

Published online: 21 October 2021, Issue date: 1 September 2022

* Corresponding author.

1. Introduction

During the past decades, the increasing availability of synchrotron radiation facilities such as synchrotron SOLEIL (the French national facility) have allowed the physician to develop a completely new set of characterization techniques. These are based on radiation-matter interactions, and include X-ray absorption spectroscopy (XAS) [1–3], anomalous wide angle X-ray scattering (AWAXS) [4–7], anomalous small angle X-ray scattering (ASAXS) [4–6] or diffraction anomalous fine structure (DAFS) [8]. Among this family of techniques, X-ray Absorption Near Edge Structure (XANES) constitutes one aspect of XAS [1–3], the other being Extended X-ray Absorption Fine Structure (EXAFS); both play pivotal roles in medical [9] as well as in biological [10–12] research.

Some of the valuable information yielded by XANES spectroscopy may be exemplified by another characterization technique, namely X-ray fluorescence (XRF), discussed previously [13–15]. XRF is one of the techniques able to identify and quantify the different elements present in a biological sample [16–18] and map them at the submicrometer scale. This elementary composition of the sample may be sufficient to establish a clinical diagnosis. This is the case for lead, the toxicity of which is intimately linked to the condition saturnism. For, the electronic state of other elements, such as chromium, can determine their toxicity. While Cr(III) is physiologically essential in sugar and lipid metabolism, Cr(VI) compounds can induce DNA damage and have potential cellular mutagenic effects [19]. XANES spectroscopy can not only establish the electronic state of Cr but also additional structural information regarding the local order around Cr atoms. The present paper will thus show how XANES spectroscopy represents an exceptional tool to investigate local structure in samples encompassing those without long range order such as molecular [20–26] and nanometer scale clusters [27–32], or amorphous compounds [33–35]. Such micrometer scale structural information allows significant correlation with the anatomical structures and thus with normal or pathological biological functions.

To this end, we will present key elements of the theory, the data analysis procedure, two experimental set ups available on the synchrotron SOLEIL (the DiffAbs and LUCIA (Line for Ultimate Characterisation by Imaging and Absorption) beamlines), and finally selected case studies which exemplify the various opportunities offered by XANES spectroscopy in medicine. These results should show clinicians how such spectroscopy can be inserted into their research, supplementing currently used vibrational spectroscopies such as μFourier Transform—InfraRed spectroscopy (μFTIR) [36–42] or Raman spectroscopy [43–45]. Finally, we will discuss the advantages and limitations of XANES spectroscopy relative to other techniques, namely Energy Loss Near Edge Structure (ELNES) and X-Ray Photoelectron Spectroscopy (XPS) which have yielded useful biomedical information [46–52].

2. Basic features of XANES spectroscopy

2.1. *Theoretical elements of XANES*

The theory of XAS can be found in several excellent publications (see for example Refs [53–59]). Some basic notions regarding this technique are summarized here to better understand its usefulness.

X-ray photons passing through matter interact with it through scattering and absorption. The absorbed intensity decreases exponentially with penetration thickness (x) (Figure 1a), as expressed by Lambert–Beer's law:

$$I_t = I_0 e^{-\mu(E)x}$$

where E is incident photon energy, $\mu(E)$ is the absorption coefficient of the sample, I_0 is the intensity of the incoming X-ray photons, and I_t is the intensity of the X-ray photons transmitted through the sample.

XAS spectroscopy studies absorption coefficient modulations as a function of the energy of incident photons near an abrupt discontinuity (Figure 1b), referred to as "absorption edge". This edge corresponds to the energy of incoming photons sufficient to eject electrons from the inner atomic shells i.e. equal to the binding energy of core-shell electrons. The discrete energies corresponding to the inner shell electrons [60] makes XAS atomically specific (Table 1), allowing the clinician to study a given element by selecting the photon energy. The edge corresponding to 1s electron ejection is referred to as K, and so on for higher electron shells: L_I for 2s electrons, L_{II} for $2p_{1/2}$, and L_{III} for $2p_{3/2}$. This so-called "absorption edge" is sometimes also referred to as the "white line" [61,62].

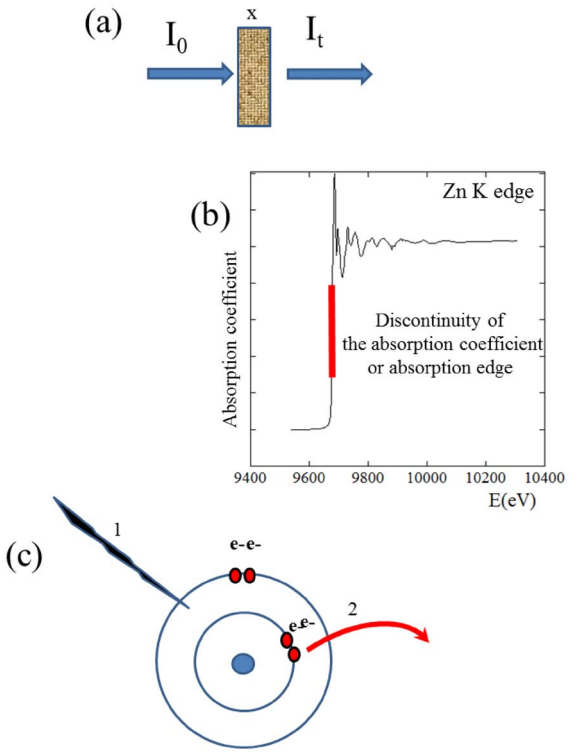

Figure 1. (a) Schematic representation of Lambert–Beer's law. (b) Discontinuity of the absorption edge observed at 9673 eV for Zn atoms. (c) A photon (1) is absorbed by the atom inducing the ejection (2) of an electron from an inner atomic shell.

Table 1. X-ray absorption edges of selected elements (keV)

Element	K-edge	L_I-edge	L_{II}-edge	L_{III}-edge
C	0.282			
N	0.397			
O	0.533			
F	0.692			
Na	1.080			
Mg	1.309			
Al	1.562	0.087	0.076	0.075
Si	1.840	0.118	0.101	0.100
P	2.143	0.153	0.130	0.129
S	2.471	0.193	0.164	0.163
Cl	2.824	0.237	0.204	0.202
Ca	4.034	0.403	0.346	0.342
Ti	4.965	0.529	0.460	0.454
Cr	5.987	0.694	0.582	0.572
Fe	7.112	0.846	0.721	0.708
Co	7.712	0.929	0.797	0.782
Ni	8.339	1.016	0.878	0.861
Cu	8.993	1.109	0.965	0.945
Zn	9.673	1.208	1.057	1.034
As	11.877	1.536	1.368	1.333
Pt	78.400	13.880	13.277	11.568

XANES spectra can be collected for all elements, from very light, e.g. nitrogen [63,64] or sulphur [65–67], and from transition metals such as Fe [68,69] to the heaviest, e.g. Pt [70–74].

After ejection, the photo-electron transits towards empty localized and continuum electronic levels, depending on its excess energy above the binding energy. On the one hand, the local symmetry in which the atom is embedded (tetrahedron, octahedron, square planar…) and the electronic structure of the atom influence the relative position and occupancy of the localized levels and thus the number and energies of the near-edge XAS signals [53–59]. On the other hand, a free photoelectron can be scattered by the surrounding atoms in a train of scattering events. The modulation of the oscillation coefficient is then sensitive to the number, chemical nature, distance, and local arrangement of the neighbouring atomic environment.

Figure 2 clearly shows the difference between XANES and EXAFS of Smithsonite ($ZnCO_3$), and Zincite (ZnO) and highlights the sensitivity of XANES spectroscopy: these two compounds corresponding to two very different Zn atomic coordination environments; Zn coordination in Smithsonite corresponds to ($N = 6$, $R = 2.11$ Å) while in Zincite it is described as ($N = 4$, $R = 1.92$ Å, $R = 1.99$ Å).

2.2. *Data analysis procedures*

Two different approaches to data treatment can be considered. As discussed by Guda *et al.* [59], the very first analysis of a XANES spectrum was performed in 1960 by Van Nordsthand [75] who carried out a systematic study on the spectra of many transition metal compounds and classified their XANES spectra according to the atomic structure and valence of

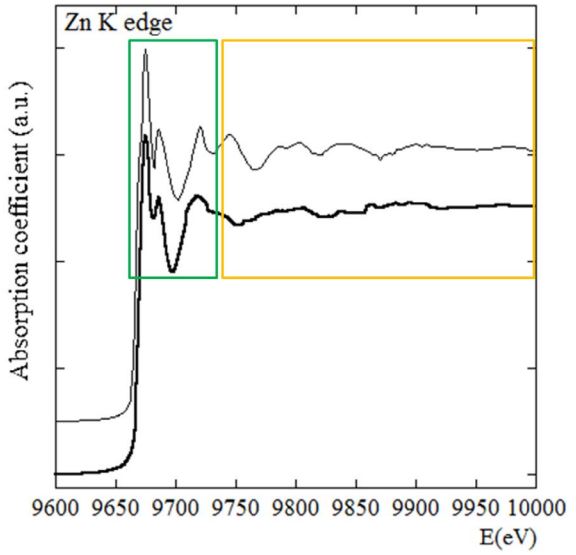

Figure 2. Repartition of the XANES (green part) and EXAFS (yellow part) parts of a XAS spectrum in the case of Zincite ($N_{ZnO} = 4$ $R = 1.92$ Å, $R = 1.99$ Å) and Smithsonite ($N_{ZnO} = 6$ $R = 2.11$ Å) (bold).

the metal element in the compound. Thus, a simple way to analyse the XANES data is to use a set of XANES spectra which correspond to reference compounds and compare them with the XANES spectra of the samples (direct comparison as fingerprint or linear combination of references). Another way to analyse the data is through numerical simulations. These methods are explained below.

2.2.1. *XANES data analysis: comparison with reference compounds*

In physiological and pathological calcifications, Ca occurs in numerous chemical phases, such as calcium oxalate, calcium phosphate, calcium carbonate, etc. as highlighted in Table 2 [76]. Ca phosphate compounds play key roles in different medical fields such as rheumatology and nephrology. Various articles [77–79] describe experiments based on fluorescence induced by electrons ejected from higher energy levels filling the core "hole" associated with photoelectron creation, to determine the chemical compound present in the sample based on the Ca/P ratio. Unfortunately, the ratio thus determined

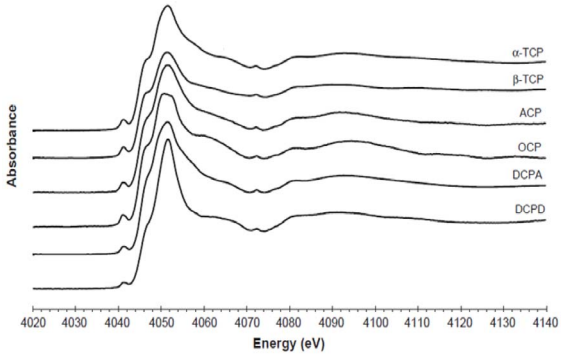

Figure 3. XANES spectra at the Ca K-edge of different non-apatitic calcium phosphate compounds (after Eicher *et al.* [100]).

(Table 2) is not sufficient to differentiate between calcium phosphate compounds.

Biological hydroxyapatite characteristic of bone [80–84] as well as pathologies of different organs such as kidney [85–88], breast [89,90], prostate [91,92] or thyroid [93,94] represents a challenging test case for chemical characterization via the Ca/P ratio. Biological apatites (CA or carbonated calcium phosphate apatite) are carbonated, and calcium- and OH-deficient [95–97]. Thus the Ca/P ratio is always less than 1.67 and photoelectron induced fluorescence is inefficient at precise determination of the chemical composition. X-Ray diffraction may yield interesting information but cannot detect the commonly occurring amorphous calcium phosphate.

In this respect, the sensitivity of XANES offers an interesting opportunity to differentiate several calcium phosphate compounds through the acquisition of spectra at the P [98] or Ca K-edges [99–101]: the shape of the absorption edge and associated features varies significantly with the crystallographic structure of the compound (Figure 3).

Moreover, in the case of calcium phosphate apatite, XANES at the Ca K-edge can provide information regarding long range order. As shown on Figure 4, XANES is not the same for well crystallized synthetic apatite (here, micrometre scale crystallised), biological apatite (nanometer scale crystallised) and amorphous biological calcium phosphate [34].

At this point, it is worth pointing out that quite similar results can be obtained by FTIR spectroscopy [36–42]. So why use XANES as a probe?

Table 2. Different calcium phosphate compounds with their stoichiometry and their Ca/P ratio

Name	Stoichiometry	Ca/P ratio
Monocalcium phosphate		
Anhydrate	$Ca(H_2PO_4)_2$	0.5
Monohydrate—MCPM	$Ca(H_2PO_4)_2H_2O$	0.5
Dicalcium phosphate		
Anhydrous—DCPA—Monetite	$CaHPO_4$	1.0
Dihydrate—DCPD—Brushite	$CaHPO_4\ 2H_2O$	1.0
Octacalcium phosphate—OCP		
Triclinic	$Ca_8(PO_4)_4(HPO_4)_2\ 5H_2O$	1.33
Apatitic	$Ca_8(PO_4)_{2.5}(HPO_4)_{3.5}\ (OH)_{0.5}$	1.33
Amorphous	$Ca_8(PO_4)_4(HPO_4)_2\ nH_2O$	1.33
Tricalcium phosphate		
α (α-TCP)or β (β-TCP)	$Ca_3(PO_4)_2$	1.5
Apatitic	$Ca_9(PO_4)_5(HPO_4)(OH)$	1.5
Amorphous Calcium phosphate—ACP	$Ca_9(PO_4)_6\ nH_2O$	1.5
μCrystallized Synthetic Hydroxyapatite—HA	$Ca_{10}(PO_4)_6(OH)_2$	1.67
Biologic (Carbonated calcium phosphate apatite or CA)	$Ca_{10-x+u}\square_{x-u}(PO_4)_{6-x}(CO_3)_x(OH)_{2-x+2u}$ with $\square$ corresponding to vacancy, $x \leq 2$ and $u \leq x/2$)	1.33–1.67
Tetracalcium phosphate TTCP	$Ca_4(PO_4)_2O$	2.00

In fact, as far as formation of Ca phosphate apatites is concerned, the amorphous surface component can be significantly altered by drying processes [102–106]. More precisely, the drying process before FTIR may alter the physicochemical integrity of a biological sample via transformation of the initial amorphous phase into CA. By limiting the element interrogated, XANES spectroscopy is compatible with various environments, including, in the case of Ca, hydrated samples. Thus for example sections of kidney can be inserted into the beam without preparation [34]. Moreover, taking advantages of the small dimensions of the probe, 2D XANES Ca K-edge distribution maps can be constructed [107].

In Figure 4, the feature labelled A reflects the effective charge and the site symmetry of Ca^{2+} ions ($3d^0$ outer shell electron configuration), and can be attributed to a 1s → 3d transition or O 2p molecular orbital. At higher energy above the "pre-peak" A, we find the most intense resonance, the "white line" [61,62], which includes a shoulder-like structure (feature B; transition 1s → 4s) and a double peak (features C1 and C2; transition 1s → 4p) the relative intensities of which depend on the crystallographic position of Ca involved (Ca(I) or Ca(II)) [99,100,108].

The L-edge of Ca [109–113] and the K-edge of P [114–116] are also sensitive to the same factors. Figure 5 shows significant differences between XANES spectra at Ca L-edge for different Ca phosphate compounds [109].

2.2.2. *XANES data analysis through numerical simulations*

There are several codes, such as Feff, FDMNES, Quantum-Espresso, CP2K [117], to simulate the XANES component [118,119], and K [120] and L [121–125] edges. It is possible to simulate various crystallographic structures, calculate the corresponding XANES spectra, and compare them to experimental data. This approach was used to precisely localize Sr^{2+} cations in a crystal of calcium phosphate apatite [126,127]. For that purpose, three structural configurations were simulated. In the first (hypothesis 1 in Figure 6), Sr^{2+} cations are surrounded only by oxygen atoms adsorbed at the surface of collagen or

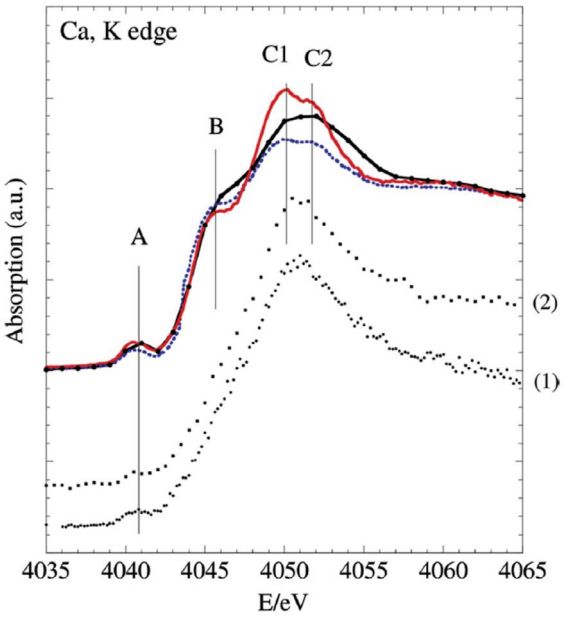

Figure 4. XANES spectra of different compounds: references (in red, HAP, well crystallized synthetic apatite; in blue, CA, biological apatite; in black, ACCP, amorphous carbonated calcium phosphate) and kidney biopsies (1) and (2) (after Carpentier *et al.* [34]).

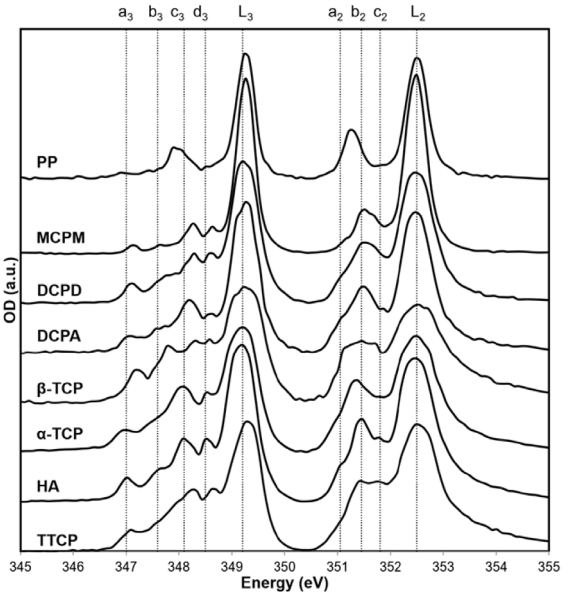

Figure 5. XANES spectra at the Ca-$L_{II,III}$-edges of several Ca-phosphate reference compounds (PP: polyphosphate). Vertical dotted lines correspond to the peak energies of HA (after Cosmidis *et al.* [109]).

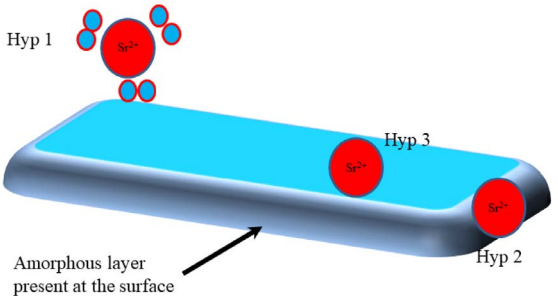

Figure 6. Schematic representation of the three structural hypotheses (Hypothesis 1, Hypothesis 2 and Hypothesis 3) regarding the localization of Sr^{2+} cations in a crystal of calcium phosphate apatite.

amorphous calcium phosphate. In the second configuration (hypothesis 2 in Figure 6), Sr^{2+} cations are engaged in the hydrated poorly crystalline apatite region present at the surface of calcium phosphate nanocrystals. Finally, a substitution of Sr^{2+} for Ca^{2+} cations can occur within Ca phosphate nanocrystals in either crystallographic site (I) or (II) (hypothesis 3 in Figure 6).

Figure 7 shows XANES simulations corresponding to each structural hypothesis in which some significant differences appear. The final data analysis step is a comparison with experimental data, from physiological and pathological calcium phosphate apatites (Figure 8). Because calcium and strontium are congeners in the periodic table, they are likely to exhibit similar chemistry and mechanistic biology, possibly explaining why physiological and pathological calcium phosphate apatites can contain Sr^{2+}.

As a preliminary conclusion, XANES spectroscopy constitutes a powerful high sensitivity biomedical tool able to discriminate even closely related compounds such as calcium carbonate or calcium oxalate [128–131], or to localize heterocations such Sr^{2+} in a calcium phosphate apatite matrix [132–134].

3. Experimental considerations

Proposals to use the synchrotron facility have to be submitted while proposal calls are open (usually

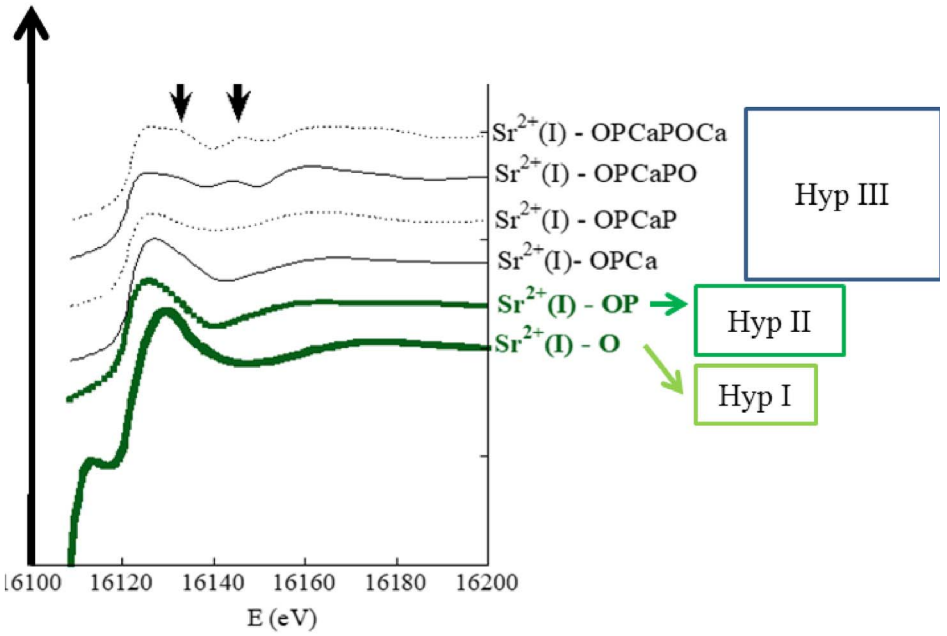

Figure 7. XANES numerical simulations for the different structural hypotheses (differences between the 3 hypotheses are supported by black arrows). Sr^{2+}(I) refers to Sr^{2+} cations in the Ca^{2+}(I) site (after Bazin *et al.* [127]).

twice a year). Feasibility and technical issues have to be addressed with the beamline scientists prior to the submission, to select the most appropriate beamline, to formulate the proposal optimally, to anticipate the experimental trajectory, define the number of samples and their preparation and observation conditions, the time needed for measurements (from a few seconds to one hour for one XANES spectrum depending on target substance concentration), and any safety considerations.

Indeed, samples may vary widely and may take the form of powders, tissues, biopsies etc. The preparation and measurement of any sample must preserve its integrity. The beamline scientists may propose various sample environments and measurement conditions to achieve this, for example, to prevent sample desiccation or beam damage. In this respect, cryo-cooling is increasingly being considered as an effective preparation technique.

Several synchrotron radiation facilities are equipped to perform XAS measurements (see for example experiments implemented on the European Synchrotron Radiation Facility (ESRF)) [135,136]. The clinician has to select the most appropriate energy range and detection limit, according to the element to be probed, its concentration, the beam characteristics, and sample heterogeneity. The SOLEIL synchrotron can acquire XANES spectra on several beamlines. Some offer very fast acquisition capabilities (less than one second, compared to conventional XANES which usually takes several minutes) allowing phase transitions or chemical reactions to be followed using quick-EXAFS, as on ROCK (Rocking Optics for Chemical Kinetics) which operates between 4.5 and 40 keV [137], and ODE (Optique Dispersive EXAFS), using dispersive EXAFS which operates between 3.5 and 25 keV [138]. Up to now, most biomedical research has been based on XANES spectroscopy performed on the DiffAbs beamline [139], where experiments can be performed using a macro (300 μm) or micro beam size (10×10 μm^2) and an energy range between 3 and 19 keV. The relevant experiments were performed at Ca [34,140], Zn [127,141], and Sr [126,127] K-edges (at about 4.086 keV, 7.112 keV, 9.659 keV and 16.104 keV respectively). Such research can be extended by XANES measurements at lower energy. On the LUCIA beamline, (Figure 9), XRF as well as XAS experiments at

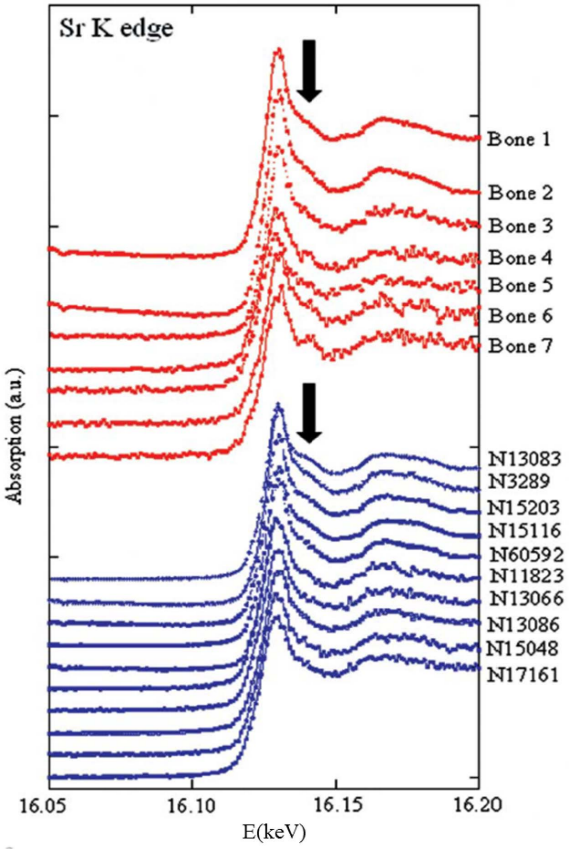

Figure 8. XANES part of X-ray absorption spectra collected at the Sr K-edge for different physiological (in red) and pathological (in blue) calcifications (after Bazin *et al.* [127]).

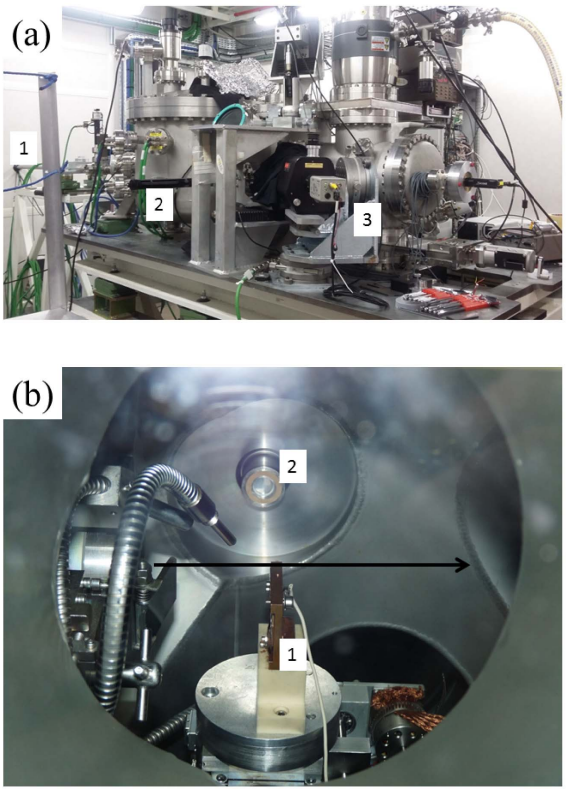

Figure 9. LUCIA experimental set-up A. 1 Synchrotron beam entry, 2 Chamber containing the final focusing mirrors and 3 Sample chamber; B Interior of the experimental chamber containing, among other apparatus, a sample holder (1) and a fluorescence detector (2). The arrow indicates the incident beam direction.

micrometric scale can be performed with photon energy between 0.8 and 8 keV and a beam size ranging from 2 mm to 2 µm [142,143]. LUCIA allows XAS experiments at the K edge of elements from Na to Fe, L edges from Ni to Gd, and M edges of rare earths and actinides. After training under the supervision of the beamline scientists, clinical teams can conduct experiments on their own.

4. Selected case studies

There are several investigations of physiological and pathological calcifications in the literature [144–146], three of which are described below. The first concerns metabolic disorders that can be studied by experiments at the K edge of metals (here, Fe) [69]. The second involves drugs developed for different purposes, namely cancer and infection, and characterizes the speciation of both light (C) and heavy (Ag and Pt) elements [147,148]. The third shows how K-edge XANES (Zn) can provide valuable clinical information about patients developing skin reactions to tattooing.

4.1. *The iron oxidation states in the substantia nigra*

Iron is essential in many human tissues (around 4 g for 70 kg body mass) and its quantity in different locations is very important [149], explaining why numerous investigations, in breast [150], prostate [151,152] and brain [153], have been published.

Brain metal homeostasis is altered in neurodegenerative diseases and the concentration, the localization and/or the chemical speciation of the elements can be modified relative to healthy individuals. These changes are often specific to the brain region affected by the neurodegenerative process. For example, iron concentration is increased in the substantia nigra (SN) of Parkinson's disease patients, although the role of metal speciation modifications in the etiological processes is still not well understood.

To determine if modification of iron speciation is involved in Parkinson's pathogenesis, Carmona *et al.* [69] have developed a methodology based on chemical element imaging and speciation, using correlative immunohistochemistry. Collecting μXRF images provided a quantitative distribution of metals in specific brain regions (Figures 10a and b). Micro-XANES defined the chemical speciation of iron in the region of interest. To produce accurate information about elemental changes in specific brain areas, these chemical imaging methods were correlated to brain tissue histology. Then, applying this methodology to the study of 6-hydroxydopamine (6-OHDA) lesioned rats (an animal model of Parkinson's disease), they showed that iron and manganese distribution differs according to the brain region mapped, although it does not differ between lesioned and non-lesioned animals (Figure 11). Additionally, iron always occurs as ferritin without any distinction between lesioned or non-lesioned animals.

Therefore, this spatially resolved study shows that iron increase in the substancia nigra might not be involved in the neurodegenerative process induced by 6-OHDA. Furthermore, it illustrates the ability to correlate immunohistochemistry and chemical element imaging at the brain level. This methodology should in a near future be successfully applied to other studies of metal dyshomeostasis in neurology.

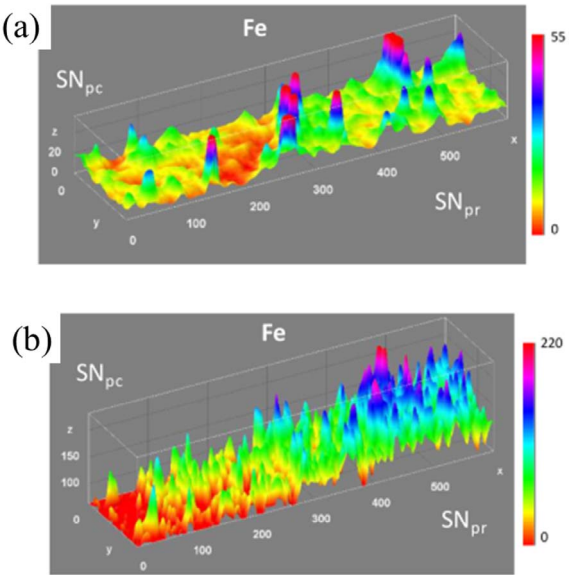

Figure 10. Representative μ-XRF distribution maps of Fe in the substantia nigra pars compacta (SNpc), appearing at the left side of the images, and substantia nigra pars reticulate (SNpr), right side of the images. (a) In the contralateral (ContraL) side of sham rat brain. (b) In the ContraL side of a 6-OHDA injured rat. x and y axis in μm; z axis in number of XRF counts (after Carmona *et al.* [69]).

4.2. *XANES investigations focusing on drugs*

In the following section, we discuss three studies selected because they have been performed at the absorption edge of elements from light (C) to heavy (Ag and Pt), showing the large range of XANES capabilities.

Drug delivery is the method or process of administering a pharmaceutical compound to optimize a therapeutic effect in humans or animals [154]. It is very important clinically clinically to preserve the chemical integrity of the drug and to be sure that the drug is inside the carrier. We can define drug carriers as biocompatible tools for the transport of molecules for pharmaceutical, cosmetic, and nutraceutical applications [155]. Guo *et al.* [147, 148] highlighted that numerous pharmaceuticals including antibiotics [156], anticancer [157] and anti-inflammatory drugs [158] etc. have been successfully loaded into bioceramic drug carriers. The first case study [147,148] relates to the incorporation of drugs in calcium silicate hydrate and is based on XANES collected at the C K-edge (Figure 12).

Guo *et al.* [147,148] considered three drug molecules, ibuprofen (IBU), alendronate sodium (ALN) and gentamicin sulfate (GS) incorporated into mesoporous spheres of calcium silicate hydrate (CSH). These three drugs display specific XANES spectra at the C–K edge (Figure 12). Because it is possible to perform XANES experiments with high

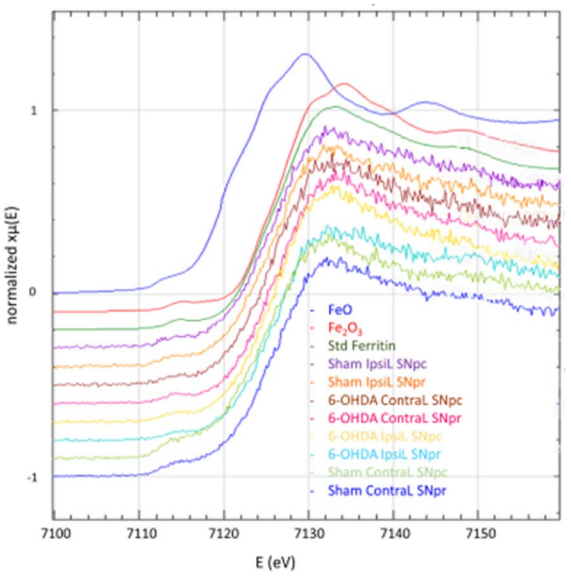

Figure 11. Fe K-edge XANES spectra for FeO, Fe_2O_3, ferritin standards and in the SNpc and SNpr for the ContraL and IpsiL brain sides of 6-OHDA injured and sham animals. All the measured spectra on brain samples show the same shape as ferritin standard (after Carmona *et al.* [69]).

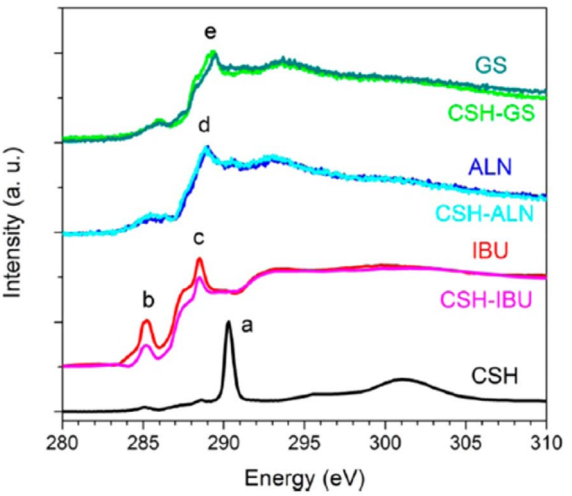

Figure 12. C K-edge XANES comparisons before and after the loading of IBU, ALN, and GS into CSH mesoporous microspheres. Feature "a" at 290.3 eV is for CO_2 adsorption in CSH; "b" at 285.2 eV is the feature of aryl ring of IBU; "c" at 288.5 eV is the 1s–π^* transition from carboxylic acid as in the case of IBU; "d" and "e" at around 289 eV are from C 1s–σ^* (C–OH/C–NH_2) of ALN and GS drug molecules, respectively (after Guo *et al.* [147,148]).

signal-to-noise ratio at the C K-edge even if the content of drug is low, this spectroscopy allows the clinician to ensure that the chemical state of the drug is preserved during incorporation into mesoporous CSH spheres Additionally, Transmission Electron Microscopy (TEM) images of CSH before/after drug loading indicated that the drug was incorporated in the carrier.

In the 2nd example, experiments were carried out at the Ag L_{III} (E = 3351 eV), S K (E = 2472 eV), and P K (E = 2145 eV) edges to study the interaction between silver ions used as antibacterial agents, and bacteria [158]. This approach reveals those chemical forms of silver which can interact with *Staphylococcus aureus* and *Escherichia coli*. The Ag L_{III}-edge XANES spectra of the bacteria are all slightly different and very different from the spectra of silver ions (silver nitrate and silver acetate) which confirms that an interaction has taken place (Figure 13). XANES thus offers the clinician a means of focusing on the interaction between Ag and bacteria at the atomic level, paving the way to optimize antibacterial agents containing Ag.

The final example considers platinum-based antitumor drugs [159,160]. We have followed two stages in our clinical investigation [70,71]. Firstly, we want to demonstrate that XRF data helps the clinician to understand the mechanisms of the nephrotoxicity which is a major limiting side effect [161] of these drugs. To this end, XRF measurements were performed on mice kidneys and on two kidney biopsies of patients treated with Pt-based anti-cancer drugs [70,71]. To the best of our knowledge, it was the first time that Pt was detected in kidney biopsies. Note that in one clinical case, the Pt contribution to the XRF spectrum is observed even 6 days after the last oxaliplatin infusion.

Secondly, we wish to show that XANES provides the clinician with the possibility of characterising the interactions between antitumor Pt-based drugs and sulfur. Wang and Guo [162] have pointed out that endogenous sulfur-containing molecules such as cysteine, methionine, glutathione, metallothionein. and albumin, affect the metabolism of platinum drugs and degrade therapeutic efficacy. It is well known in

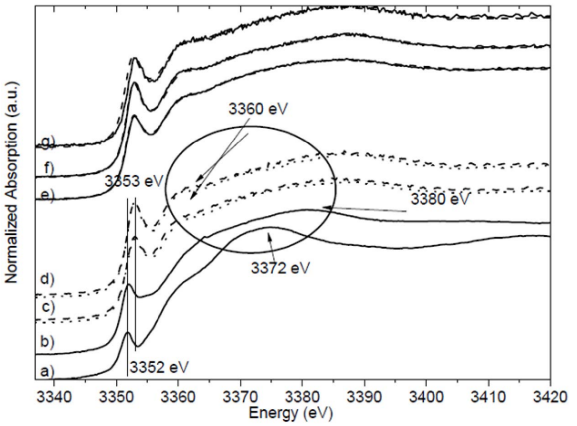

Figure 13. Silver L_{III}-edge XANES spectra of (a) silver nitrate solution (—), (b) silver acetate solution (—), (c) *E. coli* cells treated with silver nitrate (•••) and with silver acetate (– – –), and (d) *Staphylococcus aureus* cells treated with silver nitrate (•••) and with silver acetate (– – –), (e) Linear Combination Fit (LCF) of *E. coli* cells treated with silver nitrate (– – –) and the experimental results (—), and (f) LCF of *S. aureus* cells treated with silver nitrate (– – –) and the experimental results (—) (g) LCF of *Listeria monocytogenes* cells treated with silver nitrate (– – –) and the experimental results (—) (after Bovenkamp *et al.* [158]).

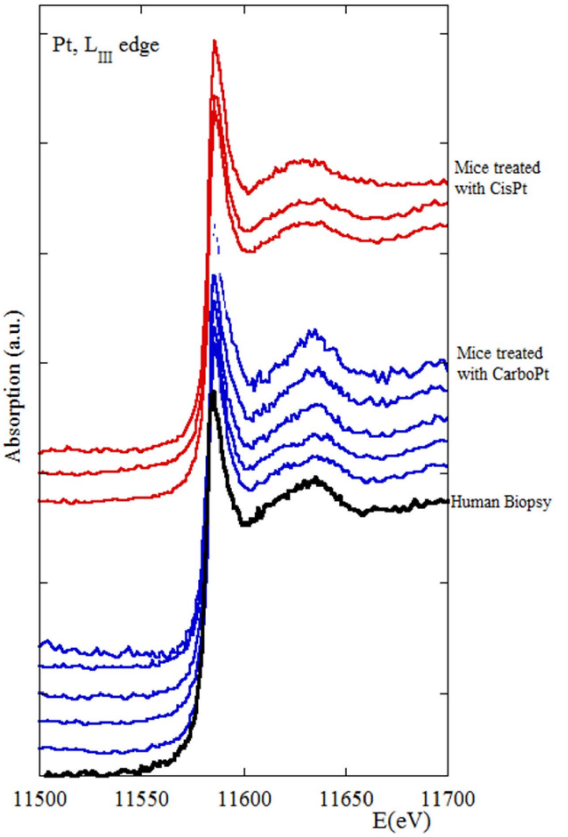

Figure 14. XANES spectra collected at the Pt-L_{III} edge for mice treated with CisPt (red), for mice treated with CarboPt (blue), and of a patient treated with Erbitux, Cisplatin and 5-Flurouracil.

heterogeneous catalysis that XANES can probe the co-ordination of sulfur by platinum [163], and determine the Pt electronic state even only present as a trace element [163–171]. Figure 14 shows the first XANES data collected at the L_{III} edge of Pt in a human biopsy. Even if such data have ultimately to be analyzed by numerical simulations to confirm S–Pt interactions, initial impressions of our complete mouse, and human biopsy, datasets seem to indicate an unchanged Pt environment.

4.3. *XANES investigation of tattoos*

The facts that tattooing has become a pervasive social phenomenon [172] and that tattoo inks contain various potentially toxic organic and inorganic substances [173,174] explain the significant increase of the prevalence of skin diseases related to tattoos. Among the metals which have been identified in skin tattoos, we focus here on Zn [175]. Quite recently, Vandebriel and De Jong [176] published a review on mammalian toxicity of ZnO nanoparticles based on published investigations between 2009 and 2011. These authors have reported that ZnO nanoparticles at most barely penetrate human skin, but they do affect skin cells in vitro. Short-term exposure results in apoptosis but not an inflammatory response, while long-term exposure shows increased reactive oxygen species generation, decreased mitochondrial activity, and the formation of tubular intercellular structures.

One of the challenges regarding the presence of Zn is discriminating between endogenous and exogenous origens. The Zn content of a 70 kg human body is around 2 g [177]. In dermatology, ZnO as well as TiO_2 minerals are utilized in sunscreens as inorganic physical sun blockers, and as a white pigment

in tattoos. In contrast to TiO_2, Raman spectroscopy is not enough sensitive to the presence of ZnO [178], while XANES, performed at the Zn K edge, provides valuable information:

ZnO can adopt three crystal structures: Wurtzite, zinc blende and rocksalt [179]. Under ambient conditions, the thermodynamically stable phase is zincite which displays a wurtzite (hexagonal $P6_3mc$ space group) structure, in which every zinc atom is tetrahedrally coordinated with four oxygen atoms [180]. We have thus regarded zincite as an appropriate reference compound for Zn in pigments.

Knowing the spatial distribution of Zn in the skin (Figure 15a) is necessary to define points of interest (POI) for probing Zn speciation. Such information is given by XRF mapping and we can see such spatial distribution of Zn on Figure 15. Comparing XANES spectra of the four POIs with that of zincite indicates the presence or absence of the pigment (Figure 15a). As we can see POI1 (1 on Figure 15b) and POI2 (2 on Figure 15b) indicate the presence of the ZnO (i.e. exogenous Zn) pigment while POI3 (3 on Figure 15b) and POI4 (4 on Figure 15b) indicate Zn^{2+} cations bound to metalloproteins (i.e. endogenous Zn) [181]. This information localises ink derived ZnO in the tissue quite precisely.

In a recent publication, we have combined XANES and Raman data to elucidate both the complex organic and inorganic chemical composition of tattoo inks in cases of keratoacanthoma. The common feature between the different clinical cases appears to be not the presence of zincite ZnO particles but the presence of a red azo pigment (PR170). Such result raises the question of the carcinogenicity of this substance which interestingly is not listed by the European Council as a carcinogenic azo-colorant [182].

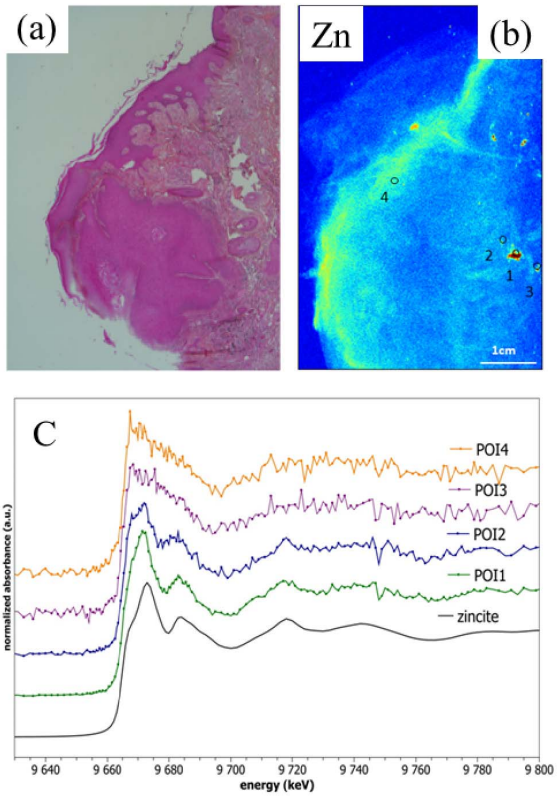

Figure 15. (a) Optical microscopy, identifying a skin cancer developed on a tattoo, Hematoxylin Eosin Saffron staining × 25. (b) Corresponding image of the spatial distribution of Zn obtained by μXRF spectroscopy in this skin cancer. Points of interest (POI) probed by Zn K-edge XANES are labelled 1 to 4. (c) XANES spectra collected at the Zn K edge for the different POIs, 1 to 4, of the skin cancer and for zincite (ZnO).

5. Other techniques to probe biological roles of metals

This is a suitable point to consider the tools able to define the role of metals in biological systems to assist diagnosis and therapy. The complementarity, adaptations, and output of each modality must be considered for each scientific case. These considerations are exemplified by a comparison of XANES spectroscopy, Energy Loss Near Edge Structure (ELNES) and XPS, which are all able to define the atomic environment around a probed atom, yielding valuable chemical, structural, and co-ordination information.

A XANES and ELNES data are subsets of XAS and EELS (electron energy-loss spectroscopy) spectra. Briefly, ELNES has higher spatial resolution (around 1 nm compared to 100 nm for XANES) while XPS is more sensitive to surface properties. ELNES and XANES have a common theoretical basis in an electron transition from a core orbital to unoccupied states and follow an electron dipole transition rule [183–186]. Thus, ELNES and XANES features provide information on the local coordination and

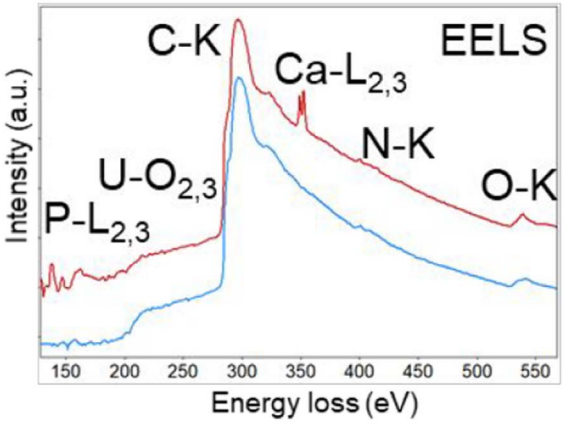

Figure 16. Typical EELS spectrum acquired from a calcium phosphate concretion (Ca and P $L_{II,III}$ edges are visible). Carbon and nitrogen (K-edges) due to biological organic material are also detected, while U, and some C and N, arises from the preparation protocol (after Gay *et al.* [51]).

chemical bonding of selected elements in the illuminated area [187]. Measurements of ELNES with a sufficient signal-to-noise ratio is limited up to about 1000 eV while XANES can be observed across all energies, effectively including almost all elements in the periodic table [188–191] which creates a natural complementarity. Both ELNES and XANES data can be analyzed either by comparison with spectra of reference compounds, or by using theoretical tools [192,193].

Major instrumental advances mean that ELNES can be used with success to investigate biomineral formation mechanisms [34–40]. Because ELNES uses electrons as a probe it must be an ultra-high vacuum technique. Using electrons as probes also means that the spatial resolution, generally governed by the diameter of the incident focused probe beam, is around one nanometre. Note that samples must be thin, i.e. <50–100 nm for such microanalysis.

Smith and McCartney [194] point out that a typical ELNES spectrum contains a monotonically decreasing background and several broad superimposed peaks, each of which has an energy that is directly related to a particular inelastic scattering process. Figure 16 shows a typical spectrum from an investigation of Randall's plaque [195], an ectopic calcification which forms at the tip of the kidney papilla [196–198].

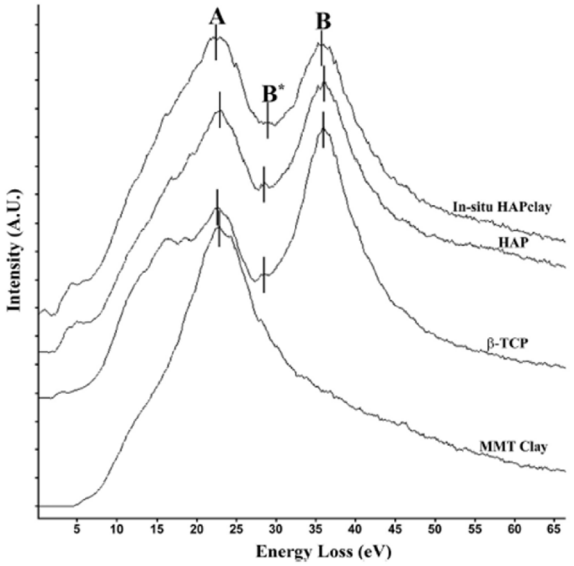

Figure 17. Energy Loss Function spectra of in-situ HAP clay, HAP, β-TCP, and modified clay. Peak A corresponds to the plasmon peak, and peaks B and B* correspond to the calcium $M_{2,3}$ edge. The spectra are separated vertically for clarity and bars denote peak position (after Payne *et al.* [199]).

The contribution of different elements within the sample (Ca, C, P, O, N), or arising from the preparation protocol, (P, U, C, Ca, N, O) are clearly visible.

Payne *et al.* [199] use such an approach to precisely identify the calcium phosphate compound in the biological sample (Figure 17). It is quite clear that a description of the structural characteristics of biominerals at the nanometre scale gives essential information concerning their formation mechanisms [200].

Even if structural information is less direct than from XANES analysis, XPS spectroscopy or electron spectroscopy can be valuable for chemical analysis. Like XANES, this spectroscopy uses photons as probes [201,202]. It measures the kinetic energy of electrons emitted from the very top (1–10 nm) of any solid surface, giving information on the electronic states of the surface region [203]. Because XPS can detect all elements, except hydrogen and helium, by their photoelectron binding energies, it is possible to obtain a precise quantitative map of surface composition. XPS thus plays major role in identification and

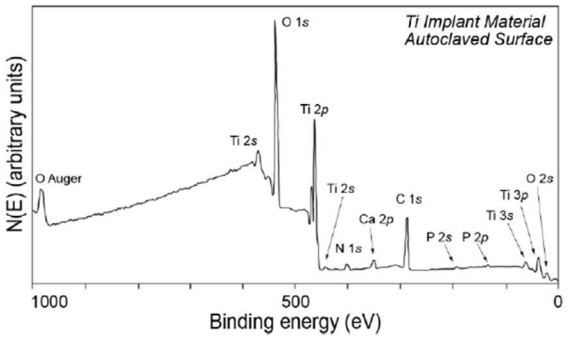

Figure 18. XPS spectrum of a titanium implant surface revealing its elementary composition at the surface (after Lach *et al.* [209].

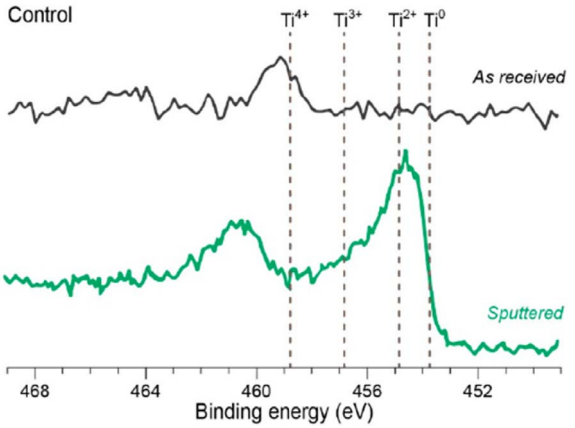

Figure 19. XPS spectrum of a titanium implant surface. Information on the electronic state of Ti is available (after Lach *et al.* [209]).

quantification of surface contaminants of biomaterials, which has long been recognized as a significant factor in predicting biocompatibility and rate of healing of implantable devices [204–206]. Also, significant recent developments in XPS allow hydrated samples to be studied, which is often essential to avoid cellular collapse [207].

Figure 18 shows a typical XPS spectrum in which it is possible to identify all the elements at the very top surface of the sample (see [208] for detection limits). Figure 19 shows that each oxidation state of Ti corresponds to a specific energy in the XPS spectra [209] which enables their discrimination (Bharti *et al.* [210]).

Finally, we would like to underline the complementarity between μFTIR [36–42] spectroscopy, considered the gold standard for chemical analysis of kidney stones, and XANES spectroscopy. Note that μFTIR spectroscopy informs on the major organic and mineral components of biological concretions, but not on trace elements. As we have described, XANES requires synchrotron facilities, so it is often convenient to characterize trace elements in the host laboratory by for example XRF (Figure 20).

In fact, for completely unknown samples, X-ray fluorescence may be the first choice analytical technique, followed by vibrational spectroscopy such μFTIR or Raman to determine more detailed chemistry, while XANES can be applied to describe the electronic state as well as the first coordination sphere of trace elements selected by their edge absorption. As emphasized by Bohic *et al.* [211], such combinations of synchrotron-based X-ray and FTIR microspectroscopies are ideal for assessing the nature and role of trace elements in biology and medicine.

6. Conclusion

While XRF spectroscopy identifies only the elements present in a biological sample, the various publications we have selected in this contribution show clearly that XANES spectroscopy offers substantial information about the local structure of biological samples, including those without long range order such as single molecules, nanometre scale particles, or amorphous compounds. XANES spectroscopy thus offers opportunities to localise and assess the metabolism of metallodrugs such as Pt based anticancer molecules, to localise nanometer scale materials such as gold nanoparticles confined in mesoporous silica (proposed to improve prognosis), and to more precisely describe the structural characteristics of pathological calcifications.

Its subcellular spatial resolution as well as its capacity to operate at room temperature and pressure constitute major advantages for biomedical research meaning, for instance, that paraffin embedded biopsies can be interrogated without any further sample manipulation. In many investigations, such a capability to directly investigate biological samples in a near native state constitutes a major advantage relative to other techniques such as EELS or XPS which require very thin samples and therefore preparation procedures which may disrupt the physicochemical

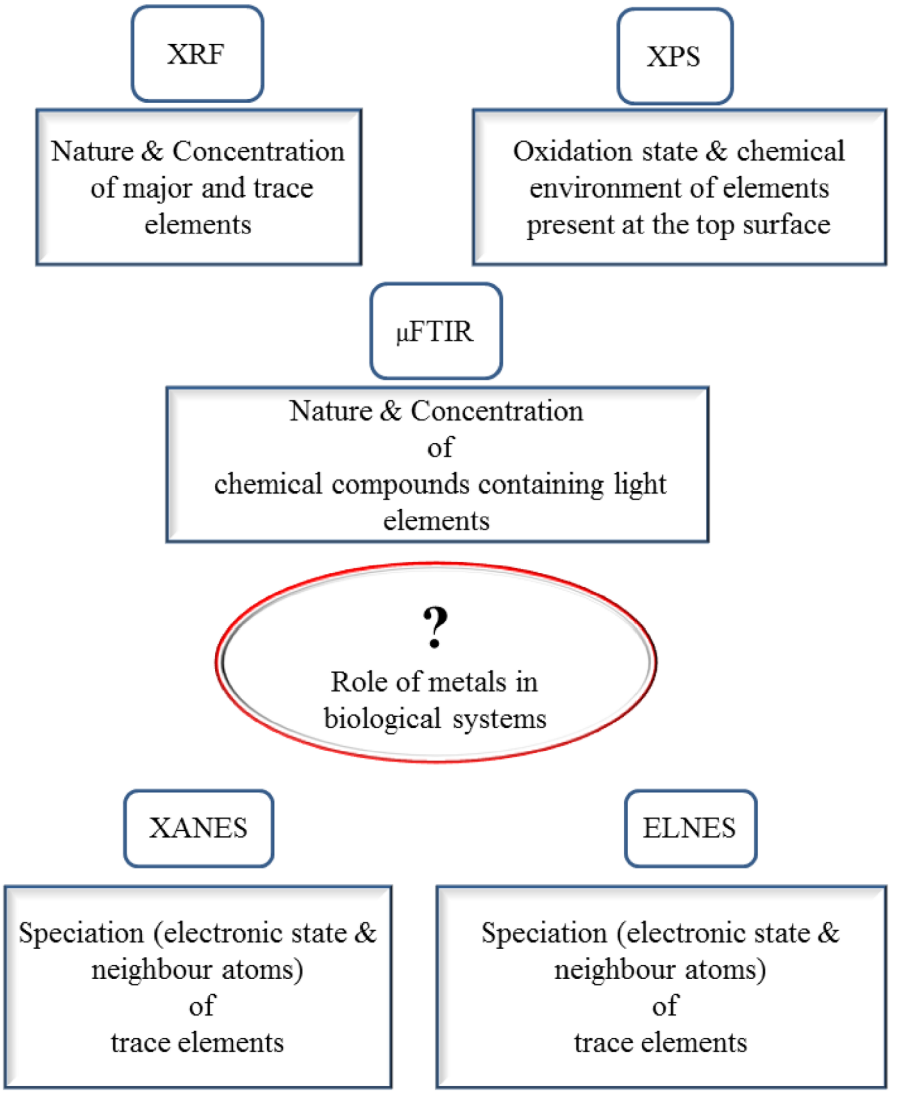

Figure 20. µSpectroscopy approaches to assess the role of metal trace elements in a biological sample.

and structural integrity of any pathological calcifications within a tissue.

Acknowledgments

This work was supported by the Physics and Chemistry Institutes of CNRS and by contracts ANR-09-BLAN-0120-02, ANR-12-BS08-0022, ANR13JSV10010-01, convergence UPMC CVG1205, Labex Matisse, Labex Michem and CORDDIM-2013-COD130042. This work was partially funded via the CNRS-CEA "METSA" French network (FR CNRS 3507) and the EU grant No. 312483-ESTEEM2. The authors are grateful to the SOLEIL Synchrotron Facility for beam time allocation and would like to very much thank the support group of SOLEIL for their help during experiment.

References

[1] D. E. Sayers, E. A. Stern, F. W. Lytle, *Phys. Rev. Lett.*, 1971, **27**, 1204-1207.
[2] F. W. Lytle, D. A. Sayers, E. A. Stern, *Phys. Rev. B*, 1975, **11**, 4825-4835.

[3] E. A. Stern, D. E. Sayers, F. W. Lytle, *Phys. Rev. B*, 1975, **11**, 4836-4846.
[4] R. W. James, *The Optical Principles of the Diffraction of X-Rays*, Bell, London, 1948.
[5] A. Guinier, *Théorie et technique de la radiocristallographie*, Dunod, Paris, 1964.
[6] B. E. Warren, *X-Ray Diffraction*, Dover, New York, 1990.
[7] D. Bazin, L. Guczi, J. Lynch, *Appl. Catal. A*, 2002, **226**, 87-113.
[8] H. Stragier, J. O. Cross, J. J. Rehr, L. B. Sorensen, C. E. Bouldin, J. C. Woicik, *Phys. Rev. Lett.*, 1992, **69**, 3064-3067.
[9] M. R. Gherase, D. E. B. Fleming, *Crystals*, 2020, **12**, article no. 10.
[10] J. G. Parsons, M. V. Aldrich, J. L. Gardea-Torresdey, *Appl. Spectrosc. Rev.*, 2002, **37**, 187-222.
[11] R. A. Metzler, R. M. Olabisi, M. Abrecht, D. Ariosa, C. J. Johnson, B. Gilbert, B. H. Frazer, S. N. Coppersmith, P. U. P. A. Gilbert, *AIP Conf. Proc.*, 2007, **882**, 51-55.
[12] O. V. Konovalov, N. N. Novikova, M. V. Kovalchuk, G. E. Yalovega, A. F. Topunov, O. V. Kosmachevskaya, E. A. Yurieva, A. V. Rogachev, A. L. Trigub, M. A. Kremennaya, V. I. Borshchevskiy, D. D. Vakhrameev, S. N. Yakunin, *Materials*, 2020, **13**, article no. 4635.
[13] D. Bazin, M. Daudon, P. Chevallier, S. Rouzière, E. Elkaim, D. Thiaudiere, B. Fayard, E. Foy, P. A. Albouy, G. André, G. Matzen, E. Véron, *Ann. Biol. Clin. (Paris)*, 2006, **64**, 125-139.
[14] S. Rouzière, D. Bazin, M. Daudon, *C. R. Chim.*, 2016, **19**, 1404-1415.
[15] S. Reguer, C. Mocuta, D. Thiaudière, M. Daudon, D. Bazin, *C. R. Chim.*, 2016, **19**, 1424-1431.
[16] G. Sagnac, "Rayons secondaires dérivés des rayons de Röntgen (seconde partie)", PhD Thesis, Faculté des sciences de Paris, Paris, France, 1900.
[17] S. Bohic, A. Simionovici, A. Snigirev, R. Ortega, G. Deves, D. Heymann, C. G. Schroer, *Appl. Phys. Lett.*, 2001, **78**, 3544-3546.
[18] J. Börjesson, M. Isaksson, S. Mattsson, *Acta Diabetol.*, 2003, **40**, S39-S44.
[19] H. Sun, J. Brocato, M. Costa, *Curr. Environ. Health Rep.*, 2015, **2**, 295-303.
[20] M. D. Hall, H. L. Daly, J. Z. Zhang, M. Zhang, R. A. Alderden, D. Pursche, G. J. Foran, T. W. Hambley, *Metallomics*, 2012, **4**, 568-575.
[21] A. A. Hummer, C. Bartel, V. B. Arion, M. A. Jakupec, W. Meyer-Klaucke, T. Geraki, P. D. Quinn, A. Mijovilovich, B. K. Keppler, A. Rompel, *J. Med. Chem.*, 2012, **55**, 5601-5613.
[22] A. A. Hummer, P. Heffeter, W. Berger, M. Filipits, D. Batchelor, G. E. Büchel, M. A. Jakupec, B. K. Keppler, A. Rompel, *J. Med. Chem.*, 2013, **56**, 1182-1196.
[23] A. Levina, J. B. Aitken, Y. Y. Gwee, Z. J. Lim, M. Liu, A. M. Singharay, P. F. Wong, P. A. Lay, *Chemistry*, 2013, **19**, 3609-3619.
[24] A. Levina, A. I. McLeod, L. E. Kremer, J. B. Aitken, C. J. Glover, B. Johannessen, P. A. Lay, *Metallomics*, 2014, **6**, 1880-1888.
[25] K. M. Shah, P. D. Quinn, A. Gartland, J. M. J. Wilkinson, *Orthop. Res.*, 2015, **33**, 114-121.
[26] F. Porcaro, S. Roudeau, A. Carmona, R. Ortega, *Trends Analyt. Chem.*, 2018, **104**, 22-41.
[27] D. Bazin, D. A. Sayers, J. J. Rehr, *J. Phys. Chem. B*, 1997, **101**, 11040-11050.
[28] D. Bazin, D. A. Sayers, J. J. Rehr, C. Mottet, *J. Phys. Chem. B*, 1997, **101**, 5332-5336.
[29] D. Bazin, J. Rehr, *Catal. Lett.*, 2003, **87**, 85-90.
[30] D. I. Sharapa, D. E. Doronkin, F. Studt, J. D. Grunwaldt, S. Behrens, *Adv. Mater.*, 2019, **31**, article no. 1807381.
[31] R. A. Davidson, D. S. Anderson, L. S. Van Winkle, K. E. Pinkerton, T. Guo, *J. Phys. Chem. A*, 2015, **119**, 281-289.
[32] S. Mourdikoudis, R. M. Pallares, N. T. K. Thanh, *Nanoscale*, 2018, **10**, 12871-12934.
[33] E. Beniash, R. A. Metzler, R. S. K. Lam, P. U. P. A. Gilbert, *J. Struct. Biol.*, 2009, **166**, 133-143.
[34] X. Carpentier, D. Bazin, P. Jungers, S. Reguer, D. Thiaudière, M. Daudon, *J. Synchrotron Radiat.*, 2010, **32**, 374-379.
[35] Y.-Y. Jiang, Z.-Q. Wang, J.-T. Chen, J. Li, Y.-J. Zhu, L.-J. Liu, X.-X. Guo, Y.-F. Hu, S.-S. He, J. Wu, F. Chen, T.-K. Sham, *Phys. Chem. Chem. Phys.*, 2020, **22**, 13108-13117.
[36] P. Franck, P. Nabet, B. Dousset, *Cell Mol. Biol.*, 1998, **44**, 273-275.
[37] P. Dumas, L. Miller, *J. Biol. Phys.*, 2003, **29**, 201-218.
[38] P. Dumas, L. Miller, *Vib. Spectrosc.*, 2003, **32**, 3-21.
[39] R. Gasper, J. Dewelle, R. Kiss, T. Mijatovic, E. Goormaghtig, *Biochim. Biophys. Acta Biomembr.*, 2009, **1788**, 1263-1270.
[40] D. Bazin, M. Daudon, *Ann. Biol. Clin.*, 2015, **73**, 517-534.
[41] M. Daudon, D. Bazin, *C. R. Chim.*, 2016, **19**, 1416-1423.
[42] M. Paraskevaidi, P. L. Martin-Hirsch, F. L. Martin, "ATR-FTIR spectroscopy tools for medical diagnosis and disease investigation", in *Nanotechnology Characterization Tools for Biosensing and Medical Diagnosis* (C. Kumar, ed.), Springer, Berlin, Heidelberg, 2018.
[43] L.-P. Choo-Smith, H. G. M. Edwards, H. P. Endtz, J. M. Kros, F. Heule, H. Barr, J. S. Robinson Jr., H. A. Bruining, G. J. Puppels, *Biopolymers*, 2002, **67**, 1-9.
[44] K. J. I. Ember, M. A. Hoeve, S. L. McAughtrie, M. S. Bergholt, B. J. Dwyer, M. M. Stevens, *NPJ Regen. Med.*, 2017, **2**, article no. 12.
[45] V. Castiglione, P.-Y. Sacré, E. Cavalier, P. Hubert, R. Gadisseur, E. Ziemons, *PLoS One*, 2018, **13**, article no. e0201460.
[46] M. M. Kłosowski, R. J. Friederichs, R. Nichol, N. Antolin, R. Carzaniga, W. Windl, S. M. Best, S. J. Shefelbine, D. W. McComb, A. E. Porter, *Acta Biomater.*, 2015, **20**, 129-139.
[47] K. Nitiputri, Q. M. Ramasse, H. Autefage, C. M. McGilvery, S. Boonrungsiman, N. D. Evans, M. M. Stevens, A. E. Porter, *ACS Nano*, 2016, **10**, 6826-6835.
[48] S. Boonrungsiman, E. Gentleman, R. Carzaniga, N. D. Evans, D. W. McComb, A. E. Porter, M. M. Stevens, *Proc. Natl. Acad. Sci. USA*, 2012, **109**, 14170-14175.
[49] V. Srot, B. Bussmann, U. Salzberger, J. Deuschle, M. Watanabe, B. Pokorny, I. J. Turinek, A. F. Mark, P. A. van Aken, *ACS Nano*, 2017, **11**, 239-248.
[50] V. Srot, U. G. K. Wegst, U. Salzberger, C. T. Koch, K. Hahn, P. Kopold, P. A. van Aken, *Micron*, 2013, **48**, 54-64.
[51] C. Gay, E. Letavernier, M.-C. Verpont, M. Walls, D. Bazin, M. Daudon, N. Nassif, O. Stephan, M. de Fruto, *ACS Nano*, 2020, **14**, 1823-1836.
[52] M. M. Lyra da Cunhaa, S. Trepout, C. Messaoudi, T.-D. Wu, R. Ortega, J.-L. Guerquin-Kern, S. Marco, *Micron*, 2016, **84**, 23-36.

[53] C. R. Natoli, D. K. Misemer, S. Doniach, F. W. Kutzler, *Phys. Rev. A*, 1980, **22**, 1104-1108.
[54] J. J. Rehr, R. C. Albers, *Rev. Mod. Phys.*, 2000, **72**, 621-654.
[55] Y. Joly, *Phys. Rev. B*, 2001, **63**, article no. 125120.
[56] I. Y. Nikiforov, I. V. Bazhin, A. B. Kolpachev, *Phys. B*, 1995, **208–209**, 113-114.
[57] J. J. Rehr, A. L. Ankudinov, *Coord. Chem. Rev.*, 2005, **249**, 131-140.
[58] G. S. Henderson, F. M. F. de Groot, B. J. A. Moulton, *Rev. Mineral. Geochem.*, 2014, **78**, 75-138.
[59] A. A. Guda, S. A. Guda, K. A. Lomachenko, M. A. Soldatov, I. A. Pankin, A. V. Soldatov, L. Braglia, A. L. Bugaev, A. Martini, M. Signorile, E. Groppo, A. Piovano, E. Borfecchia, C. Lamberti, *Cat. Today*, 2019, **336**, 3-21.
[60] R. D. Deslattes, E. G. J. Kessler, P. Indelicato, L. de Billy, E. Lindroth, J. Anton, J. S. Coursey, D. J. Schwab, J. Chang, R. Sukumar, K. Olsen, R. A. Dragoset, "X-ray transition energies by element(s), transition(s), and energy range", 2005, X-Ray Transition Energies Database, NIST Standard Reference Database 128, https://physics.nist.gov/PhysRefData/XrayTrans/Html/search.html.
[61] Y. Cauchois, *J. Phys. Radium*, 1932, **3**, 320-336.
[62] Y. Cauchois, N. F. Mott, *Philos. Mag.*, 1949, **40**, 1260-1270.
[63] R. Revel, D. Bazin, P. Parent, C. Laffon, *Catal. Lett.*, 2001, **74**, 189-192.
[64] A. W. Gillespie, F. L. Walley, R. E. Farrell, P. Leinweber, A. Schlichting, K.-U. Eckhardt, T. Z. Regier, R. I. R. Blyth, *Soil Sci. Soc. Am. J.*, 2009, **73**, 2002-2012.
[65] J. Lynch, G. Everlien, C. Leblond, D. Bazin, *J. Synchrotron Radiat.*, 1999, **6**, 661-663.
[66] I. J. Pickering, R. C. Prince, T. Divers, G. N. George, *FEBS Lett*, 1998, **441**, 11-14.
[67] A. Prange, R. Chauvistré, H. Modrow, J. Hormes, H. G. Trüper, C. Dahl, *Microbiology (Reading)*, 2002, **148**, 267-276.
[68] R. Chen, G. Chen, *J. Int. Med. Res.*, 2017, **46**, 70-78.
[69] A. Carmona, S. Roudeau, L. Perrin, C. Carcenac, D. Vantelon, M. Savasta, R. Ortega, *Front. Neurosci.*, 2019, **13**, article no. 1014.
[70] E. Esteve, D. Bazin, Ch.. Jouanneau, S. Rouzière, A. Bataille, A. Kellum, K. Provost, Ch.. Mocuta, S. Reguer, D. Thiaudiere, K. Jorissen, J. J. Rehr, A. Hertig, E. Rondeau, E. Letavernier, M. Daudon, P. Ronco, *C. R. Chim.*, 2016, **19**, 1580-1585.
[71] E. Esteve, D. Bazin, Ch.. Jouanneau, S. Rouzière, A. Bataille, A. Kellum, K. Provost, Ch.. Mocuta, S. Reguer, D. Thiaudiere, K. Jorissen, J. J. Rehr, A. Hertig, E. Rondeau, E. Letavernier, M. Daudon, P. Ronco, *C. R. Chim.*, 2016, **19**, 1586-1589.
[72] A. A. Hummer, A. Rompel, *Metallomics*, 2013, **5**, 597-614.
[73] C. K. J. Chen, P. Kappen, T. W. Hambley, *Metallomics*, 2019, **11**, 686-695.
[74] C. K. J. Chen, P. Kappen, D. Gibson, T. W. Hambley, *Dalton Trans.*, 2020, **49**, 7722-7736.
[75] R. A. Van Nordsthand, *Adv. Catal.*, 1960, **12**, 149-187.
[76] M. Banu, "Mise en forme d'apatites nanocristallines : céramiques et ciment", PhD Thesis, Insitut National polytechnique de Toulouse, Toulouse, France, 2005.
[77] S. Mondal, A. Mondal, N. Mandal, B. Mondal, S. S. Mukhopadhyay, A. Dey, S. Singh, *Bioprocess Biosyst. Eng.*, 2014, **37**, 1233-1240.
[78] J. O. Akindoyo, S. Ghazali, M. D. H. Beg, N. Jeyaratnam, *Chem. Eng. Technol.*, 201, **42**, 1805-1815.
[79] Q. Li, D. W. Chou, T. P. Price, J. P. Sundberg, J. Uitto, *Lab. Invest.*, 2014, **94**, 623-632.
[80] J. C. Elliott, *Structure and Chemistry of the Apatites and Other Calcium Orthophosphates*, Elsevier, London, 1994.
[81] M. Vallet-Regí, J. González-Calbet, *Prog. Solid State Chem.*, 2004, **32**, 1-31.
[82] D. Bazin, C. Chappard, C. Combes, X. Carpentier, S. Rouzière, G. André, G. Matzen, M. Allix, D. Thiaudière, S. Reguer, P. Jungers, M. Daudon, *Osteoporos. Int.*, 2009, **20**, 1065-1075.
[83] C. Rey, C. Combes, C. Drouet, S. Cazalbou, D. Grossin, F. Brouillet, S. Sarda, *Prog. Cryst. Growth Charact. Mater.*, 2014, **60**, 63-73.
[84] C. Combes, S. Cazelbou, C. Rey, *Minerals*, 2016, **6**, article no. 34.
[85] M. Daudon, C. A. Bader, P. Jungers, *Scanning Microsc.*, 1993, **7**, 1081-1104.
[86] M. Daudon, *Arch. Pediatr.*, 2000, **7**, 855-865.
[87] M. Daudon, H. Bouzidi, D. Bazin, *Urol. Res.*, 2010, **38**, 459-467.
[88] M. Daudon, A. Dessombz, V. Frochot, E. Letavernier, J.-P. Haymann, P. Jungers, D. Bazin, *C. R. Chim.*, 2016, **19**, 1470-1491.
[89] M. P. Morgan, M. M. Cooke, G. M. McCarthy, *J. Mammary Gland Biol. Neoplasia*, 2005, **10**, 181-187.
[90] A. Ben Lakhdar, M. Daudon, M. C. Matthieu, A. Kellum, C. Balleyguier, D. Bazin, *C. R. Chim.*, 2016, **19**, 1610-1624.
[91] A. Dessombz, P. Méria, D. Bazin, M. Daudon, *PLoS One*, 2012, **7**, article no. e51691.
[92] A. Dessombz, P. Méria, D. Bazin, E. Foy, S. Rouzière, R. Weil, M. Daudon, *Prog. Urol.*, 2011, **21**, 940-945.
[93] M. Mathonnet, A. Dessombz, D. Bazin, R. Weil, F. Triponez, M. Pusztaszeri, M. Daudon, *C. R. Chim.*, 2016, **19**, 1672-1678.
[94] J. Guerlain, S. Perie, M. Lefevre, J. Perez, S. Vandermeersch, C. Jouanneau, L. Huguet, V. Frochot, E. Letavernier, R. Weil, S. Rouziere, D. Bazin, M. Daudon, J. P. Haymann, *PLoS One*, 2019, **14**, article no. e0224138.
[95] R. Z. LeGeros, "Monographs in oral science", in *Calcium Phosphates in Oral Biology and Medicine* (H. M. Myers, ed.), vol. 15, Karger, Basel, 1991.
[96] M. Vallet-Regí, D. Arcos Navarrete, "Biological apatites in bone and teeth", in *Nanoceramics in Clinical Use: From Materials to Applications*, Royal Society of Chemistry, London, 2nd ed., 2015, 1-29.
[97] G. Cho, Y. Wu, J. L. Ackerman, *Science*, 2003, **300**, 1123-1127.
[98] D. Hesterberg, W. Zhou, K. J. Hutchison, S. Beauchemin, D. E. Sayers, *J. Synchrotron Radiat.*, 1999, **6**, 636-638.
[99] K. Asokan, J. C. Jan, J. W. Chiou, W. F. Pong, P. K. Tseng, I. N. Lin, *J. Synchrotron Radiat.*, 2001, **8**, 839-841.
[100] D. Eichert, M. Salomé, M. Banu, J. Susini, C. Rey, *Spectrochim. Acta B*, 2005, **60**, 850-858.
[101] B.-Q. Lu, N. A. Garcia, D. M. Chevrier, P. Zhang, P. Raiteri, J. D. Gale, D. Gebauer, *Cryst. Growth Des.*, 2019, **19**, 3030-3038.
[102] E. D. Eanes, "Amorphous calcium phosphate: thermodynamic and kinetic considerations", in *Calcium Phosphates in Biological and Industrial Systems* (Z. Amjad, ed.), Kluwer Academic, Dordrecht, 1998, 21-39.

[103] S. Cazalbou, C. Combes, D. Eichert, C. Rey, M. J. Glimcher, *J. Bone Miner. Metab.*, 2004, **22**, 310-317.
[104] C. Rey, C. Combes, C. Drouet, H. Sfihi, A. Barroug, *Mater. Sci. Eng. C*, 2007, **27**, 198-205.
[105] C. Rey, C. Combes, C. Drouet, A. Lebugle, H. Sfihi, A. Barroug, *Materwiss Werksttech.*, 2007, **38**, 996-1002.
[106] C. Drouet, F. Bosc, M. Banu, C. Largeot, C. Combes, G. Dechambre, C. Estournès, G. Raimbeaux, C. Rey, *Powder Technol.*, 2009, **190**, 118-122.
[107] B. Hesse, M. Salome, H. Castillo-Michel, M. Cotte, B. Fayard, C. J. Sahle, W. De Nolf, J. Hradilova, A. Masic, B. Kanngießer, M. Bohner, P. Varga, K. Raum, S. Schrof, *Anal. Chem.*, 2016, **88**, 3826-3835.
[108] B. Ravel, E. A. Stern, *Phys. B*, 1995, **208–209**, 316-318.
[109] J. Cosmidis, K. Benzerara, N. Nassif, T. Tyliszczak, F. Bourdelle, *Acta Biomater.*, 2015, **12**, 260-269.
[110] S. J. Naftel, T. K. Sham, Y. M. Yiu, B. W. Yates, *J. Synchrotron Radiat.*, 2001, **8**, 255-257.
[111] M. E. Fleet, X. Liu, *Am. Mineral.*, 2009, **94**, 1235-1241.
[112] R. A. Metzler, P. Rez, *J. Phys. Chem. B*, 2014, **118**, 6758-6766.
[113] I. M. Zougrou, M. Katsikini, M. Brzhezinskaya, F. Pinakidou, L. Papadopoulou, E. Tsoukala, E. C. Paloura, *Sci. Nat.*, 2016, **103**, article no. 60.
[114] E. D. Ingall, J. A. Brandes, J. M. Diaz, M. D. de Jonge, D. Paterson, I. McNulty, W. C. Elliott, P. Northrup, *J. Synchrotron Radiat.*, 2011, **18**, 189-197.
[115] J. Kruse, P. Leinweber, K.-U. Eckhardt, F. Godlinski, Y. Hu, L. Zuin, *J. Synchrotron Radiat.*, 2009, **16**, 247-259.
[116] J. Kruse, M. Abraham, W. Amelung, C. Baum, R. Bol, O. Kühn, H. Lewandowski, J. Niederberger, Y. Oelmann, C. Rüger, J. Santner, M. Siebers, N. Siebers, M. Spohn, J. Vestergren, A. Vogts, P. Leinweber, *J. Plant. Nutr. Soil Sci.*, 1999, **178**, 43-88.
[117] J. A. van Bokhoven, C. Lamberti, *X-Ray Absorption and X-ray Emission Spectroscopy: Theory and Applications*, Wiley, London, 2016.
[118] J. J. Rehr, J. J. Kas, M. P. Prange, A. P. Sorini, Y. Takimoto, F. Vila, *C. R. Phys.*, 2009, **10**, 548-559.
[119] F. M. F. de Groot, *J. Electron Spectrosc. Relat. Phenom.*, 1994, **61**, 529-622.
[120] F. M. F. De Groot, M. Abbate, M. van Elp, G. A. Sawatzky, Y. J. Ma, C. T. Chen, F. Sette, *J. Phys.: Condens. Matter*, 1993, **5**, 2277-2288.
[121] D. Bazin, I. Kovacs, L. Guczi, P. Parent, C. Laffon, F. De Groot, O. Ducreux, J. Lynch, *J. Catal.*, 2000, **189**, 456-462.
[122] H. Yoshida, S. Nonoyama, Y. Yazawa, T. Hattori, *Phys. Scr. T*, 2005, **115**, 813-815.
[123] D. Bazin, J. J. Rehr, *J. Phys. Chem. B*, 2003, **107**, 12398-12402.
[124] D. Bazin, L. Guczi, *Appl. Catal. A*, 2001, **213**, 147-162.
[125] R. Revel, D. Bazin, P. Parent, C. Laffon, *Catal. Lett.*, 2001, **74**, 189-192.
[126] D. Bazin, M. Daudon, C. Chappard, J. J. Rehr, D. Thiaudière, S. Reguer, *J. Synchrotron Radiat.*, 2011, **18**, 912-918.
[127] D. Bazin, A. Dessombz, C. Nguyen, H. K. Ea, F. Lioté, J. Rehr, C. Chappard, S. Rouzière, D. Thiaudière, S. Reguer, M. Daudon, *J. Synchrotron Radiat.*, 2014, **21**, 136-142.
[128] D. Bazin, X. Carpentier, I. Brocheriou, P. Dorfmuller, S. Aubert, C. Chappard, D. Thiaudière, S. Reguer, G. Waychunas, P. Jungers, M. Daudon, *Biochimie*, 2009, **91**, 1294-1300.
[129] D. Bazin, J.-P. Haymann, E. Letavernier, J. Rode, M. Daudon, *Presse Méd.*, 2014, **43**, 135-148.
[130] D. Bazin, M. Daudon, *J. Spectr. Imaging*, 2019, **8**, article no. a16.
[131] D. Bazin, E. Letavernier, J.-P. Haymann, P. Méria, M. Daudon, *Prog. Urol.*, 2016, **26**, 608-618.
[132] A. Bootchanont, W. Sailuam, S. Sutikulsombat, L. Temprom, N. Chanlek, P. Kidkhunthod, P. Suwanna, R. Yimnirun, *Ceram. Int.*, 2017, **43**, 11023-11027.
[133] A. Procopio, E. Malucelli, A. Pacureanu, C. Cappadone, G. Farruggia, A. Sargenti, S. Castiglioni, D. Altamura, A. Sorrentino, C. Giannini, E. Pereiro, P. Cloetens, J. A. M. Maier, S. Iotti, *ACS Cent. Sci.*, 2019, **5**, 1449-1460.
[134] S. Rout, N. Khandelwal, A. K. Poswal, V. Pulhani, A. V. Kumar, *Environ. Sci. Nano*, 2021, **8**, 1256-1268.
[135] A. M. Beale, A. M. J. van der Eerden, S. D. M. Jacques, O. Leynaud, M. G. O'Brien, F. Meneau, S. Nikitenko, W. Bras, B. M. Weckhuysen, *J. Am. Chem. Soc.*, 2006, **128**, 12386-12387.
[136] M. Sikora, A. Juhin, T.-Ch.. Weng, Ph. Sainctavit, C. Detlefs, F. de Groot, P. Glatzel, *Phys. Rev. Lett.*, 2010, **105**, article no. 037202.
[137] C. La Fontaine, S. Belin, L. Barthe, O. Roudenko, V. Briois, *Synchrotron Radiat. News*, 2020, **33**, 20-25.
[138] Y. Mijiti, K. Chen, J. E. F. S. Rodrigues, Z. Hu, L. Nataf, A. Trapananti, A. Di Cicco, F. Baudelet, *Phys. Rev. B*, 2021, **103**, article no. 024105.
[139] D. Bazin, R. Papoular, E. Elkaim, R. Weil, D. Thiaudière, C. Pisapia, B. Ménez, N. S. Hwang, F. Tielens, M. Livrozet, E. Bouderlique, J. P. Haymann, E. Letavernier, L. Hennet, V. Frochot, M. Daudon, *C. R. Chim.*, 2022, **25**, no. S1, 343-354.
[140] C. Nguyen, H. K. Ea, D. Thiaudiere, S. Reguer, D. Hannouche, M. Daudon, F. Lioté, D. Bazin, *J. Synchrotron Radiat.*, 2011, **18**, 475-480.
[141] A. Dessombz, C. Nguyen, H.-K. Ea, S. Rouzière, E. Foy, D. Hannouche, S. Réguer, F.-E. Picca, D. Thiaudière, F. Lioté, M. Daudon, D. Bazin, *J. Trace Elem. Med. Biol.*, 2013, **27**, 326-333.
[142] A.-M. Flank, G. Cauchon, P. Lagarde, S. Bac, M. Janousch, R. Wetter, J.-M. Dubuisson, M. Idir, F. Langlois, T. Moreno, D. Vantelon, *Nucl. Instrum. Meth. B*, 2006, **246**, 269-274.
[143] D. Vantelon, N. Trcera, D. Roy, T. Moreno, D. Mailly, S. Guilet, E. Metchalkov, F. Delmotte, B. Lassalle, P. Lagarde, A.-M. Flank, *J. Synchrotron Radiat.*, 2016, **23**, 635-640.
[144] D. Bazin, M. Daudon, C. Combes, C. Rey, *Chem. Rev.*, 2012, **112**, 5092-5120.
[145] D. Bazin, M. Daudon, *J. Phys. D*, 2012, **45**, article no. 383001.
[146] M. Daudon, D. Bazin, *J. Phys.: Conf. Ser.*, 2013, **425**, article no. 022006.
[147] X. Guo, Z. Wang, J. Wu, Y.-M. Yiu, Y. Hu, Y.-J. Zhu, T.-K. Sham, *J. Phys. Chem. B*, 2015, **119**, 10052-10059.
[148] X. Guo, J. Wu, Y.-M. Yiu, Y. Hu, Y.-J. Zhu, T.-K. Sham, *Phys. Chem. Chem. Phys.*, 2013, **15**, 15033-15040.
[149] N. Abbaspour, R. Hurrell, R. Kelishadi, *J. Res. Med. Sci.*, 2014, **19**, 164-174.
[150] A. Al-Ebraheem, J. Goettlicher, K. Geraki, S. Ralph, M. J. Farquharson, *X-Ray Spectrom.*, 2010, **39**, 332-337.
[151] W. M. Kwiatek, A. L. Hanson, C. Paluszkiewicz, M. Gałka, M. Gajda, T. Cichocki, *J. Alloys Compd.*, 2004, **362**, 83-87.

[152] K. Dziedzic-Kocurek, A. Banaś, W. M. Kwiatek, J. Stanek, *X-Ray Spectrom.*, 2008, **37**, 219-225.
[153] J. F. Collingwood, M. R. Davidson, *Front. Pharmacol.*, 2014, **5**, article no. 191.
[154] G. Tiwari, R. Tiwari, B. Sriwastawa, L. Bhati, S. Pandey, P. Pandey, S. K. Bannerjee, *Int. J. Pharm. Investig.*, 2012, **2**, 2-11.
[155] P. Trucillo, *Processes*, 2021, **9**, article no. 470.
[156] Y. F. Zhu, J. L. Shi, *Microporous Mesoporous Mater.*, 2007, **103**, 243-247.
[157] Y. F. Zhu, T. Ikoma, N. Hanagata, S. Kaskel, *Small*, 2010, **6**, 471-478.
[158] G. L. Bovenkamp, U. Zanzen, K. S. Krishna, J. Hormes, A. Prange, *Appl. Environ. Microbiol.*, 2013, **79**, 6385-6390.
[159] E. Wong, C. M. Giandomenico, *Chem. Rev.*, 1999, **99**, 2451-2466.
[160] L. Kelland, *Nat. Rev. Cancer*, 2007, **7**, 573-584.
[161] R. P. Miller, R. K. Tadagavadi, G. Ramesh, W. B. Reeves, *Toxins (Basel)*, 2010, **2**, 2490-2518.
[162] X. Wang, Z. Guo, *Anti-Cancer Agents Med. Chem.*, 2007, **7**, 19-34.
[163] A. Bensaddik, A. Caballero, D. Bazin, H. Dexpert, B. Didillon, J. Lynch, *Appl. Catal. A*, 1997, **162**, 171-180.
[164] F. W. Lytle, *J. Catal.*, 1976, **43**, 376-379.
[165] F. W. Lytle, P. S. P. Wei, R. B. Greegor, G. H. Via, J. H. J. Sinfelt, *Chem. Phys.*, 1979, **70**, 4849-4855.
[166] D. Bazin, J. Lynch, M. Ramos-Fernandez, *Oil Gas Sci. Technol. – Rev. IFP*, 2003, **58**, 667-683.
[167] R. Mom, L. Frevel, J.-J. Velasco-Vélez, M. Plodinec, A. Knop-Gericke, R. Schlögl, *J. Am. Chem. Soc.*, 2019, **141**, 6537-6544.
[168] M. D. Hall, G. J. Foran, M. Zhang, P. J. Beale, T. W. Hambley, *J. Am. Chem. Soc.*, 2003, **125**, 7524-7525.
[169] K. Provost, D. Bouvet-Muller, S. Crauste-Manciet, J. Moscovici, L. Olivi, G. Vlaic, A. Michalowicz, *Biochimie*, 2009, **91**, 1301-1306.
[170] K. Provost, D. Bouvet-Muller, S. Crauste-Manciet, L. Olivi, G. Vlaic, A. Michalowicz, *J. Phys. Conf. Ser.*, 2009, **190**, article no. 012206.
[171] A. L. M. Batista de Carvalho, A. P. Mamede, A. Dopplapudi, V. Garcia Sakai, J. Doherty, M. Frogley, G. Cinque, P. Gardner, D. Gianolioc, L. A. E. Batista de Carvalho, M. P. M. Marques, *Phys. Chem. Chem. Phys.*, 2019, **21**, 4162-4175.
[172] A. E. Laumann, A. Derick, *J. Am. Acad. Dermatol.*, 2006, **55**, 413-421.
[173] P. Laux, T. Tralau, J. Tentschert, A. Blume, S. A. Dahouk, W. Bäumler, E. Bernstein, B. Bocca, A. Alimonti, H. Colebrook, C. de Cuyper, L. Dähne, U. Hauri, P. C. Howard, P. Janssen, L. Katz, B. Klitzman, N. Kluger, L. Krutak, T. Platzek, V. Scott-Lang, J. Serup, W. Teubner, I. Schreiver, E. Wilkniß, A. Luch, *Lancet*, 2016, **387**, 395-402.
[174] G. Riffo, C. Ramírez-Lama, L. Bennun, *J. Cosmet. Dermatol. Sci. Appl.*, 2020, **10**, 33-53.
[175] B. Battistini, F. Petrucci, I. De Angelis, C. M. Failla, B. Bocca, *Chemosphere*, 2020, **245**, article no. 125667.
[176] R. J. Vandebriel, W. H. De Jong, *Nanotechnol. Sci. Appl.*, 2012, **5**, 61-71.
[177] H. C. Freake, K. Sankavaram, *Encyclopedia of Human Nutrition*, 3rd ed., Elsevier, Amsterdam, Netherlands, 2013, 437-443 pages.
[178] R. Zhang, P.-G. Yin, N. Wang, L. Guo, *Solid State Sci.*, 2009, **11**, 865-869.
[179] P. J. Perez Espitia, N. de Fátima Ferreira Soares, J. S. dos Reis Coimbra, N. J. de Andrade, R. S. Cruz, E. A. Alves Medeiros, *Food Bioprocess Technol.*, 2012, **5**, 1447-1464.
[180] S. B. Kulkarni, U. M. Patil, R. R. Salunkhe, S. S. Joshi, C. D. Lokhande, *J. Alloys Compd.*, 2011, **509**, 3486-3492.
[181] H. Colboc, D. Bazin, P. Moguelet, S. Reguer, R. Amode, C. Jouanneau, I. Lucas, L. Deschamps, V. Descamps, N. Kluger, *J. Eur. Acad. Dermatol. Venereol.*, 2020, **34**, e313-e315.
[182] P. Piccinini, S. Pakalin, L. Contor, I. Bianchi, "Safety of tattoos and permanent make-up. Adverse health effects and experience with the Council of Europe Resolution (2008)1", Tech. report, European Commission, 2016, https://publications.jrc.ec.europa.eu/repository/handle/JRC99882, published by the Publications Office of the teh European Union;.
[183] R. F. Egerton, *Electron Energy-loss Spectroscopy in the Electron Microscope*, Springer, Boston, USA, 2011.
[184] F. Hofer, F. P. Schmidt, W. Grogger, G. Kothleitner, *IOP Conf Ser.: Mater. Sci. Eng.*, 2016, **109**, article no. 012007.
[185] J. Stöhr, *NEXAFS Spectroscopy*, Springer, Berlin, Heidelberg, 1992.
[186] T. Mizoguchi, S. Kiyohara, *Microscopy*, 2020, **69**, 92-109.
[187] T. Mizoguchi, I. Tanaka, S. P. Gao, C. J. Pickard, *J. Phys.: Condens. Matter*, 2009, **21**, article no. 104204.
[188] M. Jaouen, G. Hug, V. Gonnet, G. Demazeau, G. Tourillon, *Microsc. Microanal. Microstruct.*, 1995, **6**, 127-139.
[189] D. Bolser, T. Zega, *Microsc. Microanal.*, 2014, **20**, 1706-1707.
[190] I. Y. Nikiforov, O. V. Kolpacheva, I. V. Bazhin, A. B. Kolpachev, *J. Electron Spectrosc. Relat. Phenom.*, 1994, **68**, 215-222.
[191] H. Ikeno, T. Mizoguchi, Y. Koyama, Y. Kumagai, I. Tanaka, *Ultramicroscopy*, 2006, **106**, 970-975.
[192] T. Mizoguchi, K. Tatsumi, I. Tanaka, *Ultramicroscopy*, 2006, **106**, 1120-1128.
[193] E. Stavitski, F. M. F. de Groot, *Micron*, 2010, **41**, 687-694.
[194] D. J. Smith, M. R. McCartney, *Encyclopedia of Analytical Science*, 2nd ed., Elsevier, Amsterdam, Netherlands, 2005, 84-91 pages.
[195] A. Randall, *Ann. Surg.*, 1937, **105**, 1009-1027.
[196] M. Daudon, O. Traxer, P. Jungers, D. Bazin, *AIP Conf. Proc.*, 2007, **900**, 26-34.
[197] M. Daudon, O. Traxer, J. C. Williams, D. Bazin, "Randall's Plaque", in *Urinary Tract Stone Disease* (N. P. Rao, G. M. Preminger, J. P. Kavangh, eds.), Springer, Berlin, 2010, 103-112.
[198] E. Letavernier, D. Bazin, M. Daudon, *C. R. Chim.*, 2016, **19**, 1456-1460.
[199] S. A. Payne, D. R. Katti, K. S. Katti, *Micron*, 2016, **90**, 78-86.
[200] D. Bazin, E. Letavernier, J. P. Haymann, V. Frochot, M. Daudon, *Ann. Biol. Clin.*, 2020, **78**, 349-362.
[201] C. S. Fadley, *J. Electron Spectrosc. Relat. Phenom.*, 2010, **178–179**, 2-32.
[202] P. S. Bagus, E. S. Ilton, C. J. Nelin, *Surf. Sci. Rep.*, 2013, **68**, 273-304.
[203] C. R. Brundle, B. V. Crist, *J. Vac. Sci. Technol. A*, 2020, **38**, article no. 041001.

[204] R. W. Paynter, M. W. King, R. G. Guidoin, T. Rao, *Int. J. Artif. Organs*, 1989, **12**, 189-194.
[205] J. Mouhyi, L. Sennerby, J. J. Pireaux, N. Dourov, S. Nammour, J. Van Reck, *Clin. Oral Implants Res.*, 1998, **9**, 185-194.
[206] B.-S. Kang, Y.-T. Sul, S.-J. Oh, H.-J. Lee, T. Albrektsson, *Acta Biomater.*, 2009, **5**, 2222-2229.
[207] M. Kjærvik, M. Ramstedt, K. Schwibbert, M. Dietrich, W. E. S. Unger, *Front. Chem.*, 2021, **9**, article no. 666161.
[208] A. G. Shard, *Surf. Interface Anal.*, 2014, **46**, 175-185.
[209] S. Lach, P. Jurczak, N. Karska, A. Kubi, A. Szymanska, S. Rodziewicz-Motowidło, *Molecules*, 2020, **25**, article no. 579.
[210] B. Bharti, S. Kumar, H.-N. Lee, R. Kumar, *Sci. Rep.*, 2016, **6**, article no. 32355.
[211] S. Bohic, M. Cotte, M. Salomé, B. Fayard, M. Kuehbacher, P. Cloetens, G. Martinez-Criado, R. Tucoulou, J. Susini, *J. Struct. Biol.*, 2012, **177**, 248-258.

Comptes Rendus
Chimie
2022, Vol. 25, Special Issue S1, p. 209-218
https://doi.org/10.5802/crchim.78

Microcrystalline pathologies: Clinical issues and nanochemistry / *Pathologies microcristallines : questions cliniques et nanochimie*

Opportunities given by density functional theory in pathological calcifications

Apports de la théorie de la fonctionnelle de la densité (DFT) dans les calcifications pathologiques

Frederik Tielens[*,a], **Jelle Vekeman**[b], **Dominique Bazin**[c] **and Michel Daudon**[d,e]

[a] General Chemistry (ALGC) – Materials Modelling Group, Vrije Universiteit Brussel (Free University Brussels-VUB), Pleinlaan 2, 1050 Brussel, Belgium

[b] Center for Molecular Modeling (CMM), Ghent University, Technologiepark-Zwijnaarde 46, 9052 Zwijnaarde, Belgium

[c] Université Paris-Saclay, CNRS, Institut de Chimie Physique, 91405 Orsay cedex, France

[d] UMR S1155, INSERM/UPMC, 4 Rue de la Chine, 75970 Paris Cedex 20, France

[e] AP-HP, Hôpital Tenon, Explorations fonctionnelles multidisciplinaires, 4 Rue de la Chine, 75970 Paris Cedex 20, France

E-mails: frederik.tielens@vub.be (F. Tielens), Jelle.Vekeman@vub.be (J. Vekeman), dominique.bazin@universite-paris-saclay.fr (D. Bazin), michel.daudon@aphp.fr (M. Daudon)

Abstract. Density Functional Theory has made the study of biomaterials feasible in the past years leading to better understanding of causes and possible treatments of related pathologies. Although it has been successfully applied in many fields, it has not yet consistently found its way into the field of pathological calcifications. An overview will be given of the studies where this technique has been applied in order to outline the important contributions that it can bring in the field of biomineralization. More specifically, studies on DFT calcifications from calcium oxalates and calcium phosphates, with relevance to bone formation and kidney stones, will be reviewed. Finally, a short outlook on silica mineralization will be presented as well.

Résumé. La théorie de la fonctionnelle de la densité (DFT) a rendu l'étude des biomatériaux faisable ces dernières années, conduisant à une meilleure compréhension des causes et des traitements possibles des pathologies associées. Bien que la DFT ait été appliquée avec succès dans de nombreux domaines, elle ne commence qu'a être appliquée timidement dans le domaine des calcifications pathologiques. Un aperçu sera donné des études où cette technique a été appliquée afin de souligner les contributions importantes qu'elle peut apporter dans le domaine de la biominéralisation. Plus spécifiquement, les études DFT sur les calcifications à partir d'oxalates de calcium et de phosphates

* Corresponding author.

de calcium, en rapport avec la formation osseuse et les calculs rénaux, seront examinées. Enfin, un bref aperçu de la minéralisation de la silice sera également présenté.

Keywords. Oxalates, Phosphates, DFT, Spectroscopy, Microscopy.

Mots-clés. Oxalates, Phosphates, DFT, Spectroscopie, Microscopie.

Published online: 3 June 2021, Issue date: 1 September 2022

1. Introduction

Nowadays, powerful computers and massive parallelization of numerical methods in combination with quantum chemical software offers the opportunity to address chemical and physical problems which cannot be solved analytically. Indeed, the precise calculation of energies, charge distributions and other properties in the field of computational chemistry can lead to a full understanding of molecular processes observed in experiments with the final aim of predicting them. Of course, a close interplay between theoretical and experimental methods is needed to guarantee optimal results.

Density Functional Theory (DFT) [1–3] is the most used approach to reach this goal and is being used in physics, chemistry, materials science and other related fields [4–6]. Furthermore, in medicine, DFT is a tool which aids in developing new drugs [7] or antibacterial materials [8], understanding enzyme active sites [9], improving the long-term stability of implants [10] and dental composites [11] and much more. The big advantage of DFT (and other molecular modelling tools) is that it allows building a theoretical model of real-world problems at a molecular level that is extremely hard to achieve experimentally. Furthermore, the predictive abilities allow to fast-track the experimental design of new materials and methodologies.

The big advantage of DFT (in contrast to other modelling tools) is that it offers a very good compromise between chemical correctness and computational cost. Indeed, it allows the calculation of very accurate specific properties (such as spectroscopic data) as well as a time evolution of the system through ab initio molecular dynamics. It manages this good balance between computational efficiency and accuracy by explicitly treating electronic effects (in contrast to faster, but less accurate methods such as classical molecular dynamics) at an affordable computational cost (in contrast to more accurate, but more expensive approaches such as wave function methods). Obviously this means also that there is still a limit on the size of chemical systems and the time scales that can be studied using DFT, whereby specifically the inclusion of a solvent or biological medium may be problematic as this renders the size of the system very large. Aside from these direct investigations at the DFT-level, it should be noted that DFT is often used to benchmark or fit lower-level theories for subsequent investigations on similar systems [12].

The aim of this publication is then to present recent results obtained in the field of physiological [13,14] and mostly pathological calcifications [15–17] by means of DFT. To attain this goal, we will start by a brief (more details can be found in different excellent books [18,19]) presentation of some of its underlying principles. Afterwards, a selection of recent publications will be presented, dedicated to chemical compounds—namely calcium oxalate (COM and COD) and calcium phosphate (apatite and whitlockite)—that have been identified in pathological calcifications. We will show that the use of DFT is instrumental to obtain a precise assignment of the signals present in infrared, Raman and NMR spectra, to offer important insights in the morphology of crystallites present in urine or pathological calcifications and to develop new inhibitors to stop the growing process of crystallites.

2. Main underlying principles of DFT

The existence of a wave function for every measurable system is one of the fundamental postulates of quantum mechanics. This function defines the state of the system in function of 3N variables, with N the number of electrons in the system, each having 3 spatial degrees of freedom. The knowledge of the wave functions of a system allows—in principle—to solve the fundamental equation of quantum mechanics formulated by Schrödinger [20] leading to a full understanding of the system

$$\mathrm{i}\hbar\frac{\mathrm{d}}{\mathrm{d}t}\left|\Psi(t)\right\rangle - \hat{\mathrm{H}}\left|\Psi(t)\right\rangle \tag{1}$$

whereby i is the imaginary unit, $\hbar$ is the reduced Planck constant, Ψ is the wave function, t is the time and $\hat{\mathrm{H}}$ is the Hamiltonian operator describing

all possible interactions within the system. Unfortunately, solving this equation is impossible for materials which contain more than one electron due to the quickly escalating number of variables with increasing system size.

A major breakthrough in this problem was achieved by introducing the so-called Born–Oppenheimer approximation, which significantly reduces the amount of variables that needs to be calculated [21]. This approximation uses the fact that the mass of an electron is very small compared to the mass of a nucleus and thus assumes that the electrons react instantaneously to the movement of the nuclei. As such, the terms describing the coupling between the nuclei and the electrons are discarded from the Schrödinger equation, leading to a considerable reduction in the computational cost.

A second approximation that has led to a large increase of system size within computational reach, is the Hartree–Fock method. In this method, the many-electron Hamiltonian is replaced by a one-electron Hamiltonian acting on one-electron wavefunctions (orbitals). Furthermore, the Coulomb interaction between different electrons is only represented as an average over the entire system. Although this approach leads to unexpectedly good results in general, the error margin is too large to describe many of the chemically interesting systems as the energy differences at play are often subtle. More precisely, it was found that Hartree–Fock does not consider the correlated motions of different electrons, leading to problematic descriptions of many systems. Different (partly) solutions exist to overcome these issues and to further enhance the description, but many of them are computationally quite expensive. A radically different approach was introduced by the development of the density functional theory.

The main idea of DFT is to use an electron density instead of a complicated wavefunction, reducing the number of variables to only 3 variables instead of 3N and thus making the Schrödinger equation much easier to handle. Hohenberg and Kohn [1] proved that this approximation is valid, i.e. all ground state properties of a quantum system—in particular the ground state total energy—are unique functionals of the ground state density.

Finally, it is important to underline that the success of DFT lies in a further approximation related to the calculation of the electron density from a set of mathematical functions or orbitals introduced by Kohn and Sham [22].

$$\psi_i(r) = \sum_{\nu=1}^{K} c_{\nu i}\Phi_\nu \tag{2}$$

The total energy is then decomposed into three contributions being the kinetic energy, a Coulombic energy describing the electrostatic interactions between all charged particles and the so-called exchange-correlation term describing the many-body interactions. The mathematical form of the latter term is, unfortunately, unknown and is therefore approximated by increasingly accurate functional forms. Many different approximations exist, in multiple types and flavours, but the most common family—especially for solids—are the generalized gradient approximations whereby the exchange-correlation functional depends on the gradient of the local electron density of the system.

A further issue of DFT is that it is inherently not capable of well-describing dispersion forces that are responsible for many chemical phenomena of interest. This means that specific corrections need to be introduced to circumvent this problem as, although the magnitude of a dispersion interaction is small, they dominate the behaviour of neutral physical systems at intermediate distance ranges (>0.5 nm).

Again, a plethora of methods and approximations exist, whereby the pairwise dispersion correction series proposed by Grimme *et al.* [23–26] are arguably the most popular. It is an intuitive correction term, based on the interaction between two multipoles, that is orders of magnitudes cheaper to calculate than DFT itself, making it very suitable for the calculation of large systems. The main disadvantage of this correction term is that it is empirical and needs to be fitted for every density functional it is combined with. Of course, the fitting parameters for the most common density functional are readily available although the end-user should evaluate carefully whether the fitted parameters apply for the specific system of interest.

3. Calcium oxalates

3.1. *Characterization of calcium oxalates*

Pathological calcifications containing calcium oxalates have been identified in different organs

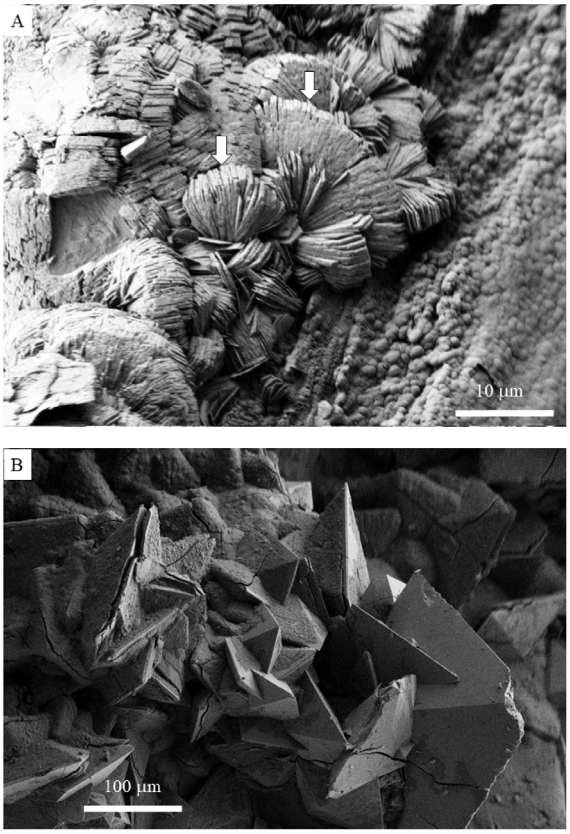

Figure 1. (A) Calcium oxalate monohydrate crystallites in kidney, (B) calcium oxalate dihydrate crystallites in prostate.

namely kidney [27], prostate [28,29] as well as thyroide [30,31]. For example in Figure 1, a calcium oxalate monohydrate crystallite in kidney can be seen as well as a calcium oxalate dihydrate crystallite in prostate. Note the significant differences in the size and in the arrangement of the crystallites in these two organs.

Regarding kidney, among the different chemical compounds which have been identified in concretions, calcium oxalate (CaOx) is the main component of more than 70% of all stones that were analysed in Western countries [32]. In general, three different crystalline forms of CaOx exist which defer in the amount of water molecules that are present in the crystal structure. The first one, calcium oxalate monohydrate (COM), or whewellite, has a 1:1 ratio between calcium oxalate units and water molecules: $CaC_2O_4 \cdot H_2O$. It is the most frequent form and is linked to hyperoxaluria [33,34]. Calcium oxalate dihydrate (COD) or weddellite has a 1:2 ratio between calcium oxalate units and water molecules ($CaC_2O_4 \cdot 2H_2O$). It is about two to three times less frequent than COM and is related to hypercalciuria [35,36]. It should be noted that, due to the presence of free-ranging water molecules inside the oxalate, the brute formula is actually $CaC_2O_4 \cdot (2 + x) \cdot H_2O$, see below. Finally, the prevalence of the third species, namely calcium oxalate trihydrate (COT) or caoxite (CaC_2O_4:H_2O = 1:3, $CaC_2O_4 \cdot 3H_2O$), is rarely observed in kidney stones.

According to a morpho-constitutional analysis [37–39], the etiology of kidney stones is based on the morphology as well as the chemical composition of the formed crystals as shown by Fourier Transform InfraRed (FT-IR) spectroscopy. Indeed, there is a correlation between the morphology of the kidney stone and the morphology of the crystallite [40,41] and therefore, the morphology of crystallites present in urine constitutes a key element to determine the underlying causes of the pathology [42]. Of course, the use of vibrational spectra (IR and Raman) implies the full understanding of the origins of the absorption and scattering bands in relation to the chemical properties of the material under investigation. The calculation of these spectra for well-defined chemical compositions can provide this understanding, enhancing the ability to interpret difficult experimental spectra obtained from natural mixed systems. Indeed, several dispersion-corrected DFT studies have been performed on calcium oxalate whereby the IR and Raman vibrational spectra were successfully predicted for the three different polyhydrates of calcium oxalate [12,43–47].

Another successful example of a DFT study on calcium oxalate was the identification of the amount and distribution of zeolitic water molecules in COD by Petit *et al.* [47]. Indeed, as mentioned before, the crystal structure of COD includes empty pores that can readily be filled by diffusing water molecules. Because of this, the crystal structure of COD is rather $CaC_2O_4 \cdot (2 + x) \cdot H_2O$ than $CaC_2O_4 \cdot 2H_2O$, whereby x represents the number of zeolitic water molecules per calcium oxalate unit. The exact value of x has been under debate for a long time until Petit *et al.* determined it through DFT studies [48]. By systematically calculating vibrational spectra for COD crystals with different values for x, they were able to show

that there are at most 4 zeolitic water molecules per unit cell ($x = 0.5$) and ideally 3.

Another important study [33] helped to resolve issues surrounding the crystal conversion from COD (being metastable) to COM. In these circumstances, the Fourier transform infrared spectra seemed to indicate the presence of the latter, while the morphology of the observed crystallites indicate presence of the former. As both forms are related to different etiologies and treatments, this posed important problems to clinicians. The DFT study was able to show, in combination with different experimental techniques, that a small amount of a less-ordered form of COM was formed that skewed the IR spectra. This resulted in the understanding that more attention should be paid to the stone morphology, rather than the spectra in these specific cases. Further on this less ordered form of COM, which had already been proposed in some experimental studies, DFT studies were needed to fully unravel the involvement of the structural water molecules in the structure and the related symmetry of the crystal [49].

Finally, we would like to note that, aside from the already mentioned experimental results such as IR and Raman spectra, also the calculation of NMR spectra is available. It was applied and validated specifically for calcium oxalates by Colas *et al.* [50]. The authors of the paper emphasized that it is yet another benchmark against which difficult experimental or clinical samples can be validated and assigned.

3.2. *Interaction between calcium oxalates and small molecules*

DFT has also been used to assess molecular interactions occurring on a COD surface which could promote an anisotropic crystal growth. More specifically, Parvaneh *et al.* [51] found that the crystallographic faces (100) and (101) of COD are hydrophilic and can therefore be solvated by a strongly bound layer of water. However, important differences in the respective adsorption mechanisms could explain the anisotropic growth of the crystals, which is favoured in the (100) direction, as observed in experiments. Similar results have been published by Debroise *et al.* [52,53] which further underlined the key role of water in the prediction of calcium oxalate morphology. More specifically, it was shown that the adsorption mechanisms of water onto the different crystal surfaces, offer the needed stabilization to obtain the experimentally found crystal morphologies.

Moreover, for many types of pathological calcifications, but especially in the case of kidney stones, crystal growth inhibitors are at the centre of several investigations. Indeed, it is well known that the growing process of crystals can be stopped or altered by ions or molecules. More specifically, the adsorption of inhibitors on specific crystal surfaces impedes the addition of surface ions, thereby reducing the rate of growth. Chung *et al.* [54] have showed by means of DFT (in combination with *in situ* atomic force microscopy) that citrate and hydroxycitrate exhibit an adsorption mechanism different from classical theory as they induce a dissolution process of the pathological crystal instead of a reduced rate of crystal growth. Similarly, experimental evidence exists suggesting that catechin (as present in green tea) has a similar effect [55]. A conclusive, explanatory DFT model, supporting these experimental findings has not yet been developed although a manuscript on this subject has been submitted by the current authors, see also Figure 2.

4. Calcium phosphates

4.1. *Characterization of calcium phosphates*

In general, it is well known that the chemistry of biological apatite is quite complex [56,57] due to a lack of Ca^{2+} and OH^- ions at the surface as well as their replacement by ions with different charges (for example CO_3^{2-} substituted for PO_4^{3-} and/or OH^-). Regarding pathological calcification, calcium phosphate apatites are present in various parts of human body [58,59] as well as on medical devices (Figure 3).

Although this makes it hard for a DFT study to capture all properties of an experimental system all at once (remember the size limit of the calculations), the method allows for a very detailed understanding of all the separate processes at work leading to an overall understanding of the system. Among such different investigations, we can quote the work of Deymier *et al.* [60] describing a mechanism by which crystal dimensions are controlled through carbonate substitution. Another study identified 2 types of carbonate substitutions and related this to the stability of the formed crystals [61]. A final example that we would like to mention here is the study of the

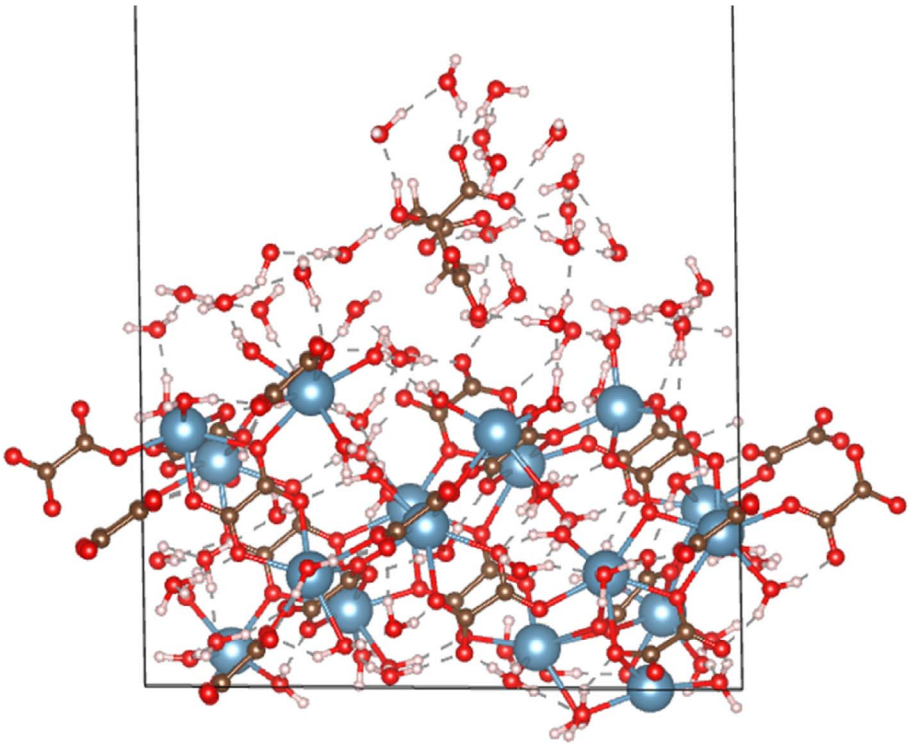

Figure 2. A citrate molecule surrounded by water molecules adsorbed onto an oxalate surface of about 15 Å × 18 Å. Brown is carbon, cyan is calcium, red is oxygen and white is hydrogen.

mobility of the carbonate anion within the channels formed by apatite [62]. These results were well in line with experimental X-ray data and revealed that the carbonate is able to move almost freely through the channel. This may have important implications for the bioactivity of the apatite structure. It is worth to underline that all these results taken together, it is clearly demonstrated that carbonate substitution is sufficient to drive the formation of bone-like crystallites.

Also a derived material, hydroxyapatite (HAP) was studied by means of DFT to unravel its paracrystalline disorder and chemical composition [63]. By combining the theoretical calculations with synchrotron X-ray total scattering data, it was possible to unravel the atomistic structure of the material. Extending the range of possible DFT-compatible techniques, Chappell *et al.* [64] have characterized the material by comparing DFT-level and experimental NMR data opening up the possibility of studying surface reactivity.

In the case of kidney infection, it is worth to underline that two chemical compounds may be related to infection namely struvite and whitlockite [65,66]. In that case, bacterial imprints (Figure 4A) can be revealed through observations at the micrometer scale by a scanning electron microscopy of the surface of calcium phosphate apatite [67,68]. In whitlockite (Figure 4B), a complex structure whereby Ca^{2+} ions are substituted by Mg^{2+} ions leads to cation vacancies and protonation of phosphate groups as can be seen in the DFT model presented in Figure 5. Again, a careful theoretical characterization is detrimental for the understanding of the formation and removal of these crystals. In that sense, an important DFT-based contribution was delivered by Debroise *et al.* [69] who were able to quantify the ability of whitlockite to form the mentioned substitutions and vacancies. By relating these defects to the resulting IR, Raman and XRD spectra, important insights into diagnosis and treatment are available.

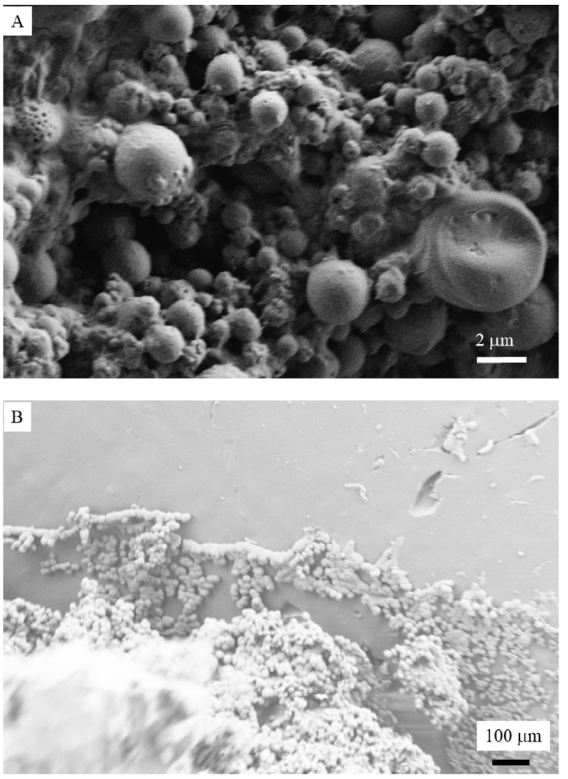

Figure 3. Spherical calcium phosphate apatite identified in thyroid calcifications (A) and on a medical device very common in urology, a JJ stent (B).

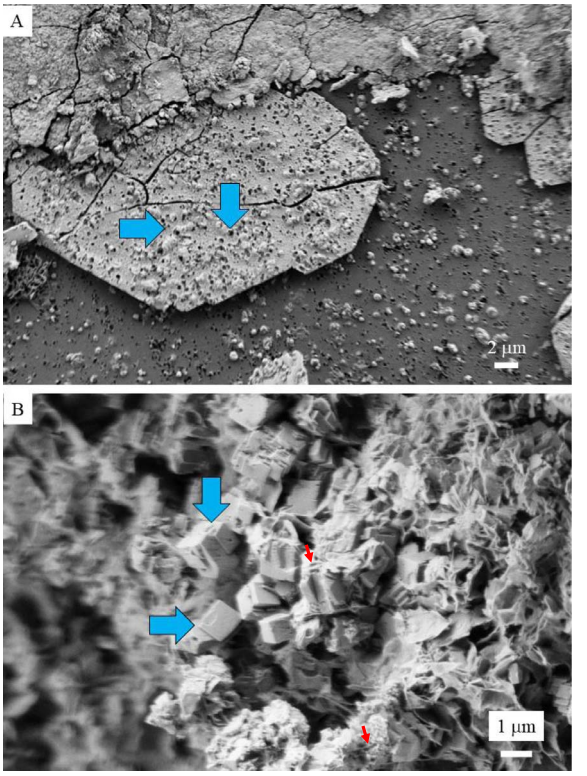

Figure 4. (A) bacterial imprints at the surface of calcium phosphate apatite deposits on a JJ stent. (B) Pseudo cubic whitlockite crystallites (blue arrows) and "bacterial imprints" (red arrows).

4.2. *Interaction between calcium phosphates and small molecules*

Most of the DFT studies dedicated to the interaction between organic and inorganic compounds have been performed within the context of physiological calcifications. As such, several studies were performed on the interface between the organic and inorganic parts in bone, namely the collagen protein and hydroxyapatite (HAP) (the most stable form of calcium phosphate in physiological conditions) [66]. A very important aspect of bone and teeth growth is the understanding of the nucleation and prenucleation phases of calcium phosphate. In that regard, an important study using DFT-driven simulations, was performed by Mancardi *et al.* [70] in identifying stable prenucleation clusters in aqueous solution.

The work of Cutini *et al.* [71] focuses on the interaction between a model of a single-collagen-strand with the most common dried P-rich (010) HAP surface. The authors discovered that the HAP adsorption process leads to a deformation of the polymer in order to create a relatively strong electrostatic interaction between the PRO carbonyl C=O group and the most exposed Ca ion of the P-rich (010) HAP surface. Other authors have investigated the interaction between water molecules and the HAP surface [69,72]. Among them, Peccati *et al.* [73] have considered a set of HAP surfaces (namely (001), (010), and (101)) and their interaction with water using DFT simulations, predicting spontaneous water dissociation on these surfaces.

Quite recently, combining multinuclear solid-state NMR spectroscopy, powder X-ray diffraction, and first principles electronic structure, Davies *et al.* [74] have underlined the fact that citrate molecules form bridges between mineral platelets

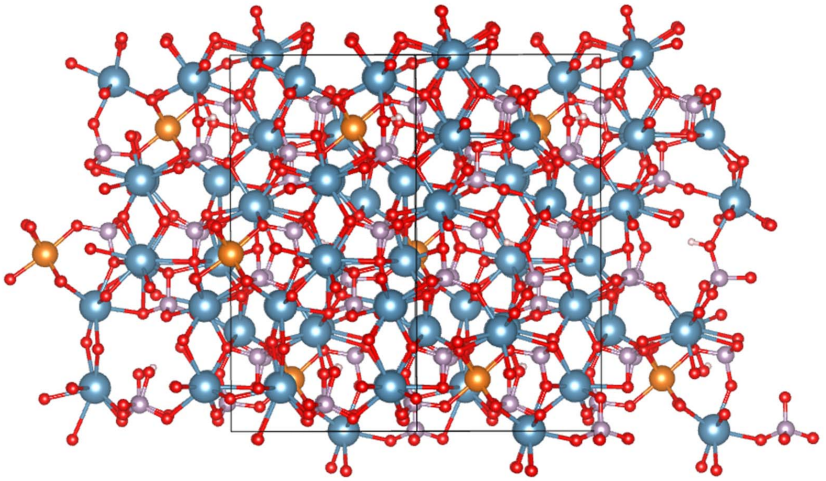

Figure 5. A DFT-based, molecular model for a Whitlockite bulk unit cell containing three Mg substitutions per unit cell of 10 Å × 9 Å × 18 Å. Blue is calcium, red is oxygen, pink is phosphorus, white is hydrogen and orange is magnesium.

in bone. In fact, citrate molecules are well known as growth inhibitors and a recent investigation done by Fernandez *et al.* [75] has considered a set of the HAP crystal growth inhibitors namely pyrophosphate, etidronate, citrate and phytate. The complete set of numerical simulation showed that the adsorption energies of the inhibitors increased in the sequence: pyrophosphate < etidronate < citrate ≪ phytate. Such sequence is in line with the increase of functional groups of the molecules bounded with the HAP surface as well as the total molecular negative charge.

Finally, it is worth to note that DFT calculations can also be used to assess the interaction between metals such as Ag and HAP. Several antimicrobial studies have clearly shown that Ag-HAp nanoparticles have excellent in vitro antibacterial activity with *E. coli*.

5. Outlook on silica DFT studies

Although rather a mineralisation than a biological calcification, silicon dioxide—or silica—is found in skin in the case of sarcoidosis [76,77] and also in kidney [78]. The chemistry of silica has been studied intensively due its importance in heterogeneous catalysis [79], yet not often at DFT level. Indeed, due to its amorphous nature and its complex solid/liquid interfaces, relatively little studies have been or are undertaken. Some of the authors of the current paper have been specializing in amorphous silica DFT modelling for over a decade. This resulted in the development of one of the first hydroxylated amorphous silica models in 2008 [80], published simultaneously with the model of the group of Ugliengo [79]. Recently, we reviewed the last decade on silica modelling with DFT [81,82].

At DFT level, aside from some studies on the interaction of small amino acids with the silica interfaces, no other work has been done related to the silica mineralisation to the best of our knowledge. This is mainly due to the complexity of the molecular structure and the large size of the models when large biological molecules are investigated. However, with the still increasing computing power we expect that in a few years more realistic biological/silica interface studies will be studied at the DFT level.

6. Conclusion

We have demonstrated, through examples from the literature, the importance of density functional theory calculations in the field of pathological calcifications. Indeed, it is clear that the capability of theoretical methods—whereby density functional theory offers a very good balance between accuracy

and computational cost—allows to zoom into the molecular level of the system of interest. Especially, the possibility to predict spectroscopic properties for different hypothesized molecular structures, allows to asses different possible models. Through careful comparison with experimental results, the validity of the proposed models can then be assessed. A careful analysis of the chemical structure of different surfaces, adsorption sites and geometries (conformations of functional groups), allows understanding and predictions that can have important repercussions at the macro level regarding prevention, diagnosis and treatment.

Acknowledgments

FT wish to acknowledge the VUB for support, among other through a Strategic Research Program awarded to his group.

References

[1] P. Hohenberg, W. Kohn, *Phys. Rev. B*, 1964, **136**, 864.
[2] R. O. Jones, *Rev. Mod. Phys.*, 2015, **87**, 897.
[3] N. Mardirossian, M. Head-Gordon, *Mol. Phys.*, 2017, **115**, 2315.
[4] D. Bazin, F. Tielens, *Appl. Catal.*, 2015, **504**, 631.
[5] F. Tielens, D. Bazin, *C. R. Chim.*, 2018, **21**, 174.
[6] I. C. Oğuz, H. Guesmi, D. Bazin, F. Tielens, *J. Phys. Chem. C*, 2019, **123**, 20314.
[7] S. LaPointe, D. A. Weaver, *Curr. Comput. Aided-Drug Des.*, 2007, **3**, 290.
[8] H. Kim, S. Mondal, B. Jang, P. Manivasagan, M. S. Moorthy, J. Oh, *Ceram. Int.*, 2018, **44**, 20490.
[9] P. E. M. Siegbahn, M. R. A. Blomberg, *Annu. Rev. Phys. Chem.*, 1999, **50**, 221.
[10] I. Y. Grubova, M. A. Surmeneva, S. Huygh, R. A. Surmenev, E. C. Neyts, *J. Phys. Chem. C*, 2017, **121**, 15687.
[11] K. Moradi, A. A. Sabbagh Alvani, *J. Aust. Ceram. Soc.*, 2020, **56**, 591.
[12] D. D. Tommaso, S. E. R. Hernández, Z. Du, N. H. Leeuw, *RSC Adv.*, 2012, **2**, 4664.
[13] E. Bonucci (ed.), *Calcification in Biological Systems*, CRC Press, Boca Raton, 1992.
[14] C. Combes, S. Cazalbou, C. Rey, *Minerals*, 2016, **6**, 34.
[15] D. Bazin, M. Daudon, C. Combes, C. Rey, *Chem. Rev.*, 2012, **112**, 5092.
[16] D. Bazin, M. Daudon, *J. Phys. D: Appl. Phys.*, 2012, **45**, article no. 383001.
[17] D. Bazin, E. Letavernier, J. P. Haymann, V. Frochot, M. Daudon, *Ann. Biol. Clin.*, 2020, **78**, 349.
[18] A. Szabo, N. S. Ostlund, *Modern Quantum Chemistry: Introduction to Advanced Electronic Structure Theory*, Dover Publications, New York, 2012.
[19] T. Helgaker, P. Jorgensen, J. Olsen, *Molecular Electronic-Structure Theory*, Wiley, New York, 2014.
[20] E. Schrödinger, *Phys. Rev.*, 1926, **28**, 1049.
[21] M. Born, R. Oppenheimer, *Ann. Phys.*, 1927, **389**, 457.
[22] W. Kohn, L. J. Sham, *Phys. Rev.*, 1965, **140**, A1133.
[23] S. Grimme, *J. Comput. Chem.*, 2006, **27**, 1787.
[24] S. Grimme, J. Antony, S. Ehrlich, H. A. Krieg, *J. Chem. Phys.*, 2010, **132**, article no. 154104.
[25] S. Grimme, S. Ehrlich, L. Goerigk, *J. Comput. Chem.*, 2011, **32**, 1456.
[26] E. Caldeweyher, C. Bannwarth, S. Grimme, *J. Chem. Phys.*, 2017, **147**, article no. 034112.
[27] D. Bazin, E. Letavernier, J.-P. Haymann, F. Tielens, A. Kellum, M. Daudon, *C. R. Chim.*, 2016, **19**, 1548.
[28] A. Dessombz, P. Méria, D. Bazin, M. Daudon, *PLoS One*, 2012, **7**, article no. e51691.
[29] A. Dessombz, P. Méria, D. Bazin, E. Foy, S. Rouzière, R. Weil, M. Daudon, *Prog. Urol.*, 2011, **21**, 940.
[30] M. Mathonnet, A. Dessombz, D. Bazin, R. Weil, F. Triponez, M. Pusztaszeri, M. Daudon, *C. R. Chim.*, 2016, **19**, 1672.
[31] J. Guerlain, S. Perie, M. Lefevre, J. Perez, S. Vandermeersch, C. Jouanneau, L. Huguet, V. Frochot *et al.*, *PLoS One*, 2019, **14**, article no. e0224138.
[32] A. P. Evan, E. M. Worcester, F. L. Coe, J. Williams, J. E. Lingeman, *Urolithiasis*, 2015, **43**, 19.
[33] D. Bazin, C. Leroy, F. Tielens, C. Bonhomme, L. Bonhomme-Coury, F. Damay *et al.*, *C. R. Chim.*, 2016, **19**, 1492.
[34] M. Daudon, E. Letavernier, V. Frochot, J.-P. Haymann, D. Bazin, P. Jungers, *C. R. Chim.*, 2016, **19**, 1504.
[35] M. Daudon, P. Jungers, D. Bazin, *AIP Conf. Proc.*, 2008, **1049**, 199.
[36] M. Daudon, P. Jungers, D. Bazin, J. C. Williams Jr., *Urolithiasis*, 2018, **46**, 459.
[37] M. Daudon, C. A. Bader, P. Jungers, *Scanning Microsc.*, 1993, **7**, 1081.
[38] M. Daudon, *Arch. Pédiatrie*, 2000, **7**, 855.
[39] M. Daudon, A. Dessombz, V. Frochot, E. Letavernier, J. P. Haymann, P. Jungers, D. Bazin, *C. R. Chim.*, 2016, **19**, 1470.
[40] M. Daudon, D. Bazin, G. André, P. Jungers, A. Cousson, P. Chevallier, E. Véron, G. Matzen, *J. Appl. Cryst.*, 2009, **42**, 109.
[41] M. Daudon, P. Jungers, D. Bazin, *New England J. Med*, 2008, **359**, 100.
[42] M. Daudon, V. Frochot, D. Bazin, P. Jungers, *C. R. Chim.*, 2016, **19**, 1514.
[43] A. Koleżyński, A. Małecki, *J. Therm. Anal. Calorim.*, 2010, **99**, 947.
[44] D. Toczek, K. Kubas, M. Turek, S. Roszak, R. Gancarz, *J. Mol. Model.*, 2013, **19**, 4209.
[45] W. Zhao, N. Sharma, F. Jones, P. Raiteri, J. D. Gale, R. Demichelis, *Cryst. Growth Des.*, 2016, **16**, 5954.
[46] A. Pintus, M. C. Aragoni, G. Carcangiu, L. Giacopetti, F. Isaia, V. Lippolis, L. Maiore, P. Meloni, M. Arca, *New J. Chem.*, 2018, **42**, 11593.
[47] K. I. Peterson, D. P. Pullman, *J. Chem. Educ.*, 2016, **93**, 1130.
[48] I. Petit, G. D. Belletti, T. Debroise, M. J. Llansola-Portoles, I. T. Lucas, C. Leroy, C. Bonhomme *et al.*, *ChemistrySelect*, 2018, **3**, 8801.
[49] M. Shepelenko, Y. Feldman, L. Leiserowitz, L. Kronik, *Cryst. Growth Des.*, 2020, **20**, 858.

[50] H. Colas, L. Bonhomme-Coury, C. C. Diogo, F. Tielens, F. Babonneau, C. Gervais, D. Bazin, D. Laurencin *et al.*, *Cryst. Eng. Commun.*, 2013, **15**, 8840.
[51] L. S. Parvaneh, D. Donadio, M. Sulpizi, *J. Phys. Chem. C*, 2016, **120**, 4410.
[52] T. Debroise, T. Sedzik, J. Vekeman, Y. Su, C. Bonhomme, F. Tielens, *Cryst. Growth Des.*, 2020, **20**, 3807.
[53] T. Debroise, E. Colombo, G. Belletti, J. Vekeman, Y. Su, R. Papoular *et al.*, *Cryst. Growth Des.*, 2020, **20**, 2553.
[54] J. Chung, I. Granja, M. G. Taylor, G. Mpourmpakis, J. R. Asplin, J. D. Rimer, *Nature*, 2016, **536**, 446.
[55] Y. Itoh, T. Yasui, A. Okada, K. Tozawa, Y. Hayashi, K. Kohri, *J. Urol.*, 2005, **173**, 271.
[56] C. Rey, C. Combes, C. Drouet, H. Sfihi, A. Barroug, *Mater. Sci. Eng. C*, 2007, **27**, 198.
[57] D. Bazin, C. Chappard, C. Combes, X. Carpentier, S. Rouzière, G. André *et al.*, *Osteoporos. Int.*, 2009, **20**, 1065.
[58] D. Bazin, J. P. Haymann, E. Letavernier, J. Rode, M. Daudon, *Presse Med.*, 2014, **43**, 135.
[59] D. Bazin, E. Letavernier, J. P. Haymann, P. Méria, M. Daudon, *Prog. Urol.*, 2016, **26**, 608.
[60] A. C. Deymier, A. K. Nair, B. Depalle, Z. Qin, K. Arcot, C. Drouet, C. H. Yoder *et al.*, *Biomaterials*, 2017, **127**, 75.
[61] R. Astala, M. J. Stott, *Chem. Mater.*, 2005, **17**, 4125.
[62] F. Peccati, M. Corno, M. Delle Piane, G. Ulian, P. Ugliengo, G. Valdrè, *J. Phys. Chem. C*, 2014, **118**, 1364.
[63] M. E. Marisa, S. Zhou, B. C. Melot, G. F. Peaslee, J. R. Neilson, *Mineral. Inorg. Chem.*, 2016, **23**, 12290.
[64] H. Chappell, M. Duer, N. Groom, C. Pickard, P. Bristowe, *Phys. Chem. Chem. Phys.*, 2008, **10**, 600.
[65] E. J. Espinosa-Ortiz, B. H. Eisner, D. Lange, R. Gerlach, *Nat. Rev. Urol.*, 2019, **16**, 35.
[66] M. Daudon, *Arch. Pédiatrie*, 2000, **7**, 855.
[67] G. Mancardi, U. Terranova, N. H. de Leeuw, *Cryst. Growth Des.*, 2016, **16**, 3353.
[68] M. Cutini, M. Corno, D. Costa, P. Ugliengo, *J. Phys. Chem. C*, 2019, **123**, 7495-7498.
[69] W. Zhao, Z. Xu, Y. Yang, N. Sahai, *Langmuir*, 2014, **30**, 13283.
[70] X. Carpentier, M. Daudon, O. Traxer, P. Jungers, A. Mazouyes, G. Matzen, E. Véron, D. Bazin, *Urology*, 2009, **73**, 968.
[71] D. Bazin, G. André, R. Weil, G. G. Mlatzen, E. Véron, X. Carpentier, M. Daudon, *Urology*, 2012, **79**, 786.
[72] X. Wang, H. Wu, X. Cheng, M. Yang, L. Zhang, *AIP Adv.*, 2020, **10**, article no. 065217.
[73] F. Peccati, C. Bernocco, P. Ugliengo, M. Corno, *J. Phys. Chem. C*, 2018, **122**, 3934.
[74] E. Davies, K. H. Muller, W. C. Wong, C. J. Pickard, D. G. Reid, J. N. Skepper, M. J. Duer, *Proc. Natl Acad. Sci.*, 2014, **111**, article no. E1354.
[75] D. Fernández, J. Ortega-Castro, J. Frau, *Appl. Surf. Sci.*, 2017, **408**, 110.
[76] H. Colboc, D. Bazin, P. Moguelet, V. Frochot, R. Weil, E. Letavernier *et al.*, *C. R. Chim.*, 2016, **19**, 1631.
[77] H. Colboc, P. Moguelet, D. Bazin, C. Bachmeyer, V. Frochot, R. Weil, E. Letavernier *et al.*, *J. Eur. Acad. Dermatol. Venereol.*, 2019, **33**, 198.
[78] A. Dessombz, D. Bazin, P. Dumas, C. Sandt, J. Sule-Suso, M. Daudon, *PLoS One*, 2011, **6**, article no. e28007.
[79] P. Ugliengo, M. Sodupe, F. Musso, I. J. Bush, R. Orlando, R. Dovesi, *Adv. Mater.*, 2008, **20**, 4579.
[80] F. Tielens, C. Gervais, J. F. Lambert, F. Mauri, D. Costa, *Chem. Mater.*, 2008, **20**, 3336.
[81] F. Tielens, M. Gierada, J. Handzlik, M. Calatayud, *Catal. Today*, 2020, **354**, 3.
[82] S. R. Stock, *Calcif. Tissue Int.*, 2015, **97**, 262.

Comptes Rendus
Chimie
2022, Vol. 25, Special Issue S1, p. 219-233
https://doi.org/10.5802/crchim.199

Microcrystalline pathologies: Clinical issues and nanochemistry / *Pathologies microcristallines : questions cliniques et nanochimie*

Profile of an "at cutting edge" pathology laboratory for pathological human deposits: from nanometer to *in vivo* scale analysis on large scale facilities

Dominique Bazin [*, a], **Ivan T. Lucas** [b], **Stéphan Rouzière** [c], **Erik Elkaim** [d], **Cristian Mocuta** [d], **Solenn Réguer** [d], **David G. Reid** [e], **Jérémie Mathurin** [a], **Alexandre Dazzi** [a], **Ariane Deniset-Besseau** [a], **Margaux Petay** [a], **Vincent Frochot** [f, g, h], **Jean-Philippe Haymann** [f, g, h], **Emmanuel Letavernier** [f, g, h], **Marie-Christine Verpont** [f, g, i], **Eddy Foy** [j], **Elise Bouderlique** [f, g, h], **Hester Colboc** [k] **and Michel Daudon** [f, g, h]

[a] Université Paris-Saclay, CNRS, Institut de Chimie Physique, 91405 Orsay cedex, France

[b] Laboratoire LISE UMR 8235 CNRS-SU, Sorbonne Université, Paris, France

[c] Université Paris-Saclay, CNRS, Laboratoire de Physique des Solides, 91405 Orsay Cedex, France

[d] Synchrotron SOLEIL, L'Orme des Merisiers Saint Aubin BP48, 91192 Gif-sur-Yvette Cedex, France

[e] Yusuf Hamied Department of Chemistry, University of Cambridge, Lensfield Road, Cambridge CB2 1EW, UK

[f] Sorbonne Université, UPMC Univ Paris 6, UMR S 1155, Paris, France

[g] INSERM, UMR S 1155, Hôpital Tenon, Paris, France

[h] Explorations fonctionnelles multidisciplinaires, AP-HP, Hôpital Tenon, Paris, France

[i] LUMIC network, F-75020 Paris, France

[j] Université Paris-Saclay, CEA, CNRS, NIMBE-LAPA, 91191 Gif-sur-Yvette, France

[k] Sorbonne Université, AP-HP, Hôpital Rothschild, Service Plaies et Cicatrisation, Paris, France

E-mails: dominique.bazin@universite-paris-saclay.fr (D. Bazin), ivan.lucas@sorbonne-universite.fr (I. T. Lucas), stephan.rouziere@u-psud.fr (S. Rouzière), erik.elkaim@synchrotron-soleil.fr (E. Elkaim), cristian.mocuta@synchrotron-soleil.fr (C. Mocuta), solenn.reguer@synchrotron-soleil.fr (S. Réguer), dgr30@cam.ac.uk (D. G. Reid), jeremie.mathurin@u-psud.fr (J. Mathurin), alexandre.dazzi@u-psud.fr (A. Dazzi), ariane.deniset@u-psud.fr (A. Deniset-Besseau), margaux.petay@u-psud.fr (M. Petay), vincent.frochot@tnn.aphp.fr (V. Frochot), jean-philippe.haymann@tnn.aphp.fr

* Corresponding author.

(J.-P. Haymann), emmanuel.letavernier@tnn.aphp.fr (E. Letavernier),
marie-christine.verpont@upmc.fr (M.-C. Verpont), eddy.foy@cea.fr (E. Foy),
elise.bouderlique@inserm.fr (E. Bouderlique), hester.colboc@aphp.fr (H. Colboc),
daudonmichel24@gmail.com (M. Daudon)

Abstract. This contribution aims to define an analysis procedure for abnormal deposits in human tissues starting from *in vivo* characterization, down to the nanoscale using major instrumentation. Such an integrated approach is based on recent literature, but particularly on our research over the last twenty years on pathological calcifications. To this end, we begin by describing four successive analytical steps, on the injury site or physician's surgery, at the hospital, at a typical physicochemical laboratory, and finally at a large scale (possibly multinational) facility. For the first step, we present various techniques which can be implemented on portable instruments. For the second step, commercial analytical setups are used. In a physicochemical laboratory, prototype or commercial setups are used and finally on large scale instruments, characterization techniques with better spatial resolution and/or higher sensitivity or techniques specific to synchrotron radiation are employed.

Keywords. Pathological calcifications, Characterization techniques, Experimental approach, Medical diagnostic, Abnormal deposits.

Published online: 27 July 2022, Issue date: 1 September 2022

1. Introduction

Pathological deposits are very common in the human body and accurate characterization is of major importance for medical care. The research described here was performed in close collaboration with several hospitals [1–4]. Pathological calcifications and abnormal deposits more generally, such as in tattoos [5] or sarcoidosis [6,7], may be intimately linked with major health problems such as cancer [8–13], infection [14–19], diabetes [20–22], or genetic disorders [23–26]. The various reviews published from either a medical [27–31] or a physicochemical point of view [1–4,22–38] have clearly underlined that characterizing deposits, of endogenous and exogenous origins, in the human body are crucial to not only assist diagnosis but also to optimise and develop specific therapy regimens.

More precisely, recent literature and the results we have gathered on different human tissues, including bone [39–41], skin [5,6,42,43], thyroid [34–46], prostate [8,47], kidney [42–51], cartilage [52–55], breast [9,56], salivary glands [57], and pancreas [58], showed that characterization by staining is often of limited utility. A more comprehensive approach has to encompass a wide range of techniques able to describe pathological calcifications at different scales. They can be classified into different families; techniques able to define elemental compositions such as X-ray fluorescence (XRF) [59,60] or energy dispersive X-ray spectroscopies (EDS) [61,62], those which describe molecular composition such as Fourier transform infrared (FTIR) [63,64] or Raman spectroscopies [65–68] as well as scattering techniques [69–72]. Imaging techniques such as scanning [61,62] and transmission electron microscopy (SEM and TEM) [73–76] or micro computed tomographic imaging [77–80] are also of prime importance. Finally, it is possible to precisely define the electronic state of some elements through X-ray photoelectron spectroscopy (XPS) [81–83] and/or their local atomic level environment using X-ray absorption spectroscopy (XAS) [84–86], electron energy-loss spectroscopy (EELS) [76,87,88] or nuclear magnetic resonance (NMR) [57,89–91].

The micrometer to nanometer scale information about abnormal deposits that these techniques yield allows an accurate description of the processes underlying the pathology, by defining morphology, elemental composition, and molecular and structural aspects. Some of these techniques can be used *in vivo* on abnormal deposits in human tissues while some can only be used on biopsy material. The application of all of these complementary techniques in the specific characterisation of abnormal human deposits is detailed in the present paper.

2. Defining an analytical procedure

We will consider the analysis procedure in four steps (Figure 1). The first is initial characterization directly on the human body using a portable analytical device at the physician's surgery or at the in-

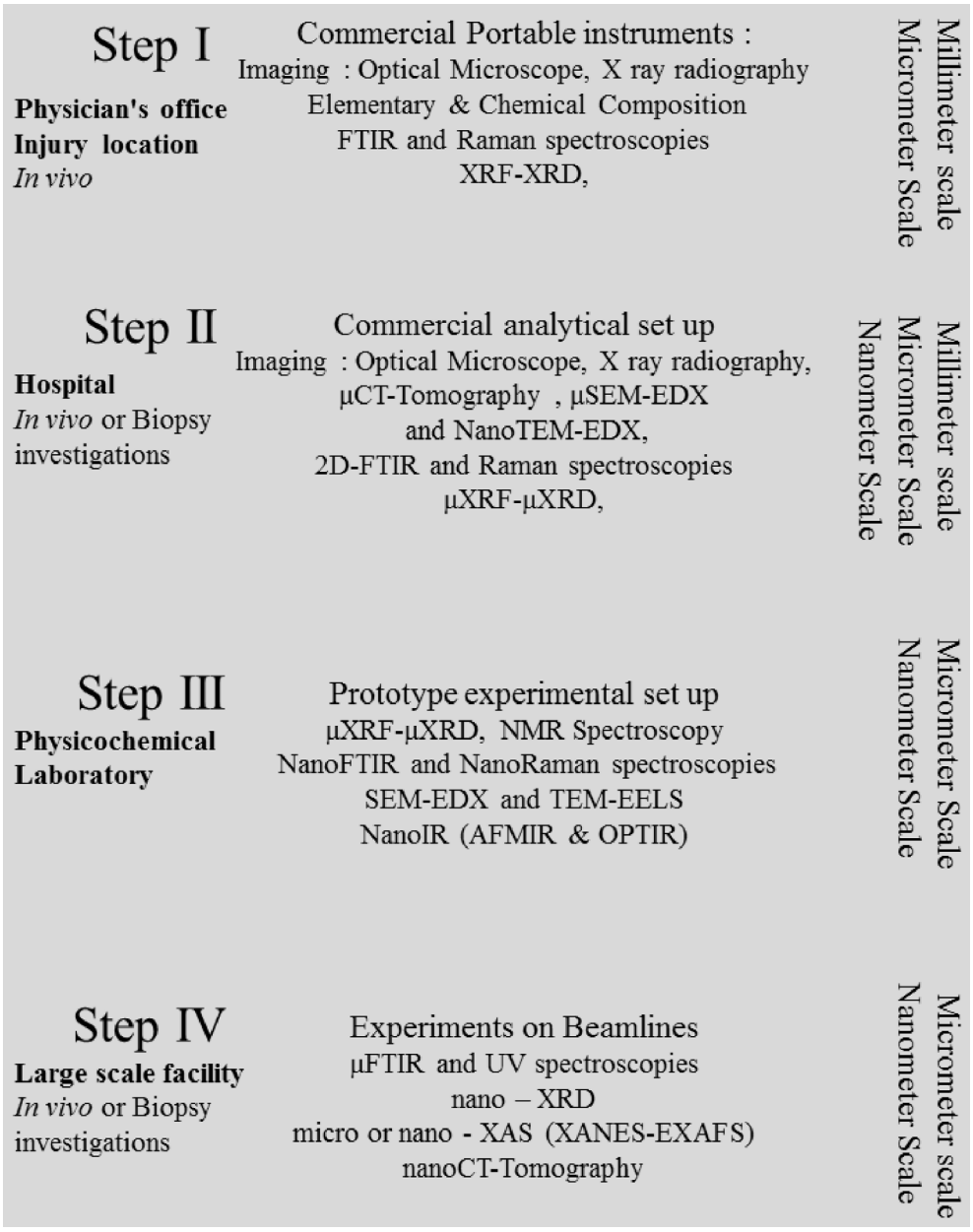

Figure 1. Various steps of the experimental approach proposed for structural and chemical investigations of pathological calcifications.

jury location depending on severity. The next would be in a hospital in which commercial analytical apparatus is available. The third step involves characterization of biopsies in a physical laboratory performing fundamental analytical research. We conclude by describing experiments requiring large scale instrumentation (often shared with other national and international users) such as synchrotron facilities. Such "photon factories" produce well-collimated and high intensity photon syn-

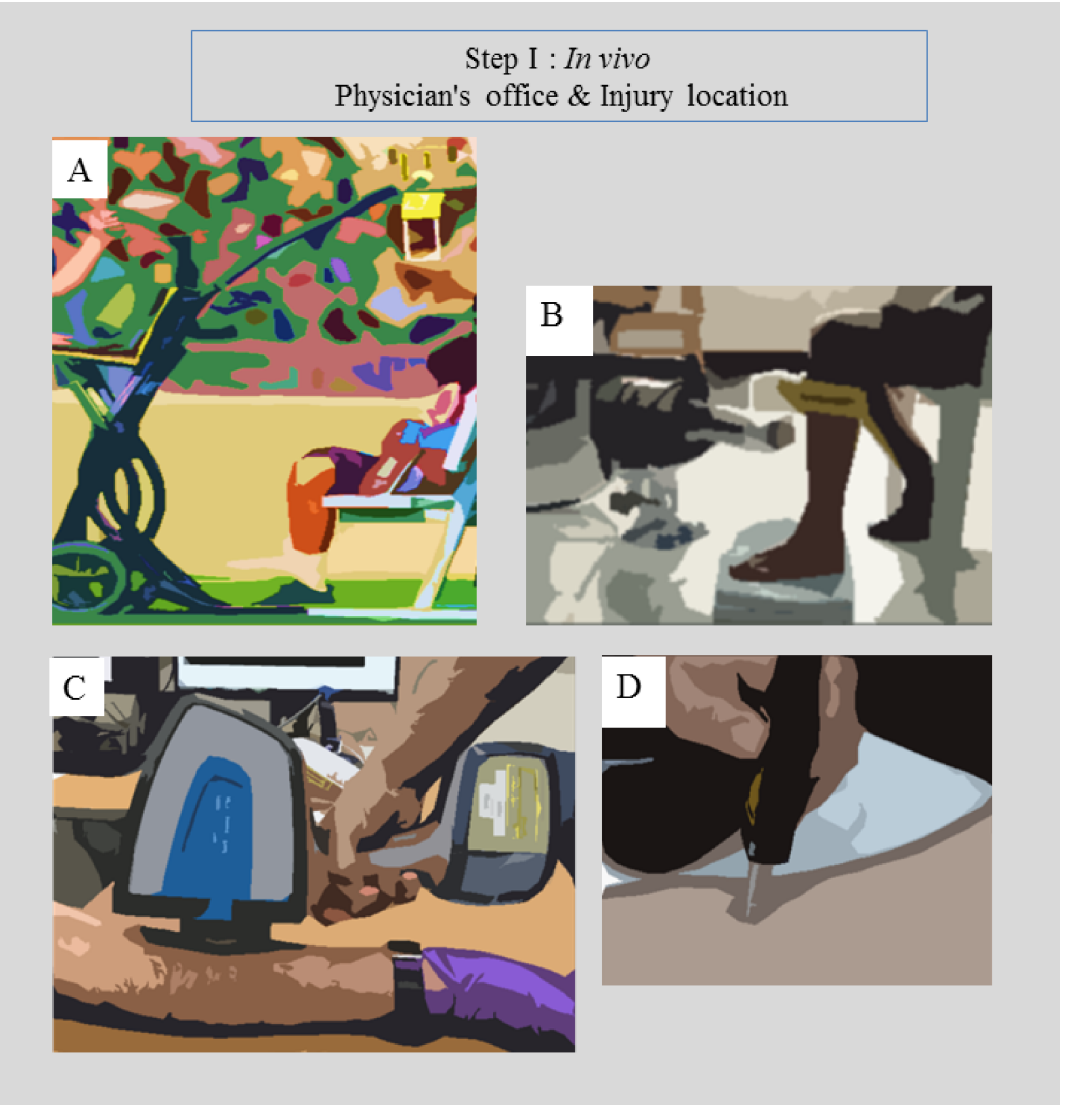

Figure 2. *In vivo* portable devices for (a) Radiography [92], (b) XRF [93], (c) FTIR [94] and (d) Raman [95] spectroscopies.

chrotron radiation beams leading to better spatial resolution and/or higher sensitivity.

2.1. *In vivo analysis at the physician's surgery or place of injury*

The *in vivo* or *in situ* (for forensic medicine) step takes account of the fact that different easy-to-implement experimental setups have been developed over the last decades (Figure 2). These include portable radiography apparatus [96], which can define an area of interest for extraction of biological samples if possible and necessary for subsequent characterization.

XRF (for elemental analysis and quantification) [97,98], FTIR [99–102] or Raman [103–105] spectroscopies (to determine the nature and amount of chemical compounds present in the sample) constitute at least three characterization techniques which can be applied *in vivo*. It is worth mentioning that biological fluids (or actual tissue in the case of

accident trauma) can also be analysed, in which case, two other techniques namely X-ray Diffraction (XRD, to determine the nature and quantity of any crystalline phases present in the sample) and tabletop SEM (for submicrometer scale surface imaging) can also be applied.

More precisely, XRD can be used to determine the crystallographic structure of unknown deposits [106,107], to identify the different crystalline phases and their composition, concentration, and average crystal dimensions [72,108]. "Tabletop" SEM is also available for observing the micrometer scale surface topology of the sample [109] and ultimately determine particle elemental composition by EDS spectroscopy [72].

2.2. *Analysis at the hospital on the patient (biopsy)*

The second step in a concerted analysis would be performed in a hospital laboratory where commercial physicochemical setups can be used (Figure 3). Investigations *in vivo* as well as on biopsies are possible. Biopsy procedures are usually performed at the hospital under and/or after radiological examination in the case of breast [110] or kidney [111]. A commercial in-lab setup provides analytical data superior to that produced by portable apparatus (better spatial resolution and sensitivity); the three techniques considered above, namely SEM, XRF and XRD can be performed directly on the biopsy sample (i.e. before paraffin embedding). Note that at Tenon Hospital nanometer scale biopsy characterization by TEM is also possible (Figure 3E).

Embedding the biopsy in a paraffin block allows the sample to be preserved and manipulated simply and safely. It also offers the opportunity to collect a set of data yielding elemental composition (through μXRF or μEDX experiments) or chemical mapping (μFTIR, μRaman or μXRD experiments), from the same sample. Note that for μXRF and μXRD experiments, it is better to use the paraffin block itself, while for μFTIR or μRaman experiments sectioning of the block into several micrometer thick slices should be considered. Microtomography may be necessary to precisely locate the abnormal deposit in the block. The resultant section can be deposited on different supports for physicochemical characterization, such as conventional glass slides, low-e microscope slides (MirrIR, Kevley Technologies, Tienta Sciences, Indianapolis) or kapton® film. It is only possible to collect a Raman spectrum and to observe the sample by SEM using conventional glass slides. Low-e microscope slides enable imaging of surface topology by SEM, or chemical characterization with μRaman and μFTIR spectroscopies. Note that other supports have been considered in hospitals in order to perform TEM observations at the nanometer scale.

2.3. *Analysis of biological samples in a physics or chemistry laboratory*

In a physics or chemistry laboratory (Figures 4 and 5), characterization using prototype experimental set ups can be performed, which may combine optics, sample holders, or detectors, developed in the laboratory. Such experiments are usually not performed in a hospital environment because the instrumentation is expensive, and the techniques are not yet on the mainstream diagnostic analysis path. The sophisticated character of these prototype setups allows significantly improved spatial resolution and/or sensitivity relative to commercial instrumentation.

Special detectors on a TEM microscope (Figure 4B) allow nanometer scale elemental analysis by Nano-EDX as well as chemical analysis by EELS. Also, the experimental set up developed at the Laboratoire de Physiques des Solides combines a multilayer mirror and a high intensity rotating-anode generator delivering a well-defined beam (100 μm size) of sufficient intensity. Using a hybrid-pixel detector and a SDD detector, one can measure XRD and XRF signals respectively at the micrometer scale rapidly (time scale between 1 and 10 min depending on the sample) (Figure 4C).

Imaging of the topology of biopsies, deposited on low-e microscope slides and based on SEM observations and chemical characterization with μRaman and/or μFTIR spectroscopies, can be complemented by NanoIR [112–122]. NanoIR, for which two experimental configurations are possible, presents novel opportunities. The first configuration is associated with 500 nm spatial resolution and is based on a pump-probe architecture using two laser sources,

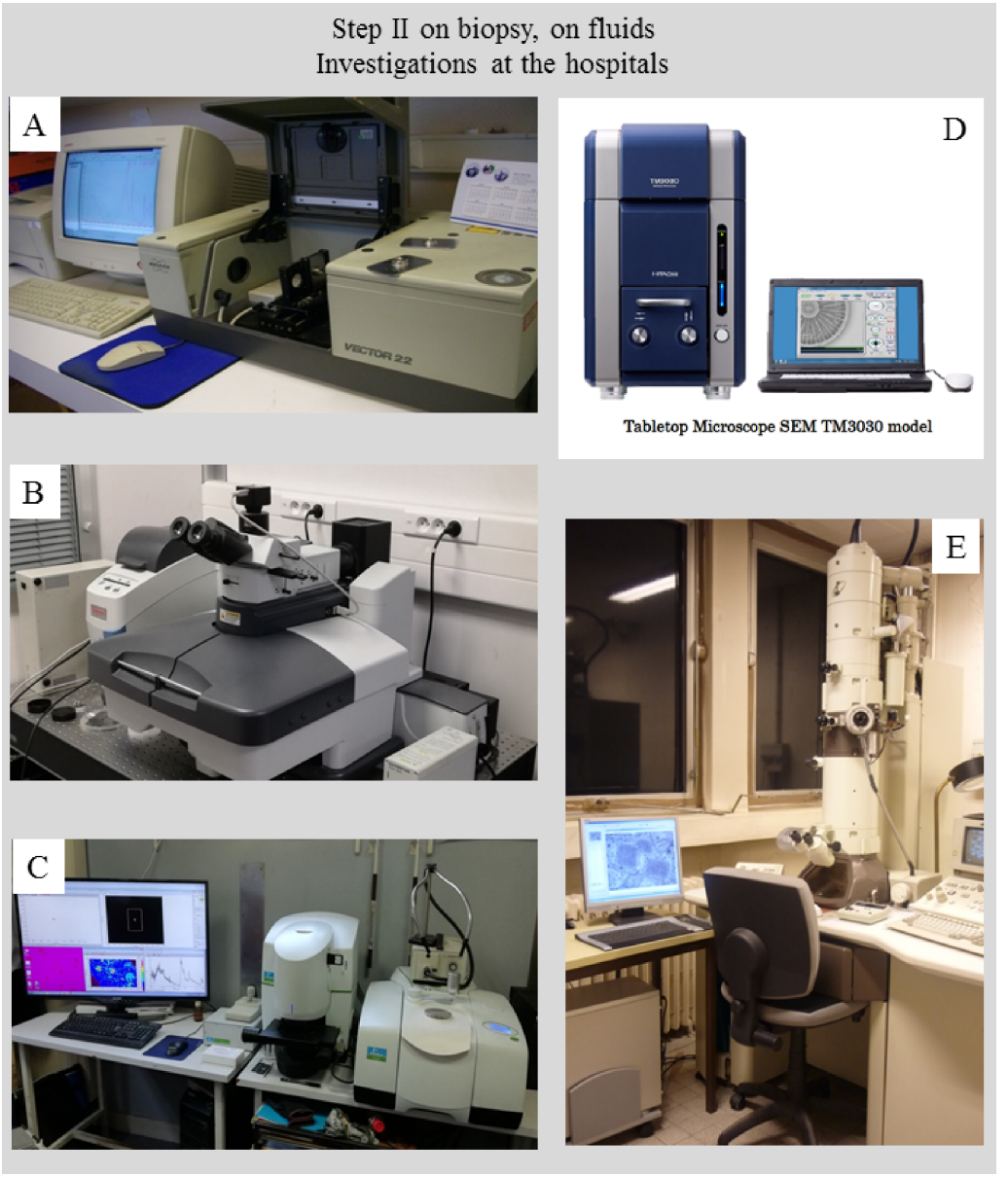

Figure 3. Tabletop commercial instruments (A) Classical FTIR experimental set up, (B) Raman experimental set up (implemented at the synchrotron SOLEIL), (C) μFTIR microscope implemented at the Service des Explorations Fonctionnelles at the Tenon Hospital, (D) Tabletop SEM (from https://www.hitachi-hightech), (E) TEM experimental set up implemented at the Tenon Hospital.

one for mid-infrared excitation (the pump) and the other one for measuring the photothermal effect (the probe) [112]. The second configuration combines an atomic force microscope (AFM) and IR lasers [115, 116] and produces a spatial resolution of 10 nm [122].

2.4. *Analysis of biological samples in a large scale facility*

The fourth and final step in a comprehensive analysis procedure uses characterization technology

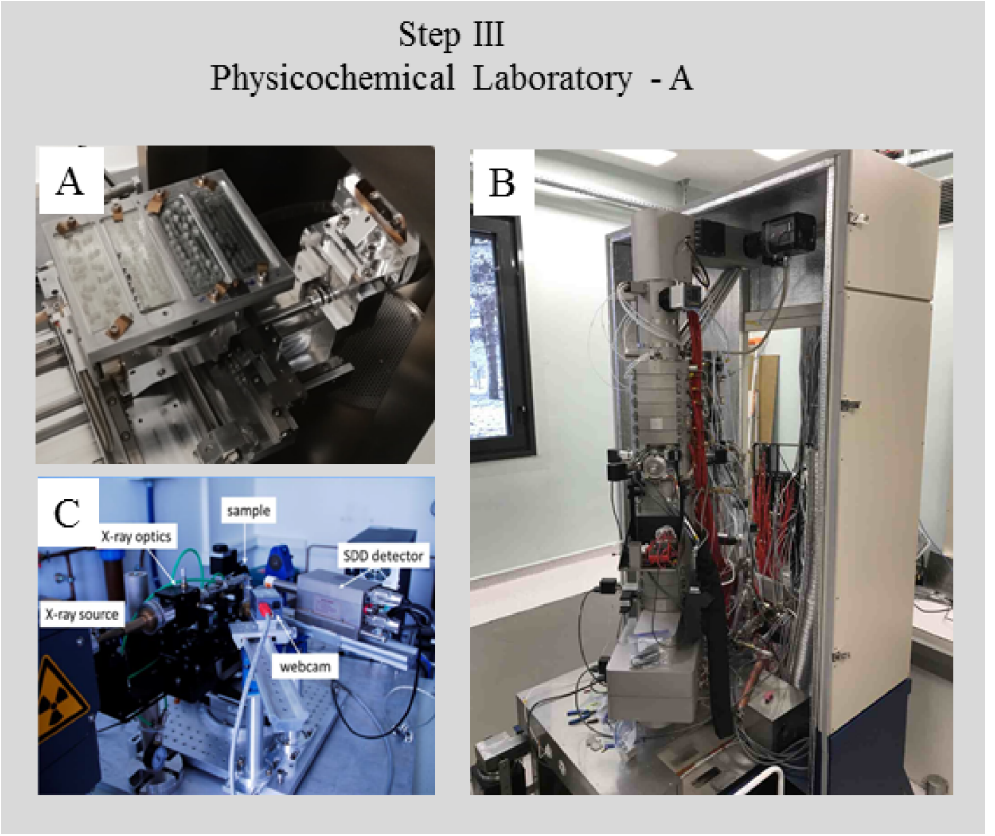

Figure 4. Forefront physics or chemistry laboratory characterization hardware, all located in the Laboratoire de Physique des Solides, Orsay. (A) SEM apparatus sample holder. (B) New transmission electron microscope. (C) An experimental device combining XRD and XRF capabilities.

usually (but not exclusively) specific to large scale instruments, which significantly increases sensitivity and/or in plane spatial resolution.

Synchrotron radiation as a submicrometer probe can be applied in several characterization techniques such as XRF or XRD. Synchrotron radiation is related to the emission of light when charged particles (electrons or positrons) moving with relativistic velocity undergo radial acceleration [123–126]. Among the important advantages of a synchrotron over a laboratory X-ray source are its large spectral range, and its brilliance (a physical characteristic encompassing the photon flux, bandwidth and the angular and lateral spread of the beam) which is more than a million times higher than that of the X-ray tube. Basically, the different beamlines on a synchrotron use a selected (but tunable) part of its energy spectrum, from terahertz to hard X-ray frequencies. This confers the advantage of being able to choose the energy of the incident beam during measurements. Two facilities are implemented in France namely SOLEIL (French national source) [127] and ESRF (European Source) [128].

van der Ent *et al.* [129] have compared different XRF approaches using either X-ray tubes, electron, proton, and synchrotron radiation as probes. While the spatial resolution of an experimental set up using a laboratory source is around 30–100 μm, it is possible to perform similar experiments on synchrotrons with a spatial resolution well below 1 μm, and down to about 50 or even 10 nm [130,131]. Also, there is a significant difference between the limits of detection which is >50 ppm in the case of a laboratory source and 0.1 ppm on synchrotron facilities. These detection limits depend intimately on the sample/matrix studied as well; the detection of heavy elements in

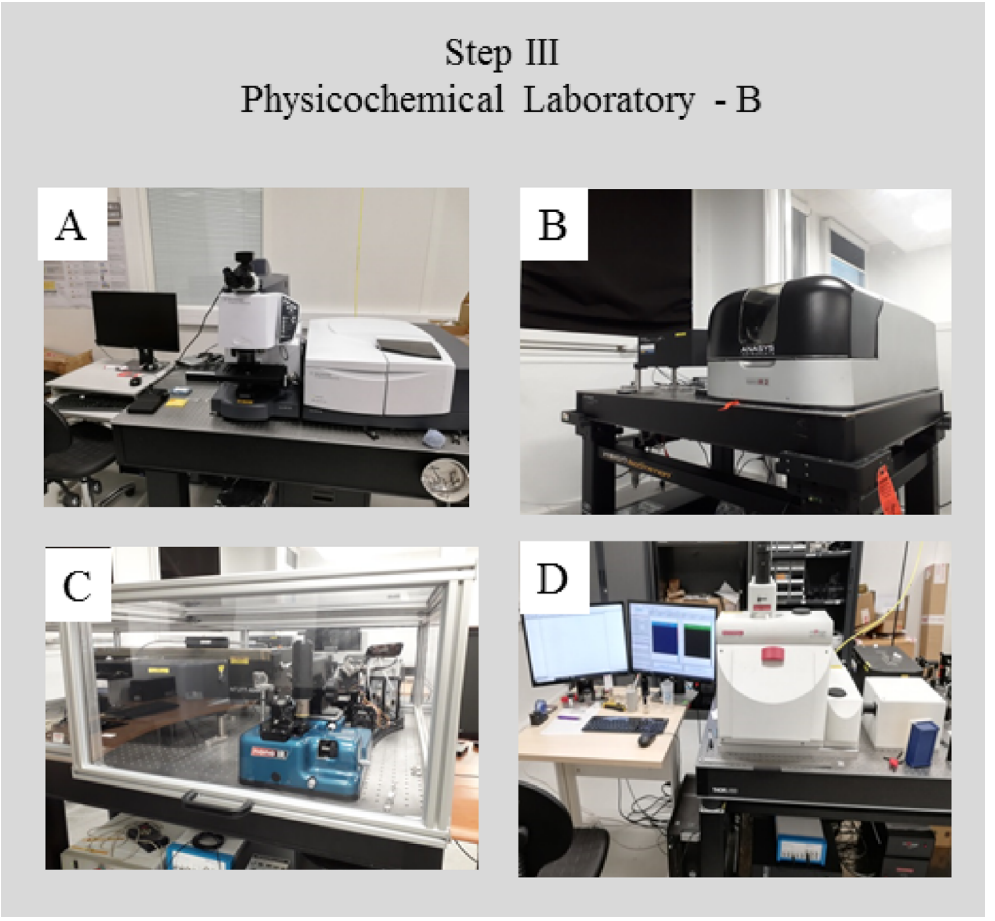

Figure 5. Characterization techniques available in a physics or chemistry laboratory (A) μFTIR spectrophotometer implemented at soleil (SMIS beamline); (B) and (C) AFMIR experimental set up implemented on the MUSIICS (MUlti Scale Infrared Imaging platform for Complex Systems, located at the institute of physics and chemistry) platform, (D) OPTIR (Optical PhotoThermal IR) experimental set up (SMIS beamline).

tissues is much more favourable than that of light elements in a matrix of heavy elements. Experimental optimization can improve the elemental detection limits to concentrations in the range 10^{-9} to 10^{-12} g/g [132,133].

A similar significant improvement pertains to X-ray scattering experiments. Implemented on synchrotron radiation facilities, these offer the opportunity of measurements on isolated and micrometer sized single crystals. Guo *et al.* [134] have shown that acquisition and assembly of complete datasets from microcrystals may be routinely carried out on synchrotron microdiffraction beamlines.

It is worth underlining that a complete new set of spectroscopies such as XAS [135,136] or UV visible spectroscopy [137–140] is available at a synchrotron radiation centre. XAS is form of spectroscopy able to describe the electronic state and the local environment of trace elements in different kinds of material including those without long range order such as nanoparticles [141–146] and amorphous compounds [147,148]. In a recent review, Ma *et al.* [149] highlighted the emergence of nanoparticles in medicine which offer novel solutions to diagnosis and treatment of chronic kidney disease.

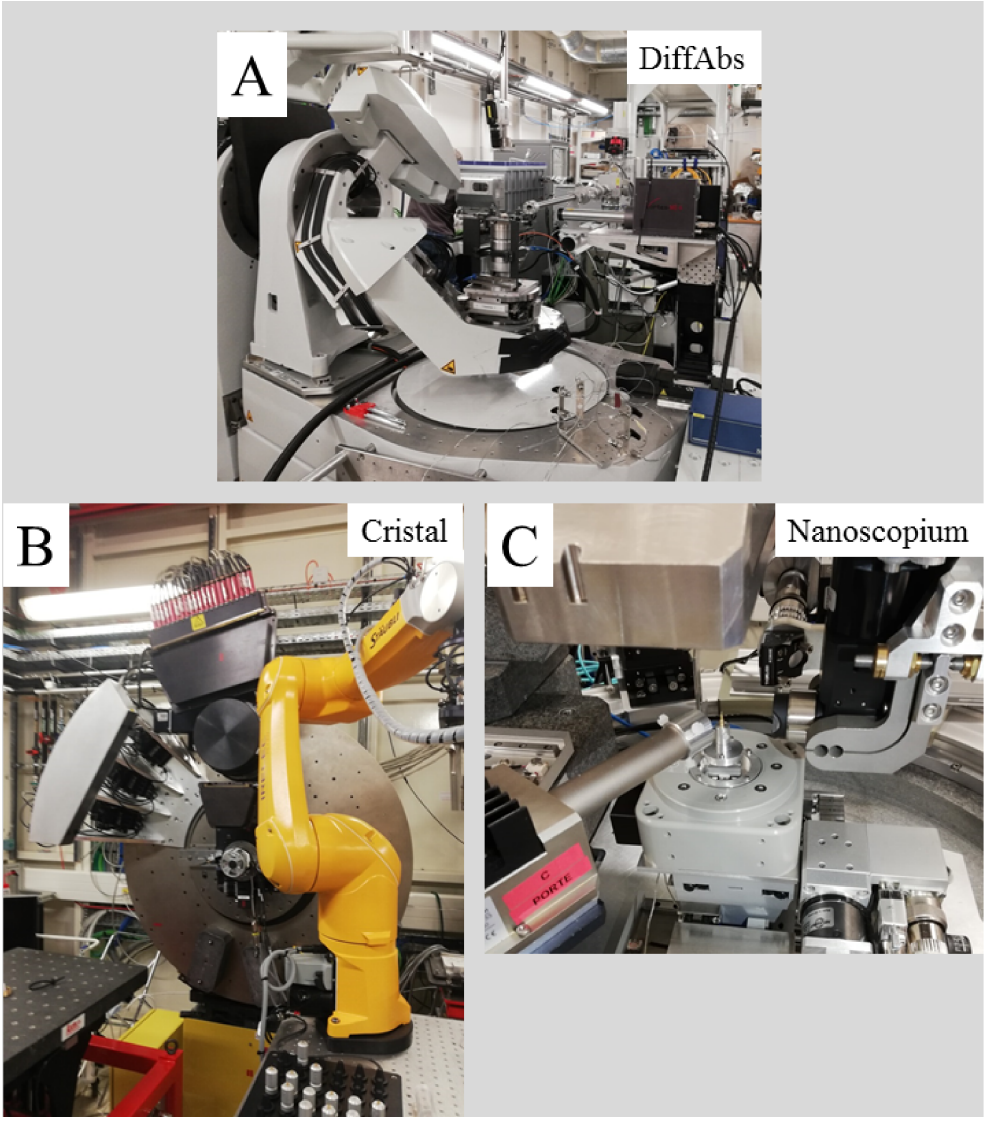

Figure 6. Three beamline experimental stations implemented on the Soleil synchrotron (A) Diffabs (details in Refs [82,83,149]), (B) Cristal (details in Refs [150–152]) and (C) Nanoscopium (details Ref. [153]).

As an example, we show in Figure 6 the different experimental beamlines we have used to characterize abnormal deposits in the human body namely Diffabs [85,86,150], Cristal [19,151] and Nanoscopium [154]. On these beamlines, XRD (Diffabs and Cristal), XAS (Diffabs) or nano-tomography (Nanoscopium) experiments can be performed. Note that other beamlines such asth the Disco beamline can be of major importance [140].

3. Sample quantity and availability

Sample quantity and availability can determine the order in which experiments are performed. Large quantities impose no priority but it must be emphasized that several scans may have to be performed several times to take possible heterogeneity into account. Obviously, if the quantity of sample is low, non-destructive characterization techniques have to be implemented first.

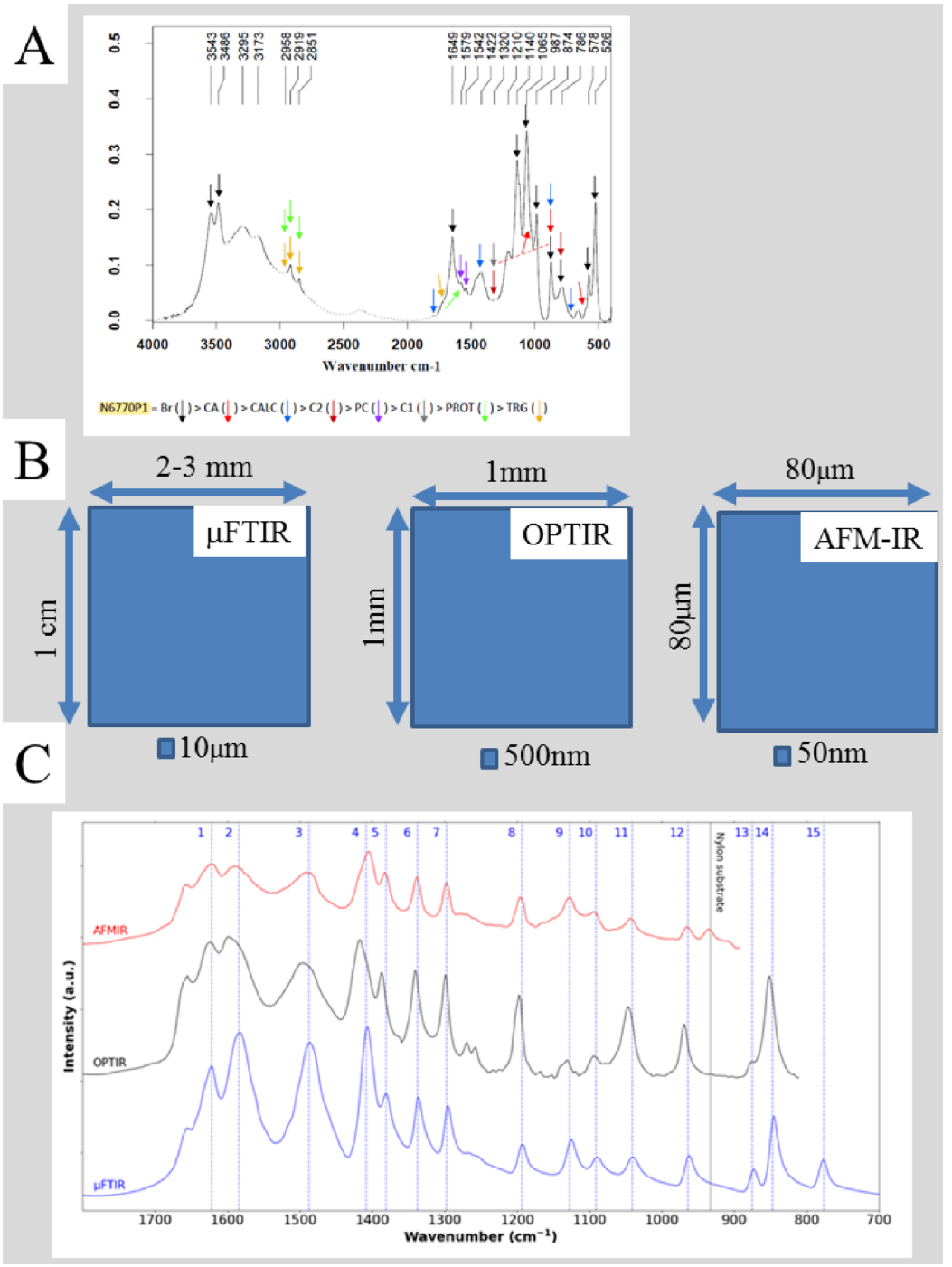

Figure 7. (A) Classical FTIR spectrum collected on part of a kidney stone dispersed in a KBr pellet; IR bands of various compounds present are indicated Br—brushite, CA—calcium phosphate apatite; CALC—calcite, C2—calcium oxalate dihydrate; PC—calcium palmitate; C1—calcium oxalate monohydrate, PROT—protein; TRG—triglycerides. (B) Typical dimensions of the maps which can be collected with µFTIR, OPTIR and AFMIR; the size of the probe for each is indicated. (C) Three IR spectra collected by the three experimental set ups—µFTIR (blue), OPTIR (black) and AFMIR (red).

Sometimes, sample quantity is simply insufficient to perform the experiments. For example, XRD experiments are performed on powder; the sample is typically inserted into a glass capillary (Ø = 0.1–1 mm) and mounted on a spinner rotating at several Hz to improve particle orientational averaging. Typically, for such experiments, less than 1 μL of powder is enclosed in small glass or kapton capillaries.

Another technique needing a relatively large amount of sample is Nuclear Magnetic Resonance (NMR) spectroscopy. In order to gather information regarding local structural changes we have to take into account that the volume of a typical widely used "standard" solid state NMR sample holder (a "magic angle spinning" rotor) in a NMR experiment is around 80 μL. Also, it is possible to probe the local environment of several elements namely ^{1}H, ^{13}C, ^{31}P.

4. Advantages and inconveniences of high spatial resolution

High spatial resolution experiments are not always the most desirable. Lower spatial resolution characterization can resolve many important clinical problems. We will examplify this by FTIR spectroscopy and the characterization of pathological renal calcification. In the case of kidney stones, several chemical compounds can be present in different proportions. Chemical compounds present at high abundance do not always define a medical diagnosis. Even a small proportion (5%) of struvite informs the clinician of bacterial infection. This factor imposes a requirement for an IR spectrum with a very high signal-to-noise ratio for there to be any possibility of detecting the presence of a small shoulder in the IR absorption bands or a small shift in their wavenumbers, which may help to distinguish up to 9 chemical compounds occurring in kidney stones.

It is very important to obtain a high quality IR spectrum from the core as well as the surface of kidney stones (Figure 7). Currently, only "classical" IR, in which measurements are performed on a small pellet, is capable of sufficiently high signal to noise. Also, high spatial resolution comes with characterization of only a small area of the sample. In the case of a kidney biopsy the calcification area can be somewhere within a length of typically around one centimetre and width 1 mm; it is clearly impractical to spend a few hours searching the whole sample for ectopic calcification at a μFTIR spatial resolution of 10 μm, or by NanoIR for which the area of interest is limited to 80 μm by 80 μm. Nevertheless, NanoIR experiments can represent the ultimate opportunity to determine chemical composition for very small deposits which cannot be characterized by μFTIR.

Finally, we must underline that polarization of the lasers used in NanoIR spectroscopy, either in the visible or the IR range, means that the intensity, and position of IR bands may vary, in the latter case by up to a few cm^{-1}. This can impose limitations on the precision of any description of abnormal biopsy deposit chemistry [122].

5. Conclusion

This paper proposes a hierarchical approach to characterize abnormal deposits in biological tissues [155], starting from *in vivo* measurements and progressing to a physicochemical description at the nanometer scale. The approach is based on a selected set of destructive and non-destructive characterization techniques which take into account the complexity of the physicochemistry of abnormal deposits in biological tissues, consistent with their exogenous and endogenous origins. Because some of these techniques need reference compounds such an approach supposes strong interactions with research teams able to generate nanomaterials [156–159]. Finally, it must be remembered that density functional theory [160,161] offers the opportunity to relate nanomaterial atomic structure to IR, Raman or XRD characteristics [162–166]. As emphasized by Khosroshahi *et al.* [167], it's time to use nanotechnology to change the conventional paradigm for analysis and diagnosis in cases of pathological deposits.

Conflicts of interest

Authors have no conflict of interest to declare.

References

[1] D. Bazin, M. Daudon, C. Combes, C. Rey, *Chem. Rev.*, 2012, **112**, 5092-5120.

[2] D. Bazin, M. Daudon, *J. Phys. D: Appl. Phys.*, 2012, **45**, article no. 383001.
[3] M. Daudon, D. Bazin, *J. Phys. Conf. Ser.*, 2013, **425**, article no. 022006.
[4] D. Bazin, M. Daudon, *J. Spectral Imaging*, 2019, **8**, article no. a16.
[5] H. Colboc, D. Bazin, P. Moguelet, S. Reguer, R. Amode, C. Jouanneau, I. Lucas, L. Deschamps, V. Descamps, N. Kluger, *J. Eur. Acad. Dermatol. Venereol.*, 2020, **34**, e313-e315.
[6] H. Colboc, D. Bazin, Ph. Moguelet, V. Frochot, R. Weil, E. Letavernier, Ch. Jouanneau, C. Frances, C. Bachmeyer, J.-F. Bernaudin, M. Daudon, *C. R. Chim.*, 2016, **19**, 1631-1641.
[7] H. Colboc, P. Moguelet, D. Bazin, C. Bachmeyer, V. Frochot, R. Weil, E. Letavernier, C. Jouanneau, M. Daudon, J. F. Bernaudin, *J. Eur. Acad. Dermatol. Venereol.*, 2019, **33**, 198-203.
[8] A. Dessombz, P. Méria, D. Bazin, M. Daudon, *PLoS One*, 2012, **7**, article no. e51691.
[9] A. Ben Lakhdar, M. Daudon, M. C. Matthieu, A. Kellum, C. Balleyguier, D. Bazin, *C. R. Chim.*, 2016, **19**, 1610-1624.
[10] J. A. M. R. Kunitake, S. Choi, K. X. Nguyen, M. M. Lee, F. He, D. Sudilovsky, P. G. Morris, M. S. Jochelson, C. A. Hudis, D. A. Muller, P. Fratzl, C. Fischbach, A. Masi, L. A. Estroff, *J. Struct. Biol.*, 2018, **202**, 25-34.
[11] K. S. Shin, M. Laohajaratsang, S. Men, B. Figueroa, S. M. Dintzis, D. Fu, *Theranostics*, 2020, **10**, 5865-5878.
[12] S. Gosling, D. Calabrese, J. Nallala, C. Greenwood, S. Pinder, L. King, J. Marks, D. Pinto, Th. Lynch, I. D. Lyburn, E. S. Hwang, Grand Challenge PRECISION Consortium, K. Rogers, N. Stone, *Analyst*, 2022, **147**, 1641-1654.
[13] S. Gosling, R. Scott, C. Greenwood, P. Bouzy, J. Nallala, I. D. Lyburn, N. Stone, K. Rogers, *J. Mammary Gland Biol. Neoplasia*, 2019, **24**, 333-342.
[14] X. Carpentier, M. Daudon, O. Traxer, P. Jungers, A. Mazouyes, G. Matzen, E. Véron, D. Bazin, *Urology*, 2009, **73**, 968-975.
[15] D. Bazin, G. André, R. Weil, G. Matzen, E. Véron, X. Carpentier, M. Daudon, *Urology*, 2012, **79**, 786-790.
[16] R. Flannigan, W. H. Choy, B. Chew, D. Lange, *Nat. Rev. Urol.*, 2014, **11**, 333-341.
[17] E. J. Espinosa-Ortiz, B. H. Eisner, D. Lange, R. Gerlach, *Nat. Rev. Urol.*, 2019, **16**, 35-53.
[18] M. Daudon, M. Petay, S. Vimont, A. Denizet, F. Tielens, J.-Ph. Haymann, E. Letavernier, V. Frochot, D. Bazin, *C. R. Chim.*, 2022, **25**, no. S1, 315-334, Online first.
[19] D. Bazin, R. J. Papoular, E. Elkaim, R. Weil, D. Thiaudière, C. Pisapia, B. Ménez, N. S. Hwang, F. Tielens, M. Livrozet, E. Bouderlique, J.-Ph. Haymann, E. Letavernier, L. Hennet, V. Frochot, M. Daudon, *C. R. Chim.*, 2022, **25**, no. S1, 343-354, Online first.
[20] E. N. Taylor, M. J. Stampfer, G. C. Curhan, *Kidney Int.*, 2005, **68**, 1230-1235.
[21] M. Daudon, B. Lacour, P. Jungers, *Nephrol. Dial. Transpl.*, 2005, **20**, 468-469.
[22] M. Daudon, E. Letavernier, R. Weil, E. Véron, G. Matzen, G. André, D. Bazin, *C. R. Chim.*, 2016, **19**, 1527-1534.
[23] M. Daudon, P. Jungers, D. Bazin, *New Engl. J. Med.*, 2008, **359**, 100-102.
[24] M. Daudon, P. Jungers, D. Bazin, *New Engl. J Med.*, 2009, **360**, 1680.
[25] A. Dessombz, E. Letavernier, J.-Ph. Haymann, D. Bazin, M. Daudon, *J. Urol.*, 2015, **193**, 1564-1569.
[26] F. Meiouet, S. El Kabbaj, M. Daudon, *C. R. Chim.*, 2022, **25**, no. S1, 281-293.
[27] D. Bazin, M. Daudon, P. Chevallier, S. Rouzière, E. Elkaim, D. Thiaudiere, B. Fayard, E. Foy, P. A. Albouy, G. André, G. Matzen, E. Véron, *Ann. Biol. Clin. (Paris)*, 2006, **64**, 125-139.
[28] D. Bazin, J.-Ph. Haymann, E. Letavernier, J. Rode, M. Daudon, *Presse Med.*, 2014, **43**, 135-148.
[29] D. Bazin, E. Letavernier, J.-P. Haymann, P. Méria, M. Daudon, *Prog. Urol.*, 2016, **26**, 608-618.
[30] D. Bazin, E. Letavernier, J.-Ph. Haymann, *C. R. Chim.*, 2016, **19**, 1395-1403.
[31] S. R. Mulay, H.-J. Anders, *N. Engl. J. Med.*, 2016, **374**, 2465-2476.
[32] D. Bazin, M. Daudon, "Nouvelles Méthodes d'étude des calculs et plaques de Randall", in *Actualités néphrologiques*, Ed. Médecine – Sciences, Flammarion, Paris, 2010, ISBN : 978–2–257–20409–7.
[33] M. Daudon, D. Bazin, "Application of physical methods to kidney stones and Randall's plaque characterization", in *Urolithiasis: Basic Science and Clinical Practice* (J. J. Talati, H. G. Tiselius, D. M. Albala, Z. Ye, eds.), Springer-Verlag, London, 2012, 683-707.
[34] L. N. Poloni, M. D. Ward, *Chem. Mater.*, 2014, **26**, 477-495.
[35] D. Bazin, Ch. Jouanneau, S. Bertazzo, Ch. Sandt, A. Dessombz, M. Réfrégiers, P. Dumas, J. Frederick, J.-Ph. Haymann, E. Letavernier, P. Ronco, M. Daudon, *C. R. Chim.*, 2016, **19**, 1439-1450.
[36] E. Tsolaki, S. Bertazzo, *Materials*, 2019, **12**, article no. 3126.
[37] D. Bazin, E. Letavernier, J. P. Haymann, V. Frochot, M. Daudon, *Ann. Biol. Clin.*, 2020, **78**, 349-362.
[38] N. Vidavsky, J. A. M. R. Kunitake, L. A. Estroff, *Adv. Healthc. Mater.*, 2021, **10**, article no. 2001271.
[39] D. Bazin, X. Carpentier, I. Brocheriou, P. Dorfmuller, S. Aubert, Ch. Chappard, D. Thiaudière, S. Reguer, G. Waychunas, P. Jungers, M. Daudon, *Biochimie*, 2009, **91**, 1294-1300.
[40] D. Bazin, C. Chappard, C. Combes, X. Carpentier, S. Rouzière, G. André, G. Matzen, M. Allix, D. Thiaudière, S. Reguer, P. Jungers, M. Daudon, *Osteoporos. Int.*, 2009, **20**, 1065-1075.
[41] Ch. Chappard, G. André, M. Daudon, D. Bazin, *C. R. Chim.*, 2016, **19**, 1625-1630.
[42] H. Colboc, J. Fontaine, D. Bazin, V. Frochot, E. Letavernier, M. Daudon, N. Laporte, S. Rouzière, M. Reby, A. Galezowski, Ch. Forasassi, S. Meaume, *J. Gerontol. A Biol. Sci. Med. Sci.*, 2022, **77**, 27-32.
[43] H. Colboc, Ph. Moguelet, E. Letavernier, V. Frochot, J.-F. Bernaudin, R. Weil, S. Rouzière, P. Senet, C. Bachmeyer, N. Laporte, I. Lucas, V. Descamps, R. Amode, F. Brunet-Possenti, N. Kluger, L. Deschamps, A. Dubois, S. Reguer, A. Somogyi, K. Medjoubi, M. Refregiers, M. Daudon, D. Bazin, *C. R. Chim.*, 2022, **25**, no. S1, 445-476.
[44] M. Mathonnet, A. Dessombz, D. Bazin, R. Weil, F. Triponez, M. Pusztaszeri, M. Daudon, *C. R. Chim.*, 2016, **19**, 1672-1678.
[45] J. Guerlain, S. Perie, M. Lefevre, J. Perez, S. Vandermeersch,

Ch. Jouanneau, L. Huguet, V. Frochot, E. Letavernier, R. Weil, S. Rouzière, D. Bazin, M. Daudon, J. P. Haymann, *PLoS One*, 2019, **14**, article no. e0224138.

[46] L. Henry, D. Bazin, C. Policar, J.-Ph. Haymann, M. Daudon, V. Frochot, M. Mathonnet, *C. R. Chim.*, 2022, **25**, no. S1, 503-515.

[47] A. Dessombz, P. Méria, D. Bazin, E. Foy, S. Rouzière, R. Weil, M. Daudon, *Prog. Urol.*, 2011, **21**, 940-945.

[48] M. Daudon, C. A. Bader, P. Jungers, *Scanning Microsc.*, 1993, **7**, 1081-1106.

[49] M. Daudon, P. Jungers, D. Bazin, *AIP Conf. Proc.*, 2008, **1049**, 199-215.

[50] M. Daudon, A. Dessombz, V. Frochot, E. Letavernier, J.-Ph. Haymann, P. Jungers, D. Bazin, *C. R. Chim.*, 2016, **19**, 1470-1491.

[51] M. Daudon, E. Letavernier, V. Frochot, J.-Ph. Haymann, D. Bazin, P. Jungers, *C. R. Chim.*, 2016, **19**, 1504-1513.

[52] C. Nguyen, H.-K. Ea, D. Bazin, M. Daudon, F. Lioté, *Arthritis Rheum.*, 2010, **62**, 2829-2830.

[53] H.-K. Ea, C. Nguyen, D. Bazin, A. Bianchi, J. Guicheux, P. Reboul, M. Daudon, F. Lioté, *Arthritis Rheum.*, 2010, **63**, 10-18.

[54] Ch. Nguyen, H. Korng Ea, D. Thiaudière, S. Reguer, D. Hannouche, M. Daudon, F. Lioté, D. Bazin, *J. Synchrotron Rad.*, 2011, **18**, 475-480.

[55] A. Gauffenic, D. Bazin, Ch. Combes, M. Daudon, H.-K. Ea, *C. R. Chim.*, 2022, **25**, no. S1, 517-534.

[56] M. Petay, M. Cherfan, A. Deniset-Besseau, E. Bouderlique, S. Reguer, A. Dazzi, J. Mathurin, M. Daudon, V. Frochot, J.-Ph. Haymann, E. Letavernier, D. Bazin, *C. R. Chim.*, 2022, **25**, no. S1, 553-576.

[57] Y. Li, D. G. Reid, D. Bazin, M. Daudon, M. J. Duer, *C. R. Chim.*, 2016, **19**, 1665-1671.

[58] C. J. Cros, D. Bazin, A. Kellum, V. Rebours, M. Daudon, *C. R. Chim.*, 2016, **19**, 1642-1664.

[59] S. Rouzière, D. Bazin, M. Daudon, *C. R. Chim.*, 2016, **19**, 1404-1415.

[60] D. Bazin, E. Foy, S. Reguer, S. Rouzière, B. Fayard, H. Colboc, J.-Ph. Haymann, M. Daudon, C. Mocuta, *C. R. Chim.*, 2022, **22**, no. S1, 165-188.

[61] D. Bazin, M. Daudon, *Ann. Biol. Clin.*, 2015, **73**, 517-534.

[62] D. Bazin, E. Bouderlique, M. Daudon, V. Frochot, J.-Ph. Haymann, E. Letavernier, F. Tielens, R. Weil, *C. R. Chim.*, 2022, **25**, no. S1, 37-60.

[63] N. Quy Dao, M. Daudon, *Infrared and Raman Spectra of Calculi*, Elsevier, Paris, 1997.

[64] M. Daudon, D. Bazin, *C. R. Chim.*, 2016, **19**, 1416-1423.

[65] V. Castiglione, P.-Y. Sacré, E. Cavalier, P. Hubert, R. Gadisseur, E. Ziemons, *PLoS One*, 2018, **13**, article no. e0201460.

[66] I. T. Lucas, D. Bazin, M. Daudon, *C. R. Chim.*, 2022, **25**, no. S1, 83-103.

[67] V. Sablinskas, S. Talmosaityte, M. Pucetaite, *C. R. Chim.*, 2022, **25**, no. S1, 73-82.

[68] V. Vuiblet, T. T. Nguyen, A. Wynckel, M. Fere, L. Van-Gulick, V. Untereiner, P. Birembaut, P. Rieu, O. Piot, *Analyst*, 2015, **140**, 7382-7390.

[69] A. Guinier, *Théorie et technique de la radiocristallographie*, Dunod, Paris, 1964.

[70] A. Le Bail, *Adv. X-Ray Anal.*, 2000, **42**, 191-203.

[71] F. Damay, D. Bazin, M. Daudon, G. André, *C. R. Chim.*, 2016, **19**, 1432-1434.

[72] D. Bazin, V. Frochot, J.-Ph. Haymann, E. Letavernier, M. Daudon, *C. R. Chim.*, 2022, **25**, no. S1, 133-147.

[73] Ph. Sciau, *Adv. Imaging Electron Phys.*, 2016, **198**, 43-67.

[74] S. J. Pennycook, M. F. Chisholm, A. R. Lupini, M. Varela, A. Y. Borisevich, M. P. Oxley, W. D. Luo, K. van Benthem, S.-H. Oh, D. L. Sales, S. I. Molina, J. García-Barriocanal, C. Leon, J. Santamaría, S. N. Rashkeev, S. T. Pantelides, *Phil. Trans. Math. Phys. Eng. Sci.*, 2009, **367**, 3709-3733.

[75] C. Verrier, D. Bazin, L. Huguet, O. Stéphan, A. Gloter, M.-Ch. Verpont, V. Frochot, J.-Ph. Haymann, I. Brocheriou, O. Traxer, M. Daudon, E. Letavernier, *J. Urol.*, 2016, **196**, 1566-1574.

[76] C. Gay, E. Letavernier, M.-Ch. Verpont, M. Walls, D. Bazin, M. Daudon, N. Nassif, O. Stephan, M. de Fruto, *ACS Nano*, 2020, **14**, 1823-1836.

[77] J. D. Boerckel, D. E. Mason, A. M. McDermott, E. Alsberg, *Stem Cell Res. Ther.*, 2014, **5**, article no. N0144.

[78] D. Bazin, C. Leroy, F. Tielens, Ch. Bonhomme, L. Bonhomme-Coury, F. Damay, D. Le Denmat, J. Sadoine, J. Rode, V. Frochot, E. Letavernier, J.-Ph. Haymann, M. Daudon, *C. R. Chim.*, 2016, **19**, 1492-1503.

[79] O. L. Katsamenis, M. Olding, J. A. Warner, D. S. Chatelet, M. G. Jones, G. G. Sgalla, B. Smit, O. J. Larkin, I. Haig, L. Richeldi, I. Sinclair, P. M. Lackie, Ph. Schneider, *Am. J. Pathol.*, 2019, **189**, 1608-1620.

[80] J. C. Williams Jr, J. E. Lingeman, M. Daudon, D. Bazin, *C. R. Chim.*, 2022, **25**, no. S1, 61-72.

[81] H. Hertz, *Ann. Physik*, 1887, **31**, 983-1000.

[82] K. Siegbahn *et al.*, *Nova Acta Regiae Soc. Sci. Ser. IV*, 1967, **20**, 1-15.

[83] F. S. Brigiano, D. Bazin, F. Tielens, *C. R. Chim.*, 2022, **25**, no. S1, 149-163.

[84] D. E. Sayers, E. A. Stern, F. W. Lytle, *Phys. Rev. Lett.*, 1971, **27**, 1204-1207.

[85] S. Reguer, C. Mocuta, D. Thiaudière, M. Daudon, D. Bazin, *C. R. Chim.*, 2016, **19**, 1424-1431.

[86] D. Bazin, S. Reguer, D. Vantelon, J.-Ph. Haymann, E. Letavernier, V. Frochot, M. Daudon, E. Esteve, H. Colboc, *C. R. Chim.*, 2022, **25**, no. S1, 189-208.

[87] R. F. Egerton, *Electron Energy-Loss Spectroscopy in the Electron Microscope*, Springer US, Boston, 2011.

[88] R. F. Egerton, *Rep. Prog. Phys.*, 2008, **72**, article no. 016502.

[89] H. Colas, L. Bonhomme-Coury, C. Diogo-Coelho, F. Tielens, F. Babonneau, C. Gervais, D. Bazin, D. Laurencin, M. Smith, J. V. Hanna, M. Daudon, C. Bonhomme, *Cryst. Eng. Commun.*, 2013, **15**, 8840-8847.

[90] A. Dessombz, G. Coulibaly, B. Kirakoya, R. W. Ouedraogo, A. Lengani, S. Rouzière, R. Weil, L. Picaut, L. Bonhomme, F. Babonneau, D. Bazin, M. Daudon, *C. R. Chim.*, 2016, **19**, 1573-1579.

[91] C. Leroy, L. Bonhomme-Coury, Ch. Gervais, F. Tielens, F. Babonneau, M. Daudon, D. Bazin, E. Letavernier, D. Laurencin, D. Iuga, J. Hanna, M. Smith, Ch. Bonhomme, *Magn. Reson.*, 2021, **2**, 1-13.

[92] AFCA Insider, "Evaluate Injuries With Portable Diagnostic X-ray From MinXray", 2022, https://insider.afca.com/

evaluate-injuries-with-portable-diagnostic-x-ray-from-minxray/.
[93] X. Zhang, A. J. Specht, E. Wells, M. G. Weisskopf, J. Weuve, L. H. Nie, *Sci. Total Environ.*, 2021, **753**, article no. 142351.
[94] Sheffield Dermatology Research, "Research".
[95] E. Guevara, J. C. Torres-Galván, M. G. Ramírez-Elías, C. Luevano-Contreras, F. J. González, *Biomed. Opt. Express*, 2018, **9**, 4998-5010.
[96] K. Eklund, R. Klefsgård, B. Ivarsson, M. Geijer, *Gerontology*, 2012, **58**, 107-111.
[97] J. Börjesson, M. Alpsten, S. Huang, R. Jonson, S. Mattsson, Ch. Thornberg, "In vivo X-ray fluorescence analysis with applications to platinum, gold and mercury in man — experiments, improvements, and patient measurements", in *Human Body Composition* (K. J. Ellis, J. D. Eastman, eds.), Basic Life Sciences, vol. 60, Springer, Boston, MA, 1993.
[98] R. Jonson, S. Mattsson, B. Unsgaard, *Phys. Med. Biol.*, 1988, **33**, 847-857.
[99] L. Brancaleon, M. P. Bamberg, T. Sakamaki, N. Kollias, *J. Invest. Dermatol.*, 2001, **116**, 380-386.
[100] A. P. M. Michel, S. Liakat, K. Bors, C. F. Gmach, *Biomed. Opt. Express.*, 2013, **4**, 520-530.
[101] A. Bauer, O. Hertzberg, A. Küderle, D. Strobel, M. A. Pleitez, W. Mäntele, *J. Biophotonics*, 2018, **11**, article no. e201600261.
[102] Y. Yarovoy, D. M. Drutis, Th. M. Hancewicz, U. Garczarek, K. P. Ananthapadmanabhan, M. Misra, *Appl. Spectrosc.*, 2019, **73**, 182-194.
[103] P. J. Caspers, G. W. Lucassen, R. Wolthuis, H. A. Bruining, G. J. Puppels, *Biospectroscopy*, 1998, **4**, S31-S39.
[104] P. J. Caspers, G. W. Lucassen, G. J. Puppels, *Biophys. J.*, 2003, **85**, 572-580.
[105] H. Lui, J. Zhao, D. McLean, H. Zeng, *Cancer Res.*, 2012, **72**, 2491-2500.
[106] A. Le Bail, D. Bazin, M. Daudon, A. Brochot, V. Robbez-Masson, V. Maisonneuve, *Acta Cryst. B*, 2009, **65**, 350-354.
[107] M. Daudon, D. Bazin, K. Adil, A. Le Bail, *Acta Cryst. E*, 2011, **67**, article no. 1458.
[108] U. Holzwarth, N. Gibson, *Nat. Nanotechnol.*, 2011, **6**, article no. 534.
[109] K. Wilkinson, J. Lundkvist, G. Seisenbaeva, V. Kessler, *Environ. Pollut.*, 2011, **159**, 311-318.
[110] M. C. Mahoney, M. S. Newell, *Radiology*, 2013, **268**, 12-24.
[111] R. N. Uppot, M. G. Harisinghani, D. A. Gervais, *Am. J. Roentgenol.*, 2010, **194**, 1443-1449.
[112] D. Fournier, F. Lepoutre, A. Boccara, *J. Phys.*, 1983, **44**, 479-482.
[113] N. Baden, H. Kobayashi, N. Urayama, *Int. J. Polym. Anal. Charact.*, 2020, **25**, 1-7.
[114] A. J. Wang, E. P. Dillon, S. Maharjan, K.-S. Liao, B. P. McElhenny, T. Tong, S. Chen, J. Bao, S. A. Curran, *Adv. Mater. Interfaces*, 2021, **8**, article no. 2001720.
[115] A. Dazzi, F. Glotin, R. Carminati, *J. Appl. Phys.*, 2010, **107**, article no. 124519.
[116] A. Dazzi, C. B. Prater, *Chem. Rev.*, 2017, **117**, 5146-5173.
[117] L. Bildstein, A. Deniset-Besseau, I. Pasini, Ch. Mazilier, Y. W. Keuong, A. Dazzi, N. Baghdadli, *Anal. Chem.*, 2020, **92**, 11498-11504.
[118] G. Latour, L. Robinet, A. Dazzi, F. Portier, A. Deniset-Besseau, M.-C. Schanne-Klein, *Sci. Rep.*, 2016, **6**, article no. 26344.
[119] E. Esteve, Y. Luque, J. Waeytens, D. Bazin, L. Mesnard, Ch. Jouanneau, P. Ronco, A. Dazzi, M. Daudon, A. Deniset-Besseau, *Anal. Chem.*, 2020, **92**, 7388-7392.
[120] D. Bazin, M. Rabant, J. Mathurin, M. Petay, A. Deniset-Besseau, A. Dazzi, Y. Su, E. P. Hessouc, F. Tielens, F. Borondic, M. Livrozet, E. Boudelicque, J.-Ph. Haymann, E. Letavernier, V. Frochot, M. Daudon, *C. R. Chim.*, 2022, **25**, no. S1, 489-502.
[121] D. Bazin, E. Bouderlique, E. Tang, M. Daudon, J.-Ph. Haymann, V. Frochot, E. Letavernier, E. Van de Perre, J. C. Williams Jr., J. E. Lingeman, F. Borondics, *C. R. Chim.*, 2022, **25**, no. S1, 105-131.
[122] J. Mathurin, A. Deniset-Besseau, D. Bazin, E. Dartois, M. Wagner, A. Dazzi, *J. Appl. Phys.*, 2022, **131**, article no. 010901.
[123] N. Al Harbi, S. Y. Lee, *Rev. Scientific Instrum.*, 2003, **74**, article no. 2540.
[124] W. Thomlinson, P. Suortti, D. Chapman, *Nucl. Instrum. Methods Phys. Res. Sect. A*, 2005, **543**, 288-296.
[125] H. Elleaume, S. Fiedler, B. Bertrand, T. Brochard, F. Estève, J. F. Le Bas, G. Le Duc, C. Nemoz, M. Renier, P. Suortti, W. Thomlinson, *Phys. Med. Biol.*, 2000, **45**, L39-L43.
[126] S. Bayat, G. Le Duc, L. Porra, G. Berruyer, C. Nemoz, S. Monfraix, S. Fiedler, W. Thomlinson, P. Suortti, C. G. Standert-skjold Nordenstam, A. R. A. Sovijarvi, *Phys. Med. Biol.*, 2001, **46**, 3287-3299.
[127] Synchrotron-Soleil, https://www.synchrotron-soleil.fr/fr.
[128] A. Laissue, H. Blattmann, M. Di Michiel, D. N. Slatkin, N. Lyubimova, R. Guzman, W. Zimmermann, S. Birrer, T. Bley, P. Kircher, R. Stettler, R. Fatzer, A. Jaggy, H. M. Smilowitz, E. Brauer, A. Bravin, G. Le Duc, C. Nemoz, M. Renier, W. Thomlinson, J. Stepanek, H.-P. Wagner, *Proc. SPIE*, 2001, **4508**, 65-73.
[129] A. van der Ent, W. J. Przybyłowicz, M. D. de Jonge, H. H. Harris, Ch. G. Ryan, G. Tylko, D. J. Paterson, A. D. Barnabas, P. M. Kopittke, J. Mesjasz-Przybyłowicz, *New Phytol.*, 2018, **218**, 432-452.
[130] Y. S. Chu, J. M. Yi, F. De Carlo, Q. Shen, W. K. Lee, H. J. Wu, C. L. Wang, J. Y. Wang, C. J. Liu, C. H. Wang, S. R. Wu, C. C. Chien, Y. Hwu, A. Tkachuk, W. Yun, M. Feser, K. S. Liang, C. S. Yang, J. H. Je, G. Margaritondo, *Appl. Phys. Lett.*, 2008, **92**, article no. 103119.
[131] X. Huang, H. Yan, E. Nazaretski, R. Conley, N. Bouet, J. Zhou, K. Lauer, L. Li, D. Eom, D. Legnini, R. Harder, I. K. Robinson, Y. S. Chu, *Sci. Rep.*, 2013, **3**, article no. 3562.
[132] M. R. Gherase, D. E. B. Fleming, *Crystals*, 2020, **10**, article no. 12.
[133] M. J. Pushie, I. J. Pickering, M. Korbas, M. J. Hackett, G. N. George, *Chem. Rev.*, 2014, **114**, 8499-8541.
[134] G. Guo, M. R. Fuchs, W. Shi, J. Skinner, E. Berman, C. M. Ogata, W. A. Hendrickson, S. McSweeneya, Q. Liu, *IUCrJ*, 2018, **5**, 238-246.
[135] D. E. Sayers, F. W. Lytle, E. A. Stern, *Adv. X-Ray Anal.*, 1970, **13**, 248-271.
[136] E. A. Stern, D. E. Sayers, F. W. Lytle, *Phys. Rev. B*, 1975, **11**, 4836-4946.
[137] F. Jamme, S. Kascakova, S. Villette, F. Allouche, S. Pallu, V. Rouam, M. Réfrégiers, *Biol. Cell.*, 2013, **105**, 277-288.
[138] F. Jamme, S. Villette, A. Giuliani, V. Rouam, F. Wien, B. Lagarde, M. Réfrégiers, *Microsc. Microanal.*, 2010, **16**, 507-514.

[139] E. Esteve, C. Jouanneau, E. Letavernier, P. Ronco, M. Daudon, D. Bazin, M. Refregiers, *Néphrol. Thér.*, 2015, **11**, 279-280.
[140] E. Estève, D. Buob, F. Jamme, Ch. Jouanneau, S. Kascakova, J. Ph. Haymann, E. Letavernier, L. Galmiche, P. Ronco, M. Daudon, D. Bazin, M. Réfrégiers, *J. Synchrotron Radiat.*, 2022, **29**, 214-223.
[141] J. Moonen, J. Slot, L. Lefferts, D. Bazin, H. Dexpert, *Phys. B*, 1995, **208**, 689-690.
[142] D. Bazin, D. Sayers, J. Rehr, *J. Phys. Chem. B*, 1997, **101**, 11040-11050.
[143] D. Bazin, D. Sayers, J. J. Rehr, C. Mottet, *J. Phys. Chem.*, 1997, **101**, 5332-5336.
[144] D. Bazin, J. Rehr, *J. Phys. Chem. C*, 2003, **107**, 12398-12402.
[145] D. Bazin, J. Rehr, *J. Phys. Chem. C*, 2011, **115**, 23233-23236.
[146] D. Bazin, J. Lynch, M. Ramos-Fernandez, *Oil Gas Sci. Technol. – Rev. IFP*, 2003, **58**, 667-683.
[147] D. Sayers, M. Paesler, *J. Phys.*, 1986, **47**, 349-356.
[148] R. Bellissent, A. Chenevas, P. Lagarde, D. Bazin, D. Raoux, *J. Non-Cryst. Solids*, 1983, **59**, 237-240.
[149] Y. Ma, F. Cai, Y. Li, J. Chen, F. Hana, W. Lin, *Bioact. Mater.*, 2020, **5**, 732-743.
[150] E. Esteve, S. Reguer, C. Boissière, C. Chanéac, G. Lugo, Ch. Jouanneau, C. Mocuta, D. Thiaudière, N. Leclercq, B. Leyh, J.-F. Greisch, J. Berthault, M. Daudon, P. Ronco, D. Bazin, *J. Synchrotron Radiat.*, 2017, **24**, 991-999.
[151] D. Bazin, M. Daudon, E. Elkaim, A. Le Bail, L. Smrcok, *C. R. Chim.*, 2016, **19**, 1535-1541.
[152] P. Gras, C. Rey, G. André, C. Charvillat, S. Sarda, C. Combes, *Acta Crystallogr. B*, 2016, **72**, 96-101.
[153] A. Somogyi, K. Medjoubi, G. Baranton, V. Le Roux, M. Ribbens, F. Polack, P. Philippot, J. P. Samama, *J. Synchrotron Radiat.*, 2015, **22**, 1118-1129.
[154] F. Brunet-Possenti, L. Deschamps, H. Colboc, A. Somogyi, K. Medjoubi, D. Bazin, V. Descamps, *J. Eur. Acad. Dermatol. Venereol.*, 2018, **32**, e442-e443.
[155] D. Bazin, *C. R. Chim.*, 2022, **25**, no. S3, Forthcoming.
[156] C. Rey, C. Combes, C. Drouet, A. Lebugle, H. Sfihi, A. Barroug, *Mater. Sci. Eng. Technol.*, 2007, **38**, 996-1002.
[157] C. Drouet, C. Rey, in *Nanostructured Biomaterials for Regenerative Medicine* (V. Guarino, M. Iafisco, S. Srpiano, eds.), Woodhead Publishing Series in Biomaterials, Elsevier, Duxford, UK, 2020, 223-254.
[158] C. Rey, C. Combes, C. Drouet, H. Sfihi, A. Barroug, *Mater. Sci. Eng. C*, 2007, **27**, 198-205.
[159] C. Combes, C. Rey, *Minerals*, 2016, **6**, article no. 34.
[160] F. Tielens, J. Vekeman, D. Bazin, M. Daudon, *C. R. Chim.*, 2022, **25**, no. S1, 209-218.
[161] D. Bazin, J. Vekeman, Q. Wang, X. Deraet, F. De Proft, H. Guesmi, F. Tielens, *C. R. Chim.*, 2022, **25**, no. S3, Online first.
[162] I. Petit, G. D. Belletti, Th. Debroise, M. J. Llansola-Portoles, I. T. Lucas, C. Leroy, Ch. Bonhomme, L. Bonhomme-Coury, D. Bazin, M. Daudon, E. Letavernier, J. Ph. Haymann, V. Frochot, F. Babonneau, P. Quaino, F. Tielens, *ChemistrySelect*, 2018, **3**, 8801-8812.
[163] Th. Debroise, E. Colombo, G. Belletti, J. Vekeman, Y. Su, R. Papoular, N. S. Hwang, D. Bazin, M. Daudon, P. Quaino, F. Tielens, *Cryst. Growth Des.*, 2020, **20**, 2553-2561.
[164] D. Bazin, F. Tielens, *Appl. Catal.*, 2015, **504**, 631-641.
[165] F. Tielens, D. Bazin, *C. R. Chim.*, 2018, **21**, 174-181.
[166] I. C. Oğuz, H. Guesmi, D. Bazin, F. Tielens, *J. Phys. Chem. C*, 2019, **123**, 20314-20318.
[167] H. T. Khosroshahi, B. Abedi, S. Daneshvar, Y. Sarbaz, A. S. Bavil, *Int. J. Biomed. Imaging*, 2017, **2017**, article no. 6141734.

Comptes Rendus
Chimie
2022, Vol. 25, Special Issue S1, p. 235-245
https://doi.org/10.5802/crchim.140

Microcrystalline pathologies: Clinical issues and nanochemistry / *Pathologies microcristallines : questions cliniques et nanochimie*

10,000 urinary stones for 10 years of analysis: a retrospective study in western Switzerland

Christine Deffert [*, a, b], **Catherine Stoermann Chopard** [c] **and Nathalie Lambeng** [a]

[a] Laboratory of Biological Fluids, Laboratory Medicine Division, Diagnostic Department, Geneva University Hospitals, 1211 Geneva, Switzerland

[b] Laboratory Medicine Division, Department of Medical Specialties, Faculty of Medicine, University of Geneva, 1206 Geneva, Switzerland

[c] Department of Nephrology, HUG, University Hospital Geneva, University of Geneva, Geneva, Switzerland

E-mails: Christine.deffert@hcuge.ch (C. Deffert), Catherine.Stoermann@hcuge.ch (C. Stoermann Chopard), nathalie.lambeng@hcuge.ch (N. Lambeng)

Abstract. Several studies have reported a worldwide increase in incidence and prevalence of nephrolithiasis, with some specificities across countries and regions. A retrospective review was performed on all urinary calculi submitted between 2009 and 2019 from a large part of the western Switzerland to our laboratory. A total of 10,437 stones were analysed and the presence of 18,804 compounds revealed. The median age of patients was 51 years and the global male-to-female ratio was 2.49:1. From 2009 to 2019, calcium oxalates containing calculi were the most frequent, followed by calcium phosphate and uric acids, the latter being more common in men, whereas carbapatite was the second most frequent component in women. Infection stone frequency remained unchanged and low, with a higher rate for women. Finally, while Randall's plaque frequency was relatively small (7.4%), patients experiencing them were significantly younger. In this review, we identified an age and gender relationship of stone composition and Randall's plaque formation in our Swiss region, which paves the way for future investigations.

Keywords. Stone composition, Nephrolithiasis, Randall's plaque, Gender, Age groups, Switzerland.

Published online: 18 January 2022, Issue date: 1 September 2022

1. Introduction

Nephrolithiasis is a frequent urologic diseases affecting more than 10% of the population, with a peak of incidence between 40 and 60 years [1,2]. Combining with a high percentage of recurrence, from 40% to 50% within ten years [3,4], this pathology has particular social and economic implications [5]. While some genetic predispositions lead to particular type of stones, life and dietary habits largely contribute to renal stone formation (review in [6,7]). Identifying the nephrolithiasis risk factors that are sometimes specific to a region or a country is of particular interest for the patients' treatment. In Switzerland there is ongoing research to improve the understanding of nephrolithiasis (Swiss Kidney Stone Cohort) [8],

* Corresponding author.

but until now, few epidemiological data are available on the demographic information of Swiss patients suffering from this pathology as well as on the composition of their calculi. The Laboratory of Biological Fluids at the Geneva University Hospitals in Switzerland receives for analysis calculi from a large part of the west of the country. The objective of this study was to take advantage of our database containing the results of 10,437 stone analyses gathered between 2009 and 2019 to investigate a possible association of gender and age with calculi composition, determine any emerging trends in stone formation, and draw a picture of nephrolithiasis in the Romandie part of Switzerland.

2. Methods

The Laboratory of Biological Fluids at the Geneva University Hospitals processes analysis of calculi received from Geneva, Vaud, Neuchatel and Valais cantons that are located in the Romandie part of Switzerland. Request analyses were received from either independent private laboratories or hospitals such as the University Hospitals of Lausanne or Geneva. A retrospective review was performed of all stones examined in our laboratory from the years 2009 to 2019. Starting from a database of 10,609 calculi collected, a total of 10,437 renal stones were selected and associated with patient's demographic information such as age and sex. These calculi were obtained by spontaneous passage, ureteroscopy, percutaneous nephrolithotomy or shockwave lithotripsy.

Stone composition was determined by morphologic examination combined with Fourier-Transformed infrared (FTIR) spectroscopy. More precisely, FTIR analysis was performed on powdered samples of the different parts of each stone by Spectrum 100 from Perkin Elmer Life (Shelton, USA) combined with an ATR accessory (Specac, Orpington, UK). The spectra were collected in the 4000–540 cm^{-1} mid infrared range at a resolution of 4 cm^{-1} with eight scans. Each spectrum was analysed by the Spectrum software (Perkin Elmer Life, Shelton, USA) and the proportion of each component was assessed. Minor components accounting for less than 5% (e.g. proteins and mucopolysaccharides) of the stone were neglected except carbapatite in Randall's plaque.

The data were analysed with GraphPad prism software using the Mann–Whitney test for comparison of age, and Chi-squared test for comparison of frequencies. Results with p value < 0.05 were considered as statistically significant.

3. Results

3.1. *Overall picture*

Between 2009 and 2019, 10,437 renal stone analyses were performed in our laboratory. The number of analysed calculi steadily increased, starting from 461 stones/year in 2009 to 1393 stones/year in 2019 (3-fold increase; Figure 1A). The male-to-female gender ratio was in favour of men (average of 2.49 ± 0.17), constant along the years and both gender contributed equally to the observed increase in the number of calculi (3.05-fold increase for women and 3.0 for men; not shown). The mean age at stone episode was 50.6 ± 11.3 years, and the difference between men and women age was statistically significant (52.3 ± 15.9 years for men and 49.8 ± 17.2 years for women ($p < 0.0001$)). Overall, the majority of patients had 41 to 60 years at stone episode (45%; Figure 1B), 26.1% had 61 to 80 years, and 20.4% had 26 to 40 years. Children ages 0 to 15 showed the lowest incidence of stone formation (1% of calculi), and patients aged 16 to 25 or above 80 years accounted for 4 and 3.8% of calculi, respectively.

The analysis of the 10,437 stones by morphological characterization and FTIR spectroscopy revealed the presence of 18,804 compounds. The majority of calculi were composed of one or two compounds (40.2% and 40.1%, respectively), but we identified at least three or more compounds in 19.7% of stones (Figure 1C). Calcium oxalates were the most frequent compounds (62.5%, Figure 1D), followed by calcium phosphates (21.9%) and uric acids (10.6%). Other identified compounds (4.9%) were urates, struvite, cystine, drugs and proteins.

3.2. *Stone composition*

3.2.1. *Calcium oxalate stones*

Calcium oxalate monohydrate (COM) was the most represented compound and found in 78.1% of stones, with a mean age of patients of 51.2 years (Table 1). Except for children below ten years, it was

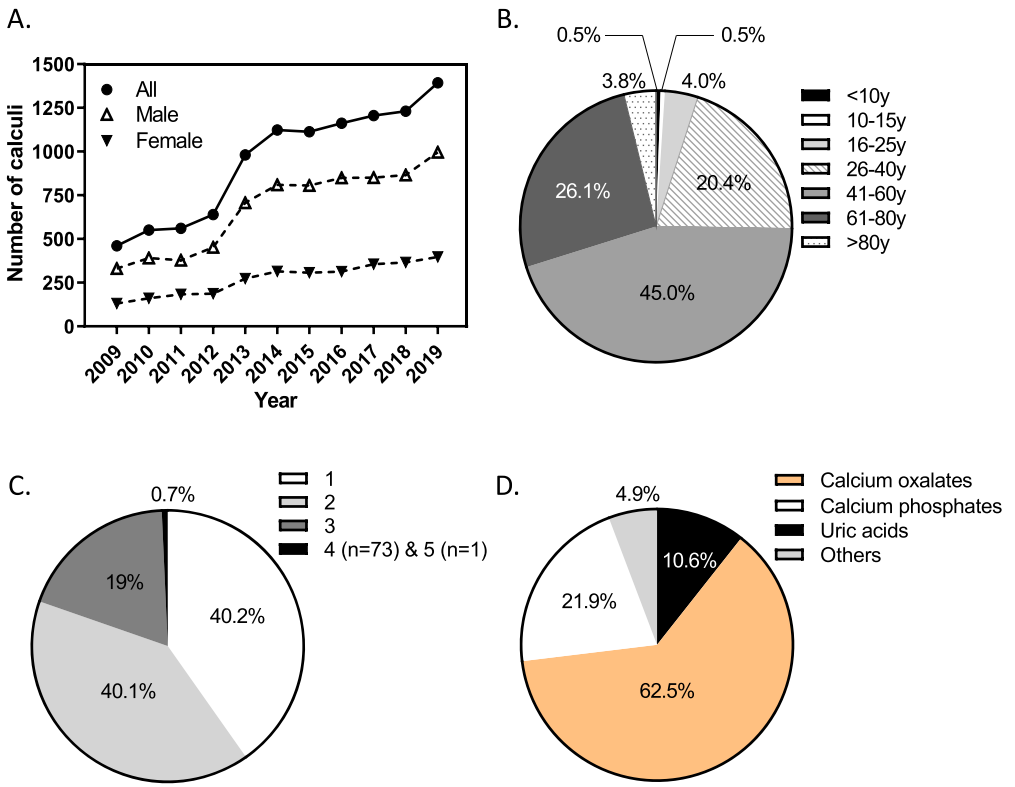

Figure 1. Stones from 2009 to 2019. (A) Number of stones by year of analysis and gender. (B) Repartition of stone episode by patient age groups. (C) Frequency of stones composed by 1, 2, 3 or more (4 or 5) components. (D) Frequency of calcium oxalates, calcium phosphates, uric acids (anhydrous uric acid and/or uric acid dihydrate), or other components (urates, struvite, cysteine, proteins, drugs) presence in all stones.

the most frequent compound in calculi whatever the gender and patient age (Table 1 and Figure 2). The mean age of women experiencing COM stones was significantly lower than that of men (49.5 versus 51.9 years, $p < 0.0001$).

Calcium oxalate dihydrate (COD) was less frequent and found in 34.4% of stones. It accounted for more than 50% of the stone in 11% of cases, with a significant higher frequency for men (11.8%) than women (8.9%, $p < 0.001$). The mean age of patients was younger (46.2 years) than for COM, regardless of sex (Table 1). In line with that, the highest COD frequency was observed for men aged 16–25 years and the presence of this compound in male stones appeared to increase between the age below ten years and 25 years before decreasing with age (Figure 2). In women, COD frequency peaked at age 10–15 years and lowered thereafter.

3.2.2. *Carbapatite stones*

Carbapatite was globally the second most frequent compound (38.1% of stones). It was mainly a minor compound, especially in men (Table 1), probably because it was the most frequent constituent of the Randall's plaque found on some calcium oxalate stones and in such cases, amounted for less than 5% of the stone. Carbapatite was the second most frequent component in adult women (Table 1 and Figure 2A) with a frequency of 51.6%, significantly higher than in men (32.7%) for whom it ranked only at the third place, after calcium oxalates. The lowest frequency was observed in girls aged 10–15 years, and in men it tended to decline with age as for COD (Figure 2).

Table 1. Distribution of urinary stones by composition

Compound	All				Women				Men			
	Total number	Frequency (%)	Age (mean, *y*)	Frequency as main component (%) (*n*)	Number	Frequency (%)	Age (mean ± SD, *y*)	Frequency as main component (%) (*n*)	Number	Frequency (%)	Age (mean ± SD, *y*)	Frequency as main component (%) (*n*)
COM	8152	78.1	51.2	61.0 (6366)	2364	79.0	49.5 ± 16.5	58.4 (1747)	5788	77.7	51.9 ± 15.0****	62 (4619)
Carbapatite	3978	38.1	47.6	11.1 (1162)	1543	51.6	47.6 ± 16.7	20.2 (603)	2435	32.7****	47.6 ± 16.2	7.5 (559)****
COD	3589	34.4	46.2	11.0 (1149)	1016	34.0	46.7 ± 17.2	8.9 (267)	2573	34.6	46.0 ± 14.5	11.8 (882)***
UA0	1413	13.5	61.7	10.5 (1094)	220	9.6	63.3 ± 13.9	5.3 (160)	1193	16.0****	61.4 ± 13.2*	12.5 (934)****
UA2	585	5.6	59.9	1.1 (118)	93	3.1	63.9 ± 13.5	0.5 (16)	492	6.6****	59.2 ± 13.0**	1.4 (102)***
STR	290	2.8	55.9	2.0 (212)	133	4.4	51.2 ± 21.4	3.3 (99)	157	2.1****	59.9 ± 21.9***	1.5 (113)****
BR	104	1.0	47.0	0.7 (76)	17	0.6	39.5 ± 14.1	0.5 (14)	87	1.2**	48.5 ± 14.5*	0.8 (62)*
UAM	94	0.9	49.2	0.4 (37)	32	1.1	46.6 ± 23.5	0.3 (8)	62	0.8	50.5 ± 28.3	0.4 (29)
UAS	67	0.6	54	0.1 (14)	8	0.3	70.1 ± 14.6	0.1 (4)	59	0.8**	51.8 ± 14.3**	0.1 (10)
Cystine	62	0.6	45.9	0.6 (62)	23	0.8	49.9 ± 19.5	0.8 (23)	39	0.5	43.6 ± 11.6	0.5 (39)
Drugs	15	0.1	55.5	0.1 (11)	2	0.07	66.5 ± 30.4	0.1 (2)	13	0.2	39 ± 12.0	0.1 (9)

COM: calcium oxalate monohydrate, COD: calcium oxalate dihydrate, UA0: anhydrous uric acid, UA2: uric acid dihydrate, STR: struvite, BR: brushite, UAM: ammonium hydrogen urate, UAS: sodium hydrogen urate, CYS: cysteine, Drugs: stones containing amoxicillin, atazanavir or 5-aminosalicyclic acid. Frequency (%): percentage of stones containing the compound. Frequency as main component: number of times (%) a component accounted for more than 50% of the stone in the whole series of 10,437 calculi. Comparison between men and women is statistically significant with **** $p < 0.0001$, *** $p < 0.001$, ** $p < 0.01$, * $p < 0.05$ (Mann–Whitney test for comparison of age and Chi-squared test for comparison of frequencies).

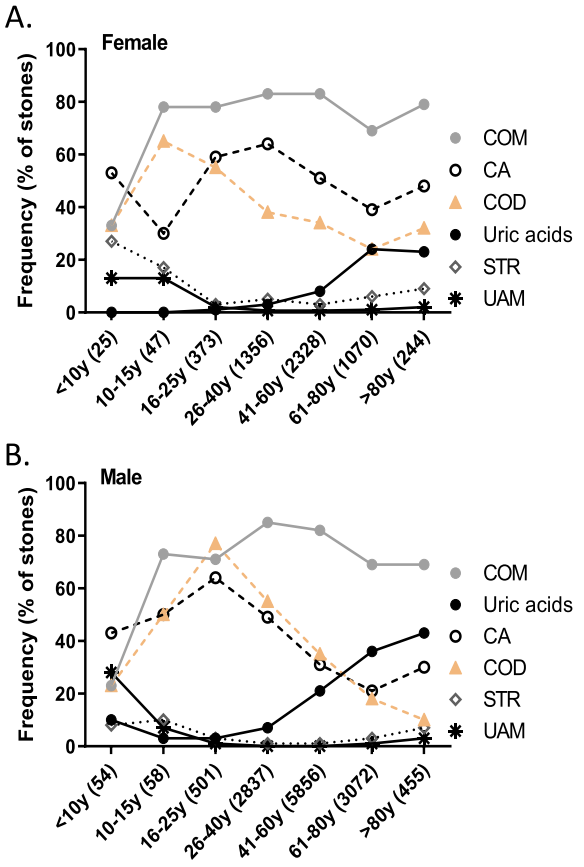

Figure 2. Component frequency by age groups and gender between 2009 and 2019.

3.2.3. *Uric acid stones*

Uric acids held the fourth place in compound frequency for both gender, reaching 13.5% for anhydrous uric acid (AU0) and 5.6% for uric acid dihydrate (AU2), with a mean age of patients of 61.7 and 59.9 years, respectively, which are the highest observed in our study (Table 1). Both type of uric acids were about twice more frequent for men than women ($p < 0.0001$, Table 1) and when it accounted for more than 50% of the stone, AU0 was the second most frequent compound for men (11% of cases) but only the fourth for women (5.3%, $p < 0.0001$), the latter being older when experiencing such calculi ($p < 0.05$ for AU0, and $p < 0.01$ for AU2). Finally, the number of uric acid stones increased with age, from the fourth decade in men but only from the sixth decade in women (Figure 2).

3.2.4. *Struvite stones*

Struvite (magnesium ammonium phosphate hexahydrate) was identified in 290 calculi (2.8% of stones; Table 1). More women than men experienced struvite calculi (4.4% and 2.1%, respectively, Table 1), with a frequency as main component also statistically different between gender (3.3% for women and 1.5% for men, $p < 0.0001$). The mean age of patient was also lower for women (51.2 versus 59.9 years, respectively; $p < 0.001$), and this was partly due to the age groups below 15 years who had the highest number of struvite calculi (Figure 2A).

3.2.5. *Brushite stones*

Brushite (dicalcium phosphate dihydrate) was identified in 104 stones (1.0% of stones; Table 1), more for men than women (1.2% and 0.6%, respectively, Table 1). The difference in the mean age of both gender (39.5 years for women and 48.5 for men) was statistically significant ($p < 0.05$).

3.2.6. *Other components*

Ammonium hydrogen or sodium hydrogen urates were present in 0.9 and 0.6% of calculi, respectively (Table 1), with a higher prevalence in younger men for the latter ($p < 0.01$, Table 1). Surprisingly, ammonium hydrogen urate was the second compound found for boys below 10 years, after calcium oxalate monohydrate, whereas it ranked at the fifth place for girls, after calcium oxalates and struvite (Figure 2).

Cystine calculi were rare: 62 from 35 patients in ten years, with a mean age of 45.9, higher in women than in men (49.9 versus 43.6 years). Cystine was the major compound in all cases.

Finally, we identified 15 stones made up of the drug atazanavir ($n = 13$, 11 patients, 1 woman and 10 men), amoxicillin (1 woman), or mesalazine (5-aminosalicylic acid, 1 man) crystals. No 2,8-dihydroxyadenine stone was detected.

3.3. *Evolution of age at stone episode*

For children below 15 years, the number of analysed calculi remained unchanged and low along the years (Figure 3). No clear evolution was observed between 2009 and 2019 for both gender at age 16–25. For men and women, the highest increase of number of stone analysed was observed for patients aged from 41 to

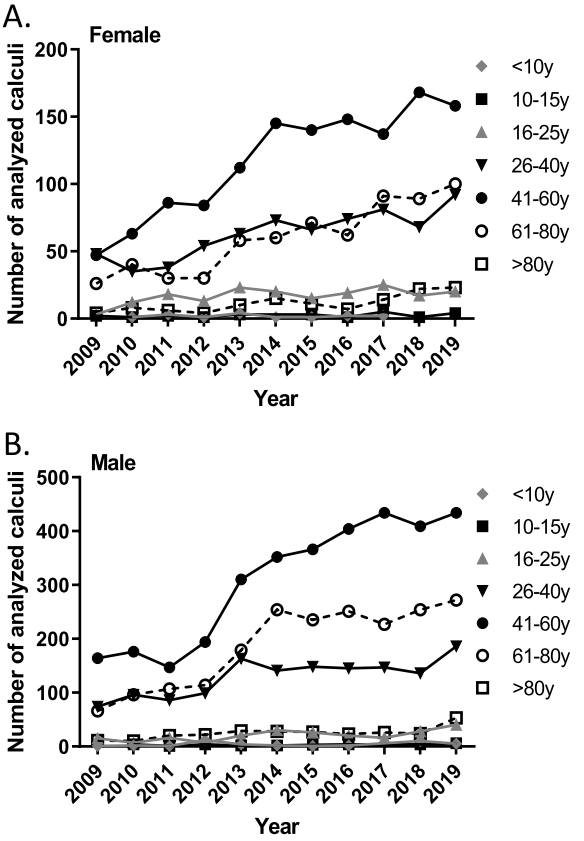

Figure 3. Number of stones by age groups and year of analysis.

60 years old (about 4-fold). This age group accounted for about half of the stones per year for men regardless of the year. Male patients of 26–40 and 61–80 years had also an increase in number of calculi, which was stronger for the latter (Figure 3B). On the contrary, the tendency of increase in stone numbers was similar for the same age groups in women (Figure 3A), but the proportion of stones for the 26–40 group age was higher than for men. Finally, all patients aged over 80 years showed also an increasing trend to have more stone episodes.

3.4. *Evolution of stone composition*

Overall no trends regarding a change in compound frequency were observed along the ten years (Figure 4), except for COD whose frequency increased along the years, particularly in women (23.1% to 47.4%; Figure 4A). Carbapatite frequency did not change, being always higher for women (Figure 4B). Anhydrous and dihydrate uric acids showed no clear tendency whatever the sex but were every year higher in men than in women (Figure 4C). Finally presence of struvite did not change along the years and was in general more frequent in women (Figure 4D).

Among the less common components, brushite had an increasing trend during the period of 2009 to 2019, especially in women (0% in 2009 to 1.3% in 2019, data not shown).

3.5. *Presence of Randall's plaque on calcium oxalate stones*

Randall's plaque (RP) is a calcium phosphate deposit at the tip of the renal papilla, considered to be at the origin of calcium oxalate stones [9]. In our laboratory, they were characterized or described only since 2015. Frequency of RP on 4829 COM-containing calculi was 7.4% irrespective of gender (Table 2). The composition of RP determined by FTIR was carbapatite in 86%, sodium urate in 6% and mixed in 1% of cases. In 7% of RP, the crystalline phase could not be identified. Only men had sodium urate in Randall's plaque (data not shown). Patients with RP were significantly younger (mean age of 45.8 versus 52.4 years, $p < 0.0001$), and this was not influenced by sex. The age group of 26 to 40 years appeared to have the highest prevalence of RP, whereas children and patients over 60 years had the lowest number of stones with RP.

4. Discussion

Environmental factors account for a large part in the development of nephrolithiasis, making epidemiological studies of particular interest to identify means of action to decrease incidence and prevalence of this disease. This descriptive and retrospective study tried to enhance the understanding of the trend over ten years regarding the chemical components of urinary tract stones. It provides the largest series of stone analyses in Switzerland, with 18,804 compounds identified in 10,437 calculi from patients living in the west and French-speaking part of the country and gathered between 2009 and 2019. To our knowledge, no comparable series has yet been described in this country.

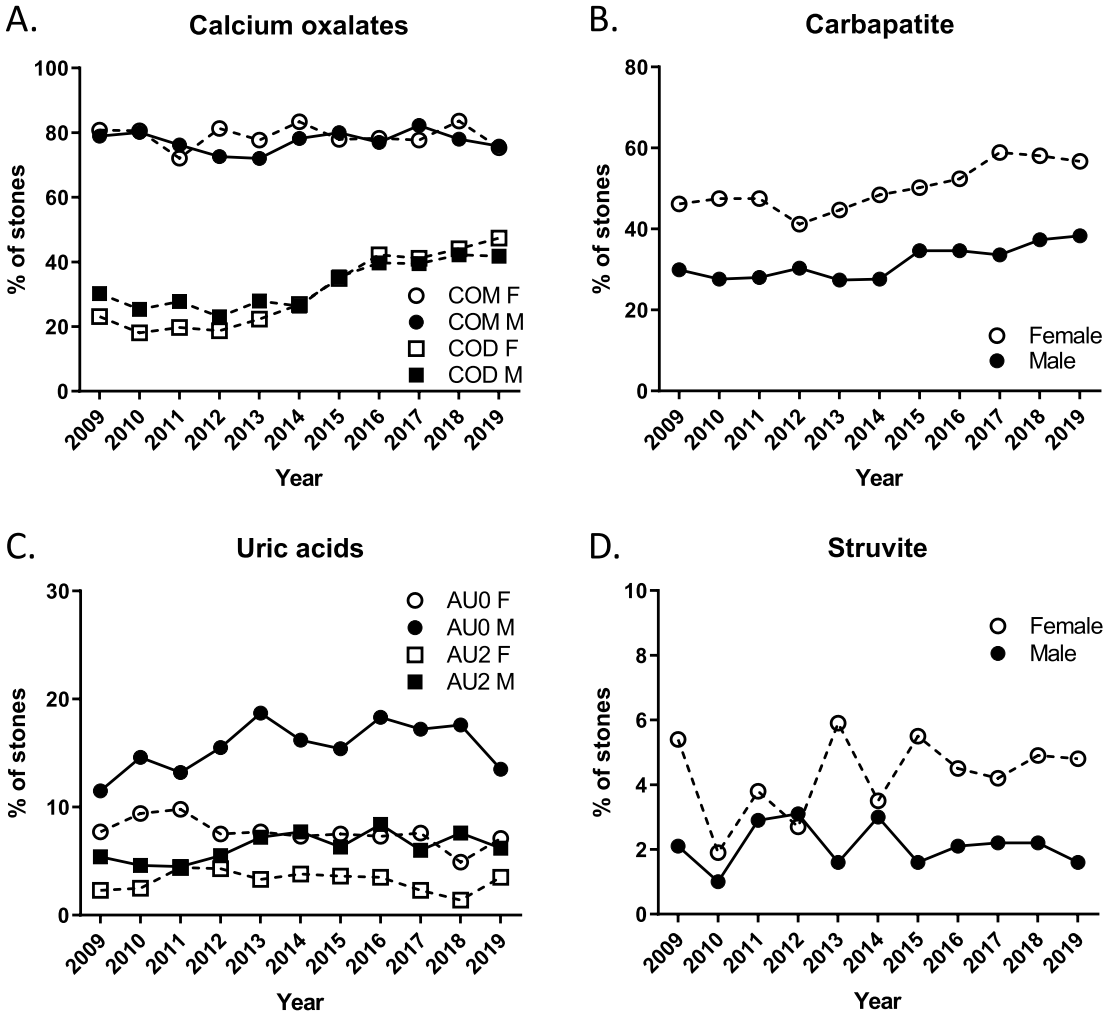

Figure 4. Evolution with time of component frequency by gender. F, female; M, male.

4.1. *Stone numbers*

The number of stones analysed has grown annually. However such a 3-fold increase in ten years cannot be explained only by a higher incidence and is also probably due to a rise in the number of sources submitting stone analyses to our laboratory.

4.2. *Age*

Analysed stones were from patients with a mean age of 50.6 years. Patients who experienced the highest number of stones were between 41 and 60 years of age. These results are similar to those described in some studies from other countries [10–14].

4.3. *Sex*

The overall male-to-female ratio was 2.49:1 and remained stable over the ten years. This proportion is between the one observed in France (2.1:1; [15]) and in Germany (2.7:1; [16]), two neighbouring countries, but largely different from the one measured in the United States (1.37:1 or 1.55:1, [17,18]).

Table 2. Prevalence of Randall's plaque among calcium oxalate monohydrate stones

Randall's plaque	All			Female			Male		
	Presence	Absence	% of RP	Presence	Absence	% of RP	Presence	Absence	% of RP
Total number of COM stones	358	4471	**7.4%**	98	1274	**7.1%**	260	3197	**7.5%**
Age (years) mean ± SD	45.8 ± 13.0	52.4 ± 15.5****		43.4 ± 12.5	51.1 ±16.6****		46.6 ± 13.1	52.9 ± 15.1****	
<15 years	1	30	**3.2%**	0	14	**0%**	1	16	**5.9%**
16–25 years	15	143	**9.4%**	7	59	**10.6%**	8	84	**8.7%**
26–40 years	114	819	**12.2%******	35	268	**11.6%***	79	551	**12.5%******
41–60 years	182	2148	**7.8%**	51	578	**7.7%**	131	1570	**8.1%**
>60 years	46	1329	**3.4%**	5	353	**1.4%**	41	976	**4.0%**

RP: Randall's plaque. Comparison of mean age between presence and absence of RP is statistically significant with $^{****}p < 0.0001$ (Mann–Whitney test). Comparison of % of RP between the 26–40 years age group and the overall frequency of RP is statistically significant with $^{****}p < 0.0001$ for the All and Male groups and $^{*}p < 0.05$ for the Female group (Chi-squared test).

4.4. *Chemical components*

In our study, the most frequent component was COM with a frequency of 78.1% followed by carbapatite (38.1%), COD (34.4%) and uric acids (19.1%). Others crystalline phases such as struvite, brushite, and urates showed a frequency below 10%. Considering components present as major compound (>50% of the stone), the highest frequency was observed for COM, carbapatite, COD and AU0. These proportions were comparable to those described for other countries [10,15]. Calcium oxalates are the most frequent compounds found in a broad majority of calculi around the world [19]. In our study, their predominance was similar to what has been observed in France. However, in our case, frequency of monohydrate calcium oxalate when present as the main component was similar for both gender, whereas French men had more stones with large amount of COM than French women [15,19]. For COD, despite an overall frequency as main component lower than in France, we also observed a statistically difference between gender, men having more calculi with COD as the major compound. Although COM-containing calculi were the most common for both gender, women's stones contained more often carbapatite (51.6% versus 32.7% for men). This ranking was found similar in other countries [13,15,17,19].

A gradual increase in frequency of uric acid stones has been observed for the recent years in different countries [6,11,14,18]. This progression seems to be due to the increase of obesity and type 2 diabetes mellitus associated with a higher susceptibility of women to develop nephrolithiasis in those cases. As in France [15], our results indicates that uric acid containing-stones rank at the fourth place in terms of number for both men and women. Their frequency also increases with age, men experiencing about twice more uric acid calculi than women [19]. In Germany, a study from 2011 put uric acid at the second most common composition in each gender [16]. In our case, the frequency of anhydrous uric acid as main component ranked at the second place but only for men. It would then be interesting to compare our results from the western and French-speaking part of Switzerland to the incidence of uric acid stones in the German-speaking part of the country.

Struvite-containing stones were less frequent in our study (2.8%) compared to others in France (4.5% [15]), in the United States (3.7% for men, 3.0% for women, [18]), but at a similar rate to the one observed in China (3%, [13]). When considering the frequency of struvite as main component, we observed a two-fold difference between women and men (3.3% versus 1.5%, respectively), which was close to the results of Daudon *et al.* [15] (2.3% versus 1.1%, respectively). As in Yang *et al.* [13], our data showed that girls below 15 years had the highest number of struvite stones illustrating the higher prevalence of urinary tract infection for this age group.

Finally, cystine frequency (0.6%) was similar to that in other countries such as France (0.9%, [15]), Germany (0.6%, [16]), China (1.1%, [12]; 0.6%, [13]), and the United States (0.4%, [18]).

4.5. *Time-related evolution of components*

Within the most frequent compounds, we did not observe any evolution over the ten years except an increase for COD frequency (23.1% to 47.4%). A gradual frequency rise of uric acid stones [6,11,14,18] was not found in our series. For these latter components, our results did not show any clear growing trend along the ten years studied as reported in a German study from 1977 to 2006 [16]. Again a comparison of our data with the incidence of uric acid stones in the German-speaking part of the country would be of interest. However, conclusion concerning uric acid stones must be made with great caution as they are the best candidate for stone dissolution by medical treatment after identification by dual-energy computed tomography, which probably leads to an underestimation of their frequency in the laboratory cohort.

4.6. *Age-related evolution of components*

Influence of age on stone composition has been known for many years. As observed in many studies, mean age of patients experiencing stones of cystine, COD, carbapatite, brushite and ammonium hydrogen urate were under 50. Conversely, the oldest patients had more uric acids as major component of their stones, which is consistent with previous observations showing a rising number of UA calculi with age [14,16,17,19]. Finally, COM was the major component in each age group except for children younger than ten years, for whom carbapatite was

the predominant component and accounted for 30% of all stones for each gender.

Uric acids showed a significant increase of 20% in oldest patients while COD decreased in the same proportion for the same age groups. Infectious components such as struvite and ammonium hydrogen urate were very common in children's stones, and struvite frequency rose in people over 80 years old.

4.7. *Sex-related evolution of components*

Our results highlighted significant differences in stone composition between women and men, especially for uric acids, COD and carbapatite. Although COM was the most common component for both gender, women's stones contained more often carbapatite (51.6% versus 32.7% for men). This ranking was found to be similar to those in other countries [13,15,17]. COD stones were also related to gender and more present in men. Furthermore, the drop of COD frequency was also initiated at the age range of 16–25 years in women while it was delayed to the age of 26–40 years in men.

Lastly, the increase of uric acid stones started later in women (from range 61–80 years) compared to men (from range 41–60 years).

4.8. *Randall's plaque*

Over the last five years, around 7.5% of COM-containing stones of our database were developed from Randall's plaque. This prevalence is low compared to others countries [10,20]. A large part of COM-containing stones were not intact when they arrived in our laboratory for analysis, which surely impaired RP's detection. Accordingly, we observed an umbilication for only 11% of stones (data not shown) which probably reflects this stone fragmentation. We also did not systemically scratch the stone umbilication to identify a RP component when RP was not visible under binocular magnifier, which certainly also decreased our RP's frequency.

Two different crystalline phases, carbapatite and sodium urates, were described with a predominance for calcium phosphate. Only men had sodium urate in Randall's plaque, which may be linked to a high level of dietary salt consumption [21], as a "Swiss survey on salt intake" revealed that dietary salt intake in the Swiss population was clearly above the international recommendation of 5 g/day, and more markedly so in men than in women [22].

Finally, as observed by Letavernier *et al.* [20], patients who showed RP were significantly younger whatever the gender.

5. Conclusion

This report is a first picture of the chemical composition of stones and influence of age and gender over the last ten years in the west of Switzerland. Although it includes a rather large number of calculi for a relatively small country (8.5 million people), this study deserves further analysis on number of stones experienced by patients, details on stone composition at first episode associated with degree of recurrence, and patient comorbidities. These will be the topics of a future publication.

Conflicts of interest

Authors have no conflict of interest to declare.

References

[1] C. D. Scales Jr, A. C. Smith, J. M. Hanley, C. S. Saigal, *Eur. Urol.*, 2012, **62**, 160-165.
[2] J. B. Ziemba, B. R. Matlaga, *Investig. Clin. Urol.*, 2017, **58**, 299-306.
[3] S. L. Ljunghall, H. Lithell, E. Skarfors, *Br. J. Urol.*, 1987, **60**, 10-13.
[4] C. Ahlstrand, H. G. Tiselius, *Urol. Res.*, 1990, **18**, 397-399.
[5] Y. Lotan, J. A. Cadeddu, C. G. Roerhborn, C. Y. C. Pak, M. S. Pearle, *J. Urol.*, 2004, **172**, 2275-2281.
[6] D. E. Zilberman, D. Yong, D. M. Albala, *Curr. Opin. Urol.*, 2010, **20**, 148-153.
[7] D. S. Goldfarb, *Adv. Chronic Kidney Dis.*, 2009, **16**, 21-29.
[8] K. Stritt, P. Bosshard, O. Bonny, P. Roth, *Rev. Med. Suisse*, 2020, **16**, 2317-2320.
[9] M. Daudon, D. Bazin, E. Letavernier, *Urolithiasis*, 2015, **43**, 5-11.
[10] V. Castiglione, F. Jouret, O. Bruyère, B. Dubois, A. Thomas, D. Waltregny, A.-C. Bekaert, E. Cavalier, R. Gadisseur, *Nephrol. Ther.*, 2015, **11**, 42-49.
[11] V. Talati, R. Soares, A. Khambati, R. Nadler, K. Perry Jr, *Urolithiasis*, 2020, **48**, 305-311.
[12] S. Wang, Y. Zhang, X. Zhang, Y. Tang, J. Li, *Int. Braz. J. Urol.*, 2020, **46**, 70-80.
[13] X. Yang, C. Zhang, S. Qi, Z. Zhang, Q. Shi, C. Liu, K. Yang, E. Du, N. Li, J. Shi, Y. Xu, *J. Clin. Lab. Anal.*, 2016, **30**, 873-879.
[14] S. Zhang, Y. Huang, W. Wu, Z. He, L. Ou, H.-G. Tiselius, G. Zeng, W. Wu, *World J. Urol.*, 2021, **39**, 3599-3605.
[15] M. Daudon, O. Traxer, E. Lechevallier, C. Saussine, *Prog. Urol.*, 2008, **18**, 802-814.

[16] T. Knoll, A. B. Schubert, D. Fahlenkamp, D. B. Leusmann, G. Wendt-Nordahl, G. Schubert, *J. Urol.*, 2011, **185**, 1304-1311.

[17] J. C. Lieske, A. D. Rule, A. E. Krambeck, J. C. Williams, E. J. Bergstralh, R. A. Mehta, T. P. Moyer, *Clin. J. Am. Soc. Nephrol.*, 2014, **9**, 2141-2146.

[18] R. Moses, V. M. Pais Jr, M. Ursiny, E. L. Prien Jr, N. Miller, B. H. Eisner, *Urolithiasis*, 2015, **43**, 135-139.

[19] M. Daudon, J.-C. Doré, P. Jungers, B. Lacour, *Urol. Res.*, 2004, **32**, 241-247.

[20] E. Letavernier, S. Vandermeersch, O. Traxer, M. Tligui, L. Baud, P. Ronco, J.-P. Haymann, M. Daudon, *Medicine (Baltimore)*, 2015, **94**, article no. e566.

[21] F. P. Muldowney, R. Freaney, M. F. Moloney, *Kidney Int.*, 1982, **22**, 292-296.

[22] A. Chappuis, M. Bochud, N. Glatz, P. Vuistiner, F. Paccaud, M. Burnier, "Swiss survey on salt intake: main results", 2011.

Comptes Rendus
Chimie
2022, Vol. 25, Special Issue S1, p. 247-267
https://doi.org/10.5802/crchim.185

Microcrystalline pathologies: Clinical issues and nanochemistry / *Pathologies microcristallines : questions cliniques et nanochimie*

The epidemiology of kidney stones in Belgium based on Daudon's morpho-constitutional classification: a retrospective, single-center study

Agnieszka Pozdzik [*,#, a, b, c], **Anwar Hamade** [#, a], **Judith Racapé** [d], **Thierry Roumeguère** [c, e], **Fleur Wolff** [f] **and Frederic Cotton** [c, f]

[a] Department of Nephrology; Brussels, Belgium Erasme Hospital, Université Libre de Bruxelles (ULB), Brussels, Belgium

[b] Department of Nephrology, Clinic de la Lithiase Rénale et du Métabolisme Minéral (CLIREMM), Centre Hospitalier Universitaire Brugmann, Université Libre de Bruxelles (ULB), Brussels, Belgium

[c] Faculty of Medicine, Université Libre de Bruxelles (ULB), Brussels, Belgium

[d] Epidemiology, Biostatistics and Clinical Research, School of Public Health, Université Libre de Bruxelles (ULB), Brussels, Belgium

[e] Department of Urology, Erasme Hospital, Université Libre de Bruxelles (ULB), Brussels, Belgium

[f] Laboratory of Chemistry, Erasme Hospital, Université Libre de Bruxelles (ULB), Brussels, Belgium

Current address: Nephrology Departement, Clinique de la Lithiase Rénale et du Métabolisme Minéral (CLIREMM), Centre Hospitalier Universitaire Brugmann, Place A. Van Gehuchten 4, 1020 Bruxelles, Belgique (A. Pozdzik)

E-mails: agnieszka.pozdzik@chu-brugmann.be (A. Pozdzik), anwar.hamade@procare.com.sa (A. Hamade), jracape@ulb.ac.be (J. Racapé), Thierry.Roumeguere@erasme.ulb.ac.be (T. Roumeguère), fleur.wolff@lhub-ulb.be (F. Wolff), frederic.cotton@lhub-ulb.be (F. Cotton)

Abstract.
Background: Increasing evidence highlights the robust clinical value of morpho-constitutional classification proposed by Daudon.

Methods: We retrospectively analyzed the data of 5480 samples submitted for Daudon's classification between 2007 and 2013 to identify the main pro-lithogenic metabolic abnormalities involved in the formation of stones in Belgium.

Results: Among 5027 stones submitted by 4975 patients, the distribution of stones steadily increased with age in both genders, reaching a maximum between 40 to 50 years and decreasing thereafter. Men

* Corresponding author.

# Contributed equally.

submitted more stones (3549) than women (1426) with global men-to-women ratio at 2.4 (1.0 to 2.79). In the whole series, type Ia was a main morpho-constitutional presentation of whewellite (surface morphology), accounting for 41.9%; the types Ib, Ic, Id and Ie corresponded to 2.2%, 0.16%, 0.94% and 0.46%, respectively. Type IIa accounted for 16.4% and types IIb and IIc for 5.7% and 0.18% of weddellite stones. Types IIIa, IIIb, IIIc and IIId accounted for 4.4%, 3.8%, 0.1% and 0.3%, of uric acid and urate stones respectively. The frequency of calcium phosphate type IVa was 4.7% followed by type IVb (3.5%), IVc (1.3%), IVd (1.4%) and IVa2 (0.3%). Type Va (cystine stones) accounted only for 1.1% and Vb for only 0.1%. The rare, but very specific types Ic, Ie, Id, IIId, IVa2 and V pointed to precise entities such as primary hyperoxaluria type 1, enteric hyperoxaluria, urinary tract abnormalities, hyperuricosuria with diarrhoea, distal tubular acidosis and cystinuria respectively. In terms of the major physico-chimical component, 75.4% of stones contained calcium oxalate (whewellite (52%) and weddellite (22.7%)), 12% calcium phosphate (carbapatite (6.7%)), and 9.8% uric acid, mainly anhydrous (9.1%). The struvite stones accounted for 106 (2.1%) and predominated in women.

Conclusions: High frequency of types Ia and IIa suggest that diet related hyperoxaluria and idiopathic hypercalciuria are the leading lithogenic disorders in Belgian kidney stone formers.

Keywords. Kidney stones, Epidemiology, Infrared spectrophotometry, Stereomicroscopy, Morpho-constitutional classification.

Published online: 30 June 2022, Issue date: 1 September 2022

1. Introduction

Kidney stone disease (KSD) is a chronic disorder of mineral metabolism with preventable acute renal manifestations and chronic extrarenal complications [1–5].

The chemical composition and the structural characteristics of kidney stone (KS) vary with age and gender and country [6]. In industrialized countries [7,8], Arabian Peninsula [9] and Maghreb [10], calcium oxalate (CaOx) accounts for the majority of KS, followed by calcium phosphate (CaP), uric acid (UA) and in a minority by cystine (Cys).

The growing prevalence of stones is likely related to dietary factors (high intake of animal protein, fructose, and salts), low water intake, hot climate, economic status, and urbanization [11–17]. Moreover, KSD is strongly associated with obesity and type 2 diabetes mellitus [18,19]. Metabolic syndrome has been identified as an independent risk factor for stone formation [20–23]. Although rare, inborn disorders need to be appropriately identified and efficiently treated as the risk of stone recurrence and loss of kidney function is high in this background [24]. Stone formation could also be promoted independently by urine flow slowdown secondary to acquired or congenital abnormalities of kidney and urinary tract (CAKUT) or urinary tract infections [25].

Therefore, each patient displays a specific combination of both biological (metabolic) abnormalities and/or clinical factors (urinary tract disease, use of some drugs, etc.) creating an individual micro- and macroenvironment driving firstly crystallization and secondly growth of urinary stones [26–32]. All the above induce prolithogenic modification in urine composition allowing formation and recurrence of stones [27]. International guidelines and recent consensus recommend a metabolic assessment of kidney stone formers (KSF) to identify the aetiology of stone and a correction of all lithogenic factors, especially in the case of recurrent disease [33,34].

Given the continuous increase in the prevalence of KSD in adults during the last 30 years, and worrying occurrence in what were previously considered lower risk groups (post-menopausal and pregnant women and the paediatric population) [35–40], KSD stands as a worldwide public healthcare burden [41,42]. Therefore, global improvement in aetiological diagnostics and collaborative care among healthcare providers in pediatrics as well as adults is urgently needed [43–46].

The morpho-constitutional classification (MCC) established by Prof Michel Daudon [47] allows very granular understanding of the whole lithogenesis process within each stone, which can vary during the patient's life [48,49]. The fundamental clinical value for clinicians of using MCC is an opportunity to accurately identify all lithogenic factors responsible for stone formation and/or recurrence as well as offering the opportunity to identify easily KSF at a high risk of recurrence [47,48,50–52].

In our laboratory we built such expertise through

theoretical learning and practice guided by the experts in this field [53]. In the present work, we report the demographic distribution of stones classified according to MCC in our centre during a five-year period. We discuss available evidence supporting our findings in terms of aetiologies proposed by MCC.

2. Materials and methods

This single-center study carried out by University Hospital Erasme in Brussels, Belgium was evaluated and approved by the local Ethic Committee (No.: P2014/444). All procedures were performed in accordance with the institutional and national ethical standards on human experimentation, and with the Helsinki Declaration of 1975, revised in 2013.

We retrospectively analyzed the results of MCC from all samples submitted to this evaluation in our department of clinical chemistry. The data for analysis were extracted from a local perspective database (GLIMS, CliniSys Group, Gent, Belgium). The KS were provided by hospitals and laboratories located in Brussels as well as from neighbouring provinces (Hainaut, Brabant-Wallon and Namur). Between January 2007 and January 2013, a total of 5480 samples were investigated. Only stones larger than 0.5 mm have been included.

The KS morphology was described under optic stereomicroscope study (MOTIC-ST-39-Series). The stones were assessed for shape, color, organization from surface throughout the section into the nucleus. After detailed morpho-constitutional analysis, each stone was classified into one of seven main morphological types and 22 subtypes. The comprehensive specification of each type and subtype has been extensively described previously and the main characteristics of MCC are summarized for non-familiar readers in Table 1 [48,50,54]. The physico-chemical components of stones were identified and semi-quantified (in %) by physical methods using FTIR spectroscopy (Bruker-Optics-FTIR-Tensor-27) as described previously [53]. Examples of photomicrographs of various stone types and corresponding FTIR spectra are depicted in Figure 1.

We recorded gender and age of all patients at the presentation, KS numbers in the submitted sample (single or multiple stones or fragments), and characteristics of the samples in terms of stone fragments or whole stones, morphological type according to the surface and section, composition (expressed in %) of each chemical component obtained by FTIR spectroscopy in global powder for all included stones.

We first expressed results as the main component accounting for more than 50% of the stone. Pure stone has been defined as a stone that contained less than 10% of other components. Secondly, we analyzed their distribution according to gender and age of KSF.

Our main aim was to analyze the epidemiology of stones according to the MCC approach and main physico-chemical component to establish their distribution according to age classes and gender and find the suggestive aetiologies.

2.1. *Statistical analysis*

The statistical analysis was performed with Statistica® (StatSoft Inc., Europe, GmbH, Hamburg, Germany). The distribution of data by gender and age intervals was tested by the Shapiro-Wilk test. The binary variables or categories are presented as a percentage. The comparison of proportions was analyzed using Pearson Chi^2 or Fisher's exact test for small sample size. A P-value lower than 0.05 was considered as statistically significant.

3. Results

Among 5480 samples we excluded 453 samples from analysis for the following reasons: urine samples without stones (71%), presence of filter material (9.7%), absence of stone (7.7%), undefined precipitation (5.3%), spurious stones (3%), tissue fibre (0.2%), tooth (0.2%) biliary stone (0.2%) or unidentified sample (0.8%).

Finally, we included all complete MCC and physico-chemical data of 5027 (96.7%) KS that fulfilled the inclusion criteria. Samples smaller than 0.5 mm were excluded.

3.1. *Global distribution of kidney stones in Brussels cohort*

The KS were provided from patients with first KS manifestation as well as during the follow-up. Single stones corresponded to 2783 (96.4%) and

Table 1. Main characteristics of surfaces and sections of kidney stones, corresponding to physical components (crystalline phase) and type of Daudon's morpho-constitutional classification. The value of this method consists in the particularly granular view of associated aetiologies pointing directly to specific diagnostic management and indirectly allowing the improvement of the therapeutic strategy

Surface	Section	MCC type/subtype	FITR component	Aetiology
Mammillary with frequent umbilication and Randall's plaque indicative of papillary origin. Color: brown	Compact concentric layers with a radiating organization. Color: brown	Ia	Whewellite	Intermittent and moderate hyperoxaluria (a high consumption of oxalate-rich foods or of hydroxyproline-rich foods, low intake of calcium) and /or low water intake resulting in low diuresis
Mammillary and rough without umbilication. Color: brown to dark brown	Compact unorganized sometimes, the presence of gaps. Color: brown, dark-brown	Ib	Whewellite	Stasis, low diuresis, crystalline, conversion form weddellite to whewellite
Budding. Color: light cream to pale yellow-brown (whitish in children)	Finely granular and poorly organized. Color: light cream to pale yellow-brown	Ic	Whewellite	Primary hyperoxaluria (most commonly type 1 related to AGXT mutation)
Smooth. Color: homogeneous, beige or pale brown	Compact with thin concentric layers. Color: beige or pale brown	Id	Whewellite	Malformative uropathy, stasis, presence of multiples stones
Locally budding, mammillary, or rough. Color: often heterogeneous, pale yellow-brown to brown	Locally unorganized and loose structure, locally more compact radiating	Ie	Whewellite	Enteric hyperoxaluria related to inflammatory bowel diseases, especially after ileal resection for Crohn's disease, in children with cystic fibrosis with a severe pancreatic deficit, after bariatric surgery such as jejuno-ileal bypass or Roux-en-Y gastrojejunal bypass
Spiculated with aggregated right angles and sharp edged bipyramidal crystals. Color: pale yellow-brown	Loose of radial crystallization. Color: pale yellow-brown	IIa	Weddellite	Hypercalciuria no matter what its cause with high urinary calcium/citrate molar ratio
Spiculated and showing aggregated bipyramidal crystals with blunt angles and ridges. Color: pale yellow-brown	Compact, unorganized crystallization. Color: pale yellow-brown	IIb	Weddellite	Both idiopathic hypercalciuria and moderate hyperoxaluria associated with stasis and low diuresis

(continued on next page)

Table 1. (continued)

Surface	Section	MCC type/subtype	FITR component	Aetiology
Rough. Color: grey-beige to dark yellow-brown	Unorganized core with a diffuse concentric compact structure at the periphery. Color: grey-beige to dark yellow-brown	IIc	Weddellite	Hypercalciuria and an obstructive anatomic abnormality with multiple stones resulting from stasis conditions.
Homogeneous smooth. Color: homogeneous, typically orange, sometimes cream, ochre or yellowish	Homogeneous compact, concentric structure with a radiating organization. Color: typically, orange	IIIa	Uric acid anhydrous	low urine pH, stasis, prostate hypertrophy, metabolic syndrome, ammoniagenesis defect
Heterogeneous embossed, rough and porous surface. Heterogeneous color from beige to brown-orange	Poorly organized section with frequent porous areas. Color: orange	IIIb	Uric acid dihydrate ± uric acid anhydrous	Insulin resistance, metabolic syndrome, type 2 diabetes, low urinary pH, ammoniagenesis defect
Homogeneous or slightly heterogeneous rough and locally porous. Color: homogeneous, cream to greyish	Unorganized porous. Color: whitish to greyish	IIIc	Urate salts, including ammonium hydrogen urate	Hyperuricosuria, no trial or alkaline urine pH, urinary tract infection by urea splitting microorganisms
Heterogeneous embossed, rough and porous, heterogeneous. Color: greyish to dark brown	Alternated layers, thick and brownish or thin and greyish, locally porous. Color: Sometimes, locally purplish	IIId	ammonium hydrogen urate	Chronic diarrhoea, electrolytes and alkali loss, high urate concentration in urine, low phosphate intake, laxative abuse
Homogeneous rough. Color: whitish to beige	Poorly organized, or diffuse concentric layers. Color: whitish to beige	IVa1	Carbapatite	Hypercalciuria and/or urinary tract infection
Embossed and varnished with small cracks. Glazed appearance. Color: homogeneous, pale brown-yellow to pale brown	Section made of compact alternated layers, thick brown-yellow and thin beige. Often, multiple nuclei (from collecting duct origin)	IVa2	Carbapatite	Inherited or acquired distal renal tubular acidosis, Sjogren syndrome, chronic hepatitis

(continued on next page)

Table 1. (continued)

Surface	Section	MCC type/subtype	FITR component	Aetiology
Heterogeneous, both embossed and rough with confluent superficial deposits. Heterogeneous color: cream to dark brown	Section made of irregularly alternating thick, whitish, and thin, brown-yellow layers	IVb	Carbapatite other calcium phosphates (±struvite)	Latent urinary tract infection, especially if they contain small amounts of ACCP, whitlockite or struvite-markers of urinary tract infection. Sometimes related to the minor defect in tubular acidification, or hypercalciuria (primary hyperparathyroidism), especially when they also contain weddellite
Homogeneous made of amalgamate crystals with blunt angles and edges	Crude radial crystallization. Color: whitish	IVc	Struvite	Urinary tract infection by urease producing bacteria
Finely rough or dappled. Color: whitish to beige	Radial crystallization with more or less visible concentric layers. Color: whitish to beige	IVd	Brushite	Hypercalciuria, primary hyperthyroidism, phosphate leak, medullary sponge kidney
Rough surface. Color: yellowish	Poorly organized, sometimes a radiating organization. Color: yellowish	Va	Cystine	Cystinuria
Smooth. Color: homogeneous, cream to yellowish	Concentric layers at the periphery, an unorganized core. Color: heterogeneous, cream (periphery) to yellowish (core)	Vb	Cystine	Cystinuria associated with inadequate diet and or medical management or urinary stasis
Homogeneous matrix soft stones. Color: cream to pale brown	Unorganized section. Color: cream to pale brown	VIa	Proteins	Urinary tract infection and chronic pyelonephritis
Heterogeneous, irregularly rough, locally scaled. Color: dark brown to black	Crude and diffuse foliated. Color: dark brown to black. Other components often present in these stones may alter the structure and the color	VIb	Proteins ± drugs or metabolic compounds	Proteins with metabolic components or drugs (quinolones, triamterene, atazanavir, . . .)

(continued on next page)

Table 1. (continued)

Surface	Section	MCC type/subtype	FITR component	Aetiology
Homogeneous, smooth surface with clefts and scales. Color: dark brown	Dark brown protein shield surrounding a loose, unorganized light core containing whewellite crystals mixed with proteins	VIc	Proteins with whewellite	Typically seen, in end stage renal disease related to relatively high calcium concentration in the urine due to chronic calcium substitution and high vitamin D intake
Various morphologies and colors according to the stone composition (infrequent purines and drugs)	Variable organization and color according to the stone composition.	VII	Miscellaneous	Other aetiologies

Adapted from Daudon M *et al.* [48] and Pozdzik A *et al.* [54].

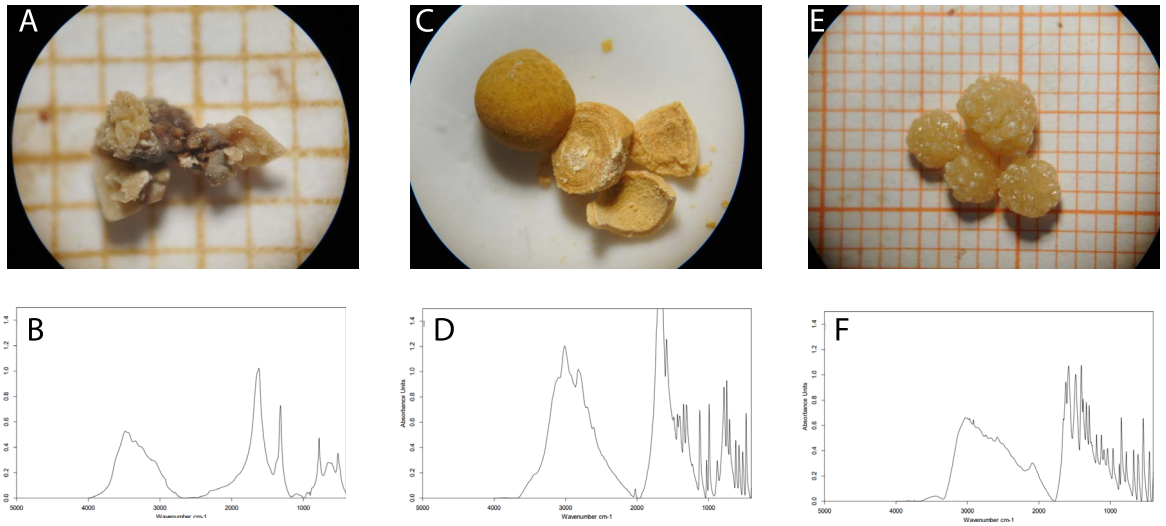

Figure 1. Illustrations of representative photomicrographs obtained during the assessment of kidney stone's morphology under optic microscope (A, C and E) and their corresponding typical FTIR absorption spectra (B, D and F). (A) Type Ia and IIa mixed stones. Type Ia is characterized by a spherical form with a smooth and dark-brown surface seen in the patients with intermittent hyperoxaluria. The surface of type IIa is typically yellow or light-brown prickly, spiculated surface due to the presence of aggregated pyramidal crystals with very sharp angles and edges, their morphology characteristic of idiopathic hypercalciuria. (B) FTIR absorption spectrum of whewellite and weddellite mixed stone shown in (A). (C) Type IIIa stones. They have a smooth, typically orange surface and their section is characterized by concentric layers with radiating organization around very well-defined nucleus. (D) FTIR absorption spectrum of anhydrous uric acid identified in type IIIA stones shown in (C). (E) Type Va stones. They have a rough crystalline surface of yellowish color (their section is typically poorly organized, sometimes a radiating organization can be found, not shown in the picture). (F) FTIR absorption spectrum of cystine identified within type Va stones shown in (E).

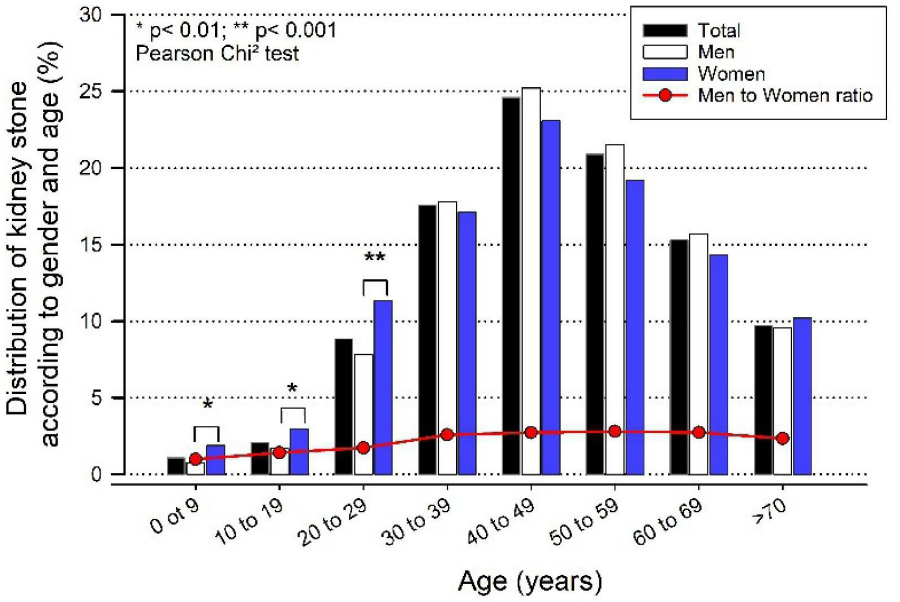

Figure 2. Global distribution of all analyzed kidney stones (n = 4975) according to gender and age classes.

Table 2. Global distribution of studied kidney stones (n = 4975) by age and according to the gender of kidney stone formers

Age (years)	All stone formers (n = 4975) Number (%)	Women (n = 1426) Number (%)	Men (n = 3549) Number (%)	Men to women ratio	P-value
0–9	54 (1.1)	27 (1.9)	27 (0.8)	1.00	*0.0005*
10–19	102 (2.1)	42 (3.0)	60 (1.7)	1.43	*0.005*
20–29	440 (8.8)	161 (11.3)	279 (7.9)	1.73	*0.0001*
30–39	874 (17.6)	244 (17.1)	630 (17.8)	2.58	*0.59*
40–49	1223 (24.6)	329 (23.1)	894 (25.2)	2.72	*0.12*
50–59	1038 (20.9)	274 (19.2)	764 (21.5)	2.79	*0.07*
60–69	760 (15.3)	204 (14.3)	556 (15.7)	2.73	*0.23*
>70	484 (9.7)	145 (10.2)	339 (9.6)	2.34	*0.57*

Statistical analyses of distribution (women *vs* men) were performed using Pearson Chi^2. Presented P-value reflect the significance of differences in the proportion (%) of kidney stones in studied groups considering the small number of kidney stones in some groups.

multiple stones to 437 (3.6%). Intact stones corresponded to 3226 (64.1%) and 1801 (35.9%) of samples corresponded to stone fragments. Stones were statistically more frequent from men (3554) than women (1473) (70.6% *vs* 29.4%, respectively).

We submitted the data of MCC for a total of 5027 stones provided by 4975 KSF for analysis by age intervals and gender (Table 2, Figure 2).

Global men-to-women ratio was 2.4 (3549 men and 1426 women) and varied from 1.43 to 2.79

(ages 10 to 19 and 50 to 59-years respectively) except for patients younger than 10 years old where male-to-female ratio was 1.0.

The number of stones increased steadily with patient age in both genders, reaching a maximum between 40 to 49 years, and decreased thereafter. The lowest number of stones (n = 54, 1.09%) was recorded in the age group between 0 to 9 years (1.8% in girls and 0.7% in boys). The highest number of stones (n = 1223, 24.6%) was found in the group aged between 40 to 49 years in both genders.

3.2. *Main morphological types of kidney stones*

Furthermore, we analyzed the age distribution of 4635 kidney stones classified according to type I, II, III, IV and V of Daudon's MCC. The lower number of stones included in this analysis is related to the fact that 362 out of 5027 KS were too small to provide a reliable classification (Tables 3 and 4). We found all morphological types in the surface and section.

Surface morphological type I accounted for 2302 KS, type II for 1145 and type III, IV and V for 466, 556 and 54, respectively.

However, the section morphological type I accounted for 2657 of KS, type II for 916 and type III, IV and V for 436, 576 and 52, respectively.

Type I composed of Whewellite (Wh) and type II composed of Weddellite (Wd) were the most frequent and predominant types in the age class 40–49 years.

Type III composed of UA progressively increased from the age class 40–49 years and reached the highest frequency after 60 years.

Type IV composed of CaP was mainly observed in age groups from 30 to 49 years and decreased slowly thereafter.

Type V composed of Cys was found mainly in age classes 20 to 29 and 30 to 39.

3.3. *Distribution of KS according to morphological subtypes and the patient's gender*

According to the *surface* morpho-constitutional subtype the statistically significant higher proportion of subtype Ia ($p < 0.0001$), IIa ($p = 0.0003$) and IIIa ($p = 0.007$) was observed in men as compared with women (Table 5). However, a statistically significant higher proportion of subtypes IVa, IVb and IVc ($p < 0.0001$, $p < 0.0001$ and $p = 0.006$ respectively) was observed in women as compared with men. The most common Ia/IIIa combination in stone surface was found in women *vs* men ($p < 0.0001$) but Ia/IIa in men *vs* women ($p < 0.0001$).

According to the *section* morpho-constitutional subtype, a significantly higher proportion of subtypes Ia, IIa and IIIa was also observed in men as compared with women ($p < 0.0001$, $p = 0.007$ and $p = 0.001$ respectively). On the other hand, subtypes IVa, IVb and IVc were observed more frequently in women as compared with men ($p < 0.0001$, $p < 0.0001$ and $p < 0.0001$ respectively, Table 6).

The rare types Ic, Ie, IIId, IVa2 and V corresponded to 0.1%, 0.4%, 0.1% 0.3% and 1.1% respectively but suggested the involvement of a very specific lithogenesis process.

Within the type V, 55 stones represented the surface morphology of type Va and the morphology Vb was found in nine (0.1% of all stones).

3.4. *Distribution according to the main physicochemical component (crystalline phase) of KS*

Stones containing mainly Wh account for the majority of KS in the whole cohort (75.4%) (Table 7).

Within 3759 CaOx stones, 2629 (52.7%) corresponded to Wh and 1130 (22.7%) to Wd. Among the 540 phosphate stones, 338 were made of CA, 106 of struvite, 62 were brushite, 30 amorphous carbonated calcium phosphate (ACCP) stones and only four octacalcium phosphate pentahydrate stones.

The UA stones accounted for 491 (9.87%) stones (UA anhydrous (UAA) 9.17 and UA dihydrate (UAD) 0.7%).

Stones containing cystine were rare and accounted for 1.2% (64 stones in whole cohort).

Protein composition was found in 44 (0.8%) of all stones. Only 86 stones were classified as miscellaneous (unknown composition). We did not detect drug(s) related stones or containing rare metabolic components such as dihydroxyadenine, xanthine, methyl-1 uric acid, ...

Table 3. Distribution of kidney stones according to the main morpho-constitutional type detected on the stone surface as a function of age ($n = 4503$)

Main surface type	0–9 years		10–19 years		20–29 years		30–39 years		40–49 years		50–59 years		60–69 years		> 70 years	
	n (%)	M/F ratio	*n* (%)	M/F ratio	*n* (%)	M/F ratio	*n* (%)	M/F ratio	*n* (%)	M/F ratio	*n* (%)	M/F ratio	*n* (%)	M/F ratio	*n* (%)	M/F ratio
I	9 (0.4)	1.25	26 (1.1)	1.60	142 (6.2)	1.15	362 (15.7)	2.41	622 (27.0)	3.26	550 (23.9)	3.09	365 (15.9)	3.84	226 (9.8)	2.75
II	15 (1.3)	0.88	38 (3.3)	1.31	173 (15.1)	3.12	281 (24.5)	4.65	297 (25.9)	3.69	189 (16.5)	3.48	103 (9.0)	1.94	49 (4.3)	1.45
III	4 (0.9)	1.00	0 (0.0)	NA	7 (1.6)	1.33	15 (3.4)	1.50	69 (15.5)	2.29	106 (23.8)	3.77	139 (31.2)	2.97	106 (23.8)	3.20
IV	19 (3.4)	1.25	16 (2.9)	1.67	53 (9.5)	0.89	101 (18.1)	0.91	117 (21.0)	0.69	96 (17.3)	1.04	83 (14.9)	1.24	71 (12.8)	1.26
V	1 (1.9)	0.00	7 (12.9)	0.75	11 (20.4)	1.75	17 (31.5)	7.50	4 (7.4)	3.00	11 (20.4)	0.57	2 (3.7)	1.00	1 (1.9)	0.00

Table 4. Distribution of kidney stones according to the main morpho-constitutional type detected in the stone section as a function of age ($n = 4637$)

Main surface type	0–9 years		10–19 years		20–29 years		30–39 years		40–49 years		50–59 years		60–69 years		> 70 years	
	n (%)	M/F ratio	*n* (%)	M/F ratio	*n* (%)	M/F ratio	*n* (%)	M/F ratio	*n* (%)	M/F ratio	*n* (%)	M/F ratio	*n* (%)	M/F ratio	*n* (%)	M/F ratio
I	6 (0.2)	1.00	32 (1.2)	1.91	179 (6.7)	1.33	435 (16.4)	2.61	736 (27.7)	3.60	628 (23.6)	3.15	409 (15.4)	3.79	409 (8.7)	3.20
II	13 (1.4)	0.44	36 (3.9)	1.33	152 (16.6)	4.07	234 (25.5)	4.40	216 (23.6)	3.49	143 (15.6)	3.18	82 (9.0)	1.65	82 (4.4)	1.35
III	1 (0.2)	NA	1 (0.2)	NA	6 (1.4)	2.00	15 (3.4)	1.50	72 (16.5)	2.79	102 (23.4)	4.94	139 (31.9)	3.48	139 (22.9)	3.30
IV	16 (2.8)	1.50	13 (2.3)	1.60	58 (10.1)	0.81	113 (19.6)	1.17	123 (21.4)	0.70	99 (17.2)	1.23	82 (14.2)	1.16	82 (12.5)	1.37
V	1 (1.9)	0.00	9 (17.3)	0.80	11 (21.1)	1.75	16 (30.8)	7.00	3 (5.8)	NA	10 (19.2)	0.25	1 (1.9)	NA	1 (1.9)	0.00

Within CaOx stones, Wh was identified as the main component of more than half of all analyzed samples ($n = 2629$) and was significantly more common in men than in women (55.1% *vs* 46.7%, $p < 0.0001$). The second most frequent crystalline phase was Wd corresponding to 1130 KS, also significantly more common in men than women (24.7% *vs* 18.9%, $p = 0.0001$).

The UAA corresponded to 457 KS mainly provided from men (9.7% *vs* 7.6%, $p = 0.02$).

In contrast, phosphate stones were less frequent (338 CA (6.8%) and 106 struvite stones (2.1%)) and were significantly more common in women as compared to men ((14.1% *vs* 3.8%, $p < 0.0001$) and (3.8% *vs* 1.4%, $p < 0.0001$) for CA and struvite respectively). Women submitted more ACCP stones than men (1.2% *vs* 0.3%, $p = 0.0001$).

3.5. *Most common physico-chemical combination of kidney stones*

In the constitutional analysis of 5027 samples, stones with a single component accounted for 2035 (40.4% pure stones), stones with two components for 1432 (28.4%) and stones with more than two components for 1560 (31%) out of the all KS. Note that minor protein content was not taken into account.

Wh was the main single component in 1621 stones and was followed by Wd and UAA (175 and 114 stones, respectively), which were observed mainly in men KSF (35.5% *vs* 25.1%, 3.9% *vs* 2.7% and 2.5% *vs* 1.7% respectively) (Table 8).

We found the most common combinations to be Wd + Wh + CA, Wd + Wh and Wd + CA (729, 620 and 307 stones).

The combinations Wd+Wh were significantly higher in men than in women (14.3% *vs* 7.8%, $p = 0.0001$) contrasting with the higher distribution of combinations Wd + Wh + CA, Wh + CA and CA + ACCP in women as compared with men (16.6% *vs* 13.8%, $p = 0.01$; 10.8% *vs* 3.3%, $p < 0.0001$ and 4.3% *vs* 0.8%, $p < 0.0001$, respectively).

3.6. *Distribution of main crystalline phase types according to patients' age and to gender*

3.6.1. *Calcium oxalate kidney stones*

Whewellite. The distribution of Wh stones (type I) increased steadily with patient age in both genders (Figure 3A). Lowest distribution was recorded

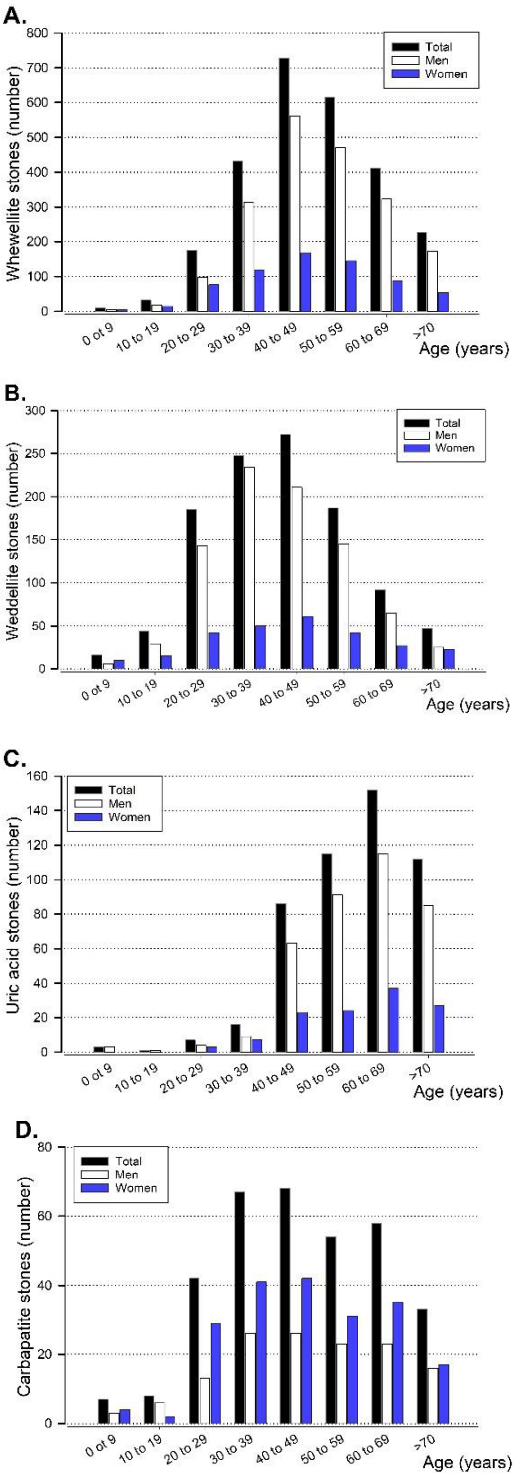

Figure 3. Kidney stone distribution by gender and age intervals according to the main physical component (crystalline phase). (A) Whewellite, (B) Weddellite, (C) Uric acid, (D) Carbapatite.

Table 5. Global and gender distribution of analyzed kidney stones according to the main morpho-constitutional type detected in the surface of stones and as a function of gender ($n = 4985$)

Stone surface type	Total ($n = 4985$) Number (%)	Women ($n = 1431$) Number (%)	Men ($n = 3554$) Number (%)	Men to women ratio	*P*-value
Type I: Calcium oxalate monohydrate (Wh)					
Ia	2088 (41.9)	530 (37.0)	1558 (43.8)	2.94	*<0.0001*
Ib	113 (2.3)	42 (2.9)	71 (2.0)	1.69	*0.04*
Ic	8 (0.2)	1 (0.1)	7 (0.2)	7.00	*NS**
Id	47 (0.9)	18 (1.3)	29 (0.8)	1.61	*0.14*
Ie	23 (0.5)	6 (0.4)	17 (0.5)	2.83	*0.78*
Type II: Weddellite (Wd)					
IIa	818 (16.4)	192 (13.4)	626 (17.6)	3.26	*0.0003*
IIb	284 (5.7)	77 (5.4)	207 (5.8)	2.69	*0.54*
IIc	9 (0.2)	3 (0.2)	6 (0.2)	2.00	*NS**
Type III: Uric acid (UA) and urate					
IIIa	222 (4.5)	46 (3.2)	176 (5.0)	3.83	*0.007*
IIIb	194 (3.9)	58 (4.1)	136 (3.8)	2.34	*0.71*
IIIc	5 (0.1)	2 (0.1)	3 (0.1)	1.50	*NS**
IIId	15 (0.3)	5 (0.4)	10 (0.3)	2.00	*NS**
Type IV: Calcium and/or magnesium phosphates					
IVa	237 (4.8)	129 (9.0)	108 (3.0)	0.84	*<0.0001*
IVb	179 (3.6)	100 (7.0)	79 (2.2)	0.79	*<0.0001*
IVc	66 (1.3)	29 (2.0)	37 (1.0)	1.28	*0.006*
IVd	72 (1.4)	21 (1.5)	51 (1.4)	2.43	*0.93*
Type V: Cystine					
Va	55 (1.1)	21 (1.5)	34 (1.0)	1.62	*0.12*
Type V: Protein					
VIa	15 (0.3)	7 (0.5)	8 (0.2)	1.14	*NS**
VIb	14 (0.3)	4 (0.3)	10 (0.3)	2.50	*NS**
Most frequently observed mixed stones					
Ia/IIa	269 (4.6)	54 (3.8)	215 (6.1)	3.98	*<0.0001*
Others	239 (4.8)	74 (5.1)	165 (4.6)	2.23	*0.43*

Statistical analyses of distribution (women *vs* men) were performed using Pearson Chi^2 or * Fisher's exact test for small group. Presented *P*-value reflects the significance of differences in the number of kidney stones in the studied groups.

between 0 and 9 years (0.3%) and highest distribution between 40 to 49 years (27.7%); patients aged more than 70 years accounted for 8.6%. Men submitted more Wh stones than women in all age classes (the men-to-women ratio varied from 1.0 to 3.6).

Weddellite. Similarly, the distribution of Wd stones (type II) increased steadily with patient age in both genders, reaching a maximum earlier between 30 and 39 years and decreasing thereafter with male predominance in all age groups except for the age classes

Table 6. Global and gender distribution of analyzed kidney stones according to the main morpho-constitutional type observed in the section of stones ($n = 4985$)

Stone section type	Total ($n = 4985$) Number (%)	Women ($n = 1431$) Number (%)	Men ($n = 3554$) Number (%)	Men to women ratio	*P*-value
Type I: Calcium oxalate monohydrate					
Ia	2499 (50.1)	612 (42.8)	1887 (53.1)	3.08	*<0.0001*
Ib	91 (1.8)	32 (2.2)	59 (1.7)	1.84	*0.17*
Ic	3 (0.1)	1 (0.1)	2 (0.1)	2.00	*NS**
Id	32 (0.6)	11 (0.8)	21 (0.6)	1.91	*0.48*
Ie	17 (0.3)	4 (0.3)	13 (0.4)	3.25	*NS**
Type II: Calcium oxalate dihydrate					
IIa	663 (13.3)	161 (11.6)	502 (14.1)	3.12	*0.007*
IIb	236 (4.7)	65 (4.5)	171 (4.8)	2.63	*0.69*
IIc	5 (0.1)	2 (0.1)	3 (0.1)	1.50	*NS**
Type III: Uric acid and urate					
IIIa	242 (4.9)	47 (3.3)	195 (5.5)	4.15	*0.001*
IIIb	186 (3.7)	48 (3.4)	138 (3.9)	2.88	*0.37*
IIIc	4 (0.1)	2 (0.1)	2 (0.1)	1.00	*NS**
IIId	1 (<0.1)	0 (0.0)	1 (<0.1)	NA	*NS**
Type IV: Calcium and/or magnesium phosphates					
IVa	203 (4.1)	108 (7.6)	95 (2.7)	0.88	*<0.0001*
IVb	163 (3.3)	89 (6.2)	74 (2.1)	0.83	*<0.0001*
IVc	140 (2.8)	63 (4.4)	77 (2.2)	1.22	*<0.0001*
IVd	69 (1.4)	20 (1.4)	49 (1.4)	2.45	*0.96*
Type V: Cystine					
Va	52 (1.0)	21 (1.5)	31 (0.9)	1.48	*0.06*
Type VI : Protein					
VIa	7 (0.1)	5 (0.4)	2 (0.1)	0.40	*0.02**
VIb	9 (0.2)	2 (0.1)	7 (0.2)	3.50	*NS**
Others	363 (7.3)	138 (9.6)	225 (6.3)	1.63	*<0.0001*

Statistical analyses of distribution (women *vs* men) were performed using Pearson Chi^2 comparison or * Fisher's exact test for small group. Presented *P*-value reflects the significance of differences in the number of kidney stones in the studied groups.

from 0 to 9. Peak distribution was observed between 40 and 49 years for women and 10 years earlier in men (Figure 3B). Men submitted more Wd stones than women in all age classes (the men-to-women ratio varied from 1.1 to 4.6, except for patients less than 10 years old where M/F ratio was lowest at 0.6).

3.6.2. *Uric acid stones*

The distribution of UA (type III) increased steadily with patient age in both genders. In our cohort, lowest distribution was recorded between age 10 to 19 years and reached a maximum between 60 to 70 years (Figure 3C). Men accounted for more KSF than women in all age classes (men-to-women ratio varied from 1.3 to 3.7).

Table 7. Global and gender distributions of analyzed kidney stones according to the main physicochemical component identified within the stones ($n = 4985$)

Main physicochemical component	Total ($n = 4985$) Number (%)	Women ($n = 1431$) Number (%)	Men ($n = 3554$) Number (%)	Men to women ratio (2.5)	*P*-value
Calcium oxalate monohydrate	2629 (52.7)	669 (46.7)	1960 (55.1)	2.9	*<0.0001*
Calcium oxalate dihydrate	1130 (22.7)	271 (18.9)	859 (24.7)	3.2	*0.0001*
Uric acid anhydrous	457 (9.2)	110 (7.7)	347 (9.8)	3.2	*0.02*
Carbapatite	338 (6.8)	202 (14.1)	136 (3.8)	0.7	*<0.0001*
Magnesium ammonium phosphate	106 (2.1)	55 (3.8)	51 (1.4)	0.9	*<0.0001*
Cystine	64 (1.3)	24 (1.7)	40 (1.1)	1.7	*0.12*
Dicalcium phosphate dihydrate	62 (1.2)	17 (1.2)	45 (1.3)	2.6	*0.82*
Proteins	44 (0.9)	15 (1.1)	29 (0.8)	1.9	*0.82*
Uric acid dihydrate	35 (0.7)	11 (0.8)	24 (0.7)	2.2	*0.72*
Amorphous carbonated calcium phosphate	30 (0.6)	18 (1.3)	12 (0.3)	0.7	*0.0001*
Octacalcium phosphate pentahydrate	4 (0.1)	2 (0.1)	2 (0.1)	1.0	*NS **
Miscellaneous	86 (1.7)	37 (2.6)	49 (1.4)	1.3	*0.35*

Statistical analyses of distribution (women *vs* men) were performed using Pearson Chi^2 comparison or Fisher's exact test (*) for small group. Presented *P*-value reflect the significance of differences in the number of kidney stones in studied groups.

3.6.3. *Calcium and magnesium phosphate stones*

In our patients, CA was the most common crystalline phase of CaP stones. CA stones (type IV) were found in 6.8% of all stones and predominated in women (14.1% *vs* 3.8% in men, $p < 0.0001$) (Figure 3D). The number of KS containing CA increased in patients older than 20 years and reached a plateau from 30 years (Figure 3D). Except for the age interval 10 to 19 years, women submitted more CA stones than men (men-to-women ratio < 1.0).

In our cohort 117 stones (2.3%) contained struvite. This crystalline phase was more frequent in women KSF as compared to men (3.8% vs 1.4%, $p < 0.0001$).

Among phosphates, whitlockite was found in 19 cases (0.4%). In all cases, whitlockite was found admixed with more abundant species, mainly CA (63.2% of cases).

4. Discussion

To our knowledge, we report the largest Belgian cohort of stone types according to Daudon's MCC and we provide a statistical analysis of their demographic distribution in relation to age classes and gender.

Within both gender categories, the overall distribution of KS increased with age, peaking at age 40 to 50 years, and decreasing thereafter as reported in Germany and France [55,56] but later than reported in Nepal (peak of prevalence 2nd and 4th decades) [57] and occurring earlier as compared with the cohort from Mayo Clinic and Northwestern University of Chicago (45.6% of age more than 60) [58, 59]. The peak age interval is shifted ten years earlier as compared with the data from the Liège region in the North-East region of Belgium [60]. The differences could be linked to a characteristic of the studied population, the patients from Liège region were older.

As reported by others [41,55,60], men submitted more stones than women and we observed male predominance for CaOx and UA stones, and female predominance for CaP stones [3,52,61–63]. The predominance of oxalate stones within mixed stones (83%) and the prevalence of UA stones (54%) in "pure" kidney stones as analyzed by FTIR spectroscopy has been recently reported also in the European part of

Table 8. Global and gender related distribution of kidney stones according to the main physicochemical component and the most frequent combination of components as determined by the analysis of a global powder of stones by FTIR spectroscopy

Main physicochemical component	Total (n = 4985) Number (%)	Women (n = 1431) Number (%)	Men (n = 3554) Number (%)	P-value
Wh	1621 (32.5)	359 (25.1)	1262 (35.5)	*<0.0001*
Wd + Wh + CA	729 (14.6)	237 (16.6)	492 (13.8)	*0.01*
Wd + Wh	620 (12.4)	111 (7.8)	509 (14.3)	*<0.0001*
Wd + CA	307 (6.2)	93 (6.5)	214 (6.0)	*0.53*
Wh + CA	271 (5.4)	154 (10.8)	117 (3.3)	*<0.0001*
UAA + UAD	254 (5.1)	58 (4.1)	196 (5.5)	*0.03*
Wd	175 (3.5)	39 (2.7)	136 (3.9)	*0.06*
UAA	114 (2.3)	25 (1.8)	89 (2.5)	*0.11*
CA + ACCP	89 (1.8)	61 (4.3)	28 (0.8)	*<0.0001*
Miscellaneous	805 (16.2)	294 (20.5)	511 (14.9)	*<0.0001*

Statistical analyses of distribution (women *vs* men) were performed using Pearson Chi^2 comparison or * Fisher's exact test for small group. Presented P-value reflects the significance of the difference in the number of kidney stones in the studied groups.

Abbreviations: Wh: whewellite; Wd: weddellite; UAA: uric acid anhydrous; CA: carbapatite; ACCP: amorphous carbonated calcium phosphate; UAD: uric acid dihydrate.

the Russian Federation [64]. In China, CaOx corresponds to 65.9% of new-onset male KSF [65].

The increase in the proportion of calcium stones mainly in women has been reported in a retrospective study of 1516 patients followed from 1980 to 2015 in the USA [66]. Talati and coworkers reported that as stone formers age, the men-to-women ratio decreased significantly from 2005 to 2015 (from 1.8 to 1.08) concomitantly with the alarming increase in the frequency of obesity in American women [59]. Additionally, Taiwanese women with stones exhibited a higher risk of chronic kidney disease (CKD) as reported by multivariate analysis (ORs 5.31; 95% CI: 3.3–13.7) [67]. These data are alarming and invite a broader revision of current management of KSF with additional focus on the prevention of CKD.

More than half of the stones mainly contained calcium oxalate: 79.8% in men and 65.6% in women. Wh accounted for 55.1% of stones in men and 46.7% in women while Wd accounted for 24.7% in men and 18.9% in women. As previously reported [26,50,68], subtype Ia indicated intermittent or moderate hyperoxaluria whereas types IIa and IIb were suggestive for hypercalciuria, whether associated or not with hyperoxaluria of dietary origin or inadequate water intake.

This hypothesis is supported by preliminary data from the retrospective cohort including 112 recurrent KSF that provide the urinary metabolic lithogenic risk factors and KS composition in adult patients from the Brussels region [69]. The physico-chemical analysis of 53 stones demonstrated that Wh has been more prevalent than Wd. In addition, subtype Ia has been found in a higher proportion than subtype IIa suggesting hyperoxaluria and hypercalciuria of dietetic origin as a main urinary abnormality. Indeed, this presumption has been confirmed by the data of 24 h urine collection performed during the first metabolic assessment. Hyperoxaluria followed by idiopathic hypercalciuria has been the most frequent direct lithogenic abnormality, in addition to the high frequency of hypernatriuresis (an indirect promoter

of lithogenesis) that has been highlighted. The authors conclude that the leading metabolic disorders involved in the formation of KS in recurrent KSF in Brussels are dietary hyperoxaluria followed by idiopathic hypercalciuria in correlation with high salt intake. These conclusions corroborate the aetiologies suggested by applying the MCC of stones to our cohort.

The recognition of the existence of Wh and Wd crystalline conversion process is crucial for the clinician. The crystalline conversion from Wd to Wh defines a specific situation when the contradiction appears between the FTIR spectroscopy information about the presence of Wh and morphological findings of bipyramidal crystallites related to Wd [26]. It is admitted that Wh indicates hyperoxaluria and Wd is related to hypercalciuria [26,48], therefore Wh and Wd indicate distinct aetiologies and thus a very different treatment. Bazin *et al.* [70] underlined that if crystalline conversion occurs, the clinician needs to focus on the stone's morphology rather than on the FTIR spectrum as the major focus for assessment of urinary abnormalities. Indeed, he demonstrated that in the case of crystalline conversion from Wd to Wh the FTIR spectra are related to the formation of amorphous whewellite. In this case, hypercalciuria suggested by the stone morphology needs to be considered as a primum movens for stone formation instead of hyperoxaluria suggested by FTIR analysis.

Although composed of Wh, the particular morphology of subtypes Ic and Ie, suggests a very distinct lithogenic process [48]. In case of Ic stone, primary hyperoxaluria (an inborn metabolic disease leading to severe systemic complications and kidney failure) should be systematically sought [45] and in the case of type Ie stone, heavy hyperoxaluria of enteric origin related to increased gut oxalate absorption (short bowel syndrome, pancreatic insufficiency, etc.) should be considered. Types Ib and Id subtypes, although composed also of Wh, are related to precise conditions such as low urine output and urinary stasis, associated or not, with kidney and urinary tract abnormalities. They were not as common in our series as reported by others [60,69].

Type III (UA) progressively increased with age from 40 and reached the highest frequency after age 60, mainly in men as reported in France, in Tunisia and USA [56,62,66]. High temperature and humidity have been reported to impact UA stone formation in Florida [7]. Any relationship between serum UA and KS has been found in a logistic regression of individual data of 6398 KSF from the UK biobank [71], corroborating the postulate of Sakhaee *et al.* [18,21,32] suggesting the major role of urinary pH in AU stone formation.

Low urine pH, recognized as a key factor of UA composed stones, has frequently been reported in observational studies of type 2 diabetic patients and overweight subjects with insulin resistance, as a factor in forming stones. Recently genetic data has reinforced this association [72,73]. During the metabolic work-up of UA stone formers the evaluation of insulin resistance should be a rule and indicate the risk of existence of metabolic syndrome. Early therapeutic interventions should be set up to prevent progression to diabetes and related cardiovascular complications [74].

The pathogenesis of type IV stones is mixed, combining hypercalciuria and alkaline urine pH higher than 6.0 [50]. The type IV stones were submitted mainly by women aged more than 30-years and accounted for 12%, similar to that reported in France (15%) [75]. A plausible hypothesis could be vitamin D and high calcium supplementation to prevent postmenopausal osteoporosis [50,51].

The subtype IVa was the most frequent in both genders and suggests the pathogenic role of hypercalciuria and/or hyperparathyroidism and/or UTI [25,75]. The subtype IVa2 accounted for 0.3% of stones and pointed to the very specific clinical entities involved in CaP formation such as alkaline urinary pH especially related to renal distal tubular acidosis whatever its origin, inherited, autoimmune, of iatrogenic origin or related to medullary sponge kidney [52,75,76].

The stones of subtype IVb indicate past or latent UTI with abnormally high alkaline urine and predominate in women, correlating with the evidence of a higher rate of UTI in women than in men [75,77]. Women with infectious stones have almost twice as high risk for postoperative fever, indicating longer antimicrobial therapy in the postoperative period [78].

Only 66 stones (1.3%) were classified as type IVc and were mainly seen in women (2.0% *vs* 1.4%, $p < 0.0001$) correlating with French data (1.2%) [48]. This type unambiguously results from UTI by urea

splitting bacteria. Within our cohort, 106 stones (2.13%) contained struvite as a main component and were mainly seen in women. In all analyzed stones and fragments the overall frequency of struvite accounted for 2.3%, similar to the frequency reported in Canada (2%), China (2.7% to 3%), Argentina (3%), Iraq (3%), Poland (3%) Italy (3.5%), but lower than the frequency reported in France (7.2%), or in Brazil (8.3%) [65,79–81]. The discrepancy between our data findings and data from Pakistan (18%) or India (23%) or data from paediatric patients from Morocco (18%) could be attributed to the differences in epidemiological characteristics of the populations studied, especially a low human development index and related low access to healthcare (late diagnosis and/or delay in accurate treatment of UTI) rather than temperature and humidity [81]. It was recently reported that neurological bladder and CAKUT contributed to 38% of infectious stones in pediatric populations [25].

The carbapatite stones admixed with struvite exhibit a high content of carbonate ions revealing UTI by urea-splitting bacteria [82]. Indeed, in analysis of the physico-chemical composition of stones the calculation of the content of carbonate ions within the carbapatite (carbonation rate, CR) is helpful to assess UTI as an aetiological factor involved in the stone's formation. Carpentier *et al.* [82] reported a close relationship between the carbonation rate of carbapatite (the amounts of carbonate ions (CO_3^{2-}) in relation to the amount of phosphate ions (PO_4^{3-}) and the number of bacterial imprints within 39 urinary idiopathic hypercalciuric stones but without struvite. This data needs more attention as identification of bacterial imprint could be helpful in controlling stone formation, in case of negative results of urine culture [83].

In the cross-sectional study including 107 KSF in tertiary hospitals in Nepal, *Escherichia coli* was the major non-urease producing organism isolated in the preoperative urine culture [57]. Recently the presence of whitlockite structures detected by SEM and synchrotron radiation has been proposed as a new criterion to identify the infectious origin of stones [84]. In our cohort only 0.3% contained whitlockite as a physical signature of non-urea splitting bacteria involvement in stone genesis.

In the absence of carbonation rate measurements, our data underestimate the prevalence of infectious stones within our cohort as we defined the infectious aetiology stones based on the presence of struvite. Indeed, it has been proposed that low CR value (<10%) in type IV stones suggest a metabolic origin without the participation of UTI; on the contrary CR > 15% indicates the involvement of past or actual UTI in the lithogenesis [82].

The association between the presence of struvite identified by FTIR analysis and type II morphology was suggestive for both UTI by urea-splitting bacteria and hypercalciuria in the patient. Interestingly 54% of paediatric patients (n = 111) with infectious stones (22%) presented hypercalciuria [25]. Indeed, evidence suggest that oral vitamin D supplementation may induce hypercalciuria among children under five years of age [85].

The cumulative frequency of stones containing carbapatite, struvite, brushite, ACCP was 10.8% in our study, corroborating the average cumulative frequency of all calcium and magnesium phosphate stones (9%) analyzed in the smaller series of stones from different countries (n = 1204) as recently reported by Halinski *et al.* [80].

Stones with type IVd morphology accounted for 1.4% and 62 stones (1.24%) were composed mainly of brushite in our experience. Type IVd has been reported in 14% of patients with primary hyperthyroidism in some series [86].

Distinctive morphology of V allowed us the diagnosis of cystinuria [87,88]. The subtype Va is pathognomonic of a heavy cystinuria.

In our series, the subtype Vb was less common, and its frequency was similar to that reported by Daudon *et al.* (0.1% *vs* 10%). The type Vb stones suggest uncontrolled cystinuria associated with inadequate diet and/or medical management or urinary stasis.

We recognize the limitations of our study, including the absence of concomitant 24 h urine collection data to correlate the urinary abnormalities with the aetiologies evoked as suggested by MCC. Such correlation has been previously reported for Wh and Wd stones. Lithogenic factors identified in the 24 h urine collection correlate with the main stone composition identified by physical methods, although the morphological type of KS is unknown in those reports [89–91]. The discordance between the findings from 24 h urine collection and aetiologies evoked by MCC occurs mainly in case of intermittent hyperoxaluria and hypercalciuria, especially if the patient already performed diet and/or hydration

habit modifications. Unfortunately, in every day clinical practice this is by far the most frequent clinical scenario as the patient undergoes metabolic evolution at least two months after the acute manifestation or urological intervention (according to current guidelines). In this context, the identification of prior urine metabolic abnormalities involved in initiation and growth of stones could be revealed only by adequate morphological and physicochemical analysis of stones as described by Daudon [2], which should integrate a metabolic work-up guidelines as previously proposed.

Astonishingly, there is discrepancy between the propositions of the "best" stone classification. Thongprayoon Ch and coworkers [42] proposed a classification of kidney stones according to major chemical composition into the following seven mutually exclusive groups: calcium oxalate (if majority), hydroxyapatite (if majority), uric acid (if any), struvite (if any), brushite (if any), cystine (if any) and others (including stones composed of drugs). However it has been admitted that classification based on chemical analysis is too inadequate to accurately recognize KS components, and could even fail to detect certain elements, such as rare purine stones and drug-induced stones [92].

Recently Williams and coworkers [93] have reported the value of micro-CT technique alone to successfully identify majority of the apatite, brushite, uric acid, and struvite stones and additionally the three-dimensional nature of micro-CT also allows the visualization of surface features in stones, which is valuable for the study of stone formation. The limitation observed by the authors concerned the detection of small quantities well below 1% of minor minerals, such as apatite in CaOx or calcium salts in UA stones.

Our results highlight the need for field-specific standardization of clinical protocols in terms of stone assessment procedures, as well as in defining clinically relevant metadata including MCC type and physical composition of stones considering the initiative of European Renal Stone Network for a common database for observational research [94,95].

Currently the Daudon's MCC remains a gold standard method in KSF assessment [52,96].

4.1. *Conclusions*

According to Daudon's MCC, the leading metabolic disorders involved in lithogenesis in the Belgian population are intermittent hyperoxaluria (Ia), hypercalciuria (IIa), hypercalciuria ± hyperoxaluria ± hypocitraturia (IIb), low urine pH or stasis (IIIa) and diabetes with metabolic syndrome (IIIb). Rare morphologies, types Ie, Id, IId and IVa2 point to precise clinical entities such as enteric hyperoxaluria, urinary tract abnormalities, hyperuricosuria with diarrhoea and distal tubular acidosis respectively. In a few cases, very distinctive morphology such as Ic and V allowed the rapid diagnosis of primary hyperoxaluria type 1 and cystinuria respectively, both severe inborn disorders of metabolism.

Based on our and other experiences, we emphasize that international guidelines for the assessment and management of KSF need to be actualized and should strongly highlight the contribution of Daudon's MCC to the clinical reasoning of physicians.

Abbreviations

ACCP	amorphous carbonated calcium phosphate
CA	carbapatite
CaP	calcium phosphate
CKD	chronic kidney disease
CAKUT	congenital anomalies of the kidney and/or urinary tract
CaOx	calcium oxalate
Cys	cystine
FTIR	Fourier Transform Infrared (Spectroscopy)
[H] KS	kidney stones
KSD	kidney stones disease
KSF	kidney stones formers
MAP	magnesium ammonium phosphate hexahydrate
MCC	morpho-constitutional classification
UA	uric acid
UAA	uric acid anhydrous
UAD	uric acid dihydrate
UTI	urinary tract infection
Wd	weddellite
Wh	whewellite

Conflicts of interest

None declared.

Authors' contributions

AP: Contributed substantially to the conception and design of the study, the acquisition of data, or the analysis and interpretation. Supervised the research, drafted or provided critical revision of the article, provided final approval of the version to publish;
AH: Contributed substantially to the conception and design of the study, the acquisition and the analysis and interpretation, drafted or provided critical revision of the article, provided final approval of the version to publish;
JR: Performed bioinformatic analyses. Drafted or provided critical revision of the article, provided final approval of the version to publish;
TR: Provided the data;
FW: Provided the data, contributed substantially to the analysis and interpretation of data, provided critical revision of the article;
FC: Contributed substantially to the conception and design of the study, the acquisition of data, or the analysis and interpretation, provided critical revision of the article.

Funding

No funding supported this study.

Acknowledgments

The authors would like to acknowledge Dr. Khashayar Sakhaee and Dr. Naim Maalouf (University of Texas Southwestern Medical Center, Dallas, Texas, USA) for helpful discussions during the preparation of this manuscript.

References

[1] C. D. Scales Jr., G. E. Tasian, A. L. Schwaderer, D. S. Goldfarb, R. A. Star, Z. Kirkali, *Clin. J. Am. Soc. Nephrol.*, 2016, **11**, 1305-1312.
[2] A. Pozdzik, N. Maalouf, E. Letavernier, I. Brocheriou, J. J. Body, B. Vervaet, C. Van Haute, J. Noels, R. Gadisseur, V. Castiglione *et al.*, *J. Nephrol.*, 2019, **32**, 681-698.
[3] S. K. Yarovoy, R. V. Royuk, *Urologiia*, 2021, **3**, 33-38.
[4] C. Ganesan, I. C. Thomas, R. Romero, S. Song, S. Conti, C. Elliott, G. M. Chertow, M. K. Tamura, J. T. Leppert, A. C. Pao, *J. Bone Miner. Res.*, 2021, **36**, 872-878.
[5] K. Sakhaee, N. M. Maalouf, J. Poindexter, B. Adams-Huet, O. W. Moe, *J. Urol.*, 2017, **197**, 1472-1477.
[6] I. Sorokin, C. Mamoulakis, K. Miyazawa, A. Rodgers, J. Talati, Y. Lotan, *World J. Urol.*, 2017, **35**, 1301-1320.
[7] C. Grant, G. Guzman, R. P. Stainback, R. L. Amdur, P. Mufarrij, *J. Endourol.*, 2018, **32**, 973-977.
[8] C. Roger, N. Abid, L. Dubourg, C. Auvergnon, S. Lemoine, C. Machon, *Prog. Urol.*, 2020, **30**, 339-345.
[9] W. G. Robertson, H. Hughes, *Scanning Microsc.*, 1993, **7**, 391-401, discussion 401–402.
[10] F. Abbassene, A. Maizia, N. Messaoudi, L. Bendahmane, H. Boukharouba, M. Daudon, A. Addou, *Tunis Med*, 2020, **98**, 396-403.
[11] J. J. Crivelli, N. M. Maalouf, H. J. Paiste, K. D. Wood, A. E. Hughes, G. R. Oates, D. G. Assimos, *J. Urol.*, 2021, **206**, 517-525.
[12] D. S. Goldfarb, J. Hirsch, *Med. Hypotheses*, **85**, 953-957.
[13] P. M. Ferraro, E. I. Mandel, G. C. Curhan, G. Gambaro, E. N. Taylor, *Clin. J. Am. Soc. Nephrol.*, 2016, **11**, 1834-1844.
[14] E. N. Taylor, G. C. Curhan, *Kidney Int.*, 2008, **73**, 207-212.
[15] R. J. Johnson, S. E. Perez-Pozo, J. L. Lillo, F. Grases, J. D. Schold, M. Kuwabara, Y. Sato, A. A. Hernando, G. Garcia, T. Jensen *et al.*, *BMC Nephrol.*, 2018, **19**, article no. 315.
[16] P. M. Ferraro, M. Bargagli, A. Trinchieri, G. Gambaro, *Nutrients*, 2020, **12**, 779-795.
[17] E. N. Taylor, M. J. Stampfer, G. C. Curhan, *J. Am. Soc. Nephrol.*, 2004, **15**, 3225-3232.
[18] K. Sakhaee, *J. Nephrol.*, 2014, **27**, 241-245.
[19] I. A. Bobulescu, N. M. Maalouf, G. Capolongo, B. Adams-Huet, T. R. Rosenthal, O. W. Moe, K. Sakhaee, *Am. J. Physiol. Renal Physiol.*, 2013, **305**, F1498-F1503.
[20] F. Qiu, Y. Xu, X. Ji, J. Pu, J. Zhou, Y. Huang, *Transl. Androl. Urol.*, 2021, **10**, 3646-3655.
[21] K. Sakhaee, B. Adams-Huet, O. W. Moe, C. Y. Pak, *Kidney Int.*, 2002, **62**, 971-979.
[22] K. Sakhaee, N. M. Maalouf, *Semin. Nephrol.*, 2008, **28**, 174-180.
[23] M. Daudon, B. Lacour, P. Jungers, *Urol. Res.*, 2006, **34**, 193-199.
[24] G. Gambaro, E. Croppi, D. Bushinsky, P. Jaeger, A. Cupisti, A. Ticinesi, S. Mazzaferro, A. D'Addessi, P. M. Ferraro, *J. Urol.*, 2017, **198**, 268-273.
[25] C. Rauturier, C. Machon, D. Demede, L. Dubourg, J. Bacchetta, A. Bertholet-Thomas, *Eur. J. Pediatr.*, 2021, **180**, 3555-3563.
[26] M. Daudon, R. J. Reveillaud, *Nephrologie*, 1984, **5**, 195-201.
[27] P. M. Ferraro, A. Ticinesi, T. Meschi, A. Rodgers, F. Di Maio, P. Fulignati, L. Borghi, G. Gambaro, *J. Urol.*, 2018, **200**, 1082-1087.
[28] E. N. Taylor, G. C. Curhan, *Nephron Physiol.*, 2004, **98**, 55-63.
[29] B. A. Vervaet, P. C. D'Haese, M. E. De Broe, A. Verhulst, *Nephrol. Dial. Transplant.*, 2009, **24**, 3659-3668.
[30] B. A. Vervaet, A. Verhulst, M. E. De Broe, P. C. D'Haese, *Urol. Res.*, 2010, **38**, 249-256.
[31] O. W. Moe, *Lancet*, 2006, **367**, 333-344.
[32] K. Sakhaee, N. M. Maalouf, B. Sinnott, *J. Clin. Endocrinol. Metab.*, 2012, **97**, 1847-1860.

[33] A. Skolarikos, M. Straub, T. Knoll, K. Sarica, C. Seitz, A. Petrik, C. Turk, *Eur. Urol.*, 2015, **67**, 750-763.
[34] J. C. Williams Jr., G. Gambaro, A. Rodgers, J. Asplin, O. Bonny, A. Costa-Bauza, P. M. Ferraro, G. Fogazzi, D. G. Fuster, D. S. Goldfarb *et al.*, *Urolithiasis*, 2021, **49**, 1-16.
[35] D. J. Sas, *Clin. J. Am. Soc. Nephrol.*, 2011, **6**, 2062-2068.
[36] W. Wang, J. Fan, G. Huang, J. Li, X. Zhu, Y. Tian, L. Su, *Sci. Rep.*, 2017, **7**, article no. 41630.
[37] M. Prochaska, E. N. Taylor, G. Curhan, *J. Urol.*, 2018, **200**, 823-828.
[38] Y. Li, D. Bayne, S. Wiener, J. Ahn, M. Stoller, T. Chi, *J. Pediatr. Urol.*, 2020, **16**, 373.e1-373.e6.
[39] C. D. Scales Jr., A. C. Smith, J. M. Hanley, C. S. Saigal, *Eur. Urol.*, 2012, **62**, 160-165.
[40] A. Chewcharat, G. Curhan, *Urolithiasis*, 2021, **49**, 27-39.
[41] W. Kittanamongkolchai, L. E. Vaughan, F. T. Enders, T. Dhondup, R. A. Mehta, A. E. Krambeck, C. H. McCollough, T. J. Vrtiska, J. C. Lieske, A. D. Rule, *Mayo Clin. Proc.*, 2018, **93**, 291-299.
[42] C. Thongprayoon, A. E. Krambeck, A. D. Rule, *Nat. Rev. Nephrol.*, 2020, **16**, 736-746.
[43] D. Bos, E. Abara, M. S. Parmar, *Can. Urol. Assoc. J.*, 2014, **8**, E795-E804.
[44] D. I. Chu, G. E. Tasian, L. Copelovitch, *Curr. Treat. Options Pediatr.*, 2016, **2**, 104-111.
[45] A. Pozdzik, C. David, J. Vekeman, F. Tielens, M. Daudon, *IJU Case Rep.*, 2021, **4**, 235-238.
[46] J. Vekeman, J. Torres, C. E. David, E. Van de Perre, K. M. Wissing, E. Letavernier, D. Bazin, M. Daudon, A. Pozdzik, F. Tielens, *Nanomaterials (Basel)*, 2021, **11**, 1763-1775.
[47] M. Daudon, C. A. Bader, P. Jungers, *Scanning Microsc.*, 1993, **7**, 1081-1104, discussion 1104–1106.
[48] M. Daudon, A. Dessombz, V. Frochot, E. Letavernier, J.-P. Haymann, P. Jungers, D. Bazin, *C. R. Chim.*, 2016, **19**, 1470-1491.
[49] M. Corrales, S. Doizi, Y. Barghouthy, O. Traxer, M. Daudon, *Eur. Urol. Focus*, 2021, **7**, 13-21.
[50] J. Cloutier, L. Villa, O. Traxer, M. Daudon, *World J. Urol.*, 2015, **33**, 157-169.
[51] V. Frochot, M. Daudon, *Int. J. Surg.*, 2016, **36**, 624-632.
[52] M. Daudon, P. Jungers, D. Bazin, J. C. Williams Jr., *Urolithiasis*, 2018, **46**, 459-470.
[53] F. Cotton, F. Wolff, I. Simon, M. Idrissi, C. Tielemans, M. Vanden Bossche, T. Roumeguere, A. Pozdzik, *Rev. Med. Brux.*, 2014, **35**, 243-249.
[54] A. Pozdzik, C. Van Haute, N. Maalouf, E. Letavernier, J. C. Williams, K. Sakhaee, *Urolithiasis*, 2021, **49**, 493-494.
[55] T. Knoll, A. B. Schubert, D. Fahlenkamp, D. B. Leusmann, G. Wendt-Nordahl, G. Schubert, *J. Urol.*, 2011, **185**, 1304-1311.
[56] M. Daudon, J. C. Dore, P. Jungers, B. Lacour, *Urol. Res.*, 2004, **32**, 241-247.
[57] S. Ranjit, A. K. Singh, *JNMA J. Nepal Med. Assoc.*, 2020, **58**, 871-874.
[58] J. C. Lieske, A. D. Rule, A. E. Krambeck, J. C. Williams, E. J. Bergstralh, R. A. Mehta, T. P. Moyer, *Clin. J. Am. Soc. Nephrol.*, 2014, **9**, 2141-2146.
[59] V. M. Talati, R. M. O. Soares, A. Khambati, R. B. Nadler, K. T. Perry Jr., *Urolithiasis*, 2020, **48**, 305-311.
[60] V. Castiglione, F. Jouret, O. Bruyere, B. Dubois, A. Thomas, D. Waltregny, A. C. Bekaert, E. Cavalier, R. Gadisseur, *Nephrol. Ther.*, 2015, **11**, 42-49.
[61] M. Daudon, L. Estepa, B. Lacour, P. Jungers, *J. Nephrol.*, 1998, **11**, 51-55.
[62] A. Alaya, A. Nouri, M. Belgith, H. Saad, I. Hell, W. Hellara, R. Jouini, M. F. Najjar, *Actas Urol. Esp.*, 2012, **36**, 171-177.
[63] S. Bouslama, A. Boutefnouchet, B. Hannache, T. Djemil, A. Kadi, A. Dahdouh, S. Saka, M. Daudon, *Prog. Urol.*, 2016, **26**, 41-49.
[64] V. I. Smirnova, D. G. Lebedev, S. V. Lapin, V. L. Emanuel, R. V. E, *Urologiia*, 2021, **6**, 20-24.
[65] Z. Ye, G. Zeng, H. Yang, J. Li, K. Tang, G. Wang, S. Wang, Y. Yu, Y. Wang, T. Zhang *et al.*, *BJU Int.*, 2020, **125**, 801-809.
[66] L. H. R. Xu, B. Adams-Huet, J. R. Poindexter, N. M. Maalouf, O. W. Moe, K. Sakhaee, *J. Urol.*, 2017, **197**, 1465-1471.
[67] T. M. Chien, Y. M. Lu, C. C. Li, W. J. Wu, H. W. Chang, Y. H. Chou, *Biol. Sex Differ.*, 2021, **12**, article no. 40.
[68] M. Daudon, *Rev. Med. Suisse Romande*, 2004, **124**, 445-453.
[69] M. El Mallouli, C. Van Haute, D. Barglazan, M. P. Lebitasy, W. G. Robertson, A. Pozdzik, *Rev. Med. Brux.*, 2021, **42**, 155-166.
[70] D. Bazin, C. Leroy, F. Tielens, C. Bonhomme, L. Bonhomme-Coury, F. Damay, D. Le Denmat, J. Sadoine, J. Rode, V. Frochot *et al.*, *C. R. Chim.*, 2016, **19**, 1492-1503.
[71] R. K. Narang, G. G. Gamble, R. Topless, M. Cadzow, L. K. Stamp, T. R. Merriman, N. Dalbeth, *Am. J. Kidney Dis.*, 2021, **78**, 210-218.
[72] S. Yuan, S. C. Larsson, *Mol. Genet. Metab.*, 2021, **134**, 212-215.
[73] F. C. Torricelli, S. De, S. Gebreselassie, I. Li, C. Sarkissian, M. Monga, *Urology*, 2014, **84**, 544-548.
[74] M. Daudon, P. Jungers, *Curr. Diab. Rep.*, 2007, **7**, 443-448.
[75] M. Daudon, H. Bouzidi, D. Bazin, *Urol. Res.*, 2010, **38**, 459-467.
[76] A. Dessombz, E. Letavernier, J. P. Haymann, D. Bazin, M. Daudon, *J. Urol.*, 2015, **193**, 1564-1569.
[77] L. Maurice-Estepa, P. Levillain, B. Lacour, M. Daudon, *Scand. J. Urol. Nephrol.*, 1999, **33**, 299-305.
[78] L. Peng, Z. Xu, J. Wen, W. Zhong, G. Zeng, *World J. Urol.*, 2021, **39**, 1277-1285.
[79] F. Meiouet, S. El Kabbaj, M. Daudon, *Prog. Urol.*, 2019, **29**, 173-182.
[80] A. Halinski, K. H. Bhatti, L. Boeri, J. Cloutier, K. Davidoff, A. Elqady, G. Fryad, M. Gadelmoula, H. Hui, K. Petkova *et al.*, *Arch. Ital. Urol. Androl.*, 2021, **93**, 307-312.
[81] T. D. S. Cunha, A. Rodriguez, I. P. Heilberg, *J. Bras. Nefrol.*, 2020, **42**, 454-460.
[82] X. Carpentier, M. Daudon, O. Traxer, P. Jungers, A. Mazouyes, G. Matzen, E. Veron, D. Bazin, *Urology*, 2009, **73**, 968-975.
[83] D. Bazin, G. Andre, R. Weil, G. Matzen, V. Emmanuel, X. Carpentier, M. Daudon, *Urology*, 2012, **79**, 786-790.
[84] D. Bazin, R. J. Papoular, E. Elkaim, R. Weil, D. Thiaudière, C. Pisapia, B. Ménez, N. S. Hwang, F. Tielens, M. Livrozet *et al.*, *C. R. Chim.*, 2022, **25**, no. S1, 343-354.
[85] S. L. Huey, N. Acharya, A. Silver, R. Sheni, E. A. Yu, J. P. Pena-Rosas, S. Mehta, *Cochrane Database Syst. Rev.*, 2020, **12**, article no. CD012875.
[86] I. Simon, T. Roumeguere, F. Devuyst, F. Cotton, B. N. Tang, M. Cappello, S. Corbetta, M. Idrissi, A. Pozdzik, J. Nortier, *Rev. Med. Brux.*, 2015, **36**, 172-176.

[87] R. Belhadj, O. Marrakchi, L. Zerelli, A. Mohsni, M. Chebil, J. Abdelmoula, *Tunis. Med.*, 2008, **86**, 556-559.
[88] A. Kamoun, M. Daudon, J. Abdelmoula, M. Hamzaoui, B. Chaouachi, T. Houissa, A. Zghal, S. Ben Ammar, C. Belkahia, R. Lakhoua, *Pediatr. Nephrol.*, 1999, **13**, 920-925, discussion 926.
[89] J. R. Asplin, J. Lingeman, R. Kahnoski, H. Mardis, J. H. Parks, F. L. Coe, *J. Urol.*, 1998, **159**, 664-668.
[90] M. A. Cameron, N. M. Maalouf, B. Adams-Huet, O. W. Moe, K. Sakhaee, *J. Am. Soc. Nephrol.*, 2006, **17**, 1422-1428.
[91] F. C. Torricelli, S. De, X. Liu, J. Calle, S. Gebreselassie, M. Monga, *J. Endourol.*, 2014, **28**, 735-738.
[92] M. Daudon, P. Jungers, *Drugs*, 2004, **64**, 245-275.
[93] J. C. Williams Jr., J. E. Lingeman, M. Daudon, D. Bazin, *C. R. Chim.*, 2022, **25**, no. S1, 61-72.
[94] P. M. Ferraro, R. Unwin, O. Bonny, G. Gambaro, *J. Nephrol.*, 2021, **34**, 1337-1346.
[95] P. M. Ferraro, M. A. Arrabal-Polo, G. Capasso, E. Croppi, A. Cupisti, T. Ernandez, D. G. Fuster, J. A. Galan, F. Grases, E. J. Hoorn *et al.*, *Urolithiasis*, 2019, **47**, 219-224.
[96] C. Pricop, M. Ivanuta, A. Stan, D. T. Anton-Paduraru, G. D. Radavoi, V. Jinga, T. M. Proca, D. Puia, *Rom. J. Morphol. Embryol.*, 2020, **61**, 1227-1233.

Comptes Rendus
Chimie
2022, Vol. 25, Special Issue S1, p. 269-279
https://doi.org/10.5802/crchim.116

Microcrystalline pathologies: Clinical issues and nanochemistry / *Pathologies microcristallines : questions cliniques et nanochimie*

Medullary sponge kidney: what kind of stones?

Michel Daudon *, [a, b], **Vincent Frochot** [a, b], **Dominique Bazin** [c], **Jean-Philippe Haymann** [a, b] and **Emmanuel Letavernier** [a, b]

[a] Service des Explorations Fonctionnelles, Hôpital Tenon, APHP, 75020 Paris, France

[b] INSERM UMRS 1155, Sorbonne Université, Hôpital Tenon, 75020 Paris, France

[c] Institut de Chimie Physique, UMR CNRS 8000, Université Paris Sud, 91400 Orsay, France

E-mails: daudonmichel24@gmail.com, m.daudon@infonie.fr (M. Daudon), vincent.frochot@aphp.fr (V. Frochot), dominique.bazin@universite-paris-saclay.fr (D. Bazin), jean-philippe.haymann@aphp.fr (J.-P. Haymann), emmanuel.letavernier@aphp.fr (E. Letavernier)

Abstract. Medullary sponge kidney (MSK) is an anomaly of the kidney with cystic enlargement of distal tubules generating stasis zones where calcium salt deposits may form and grow locally. From an epidemiological point of view, MSK is reported in 2% to more than 20% of calcium stone formers. The association of stasis and various metabolic disorders explains a high recurrence rate of stones in affected patients. The composition of stones has been poorly investigated. The aim of this study is to compare stone composition and morphology in MSK and non-MSK patients.

Material and methods: 1036 stones from MSK patients and 31,494 stones from non-MSK patients were submitted to a morpho-constitutional analysis based on morphological typing under stereo microscope and precise characterization of chemical and crystalline phases by Fourier transform infrared spectroscopy.

Results and discussion: Regarding patients, the male to female ratio was significantly lower in MSK vs non-MSK subjects (1.48 vs 2.09, $p < 0.00001$). The recurrence rate was significantly higher in MSK patients (85.0% vs 39.5% in non-MSK, $p < 0.000001$). Stones were more often spontaneously passed in MSK vs non-MSK subjects (45.7% vs 34.6%, $p < 0.000001$). Stones were mainly composed of calcium oxalate in both groups (66.3% vs 72.5%). However, the slight decrease in the occurrence of calcium oxalate stones was mainly supported by weddellite calculi, less frequent in MSK (17.0% vs 21.6% in non-MSK, $p < 0.001$). The main point was the high proportion of stones mainly composed of calcium phosphates: 28.9% in MSK vs 13.9% in non-MSK patients) with a high proportion of stones exhibiting a IVa2 morphology which is a marker for distal tubular acidification defect (12.1% in MSK vs 0.4% in non-MSK patients, $p < 0.000001$). Finally, while stones nucleated from a papillary Randall's plaque were found with a similar frequency in both groups, calcium phosphate nucleus was significantly more frequent in MSK than in non-MSK stones (68.8% vs 48.9%, $p < 0.000001$), suggesting a frequent initiation of stones from calcium phosphate plugs in distal tubules ectasias.

Keywords. Medullary sponge kidney, Calculi, Stone analysis, Morphology, Calcium phosphates, Calcium oxalates.

Published online: 15 October 2021, Issue date: 1 September 2022

* Corresponding author.

1. Introduction

Medullary sponge kidney (MSK) is a common anomaly in recurrent stone formers who present more severe stone disease than other conditions [1–3]. MSK is a congenital disease with a familial transmission in some cases where GNDF/RET genes mutations were suspected to play a major role to explain abnormal development of the kidneys in affected patients [4–6]. The occurrence of MSK among stone formers is controversial in the literature, ranging from 2% up to 25% [7–14]. Indeed, tubular ectasias may be located only in a caliceal group of one kidney or may be extended to all calices of both kidneys, making very diverse the clinical expression of this malformative uropathy. In addition, metabolic disorders that favour urine supersaturation and crystal formation may be diverse, including hypercalciuria, hyperoxaluria, hypocitraturia, hypomagnesuria. As a result, clinical signs of the disease range from the absence of any kind of stones to multiple and recurrent stones with nephrocalcinosis affecting one or both kidneys. It is largely accepted that stones are made of calcium salts, including calcium oxalate and calcium phosphate, but also in some cases uric acid [2,10,15]. However, very few studies have investigated more precisely the stone composition and morphology in MSK patients [13,14,16,17]. Examining our stone database, we found that about one thousand calculi analysed in our lab were from patients suffering from MSK. The aim of this work is to provide accurate information regarding composition and morphology of the stones associated with MSK and to compare these data with the ones recorded in common stone disease.

2. Materials and methods

From 1990 to 2020, we received about 77,500 stones for morpho-constitutional analysis based on optical examination of the surface and the section of the stones in order to classify them according to a morphological type completed by a sequential infrared analysis from the core to the surface providing a quantitative crystalline composition as previously described [18–20]. Among them, 32,532 stones were accompanied with a query sheet providing clinical information on comorbidities and the presence or not of urological or kidney anomalies: 31,494 stones came from patients without any malformative anomaly (control group) while 1036 stones came from MSK patients. In case the query sheet mentioned MSK and other clinical disease such as primary hyperparathyroidism, renal tubular acidosis or other cause of nephrocalcinosis, the stone was excluded from the study. MSK diagnosis was made by trusted urologists or nephrologists aware of the limitations of imaging for such a diagnosis. Most urologists who mentioned MSK have performed endoscopic examination of the kidney(s). For nephrologists, the diagnosis was based on the results of a CT scan with injection of contrast product and furosemide and, for the oldest cases, on the results of an intravenous urography.

Scanning electron microscopy was performed on a selected sample of MSK stones to better describe crystal morphologies and stone organization. For this purpose, surface and section of selected stones were examined using a FEI/Philips XK-40 environmental scanning electron microscope. Such apparatus does not need conductive coating and permits direct observation of the sample.

Statistical comparisons were based on the Chi-square test and Fisher's exact test when appropriate. Statistical significance was considered for $p < 0.05$.

3. Results

3.1. *Patients*

Demographic and clinical data are summarized in Table 1. Among 31,494 patients without MSK, 21,315 were males and 10,179 were females (sex ratio M/F = 2.09). Among 1036 patients with MSK, 618 were males and 418 were females (sex ratio = 1.48; $p < 0.00001$ vs non-MSK patients). Recurrence of clinically symptomatic stone episodes accounted for 85% of cases in MSK vs 39.6% in non-MSK patients ($p < 0.000001$). Because many MSK patients had multiple stones in one or both kidneys, it is difficult to conclude that a new stone episode is actually a stone recurrence. By contrast, in non-MSK patients, it is easier to assert stone recurrence when imaging reveals the patient is stone-free after a previous stone. Males were more prone than females to recurring stones in non-MSK patients (41.4% vs 35.9%, $p < 0.000001$). No significant difference was found in MSK patients (M: 86.7%, F: 82.2%, NS).

The mean age of MSK patients was moderately lower than in non-MSK patients (45.5 ± 13.3 vs 48.3

Table 1. Demographic and clinical data

	MSK			Non-MSK		
	Males	Females	Total	Males	Females	Total
Number	618	418	1036	21,315	10,179	31,494
Mean age	45.5 ± 12.6	45.9 ± 13.7	45.5 ± 13.3	48.4 ± 14.4	48.1 ± 16.4	48.3 ± 15.3
BMI (kg/m^2)	25.0 ± 3.7	23.8 ± 6.4	24.6 ± 5.0	25.8 ± 4.4	25.8 ± 6.3	25.8 ± 5.2
Stone recurrence	86.7[a]	82.2[a]	85.0[a]	41.3[1]	35.7	39.5

[a] $p < 0.000001$ vs non-MSK.

[1] $p < 0.000001$ vs females in the same group.

Table 2. Mode of stone removal

	MSK			Non-MSK		
	Males	Females	Total	Males	Females	Total
Spontaneously passed	328 (53.1)[d,5]	145 (34.7)[a]	473 (45.7)[d]	8066 (37.8)[5]	2841 (27.9)	10,907 (34.6)
Endoscopy	167 (27.0)[c,4]	178 (42.6)	345 (33.3)	7425 (34.8)[5]	3986 (39.2)	11,411 (36.2)
ESWL	72 (11.6)	35 (8.4)[a]	107 (10.3)[a]	2987 (14.0)	1321 (13.0)	4308 (13.7)
NLPC	27 (4.4)[a]	31 (7.4)[a]	58 (5.6)[b]	1611 (7.6)[5]	1228 (12.1)	2839 (9.0)
Surgery	16 (2.6)[a,1]	24 (5.7)	40 (3.9)[a]	1102 (5.2)	746 (7.3)	1848 (5.9)
Coelioscopy	0	0	0	13 (<0.1)	11 (0.1)	24 (<0.1)
Unknown	8 (1.3)	5 (1.2)	13 (1.25)	111 (0.5)	46 (0.45)	157 (0.5)
Total	618	418	1036	21,315	10,179	31,494

[a] $p < 0.01$; [b] $p < 0.001$; [c] $p < 0.0001$; [d] $p < 0.000001$ vs non-MSK.

[1] $p < 0.01$; [2] $p < 0.001$; [3] $p < 0.0001$; [4] $p < 0.00001$; [5] $p < 0.000001$ vs females in the same group.

± 15.3 years, $p < 0.000001$). BMI was similar in both groups at the upper limit of the normal range (24.6 ± 5.0 in MSK vs 25.8 ± 5.2 kg/m^2 in non-MSK subjects, NS).

3.2. *Urological procedures*

Whilst only 34.6% of stones are spontaneously passed in non-MSK patients, we found that 45.7% of the stones were expelled without any urological procedure in MSK subjects ($p < 0.000001$), the proportion increasing up to 53.1% in male patients. A urological treatment was required for removal of 54.3% of the stones. As shown in Table 2, percutaneous nephrolithotomy was performed in 5.6% of cases and ESWL was used in 10.3% of cases. The most common treatment for stone removal was endoscopy, including JJ stents, rigid or flexible ureteroscope, and basket to trap stones. Endoscopic procedures were applied in 33.3% of cases. Open surgery accounted for only 3.9% of urological treatment and for less than 1% of cases in recent years.

3.3. *Stones*

3.3.1. *Main component*

Calcium oxalate was the main component in 76.2% of stones in MSK males and 51.7% in MSK females (Table 3). Such difference between genders was also found in non-MSK patients. Of note, among crystalline phases of calcium oxalate, weddellite was significantly less frequent in MSK patients ($p < 0.0001$).

The striking difference between MSK and non-MSK stones was the very high proportion of stones mainly composed of calcium phosphates in the case of MSK (28.9% vs 13.8%, $p < 0.000001$) in both genders. As shown in Table 3, carbapatite and brushite

Table 3. Main components in MSK and non-MSK related stones

Main component	MSK			Non-MSK		
	Males	Females	Total	Males	Females	Total
N	618	418	1036	21,315	10,179	31,494
Calcium oxalate	471 (76.2)^{3}	216 (51.7)^{v}	687 (66.3)	16,759 (78.6)^{z}	6079 (59.8)	22,838 (72.5)^{c}
Whewellite	341 (55.2)^{2}	167 (40.0)	508 (48.9)	11,402 (53.5)^{z}	4627 (45.5)	16,029 (50.9)
Weddellite	130 (21.0)^{1}	49 (11.7)	179 (17.0)	5357 (25.1)^{z}	1452 (14.3)	6809 (21.6)^{b}
Calcium phosphate	118 (19.1)^{*,3}	181 (43.3)^{y}	299 (28.9)	1737 (8.1)^{z}	2612 (25.7)	4349 (13.8)^{e}
Carbapatite (CA)	87 (14.1)^{*,3}	166 (39.7)^{y}	253 (24.4)	1307 (6.1)^{z}	2369 (23.3)	3676 (11.7)^{e}
CA without MAP	77 (12.5)^{**,1}	144 (34.4)^{z}	221 (21.3)	998 (4.7)^{z}	1553 (15.3)	2551 (8.1)^{e}
Brushite	27 (4.4)*	13 (3.1)^{v}	40 (3.9)	380 (1.8)	150 (1.5)	530 (1.7)^{d}
Presence of brushite	47 (7.6)***	24 (5.7)^{v}	71 (6.9)	650 (3.0)	300 (3.0)	950 (3.0)^{e}
Other calcium phosphates	4 (0.6)	2 (0.5)	6 (0.6)	50 (0.2)^{z}	93 (0.9)	143 (0.5)
Struvite (MAP)	0	1 (0.2)^{v}	1 (0.1)	143 (0.7)^{z}	251 (2.5)	394 (1.3)^{b}
Presence of MAP	9 (1.5)^{2}	30 (7.2)^{v}	39 (3.8)	563 (2.6)^{z}	1189 (11.7)	1752 (5.6)
Uric acid and urates	22 (3.6)**	14 (3.3)^{v}	36 (3.5)	2102 (9.9)^{z}	770 (7.6)	2872 (9.1)^{e}
Uric acid anhydrous	21 (3.4)*	12 (2.9)^{v}	33 (3.2)	1767 (8.3)^{z}	650 (6.4)	2417 (7.7)^{e}
Uric acid dihydrate	1 (0.2)*	0	1 (0.1)	299 (1.4)^{y}	73 (0.7)	372 (1.2)
Ammonium urate	0	1 (0.2)	1 (0.1)	29 (0.1)^{x}	42 (0.4)	71 (0.2)
Cystine	3 (0.5)	1 (0.2)^{v}	4 (0.4)	252 (1.2)^{z}	212 (2.1)	464 (1.5)^{a}
Proteins	4 (0.6)	4 (1.0)	8 (0.8)	160 (0.8)^{v}	109 (1.1)	269 (0.9)
Others	0	1 (0.2)	1 (0.1)	169 (0.8)^{v}	151 (1.5)	320 (0.3)
Total	618 (100)	418 (100)	1036 (100)	21,315 (100)	10,179 (100)	31,494 (100)

$^{a}p < 0.01$; $^{b}p < 0.001$; $^{c}p < 0.0001$; $^{d}p < 0.00001$; $^{e}p < 0.000001$ vs MSK.

$^{1}p < 0.001$; $^{2}p < 0.00001$; $^{3}p < 0.000001$ vs MSK females.

$^{*}p < 0.0001$; $^{**}p < 0.00001$; $^{***}p < 0.000001$ vs non-MSK males.

$^{v}p < 0.01$; $^{w}p < 0.001$; $^{x}p < 10^{-4}$; $^{y}p < 10^{-5}$; $^{z}p < 10^{-6}$ vs non-MSK females.

were two times more frequent in MSK patients. Despite stasis induced by tubular ectasias, infection stones seemed infrequent since the presence of struvite was not increased in MSK vs non-MSK patients. In agreement with such observation, the mean content of carbapatite in MSK stones was significantly increased by comparison with non-MSK stones in both genders (17.4% of stone weight in average in MSK vs 9.4% in non-MSK), the difference being more marked in female (26.6% vs 13.7%, $p < 0.000001$) than in male patients (12.2% vs 7.1%, $p < 0.0001$).

3.3.2. *Stone morphology*

Regarding stone morphology, which is an important marker in addition to stone composition for the relation to etiology [21,22], the first message deduced from morpho-constitutional stone analysis was that pure stone types (Table 4) were significantly less frequent in MSK patients (33.9% vs 44.6% in non-MSK patients, $p < 0.000001$). As observed in common stone disease, the main type was Ia (13% vs 18.6%, $p < 0.00001$ MSK vs non-MSK), followed by IVa2 stones (5.2% vs 0.4%, $p < 0.000001$ MSK vs non-MSK) and by IIa or IIb stones (5.0% vs 9.0%, $p < 0.00001$ MSK vs non-MSK).

Interestingly, IVa2 morphology, which is a marker for distal acidification defect [23] was thirty times more frequent in MSK patients. IVa2 morphology was observed as pure or mixed type on the surface or within the stones with a high frequency in MSK patients: 12.1% vs 0.4% in non-MSK ($p < 0.000001$). The occurrence of type IVa2 was significantly higher in female than in male patients (20.6% vs 6.0%, $p < 0.000001$).

Table 4. Pure morphological types

Morphological type	MSK			Non-MSK		
	Males	Females	Total	Males	Females	Total
Ia	94 (15.2)[a]	41 (9.8)[a]	135 (13.0)[c]	4295 (20.2)[4]	1565 (15.4)	5860 (18.6)
Ib	0	1 (0.2)	1 (0.1)	162 (0.8)	72 (0.7)	234 (0.7)
Ic	0	0	0	23 (0.1)	10 (0.1)	33 (0.1)
Id	1 (0.2)	3 (0.7)	4 (0.4)	125 (0.6)	53 (0.5)	178 (0.6)
Ie	0	0	0	79 (0.4)	44 (0.4)	123 (0.4)
IIa or IIb	43 (7.0)[a,1]	9 (2.2)[a]	52 (5.0)[c]	2272 (10.7)[4]	573 (5.6)	2845 (9.0)
IIIa	1 (0.2)	0	1 (0.1)[a]	244 (1.1)[2]	65 (0.6)	309 (1.0)
IIIb	15 (2.4)[b]	5 (1.2)[a]	20 (1.9)[c]	1232 (5.8)	453 (4.4)	1685 (5.4)
IIIc	0	0	0	50 (0;2)	27 (0.3)	77 (0.2)
IIId	0	0	0	2 (0.01)	14 (0.1)	16 (0.05)
IVa1	11 (1.8)	16 (3.8)	27 (2.6)	177 (0.8)[4]	440 (3.3)	617 (2.0)
IVa2	8 (1.3)[c,4]	46 (11.0)[d]	54 (5.2)[d]	49 (0.2)[4]	74 (0.7)	123 (0.4)
IVb	5 (0.8)[3]	24 (5.7)	29 (2.8)	260 (1.2)[4]	773 (7.6)	1033 (3.3)
IVc	0	0	0	26 (0.1)	38 (0.4)	64 (0.2)
IVd	10 (1.6)	7 (1.7)	17 (1.6)[a]	180 (0.8)	76 (0.7)	256 (0.8)
Va or Vb	2 (0.3)	0	2 (0.2)[a]	218 (1.0)	175 (1.7)	393 (1.2)
VIa, b or c	3 (0.5)	0	3 (0.3)	134 (0.6)	52 (0.5)	186 (0.6)
Others	1 (0.2)	5 (1.2)	6 (0.6)	95 (0.4)	32 (0.3)	127 (0.4)
Total	194 (31.4)[d]	157 (37.6)[a]	351 (33.9)[d]	9623 (45.1)	4536 (44.6)	14,159 (45.0)

[a] $p < 0.01$; [b] $p < 0.001$; [c] $p < 0.00001$; [d] $p < 0.000001$ vs non-MSK.

[1] $p < 0.001$; [2] $p < 0.0001$; [3] $p < 0.00001$; [4] $p < 0.000001$ vs females in the same group.

Examples of stone morphology in MSK patients are given in Figures 1 and 2 for examination under stereo microscope and in Figure 3 for SEM examination. One of the main features of the stones produced by these patients was the high diversity of stone composition and morphology among calculi produced by the same patient. There was no similar finding in non-MSK patients (Table 5).

In more than 12% of cases (thirty times more frequent than in non-MSK patients), IVa2 type (white arrows on Figures 1C and E) is observed among the stones, suggesting distal acidification defect in the patients.

As shown in Table 5, mixed types were more frequent in MSK patients. The main associations were type Ia or Ib mixed with type IIa or IIb (26.9%), ternary associations of type Ia or Ib mixed with type IIa or IIb mixed with type IVa or IVb (14.6%) and associations of type IIa or IIb mixed with type IVa or IVb (11.1%). These associations accounted for more than 52% of all stones in MSK patients.

3.3.3. *Stone nucleus*

As a result of the high occurrence of stone fragmentation by extracorporeal lithotripsy or in situ fragmentation by laser during ureteroscopic procedures, stone nucleus was available in only 816 stones from MSK patients and 24,079 stones from non-MSK patients. Main components found in stone nucleus are gathered together in Table 6.

In MSK patients, 68.8% of all stones (vs 48.9% in non-MSK patients) were initiated from a calcium phosphate nucleus ($p < 0.000001$). However, the occurrence of RP was similar in both groups (Table 6). Calcium oxalate nuclei accounted for 21.2% of stones from MSK patients and weddellite was involved only in 5.5% of cases. The main components of RP in MSK are given in Table 7.

Table 5. Mixed morphological types

Mixed types	MSK			Non-MSK		
	Males	Females	Total	Males	Females	Total
I + II*	207 (33.5)[b,4]	72 (17.2)	279 (26.9)	5562 (26.1)[4]	1833 (18.0)	7395 (23.5)
II + IV*	65 (10.5)	50 (12)	115 (11.1)	2419 (11.3)	1280 (12.6)	3689 (11.7)
I + II + IV*	79 (12.8)[c]	72 (17.2)[c]	151 (14.6)[c]	1205 (5.6)[3]	729 (7.2)	1934 (6.1)
I + III*	11 (1.8)	4 (1.0)	15 (1.4)	479 (2.2)	154 (1.5)	633 (2.0)
I* + IVa1	6 (1.0)[2]	19 (4.5)	25 (2.4)	197 (0.9)[4]	350 (3.4)	547 (1.7)
IVa1 + IVd	13 (2.1)[c]	5 (1.2)	18 (1.7)[b]	84 (0.4)	50 (0.6)	134 (0.4)
IVd + II*	7 (1.1)	0	7 (0.7)	134 (0.6)	44 (0.4)	178 (0.6)
II* + IVa1 + IVd	4 (0.6)	2 (0.5)	6 (0.6)	98 (0.5)	39 (0.4)	137 (0.4)
I + II + III*	3 (0.5)	2 (0.5)	5 (0.5)	174 (0.8)	73 (0.7)	247 (0.8)
Ia + II* + IVd	3 (0.5)	2 (0.5)	5 (0.5)	21 (0.1)	4 (<0.1)	25 (<0.1)
Ia + IVa2 + IVd	3 (0.5)	0	3 (0.3)	0	0	0
IVa + VIb	5 (0.8)	2 (0.5)	7 (0.7)	106 (0.5)[4]	205 (2.0)	311 (1.0)
Others	21 (3.4)[a,1]	31 (7.4)	52 (5.0)	1213 (5.7)[4]	882 (8.7)	2095 (6.7)
Total	424 (68.6)[c]	261 (62.4)[a]	685 (66.1)[c]	11,692 (54.9)	5643 (55.4)	17,335 (55.0)

*Subtypes a or b for each type.

[a] $p < 0.01$; [b] $p < 0.0001$; [c] $p < 0.000001$ vs non-MSK.

[1] $p < 0.01$; [2] $p < 0.001$; [3] $p < 0.00001$; [4] $p < 0.000001$ vs females in the same group.

4. Discussion

To the best of our knowledge, this series is the largest database regarding stone characteristics from MSK patients. The first information deduced from this cohort is the relatively low male to female sex ratio (1.48/1) in comparison to the control group (2.09/1, $p < 0.000001$). Thus, women seem more prone than men to present canalicular ectasias and stones in this context, confirming the previous reports of Yagisawa *et al.* [10] and Fabris *et al.* [2]. The second point is the high stone recurrence rate in MSK patients (85% vs 39.5% in non-MSK, $p < 0.000001$) as underlined by several authors [2,24,25]. Of note, stones in MSK patients have a high propensity to expel spontaneously as shown in Table 2 (45.7% vs 34.6% in non-MSK patients, $p < 0.000001$). Spontaneous stone passage is more frequent in men than in women (53.1% vs 34.7%, $p < 0.000001$). The high rate of stone activity in MSK patients may be explained by stasis in tubular ectasias, in addition to metabolic risk factors found as frequently as in other stone patients, mainly hypercalciuria and hypocitraturia, and less frequently hyperoxaluria and hyperuricosuria [2,10,26].

Stone composition shows that calcium oxalate is the main component of 76.2% of stones in males and 51.7% in females. Among crystalline phases, weddellite, which can be considered as a calcium-dependent species [27–30] appears to be less frequent in MSK patients while hypercalciuria is often reported as a frequent finding among metabolic factors explaining stone formation [1,2,8,24,26]. However, in agreement with our data, other studies report a less frequent occurrence of hypercalciuria in MSK patients when compared to other stone formers [10].

Stone composition and morphology are both highly suggestive of high occurrence of an acidification defect in MSK patients. Arguments for this are the high proportion of calcium phosphate containing stones (28.9% vs 13.9% in non-MSK patients, $p < 0.000001$), including carbapatite and brushite crystalline species and the very high proportion of type IVa2 as morphologic characteristics of surface and/or inner structure of the calculi (12.1% vs 0.3% in non-MSK, $p < 0.000001$). This finding is especially true for stones from female patients: 20.6% vs 6.0% in males, $p < 0.000001$). Hypocitraturia, which is considered as a marker for renal acidifica-

Table 6. Main component of the stone nucleus

Component	MSK			Non-MSK		
	Males	Females	Total	Males	Females	Total
Ca oxalates	144 (29.1)	74 (23.0)	218 (26.7)	6981 (42.3)	2330 (30.7)	9311 (38.7)
COM	110 (22.2)[d]	63 (19.6)	173 (21.2)[e]	5124 (31.0)[2]	1801 (23.7)	6925 (28.8)
COD	34 (6.9)[b]	11 (3.4)[a]	45 (5.5)[d]	1857 (11.3)[2]	529 (7.0)	2386 (9.9)
Ca phosphates	326 (65.9)[f]	235 (73.2)[f]	561 (68.8)[f]	7606 (46.1)[2]	4165 (55.0)	11,772 (48.9)
Carbapatite	304 (61.4)[f]	223 (68.5)[f]	527 (64.6)[f]	7231 (43.8)[2]	3946 (52.1)	11,177 (46.4)
Brushite	10 (2.0)[c]	2 (0.6)	12 (1.5)[b]	113 (0.7)	35 (0.5)	148 (0.6)
Other CaP	12 (2.4)	10 (3.1)	22 (2.7)	262 (1.6)	184 (2.4)	447 (1.9)
Struvite	1 (0.2)	0	1 (0.1)	78 (0.5)[2]	187 (2.5)	265 (1.1)
Uric acids	15 (3.0)[d]	9 (2.8)[b]	24 (2.9)[e]	1308 (7.9)	516 (6.8)	1824 (7.6)
Urates	1 (0.2)	2 (0.6)	3 (0.4)	51 (0.3)	57 (0.7)	108 (0.4)
Cystine	3 (0.6)	1 (0.3)	4 (0.5)	173 (1.0)	129 (1.7)	302 (1.3)
Proteins	4 (0.8)	2 (0.6)	6 (0.7)	189 (1.1)	104 (1.4)	293 (1.2)
Others	1 (0.2)	1 (0.3)	2 (0.2)	114 (0.7)	90 (1.2)	204 (0.8)
RP	153 (30.9)[1]	54 (16.8)	207 (25.4)	4459 (27.0)[2]	1447 (19.1)	5906 (24.5)
Total	495	321	816	16,501	7578	24,079

Other CaP = whitlockite, octacalcium phosphate pentahydrate, amorphous carbonated calcium phosphate.

RP = Randall's plaque.

[a] $p < 0.05$; [b] $p < 0.01$; [c] $p < 0.001$; [d] $p < 0.0001$; [e] $p < 0.00001$; [f] $p < 0.000001$ vs non-MSK.

[1] $p < 0.00001$; [2] $p < 0.000001$ vs females in the same group.

Table 7. Components of Randall's plaques in MSK patients

Components found in RP	MSK
Carbapatite	205 (99.0)
ACCP	18 (8.7)
Monosodium hydrogen urate	6 (2.9)
Brushite	2 (1.0)

tion defect (in the absence of urinary tract infection) was often described as a major metabolic disorder in MSK patients [2,10,26] and several works confirm an acidification defect in MSK patients [31,32] even if other studies failed to demonstrate any abnormal response to dynamic acidification tests [33]. In our experience, proven severe distal acidification defect responsible for stone formation is associated with a very high proportion of calcium phosphate-rich stones exhibiting the type IVa2 morphology [23,34]. Thus, the relatively high proportion (12.1%) of MSK patients producing IVa2 stones suggests a high occurrence of distal acidification defects in this context but affecting less than 50% of MSK patients. Of note, the occurrence of IVa2 morphology was three times more frequent in females than in males without any evident explanation. Perhaps MSK women in our series presented with more extended and severe form of MSK, but we have no radiographic data to confirm such hypothesis.

Another interesting point regarding stone morphology is the relatively high occurrence of mixed stones in MSK patients (66.1% vs 55% in non-MSK subjects, $p < 0.000001$), the difference being more marked in males (68.6% in MSK vs 54.9% in non-MSK patients). About 16.5% of stones exhibit three different morphological types, which is two times more than in non-MSK patients (7.4%).

Regarding stone nucleation, we underlined in previous reports that about 50% of calcium stones were

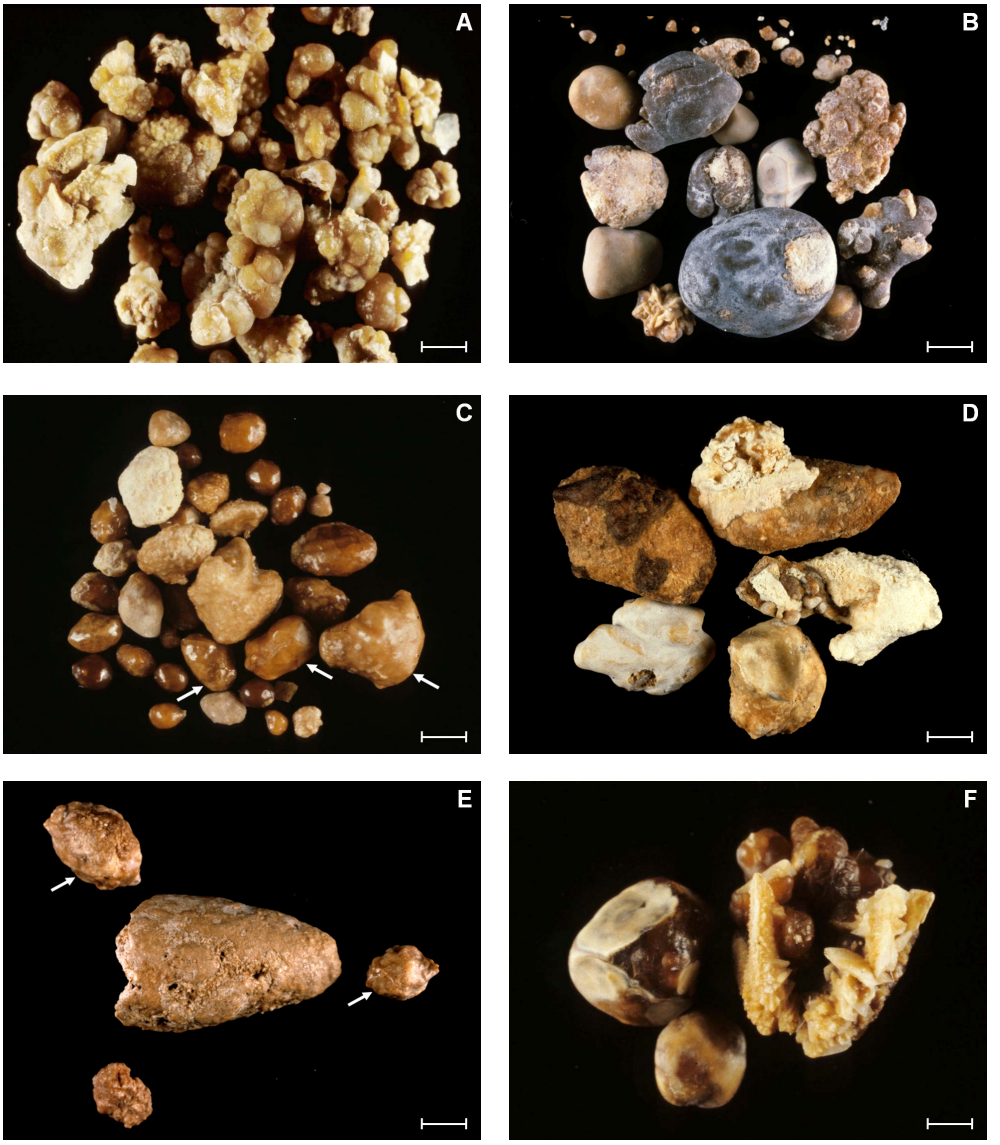

Figure 1. Heterogeneity of stone morphology and composition in MSK patients. Each photograph shows multiple stones spontaneously passed by one patient. Figures A, B and F show calculi mainly composed of calcium oxalate monohydrate mixed with calcium oxalate dihydrate and containing only small proportions of carbapatite. Figures C–E illustrate calcium stones where calcium oxalate monohydrate and calcium oxalate dihydrate are associated with high proportions of carbapatite which is the main component of calculi in Figure E. Bars = 2 mm.

initiated from a calcium phosphate nucleus even when the stone was nearly pure in calcium oxalate [35]. A significant part of these stone nuclei were made of a Randall's plaque (RP), a papillary calcification mainly composed of carbapatite [36,37]. In MSK patients, the frequency of RP as the nucleus of calcium stones was similar to that observed in non-MSK patients. However, we observed an increased proportion of stones initiated from a calcium phosphate (68.8% vs 48.9% in non-MSK, $p < 0.000001$). A high occurrence of calcium phosphate plugs in tubular ectasias may explain this phenomenon.

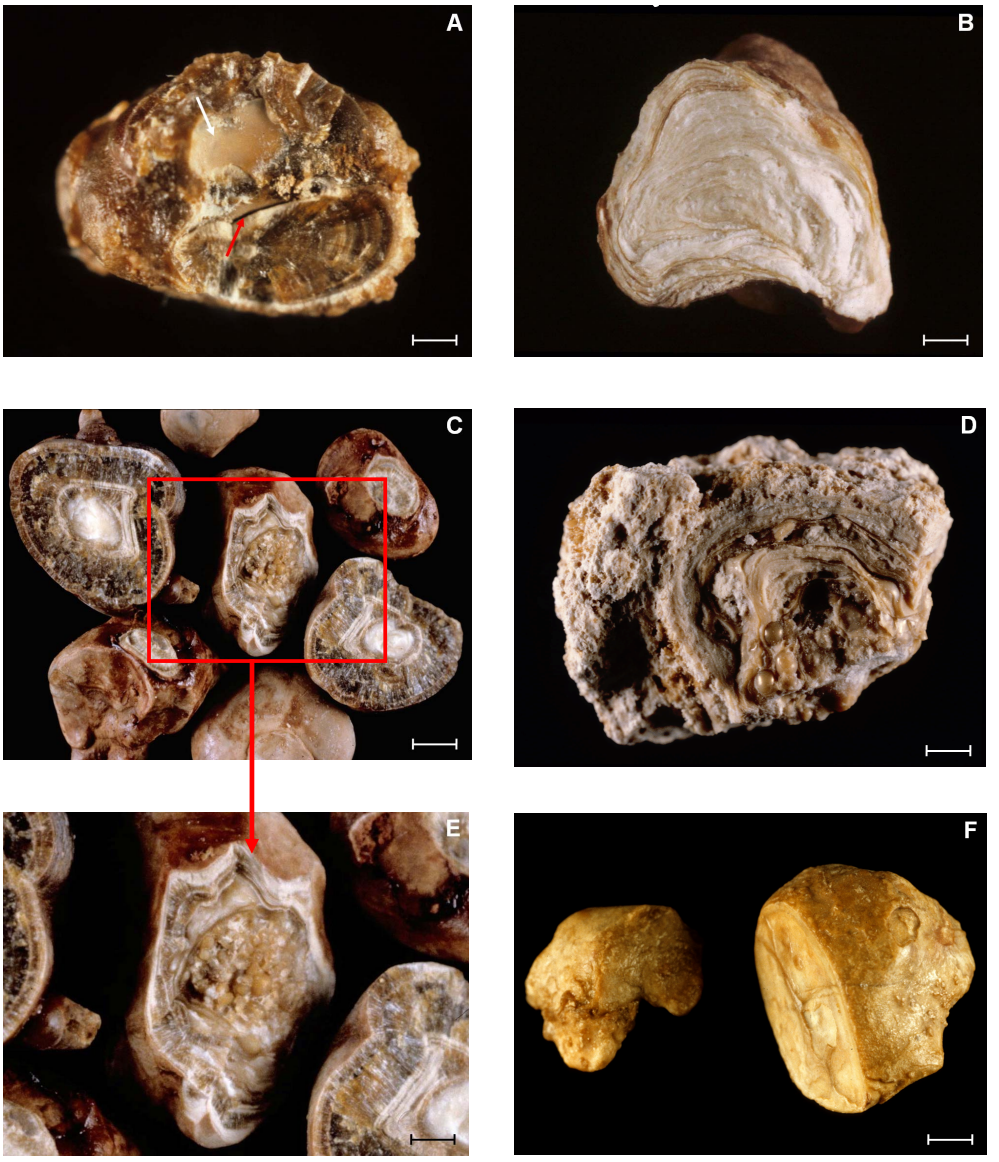

Figure 2. Examples of inner structure of stones formed in MSK patients. (A) Stone section showing that two initial stones have secondly merged to form only one stone. The partition line between the two stones is indicated by the red arrow. Of note, one of the stones was initially in straight contact with another stone as suggested by the presence of a joining face (white arrow). Bar = 1 mm. (B) Stone section made of numerous concentric cream to pale yellow-brown layers mainly composed of carbapatite. Bar = 1 mm. (C) Stone sections mainly made of calcium oxalate monohydrate (brown crystalline layers with radial organization) surrounding a whitish core made of carbapatite. Bar = 1 mm. Of note, in Figures D and E, which is a magnification of Figure C, the stone core is made of multiple type IVa2 spheres of carbapatite first formed within collecting ducts of the kidney. Bars 1D = 1 mm; 1E = 0.5 mm. (F) Another example of MSK stones mainly composed of carbapatite whose inner structure corresponds to IVa2 morphology which is highly suggestive of distal acidification defects. Bar = 1 mm.

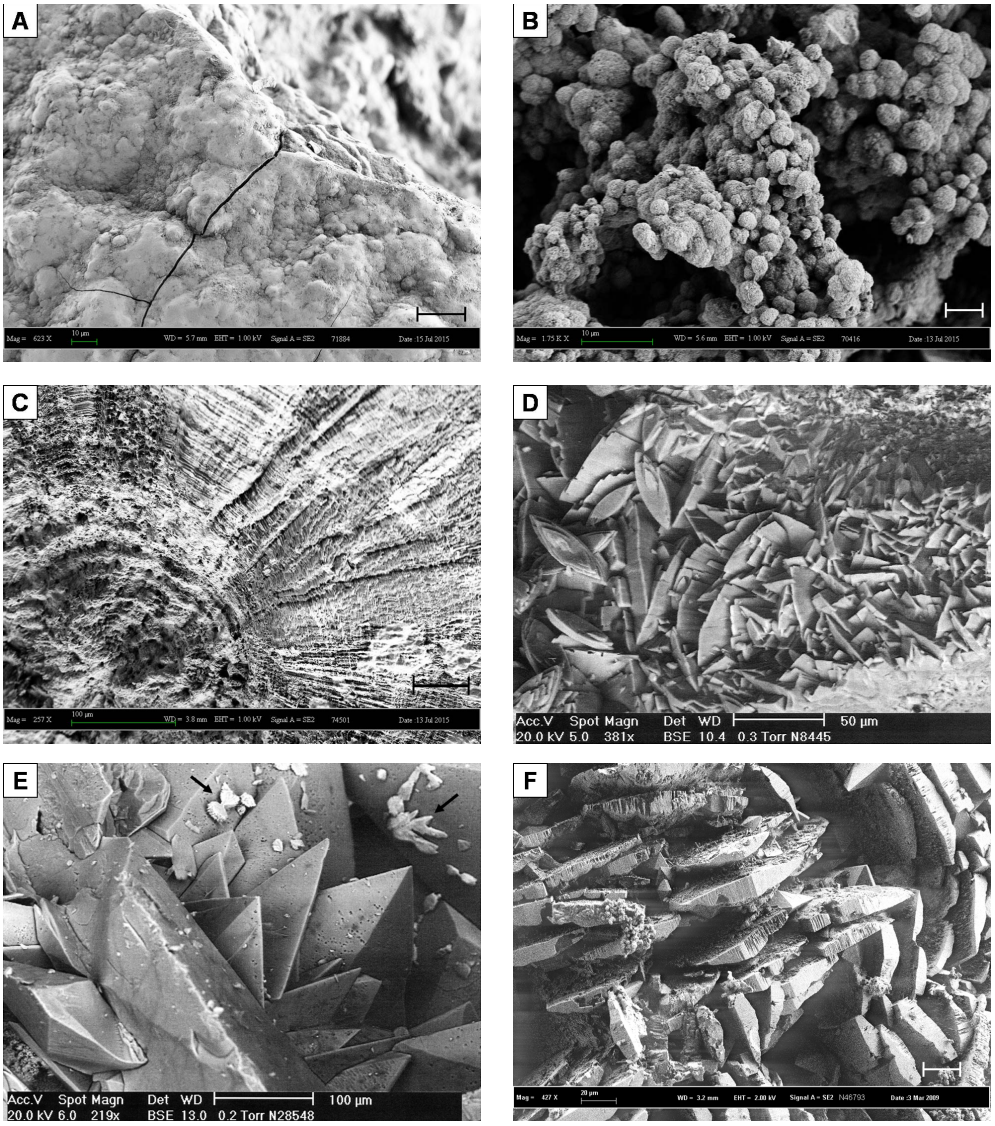

Figure 3. Scanning electron microscopy photographs of MSK stones. (A) Type IVa2 surface, embossed with cracks. Bar = 20 µm. (B) Inner loose layer with carbapatite spherules. Bar = 5 µm. (C) Section of type Ia stone with concentric layers and radial crystallization. Bar = 50 µm. (D) Whewellite crystals poorly organized in deep layers of a stone. Bar = 50 µm. (E) Periphery of a MSK stone with weddellite crystals locally covered by small aggregates of whewellite crystals (black arrows). Bar = 100 µm. (F) Typical crystals of brushite at the surface of a type IVd stone. Bar = 20 µm.

As evidenced by stone analysis, not all MSK patients suffer renal acidification defect. On the other hand, metabolic evaluation of patients in various series found a variety of metabolic disorders as reported in non-MSK, suggesting that some patients, independently of their tubular ectasias, may present risk factors of stone formation related to other causes such as metabolic syndrome or diabetes mellitus. Thus, it is not surprising to find uric acid stones in MSK patients. Of note, 83.3% of MSK patients producing uric acid stones in our database were overweight or obese. However, we can note that uric acid

calculi account for only 3.5% of the series, i.e., three times less than in common stone formers. We found also a small proportion (0.4%) of cystine stones.

A limitation of our study is that MSK diagnosis was made by different ways, either endoscopic examination for urologists or intravenous urography or CT scan in other cases. We cannot rule out false negative cases (undiagnosed MSK) but the number of false positive cases was probably limited by the fact that most of stones analysed were sent by trusted urologists or nephrologists aware of the limitations of MSK diagnosis. Of note, repeated misdiagnosis of MSK would have blunted the differences between MSK and non-MSK-related kidney stones.

5. Conclusion

Kidney stones developed in MSK patients present morphological and compositional characteristics significantly different from that observed in non-MSK stones. Both stasis and metabolic disorders may contribute to stone formation. The key point of our results is the high proportion of calcium phosphates, as main components of the stones and even more as the nucleus of a large number of MSK calculi. These data are in agreement with a more frequent acidification defect than in other clinical contexts of stone disease as suggested by the literature and also in our study by the high frequency of stones exhibiting IVa2 morphology.

References

[1] J. H. Parks, F. L. Coe, A. L. Strauss, *New Engl. J. Med.*, 1982, **306**, 1086-1091.

[2] A. Fabris, A. Lupo, P. Bernich, C. Abaterusso, N. Marchionna, A. Nouvenne, G. Gambaro, *Clin. J. Am. Soc. Nephrol.*, 2010, **5**, 1663-1668.

[3] M. Daudon, O. Traxer, P. Jungers, *Lithiase Urinaire*, 2nd ed., Médecine-Sciences, Lavoisier, Paris, 2012, 672 pages.

[4] R. Torregrossa, F. Anglani, A. Fabris, A. Gozzini, A. Tanini, D. Del Prete, R. Cristofaro, L. Artifoni, C. Abaterusso, N. Marchionna, A. Lupo, A. D'Angelo, G. Gambaro, *Clin. J. Am. Soc. Nephrol.*, 2010, **5**, 1205-1210.

[5] A. Fabris, F. Anglani, A. Lupo, G. Gambaro, *Nephrol. Dial. Transpl.*, 2013, **28**, 1111-1119.

[6] T. H. Imam, H. Patail, H. Patail, *Int. J. Nephrol. Renov.*, 2019, **12**, 213-218.

[7] J. N. Lavan, F. C. Neale, S. Posen, *Med. J. Aust.*, 1971, **2**, 1049-1061.

[8] M. O'Neill, N. A. Breslau, C. Y. C. Pak, *J. Am. Med. Assoc.*, 1981, **245**, 1233-1236.

[9] M. Laube, B. Hess, F. Terrier, P. Vock, P. Jaeger, *Schweiz Rundsch. Med. Prax.*, 1995, **84**, 1224-1230.

[10] T. Yagisawa, C. Kobayashi, T. Hayashi, A. Yoshida, H. Toma, *Am. J. Kidney Dis.*, 2001, **37**, 1140-1143.

[11] J. M. Ginalski, L. Portmann, P. Jaeger, *Am. J. Roentgenol.*, 1990, **155**, 299-302.

[12] E. Thomas, Y. Witte, J. Thomas, G. Arvis, *Prog. Urol.*, 2000, **10**, 29-35.

[13] E. R. Yendt, S. Jarzylo, M. Cohanim, in *Urolithiasis* (V. R. Walker, R. A. L. Sutton, E. C. B. Cameron, eds.), Plenum Press, New-York, 1989, 383-386.

[14] F. Hildebrandt, P. Jungers, C. Robino, J. P. Grünfeld, in *Diseases of the Kidney and Urinary Tract* (R. W. Schrier, ed.), Lippincott Williams & Wilkins, Boston, 2001, 521-546.

[15] E. F. McPhail, M. T. Gettman, D. E. Patterson, L. J. Rangel, A. E. Krambeck, *Urology*, 2012, **79**, 277-281.

[16] P. Jungers, P. Conort, M. Daudon, *Eurobiol.*, 2001, **34**, 51-55.

[17] M. Daudon, F. Cohen-Solal, B. Lacour, P. Jungers, *Prog. Urol.*, 2003, **13**, 1320-1329.

[18] M. Daudon, M. F. Protat, R. J. Réveillaud, *Ann. Biol. Clin.*, 1978, **36**, 475-489.

[19] M. Daudon, C. Bader, P. Jungers, *Scanning Microsc.*, 1993, **7**, 1081-1106.

[20] M. Daudon, A. Dessombz, V. Frochot, E. Letavernier, J. P. Haymann, P. Jungers, D. Bazin, *C. R. Chim.*, 2016, **19**, 1470-1491.

[21] M. Daudon, P. Jungers, in *Urolithiasis: Basic Science and Clinical Practice* (J. J. Talati, H. G. Tiselius, D. M. Albala, Z. Ye, eds.), Springer Verlag, London, 2012, 113-140.

[22] J. Cloutier, L. Villa, O. Traxer, M. Daudon, *World J. Urol.*, 2015, **33**, 157-169.

[23] A. Dessombz, E. Letavernier, J. P. Haymann, D. Bazin, M. Daudon, *J. Urol.*, 2015, **193**, 1564-1569.

[24] A. P. Evan, E. M. Worcester, J. C. Williams Jr., A. J. Sommer, J. E. Lingeman, C. L. Phillips, F. L. Coe, *Anat. Rec. (Hoboken)*, 2015, **298**, 865-877.

[25] W. Cheungpasitporn, C. Thongprayoon, B. A. Brabec, W. Kittanamongkolchai, S. B. Erickson, *Clin. Kidney J.*, 2016, **9**, 866-870.

[26] E. Cicerello, M. Ciaccia, G. Cova, M. Mangano, *Arch. Ital. Urol. Androl.*, 2019, **91**, 102-106.

[27] B. T. Murphy, L. N. Pyrah, *Br. J. Urol.*, 1962, **34**, 129-159.

[28] M. Daudon, R. J. Réveillaud, *Néphrologie*, 1984, **5**, 195-201.

[29] J. R. Asplin, J. E. Lingeman, R. Kahnoski, H. Mardis, J. H. Parks, F. L. Coe, *J. Urol.*, 1998, **159**, 664-668.

[30] M. Daudon, E. Letavernier, V. Frochot, J. P. Haymann, D. Bazin, P. Jungers, *C. R. Chim.*, 2016, **19**, 1504-1513.

[31] E. Higashihara, K. Nutahara, K. Tago, A. Veno, T. Nijima, *Kidney Int.*, 1984, **25**, 453-459.

[32] P. J. Osther, A. B. Hansen, H. F. Rohl, *Br. J. Urol.*, 1988, **61**, 392-394.

[33] P. Houillier, F. Leviel, M. Daudon, M. Paillard, P. Jungers, in *Urolitihasis* (V. R. Walker, R. A. L. Sutton, E. C. Bert Cameron, C. Y. C. Pak, W. G. Robertson, eds.), Plenum Press, New York, 1989, 375-377.

[34] M. Daudon, H. Bouzidi, D. Bazin, *Urol. Res.*, 2010, **38**, 459-467.

[35] M. Daudon, *Ann. Urol.*, 2005, **39**, 209-231.

[36] M. Daudon, O. Traxer, P. Jungers, D. Bazin, *Am. Instit. Phys. Conf. Proc.*, 2007, **900**, 26-34.

[37] M. Daudon, D. Bazin, E. Letavernier, *Urolithiasis*, 2015, **43**, 5-11.

Comptes Rendus
Chimie
2022, Vol. 25, Special Issue S1, p. 281-293
https://doi.org/10.5802/crchim.160

Microcrystalline pathologies: Clinical issues and nanochemistry / *Pathologies microcristallines : questions cliniques et nanochimie*

The type Ic morphology of urinary calculi: an alert to primary hyperoxaluria? Experience with 43 Moroccan children

Faïza Meiouet [*, a], **Saâd El Kabbaj** [a] **and Michel Daudon** [b]

[a] Laboratoire de Recherche et d'Analyses Médicales de la Gendarmerie Royale, Avenue Ibn Sina, Agdal, Rabat, Maroc

[b] Laboratoire des Lithiases, Service des Explorations Fonctionnelles, Hôpital Tenon, APHP, Paris, France

E-mails: fmeiouet@lram-fgr.ma (F. Meiouet), selkabbaj@lram-fgr.ma (S. El Kabbaj), daudonmichel24@gmail.com (M. Daudon)

Abstract. Primary hyperoxaluria is the most severe stone disease responsible for multiple stone recurrence and impairment of kidney function. It is a rare inherited disease with an autosomal transmission. Due to the high proportion of consanguineous marriages by comparison to other areas in the world, this pathology is more frequent in North Africa. Stones are made of calcium oxalate monohydrate, which is not unique to the disease and cannot help physicians for the diagnosis. By contrast, stone morphology may be a useful marker of the pathology. We report our experience based on 614 stones from Moroccan children analyzed by infrared spectroscopy and examined by stereomicroscopy for the determination of their morphological type. Our results show that 85 stones (13.8%) exhibit a type Ic morphology, strongly suggestive of the disease in children patients. It was confirmed in all subjects of a subgroup of 43 patients who benefited from urinary biochemical explorations revealing whewellite crystalluria and a very high oxalate to creatinine ratio.

Keywords. Primary hyperoxaluria, Type Ic, Stone morphology, Infrared spectroscopy, Whewellite, Crystalluria.

Published online: 15 March 2022, Issue date: 1 September 2022

1. Introduction

Primary hyperoxaluria (PH) is one of the most severe hereditary kidney stone diseases and is caused by defects in glyoxylate metabolism, resulting in overproduction of oxalate and eventually end stage renal disease (ESRD). Three different genetic forms have been identified to date, related to mutations on three genes coding for three enzymes, namely alanine glyoxylate aminotransferase (PH1) [1,2], glyoxylate reductase hydroxypyruvate reductase (PH2) [3,4] and 4-hydroxy-2-oxo-glutarate aldolase 1 (PH3) [5,6]. In all cases, the high production of oxalate, mainly by the liver, is the cause of recurrent urolithiasis and nephrocalcinosis which are the main markers of the disease. At the stage of severe chronic kidney disease, plasma oxalate increase leads to a systemic

* Corresponding author.

oxalosis characterized by calcium oxalate deposits in all tissues, in particular bones and the cardiovascular system [7,8]. Furthermore, it accounts for 1 to 2% of cases of pediatric ESRD, according to registries from Europe, the United States, and Japan [1,9,10], but it appears to be more prevalent in countries in which consanguineous marriages are common (with a prevalence of 10% or higher in some North African and Middle Eastern nations), but it is certainly underestimated [11]. From an epidemiological point of view, PH1 is the most frequent (60–75% of cases) and unfortunately the most severe form of the disease. Theoretically, the diagnosis of PH should be based on the measurement of oxalate in urine and/or blood and confirmed by genetic determination of the gene mutations. Unfortunately, for economic reasons and logistics, these tools are not available in many countries around the world, thus inducing an absence of diagnosis or a delay in the diagnosis of this pathology with dramatic consequences for the patient [1,12, 13]. Moreover, due to inadequate pre-analytical conditions by untrained laboratories, oxalate measurement in urine may fail to demonstrate elevated levels because of oxalate loss as a result of massive calcium oxalate crystalluria. Even in western countries, the diagnosis may be missed because the clinical course of the disease is only calcium oxalate stone disease, the composition of calculi being very common since they are made of calcium oxalate, the main component of about 70–90% of the stones throughout the world. Thus, a number of PH cases are diagnosed in patients with ESRD and even after a failed kidney transplant [13–15]. Actually, data from PH cohorts in industrialized countries show that the diagnosis was only made after progression to ESRD in more than 30% of patients [1,9,12,16].

The number of PH cases in Morocco is currently unknown because PH is under-diagnosed. The objective of this study on a group of Moroccan children is to show that calcium oxalate monohydrate (COM) stone with type Ic morphology is associated with high oxalate excretion, which should lead to PH investigation and genetic assessment.

2. Material and methods

2.1. *Study population*

This study was based on the current morpho-constitutional stone analysis [17,18] performed routinely in the Laboratoire de Recherches et d'Analyses Médicales de la Gendarmerie Royale in Morocco. From 1999 to 2020, we analyzed urinary calculi from 614 children aged less than 18 years old, i.e., 419 boys and 195 girls. Because type Ic morphology of stones has been described as a strong marker suggesting PH [18,19], we focused our attention on patients who formed COM stones with a type Ic morphology. Of our 614 patients, 85 children (53 boys, 32 girls) met this criterion. However, urine samples required for determining oxalate concentration and the oxalate to creatinine ratio were not available for all patients. Only 43 patients who formed Ic-type calculi were able to benefit from additional biochemical exploration including the study of crystalluria and oxalate assay in urine samples. They were compared to a control group of 92 children (55 boys, 37 girls aged from 1 month to 17 years old) who produced stones with other morphological types including only 10 patients with type Ia stones. Ideally, the control group should have included pure calcium oxalate stones with morphologies other than type Ic, but this group, very common in adult patients, hardly exists in children in our series where many stones have an infectious component and include either phosphates or ammonium urate. None of the patients presented with chronic pancreatitis or inflammatory bowel disease or other cause of absorptive hyperoxaluria.

2.2. *Methods*

2.2.1. *Morpho-constitutional analysis of urinary stones*

Each calculus was checked for its morphological characteristics using a stereomicroscope to define the morphological type according to the previously reported classification [17,18] and to select the representative parts of the stone (core, inner layers and surface) for specific infrared analysis. Among calcium oxalate stones, it was shown that type I stones mainly formed of COM are related to hyperoxaluria. By contrast, type II stones are mainly associated to hypercalciuria. Type I may be subdivided in five subtypes, namely Ia, Ib, Ic, Id and Ie [20–22]. Type Ia stones are essentially related to intermittent hyperoxaluria from dietary origin while type Ic stones are very widely associated with PH and type Ie stones to enteric hyperoxaluria. Type Ic stones, that are strongly

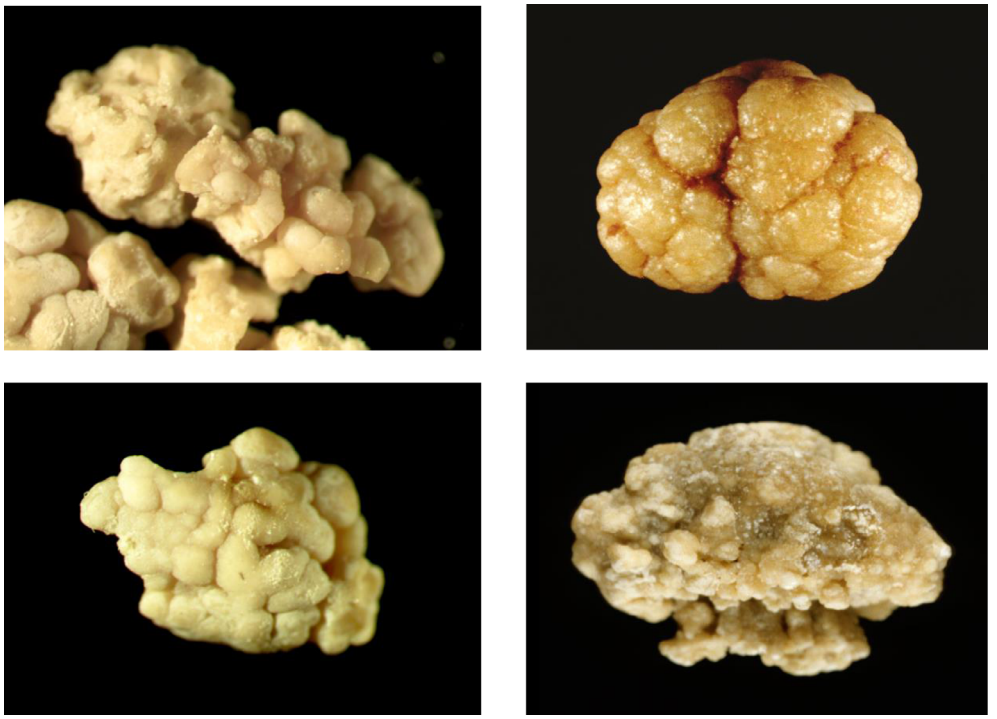

Figure 1. Morphological aspect of pure type Ic calcium oxalate monohydrate stones (surface).

suggestive for PH have a particular morphology characterized by a pale, yellowish budding surface and a loose, finely granular and unorganized section with light color, cream to pale yellow-brown as shown in Figures 1 (surface) and 2 (section). Stone morphology is very different from that observed in common type Ia COM stones resulting from dietary habits and/or low diuresis. As shown in Figure 3, type Ia COM stones are characterized by a dark-brown smooth surface with nipples. The stone section is dark-brown in color and made of concentric layers with radial crystallization.

A sequential infrared analysis is the second step of the morpho-constitutional analysis. For this purpose, a fraction of 1–2 mg of each calculus sample selected under the stereomicroscope was pulverized and crushed in 100–200 mg of pure and dry potassium bromide for IR spectroscopy analysis [25]. The mixture was transformed into a transparent pellet of 13 mm in diameter using a press under a pressure of 10 tons/cm^2 as previously described [25]. The pellet was then placed in a special holder and inserted into the infrared spectrophotometer for analysis. The instrument used was a Nicolet IS10 Fourier transform infrared spectrometer from Thermo-Nicolet. The infrared spectra were recorded on the wavelength range from 2.5 to 25 μm (4000–400 cm^{-1}) with a resolution of 4 cm^{-1}. Air was used as the reference. The resulting spectra were identified by comparison with available reference spectra [25,26]. Thereafter, in order to assess the total composition of the stone, each calculus was pulverized in its totality and a fraction of the powder was again used to prepare a pellet to be analyzed.

2.2.2. *Crystalluria studies*

For half of the patients with type Ic stones ($n = 43$), at least one and often several urine samples were available for metabolic evaluation and crystalluria analysis. We performed crystalluria studies to confirm the diagnosis and for the follow-up of the patients. Thus, we examined 173 crystalluria in fresh first-voided morning urine samples, according to a uniform protocol described elsewhere [27]. In short, urine samples brought to the laboratory within 2 hours of voiding were kept at room temperature

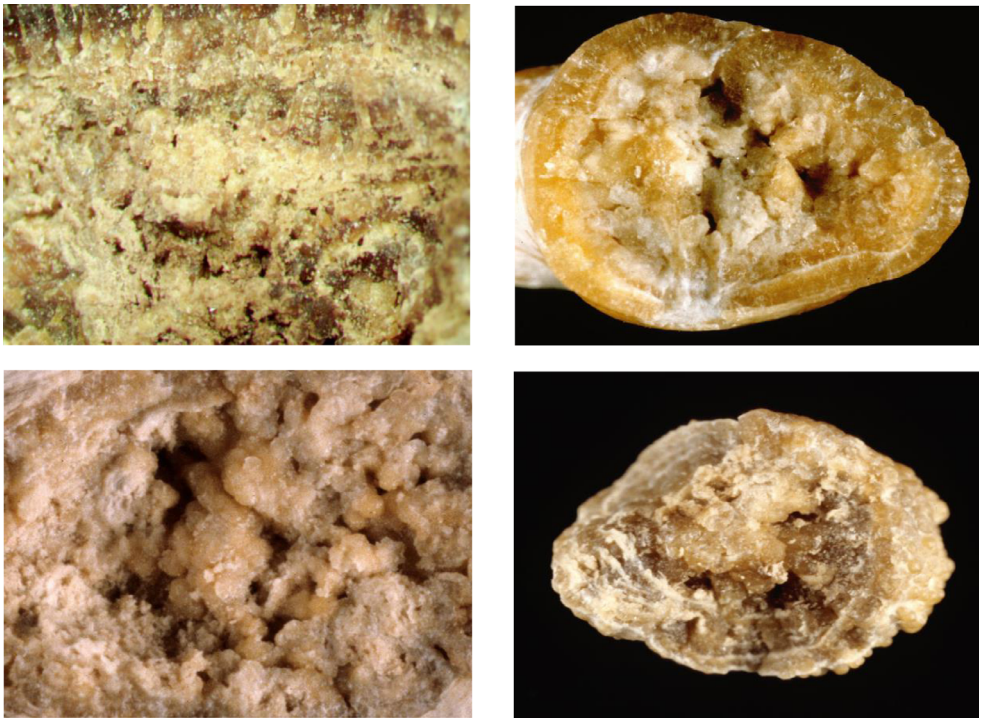

Figure 2. Examples of poorly organized inner section of type Ic stones [23,24].

and were rapidly processed. Urine-specific gravity and pH were measured. Undiluted urine was then homogenized by gentle shaking and turning over (neither centrifuged nor filtered) and immediately placed in a Malassez cell (CML, Nemours, France) containing 10 mm^3, then examined by light microscopy using a polarizing microscope (Nikon, Champigny-sur-Marne, France). The entire cell was examined at ×200 magnification to localize crystals and aggregates, then at ×400 magnification (high power field). All crystals and aggregates were counted on the entire cell. The results were expressed as number of crystals by mm^3.

2.2.3. *Metabolic evaluation*

Because it is very difficult to collect reliable 24 h-urine samples in children for biochemistry measurements, we determined the concentrations of urine solutes in the first-voided morning urine samples. In every sample, urinary concentrations of calcium, magnesium, phosphate, sodium, urate, urea, proteins and creatinine were measured. All parameters were determined on a Roche Cobas 8000 analyzer. Oxalate concentration was measured enzymatically with oxalate oxydase at 590 nm (Oxalate kit reference: 2401, SOBIODA, France). Citrate concentration was enzymatically determined by UV spectroscopy with citrate lyase at 340 nm.

Lithogenic risk thresholds for oxalate, citrate, magnesium, urate, phosphate and calcium were defined as follows [28–30]: oxalate > 0.3 mmol/l, citrate < 1 mmol/l, calcium > 3.8 mmol/l, magnesium < 2 mmol/l, urate > 2 mmol/l at pH < 5.5 and >3.5 mmol/l at pH > 6, phosphate > 13 mmol/l at pH > 7.5 and >24 mmol/l at pH < 6.5.

In order to assess the excretion of oxalate, we calculated the ratio of oxalate concentration to creatinine concentration, which is considered a strong marker for heavy hyperoxaluria of genetic origin [31, 32]. The reference values used to interpret the oxalate/creatinine ratio (mmol/mmol) by age group are: ≤6 months: <0.36; 7–12 months: <0.23; 1–2 years: <0.18; 3–<5 years: <0.10; 5–<12 years: <0.08; ≥12 years: <0.07 [31].

Data are presented as means ± SEM. Intergroup comparisons used Student t-test, or analysis of

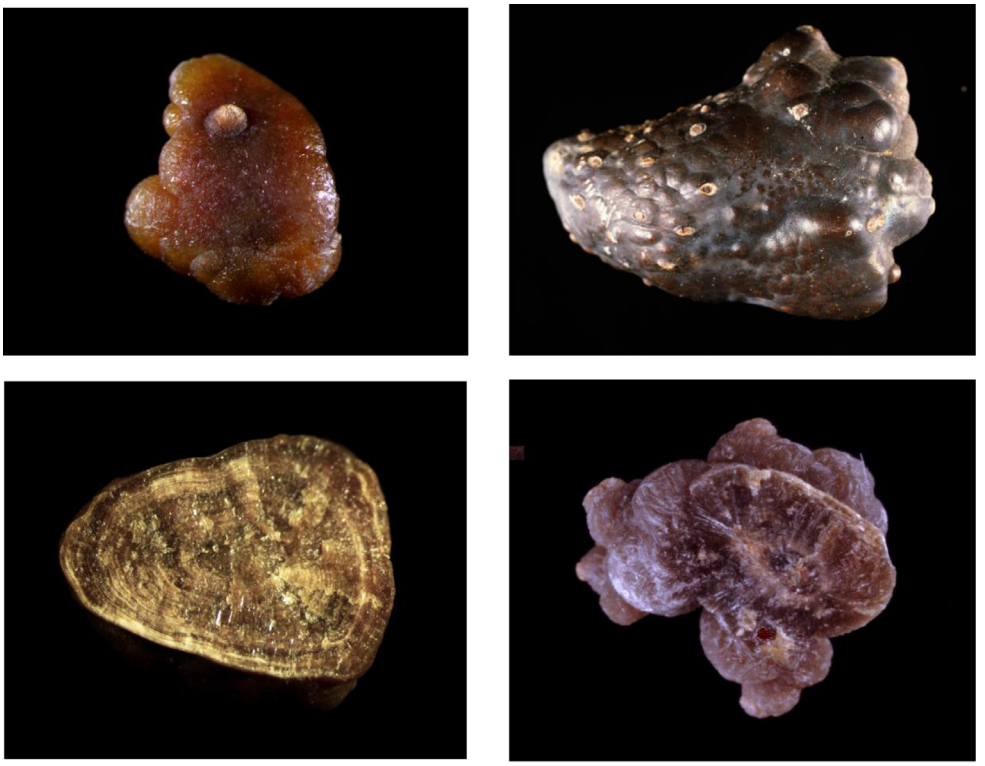

Figure 3. Examples of surface and inner section of common type Ia COM stones [23].

variance (ANOVA) for continuous variables, and the χ^2 and Fisher's exact tests for categorical variables. A p value less than 0.05 was considered statistically significant. Statistical procedures used the SPSS.23 software.

3. Results

3.1. *Localization of calculi*

The anatomical localization was specified for 55 stones (64.7% of cases). The stones were found within the kidney in 84% of cases, in the ureter in 8% and in the bladder in 8%. No statistical difference was found between girls and boys regarding stone location.

3.2. *Infrared analysis*

The results of stone analysis by Fourier transform infrared (FTIR) spectroscopy are summarized in Table 1. The results are expressed as the main component for each stone. Type Ic morphology being reported as pathognomonic of PH [19,33,34], it deserved special attention including at the infrared spectrum level where some differences could be observed by comparison with common COM spectra .

COM was the most frequent main component of stones, found in 248 calculi (40.4%), followed by MAP (114 stones, 18.6%) and COD (65 stones, 10.6%). However, only 110 stones contained more than 95% COM. Among the 85 Moroccan children who had type Ic calculi, 83 formed stones containing more than 95% COM. They accounted for 75.5% of cases. One stone with Ic morphology actually had a mixed morphology Ic + IIa and contained 82% COM and 18% COD. The last one contained 90% COM and 10% carbapatite.

The molecular and crystalline identification of different areas of the type Ic COM stones analyzed by FTIR spectroscopy showed a chemical composition similar to that of most urinary calculi, i.e., mainly consisting of calcium oxalate monohydrate (COM, whewellite) which was the main component

Table 1. Frequency of main components identified in Moroccan children stones

Main component	Girls ($n = 195$)	Boys ($n = 419$)	Overall ($n = 614$)
COM	107 (54.9)	141 (33.7)	248 (40.4%)
COD	22 (11.3)	43 (10.3)	65 (10.6%)
Carbapatite	15 (7.7)	45 (10.7)	60 (9.8%)
Brushite	1 (0.5)	1 (0.2)	2 (0.3%)
Struvite	18 (9.2)	96 (22.9)	114 (18.6%)
Uric acid	3 (1.5)	15 (3.6)	18 (2.9%)
Ammonium urate	17 (8.7)	41 (9.8)	58 (9.4%)
Cystine	5 (2.6)	28 (6.7)	33 (5.4%)
Xanthine	2 (1.0)	2 (0.5)	4 (0.7%)
Drugs	3 (1.5)	4 (1.0)	7 (1.1%)
Others (proteins, lipids,...)	2 (1.0)	3 (0.7)	5 (0.8%)

of all stones. COM is characterized by its bands on the infrared spectrum at 1619 cm^{-1}, 1316 cm^{-1} and 780 cm^{-1} (Figure 4). Of note, by contrast with synthetic whewellite, the infrared spectrum of all urinary stones exhibits an additional broad vibration about 1100 cm^{-1} (black arrow in Figure 4A), the intensity of which being close to the absorption of the minor peak of whewellite at 886 cm^{-1}. That vibration does not belong to whewellite and results from the ν_3 vibration of the PO_4 group present in organic material such as uropontin which is known to have a strong affinity for several crystalline faces (100/121) of COM [35]. It has been shown that this organic phosphate may be converted into apatite after pyrolysis of COM stones [36].

The comparison between type Ia and type Ic stones regarding the ratio of peak heights 1100/949 cm^{-1} is particularly interesting from a clinical point of view. For type Ia stones, the ratio was >1 in 72.3% of cases, around 1 in 17% of cases and slightly decreased below 1 but greater than 0.7 in only 10.7% of cases. By contrast, in type Ic stones, the ratio was >1 in only 3.6% of cases, about 1 in 7.1% of cases and below 1 in 89.3% of cases. Of note, among type Ic stones with a decreased ratio, 80% of stones had a ratio below 0.7.

3.3. *Demographic profile of type Ic stone formers*

The mean age (±SD) of the patients was 7.09 ± 3.7 years. The patient's age ranged from 1 to 17 years among boys with an average age of 7.5 ± 3.8 years and from 1 to 15 years in girls with an average age of 6.45 ± 3.5 years. Figure 5 shows the patient's age at the first stone episode. Of note, 28.2% of stones were observed before the age of 5, 47.1% in patients aged from 5 to 10 years and 24.7% above the age of 10 years. The mean male to female ratio for the whole series was 1.66.

3.4. *Crystalluria*

Among those children with COM stones of type Ic morphology, 43 patients provided spot urine for examining biochemistry and crystalluria. In all cases, abundant crystalluria mainly composed of typical COM oval crystals with depressed core (Figure 6) was observed. Usually, voluminous aggregates of COM crystals are also observed (Figure 7). The average number of crystals was 151 ± 12 /mm^3 and the global crystal volume for COM was 14,632 ± 1225 $\mu m^3/mm^3$ as calculated according to the previously published formula [37]: $N \times L^3 \times 0.19$ (where N is the number of crystals/mm^3 and L is the mean size of the crystals). By contrast, in urine samples that have hyperoxaluria (oxalate concentration above 0.3 mmol/l) for various reasons in the absence of primary hyperoxaluria, the average number of whewellite crystals was 6 /mm^3 and the corresponding crystal volume was 350 $\mu m^3/mm^3$ ($p < 0.0001$). These results, like stone morphology, highly suggested primary hyperoxaluria in this cohort of patients [7,19,33,34,37–39].

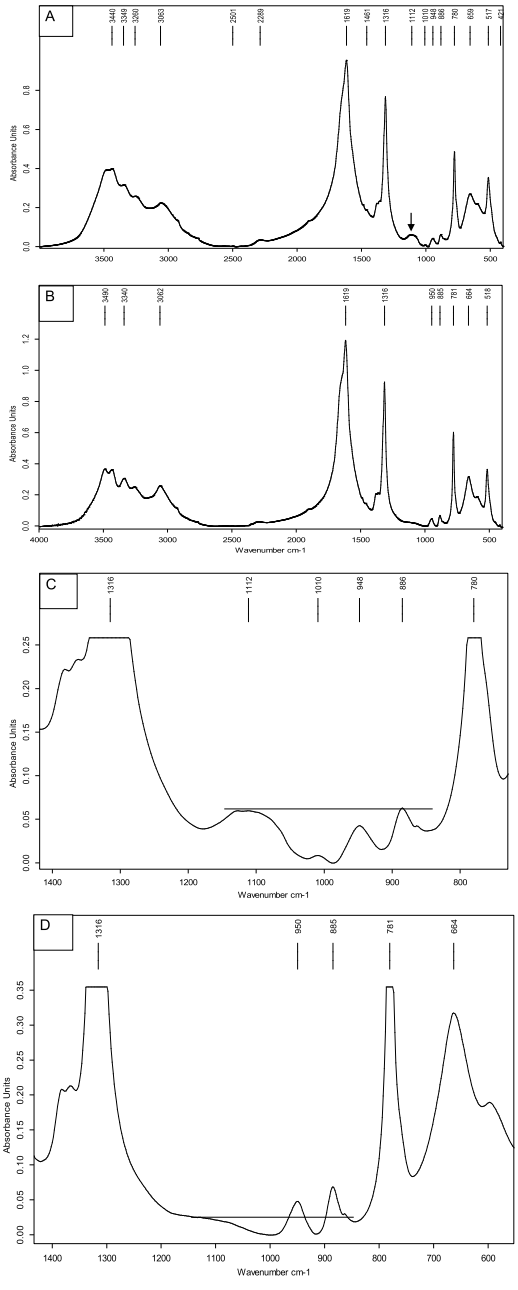

Figure 4. Infrared spectra of pure calcium oxalate monohydrate (COM) stones: (A) spectrum of common biological whewellite; (B) spectrum of whewellite found in a number (not all) type Ic stones; (C) detailed part of the spectrum shown in Figure 4A; (D) detailed part of the spectrum shown in Figure 4B (note the weak absorbance of the 1100 cm^{-1} area by comparison with Figure 4C).

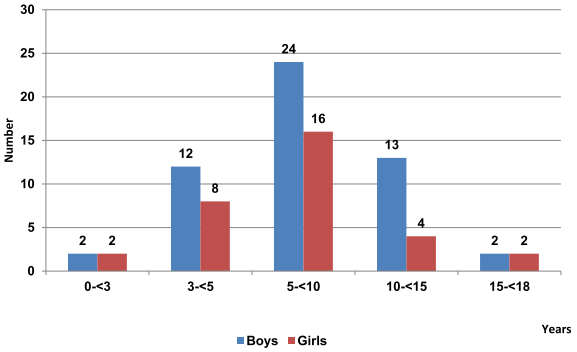

Figure 5. Distribution of type Ic morphology according to patient's age.

3.5. *Biochemical examination of first morning urine samples*

The different urinary parameters evaluated in type Ic COM stone formers and in the control group are summarized in Table 2. Of note, no significant difference between boys and girls was found for any parameter, neither in the patients with type Ic COM stone nor in the control group.

Our data showed that hyperoxaluria was the most common abnormality and was coexisting with a dramatically elevated urinary oxalate-to-creatinine ratio in all the children with type Ic stones as previously reported in PH patients [1,31]. The mean value for oxalate concentration in type Ic COM stone formers was 1.01 ± 0.042 mmol/l (vs 0.136 ± 0.029 mmol/l in the control group, $p < 0.0001$). All but one urine samples exhibited oxaluria >0.3 mmol/l, i.e. above the threshold value of oxalate for the crystallization risk of calcium oxalate [40]. Of note, the oxalate to creatinine ratio was high (0.1 mmol/mmol) for this patient. In the control group, 83 samples (90.2%) had a concentration level of oxalate below 0.3 mmol/l ($p < 0.0001$). Very high level of the oxalate/creatinine ratio was observed in type Ic COM stone formers: 0.26 ± 0.012 vs 0.03 ± 0.010 in the control group, $p < 0.0001$ suggesting the diagnosis of PH in the absence of other cause of hyperoxaluria. Hypocitraturia was coexisting in 66.7% of the samples and low calcium concentration <1 mmol/l was observed in 56.7% of the cases. These findings were similar in the control group: 64.1% of the patients had citrate concentration in urine below 1 mmol/l and 55 subjects (59.8%) had urine calcium concentration below 1 mmol/l.

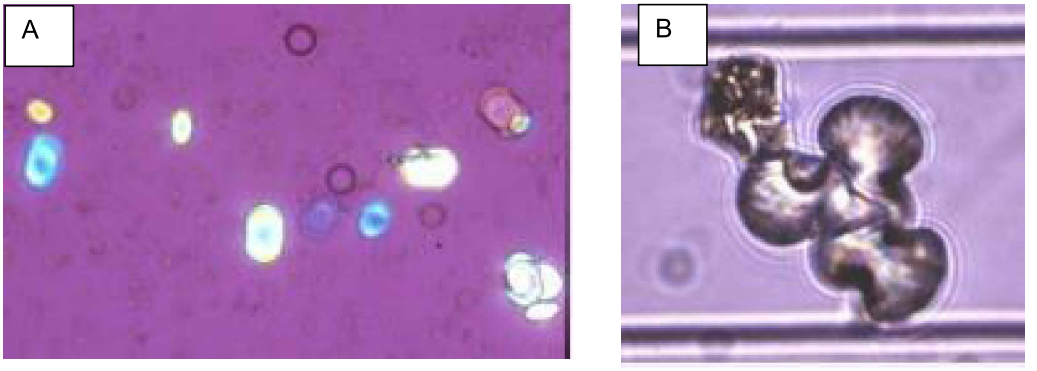

Figure 6. Oval crystals of whewellite with a depressed center. (A) Polarized light; (B) white light.

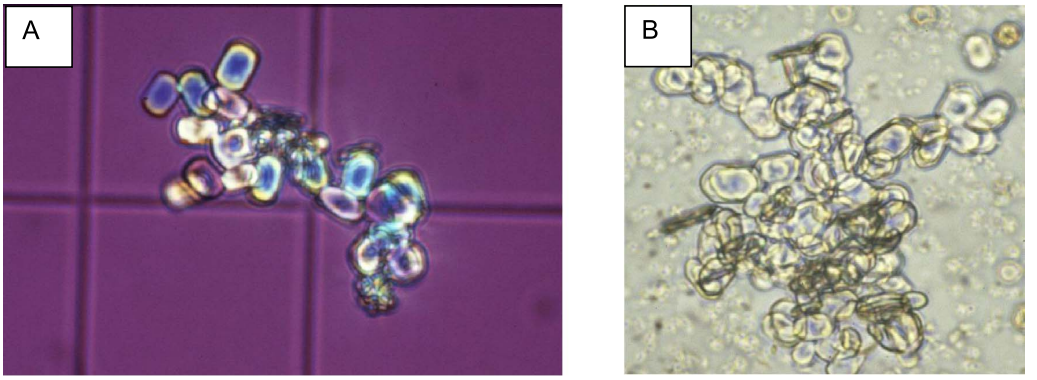

Figure 7. Voluminous aggregates of whewellite crystals. (A) Polarized light; (B) white light.

By contrast, only 4.8% of urine samples from type Ic COM stone formers presented with hypomagnesuria (Mg concentration < 2 mmol/l) while that criterion was observed in 44.6% of the subjects in the control group. Of note, proteinuria was slightly increased in type Ic COM stone formers (0.24 ± 0.04 g/l vs 0.15 ± 0.03 g/l in CG, $p = 0.002$), perhaps as a marker of some degree of kidney damage.

Figure 8 shows the correlation between urinary oxalate concentration and oxalate/creatinine ratio with a distinct distribution of the two groups.

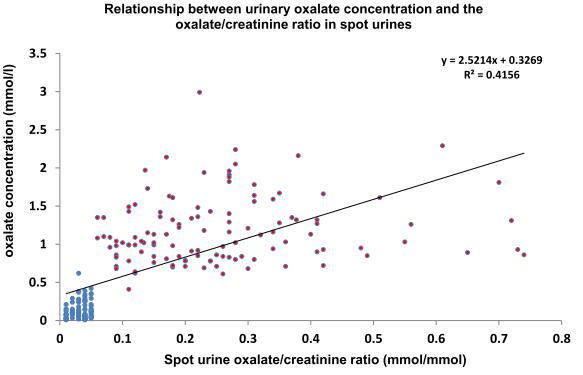

Figure 8. Relationship between oxalate and oxalate/creatinine ratio in spot morning urines of type Ic stone formers and control groups. Blue circles = control group; red circles = type Ic stone formers.

3.6. *Influence of age*

As seen above, the clinical significance of the oxalate to creatinine ratio is changing with patient's age. It is also a common finding for other urinary solutes of interest for stone disease like calcium or uric acid.

Table 2. Urinary biochemical evaluation in first-morning urine samples of children with type Ic COM stones and in the control group

Number	Type Ic COM stone formers 43		Control group 92		*P* value Ic stones vs CG
	Mean ± SEM	Median	Mean ± SEM	Median	
Age	7.09 ± 0.74	6.0	8.36 ± 0.51	8.5	NS
pH	6.07 ± 0.11	5.90	6.04 ± 0.08	5.93	NS
Specific gravity	1012.8 ± 1.0	1013	1010.6 ± 0.7	1010	NS
Creatinine (mmol/l)	5.11 ± 0.62	4.25	4.78 ± 0.43	3.74	NS
Calcium (mmol/l)	1.03 ± 0.29	0.73	1.63 ± 0.2	0.68	NS
Phosphate (mmol/l)	14.6 ± 1.5	11.9	13.1 ± 1.0	10.9	NS
Sodium (mmol/l)	63.9 ± 3.6	53	32.2 ± 2.4	32	<0.0001
Magnesium (mmol/l)	4.94 ± 0.46	3.94	3.03 ± 0.32	2.53	NS
Urate (mmol/l)	2.06± 0.22	1.56	1.70 ± 0.15	1.22	0.02
Oxalate (mmol/l)	1.010 ± 0.042	0.9	0.136 ± 0.029	0.1	<0.0001
Citrate (mmol/l)	0.70 ± 0.12	0.39	0.89 ± 0.08	0.57	NS
Proteins (g/l)	0.24 ± 0.04	0.14	0.15 ± 0.03	0.09	0.002
Urea (mmol/l)	205.9 ±18.8	190.7	186.9 ± 12.8	162.0	NS
Ratio calcium/creatinine (mmol/mmol)	0.21± 0.06	0.17	0.42 ± 0.04	0.20	NS
Ratio oxalate/creatinine (mmol/mmol)	0.27 ± 0.012	0.26	0.03 ± 0.010	0.03	<0.0001

The explanation is that, at birth, tubular immaturity is common and may affect either proximal or distal tubular cells or both, modifying secretion and reabsorption of these substances. It is the reason why the oxalate to creatinine ratio may be high at birth, for example about 0.1 mmol/mmol without any genetic disease. In normal subjects, the ratio should decrease rapidly over time to 0.03 mmol/mmol. If we subdivide our series of patients in age classes, we can observe the change in oxalate to creatinine ratio (Figure 9). Age classes were defined as follows: class 1: <1 year; class 2: 1–2 years; class 3: 3–<5 years; class 4: 5–<12 years; class 5: ≥12–<18 years. Because class 1 and class 2 included only 2 patients either in the control group or in the type Ic stone group, these age classes were not shown on the figure below. The highest value of the oxalate to creatinine ratio was observed in the age class 3 with a median value at 0.33 for type Ic stone patients and ten times lower at 0.04 for the control group ($p < 0.0001$). As expected, the ratio decreased with age in both groups, by about 50% in the age class 4 for PH patients, and by about 25% in the control group. Then, the ratio slightly decreased in class 5 for both groups.

4. Discussion

PH is the most severe lithogenic disease associated with highly recurrent stone formation and gradual deterioration of kidney function. Thus, it is of prime importance to identify early this disease because treatment with vitamin B6 is able to reduce effectively oxalate excretion in about 25% of PH1 patients, which may stop or delay the impairment of kidney function [41–43]. Moreover, very promising therapy based on siRNA treatments able to reduce the oxalate synthesis by the liver is now available [44,45]. Actually, diagnostic delay is still responsible for ESRD in at least one third of the patients. Several explanations for such delayed diagnosis may be proposed: non typical course of the disease, common crystalline composition of the stones, inaccessibility to oxalate testing, false results of the dosages as a consequence of inadequate pre-analytical conditions, high cost of genetic studies, and so on. However, almost all of the patients who suffer PH throughout the world had recurrent stones and these stones can be analyzed. Unfortunately, an accurate identification of the crystalline compounds based on

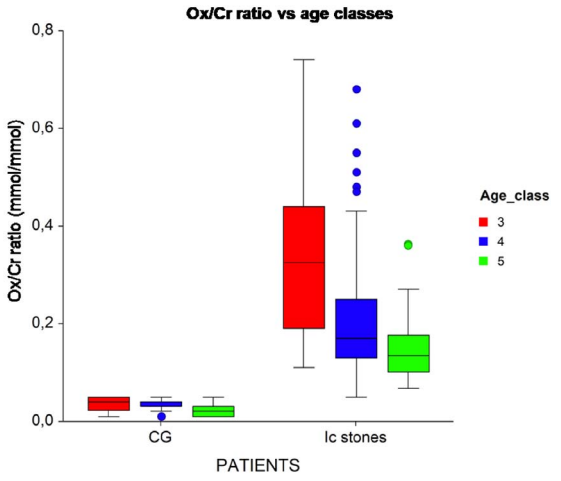

Figure 9. Evolution of the oxalate/creatinine ratio (mmol/mmol) according to patient's age. CG = control group; Ic stones = type Ic COM stone formers; Age classes: 3 = 3–<5 years; 4 = 5–<12 years; 5 = 12–<18 years.

physical methods such as infrared or Raman spectroscopy or X-ray diffraction is not sufficient to guide the diagnosis because they only identify COM which is the most common component of urinary stones. Fortunately, the study of stone morphology, although not much used around the world, could be of great help, as shown by this study. It may help the diagnosis instantly and is very inexpensive and not so time-consuming by comparison to other methods such as infrared spectroscopy alone when considering the additional benefit for the etiological orientation of stone disease. Morphological classification of the stones constitutes the preliminary work to the genetic study that will confirm the diagnosis of primary hyperoxaluria, the type of PH (PH1, PH2, and PH3) and the characterization of the genes' mutations that may be relevant for the medical management of the disease.

Several works emphasized the link between stone morphology and the cause of hyperoxaluria [19,33,46]. They highlight the interest of performing a morphological classification of the stones in addition to stone composition. This is in agreement with the results observed in a study involving 124 patients affected with PH1 and where most calculi exhibited a peculiar morphology with COM composition identified by FTIR and scanning electron microscopy (SEM) [34].

In case of inherited lithogenic diseases, like PH, the main clinical interest of morphological analysis of the stones by optical examination is to orient immediately the diagnosis to severe diseases, especially when diagnosis by other methods is not easy to perform.

In our series of 614 stones from children, we found that COM was the main component in 248 cases (40.4%) confirming our previous observations [47] while calcium oxalate dihydrate accounted only for 10.6% of cases. It is well known that hyperoxaluria favors COM (as opposed to calcium oxalate dihydrate) which is favored by hypercalciuria [28,40]. Thus, our results suggest that hyperoxaluria is more prevalent than hypercalciuria in the formation of urinary calculi in Moroccan children. Of interest is the morphology of stones containing 90% or more of COM (n = 123, i.e., 20% of all stones and 49.6% of stones mainly composed of COM). We found that type Ic stones accounted for 83 cases (13.5% of the series and 67.5% of stones containing at least 90% COM). Two stones had a mixed morphology, Ic + IIa in one case, Ic + IVa in the other. They contained 20% of COD and 12% of carbapatite respectively. It was shown that COM stones with a type Ic morphology are most strongly associated with primary hyperoxaluria [18,19,33]. In our series of stones, which today include 614 samples from 419 boys and 195 girls, type Ic morphology was observed in 85 calculi (13.8%). Infrared analysis of these stones revealed a high proportion (89.3%) of stones with a decreased ratio of peak heights 1100/949 cm^{-1} by comparison to common type Ia stones. From a clinical point of view, the band at 1100 cm^{-1}, which corresponds to organic material deposited on the crystals can be considered as a marker of slow and/or intermittent growth of the whewellite stone. By contrast, when whewellite crystals are abundant and rapidly formed and aggregated, as in primary hyperoxaluria, such organic material is often less incorporated to the crystal aggregates and we observe that the relative intensity of the peak at 1100 cm^{-1} is then significantly decreased as shown in Figure 4D. In our experience, this finding is in agreement with a rapid crystallization of whewellite due to heavy hyperoxaluria.

Biological data were available for a subset of 43 patients with type Ic stones. All of these patients had

a high oxalate to creatinine ratio for their age class. These data suggest that a high percentage of COM stone formers in Moroccan children may have PH. These data seem in agreement with other reports: due to the high degree of consanguinity [48], the prevalence of homozygous primary hyperoxaluria was found significantly higher in North Africa than in the industrialized countries [49].

Moreover, crystalluria of 43 children with type Ic COM stones showed many COM crystals (Whewellite) with an oval or dumb-bell shape, commonly associated with high levels of urine oxalate [50]. These results indicate a very active calcium oxalate crystallization. This is in agreement with other reports [39]. The global crystal volume of COM was very high (14,632 ± 1225 $\mu m^3/mm^3$). Of note, the average number of COM crystals found in our series of patients was below the threshold published by Cochat *et al.* The explanation is that recommendations published in Nephrology, Dialysis and Transplantation intended to alert the reader on the very suggestive criteria of the disease to encourage them to undertake further investigations [7]. In our experience, about 70% of patients who have urine samples that contain more than 200 COM crystals per mm^3 suffer from primary hyperoxaluria. However, according to our data, a threshold of 150 COM crystals per mm^3 could be a better value to systematically look for primary hyperoxaluria.

In addition to the abundance of whewellite crystalluria observed in all these urines, the regular biological monitoring of these children has revealed significant abnormalities, particularly hyperoxaluria with a very high oxalate/creatinine ratio for the whole series: mean ± SEM = 0.27 ± 0.012 mmol/mmol, range: 0.1 to 0.7 mmol/mmol, vs 0.03 ± 0.01 mmol/mmol in children who do not suffer from primary hyperoxaluria ($p < 0.0001$). Thus, we can confirm that type Ic morphology for urinary stones is a very interesting marker to orient easily physicians toward primary hyperoxaluria, which still need further analysis to be confirmed. Of note, among our 85 children with type Ic stones, 14 have had a genetic analysis. In all cases, mutations of the gene AGXT responsible for PH1 have been identified.

We have also noted low levels of urinary calcium in our series. This finding has been reported by others authors, specifying this decrease in PH1 and PH2 and not in PH3 where the level of urinary calcium may vary and in some instances is quite high [8,51]. Among the other parameters studied, magnesium measurement was performed in our study because of its protective role against urolithiasis. We found very few cases of hypomagnesuria by comparison with the control group (4.8% vs 44.6%, $p < 0.001$). This could be explained by conservative treatment of these children based on a supplementation with pyridoxine and magnesium (MAGNE-B6®) [43]. In contrast, hypocitraturia as a lithogenic risk factor was observed in our series with a significant proportion (72.1%) whereas citrate is known to prevent crystallization of calcium salts [17]. Our observation of hypocitraturia in paediatric stone-formers has previously been described by several authors in children stone formers [52–54]. Despite the low proportion of urinary calcium above 3.8 mmol/l, the high occurrence of hypocitraturia, although similar to that observed in the control group, could be an argument for supplementation with potassium and/or magnesium citrate.

Regarding calcium oxalate crystal phase, a controversy has been raised by some authors who found COD crystals in stones from PH patients [55]. This finding is not surprising because crystalline phases of calcium oxalate first depend on the calcium to oxalate ratio and may be influenced by various other urine parameters such as ionic strength and the citrate content for example. Contrary to the claims of these authors, whewellite found in stones from PH patients does not come from a crystalline conversion of weddellite, which is a common finding in the case of stones related to dietary conditions. In the case of PH, COM crystals are directly formed from the high content of oxalate in urine as previously reported [34,40] and confirmed by the crystalluria studies of the present work. All the patients who present with PH have COM crystals in their urine. Moreover, COM is often the unique crystal phase observed in such patients. However, in PH patients who have, in addition to hyperoxaluria, normal or increased urinary calcium, sometimes COD crystals may be observed in association with COM.

This study has at least three limitations: first, genetic diagnosis was only available for a small number of patients. Second, only half of the patients with a type Ic stone provided a urine sample for crystalluria study and biochemical evaluation. Third, our control group is not perfect because only a small num-

ber of urine samples from other types I stone formers was available for biochemical comparisons. Nevertheless, all samples from patients with type Ic stones show heavy COM crystalluria, heavy hyperoxaluria and very high oxalate to creatinine ratio, all markers of primary hyperoxaluria.

5. Conclusion

This study confirms the clinical interest of morphological classification associated with the identification of crystalline components by physico-chemical methods. It highlights correlation between the type Ic morphology of COM stones in Moroccan stone children, the presence of COM crystalluria, the high concentration of oxalate in urine as well as the high values of the oxalate/creatinine ratio usually accepted as a strong marker of primary hyperoxaluria in the absence of bowel diseases. Because measurement of oxalate in biological fluids is not easily available and due to its scarcity, primary hyperoxaluria is often misdiagnosed or diagnosis is delayed, leading to an impairment of kidney function. Nevertheless, early diagnosis is crucial, and can be implemented by a morpho-constitutional analysis of the first calculus identified in the child. Type Ic morphology is a very useful tool for the detection of the disease while stone composition is not suggestive.

Genetic diagnosis, now more easily available, is mandatory to identify potential mutations invested in the process and help in the clinical management of the patients.

Conflicts of interest

Authors have no conflict of interest to declare.

References

[1] B. Hoppe, C. B. Langmann, *Pediatr. Nephrol.*, 2003, **18**, 986-991.
[2] C. J. Danpure, *Nephron Exp. Nephrol.*, 2004, **98**, e39-e44.
[3] S. A. Johnson, G. Rumsby, D. Cregeen, S. A. Hulton, *Pediatr. Nephrol.*, 2002, **17**, 597-601.
[4] D. P. Cregeen, E. L. Williams, S. Hulton, G. Rumsby, *Hum. Mutat.*, 2003, **22**, 497.
[5] C. G. Monico, S. Rossetti, R. Belostotsky, A. G. Cogal, R. M. Herges, B. M. Seide, J. B. Olson, E. J. Bergstrahl, H. J. Williams, W. E. Haley, Y. Frishberg, D. S. Milliner, *Clin. J. Am. Soc. Nephrol.*, 2011, **6**, 2289-2295.
[6] C. Martin-Higueras, S. F. Garrelfs, J. W. Groothoff, D. E. Jacob, S. H. Moochhala, J. Bacchetta, C. Acquaviva, M. Zaniew, P. Sikora, B. B. Beck, B. Hoppe, *Kidney Int.*, 2021, **100**, 621-635.
[7] P. Cochat, S. A. Hulton, C. Acquaviva, C. J. Danpure, M. Daudon, M. De Marchi, S. Fargue, J. Groothoff, J. Harambat, B. Hoppe, N. V. Jamieson, M. J. Kemper, G. Mandrile, M. Marangella, S. Picca, G. Rumsby, E. Salido, M. Straub, C. S. van Woerdent, *Nephrol. Dial. Transplant.*, 2012, **27**, 1729-1736.
[8] P. Cochat, G. Rumsby, *N. Engl. J. Med.*, 2013, **369**, 649-658.
[9] T. Takayama, M. Nagata, A. Ichiyama, S. Ozono, *Am. J. Nephrol.*, 2005, **25**, 297-302.
[10] J. Harambat, K. J. van Stralen, L. Espinosa, J. W. Groothoff, S. A. Hulton, R. Cerkauskiene, F. Schaefer, E. Verrina, K. J. Jager, P. Cochat, *Clin. J. Am. Soc. Nephrol.*, 2012, **7**, 458-465.
[11] M. Jellouli, M. Ferjani, K. Abidi, C. Zarrouk, O. Naija, J. Abdelmoula, T. Gargah, *Saudi J. Kidney Dis. Transplant.*, 2016, **27**, 526-532.
[12] S. M. van der Hoeven, C. S. van Woerden, J. W. Groothoff, *Dial. Transplant.*, 2012, **27**, 3855-3862.
[13] D. F. Du, Q. Q. Li, C. Chen, S. M. Shi, Y. Y. Zhao, J. P. Jiang, D. W. Wang, H. Guo, W. J. Zhang, Z. S. Chen, *Curr. Med. Sci.*, 2018, **38**, 749-757.
[14] C. Madiwale, P. Murlidharan, N. K. Hase, *J. Postgrad. Med.*, 2008, **54**, 206-208.
[15] G. Spasovski, B. B. Beck, N. Blau, B. Hoppe, V. Tasic, *Int. Urol. Nephrol.*, 2010, **42**, 825-829.
[16] P. Sikora, M. Zaniew, R. Grenda, K. Jobs, J. Rubik, J. Zawadzki, M. Myślak, M. Durlik, F. Erger, B. Bieniaś, B. Hoppe, B. B. Beck, *Pol. Arch. Intern. Med.*, 2020, **130**, 1053-1063.
[17] M. Daudon, in *Lithiase Urinaire* (P. Jungers, M. Daudon, A. Le Duc, eds.), Flammarion Médecine-Sciences, Paris, 1989, 35-113.
[18] M. Daudon, C. Bader, P. Jungers, *Scanning Microsc.*, 1993, **7**, 1081-1106.
[19] M. Daudon, L. Estépa, B. Lacour, P. Jungers, *J. Nephrol.*, 1998, **11**, 51-55.
[20] M. Daudon, O. Traxer, P. Jungers, *Lithiase Urinaire*, second ed., Lavoisier Médecine-sciences, Paris, 2012.
[21] J. Cloutier, L. Villa, O. Traxer, M. Daudon, *World J. Urol.*, 2015, **33**, 157-169.
[22] M. Daudon, A. Dessombz, V. Frochot, E. Letavernier, J. P. Haymann, P. Jungers, D. Bazin, *C. R. Chim.*, 2016, **19**, 1470-1491.
[23] M. Daudon, P. Jungers, in *Urolithiasis: Basic Science and Clinical Practice* (J. J. Talati, H. G. Tiselius, D. M. Albala, Z. Ye, eds.), Springer Verlag, London, 2012, 113-140.
[24] M. Corrales, S. Doizi, Y. Barghouthy, O. Traxer, M. Daudon, *Eur. Urol. Focus*, 2021, **7**, c13-c21.
[25] M. Daudon, M. F. Protat, R. J. Réveillaud, *Ann. Biol. Clin.*, 1978, **36**, 475-478.
[26] Q. D. Nguyen, M. Daudon, *Infrared and Raman Spectra of Calculi*, Elsevier, Paris, 1997.
[27] C. A. Bader, A. Chevalier, C. Hennequin, P. Jungers, M. Daudon, *Scanning Microsc.*, 1994, **8**, 215-232.
[28] M. Daudon, P. Jungers, *Nephron Physiol.*, 2004, **98**, 31-36.
[29] M. Daudon, C. Hennequin, G. Boujelben, B. Lacour, P. Jungers, *Kidney Int.*, 2005, **67**, 1934-1943.
[30] M. Daudon, *Néphrol. Thér.*, 2015, **11**, 174-190.

[31] P. Cochat, E. Bérard, *Néphrologie Pédiatrique*, Doin, Paris, 2011.
[32] C. von Schnakenburg, D. J. Byrd, K. Latta, G. S. Reusz, D. Graf, J. Brodehl, *Eur. J. Clin. Chem. Clin. Biochem.*, 1994, **32**, 27-29.
[33] M. Daudon, P. Jungers, D. Bazin, *New Engl. J. Med.*, 2008, **359**, 100-102.
[34] M. Daudon, D. Bazin, G. André, P. Jungers, A. Cousson, P. Chevalier, E. Véron, G. Matzen, *J. Appl. Crystallogr.*, 2009, **42**, 109-115.
[35] B. Grohe, A. Taller, P. L. Vincent, L. D. Tieu, K. A. Rogers, A. Heiss, E. S. Sorensen, S. Mittler, H. A. Goldberg, G. K. Hunter, *Langmuir*, 2009, **25**, 11635-11646.
[36] M. Daudon, M. F. Protat, R. J. Réveillaud, H. Jaeschke-Boyer, *Fortsch. Urol. Nephrol.*, 1981, **17**, 311-321.
[37] M. Daudon, V. Frochot, D. Bazin, P. Jungers, *C. R. Chim.*, 2016, **19**, 1514-1526.
[38] M. Daudon, *EMC - Néphrologie*, 2013, **10**, 1-15, [Article 18-026-C-50].
[39] J. A. T. Poloni, C. D. Garcia, L. N. Rotta, M. A. Perazella, *Kidney Int.*, 2016, **89**, 250.
[40] M. Daudon, E. Letavernier, V. Frochot, J. P. Haymann, D. Bazin, P. Jungers, *C. R. Chim.*, 2016, **19**, 1504-1513.
[41] C. G. Monico, S. Rossetti, J. B. Oloson, D. S. Milliner, *Kidney Int.*, 2005, **67**, 704-709.
[42] B. Hoppe, B. B. Beck, D. S. Milliner, *Kidney Int.*, 2009, **75**, 1264-1271.
[43] E. Lorenz, J. C. Lieske, B. M. Seide, A. M. Meek, J. B. Olson, E. J. Bergstralh, D. S. Milliner, *Am. J. Transplant.*, 2014, **14**, 1433-1438.
[44] D. S. Milliner, *Mol. Ther.*, 2016, **24**, 666-667.
[45] L. J. Scott, S. J. Keam, *Drugs.*, 2021, **81**, 277-282.
[46] F. Cohen-Solal, B. Lacour, P. Jungers, M. Daudon, *XXIIème Symposium Gambro*, Gambro, 2001, 90-97 pages.
[47] F. Meiouet, S. El Kabbaj, M. Daudon, *Prog. Urol.*, 2019, **29**, 173-182.
[48] I. C. Jaouad, S. C. Elalaoui, A. Sbiti, F. Elkerh, L. Belmahi, A. Sefiani, *J. Biosoc. Sci.*, 2009, **41**, 575-581.
[49] A. Kamoun, R. Lakhoua, *Pediatr. Nephrol.*, 1996, **10**, 479-482.
[50] M. Daudon, V. Frochot, *Clin. Chem. Lab. Med.*, 2015, **53**, S1479-S1487.
[51] B. Hoppe, *Nat. Rev. Nephrol.*, 2012, **8**, 467-475.
[52] G. Lama, M. G. Carbone, N. Marrone, P. Russo, G. Spagnulo, *Child. Nephrol. Urol.*, 1990, **10**, 81-84.
[53] T. Akçay, D. Konukoglu, C. Celik, *Arch. Dis. Child.*, 1996, **74**, 350-351.
[54] A. Tekin, S. Tekgul, N. Atsu, A. Sahin, H. Ozen, M. Bakkaloglu, *J. Urol.*, 2000, **164**, 162-165.
[55] D. E. Jacob, B. Grohe, M. Gessner, B. B. Beck, B. Hoppe, *PLoS One*, 2013, **8**, article no. e70617.

Comptes Rendus
Chimie
2022, Vol. 25, Special Issue S1, p. 295-306
https://doi.org/10.5802/crchim.109

Microcrystalline pathologies: Clinical issues and nanochemistry / *Pathologies microcristallines : questions cliniques et nanochimie*

Drug-induced nephrolithiasis and crystalluria: the particular case of the sulfasalazine derivatives

Guillaume Chebion [*, a], **Estelle Bugni** [b], **Vincent Gerin** [c], **Michel Daudon** [d, e] **and Vincent Castiglione** [f]

[a] Sorbonne Université, Paris, France

[b] ProBioQual, Lyon, France

[c] Laboratoire de Biologie Médicale, Clinique Saint-Pierre, Ottignies, Belgique

[d] Service des Explorations Fonctionnelles, Hôpital Tenon, APHP, Paris, France

[e] INSERM UMRS 1155, Sorbonne Université, Hôpital Tenon, Paris, France

[f] Département de Chimie Clinique, CHU de Liège, Belgique

E-mails: chebion.guillaume@gmail.com (G. Chebion), e.bugni@probioqual.com (E. Bugni), vincentgerin@yahoo.fr (V. Gerin), daudonmichel24@gmail.com (M. Daudon), v.castiglione@chuliege.be (V. Castiglione)

Abstract.

Introduction: Drug-induced calculi are rarely reported in literature but represent a seldom reported complication of long-term or high-dose prescription of certain medications. We review here some drugs involved in stone formation from first case reports of sulfonamides in the 1930s to protease inhibitors and sulfadiazine with more recent emergence of HIV and opportunistic infections. Finally, we will study in particular sulfasalazine and mesalazine, two different forms of a drug used for treatment of ulcerative colitis or Crohn's disease.

Material and methods: Review of the literature and report of a series of ten new cases of mesalazine-induced nephrolithiasis.

Results and discussion: Ten patients (eight women and two men) produced stones spontaneously passed ($n = 9$) or surgically removed ($n = 1$). Patients received mesalazine either for ulcerative colitis ($n = 6$) or Crohn's disease ($n = 4$). The daily oral dose was 4 g/d in nine patients and only 2 g/d in one subject. The duration of medication before stone episode ranged from one month up to 15 years with an average of four years. Stone analysis found pure mesalazine in all stones analyzed ($n = 9$). Rod-shaped crystals found in urine of one patient (stone unavailable) were identified as mesalazine by Fourier transform infrared spectroscopy.

* Corresponding author.

Conclusion: We report the largest case-series of mesalazine nephrolithiasis, and the first case of mesalazine crystalluria to date. Nonmetabolized mesalazine composition of concretions suggests peculiar drug absorption and/or metabolism in these patients. Of note, women seem to be more affected by this side effect.

Keywords. Drug-induced kidney stones, Sulfamides, Triamterene, Protease inhibitors, Sulfasalazine, Mesalazine (5-ASA).

Published online: 17 September 2021, Issue date: 1 September 2022

1. Introduction

Drug-induced nephrolithiasis is rarely discussed in medical literature except through isolated case reports. From an epidemiological point of view, only few data are available from laboratories that have analyzed urinary stones by physical methods such as infrared spectroscopy or X-ray powder diffraction [1–3]. In 1989, Jungers *et al.* have reported a 2% incidence of drug-induced urolithiasis [4]. Due to changes in drug availability with time, such incidence seems to be decreasing in the last decades [5]. Although it is uncommon, it is a seldom reported complication of the long-term and/or high-dose prescription of certain drugs with high renal excretion [5,6]. Among these, the first drugs identified leading to nephrolithiasis and/or crystal nephropathy are sulfonamides [7]. Since the end of the 1930s, the first cases of kidney stones and renal failure related to the use of these products were reported, yet, widely prescribed for their antibiotic properties [7–10]. Subsequently, the evolution of the pharmacopoeia with the development of more soluble sulfonamides gradually made the clinicians forget the renal risks associated with the crystallization of these products, even if some sporadic publications have described cases of urolithiasis or acute renal failure in patients treated with different sulfonamides antibiotics [11–16]. For more than forty years, the presence of numerous drugs, namely foscarnet [17–19], atazanavir [20,21], and cisplatin [22,23] have been reported as causative of nephrolithiasis and/or crystalline nephropathy or have been identified in kidneys.

2. Main drugs involved in nephrolithiasis

2.1. *Triamterene*

At the end of the 1970s, nephrologists lost sight of sulfonamides, supplanted by a new molecule, triamterene, an antihypertensive of the pteridine family. In large studies conducted in the United States with laboratory analysis through physical methods such as X-ray diffraction or infrared spectrophotometry, it has been shown that 0.4% of all calculi analyzed by these laboratories were made, totally or partially, of triamterene metabolites [24–27].

In Europe, and particularly in France, this drug has been identified with the same frequency as in the United States [28], which means that triamterene was the main cause of drug-induced stones in the world for nearly a decade, with also several reported cases of triamterene-induced crystal nephropathies [29,30].

Studies conducted to identify risk factors for crystallization of triamterene [31] have shown less solubility in acidic urine vs alkaline urine and, above all, that low urine pH reduces its tubular reabsorption. Furthermore, the hepatic metabolism of triamterene led to the predominant formation of 4′-hydroxytriamterene sulfate with high urinary excretion (Figure 1). This metabolite was often abundant, sometimes predominant, and even almost pure in some stones [28,32].

2.2. *Glafenin*

Triamterene shared, at least in France, the first place among lithogenic drugs with another molecule, glafenin (not FDA approved, banned in early 1990s in Europe). It was a non-steroidal anti-inflammatory drug (NSAID) from the 4-amino-quinoline family which was widely prescribed by general practitioners, rheumatologists, and dentists because of its effective analgesic properties [33]. Several dozen cases of renal lithiasis (as well as biliary) were described between 1980 and 1993 [6,34–38]. Glafenin-induced lithogenesis appeared to be related to the concomitant presence of bacteria in urine. Glafenin was metabolized by the liver and eliminated primarily by the kidney in the form of glucuronide glafenic acid, a soluble derivative without reason to crystallize. However, the stones were composed of free glafenic

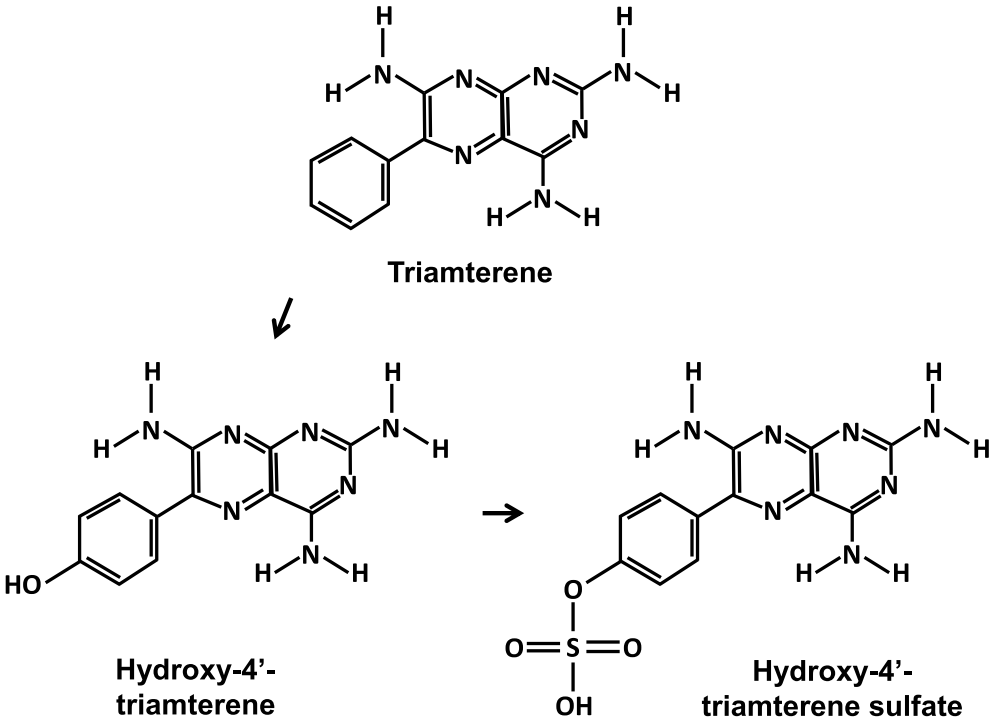

Figure 1. Triamterene and its major urinary metabolites.

acid and, to a lesser extent, of free 4-hydroxy-glafenic acid, therefore unconjugated, and poorly soluble in urine (Figure 2).

As the glucuronidation properties are important in the liver, ensuring detoxification of many substances, the hepatic origin of free glafenic acid was unlikely. Moreover, it is known that certain bacteria have very active beta-glucuronidases which have been shown to be implicated in bilirubin deconjugation, at the origin of certain pigment gallstones [39,40]. More than 80% of patients who developed glafenic acid stones were found to have a clinically symptomatic urinary tract infection, which is quite unusual in drug-induced stones [5].

Identified species were mainly Escherichia coli, a species known to possess glucuronidases, and, more rarely, Proteus mirabilis which by its capacity to strongly increase the urinary pH, can saponify the glucuronide function.

Apart from renal lithiasis, perhaps linked to a particular environment, glafenin has been shown to be a nonexceptional cause of degradation of renal function, sometimes of crystalline origin, but above all for reasons of renal toxicity linked to immunoallergic reactions [41,42], which led to the publication of a special issue of the Presse Médicale journal in 1972 [43] and to the withdrawal of this molecule in 1992 after multiple cases, sometimes fatal, of anaphylactic shock and liver toxicity.

2.3. *Protease inhibitors*

In the 1990s came the protease inhibitors used in tri-therapies against HIV, first indinavir sulfate [44–48] then barely ten years later, atazanavir [49–60]. In both cases, nephrolithiasis was explained by the short drug half life and its high urinary excretion, leading within 90–120 min after intake, to a peak elimination of poorly soluble unchanged form. As for sulfonamides and other drugs able to crystallize in the urinary tract, nephrolithiasis [49–51] and/or crystalline nephropathy [52–60] cases were reported, new anti-retroviral drug protocols with the appearance of new molecules have led to a significant reduction in stones and drug-induced renal complications over the past five years.

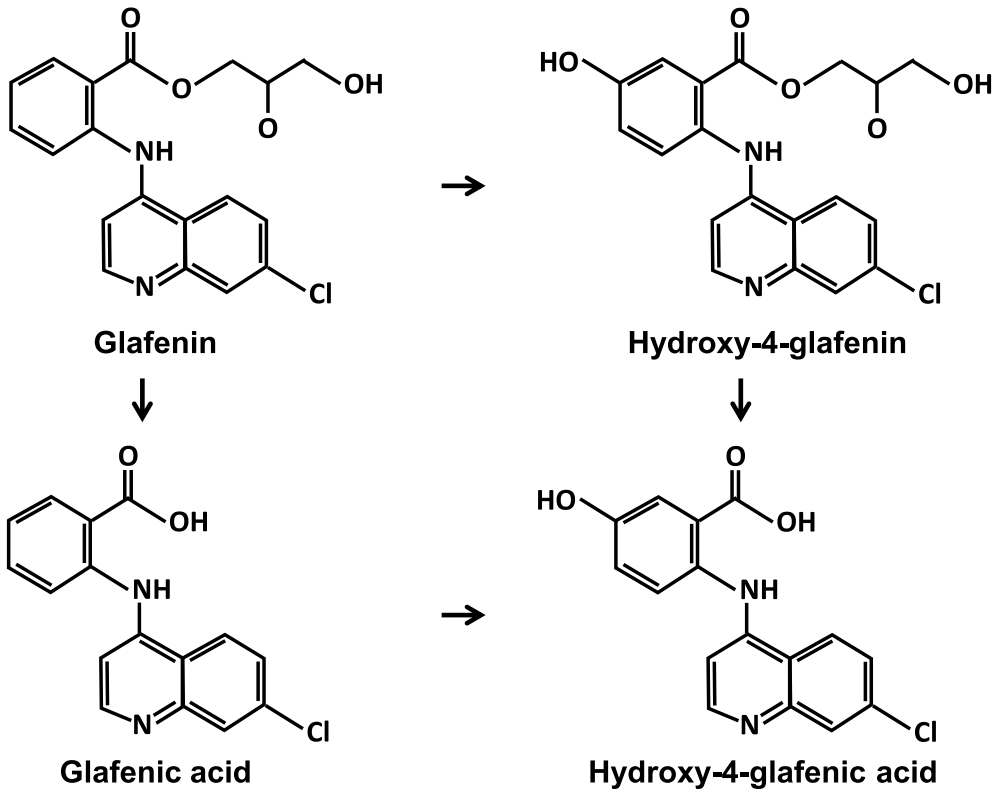

Figure 2. Glafenin and metabolites.

2.4. *Antibiotics*

Certain molecules from antiseptics or antibiotics class, such as amoxicillin, ceftriaxone, ciprofloxacin or vancomycin, are still occasionally reported as drug nephrolithiasis [61–67] and more often responsible for crystalline-induced nephropathies [68–83]. It should be noted that ceftriaxone and ciprofloxacin crystallize in the form of salts, calcium for ceftriaxone, magnesium for ciprofloxacin, which suggests that the individual metabolic status of the patient may be involved in the crystallogenic risk of these drugs [84,85].

2.5. *Sulfadiazine*

In the context of the opportunistic infections in AIDS patients [86], cases of lithiasis and acute renal failure reappeared in the early 1990s, induced by a first-generation sulfonylurea, sulfadiazine, the only one still currently used in clinical practice (Figure 3). It is still effective against severe forms of toxoplasmosis as the small size of the molecule allows it to cross the blood–brain barrier, but clinicians had forgotten how to avoid renal complications related to the high-dose prescription of this molecule, often several grams per day [87–91].

Sulfadiazine leads to stone formation and crystalline-induced acute kidney injury due to the low solubility in acidic urine of the molecule and its main metabolite, N-acetylsulfadiazine, mainly excreted by the kidney. Not all sulfonamides used have this propensity to easily crystallize in urine, either because of a lower dosage, a better solubility, or finally because of their own metabolism limiting their urinary excretion.

3. Sulfasalazine and mesalazine

In this work we addressed the specific case of sulfasalazine. It is a sulfonylurea that has been used

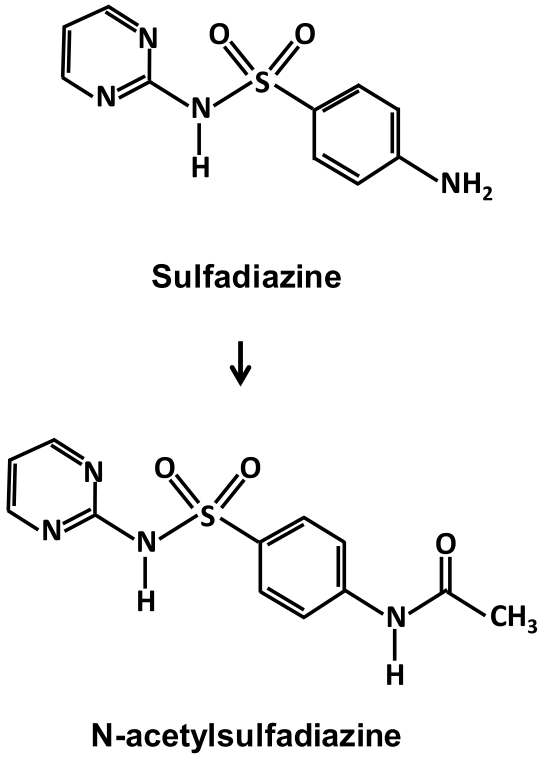

Figure 3. Molecular structure of sulfadiazine and N-acetylsulfadiazine identified in nephrolithiasis and crystal nephropathies.

for several decades for the treatment of inflammatory bowel diseases, mainly in ulcerative colitis and Crohn's disease [92]. It is also used to a lesser extent in the treatment of rheumatoid arthritis [93]. To our knowledge, this is the only drug which has led over the last thirty years to two different forms of nephrolithiasis and urinary crystallization, one concerning sulfapyridine, the other 5-aminosalicylic acid, two molecules resulting from the catabolism of sulfasalazine.

Sulfasalazine, also called salazosulfapyridine (Figure 4), is used per os at high doses as starting treatment (4–6 g/d) and at lower doses (2–3 g/d) for the long-term maintenance treatment.

About 20% of the ingested dose is absorbed through the digestive mucosa and metabolized in the liver. The peak serum concentration is reached between 3 to 12 h after taking the drug, depending on the individual. Sulfasalazine is essentially cleaved by the gut microbiota into sulfapyridine and 5-aminosalicylic acid (5-ASA, also named mesalamine or mesalazine), which constitute two active forms of the drug in the digestive mucosa (Figure 4).

The absorption of these metabolites is considered to be low, but variable depending on the individual and the condition of the intestinal mucosa. Sulfapyridine is absorbed much faster and importantly than mesalazine. Both of them can undergo hepatic acetylation, the speed and extent of which depend on the acetylation functions of the liver (with genetic and other drug intake influence) [94].

The N-acetylated derivatives (Figure 5) essentially are eliminated in the urine [95]. Due to their low solubility, they can lead to the formation of crystals and stones in the urinary tract. The use of sulfapyridine for its antiseptic properties in the 1940s had already led to cases of crystal nephropathies, including several fatal cases, observed in particular among certain Indian soldiers of the British army, after administration of doses of ≥4 g/d, while most patients were hydrated and had alkaline urine [96–100]. Hypersensitivity related to the ethnicity of the subjects had been mentioned [101].

Forty years later, the use of sulfasalazine, transformed by the gut microbiota into sulfapyridine, corresponds to a slightly different context, but which does not exclude the complications initially reported for sulfapyridine. The cleavage of sulfasalazine by intestinal bacteria releases quantities of sulfapyridine, a part of which may be more or less rapidly absorbed and transported to the liver where it is transformed into an N-acetyl derivative which will then be mainly excreted in the urine. In fact, as early as 1993, a first case of N-acetylsulfapyridine lithiasis was described by Sillar and Kleinig [102] in a patient treated with sulfasalazine and the following year a new case of bilateral lithiasis composed of N-acetylsulfapyridine was reported by Erturk *et al.* [103]. Several other cases of urolithiasis were then reported [104–108] and also several cases of kidney injury resulting from crystal deposition in the parenchyma [105,106,109].

Following various studies on the mode of action of sulfasalazine, it quickly became clear that 5-ASA released by bacterial hydrolysis of sulfasalazine represented an interesting compound due to its lower digestive absorption and its longer action *in situ*. For this reason, 5-ASA, also called mesalazine, replaced sulfasalazine just over two decades ago. Considered to be the main active anti-inflammatory metabolite, mesalazine is effective in the treatment of ulcerative

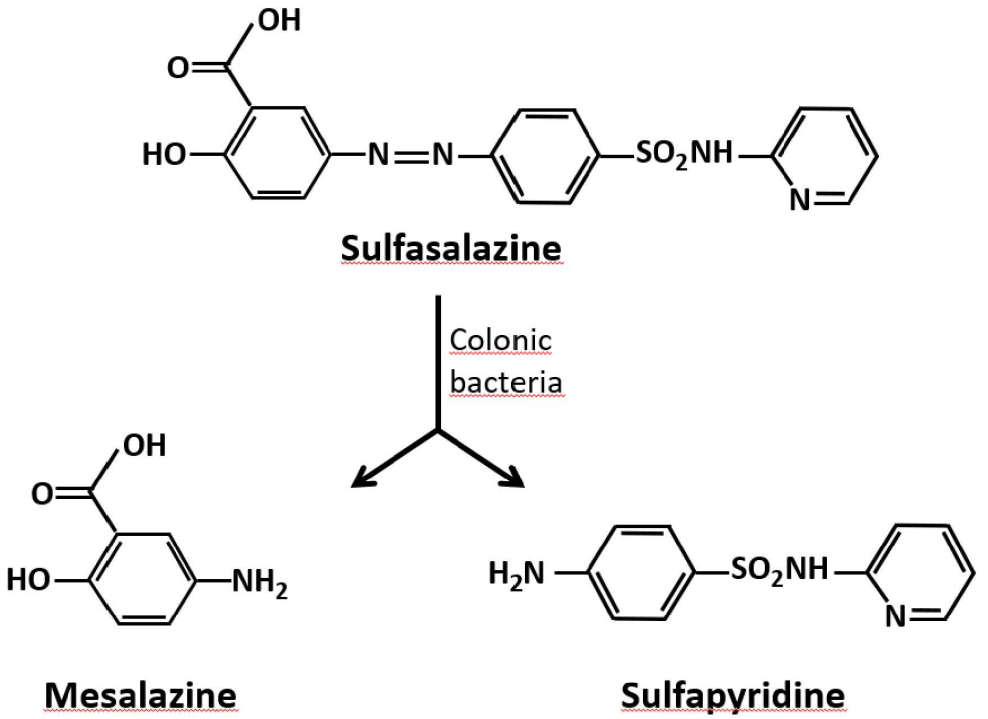

Figure 4. Simplified metabolism of sulfasalazine in the digestive tract.

colitis and moderate forms of Crohn's disease [110]. Its efficacy is considered to be proportional to its intraluminal concentration [111,112]. It is used orally (tablets or granules) or rectally (suppositories or suspension) at doses of 2–4 g/d.

The absorption of mesalazine from the intestinal mucosa appears to be variable among individuals and slower than that of sulfapyridine. Overall, its absorption is estimated to be around 60% of the ingested dose, around 35% in the small intestine and 25% in the colon. The absorbed mesalazine is then metabolized by the liver and other tissues to the N-acetyl derivative which is mainly excreted in the urine [113]. In fact, several dozens of cases of tubulointerstitial nephritis during mesalazine treatment have been reported, but no case of lithiasis [114,115]. The retained mechanism was cellular nephrotoxicity by analogy with aspirin and phenacetin [114]. The first cases of 5-ASA nephrolithiasis were described in 2013, one by Hasan and Tiselius [116], the other by Jacobsson *et al.* [117]. The first observation concerned a 32-year-old woman treated with mesalazine at a dose of 6 g/d for ulcerative colitis. The stones were spontaneously expelled. They were analyzed by the Herring laboratory in the USA that revealed they were composed of free mesalazine. Reducing the dose to 2 g/d with increased diuresis prevented recurrence. In the second case, it was also a 32-year-old woman treated during only six months with mesalazine at an unknown dosage. The patient expelled several stones identified as derivatives of mesalazine, without further indication. In 2018, a third case was reported in a 23-year-old woman treated for four years for ulcerative colitis with mesalazine at a dose of 4 g/d, plus local administration of 500 mg [118]. She presented with a left renal colic rapidly resolving with medical management. A computerized tomography without injection did not show any stone. No stones were recovered, but the following year, during a new renal colic, the patient expelled small orange-colored stones of which infrared analysis revealed to be composed of mesalazine. The following year, Simsek and de Boer described the case of a 33-year-old woman receiving 4 g/d of mesalazine for ulcerative colitis, who began to spontaneously expel stones after six months of treatment while she had no history of nephrolithiasis [119]. The calculi were composed of 85% mesalazine without specifying the other pos-

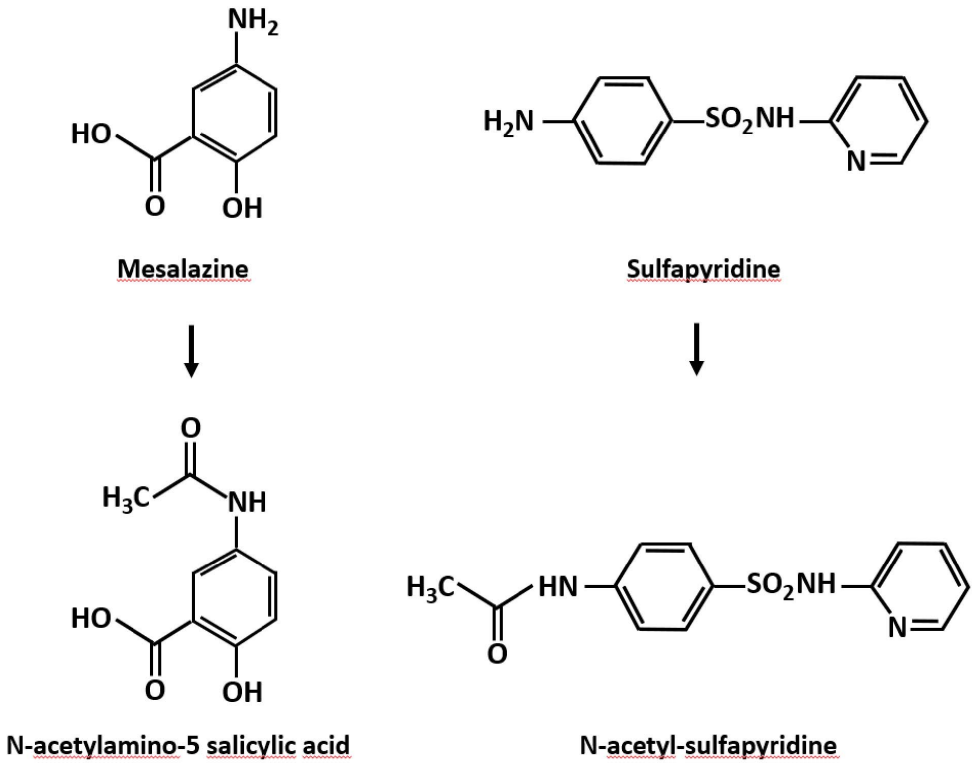

Figure 5. N-acetyl derivatives of sulfasalazine metabolites.

sible compounds. On the occasion of this case report, the authors recall that 48 cases of urolithiasis under treatment with mesalazine were the subject of reports to the European Pharmacovigilance Commission (Eudra Vigilance), but that only the four cases reported above have demonstrated the presence of the drug in the stones. Two other cases were reported in 2020 by Vilchez *et al.* in subjects treated over several years with 4 g/d of mesalazine [120]. Finally, data from FDA reports updated in March 2021 implied 64 cases of kidney stones while patients were treated with mesalazine [121] with no detailed information regarding stone composition.

4. Case presentation

A series of cases is presented here, of ten patients with mesalazine kidney stones, collected between 2014 to 2020 (8 women and 2 men), being the biggest case-series to date. They were treated either for ulcerative colitis or for Crohn's disease with daily doses of mesalazine between 2 g (n = 1) and 4 g (n = 9). The data for each patient are summarized in Table 1.

The average age was 34.8 years, the disease had been progressing for 4.5 years without flare-up while on treatment. All patients had normal kidney function. Patients had been taking the treatment for four years on average before the first stone event. None of them had previous history of nephrolithiasis, most of the calculi were spontaneously passed, and six of the ten patients stopped the treatment due to this side effect.

All stones and crystals were identified as pure mesalazine by Fourier transform infrared (FTIR) spectroscopy or X-ray diffraction. The infrared spectrum is presented in Figure 6.

The stones had a particular morphology, with a rough orange- or pink-colored surface. The section was identical to the surface without detectable organization. For one of the patients, the stone could not be recovered, but the examination of the

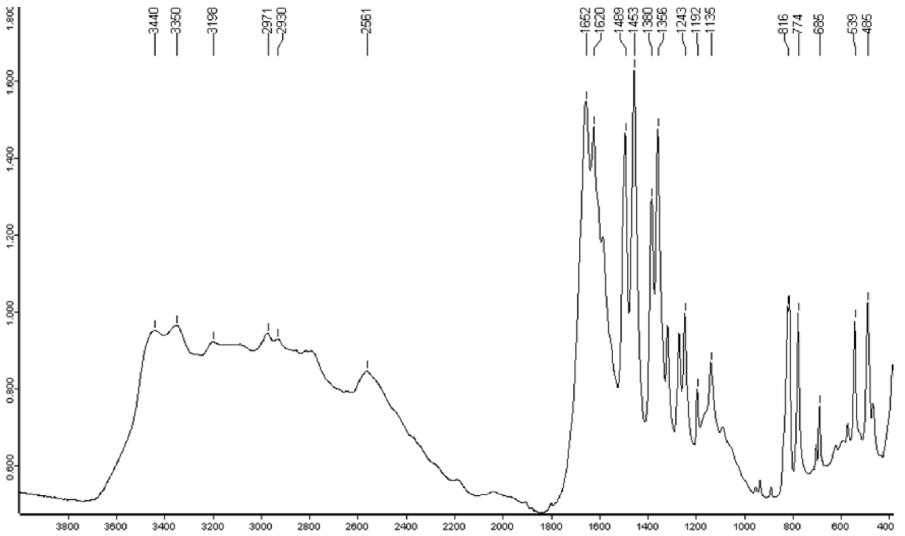

Figure 6. Infrared spectrum of mesalazine (5-aminosalicylic acid) stone. *Y*-axis: infrared absorption intensity; *X*-axis: wavelength (cm^{-1}).

Table 1. Patient characteristics

Patient characteristics	1	2	3	4	5	6	7	8	9	10
Sex category	Female	Female	Female	Female	Male	Female	Female	Female	Female	Male
Age (years old)	29	50	29	44	30	24	38	33	60	48
Pathology	UC_1	CD_2	UC	CD	UC	UC & CD	CD	CD	UC	UC
Number of year of disease progression (years)	1	15	6	7 Mo_3	4	3	2	15	12	4 Mo_3
Nature of material identified	Stone	Stone	Stone	Stone	Stone	Stone* + Crystalluria	Stone	Stone	Stone	Stone
History of previous nephrolithiasis under 5-ASA	No	No	No	No	No	No	No	Yes	Yes	No
Posology of medication (g/d)	4	4	4	4	2	4	4	4	4	4
Route of admission	po_4	po	po	po	po	po	po	po	po	po
Duration of medication intake before stone (years)	1	2	6	0.5	1 Mo_3	3	0.5	15	12	4 Mo_3
Stone treatment	$Spont_5$	JJ stent	Spont	Spont	Spont	Spont	Spont	Spont	Spont	Spont
Treatment discontinuation	Yes	Yes	No	Yes	Yes	Yes	Yes	No	No	No
Stone recurrence	No	No	Yes	No	No	No	No	No	No	No
Other lithogenic drugs	No	No	No	No	No	No	No	No	No	No

Legend: Ulcerative $colitis_1$, Crohn's $disease_2$, $Months_3$, Per OS_4, Spontaneous $emission_5$, Stone not available for analysis*.

urine revealed the presence of needle-shaped or rod-shaped crystals, more or less aggregated, whose infrared spectrum after centrifugation and drying of the sediment revealed that they were made from pure mesalazine (Figure 7).

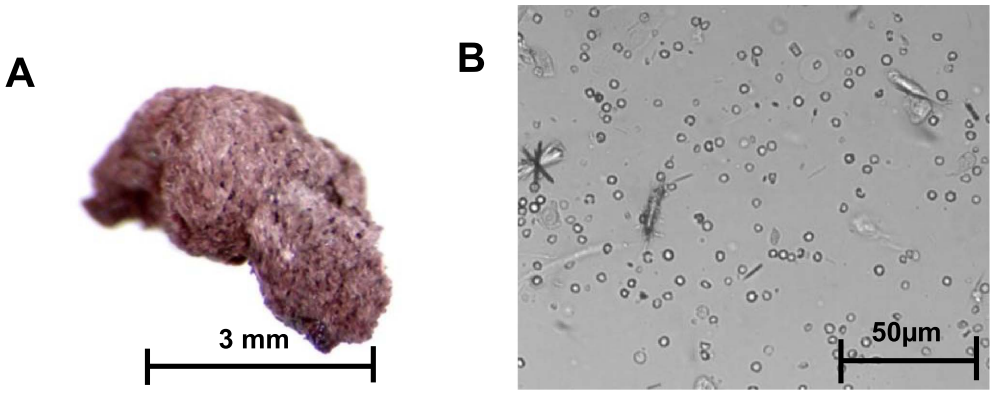

Figure 7. A. Mesalazine stone; B. Mesalazine crystalluria, original magnification: 400×.

5. Discussion

From a general point of view, drugs may be divided into two different categories according to the mechanism involved in calculi formation [5,122]. The first one includes poorly soluble drugs that favor crystallization and calculi formation. The second category includes drugs that enhance calculi formation through their metabolic effects (loop diuretics, carbonic anhydrase inhibitors, laxatives).

In the case of mesalazine, only the unmetabolized drug was clearly identified in urinary stones and crystals. Although no study has been carried out to date to verify it and understand its mechanisms, it can be thought that the formation of urinary stones composed of mesalazine is preceded by a digestive absorption of this compound greater than in other subjects, may be due to a peculiar digestive environment or metabolism.

Furthermore, patients with inflammatory bowel disease suffer from chronic hydro electrolytic losses, increasing therefore the urinary concentration of the drug above its solubility product, thus favoring its crystallization. Moreover, due to the more rapid urinary excretion (approximately 1 h) [123] of nonmetabolized mesalazine by comparison to that of N-acetyl derivative, one would expect, as it had been observed for protease inhibitors [5] at a peak excretion within two hours of absorption. In addition, in low acetylators for genetic reasons or because of multiple drugs therapy, it is reasonable to expect higher mesalazine concentrations in plasma and urine, with an increased risk of crystallization in urine.

In patients with normal renal function, the plasma concentration of mesalazine can reach 2–3 µg/mL [108], which suggests an urinary excretion of 20–30 mg within 60–120 min after absorption of the product. In patients with low urine output (1 L/d, or 40 mL/h), a urine concentration of 600–650 mg/L can be predicted and it can probably be higher in subjects with very low urine output. Knowing that the urinary solubility of mesalazine is approximately 800 mg/L [112], it is quite possible that, if the circumstances are favorable (higher dosage, increased digestive absorption, less hepatic N-acetylation, low diuresis, urine pH < 6), mesalazine supersaturation can lead to crystallization in the kidneys and urinary tract.

Renal toxicity of 5-ASA has been well documented, yet, none of our patients experienced renal impairment. Perhaps, as recently reported for vancomycin, mesalazine-related kidney injury could be, at least in part, related to crystallization of the drug [71]. To prevent such consequences, it could be relevant to increase water intake associated to the drug intake and within 2 h after, as has been shown to be efficacious for preventing stones with indinavir [6].

Of note, among our 9 cases of mesalazine stones, all were made of pure mesalazine. No metabolic

compound neither acetylated metabolites were detected in the stones by FTIR spectroscopy. Another remarkable point of our small cohort of patients is the very high gender ratio F/M, which was equal to 4.0 while the sex ratio F/M for common stone disease is about 0.5 or less in western countries. However, it seems that women are slightly more exposed than men to inflammatory bowel diseases, especially for Crohn's disease. A sex ratio F/M was reported ranging from 1.1 to 1.35 for ulcerative colitis and from 1.18 to 1.65 for Crohn's disease [124–127], i.e., a female to male ratio significantly lower than in our series of stone cases. Such a finding suggests a special sensitivity of women to the risk of forming mesalazine stones. However, it was not reported that women have a mesalazine metabolism significantly different from that observed in men. Further studies are required to explain such difference between genders.

6. Conclusion

Drug-containing stones are infrequent and result in most cases from specific characteristics of the drug, i.e., high dosage, high urine excretion, low solubility of the drug or its metabolites. Regarding mesalazine, the occurrence of urine crystallization could be underestimated. Several factors may be involved in stone formation: higher absorption of mesalazine by the gut, lower acetylation of the drug by the liver, lower urine volume than in patients free of stones, all of which deserve further investigations.

References

[1] M. Daudon, M. F. Protat, R. J. Réveillaud, *Ann. Biol. Clin. (Paris)*, 1983, **41**, 239-249.
[2] R. Asper, *Clin. Chem.*, 1986, **24**, 767-768.
[3] A. Rapado, M. L. Traba, C. Caycho, L. Cifuentes-Delatte, *Contrib. Nephrol.*, 1987, **58**, 25-29.
[4] P. Jungers, M. Daudon, A. Le Duc, *Lithiase Urinaire*, Flammarion, Paris, 1989.
[5] M. Daudon, P. Jungers, *Drugs*, 2004, **64**, 245-275.
[6] M. Daudon, V. Frochot, D. Bazin, P. Jungers, *Drugs*, 2018, **78**, 163-201.
[7] W. Antopol, H. Robinson, *Proc. Soc. Exp. Biol. Med.*, 1939, **40**, 428-439.
[8] R. W. Barnes, G. K. Kawaichi, *J. Urol.*, 1943, **49**, 324-330.
[9] A. Abaza, "Sulfamidothérapie intestinale", in *Acquisitions médicales récentes dans les pays alliés*, Doin & Cie, Paris, 1946, 260-283.
[10] D. Lehr, *Ann. N. Y. Acad. Sci.*, 1957, **69**, 417-447.
[11] H. Otto, V. Allesch, *Urologe*, 1969, **8**, 202-204.
[12] W. H. Siegel, *J. Urol.*, 1977, **117**, 397.
[13] M. Rincé, P. Dudognon, C. Moesch, C. Leroux-Robert, *Paraplegia*, 1992, **30**, 750-751.
[14] D. M. Albala, E. L. Prien, H. A. Galal, *J. Endourol.*, 1994, **8**, 401-403.
[15] C. Catalano-Pons, S. Bargy, D. Schlecht, M. D. Tabone, G. Deschênes, A. Bensman, T. Ulinski, *Pediatr. Nephrol.*, 2004, **19**, 928-931.
[16] F. de Liso, G. Garigali, C. FerrarisFusarini, M. Daudon, G. B. Fogazzi, *Clin. Chim. Acta*, 2016, **452**, 106-108.
[17] H. Beaufils, G. Deray, C. Katlama, E. Dohin, D. Henin, V. Sazdovitch, C. Jouanneau, *Lancet*, 1990, **336**, 755.
[18] L. Maurice-Estepa, M. Daudon, C. Katlama, C. Jouanneau, V. Sazdovitch, B. Lacour, H. Beaufils, *Am. J. Kidney Dis.*, 1998, **32**, 392-400.
[19] A. Dessombz, D. Bazin, P. Dumas, C. Sandt, J. Sule-Suso, M. Daudon, *PLoS One*, 2011, **6**, article no. e28007.
[20] H. R. Chang, P. M. Pella, *N. Engl. J. Med.*, 2006, **355**, 2158-2159.
[21] V. Frochot, D. Bazin, E. Letavernier, C. Jouanneau, J. P. Haymann, M. Daudon, *C. R. Chim.*, 2016, **19**, 1565-1572.
[22] N. Pabla, Z. Dong, *Kidney Int.*, 2008, **73**, 994-1007.
[23] E. Esteve, D. Bazin, C. Jouanneau, S. Rouzière, A. Bataille, A. Kellum, K. Provost, C. Mocuta, S. Reguer, K. Jorissen, J. J. Rehr, A. Hertig, E. Rondeau, E. Letavernier, J. P. Haymann, M. Daudon, P. Ronco, *C. R. Chim.*, 2016, **19**, 1586-1589.
[24] B. Ettinger, N. O. Oldroyd, F. Sorgel, *JAMA*, 1980, **244**, 2443-2445.
[25] R. A. Carey, M. M. Beg, C. F. McNally, P. Tannenbaum, *Clin. Ther.*, 1984, **6**, 302-309.
[26] D. P. Dooley, M. E. Callsen, J. A. Geiling, *Mil. Med.*, 1989, **154**, 126-127.
[27] M. C. Carr, E. L. Prien Jr, R. K. Babayan, *J. Urol.*, 1990, **144**, 1339-1340.
[28] M. Daudon, M. F. Protat, R. J. Réveillaud, *Néphrologie*, 1982, **3**, 119-123.
[29] D. Farge, M. W. Turner, D. R. Roy, S. Jothy, *Am. J. Kidney Dis.*, 1986, **8**, 445-449.
[30] L. F. Roy, J. P. Villeneuve, A. Dumont, L. R. Dufresne, M. A. Duran, C. Morin, J. Jobin, *Am. J. Nephrol.*, 1991, **11**, 486-488.
[31] P. G. Werness, J. H. Bergert, L. H. Smith, *J. Lab. Clin. Med.*, 1982, **99**, 254-262.
[32] F. Sorgel, B. Ettinger, L. Z. Benet, *J. Urol.*, 1985, **134**, 871-873.
[33] F. Ginsberg, R. P. Bourguignon, P. Smets, J. P. Famaey, *Curr. Med. Res. Opin.*, 1983, **8**, 562-569.
[34] R. J. Réveillaud, M. Daudon, M. F. Protat, M. Rymer, E. Amar, J. Pottier, *Néphrologie*, 1980, **1**, 3-8.
[35] M. Daudon, M. F. Protat, R. J. Réveillaud, *Ann. Biol. Clin.*, 1983, **41**, 105-111.
[36] M. Normand, J. L. Cayotte, M. Gottis-Normand, C. Patouraux, *Néphrologie*, 1985, **6**, 33.
[37] M. Daudon, R. J. Réveillaud, B. Bigorie, *Presse Méd.*, 1988, **17**, 869.
[38] C. Moesch, M. Daudon, J. Leymarie, C. Raby, *Eur. J. Clin. Chem. Clin. Biochem.*, 1993, **31**, 329-333.
[39] F. Lammert, K. Gurusamy, C. W. Ko, J. F. Miquel, N. Méndez-Sánchez, P. Portincasa, K. J. van Erpecum, C. J. van Laarhoven, D. Q. H. Wang, *Nat. Rev. Dis. Primers*, 2016, **2**, article no. 16024.

[40] I. A. D. Bouchier, *Keio J. Med.*, 1992, **41**, 1-5.
[41] A. Davido, P. Hallali, T. Boutchnei, *Rev. Med. Int.*, 1989, **10**, 113-117.
[42] B. H. Stricker, R. R. de Groot, J. H. Wilson, *Lancet*, 1990, **336**, 943-944.
[43] M. Gaultier, C. Bismuth, M. L. Efthymiou, L. Morel-Maroger, A. Romion, *Nouv. Presse Méd.*, 1972, **1**, 3125-3128.
[44] M. Daudon, L. Estepa, J. P. Viard, D. Joly, P. Jungers, *Lancet*, 1997, **349**, 1294-1295.
[45] S. P. Blake, M. M. J. McNicholas, V. Raptopoulos, *Am. J. Roentgenol.*, 1998, **171**, 717-720.
[46] C. P. Sundaram, B. Saltzman, *J. Endourol.*, 1999, **13**, 309-312.
[47] M. Jaradat, C. Phillips, M. N. Yum, H. Cushing, S. Moe, *Am. J. Kidney Dis.*, 2000, **35**, article no. E16.
[48] J. S. Herman, N. J. Ives, M. Nelson, B. G. Gazzard, P. J. Easterbrook, *J. Antimicrob. Chemother.*, 2001, **48**, 355-360.
[49] J. Pacanowski, J. M. Poirier, I. Petit, J. L. Meynard, P. M. Girard, *AIDS*, 2006, **20**, 2131.
[50] C. Couzigou, M. Daudon, J. L. Meynard, F. Borsa-Lebas, D. Higueret, L. Escaut, D. Zucman, J. Y. Liotier, J. L. Quencez, K. Asselah, T. May, D. Neau, D. Vittecoq, *Clin. Infect. Dis.*, 2007, **45**, e105-e108.
[51] K. M. Chan-Tack, M. M. Truffa, K. A. Struble, D. B. Birnkrant, *AIDS*, 2007, **21**, 1215-1218.
[52] Y. Moriyama, Y. Minamidate, M. Yasuda, H. Ehara, M. Kikuchi, T. Tsuchiya, T. Deguchi, H. Tsurumi, *Urol. Res.*, 2008, **36**, 275-277.
[53] Y. Hamada, T. Nishijima, K. Watanabe, H. Komatsu, K. Tsukada, K. Teruya, H. Gatanaga, Y. Kikuchi, S. Oka, *Clin. Infect. Dis.*, 2012, **55**, 1262-1269.
[54] M. Lafaurie, B. De Sousa, D. Ponscarme, N. Lapidus, M. Daudon, L. Weiss, C. Rioux, E. Fourn, C. Katlama, J. M. Molina, *PLoS One*, 2014, **9**, article no. e112836.
[55] K. T. Tashima, J. Horowitz, S. Rosen, *N. Engl. J. Med.*, 1997, **336**, 138-140.
[56] F. Martinez, H. Mommeja-Marin, L. Estepa-Maurice, H. Beaufils, M. Bochet, M. Daudon, G. Deray, C. Katlama, *Nephrol. Dial. Transplant.*, 1998, **13**, 750-753.
[57] D. W. Grabe, G. Eisele, C. Miller, J. Singh, D. Stein, *Clin. Nephrol.*, 1999, **51**, 181-183.
[58] U. C. Brewster, M. A. Perazella, *Am. J. Kidney Dis.*, 2004, **44**, e81-e84.
[59] H. Izzedine, M. B. M'Rad, A. Bardier, M. Daudon, D. Salmon, *AIDS*, 2007, **21**, 2357-2358.
[60] D. Viglietti, J. Verine, N. De Castro, A. Scemla, M. Daudon, D. Glotz, E. Pillebout, *Antivir. Ther.*, 2011, **16**, 119-121.
[61] P. Cochat, N. Cochat, M. Jouvenet, D. Floret, C. Wright, X. Martin, J. J. Vallon, L. David, *Nephrol. Dial. Transplant.*, 1990, **5**, 974-976.
[62] G. Feher, A. Benczik, E. Szabo, I. Réthy, M. Berényi, *Orv. Hetil.*, 1999, **140**, 769-771.
[63] R. A. de Moor, A. C. Egberts, C. H. Schroder, *Eur. J. Pediatr.*, 1999, **158**, 975-977.
[64] S. Chutipongtanate, V. Thongboonkerd, *Biochem. Biophys. Res. Commun.*, 2011, **406**, 396-402.
[65] X. Shen, W. Liu, X. Fang, J. Jia, H. Lin, M. Xu, H. Geng, *Int. Urol. Nephrol.*, 2014, **46**, 1909-1914.
[66] N. Chopra, P. L. Fine, B. Price, I. Atlas, *J. Urol.*, 2000, **64**, 438.
[67] M. F. Najjar, M. Rammah, A. Oueslati, F. M'Henni, M. A. Ben Amor, H. Zouaghi, *Biologiste*, 1988, **22**, 215-220.
[68] N. Li, X. Zhou, J. Yuan, G. Chen, H. Jiang, W. Zhang, *Pediatrics*, 2014, **133**, e917-e922.
[69] W. R. Gerritsen, A. Peters, F. C. Henny, J. R. Brouwers, *Nephrol. Dial. Transplant.*, 1987, **2**, 382-383.
[70] R. Montagnac, C. Briat, F. Schillinger, H. Sartelet, P. Birembaut, M. Daudon, *Néphrol. Thér.*, 2005, **1**, 44-51.
[71] P. Stratta, E. Lazzarich, C. Canavese, C. Bozzola, G. Monga, *Am. J. Kidney Dis.*, 2007, **50**, 330-335.
[72] K. Kammoun, F. Jarraya, S. Makni, L. Ben Mahmoud, M. Kharrat, M. Ben Hmida, K. Zeghal, T. Boudawara, J. Hachicha, *Iran J. Kidney Dis.*, 2014, **8**, 240-242.
[73] M. Khan, L. M. Ortega, N. Bagwan, A. Nayer, *J. Nephropathol.*, 2015, **4**, 29-31.
[74] R. Goli, K. K. Mukku, S. B. Raju, M. S. Uppin, *Indian J. Nephrol.*, 2017, **27**, 231-233.
[75] D. P. Jones, L. Gaber, G. R. Nilsson, E. D. Brewer, F. B. Stapleton, *Clin. Pediatr. (Phila)*, 1993, **32**, 735-739.
[76] J. J. Boffa, H. De Preneuf, L. Bouadma, M. Daudon, J. L. Pallot, *Presse Méd.*, 2000, **29**, 699-701.
[77] L. Labriola, M. Jadoul, M. Daudon, Y. Pirson, M. Lambert, *Clin. Nephrol.*, 2003, **59**, 455-457.
[78] C. Rafat, J. P. Haymann, S. Gaudry, V. Labbé, R. Miguel-Montanes, N. Dufour, M. Daudon, D. Dreyfuss, J. D. Ricard, *Kidney Int.*, 2014, **86**, 1065-1066.
[79] A. S. Garnier, J. Dellamaggiore, B. Brilland, L. Lagarce, P. Abgueguen, A. Furber, E. Legrand, J. F. Subra, G. Drablier, J. F. Augusto, *J. Clin. Med.*, 2020, **9**, article no. 2022.
[80] L. Thomas, C. Le Beller, T. Trenque, J. Michot, M. Zenut, E. Letavernier, N. Mongardon, D. Vodovar, *Br. J. Clin. Pharmacol.*, 2020, **86**, 2256-2265.
[81] T. P. Lodise, N. Patel, B. M. Lomaestro, K. A. Rodvold, G. L. Drusano, *Clin. Infect. Dis.*, 2009, **49**, 507-514.
[82] Y. Luque, K. Louis, C. Jouanneau, S. Placier, E. Estève, D. Bazin, E. Rondeau, E. Letavernier, A. Wolfromm, C. Gosset, A. Boueilh, M. Burbach, P. Frère, M. C. Verpont, S. Vandermeersch, D. Langui, M. Daudon, V. Frochot, L. Mesnard, *J. Am. Soc. Nephrol.*, 2017, **28**, 1723-1728.
[83] E. Esteve, Y. Luque, J. Waeytens, D. Bazin, L. Mesnard, C. Jouanneau, P. Ronco, A. Dazzi, M. Daudon, A. Deniset-Besseau, *Anal. Chem.*, 2020, **92**, 7388-7392.
[84] M. Zupancic, P. Bukovec, *Acta Pharm.*, 1996, **46**, 221-228.
[85] E. Steadman, D. W. Raisch, C. L. Bennett, J. S. Esterly, T. Becker, M. Postelnick, J. M. McKoy, S. Trifilio, P. R. Yarnold, M. H. Scheetz, *Antimicrob. Agents Chemother.*, 2010, **54**, 1534-1540.
[86] C. Cuervo, J. González, V. Rives, M. A. Vicente, *AAPS Pharm. Sci. Tech.*, 2013, **14**, 128-132.
[87] L. G. Carbone, B. Bendixen, G. B. Appel, *Am. J. Kidney Dis.*, 1988, **12**, 72-75.
[88] S. Christin, A. Baumelou, S. Bahri, M. Ben Hmida, G. Deray, C. Jacobs, *Nephron*, 1990, **55**, 233-234.
[89] J. M. Molin, X. Belenfant, T. Doco-Lecompte, J. M. Idatte, J. Modai, *AIDS*, 1991, **5**, 587-589.
[90] R. Hein, R. Brunkhorst, W. F. Thon, I. Schedel, R. E. Schmidt, *Clin. Nephrol.*, 1993, **39**, 254-256.
[91] J. L. Potter, W. G. Kofron, *Clin. Chim. Acta*, 1994, **230**, 221-224.

[92] S. Coward, M. E. Kuenzig, G. Hazlewood, F. Clement, K. McBrien, R. Holmes, R. Panaccione, S. Ghosh, C. H. Seow, A. Rezaie, G. G. Kaplan, *Inflamm. Bowel Dis.*, 2017, **23**, 461-472.
[93] G. L. Plosker, K. F. Croom, *Drugs*, 2005, **65**, 1825-1849.
[94] D. Teshima, B. Hino, K. Makino, T. Yano, Y. Itoh, Y. Joh, M. Iida, R. Oishi, *J. Clin. Pharm. Ther.*, 2003, **28**, 239-242.
[95] C. J. Buggé, S. R. Gautam, L. E. Parke, J. T. Mason, D. B. Garcia, *J. Pharm. Sci.*, 1990, **79**, 1095-1098.
[96] J. Carson, G. S. Smith, *Lancet*, 1942, **2**, 359.
[97] R. C. S. Benson, R. C. Percival, *Lancet*, 1942, **2**, 360.
[98] H. Burt-White, A. G. Johnson, *Br. Med. J.*, 1943, **2**, 508.
[99] A. Nicoll, J. R. Army, *Med. Corps.*, 1947, **89**, 135-138.
[100] B. L. Raina, *Indian Med. Gaz.*, 1946, **81**, 505-506.
[101] C. W. Nealey, *Br. Med. J.*, 1946, **1**, 202.
[102] D. B. Sillar, D. Kleinig, *Br. J. Urol.*, 1993, **71**, 750-751.
[103] E. Erturk, J. B. Casemento, K. R. Guertin, A. S. Kende, *J. Urol.*, 1994, **151**, 1605-1606.
[104] R. Yanagisawa, T. Kamijo, Y. Nagase, *Nihon Hinyokika Gakkai Zasshi*, 1999, **90**, 462-465.
[105] M. Saito, C. Takahashi, G. Ishida, H. Kadowaki, S. Hirakawa, I. Miyagawa, *J. Urol.*, 2001, **165**, 1985-1986.
[106] P. J. Russinko, S. Agarwal, M. J. Choi, P. J. Kelty, *Urology*, 2003, **62**, 748.
[107] A. S. De Koninck, L. A. Groen, H. Maes, A. G. Verstraete, V. Stove, J. R. Delanghe, *Clin. Lab.*, 2016, **62**, 235-239.
[108] K. Ogawa, K. Sakaguchi, S. Oka, S. Nagamoto, K. Kurosawa, S. Urakami, T. Okaneya, *Nihon Hinyokika Gakkai Zasshi*, 2019, **110**, 41-46.
[109] M. Durando, H. Tiu, J. S. Kim, *Am. J. Kidney Dis.*, 2017, **70**, 869-873.
[110] A. K. Azad Khan, J. Piris, S. C. Truelove, *Lancet*, 1977, **2**, 892-895.
[111] D. L. French, J. W. Mauger, *Pharm. Res.*, 1993, **10**, 1285-1290.
[112] P. Desreumaux, S. Ghosh, *Aliment. Pharmacol. Ther.*, 2006, **24**, 2-9.
[113] H. D. Cohen, K. M. Das, *J. Clin. Gastroenterol.*, 2006, **40**, S150-S154.
[114] G. Corrigan, P. E. Steven, *Aliment. Pharmacol. Ther.*, 2000, **14**, 1-6.
[115] J. P. Gisbert, Y. González-Lama, *J. Matér. Inflamm. Bowel Dis.*, 2007, **13**, 629-638.
[116] M. N. Hasan, H. G. Tiselius, *Urolithiasis*, 2013, **41**, 271-272.
[117] H. Jacobsson, J. Eriksen, P. Karlén, *Am. J. Case Rep.*, 2013, **14**, 551-553.
[118] B. Corbery, S. Lebdai, S. Borojeni, P. Bigot, A. R. Azzouzi, T. Culty, *Urol. J.*, 2018, **15**, 54-55.
[119] M. Simsek, N. K. H. de Boer, *Am. J. Gastroenterol.*, 2019, **114**, 1359-1360.
[120] A. Vilchez, J. A. Orts, S. F. Scheirs, G. Benavent, *Arch. Esp. Urol.*, 2020, **73**, 561-564.
[121] eHealthMe, "Mesalamine and kidney stones, a phase IV clinical study of FDA data—eHealthMe [Internet]", 2021, available at: https://www.ehealthme.com/ds/mesalamine/kidney-stones.
[122] M. C. Sighinolfi, A. Eissa, L. Bevilacqua, A. Zoeir, S. Ciarlariello, E. Morini, S. Puliatti, V. Durante, P. L. Ceccarelli, S. Micali, G. Bianchi, B. Rocco, *Paediatr. Drugs*, 2019, **21**, 323-344.
[123] U. Klotz, K. E. Maier, *Dig. Dis. Sci.*, 1987, **32**, S46-S50.
[124] M. D. Kappelman, S. L. Rifas-Shiman, K. Kleinman, D. Ollendorf, A. Bousvaros, R. J. Grand, J. A. Finkelstein, *Clin. Gastroenterol. Hepatol.*, 2007, **5**, 1424-1429.
[125] M. Barreiro-de Acosta, F. Magro, D. Carpio, P. Lago, A. Echarri, MD, J. Cotter, S. Pereira, R. Goncalves, A. Lorenzo, L. Carvalho, J. Castro, L. Barros, J. Amil Dias, S. Rodrigues, F. Portela, C. Dias, A. da Costa-Pereira, *Inflamm. Bowel Dis.*, 2010, **16**, 1227-1238.
[126] J. D. Betteridge, S. P. Armbruster, C. Maydonovitch, G. R. Veerappan, *Inflamm. Bowel Dis.*, 2013, **19**, 1421-1427.
[127] B. César da Silva, A. Castro Lyra, R. Rocha, G. Oliveira Santana, *World J. Gastroenterol.*, 2014, **20**, 9458-9467.

Comptes Rendus
Chimie
2022, Vol. 25, Special Issue S1, p. 307-314
https://doi.org/10.5802/crchim.91

Microcrystalline pathologies: Clinical issues and nanochemistry / *Pathologies microcristallines : questions cliniques et nanochimie*

Lateralization of uric acid stones on the left side

Emmanuel Letavernier *, [a, b, c], **Martin Flamant** [d, e], **Claude Marsault** [f], **Jean-Philippe Haymann** [a, b, c], **Guillaume Müller** [g], **Luca Villa** [g], **Jonathan Cloutier** [g], **Olivier Traxer** [a, g] **and Michel Daudon** *, [a, b, c]

[a] Sorbonne université, UMR S 1155, F-75020, Paris, France

[b] INSERM, UMR S 1155, F-75020, Paris, France

[c] Explorations fonctionnelles multidisciplinaires, AP-HP, Hôpital Tenon, F-75020, Paris, France

[d] Université Denis Diderot Univ Paris 07, UMR S 1149, F-75018, Paris, France

[e] Explorations Fonctionnelles Multidisciplinaires, AP-HP, Hôpital Bichat F-75018, Paris, France

[f] Service de Radiologie, AP-HP, Hôpital Tenon, F-75020, Paris, France

[g] Service d'Urologie, AP-HP, Hôpital Tenon, F-75020, Paris, France

Current address: Service des Explorations Fonctionnelles Multidisciplinaires, Hôpital TENON, 4 rue de la Chine, 75020 Paris, France (E. Letavernier, M. Daudon)

E-mails: emmanuel.letavernier@aphp.fr (E. Letavernier), martin.flamant@aphp.fr (M. Flamant), marsaultclaude@gmail.com (C. Marsault), jean-philippe.haymann@aphp.fr (J.-P. Haymann), guillaumuller@gmail.com (G. Müller), l.villa@hotmail.it (L. Villa), jonathan.cloutier.2@ulaval.ca (J. Cloutier), olivier.traxer@aphp.fr (O. Traxer), michel.daudon@aphp.fr (M. Daudon)

Abstract. The analysis of 35,087 kidney stones revealed that 60% of uric acid stones originate from the left kidney whereas other stones are homogeneously distributed ($p < 0.001$). The analysis of (i) lateralized urine samples collected during ureteroscopy and (ii) urine from patients grafted with left or right kidney, did not reveal any difference in urine from left and right kidney. Patients affected by uric acid stones had significantly more cysts, predominating in the left kidney, than patients affected by calcium oxalate stones ($p < 0.001$). This set of experiments suggests that renal cysts are associated to uric acid stone lateralization on the left side.

Keywords. Uric acid, Nephrolithiasis, Lateralization, Renal cyst, Polycystic kidney disease.

Published online: 9 August 2021, Issue date: 1 September 2022

* Corresponding authors.

1. Introduction

Urolithiasis prevalence is increasing in all industrialized countries, affecting more than 10% of the population [1–4]. Among renal stone formers, uric acid stones affect 10% of patients, mainly men after the fourth decade [5,6]. During the past years, several studies have shown evidence that metabolic syndrome and type 2 diabetes are associated with an increased risk of uric acid stone [7–10]. Uric acid crystals and stone formation are specifically promoted by increased uric acid urinary concentration, due to purine and fructose consumption, and by low urinary pH [10–12]. Permanent acid urine over a 24-h period is a hallmark of metabolic syndrome and type 2 diabetes, due to impaired ammoniagenesis and to an increased daily net acid excretion in uric acid stone formers [10–13]. Beyond these well recognized biological risk factors for uric acid stones, data from a large stone database provided evidence that uric acid stones originate mainly from the left kidney, whereas other stones are more homogenously distributed in both kidneys [4]. This original observation suggests that left kidney may conceal a specific risk factor for uric acid stone formation and we show herein that uric acid stone formers have an increased frequency of renal cysts in the left kidney.

2. Patients and methods

2.1. *Morphoconstitutional analysis of renal stones*

The Cristal laboratory has been collecting stones sent for identification and classification from >200 hospitals in France during several decades. Morphologic examination and classification of urinary stone surface and section were combined with Fourier transform infrared spectroscopy (FTIR) to classify stones and identify the different crystalline phases [14,15]. Starting from a database of more than 78,000 urinary stones collected in adults between 1990 and 2020, stones whose origin side (left or right kidney) was certain have been selected, limiting the study to 38,349 stones. Other clinical data including the notion of diabetes were recorded in the database when available. The proportions of the main stone components were assessed, as well as the internal structure of the stone according to FTIR and to the morphoconstitutional stone classification [14,15]. All stones have been analyzed by a single investigator (MD).

2.2. *Lateralization of uric acid renal excretion and urine pH in kidney stone formers*

To assess whether kidney side would influence uric acid excretion or urine pH in kidney stone formers, we measured uric acid and pH in urine from left or right kidney collected during reno-ureteroscopic procedures. Urine samples were collected in 38 renal stone formers at the beginning of reno-ureteroscopic procedures in the left (22 patients) or the right kidney (16 patients) in a single center (Tenon Hospital, Paris). In parallel, bladder urine (i.e. mixed urine from the left and the right kidney) was collected. We deliberately did not collect urine from both kidneys during the same procedure to stay in the routine practice procedure and avoid any risk of ureteral or kidney damage on the other side. Serum samples were collected during preoperative check-up. All patients gave a written consent and the procedure was in accordance with routine practice. Serum and urine parameters including uric acid, creatinine, and pH were assessed as previously described [16].

We assessed uric acid/creatinine ratio in urine and uric acid fractional excretion defined by the formula: (urine uric acid $*$ serum creatinine)/(serum uric acid $*$ urine creatinine). The lateralization ratio was defined by the (left or right kidney uric acid/creatinine)/(bladder uric acid/creatinine) ratio. Urinary pH was measured in all samples.

2.3. *Uric acid fractional excretion and pH in renal transplant kidneys*

To assess whether kidney side would influence uric acid excretion or urine pH, we also measured urinary uric acid and pH in a cohort of renal graft recipients who received either a left or a right kidney. Uric acid fractional excretion and fasting urine pH were analyzed retrospectively in 181 renal transplant recipients whose data had been recorded in the Bichat Hospital (Paris) transplant recipient cohort [17]. Renal transplant recipients had a systematic measure of GFR 3 months or one year after kidney graft and uric acid fractional excretion was calculated as stated above.

2.4. *CT-scan analysis of kidneys in uric acid and calcium oxalate stone formers*

To assess whether uric acid stone formation would be influenced by morphological changes in the left kidney, we assessed kidney and urinary tract morphology by CT-scan in uric acid stone formers. We analyzed CT-scans of uric acid stone formers who fulfilled the following criteria: (1) uric acid stones analyzed in the Cristal laboratory and (2) CT-scan performed in the radiology unit of Tenon Hospital at ±1 year from stone removal or expulsion. Overall, 25 patients fulfilled the criteria (23 males/2 females, mean age 62 years). A control group of 25 patients matched by age and sex and affected by calcium oxalate stones who performed a CT-scan in the same conditions was designed (23 males/2 females, mean age 60 years). In the view of the high number of cysts observed in left kidneys of uric acid stone formers, a trained radiologist (CM) reviewed all CT-scans retrospectively (unblinded procedure as uric acid density is lower than calcium oxalate). Renal or ureteral malformations including the presence of cysts and the number, size and type of renal cysts were recorded.

2.5. *Statistical analyses*

χ^2 test was used for epidemiological data. Fisher's exact test and Mann–Whitney test were used to compare other categorical or quantitative variables, respectively. Reported values represent mean ± SEM and median ± interquartile range-IQR. A p value < 0.05 was considered significant. Statistics were performed independently by two authors using both NCSS 6.0 and Statview softwares.

3. Results

3.1. *Uric acid renal stones lateralization*

Among more than 78,000 renal stones analyzed between 1990 and 2020, 38,349 stones from adult patients, whose origin (left or right kidney) was certain, were identified. Among these stones 3195 had uric acid as main component and 61% of these stones originated from the left kidney ($p < 0.001$), a specific feature of uric acid stones since stones made principally of calcium oxalate (monohydrate/whewellite and dihydrate/weddellite), carbapatite, brushite, struvite, or cystine were more homogeneously distributed (Figure 1). The notion of diabetes was recorded for 416 patients whose uric acid stone was analyzed. Among these diabetic patients, the lateralization ratio (left/right kidney stones) was lower than in all other patients affected by uric acid stones (1.26 versus 1.6; $p = 0.02$, Figure 1).

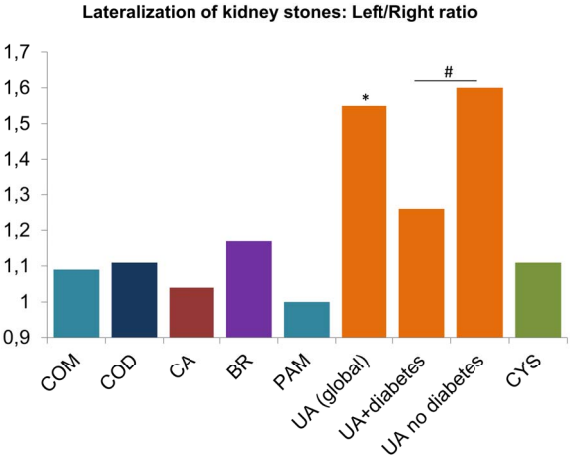

Figure 1. Lateralization of uric acid stones on the left side. Lateralization ratio (number of left kidney stones/number of right kidney stones) is shown for 38,349 stones whose main component is calcium oxalate monohydrate (COM), calcium oxalate dihydrate (COD), apatite (CA), brushite (BR) uric acid (UA, global and with/without notion of diabetes), struvite (PAM) or cystine (CYS). *: $p < 0.001$. Lateralization ratio was significantly lower when patients affected by uric acid stones were known to be affected by diabetes (#: $p = 0.02$).

3.2. *Similar composition of urine from left and right kidneys*

Uric acid supersaturation in urine is driven by (i) low pH and (ii) high uric acid concentration: both parameters were analyzed in urine from left and right kidneys during renoureteroscopy and in kidney allograft recipients. Uric acid/creatinine median ratio was similar in urine collected in both left and right kidney at the beginning of ureteroscopic interventions performed in routine practice (0.35 [0.30, 0.48] mmol/mmol and 0.32 [0.17, 0.39]

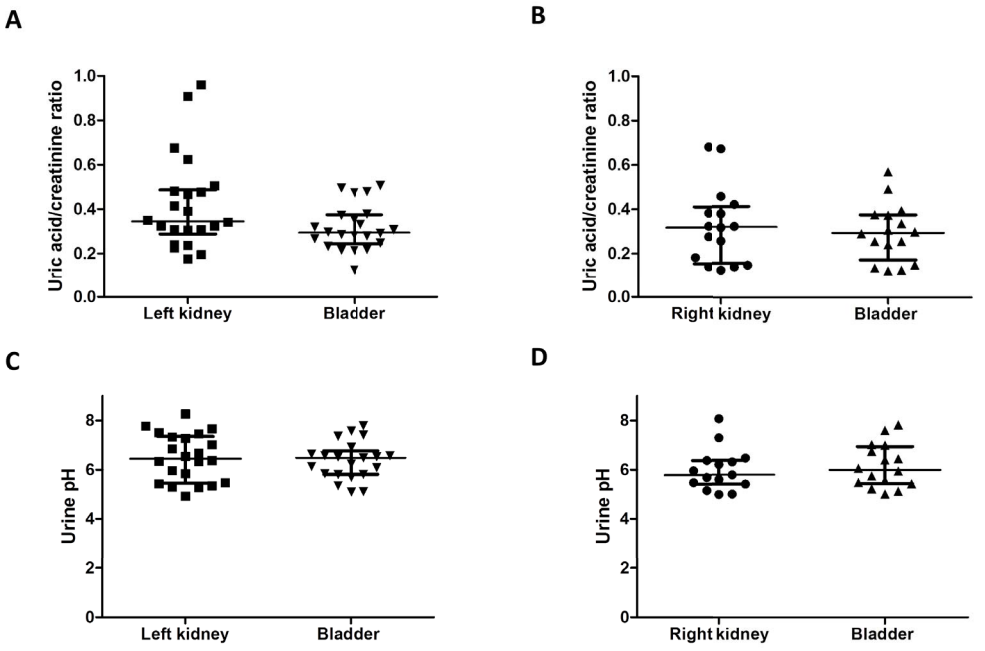

Figure 2. (A,B) Absence of lateralization of uric acid excretion in kidney stone formers. Uric acid/creatinine ratio was measured at the same time in the urine from the left or the right kidney at the beginning of reno-ureteroscopic procedures and in the bladder of 38 patients (mixed urine from both kidneys). We did not see a significant lateralization of uric acid excretion on the left side. Results are shown as median ± IQR. (C,D) Absence of lateralization of urine pH in kidney stone formers. pH was measured at the same time in the urine from the left or the right kidney at the beginning of reno-ureteroscopic procedures and in the bladder of 38 patients (mixed urine from both kidneys). We did not observe a lower pH on the left side. Results are shown as median ± IQR (brackets show IQR 25–75).

mmol/mmol respectively (p = 0.15, Figures 2(A) and (B)). When compared to the bladder urine (integrating left and right kidney uric acid secretion), there was no significantly increased uric acid excretion in the left kidney (left and right lateralization ratio respectively at 1.19 [0.97, 1.78] and 1.05 [1.00, 1.20], p = 0.31). In the same vein, urinary pH did not differ significantly in lateralized or mixed urines. Urinary median pH from the left and right kidney was at 6.45 [5.55, 7.31] and 5.78 [5.44, 6.34] respectively (p = 0.11, Figures 2(C) and (D)). Among the 38 patients whose urine has been analyzed, most had calcium oxalate stones and uric acid stones have been reported in 3 patients only. Of notice, these three patients had a left lateralization ratio of uric acid at 1.26, 1.81 and 2.41 respectively.

In addition, uric acid fractional excretion and urinary pH were analyzed in 181 renal transplant recipients who received either a right (n = 71) or a left kidney (n = 110). Kidney side (in the donor) did not affect significantly uric acid fractional excretion or fasting urinary pH in the recipient (Figures 3(A), (B)).

3.3. *CT-scan analysis of kidneys in uric acid and calcium oxalate stone formers*

To assess whether kidney structure would be related to uric acid stone formation, CT-scan were retrospectively analysed in 25 kidney stone formers affected by uric acid urolithiasis and 25 patients affected by calcium oxalate urolithiasis. The frequency of renal cysts was higher in patients affected by uric acid stones (68%) than in calcium oxalate stone formers (16%, $p < 0.001$). In uric acid stone formers, 9 had left renal cysts, 7 had bilateral cysts and 1 had right renal cysts (Figures 4(A)–(C)). Cysts were often multiple

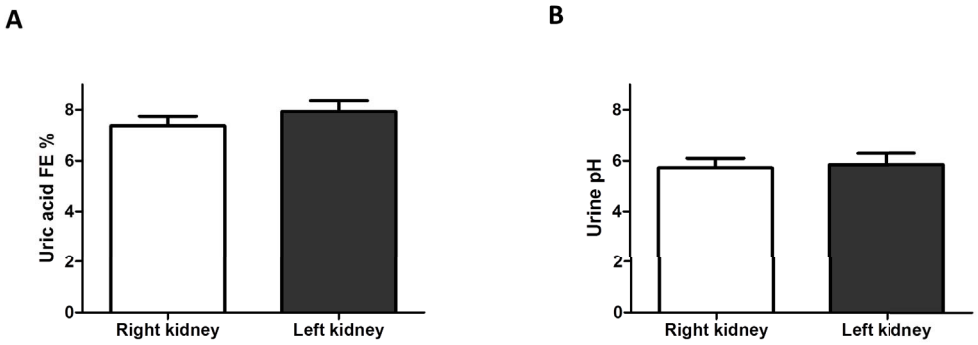

Figure 3. (A) Uric acid excretion in renal transplant recipients grafted with left or right kidney from the donor. Uric acid fractional excretion (FE) was similar in renal transplant recipients who received either a right or a left kidney. Results are shown as mean ± SEM. (B) Fasting urine pH in renal transplant recipients grafted with left or right kidney from the donor. Fasting urine pH was similar in renal transplant recipients who received either a right or a left kidney. Results are shown as mean ± SEM.

in affected kidneys. Two patients had left parapyelic cysts and 2 had bilateral parapyelic cysts. Among the 25 patients affected by calcium oxalate stones, only 2 had left renal cysts and 2 had right renal cysts. Kidney stones were evidenced in CT-scans but there was no evidence for close relationships between cysts and stones or chronic obstruction (Figures 4(A), (B)). None of these patients was affected by autosomal dominant polycystic kidney disease (ADPKD).

4. Discussion

Based upon a collection of 38,349 stones from adult stone formers, 3195 were made of uric acid (main component) and predominated in the left kidney. Although a moderate left/right lateralization was observed in calcium oxalate (1.09 and 1.11 for whewellite and weddellite as main component, respectively), brushite (1.17) and cystine (1.11) stone formers, the lateralization ratio was dramatic in uric acid stone formers (1.55, more than 61% in the left kidney). In addition, CT-scan analysis evidenced an association between uric acid stones and left renal cysts.

Previous studies evidenced a trend toward lateralization of kidney stones in the left kidney. For instance, Buck *et al.* have observed in 127 normocalciuric stone formers that 50.4% had left kidney stones and 41.7% right kidney stones, and in 148 hypercalciuric patients that 46.6% had left kidney stones and 40.6% right kidney stones [18]. Nevertheless, stone composition was not assessed and left lateralization was not statistically significant.

Uric acid crystals and kidney stones are promoted by (i) urinary uric acid concentration, due to low diuresis and/or increased uric acid excretion and (ii) low urine pH. Acid urine pH results mainly from decreased renal ammoniagenesis, a common setting in diabetes and metabolic syndrome, and from an increased acid load [7–13]. The increasing prevalence of obesity, metabolic syndrome and diabetes may explain why uric acid urolithiasis is relatively frequent in industrialized countries, resulting in about 10% of renal stones [4–6]. Our studies provide evidence for the first time to our knowledge that more than 60% of uric acid stones originate from the left kidney, a specific feature since other stones are equally distributed in both kidneys. Interestingly, the lateralization ratio was significantly lower in patients declared to be diabetic (1.26). Uric acid stones may form in both kidneys in patients affected by diabetes with low urine pH, whereas local factors may increase the risk of uric acid stone formation in the left kidney.

Based upon the analysis of urine biochemistry from the left or the right kidney collected in kidney stone formers, we did not find a lateralization of uric acid excretion or a lower pH in urine from the left kidney. Of notice, most of patients were affected by calcium oxalate stones, consistent with kidney stones epidemiology. In addition, left or right grafted kidneys do not differ statistically regarding uric acid excretion or urinary pH. Overall, these results rule

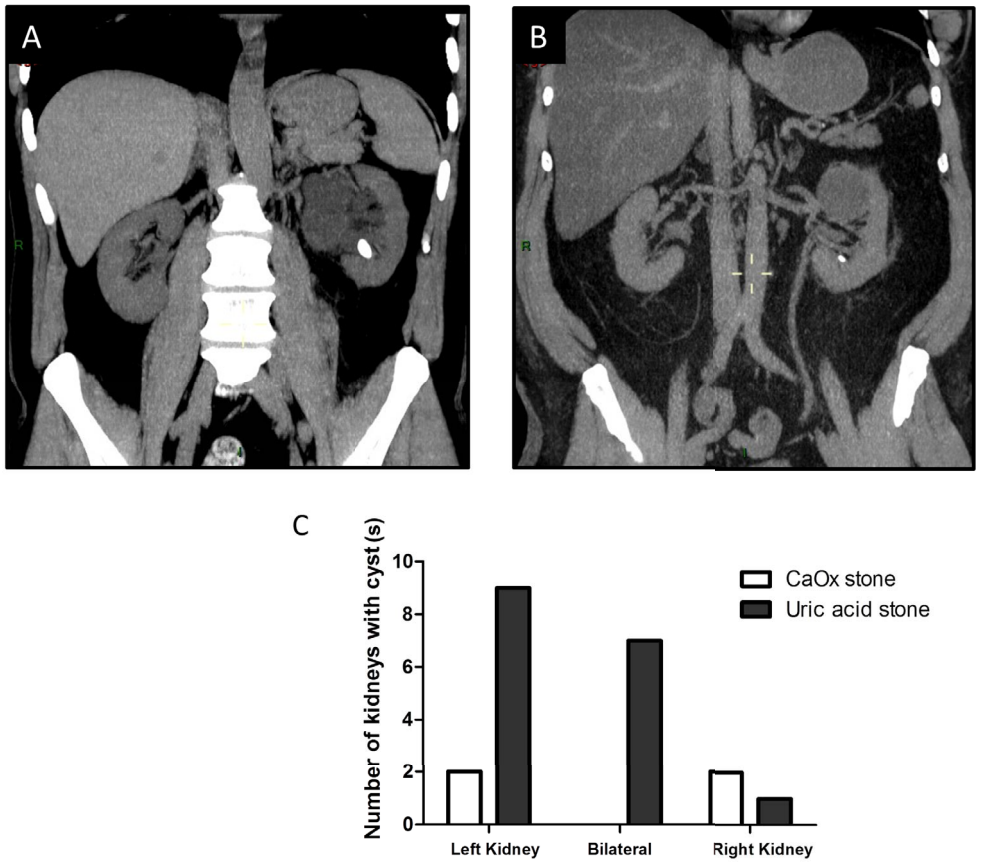

Figure 4. (A,B) Representative CT-scans from patients affected by renal cysts and uric acid stones. Patients were sometimes affected by (multiple) parapyelic cysts or isolated cysts without clear evidence of spatial relationships between stones and cysts. (C) Number of left, right or bilateral cysts in 25 uric acid stone formers (SF) and 25 calcium oxalate (CaOx) stone formers. We observed a dramatic number of left renal cysts in uric acid stone formers when compared to control CT-scans performed in 25 CaOx stone formers ($p < 0.001$).

out the hypothesis that kidney side would influence kidney physiology, at least in calcium oxalate stone formers and kidney donors.

Nevertheless, patients affected by uric acid stones are more frequently affected by renal cysts than renal calcium oxalate stone formers, particularly in the left kidney.

On the one hand, it has been reported that both hyperuricemia and high uric acid fractional excretion are independent "risk factors" for the presence of simple renal cysts [19]. The presence of renal cysts might be a consequence of hyperuricemia and/or increased uric acid excretion, potentially through the formation of urate crystals in renal tissue or uric acid crystals in renal tubules.

On the other hand, the presence of cysts could be responsible for uric acid crystal formation or aggregation. Kidney cysts are the ending product of tubular alterations resulting in tubule dilation and inverse cellular polarity associated with aberrant ionic transports [20]. The content of renal cysts was analyzed, revealing an increased uric acid and urea concentration in cystic fluid compared to plasmatic levels whereas electrolyte concentrations were similar [21]. We may therefore hypothesize that tubular cells undergoing cystic formation would be responsible for locally increased uric acid and/or increased proton excretion. Interestingly, the proportion of uric acid stones has been previously described to be high in patients affected by ADPKD, due to *PKD1* or *PKD2*

genes mutation [22,23]. A majority of ADPKD patients has a low urinary pH (<5.5), probably due to a defect in ammoniagenesis but the underlying mechanisms remain elusive [23–25]. It seems likely that low urinary pH in polycystic patients, in addition to the distorted renal structure, may enhance uric acid stone risk. It has been shown that *Pkd1* ± mice on 129/Sv genetic background (which are not affected by renal cysts) develop increased uric acid excretion when compared to controls. Surprisingly, the nestin-Cre *Pkd1*-targeted cystic mice, on a c57bl/6 genetic background, do not have increased uric acid excretion [26]. The mechanisms underlying the role of *Pkd1* in uric acid transport remain unknown. Another hypothesis is that renal distortion due to cysts may promote urine stasis and crystal formation, growth or aggregation. However, these hypotheses do not address why uric acid stones are lateralized on the left side.

Previous studies have shown that renal malformations are more often found on the left side, including renal agenesis/aplasia, renal ectopia, pelviureteral junction obstruction and non-obstructive non-refluxing megaureter [27]. Of notice, unilateral multicystic dysplastic kidneys are more frequently located on the left side [28]. It has been hypothesized that genes that are differentially expressed at both sides of the embryo during development would be involved in unilateral kidney malformations. Among these genes, those involved in the cilium function are particularly of interest since they are involved both in abnormal left–right body axis and cystic diseases. For instance, mutations of *INVS* causing nephronophtisis type 2 or mutations of *BBS* genes responsible for Bardet–Biedl Syndrome are related to renal cyst formation and, in some cases, random left–right axis specification resulting in situs inversus [29,30]. Mice affected by *nek8* or *pkd2* loss develop cystic kidney disease and left–right asymetric defect [31]. We may hypothesize that the predominance of renal cysts in the left kidney would explain the lateralization of uric acid stones.

Our study suffers from limitations. It would be of interest to assess whether uric acid stone formers affected by isolated left cysts have an increased uric acid fractional excretion or lower urine pH in the left kidney. Although we analyzed lateralized uric acid excretion in a large number of patients, only 3 were affected by uric acid stones. Interestingly, left lateralization ratio of uric acid seemed increased in 2 of them but we did not collect data relative to kidney morphology in these uric acid stone formers and the number of patients was too low to draw any conclusion. To date, we have no proof that isolated cysts or nephrons undergoing cystic formation modify urine composition.

In conclusion, we describe that uric acid stones predominate on the left side and are frequently associated with left renal cysts. These observations deserve further studies to identify genes involved in left renal cysts and uric acid stone formation.

Conflicts of interest

The authors declare no conflict of interest.

References

[1] A. Trinchieri, F. Coppi, E. Montanari, A. Del Nero, G. Zanetti, E. Pisani, *Eur. Urol.*, 2000, **37**, 23-25.

[2] K. K. Stamatelou, M. E. Francis, C. A. Jones, L. M. Nyberg, G. C. Curhan, *Kidney Int.*, 2003, **63**, 1817-1823.

[3] M. S. Pearle, E. A. Calhoun, G. C. Curhan, *J. Urol.*, 2005, **173**, 848-857.

[4] M. Daudon, *Ann. Urol. (Paris)*, 2005, **39**, 209-231.

[5] K. Sakhaee, *J. Nephrol.*, 2014, **27**, 241-245.

[6] R. Moses, V. M. Jr Pais, M. Ursiny, E. L. Jr Prien, N. Miller, B. H. Eisner, *Urolithiasis*, 2015, **43**, 135-139.

[7] O. W. Moe, N. Abate, K. Sakhaee, *Endocrinol. Metab. Clin. North. Am.*, 2002, **31**, 895-914.

[8] N. Abate, M. Chandalia, A. V. Jr Cabo-Chan, O. W. Moe, K. Sakhaee, *Kidney Int.*, 2004, **65**, 386-392.

[9] M. Daudon, B. Lacour, P. Jungers, *Nephrol. Dial. Transplant.*, 2005, **20**, 468-469.

[10] M. Daudon, O. Traxer, P. Conort, B. Lacour, P. Jungers, *J. Am. Soc. Nephrol.*, 2006, **17**, 2026-2033.

[11] M. A. Cameron, N. M. Maalouf, B. Adams-Huet, O. W. Moe, K. Sakhaee, *J. Am. Soc. Nephrol.*, 2006, **17**, 1422-1428.

[12] N. M. Maalouf, M. A. Cameron, O. W. Moe, K. Sakhaee, *Clin. J. Am. Soc. Nephrol.*, 2010, **5**, 1277-1281.

[13] I. A. Bobulescu, N. M. Maalouf, G. Capolongo, B. Adams-Huet, T. R. Rosenthal, O. W. Moe, K. Sakhaee, *Am. J. Physiol. Renal. Physiol.*, 2013, **305**, F1498-F1503.

[14] M. Daudon, R. Donsimoni, C. Hennequin, S. Fellahi, G. Le Moel, M. Paris, S. Troupel, B. Lacour, *Urol. Res.*, 1995, **23**, 319-326.

[15] M. Daudon, C. A. Bader, P. Jungers, *Scanning Microsc.*, 1993, **7**, 1081-1104.

[16] E. Letavernier, O. Traxer, M. Daudon, M. Tligui, J. Hubert-Brierre, D. Guerrot, A. Sebag, L. Baud, J. P. Haymann, *Clin. J. Am. Soc. Nephrol.*, 2011, **6**, 1149-1154.

[17] I. Masson, M. Flamant, N. Maillard, A. D. Rule, F. Vrtovsnik, M. N. Peraldi, L. Thibaudin, E. Cavalier, E. Vidal-Petiot, C. Bonneau, O. Moranne, E. Alamartine, C. Mariat, P. Delanaye, *Transplantation*, 2013, **95**, 1211-1217.

[18] A. C. Buck, W. F. Sampson, C. J. Lote, N. J. Blacklock, *Br. J. Urol.*, 1981, **53**, 485-491.
[19] Y. Han, M. Zhang, J. Lu, L. Zhang, J. Han, F. Zhao, H. Chen, Y. Bao, W. Jia, *Sci. Rep.*, 2017, **7**, article no. 3802.
[20] P. D. Wilson, *Biochim. Biophys. Acta*, 2011, **1812**, 1239-1248.
[21] R. M. Scarpa, M. Sorgia, A. De Lisa, G. Campus, M. Usai, R. Migliari, E. Usai, *Arch. Ital. Urol. Nefrol. Androl.*, 1991, **63**, 113-117.
[22] M. Daudon, F. Cohen-Solal, B. Lacour, P. Jungers, *Prog. Urol.*, 2003, **13**, 1320-1329.
[23] V. E. Torres, S. B. Erickson, L. H. Smith, D. M. Wilson, R. R. Hattery, J. W. Segura, *Am. J. Kidney Dis.*, 1988, **11**, 318-325.
[24] V. E. Torres, D. M. Wilson, R. R. Hattery, J. W. Segura, *Am. J. Kidney Dis.*, 1993, **22**, 513-519.
[25] V. E. Torres, P. C. Harris, Y. Pirson, *Lancet*, 2007, **369**, 1287-1301.
[26] R. R. Ferraz, J. M. Fonseca, G. G. Germino, L. F. Onuchic, I. P. Heilberg, *Urolithiasis*, 2014, **42**, 301-307.
[27] M. F. Schreuder, *Kidney Int.*, 2011, **80**, 740-745.
[28] M. F. Schreuder, R. Westland, J. A. van Wijk, *Nephrol. Dial. Transplant.*, 2009, **24**, 1810-1818.
[29] T. Mochizuki, Y. Saijoh, K. Tsuchiya, Y. Shirayoshi, S. Takai, C. Taya, H. Yonekawa, K. Yamada, H. Nihei, N. Nakatsuji, P. A. Overbeek, H. Hamada, T. Yokoyama, *Nature*, 1998, **395**, 177-181.
[30] S. J. Ansley, J. L. Badano, O. E. Blacque, J. Hill, B. E. Hoskins, C. C. Leitch, J. C. Kim, A. J. Ross, E. R. Eichers, T. M. Teslovich, A. K. Mah, R. C. Johnsen, J. C. Cavender, R. A. Lewis, M. R. Leroux, P. L. Beales, N. Katsanis, *Nature*, 2003, **425**, 628-633.
[31] D. K. Manning, M. Sergeev, R. G. van Heesbeen, M. D. Wong, J. H. Oh, Y. Liu, R. M. Henkelman, I. Drummond, J. V. Shah, D. R. Beier, *J. Am. Soc. Nephrol.*, 2013, **24**, 100-112.

Comptes Rendus
Chimie
2022, Vol. 25, Special Issue S1, p. 315-334
https://doi.org/10.5802/crchim.159

Microcrystalline pathologies: Clinical issues and nanochemistry

Urinary tract infection inducing stones: some clinical and chemical data

Michel Daudon [*, a, b, c], **Margaux Petay** [d], **Sophie Vimont** [b, c, e], **Ariane Deniset** [d], **Frederik Tielens** [f], **Jean-Philippe Haymann** [a, b, c], **Emmanuel Letavernier** [a, b, c], **Vincent Frochot** [a, b, c] **and Dominique Bazin** [d, g]

[a] Explorations fonctionnelles multidisciplinaires, AP-HP, Hôpital Tenon, Paris, France

[b] Sorbonne Universités, UPMC Univ Paris 6, UMR S 1155, Paris, France

[c] INSERM, UMR S 1155, Paris, France

[d] Institut de Chimie Physique, UMR CNRS 8000, Bâtiment 350, Université Paris Saclay, 91405 Orsay cedex, France

[e] Département de bactériologie, AP-HP, Hôpital Saint-Antoine, Paris, France

[f] Eenheid Algemene Chemie (ALGC) – Materials Modelling Group, Vrije Universiteit Brussel (VUB), Pleinlaan 2, 1050 Brussel, Belgium

[g] Laboratoire de Physique des Solides, UMR CNRS 8502, Bâtiment 510, Université Paris Saclay, 91405 Orsay cedex, France

E-mails: daudonmichel24@gmail.com (M. Daudon), margaux.petay@universite-paris-saclay.fr (M. Petay), sophie.vimont@aphp.fr (S. Vimont), ariane.deniset@universite-paris-saclay.fr (A. Deniset), frederik.tielens@vub.be (F. Tielens), jean-philippe.haymann@aphp.fr (J.-P. Haymann), emmanuel.letavernier@aphp.fr (E. Letavernier), vincent.frochot@aphp.fr (V. Frochot), dominique.bazin@universite-paris-saclay.fr (D. Bazin)

Abstract. Most papers on kidney stones arising from infection concentrate on the mineral struvite. In this contribution, we would like to call attention to other mineral phases such as highly carbonated calcium phosphate apatite, ammonium urate, and whitlockite, by presenting clinical and chemical data. We start with epidemiological data which emphasize the increase in the prevalence of kidney stones related to infection. Then we present a statistical analysis of more than 85,000 stones which have been analysed at the Laboratoire des Lithiases of Assistance Publique-Hôpitaux de Paris which gives insights regarding the link between urinary tract infection and struvite, carbonated calcium phosphate apatite (carbapatite), and also surprisingly whitlockite. Some information regarding the pathogenesis of kidney stones linked to infection, the nature of the bacteria which have been identified, and the approach to precisely analyse infrared spectra to identify struvite, carbapatite, and whitlockite, conclude this first part. To complete this clinical description, we describe the crystallographic structure and the chemistry of three relevant compounds namely carbonated calcium phosphate, struvite, and whitlockite. To conclude this second part, the dependence of crystallite morphology of struvite on pH and on the presence, or absence, of bacteria, is described. Based on clinical and

* Corresponding author.

chemical data, it is becoming clear that struvite is not the only mineral intimately related to renal infectious processes, but that whitlockite and carbapatite with a high carbonation rate are strongly associated with urinary tract infection as well.

Keywords. Infection-induced calculi, Struvite, Whitlockite, Amorphous carbonated calcium phosphate, Carbapatite, Carbonation rate, Urease-splitting bacteria.

Published online: 15 March 2022, Issue date: 1 September 2022

1. Introduction

Urinary tract infections (UTI), ranging from uncomplicated cystitis to severe pyelonephritis and nephrolithiasis, are the third most common type of infection in human medicine (after respiratory and alimentary infections), affecting 150 million people each year worldwide [1,2]. As reported by Flores-Mireles *et al.* [3], the societal costs of these infections, including health care costs and time missed from work, are approximately US$3.5 billion per year in the United States alone.

Regarding clinical presentation, UTI is associated with flank or abdominal pain (70%), typical renal colic (rare), fever (26%), gross haematuria (18%), and sepsis (1%), but can be asymptomatic (8%—incidental diagnosis). Infection of the urinary system may lead to the formation of concretions [4–9] as well as an incrustation of JJ stents [10–13]. It is well known that infection stones form secondary to urease-splitting organisms such as *Proteus*, *Klebsiella*, *Pseudomonas*, or *Staphylococcus*, among others. With elevated urine pH due to infection of the urinary tract, the patient becomes prone to form magnesium ammonium phosphate hexahydrate (MAP or struvite), carbonated calcium phosphate apatite (carbapatite or CA), or amorphous carbonated calcium phosphate (ACCP) stones [14,15].

It is worth noting that while infection can initiate the stone, it can also contribute to the progression of a pre-existing metabolic stone: in practice, the reality is undoubtedly more complex. Letavernier [16] suggests that a urinary metabolic anomaly such as hypercalciuria could favour crystallization of calcium phosphate in the presence of non-ureasic bacteria like *Escherichia coli*. It is a new concept in addition to classical situations described by Miano *et al.* [17] which consider two different clinical pictures: stones that develop following UTI, and stones complicated by UTI (stones with infection) which are metabolic stones that passively trap bacteria from coexistent UTIs and may or may not contain calcium.

This short review provides an overview of infection kidney stones (IKS) and treats both clinical and chemical data. We will start by considering epidemiologic data which indicate a significant increase in the prevalence of IKS. Thanks to the data bank from the Laboratoire des Lithiases of Assistance Publique-Hôpitaux de Paris which details the chemical composition of kidney stones determined by Fourier Transform InfraRed (FTIR) spectroscopy [18,19] as well as clinical data from more than 85,000 patients, we will establish a significant relationship between UTI and different chemical compounds namely MAP, CA, ACCP and whitlockite (Wk). Information on the pathogenesis of IKS as well as the nature of the bacteria identified in the patients concludes this section. To complete this clinical description, the crystallographic structure and chemistry of three chemical compounds, namely MAP, CA and Wk, are presented, concluding with descriptions of crystallite morphology of these three chemical phases in the presence or absence of bacteria.

2. Clinical data regarding IKS

2.1. *Some epidemiological data*

In developing countries, major differences in the incidence of infection stones have been observed depending on continent and region, from 2.7% in Asia Minor to 13% in South America and 42.9% in Sub-Saharan Africa. These differences reflect the infectious risk factors specific to certain populations, such as nutrition and availability of modern medicine and antibiotics in each specific area [20].

Considering all criteria from stone analysis suggestive of infection-related stones, we and others [18, 21,22] in industrialized countries observed a decrease of infection stones over several decades before 2000, but a constant increase in the proportion of stones related to infection in both sexes thereafter (Figure 1). Such a significant increase may be due to different factors such as the evolution of bacteria resistant to antibiotics, or more limited access to medicine. Of note, the relative proportion of UTI

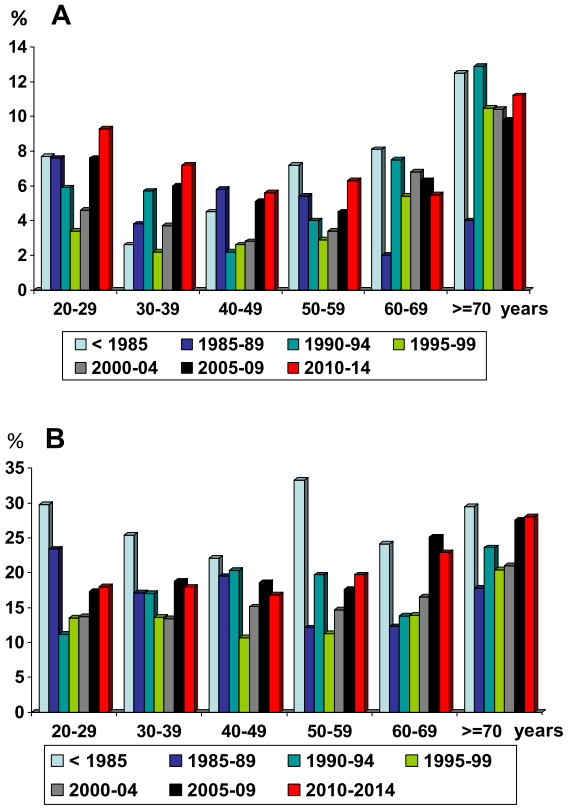

Figure 1. Evolution of infection stones in humans as a function of age and time period: A = men; B = women (from Ref. [18]). After a constant decrease in the proportion of infection stones in the second part of the twentieth century, we observed a new increase of infection stones at the beginning of the twenty-first century.

stone occurrence in men ranged from 3.2 to 10.1% and was slightly higher at the extremes of life [21]. As shown in Figures 1A and B, infection stones occur more frequently in female than in male patients across all ages.

2.2. *Chemical phases related to clinically indicated UTI*

Each stone sent for analysis in our lab is accompanied by an information sheet including anthropometric and clinical data. A clinically symptomatic urinary tract infection is one of the queries. Based on the data bank, the relationship between UTI and the main chemical compound present in the chemical composition of the stones removed from patients is summarized in Table 1. Consistent with the literature, the first compound in Table 1 is struvite, considered as a strong marker of this lithogenic process [23–30]. We note surprisingly that UTI was clinically identified in only 65.8% of cases where the stone contains any proportion of struvite. The link is slightly stronger for stones mainly composed of struvite (71.2%).

The statistical analysis (Table 1) clearly implicates a new compound as strongly related to UTI, namely Wk. Actually, more than 50% of patients with whitlockite stones had clinically recognized UTI. Such a result is in line with previous publications in which the content of Wk in kidney stones greater than 20%, estimated by FTIR, was related to infection with a high degree (80% of cases) [31]. Such relationship has been found also in a recent publication dedicated to Wk [32].

Considering CA, we also found a relationship between this compound and UTI. More precisely, we have previously noticed a significant association between a high CO_3^{2-}/PO_4^{3-} ratio in CA, and both the presence of ACCP as determined by FTIR, and the presence of bacterial imprints as shown by scanning electron microscopy (SEM) [33–37]. Ammonium urate (AmUr) is another chemical compound in Table 1 related to UTI [36–38]. Quite recently, Chou *et al.* [39] have noticed that comorbidities of ammonium acid urate urolithiasis stones included chronic kidney disease (60%), UTI (52%), irritable bowel syndrome (36%), and gout (28%). For stones composed of the other compounds, namely brushite (Br), cystine (CYS), uric acid, or calcium oxalates, less than 25% of patients had a urinary tract infection ($p < 10^{-3}$).

While MAP, Wk, and apatite have been identified in concretions at the surface of JJ stents, it seems that Wk is quite rare among the chemical phases present. Indeed, in a recent study on the mechanical properties of used JJ stents [40–42], chemical analysis of the calcifications at the surface of 52 stents shows the presence of different chemicals including ACCP, CA, Br, octacalcium phosphate pentahydrate (OCP), MAP, AmUr, weddellite (calcium oxalate dihydrate or COD), whewellite (calcium oxalate monohydrate or COM), CYS, mucopolysaccharides (MPS), proteins (PRO), and triglycerides (TRG), but no Wk. Such chemical specificity for the JJ stent is confirmed by a statistical study based on 1676 JJ stents char-

Table 1. Relationship between UTI and the chemical composition of stones determined by FTIR spectroscopy

Main crystalline or amorphous phase	Number of UTI*	Number of patients without recognized UTI	Occurrence of UTI (%)
Struvite	477	193	71.2[d]
Wk	35	31	53.0[a,c,e]
ACCP	21	20	51.2[a]
CA with CO_3 rate ≥ 15%	354	323	52.3[a,d]
OCP	21	42	33.3
CA (overall)	1024	2276	31.0[b]
AmUr	27	62	30.3[b]
Brushite	160	579	21.7[g]
UA0	542	2558	17.5
CYS	89	427	17.3
UA2	47	402	10.5[f]
COM	1900	16,675	10.2
COD	613	7148	7.9
Total	4956	30,413	14.0

*UTI was defined as UTI clinically diagnosed on the basis of urine culture and biological signs in patients. COM = calcium oxalate monohydrate, COD = calcium oxalate dihydrate, Cys = cystine, OCP = octacalcium phosphate pentahydrate, UA0 = uric acid anhydrous, UA2 = uric acid dihydrate.

[a] $p < 0.01$ vs MAP; [b] $p < 10^{-6}$ vs MAP.

[c] $p < 0.001$ vs CA; [d] $p < 10^{-6}$ vs CA.

[e] $p < 10^{-6}$ vs metabolic compounds (UA0, UA2, CYS, COM, COD).

[f] $p < 0.001$ vs AU0.

[g] $p < 10^{-4}$ vs Wk, UA2, COM, COD.

acterized at the Crystal Laboratory of Tenon Hospital; only one device had Wk as a major component, and Wk was present in 26 other stents. These observations correspond to 1.6% of cases, while in kidney stones the occurrence of Wk is equivalent to 4.4%. Note that, in the case of MAP, the same percentage is observed for both kidney stones and the JJ stent i.e. 7.2% [37].

2.3. *Pathogenesis of IKS*

The literature indicates clearly that the pathogenesis of IKS is the consequence of a high urine pH and of the production of NH_4^+ ions as a result of urea hydrolysis by bacterial urease [5,9,43,44]. As noted by Konieczna *et al.* [45], urease (urea amidohydrolase) was the first enzyme to be crystallized (1926). It was also the first enzymatic protein in which nickel ions were observed [46].

Hydrolysis of urea by urease is a complex process [45]. The first step generates one molecule of ammonia and one of carbamate appears. In aqueous solution, carbamate spontaneously converts into the second ammonia molecule and carbonic acid. Protonation of ammonia (Figure 2) results in a pH increase.

High urine pH also results in an increased calcium phosphate supersaturation, which facilitates the formation of insoluble salts such as CA and ACCP (Figure 3). However, other changes of urine biochemistry result from ureolysis, such as an increase in CO_3^{2-} ions that may end up incorporated within CA and ACCP structures.

As Figure 3 shows, four chemical phases com-

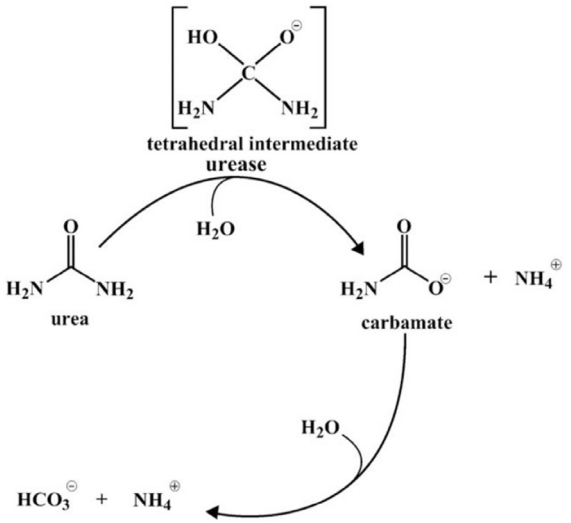

Figure 2. Mechanism of urea hydrolysis (Konieczna *et al.* [45]).

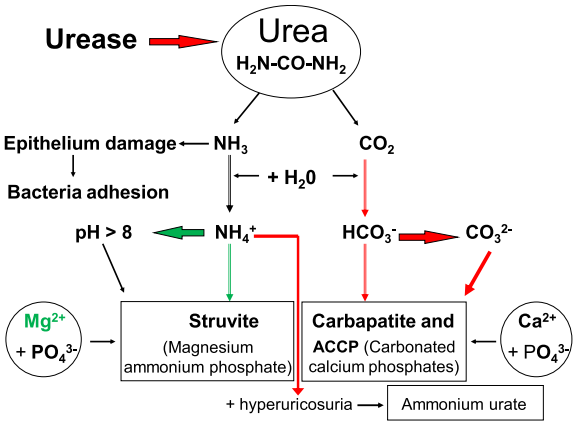

Figure 3. Pathogenesis of infection stones induced by urease-producing bacteria.

monly occur, namely struvite, ACCP, CA and AmUr. Other chemical phases may be present in IKS but an agglomeration of small crystallites trapped in the biofilm produced by bacteria could be an explanation of the presence of these, which may be related to other metabolic disorders as well.

From a clinical point of view, one cannot completely exclude the possibility of struvite stones related to conditions other than UTI if urine biochemistry is similar (for other pathological reasons) to that produced by urea-splitting bacteria. To date, no reports of such conditions have appeared in humans. Thus, our discussion of the potential link between UTI and various crystalline phases identified in urinary calculi will omit any unsubstantiated causes of struvite formation.

2.4. *Nature of the bacteria related to UTI*

As reported in several publications [47–51], the most common pathogens in UTI are the members of the Enterobacterales order (Gram-negative bacteria found in the gut, namely *Escherichia coli*, *Klebsiella* spp., pathogens of the CES group (*Citrobacter–Enterobacter–Serratia*), members of the Proteae tribe (*Proteus–Providencia–Morganella*) with a very high proportion of urease-positive strains; other causative agents include Gram-positive cocci (*Enterococcus* spp., *Streptococcus* spp., *Staphylococcus saprophyticus*, *Staphylococcus epidermidis* and *Staphylococcus aureus*), non-fermenting Gram-negative bacteria (*Pseudomonas* spp. and *Acinetobacter* spp.), atypical microorganisms (*Mycoplasma*, *Ureaplasma* species) and yeasts (*Candida* spp.).

A generally urease negative species is *Escherichia coli*, among strains of which only about 1% of urease-positive isolates were found. In Table 2 we summarize the main micro-organisms identified in urine samples from 980 patients of our cohort with urinary stones containing any proportion of MAP. Urea-splitting bacteria were most frequent (72.0%).

Table 3 shows that the distribution of micro-organism strains in urine from patients who have formed Wk-containing stones is different from that observed for MAP stones.

3. Infrared spectroscopy identification of MAP and Wk

Infrared spectroscopy is one of the most common physical techniques used for stone analysis [52–60]. An infrared spectrum can be considered as the fingerprint of a compound or a mixture of several components in various proportions. However, because minerals, in particular phosphate compounds, exhibit broad peaks and are often present as mixtures in the same stone, it may sometimes be difficult to identify each crystalline phase accurately.

However, for clinical purposes, it is very important to detect the presence of certain components such as

Table 2. Microorganisms identified in urine of stone formers with MAP-containing calculi

Bacterial strain	Number of cases	%	Urease
Proteus mirabilis	528	53.9	+
Escherichia coli	188	19.2	−
Pseudomonas aeruginosa	53	5.4	+
Enterococcus faecalis	48	4.9	−
Klebsiella pneumoniae	42	4.3	+
Staphylococcus aureus	29	3.0	+
Enterobacter cloacae	25	2.6	−
Staphylococcus epidermidis	15	1.5	+
Corynebaterium urealyticum	13	1.3	+
Serratia marcescens	7	0.7	+
Citrobacter freundii	7	0.7	−
Candida albicans	6	0.6	−
Morganella morganii	5	0.5	+
Providencia stuartii	4	0.4	+
Proteus vulgaris	4	0.4	+
Staphylococcus saprophyticus	4	0.4	+
Ureaplasma urealyticum	2	0.2	+
Total	980	100.0	

Table 3. Occurrence of micro-organisms identified in urine samples from patients who form stones without MAP

Bacterial strain	Patients with Wk-containing stones		Patients with stones without Wk		p vs Wk stones
	Number	%	Number	%	
Proteus mirabilis	20	11.8	134	10.7	NS
Escherichia coli	99	58.6	632	50.2	NS
Pseudomonas aeruginosa	24	14.2	83	6.6	0.001
Enterococcus faecalis	7	4.1	124	9.9	NS
Klebsiella pneumoniae	7	4.1	68	5.4	NS
Staphylococcus sp.	5	3.0	88	7.0	NS
Enterobacter cloacae	2	1.2	24	1.9	NS
Corynebaterium sp.	3	1.8	3	0.2	
Citrobacter freundii	2	1.2	16	1.2	NS
Candida albicans	—	—	21	1.7	
Others	—	—	65	5.2	—
Total	169	100.0	1258	100.0	

MAP or Wk that may be markers for urinary tract infection as the cause of the stone. When MAP is the main component, it is easy to identify as shown in the infrared spectrum of pure struvite in Figure 4. Its main characteristics are a very strong ν_3 PO_4^{3-} vibration at 1005 cm^{-1} with a strong and broad absorp-

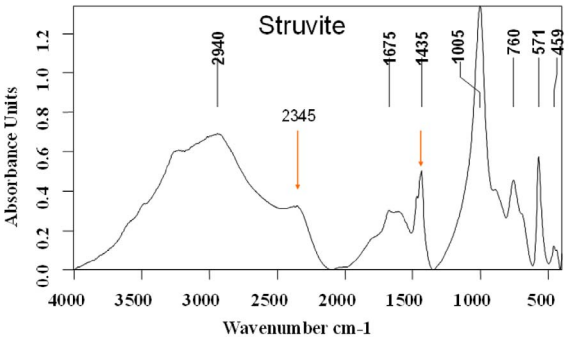

Figure 4. Struvite infrared spectrum.

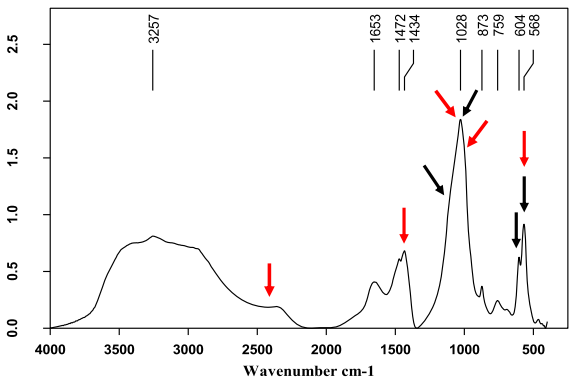

Figure 5. Mixed struvite (red arrows) and calcium phosphate (black arrows) stone.

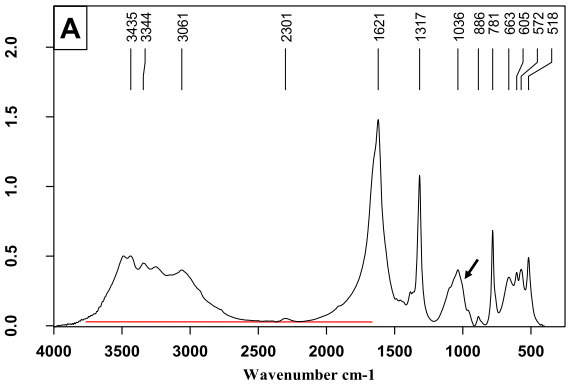

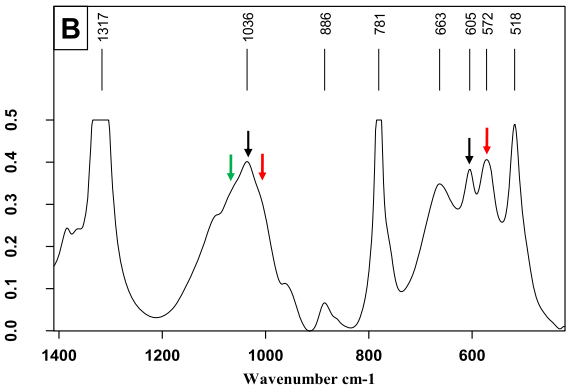

Figure 6. Mixed calcium stone mainly containing calcium oxalate monohydrate with small proportions of ACCP (green arrow), CA (black arrows) and MAP (red arrows). (A) FTIR spectrum on the wavenumber range 4000–400 cm^{-1}. (B) Enlargement of a portion of Figure 6A to better see the shoulders on the broad ν_3 phosphate band.

tion between 3700 and 2100 cm^{-1} due to ν_3 stretching vibrations of hydrogen peaks of the six water molecules and of the $NH4^+$ group, with a decrease on the right side as a pseudo-plateau between 2500 and 2345 cm^{-1} [61,62]. Another interesting vibration is the ν_2 bending peak of the ammonium group at 1435 cm^{-1}. Finally, a ν_2 peak of the PO_4^{3-} group can be observed at 571 cm^{-1}. Note that ν_2 and ν_4 bending vibrations of water molecules can be seen at 1675 and 760 cm^{-1} respectively.

When MAP is a minor component in a phosphate mixture, it is of prime importance to detect its infrared bands, mainly the plateau at 2345 cm^{-1}. The ν_2 peak of NH_4^+ is also relevant. In the case of very common mixtures of MAP with carbonated calcium phosphates, it is often shifted on the right side due to its association with the ν_3 stretching band of the CO_3^{2-} group. Finally, the ν_3 PO_4^{3-} peak of MAP can be obscured by the broad ν_3 PO_4^{3-} peak of other phosphates between 1020 and 1040 cm^{-1}.

As shown in Figure 5, in calcium orthophosphate mixtures containing less than 30% MAP, the pseudo-plateau arising at 2345 cm^{-1} is less intense, the ν_3 PO_4^{3-} peak at 1035–1030 cm^{-1} is slightly shifted towards lower wavenumbers and the edge of the peak to the right is a discrete shoulder at about 1005 cm^{-1} (red arrows).

The same criteria can be useful when MAP is only present as a small proportion of the mixture. For example, the spectrum in Figure 6 mainly shows whewellite (calcium oxalate monohydrate), carbapatite (10%), and struvite (≤5%). Note that the pseudo-plateau between 2500 and 2345 cm^{-1} is only very slightly above the baseline at 2100–

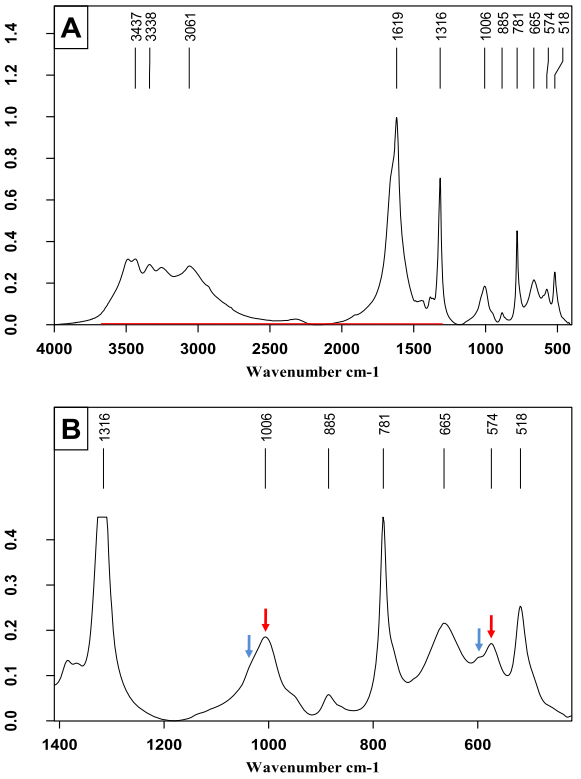

Figure 7. Another mixed stone containing struvite. (A) FTIR spectrum on the wavenumber range 4000–400 cm^{-1}. Note the presence of a plateau between 2500 and 2345 cm^{-1} indicative of struvite. (B) Enlargement of a portion of Figure 7A to see more easily some details of the phosphate bands. Shoulders at 1035 and 600 cm^{-1} correspond to CA bands (blue arrows) while peaks at 1006 and 574 cm^{-1} (red arrows) correspond to struvite. Other peaks indicate the presence of calcium oxalate monohydrate.

2150 cm^{-1}. However, other markers of MAP can be used such as the discrete shoulder at 1005 cm^{-1} (black arrow) and that to the left of the ν_4 PO_4 peak at 572 cm^{-1} (red arrow on the expanded spectrum in Figure 6B).

The expanded spectrum (Figure 6B) reveals a third phosphate, namely ACCP, detected by the slight convexity (green arrow) between the ν_3 PO_4^{3-} peak of carbapatite at 1036 cm^{-1} and its left-hand shoulder at 1097 cm^{-1} [63,64].

The final spectrum (Figure 7) shows a mainly

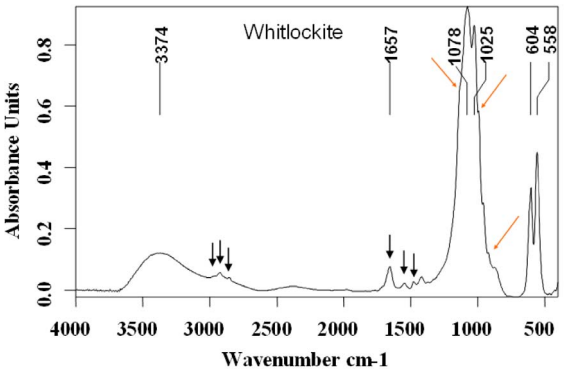

Figure 8. Whitlockite infrared spectrum.

whewellite composition, with struvite content less than 15%. The pseudo-plateau at 2345 cm^{-1} is more prominent and the ν_3 PO_4^{3-} peak at 1005–1006 cm^{-1} is not shifted, due to a very low proportion of calcium phosphates.

Nevertheless, the spectrum expansion in Figure 7B reveals shoulders due to the presence of CA (blue arrows) on the left of the struvite peaks. CA accounted for less than 10% of the mixture.

Whitlockite is another compound often related to urinary tract infection. Its infrared spectrum is shown in Figure 8 where a small proportion of proteins may also be detected (black arrows).

Characteristic vibrations for Wk are observed as a strong band with two maxima at 1078 (ν_3 HPO_4^{2-}) and 1025 (ν_3 PO_4^{3-}) cm^{-1} with shoulders at 1135 and 990 cm^{-1} (red arrows). A third shoulder can be observed at 922 cm^{-1} (red arrow). Note the peak at 1078 cm^{-1} is more intense than the one at 1025 cm^{-1}. The ν_2 and ν_4 PO_4^{3-} bending vibrations are observed at 603 and 558 cm^{-1}.

As with MAP, Wk is rarely the only phosphate present. It is almost always accompanied by CA. In such cases, the ν_4 PO_4^{3-} band of Wk at 558 cm^{-1} is slightly shifted above 560 cm^{-1}. Thus Figure 9 shows an infrared spectrum where whewellite is the main component accompanied by a small proportion of Wk (about 7–8%) and of CA (≤5%).

In cases where CA is the main component (Figure 10), it is of prime importance to look for other phosphates and particularly Wk. For this purpose, one must detect a shoulder at 990 cm^{-1} to the right of the ν_3 stretching band of CA and another shoulder to its left side at about 1135 cm^{-1}

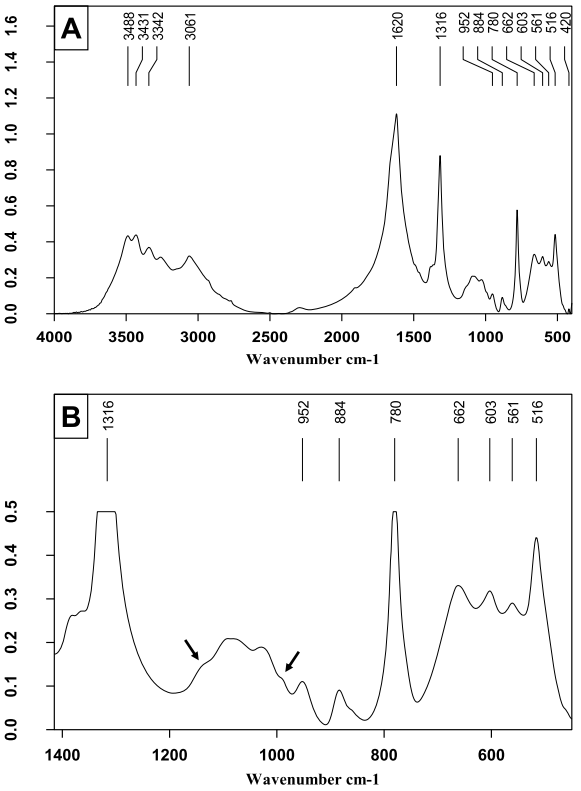

Figure 9. Kidney stone mainly containing whewellite accompanied by a small proportion of whitlockite (about 7–8%) and of carbapatite (less than 5%). (A) FTIR spectrum on the wavenumber range 4000–400 cm^{-1}. (B) Enlargement of a portion of Figure 9A to better see some details of the phosphate bands: shoulders of the whitlockite at 1135 and 991 cm^{-1} are marked by the black arrows.

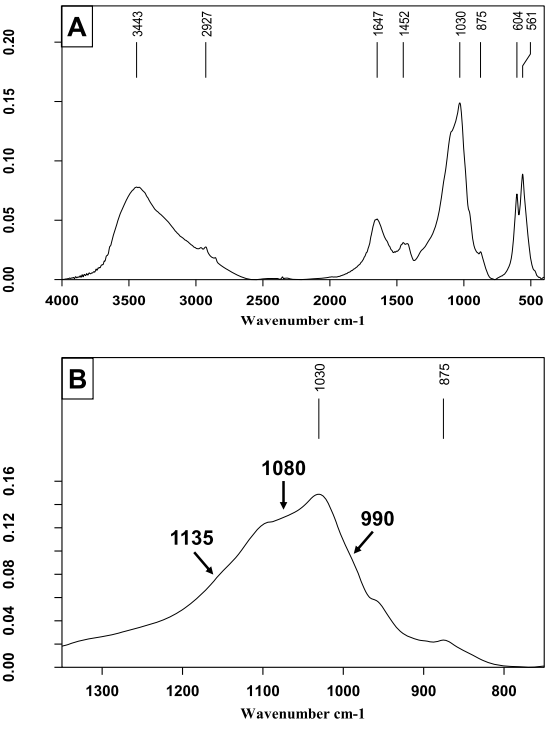

Figure 10. Carbapatite and whitlockite stone. (A) FTIR spectrum on the wavenumber range 4000–400 cm^{-1}. (B) Enlargement of a portion of Figure 10A to see some details of the phosphate bands, especially shoulders of whitlockite at 1135 and 990 cm^{-1}.

(see the expanded spectrum). Note that, in addition, the spectrum shows a small proportion of proteins (ν_3 C–H stretching bands between 2860 and 2960 cm^{-1}).

4. Physicochemical data regarding IKS

4.1. *Crystallographic structure of chemical phases related to infection*

4.1.1. *Struvite*

This compound was named after Heinrich Christoph Gottfried von Struve (1772–1851) of the Russian diplomatic service who was a co-founder of a natural science museum in Hamburg. Struvite ($MgNH_4PO_4{\cdot}6H_2O$), a white inorganic crystalline mineral, crystallizes in the orthorhombic system with cell dimensions $a = 6.941 \pm 0.002$ Å, $b = 6.137 \pm 0.002$ Å, $c = 11.199 \pm 0.004$ Å. The space group is $Pmn2_1$ and there are two molecules in the unit cell [65–70]. Figure 11A shows the atomic scale structure of struvite and Figure 11B the morphology of the struvite crystal [68]. As we will see, struvite may present very different morphologies.

4.1.2. *Carbapatite*

The mineral's name is derived from the Greek word $\alpha\pi\alpha\tau\epsilon\acute{\iota}\nu$ (apatein), which means to deceive or to be misleading. The crystallographic structure of calcium phosphate hydroxyapatite (HAP) is well known. The space group is $P6_3/m$ (Figure 12A), the

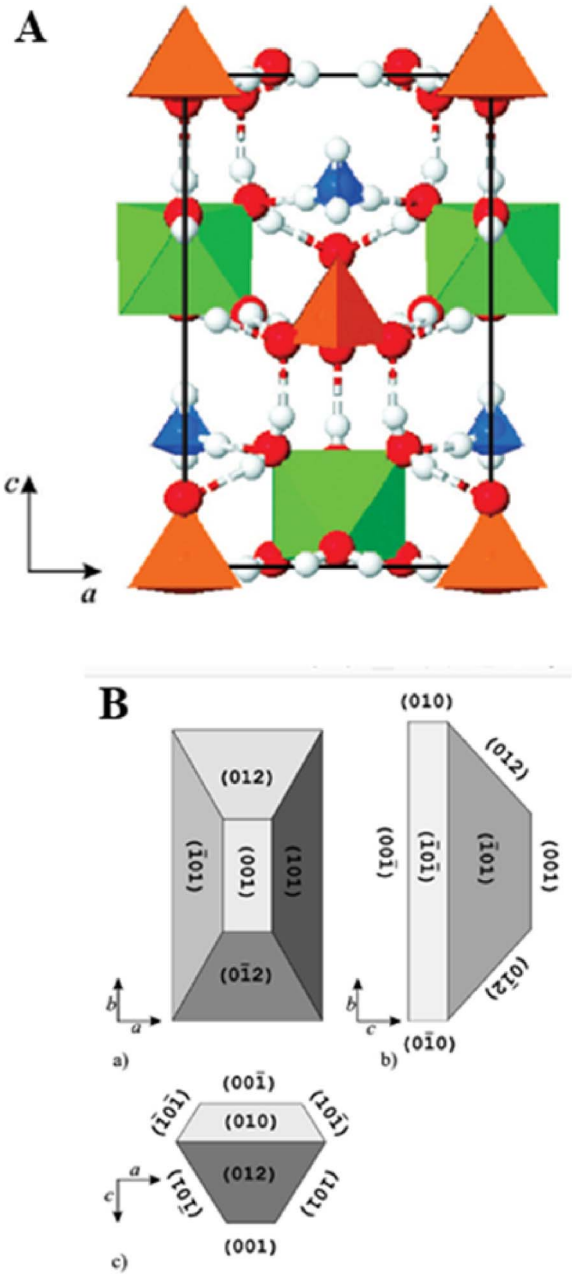

Figure 11. (A) The structure of struvite: PO_4^{3-} and NH_4^+ tetrahedra and $Mg[H_2O]_6^{2+}$ octahedra—orange, blue, and green polyhedra, respectively; O and H atoms—red and white balls, respectively; *c*-axis is polar; plane of observation: (010). (B) Crystallographic faces of struvite crystals (from Prywer *et al.*, 2009 [68]).

values for the crystallographic parameters being $a = b = 9.41844$ Å, $c = 6.88374$ Å [71–77].

Biological apatites have some structural specificities. These arise firstly from the stoichiometric formula which in reality is not the canonical $Ca_{10}(PO_4)_6(OH)_2$ but in practice $Ca_{10-x+u}\square_{x-u}(PO_4)_{6-x}(CO_3)_x(OH)_{2-x+2u}\square_{x-2u}$ where squares correspond to vacancies or additional cations and anions while x and u values are as follows: $0 < x < 2$ and $0 < u < x$. Such complexity takes into account substitution processes [78–80] as well as Ca^{2+} and OH^- vacancies [81,82] (Figure 12B). In the case of biological apatites, the diffraction peak ($hkl = 002$) is sharper than the other peaks, indicating the anisotropy of nanocrystals (needle and/or platelet-like morphology) [83]. Note that a structured hydrated layer exists at the surface of biological apatite which serves as an exchange area with the biological environment (Figure 12C) [84–87].

4.1.3. *Whitlockite*

Whitlockite was named after Herbert Percy Whitlock (1868–1948), a curator of minerals at the American Museum of Natural History in New York (USA). Wk is a complex material which involves cation substitutions, cation vacancies, and protonation of phosphate groups [88–90]. Using quantum chemical structural optimization by Density Functional Theory (DFT) calculations, Debroise *et al.* [90] were able to quantify the ability of Wk to hold these substitutions and vacancies in preferential sites. The impact of Ca^{2+}/Mg^{2+} substitutions on X-ray diffraction (XRD), IR, and Raman characteristics fell within the scope of DFT and compared with experiment. In particular, the crystallographic positions of the vacancy and optimal Ca^{+2}/Mg^{2+} substitution sites were identified (Figure 13). Mg^{2+} concentration could be quantified from the variation in length of the unit cell parameters. Also, they show clearly that Raman spectroscopy is very sensitive to the Mg^{2+} substitutions and to the presence of impurities such as Fe^{2+}. The theoretical IR spectra enabled unequivocal assignment of observed spectral bands to specific vibrations. As with Raman, IR spectra were found to be very sensitive to the presence of defects, and the Mg^{2+} concentration.

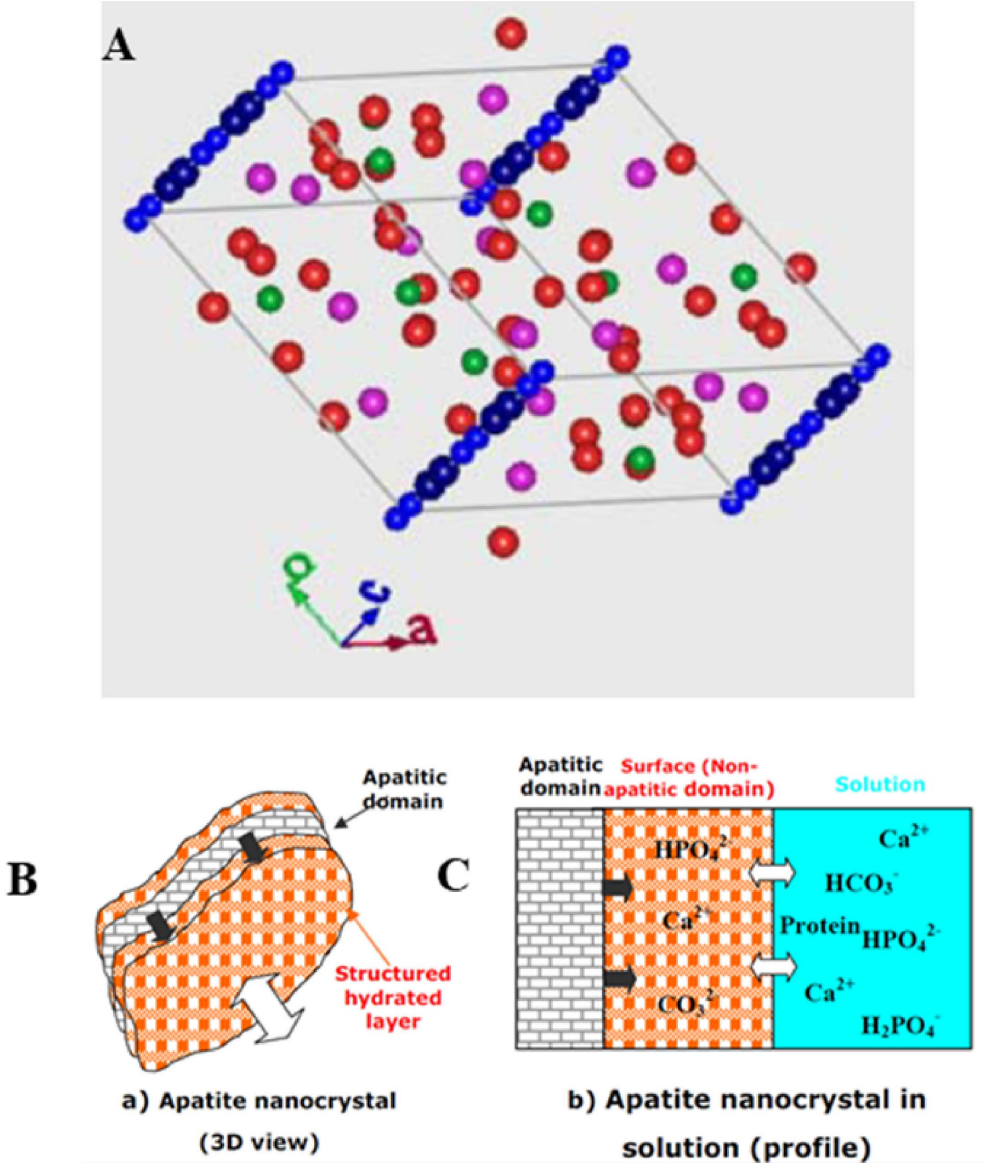

Figure 12. (A) Spatial distribution of different atoms in HAP. Hydrogen and oxygen atoms of the hydroxyl groups represented in blue are located on the *c*-axis. (B) and (C) Schematic model of the surface hydrated layer of poorly crystalline apatite nanocrystals (from Refs. [84,85]).

4.2. *Synthesis of chemical phases related to IKS*

In this section, we will not describe the synthesis of calcium phosphate apatite as its presence in bone has resulted in a considerable literature (see for example [91–97]).

4.2.1. *The case of struvite*

Several papers, arising in two very different research fields, wastewater treatments, and medicine, describe the synthesis of MAP [98–111]. Different precursors have been used in *in vitro* experiments. For example, introduction of Mg^{2+} cations can be performed by addition of $MgSO_4$, $MgCl_2{\cdot}6H_2O$,

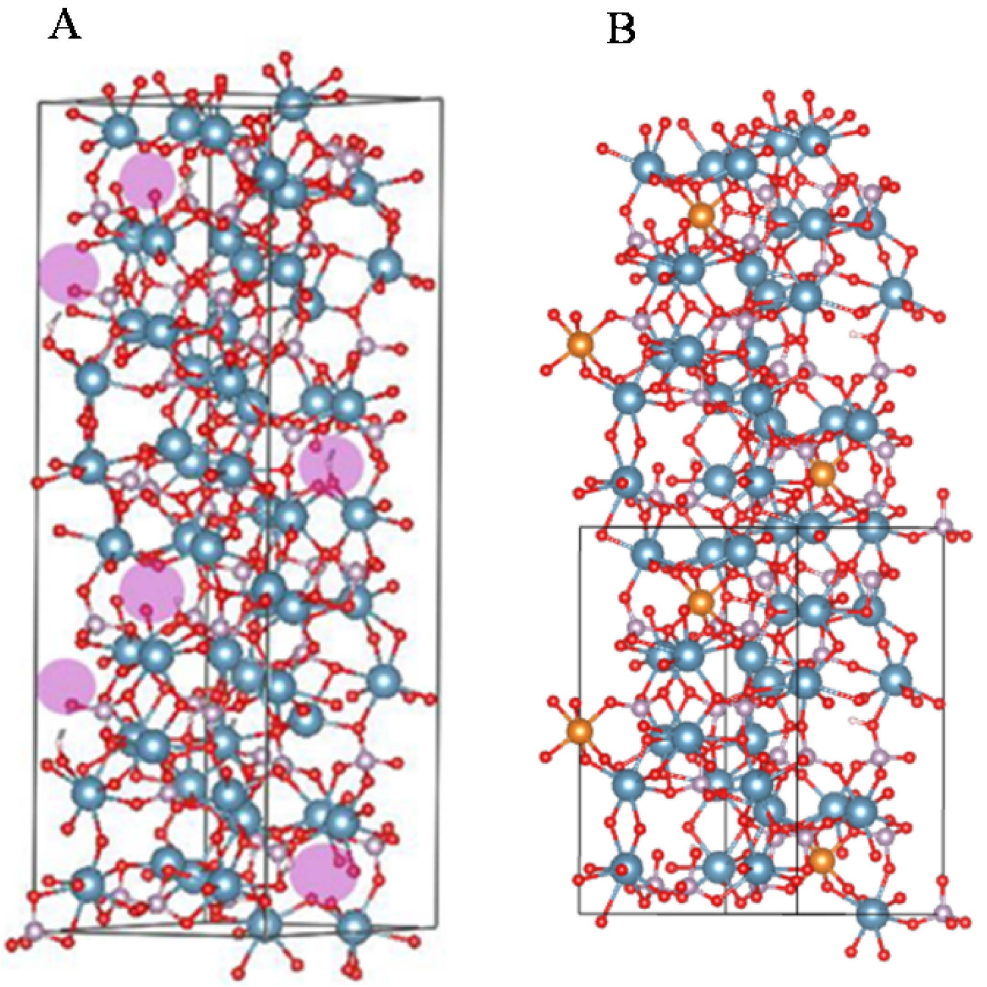

Figure 13. (A) Whitlockite unit cell showing vacancies indicated by purple spheres, which correspond to the crystallographic Ca^{2+} site number 4. (B) Whitlockite unit cell showing the half unit cell with $3Mg^{2+}$ substitutions on the Ca^{2+} sites. Crystallographic site 5 was found to be the most favourable energetically for substitution by Mg^{2+}. Ca: blue, Mg: gold, P: grey, O: red and H: white (from Debroise *et al.* [90]).

$C_4H_6MgO_4$ to the synthesis solution. In the case of Ca^{2+} cations, $CaCl_2{\cdot}2H_2O$ is usually used. Some of these synthetic struvite crystals, such as the one published by Manzoor *et al.* [106], have been obtained in the presence of creatine.

In urine, crystallization of struvite is highly dependent on pH and relative concentrations of magnesium, phosphate and ammonium as shown in Figure 14.

For a similar magnesium ammonium phosphate molar product (pMAP), the relative concentrations of ions involved in pMAP can be very different as shown in Table 4, explaining the fact that bacterial urease activity is not the unique condition for struvite crystallization and that the urine biochemistry of the patient can also be involved (Figure 15). Nevertheless, as shown in Figure 14, urine pH is a very strong determinant for MAP crystallization. Below pH 6.5, the concentrations of magnesium, ammonium, and phosphate, required for MAP formation are too high to correspond to any physiological or pathological condition; this is why MAP in urinary concretions is commonly considered a marker of alkaline urine related to urinary tract infection by urea-splitting bac-

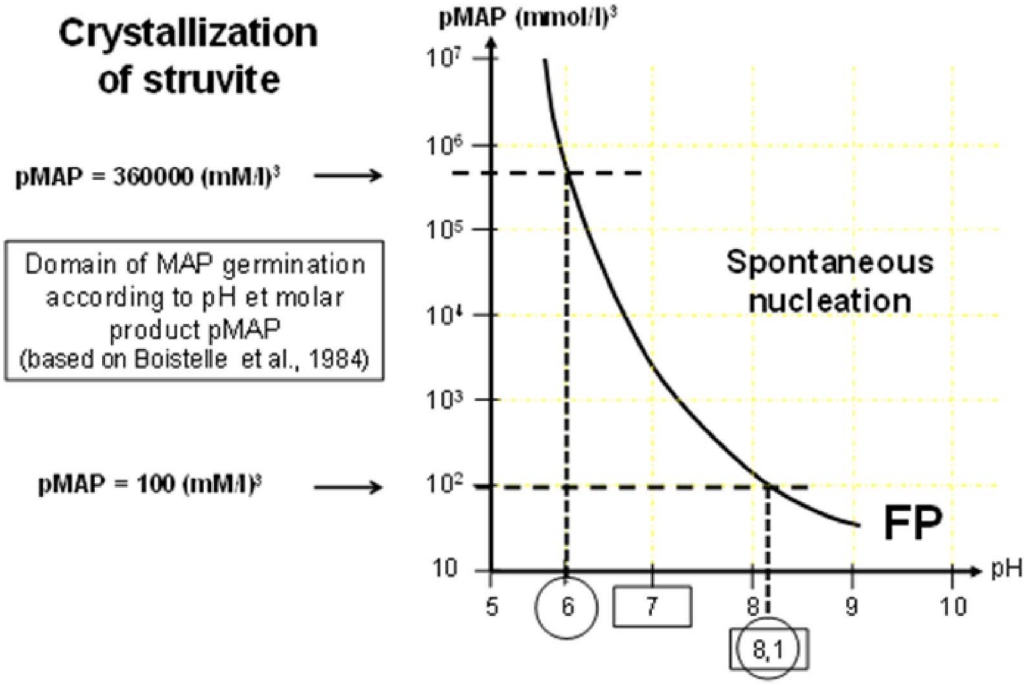

Figure 14. Crystallization of struvite is highly dependent on urine pH. FP is the formation product of MAP, i.e., the limit of pMAP above which MAP crystals spontaneously form in urine.

teria.

As shown in Table 4, the FP for MAP required for crystallization is very high for pH < 6.8 and rarely encountered in urine. In cases of UTI by urea-splitting bacteria, the increase of urine pH by production of NH_3 from urea strongly reduces the pMAP needed for crystallization, mainly encountered in UTI by microorganisms with urease. However, metabolic conditions which allow MAP crystallization without infection should not be ruled out. This might explain the discrepancy between the occurrence of clinically recognized UTI reported by physicians and the presence of MAP in stones although to date no metabolic condition has been clearly identified as a cause of MAP stones without UTI in humans.

However, such conditions have occasionally been reported in animals [111]. Another explanation is related to the time elapsed between stone formation and stone removal. In the absence of clinically recorded UTI with stones that contain MAP, we noted that MAP was mainly located in the nucleus of the stone (89.8% of cases), which could be a marker for a transient episode of UTI.

As shown in Figure 15, the urinary excretion of solutes markedly reflects the risk of crystallization of a given species. For example, in the case of MAP and brushite crystals, and to a lesser extent for ACCP, the excretion of phosphate ions is significantly higher than for other crystalline species, irrespective other parameters such as urine pH.

4.2.2. *The case of whitlockite*

Only a few publications report the synthesis of Wk [113–118], among them note the work of Jang *et al.* introducing a new synthetic route to pure Wk nanocrystals precipitated under Mg^{2+}-rich and physiological conditions [114]. Qi *et al.* [115] generated Wk microspheres which displayed high biocompatibility and an excellent ability to promote adhesion and spreading of MC-3T3 osteoblasts using a novel microwave-assisted method. Also, hydrothermal growth of Wk on a β-TCP surface to enhance osteogenesis has been investigated by Guo *et al.* [116]. Finally, Wk nanoparticles can also be prepared by precipitation using calcium hydroxide and magnesium hydroxide [117].

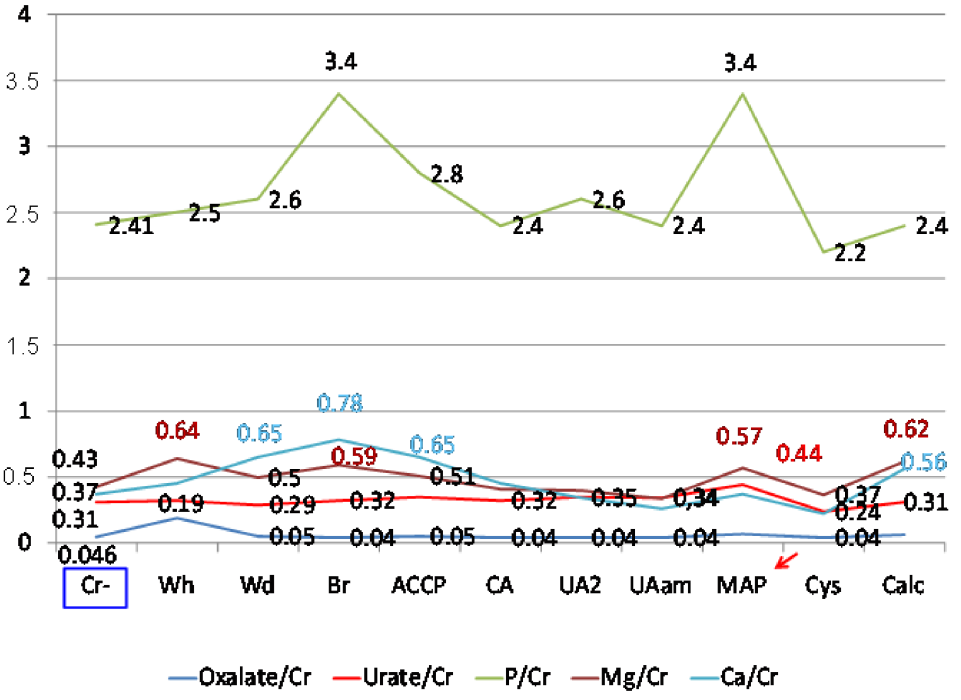

Figure 15. On the *y* axis, are shown the mean values of oxalate to creatinine ratio (—), urate to creatinine ratio (—), phosphate to creatinine ratio (—), magnesium to creatinine ratio (—) and calcium to creatinine ratio (—) for the different crystalline phases described below. Cr^{-} = absence of crystals. Crystalline phases: Wh = whewellite; Wd = weddellite; Br = brushite; ACCP = amorphous carbonated calcium phosphate; CA = carbapatite; UA2 = uric acid dihydrate; UAam = uric acid amorphous; MAP = struvite; Cys = cystine; Calc = calcite.

Recently, Wang *et al.* [118] have developed an interesting synthesis of Wk nanocrystals using a tri-solvent system for the solid–liquid–solution process, which offers the opportunity to generate Wk nanocrystals with tuneable size, morphology (nanoplates, nanospheres), and surface properties (hydrophobic, hydrophilic), impossible to achieve using the traditional precipitation method.

Regarding the role of pH in the synthesis of Wk, it is worth underlining that, as noted by Jang *et al.* [114], Wk had greater stability than HAP in acidic conditions below pH 4.2. These authors also confirmed that calcium phosphate apatite can directly transform into Wk under appropriate acidic pH conditions with a sufficient Mg^{2+} cations content in the medium.It is notable that, in urinary stones, Wk has occurred mixed with MAP in 11.3% of cases and that a mixture of WK and MAP was found in the same layers of more than 100 stones, suggesting that acidic conditions are not required for Wk formation under biological conditions.

4.3. *Crystallite morphology of chemical phases related to IKS*

4.3.1. *Morphology of MAP crystallites*

Various publications have reported the morphology of MAP crystallites [112,119]. Prywer *et al.* [112] have used scanning electron microscopy to correlate crystal morphology with the pH of artificial urine (Figure 16).

As shown by Daudon and Frochot [120], MAP is highly dependent on urinary pH and may occur in a range between 6.8 and 9.0 (Figure 17).

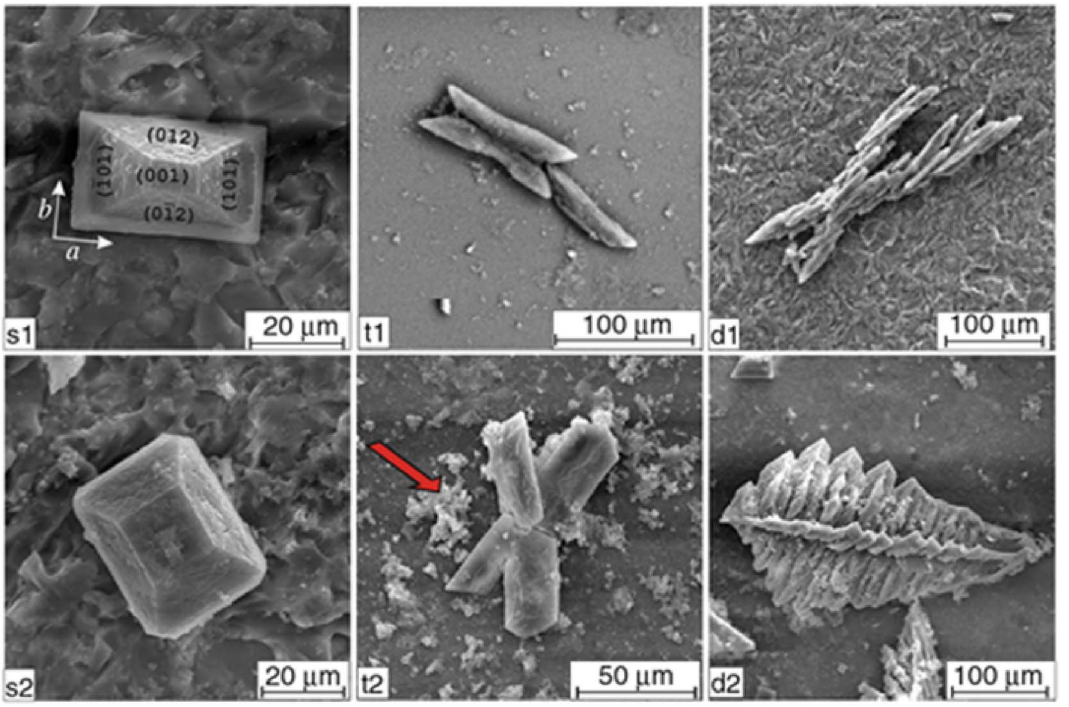

Figure 16. SEM micrographs illustrating the dependence of morphology and habits of struvite on pH of artificial urine; left column: single hemimorphic crystals obtained at pH range 7.2–9.0; middle column: contact (t1) and penetration (t2) twins obtained at pH range 9.0–9.5; right column: X-shaped (d1) and fern-leaf (d2) dendritic crystals obtained at the highest pH values (pH 9.5); arrow indicates CA precipitation (from Prywer *et al.* [112]).

At this point, it is worth underlining those bacteria are able to affect and modify the dimensions or the morphology of MAP crystals [112,119–123]. For example, the results of Sun *et al.* [123] show that MAP particles produced in the presence of bacteria are larger than in the absence. It is possible that bacterial biomolecules may act as templates to induce the nucleation, growth, and aggregation of struvite crystals.

4.3.2. *Morphology of CA and Wk crystallites*

Several investigators have reported the presence of bacterial imprints in renal stones using transmission and scanning electron microscopy [124–126]. Indeed, this approach may help identify bacteria that may contribute to stone formation, even though urine culture results might be negative.

More specifically, it was reported that in IKS bacterial imprints are only observed on areas composed of CA and not on MAP crystals [127], as has also been observed in IKS containing Wk (Figure 18). In a contribution to this special issue we have shown that Wk crystallites display a specific morphology [32].

5. Conclusions and perspectives

The comprehensive set of clinical and physicochemical data presented in this contribution shows clearly that IKS display a complex chemistry which is clearly not limited to struvite. For the clinician, such chemical complexity calls for a precise analysis of different infrared spectra related to the core and the surface of a kidney stone. With the increase of bacterial antibiotic resistance and the paucity of new antibiotics (as underlined by the World Health Organization),[1] it is

[1] https://www.who.int/news/item/17-01-2020-lack-of-new-antibiotics-threatens-global-efforts-to-contain-drug-resistant-infections.

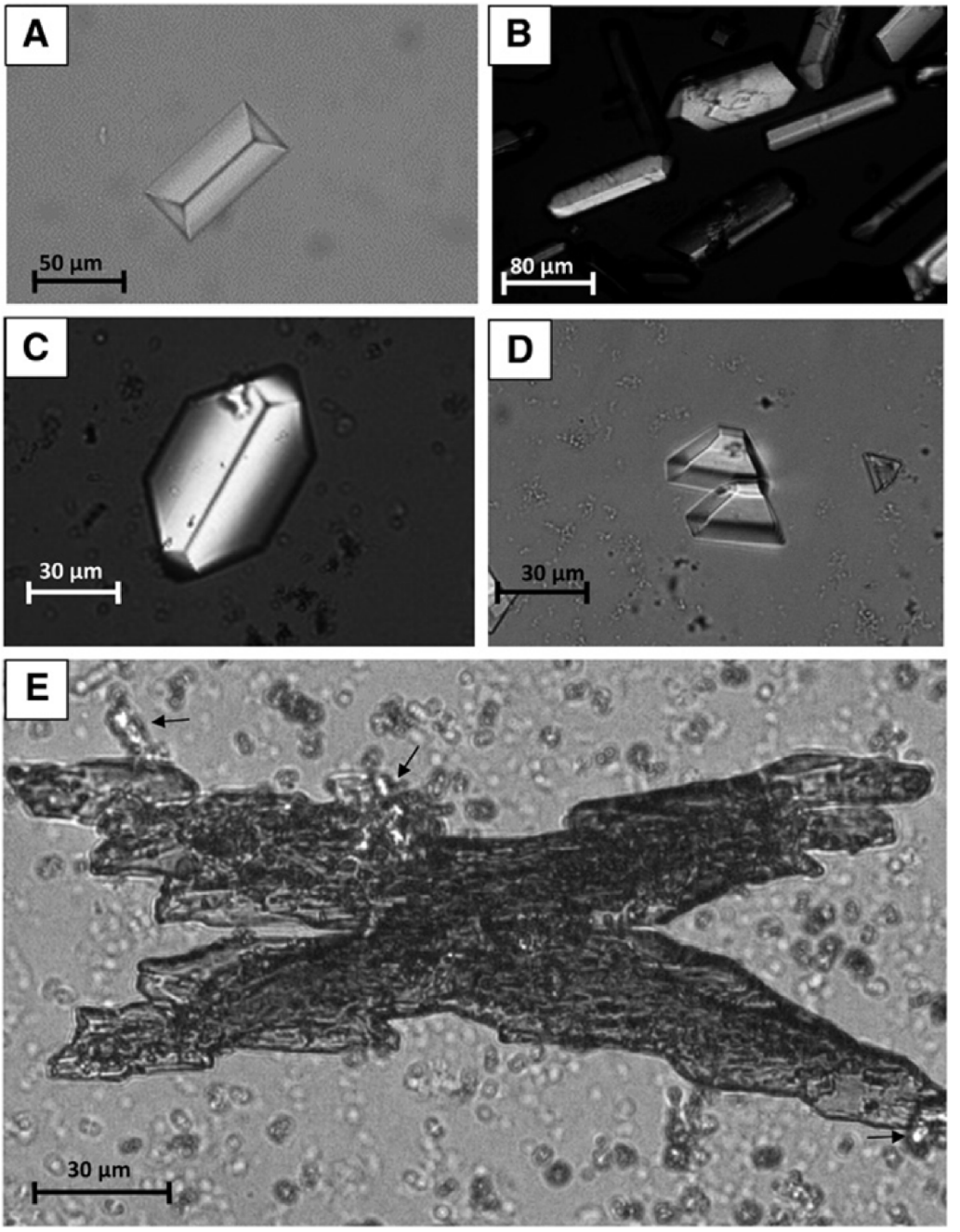

Figure 17. MAP crystals as seen under polarized light (from Daudon and Frochot, 2015 [120]). (A) A coffin-shaped crystal of MAP. (B) Rod-shaped and coffin-shaped crystals of MAP. (C) A hexagonal crystal of MAP and small agglomerates of amorphous carbonated calcium phosphate grains. (D) Trapezoidal crystals of MAP. (E) A large X-shaped dendritic crystal of MAP with birefringent small aggregates of ammonium hydrogen urate crystals (black arrows).

Table 4. Formation product (FP) for MAP (pMAP) at different urinary pH and ion concentrations (adapted from Boistelle *et al.* 1984 [110])

Ion concentration (mmol/L)			Formation product (FP) of pMAP ($\mu mol/L^3$)	pH at FP
Mg	PO_4	NH_4		
1	5	10	50	8.7
1	10	15	150	8.0
1	10	50	500	7.45
2	20	20	800	7.3
3	20	30	1800	6.95
2	10	100	2000	7.0
2	100	10	2000	7.0
4	30	30	3600	6.8
6	30	40	7200	6.75
3	10	300	9000	6.7
7	30	50	10,500	6.65
7	40	80	22,400	6.5
7	50	100	35,000	6.4
7	100	200	140,000	6.15
8	150	300	360,000	6.0

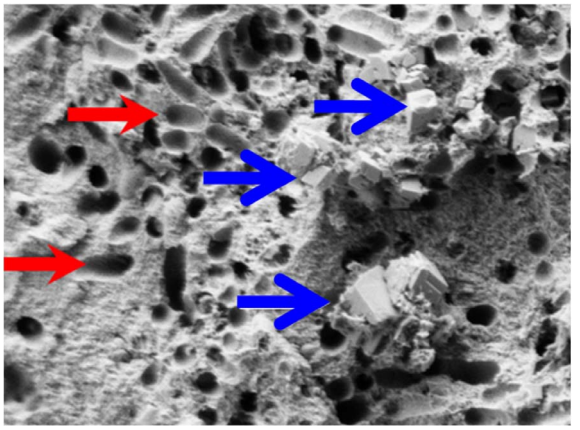

Figure 18. SEM image showing bacterial imprints (red arrows) in a stone made of whitlockite (blue arrows) mixed with carbapatite.

quite clear that IKS constitute a major topic of interest for the medical community. It is thus of primary importance to accurately detect the presence of MAP and Wk in urinary stones as well as to precisely measure the carbonation rate of calcium phosphate apatite by FTIR spectroscopy.

Conflicts of interest

Authors have no conflict of interest to declare.

References

[1] W. E. Stamm, S. R. Norrby, *J. Infect. Dis.*, 2001, **183**, S1-S4.

[2] B. Foxman, *Infect. Dis. Clin. North Am.*, 2014, **28**, 1-13.

[3] A. L. Flores-Mireles, J. N. Walker, M. Caparon, S. J. Hultgren, *Nat. Rev. Microbiol.*, 2015, **13**, 269-284.

[4] A. E. Krambeck, N. F. Khan, M. E. Jackson, J. E. Lingeman, J. A. McAteer, J. C. Williams, *J. Urol.*, 2010, **184**, 1543-1549.

[5] R. Flannigan, W. H. Choy, B. Chew, D. Lange, *Nat. Rev. Urol.*, 2014, **11**, 333-341.

[6] J. Prywer, M. Olszynski, *Curr. Med. Chem.*, 2017, **24**, 292-311.

[7] W. L. Strohmaier, "Infection induced urinary stones. Version: 2018-02-27", in *Urogenital Infections and Inflammations* (T. E. Bjerklund Johansen, F. M. E. Wagenlehner, T. Matsumoto, Y. H. Cho, J. N. Krieger, D. Shoskes, K. G. Naber, eds.), German Medical Science GMS Publishing House, Duesseldorf, 2017.

[8] J. L. Bauza, E. C. Pieras, F. Grases, V. Tubau, J. Guimerà, X. A. Sabaté, P. Pizà, *Med. Hypotheses*, 2018, **118**, 34-35.

[9] E. J. Espinosa-Ortiz, B. H. Eisner, D. Lange, R. Gerlach, *Nat. Rev. Urol.*, 2019, **16**, 35-53.

[10] D. W. L. Hukins, D. S. Hickey, A. P. Kennedy, *Br. J. Urol.*, 1983, **55**, 304-305.

[11] D. Stickler, L. Ganderton, J. King, J. Nettleton, C. Winters, *Urol. Res.*, 1993, **21**, 407-411.

[12] D. J. Stickler, *J. Intern. Med.*, 2014, **276**, 120-129.

[13] C. E. Chenoweth, C. V. Gould, S. Saint, *Infect. Dis. Clin. North Am.*, 2014, **28**, 105-119.

[14] R. Golan, K. L. Cooper, O. Shah, *Rev. Urol.*, 2020, **22**, 52-56.

[15] N. Karki, S. W. Leslie, "Struvite and triple phosphate renal calculi. [Updated 2021 Aug. 12]", in *StatPearls [Internet]*, StatPearls Publishing, Treasure Island (FL), 2021.

[16] E. Letavernier, "Quel est le profil métabolique des patients qui développent des calculs d'infection ? Calculs infectieux sans struvite", in *Communication aux 20*émes *Confrontations Clinico-Biologiques sur la Lithiase Urinaire* (Paris, France), 2015.

[17] R. Miano, S. Germani, G. Vespasiani, *Urol. Int.*, 2007, **79**, 32-36.

[18] M. Daudon, M. Livrozet, D. Bazin, J. P. Haymann, E. Letavernier, "Proceedings of the 24e Confrontations Clinico-Biologiques sur la Lithiase Urinaire" (Paris, France), 2019, 8-18.

[19] D. Bazin, M. Daudon, *Ann. Biol. Clin.*, 2015, **73**, 517-534.

[20] M. Daudon, B. Bounxouei, F. Santa Cruz, S. Leite da Silva, B. Diouf, F. F. Angwafoo 3rd, J. Talati, G. Desrez, *Prog. Urol.*, 2004, **14**, 1151-1161.

[21] M. Daudon, J. C. Doré, B. Lacour, *Urol. Res.*, 2004, **32**, 241-247.

[22] R. Moses, V. M. Pais Jr., M. Ursiny, E. L. Prien Jr., N. Miller, B. H. Eisner, *Urolithiasis*, 2015, **43**, 135-139.

[23] D. L. Lamm, S. A. Johnson, A. M. Friedlander, R. F. Gittes, *Urology*, 1977, **10**, 418-421.

[24] D. P. Griffith, *Kidney Int.*, 1978, **13**, 372-382.

[25] D. P. Griffith, *Urol. Res.*, 1979, **7**, 215-221.

[26] M. I. Resnick, *Urol. Clin. North Am.*, 1981, **8**, 265-276.

[27] S. P. Lerner, M. J. Gleeson, D. P. Griffith, *J. Urol.*, 1989, **141**, 753-758.

[28] T. D. Cohen, G. M. Preminger, *Semin. Nephrol.*, 1996, **16**, 425-434.

[29] J. S. Rodman, *Nephron*, 1999, **81**, 50-59.

[30] J. C. Williams Jr., A. J. Sacks, K. Englert, R. Deal, T. L. Farmer, M. E. Jackson, J. E. Lingeman, J. A. McAteer, *J. Endourol.*, 2012, **26**, 726-731.

[31] L. Maurice-Estepa, P. Levillain, B. Lacour, M. Daudon, *Scand. J. Urol. Nephrol.*, 1999, **33**, 299-305.

[32] D. Bazin, R. J. Papoular, E. Elkaim, R. Weil, D. Thiaudière, C. Pisapia, B. Ménez, N. S. Hwang, F. Tielens, M. Livrozet, E. Bouderlique, J.-P. Haymann, E. Letavernier, L. Hennet, V. Frochot, M. Daudon, *C. R. Chimie*, 2022, **25**, no. S1, 343-354.

[33] X. Carpentier, M. Daudon, O. Traxer, P. Jungers, A. Mazouyes, G. Matzen, E. Véron, D. Bazin, *Urology*, 2009, **73**, 968-975.

[34] M. Daudon, H. Bouzidi, D. Bazin, *Urol. Res.*, 2010, **38**, 459-467.

[35] K. M. Englert, J. A. McAteer, J. E. Lingeman, J. C. Williams Jr., *Urolithiasis*, 2013, **41**, 389-394.

[36] M. Daudon, C. A. Bader, P. Jungers, *Scan. Microsc.*, 1993, **7**, 1081-1104.

[37] M. Daudon, A. Dessombz, V. Frochot, E. Letavernier, J.-P. Haymann, P. Jungers, D. Bazin, *C. R. Chim.*, 2016, **19**, 1470-1491.

[38] A. Hesse, H.-G. Tiselius, A. Jahnen (eds.), *Urinary Stones*, Karger, Basel, 2002.

[39] Y.-H. Chou, C.-N. Huang, W.-M. Li, S.-P. Huang, W.-J. Wu, C.-C. Tsai, A.-W. Chang, S.-M. Chen, Y.-L. Lin, Y.-P. Lin, *Kaohsiung J. Med. Sci.*, 2012, **28**, 259-264.

[40] C. Poulard, A. Dessombz, M. Daudon, D. Bazin, *C. R. Chim.*, 2016, **19**, 1597-1604.

[41] E. Van de Perre, G. Reichman, D. De Geyter, C. Geers, K. M. Wissing, E. Letavernier, *Front. Med.*, 2020, **7**, article no. 609024.

[42] P. Calvó, J. L. Bauza, F. Julià, J. Guimerá, E. C. Pieras, A. Costa-Bauzá, F. Grases, *C. R. Chimie*, 2022, **25**, no. S1, 425-430.

[43] A. Trinchieri, *Urologia*, 2014, **81**, 93-98.

[44] E. L. Prien, *Clin. Microbiol. Newslett.*, 1990, **12**, 129-132.

[45] I. Konieczna, P. Żarnowiec, M. Kwinkowski, B. Kolesińska, J. Frączyk, Z. Kamiński, W. Kaca, *Curr. Protein Pept. Sci.*, 2012, **13**, 789-806.

[46] H. L. T. Mobley, M. D. Island, R. P. Hausinger, *Microbiol. Rev.*, 1995, **59**, 451-480.

[47] K. H. Bichler, E. Eipper, K. Naber, V. Braun, R. Zimmermann, S. Lahme, *Int. J. Antimicrob. Ag.*, 2002, **19**, 488-498.

[48] B. Wiedemann, A. Heisig, P. Heisig, *Antibiotics*, 2014, **3**, 341-352.

[49] J. D. Sobel, D. Kaye *et al.*, "Chapter 74—Urinary tract infections", in *Mandell, Douglas, and Bennett's Principles and Practice of Infectious Diseases* (J. E. Bennett *et al.*, eds.), Elsevier, Philadelphia, 8th ed., 2015, 886-913.e3.

[50] Y. M. Romanova, N. S. Mulabaev, E. R. Tolordava, A. V. Seregin, I. V. Seregin, N. V. Alexeeva, T. V. Stepanova, G. A. Levina, O. I. Barhatova, N. A. Gamova, S. A. Goncharova, L. V. Didenko, I. V. Rakovskaya, *Mol. Genet. Mikrobiol. Virol.*, 2015, **2**, 20-25.

[51] M. Gajdács, M. Ábrók, A. Lázár, K. Burián, *Sci. Rep.*, 2020, **10**, article no. 17658.

[52] N. Quy Dao, M. Daudon, *Infrared and Raman Spectra of Calculi*, Elsevier, Paris, 1997.

[53] L. M. Estepa, P. Levillain, B. Lacour, M. Daudon, *Clin. Chem. Lab. Med.*, 1999, **37**, 1043-1052.

[54] F. Cohen-Solal, B. Dabrowsky, J. C. Boulou, B. Lacour, M. Daudon, *Appl. Spectrosc.*, 2004, **58**, 671-678.

[55] D. Bazin, M. Daudon, "Nouvelles Méthodes d'étude des calculs et plaques de Randall", in *Actualités néphrologiques Jean Hamburger* (P. Lesavre, T. Drüeke, C. Legendre, P. Niaudet, eds.), Flammarion — Médecine, Paris, 2010, 75-98.

[56] M. Daudon, D. Bazin, "New techniques to characterize kidney stones and Randall's plaque", in *Urolithiasis: Basic Science and Clinical Practice* (J. J. Talati, H. G. Tiselius, D. M. Albala, Z. Ye, eds.), Springer, London, 2012, 683-707.

[57] D. Bazin, J.-P. Haymann, E. Letavernier, J. Rode, M. Daudon, *Presse Med.*, 2014, **43**, 135-148.

[58] M. L. Giannossi, *J. X-ray Sci. Technol.*, 2015, **23**, 401-407.

[59] M. Daudon, D. Bazin, *C. R. Chim.*, 2016, **19**, 1416-1423.

[60] D. Bazin, E. Letavernier, J.-P. Haymann, P. Méria, M. Daudon, *Prog. Urol.*, 2016, **26**, 608-618.

[61] D. Sidorczuk, M. Kozanecki, B. Civalleri, K. Pernal, J. Prywer, *J. Phys. Chem. A*, 2020, **124**, 8668-8678.

[62] K. Suguna, M. Thenmozhi, C. Sekar, *Bull. Mater. Sci.*, 2012, **35**, 701-706.

[63] C. Rey, M. Shimizu, B. Collins, M. J. Glimcher, *Calcif. Tissue Int.*, 1990, **46**, 384-394.

[64] M. E. Fleet, *Am. Mineral.*, 2017, **102**, 149-157.

[65] A. Whitaker, J. W. Jeffery, *Acta Crystallogr. B*, 1970, **26**, 1429-1440.
[66] F. Abbona, R. Boistelle, *J. Cryst. Growth*, 1979, **46**, 339-354.
[67] G. Ferraris, H. Fuess, W. Joswig, *Acta Crystallogr. B*, 1986, **42**, 253-258.
[68] J. Prywer, A. Torzewska, *Cryst. Growth Des.*, 2009, **9**, 3538-3543.
[69] Z. Romanowski, P. Kempisty, J. Prywer, S. Krukowski, A. Torzewska, *J. Phys. Chem. A*, 2010, **114**, 7800-7808.
[70] J. Prywer, L. Siero, A. Czylkowska, *Crystals*, 2019, **9**, article no. 89.
[71] S. Naray-Szabo, *Z. Kristallogr. Kristallgeom. Kristallphys. Kristall Chem.*, 1930, **75**, 387-398.
[72] J. C. Elliot, P. E. Mackie, R. A. Young, *Science*, 1973, **180**, 1055-1057.
[73] J. C. Elliot, E. Dykes, P. E. Mackie, *Acta Crystallogr. B*, 1981, **37**, 435-438.
[74] J. C. Elliot, *Structure and Chemistry of the Apatites and Other Calcium Orthophosphates*, Elsevier, Amsterdam, 1994.
[75] T. J. White, D. Zhi Li, *Acta Crystallogr. B*, 2003, **59**, 1-16.
[76] M. Vallet-Reg, M. J. Gonzalez-Calbet, *Prog. Solid State Chem.*, 2004, **32**, 1-31.
[77] D. Bazin, C. Chappard, C. Combes, X. Carpentier, S. Rouzière, G. André, G. Matzen, M. Allix, D. Thiaudière, S. Reguer, P. Jungers, M. Daudon, *Osteoporos Int.*, 2009, **20**, 1065-1075.
[78] Y. Suetsugu, Y. Takahashi, F. P. Okamura, J. Tanaka, *J. Solid State Chem.*, 2000, **155**, 292-297.
[79] T. Tite, A.-C. Popa, L. M. Balescu, I. M. Bogdan, I. Pasuk, J. M. F. Ferreira, G. E. Stan, *Materials (Basel)*, 2018, **11**, article no. 2081.
[80] Y. Jiang, Z. Yuan, J. Huang, *Mater. Technol.*, 2020, **35**, 785-796.
[81] C. Rey, J. L. Miquel, L. Facchini, A. P. Legrand, M. J. Glimcher, *Bone*, 1995, **16**, 583-586.
[82] C. K. Loong, C. Rey, L. T. Kuhn, C. Combes, Y. Wu, S. H. Chen, M. J. Glimcher, *Bone*, 2000, **26**, 599-602.
[83] H. M. Kim, C. Rey, M. J. Glimcher, *J. Bone Miner. Res.*, 1995, **10**, 1589-1601.
[84] C. Combes, S. Cazalbou, C. Rey, *Minerals*, 2016, **6**, article no. 34.
[85] D. Eichert, C. Drouet, H. Sfihi, C. Rey, C. Combes, *Nanocrystalline Apatite Based Biomaterials: Synthesis, Processing and Characterization*, Nova Science Publishers Inc., New York, NY, USA, 2009.
[86] J. Gómez-Morales, M. Iafisco, J. M. Delgado-López, S. Sarda, C. Drouet, *Prog. Cryst. Growth Character. Mater.*, 2013, **59**, 1-46.
[87] C. Drouet, M. Aufray, S. Rollin-Martinet, N. Vandecandelaère, D. Grossin, F. Rossignol, E. Champion, A. Navrotsky, C. Rey, *Am. Mineral.*, 2018, **103**, 550-564.
[88] C. Calco, R. Gopal, *Am. Mineral.*, 1975, **60**, 120-133.
[89] H. L. Jang, K. Jin, J. Lee, K. Kim, S. H. Nahm, K. S. Hong, K. T. Nam, *ACS Nano*, 2014, **8**, 634-641.
[90] T. Debroise, E. Colombo, G. Belletti, J. Vekeman, Y. Su, R. Papoular, N. S. Hwang, D. Bazin, M. Daudon, P. Quaino, F. Tielens, *Cryst. Growth Des.*, 2020, **20**, 2553-2561.
[91] S. I. Stupp, G. W. Ciegler, *J. Biomed. Mater. Res.*, 1992, **26**, 169-183.
[92] B. Viswanath, N. Ravishankar, *Biomaterials*, 2008, **29**, 4855-4863.
[93] Y. Wang, S. Von Euw, F. M. Fernandes, S. Cassaignon, M. Selmane, G. Laurent, G. Pehau-Arnaudet, C. Coelho, L. Bonhomme-Coury, M.-M. Giraud-Guille, F. Babonneau, T. Azaïskofina, N. Nassif, *Nat. Mater.*, 2013, **12**, 1144-1153.
[94] C. Combes, C. Rey, *Acta Biomater.*, 2010, **6**, 3362-3378.
[95] N. Nassif, F. Martineau, O. Syzgantseva, F. Gobeaux, M. Willinger, T. Coradin, S. Cassaignon, T. Azaïs, M. M. Giraud-Guille, *Chem. Mater.*, 2010, **22**, 3653-3663.
[96] C. Rey, C. Combes, C. Drouet, S. Cazalbou, D. Grossin, F. Brouillet, S. Sarda, *Progr. Cryst. Growth Character. Mater.*, 2014, **60**, 63-73.
[97] D. P. Minh, N. D. Tran, A. Nzihou, P. Sharrock, *Mater. Res. Bull.*, 2014, **51**, 236-243.
[98] S. Shaddel, S. Ucar, J.-P. Andreassen, S. W. Østerhu, *J. Environ. Chem. Eng.*, 2019, **7**, article no. 102918.
[99] A. Capdevielle, E. Sorová, B. Biscans, F. Béline, M.-L. Daumer, *J. Hazard. Mater.*, 2013, **244–245**, 357-369.
[100] H. Li, Q.-Z. Yao, Y.-Y. Wang, Y.-L. Li, G.-T. Zhou, *Sci. Rep.*, 2015, **5**, article no. 7718.
[101] B. Suyamud, J. Ferrier, L. Csetenyi, D. Inthorn, G. M. Gadd, *Environ. Microb.*, 2020, **22**, 1588-1602.
[102] S. Sutiyono, L. Edahwati, D. S. Perwitasari, S. Muryanto, J. Jamari, A. P. Bayuseno, *MATEC Web Conf.*, 2016, **58**, article no. 01006.
[103] V. V. Vol'khin, D. A. Kazakov, G. V. Leont'eva, Y. V. Andreeva, E. A. Nosenko, M. Y. Siluyanova, *Russ. J. Appl. Chem.*, 2015, **88**, 1986-1996.
[104] H. Li, Q.-Z. Yao, S.-H. Yu, Y.-R. Huang, X.-D. Chen, S.-Q. Fu, G.-T. Zhou, *Am. Mineral.*, 2017, **102**, 381-390.
[105] B. Tansel, G. Lunn, O. Monje, *Chemosphere*, 2018, **194**, 504-514.
[106] M. A. P. Manzoor, M. Mujeeburahiman, S. R. Duwal, P. D. Rekha, *Biocatal. Agricult. Biotechnol.*, 2019, **17**, 566-570.
[107] D. Kim, C. Olympiou, C. P. McCoy, N. J. Irwin, J. D. Rimer, *Chemistry*, 2020, **26**, 3555-3563.
[108] A. N. Kofina, P. G. Koutsoukos, *Cryst. Growth Des.*, 2005, **5**, 489-496.
[109] H. Li, Q.-Z. Yao, Z.-M. Dong, T.-L. Zhao, G.-T. Zhou, S.-Q. Fu, *ACS Sustain. Chem. Eng.*, 2019, **7**, 2035-2043.
[110] R. Boistelle, F. Abbona, Y. Berland, M. Granvuillemin, M. Olmer, *Nephrologie*, 1984, **5**, 217-221.
[111] G. Sanders, A. Hesse, D. B. Leusmann, *Scan. Electron Microsc.*, 1986, **4**, 1713-1720.
[112] J. Prywer, A. Torzewska, T. Plocinski, *Urol. Res.*, 2012, **40**, 699-707.
[113] S. Rowles, *Bull. Soc. Chim. Fr.*, 1968, 1798-1802.
[114] H. L. Jang, H. K. Lee, K. Jin, H.-Y. Ahn, H.-E. Lee, K. T. Nam, *J. Mater. Chem. B*, 2015, **3**, 1342-1349.
[115] C. Qi, Y.-J. Zhu, F. Chen, J. Wu, *J. Mater. Chem. B*, 2015, **3**, 7775-7786.
[116] X. Guo, X. Liu, H. Gao, X. Shi, N. Zhao, Y. Wang, *J. Mater. Sci. Technol.*, 2017, **34**, 1054-1059.
[117] N. S. M. Pillai, K. Eswar, S. Amirthalingam, U. Mony, P. K. Varma, R. Jayakumar, *ACS Appl. Biomater.*, 2019, **2**, 865-873.
[118] C. Wang, K.-J. Jeong, H. J. Park, M. Lee, S.-C. Ryu, D. Y. Hwang, K. H. Namb, I. H. Han, J. Lee, *J. Colloid Interface Sci.*, 2020, **569**, 1-11.
[119] J. Prywer, A. Torzewska, *Cryst. Res. Technol.*, 2009, **45**, 1283-1289.

[120] M. Daudon, V. Frochot, *Clin. Chem. Lab. Med.*, 2015, **53**, S1479-S1487.
[121] R. R. Sadowski, J. Prywer, A. Torzewska, *Cryst. Res. Technol.*, 2014, **49**, 478-489.
[122] A. Sinha, A. Singh, S. Kumar, S. K. Khare, A. Ramanan, *Water Res.*, 2014, **54**, 33-43.
[123] J. Sun, L. Chen, X. Wang, S. Cao, W. Fu, W. Zheng, *Chemistry*, 2012, **42**, 445-448.
[124] L. CifuentesDelatte, M. Santos, *Eur. Urol.*, 1977, **3**, 96-99.
[125] L. CifuentesDelatte, *Composicion y estructura de los calculosrenales*, Ed. Salvat, Barcelona, 1984.
[126] D. B. Leusmann, *Pathog. Klin. Harnsteine*, 1982, **8**, 275-280.
[127] D. Bazin, G. André, R. Weil, G. Matzen, E. Véron, X. Carpentier, M. Daudon, *Urology*, 2012, **79**, 786-790.

Comptes Rendus
Chimie
2022, Vol. 25, Special Issue S1, p. 335-341
https://doi.org/10.5802/crchim.126

Microcrystalline pathologies: Clinical issues and nanochemistry

Chronic urine acidification by fludrocortisone to treat infectious kidney stones

Arnaud Lionet[*,a], **Camille Roger**[a], **Xavier Biardeau**[b], **Michel Daudon**[c,d] and **Emmanuel Letavernier**[c,d]

[a] Service de Néphrologie et Transplantation Rénale, Hôpital Huriez, 1 rue Polonovski, CHRU-Lille, Lille, France

[b] Service d'Urologie, d'Andrologie et de Transplantation Rénale, Hôpital Huriez, 1 rue Polonovski, CHRU-Lille, Lille, France

[c] Service des Explorations Fonctionnelles, Hôpital Tenon, AP-HP, 4, rue de la Chine, 75970 Paris Cedex 20, France

[d] UMRS 1155, Sorbonne Université, Hôpital Tenon, 75970 Paris Cedex 20, France

E-mails: arnaud.lionet@chu-lille.fr (A. Lionet), Camille.roger@chru-lille.fr (C. Roger), Xavier.biardeau@chru-lille.fr (X. Biardeau), daudonmichel24@gmail.com (M. Daudon), emmanuel.letavernier@aphp.fr (E. Letavernier)

Abstract. Chronic urinary tract infections by urease-producing bacteria may increase urine pH and promote thereby the formation of recurrent kidney stones made of highly carbonated calcium phosphate apatite and struvite, a magnesium ammonium phosphate. To date, there is no safe and effective treatment decreasing urine pH on a long term. We hypothesized that fludrocortisone, a mineralocorticoid, would decrease urine pH by increasing proton secretion in the kidney collecting tubule. We report three cases of patients with kidney stone suffering from chronic urinary infection by urease-producing germs, treated by fludrocortisone on a long term. Urine pH decreased sustainably over several months and tolerance was good.

Keywords. Kidney stone, Infection, Urine pH, Fludrocortisone, Crystallization.
Published online: 10 November 2021

1. Introduction

Infectious urolithiasis accounts for 10 to 15% of all urinary stones [1]. The development of infection-related urinary stones is promoted by alkaline urine. Actually, chronic urinary tract infection by urease-producing bacteria increases pHu. The bacterial urease hydrolyses urea to produce ammonia and carbamate, then carbamate rapidly hydrolysis to ammonia and carbonic acid. Urease activity increases thereby pHu, frequently above 7.0, promoting calcium phosphate supersaturation (apatite, pKa 6.8) and its crystallization in urine. Calcium phosphate stones promoted by urea-splitting bacteria frequently contain

* Corresponding author.

high amounts of carbonate due to increased bicarbonate concentration in urine [2]. Calcium phosphate phases are mainly carbonated apatite (CA) and amorphous carbonated calcium phosphate (ACCP). Magnesium ammonium phosphate (struvite) is also frequently identified in infectious stones. The presence of struvite even in small amounts in urinary stones is pathognomonic for the presence of urease-producing bacteria. The crystallization of struvite is promoted by both increase in pHu (pKa 7.2) and increase in ammonia production; the role of magnesium in its formation remains poorly understood [3, 4]. Finally, infectious stones may contain ammonium urate (AmUr), usually as a minor component, whose crystallization is promoted by alkaline pH (pKa 7.95) and high concentration of ammonia (and urate) [5,6].

Urine culture from patients with infectious stone may be negative or reveal the presence of other bacteria without urease activity, suggesting that low-grade urease-producing bacteria are present in the kidney stone vicinity but may not be always successfully identified [7–9]. Both gram-positive and gram-negative species can have urease activity. The most frequently incriminated bacteria with urease activity are *Proteus mirabilis*, *Staphylococcus*, *Pseudomonas*, *Providencia* and *Klebsiella*.

Because the supersaturation of struvite, AmUr and CA is increased by alkaline pH, acidification of urine can be helpful in the management of infectious stone [10]. Moreover, urine alkalinization may be promoted by a lack of proton supply in the distal part of the renal tubule (distal tubular acidosis), by chronic digestive loss of hydrochloric acid (vomiting or gastric aspiration) or by ion exchange (chloride and bicarbonate) in patients affected by urinary diversion with intestinal segments. The latter case is at risk for chronic colonization by urea-splitting germs.

Direct delivery of acid valences through ammonium (sulfate, nitrite or chloride) or oral L-methionine (metabolized to sulfate and hydrogen ions) has been tested to acidify urine of patients suffering from infectious urolithiasis [11]. However, this strategy induces gastrointestinal tract irritation and systemic hyperchloremic acidosis with headaches and dizziness.

Therefore, we suggest a new way to sustainably acidify urine by increasing tubular proton secretion in the collecting duct. For this purpose, we were inspired by the acute urine acidification tests described by Walsh *et al.* [12]. Indeed, this study demonstrated capacity of the distal part of the nephron to acidify urine after a single administration of 1200 μg fludrocortisone, a mineral corticoid. The acidification capacities of the kidney were considered as preserved if pHu decreased lower than 5.3 after a single dose. Fludrocortisone induces principal cell sodium reabsorption and alpha-intercalated cells H^+ secretion in the distal nephron [13]. However, this high dose of fludrocortisone is not acceptable for a daily use. We hypothesized that fludrocortisone on a long term and at a milder dose (100 μg BID) would reduce pHu and could thereby prevent infectious stone formation (Figure 1). We present herein the preliminary results obtained in three patients treated on a long term with fludrocortisone for urinary infectious stone.

2. Patients and methods

We report three cases of patients referred to our nephrology unit for urolithiasis. All patients were affected by infectious urolithiasis and had high pHu. None of them had conditions that would have contraindicated the use of fludrocortisone, i.e. hypersensitivity to fludrocortisone, cirrhosis, hypertension and heart failure, thyroid disease, myasthenia or ocular infection due to herpes simplex virus. After receiving information relative to potential side effects, they all gave informed consent for testing the mineralocorticoid treatment on a long term, to acidify their urine. Fludrocortisone (Flucortac®) was started at 50 μg BID, with monitoring of serum potassium level and pHu. If the pHu did not fall below 7, the dosage of fludrocortisone was increased to 100 μg BID with a new control of serum potassium level. Clinical tolerance was assessed in parallel.

3. Results

3.1. *Patient no. 1*

Patient 1 was a 28-year-old man with spinal muscular atrophy type 1. He was bedridden, diabetic, with gastrostomy feeding, indwelling urinary catheter and mechanical ventilation by tracheostomy. Enteral nutrition provided 1.397 kcal and hydration was 1.5 l/24 h. His body mass index (BMI) was 18. The first stone episode occurred when he was 7 years

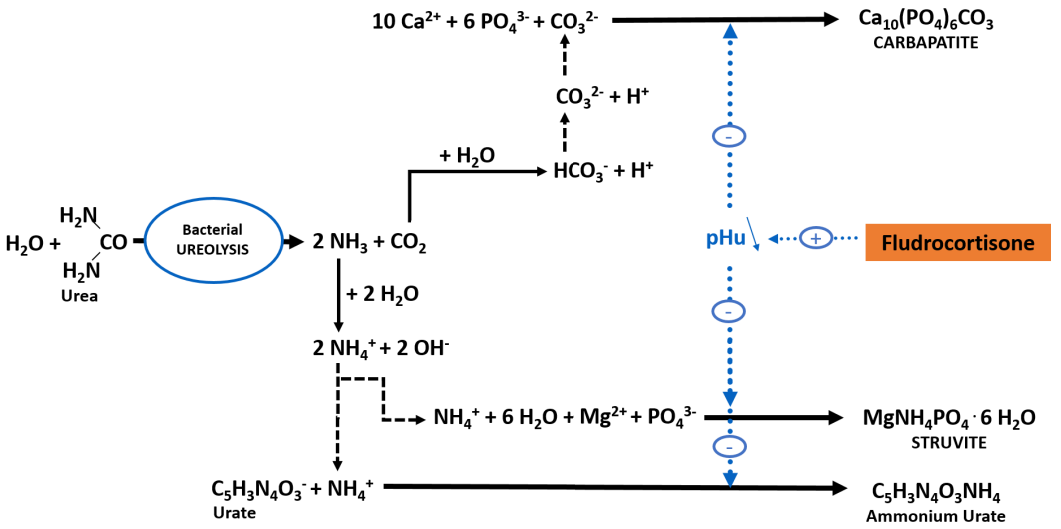

Figure 1. Concept of the use of fludrocortisone for slowing down the process of infectious urolithiasis. Blue dotted arrow: representation of the effect (positive or negative) of fludrocortisone on pHu and of pHu on the formation of carbapatite, struvite and ammonium urate; black arrow: chemical reaction; black dotted arrow: origin of the molecules (i.e. it is not the exact chemical reaction).

old. He experienced five extracorporeal shock-wave lithotripsies and was hospitalized several times for urinary tract infections and sepsis. At the age of 26, stone formation accelerated with the need for four ureteroscopy (URS) treatments, and two admissions in intensive care unit in 24 months. The spectro-morphometric analysis concluded in ammonium urate stones of subtype IIId, composed of 90% ammonium urate, 5% CA and 5% struvite. Biological assessment (Table 1) revealed a serum creatinine at 0.9 mg/l (7.9 µmol/l), a 24 h urine volume at 1.4 l containing urea 13 g (216 mmol)/24 h, uric acid 363 mg (2.15 mmol)/24 h, Na^+ 45 mmol/24 h, K^+ 38 mmol/24 h, Cl^- 41 mmol/24 h, Ca^{2+} 13 mg (0.32 mmol)/24 h and oxalate 15 mg (166 µmol)/24 h. Urine pH was 8.0. The cytobacteriological examinations of the urine (CBEU) revealed the presence of three different urease-producing bacteria: *Pseudomonas aeruginosa*, *Serratia marcescens* and *Proteus mirabilis*. Flucortac® treatment was started at 50 µg BID and increased to 100 µg BID. Urine pH decreased from 8 to 5 (month 1), 7 (month 2) and 6 (month 3, Figure 2). A CT-scan performed 3 months after initiation of fludrocortisone showed stable kidney stones and the presence of a bladder stone at the end of the ureteral catheter. The

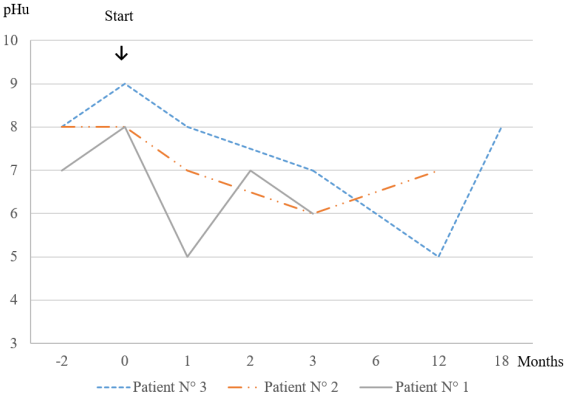

Figure 2. pHu before and after treatment by fludrocortisone.

stones were removed by flexible ureteroscopy. The stones were CA subtype IVa, consisting of 90% CA, 5% ammonium urate and 5% struvite. Under treatment, the patient presented mild lumbar oedema without hypertension. He experienced an episode of hypokalaemia rapidly corrected by potassium oral supplementation.

Table 1. Biological values before and after fludrocortisone

	Patient no. 1		Patient no. 2		Patient no. 3	
Delay after fludrocortisone (months)	0	3	0	4	0	8
Serum						
Creatinine mg/L (μmol/L)	0.9 (7.9)	0.9 (7.9)	4.1 (36.2)	4.2 (37.1)	5.2 (45.9)	8 (70.7)
Potassium (mEq/L)	3.9	3.5	5.7	3.7	4	4.8
Bicarbonate (mmol/L)	21	22	20	31	28	31
Urine						
24 h Volume (L)	1.4	2	2.2	2.4	1.7	1.5
BUN g/24 h (mmol)	13 (216)	10 (166)	10.3 (171)	10.6 (176)	15 (245)	16.4 (275)
Creatinine mg/24 h (μmol/24 h)	54 (477)	20 (176)	440 (3890)	380 (3360)	510 (4508)	626 (5533)
Calcium mg/L (mmol/L)	9 (0.22)	38 (0.94)	97 (2.42)	34 (0.84)	51 (1.27)	26 (0.64)
Calcium mg/24 h (mmol/24 h)	13 (0.32)	76 (1.89)	213 (5.31)	94 (2.34)	87 (2.17)	39 (0.97)
Phosphorus mg/L (mmol/L)	—	182 (5.8)	20 (0.64)	140 (4.51)	222 (7.16)	522 (16.8)
Phosphorus mg/24 h (mmol/24 h)	—	364 (11.74)	44 (1.4)	336 (10.8)	377 (12.16)	783 (25.25)
Uric acid mg/L (mmol/L)	250 (1.48)	—	125 (0.74)	140 (0.83)	272 (1.61)	324 (1.92)
Uric acid mg/24 h (mmol/24 h)	363 (2.15)	—	275 (1.63)	336 (1.99)	462 (2.74)	486 (2.89)
Oxalate mg/24 h (μmol/24 h)	15 (166)	—	17 (188)	22 (244)	<2 (22)	<2 (22)
Oxalate mg/L (μmol/L)	10.7 (188)		7.7 (85.5)	9.1 (101.6)	<2 (22)	<2 (22)
pHu	7	6	8	6	8	5
CBEU	*P. aeruginosa* *S. marcescens* *P. mirabilis*	—	*K. pneumoniae*	*E. coli* and *P. aeruginosa*	*E. coli*	*E. coli*

3.2. *Patient no. 2*

Patient 2 was a 40-year-old woman patient with spina bifida. A lumbosacral myelomeningocele-induced hydrocephalus was treated with a ventricular peritoneal shunt. She was affected by paraplegia, osteoporosis and neurogenic bladder symptoms. A trans-ileal ureterostomy (Bricker's diversion) was performed in 2013. After the Bricker's diversion, she had episodes of hyperkalaemia and a mild hyperchloremic acidosis (chloride 113 meq/l, CO_2 20 meq/l), attributed to ion exchanges between the urine and blood through the digestive mucosa. She received sodium polystyrene sulfonate to decrease serum potassium levels. Two large stones were incidentally identified in the right kidney in 2016, measuring 25 × 13 mm and 20 × 16 mm and with a low density on CT-scan (530 Hounsfield Units). The patient underwent two flexible ureteroscopies during the next two years, due to the recurrence of kidney stones in the right kidney. Unfortunately, none of the stones were analysed. After an increase in drinking water, the urine tests showed: pHu 8, diuresis 2.2 l/24 h, urea 10.3 g (171 mmol)/24 h, Ca^2 + 213 mg (5.31 mmol)/24 h, phosphorus 44 mg (0.64 mmol)/24 h, uric acid 275 mg (1.63 mmol)/24 h and oxalate 17 mg (188 μmol)/24 h. CBEU identified two urea-splitting bacteria, *Klebsiella pneumoniae* and *Proteus mirabilis*. Flucortac® was started at 50 μg BID then increased to 100 μg BID. Urine pH decreased from 8 to 7 (month 1), 6 (month 3), 7 (month 6) and 7 (month 12). Concomitantly, serum potassium levels decreased and sodium polystyrene sulfonate was discontinued. The patient developed slight oedema of the lower limbs without arterial hypertension.

3.3. *Patient no. 3*

Patient 3 was a 26-year-old woman with spina bifida. Myelomeningocele was also responsible for hydrocephalus, paraplegia and neurological bladder. A trans-ileal ureterostomy was performed

in 2017. Two renal stones appeared one year after the surgery. They were removed with flexible ureteroscopy but not analysed. The disease recurred, with three new kidney stones over two years. Urine analysis found: diuresis 1.7 l/24 h, pHu 8 and 9, Na^+ 85 mEq/24 h, uric acid 462 mg (2.74 mmol)/24 h, Ca^{2+} 87 mg (2.17 mmol)/24 h, phosphorus 377 mg (12.16 mmol)/24 h, urea 15 g (245 mmol)/24 h, oxalate <2 mg/24 h (<22 μmol). CBEU was positive for *Escherichia coli* but no urease-producing bacteria could be evidenced. Flucortac® was started at 50 μg BID. Under treatment, the urine pH dropped: 9 (month 0), 8 (month 1), 7 (month 3), 6 (month 5). At 1 year the urine pH was 5. At that time, the patient was under antibiotic treatment for an infection of the vertebral osteosynthesis pin. The patient described spontaneous expulsion of stones through the ileal stoma. CT-scan at 12 months showed a single 6 mm stone in the left kidney. Eighteen months after initiation of the treatment the urine pH was back to 8. The patient did not develop oedemas, hypertension or hypokalaemia.

4. Discussion

We report the use of mineralocorticoids in three patients in order to acidify their urine. All three presented typical characteristics of patients with infectious stone: reduced mobility, presence of bacteria with urease activity responsible for increased pHu, multiple urological interventions and in two out of three cases a urinary intestinal diversion. Patients' pHu were between 7 and 9 before treatment and decreased in all cases with fludrocortisone. We thus observed efficient urine acidification for these patients while the dose of mineralocorticoid used was six times less than proposed by Walsh *et al.* for the acute functional acidification test [12]. Some preliminary studies allowed us to hope for these results. Aperia *et al.* studied the urine acidifying power of mineralosteroids in 1974 [14]. The test consisted of an ammonium chloride load and a bicarbonate infusion, before and after 4 to 6 days of mineralocorticoid treatment in five young girls. The children received 400 μg/1.73 m^2 body surface/day of fluorohydrocortisone with a supplement of potassium. In all patients the urine acidification occurred during fluorohydrocortisone administration.

There is probably an attenuation of the urine acidification effect over time, as shown by the pHu of patients 2 and 3, which was above 7 after one year of treatment. This loss of efficacy over time could be due to the adaptation of bacteria with the induction of urease enzyme activity and/or to the loss of urine acidification capacity by the distal nephron. Even if urine acidification might not persist through time, the use of fludrocortisone may be of help to slow down infectious urolithiasis formation. Although this benefit cannot be stated with certainty in our patients, patient no. 1 modified his urolithiasis profile. Indeed, kidney stone components changed from 90% AmUr (pKa 7.95) to 95% CA (pKa 6.8). This change in crystalline nature could reflect the decrease in pHu. For patients no. 2 and no. 3 we can only note the absence of new stone formation without being able to affirm that this is due to fludrocortisone.

pHu is directly influenced by the presence of bacteria. But variations in pHu can also influence the bacteria behaviour in the urinary tract. Urine acidification could reduce bacterial growth and decrease its cytoadherence [15,16]. It could also have a synergistic effect with antibiotics since the activity of many antibiotics becomes optimal with acid pH [17,18]. However, antibacterial effects of acid pH have been demonstrated only *in vitro*. In a polymicrobial environment it cannot be excluded that acidification leads to the emergence of a subgroup of acidophilic bacteria. It remains to be determined whether fludrocortisone allows a significant decrease in urine pH to obtain an antibacterial effect.

Treatment with fludrocortisone needs to be done with caution, as patients may be affected by short-term and long-term side effects, particularly electrolyte imbalance. There is a risk of sodium retention contraindicating its use in patients affected by uncontrolled hypertension, cirrhosis and heart failure. Fludrocortisone-induced fluid retention resulted in oedema in two of our patients. Oedema was limited and the use of diuretics was not necessary. If the situation had required it, we would have had the choice of either discontinuing fludrocortisone administration or adding a diuretic. In this case, the use of a loop diuretic would increase the flow of sodium to the distal nephron and, in theory, maintain (or even increase) the acidifying power of the urine by fludrocortisone. The second early adverse effect observed was hypokalaemia in patient no. 1.

Metabolic alkalosis and hypokalaemia are due to the urinary excretion of H^+ and potassium, respectively, under the action of fludrocortisone. Hypokalaemia is easily detected by blood tests and can be corrected by oral potassium supplementation. These biological modifications can sometimes be beneficial for the patients. This was the case for patient no. 2 who had a trans-ileal urine diversion. In this type of surgery, the contact of the urine with the digestive mucosa is responsible for chloride/bicarbonate ion exchanges which lead to hyperchloremic metabolic acidosis and hyperkalaemia. In this case, fludrocortisone can help to correct the metabolic acidosis and thus control hyperkalaemia. Long-term use of fludrocortisone could expose patients to hepatic glycogen accumulation that could adversely affect nitrogen balance if protein intake is inadequate [19,20]. Fludrocortisone may also increase bone turnover inducing osteoporosis with increased urinary calcium excretion [19,21]. However, urine calcium excretion was relatively low in the three patients. The main risk with a long-term use of fludrocortisone remains adrenal insufficiency. It results from a progressive inhibition of corticotrophin secretion by fludrocortisone. This inhibition occurs at prolonged and high doses (400 μg/day) of fludrocortisone [22]. Moreover, patients with infectious urinary lithiasis present high risk for urinary tract sepsis with acute exacerbation of underlying adrenal insufficiency. Therefore, fludrocortisone dose should be less than 400 μg/day and/or prescribed for a limited period of time. Patients and caregivers should be informed and educated about the risk of adrenal insufficiency in the event of sepsis on fludrocortisone. In this way, bacterial infections can be treated quickly and adrenal insufficiency detected early. Risk of malnutrition should also be prevented, and osteoporosis should be detected and treated in case of treatment duration over one year.

Infectious stones are a serious cause of morbidity and mortality for which treatment is still unsatisfactory. These fast-growing stones may reappear quickly, within 4 to 6 weeks following surgery [23,24]. Complete removal of stones by surgery is essential: patients with struvite stone fragments three months after a surgery have a higher rate of stone progression (+78%) than stone-free patients [25]. Antibiotics have a pertinent role pre-operatively, post-operatively and potentially in the presence of residual stone fragments. However, evidence for specific antibiotic regimens is lacking and guidelines are not prescriptive regarding the nature of the molecules to be used, their dose and duration of treatment [26–29]. Other treatment strategies have failed. The urease inhibitor (acetohydroxamic acid) has only shown a modest benefit with many side effects (22 to 62%) and is no longer used [30–32]. Citrate forms protective complexes with Ca^{2+} and Mg^{2+}, limiting in theory stone formation, but is lost in infectious conditions due to the metabolism of citrate by bacteria [18]. Thus, after supporting surgery with antibiotics, secondary prevention of infectious stones is often disappointing and limited to increased water intake and correction of potential nutritional risk factors. New therapeutics are therefore required and we think that the use of fludrocortisone in order to acidify urine deserves further investigation. Its use in a selected population seems to be safe but the modality of use must be specified and its effectiveness monitored. Fludrocortisone could be particularly useful for patients with digestive urine diversion to prevent or treat hyperchloremic acidosis and hyperkalaemia. This treatment could also be used as secondary prevention after surgery of infectious stones.

Our study suffers from limitations. The most important is the lack of a control group. In the absence of a control group, we cannot state that the changes in pHu that we observed in our patients are totally attributable to fludrocortisone. Although the pHu decreased in the three cases, the limited number of patients did not allow to draw any definitive conclusion and we could not perform relevant statistical analyses. Moreover, pHu may vary during the day. These variations depend on the pharmacokinetics of Flucortac® but also on food intake. Further studies may focus on pHu variations over the diurnal cycle under treatment. Finally, as evidenced by patient no. 3, urine acidification can be influenced by the use of antibiotics if they are effective on the urease-producing bacteria present in the urinary tract. Nevertheless, pHu dropped early and sustainably in patient no. 3, before the onset of antibiotics.

5. Conclusion

Fludrocortisone appears to be a potential therapeutic tool in the treatment of infectious urolithiasis. It

may actually decrease pHu by increasing proton secretion by the distal nephron. The expected benefit of this treatment is to increase the solubility of struvite, AmUr and CA with also potential antibacterial effects. Moreover, fludrocortisone use could decrease the risk of hyperchloremic acidosis induced by digestive urine diversions. We reported three cases with decreased pHu after fludrocortisone use and good tolerance. Further studies are needed to determine the best strategy for the use of this therapy (patient typology, dosage, presence of concomitant antibiotics use, duration) and to confirm clinical benefits for the patients.

References

[1] M. Daudon, H. Bouzidi, D. Bazin, *Urol. Res.*, 2010, **38**, 459-467.

[2] X. Carpentier, M. Daudon, O. Traxer, P. Jungers, A. Mazouyes, G. Matzen *et al.*, *Urology*, 2009, **73**, 968-975.

[3] R. Flannigan, W. H. Choy, B. Chew, D. Lange, *Nat. Rev. Urol.*, 2014, **11**, 333-341.

[4] D. Bazin, R. J. Papoular, E. Elkaim, R. Weil, D. Thiaudière, C. Pisapia *et al.*, *C. R. Chim.*, 2022, **25**, no. S1, 343-354.

[5] J. S. Elliot, R. F. Sharp, L. Lewis, *J. Urol.*, 1959, **81**, 366-368.

[6] J. S. Elliot, W. L. Quaide, R. F. Sharp, L. Lewis, *J. Urol.*, 1958, **80**, 269-271.

[7] P. Mariappan, G. Smith, S. A. Moussa, D. A. Tolley, *BJU Int.*, 2006, **98**, 1075-1079.

[8] P. Mariappan, G. Smith, S. V. Bariol, S. A. Moussa, D. A. Tolley, *J. Urol.*, 2005, **173**, 1610-1614.

[9] H. Shafi, Z. Shahandeh, B. Heidari, F. Sedigiani, A. A. Ramaji, Y. R. Y. Pasha *et al.*, *Saudi J. Kidney Dis. Transpl.*, 2013, **24**, 418-423.

[10] D. Heimbach, D. Jacobs, S. C. Müller, A. Hesse, *Urol. Int.*, 2002, **69**, 212-218.

[11] M. Abou Chakra, A. E. Dellis, A. G. Papatsoris, M. Moussa, *Expert Opin. Pharmacother.*, 2020, **21**, 85-96.

[12] S. B. Walsh, D. G. Shirley, O. M. Wrong, R. J. Unwin, *Kidney Int.*, 2007, **71**, 1310-1316.

[13] C. A. Wagner, *Nephron Physiol.*, 2014, **128**, 26-34.

[14] A. Aperia, U. Berg, O. Broberger, *Acta Paediatr. Scand.*, 1974, **63**, 209-219.

[15] D. Bach, *Fortschr. Med.*, 1985, **103**, 421-424.

[16] R. Fünfstück, E. Straube, O. Schildbach, U. Tietz, *Med. Klin. Munich Ger. 1983*, 1997, **92**, 574-581.

[17] N. Frimodt-Møller, *Int. J. Antimicrob. Agents*, 2002, **19**, 546-553.

[18] A. Hesse, D. Heimbach, *World J. Urol.*, 1999, **17**, 308-315.

[19] M. Rahman, F. Anjum, in *StatPearls*, StatPearls Publishing, Treasure Island (FL), 2021.

[20] T. Kuo, A. McQueen, T.-C. Chen, J.-C. Wang, *Adv. Exp. Med. Biol.*, 2015, **872**, 99-126.

[21] J. M. Brown, A. Vaidya, *Curr. Opin. Endocrinol. Diabetes Obes.*, 2014, **21**, 193-201.

[22] Yumpu.com, "Traitements-par-la-fludrocortisone-cnhim. yumpu.com.", 2003, [cited 2021 Apr 23]. Available from https://www.yumpu.com/fr/document/view/31862253/traitements-par-la-fludrocortisone-cnhim.

[23] K.-H. Bichler, E. Eipper, K. Naber, V. Braun, R. Zimmermann, S. Lahme, *Int. J. Antimicrob. Agents*, 2002, **19**, 488-498.

[24] K. Evans, R. A. Costabile, *J. Urol.*, 2005, **173**, 858-861.

[25] E. M. Beck, R. A. Riehle, *J. Urol.*, 1991, **145**, 6-9.

[26] A. F. Bierkens, A. J. Hendrikx, K. E. Ezz el Din, J. J. de la Rosette, A. Horrevorts, W. Doesburg *et al.*, *Eur. Urol.*, 1997, **31**, 30-35.

[27] M. Dion, G. Ankawi, B. Chew, R. Paterson, N. Sultan, P. Hoddinott *et al.*, *Can. Urol. Assoc. J.*, 2016, **10**, E347-E358.

[28] G. M. Preminger, D. G. Assimos, J. E. Lingeman, S. Y. Nakada, M. S. Pearle, J. S. Wolf *et al.*, *J. Urol.*, 2005, **173**, 1991-2000.

[29] H. G. Tiselius, D. Ackermann, P. Alken, C. Buck, P. Conort, M. Gallucci *et al.*, *Eur. Urol.*, 2001, **40**, 362-371.

[30] D. P. Griffith, M. J. Gleeson, H. Lee, R. Longuet, E. Deman, N. Earle, *Eur. Urol.*, 1991, **20**, 243-247.

[31] D. P. Griffith, F. Khonsari, J. H. Skurnick, K. E. James, *J. Urol.*, 1988, **140**, 318-324.

[32] J. J. Williams, J. S. Rodman, C. M. Peterson, *N. Engl. J. Med.*, 1984, **311**, 760-764.

Comptes Rendus
Chimie
2022, Vol. 25, Special Issue S1, p. 343-354
https://doi.org/10.5802/crchim.80

Microcrystalline pathologies: Clinical issues and nanochemistry

Whitlockite structures in kidney stones indicate infectious origin: a scanning electron microscopy and Synchrotron Radiation investigation

Dominique Bazin [*,a], **Robert J. Papoular** [b], **Erik Elkaim** [c], **Raphael Weil** [d], **Dominique Thiaudière** [c], **Céline Pisapia** [e], **Benedicte Ménez** [e], **Nathaniel S. Hwang** [f], **Frederik Tielens** [g], **Marine Livrozet** [h,i], **Elise Bouderlique** [h,i], **Jean-Philippe Haymann** [h,i], **Emmanuel Letavernier** [h,i], **Louis Hennet** [j], **Vincent Frochot** [h,i] **and Michel Daudon** [h,i]

[a] Université Paris-Saclay, CNRS, Institut de Chimie Physique, 310 rue Michel Magat, 91400 Orsay, France

[b] Saclay Institute for Matter and Radiation (IRAMIS), Laboratoire Léon Brillouin, CEA-Saclay, 91191 Gif sur Yvette Cedex, France

[c] Synchrotron SOLEIL, L'Orme des Merisiers, Saint-Aubin - BP 48, 91192 Gif-sur-Yvette Cedex, France

[d] Université Paris-Saclay, CNRS, Laboratoire de Physique des Solides, Université Paris Sud, 91400 Orsay, France

[e] Université de Paris, Institut de physique du globe de Paris, CNRS - 1, rue Jussieu - 75238 Paris Cedex 05, France

[f] School of Chemical and Biological Engineering, NBio Institute, Institute of Chemical Processes, Seoul National University, Seoul, 151-744, Republic of Korea

[g] General Chemistry (ALGC) - Materials Modelling group, Vrije Universiteit Brussel (Free University Brussels-VUB), Pleinlaan 2, 1050 Brussel, Belgium

[h] INSERM, UMRS 1155, Sorbonne Université, Hôpital Tenon, 75020 Paris, France

[i] Service d'explorations fonctionnelles, Hôpital Tenon, AP-HP, 4, rue de la Chine, 75020 Paris Cedex 20, France

[j] ICMN, UMR7374, CNRS, 45071 Orléans Cedex 2, France

E-mails: dominique.bazin@universite-paris-saclay.fr (D. Bazin), robert.papoular@cea.fr (R. J. Papoular), erik.elkaim@synchrotron-soleil.fr (E. Elkaim), raphael.weil@u-psud.fr (R. Weil), dominique.thiaudiere@synchrotron-soleil.fr (D. Thiaudière), pisapia@ipgp.fr (C. Pisapia), menez@ipgp.fr (B. Ménez), nshwang@snu.ac.kr (N. S. Hwang), frederik.tielens@vub.be (F. Tielens), Marine.livrozet@aphp.fr (M. Livrozet), Eliseboud@aol.com (E. Bouderlique), jean-Philippe.haymann@aphp.fr (J.-P. Haymann), emmanuel.letavernier@aphp.fr (E. Letavernier), louis.hennet@cnrs-orleans.fr (L. Hennet), vincent.frochot@aphp.fr (V. Frochot), michel.daudon@aphp.fr (M. Daudon)

[*] Corresponding author.

Abstract. In this contribution dedicated to kidney stones containing Whitlockite (Wk), we addressed three questions, namely, the presence of iron in Wk, the relationship between bacterial imprints and the presence of Wk, and finally the relationship between the crystal size of Wk-bearing stones and infection. The complete dataset indicates that iron is not present in our Wk stoichiometry. We also note the presence of bacterial imprints for kidney stones with a high, but sometimes a low content, of Wk. Finally, we propose FE-SEM as a diagnostic tool for stone patients who have a negative urine culture associated with kidney stones containing less than 20% by weight Wk, a low level of carbonate in apatite, and no struvite. Such a diagnostic tool would represent a significant benefit to the clinician.

Keywords. Kidney stone, Infection, Whitlockite, Diagnosis, X-ray scattering, SEM.
Published online: 20 May 2021

1. Introduction

Numerous studies have underlined a significant global increase in prevalence and incidence of nephrolithiasis [1–4]. Part of this increase is related to the relationship between urolithiasis and major public health problems such as metabolic syndrome [5,6]. Urinary tract infection (UTI) leading to the formation of kidney stones can also be considered a relevant factor [7,8]. In view of the increase in infection-related stones over the past two decades, UTI must always be considered a significant possible cause of urolithogenesis [9–13].

Several kidney stone chemical phases are related to kidney infection [14–18]. Among them we can cite calcium phosphate apatite with a high level of carbonate [19–21], ammonium urate [22], struvite [23–26] and whitlockite (Wk) [27,28]. High carbonate calcium phosphate apatite and struvite are related to urease-producing bacteria, while Wk may be related to infection by non-urease-producing bacteria. There is another major difference between struvite and Wk. While the presence of struvite (independently of its weight fraction) is directly related to infection, the weight fraction of Wk in kidney stones, estimated by Fourier transform infrared spectroscopy (FTIR), was related to infection with a high degree (80%) of statistical significance if greater than 20% [15].

For further insight into the relationship between infection and kidney stones containing Wk without struvite, we have used physicochemical characterization techniques [29–32] to obtain a precise multiscale description of such concretions [33–37]. First, by analogy with geological studies [38], we assessed the presence of iron in Wk by X-ray fluorescence (XRF) [39–41] using synchrotron radiation (SR) as a probe [42–46]. Iron in Wk may modify the position of IR absorption bands and thus may confuse the analysis of IR spectra. Then, we address the size of Wk nanocrystals for an initial set of infection-related kidney stones containing more than 20% Wk in weight, using SR-wide angle X-ray scattering (WAXS) [47–52]. We use the definition of the terms "nanocrystals" and "crystallites" of Van Meerssche and Feneau-Dupont, i.e. crystallites (typically measuring tens of micrometres) composed of accretions of nanocrystals (typically measuring hundreds of nanometres), to describe the structural hierarchy of pathological calcifications [53].

For the first set of kidney stones, field emission scanning electron microscopy (FE-SEM) observations allowed precise crystallite definition in order to ultimately pinpoint bacterial imprints. For the second set, containing less than 20% by weight Wk, FE-SEM was also performed for bacterial imprints to establish a possible infection process. Such a multiscale approach taking into account chemistry and morphology has already been used to develop new diagnostic tools, or to deduce the very first steps of calcification pathogenesis [54–59].

2. Materials and methods

2.1. *Samples*

Kidney stones (Tenon Hospital) from 31 patients (12 males, 19 females) were investigated (see Tables 1 and 2).

2.2. *Investigational tools*

Initial analysis was carried out at the hospital using a stereomicroscope for morphological typing and a FTIR spectrometer to accurately determine stone composition [60–63]. FT-IR experiments were performed in transmission mode using a FTIR spectrometer Vector 22 (Bruker Optics, Marne-la-Vallée,

Table 1. Clinical data for the first set of kidney stones containing more than 20% in weight of Wk and related to infection

	Sex, age (year)	Location	Chemical composition estimated through FTIR	Carbonate level	Crystal size estimated through WAXS
T10508	F, 59	Staghorn_Kidney	38% CA, 28% Wk, 20% glafenic acid, 10% Prot, 4% C1	/	
T12487	F, 54	Ureter	50% CA, 23% Wk, 20% C1, 7% Prot	5%	/
T12900	M, 55	Kidney	35% CA, 25% Wk, 25% ACCP,10% C1,5% Prot		
T17405	M, 65	Kidney	50% CA, 25% Wk, 20% ACCP, 5% Prot	19%	/
T17615	M, 36	Bladder	40% CA, 28% Wk, 26% ACCP, 4% Prot, 2% C2		
T29735	F, 59	Urinary tract	30% CA, 25% Wk, 20% ACCP, 15% Prot, 5% TGL, 5% C2	19%	/
T32616	F, 22	Kidney	30% Wk, 21% C1, 20% CA, 15% C2, 7% Prot	7%	290 nm ± 10 nm
T38693	M, 52	Staghorn	35% Wk, 24% C1, 19% CA, 16% C2, 8% Prot	7%	/
T38952	M, 3	Urethra	40% Wk, 13% C1, 20% CA, 15% ACCP, 5% C2, 7% Prot	5%	90 nm ± 10 nm
T43068	F, 54	Kidney	66% Wk, 19% CA, 9% Prot, 6% C1	/	30 nm ± 10 nm
T43736	M, 4	Kidney	67% Wk, 3% C1, 20% CA, 10% Prot	6%	250 nm ± 10 nm
T44112	M, 87	Expelled	42% Wk, 20% C1, 20% CA, 11% C2, 7% Prot	7%	/
T45449	F, 39	Ureter	75% Wk, 12% Prot, 8% CA, 3% C1, 2% TGL	/	330 nm ± 10 nm
T51263	M, 70	Urinary tract	75% Wk, 12% Prot, 10% CA, 3% C1	/	330 nm ± 10 nm
T52975	F, 89	Urinary tract	60% Wk, 25% CA, 10% Prot, 5% TGL	10%	130 nm ± 10 nm
T55785	F, 54	Kidney	50% Wk, 7% C1, 33% CA, 10% Prot,	5%	190 nm ± 10 nm
T58866	F, 77	Tubular	52% Wk, 25% CA, 15% ACCP, 8% Prot,	25%	/
T71739	F, 69	Kidney	45% Wk, 25% CA, 22% ATZ 8% Prot,	/	/
T74647	F, 72	Ureter	75% Wk, 20% CA, 5% Prot	8%	90 nm ± 10 nm
T74808	M, 34	Prostate urethra	26% Wk, 21% C2, 17% Br, 14% CA, 10% OCP, 7% Prot, 3% C1, 2% TGL	6%	120 nm ± 10 nm

Wk = whitlockite; Br = brushite; CA = carbonated calcium apatite; C1 = whewellite; C2 = weddellite; ACCP = amorphous carbonated calcium phosphate; Prot = protein; TGL = triglycerides; ATZ = atazanavir; OCP = octacalcium phosphate.

France) covering the mid-infrared range from 2.5 to 25 μm.

A Zeiss SUPRA55-VP scanning electron microscope with an energy-dispersive X-ray (EDX) spectrometer was used for direct microstructure observation. Images were obtained without any conductive coating on the sample. This field emission gun microscope can operate at 0.5–30 kV accelerating voltage. High resolution observations were obtained around 1 kV using two secondary electron detectors: an in-lens and an Everhart–Thornley detector [64]. Note that such observations allow the clinician to determine the morphology of crystallites which is a major parameter in nephrology [65–68].

One set of X-ray fluorescence experiments as well as three sets of X-ray scattering measurements were conducted at the synchrotron facility SOLEIL (Saint-Aubin, France). The X-ray fluorescence experiments were carried out at the Diffabs beamline (e.g. Figure 1). The main optical system includes a fixed-exit double crystal monochromator composed of two independent Si(111) crystals and located between two long mirrors (50 nm Rh-coated Si) [25].

The X-ray scattering experiments were performed at the Cristal beamline during two consecutive SOLEIL synchrotron sessions, using first a 18.446 keV ($\lambda = 0.67212$ Å) and then a 17.017 keV ($\lambda = 0.72857$ Å) monochromatic beam. Note that the monochromator was calibrated using a standard LaB_6 powder (NIST SRM 660b). The samples, introduced in kapton capillaries (ø = 0.7 mm), were mounted on a spinner rotating at 5 Hz to improve particle orientational averaging. Data were collected in Debye–Scherrer mode using a 21 Si(111) crystal analyser. With this setup and for each sample, two high angular resolution diagrams recorded in about one

Table 2. Clinical data related to the second set of struvite-free kidney stones containing less than or equal to 20% in weight of Wk and a low carbonate level for the apatite

	Sex, age (year)	Location	Chemical composition estimated through FTIR	Apatite carbonate level
T3347	M, 86	Bladder	70% CA, 15% Wk, 10% C2, 5% C1	9%
T4216	F, 31	Ureter	60% C2, 20% CA, 12% Wk, 8% Prot	/
T9261	M	Bladder	69% CA, 18% Wk, 8% C2, 3% C1, 2% Prot	8%
T9491	F, 43	Ureter	55% CA, 18% C1, 15% Wk, 8% Prot	3%
T10410	M, 65	Kidney	61% CA, 16% Wk, 15% C1, 8% Prot	6%
T11564	F, 40	Urinary tract	70% CA, 15% Wk, 7% C2, 5% OCP, 3% C1	7%
T11866	F, 58	Ureter	35% CA, 33% C1, 17% Wk, 15% C2	6%
T18382	F, 34	Ureter	52% CA, 30% C1, 14% Wk, 4% Prot	4%
T22610	F, 68	Kidney	45% CA, 20% Wk, 17% C1, 10% Prot, 8% ACCP	/
T33101	F, 50	Kidney	45% CA, 30% C1, 18% Wk, 7% Prot	10%

Wk = whitlockite; Br = brushite; CA = carbonated calcium apatite; C1 = whewellite; C2 = weddellite; ACCP = amorphous carbonated calcium phosphate; Prot = protein; TGL = triglycerides; ATZ = atazanavir; OCP = octacalcium phosphate.

hour were summed since sample degradation under the X-ray beam was not significant (Figure 2). Details regarding the experimental set up can be found in reference [69]. To allow for their subsequent superimposition in the same figures, all the collected X-ray diffractograms were first preprocessed using the freely available Graphical User Interface WINPLOTR software [70]. The mean size of the coherently diffracting crystals was calculated using the GSAS software [71].

3. Results and comments

As emphasized by Borghi *et al.* [72], the relationship between nephrolithiasis and urinary tract infections is complex and difficult to analyse both from a pathophysiological and clinical point of view. This has prompted several investigations to understand the relationship between infection and urinary stones [73,74], most of them focussing on struvite [75–81]. Here we attempt to broaden the scope of studies of this pathogenesis by describing in detail the physicochemical characteristics of stones containing Wk without struvite. At this point, it is worth bearing in mind that Wk has been reported in different parts of the body including lungs [82], breast [83], gallstone [84], prostate [85,86], aorta [87], bone [88], cartilage [89] and salivary glands [90], and to note that emerging evidence indicates that bacteria are present in and contribute to other calcifications such as vascular calcification [91].

Wk has also been identified as a kidney stone component [92–94]. While several publications concentrate on kidney stones containing struvite, little is known regarding the relationship between infection and kidney stones containing Wk. Interestingly, hyperthermophilic bacteria (70–110 °C) have been shown to be able to convert an amorphous calcium phosphate phase into fully crystalline Wk mineral, and spherulitic clusters that we interpret to be hydroxyapatite-like nanocrystals [95].

One of the various geological studies of Wk [96–98] underlines the presence of iron in the crystallographic structure [38]. To assess the presence of this element in Wk of biological origin, we began our investigation with SR-XRF experiments. Figure 1 shows X-ray fluorescence spectra of different kidney stones. The presence of Ca as well as Zn has been already discussed [44,45,99–102]. Note that although the Zn signals are more prominent than those of Ca, it doesn't indicate higher Zn content. Various correction procedures have to account for the self-absorbing matrix and the fact that measurements have been performed in air, the nature of the matrix, absorption by air, incident beam energy, and the ionization and X-ray emission cross-sections associated

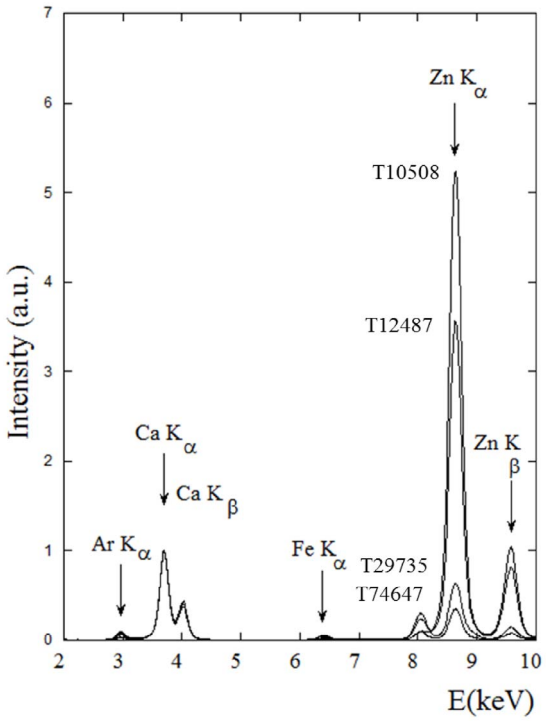

Figure 1. Normalized X-ray fluorescence spectra (the contribution of Ca is set to 1) collected for different kidney stones (T10508, T12487, T29735, T74647) containing Wk. The contributions of Ca (K_α = 3.691 keV, K_β = 4.012 keV), Zn (K_α = 8.638 keV, K_β = 9.572 keV) are clearly visible. Note the absence of a significant contribution from possible iron.

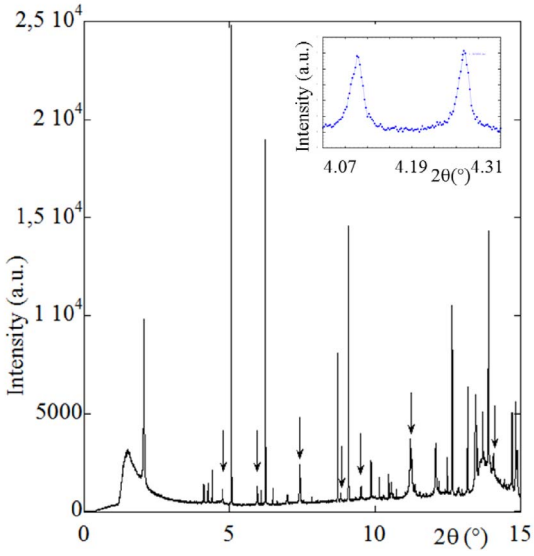

Figure 2. Typical high resolution X-ray powder diffractogram measured on the Cristal beamline for sample T74808 (λ = 0.67212 Å). The whitlockite diffraction peaks are marked with an arrow. Note the prominent 010 reflection of the octacalcium phosphate (OCP) crystalline phase, which occurs at 2θ = 2.051° and two other Bragg reflections [100,110] pertaining to OCP for 2θ = 4.117° and 4.261°, respectively (see inset). Note that the associated OCP phase has only been detected by FTIR spectroscopy through detailed analysis based on spectral derivatives. OCP indicates possible hypercalciuria without any link with infection. Accordingly, we will not discuss the presence of this compound further.

with each element [103,104]. In our case, the experiment was optimized for the X-ray fluorescence of Zn (K_α = 8.638 keV, K_β = 9.572 keV).

As the majority of the fluorescence events arise from photons with energy just above the absorption edge, the SR-XRF sensitivity is optimized for elements with X-ray fluorescence lines just below the monochromatic excitation energy, which in this case is Zn. In addition, X-ray production cross-sections are a function of Z^4 for SR-XRF, where Z is the atomic number of the target element. Finally, characteristic Zn X-ray emissions occur at higher energy than those of Ca (K_α = 3.691 keV, K_β = 4.012 keV), which is thus more susceptible to absorption and significantly affected by air between the sample and the detector.

The intensity of Zn X-ray fluorescence seems to be related to the carbonated calcium apatite (CA) content. High intensity values correspond to samples with a high CA content (38% CA for 10508, 50% CA for T12487) and weak ones to lower (30% CA for 29735, 20% CA for T74647). Note the weak signal for Zn X-ray fluorescence for sample T74647 which contains 75% by weight Wk. In all these measurements the absence of a significant contribution from iron is striking, implying the stoichiometric formula $Ca_9Mg(HPO_4)(PO_4)_6$ for kidney stones containing Wk.

Iron is an element of considerable biological im-

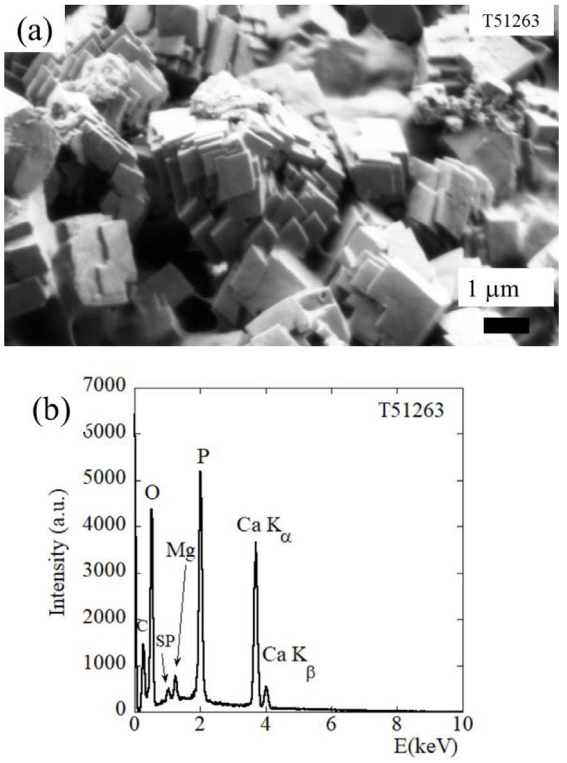

Figure 3. Sample T51263 (75% Wk, 12% Prot, 10% CA, 3% C1) (a) characteristic pseudocubic morphology of Wk as seen by FE-SEM and corresponding EDX spectrum (b) in which the contributions of C (K_α = 0.277 keV), O (K_α = 0.525 keV), Mg (K_α = 1.253 keV), P (K_α = 2.014 keV), and Ca (K_α = 3.691 keV, K_β = 4.012 keV) are clear. Note the presence of a sum peak (SP) due to the coincidence of two O K_α photons.

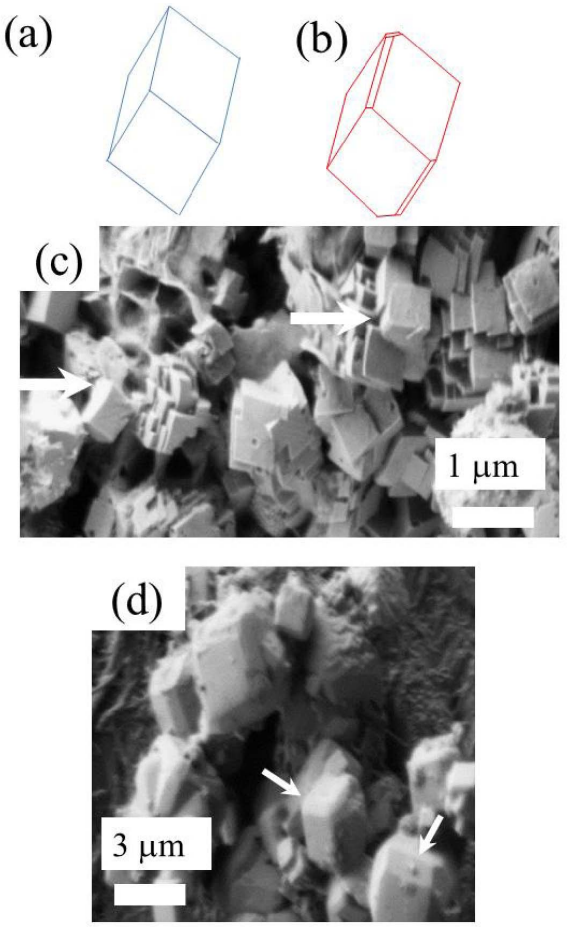

Figure 4. (a, b) The morphologies for Wk crystals. Reprinted from [96], with the permission of Mineralogical Society of America. (c) SEM observation of the Wk part of kidney stones related to infection. (d) SEM observation of breast calcifications made of Wk.

portance due instance to its presence in major proteins such as haemoglobin, and links to some genetic diseases; for this reason we have already proposed the use of X-ray fluorescence to detect it in biological tissue [105,106]. It is quite clear that there is no iron in the stoichiometric formulation of biological Wk.

Next, SEM observations were made on kidney stones with high Wk content; these (Figure 3a) clearly show pseudocubic crystallites with a trigonal geometry. Associated EDX spectra shows contributions of the different elements in the Wk stoichiometric formula $Ca_9Mg(HPO_4)(PO_4)_6$, namely O, P, Mg and Ca (Figure 3b). One interesting fact lies on the morphology of Wk crystallites.

According to Frondel [96], crystals are usually simple rhombohedra as shown in Figure 4a, but are sometimes modified by small faces as shown in Figure 4b. Here, we have always observed the first one (white arrows on Figure 4c). However, in the case of synthetic Wk [107,108] as well as in the case of breast cancer, the second morphology was observed (white arrows on Figures 4d,e). It seems thus that in the case of infection, the local biochemical environment defined by the kidney and/or by the bacteria induce the formation of Wk crystallites with a peculiar morphology.

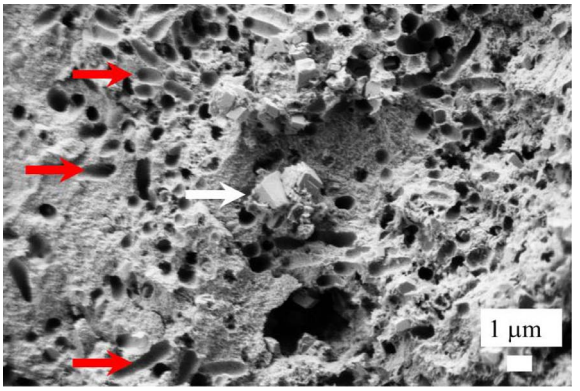

Figure 5. Bacterial imprints (red arrows) observed close to Wk crystallites (white arrow).

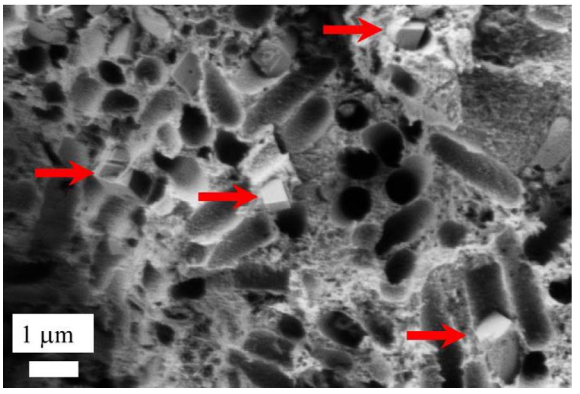

Figure 6. Wk crystallites (red arrows) present in bacterial imprints.

The mineralogical composition of the kidney stones as given by FTIR spectroscopy (Tables 1 and 2) explains the presence of carbon (Figure 3b). In kidney stones containing a high level of Wk, bacterial cell imprints are clearly visible at the surface of and probably within the apatitic part of the kidney stones (red arrows in Figure 5) but not at the surface of Wk crystallites (white arrow on Figure 5) [109].

Finally, at higher magnification, it is possible to observe Wk crystallites in bacterial imprints (red arrows on Figure 6). Such an observation is consistent with the fact that, as previously emphasized, an intimate link exists between Wk and bacteria [15].

In some kidney stones, FE-SEM did not reveal a large number of automorphic Wk crystallites. Instead some microscale crystallites were observed (red arrows on Figure 7a) in which EDX clearly shows contributions from Mg (Figure 7b).

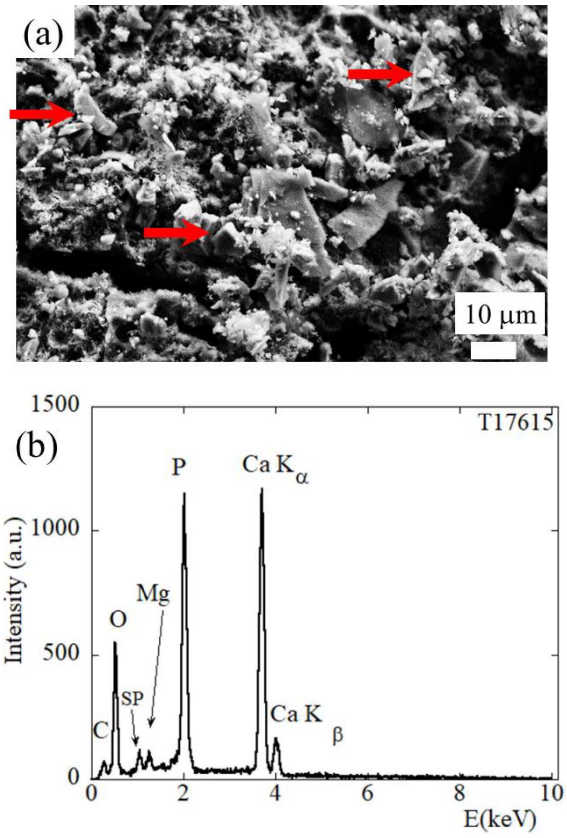

Figure 7. Sample T17615 (40% CA, 28% Wk, 26% ACCP, 4% Prot, 2% C2) (a) Wk (red arrows) as observed by its trigonal morphology in FE-SEM, and corresponding EDX spectrum (b) showing contributions from C (K_α = 0.277 keV), O (K_α = 0.525 keV), Mg (K_α = 1.253 keV), P (K_α = 2.014 keV), Ca (K_α = 3.691 keV, K_β = 4.012 keV). Note the presence of a sum peak (SP) due to the coincidence of two O K_α photons.

The second part of this investigation on the first set of kidney stones (with Wk content greater than 20% by weight) focuses on the size of the Wk nanocrystals, characterized using high resolution X-ray powder diffraction on selected examples (Figure 2).

For one sample, it was possible to measure the mean size of the coherently diffracting crystals. For the other samples, we used the Scherrer formula [110,111] $D(2\theta) = K\lambda/L\cos(\theta)$, a relationship between

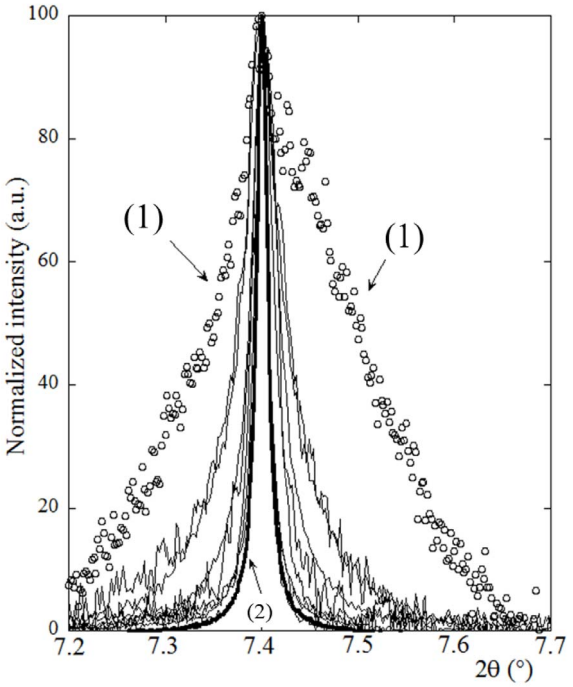

Figure 8. Widths of the Wk-specific scattering Bragg peak (2 −1 0 reflection, d = 5.165 Å) for those kidney stones measured. Note in particular: (1-white circle) = T43068 (66% Wk), (2-bold solid line) = T51263 (75% Wk). Note that the wavelength chosen to superimpose all X-ray diffractograms is 0.67212 Å, as in Figure 2.

D(2θ), the diameter of the crystallites, and the width of the scattering peak L. Note that K is a dimensionless geometrical factor of the order of 1 related to the specific shape of the targeted nanocrystal. As reported previously, this factor was set to unity in our evaluation of the crystal size [112].

Such simple analysis supposes similar peak broadening due to microstrain for all the samples and an isotropic morphology for the Wk crystals (which is the case for the automorphic crystals) [113]. Figure 8 shows that the scattering peak characteristic of Wk in the different experimental diffractograms displayed very different widths. In fact, it was impossible to investigate kidney stones with lower Wk content using X-ray scattering, suggesting that Wk exists in an amorphous state in low Wk content stones.

Table 1 shows that the size distribution of the Wk nanocrystals is quite large, which may be a function of various chemical parameters such as pH and ionic concentration as shown in a recent investigation of struvite [114]. These results seem to indicate that there is no specific size for the Wk crystals when there is an infection.

To understand the relationship between Wk in kidney stones, and infection, the foregoing structural description of Wk has to be complemented by chemical information. The ratio of Mg/Ca in stoichiometric Wk is 0.0643. In urine, this ratio is around 0.4 if we consider that normal calcium excretion is around 5 mmol/day and magnesium excretion is around 2 mmol/day. The normal value for phosphate is around 20 mmol/day, so all the elements present in the stoichiometric formula of Wk are present and so Wk biogenesis may well occur alongside that of CA.

In fact, the formation of CA as well as Wk requires destabilisation of the water molecules around the Ca^{2+} and Mg^{2+} cations. Based on molecular dynamics simulations using a polarizable potential, Jiao *et al.* [115] have shown that the lifetime of water molecules in the first solvation shell of Mg^{2+} is on the order of hundreds of picoseconds, in contrast to only a few picoseconds for Ca^{2+}, K^{+}, or Na^{+}. Such a simulation indicates that the stability of water molecules around Mg^{2+} is higher than the one around Ca^{2+}, favouring the formation of CA over Wk, the formation of the first one is hence favoured. To promote the formation of Wk, the first hydration shell of Mg^{2+} cations has to be destabilized. We propose that this may be achieved by physisorption of Mg^{2+} at the surface of bacteria [116].

Several points lead to the proposition that bacteria may play a key role in this destabilization process. Firstly, among one hundred chemical phases identified in kidney stones only two common ones contain Mg^{2+}, namely struvite and Wk, and these two chemical phases are related to infection. Secondly, Mg^{2+} cations play a key role in bacterial metabolism [117,118]. Finally, we have observed Wk crystallites inside bacterial imprints. These facts indicate the possibility of destabilization of the Mg^{2+} hydration shell by bacteria. Note that such a hypothesis also implies that for bacteria with urease, the decomposition of urea constitutes a much favourable pathway, leading to the formation of struvite and highly carbonated apatite, than the formation of Wk.

Finally, we consider a set of kidney stones (Table 2) with Wk content equal to or less than 20% by weight.

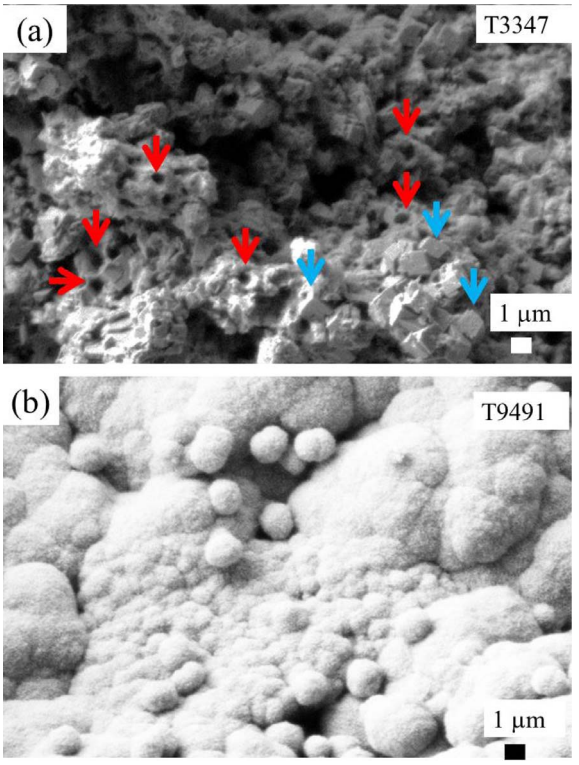

Figure 9. (a) For sample T3347 (15% by weight), very small Wk crystallites (blue arrows) as well as bacterial imprints (red arrows) are observed. (b) Bacterial imprints and Wk crystallites are not observed for the sample T9491 (Wk-free based on FTIR estimates).

In some samples, bacterial imprints were observed along with Wk crystallites, as in sample T3347 (Figure 9a). For other stones, no bacterial imprints, or Wk crystallites, could be detected (Figure 9b). Even though our sample number is quite low, this suggests that in the case of infection, Wk crystallites are observed. Otherwise, Wk may be present but in an amorphous state.

What is the benefit of these investigations to the clinician? Firstly, we confirm that kidney stones containing more than 20% by weight of Wk are related to infection. This is consistent with previous studies which indicate a content of 25% in weight of Wk [15]. Second, this study proposes a new approach for the characterization of kidney stones containing less than 20% by weight of Wk, a low level of carbonate in apatite, and no struvite, in patients presenting a negative urine culture. At this point, we must underline that according to the data gathered in our laboratory, which are based on the analysis of 70,728 kidney stones, 3171 kidney stones contain Wk. Among these, 1728 contain less than 20% in weight of Wk, a low level of carbonate in the apatite and no struvite, and are associated with a negative urine culture. For these 1728 stones, which correspond to 2.5% of the patients, the relationship with infection is not clear. In the present instance, we found that 4 stones out of a set of 11 presented bacterial imprints by FE-SEM.

We propose that, for these patients, FE-SEM could represent a significant diagnostic tool able to disclose possible infection. If FE-SEM underlines the presence of bacterial imprints, there are two possibilities to explain such observation. Is the stone linked to previous infection? In that case the clinical data doesn't contain such information and it is of primary importance to have such information regarding etiology. Is the stone linked to present infection? In that case, the lithogenic process is active for the patient and antibiotic have to be given. In both cases, it is clear that FE-SEM bring major information to the clinician.

We propose thus that for patients having kidney stones without struvite, carbapatite with a low level of carbonate and a low content of Wk, FE-SEM could represent a significant diagnostic tool able to disclose possible infection.

4. Conclusion

These investigations focused on kidney stones containing Wk, a mineral closely correlated with bacterial infection when its content is greater than 20% by weight by FTIR spectroscopy. Firstly, we stress that iron is not present in Wk when the latter occurs in kidney stones. Secondly, FE-SEM supports the relationship between Wk and infection. Bacterial imprints were observed in all the kidney stones containing higher than 20% by weight Wk. Moreover, WK related to infection seems to have a specific morphology. Thirdly, a measurement of Wk crystal size has been performed by X-ray diffraction based on the width of a specific diffraction peak (i.e. [210]). A detailed analysis of the high resolution X-ray powder diffratograms indicates a large distribution of crystal sizes between samples. It seems thus that Wk

content, but not crystal size, in kidney stones correlates with infection. Finally, based on FE-SEM observations as well as molecular dynamics' simulations, we propose that bacteria are able to destabilize the first hydration shell of Mg^{2+} cations. For bacteria with urease, the decomposition of urea to ammonia provides a more favourable chemical pathway, to struvite and carbonated apatite, than to Wk.

In conclusion, we propose FE-SEM as a diagnostic tool for patients with kidney stones containing less than 20% Wk, a low level of carbonate in apatite, without struvite, and with a negative urine culture. FE-SEM observations will give direct evidence of bacterial imprints at the surface. These may eventually be observed through tomography, if experimental configurations such as Nanoscopium [119,120] or Anatomix [121] are able to deal with biological samples with low acquisition time and submicrometer spatial resolution.

Acknowledgments

This work was supported by the Physics and Chemistry Institutes of Centre national de la recherche scientifique and by contracts ANR-09-BLAN-0120-02, ANR-12-BS080022, ANR-13-JSV-10010-01, convergence UPMC CVG1205 and CORDDIM-2013-COD130042.

References

[1] M. Daudon, *Annales d'urologie*, 2005, **39**, 209.
[2] V. Romero, H. Akpinar, D. G. Assimos, *Rev. Urol.*, 2010, **12**, article no. e86.
[3] T. Knoll, *European Urology Supp.*, 2010, **9**, 802.
[4] I. Sorokin, C. Mamoulakis, K. Miyazawa, A. Rodgers, J. Talati, Y. Lotan, *World J. Urol.*, 2017, **35**, 1301.
[5] M. Daudon, O. Traxer, P. Conort, B. Lacour, P. Jungers, *J. Am. Soc. Nephrol.*, 2006, **17**, 2026.
[6] M. Daudon, E. Letavernier, R. Weil, E. Véron, G. Matzen, G. André, D. Bazin, *C. R. Chim.*, 2016, **19**, 1527.
[7] K. Brandenburg, T. Schürholz, *World J. Biol. Chem.*, 2015, **6**, 71.
[8] L. N. Schultz, J. Connolly, E. Lauchnor, T. A. Hobbs, R. Gerlach, "Struvite Stone Formation by Ureolytic Biofilm Infections", in *The Role of Bacteria in Urology* (D. Lange, B. Chew, eds.), Springer International Publishing, Lausanne, 2016, 41-49.
[9] E. J. Espinosa-Ortiz, B. H. Eisner, D. Lange, R. Gerlach, *Nat. Rev. Urol.*, 2019, **16**, 35.
[10] M. Daudon, O. Traxer, E. Lechevallier, C. Saussine, *Prog. Urol.*, 2008, **18**, 802.
[11] J. E. Paonessa, E. Gnessin, N. Bhojanic, J. C. Williams Jr., J. E. Lingeman, *J. Urol.*, 2016, **196**, 769.
[12] J. Prywer, M. Olszynski, *Curr. Med. Chem.*, 2017, **24**, 292.
[13] D. O'Kane, A. Kiosoglous, K. Jones, *BMJ Case Rep.*, 2013, **2013**, article no. bcr2013009087.
[14] M. Daudon, C. A. Bader, P. Jungers, *Scanning Microsc.*, 1993, **7**, 1081.
[15] L. Maurice-Estepa, P. Levillain, B. Lacour, M. Daudon, *Scand. J. Urol. Nephrol.*, 1999, **33**, 299.
[16] H. M. Abrahams, M. L. Stoller, *Curr. Opin. Urol.*, 2003, **13**, 63.
[17] M. Daudon, P. Jungers, D. Bazin, *AIP Conf. Proc.*, 2008, **1049**, 199.
[18] M. Daudon, P. Jungers, D. Bazin, J. C. Williams Jr., *Urolithiasis*, 2018, **46**, 459.
[19] X. Carpentier, M. Daudon, O. Traxer, P. Jungers, A. Mazouyes, G. Matzen, E. Véron, D. Bazin, *Urology*, 2009, **73**, 968.
[20] M. Daudon, H. Bouzidi, D. Bazin, *Urol. Res.*, 2010, **38**, 459.
[21] K. M. Englert, J. A. McAteer, J. E. Lingeman, J. C. Williams Jr., *Urolithiasis*, 2013, **41**, 389.
[22] A. Hesse, H.-G. Tiselius, A. Jahnen (eds.), *Urinary Stones*, Karger, Basel, 2002.
[23] M. T. Gettman, J. W. Segura, *J. Endourol.*, 1999, **13**, 653.
[24] D. Bazin, G. André, R. Weil, G. Matzen, E. Véron, X. Carpentier, M. Daudon, *Urology*, 2012, **79**, 786.
[25] M. A. P. Manzoor, B. Singh, A. K. Agrawal, A. B. Arun, M. Mujeeburahiman, P. D. Rekha, *PLoS One*, 2018, **13**, article no. e0202306.
[26] P. Das, G. Gupta, V. Velu, R. Awasthi, K. Dua, H. Malipeddi, *Biomed. Pharmacother.*, 2017, **96**, 361.
[27] M. Daudon, *Archives de Pédiatrie*, 2000, **7**, 855.
[28] M. Daudon, A. Dessombz, V. Frochot, E. Letavernier, J. P. Haymann, P. Jungers, D. Bazin, *C. R. Chim.*, 2016, **19**, 1470.
[29] S. Reguer, C. Mocuta, D. Thiaudière, M. Daudon, D. Bazin, *C. R. Chim.*, 2016, **19**, 1424.
[30] D. Bazin, M. Daudon, *Ann. Biol. Clin.*, 2015, **73**, 517.
[31] D. Bazin, C. Jouanneau, S. Bertazzo, C. Sandt, A. Dessombz, M. Réfrégiers, P. Dumas, J. Frederick, J.-P. Haymann, E. Letavernier, P. Ronco, M. Daudon, *C. R. Chim.*, 2016, **19**, 1439.
[32] M. Daudon, D. Bazin, *J. Phys.: Conf. Ser.*, 2013, **425**, article no. 022006.
[33] D. Bazin, M. Daudon, *J. Phys. D: Appl. Phys.*, 2012, **45**, article no. 383001.
[34] D. Bazin, M. Daudon, C. Combes, C. Rey, *Chem. Rev.*, 2012, **112**, 5092.
[35] A. L. Rodgers, *Urolithiasis*, 2017, **45**, 27.
[36] M. Li, J. Zhang, L. Wang, B. Wang, C. V. Putnis, *J. Phys. Chem. B*, 2018, **122**, 1580.
[37] P. Chatterjee, A. Chakraborty, A. K. Mukherjee, *Spectrochim. Acta Part A*, 2018, **200**, 33.
[38] R. Gopal, C. Calvo, *Nat. Phys. Sci.*, 1972, **237**, 30.
[39] M. de Broglie, *C. R. Acad. Sci. Paris*, 1913, **157**, 924.
[40] M. Daudon, D. Bazin, "Application of physical methods to kidney stones and randall's plaque characterization", in *Urolithiasis* (J. Talati, H. G. Tiselius, D. Albala, Z. Ye, eds.), Springer, London, 2012.
[41] S. Rouzière, D. Bazin, M. Daudon, *C. R. Chim.*, 2016, **19**, 1404.
[42] D. Bazin, X. Carpentier, O. Traxer, D. Thiaudière, A. Somo-

gyi, S. Reguer, G. Waychunas, P. Jungers, M. Daudon, *J. Synchrotron Rad.*, 2008, **15**, 506.
[43] D. Bazin, M. Daudon, P. Chevallier, S. Rouziere, E. Elkaim, D. Thiaudière, B. Fayard, E. Foy, P. A. Albouy, G. André, G. Matzen, E. Véron, *Ann. Biol. Clin.*, 2006, **64**, 125.
[44] X. Carpentier, D. Bazin, C. Combes, A. Mazouyes, S. Rouzière, P. A. Albouy, E. Foy, M. Daudon, *J. Trace Elements Med. Biol.*, 2011, **25**, 160.
[45] A. Dessombz, C. Nguyen, H. K. Ea, S. Rouzière, E. Foy, D. Hannouche, S. Réguer, F.-E. Picca, D. Thiaudière, F. Lioté, M. Daudon, D. Bazin, *J. Trace Elements Med. Biol.*, 2013, **27**, 326.
[46] D. Bazin, M. Daudon, *J. Spectral Imaging*, 2019, **8**, article no. a16.
[47] D. Bazin, D. A. Sayers, J. J. Rehr, *J. Phys. Chem. B*, 1997, **101**, 11040.
[48] D. Bazin, L. Guczi, J. Lynch, *App. Cat. A*, 2002, **226**, 87.
[49] M. T. D. Orlando, L. Kuplich, D. O. de Souza, H. Belich, J. B. Depianti, C. G. P. Orlando, E. F. Medeiros, P. C. M. da Cruz, L. G. Martinez, H. P. S. Corrêa, R. Ortiz, *Powder Diffr. Suppl.*, 2008, **23**, S59.
[50] D. Bazin, C. Chappard, C. Combes, X. Carpentier, S. Rouzière, G. André, G. Matzen, M. Allix, D. Thiaudière, S. Reguer, P. Jungers, M. Daudon, *Osteoporosis Int.*, 2009, **20**, 1065.
[51] T. Yapanoglu, A. Demirel, S. Adanur, H. Yüksel, O. Polat, *Turkish J. Med. Sci.*, 2010, **40**, 415.
[52] H. Almarshad, A. Alsharari, *J. Med. Imaging Health Inform.*, 2018, **8**, 655.
[53] M. Van Meerssche, J. Feneau-Dupont, *Introduction à la Cristallographie et à la Chimie Structurale*, Vander, Louvain, 1973.
[54] E. Bouderlique, E. Tang, J. Perez, A. Coudert, D. Bazin, M.-C. Verpont, C. Duranton, I. Rubera, J.-P. Haymann, G. Leftheriotis, L. Martin, M. Daudon, E. Letavernier, *Am. J. Pathol.*, 2019, **189**, 2171.
[55] J. Guerlain, S. Perie, M. Lefevre, J. Perez, S. Vandermeersch, C. Jouanneau, L. Huguet, V. Frochot, E. Letavernier, R. Weil, S. Rouzière, D. Bazin, M. Daudon, J. P. Haymann, *PLoS One*, 2019, **14**, article no. e0224138.
[56] E. Esteve, Y. Luque, J. Waeytens, D. Bazin, L. Mesnard, C. Jouanneau, P. Ronco, A. Dazzi, M. Daudon Deniset-Besseau, *Anal. Chem.*, 2020, **92**, 7388.
[57] D. Bazin, J.-P. Haymann, E. Letavernier, J. Rode, M. Daudon, *La Presse médicale*, 2014, **43**, 135.
[58] M. L. Giannossi, *J. X-Ray Sci. Technol.*, 2015, **23**, 401.
[59] E. Tsolaki, S. Bertazzo, *Materials*, 2019, **12**, 3126.
[60] N. Quy Dao, M. Daudon, *Infrared and Raman Spectra of Calculi*, Elsevier, Paris, 1997.
[61] L. Estepa, M. Daudon, *Biospectroscopy*, 1997, **3**, 347.
[62] M. Daudon, D. Bazin, *C. R. Chim.*, 2016, **19**, 1416.
[63] D. Bazin, E. Letavernier, J. P. Haymann, P. Méria, M. Daudon, *Progrès en Urol.*, 2016, **26**, 608.
[64] F. Brisset, M. Repoux, J. Ruste, F. Grillon, F. Robaut, *Microscopie Electronique à Balayage et Microanalyses*, EDP Sciences, France, 2009, ISBN: 978-2-7598-0082-7.
[65] M. Daudon, P. Junger, D. Bazin, *New England J. Med.*, 2008, **359**, 100.
[66] A. Dessombz, E. Letavernier, J.-P. Haymann, D. Bazin, M. Daudon, *J. Urol.*, 2015, **193**, 1564.
[67] E. Letavernier, G. Kauffenstein, L. Huguet, N. Navasiolava, E. Bouderlique, E. Tang, L. Delaitre, D. Bazin, M. de Frutos, C. Gay, J. Perez, M. C. Verpont *et al.*, *J. Am. Soc. Nephrol.*, 2018, **29**, 2337.
[68] H. Bilbault, J. Perez, L. Huguet, S. Vandermeersch, S. Placier, N. Tabibzadeh, V. Frochot, E. Letavernier, D. Bazin, M. Daudon, J.-P. Haymann, *Sci. Rep.*, 2018, **8**, 16319.
[69] D. Bazin, M. Daudon, E. Elkaim, A. Le Bail, L. Smrcok, *C. R. Chim.*, 2016, **19**, 1535.
[70] T. Roisnel, J. Rodriguez-Carvajal, *Mater. Sci. Forum*, 2001, **378–381**, 118.
[71] A. C. Larson, R. B. Von Dreele, *General Structure Analysis System (GSAS)*, vol. 86, Los Alamos National Laboratory Report LAUR, 2004.
[72] L. Borghi, A. Nouvenne, T. Meschi, *Nephr. Dial. Transpl.*, 2012, **27**, 3982.
[73] J. L. Bauza, E. C. Pieras, F. Grases, V. Tubau, J. Guimera, X. A. Sabate, P. Piza, *Med. Hypotheses*, 2018, **118**, 34.
[74] A. L. Schwaderer, A. J. Wolfe, *Ann. Transl. Med.*, 2017, **5**, 32.
[75] J. Prywer, M. Olszynski, E. M. Brzoska, *Cryst. Growth Des.*, 2017, **17**, 5953.
[76] J. Prywer, A. Torzewska, *Cryst. Growth Des.*, 2009, **9**, 3538.
[77] J. Prywer, R. Sadowski, A. Torzewska, *Cryst. Growth Des.*, 2015, **15**, 1446.
[78] J. Prywer, A. Torzewska, *Sci. Rep.*, 2019, **9**, 17061.
[79] S. B. Streem, G. Lammert, *J. Urol.*, 1992, **147**, 563.
[80] E. De Lorenzis, A. B. Alba, M. Cepeda, J. A. Galan, P. Geavlete, S. Giannakopoulos, I. Saltirov, K. Sarica, A. Skolarikos, S. Stavridis, E. Yuruk *et al.*, *Eur. J. Clin. Microbiol. Infect. Dis.*, 2020, **39**, 1971.
[81] A. R. Izatulina, A. M. Nikolaev, M. A. Kuz'mina, O. V. Frank-Kamenetskaya, V. V. Malyshev, *Crystals*, 2019, **9**, 259.
[82] R. Lagier, C. A. Baud, *Pathol. Res. Pract.*, 2003, **199**, 329.
[83] R. Scott, N. Stone, C. A. Kendall, K. Geraki, K. Rogers, *NPJ Breast Cancer*, 2016, **2**, 16029.
[84] A. Cariati, *Clin. Res. Hepatol. Gastroenterol.*, 2013, **37**, article no. e69.
[85] A. Dessombz, P. Méria, D. Bazin, E. Foy, S. Rouzière, M. Daudon, *Progrès en Urologie*, 2011, **21**, 940.
[86] A. Dessombz, P. Méria, D. Bazin, M. Daudon, *PLoS One*, 2012, **7**, article no. e51691.
[87] J. D. Reid, M. E. Andersen, *Atherosclerosis*, 1993, **101**, 213.
[88] F. A. Shah, B. E. J. Lee, J. Tedesco, C. L. Wexell, C. Persson, P. Thomsen, K. Grandfield, A. Palmquist, *Nano Lett.*, 2017, **17**, 6210.
[89] C. A. Scotchford, S. Y. Ali, *Ann. Rheum. Dis.*, 1995, **54**, 339.
[90] L. S. Burnstein, A. L. Boskey, P. J. Tannenbaum, A. S. Posner, I. D. Mandel, *J. Oral. Pathol.*, 1979, **8**, 284.
[91] A. Clifford, G. S. Hoffman, *Curr. Opin. Rheumatol.*, 2015, **27**, 397.
[92] J. Gervasoni, A. Primiano, P. M. Ferraro, A. Urbani, G. Gambaro, S. Persichilli, *J. Chem.*, 2018, article no. 4621256.
[93] J. Cloutier, L. Villa, O. Traxer, M. Daudon, *World J. Urol.*, 2015, **33**, 157.
[94] S. R. Khan, M. S. Pearle, W. G. Robertson, G. Gambaro, B. K. Canales, S. Doizi, O. Traxer, H.-G. Tiselius, *Nat. Rev. Dis. Primers*, 2016, **2**, 16008.
[95] M. Haddad, H. Vali, J. Paquette, S. R. Guiot, *PLoS One*, 2014, **9**, article no. e89480.

[96] C. Frondel, *Am. Mineral.*, 1941, **26**, 145.
[97] T. Debroise, E. Colombo, G. Belletti, J. Vekeman, Y. Su, R. Papoular, N. S. Hwang, D. Bazin, M. Daudon, P. Quaino, F. Tielens, *Cryst. Growth Des.*, 2020, **20**, 2553.
[98] C. Calvo, R. Gopal, *Am. Mineral.*, 1975, **60**, 120.
[99] D. Bazin, P. Chevallier, G. Matzen, P. Jungers, M. Daudon, *Urol. Res.*, 2007, **35**, 179.
[100] D. Bazin, X. Carpentier, I. Brocheriou, P. Dorfmuller, S. Aubert, C. Chappard, D. Thiaudière, S. Reguer, G. Waychunas, P. Junger, M. Daudon, *Biochimie*, 2009, **91**, 1294.
[101] E. Esteve, D. Bazin, C. Jouanneau, S. Rouzière, A. Bataille, A. Kellum, K. Provost, C. Mocuta, S. Reguer, P. Ronco, J. Rehr, J.-P. Haymann, E. Letavernier, A. Hertig, *C. R. Chim.*, 2016, **19**, 1580.
[102] E. Esteve, D. Bazin, C. Jouanneau, S. Rouzière, A. Bataille, A. Kellum, K. Provost, C. Mocuta, S. Reguer, P. Ronco, J. Rehr, J.-P. Haymann, E. Letavernier, A. Hertig, *C. R. Chim.*, 2016, **19**, 1586.
[103] R. M. Rousseau, *Spectrochim. Acta B*, 2006, **61**, 759.
[104] I. L. Thomas, M. T. Haukka, D. H. Anderson, *Anal. Chim. Acta*, 1979, **105**, 177.
[105] S. Kascakova, C. M. Kewish, S. Rouzière, F. Schmitt, R. Sobesky, J. Poupon, C. Sandt, B. Francou, A. Somogyi, D. Samuel, E. Jacquemin, A. Dubart-Kupperschmitt *et al.*, *J. Path.: Clin. Res.*, 2016, **2**, 175.
[106] E. Esteve, S. Reguer, C. Boissiere, C. Chanéac, G. Lugo, C. Jouanneau, C. Mocuta, D. Thiaudière, N. Leclercq, B. Leyh, J. F. Greisch, J. Berthault, M. Daudon, P. Ronco, D. Bazin, *J. Synchrotron Radiat.*, 2017, **24**, 991.
[107] H. D. Kim, H. L. Jang, N. Y. Ahn, H. K. Lee, J. Park, E.-S. Lee, E. A. Lee, Y.-H. Jeong, D.-G. Kim, K. T. Nam, N. S. Hwang, *Biomaterials*, 2017, **112**, 31.
[108] H. L. Jang, K. Jin, J. Lee, Y. Kim, S. H. Nahm, K. S. Hong, K. T. Nam, *ACS Nano*, 2014, **8**, 634.
[109] C. Millo, S. Dupraz, M. Ader, F. Guyot, C. Thaler, E. Foy, B. Ménez, *Geochim. Cosmochim. Acta*, 2012, **98**, 107.
[110] P. Scherrer, *Nachr Ges Wiss Göttingen*, 1918, **26**, 98.
[111] A. L. Patterson, *Phys. Rev.*, 1939, **56**, 978.
[112] D. Bazin, M. Daudon, G. André, R. Weil, E. Véron, G. Matzen, *J. Appl. Cryst.*, 2014, **47**, 719.
[113] H. Klug, L. Alexander, *X-Ray Diffraction Procedures for Polycrystalline and Amorphous Materials*, 2nd ed., Wiley, New York, 1974.
[114] S. Shaddel, S. Ucar, J. P. Andreassen, S. W. Østerhus, *J. Environ. Chem. Eng.*, 2019, **7**, article no. 102918.
[115] D. Jiao, C. King, A. Grossfield, T. A. Darden, P. Ren, *J. Phys. Chem. B*, 2006, **110**, 18553.
[116] H. H. Tuson, D. B. Weibel, *Soft Matter*, 2013, **9**, 4368.
[117] C. Cutinell, F. Galdiero, *J. Bacteriol.*, 1967, **93**, 2022.
[118] X. Yuntao, L. Yang, *Sci. Rep.*, 2016, **6**, 20628.
[119] K. Medjoubi, G. Baranton, A. Somogyi, *Microsc. Microanal.*, 2018, **24**, 252.
[120] F. Brunet-Possenti, L. Deschamps, H. Colboc, A. Somogyi, K. Medjoubi, D. Bazin, V. Descamps, *J. Eur. Acad. Derm. Venereol.*, 2018, **32**, article no. e442.
[121] T. Weitkamp, M. Scheel, J. Perrin, V. Le Roux, V. Joyet, S. Chaouchi, H. G. Pais, J.-L. Giorgetta *et al.*, *Microsc. Microanal.*, 2018, **24**, 244.

Comptes Rendus
Chimie
2022, Vol. 25, Special Issue S1, p. 355-372
https://doi.org/10.5802/crchim.93

Microcrystalline pathologies: Clinical issues and nanochemistry

Inflammation and injury: what role do they play in the development of Randall's plaques and formation of calcium oxalate kidney stones?

Saeed R. Khan[a]

[a] Department of Pathology, Immunology and Laboratory Medicine, College of Medicine, University of Florida, Gainesville, Florida, USA
E-mail: khan@pathology.ufl.edu

Abstract. Urinary supersaturation is important for crystallization and likely cause of stone formation on ductal plugs. Formation of idiopathic stones that develop on Randall's plaques in the presence of low supersaturation is, however, dependent upon immunological responses of the kidneys. Experimental data suggests osteogenic and inflammatory processes playing pivotal role in plaque formation and its exposure to the pelvic urine which is necessary for stone development. Inflammatory and crystallization modulating molecules are released into the urine, becoming incorporated within the crystals and stones as organic matrix. Many of these molecules play roles in both inflammation and crystallization.

Keywords. Randall's plaque, Calcium oxalate, Idiopathic kidney stones, Hyperoxaluria, Hypercalciuria, Inflammation, Osteogenesis.
Published online: 28 July 2021

1. Introduction

Most idiopathic kidney stones are composed of an organic matrix and crystals of calcium oxalate (CaOx) mixed with small amounts of apatitic calcium phosphate (CaP). Consensus is that these CaOx stones are formed in association with Randall's plaques (RP) or Randall's plugs (RPg) on the renal papillae [1–3]. The plaques are suburothelial deposits of hydroxyapatite and originate deep inside the papillary tissue, suggested to start in the basement membrane of the loops of Henle. The plugs are crystalline deposits in the terminal collecting ducts. This article explores the role of inflammation and injury in the pathogenesis of CaOx kidney stones with emphasis on the development of RPs and production of stone matrix contents.

2. Randall's plaques

Plaques are suburothelial deposits of biological apatite on renal papillary surface [1,4–6]. They start as interstitial deposits of CaP deep in the renal papillary tip and are common in both the stone formers and non-stone formers. All of the plaques, however, are not associated with or support kidney stone formation [7]. It has been proposed that plaque formation starts as concentrically laminated spherulitic CaP crystals in the tubular basement (Figures 1, 2), most likely that of loops of Henle. Such crystals, 0.5–2 μm across, are seen in the tubular basement membrane and renal interstitium. The calcification pro-

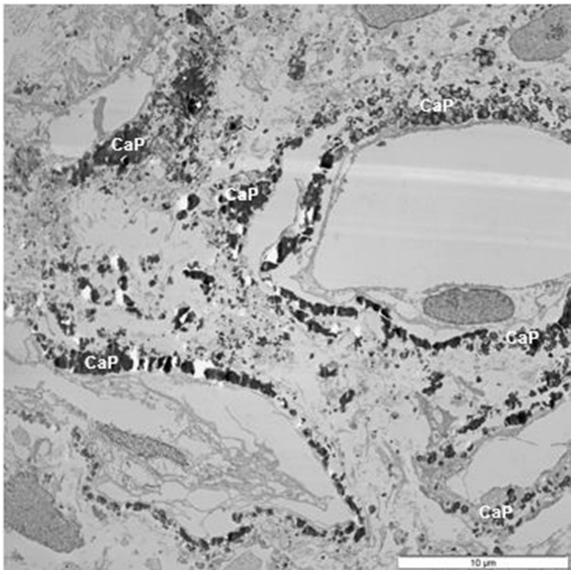

Figure 1. TEM of a section of renal papilla from CaOx kidney stone former. There are a number of damaged tubules surrounded by calcium phosphate (CaP) deposits.

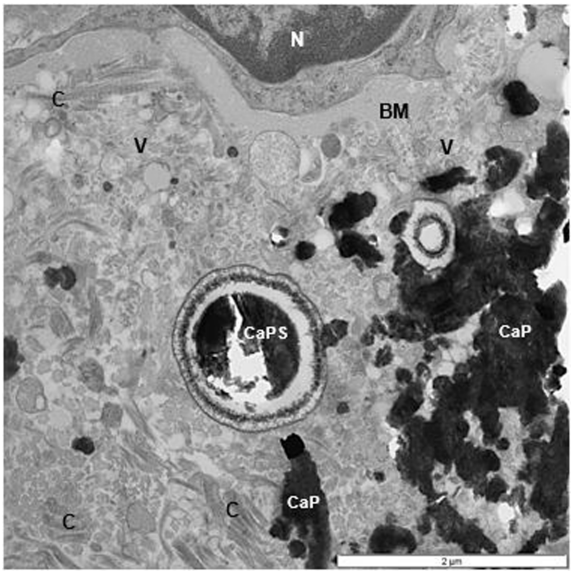

Figure 2. TEM of renal interstitium of a stone former showing aggregated calcium phosphate (CaP) deposits as well as a spherical (CaPs). Interstitium is filled with collagen (C) and other unidentified fibers, and vesicles (V). Part of a normal appearing epithelial cell with nucleus (N) and basement membrane are also seen.

ceeds from the tubular basement membrane through the interstitium and reaches the base of the papillary surface urothelium. Erosion of the covering urothelium exposes the underlying crystalline plaque to the urine with its various urinary components. Stones form on the exposed plaque by the addition of crystals on the exposed surface through nucleation, growth and aggregation. The interstitial calcifications include highly dense deposits of elongated calcified strands aggregated with spherulitic units of varying diameters. In addition, collagen fibers, unidentified fibrillary material, (Figures 2, 3) membrane-bound vesicles, and cellular degradation products are also detectable [8]. The results of electron diffraction of the calcified deposits demonstrated a range of crystallinity with the center being more crystalline than the periphery. Higher magnification of the plaques as shown in Figures 2 and 3 clearly demonstrate that spherulites and other crystals are actually a complex of crystals and organic matrix, so called biocrystals. Plaques also express osteopontin (OPN), heavy chain of inter-α-trypsin-inhibitor [2,9], and zinc [10].

A number of hypotheses have been put forward to explain the pathogenesis of Randall's plaque. One theory proposes that calcium excretion plays a central role in the development of the plaques [11]. This theory describes plaque and stone formation as basically a supersaturation dependent chemical reaction between various ions. The proposed mechanism involves decreased reabsorption of calcium in the proximal tubule leading to increased calcium in the thick ascending limbs of the loop and reabsorption into the interstitium. This leads to an increased supersaturation for CaP in the interstitium around the limbs of the loops of Henle promoting the formation of CaP crystals [12,13]. Proponents of the hypercalciuria theory reported the absence of any signs of cell injury, inflammation, interstitial fibrosis or intratubular crystal deposition.

Other studies of renal papillary tips from idiopathic stone formers have reported the existence of cellular injury and inflammation in association with the interstitial RPs. Analysis of kidneys obtained from patients undergoing radical nephrectomy showed the presence of mineral deposits in all human renal tissues with as well as without the RPs. Both intratubular and interstitial crystalline deposits were

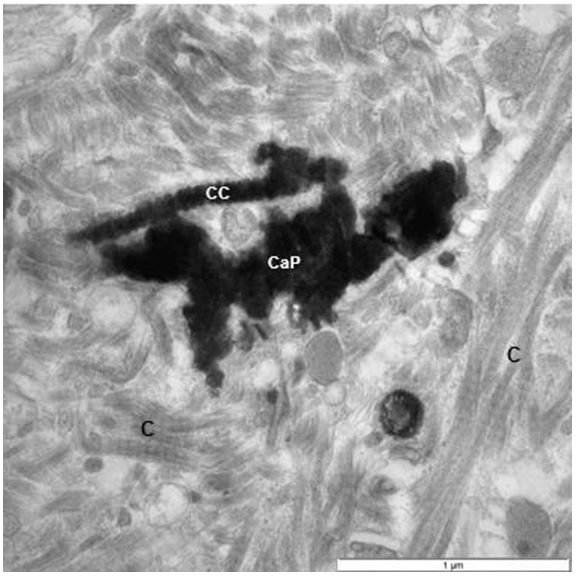

Figure 3. TEM of renal interstitium of a stone former filled with CaP deposits and masses of fibrillary material. Some of them clearly collagenous (C). One of the collagen strands appears to have been calcified (CC).

discovered, intratubular in the outer medulla, and interstitial in the papillary tips in close alignment with the vasa recta. A positive correlation was found between proximal intratubular and the distal interstitial crystal deposition. Both types of deposits were made of CaP but intratubular deposits were comprised of large spherical aggregates of several hundred nanometer long plate or needle shaped crystals while interstitial deposits contained small spherical entities united together and embedded in a collagenous matrix. Both types of deposits stained positive for OPN, osteocalcin (OC) and bone specific protein (BSP) [14]. Additionally, vasa recta and renal tubules were also positive for OPN and OC. It was concluded that both vasa recta and renal tubules participate in interstitial calcification and perhaps proximal intratubular CaP deposition stimulates distal interstitial deposition [15]. It is interesting to note that OPN, OC and BSP are osteoblast markers and play a well-established role in vascular calcification. OPN is a known participant in inflammation and a well-known modulator of mineralization. It is ubiquitous in matrices of soft tissue calcifications, RPs and stone and urinary crystal. Osteocalcin is found in matrices of both the bone and stone matrices [16,17]. Bone specific protein is involved in both physiological and pathological conditions [18–20].

Our ultrastructural observations of the renal papillae from both the primary hyperoxaluric [21], as well as idiopathic stone formers [8], have shown clear signs of cellular injury and inflammation. Histological examination of paraffin embedded papillectomy specimens from a patient with malabsorption revealed interstitial fibrosis, and focal epithelial hyperplasia in association with PAS (periodic acid schiff) positive calcification [21]. Ultrastructural analysis of the calcified areas disclosed enlarged interstitium filled with myofibroblasts, abundant collagen, unidentified fibrils, and necrotic cellular debris. Tubular epithelial cells appeared necrotic with swollen mitochondria and vesiculating endoplasmic reticulum. Basement membrane of the epithelial cells appeared thickened and multilayered. CaP deposits included 120–150 nm diameter laminated spherules with needle-shaped crystals. In addition, there were large electron dense deposits of CaP which were surrounded on the periphery by vesicular and fibrillary material.

Ultrastructural analysis of renal papillary tissue obtained from 15 idiopathic stone patients through cold cup biopsy revealed pathology somewhat similar to that described above [8]. Two basic configurations of crystals, both identified as basic CaP, were seen in the renal interstitium (Figures 2, 3). Spherical, 0.5–2 µm in diameter, concentrically laminated units were found throughout, within the tubular basement membrane as well as interstitium. Some of them retained concentrically arranged needle-shaped crystallites while others lost them during processing leaving behind the organic matrix as crystal ghosts. Large electron dense calcifications were aggregates of elongated calcified strands mixed with spherulites and were located mainly in the interstitium. They were surrounded by collagen fibers, membrane bound calcified and non-calcified vesicles and a variety of cellular degradation products. Peripheral strands showed a distinct banding pattern, reminiscent of the banding pattern of close by collagen fibers. Center of the large deposits was more compact and appeared more crystalline with radiating needle-shaped crystallites compared to the surface which was less compact and crystalline. Elec-

tron diffraction confirmed ultrastructural observations that central hydroxyapatite was more crystalline than the peripheral ones. The epithelial cells with large numbers of spherical CaP crystals in their basement membrane, appeared necrotic. The interstitium was replete with membrane bound vesicles, other forms of cellular degradation products, collagen and other fibriller material. Lumens of some tubules appeared blocked with cellular degradation products and perhaps even CaP crystals.

Nanoscale studies of incipient and fully developed Randall's plaque using field emission scanning electron microscopy with energy-dispersive X-ray microanalysis, μ-Fourier transform infrared spectroscopy, cryo-transmission electron microscopy coupled with selected area electron diffraction and electron energy loss spectroscopy showed the presence of microcalcifications around both the loops of Henle and vasa recta [22,23]. Two types of micro-calcifications were identified including calcified vesicles and mineral granules both containing CaP with carbonate in their cores. Secondary calcifications were found embedded in a fibrillary organic material.

A recent study using a combination of techniques including micro-CT imaging, multiphoton and confocal fluorescence imaging and infrared microscopy found a blue autofluorescence signature unique to RP, suggesting a unique nature of the molecules within [24]. Based upon its intrinsic fluorescence, fibrillar collagen was identified in the plaque.

Another study investigated the presence of crystals and the expression of known kidney stone related genes in kidneys from stone formers and non-stone formers [25]. Calcific crystal deposits were found in both groups. Stone formers kidneys showed significantly more crystals in renal medullas and papillae. More crystals were seen in the papillae of stone formers than those of controls. There were signs of crystal movement from tubular lumen to the interstitium. Osteopontin expression was higher and that of THP lower in stone formers papillae. Expression of superoxide dismutase was also low, indicating signs of oxidative stress. The presence of renal papillary crystals was determined to be significantly related to stone formation (odds ratio 5.55, 95% confidence interval 1.08–37.18, $P = 0.0395$). Based upon the observations of the presence of intratubular crystals in proximal medullary tubules and interstitial crystals later in the renal papillae, a new theory entitled, "upstream mineral formations initiate downstream Randall's plaque" has been presented [26].

Investigation of renal papillary tissue using the technique of genome-wide gene expression profiling revealed considerable differences between the tissue from idiopathic CaOx stone formers and controls. Differences were also found between stone formers Randall's plaque and non-Randall's plaque tissues. There was an increase in the expression of *LCN2*, *IL11*, *PTGS1*, *GPX3* and *MMD*, and decrease of *SLC12A1* and *NALCN* in the renal papillary tissue associated with Randall's plaque compared with the normal non-plaque associated papillary tissue [27]. There was also an increase in number of immune cells and apoptotic cells in renal tissue associated with Randall's plaque compared with non-plaque associated renal papillary tissue. The above mentioned genes play important roles in inflammatory processes. There is also an increase in M1 macrophage related genes and a decrease in M2 macrophage related genes in renal papillary tissue of stone patients [28]. Presence of giant cells in the renal interstitium, where crystals are surrounded by macrophages, is a well-known occurrence [29].

A study of renal papillary tips of kidney stone patients utilizing the technique of quantitative PCR showed a significant increase, compared to controls, in the presence of inflammatory cytokine, *CCL2*, *CCL5*, *CCL7*, CC-chemokine receptor 2 (*CCR2*), *CD40*, macrophage colony-stimulating factor 1 receptor (*CSF1*), CXC-chemokine ligand 9 (*CXCL9*), *CXCL10*, Fas ligand (*FASLG*), receptor interacting serine–threonine kinase 2 (*RIPK2*), e-selectin (*SELE*) and Toll-like receptor 3 (*TLR3*), irrespective of the stone type [30].

2.1. *Randall's plugs*

Randall described two types of renal papillary lesions, Type 1 and Type 2, as sites for future stone formation. Plaque 1 is now generally known as Randall's plaque and Type 2 plaque is mostly referred as ductal plug. Plaques are present on the papillary surface while plugs are crystalline deposits clogging the openings of the terminal collecting ducts [1,6,31]. As discussed above, Randall's plaques are deposits of mostly apatitic CaP crystals and are found in

idiopathic CaOx, brushite, primary hyperparathyroid, small bowel resection, ileostomy stone disease [4]. The composition of ductal plugs varies. Plugs can be apatitic in primary hyperparathyroid stone formers, mixed with CaOx in brushite stone formers, obesity bypass patients, patients with small bowel resection, renal tubular acidosis. Ductal plugs can also be apatite mixed with urate in ileostomy stone formers [4]. The Randall's plugs of stone patients with primary hyperoxaluria are made of CaOx [4,21]. Plugging is also common in non-stone forming kidneys where it is mainly composed of carbonate apatite and amorphous CaP [32].

Obviously, plug formation is a result of crystal retention within the terminal collecting ducts. Results of animal model and tissue culture studies clearly show that crystals can be retained by either attachment to the epithelial surface or aggregation during excessive supersaturation [33–35]. Crystal nucleation, and aggregation can be supported by the membranous products of renal tubular injury [36–38]. Massive crystallization is possible in the presence of acute or persistent urinary supersaturation and excretion of poorly soluble salts and cause tubular plugging in any section of the renal tubules [32]. Examples include CaOx ductal plugs in patients with primary hyperoxaluria [21,39], or cystine crystal plugs in the cystine stone formers [39]. The overgrowth on plugs will form an attached stones. Parts of a stone may break off and act as nidus for an unattached stone [6,40]. Plugs are exposed to two different environments, tubular and pelvic, with different urinary composition. As a result the final product, the stone, may have one crystalline type on the tubular side and another on the pelvic side. Thus an apatite nucleus may have brushite on the one side and CaOx on the other [41].

3. Organic matrix of idiopathic kidney stones

Calcium oxalate kidneys stones, like other stones, are composed of crystals (Figure 4) mixed with small amounts of a pervasive organic matrix (Figures 5, 6) which contains carbohydrates, proteins and lipids [37,42,43]. The matrix composition varies between various stone types. There is more matrix material in the outer layers of the stones than their centers and its make-up may change from the surface to the center. Urinary crystals isolated from the human urine or produced *in vitro* in human urine also contain an organic matrix. Similarly CaOx and CaP crystals and stones produced experimentally in rats also contain an organic matrix, indicative of universal phenomenon of incorporation of biological substances from the immediate environment into the growing crystals. Both chromatograph, biochemical and microscopic techniques have been used to study various aspects of organic matrix.

3.1. *Results of biochemical, chromatographic, and spectrophotometric analyses*

Ever since Boyce described Substance A as the major component of stone matrix, several studies have examined matrix composition using ever more sophisticated techniques with a significant increase in the number of components identified. Recent studies, using a variety of methods, have identified up to 1059 unique proteins in stone matrix [44].

Dussol *et al.* analyzed soluble matrix of 5 different types of kidney stones using electrophoretic techniques [45], and identified 13 proteins. Human serum albumin, α1-antitrypsin, α1-microglobulin, were three of the nine proteins common in all types of stones. B2-microglobulin was found only in CaOx stone matrix. THP was not found in matrix of any of the stones.

Canales *et al.* used mass spectroscopy to analyze matrix of 25 stones including 9 CaOx monohydrate (COM), 4 CaOx dihydrate (COD), 9 apatite and 3 brushite stones [46]. A total of 113 proteins were identified. 42 proteins were unique to CaOx, 36 to CaP and 35 were common in both. Calgranulin A and B, hemoglobin α and β chains, fibrinogen, Tamm–Horsfall protein (THP), α 1 antitrypsin, and vitronectin were found in more than 10 stones. Gene ontology analysis showed that COM stones matrix contained more cell structure, cell membrane, intracellular transport proteins and coagulative proteins while the matric of apatite stones contained more immunity and defense proteins. Proteins involved in inflammatory processes were common in both CaOx and CaP stones.

Marchant *et al.* analyzed the organic matrix of stones obtained from 5 patients. They used a variety of techniques including spectrophotometry and one-dimensional polyacrylamide electrophoresis [47]. A total of 158 proteins were identified with

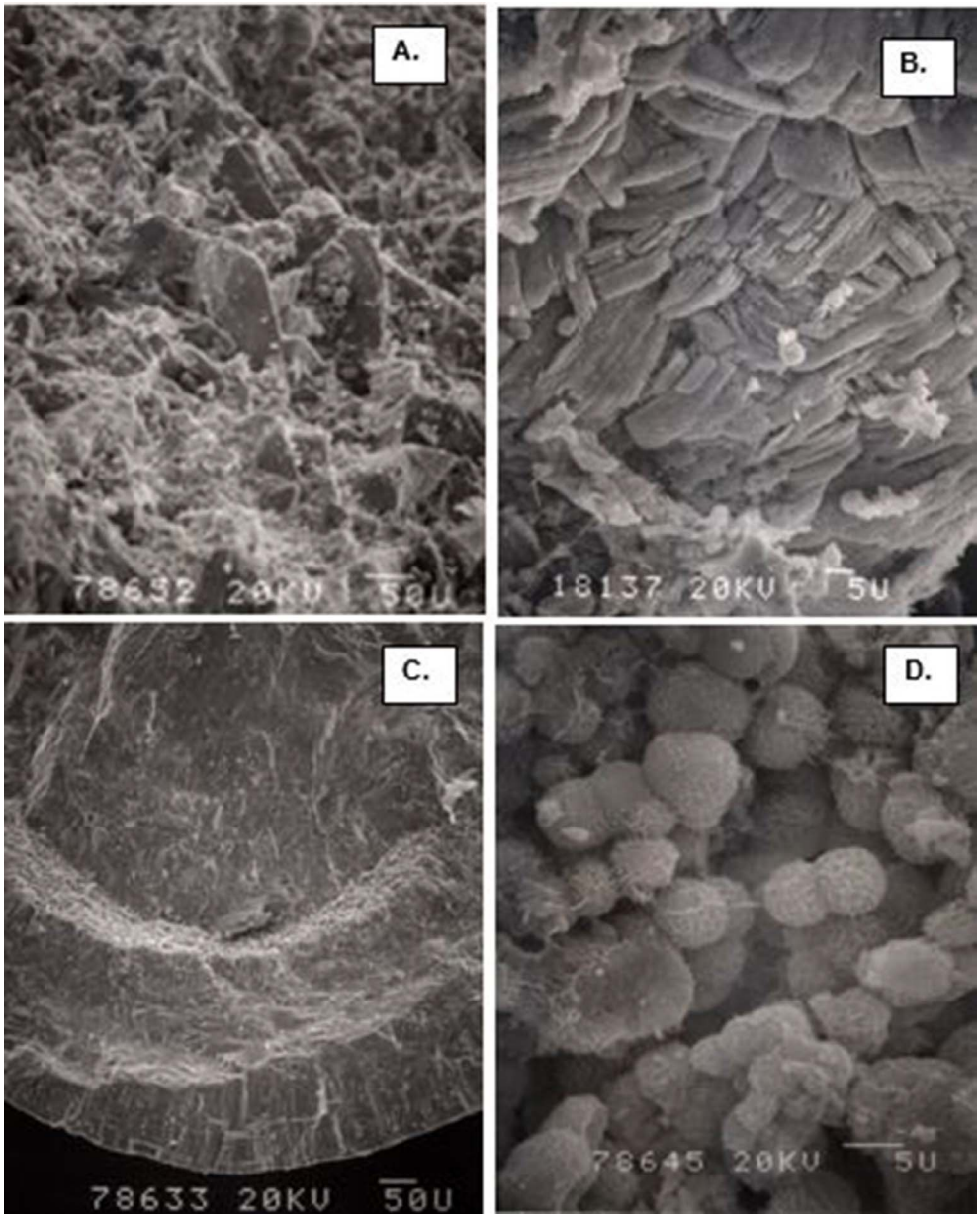

Figure 4. Calcium oxalate (CaOx) kidneys stone examined using scanning electron microscopy (SEM). (A) Stone surface showing CaOx dihydrate (COD) crystals sticking out on the surface. (B) Stone surface showing tops of the tabular CaOx monohydrate (COM) crystals. (C) Fractured surface showing COM crystals organized in concentric laminations. (D) Spherical calcium phosphate crystals.

28 of them detected in all three LC-MS analyses. Proteins included such commonly known ones as THP, OPN, calgranulins, and albumin. Gene ontology analyses suggested that 61% had extracellular origin, 36% intracellular and 3% intra-/extracellular. Ingenuity pathway analyses identified tumorigenesis, immunological disease and inflammatory disease.

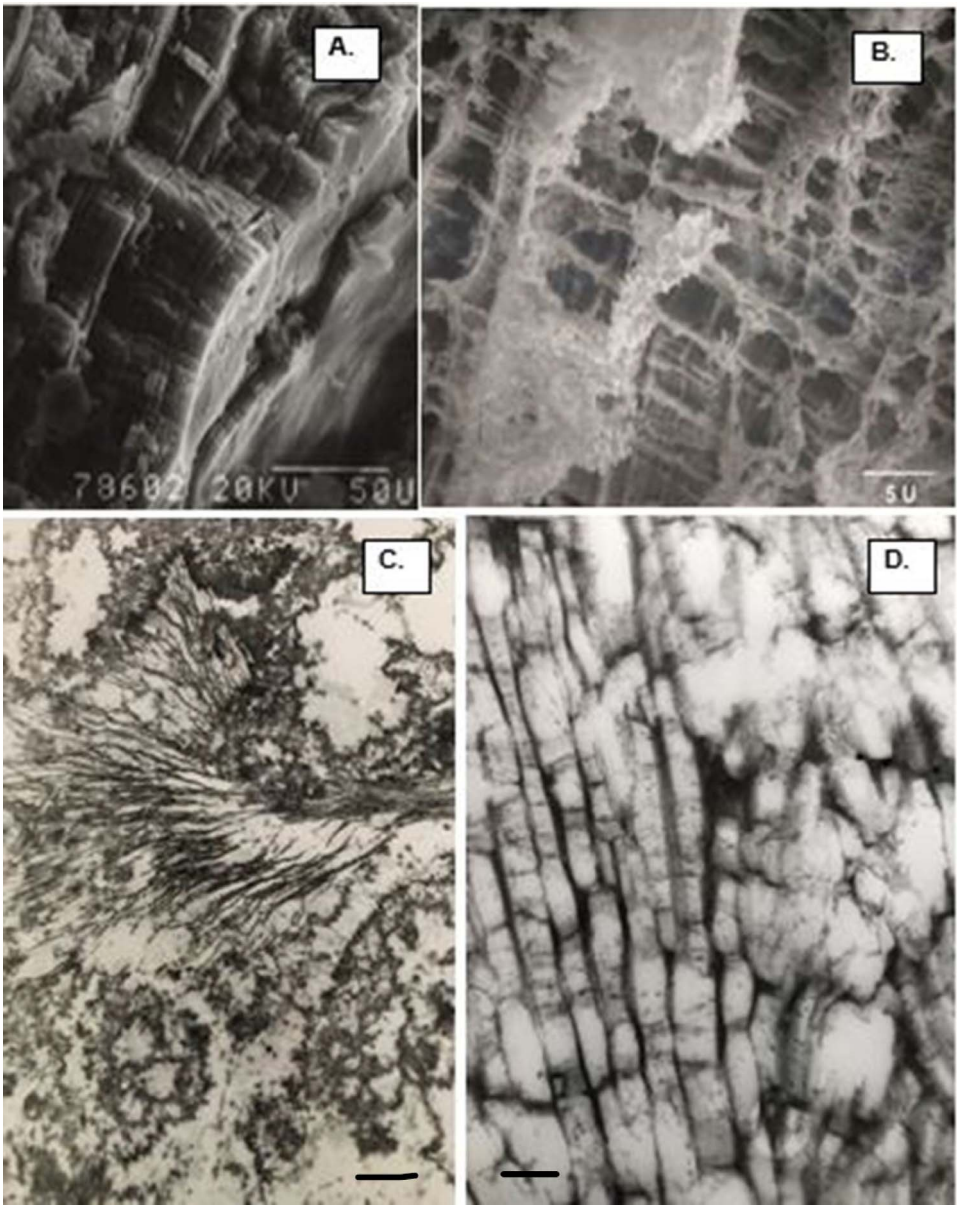

Figure 5. SEM and TEM appearance of demineralized COM stones demonstrating ubiquitous nature of the organic matrix, and its intimate association with the crystalline components of the stone. Stone pieces were demineralized and then processed for electron microscopy. The stone and crystals maintained their architecture even after the removal of the crystalline component. (A) Low magnification SEM appearance of demineralized COM stone, very much similar to the non-demineralized stone shown in Figure 4(C). (B) SEM of the fractured ghosts of tabular COM crystals showing loss of the crystals, leaving behind the organic matrix which allowed the ghost to maintain tabular morphology. COM crystals tightly organized in radial striations and concentric laminations. (C) TEM appearance of a COM stone showing ghosts of both the tabular COM and spherical CaP crysals. The interface is occupied by the organic matrix. Bar = 1 μm. (D) TEM of the cross section of tabular COM crystals demonstrating the inter and intra-crystalline electron dense organic matrix. Bar = 0.2 μm.

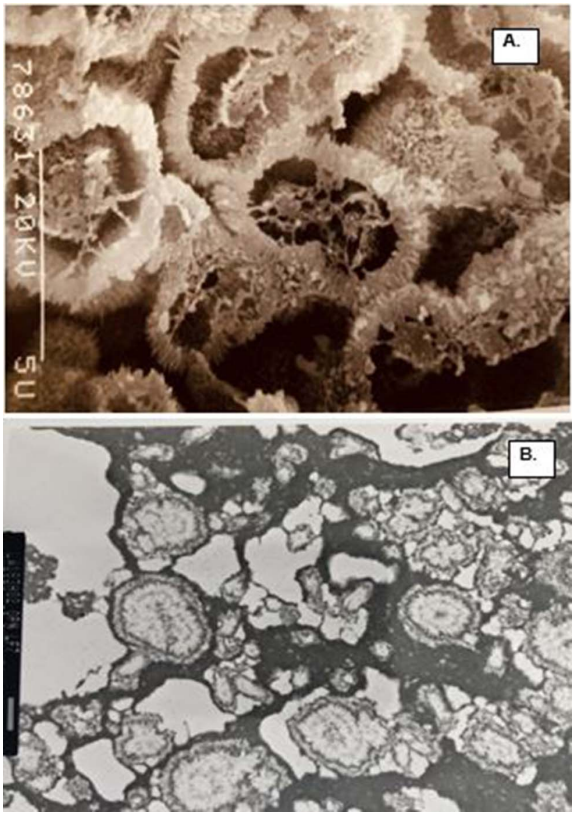

Figure 6. Organic matrix of the CaP crystals in a COM stone. (A) SEM of the fractured demineralized spherical CaP crystals. There is electron dense organic matrix in the center as well as on the surface. Closer look at the surface show needle shaped appearance. (B) TEM of the CAP crystal ghosts showing electron dense material organized on the periphery and also present in the center, similar to what is shown in A. Bar = 1 μm.

Okumura *et al.* examined CaOx stones obtained from 9 stone patients and their organic matrix was analyzed using nanoLC-MALDI-tandem mass spectrometry following in-solution protein digestion [48]. A total of 92 proteins were identified and included proteins of kidney, blood and leukocyte origin. Osteopontin, prothrombin, THP, serum albumin, Calgranulins, Fetuin A, Lactotransferin, myeloperoxidase were common to all stones. There was an inverse relationship between Prothrombin and Calgranulins. Some samples had more Prothrombin and OPN while others more Calgranulins. Calgranulins rich stones were also rich in myeloperoxidase and lactotransferin.

Boonla *et al.* analyzed proteome of stone matrix and urine obtained from same patient to identify the urinary proteins that become part of the stone matrix. Proteins known to be involved in inflammation and fibrosis were detected in both the urine and stone matrix of stone patients [49]. Eighteen proteins with a role in immunity, inflammation, coagulation and fibrosis were common to stone matrix and patient urine and were absent from normal healthy human urine. Calgranulin A, a calcium binding protein with important role in inflammation was suggested to be a urinary marker of nephrolithiasis.

Rodgers group applied solid state nuclear magnetic resonance spectroscopy technique to characterize the biomolecular composition of phosphate stones. They detected varying amounts of proteins, glycosaminoglycans (GAGS) and lipids. Their analysis showed that GAGS and proteins, "composited into or onto the mineral lattice by strong physicochemical interactions" [50]. Interestingly, their results also showed that CaOx and uric acid, when present, existed as separate entities, no direct epitaxial-like relationship.

3.2. *Results of microscopic and immunehistochemical analyses*

Results of the studies discussed above have provided significant information about the composition of stone matrix and have identified more than a thousand proteins. These studies have provided some indication about the matrix origin as well as clues for stone pathogenesis. The role of matrix is however, still uncertain. To appreciate the role we have to know the exact location of matrix and its components in the stones and their association with the crystals. Boyce and associates realized the significance of such information and performed some of the earliest histological and histochemical examinations of kidney stones [51–53]. We performed a number of light and electron microscopic studies of decalcified CaOx crystals and stones, both from stone patients and those produced experimentally in rats, to localize various matrix components. Scanning electron microscopy and energy dispersive X-ray microanalysis of CaOx stones after staining with

colloidal iron showed the presence of acidic mucosubstances in association with CaOx crystals [54]. But stones, particularly CaOx kidney stones, being highly crystalline, it is difficult to perform critical microscopic studies of their organic matrix. Therefore, we developed a technique involving decalcification of stone sections using 0.25 M ethylenediaminetetracetic acid (EDTA), after embedding them in agar, which allowed full or partial removal of crystals without excessively disturbing the matrix material [55]. Crystals were replaced by crystal ghosts (Figures 5, 6) and could be easily processed for various microscopic and immune-histochemical techniques. Light and electron microscopic examination of decalcified stones, helped localize the organic matrix and its various components within the stones and demonstrated that matrix is ubiquitous within the stones and is present not only on crystals surfaces but also within them [56–58]. Crystal ghosts generally maintained the original shape of the crystals. Ghosts of CaOx monohydrate crystals appeared as radially arranged tabular units, showing concentric laminations and radial striations (Figure 5). Those of CaOx dihydrate appeared dipyramidal while those of apatite as spherical units. Matrix contains both amorphous and fibrous components and could be stained just like any other tissue components. Staining of demineralized stones with Sudan Black B showed sudanophilic material within the intercrystalline spaces indicating its lipidic nature [59]. The presence of lipids in the intercrystalline spaces was further confirmed through transmission electron microscopy after malachite green staining [60]. Ultrastructural studies of kidney stones, crystal deposits induced in experimental hyperoxaluric rats, as well as those produced in human urine *in vitro*, showed the presence of proteins, membranes and lipids in their matrices [37]. Crystal ghosts of both CaOx and CaP were made of amorphous material and were associated with fibrillary, amorphous and membranous elements including membrane bound vesicles. Transmission electron microscopy and backscattered electron microscopy of crystal ghosts revealed the presence of organic material on the surface as well as inside the CaOx and CaP crystals and was organized in discrete layers. In addition the interface between CaOx and CaP crystals was occupied by an amorphous organic material [61].

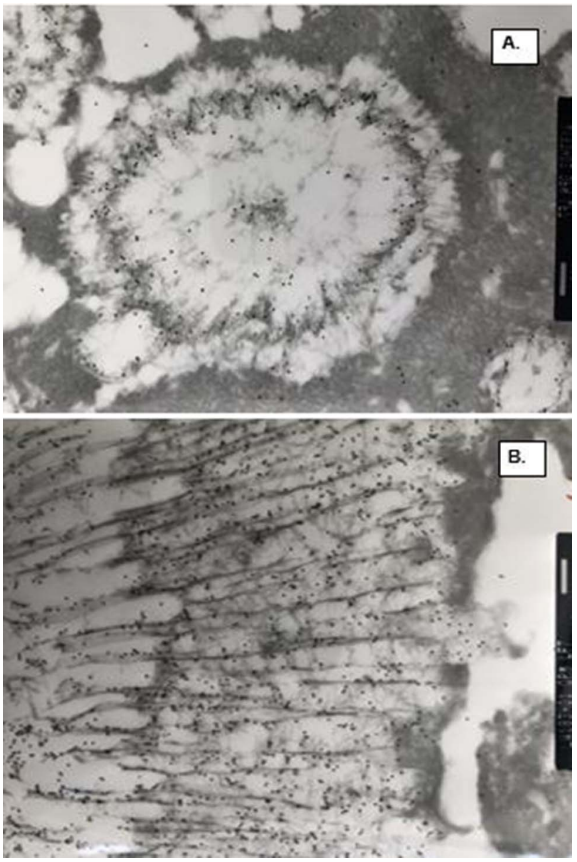

Figure 7. TEM of the CaP and COM crystal ghosts stained for osteopontin (black dots) demonstrating its substantial presence in the matrix. (A) Spherical CaP ghosts. OPN is specifically present in the electron dense organic matrix in the center and on the periphery of the ghosts. Electron dense amorphous material outside the spherical units is not stained. (B) Tabular COM ghosts. OPN is specifically associated with the inter and intra-crystalline organic matrix of the ghosts. Electron dense materials outside the ghosts is negative for OPN. Bar = 200 nm.

We also performed ultrastructural immunodetection of OPN, THP and albumin, the three most common organic matrix proteins, in the CaOx crystals of the human stone and those produced in a rat model [16]. Osteopontin was a prominent constituent of CaOx crystals and stones (Figures 7, 8). Intense labelling for OPN was seen in the nucleus,

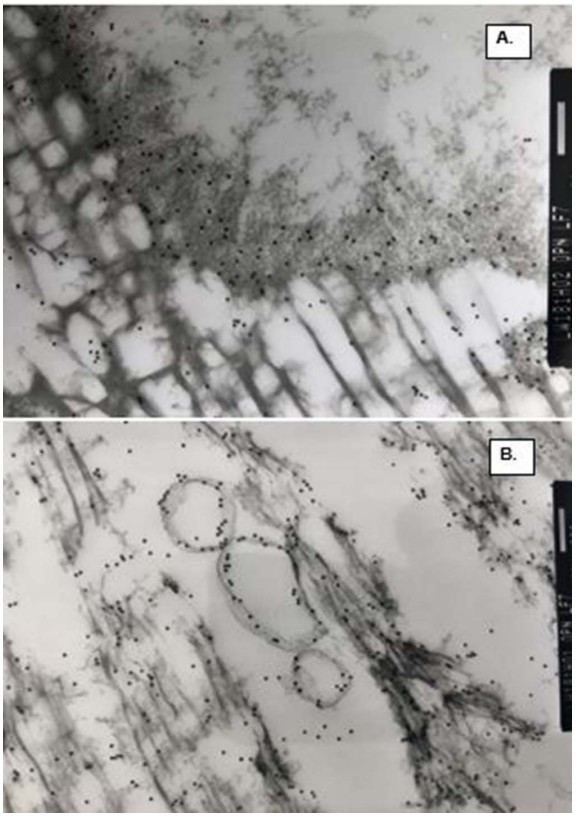

Figure 8. OPN staining in demineralized COM stones. (A) Interface between ghosts of CaP and COM is occupied by OPN positive electron dense organic matrix. (B) OPN positive vesicles in between the ghosts of tabular COM crystals.

laminas and striations of crystal ghost from rat urine. Similarly, concentric laminas and radial striations of human CaOx kidney stones were also intensely positive for OPN. CaOx crystal ghosts were negative for THP and albumin. Labelling for THP was mostly seen on the stone surface. Similarly, albumin was seen on stone surface and between crystals but not in direct contact with the crystals. Organic material between the Cox and CaP crystals stained positive for OPN.

4. Discussion

Results of most current studies indicate that, (1) renal papillae of idiopathic CaOx kidney stone formers show signs of injury and inflammation; and (2) organic matrix of calcific kidney stones contains biomolecules known to be involved in immune response and inflammation (Table 1). It is however unclear whether injury and inflammation play a causative role in the development of RP and stones. It has been suggested that Randall's plaque development is dependent upon an increase in urinary calcium [11]. Calcium reabsorption is decreased in the proximal tubules (PT), hence more calcium reaches the thick ascending limbs of the loop. Calcium reabsorption into the interstitium is increased, increasing the supersaturation thus promoting the formation of interstitial plaques [12,13,62]. Surprisingly they did not find any sign of injury or inflammation associated with the plaque as well as crystal deposits in the nearby tubules. Surprising, because results of earlier studies including those of Randall implied calcification in association with injury. Randall suggested "that calcium plaques appear to be a natural reparative process to some form of tubule damage, the occurrence of which is in much higher incidence than actual frequency of renal stone" [63]. Electron microscopic study of necropsy material by Haggit and Pitcock described calcification as spherical laminated electron-dense bodies in the papillary interstitium and basement membrane of collecting ducts [7]. They showed excessive deposition of collagen in the papillary interstitium, tubular epithelial necrosis and thickening of the tubular epithelial basement membrane. We have always found signs of tubular and interstitial injury in association with Randall's plaque in renal papillae from idiopathic kidney stone formers [6]. Additionally, in every animal model study and every tissue culture study where renal epithelial cells become exposed to crystals or even high oxalate, there are signs of oxidative stress which eventually leads to cellular injury [33,34,64–74]. Some studies of both CaOx and CaP nephrocalcinosis have also shown signs of osteogenic transformation of renal tubular epithelial cells [75–77]. In addition, hypercalciuria, genetic or induced by other means, by itself leads only to tubular deposition of crystals [69]. Interstitial crystals have so far only been seen in animal models of nephrocalcinosis with a deficiency of crystal inhibitors such as pyrophosphate, OPN and THP [78–82].

It has been proposed that Randall's plaque and stone formation [6,38,83], are mechanistically a form of ectopic calcification, pathological deposition of mostly CaP in the soft tissue, analogous to vascu-

Table 1. Biomolecules involved in both, the inflammation and idiopathic CaOx stone disease

Molecule	Description	Immune function	Findings in Nephrolithiasis
α-1 microglobulin (A1M)	A reductase that degrades heme and removes free radicals and oxidizing agents from tissue. It is induced by reactive oxygen species and broken down in the kidney	Urinary marker for renal inflammation & hypertension	CaOx crystallization inhibitor, present in KS matrix
Albumin (ALB)	Globular protein commonly found in blood and has a good binding capacity for water, Ca(2+), Na(+), K(+), fatty acids, and hormones	Decrease in response to inflammation. Hypoalbuminemia is a predictor of mortality in patients with chronic renal failure	Promotes crystallization and crystal adhesion, present in KS matrix
Bikunin	A single glycosaminoglycan chain, is a plasma serine protease inhibitor	Anti-inflammatory	CaOx crystallization inhibitor, present in KS matrix
Calgranulin (S100)	S100 calcium-binding protein family (A8, A9, A12) that is expressed in multiple cell types, including renal epithelial cells and neutrophils	Inflammatory, act as damage-associated molecular pattern (DAMP) proteins, signaling through the receptor for advanced glycation end products (RAGE), and acting as endogenous toll-like receptor 4 (TLR4) ligands	Inhibitor of CaOx crystallization in urine, present in KS matrix
Fetuin-A	Also known as alpha-2-HS-glycoprotein (AHSG), is a human plasma glycoprotein belonging to the cystatin proteases inhibitors family that has a calcium phosphate-binding site and TGF (transforming growth factor)-β cytokine-binding motif	Anti-inflammatory (stimulates anti-inflammatory cationic polyamines and directly inhibits PAMP-induced HMGB1 release by innate immune cells)	Binds to CaP to form nanoparticles and promotes crystal aggregation, present in KS matrix
Fibronectin	Glycoprotein of the extracellular matrix that binds to integrins, collagen, fibrin, and heparan sulfate proteoglycans	Modulator of inflammation	Inhibitor of CaOx crystallization and adhesion, present in KS matrix
Heparin sulfate (HS)	A linear polysaccharide that occurs as a proteoglycan which is capable of binding Wnt	Pro-inflammatory by assisting macrophage attachment and chemokine binding	Inhibitor of CaOx crystal growth and adhesion, present in KS matrix
Inter-α-inhibitor (IαI)	A plasma proteins consisting of three of four heavy chains selected from the group ITIH1, ITIH2, ITIH3, ITIH4 and one light chain selected from the group AMBP which function as protease inhibitors. IαI form complexes with HA	Anti-inflammatory	Inhibitor of CaOx crystallization and adhesion, present in KS matrix
Matrix-gla-protein (MGP)	A member of a family of vitamin-K2 dependent, Gla-containing proteins that binds to calcium. It acts as an inhibitor of vascular mineralization and plays a role in bone organization	Anti-inflammatory	Inhibitor of mineralization, present in KS matrix
Osteonectin	Also known as secreted protein acidic and cysteine rich (SPARC), is a calcium binding glycoprotein that belongs to the matricellular protein family and is expressed in remodeling tissues, such as bone, mucosa of the gut, and healing wounds	Anti-inflammatory (may regulate macrophage viability and chronic immune response)	Inhibitor of CaOx crystal growth and adhesion

(continued on next page)

Table 1. (continued)

Molecule	Description	Immune function	Findings in Nephrolithiasis
Osteopontin (OPN)	A phosphorylated glycoprotein that binds integrins and functions as a mediator of cell adhesion, migration, immune responses, and tissue repair	Pro-inflammatory cytokine	Both a promoter and inhibitor calcification, crystal aggregation and attachment; present in KS matrix
Phospholipids	Components of cellular membranes	Membrane exposure to reactive oxygen species creates oxidized phospholipids which are potent anti-inflammatory mediators	Membrane lipids provide site for face selective crystal nucleation, aggregation and retention within the kidneys
Prothrombin fragment 1	Peptide formed during conversion of prothrombin to thrombin; excreted in urine	Binds calcium and is involved in coagulation, as well as in the recruitment and activation of immune cells	Inhibitor of crystal growth and aggregation, present in KS matrix
Tamm–Horsfall protein (THP)	Also known as uromodulin, is a large glycoprotein in the ascending limb of the loop of Henle extending into the early portion of the distal tubule and is the most abundant protein excreted in normal urine	Modulator of inflammation	Important modulator of CaOx crystallization and aggregation in urine as well as CaOx adhesion to uroepithelium, present in KS matrix

Modified from Khan *et al.* [69].

lar/valvular calcification (VC) during atherosclerosis (Table 2) [1,69,83,84]. Reactive oxygen species play a crucial role in both VC and stone formation [66,68,85,86]. Vascular calcification involves osteogenic transformation of vascular smooth muscle cells (VSMC) [87–90], in the presence of high calcium and phosphate. Reactive oxygen species play crucial role [66,68,85,86]. The transcription factors, Runt-related transcription factor 2 (RUNX2), osterix and msh homeobox 2 (MSX-2) are upregulated. Bone morphogenetic proteins and Wnt signaling pathways are activated [84,91]. Calcification starts in membrane bound matrix vesicles or exosomes [92], produced by the transformed VSMC cells. Apoptotic bodies produced by the deaths of many other cells including lymphocytes and macrophages can also behave as matrix vesicles [90,93–96]. The matrix vesicles contain certain proteins and lipids that help crystal nucleation. Once formed, needle shaped CaP crystals pierce through the limiting membrane of the vesicles inducing mineralization of the surrounding extracellular matrix such as collagen, and support onward movement of the mineralization front [90,97]. RPs contain both empty and calcified vesicles [8,23], normal and calcified collagen fibers [8,24], membranous cellular degradation products, and express various mineralization modulators such as OPN [27,98]. Progression of mineralization is accomplished by calcification of apoptotic bodies and collagen fibers in the extracellular matrix. These features are similar to what happens during vascular calcification as briefly reviewed above. Osteogenic changes and expression of transcription factors in association with RPs has been suggested but not been confirmed [99,100]. The appearance of transcription factors may be transient or below the level of detection by immunohistochemical means. It has however, been reported in rat models of CaOx and CaP nephrolithiasis [76,77]. Macrophages play a significant role in both vascular and renal papillary calcification. Pro-inflammatory macrophages are implicated in vascular plaque calcification while anti-inflammatory ones with plaque regression [101–103]. Macrophages are common around renal interstitial crystals and pro-inflammatory macrophage genes are increased while anti-inflammatory macrophage genes are decreased in the kidneys of patients with kidney stones [28,104–106].

Almost all the recent studies of organic matrix of idiopathic CaOx kidney stones, have concluded that injury and inflammation are significant contributors to the formation of matrix constituents. Over a thousand proteins have so far been identified therein. Many of them participate in immune re-

Table 2. Features common to vascular and renal calcification

	Vascular calcification	Renal calcification
Reactive oxygen species involvement	ROS activate many steps in calcification. Both Mitochondria and NADPH are involved in ROS production	Crystals and high oxalate induce ROS production by renal epithelium. Mitochondria and NADPH oxidase are involved in ROS production
Inflammation	Activation of NLRP 3 inflammasome is required for VSMC calcification	Activation of NLRP3 Inflammasome
Osteogenic transformation (OT)	OT of VSMC	OT of renal tubular epithelial cells
Transcription factors involved	RUNX2 and Osterix	RUNX1 and 2, Osterix
Bone specific gene and protein expression	BMP, OPN, OCN, MGP	BMP, OPG, OPN, MGP, Osteocalcin, Osteonectin, Fibronectin
Mineralization modulators	OPN, OCN, MGP, Fetuin, Lipids	OPN, MGP, Fetuin, Osteocalcin, Lipids, THP
Monocyte/ macrophages	Macrophages play critical role in plaque calcification. M1 macrophages associated with plaque calcification and M2 with plaque regression	Macrophages are common around interstitial crystals. M1 related genes are upregulated and M2 related genes are downregulated in kidneys of stone patients
Matrix vesicles/ exosomes/apoptotic bodies	VC starts in membrane bound vesicles produced by transformed VSMC and apoptotic bodies produced by death of lymphocytes and macrophages	Membrane bound vesicles are associated with both intratubular and interstitial calcifications and are likely starting point for interstitial calcification
Mineralization progress	Mineralization continues by calcification of apoptotic bodies and collagen fibers in extracellular matrix	Mineralization continues by calcification of apoptotic bodies and collagen fibers in extracellular matrix

Results based on animal model, cell culture as well as limited number of clinical studies. (From Khan *et al.* [69].)

sponse and are also well-known modulators of crystallization in the urine (Table 1) [1,69,107–112]. Osteopontin, a phosphorylated glycoprotein, the most common matrix constituent, is a pro-inflammatory cytokine and can act as both a promoter and inhibitor of crystal formation, aggregation and attachment to epithelial surfaces. Urinary prothrombin fragment 1 is formed during conversion of prothrombin to thrombin and is excreted in urine. It binds calcium and plays a role in coagulation, and recruitment and activation of immune cells. It is an inhibitor of crystal growth and aggregation. Of the many proteins present in the urine, CaOx crystals selectively incorporate OPN and UPFT-1 [16,113–115]. Albumin is common in blood, urine and stone matrix. It promotes crystal formation and adhesion. Albumin production is reduced in response to inflammation and hypoalbuminaemia is considered a mortality predictor in patients with renal failure. Calgranulins, a family of S100 calcium binding proteins function as damage associated molecular pattern signaling through the receptor for advanced glycation products and as endogenous ligands for tool-like receptor. They are common in stone matrix and have been shown to inhibit CaOx crystallization in urine. Tamm–Horsfall Protein or uromodulin, a large glycoprotein expressed mainly in ascending limb of the loop of Henle and proximal part of the distal tubule,

is excreted in the urine in large amounts. It modulates certain steps in inflammation as well as CaOx crystallization and their retention within the kidneys. Inter alpha trypsin inhibitor is a plasma protein complex of a light chain covalently bound to heavy chains 1 and 2. Both light and heavy chains are excreted in the urine and have been shown to inhibit CaOx crystallization and adhesion to tubular epithelium. Matrix-GLA protein contains glutamate residues requiring vitamin K for activation, and functions primarily as an inhibitor of vascular calcification. Fetuin A is plasma glycoprotein, has CaP and TGFB cytokine binding sites and has anti-inflammatory properties.

Macromolecules inhibitors of crystallization present in the kidneys and urine, such as MGP, OPN and Fetuin A, are also inhibitors of mineralization of vascular smooth muscle [84]. MGP inhibits vascular calcification [116] and regulates activities of bone morphogenetic protein 2 (BMP2) [117]. Even though it was first isolated from bone [118], the expression of *MGP* mRNA is fivefold higher in rat kidneys than in bone [119]. There is widespread arterial calcification in $Mgp^{-/-}$ mice, which starts as amorphous CaP, and eventually transforms into hydroxyapatite and carbonate apatite [120]. MGP may also play a role in kidney stone formation. *MGP* polymorphisms might be involved in the development of CaOx kidney stone disease in Japanese [121] and Chinese patients [122].

Fetuin A, which is encoded by *AHSG*, has high affinity for CaP and is highly enriched in both mineralized tissues [123] and pathological calcifications [124]. Knocking out AHSG gene in mice causes extensive soft tissue calcification [123]. In humans, cardiovascular calcification and aortic stiffness in patients with kidney failure is associated with serum Fetuin A deficit [125,126]. The urine, kidneys and serum of kidney stone patients have lower Fetuin A levels than healthy controls [127].

Osteopontin is highly phosphorylated with multiple functions and plays a role in both calcification and inflammation [128–130]. It is modulator of crystallization of CaOx as well as CaP and is prominent in both mineralized tissue and soft tissue calcifications. Knockout of OPN leads to deposition of CaOx in hyperoxaluric mice [111]. It is a chemoattractant for macrophages and T-cells and involved in secretion of IL-3, IL-10, IL-12, interferon-γ, integrin αvB3, NF$\kappa\beta$. *SPP1* gene that encodes for OPN, is upregulated in renal tissues of kidney stone patients [28].

Lipids and membranes are present in both the kidney stone matrix as well as vascular calcification. Oxidative stress and inflammation are considered two major pathological mechanisms for endothelial dysfunction. Membrane bound extracellular vesicles derived from smooth muscle cells, valvular interstitial cells and macrophages act similar to matrix vesicles and act as mediators of calcification [92,131]. We have found that lipid contents of the kidney stone matrix [132], as well as tubular epithelial brush border membrane vesicles can act as mediator of both CaP and CaOx crystallization *in vitro* [36,133]. Stone formers urine contains more acidic phospholipids, considered to be involved in promoting calcification, than the urine of non-stone formers [134]. The ultrastructure of human calcified aortic valve [92], appears to be analogous to the ultrastructure of Randall's plaque seen in the kidneys of patients with idiopathic CaOx kidney stones [1,8,69]. Both show membrane bound vesicles with and without needle shaped crystals associated with collagen fibers.

As far as the presence of organic matrix is concerned, all calcifications, physiological or pathological, either human or animal, have a matrix. Apparently any biomolecule present at the site of calcification becomes incorporated into the organic matrix. However some, such as OPN and urinary prothrombin fragment 1, and perhaps inter-alpha-inhibitors are preferentially and specifically incorporated into the crystals. Thus crystals are actually not pure crystals with a protein coat but bio-crystal unit.

A review of the current literature about Randall's plaques, plugs and idiopathic CaOx kidney stone and experimental data obtained through animal model and tissue culture studies discussed above indicates that: (1) at least the early steps of stone pathogenesis are more complicated than simple increase in urinary supersaturation; (2) there is oxidative stress, injury and inflammation at some stages during stone pathogenesis; (3) intratubular crystallization and parenchymal crystal deposition is a common occurrence. Based upon these observations, we have proposed that hypercalciuria, hyperoxaluria and hypocitraturia induce tubular crystallization activating

many systems including renin–angiotensin system and nicotinamide adenine dinucleotide phosphate (NADPH) oxidase, leading to an increase in the production of reactive oxygen species (ROS). In response, exposed cells produce crystallization modulators such as OPN, matrix Gla protein (MGP), bone morphogenetic proteins (BMPs) and alkaline phosphatase (ALP). Activation of NOD-, LRR- and pyrin domain-containing protein 3 (NLRP3) inflammasome, causes the production of caspases and inflammatory cytokines that promote macrophage infiltration. Under normal conditions inhibitors keep the crystals small which are passed out during urination. Some of the crystals are taken in by the cells and are phagocytosed. Some are extruded into the interstitium where they attract macrophages and are taken care of by them. However, in the presence of continuing high calcium, oxalate and low citrate, as is possible in many kidney stone formers, there is development of oxidative stress and epithelial cells are unable to produce sufficient amounts of inhibitors. Epithelial cells undergo osteogenic changes, produce inflammatory cytokines attracting macrophages and their transformation from anti-inflammatory to pro-inflammatory. This leads to inflammation and deposition of collagen. Transformed epithelial cells, cellular apoptosis as well as macrophages produce calcifying vesicles. From then on, interstitial calcification progresses through the mineralization of collagen and other components of the extracellular matrix. Growing outward it reaches the sub-urothelial space on papillary surface and appears as Randall's plaque. Exposure of the plaque to the pelvic urine might be brought about by metalloprotease mediated disruption of the tight junctions between cells of the covering urothelium. Involvement of matrix metalloproteinases (MMP) in crystal associated diseases of the kidneys has, so far not been investigated. MMPs are increased by oxidative stress and inflammation and a number of MMPs are known to play a role in a variety of kidney diseases [135,136], including vascular calcification in chronic kidney disease [137]. Some of the proposed steps are summarized in Figure 9.

Once RP's become exposed to the urine, stones develop by the addition of CaOx crystals which can either happen by crystal nucleation on the exposed plaque or by accretion of CaOx crystals formed independently in the surrounding urine. Crystallization will depend upon the presence of calcium, and oxalate as well as various crystallization modulators present in th urine. It should, however, be recognized that CaOx crystals will not be depositing or nucleating on CaP crystals. Both CaOx and CaP crystals as well as the plaque are covered by an organic matrix. Therefore CaOx crystals would most probably nucleate on the organic material present on the CaP crystals or plaque. If there is any specificity of interaction between the two types of crystals, it is based upon the specific macromolecule present on crystal surfaces. For example, OPN shown to be specifically incorporated into the CaOx crystals is well known for its crystal nucleation capabilities when adsorbed onto a surface.

The formation of ductal plugs is dependent upon the supersaturation. Acute and or persistent supersaturation will result in excessive crystallization reducing their movement with the urine. Slowing will allow the aggregates to increase their mass and further reduce their pace through the tubules eventually blocking their lumens. Bends in the tubules as well as changes in their luminal diameter will also hamper movement of crystal aggregates. Blockage of the openings of the terminal collecting ducts would create a lesion exposed to the pelvic urine. From this point, further growth will most likely be similar to that what happens on the exposed Randall's plaque discussed above. Crystalline overgrowth and development of stone will depend upon the concentration of calcium, oxalate, citrate as well as many macromolecular modulators of crystallization present in the pelvic urine.

5. Conclusions

Kidney's immune system responds to the abnormal excretion of stone forming ions and salts by producing macromolecules to control and inhibit crystallization within the renal tubules. Most of the small crystals are expelled as crystalluria. Others are dispatched into the interstitium where macrophages are responsible for their disposal. Failure of the normal appropriate renal response leads to injury, inflammation and the formation of the plaques and plugs. Many of the calcium binding macromolecules produced to modulate and inhibit crystallization, become incorporated into the crystals and become part of the organic matrix of the stones. The matrix is

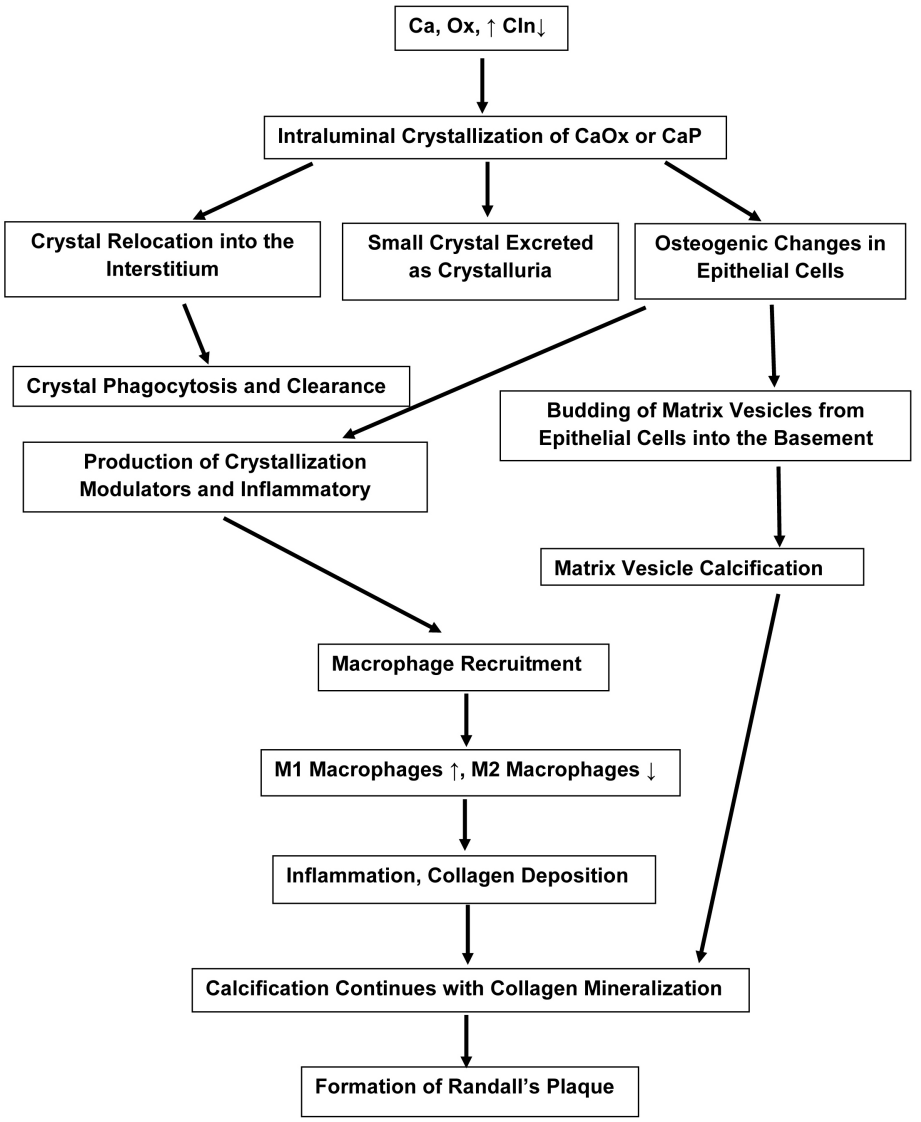

Figure 9. Proposed scheme for the development of Randall's plaques based upon experimental and clinical data as discussed. Urinary supersaturation with respect to the CaOx and CaP, which is mainly a result of high calcium (Ca) and oxalate (Ox) and lower crystallization inhibitory potential (CIn), is increased. Transient increase produce small crystals which are excreted in the urine. Some of the crystals are endocytosed, moved into the interstitium leading to their clearance. Persistent but mild increase in supersaturation and continued production of intraluminal crystals provokes an immunological response. There are osteogenic changes and production of inflammatory and crystallization modulatory molecules. There is production of matrix vesicles through budding from the epithelial cells into the basement membrane, as well as degradation of interstitial elements and macrophages. Calcification continues with the mineralization of collagen, matrix vesicles and cellular degradation products, eventually reaching the base of the urothelium. It is now ready to be exposed to the pelvic urine through the urothelial loss and become a nidus for the development of a stone.

neither a glue nor a mortar binding individually-produced inorganic crystals but a component of the bio-crystals, biological CaP or CaOx.

Conflicts of interest

The author declares no conflict of interest.

References

[1] S. R. Khan *et al.*, *Nat. Rev. Dis. Primers*, 2016, **2**, article no. 16008.
[2] A. Evan *et al.*, *Kidney Int.*, 2006, **69**, 1313-1318.
[3] M. Daudon, D. Bazin, E. Letavernier, *Urolithiasis*, 2015, **43**, 5-11.
[4] F. L. Coe *et al.*, *Urol. Res.*, 2010, **38**, 239-247.
[5] A. P. Evan, R. J. Unwin, J. C. Williams Jr, *Nephron. Physiol.*, 2011, **119**, 49-53.
[6] S. R. Khan, B. K. Canales, *Urolithiasis*, 2015, **43**, 109-123.
[7] R. C. Haggit, J. A. Pitcock, *J. Urol.*, 1971, **106**, 342-347.
[8] S. R. Khan *et al.*, *J. Urol.*, 2012, **187**, 1094-1100.
[9] A. P. Evan *et al.*, *Kidney Int.*, 2007, **72**, 1503-1511.
[10] X. Carpentier *et al.*, *J. Trace Elem. Med. Biol.*, 2011, **25**, 160-165.
[11] R. L. Kuo *et al.*, *Kidney Int.*, 2003, **64**, 2150-2154.
[12] F. L. Coe, A. Evan, E. Worcester, *Clin. J. Am. Soc. Nephrol.*, 2011, **6**, 2083-2092.
[13] F. L. Coe, E. M. Worcester, A. P. Evan, *Nat. Rev. Nephrol.*, 2016, **12**, 519-533.
[14] L. Chen *et al.*, *PLoS One*, 2017, **12**, article no. e0187103.
[15] S. V. Wiener *et al.*, *Connect Tissue Res.*, 2018, **59**, 102-110.
[16] M. D. McKee, A. Nanci, S. R. Khan, *J. Bone Miner. Res.*, 1995, **10**, 1913-1929.
[17] A. N. Kapustin, C. M. Shanahan, *Arterioscler. Thromb. Vasc. Biol.*, 2011, **31**, 2169-2171.
[18] J. A. Gordon *et al.*, *Bone*, 2007, **41**, 462-473.
[19] N. X. Chen, S. M. Moe, *Semin. Nephrol.*, 2004, **24**, 61-68.
[20] C. M. Shanahan *et al.*, *Z. Kardiol.*, 2000, **89**, 63-68.
[21] S. R. Khan, B. Finlayson, R. Hackett, *Urology*, 1984, **23**, 194-199.
[22] C. Verrier *et al.*, *J. Urol.*, 2016, **196**, 1566-1574.
[23] C. Gay *et al.*, *ACS Nano.*, 2020, **14**, 1823-1836.
[24] S. Winfree *et al.*, *Urolithiasis*, 2021, **49**, 123-135.
[25] A. Okada *et al.*, *BMC Urol.*, 2018, **18**, article no. 19.
[26] R. S. Hsi *et al.*, *BJU Int.*, 2017, **119**, 177-184.
[27] K. Taguchi *et al.*, *J. Am. Soc. Nephrol.*, 2017, **28**, 333-347.
[28] K. Taguchi *et al.*, *Sci. Rep.*, 2016, **6**, article no. 35167.
[29] L. Anderson, D. J. Mc, *Surg. Gynecol. Obstet.*, 1946, **82**, 275-282.
[30] A. Y. Sun *et al.*, *J. Endourol.*, 2018, **32**, 236-244.
[31] A. Randall, *J. Urol.*, 1940, **44**, 580-589.
[32] L. Huguet *et al.*, *Urolithiasis*, 2018, **46**, 333-341.
[33] S. R. Khan, *Urol. Res.*, 1995, **23**, 71-79.
[34] S. R. Khan, *Arch. Ital. Urol. Androl.*, 2011, **83**, 1-5.
[35] S. R. Khan, *Urolithiasis*, 2017, **45**, 75-87.
[36] S. R. Khan *et al.*, *Calcif. Tissue Int.*, 2000, **66**, 90-96.
[37] S. R. Khan *et al.*, *Calcif. Tissue Int.*, 1996, **59**, 357-365.
[38] S. R. Khan *et al.*, *Kidney Int.*, 2002, **62**, 2062-2072.
[39] F. L. Coe *et al.*, *Urol. Res.*, 2010, **38**, 147-160.
[40] M. P. Linnes *et al.*, *Kidney Int.*, 2013, **84**, 818-825.
[41] J. C. Williams Jr *et al.*, *Urol. Res.*, 2010, **38**, 477-484.
[42] S. R. Khan, D. J. Kok, *Front. Biosci.*, 2004, **9**, 1450-1482.
[43] S. D. Roberts, M. I. Resnick, *J. Urol.*, 1986, **135**, 1078-1083.
[44] F. A. Witzmann *et al.*, *Proteome Sci.*, 2016, **14**, article no. 4.
[45] B. Dussol *et al.*, *Urol. Res.*, 1995, **23**, 45-51.
[46] B. K. Canales *et al.*, *Urology*, 2010, **76**, article no. 1017 e13–e20.
[47] M. L. Merchant *et al.*, *Am. J. Physiol. Renal. Physiol.*, 2008, **295**, F1254-F1258.
[48] N. Okumura *et al.*, *PLoS One*, 2013, **8**, article no. e68624.
[49] C. Boonla *et al.*, *Clin. Chim. Acta*, 2014, **429**, 81-89.
[50] D. G. Reid *et al.*, *J. Urol.*, 2011, **185**, 725-730.
[51] W. H. Boyce, N. M. Sulkin, *J. Clin. Invest.*, 1956, **35**, 1067-1079.
[52] W. H. Boyce, F. K. Garvey, *J. Urol.*, 1956, **76**, 213-227.
[53] W. H. Boyce, J. S. King Jr, *J. Urol.*, 1959, **81**, 351-365.
[54] S. R. Khan, R. L. Hackett, *Scan. Electron. Microsc.*, 1986, 761-765.
[55] S. R. Khan, B. Finlayson, R. L. Hackett, *J. Urol.*, 1983, **130**, 992-995.
[56] S. R. Khan, R. L. Hackett, *Calcif. Tissue Int.*, 1987, **41**, 157-163.
[57] S. R. Khan, R. L. Hackett, *Scan. Electron. Microsc.*, 1984, 935-941.
[58] S. R. Khan, R. L. Hackett, *J. Urol.*, 1993, **150**, 239-245.
[59] S. R. Khan, P. N. Shevock, R. L. Hackett, *Calcif. Tissue Int.*, 1988, **42**, 91-96.
[60] S. R. Khan, *Scan. Microsc.*, 1995, **9**, 597-614, discussion 614–616.
[61] S. R. Khan, *J. Urol.*, 1997, **157**, 376-383.
[62] A. P. Evan *et al.*, *Am. J. Physiol. Renal. Physiol.*, 2018, **315**, F1236-F1242.
[63] A. Randall, *Ann. Surg.*, 1937, **105**, 1009-1027.
[64] S. Thamilselvan, R. L. Hackett, S. R. Khan, *J. Am. Soc. Nephrol.*, 1999, **10**, S452-S456.
[65] M. H. Khaskhali, K. J. Byer, S. R. Khan, *Urol. Res.*, 2009, **37**, 1-6.
[66] S. R. Khan, *Urol. Res.*, 2012, **40**, 95-112.
[67] S. R. Khan, *Kidney Int.*, 2007, **71**, 83, author reply 83–84.
[68] S. R. Khan, *J. Urol.*, 2013, **189**, 803-811.
[69] S. R. Khan, B. K. Canales, P. R. Dominguez-Gutierrez, *Nat. Rev. Nephrol.*, 2021, **17**, 417-433.
[70] S. R. Khan, *Urol. Res.*, 2006, **34**, 86-91.
[71] S. Joshi, W. Wang, S. R. Khan, *PLoS One*, 2017, **12**, article no. e0185009.
[72] S. R. Mulay *et al.*, *J. Clin. Invest.*, 2013, **123**, 236-246.
[73] S. R. Mulay, H. J. Anders, *Nat. Rev. Nephrol.*, 2017., **13**, 226-240.
[74] I. Ludwig-Portugall *et al.*, *Kidney Int.*, 2016, **90**, 525-539.
[75] S. R. Khan, S. Joshi, W. Wang, *J. Am. Soc. Nephrol.*, 2014, **25**, article no. 101A.
[76] S. Joshi *et al.*, *Biochim. Biophys. Acta*, 2015, **1852**, 2000-2012.
[77] Z. Jia *et al.*, *Urology*, 2014, **83**, article no. 509.
[78] E. Letavernier *et al.*, *J. Am. Soc. Nephrol.*, 2018, **29**, 2337-2347.
[79] V. Pomozi *et al.*, *J. Invest. Dermatol.*, 2019, **139**, 1082-1088.
[80] S. R. Khan, P. A. Glenton, *Am. J. Physiol. Renal Physiol.*, 2008, **294**, F1109-F1115.

[81] Y. Liu *et al.*, *Am. J. Physiol. Renal Physiol.*, 2010, **299**, F469-F478.
[82] L. Mo *et al.*, *Am. J. Physiol. Renal Physiol.*, 2007, **293**, F1935-F1943.
[83] G. Gambaro *et al.*, *J. Nephrol.*, 2004, **17**, 774-777.
[84] R. C. Shroff, C. M. Shanahan, *Semin. Dial.*, 2007, **20**, 103-109.
[85] N. X. Chen, K. D. O'Neill, S. M. Moe, *Kidney Int.*, 2018, **93**, 343-354.
[86] C. H. Byon *et al.*, *J. Biol. Chem.*, 2008, **283**, 15319-15327.
[87] S. Jono *et al.*, *Circ. Res.*, 2000, **87**, E10-E17.
[88] A. N. Kapustin *et al.*, *Circ. Res.*, 2011, **109**, e1-e12.
[89] A. N. Kapustin, C. M. Shanahan, *Trends Cardiovasc. Med.*, 2012, **22**, 133-137.
[90] C. M. Shanahan *et al.*, *Circ. Res.*, 2011, **109**, 697-711.
[91] F. Zhu *et al.*, *J. Cell. Physiol.*, 2012, **227**, 2677-2685.
[92] J. B. Krohn *et al.*, *J. Physiol.*, 2016, **594**, 2895-2903.
[93] L. Zazzeroni, G. Faggioli, G. Pasquinelli, *Eur. J. Vasc. Endovasc. Surg.*, 2018, **55**, 425-432.
[94] M. Schoppet *et al.*, *Kidney Int.*, 2008, **73**, 384-390.
[95] M. Murshed, M. D. McKee, *Curr. Opin. Nephrol. Hypertens.*, 2010, **19**, 359-365.
[96] E. E. Golub, *Semin. Immunopathol.*, 2011, **33**, 409-417.
[97] A. L. Durham *et al.*, *Cardiovasc. Res.*, 2018, **114**, 590-600.
[98] A. P. Evan *et al.*, *Kidney Int.*, 2005, **68**, 145-154.
[99] S. R. Khan, G. Gambaro, *Anat. Rec. (Hoboken)*, 2016, **299**, 5-7.
[100] A. P. Evan *et al.*, *Anat. Rec. (Hoboken)*, 2015, **298**, 865-877.
[101] G. Chinetti-Gbaguidi *et al.*, *Circ. Res.*, 2017, **121**, 19-30.
[102] C. M. Shanahan, *Curr. Opin. Nephrol. Hypertens.*, 2005, **14**, 361-367.
[103] A. Shioi, Y. Ikari, *J. Atheroscler. Thromb.*, 2018, **25**, 294-303.
[104] J. Xi *et al.*, *J. Cell. Physiol.*, 2019, **234**, 11463-11473.
[105] R. de Water *et al.*, *Am. J. Kidney Dis.*, 1999, **33**, 761-771.
[106] R. de Water *et al.*, *Am. J. Kidney Dis.*, 2000, **36**, 615-625.
[107] D. J. Kok, S. R. Khan, *Kidney Int.*, 1994, **46**, 847-854.
[108] R. L. Ryall, *Nephron. Physiol.*, 2004, **98**, 37-42.
[109] E. M. Worcester, *J. Am. Soc. Nephrol.*, 1994, **5**, 46-53.
[110] A. M. Beshensky *et al.*, *J. Am. Soc. Nephrol.*, 2001, **12**, 2108-2116.
[111] J. A. Wesson *et al.*, *J. Am. Soc. Nephrol.*, 2003, **14**, 139-147.
[112] S. R. Khan, *Urol. Int.*, 1997, **59**, 59-71.
[113] F. Atmani, P. A. Glenton, S. R. Khan, *Urol. Res.*, 1998, **26**, 201-207.
[114] A. M. Stapleton, R. J. Simpson, R. L. Ryall, *Biochem. Biophys. Res. Commun.*, 1993, **195**, 1199-1203.
[115] S. Maslamani, P. A. Glenton, S. R. Khan, *J. Urol.*, 2000, **164**, 230-236.
[116] L. J. Schurgers, E. C. Cranenburg, C. Vermeer, *Thromb. Haemost.*, 2008, **100**, 593-603.
[117] C. M. Shanahan *et al.*, *Crit. Rev. Eukaryot. Gene Expr.*, 1998, **8**, 357-375.
[118] P. A. Price, M. R. Urist, Y. Otawara, *Biochem. Biophys. Res. Commun.*, 1983, **117**, 765-771.
[119] J. D. Fraser, P. A. Price, *J. Biol. Chem.*, 1988, **263**, 11033-11036.
[120] O. Gourgas *et al.*, *Arterioscler. Thromb. Vasc. Biol.*, 2018, **38**, 363-372.
[121] B. Gao *et al.*, *J. Urol.*, 2007, **177**, 2361-2365.
[122] X. Lu *et al.*, *Gene*, 2012, **511**, 127-130.
[123] W. Jahnen-Dechent *et al.*, *J. Mol. Med. (Berl.)*, 2008, **86**, 379-389.
[124] S. M. Moe *et al.*, *Kidney Int.*, 2005, **67**, 2295-2304.
[125] M. Ketteler *et al.*, *Kidney Int. Suppl.*, 2003, **63**, S84-S87.
[126] M. L. Ford *et al.*, *Hypertension*, 2010, **55**, 1110-1115.
[127] A. Mehrsai *et al.*, *Cent. European. J. Urol.*, 2017, **70**, 394-399.
[128] M. Mazzali *et al.*, *QJM*, 2002, **95**, 3-13.
[129] S. A. Steitz *et al.*, *Am. J. Pathol.*, 2002, **161**, 2035-2046.
[130] C. M. Giachelli, S. Steitz, *Matrix Biol.*, 2000, **19**, 615-622.
[131] S. E. New, E. Aikawa, *Arterioscler. Thromb. Vasc. Biol.*, 2013, **33**, 1753-1758.
[132] S. R. Khan, P. N. Shevock, R. L. Hackett, *J. Urol.*, 1988, **139**, 418-422.
[133] J. M. Fasano, S. R. Khan, *Kidney Int.*, 2001, **59**, 169-178.
[134] S. R. Khan, P. A. Glenton, *Br. J. Urol.*, 1996, **77**, 506-511.
[135] J. M. Catania, G. Chen, A. R. Parrish, *Am. J. Physiol. Renal. Physiol.*, 2007, **292**, F905-F9011.
[136] O. Zakiyanov *et al.*, *Kidney Blood Press. Res.*, 2019, **44**, 298-330.
[137] N. X. Chen *et al.*, *Am. J. Nephrol.*, 2011, **34**, 211-219.

Comptes Rendus
Chimie
2022, Vol. 25, Special Issue S1, p. 373-391
https://doi.org/10.5802/crchim.102

Microcrystalline pathologies: Clinical issues and nanochemistry

Randall's plaque as the origin of idiopathic calcium oxalate stone formation: an update

Els Van de Perre [a,*], Dominique Bazin [b], Vincent Estrade [c], Elise Bouderlique [d], Karl Martin Wissing [a], Michel Daudon [d,e] and Emmanuel Letavernier [d,e]

[a] Vrije Universiteit Brussel (VUB), Universitair Ziekenhuis Brussel (UZ Brussel), Nephrology Department, Brussels, Belgium

[b] Université Paris-Saclay, CNRS, Institut de Chimie Physique, 91405, Orsay, France

[c] Centre Hospitalier Universitaire Pellegrin, Urology Department, Bordeaux, France

[d] Sorbonne Université, Institut National de la Santé et de la Recherche Médicale (INSERM), Unité Mixte de Recherche UMR S 1155, Paris, France

[e] Assistance Publique - Hôpitaux de Paris, Hôpital Tenon, Service des Explorations Fonctionnelles Multidisciplinaires, Paris, France

E-mails: Els.vandeperre@uzbrussel.be (E. Van de Perre), Dominique.bazin@universite-paris-saclay.fr (D. Bazin), Vincent.estrade@gmail.com (V. Estrade), Eliseboud@aol.com (E. Bouderlique), KarlMartin.Wissing@uzbrussel.be (K. M. Wissing), Michel.daudon@aphp.fr (M. Daudon), Emmanuel.letavernier@aphp.fr (E. Letavernier)

Abstract. The majority of idiopathic calcium oxalate kidney stones form on the Randall's plaque, a subepithelial calcium phosphate plaque at the renal papilla. The formation mechanisms of the Randall's plaque and associated calcium oxalate stones remain incompletely understood. This article provides an historical overview of the research performed on this topic, describes the current epidemiological trends of Randall's plaque-associated kidney stone formation and reviews the suggested formation mechanisms of Randall's plaque and associated calcium oxalate stones. Finally, this overview highlights the recent advances made on the subject, including the development of an animal model.

Keywords. Randall's plaque, Calcium phosphate, Calcium oxalate stones, Kidney stones, Nephrolithiasis.

Published online: 17 August 2021

1. Introduction

Nephrolithiasis is extremely common, with estimated prevalence of 10.6% in males and 7.1% in females in the United States of America [1]. In 66.0–93.0% of kidney stones, the main component is calcium oxalate, comprising calcium oxalate monohydrate (COM) in 42.8–74.4% and calcium oxalate dihydrate (COD) in 18.6–23.2% [2,3]. Up to 90% of calcium oxalate kidney stones are categorized as idiopathic as no causative hereditary or acquired disease can be detected [4]. The exact mechanism of

* Corresponding author.

idiopathic calcium oxalate stone formation remains to be elucidated but the majority of these stones appears to form by a process of heterogeneous nucleation on a subepithelial calcium phosphate plaque at the papilla, known as the Randall's plaque.

The plaque is named after Alexander Randall, who, in the 1930's, described the presence of a subepithelial interstitial calcium plaque at the renal papilla in 19.6% of 1154 pairs of cadaveric kidneys, as an initiating lesion that precedes kidney stone formation [5,6]. Randall observed that some of the plaques lost their epithelial lining and hypothesized that they would act as a nidus for subsequent stone formation after their exposure to calyceal urine. Actually, Randall reported small calculi attached to the calcium plaque in 2.3% of patients. Additionally, he found several kidney stones to display a smooth depression, indicative of prior papillary attachment and on some of them, remnants of the calcium plaque.

Randall additionally described a second, less frequently occurring papillary lesion, now known as tubular plugs or Randall's plugs, which consists of crystal deposition in the lumina of the collecting ducts [6]. Tubular plugging rather than interstitial calcium phosphate plaque formation has been hypothesized as the initiating lesion for brushite stone formation and for kidney stones formed in patients with primary hyperparathyroidism, enteric hyperoxaluria and distal renal tubular acidosis [7–9]. The subject of tubular plugging is however not the topic of this overview.

Randall's groundbreaking publications concerning the interstitial calcium plaque were followed by several reports of his contemporaries, who confirmed the presence of papillary plaques in cadaveric kidneys and nephrectomy samples with attached stones in a proportion of these plaques [10–13].

After a long period with few publications on the matter, research on the subject of Randall's plaque regained new interest at the end of the 20th century, likely driven by the increased performance of urologic endoscopy, during which Randall's plaques can be directly visualized at the papillary tip and due to the increased prevalence of Randall's plaque-associated kidney stone formation. Especially the formation mechanism of Randall's plaque, which remains incompletely understood, has been addressed in many publications during the last two decades.

2. Epidemiology

Early publications by Randall [5], Rosenow [10], Vermooten [12] and Haggitt and Pitcock [14] reported the presence of papillary plaques in 8.3–23.0% of unselected autopsy kidney specimens, detected by macroscopic or hand lens examination. The papillary plaques were described as cream-coloured to white lesions, with size ranging from 1–2 mm to a surface occupying the entire papilla. Vermooten [12] described a difference in prevalence between the Caucasian and the native South African population, with respectively 17.2 and 4.3% of subjects displaying Randall's plaque.

Light microscopic examinations of papillary tissue of unselected autopsy kidneys and nephrectomy samples, including kidneys affected by nephrolithiasis, could detect medullary calcifications in all kidneys in the reports of Anderson and McDonald [13] and Haggitt and Pitock [14], while Anderson could only detect calcifications in 12% of autopsy kidneys [11]. It has to be mentioned that in the last study children and infants formed 36% of the study population, with only 5.7% of them displaying Randall's plaque and frequently examination on only one renal section, not always containing papillary tissue, was performed. Finally, Ruggera *et al.* [15] reported interstitial calcifications detected by microscopic examination in 42.9% of papillary biopsies performed during ureterorenoscopy in stone-forming patients.

Optical microscopy of eliminated kidney stones grown on Randall's plaque typically reveals a papillary umbilication, the imprint of the previous papillary attachment, which can be found as an irregular depression, while some stones can display plaque remnants at the umbilication as well [16] (Figure 1). Daudon *et al.* [16] described papillary umbilication in 19.5% of 45,774 examined calculi. The rates augment to 39.0% taking only spontaneously eliminated stones into account and even to 66.1% considering only spontaneously passed COM stones [4]. Cifuentes Delatte *et al.* described papillary umbilication in 28.4% of 500 spontaneously passed stones [17] and plaque remnants in 72.4% of 87 umbilicated kidney stones [18]. Letavernier *et al.* [19] reported 34.1% of 30149 intact calcium oxalate stones to show Randall's plaque remnants.

Recently, micro-computed tomographic imaging (micro-CT), using 3-dimensional X-ray imaging

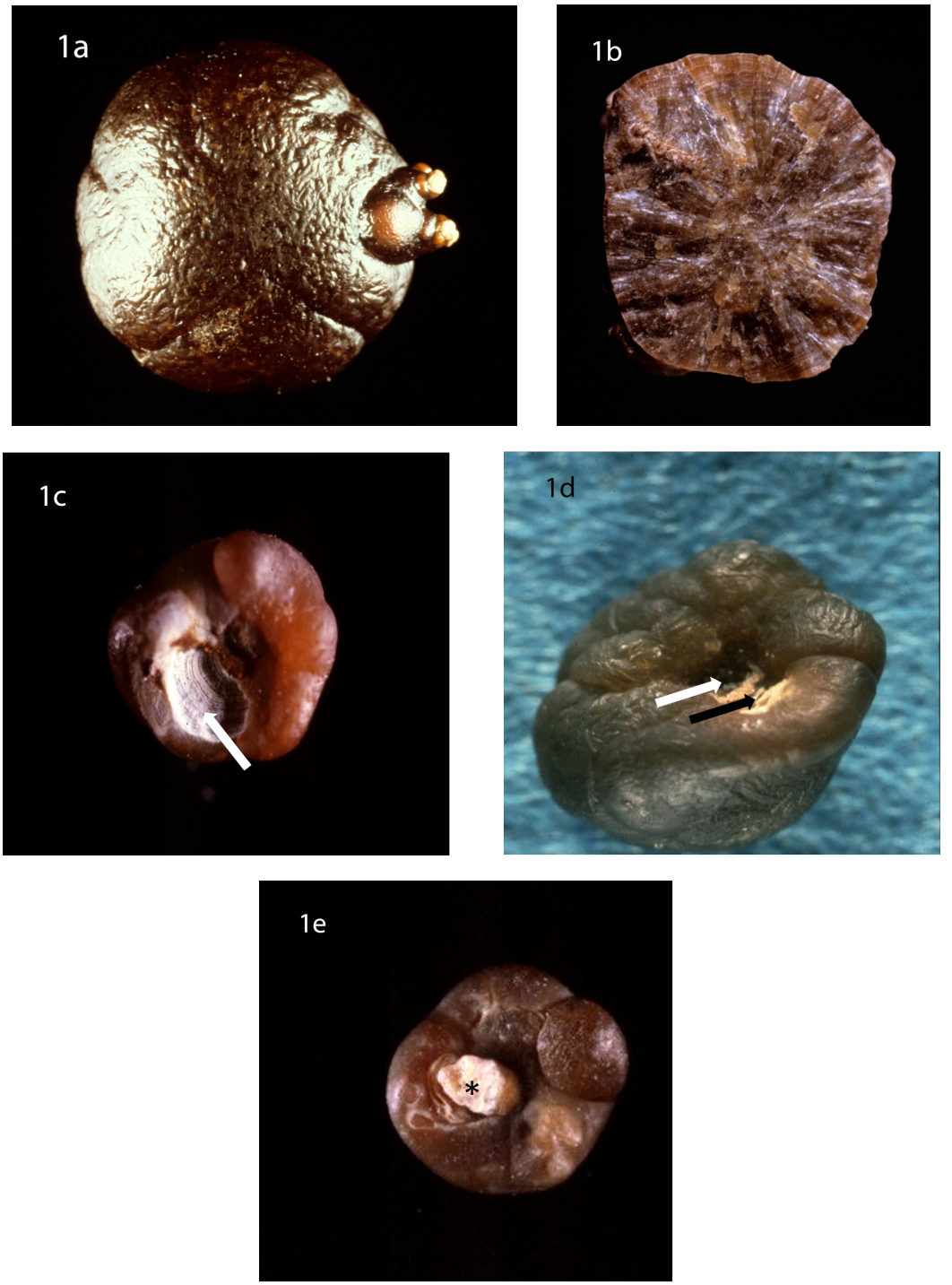

Figure 1. (a) Optical microscopy showing COM stone without papillary umbilication and without Randall's plaque. (b) Optical microscopy showing sectioned COM stone without papillary umbilication and without Randall's plaque. (c) Optical microscopy showing COM stone with papillary umbilication. (d) Optical microscopy showing COM stone with papillary umbilication and plaque remnants. (e) Optical microscopy showing COM stone with Randall's plaque. White arrow: papillary umbilication, black arrow: Randall's plaque remnants, asterisk: massive Randall's plaque.

with microscopic level resolution was introduced by Williams *et al.* [20], who reported the technique to be able to detect calcium phosphate deposits in papillary tissue samples and in eliminated kidney stones.

Rates of Randall's plaque detected by endoscopic urological procedures including ureterorenoscopy and percutaneous techniques are much higher compared to the rates detected by optical microscopy as current urological techniques including shockwave, ultrasound and laser frequently destroy kidney stones and Randall's plaques, resulting in loss of the plaque or papillary umbilication for optical microscopy. Endoscopic urological examination reveals Randall's plaques as irregular, glossy, whitish lesions surrounding the opening of the collecting ducts [7,9] (Figure 2). In American studies performing endoscopic urology, Randall's plaque was detected in 73.7–100.0% of stone-forming patients [9,21,22], with 47.8–100.0% of idiopathic calcium stone formers showing evidence of attached stones at the Randall's plaques [22,23]. European studies have reported lower rates and detected Randall's plaque in 56.7% of 289 stone formers [24].

A difference in density, determined by computed tomography attenuation values between renal papilla of stone formers and non-stone formers respectively has been reported [25,26]. In 2013, a study comparing papillary surface plaque coverage determined during percutaneous nephrolithotomy and by means of single- or dual-energy helical computed tomography, reported the absence of correlation between the radiological and endoscopic results and concluded current computed tomography techniques not able to detect Randall's plaque [27]. Indeed, only huge Randall's plaque can be visualized with computed tomography. In the future, novel techniques with higher spatial resolution, reduced image noise and improved material differentiation might constitute a good means for the non-invasive detection of Randall's plaque [28].

Although less prevalent than in stone formers [21, 29] and displaying lower papillary tissue plaque coverage [30], Randall's plaques are also detected in non-stone-forming patients, supporting the theory of their formation as a precursor lesion for kidney stone formation, with subsequent pathogenic steps required for actual kidney stone formation. Light microscopic examination could detect papillary calcifications in 69.4% of 62 cadaveric kidneys of non-stone formers [31]. Endoscopic urology detected Randall's plaque in 42.9% of seven non-stone-forming patients in an American study [21], while the rate was 27.7% of 173 non-stone-forming patients in a European study [24]. Finally, incipient papillary Randall's plaque could be detected in 72.7% of non-stone formers [32].

Endoscopic urological studies reported Randall's plaque to uniformly affect all or nearly all papilla [9, 21,22,24]. Verrier *et al.* [32] observed that nearly all examined papilla were affected by incipient interstitial calcifications, suggesting that the process of Randall's plaque formation a minima is extremely frequent.

Randall's plaque has been described in children [33,34]. Epidemiological data [19] demonstrate that the proportion of kidney stones formed on Randall's plaque is maximal in the age category of 20–29 years and that this proportion reduces with age, as opposed to the initial idea that plaque formation and associated kidney stone formation increases with age [12]. Additionally, the age of the patients presenting the largest proportion of Randall's plaque-associated kidney stone formation has decreased during the last decades [35].

The frequency of Randall's plaque-associated stone formation is rising. In France, a significant increase in proportion of calcium oxalate stones formed on Randall's plaque between the early 1980's and the early 2010's, in both males and females, but most pronounced in young females was reported [19,35]. In general, the proportion of Randall's plaque-associated kidney stone formation increased from 5.7% in the period 1978–1985 to 23.3% during the period 2000–2006 [16,19]. Additionally, the proportion of papillary tissue covered by Randall's plaque is correlated with the number of stones formed [30], supporting the theory of Randall's plaque as an initiating lesion for kidney stone formation and highlighting the plaque's relevance for recurrent stone formation. The increasing proportion of calcium oxalate stone formation on Randall's plaque is hypothesized to contribute to the rising frequency of calcium oxalate kidney stone formation in general [36–38]. Additional epidemiological studies are needed to confirm these findings but are impeded by the frequent loss of papillary umbilication and plaque remnants due to urological

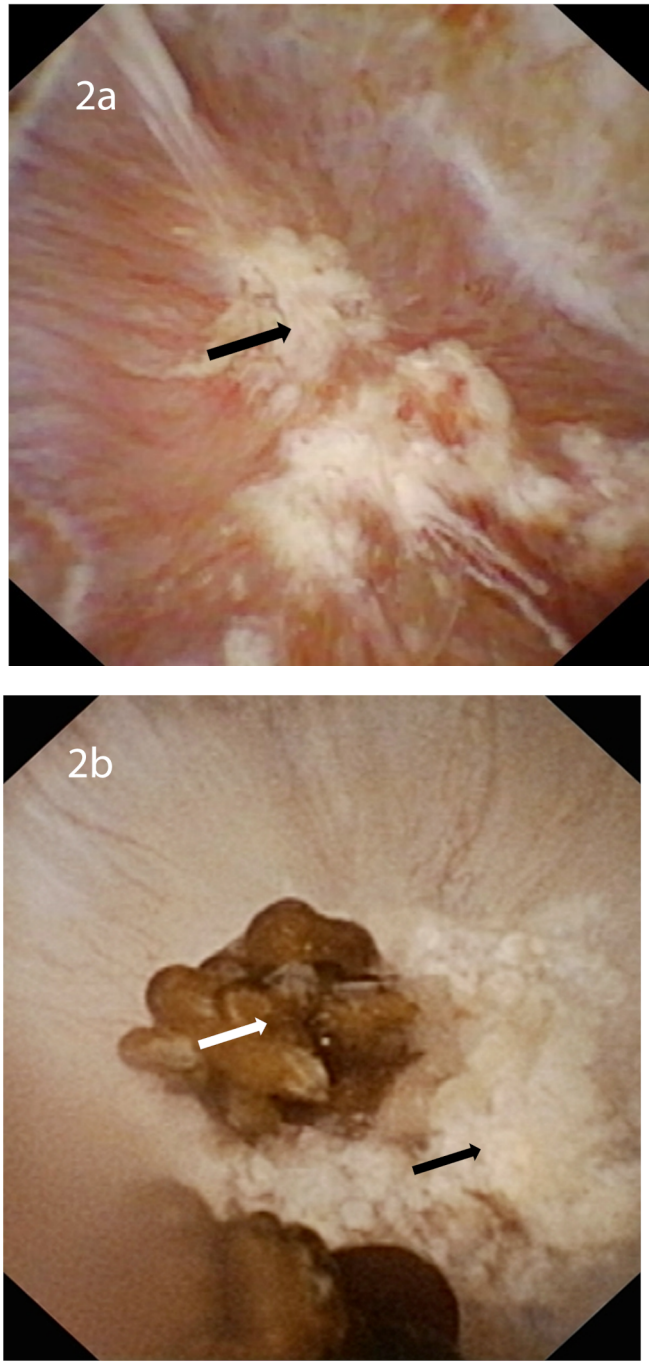

Figure 2. (a) Endoscopic urological view of Randall's plaques at the papilla, visible as irregular, glossy, whitish lesions. (b) Endoscopic urological view of Randall's plaques with attached COM stones. Black arrow: Randall's plaque, white arrow: COM stone.

fragmentation techniques and by the non-universal use of morphoconstitutional stone analysis [39–41] comprising optic microscopy and Fourier-transform infrared spectroscopy (FTIR) [42] or X-ray analysis as the gold standard for kidney stone analysis and Randall's plaque detection.

3. Update on the mechanism of Randall's plaque formation

3.1. *Historical data*

Already at the initial description by Randall [5] and later confirmed by other authors [13,14,43,44], it was reported that Randall's plaque consists of interstitial calcification, with sparing of the tubular lumina, nor were calcifications found in the cytoplasm of tubular cells [14]. Initially, Randall hypothesized that plaque formation begins at the basement membranes of the collecting tubules, initiated by lesions at its epithelium [5]. In the same time period, Vermooten described the localization of the calcifications not only at the collagen fibers of the basement membrane of collecting tubules but also at collagen fibers of the vasa recta and in the interstitium [12,43]. In 1970, Cooke was the first to report the calcifications to be related to the basement membrane of the thin limbs of the loop of Henle [31]. At the end of the 20th century, Stoller *et al.* [44] supported the findings of Vermooten [12,43] and reported the calcifications to be located at the basement membrane of the collecting tubules, the interstitium and the vasa recta.

3.2. *Randall's plaque formation begins in the basement membranes of the thin limbs of Henle's loop and of the vasa recta*

Although the exact mechanism of Randall's plaque formation as an ectopic calcification remains to be elucidated, it has been demonstrated that Randall's plaque formation begins in the basement membranes of the thin limbs of the loops of Henle and of the vasa recta at the tip of the renal papilla, with subsequent spreading into the interstitial tissue to the suburothelium [7,32]. Electron microscopy shows that at incipient Randall's plaques and papillary tissue adjacent to Randall's plaques, calcifications can be found around the basement membranes of the thin loop of Henle and of the vasa recta, in close contact with collagen bundles. Calcifications can be found as isolated, small, spherical homogeneous electron-dense deposits but can also be detected as larger deposits with a multilaminated morphology showing radial crystallization [7, 32,45]. The small spherical deposits can merge to form larger depositions, forming syncytia and losing their identity, spreading in the interstitium, in close contact with collagen bundles and organizing into complete or incomplete rings or cuffs, surrounding the thin loops and the vasa recta. Completely surrounded tubules may show cytoplasm vacuolization or basement membrane detachment as signs of cellular damage. Evan *et al.* [7], supported by later publications [46], confirmed the absence of crystals in vascular and tubular cells even in larger plaques and reported also the tubular lumina to remain free, except for extensive calcification. The interstitial deposits can extend to and surround the collecting tubules as described by Stoller *et al.* [44], without affecting the collecting tubular cells, but it is clear that the collecting tubules are not the initial site of Randall's plaque formation [7,32].

Scanning electron microscopy of a Randall's plaque typically shows the presence of calcified tubules and calcified blood vessels [18] (Figure 3). Linnes [9] described in approximately 40% of patients with Randall's plaque the occurrence of tubular plugs, evidenced by means of ureterorenoscopy. Also Verrier *et al.* [32] reported tubular plugs consisting of carbonated apatite and amorphous calcium phosphate to be present in 79.6% of papillary tissues with or without incipient Randall's plaques, but the plugs were not in contact with the interstitial calcifications, suggesting that the formation of incipient Randall's plaque is not related to these intratubular crystals. The role of tubular plugs and their interaction with interstitial calcium phosphate deposition remains unknown.

3.3. *In situ calcium phosphate precipitation driven by calcium phosphate supersaturation and the role of hypercalciuria*

The mechanism for calcium phosphate deposition at the basement membrane of the thin loops of Henle and of the vasa recta is incompletely elucidated but

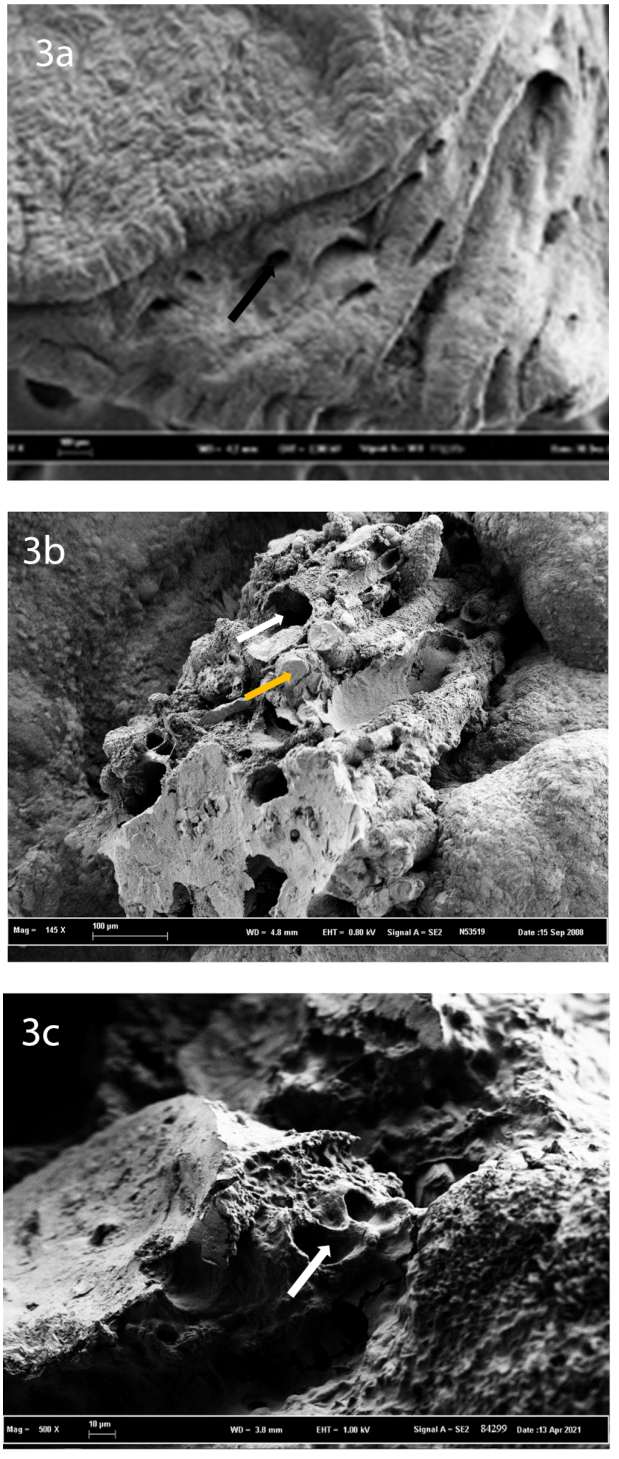

Figure 3. (a) Scanning electron microscopy showing a normal papilla. (b) Scanning electron microscopy showing a Randall's plaque fragment in a kidney stone with calcified tubules and tubular plugs. (c) Scanning electron microscopy showing a Randall's plaque fragment in a kidney stone with calcified tubules. Black arrow: opening of a collecting duct, white arrow: calcified tubule, orange arrow: calcium phosphate tubular plug.

a process of in situ calcium phosphate precipitation, driven by high local calcium phosphate supersaturation, influenced by high calcium concentration and high pH is assumed. As no intracytoplasmic crystals or calcifications in the tubular epithelial cells are detected [7] and incipient Randall's plaque are not in contact with tubular plugs [32], a process of intratubular calcium phosphate crystal formation, driven by high calcium phosphate supersaturation in the tubular fluid of Henle's loop [47] with subsequent paracellular or transcellular transport-like endocytosis [48], resulting in basolateral release of calcium phosphate crystals or increased calcium phosphate excretion is less likely. The hypothesis of in situ interstitial calcium phosphate crystal formation is supported by the description of a medullary concentration gradient for calcium, caused by passive calcium diffusion from the loops of Henle, predominantly at the thick ascending limb, and from the descending vasa recta [49–51]. It is hypothesized that high calcium delivery out of the proximal tubule, as seen in idiopathic hypercalciuria, where there is reduced proximal tubular calcium reabsorption [52], results in increased passive calcium diffusion at the thick ascending limb of Henle, increasing the medullary calcium concentration. Descending vasa recta tend to wash this outer medullary calcium to the inner medulla but are permeable to calcium, resulting in passive calcium diffusion to the interstitium, increasing the medullary calcium concentration and contributing to the calcium phosphate supersaturation at the papillary tip. Additionally, reduced water reabsorption at the collecting duct due to increased serum calcium levels at the vasa recta, can additionally increase calcium phosphate supersaturation [53]. Finally, it has been hypothesized that there is a high papillary pH in patients with Randall's plaque [54], further contributing to high papillary calcium phosphate supersaturation. Calcium diffusion from the thin limbs of Henle's loop is assumed to contribute very little to the high calcium phosphate supersaturation at their basement membranes as no vectorial calcium or phosphate transport occurs at this site and the permeability for calcium and phosphate is very low. The diffusion of calcium from the descending vasa recta close to the thin limbs is assumed to be the major source of calcium phosphate supersaturation at the interstitium in their vicinity. In fact, the basement membranes of the thin limbs of the loop of Henle are thick, composed of collagen and mucopolysaccharides, an electrostatically charged matrix, easily attracting calcium phosphate with progressive calcification. Recently, Evan *et al.* [55] demonstrated that Randall's plaque formation begins at the ascending thin limbs of Henle's loop and not at the descending thin limbs. These findings support the theory of calcium washdown from the interstitial tissue at the thick ascending limb to the interstitial tissue at the papillary tip and the ascending thin limbs by the vasa recta, as the descending vasa recta are preferentially located near the ascending thin limbs of Henle's loop and as the ascending thin limbs are impermeable to water as opposed to the descending thin limbs [56], impairing dilution of the local high interstitial calcium concentration.

In this "vas washdown" theory, with subsequent in situ calcium phosphate precipitation at the basement membranes of the vasa recta and of the thin limbs of the loop of Henle, calcium concentration of the tubular fluid delivered to the thick ascending limb is an important determinant of Randall's plaque formation. Many findings support this. First, idiopathic hypercalciuria is the most common metabolic abnormality in idiopathic calcium oxalate stone formers [57]. The coverage of papillary tissue by Randall's plaque is correlated with calciuria [29,58]. Randall's plaque is more pronounced in idiopathic hypercalciuric stone formers compared to other stone formers [8]. The importance of calciuria could also explain the difference in frequency of Randall's plaque described by Vermooten [10] between Caucasian subjects and the native South African population, who are known to have lower levels of calciuria. Finally, in a study comparing calcium oxalate stone formers related and unrelated to Randall's plaque, Letavernier *et al.* [19] described higher serum levels of osteocalcin to be associated with Randall's plaque formation, and to a lesser extent increased serum calcium levels and phosphate reabsorption rate. As the osteocalcin gene has a vitamin D receptor response element in its promotor region, increased osteocalcin levels are a marker of vitamin D receptor activation. These findings suggest the implication of vitamin D activation in Randall's plaque formation. Activated vitamin D (1,25-OH_2-vitamin D), by means of increased gastro-intestinal calcium absorption, is an important mediator of renal calcium excretion.

Letavernier *et al.* [19] speculated that the increased prevalence of Randall's plaque-associated kidney stone formation might be partly attributed to the increased use of vitamin D supplements. Although controversial, some publications have reported the relationship between vitamin D supplements and kidney stone formation, especially when combined with calcium supplements [59]. Recently, combined administration of vitamin D and calcium resulted in accelerated calcification in an animal model of Randall's plaque formation [60]. The role of vitamin D supplementation in the formation of Randall's plaque in predisposed subjects was again raised by the authors but remains a subject of controversy and debate.

According to this theory, measures that augment proximal tubular calcium reabsorption and hence reduce calcium delivery to the thick ascending limb, like thiazide diuretics and low sodium diet, could reduce Randall's plaque formation. On the other hand, increased Randall's plaque formation can be generated by further increase in calcium phosphate supersaturation at the papillary tip, which is typically induced by a Western diet rich in salt and protein, the major dietary determinants of renal calcium excretion. Additionally, high protein intake results in high urinary phosphate excretion and an acid load, leading to basolateral, interstitial bicarbonate excretion in parallel to tubular proton excretion by alpha-intercalated cells of the collecting ducts, additionally raising calcium phosphate supersaturation. Indeed, besides correlation with calciuria and low urinary volume, Kuo *et al.* [29] described low urinary pH to correlate with Randall's plaque papillary coverage.

3.4. *Crystalline and organic composition of Randall's plaque*

The main crystalline components of Randall's plaque are carbonated apatite (carbapatite) and amorphous carbonated calcium phosphate [4]. Amorphous carbonated calcium phosphate is more predominantly found at the core of the Randall's plaque, suggesting that it is the first crystalline phase formed, with subsequent formation of the more stable apatite at the surface [61]. Sodium hydrogen urate can be detected in 3.4% of Randall's plaque identified during morphoconstitutional kidney stone analysis [4,62]. Additionally, whitlockite is detected in 1.0% of Randall's plaques, identified at kidney stone surface [4] and has also been observed in incipient Randall's plaque in the papilla [32]. Brushite can be detected in 0.34% of Randall's plaques, identified at kidney stone surface [4]. Finally, minor compounds including octacalcium phosphate, struvite, calcite, uric acid, bobierrite, ammonium urate, potassium urate, opaline silica and porphyrines have been detected as well [4,17]. The variety of the different crystalline phases detected at the Randall's plaque and the variable levels of carbonation, ranging between 5 and 35% [16] likely reflect the involvement of different formation mechanisms.

Randall's plaque contains an organic matrix rich in proteins, glycosaminoglycans and lipids, containing collagen fibers and other yet unidentified fibrillary material, membrane vesicles and other cellular degradation products [45,63]. Already described by Haggitt and Pitcock in 1971 [14], electron microscopy shows that deposits can have a multilaminated morphology [7,32]. The lamination reflects the alternating layers between mineral phases as shown by the light regions and organic material represented by the electron-dense layers [64,65]. Evan *et al.* [65] reported that all mineral deposits, even the smallest, are surrounded by organic material, with larger deposits described to "float in an organic sea". Already reported in historical papers [12,43], Khan *et al.* [45] confirmed the mineral spherical deposits to be in close association with collagen fibers and described the presence of membrane vesicles. The authors hypothesized that in the process of aggregation and merging of the initial spherical mineral deposits to form larger deposits, collagen and membranous degradation products interact with the enlarging calcification, getting calcified as well. Very recently, Gay *et al.* [63] demonstrated at higher magnification that, although plaques are located in collagen-rich regions, there is a gap between the collagen fibers and microcalcifications in the incipient calcium plaque, assuming no close interaction with collagen in the early steps of Randall's plaque formation. The authors confirmed the findings of Khan *et al.* [45] and reported the presence of vesicles containing calcium phosphate crystals. A predominant macromolecule detected at Randall's plaque is osteopontin [66], which is located at the interface of the apatite crystal and the surrounding organic matrix [65]. The exact role of this crystallization modulator [67,68],

which is also implicated in pathological vessel calcification [69] and bone mineralization, is unknown. Other macromolecules detected at Randall's plaque organic matrix include osteocalcin, bone sialoprotein and inter-alpha-trypsin inhibitor heavy chain 3 [70].

Very recently, Winfree *et al.* [71] described, in a study using microscopic fluorescence, an autofluorescence signal unique to Randall's plaque, present on calcium oxalate stones and in papilla and different from the signal detected from the attached stone. As autofluorescence originates from proteins and metabolites, these findings suggest the presence of a unique, yet unidentified proteinaceous or metabolic deposition in the organic components of Randall's plaque, which is absent in stone matrix and urine. Such results may be in line with the presence of some specific metalloproteins in the Randall's plaque. Actually, high levels of zinc [72] have been identified at Randall's plaque, that may be related to inflammatory processes and to the presence of metalloproteinases.

3.5. *Alternative theories on Randall's plaque formation*

3.5.1. *The vascular theory of Randall's plaque formation*

The vascular theory of Randall's plaque formation, postulated by Stoller and colleagues [73,74], hypothesizes that injury to the vasa recta located at the renal papilla, could lead to an atherosclerosis-like reaction resulting in vessel wall calcification, through the implication of oxidative stress and production of reactive oxygen species (ROS). Erosion of the vessel wall calcification into the surrounding interstitium could subsequently lead to Randall's plaque formation. Vasa recta at the renal papillary tip are hypothesized to be especially prone to injury due to several reasons: the changing blood flow from laminar to turbulent, the hypoxic and hyperosmolar environment and the decreased vascular resistance and flow velocity in the ascending vessels. The theory is supported by the association between cardiovascular disease [75], aortic and coronary artery calcification [76], cardiovascular risk factors like hypertension [77], metabolic syndrome, obesity [78] and diabetes mellitus [79] and kidney stone disease. Additionally, similarities between vascular calcification and Randall's plaque formation are reported, comprising the involvement of collagen and membrane vesicles and peripheral growth of the calcification [45], the implication of inflammation and oxidative stress [80], involvement of the same macromolecules regulating urine crystallization and vascular calcification like osteopontin, similarities between the different types of calcifications involved at incipient Randall's plaque and cardiovascular calcification [63] and the detection of lipid droplets in interstitial cells of the medulla [81]. Additionally, the protective effect of statins for the development of kidney stones was described, suggesting the involvement of a common pathogenic step [82]. So far however, no report has described the presence of plaques or calcifications in the vasa recta, which disproves this theory.

3.5.2. *Theory involving progression of proximal intratubular calcifications*

Recently, several publications [83–85] provide arguments to support a novel version of a hypothesis postulated in 1954 by Carr [86] in which the distal interstitial Randall's plaque is hypothesized to be formed secondary to intratubular crystal deposition in the proximal upper medulla and using the "medullo-papillary complex" as a functional unit, consisting of a papilla with the corresponding medulla, displaying specific pressure and chemical gradients. Micro-CT and electron microscopy of nephrectomy samples showed the presence of proximal intratubular calcifications in all kidneys, even in those without Randall's plaques. The amount of proximal intratubular crystal deposition correlated with the presence of Randall's plaque interstitial distal mineralization. The theory postulates that proximal intratubular crystal deposition, caused by high calcium phosphate supersaturation in short nephrons that display low fluid velocity, precedes distal interstitial calcification due to changes in fluid dynamics secondary to obstructed tubular lumina in the proximal medulla.

3.5.3. *The involvement of cellular osteogenic differentiation*

Another theory on Randall's plaque formation hypothesizes the involvement of osteogenic differentiation of cells like pericytes, fibroblasts, vasa recta en-

dothelial cells and/or tubular epithelial cells. First, osteopontin, the main protein identified in Randall's plaque [65], is also a known marker of osteogenesis. Additionally, increased expression of the osteogenic markers Runt-related transcription factor 2 (Runx2), osteocalcin and osteopontin has been reported in Randall's plaque papillary tissue compared to normal papillary tissue [87]. Mezzabotta *et al.* [88], performing experiments on papillary cells from a medullary sponge kidney (MSK) patient, reported spontaneous calcium phosphate deposition and osteogenic differentiation with expression of osteogenic markers by cells resembling pericytes or stromal stem cells. The authors hypothesized that the papilla might be a perivascular niche where pericytes, involved in other ectopic calcification processes and present around the vasa recta can undergo osteogenic differentiation leading to Randall's plaque formation. These findings were however contradicted by a study of Evan *et al.*, who could not detect interstitial mineral deposition in areas positive for Runx2 and osteoblast transcription factor (osterix) gene expression in papillary biopsies of MSK patients [89]. Additionally, no Runx2 or osterix gene expression was observed at Randall's plaque in idiopathic calcium stone formers. Zhu *et al.* [87] showed that under osteogenic conditions also renal interstitial fibroblasts can display an osteogenic phenotype, forming calcium phosphate nodules similar to Randall's plaque calcium phosphate deposition, with increased expression of osteogenic markers, hypothesizing the implication of osteogenic differentiation of fibroblasts in the formation of Randall's plaque. Finally, Priante *et al.* [90] reported the osteogenic differentiation of human renal proximal tubular cells with expression of osteogenic markers and leading to deposition of calcium phosphate crystals in osteogenic conditions. Also Khan *et al.* [91,92] hypothesize that cellular osteogenic differentiation is implicated in Randall's plaque formation and postulate that in conditions of stress, like exposure to calcium oxalate crystals, hyperoxaluria, hypercalciuria or hypocitraturia, renal epithelial cells or vasa recta endothelial cells undergo osteogenic differentiation, associated with increased expression of osteogenic markers, reduced expression of crystallization inhibitors like fetuin and matrix Gla protein and the release of membrane vesicles.

4. Mechanism of stone formation

The disruption of the papillary epithelium with subsequent exposure of the plaque to the calyceal urine [45,93] occurs through an unknown mechanism, although the involvement of matrix metalloproteinases and sheer force due to the growth of the plaque has been suggested [94].

Although Randall initially hypothesized Randall's plaque to act as a nidus for the formation of different types of stones including calcium oxalate, calcium phosphate and uric acid [6], it is now known that the bulk of stones formed on Randall's plaque are COM stones [17,46]. Analysed by FTIR, 89.5% of 10462 Randall's plaque-associated kidney stones were made of COM pure or mixed with COD [62]. Alternatively, 88% of calcium oxalate stone formers have endoscopic evidence of Randall's plaque [21] and 66.1% of spontaneously passed COM stones display papillary umbilication [4]. Randall's plaque was most common in calcium oxalate stone formers compared to stone formers of other stone types [58]. Additionally, the crystalline phase in direct contact with the Randall's plaque is almost exclusively COM [16] (Figure 4). Other crystalline phases may be present, like COD, hydroxyapatite and uric acid but these are not in direct contact with the Randall's plaque [35,93]. Calcium oxalate crystal nucleation is driven by calcium oxalate supersaturation, influenced by urinary volume, urinary calcium and oxalate concentration and concentration of crystallization inhibitors like citrate.

At this point, it is worth to recall some physicochemical properties of biological apatites to assess the interface between the Randall's plaque and COM crystallites. Biological apatites which belong to physiological or pathological calcifications share physicochemical characteristics [95–97]. The morphology of biological apatite nanocrystals can be described as a thin platelet morphology elongated towards the c-axis with crystal size of less than 50–100 nm length and a few nanometers of thickness [98]. As discussed in detail in several papers [99–101], it seems that apatite nanocrystals display an apatitic core and a more or less structured surface hydrated layer including non-apatitic domains. As discussed previously, on this amorphous surface of biological apatite, proteins are present, with Tamm–Horsfall protein (THP) and osteopontin identified at the interface. Such struc-

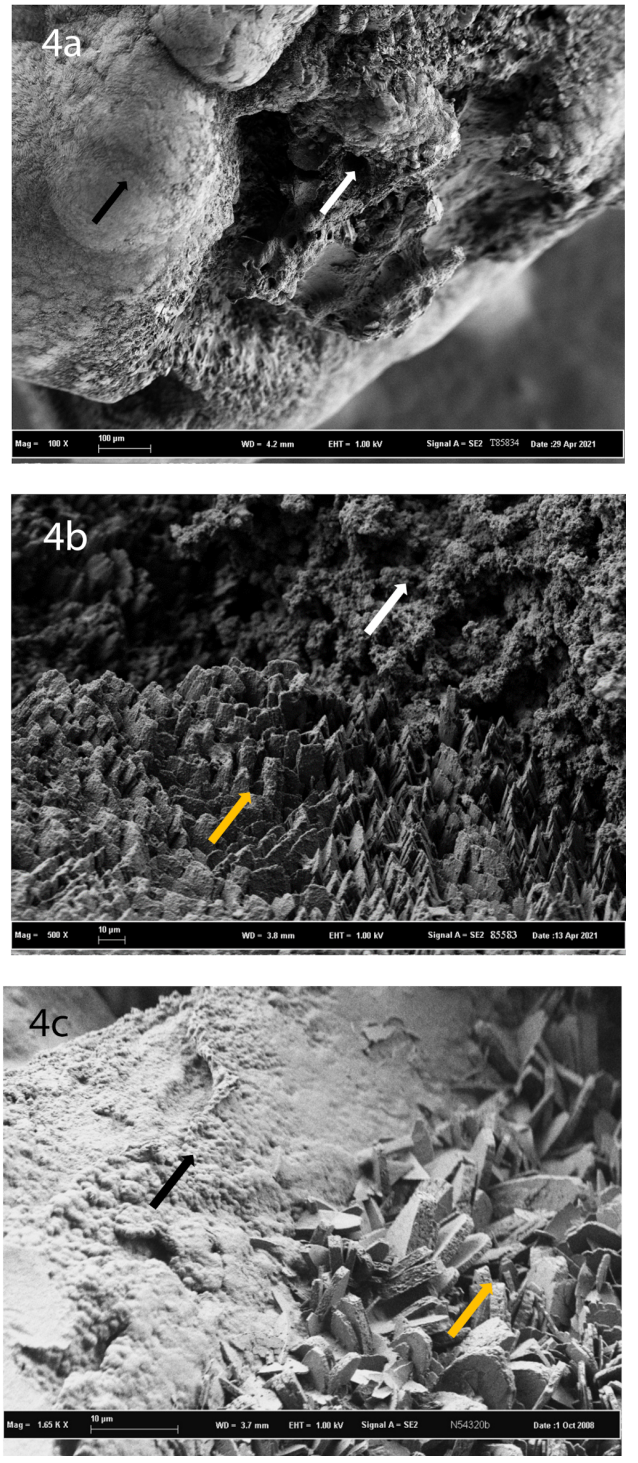

Figure 4. (a–c) Scanning Electron Microscopy showing the interface of Randall's plaque and COM crystals at different magnification. (a) Black arrow: COM stone, white arrow: Randall's plaque. (b) White arrow: carbonated apatite spherical deposits at Randall's plaque, orange arrow: COM crystals. (c) Black arrow: carbonated apatite spherical deposits at Randall's plaque, orange arrow: COM crystals.

tural characteristics are thus not compatible with an epitaxy between the Randall's plaque and COM crystals [102,103]. As illustrated by Figure 4c, large randomly oriented COM crystals are trapped on a phase of carbapatite crystals embedded in proteins acting as a "glue" [104]. This mechanism explains why patients without risk to generate kidney stones (the size of COM crystals is compatible with natural expulsion) become at risk due to the presence of the Randall's plaque.

Other mechanisms of calcium oxalate stone formation on Randall's plaque have been proposed. First, the efficient nucleation of calcium oxalate by apatite has been demonstrated in vitro [102,103]. Evan *et al.*, in a study on biopsy specimens comprising papillary stones with their renal attachment [93], described the plaque, exposed to calyceal urine, to be covered by a "ribbon" composed of alternating layers of organic material and mineral phases, which were identified by FTIR as amorphous phosphate. Eventually, progressing through the alternating layers of the interface, the authors reported that calcium oxalate crystals get mixed with apatite and progressively become the dominant mineral phase, resulting in calcium oxalate stone formation. Also Khan *et al.* reported Randall's plaque crystal deposits to be present under a fibrous layer [45] and hypothesized that stone growth occurs by organic matrix-associated nucleation of calcium oxalate or by the transformation of the outer layer of calcium phosphate crystals into calcium oxalate crystals [91]. It has been suggested that in case of low diuresis or high acid load, proton secretion in the distal nephron results in low urinary pH leading to dissolution of calcium phosphate crystals, giving rise to increased calcium concentration and increasing calcium oxalate supersaturation, resulting in replacement of the external calcium phosphate crystals at the plaque by calcium oxalate crystals by a process of crystal dissolution and recrystallization [105–107]. Sethmann *et al.* [46] however described in a study examining papillary stones the presence of an initial layer of COM crystals at the surface of the Randall's plaque, subsequently covered by a "crust" containing calcium phosphate, suggesting no macromolecular interface at COM crystal precipitation.

5. Recent developments

Recently, research on Randall's plaque is not just merely focusing on factors influencing urinary lithogenicity or supersaturation but also recognizes factors aiding crystal nucleation or crystal germination, as the first step of Randall's plaque formation [108], like membrane vesicles, which can be linked to inflammation.

5.1. *The role of membrane vesicles in crystal nucleation*

The presence of membrane vesicles at Randall's plaque was first described by Khan *et al.* [45] and later confirmed by Verrier *et al.* [32]. Recently, in their nanoscale analysis of incipient Randall's plaque, the same research group [63] confirmed these observations as they described the presence of different types of calcifications. Next to the earlier described microcalcifications, situated at collagen-rich areas, which can either be homogeneous, rounded, electron-dense, small spheres with an approximate diameter of 50 nm or display a larger, multilaminated morphology with 0.5–2 μm diameter [45], they observed various types of nanocalcifications: solitary mineral particles with an average diameter of 100 nm, but also vesicles with a nitrogen-rich "membrane". These membrane vesicles contain nanocrystals with a diffraction pattern that suggests the presence of crystalline apatite and can be found solitary or in clusters, giving rise to larger depositions and subsequently form microcalcifications. Membrane vesicles or exosomes, consisting of phospholipids can be liberated by all cell types as a response to certain physiological and pathological stimuli and have been suggested to be implicated in other physiological and pathological calcification processes including bone formation [109] and vascular calcification [110]. In vitro, it has been demonstrated that phospholipids induce apatite precipitation [111]. In animal models, experimentally induced calcium oxalate crystals are always accompanied by membrane fragments [112]. Although it remains unclear from which cells these membrane vesicles are released, their presence at the incipient Randall's plaque, their

nanocrystal content and the analogy with other calcification processes lead the authors to hypothesize membrane vesicles to be implicated in the very first steps of Randall's plaque formation by aiding the heterogeneous nucleation of calcium phosphate.

In addition, Gay *et al.* [63] described a variety of compositions of different mineral particles. All mineral particles were mainly composed of calcium phosphate but more than half of them additionally had calcium carbonate located at their centre, while other mineral particles do not contain calcium carbonate but display high amounts of organic compounds. The authors suggested that both carbonate and organic compounds act as driving factors for nucleation of the respective mineral particles.

5.2. *The role of inflammation, oxidative stress and immunity*

Although Evan *et al.* [7] explicitly reported the absence of cellular injury, inflammation and interstitial fibrosis, recently, the involvement of the immune system, inflammation, oxidative stress, apoptosis and kidney injury in the pathogenesis of Randall's plaque and in the formation of calcium stones in general, has received much attention [113–115].

First, certain biomolecules detected at Randall's plaque, including THP, osteopontin and inter-alpha-trypsin inhibitor are also implicated in the immune/inflammatory system. Additionally, the high zinc content of Randall's plaque described by Carpentier *et al.* [72] points towards an inflammatory mechanism involved in Randall's plaque formation, as zinc has been demonstrated to be implicated in inflammation [116,117]. Further, the presence of sodium hydrogen urate, although rare, in Randall's plaque, was accompanied by various cells, suggesting an inflammatory process [62]. It is known that not only sodium hydrogen urate, but also many other crystals, are involved in inflammation by triggering the nod-like receptor protein 3 (NLRP3) inflammasome pathway and other pathways leading to IL-1 production and innate immune cell recruitment [118]. Additionally, Taguchi *et al.* [66] described the upregulation of gene expression pathways associated with inflammation, oxidative stress and kidney injury and the increased expression of proinflammatory cytokines, immune cells and cellular apoptosis in Randall's plaque tissue compared to non-Randall's plaque papillary tissue of calcium oxalate stone formers. Sun *et al.* [119] reported increased gene expression of inflammatory cytokines in papillary tissue of stone formers compared to controls, with the upregulation of CCL-2, CCL-7, CCR-2 and CSF1 suggesting the involvement of monocyte activation. Microarray analysis of genes expressed in renal papillary tissue of stone formers demonstrates an upregulation of genes associated with an M1 inflammatory macrophage phenotype and downregulation of genes linked to an M2 anti-inflammatory macrophage phenotype [120]. In fact, two macrophage phenotypes have been described with M2 anti-inflammatory macrophages being associated with crystal phagocytosis, suppression of stone formation and suppression of inflammatory damage, while M1 inflammatory macrophages would be associated with stone formation [121].

Animal and in vitro experiments have demonstrated that intratubular calcium oxalate crystals, formed in conditions of hyperoxaluria, induce an inflammatory response, that implicates ROS production, increased NLRP3 inflammasome activation and expression of inflammation-related genes and increased synthesis of molecules implicated in the inflammatory cascade including osteopontin, matrix Gla protein, fetuin and monocyte chemoattractant protein-1 (MCP-1) [122,123]. The inflammatory response leads to monocytes migration, surrounding intratubular and interstitial calcium oxalate crystals [112], followed by in situ monocytes differentiation towards macrophages. Depending on the local cytokine milieu and influenced by other mediators, a preferential differentiation towards an inflammatory macrophage phenotype is induced, resulting in tissue damage through the production of ROS and bioactive lipids like prostanoids and leukotrienes versus differentiation towards an anti-inflammatory phenotype, associated with crystal phagocytosis and prevention of kidney injury. M2 anti-inflammatory macrophages have been shown to clear calcium oxalate crystals by processes of clathrin-mediated endocytosis and phagocytosis, followed by release of inflammatory cytokines by the macrophages, leading to the additional recruitment of macrophages, neutrophils and dendritic cells. Patel *et al.* [124] hypothesized that an imbalance between oxidative and antioxidative forces with increased ROS production, induced by excessive calcium oxalate crystal depo-

sition, may result in mitochondrial damage of the monocytes, leading to impaired crystal elimination capacities and perhaps resulting in macrophage polarization towards an inflammatory phenotype and further enhancing tissue inflammation. Additionally, a possible role of the NLRP3 inflammasome [125] and the androgen receptor [126] in the differential polarization towards an inflammatory macrophage phenotype and tissue damage caused by calcium oxalate crystals has been suggested. Alternatively, the implication of Sirtuin 3 [127], a mitochondrial enzyme that decreases the production of ROS, in the preferential anti-inflammatory polarization of macrophages has been proposed. Finally, while short period exposure to calcium oxalate crystals induces an anti-inflammatory macrophage phenotype, prolonged exposure results in switch to a proinflammatory phenotype [128].

Although most animal and in vitro studies have focused on calcium oxalate crystals, some in vitro studies have reported similar reactions of renal epithelial cells after exposure to calcium phosphate crystals including cellular injury, increased production of ROS, cellular injury, upregulation of inflammatory mediators, production of MCP-1 and increased apoptotic activity [123,129,130].

Of note, most of the animal models based upon urinary calcium oxalate crystallization induce crystalline nephropathies (intratubular crystal precipitation) rather than kidney stone formation. Whether calcium oxalate crystals forming stones in urinary cavities induce inflammatory processes has not been proven in humans.

It is hypothesized that repeated and continuous exposure of renal epithelial cells to conditions like hyperoxaluria, hypercalciuria, calcium oxalate or calcium phosphate crystals induces oxidative stress and an inflammatory cascade including polarization towards an inflammatory macrophage phenotype and possibly the production of membrane vesicles as a facilitator of calcium phosphate nucleation. The ensuing continuous inflammation can lead to papillary damage, collagen deposition and calcification and ultimately Randall's plaque formation. An alternative hypothesis suggests the implication of inflammation only in the process of urothelial rupture after interstitial calcium phosphate deposition, resulting in exposure of the plaque to the calyceal urine and subsequent aggregation of calcium oxalate crystals [130].

Despite these findings, patients exhibiting Randall's plaque seem not prone to develop chronic kidney disease, although exact data on this subject are lacking.

5.3. *Development of an animal model and the role of inorganic pyrophosphate*

Advances in the knowledge of the formation mechanism of Randall's plaque have partly been hampered by the lack of an appropriate animal model of Randall's plaque formation. In the past, hyperoxaluric animal models [112,131,132] developed intratubular calcium oxalate crystal deposits with subsequent stone formation while animal models of hypercalciuria [133,134] developed intratubular calcium phosphate deposits with subsequent stone formation. $Npt2^{-/-}$ mice, knockout of NPT2 (SLC34A1), a Na^+-dependent phosphate transport protein 2A expressed on the luminal surface of the proximal tubule, produce both interstitial and intratubular deposits [135], just like THP-deficient mice [136,137]. Osteopontin-deficient animals did not consistently show interstitial calcifications [137,138]. Finally, Na^+/H^+ exchanger regulatory factor-1 (NHERF-1) knockout mice develop interstitial calcifications that are however not located at the basement membrane of the thin loops of Henle [139]. In conclusion, no model of interstitial calcification deposition as seen in Randall's plaque was developed until recently.

Pseudoxanthoma elasticum is a hereditary disorder characterized by ectopic calcification of elastic fibers in skin, retina and peripheral arteries. The disease is caused by mutations in the *ABCC6* gene, which encodes an ATP-binding cassette transporter, implicated in extracellular release of ATP, which due to its catabolism by ectonuclotide pyrophosphatase phosphodiesterase-1 (ENPP1) is the major source of inorganic pyrophosphate [140]. Inorganic pyrophosphate is a long known mineralization inhibitor and acts through inhibition of calcium phosphate crystallization and precipitation [141]. Low serum levels of inorganic pyrophosphate have been detected in patients with pseudoxanthoma elasticum [140]. Up to 39.8% of pseudoxanthoma elasticum patients have a history of nephrolithiasis [142,143], with morphoconstitutional stone analysis and results from computed tomography in a few patients suggesting a

Randall's plaque-driven stone formation. Rare cases reported even nephrocalcinosis [144,145]. *Abcc6*$^{-/-}$ mice have lower inorganic pyrophosphate urinary excretion and serum levels compared to controls and spontaneously develop interstitial calcifications at the tip of renal papilla with ageing [143]. The demonstrated interstitial calcifications are similar to the calcifications of Randall's plaque, namely located at the basement membrane of the loops of Henle and the vasa recta specifically at the tip of the renal papilla, consisting of spherulites with alternating concentric layers of calcium phosphate and organic compounds and containing apatite and amorphous calcium phosphate [143]. Supplementation with inorganic pyrophosphate results in increased serum inorganic pyrophosphate levels and reduced tissue calcifications [146–148], while combined administration of vitamin D and calcium accelerated interstitial calcifications in *Abcc6*$^{-/-}$ mice [60]. The *Abcc6*$^{-/-}$ mice animal model of Randall's plaque formation hence suggests the role of inorganic pyrophosphate in the formation of Randall's plaque, while the presence of merely hyperoxaluria, hypercalciuria or deficiency in macromolecules is insufficient to constitute a reliable model of Randall's plaque formation. In fact, not all studies were able to find a difference in urinary calcium excretion between calcium oxalate stone formers with and without Randall's plaque respectively [19,149] and urinary calcium excretion in *Abcc6*$^{-/-}$ was not different compared to wild type mice, suggesting that hypercalciuria is insufficient for the development of Randall's plaque and that additional deficiency of inhibitors like inorganic pyrophosphate is mandatory. Low urinary levels of inorganic pyrophosphate have been reported in stone formers [150–153], but currently it is unknown if patients with Randall's plaque display lower urinary levels of inorganic pyrophosphate compared to patients with stone formation unrelated to Randall's plaque. Measurement of inorganic pyrophosphate levels has been difficult in the past due to absence of reliable methods and the very low concentrations of inorganic pyrophosphate. As it has been demonstrated that oral pyrophosphate is partly absorbed [154] and increases serum levels, inorganic pyrophosphate supplementation can possibly constitute a treatment option for the prevention of Randall's plaque formation in the future.

6. Conclusion

The recent development of an animal model of Randall's plaque formation will likely accelerate research on Randall's plaque and associated kidney stone formation and will hopefully bring clarity to the exact formation mechanism of both Randall's plaque and associated calcium oxalate kidney stones. Additionally, the identification of inorganic pyrophosphate as a probable important determinant for the development of Randall's plaque leads to not only additional, so far unresolved, questions and problems like the development of reliable inorganic pyrophosphate measurement methods but also to some hopeful prospects for the future, as inorganic pyrophosphate supplementation might constitute a treatment option in patients with Randall's plaque-associated kidney stone formation.

References

[1] C. D. Scales Jr., A. C. Smith, J. M. Hanley, C. S. Saigal, *Eur. Urol.*, 2012, **62**, 160-165.
[2] M. S. Ansari, N. P. Gupta, A. K. Hemal, P. N. Dogra, A. Seth, M. Aron, T. P. Singh, *Int. J. Urol.*, 2005, **12**, 12-16.
[3] M. Daudon, R. Donsimoni, C. Hennequin, S. Fellahi, G. Le Moel, M. Paris, S. Troupel, B. Lacour, *Urol. Res.*, 1995, **23**, 319-326.
[4] M. Daudon, D. Bazin, E. Letavernier, *Urolithiasis*, 2015, **43**, 5-11.
[5] A. Randall, *Ann. Surg.*, 1937, **105**, 1009-1027.
[6] A. Randall, *J. Urol.*, 1940, **44**, 580-589.
[7] A. P. Evan, J. E. Lingeman, F. L. Coe, J. H. Parks, S. B. Bledsoe, Y. Shao, A. J. Sommer, R. F. Paterson, R. L. Kuo, M. Grynpas, *J. Clin. Invest.*, 2003, **111**, 607-616.
[8] F. L. Coe, A. P. Evan, J. E. Lingeman, E. M. Worcester, *Urol. Res.*, 2010, **38**, 239-247.
[9] M. P. Linnes, A. E. Krambeck, L. Cornell, J. C. Williams Jr., M. Korinek, E. J. Bergstralh, X. Li, A. D. Rule, C. M. McCollough, T. J. Vrtiska, J. C. Lieske, *Kidney Int.*, 2013, **84**, 818-825.
[10] E. C. Rosenow, *J. Urol.*, 1940, **44**, 19-28.
[11] W. A. D. Anderson, *J. Urol.*, 1940, **44**, 29-34.
[12] V. Vermooten, *J. Urol.*, 1941, **46**, 193-200.
[13] L. Anderson, D. J. McDonald, *Surg. Gynecol. Obstet.*, 1946, **82**, 275-282.
[14] R. C. Haggitt, J. A. Pitcock, *J. Urol.*, 1971, **106**, 342-347.
[15] L. Ruggera, G. Gambaro, P. Beltrami, G. Martignoni, F. Zattoni, *J. Endourol.*, 2011, **25**, 25-30.
[16] M. Daudon, O. Traxer, P. Jungers, M. Bazin, *AIP Conf. Proc.*, 2007, **900**, 26-34.
[17] L. Cifuentes Delatte, J. Minon-Cifuentes, J. A. Medina, *J. Urol.*, 1987, **137**, 1024-1029.
[18] L. Cifuentes Delatte, J. L. Minon-Cifuentes, J. A. Medina, *J. Urol.*, 1985, **133**, 490-494.

[19] E. Letavernier, S. Vandermeersch, O. Traxer, M. Tligui, L. Baud, P. Ronco, J. P. Haymann, M. Daudon, *Medicine (Baltimore)*, 2015, **94**, article no. e566.
[20] J. C. J. Williams, J. E. Lingeman, F. L. Coe, E. M. Worcester, A. P. Evan, *Urolithiasis*, 2015, **43**, 13-17.
[21] R. K. Low, M. L. Stoller, *J. Urol.*, 1997, **158**, 2062-2064.
[22] B. R. Matlaga, J. C. J. Williams, S. C. Kim, R. L. Kuo, A. P. Evan, S. B. Bledsoe, F. L. Coe, E. M. Worcester, L. C. Munch, J. E. Lingeman, *J. Urol.*, 2006, **175**, 1720-1724.
[23] N. L. Miller, D. L. Gillen, W. J. C. Jr., A. P. Evan, S. B. Bledsoe, F. L. Coe, E. M. Worcester, B. R. Matlaga, L. C. Munch, J. E. Lingeman, *BJU Int.*, 2009, **103**, 966-971.
[24] X. Carpentier, M. Daudon, D. Bazin, O. Traxer, *Sémin. Urol. Néphrol.*, 2009, **35**, 86-90.
[25] A. Ciudin, M. P. Luque Galvez, R. S. Izquierdo, M. G. Diaconu, A. F. de Castroa, V. Constantin, J. R. Alvarez-Vijande, C. Nicolau, A. A. Asensio, *Urology*, 2013, **81**, 246-249.
[26] N. M. Bhuskute, W. W. Yap, T. M. Wah, *Eur. J. Radiol.*, 2009, **72**, 470-472.
[27] A. E. Krambeck, J. C. Lieske, X. Li, E. J. Bergstralh, A. D. Rule, D. Holmes 3rd, C. M. McCollough, T. J. Vrtiska, *Urology*, 2013, **82**, 301-306.
[28] A. Somogyi, K. Medjoubi, G. Baranton, V. Le Roux, M. Ribbens, F. Polack, P. Philippot, J. P. Samama, *J. Synchrotron Radiat.*, 2015, **22**, 1118-1129.
[29] R. L. Kuo, J. E. Lingeman, A. P. Evan, R. F. Paterson, J. H. Parks, S. B. Bledsoe, L. C. Munch, F. L. Coe, *Kidney Int.*, 2003, **64**, 2150-2154.
[30] S. C. Kim, F. L. Coe, W. W. Tinmouth, R. L. Kuo, R. F. Paterson, J. H. Parks, L. C. Munch, A. P. Evan, J. E. Lingeman, *J. Urol.*, 2005, **173**, 117-119.
[31] S. A. Cooke, *Br. J. Surg.*, 1970, **57**, 890-896.
[32] C. Verrier, D. Bazin, L. Huguet, O. Stéphan, A. Gloter, M.-C. Verpont, V. Frochot, J.-P. Haymann, I. Brocheriou, O. Traxer, M. Daudon, E. Letavernier, *J. Urol.*, 2016, **196**, 1566-1574.
[33] A. Darves-Bornoz, T. Marien, J. Thomas, G. Fiscus, J. Brock 3rd, D. Clayton, N. J. Miller, *J. Endourol.*, 2019, **33**, 863-867.
[34] K. Bouchireb, O. Boyer, C. Pietrement, H. Nivet, H. Martelli, O. Dunand, F. Nobili, G. L. Sylvie, P. Niaudet, R. Salomon, M. Daudon, *Nephrol. Dial. Transplant.*, 2012, **27**, 1529-1534.
[35] M. Daudon, *Ann. Urol. (Paris)*, 2005, **39**, 209-231.
[36] A. Trinchieri, *Urol. Res.*, 2006, **34**, 151-156.
[37] V. Romero, H. Akpinar, D. G. Asimos, *Rev. Urol.*, 2010, **12**, e86-e96.
[38] J. B. Ziemba, B. R. Matlaga, *Investig. Clin. Urol.*, 2017, **58**, 299-306.
[39] M. Daudon, C. A. Bader, P. Jungers, *Scanning Microsc.*, 1993, **7**, 1081-1104.
[40] M. Daudon, *Arch. Pédiat.*, 2000, **7**, 855-865.
[41] M. Daudon, A. Dessombz, V. Frochot, E. Letavernier, J.-P. Haymann, P. Jungers, D. Bazin, *C. R. Chim.*, 2016, **19**, 1470-1491.
[42] M. Daudon, D. Bazin, *C. R. Chim.*, 2016, **19**, 1416-1423.
[43] V. Vermooten, *J. Urol.*, 1942, **48**, 27-37.
[44] M. L. Stoller, R. K. Low, G. S. Shami, V. D. McCormick, R. L. Kerschmann, *J. Urol.*, 1996, **156**, 1263-1266.
[45] S. R. Khan, D. E. Rodriguez, L. B. Gower, M. Monga, *J. Urol.*, 2012, **187**, 1094-1100.
[46] I. Sethmann, G. Wendt-Nordahl, T. Knoll, F. Enzmann, L. Simon, H. J. Kleebe, *Urolithiasis*, 2017, **45**, 235-248.
[47] J. R. Asplin, N. S. Mandel, F. L. Coe, *Am. J. Physiol.*, 1996, **270**, F604-F613.
[48] J. C. Lieske, R. Norris, H. Swift, F. G. Toback, *Kidney Int.*, 1997, **52**, 1291-1301.
[49] M. Tournus, N. Seguin, B. Perthame, S. R. Thomas, A. Edwards, *Am. J. Physiol. Renal Physiol.*, 2013, **305**, F979-F994.
[50] M. Martin, A. Hadj Aissa, G. Baverel, M. Pellet, *J. Physiol. (Paris)*, 1975, **70**, 159-172.
[51] R. Hautmann, A. Lehmann, S. Komor, *Eur. J. Clin. Invest.*, 1980, **10**, 173-176.
[52] E. M. Worcester, F. L. Coe, A. P. Evan, K. J. Bergsland, J. H. Parks, L. R. Willis, D. L. Clark, D. L. Gillen, *Am. J. Physiol. Renal Physiol.*, 2008, **295**, F1286-F1294.
[53] D. A. Bushinsky, *J. Clin. Invest.*, 2003, **111**, 602-605.
[54] H. G. Tiselius, "Solution chemistry of supersaturation", in *Kidney Stones: Medical and Surgical Management* (F. L. Coe, M. J. Favus, C. Y. C. Pak *et al.*, eds.), Lippincott Raven, Philadelphia, 1996, 33-64.
[55] A. P. Evan, F. L. Coe, J. Lingeman, S. Bledsoe, E. M. Worcester, *Am. J. Physiol. Renal Physiol.*, 2018, **315**, F1236-F1242.
[56] G. Wei, S. Rosen, W. H. Dantzler, T. L. Pannabecker, *Am. J. Physiol. Renal Physiol.*, 2015, **309**, F627-F637.
[57] E. M. Worcester, F. L. Coe, *Semin. Nephrol.*, 2008, **28**, 120-132.
[58] R. K. Low, M. L. Stoller, C. K. Schreiber, *J. Endourol.*, 2000, **14**, 507-510.
[59] E. Letavernier, M. Daudon, *Nutrients*, 2018, **10**, article no. 366.
[60] E. Bouderlique, E. Tang, J. Perez, A. Coudert, D. Bazin, M.-C. Verpont, C. Duranton, I. Rubera, J.-P. Haymann, G. Leftheriotis, L. Martin, M. Daudon, E. Letavernier, *Am. J. Pathol.*, 2019, **189**, 2171-2180.
[61] X. Carpentier, D. Bazin, P. Jungers, S. Reguer, D. Thiaudière, M. Daudon, *J. Synchrotron Radiat.*, 2010, **17**, 374-379.
[62] D. Bazin, E. Letavernier, C. Jouanneau, P. Ronco, C. Sandt, P. Dumas, G. Matzen, E. Véron, J.-P. Haymann, O. Traxe, P. Conort, M. Daudon, *C. R. Chim.*, 2016, **19**, 1461-1469.
[63] C. Gay, E. Letavernier, M.-C. Verpont, M. Walls, D. Bazin, M. Daudon, N. Nassif, O. Stephan, M. de Fruto, *ACS Nano*, 2020, **14**, 1823-1863.
[64] F. F. Amos, L. Dai, R. Kumar, S. R. Khan, L. B. Gower, *Urol. Res.*, 2009, **37**, 11-17.
[65] A. P. Evan, F. L. Coe, S. R. Rittling, S. M. Bledsoe, Y. Shao, J. E. Lingeman, E. M. Worcester, *Kidney Int.*, 2005, **68**, 145-154.
[66] K. Taguchi, S. Hamamoto, A. Okada, R. Unno, H. Kamisawa, T. Naiki, R. Ando, K. Mizuno, N. Kawai, K. Tozawa, K. Kohri, T. Yasui, *J. Am. Soc. Nephrol.*, 2017, **28**, 333-347.
[67] T. Wada, M. D. McKee, S. Steitz, C. M. Giachelli, *Circ. Res.*, 1999, **84**, 166-178.
[68] S. Ito, T. Saito, K. Amano, *J. Biomed. Mater. Res. A*, 2004, **69**, 11-16.
[69] S. M. Moe, K. D. O'Neill, D. Duan, S. Ahmed, N. X. Chen, S. B. Leapman, N. Fineberg, K. Kopecky, *Kidney Int.*, 2002, **61**, 638-647.
[70] A. P. Evan, S. Bledsoe, E. M. Worcester, F. L. Coe, J. E. Lingeman, K. J. Bergsland, *Kidney Int.*, 2007, **72**, 1503-1511.
[71] S. Winfree, C. Weiler, S. B. Bledsoe, T. Gardner, A. J. Sommer, A. P. Evan, J. E. Lingeman, A. E. Krambeck, E. M. Worcester,

T. M. El-Achkar, J. C. Williams Jr., *Urolithiasis*, 2021, **49**, 123-135.
[72] X. Carpentier, D. Bazin, C. Combes, A. Mazouyes, S. Rouzière, P.-A. Albouy, E. Foy, M. Daudon, *J. Trace Elem. Med. Biol.*, 2011, **25**, 160-165.
[73] M. L. Stoller, M. V. Meng, H. M. Abrahams, J. P. Kane, *J. Urol.*, 2004, **171**, 1920-1924.
[74] E. R. Taylor, M. L. Stoller, *Urolithiasis*, 2015, **43**, 41-45.
[75] R. T. Alexander, B. R. Hemmelgarn, N. Wiebe, A. Bello, S. Samuel, S. W. Klarenbach, G. C. Curhan, M. Tonelli, *Clin. J. Am. Soc. Nephrol.*, 2014, **9**, 506-512.
[76] L. Shavit, D. Girfoglio, V. Vijay, D. Goldsmith, P. M. Ferraro, S. H. Moochhala, R. Unwin, *Clin. J. Am. Soc. Nephrol.*, 2015, **10**, 278-285.
[77] F. Madore, M. J. Stampfer, E. B. Rimm, G. C. Curhan, *Am. J. Hypertens.*, 1998, **11**, 46-53.
[78] E. N. Taylor, M. J. Stampfer, G. C. Curhan, *JAMA*, 2005, **293**, 455-462.
[79] E. N. Taylor, M. J. Stampfer, G. C. Curhan, *Kidney Int.*, 2005, **68**, 1230-1235.
[80] Y. Tada, S. Yano, T. Yamaguchi, K. Okazaki, N. Ogawa, M. Morita, T. Sugimoto, *Horm. Metab. Res.*, 2013, **45**, 267-272.
[81] R. E. Druilhet, M. L. Overturf, W. M. Kirkendall, *Int. J. Biochem.*, 1978, **9**, 729-734.
[82] R. L. Sur, J. H. Masterson, K. L. Palazzi, J. O. L'Esperance, B. K. Auge, D. C. Chang, M. L. Stoller, *Clin. Nephrol.*, 2013, **79**, 351-355.
[83] R. S. Hsi, K. Ramaswamy, S. P. Ho, M. L. Stoller, *BJU Int.*, 2017, **119**, 177-184.
[84] L. Chen, R. S. Hsi, F. Yang, B. A. Sherer, M. L. Stoller, S. P. Ho, *PLoS One*, 2017, **12**, article no. e0187103.
[85] S. V. Wiener, L. Chen, A. R. Shimotake, M. Kang, M. L. Stoller, S. P. Ho, *Connect. Tissue Res.*, 2018, **59**, 102-110.
[86] R. J. Carr, *Br. J. Urol.*, 1954, **26**, 105-117.
[87] Z. Zhu, F. Huang, W. Xia, H. Zeng, M. Gao, Y. Li, F. Zeng, H. Cheng, J. Chen, Z. Chen, Y. Li, Y. Cui, H. Chen, *Front. Cell Dev. Biol.*, 2020, **8**, article no. 596363.
[88] F. Mezzabotta, R. Cristofaro, M. Ceol, D. Del Prete, G. Priante, A. Familiari, A. Fabris, A. D'Angelo, G. Gambaro, F. Anglani, *J. Cell. Mol. Med.*, 2015, **19**, 889-902.
[89] A. P. Evan, E. M. Worcester, J. C. Williams Jr., A. J. Sommer, J. E. Lingeman, C. L. Phillips, F. L. Coe, *Anat. Rec. (Hoboken)*, 2015, **298**, 865-877.
[90] G. Priante, M. Ceol, L. Gianesello, C. Furlan, D. Del Prete, F. Anglani, *Cell Death Discov.*, 2019, **5**, article no. 57.
[91] S. R. Khan, B. K. Canales, *Urolithiasis*, 2015, **43**, 109-123.
[92] S. R. Khan, G. Gambaro, *Anat. Rec. (Hoboken)*, 2016, **299**, 5-7.
[93] A. P. Evan, F. L. Coe, J. E. Lingeman, Y. Shao, A. J. Sommer, S. B. Bledsoe, J. C. Anderson, E. M. Worcester., *Anat. Rec. (Hoboken)*, 2007, **290**, 1315-1323.
[94] S. R. Khan, M. S. Pearle, W. G. Robertson, G. Gambaro, B. K. Canales, S. Doizi, O. Traxer, H.-G. Tiselius, *Nat. Rev. Dis. Primers*, 2017, **3**, article no. 17001.
[95] D. Bazin, C. Chappard, C. Combes, X. Carpentier, S. Rouzière, G. André, G. Matzen, M. Allix, D. Thiaudière, S. Reguer, P. Jungers, M. Daudon, *Osteoporos. Int.*, 2009, **20**, 1065-1075.
[96] D. Bazin, M. Daudon, C. Combes, C. Rey, *Chem. Rev.*, 2012, **112**, 5092-5120.
[97] D. Bazin, J.-P. Haymann, E. Letavernier, J. Rode, M. Daudon, *Presse Med.*, 2014, **43**, 135-148.
[98] P. Pascaud, "Apatites nanocristallines biomimétiques comme modèles de la réactivité osseuse : Étude des propriétés d'adsorption et de l'activité cellulaire d'un bisphosphonate, le tiludronate", PhD Thesis, Université de Toulouse, France, 2012.
[99] C. Rey, C. Combes, C. Drouet, A. Lebugle, H. Sfihi, A. Barroug, *Mater. Sci. Eng.*, 2007, **27**, 198-205.
[100] C. Drouet, C. Rey, *Nanostructured Biomaterials for Regenerative Medicine*, Woodhead Publishing Series in Biomaterials, Woodhead Publishing, 2020, 223-254 pages.
[101] C. Gervais, C. Bonhomme, D. Laurencin, *Solid State Nucl. Magn. Reason.*, 2020, **107**, article no. 101663.
[102] J. L. Meyer, J. H. Bergert, L. H. Smith, *Clin. Sci. Mol. Med.*, 1975, **49**, 369-374.
[103] B. Xie, T. J. Halter, B. M. Borah, G. H. Nancollas, *Cryst. Growth Des.*, 2015, **15**, 204-211.
[104] D. Bazin, M. Daudon, *J. Phys. D Appl. Phys.*, 2012, **45**, article no. 383001.
[105] H. G. Tiselius, *Urol. Res.*, 2011, **9**, 231-243.
[106] I. Sethmann, B. Grohe, H. J. Kleebe, *Mineral Mag.*, 2014, **78**, 91-100.
[107] H. G. Tiselius, *Urolithiasis*, 2013, **41**, 369-377.
[108] D. Bazin, E. Letavernier, J. P. Haymann, V. Frochot, M. Daudon, *Ann. Biol. Clin.*, 2020, **78**, 349-362.
[109] J. C. Anderson, *Clin. Orthop. Relat. Res.*, 1995, **314**, 266-280.
[110] I. Zazzeroni, G. Faggioli, G. Pasquinelli, *Eur. J. Vasc. Endovasc. Surg.*, 2018, **55**, 425-432.
[111] D. Skrtic, E. D. Eanes, *Bone Miner.*, 1992, **16**, 109-119.
[112] S. R. Khan, B. Finlayson, R. L. Hackett, *Am. J. Pathol.*, 1982, **107**, 59-69.
[113] S. R. Khan, B. K. Canales, P. R. Dominguez-Gutierrez, *Nat. Rev. Nephrol.*, 2021, **17**, 417-433.
[114] P. R. Dominguez-Gutierrez, E. P. Kwenda, S. R. Khan, B. K. Canales, *Curr. Opin. Urol.*, 2020, **30**, 183-189.
[115] S. R. Khan, *Transl. Androl. Urol.*, 2014, **3**, 256-276.
[116] B. Bao, A. S. Prasad, F. W. Beck, D. Snell, A. Suneja, F. H. Sarkar, N. Doshi, J. T. Fitzgerald, P. Swerdlow, *Transl. Res.*, 2008, **152**, 67-80.
[117] H. Haase, J. L. Ober-Blöbaum, G. Engelhardt, S. Hebel, A. Heit, H. Heine, L. Rink, *J. Immunol.*, 2008, **181**, 6491-6502.
[118] F. Martinon, V. Petrilli, A. Mayor, A. Tardivel, J. Tschopp, *Nature*, 2006, **440**, 237-241.
[119] A. Y. Sun, B. Hinck, B. R. Cohen, K. Keslar, R. J. Fairchild, M. Monga, *J. Endourol.*, 2018, **32**, 236-244.
[120] K. Taguchi, A. Okada, S. Hamamoto, R. Unno, Y. Moritoki, R. Ando, K. Mizuno, K. Tozawa, K. Kohri, T. Yasui, *Sci. Rep.*, 2016, **6**, article no. 35167.
[121] S. Kusmartsev, P. R. Dominguez-Gutierrez, B. K. Canales, V. G. Bird, J. Vieweg, S. R. Khan, *J. Urol.*, 2016, **195**, 1143-1151.
[122] A. Okada, T. Yasui, Y. Fujii, K. Niimi, S. Hamamoto, M. Hirose, Y. Kojima, Y. Itoh, K. Tozawa, Y. Hayashi, K. Kohri, *J. Bone Miner. Res.*, 2010, **25**, 2701-2711.
[123] T. Umekawa, N. Chegini, S. R. Khan., *Nephrol. Dial. Transplant.*, 2003, **18**, 664-669.
[124] M. Patel, V. Yarlagadda, O. Adedoyin, V. Saini, D. G. Assimos, R. P. Holmes, T. Mitchell, *Redox Biol.*, 2018, **15**, 207-215.
[125] H. J. Anders, B. Suarez-Alvarez, M. Grigorescu, O. Foresto-

Neto, S. Steiger, J. Desai, J. A. Marschner, M. Hanorpisheh, C. Shi, J. Jordan, L. Müller, N. Burzlaff, T. Bäuerle, S. R. Mulay, *Kidney Int.*, 2018, **93**, 656-669.
[126] W. Zhu, Z. Zhao, F. Chou, L. Zuo, T. Liu, S. Yeh, D. Bushinsky, G. Zeng, C. Chang, *Cell Death Dis.*, 2019, **10**, article no. 275.
[127] J. Xi, Y. Chen, J. Jing, Y. Zhang, C. Liang, Z. Hao, L. Zhang, *J. Cell. Physiol.*, 2019, **234**, 11463-11473.
[128] P. R. Dominguez-Gutierrez, S. Kusmartsev, B. K. Canales, S. R. Khan, *Front. Immunol.*, 2018, **9**, article no. 1863.
[129] K. Aihara, K. J. Byer, S. R. Khan, *Kidney Int.*, 2003, **64**, 1283-1291.
[130] C. Escobar, K. J. Byer, H. Khaskheli, S. R. Khan, *J. Urol.*, 2008, **180**, 379-387.
[131] Y. H. Chen, H. P. Liu, H. Y. Chen, F. J. Tsai, C. H. Chang, Y. J. Lee, W. Y. Lin, W. C. Chen, *Kidney Int.*, 2011, **80**, 369-377.
[132] S. R. Khan, P. A. Glenton, K. J. Byer, *Kidney Int.*, 2006, **70**, 914-923.
[133] E. Letavernier, C. Verrier, F. Goussard, J. Perez, L. Huguet, J.-P. Haymann, L. Baud, D. Bazin, M. Daudon, *Kidney Int.*, 2016, **90**, 809-817.
[134] D. A. Bushinsky, M. D. Grynpas, E. L. Nilsson, Y. Nakagawa, F. L. Coe, *Kidney Int.*, 1995, **48**, 1705-1713.
[135] S. R. Khan, P. A. Glenton, *Am. J. Physiol. Renal Physiol.*, 2008, **294**, F1109-F1115.
[136] Y. Liu, L. Mo, D. S. Goldfarb, A. P. Evan, F. Liang, S. R. Khan, J. C. Lieske, X. R. Wu, *Am. J. Physiol. Renal Physiol.*, 2010, **299**, F469-F478.
[137] L. Mo, L. Liaw, A. P. Evan, A. J. Sommer, J. C. Lieske, X. R. Wu, *Am. J. Physiol. Renal Physiol.*, 2007, **293**, F1935-F1943.
[138] J. A. Wesson, R. J. Johnson, M. Mazzali, A. M. Beshensky, S. Stietz, C. Giachelli, L. Liaw, C. E. Alpers, W. G. Couser, J. G. Kleinman, J. Hughes, *J. Am. Soc. Nephrol.*, 2003, **14**, 139-147.
[139] S. Shenolikar, J. W. Voltz, C. M. Minkoff, J. B. Wade, E. J. Weinman, *Proc. Natl. Acad. Sci. USA*, 2002, **99**, 11470-11475.
[140] R. S. Jansen, S. Duijst, S. Mahakena, D. Sommer, F. Szeri, A. Varadi, A. Plomp, A. A. Bergen, R. P. J. Oude Elferink, P. Borst, K. van de Wetering, *Arterioscler. Thromb. Vasc. Biol.*, 2014, **34**, 1985-1989.
[141] H. Fleisch, *Kidney Int.*, 1978, **13**, 361-371.
[142] A. Legrand, L. Cornez, W. Samkari, J. M. Mazzella, A. Venisse, V. Boccio, K. Auribault, B. Keren, K. Benistan, D. P. Germain, M. Frank, X. Jeunemaitre, J. Albuisson, *Genet. Med.*, 2017, **19**, 909-917.
[143] E. Letavernier, G. Kauffenstein, L. Huguet, N. Navasiolava, E. Bouderlique, E. Tang, L. Delaitre, D. Bazin, M. de Frutos, C. Gay, J. Perez, M. C. Verpont, J.-P. Haymann, V. Pomozi, J. Zoll, O. Le Saux, M. Daudon, G. Leftheriotis, L. Martin, *J. Am. Soc. Nephrol.*, 2018, **29**, 2337-2347.
[144] H. Seeger, N. Mohebbi, *Kidney Int.*, 2016, **89**, 1407.
[145] R. Chraibi, N. Ismaili, F. Belgnaoui, N. Akallal, J. Bouhllab, K. Senouci, B. Hassam, *Ann. Dermatol. Venereol.*, 2007, **134**, 764-766.
[146] V. Pomozi, C. Brampton, K. van de Wetering, J. Zoll, B. Calio, K. Pham, J. Owens, J. Mahr, S. Moisyadi, A. Varadi, L. Martin, C. Bauer, J. Erdmann, Z. Aherrahrou, O. Le Saux, *Am. J. Pathol.*, 2017, **187**, 1258-1272.
[147] V. Pomozi, C. B. Julian, J. Zoll, K. Pham, S. Kuo, N. Tokesi, L. Martin, A. Varadi, O. Le Saux, *J. Invest. Dermatol.*, 2019, **139**, 1082-1088.
[148] D. Dedinszki, F. Szeri, E. Kozak, V. Pomozi, N. Tokesi, T. R. MEzei, K. Merczel, E. Letavernier, E. Tang, O. Le Saux, T. Aranyi, K. van de Wetering, A. Varadi, *EMBO Mol. Med.*, 2017, **9**, 1463-1470.
[149] E. Pieras, A. Costa-Bauza, M. Ramis, F. Grases, *Sci. World J.*, 2006, **6**, 2411-2419.
[150] N. B. Roberts, J. Dutton, T. Helliwell, P. J. Rothwell, J. P. Kavanagh, *Ann. Clin. Biochem.*, 1992, **29**, 529-534.
[151] R. G. Russell, A. Hodgkinson, *Clin. Sci.*, 1966, **31**, 51-62.
[152] H. Fleisch, S. Bisaz, *Nature*, 1962, **195**, article no. 911.
[153] J. A. Munoz, M. Lopez-Mesas, M. Valiente, *Anal. Chim. Acta*, 2010, **658**, 204-208.
[154] E. Letavernier, E. Bouderlique, J. Zaworski, L. Martin, M. Daudon, *Int. J. Mol. Sci.*, 2019, **20**, article no. 6353.

Comptes Rendus
Chimie
2022, Vol. 25, Special Issue S1, p. 393-405
https://doi.org/10.5802/crchim.92

Microcrystalline pathologies: Clinical issues and nanochemistry

Inflammation plays a critical role in 2,8-dihydroxyadenine nephropathy

Elise Bouderlique [a,b], Ellie Tang [a,b], Joëlle Perez [a,b], Hang-Korng Ea [c,d,e], Felix Renaudin [c,d,e], Amélie Coudert [c,e], Sophie Vandermeersch [a,b], Dominique Bazin [f], Jean-Philippe Haymann [a,b,g], Camille Saint-Jacques [a,b,g], Vincent Frochot [a,b,g], Michel Daudon [a,b,g] and Emmanuel Letavernier [*,a,b,g]

[a] Sorbonne Universités, UPMC Univ Paris 06, UMR S 1155, F-75020, Paris, France

[b] INSERM, UMR S 1155, F-75020, Paris, France

[c] Université de Paris, département de médecine générale, 75018 Paris, France

[d] Hôpital Lariboisière, service de rhumatologie, pôle locomoteur, AP-HP, 2, rue Ambroise Paré 75010 Paris, France

[e] INSERM U1132 Bioscar, Paris 75010, France

[f] Laboratoire de Chimie Physique, CNRS UMR 8000, Université Paris XI, 91405 Orsay, France

[g] Physiology Unit, AP-HP, Hôpital Tenon, F-75020, Paris, France

Current address: Service des Explorations Fonctionnelles Multidisciplinaires, Hôpital TENON, 4 rue de la Chine, 75020 Paris, France (E. Letavernier)

E-mails: elise.bouderlique@inserm.fr, ellieyali.tang@hotmail.com, perezjoelle@yahoo.fr, hang-korng.ea@aphp.fr, Felix.renaudin@gmail.com, amelie.coudert@inserm.fr, sophie.vandermeersch@upmc.fr, dominique.bazin@u-psud.fr, jean-philippe.haymann@aphp.fr, camille.saint-jacques@aphp.fr, vincent.frochot@aphp.fr, michel.daudon@aphp.fr, emmanuel.letavernier@aphp.fr

Abstract. Adenine phosphoribosyltransferase (APRT) deficiency is a genetic disease characterized by an increased production of 2,8 dihydroxyadenine (2,8-DHA) precipitating in urine, leading to a crystalline nephropathy and end-stage renal disease. Here, we describe the high prevalence of granuloma (88%) in biopsies from patients with APRT deficiency. A murine model of 2,8-DHA nephropathy was generated, showing that anakinra or dexamethasone, combined with allopurinol, improved renal function to a larger extent than allopurinol alone, the standard therapy. Inflammation plays a critical role in the development of 2,8-DHA nephropathy, and therapy based upon drugs targeting innate immunity could improve renal function recovery.

Keywords. 2,8-Dihydroxyadenine, Adenine phosphoribosyl transferase (APRT), Kidney, Inflammation, Interleukin-1 beta.

Published online: 9 August 2021

* Corresponding author.

1. Introduction

Adenine phosphoribosyltransferase (APRT) deficiency is an autosomal recessive genetic dis-

ease [1–4]. This purine metabolism disorder results in an increased production and urinary excretion of 2,8 dihydroxyadenine (2,8-DHA) which is poorly soluble in urine, leading to recurrent urolithiasis and crystalline nephropathy. Actually, the main feature of this disease is the development of a chronic kidney disease resulting from crystallites precipitation in renal tubule, engulfment of crystallites by tubular epithelial cells and interstitial accumulation of 2,8-DHA and, finally, renal fibrosis. In the absence of a specific treatment, patients develop end-stage renal disease (ESRD). As renal transplantation does not cure the enzymatic deficiency, kidney transplant recipients are also affected by a high rate of recurrence leading to graft loss if the disease has not been diagnosed previously [5–7].

The disease is considered to be very rare and a majority of the cases have been reported in Iceland, France and Japan [4,8–11]. A missense (homozygous) mutation in exon 3 (Asp65Val) accounts for all cases of APRT deficiency in Iceland, suggesting the existence of a founder effect [4,12]. In Japan, a missense mutation in exon 5 (Met136MThr) affects 70% of patients [11]. By contrast, in 53 cases of APRT deficiency (from 43 families) identified at a single institution in France, 18 distinct mutations have been identified [9]. As suggested by Edvardsson *et al.* APRT could be massively unrecognized [4]. Actually, the estimated pathogenic mutation frequency in various populations could range from 0.4 to 1.2% [3,4, 10]. This suggests that homozygous or compound heterozygous carriers should be at least 1:50,000–100,000, i.e. 3000 cases in the USA and 9000 cases in Europe for instance. On the other hand, a recent study based upon six population genomic databases reported that the large number of cases in Japan and Iceland was consistent with a founder effect in these populations. In other countries, the minor allele frequency of pathogenic variants seems relatively low, suggesting that there is no widespread underdiagnosis of this nephropathy [13]. In France, many cases have been diagnosed with the help of crystalluria, morphoconstitutional kidney stone analysis including Fourier transform infrared (FTIR) spectroscopy and FTIR microscopy evidencing the crystalline phase in kidney biopsies, including kidney graft biopsies [9,14–16]. Measurement of enzyme activity in red blood cell lysates and genetic analyses were usually performed after identification of crystals and one may hypothesize that many patients with undiagnosed chronic kidney disease are affected by APRT deficiency. The widespread use of whole-exome sequencing in patients with unidentified nephropathy and who are candidates for an allograft should be informative in a near future.

There is a need for an early diagnosis as there is an efficient treatment: xanthine oxidoreductase inhibitors, allopurinol and febuxostat, which decrease 2,8-DHA synthesis and excretion in urine [17]. If initiated early, a lifelong therapy associated with high fluid intake may stabilize kidney function. Nevertheless, renal function recovery is often limited and there may be a place for other therapeutics to improve renal function recovery [7,18].

Klinkhammer *et al.* highlighted recently the important role of innate immunity in 2,8-DHA crystalline nephropathy, and described the presence of granuloma in a murine model of the disease [19]. As we have observed frequent and massive macrophage infiltrates and granuloma-like structures in biopsies from patients affected by APRT, we assessed systematically inflammatory infiltrates in a series of 17 biopsies. We performed *in vivo* animal studies to highlight the role of inflammation in this disease. In addition, we hypothesized that targeting the immune response induced by 2,8-DHA crystalline deposits might be protective and showed that corticosteroids or anakinra may improve renal outcome, when added to the conventional therapy (allopurinol), in a model of 2,8-DHA nephropathy.

2. Material and methods

2.1. *Human kidney tissue biopsies*

Seventeen biopsies from 17 patients affected by APRT deficiency were analyzed, including 12 biopsies performed in kidney grafts. All biopsies were sent to Tenon and Necker hospitals, Paris, to diagnose the nature of the crystalline nephropathy. Kidney tissues were fixed in formalin and embedded in paraffin. Four micrometer tissue sections were deposited on low emission microscope slides (MirrIR, Keveley Technologies, Tienta Sciences, Indianapolis, IN, USA). FTIR hyperspectral images were recorded with a Spectrum spotlight 400 FTIR imaging system (Perkin Elmer Waltham, MA, USA), with a spatial resolution of 6.25 μm and a spectral

resolution of 4 cm^{-1}. The spectra were recorded in the 4000–700 cm^{-1} mid-Infrared range. Each spectral image, covering a substantial part of the tissue, consisted of about 30,000 spectra. Histopathological lesions were analyzed in 4 μm sections stained with Masson Trichrome and Hematoxylin/Eosin staining, by two independent nephrologists trained in renal pathology. 2,8-DHA was identified using μ Fourier Transform InfraRed spectrometry in the 17 biopsies. For immunohistochemistry experiments, kidneys sections were dewaxed, heated in citric acid solution and next incubated with one of the following primary antibodies overnight at 4 °C: Anti-CD3 (Polyclonal, A0452 (Dako, Agilent, Santa Clara, CA, USA), Rabbit anti-mouse CD3 (Polyclonal, ab5690, Abcam, Cambridge, MA, USA), Rat anti-mouse pan-macrophages (Oxford Biotech, Oxford, UK), Anti-CD68 (PG-M1, M0876, Dako, Agilent, Santa Clara, CA, USA), Anti-CD163 (ab182422, Abcam, Cambridge, MA, USA). After washing, immunostaining was revealed with Histofine secondary antibodies (Nichirei Biosciences, Tokyo, Japan) and then revealed with AEC (k34769, Dako, Santa Clara, USA). Nuclei were counterstained with hematoxylin. Negative controls were performed by omitting the primary antibody. Tissue sections deposited on Mirr IR slides were examined with a Zeiss SUPRA55-VP Field Emission scanning Electron Microscope (Zeiss France, Marly-le-Roi, France). Measurements were performed at a low voltage (1.4 keV).

2.2. *Crystal synthesis*

2,8-DHA crystals were obtained from kidney stones containing 100% 2,8-DHA according to FTIR analysis. Stone fragments were ground in a mortar with 100% pure ethanol. Crystals were filtered in 100 μm sieve before washing in ethanol and warm sterilization. Monosodium urate (MSU) crystals were prepared with 500 mL of boiling water and 2 g of uric acid (U2625, Sigma Aldrich, St Louis, MO, USA). pH solution was maintained at 8 by adding NaOH (1 M). Solution was cooled and kept 24 h during crystals formation. Crystals were filtered in 100 μm sieve before washing in ethanol and warm sterilization and characterized by FTIR analysis. Monoclinic calcium pyrophosphate dihydrate (mCPPD) crystals were synthesized and characterized as previously reported [20]. mCPPD crystals were characterized by X-ray diffraction (Seifert XRD-3000TT diffractometer with Cu Kα radiation, in the 2θ range 2°–70° with step size 0.02° and scan step time 16 s at 298 K), FTIR spectroscopy (Thermo Nicolet 5700 Fourier-transform infrared spectrometer) and scanning electron microscopy (SEM, Leo 435 VP microscope). All crystals were dispersed by brief sonication and suspended at 2 mg/mL in phosphate buffered saline (PBS). They were prepared under endotoxin-free conditions and tested negative with Pierce Limulus amebocyte Assay (Thermo Fisher Scientific, Waltham, MA, USA).

2.3. *Animal models*

Eight-week old male C57Bl/6J mice were used for *in vivo* experiments. After purchase, mice were housed one week before experimentation. All mice were housed and bred in similar conditions at INSERM UMR S 1155 Mouse Facility, with a 12-h dark/light cycle. All mice received standard chow (or adenine-enriched diet). All animal procedures were performed in accordance with the European Union and National Institutes of Health guidelines for the care and use of laboratory animals (Comité d'Ethique en Experimentation Charles Darwin C2EA-05). The project was authorized by the Health Ministry and local Ethics Committee (authorization numbers #13902 and #16615).

2.3.1. *Mouse air-pouch model*

Eight-week old male C57Bl/6J mice were used to perform an air-pouch model (six animals/group). Air pouches were created by two dorsal subcutaneous injections of 3 mL of sterile air (day 0 and day 3), under isoflurane anesthesia. At day 6, PBS (1 mL) in control mice or crystals (2,8-DHA, mCPPD or MSU, 1 mg/mL, diluted in PBS) were injected directly into the air pouch. Six hours after crystal stimulation, air pouch lavages were performed and collected for cytokine quantification and cell isolation. Infiltrated cells were counted and phenotyped by flow cytometry. IL-1β cytokine production in supernatants or air pouch lavages was measured in the 6 animals (one missing data in the MSU group) by using ELISA kit (Invitrogen-Thermo fisher scientific, Waltham, MA, USA).

2.3.2. *Flow cytometry*

10^5 cells from air pouch lavages were stained with anti-F4/80-APC (clone REA126; Miltenyi Biotechnology, Bergish Gladbach, Germany) and anti-Ly6G-PE mouse monoclonal antibodies and clone 1A8 (Miltenyi Biotechnology, Bergish Gladbach, Germany) for 20 min at 4 °C, washed in PBS and analyzed with a BD FACS Canto II cytometer (BD Biosciences, Franklin Lakes, NJ, USA). Data were analyzed with BDFACS Diva software (BD Biosciences, Franklin Lakes, NJ, USA).

2.3.3. *Adenine model*

Thirty-two animals had a free access to tap water and received adenine enriched diet (chow containing 0.25% adenine, A8626 Sigma Aldrich, St-Louis, MO, USA) during 4 weeks to induce a 2,8-DHA nephropathy. After two weeks of adenine-enriched diet, animals were divided in 4 groups of 8 animals: control, allopurinol, dexamethasone and allopurinol, anakinra and allopurinol. Except control animals, all groups received allopurinol in tap water at 250 mg/L during the 2 last weeks as the standard therapy against 2,8-DHA. Each group received 100 µL/day subcutaneous injections during these two last weeks, with either isotonic sodium chloride (control and allopurinol groups), dexamethasone (1 mg/kg/day–Mylan, Canonsburg, PA, USA) or anakinra (100 mg/kg/day–Sobi France, Puteaux, France).

Animals were sacrificed 4 weeks after initiation of the adenine-enriched diet, blood and kidneys were collected. Blood samples were collected to assess serum urea, serum creatinine and serum uric acid levels with an IDS-iSYS automat (Immunodiagnostic Systems Holdings PLC, Pouilly-en-Auxois, France).

Left kidneys were fixed in formaldehyde and embedded in paraffin. X-ray computed tomography imaging of the left kidney was performed using a Skyscan 1272 (Bruker, Anvers, Belgium). A 6 µm resolution scale was obtained. Data were reconstructed using N-recon software (Bruker, Anvers, Belgium). The Mimics Innovation suite 20.0 (Materialise, Leuven, Belgium) was used to perform three-dimensional modeling of crystalline deposits in the kidney and quantify crystalline volume. Four-µm thick sections were stained with Masson trichromic solution and Hematoxylin/Eosin standard protocol to reveal 2,8-DHA deposits in polarized light, or with sirius red in picric acid solution to assess fibrosis. A morphometric analysis of fibrosis tissue surface was performed with the Image J software (NIH) on 5 representative fields at ×200 magnification by using polarized light. For each animal, the mean value has been considered.

Crystalline deposits observed in tissue sections were characterized using FTIR microscopy as described above. Four-µm tissue sections were deposited on low-emission microscope slides (MirrIR; Keveley Technologies, Tienta Sciences, Indianapolis, USA) and FTIR hyperspectral images were recorded with a Spectrum spotlight 400 FT-IR imaging system (PerkinElmer, Waltham, USA).

2.3.4. *Quantitative RT-PCR*

mRNA from kidney was extracted using Trizol solution (Life Technologies BRL, Gaithersburg, MD, USA). RNA concentration was measured by using NanoDrop1000 spectrophotometer (Thermo Scientific, Waltham, MA, USA). RT-PCR was performed using SYBR green and specific probes on the light cycler 480 (Roche Diagnostic). Specific primers for TNF-α ForTCTTCTCATTCCTGCTTGTGG, RevATGAGAGGGAGGCCATTTG and IL1-β ForTGTAATGAAAGACGGCACACC RevTCTTCTTTGGGTATTGCTTGG, PCR was also carried out for the housekeeping gene HPRT ForGGAGCGGTAGCACCTCCT RevCTGGTTCATCATCGCTAATCAC to normalize the Q-PCR results, using Roche LightCycler 2.0 software (Roche Diagnostics Indianapolis, IN, USA). Results are expressed as $2^{-\Delta\Delta CT}$, where CT is the cycle threshold number.

2.4. *Statistical analyses*

Data are expressed as mean (±SEM). Data were analyzed with non-parametric tests (Kruskal Wallis followed by post hoc tests and Mann–Whitney test), using Statview and GraphPad Prism 7.0 softwares (GraphPad Software Inc., San Diego, CA, USA). The level of significance was set at <0.05.

3. Results

3.1. *Clinical study*

The histological lesions and the presence and type of inflammatory cells were assessed in kidney biopsies

from 17 patients, including 12 biopsies performed in renal transplant recipients. Acute tubular lesions were noticed in all biopsies and features of tubular atrophy and interstitial fibrosis were significant in 14 biopsies. Crystallites morphology was heterogeneous with irregular structures (N = 17), round shaped (N = 16) or ring-shaped (N = 10) deposits (Figure 1A–D). Crystallites were present in the tubular lumen (N = 16), in tubular cells (N = 17) and in the interstitial tissue (N = 12). Under polarized light, deposits were frequently radial (N = 17), sometimes needle-like (N = 7) and the typical "maltese cross" aspect was evidenced in 6 biopsies. In all biopsies, the presence of 2,8-DHA had been previously confirmed by FTIR microscopy. Scanning electron microscopy revealed the topography of the birefringent deposits (Figure 1E).

The presence of epithelioid granuloma was observed in 15/17 biopsies (88%). These granulomas were centered by 2,8-DHA crystals and made of epithelioid cells and giant multinucleated cells (Figure 1A–D). Immunostaining confirmed that granulomas contained mainly macrophages, with a predominance of macrophages type M2 (CD163+) over macrophages type M1 (CD68+), and T-cells (CD3+) (Figure 1F–H).

4. *In vivo* air-pouch model

To confirm whether 2,8-DHA crystals may induce an innate immune response, an air-pouch model was generated in C57Bl/6J mice. In this model, MSU crystals and monoclinic pyrophosphate dihydrate (mCPPD) crystals were used as a positive control to induce white blood cell chemotaxis, and IL-1β synthesis. 2,8-DHA crystals increased significantly white blood cell recruitment at 6 h in the air-pouch in comparison with controls (p = 0.002, n = 6/group, Figure 2A) but also in comparison with MSU (p = 0.01, n = 6/group). The number of macrophages was significantly increased by 2,8-DHA crystals in comparison with control and MSU crystals (p = 0.002 and p = 0.01 respectively, n = 6/group, Figure 2B), as well as the number of neutrophils (p = 0.002 vs controls and MSU crystals, n = 6/group, Figure 2C). IL-1β synthesis was also significantly increased by 2,8-DHA crystals in comparison with controls (p = 0.01, n = 6/group, Figure 2D), but there was a non-significant trend toward higher IL-1β in animals exposed to mCPPD and MSU crystals in comparison with controls.

5. *In vivo* 2,8-DHA nephropathy model

Exposure of mice to a diet enriched in adenine led to the precipitation of crystals in kidney tubules, and FTIR spectroscopic microscopy performed in several control mice confirmed that crystals were actually made of 2,8-DHA (Figure 3A,B). To assess the amount of crystallites in the kidneys, a 3-dimensional assessment of the whole-kidney crystalline volume was measured by CT-scan and evidenced that allopurinol, alone or in association with dexamethasone or anakinra, reduced significantly the volume of 2,8-DHA deposits as expected when compared to control group (p = 0.0002, p = 0.0002 and p = 0.0003 respectively, N = 8/group, Figure 4F). The addition of corticosteroids or anakinra to allopurinol did not reduce further the whole crystalline volume in comparison with allopurinol alone ($p = NS$, n = 8/group, Figure 4F).

Renal function was impaired in all groups of mice exposed to 2,8-DHA. Serum creatinine level was significantly higher in control mice than in groups receiving allopurinol alone (p = 0.019, N = 8/group Figure 5A), allopurinol+dexamethasone or allopurinol+anakinra (p = 0.02 and p = 0.01, respectively, n = 8/group, Figure 5A). Of note, mice exposed to anakinra and allopurinol had a lower serum creatinine level than mice exposed to allopurinol alone (p = 0.009, N = 8/group, Figure 5A). Serum urea level was lower in the anakinra+allopurinol group when compared to the control group (p = 0.037, n = 8/group, Figure 5B) but also in comparison with allopurinol and allopurinol+dexamethasone groups (p = 0.02 and 0.028, respectively, N = 8/group, Figure 5B). Renal fibrosis assessed by morphometry (sirius red in polarized light) was also significantly decreased in mice treated with anakinra and allopurinol when compared to controls (p = 0.01, N = 8/group (Figure 5C,D). A non-significant trend toward less fibrosis was observed in mice receiving allopurinol and allopurinol+dexamethasone. Unexpectedly, the expression of IL-1β was markedly increased in mice treated with allopurinol alone when compared to controls (p = 0.028, N = 8/group, Figure 5E), despite a lower number of crystalline deposits. Mice exposed to anakinra/allopurinol had a

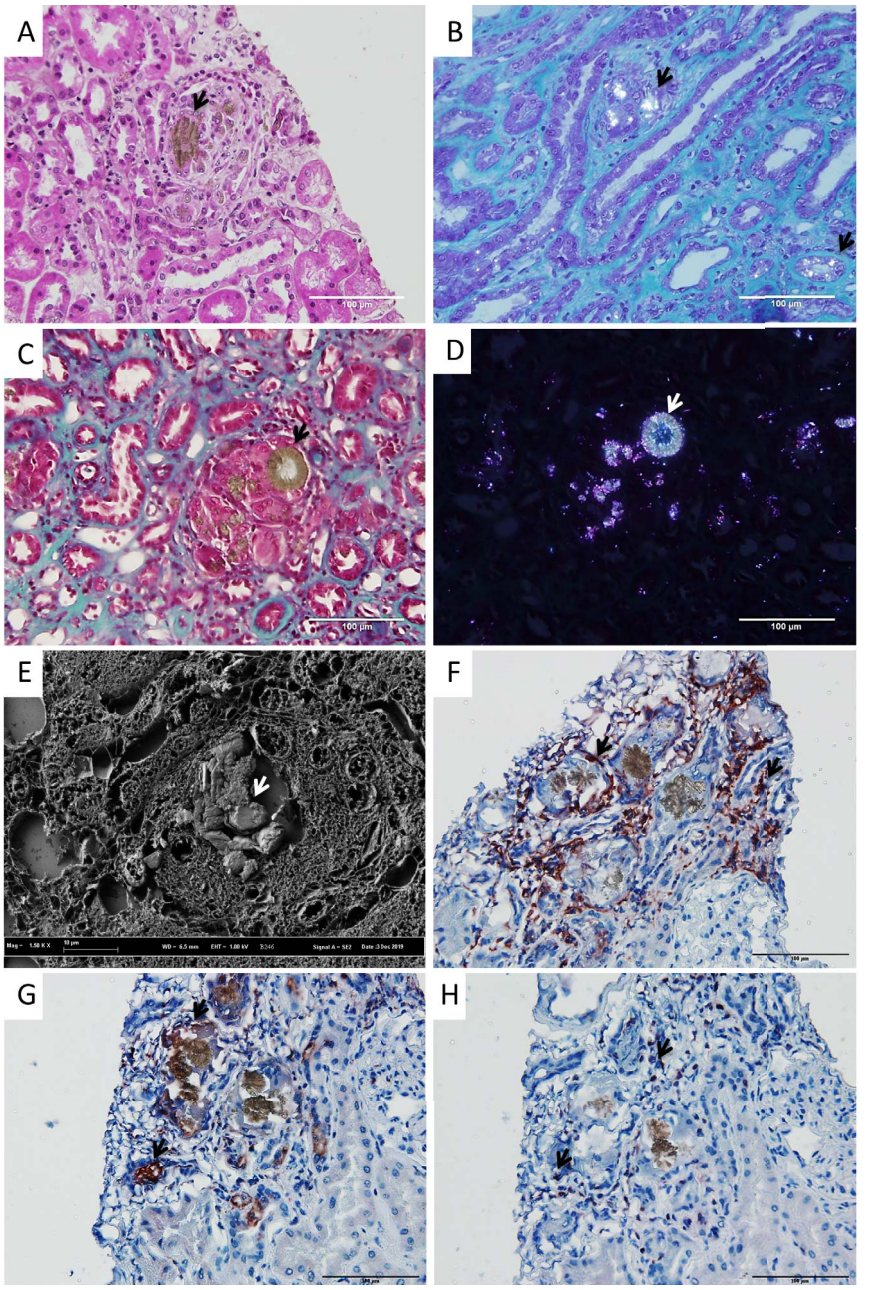

Figure 1. Typical crystalline deposits in kidney biopsies from patients affected by 2,8-DHA nephropathy. Crystallites were present in the tubular lumen and in the interstitial tissue and were frequently surrounded by granuloma containing epithelioid and giant cells (arrows, Figure 1A–D). Polarized light evidenced the presence of crystals in interstitial tissue and tubular cells (Figure 1B) and inside granuloma (Figure 1D). Scanning electron microscopy revealed the topography of deposits (Figure 1E). Immunohistochemistry revealed the presence of M2 type macrophages (arrows, CD163+, Figure 1F: crop showing the organization of macrophages around crystals), M1 type macrophages (arrows, CD68+, Figure 1G: crop showing the organization of macrophages around crystals) and lymphocytes (arrows, CD3+, Figure 1H) in granulomas surrounding 2,8-DHA crystallites. Negative controls did not evidence significant background staining (not shown).

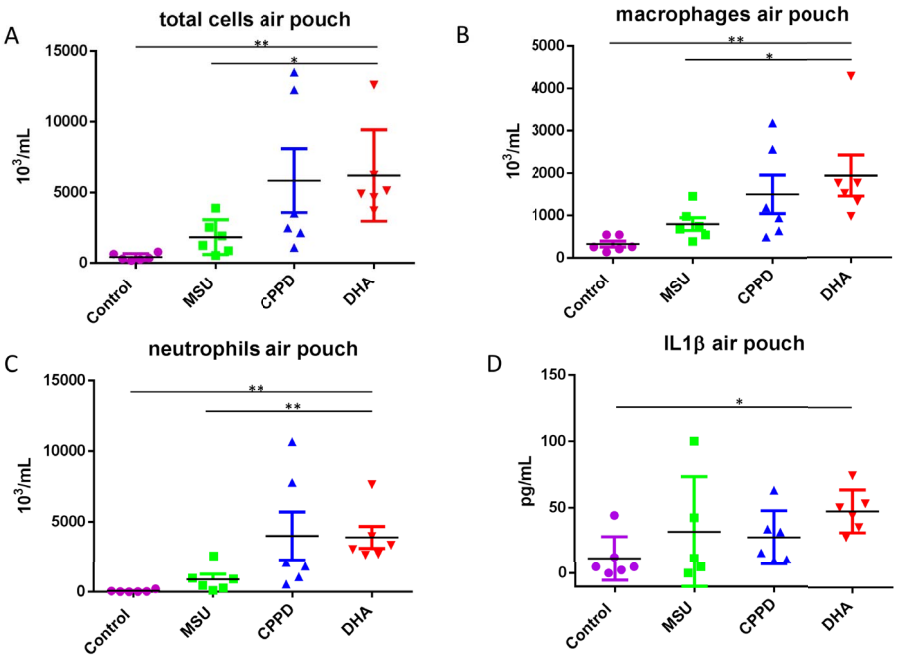

Figure 2. Air-pouch model. 2,8-DHA crystals increased significantly white blood cell recruitment at 6 h in the air-pouch in comparison with controls ($^{**}p = 0.002$, $n = 6$/group, Figure 2A) but also in comparison with MSU ($^{*}p = 0.01$, $n = 6$/group, Figure 2A). The number of macrophages was significantly increased by 2,8-DHA crystals in comparison with control and MSU crystals ($^{**}p = 0.002$ and $^{*}p = 0.01$ respectively, $n = 6$/group, Figure 2B), as well as the number of neutrophils ($^{**}p = 0.002$ vs controls and MSU crystals, $n = 6$/group, Figure 2C). There was no significant difference in white blood cells recruitment between mCPPD and DHA crystals (Figure 2A–C). IL-1β synthesis was also significantly increased by 2,8-DHA crystals in comparison with controls ($^{*}p = 0.01$, $n = 5$ or 6/group, Figure 2D). MSU: Monosodium urate; mCPPD: monoclinic calcium pyrophosphate dihydrate.

lower expression of IL-1β than controls and mice exposed to allopurinol alone ($p = 0.015$ and 0.0002, respectively, $N = 8$/group, Figure 5E). Mice exposed to allopurinol+dexamethasone had a lower expression of IL-1β than mice exposed to allopurinol alone ($p = 0.015$, $N = 8$/group, Figure 5E). TNF-α was reduced only in the allopurinol+anakinra group vs allopurinol alone ($p = 0.01$, $N = 8$/group, Figure 5F). Inflammatory infiltrate was less important in mice treated with anakinra and corticosteroids but infiltrates and granuloma were focal and therefore difficult to quantify (Figure 6).

6. Discussion

We describe herein that granuloma are frequent in a large series of kidney biopsies from patients affected by 2,8-DHA nephropathy and that 2,8-DHA crystals induce an important innate immune response *in vivo*. Moreover, in a murine model of 2,8-DHA nephropathy, anakinra and dexamethasone, combined with allopurinol, improved renal function to a larger extent than allopurinol alone, the current standard therapy.

The lesions observed in kidney biopsies from patients affected by APRT deficiency have been described since decades but little attention has been paid to granuloma and inflammatory infiltrates. By contrast, inflammation and the role of the NLRP3 inflammasome have been described more extensively in 2,8-DHA murine models, promoted by adenine-enriched diet [21,22]. It has been evidenced that NLRP3 pharmacological inhibition, limiting innate immunity and inflammation, could be protective

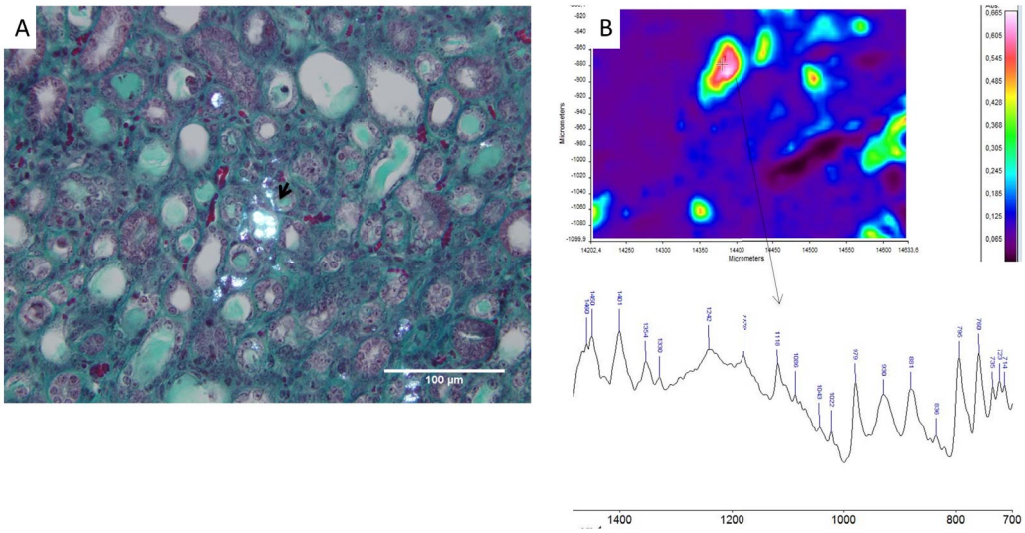

Figure 3. 2,8-DHA murine model. Typical crystals observed in polarized light after 4 weeks of adenine-enriched diet in kidney tissue in a control mouse (Figure 3A). FTIR microscopic analysis confirmed the nature of the crystalline phase: 2,8-DHA (Figure 3B, representative spectrum).

against crystalline nephropathies induced by calcium oxalate or 2,8-DHA crystal deposits [21,23, 24]. More recently, the presence of granuloma in a murine model of 2,8-DHA nephropathy has been highlighted [19].

As we observed massive inflammatory infiltrates and large granuloma in a series of human biopsies, we hypothesized that targeting innate immune pathways could be protective against renal lesions induced by 2,8-DHA, in addition to the conventional therapy (allopurinol or febuxostat). Actually, among 17 biopsies with FTIR-proven 2,8-DHA crystals in the tissue, epithelioid granuloma were present in 15 biopsies and centered by 2,8-DHA crystallites. 2,8-DHA crystals induced IL-1β synthesis *in vivo*, a result consistent with the biological effect of other particulate inflammasome activators, particularly sodium urate [25]. Interestingly, it has been shown recently in a rodent model of 2,8-DHA nephropathy that TNF receptor 1 was an important mediator of crystal clearance and inflammation [19]. Mice deficient in *Tnfr* 1 gene have reduced lesions and inflammation when exposed to 2,8-DHA nephropathy. In the view of these results the authors suggested that targeting the TNF/TNFR pathway could be a potential option to treat 2,8-DHA nephropathy, as previously shown in calcium oxalate nephropathy [26]. Although TNF-α is a potentially interesting target, we focused our attention on IL-1β because drugs inhibiting IL-1β pathway have been shown to be efficient in crystallopathies, especially gout and chondrocalcinosis [27]. In the air pouch model, the dramatic increase in IL-1β synthesis in response to 2,8-DHA crystals which correlated with white blood cell recruitment, led us to test drugs interfering with innate immunity in a murine 2,8-DHA model, dexamethasone and anakinra. The two murine models were complementary: the air-pouch model allowed a precise quantification of white-blood cells recruitment and IL-1β synthesis in response to 2,8-DHA crystals, whereas the 2,8-DHA nephropathy model highlighted the role of anti-inflammatory drugs, in addition to allopurinol, on renal function and renal tissue lesions. To date, the gold standard therapy against 2,8-DHA nephropathy is xanthine oxidoreductase inhibition, by allopurinol and in some cases febuxostat [17]. These drugs inhibit the conversion of adenine, produced in excess due to APRT deficiency, to 2,8-DHA which precipitates in urine. This lifelong therapy can prevent urolithiasis recurrence, stabilize renal function and sometimes ameliorate the glomerular filtration rate if prescribed early, but renal function recovery may be incomplete, especially after acute renal failure episodes [6,7]. In the

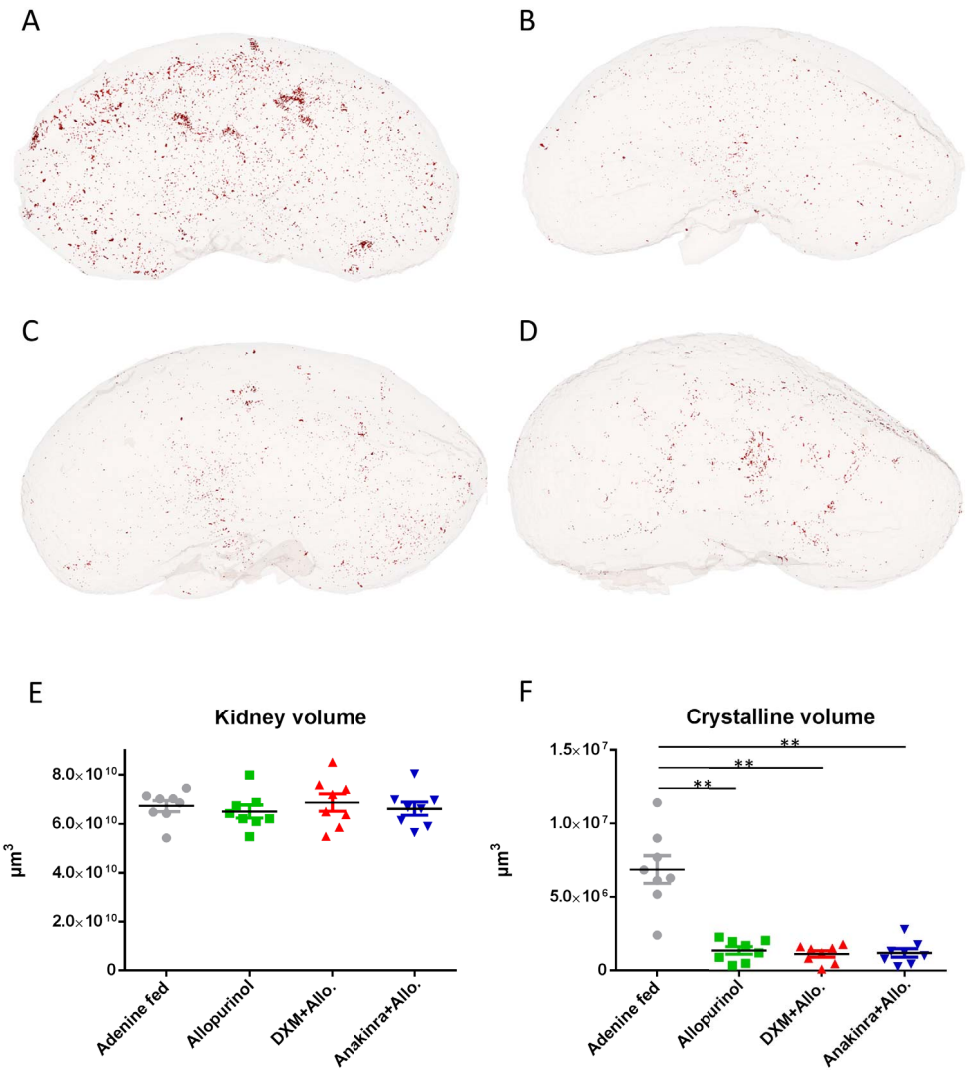

Figure 4. 3D measurement of crystalline volume. The 3-dimensional assessment of the crystalline volume was measured by CT-scan in the adenine fed (control) group (Figure 4A, 2,8-DHA crystallites in red), allopurinol group (Figure 4B), allopurinol+dexamethasone (Figure 4C) and allopurinol+anakinra (Figure 4D). Total volume of the kidneys was not affected by treatment in any group (Figure 4E). Allopurinol reduced significantly the volume of 2,8-DHA deposits as expected when compared to control group ($^{**}p = 0.0002$, Figure 4F). Crystalline volume reduction was also significant (vs adenine fed controls) in the allopurinol+dexamethasone (DXM+Allo.) and in the allopurinol+anakinra (Anakinra+Allo.) groups ($^{**}p = 0.0002$ and $p = 0.0003$ respectively, $N = 8$/group, Figure 4F). The addition of dexamethasone or anakinra to allopurinol did not reduce further the whole crystalline volume in comparison with allopurinol alone (p = NS, $n = 8$/group, Figure 4F). DXM: dexamethasone; Allo.: allopurinol.

view of human renal histology and air-pouch model results, we hypothesized that anti-inflammatory drugs could be of help in a murine model of 2,8-DHA, in addition to allopurinol, the standard therapy. Although non-specific, corticosteroids are still the main drugs used to control innate immunity, and have been shown to be efficient in renal granulomatous diseases such as sarcoidosis [28]. Anakinra

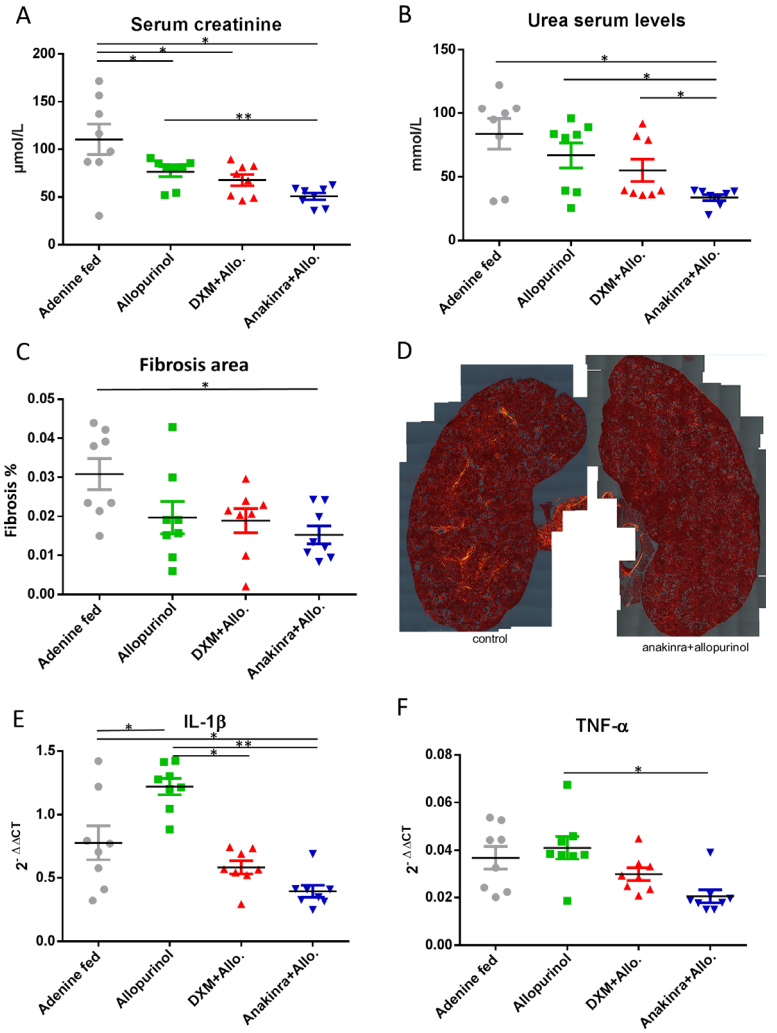

Figure 5. Renal function, inflammation and fibrosis. Serum creatinine was significantly higher in control adenine fed mice than in groups receiving allopurinol alone ($^{*}p = 0.019$, $N = 8$/group Figure 5A), allopurinol+dexamethasone (DXM+Allo.) or allopurinol+anakinra (Anakinra+Allo.) ($^{*}p = 0.02$ and $^{*}p = 0.01$, respectively, $n = 8$/group, Figure 5A). Mice exposed to anakinra and allopurinol had a lower serum creatinine level than mice exposed to allopurinol alone ($^{**}p = 0.009$, $N = 8$/group, Figure 5A). Serum urea levels were improved in the allopurinol+anakinra group when compared to control group ($^{*}p = 0.037$, $n = 8$/group, Figure 5B) but also in comparison with allopurinol and allopurinol+dexamethasone groups ($^{*}p = 0.02$ and 0.028, respectively, $N = 8$/group, Figure 5B). Renal fibrosis assessed by morphometry (sirius red in polarized light) was significantly decreased in mice treated with allopurinol+anakinra when compared to controls ($^{*}p = 0.01$, $N = 8$/group, Figure 5C,D; mosaics: left: control kidney, right: allopurinol+anakinra kidney). A non-significant trend toward less fibrosis was observed in mice receiving allopurinol and allopurinol/steroids. The expression of IL-1β was markedly increased in mice treated with allopurinol alone when compared to controls ($^{*}p = 0.028$, $N = 8$/group, Figure 5E). Mice exposed to allopurinol+anakinra had a lower expression of IL-1β than controls and mice exposed to allopurinol alone ($^{*}p = 0.015$ and $^{**}0.0002$, respectively, $N = 8$/group, Figure 5E). Mice exposed to allopurinol+dexamethasone had a lower expression of IL-1β than mice exposed to allopurinol alone ($^{*}p = 0.015$, $N = 8$/group, Figure 5E). TNF-α was reduced only in the anakinra/allopurinol group vs allopurinol alone ($^{*}p = 0.01$, $N = 8$/group, Figure 5F). IL-1β: interleukin-1 beta; TNF-α: Tumor necrosis factor alpha; DXM: dexamethasone; Allo.: allopurinol.

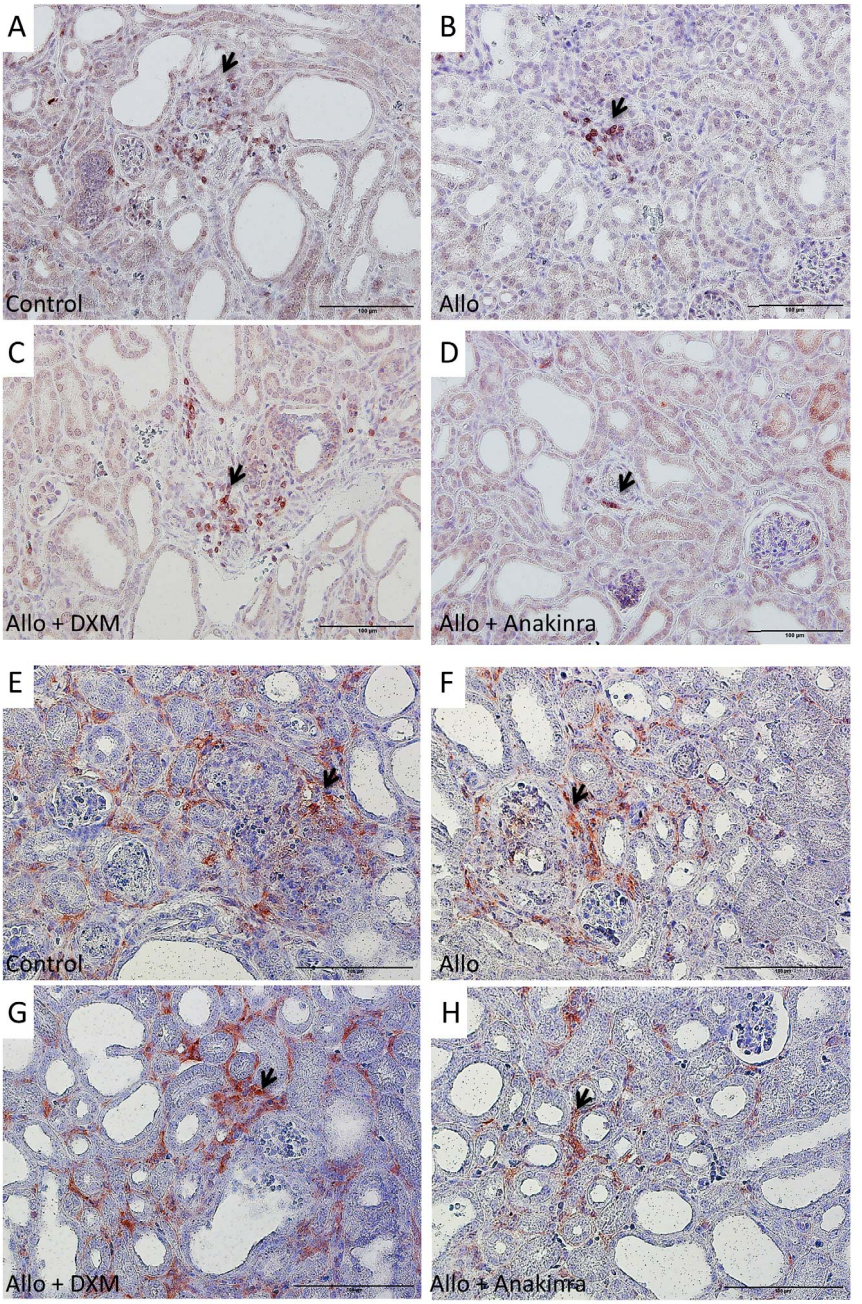

Figure 6. Inflammatory infiltrate in the murine model of nephropathy. Lymphocytes infiltrate (anti CD3 antibody) was less important in mice treated with anakinra (Figure 6D) and to a lesser extent with DXM (Figure 6C) than in control mice (Figure 6A) and in mice treated with allopurinol alone (Figure 6B). Macrophages (anti pan-macrophages antibody) were less present in mice treated with anakinra (Figures 6H) and DXM (Figure 6G) than in control mice (Figure 6E) and in mice treated with allopurinol alone (Figure 6F). Negative controls evidenced a mild background staining (not shown). DXM: dexamethasone; Allo: allopurinol.

is a recombinant, and slightly modified, human interleukin 1 receptor antagonist protein. It has been developed to treat rheumatoid arthritis and is also useful to manage gout attacks and to a larger extent diseases involving NLRP3 inflammasome activation and IL-1β synthesis [27].

The addition of anakinra or dexamethasone to allopurinol improved significantly renal function and renal lesions in the murine model of 2,8-DHA nephropathy. Of note, dexamethasone may have increased serum urea levels through its catabolic effect, limiting the decrease in serum urea due to improvement of renal function. Interestingly, allopurinol decreased significantly, as expected, the amount of crystalline deposits in renal tissue but the addition of steroids or anakinra did not reduce further the crystalline global volume, suggesting that these anti-inflammatory drugs protected renal tissue against fateful damages induced by inflammation and fibrosis but did not reduce significantly crystal adhesion or retention in tubules.

Anakinra has already been tested in another crystalline nephropathy model induced by calcium-oxalate tubular crystallites. Mulay *et al.* have shown first that IL-1 blockade by anakinra protected from renal failure in calcium oxalate nephropathy but in more recent models, anakinra did not improve renal function in a calcium oxalate nephropathy model [23,24]. In a murine model of 2,8-DHA crystalline nephropathy, inhibition of NLRP3 inflammasome by a specific inhibitor had demonstrated its efficiency to reduce IL-1β synthesis and kidney fibrosis [21]. One may hypothesize that purine-mediated IL-1β synthesis may be particularly important in response to 2,8-DHA crystals.

The most surprising observation was the significantly increased expression of IL-1β and TNF-α in the kidneys of mice treated with allopurinol alone. It seems unlikely that allopurinol by itself would be pro-inflammatory and we have no clear explanation but a parallel may be drawn with another crystallopathy: gout. Actually, the onset of treatments decreasing serum urate levels in gouty patients is associated with acute gout flares. The underlying mechanism is unknown but it has been hypothesized that urate lowering may lead to large crystals or tophi destabilization and induce pro-inflammatory pathways, this is the reason why allopurinol and febuxostat are classically associated with colchicine to prevent gout flares during the first months of the therapy [29]. One may also hypothesize that in the 2,8-DHA nephropathy model, allopurinol would be overall beneficial by lowering 2,8-DHA crystals formation (as observed in our model) but, on the other hand, could "activate" transiently pro-inflammatory pathways through destabilization of 2,8-DHA crystallites. This mechanism remains hypothetical to date and deserves further studies but this observation stresses even more the potential benefit of a short-term therapy based upon steroids or anakinra when initiating the treatment of 2,8-DHA nephropathy by allopurinol or febuxostat.

One of the main strength of our study is the demonstration, in a significant number of human biopsies and in murine models, that inflammation plays a role in the lesions induced by 2,8-DHA crystals. The significant improvement of renal function by anakinra and dexamethasone definitively proves the key role of innate immunity in this model and opens new potential clinical perspectives. Our study has some limitations. In murine *in vivo* models, we evidenced that cytokine synthesis was decreased significantly in mice exposed to anakinra and dexamethasone but, unlike in the air pouch model, we could not quantify precisely the number of immune cells in the kidney tissue. Moreover, although we confirmed that the crystalline deposits were actually made of 2,8-DHA, the *in vivo* model is based upon administration of adenine, and not a genetic murine model based upon APRT deficiency [30,31].

As a conclusion, inflammation and innate immunity play a critical role in 2,8-DHA nephropathy. Steroids or drug targeting IL-1 pathway are efficient to protect renal function and tissue in experimental models, when added to the standard therapy. As the disease is rare, it does not seem feasible to test these drugs in a randomized controlled study but the risk of a transient treatment by steroids or anakinra seems low in comparison with the potential benefit. The observation of granuloma in the renal biopsy could be of help before initiating this type of treatment. For instance, there is no doubt that steroids are useful against granulomatous lesions due to renal sarcoidosis. Unfortunately, APRT deficiency is frequently diagnosed in renal transplant recipients: the use of corticosteroids has decreased in renal transplantation during the past decades, in the view of their long-term side effects, but a transient treatment targeting

innate immunity when inflammatory infiltrate is observed in the graft seems a reasonable option, especially when allopurinol or febuxostat is initiated. Additional studies are still warranted, including the assessment of plasma and/or urinary biomarkers for inflammatory activity in the kidney of patients affected by 2,8-DHA nephropathy.

References

[1] G. Bollée, J. Harambat, A. Bensman, B. Knebelmann, M. Daudon, I. Ceballos-Picot, *Clin. J. Am. Soc. Nephrol.*, 2012, **7**, 1521-1527.

[2] I. Ceballos-Picot, J. L. Perignon, M. Hamet, M. Daudon, P. Kamoun, *Lancet*, 1992, **339**, 1050-1051.

[3] Y. Hidaka, T. D. Palella, T. E. O'Toole, S. A. Tarlé, W. N. Kelley, *J. Clin. Investig.*, 1987, **80**, 1409-1415.

[4] V. Edvardsson, R. Palsson, I. Olafsson, G. Hjaltadottir, T. Laxdal, *Am. J. Kidney Dis.*, 2001, **38**, 473-480.

[5] E. R. Gagné, E. Deland, M. Daudon, L. H. Noël, T. Nawar, *Am. J. Kidney Dis.*, 1994, **24**, 104-107.

[6] G. Bollée, P. Cochat, M. Daudon, *Can. J. Kidney Health Dis.*, 2015, **2**, article no. 31.

[7] M. Zaidan, R. Palsson, E. Merieau, E. Cornec-Le Gall, A. Garstka, U. Maggiore, P. Deteix, M. Battista, E.-R. Gagné, I. Ceballos-Picot, J.-P. Duong Van Huyen, C. Legendre, M. Daudon, V. O. Edvardsson, B. Knebelmann, *Am. J. Transplant.*, 2014, **14**, 2623-2632.

[8] I. Ceballos-Picot, M. Daudon, J. Harambat, A. Bensman, B. Knebelmann, G. Bollée, *Nucleosides Nucleotides Nucleic Acids*, 2014, **33**, 241-252.

[9] G. Bollée, C. Dollinger, L. Boutaud, D. Guillemot, A. Bensman, J. Harambat, P. Deteix, M. Daudon, B. Knebelmann, I. Ceballos-Picot, *J. Am. Soc. Nephrol.*, 2010, **21**, 679-688.

[10] A. Sahota, J. Chen, S. A. Boyadjiev, M. H. Gault, J. A. Tischfield, *Hum. Mol. Genet.*, 1994, **3**, 817-818.

[11] N. Kamatani, M. Hakoda, S. Otsuka, H. Yoshikawa, S. Kashiwazaki, *J. Clin. Investig.*, 1992, **90**, 130-135.

[12] V. O. Edvardsson, D. S. Goldfarb, J. C. Lieske, L. Beara-Lasic, F. Anglani, D. S. Milliner, R. Palsson, *Pediatr. Nephrol.*, 2013, **28**, 1923-1942.

[13] H. L. Runolfsdottir, J. A. Sayer, O. S. Indridason, V. O. Edvardsson, B. O. Jensson, G. A. Arnadottir, S. A. Gudjonsson, R. Fridriksdottir, H. Katrinardottir, D. Gudbjartsson, U. Thorsteinsdottir, P. Sulem, K. Stefansson, R. Palsson, *Eur. J. Hum. Genet.*, 2021, 1061-1070.

[14] M. Daudon, P. Jungers, *Nephron Physiol.*, 2004, **98**, 31-36.

[15] V. Frochot, M. Daudon, *Int. J. Surg.*, 2016, **36**, 624-632.

[16] G. Garigali, G. Marra, V. Rizzo, F. de Liso, A. Berrettini, M. Daudon, G. B. Fogazzi, *Clin. Chim. Acta*, 2019, **492**, 23-25.

[17] V. O. Edvardsson, H. L. Runolfsdottir, U. A. Thorsteinsdottir, I. M. S. Agustsdottir, G. S. Oddsdottir, F. Eiriksson, D. S. Goldfarb, M. Thorsteinsdottir, R. Palsson, *Eur. J. Intern. Med.*, 2018, **48**, 75-79.

[18] H. L. Runolfsdottir, R. Palsson, I. M. S. Agustsdottir, O. S. Indridason, J. Li, M. Dao, B. Knebelmann, D. S. Milliner, V. O. Edvardsson, *Transplantation*, 2020, **104**, 2120-2128.

[19] B. M. Klinkhammer, S. Djudjaj, U. Kunter, R. Palsson, V. O. Edvardsson, T. Wiech, M. Thorsteinsdottir, S. Hardarson, O. Foresto-Neto, S. R. Mulay, M. J. Moeller, W. Jahnen-Dechent, J. Floege, H.-J. Anders, P. Boor, *J. Am. Soc. Nephrol.*, 2020, **31**, 799-816.

[20] P. Gras, C. Rey, O. Marsan, S. Sarda, C. Combes, *Eur. J. Inorg. Chem.*, 2013, **2013**, 5886-5895.

[21] I. Ludwig-Portugall, E. Bartok, E. Dhana, B. D. G. Evers, M. J. Primiano, J. P. Hall, B. S. Franklin, P. A. Knolle, V. Hornung, G. Hartmann, P. Boor, E. Latz, C. Kurts, *Kidney Int.*, 2016, **90**, 525-539.

[22] C. Okabe, R. L. Borges, D. C. de Almeida, C. Fanelli, G. P. Barlette, F. G. Machado, S. C. A. Arias, D. M. A. C. Malheiros, N. O. S. Camara, R. Zatz, C. K. Fujihara, *Am. J. Physiol. Renal. Physiol.*, 2013, **305**, F155-F163.

[23] H.-J. Anders, B. Suarez-Alvarez, M. Grigorescu, O. Foresto-Neto, S. Steiger, J. Desai, J. A. Marschner, M. Honarpisheh, C. Shi, J. Jordan, L. Müller, N. Burzlaff, T. Bäuerle, S. R. Mulay, *Kidney Int.*, 2018, **93**, 656-669.

[24] S. R. Mulay, O. P. Kulkarni, K. V. Rupanagudi, A. Migliorini, M. N. Darisipudi, A. Vilaysane, D. Muruve, Y. Shi, F. Munro, H. Liapis, H.-J. Anders, *J. Clin. Investig.*, 2013, **123**, 236-246.

[25] F. Martinon, V. Pétrilli, A. Mayor, A. Tardivel, J. Tschopp, *Nature*, 2006, **440**, 237-241.

[26] S. R. Mulay, J. N. Eberhard, J. Desai, J. A. Marschner, S. V. R. Kumar, M. Weidenbusch, M. Grigorescu, M. Lech, N. Eltrich, L. Müller, W. Hans, M. Hrabě de Angelis, V. Vielhauer, B. Hoppe, J. Asplin, N. Burzlaff, M. Herrmann, A. Evan, H.-J. Anders, *J. Am. Soc. Nephrol.*, 2017, **28**, 761-768.

[27] A. So, T. De Smedt, S. Revaz, J. Tschopp, *Arthritis Res. Ther.*, 2007, **9**, article no. R28.

[28] R. Bergner, C. Löffler, *Curr. Opin. Pulm. Med.*, 2018, **24**, 513-520.

[29] A. Latourte, T. Bardin, P. Richette, *Rheumatology (Oxford)*, 2014, **53**, 1920-1926.

[30] S. J. Engle, M. G. Stockelman, J. Chen, G. Boivin, M. N. Yum, P. M. Davies, M. Y. Ying, A. Sahota, H. A. Simmonds, P. J. Stambrook, J. A. Tischfield, *Proc. Natl. Acad. Sci. USA*, 1996, **93**, 5307-5312.

[31] N. J. Redhead, J. Selfridge, C. L. Wu, D. W. Melton, *Hum. Gene Ther.*, 1996, **7**, 1491-1502.

Comptes Rendus
Chimie
2022, Vol. 25, Special Issue S1, p. 407-416
https://doi.org/10.5802/crchim.162

Microcrystalline pathologies: Clinical issues and nanochemistry

Endoscopic *in-situ* recognition of urinary stones during LASER-induced stone fragmentation: a modern, effective and essential approach in the diagnostic process in urolithiasis

Vincent Estrade [a,*], Baudouin Denis de Senneville [b], Laurent Facq [b] and Michel Daudon [c]

[a] Department of Urology, CHU Pellegrin, Place Amélie Raba Léon 33000 Bordeaux, France

[b] Univ. Bordeaux, CNRS, INRIA, Bordeaux INP, IMB, UMR 5251, F-33400 Talence, France

[c] INSERM UMRS 1155, Sorbonne University, Tenon Hospital, Paris, France

E-mails: vincent.estrade@gmail.com (V. Estrade), bdenisde@math.u-bordeaux.fr (B. Denis de Senneville), laurent.facq@math.u-bordeaux.fr (L. Facq), daudonmichel24@gmail.com (M. Daudon)

Abstract. Examination of stone morphologies shows a great potential for the etiological diagnosis of stone disease. Endoscopic Stone Recognition (ESR) can thereby provide essential morpho-constitutional analysis of stones *in-situ*, and becomes a method of choice for an effective management of patients with kidney stones.

Here, we show that both visual and automatic ESR can be performed within a LASER-induced spraying session. ESR may therefore be beneficial to still apply an etiological approach in lithiasis. We discuss the added value of Artificial Intelligence in the entire patient care process. Prospects and requirements for widespread applications of ESR in a clinical practice are evaluated.

Keywords. Morpho-constitutional analysis of urinary stones, Endoscopic diagnosis, Automatic recognition, Deep learning, Etiology.

Published online: 15 March 2022

1. Introduction

Analysis of stone composition allows establishing dedicated treatments that can eliminate stones with a reduced probability of relapses. To this end, non-enhanced computed tomography (CT) is currently the first step of an etiological approach by a urologist. Zhang *et al.* showed that dual-source dual-energy CT can predict common stone composition for both pure and mixed stones [1]. However, the limitations of such an approach mainly lie in (1) a substantial radiation exposure, (2) an accuracy of the results directly dependent on the extraction quality

* Corresponding author.

of the piece of stone, (3) the fact that this approach does not give access to the morphological aspect of urinary stones, which may be the key for an accurate etiological diagnosis [2,3].

Alternatively, a morpho-constitutional examination of urinary stones becomes a method of choice [2–5]. It is now well established that such examinations play an essential role in the etiological diagnosis, as explained in the international morpho-constitutional classification of urinary stones [5]. This analysis can be performed during a post-operative session by a biologist and consists of collecting morpho-constitutional information based on both microscopic morphology, using binocular stereomicroscope, and infrared spectroscopy recognition (FTIR). Alternatively, Endoscopic Stone Recognition (ESR), which is conducted by a urologist, can also conveniently provide essential morphological observations of stones *in-situ* during pre- and intra-operative sessions [6,7].

In this article, the principles of ESR are reviewed; then, various LASER technologies designed for kidney stone fragmentation are presented. ESR, which can be supported by Artificial Intelligence (AI), may find a widespread use in a clinical practice. The requirements for such a generalized use are described.

2. Basic principles of ESR

ESR-based analysis is, to a certain extent, similar to that applied by a biologist in a dedicated laboratory: detailed knowledge on the classification of the different types of stone surface, section and nuclei is a prerequisite; this expertise encompasses the use of well-established stone descriptions obtained with microscopy images *ex-vivo* [2] and endoscopic images *in-situ* [6,7] classified with respect to the nomenclature established by Corrales *et al.* [5]. A relatively fast learning curve was reported when urologists following the ESR training encountered the most frequent stone morphologies, such as: stones with a single crystalline component [8], calcium oxalate monohydrate (COM) (also referred to as type I, subdivided in subtypes Ia, Ib, Ic, Id or Ie—subscripts in the Latin alphabet differentiate morphological subtypes, each of them being associated with a specific etiology), calcium oxalate dihydrate (COD, morphological type II subdivided as IIa and IIb subtypes) and uric acid (UA, morphological type III subdivided as IIIa and IIIb subtypes) [9]. However, a much steeper learning curve was needed when calcium phosphates or mixed stone morphologies are involved [7,8]; this issue may limit ESR translation to daily clinical practice [9].

3. LASER devices for kidney stone fragmentation

Since the beginning of the 2000's, the LASER Holmium-Yag technology is accessible to any urologist for urinary-stone treatments [10]. Thanks to recent technological innovations, LASER spraying of all types of stones is now feasible and two main interventional strategies were implemented:

1. "Pop corning" mode: using moderate LASER frequencies ranging from 10 to 15 Hz, the urologist can either (i) split a stone in two parts or (ii) fragment it into small pieces. Stone fragments of a size of 250–500 μm can be collected, thus allowing for post-operative examinations of the microscopic morphology [10–15].
2. "Dusting" mode: using higher LASER frequencies ranging from 20 to 320 Hz, the operator can conveniently spray the stone [13]. Since 2017, this is achievable using Holmium-Yag devices by means of the "Moses Effect" [12] and, more recently, using Thulium Fiber LASER (TFL) devices. There, micro fragments below 250 μm are created, 20 μm being generally the wanted size [14].

Both the Holmium-Yag using "Moses Effect" and TFL devices thus appear effective technological revolutions able to quickly operate in interventional theaters [12,13,16]. This technological breakthrough has a clearly obvious therapeutic objective: to eliminate the presence of any stone fragments at the end of the interventional procedure. In addition, therapeutic approaches have been rated for decades by both urologists and manufacturers according to their capability to eliminate stone fragments.

However, LASER fragmentation of stones, when achieving "dusting" modes [11–15], has two consequences that hamper the etiological approach in lithiasis:

1. High frequency LASER stone fragmentation irreversibly hampers the morphological analysis of the targeted stones [14,15]. FTIR dust examinations of the stone powder, with a fragment size below 250 μm, may not provide sufficient information for the lithogenic stage.
2. IR spectra can be modified when the LASER stone fragmentation is achieved in dusting mode with or without high-frequency TFL or "Moses Effect" [14,15], which hampers FTIR dust examinations. Keller *et al.* observed IR-conversion of several crystalline elements *in-vitro* during "Moses Effect", in particular IR changes from COD towards COM, IR changes from carbapatite towards amorphous carbonated calcium phosphate, MAP in newberyite and BR in monetite as well as IR changes from brushite towards carbapatite (see Figure 1 and Table 1) [14,15].

The so-called "stone free rate" therapeutic objective [10–15,17] is therefore now achievable. However, it must be underlined that the morphological type and related etiology are better indicators of stone recurrence than stone composition only. Hence, the absence of intra-operative examination (in other terms: no morphological data) may preclude the robustness of the etiological approach in lithiasis and relapse prevention [5].

Fortunately, it has been reported that visual examinations of stone can be obtained using ESR before and during LASER destruction [7,8]. While recent (chronological) lithogenic events are observable on the stone surface, older events are located on a stone section and are accessible during LASER fragmentation. The stone nucleus, which is the oldest part, can thereby provide information about the initial lithogenic context. Recently, Estrade *et al.* demonstrated that these examinations can be readily supplemented by observations of the stone section and nucleus if the urologist carefully splits the stone in two parts using LASER [8].

The traceability of the morphology of the surface, the section and the nucleus of a urinary stone can be recorded, thus allowing a retrospective expertise, if necessary, by a biologist, an expert urologist or machine learning. Therefore, intra-operative ESR and post-operative infrared (FTIR) examinations of LASER-fragmented stones are crucial to preserve an etiological approach in lithiasis.

4. Towards automatic intra-operative ESR

Black *et al.* recently have shown that artificial intelligence (AI) applied to various types of microscopic images of stones *ex-vivo* is a promising tool for automatic ESR (AESR) [18]. While Serrat *et al.* fed texture and color features of stones into a random forest classifier [19], Black *et al.* obtained much improved scores using a deep Convolutional Neural Network (CNN) [18]. However, both approaches used *ex-vivo* stone fragments placed into a controlled environment. Hence, images were not disturbed by motion blur, specular reflections or scene illumination variations, as it is encountered in common practice during an intra-operative endoscopic imaging session. Martinez *et al.* showed the potential of AESR approaches using *in-situ* images of pure stones acquired in a clinical setting with ureteroscopes [20]. More recently, from intra-operative endoscopic images, first AESR clinical results evidencing morphological elements that constituted both pure and mixed urinary stones *in-situ* have been reported [21]. As an illustration, Table 2 reports typical preliminary AESR results obtained with six morphology classes (four pure stones: Ia/COM, Ia active, IIb/COD and IIIb/UA, and two mixed stones divided into two morphologies: Ia/COM + IIb/COD and Ia/COM + IIIb/UA) from images obtained before LASER fragmentation. In this study, a urologist (VE, 20 years of experience) prospectively examined intra-operative endoscopic digital images of stones acquired between January 2018 and November 2020 (single center) using a flexible digital ureterorenoscope (Olympus URF-V CCD sensor). Images from 436 urinary stones were collected (pure stones: Ia/COM = 221, Ia active = 32, IIb/COD = 66, IIIb/UA = 31; mixed stones: Ia/COM + IIb/COD = 74, Ia/COM + IIIb/UA = 12). A deep convolutional neural network (CNN), ResNet-152-V2 [22], was trained to predict stone types from collected images. For the statistical analysis, stones were randomly divided into training (70%) and testing (30%) sets (stratified split/10 trials) [23]. In average, the accuracy was higher than 86% for both pure and mixed stones with the experimental setup used [21].

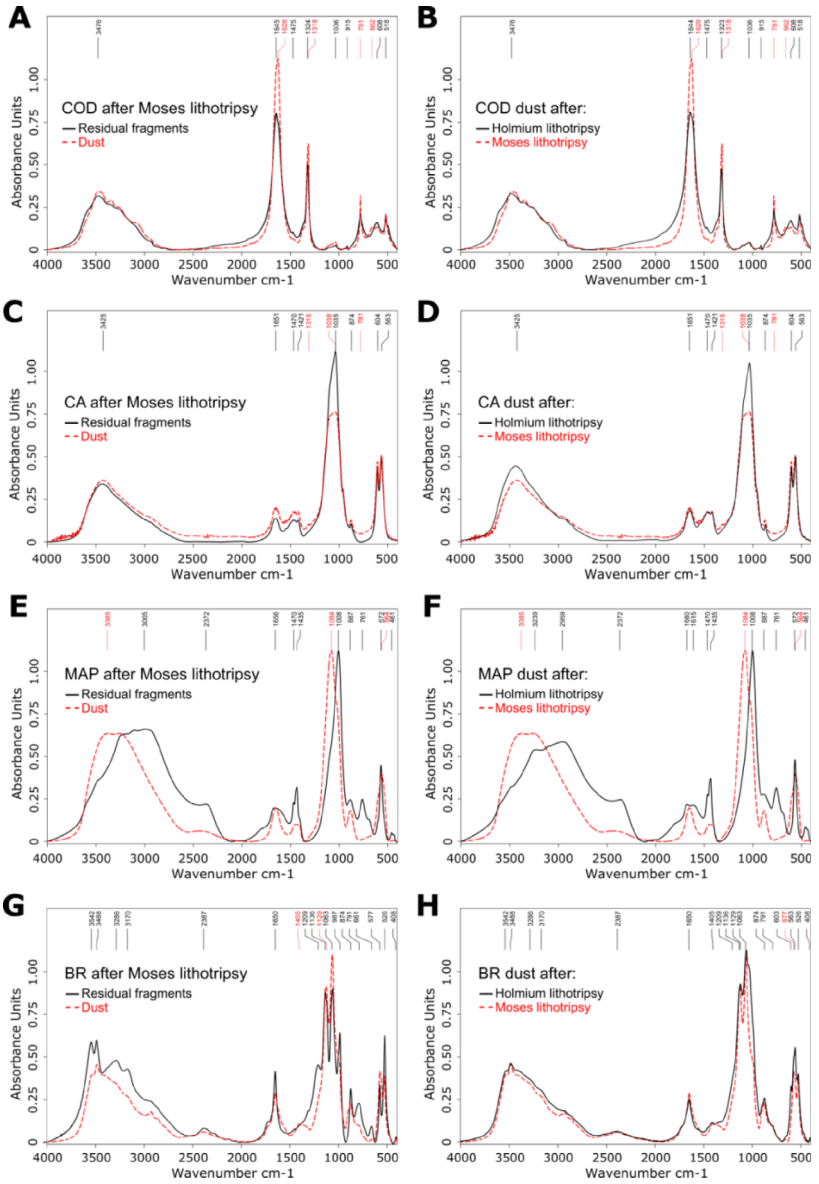

Figure 1. Constitutional analysis by Fourier transform infrared spectroscopy. Comparison between residual fragments and stone dust revealed spectra changes for several constitutional stone types. (A) Conversion from COD towards COM in dust after Moses lithotripsy. (B) The conversion from COD towards COM in dust was more pronounced after Moses lithotripsy compared to conventional Holmium lithotripsy. (C) Changes towards an amorphous phase in CA dust after Moses lithotripsy with flattening and displacement of the 1035 cm^{-1} band. (D) A spectral change of CA dust was only found after Moses lithotripsy, but not after conventional Holmium lithotripsy. (E) Changes towards a differing and amorphous crystalline phase in MAP dust after Moses lithotripsy. (F) A spectral change of MAP dust was only found after Moses lithotripsy, but not after conventional Holmium lithotripsy. (G) Changes from BR towards CA after Moses lithotripsy. (H) Spectral changes were found in CA dust both after Moses and conventional Holmium lithotripsy. Figure and caption reproduced with permission from Keller *et al.* [15].

Table 1. Observations from morpho-constitutional analysis of stone dust after TFL lithotripsy

Stone type	Preserved characteristics from initital stones?	Morphological analysis (SEM)	Constitutional analysis (FTIR)
COM	Yes	Preserved lamellar organization	Preserved major bands at 1617, 1315 and 781 cm^{-1}
COD	Partially	Almost complete loss of bipyramidal organization	Displacement of major bands from 1645 and 1324 cm^{-1} to 1624 and 1318 cm^{-1}, respectively, as well as appearance of a prominent band at 781 cm^{-1} indicating a conversion from COD to COM
UA	No	Altered organization with appearance of a needle-like organization	Major bands at 3603, 1613, 1531 and 1003 cm^{-1}, indicating a conversion from UA to sodium hydrogen urate monohydrate
CA	Yes	Preserved organization with spherical particles within more smooth blocks	Preserved major bands at 1035, 604 and 563 cm^{-1}
STR	No	Loss of the encased monodirectional needle organization resulting in a pile of randomly configured needles that are partially attached to each other	Loss of the ammonium bands at 1470 and 1435 cm^{-1}. Very large and displaced major band at 1014 cm^{-1} indicating a conversion from STR to newberyite
BR	Partially	Partially preserved longitudinal beguette-like organization	Displacement of major bands from 1136 and 1063 cm^{-1} to 1134 and 1066 cm^{-1}, respectively, as well as the appearance of major bands at 1002 and 564 cm^{-1}, as well as additional bands at 1406 and 892 cm^{-1}, indicating a convrsion from BR to monetite
CYS	Partially	Preserved layered organization, with an almost complete loss of the hexagonal organization	Loss of the 1656 cm^{-1} band, unusually prominent band at 1622 cm^{-1} and large, prominent and displaced band at 1337 cm^{-1}, indicating a profound change in crystalline organization

Table and caption reproduced with permission from Keller *et al.* 2020 [14].

SEM: scanning electron microscopy, FTIR: fourier transform infrared spectroscopy, COM: calcuum oxalate monohydrate, COD: calcium oxalate dihydrate, UA: uric acid, CA: carbapatite, STR: struvite, BR: brushite, CYS: cystine.

5. Requirements of intra-operative AESR in the etiological approach

ESR can be supported by a computer-assisted approach, which may deliver reproducible results and minimizes operator dependency. In our opinion, it is imperative to build-up a digital endoscopic image database annotated according to the criteria published in 2020 [7]. However, several issues still need to be addressed for a wide AESR integration into a clinical routine.

First, it is difficult to obtain a gold standard database of annotated stone images, which is a necessary prerequisite for the training of an IA network [24,25].

Table 2. Diagnostic performance of a CNN classifier (ResNet-152-V2) to predict the surface of pure stones COM, COD and AU with respective morphologies (Ia, Ia active, IIb and IIIb) and mixed stones COM+COD and COM + AU with morphologies (Ia + IIb and Ia + IIIb) from collected images

Kidney type	Accuracy (%)	AUROC	Sensitivity (%)	Specificity (%)	PPV (%)	NPV (%)	FPR (%)	FNR (%)
Ia	86 ± 2	0.86 ± 0.02	89 ± 3	84 ± 5	85 ± 4	88 ± 3	16 ± 5	11 ± 3
Ia active	93 ± 1	0.75 ± 0.06	53 ± 13	97 ± 1	64 ± 8	96 ± 1	3 ± 1	47 ± 13
IIb	93 ± 1	0.86 ± 0.04	77 ± 9	96 ± 1	74 ± 6	96 ± 1	4 ± 1	23 ± 9
IIIb	98 ± 1	0.95 ± 0.04	92 ± 7	98 ± 1	81 ± 11	99 ± 1	2 ± 1	8 ± 7
Ia + IIb	89 ± 3	0.79 ± 0.04	63 ± 8	94 ± 3	70 ± 9	92 ± 1	6 ± 3	37 ± 8
Ia + IIIb	98 ± 1	0.66 ± 0.16	33 ± 3	100 ± 1	52 ± 47	98 ± 1	0 ± 1	67 ± 31

AUROC: area under the ROC (Receiver Operating Characteristic) curve; PPV: positive predictive value; NPV: negative predictive value; FPR: false predictive rate; FNR: false negative rate.

On the one hand, infrared spectroscopy can be used as a gold standard, but its accuracy relies on the equipment used, the reference spectra and the qualification of the operator. On the other hand, one can use ESR as a gold standard, but any subjectivity or potential selection bias of the endo-urologist may be present in the annotated dataset. We believe that a concordance study between endoscopic and microscopy examinations, as described in [7], may provide a database of confirmed annotated ESR image of stones corresponding to specific aetiologies or lithogenic mechanisms.

Second, AI generally relies on a large amount of labeled training images to provide accurate stone predictions [22,23]; however, a sufficient amount of images is hardly achievable in the context of rare diseases. This is problematic on the clinical level because such pathologies are precisely those in need for a rapid and reliable management. Therefore, AI algorithms must be improved in order to further reduce the amount of training data, thereby allowing AESR of rare stone diseases with a satisfactory reliability. Several paths of investigation may be taken to reach this goal; for instance, training databases may be conveniently supplemented by high-quality *ex-vivo* images of complete and fractioned stones [7,21]. In addition, an interesting aspect to explore is the potential benefit of AI classification algorithms upon clustering of different stone types, but also the impact of possible overlaps between these clusters. Ultimately, the development of specific image filtering algorithms and the automatic segmentation of relevant image regions of interest should allow reducing the amount of training samples needed, and may give access to rather reliable AESR workflows for specific stone types.

Third, it must be underlined that a general problem with the deep neural network approach lies in the difficulty to interpret and understand what the model has learned. Regularly called "black box" algorithms, deep neural networks are often questioned because of their lack of explicitness; computer-assisted predictions of stone morphologies may thus be hardly explainable. However, a general interest in AI techniques designed to address such a key point is growing in order to devise robust validation procedures. In particular, recent AI studies underlined the benefit of generating maps to properly understand where the deep learning algorithm of interest was "looking" in the endoscopic image to make its decision [26]. In that regard, recent efforts must be reported in the identification of the learned patterns by AI models. During endoscopy, it is essential to highlight the most characteristic locations inferred by the network in the endoscopic image of interest. Figures 2 and 3, reproduced from [21], illustrate the usefulness of providing deep CNN-algorithm based "attention" maps to explain predictions computed by deep CNNs. In these figures, "attention" maps are overlaid onto the endoscopic image in order to visually assess whether CNN-derived hallmarks corroborate with clinically relevant stone features. In the presented results, hot (red) spots were found on relevant urological features in 98% of the

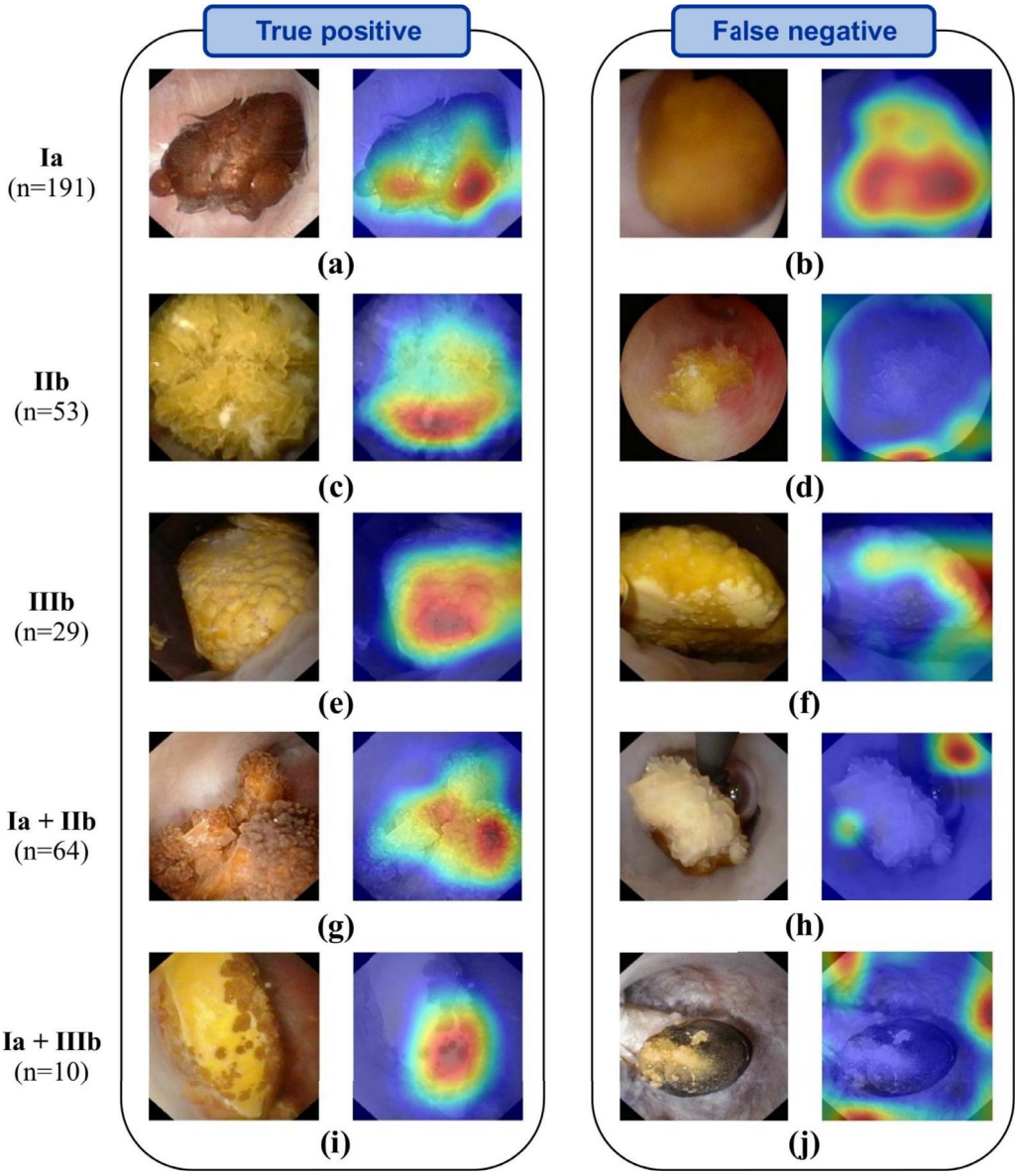

Figure 2. Representative automatic ESR results obtained before LASER fragmentation (surface image). Examples of both correctly (left panel) and misclassified images (right panel; type reported on the far left is not recognized by the network) are shown. *In-situ* surface images (left image of each panel) are reported for each stone composition. Ia/COM, IIb/COD and IIIb/UA pure morphologies are reported in the first three rows. For each mixed stone (last two rows), a mixture of the corresponding pure morphologies is visible. Activation maps (right image of each panel) show areas where the network concentrates its attention. Figure and caption reproduced with permission from Estrade *et al.* [21].

correctly classified ("True positive") images (see images in left columns in Figures 2 and 3). Conversely, hot spots were observable outside the stone in 33% and 25% of misclassified surface and section images, respectively (see for example Figures 2d, 2j or 3b). Such a tool may be a great asset for urologists to

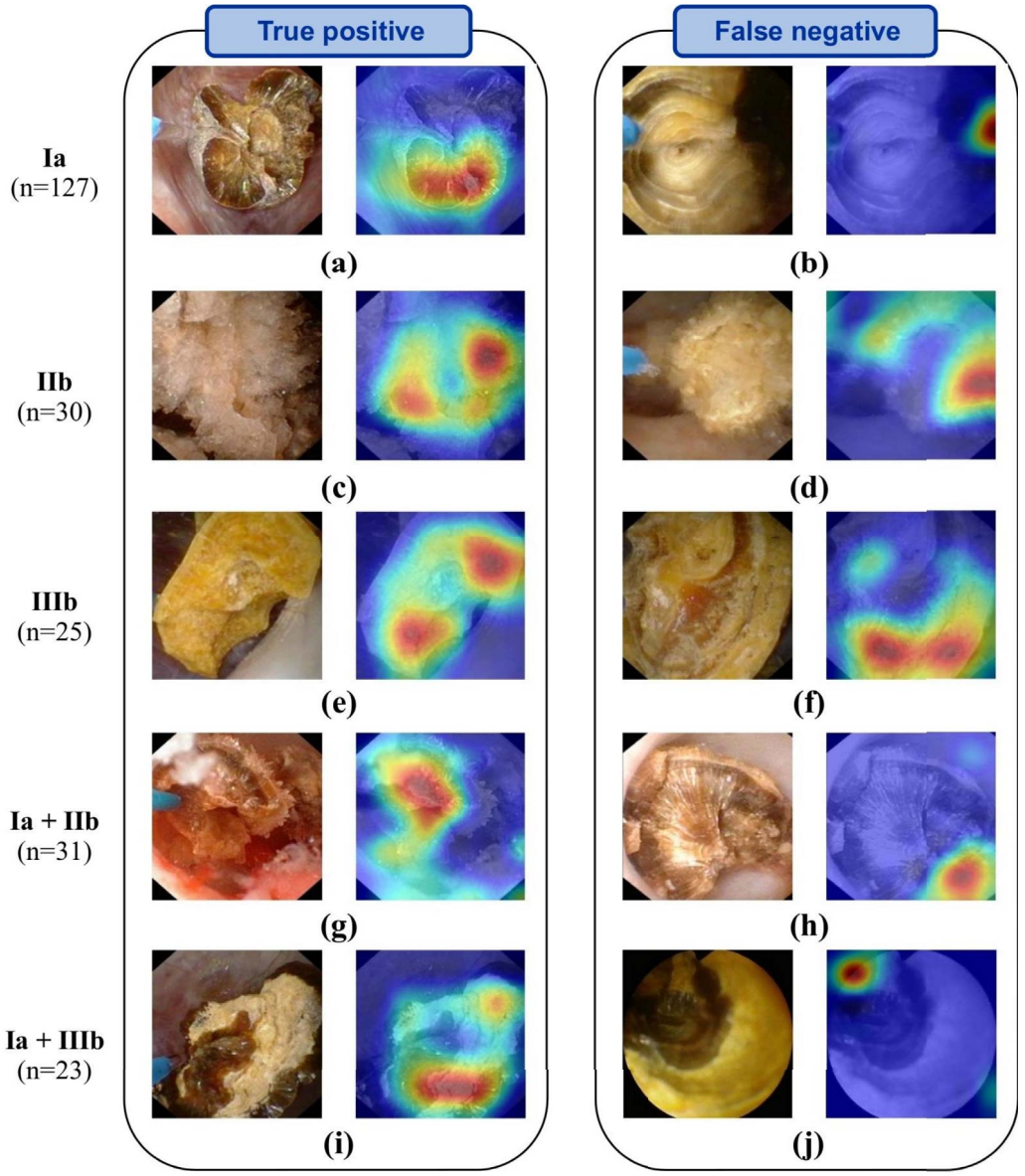

Figure 3. Representative automatic ESR results obtained after LASER fragmentation (section images). Examples of both correctly (left panel) and misclassified images (right panel: type reported on the far left is not recognized by the network) are shown. *In-situ* section images (left image of each panel) are reported for each stone composition. Ia/COM, IIb/COD and IIIb/UA pure morphologies are reported in the first three rows. For each mixed stone (last two rows), a mixture of the corresponding pure morphologies is visible. Activation maps (right image of each panel) show areas where the network concentrates its attention. Figure and caption reproduced with permission from Estrade *et al.* [21].

intra-operatively understand the predictions made by the AI model.

Nevertheless, it must be stressed that the infrared (SPIR) examination of stone powder by a dedicated laboratory remains essential to perform in order the morpho-constitutional stone analysis to provide additional and complementary information [2–7]. In our opinion, the combination of intra-operative ESR

and post-operative infrared (FTIR) examinations of laser-fragmented stones may further improve the etiological approach by urologists in lithiasis [21]. However, it must be reported that, after LASER stone fragmentation, only a few stone fragments may be available for a subsequent IR stone analysis. It may thus be difficult to attribute the collected fragments to the different areas in the stone that can be observed within an endoscopic session. Collecting non- or partially-fragmented stones may be preferable since outer stone surface and different layers of inner stone (after cutting or crushing) can be recorded. In such a case, corresponding portion of the stone may therefore be easily sampled and sent for IR analysis.

6. Conclusions

LASER spraying of all types of urinary stones became common practice. Similarly, morpho-constitutional examination of urinary stones becomes a method of choice for the effective management of patients suffering from kidney stones and regarding the prevention of stone recurrence [2–5]. While urologists following the ESR training experience a relatively fast learning curve when they encounter the most frequent stone morphologies, they need more practice when calcium phosphate or mixed stones morphologies are involved. Trained on confirmed high-quality endoscopic images annotated according to the criteria published by Estrade and colleagues [7], AI proves to be a good candidate for automatic ESR of the morphological elements composing urinary stones. Recent works demonstrated that AI is a promising tool to identify both pure and mixed kidney stone compositions from endoscopic images acquired intra-operatively [20,21]. ESR performed before complete LASER-induced spraying may thereby be beneficial to maintain an etiological approach in lithiasis. The combination of automatic intra-operative ESR and post-operative infrared examinations of laser-fragmented stones may improve the etiological approach in lithiasis [7,21].

In our opinion, it is imperative to extend ESR learning in the curriculum of urologists and further improve current AI developments; hence, we believe that such objectives must be highly prioritized by urological and scientific communities.

Abbreviations

AESR	Automated Endoscopic Stone Recognition
AI	Artificial Intelligence
AUROC	Area Under the ROC curve
BR	Brushite
CA	Carbapatite
CNN	Convolutional Neural Network
COD	Calcium Oxalate Dihydrate
COM	Calcium Oxalate Monohydrate
CT	Computed Tomography
CYS	Cystine
DSDECT	Dual-Source Dual-Energy Computed Tomography
ESR	Endoscopic Stone Recognition
FNR	False Negative Rate
FPR	False Predictive Rate
FTIR	Fourier Transform InfraRed spectroscopy
Grad-CAM	Gradient-weighted Class Activation Mapping
Ho-Yag	Holmium-Yag LASER
IR	Infra Red
LASER	Light Amplification by Stimulated Emission of Radiation
MAP	Magnesium Ammonium Phosphate (struvite)
NPV	Negative Predictive Value
PPV	Positive Predictive value
ROC	Receiver Operating Characteristic
STR	Struvite
TFL	Thulium Fiber LASER
UA	Uric Acid
VE	Vincent Estrade

Conflicts of interest

Authors have no conflict of interest to declare.

Acknowledgments

Experiments presented in this paper were carried out using the PlaFRIM experimental test-bed and supported by Inria, CNRS (LABRI and IMB), Université de Bordeaux, Bordeaux INP and Conseil Régional

d'Aquitaine (see https://www.plafrim.fr/). The authors gratefully acknowledge the support of NVIDIA Corporation (Santa Clara, CA, USA) after their donation of a TITAN X GPU used in this research.

References

[1] G. Zhang, H. Sun, H. Xue *et al.*, *Clin. Radiol.*, 2016, **71**, 1178-1183.
[2] M. Daudon, A. Dessombz, V. Frochot *et al.*, *C. R. Chim.*, 2016, **19**, 1470-1491.
[3] J. Cloutier, L. Villa, O. Traxer *et al.*, *World J. Urol.*, 2015, **33**, 157-169.
[4] M. Daudon, P. Jungers, D. Bazin *et al.*, *Urolithiasis*, 2018, **46**, 459-470.
[5] M. Corrales, S. Doizi, Y. Barghouthy *et al.*, *Eur. Urol. Focus*, 2020, **7**, 13-21.
[6] V. Estrade, M. Daudon, P. Méria *et al.*, *Prog. Urol. FMC*, 2017, **27**, F26-F35.
[7] V. Estrade, B. Denis de Senneville, P. Meria *et al.*, *Br. J. Urol. Int.*, 2020, **128**, 319-330.
[8] G. Sampogna, D. Basic, P. Geavlete *et al.*, *Actas Urol. Esp.*, 2021, **45**, 154-159.
[9] C. Bergot, G. Robert, J. C. Bernhard *et al.*, *Prog. Urol.*, 2019, **29**, 312-317.
[10] E. Emiliani, M. Talso, S. Y. Cho *et al.*, *J. Urol.*, 2017, **198**, 702-706.
[11] S. Doizi, E. X. Keller, V. De Coninck *et al.*, *Nat. Rev. Urol.*, 2018, **15**, 653-654.
[12] E. Ventimiglia, O. Traxer, *J. Endourol.*, 2019, **33**, 353-357.
[13] O. Traxer, E. X. Keller, *World J. Urol.*, 2020, **38**, 1883-1894.
[14] E. X. Keller, V. De Coninck, S. Doizi *et al.*, *World J. Urol.*, 2020, **39**, 1693-1698.
[15] E. X. Keller, V. de Coninck, M. Audouin *et al.*, *J. Biophoton.*, 2019, **12**, article no. e201800227.
[16] V. Andreeva, A. Vinarov, I. Yaroslavsky *et al.*, *World J. Urol.*, 2020, **38**, 497-503.
[17] A. Srisubat, S. Potisat, B. Lojanapiwat, V. Setthawong, M. Laopaiboon, *Cochrane Database Syst. Rev.*, 2014, article no. CD007044.
[18] K. M. Black, H. Law, A. Aldoukhi *et al.*, *Br. J. Urol. Int.*, 2020, **125**, 920-924.
[19] J. Serrat, F. Lumbreras, F. Blanco *et al.*, *Expert Syst. Appl.*, 2017, **89**, 45-51.
[20] A. Martinez, D. H. Trinh, J. El Beze *et al.*, in *Annual International Conference of the IEEE Engineering in Medicine & Biology Society* (Montreal, QC, Canada), IEEE, 2020, 1936-1939.
[21] V. Estrade, M. Daudon, E. Richard *et al.*, *Br. J. Urol. Int.*, 2021, **129**, 234-242.
[22] K. He, X. Zhang, S. Ren *et al.*, in *IEEE Conference on Computer Vision and Pattern Recognition (ICVPR)* (Las Vegas, NV, USA), IEEE, 2016, 770-778.
[23] R. Kohavi, in *Proceedings of the 14th International Joint Conference on Artificial Intelligence* (Montreal, QC, Canada), vol. 2, Morgan Kaufmann Publishers Inc., 1995, 1137-1143.
[24] R. Siener, N. Buchholz, M. Daudon *et al.*, *PLoS One*, 2016, **11**, article no. e0156606.
[25] B. Yang, D. Veneziano, B. K. Somani, *Curr. Opin. Urol.*, 2020, **30**, 782-787.
[26] R. R. Selvaraju, M. Cogswell, A. Das *et al.*, in *IEEE International Conference on Computer Vision (ICCV)* (Venice, Italy), IEEE, 2017, 618-626.

Comptes Rendus
Chimie
2022, Vol. 25, Special Issue S1, p. 417-423
https://doi.org/10.5802/crchim.106

Microcrystalline pathologies: Clinical issues and nanochemistry

A novel laser lithotripsy system with automatic target recognition: from bench to bedside

Daniel Schlager [a,*], Antonia Schulte [a], Lea Kraft [a], Christian Gratzke [a], Rodrigo Suárez-Ibarrola [a], Mehmet Yilmaz [a] and Arkadiusz Miernik [a]

[a] Department of Urology, Faculty of Medicine, University of Freiburg - Medical Centre, Freiburg, Germany

E-mails: daniel.schlager@uniklinik-freiburg.de (D. Schlager), antonia.schulte@uniklinik-freiburg.de (A. Schulte), lea.kraft@uniklinik-freiburg.de (L. Kraft), christian.gratzke@uniklinik-freiburg.de (C. Gratzke), rodrigo.suarez@uniklinik-freiburg.de (R. Suárez-Ibarrola), mehmet.yilmaz@uniklinik-freiburg.de (M. Yilmaz), arkadiusz.miernik@uniklinik-freiburg.de (A. Miernik)

Abstract. While employing the Holmium YAG laser, photonic technologies can help detect urinary stones and enhance safety for the patient. Our research group recently found that continuous monitoring of the fluorescence spectra of urinary calculi suffices to distinguish between stone, tissue, and endoscope components precisely and in real time. We hereby introduce our new automatic target identification system and the results of experimental studies we conducted. In this study, we review the research on *in vitro* and *in vivo* experiments we conducted developing and characterizing a novel target system, and summarize the key features of this new technology. This new system using intraoperative autofluorescence monitoring, enables the detection of the laser's target by analyzing the fluorescent spectra reflected from the target. The energy pulses are only emitted when a urinary stone is within reach of the laser fiber tip. Our experiments revealed that this autofluorescence-based automatic target recognition lithotripsy system delivers valuable diagnostic information to the surgeon in real time. Our system recognizes potential target structures via implemented fluorescence detection. After setting a fluorescence intensity threshold level, a feedback mode was employed that autonomously controls the Ho:YAG laser. During this procedure, the pulse emissions were controlled only by our system, not by the surgeon. The safety and effectiveness of this system has been successfully proven in animal studies. This new target system with a feedback mechanism provides certainty that even in the event of unintentional laser activation, the laser emission is blocked, thus preventing tissue damage and unnecessary heat generation. Ours is a promising approach with the potential to be used in various future urological and non-urological applications primarily to enhance patients' safety.

Keywords. Urinary stone disease, Urolithiasis, Automatic target recognition, Laser lithotripsy, Lithotripsy.

Published online: 17 August 2021

* Corresponding author.

1. Introduction

Urinary stones are common all over the world [1]. Thanks to recent technological developments in medical engineering, laser lithotripsy is now the first-line treatment modality in endoscopic surgical urolithiasis treatment [2]. The Holmium:YAG (Ho:YAG) laser is the most popular technology employed in lithotripsy for over 20 years, and is still considered the gold standard [3]. However, the high energy applied during the procedure, the strong absorption of laser light in water, anatomical factors, and inadequate surgical experience can all contribute to injuries to surrounding tissues in the urinary tract and to endoscope damage [4]. Beyond this direct effect, insufficient irrigation during an endourological laser intervention might cause an uncontrolled temperature rise that damages adjacent tissue indirectly and delayed in time [5]. Photonic technologies have recently been used to experimentally identify urinary stones to increase safety while employing the Ho:YAG laser [6]. More recently, Winfree *et al.* applied an autofluorescent imaging method to facilitate identification of Randall's plaque [7].

Our research group found that continuous monitoring of the fluorescence spectra of urinary calculi is sufficient to distinguish precisely and in real time between stone, tissue, and endoscope components [8]. Relying on the foundation of this basic research work, our group developed a target identification system that autonomously supports the surgeon during lithotripsy to enable automatic real-time urinary stone detection via autofluorescence. For this review we introduce our new automatic target identification system and the results of the experimental studies we conducted.

The aim of this study was to provide basic scientific evidence for the development of an autofluorescence-based imaging system for real-time urinary stone target identification and subsequent experimental evaluation for performance, reliability and safety in an *in vivo* animal study.

2. Materials and methods

In the initial study we developed a fiber-based autofluorescence measurement system consisting of commercially available components to analyze spectral information [8]. The excitation laser light was emitted by a 15 mW diode pumped, solid state FDSS532 laser (CryLas, Berlin, Germany) and was connected to an optical core therapeutic fiber with a 365 mm core (PercuFib optical core treatment fiber, LISA laser products, Katlenburg-Lindau, Germany). Fluorescent light re-entering the fiber was separated from the excitation light with a beam splitter and analyzed on a fiber-coupled spectrometer. Fluorescence signals were collected and evaluated in random areas on the stones. The spectra of 82 human kidney stones were analyzed and compared to porcine urinary tract tissue and polytetrafluoroethylene coating of a common ureterorenoscopic working channel in a series of standardized measurements (Figure 1). Artificial stones made of pure inorganic components were also analyzed. Each sample's chemical composition was consistently analyzed by an infrared spectrometer.

In the second experiment, we developed a real-time compact demonstration system based on the aforementioned laboratory setup to make automatic identification possible [9]. In this system, the Ho:YAG laser was connected to a therapeutic laser fiber, so that the entire system was equipped with all the technical components needed for automatic target identification during stone treatment. Most importantly, this setup actively utilized a feedback loop between the spectral detection unit and Ho:YAG laser. First, the setup was applied in a simulated surgical intervention in a porcine kidney *in vitro*. The experimental setup is descripted in Figures 1 and 2. Finally, the performance was assessed performing conventional Ho:YAG laser lithotripsy with and without target recognition in an *in vivo* setting in an animal study on domestic pigs [10]. Laser lithotripsy procedures were performed in the porcine collecting system of the kidney, in the ureter and bladder after retrograde placement of human stone material in the porcine urinary tract under general anesthesia. These experiments were approved by the Ethics Committee of the Albert-Ludwigs University of Freiburg, Germany (IRB: 296/15). To detect and evaluate any tissue damage related to the intervention and laser light's endoluminal application, the entire urinary tract was surgically removed and examined by a pathologist. The experimental setup can be seen in Figure 2.

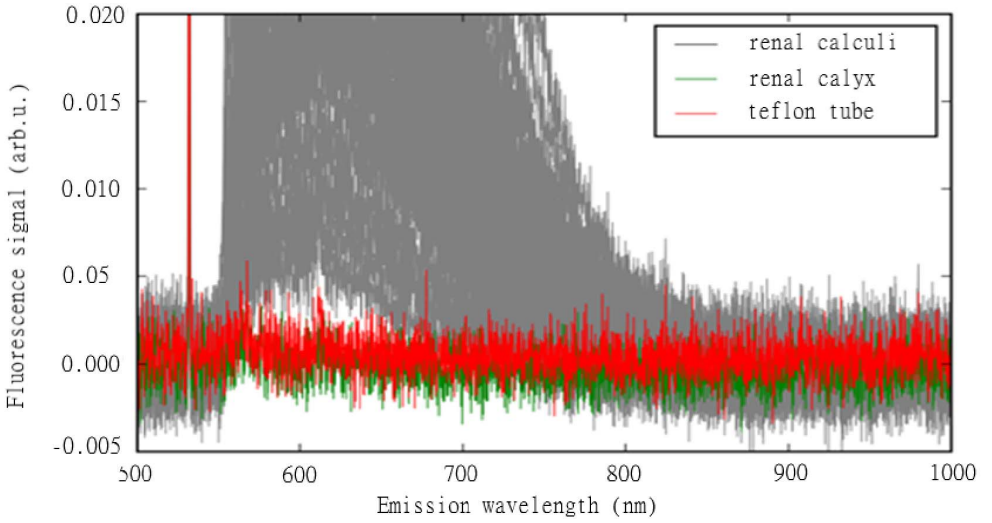

Figure 1. Autofluorescence measurement of urinary stone fragments, teflon element and tissue.

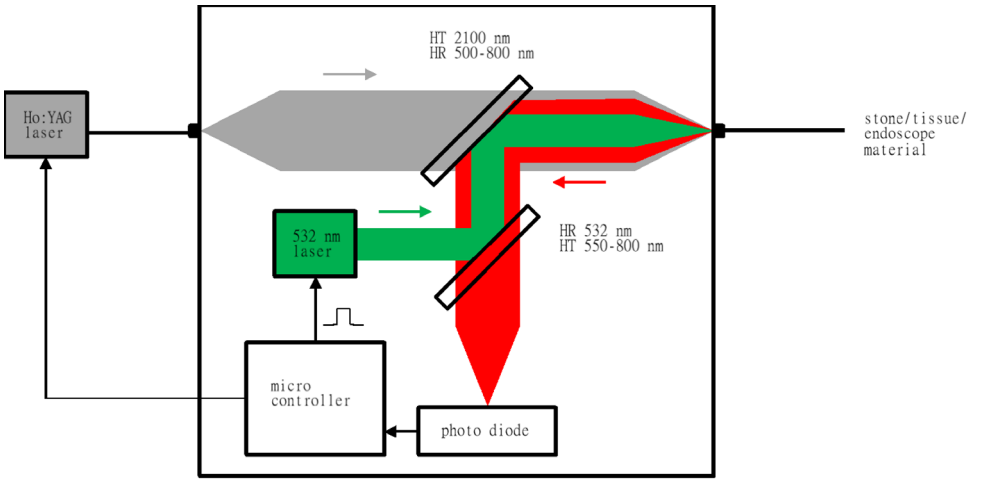

Figure 2. System setup including the measurement system and therapeutic laser.

3. Results

In our spectral analyses of various human urinary stones, tissue material from the urinary tract, and surgical instrument (endoscope components) using autofluorescence, we were able to define the spectral characteristics of each of these objects. The shapes of the spectra originating in urinary stones of different composition were similar, which meant that the autofluorescence signals were unable to distinguish between the stones' chemical compositions. Although the stones' signal amplitudes varied, all signals were significantly stronger than the measurement values originating from the tissue samples and endoscope components. Note that all the human stones examined in these experiments emitted significantly higher signal values than all the other targeted objects. We found that the weakest stone signal was 3.6 times stronger than the strongest signal from porcine kidney tissue (mean ± SD 0.038 ± 0.043 vs 0.00058 ± 0.00058 arbitrary units). Furthermore, we detected no fluorescence signal from endoscope components.

In our *in vitro* study, the stones' mean SD autofluorescence signal amplitudes ranged from 142 ± 29 to 1521 ± 152 ADU (analog-to-digital units), while emissions from tissue and the endoscope coating were practically negligible. All the stone signals were significantly stronger than those from tissue and endoscope components. We discovered that when the minimum threshold is defined as tissue plus six standard deviations, this results in 14 ADU. If the Ho:YAG laser was deactivated under that aforementioned threshold, the emission of laser light on the tissue or endoscope could be prevented. The distance between the laser tip and targeted object is known to play an essential role in ensuring efficient stone disintegration. We observed that the Ho:YAG laser operates optimally when the distance between the fiber tip and target is within a 0.1–0.5 mm range. Note that if a urinary stone emits an average fluorescent signal and is at a distance of more than about 1 mm from the fiber tip, the laser will be blocked. We also experimentally confirmed that automatic target recognition works at threshold values between 50 and 200 ADU. It is important to note, that while the laser was activated during the lithotripsy procedure, only the detection system was controlling its pulse emission—not the surgeon. During *in vivo* usage of this system, we observed no incorrectly emitted laser energy or tissue damage, or any impact on endoscopes.

In our *in vivo* experiment, lithotripsy could be performed successfully with both a standard laser and new target system (Figure 3). No macroscopic damage was detected in the tissue after treatment with this new device. We observed no organ perforation or any other severe lesion in the urinary tract whatsoever in fluoroscopic, macroscopic, and pathological investigations. No relevant thermal damage was detected even in the microscopic and histological work-up.

Furthermore, we found that cumulative laser energy was reduced during each procedure while the target recognition system was active. The energy applied lessened significantly with an average reduction of over 30% (27.1% for ureter stone, 52.2% for kidney stone, 17.1% for bladder stone lithotripsy). In addition, according to the personal assessment of the surgeon who conducted the animal studies, the new laser setup functions smoothly and does not hinder workflow.

4. Discussion

The increasing clinical need to prevent tissue damage from laser light emitted from laser systems has inspired research on novel photonic technologies. Lange *et al.* was the first group to demonstrate that autofluorescence is capable of distinguishing between urinary stones and human tissue [6]. Other research groups also proved that tissue and stone differentiation is feasible via target autofluorescence spectra [11,12]. To transform these findings and technology into therapeutic application, we developed an advanced autofluorescence monitoring system integrated into a Holmium laser system that allows real-time target recognition during laser lithotripsy. This setup proved able to inform the surgeon about the object in front of the laser fiber's tip in real time, that is, when stone material is within the laser's therapeutic range. Once a fluorescence intensity threshold level has been set, the feedback mode then functions to autonomously control the Ho:YAG laser. During the procedure, the emission of energy was monitored independently by the feedback system, emitting laser energy only when it "recognized" stone material. The safety and efficiency of the present setup was successfully proven in animal models [10]. Our observations have also been confirmed histologically.

Urinary stones expose characteristic autofluorescent spectra particularly when excited at the wavelength of 520 nm [8]. An essential aim of our project was to define the appropriate wavelength to trigger the targeted object's excitation, as this would enable us to detect any kind of chemical composite of the stone. Interestingly, stones possessing the same chemical composition reveal different wavelengths upon fluorescent excitation [8]. A stone's wavelength spectrum is most likely determined by proteins on its surface, and it is most likely these proteins that cause the characteristic autofluorescent properties, rather than the chemical composition. This hypothesis is supported by the evidence that chemically pure compounds (e.g. pure calcium) emit no fluorescence spectra when excited at this wavelength [8].

This new system monitoring intraoperative autofluorescence only allows the laser to emit energy for therapeutic purposes when the stone is within an appropriate distance to the stone surface. The spectra monitoring unit is attached to the therapeutic laser by a glass fiber. The system is equipped with a double

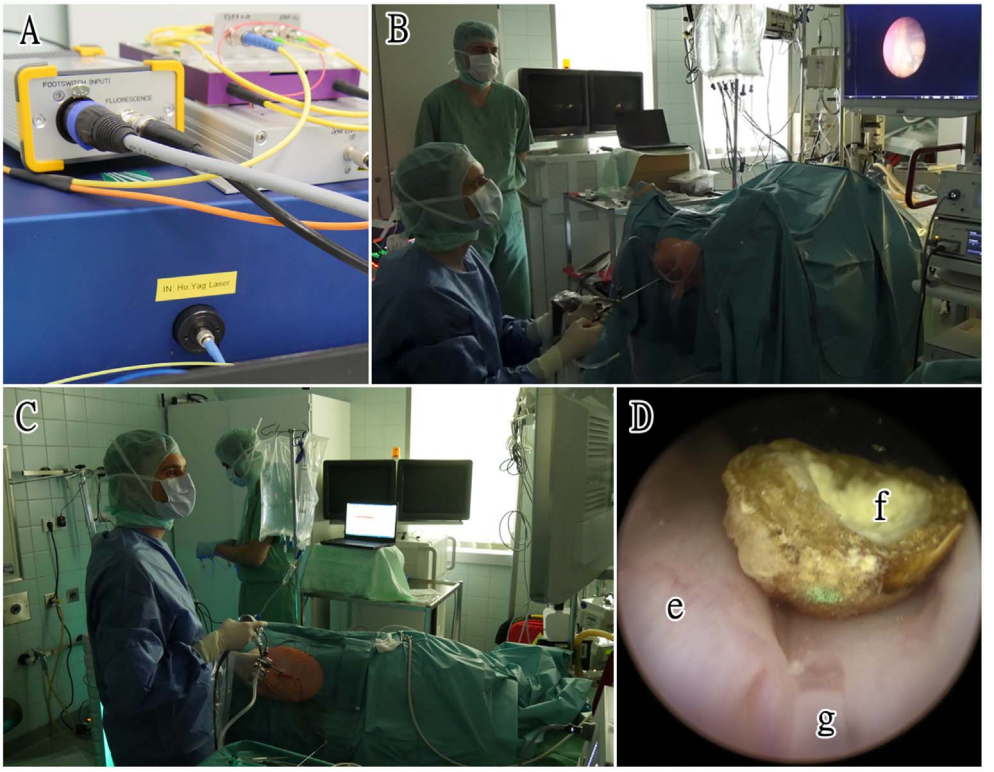

Figure 3. Presentation of the animal studies: (A) experimental setup of the system; (B) ureteroscopy procedure using the novel laser system (C) percutaneous nephrolithotomy procedure using the novel laser system; (D) endoscopic image from laser lithotripsy—(e) Urinary bladder mucosal (f) Urinary stone, (g) Laser fiber tip.

control mechanism. The general on-and-off switch is regulated by operating a foot pedal. The monitoring unit also communicates with the treatment laser. It is the surgeon who is in control of turning the entire system on and off. If the foot pedal remains pressed, the system is active. Moreover, the target object must be detected correctly, as only then will energy be emitted. If the foot pedal is not pressed down, it does not matter whether the fiber tip is correctly placed on the target object. In that case, no laser light energy is applied at all. When the system is in the active mode, the surgeon only needs to navigate the endoscope with the treatment fiber in place to the target stone.

Although laser lithotripsy at its current developmental stage might be considered safe and efficient, its most annoying limitation is the uncontrolled and not fully controlled energy release during surgery and its potential damage to surrounding tissues. It is a fact that while direct physical lesions rarely occur, secondary thermal injuries caused by the effect of excessive heat production in the urinary tract can eventually trigger adverse events [5,13]. Various strategies have been proposed to prevent accidental damage, such as keeping the laser fiber tip coated for better identification and keeping it at a reasonable safety distance from the optical tip of the scope, regularly cutting the fiber tip to prevent retrograde laser emission [14]. The Ho:YAG laser has a therapeutic range of 1–3 mm in liquid. In standard lithotripsy with a Ho:YAG laser system, the emission of high-energy pulses depends solely on the surgeon. When the surgeon presses the foot pedal while the stone is right in front of the laser fiber tip, laser energy is transferred to the stone through the fluid in between. Due to a continuous exchange of irrigation fluid, and to mechanical forces resulting from the laser–target interaction, the stone may move away from laser's fiber tip. When that happens, laser energy is unavailable for fragmenting the calculus, but it suffices to heat

the surrounding liquid. The endoscope can also be damaged if the laser fiber is accidentally retracted too far during treatment [4]. Another potential problem is that by delivering energy in an undesirably large space between the stone and the laser fiber tip, the force of retropulsion becomes excessive and causes the stones' dislocation. Specifically, if the urinary tract anatomy is unfavorable, situations may arise in which visualization of the intended target becomes difficult. When the threshold values are accurately set, the energy is absorbed almost exclusively by the stone surface, thus minimizing retropulsion.

The greatest contribution of our system to the lithotripsy procedure is that it detects stone and tissue automatically, and that it is *completely surgeon-independent,* requiring no action by or input from the surgeon during lithotripsy. Thanks to this detection function that the feedback mechanism provides, the surgeon can focus solely on navigating and the lithotripsy procedure without having to worry about damaging the tissue.

In addition to reducing the risk of tissue injuries and contributing to a safer, more efficient surgery, our system has further advantages in terms of its clinical performance. We have demonstrated that the total amount of energy required for sufficient and successful fragmentation dropped by about 30%. By preventing endoscope damage, utilizing our system might also deliver a positive economic effect. Another potential benefit of this new technology is that it will be easier to operate by less experienced surgeons or urology residents in training still in a steep learning curve. Thanks to the automatic, surgeon-independent therapy monitoring function, the stress and anxiety associated with a lithotripsy intervention could be minimized. This innovative technology can also be adapted to other laser types as a hardware add-on. Our new target system holds promise for substantial improvements in laser lithotripsy in the future.

Our system has some limitations. While using this system, temperature changes in the operation area are not measured. The long-term thermal effect of temperature changes on human urinary tract tissue is not completely understood [5]. In addition, it is not yet clear how effective this system is when applying different stone disintegration techniques. Its main limitation is that we have not yet gained any practical experience from procedures in humans. However, since this technical approach has proven safe and robust in the preclinical setting and animal model, our group recently started a clinical pilot study with the system being applied for human laser lithotripsy.

5. Conclusion

In this review we summarized our research and development on a novel laser system providing a real-time treatment-monitoring unit using autofluorescence to distinguish urinary stone targets during laser lithotripsy from urothelial tissue and endoscope components. We found this technology to work reliably and be safe in experimental preclinical settings and animal trials. We are currently preparing for its first in-human use.

Author disclosure statement

A. Miernik receives research funds of the German Federal Ministry of Education and Research, Berlin (D). He receives support for his travel activities from the European Society of Urology, Arnhem (NL), and the German Society of Urology, Düsseldorf (D). Furthermore, A. Miernik is consulted for: KLS Martin, Tuttlingen (D), Avateramedical, Jena (D), LISA LaserProducts GmbH, Katlenburg-Lindau (D), Schoelly fiberoptics GmbH, Denzlingen (D), Dornier MedTech Laser GmbH (D), Medi-Tate Ltd. (IL, USA) and B. Braun New ventures GmbH, Freiburg (D). A. Miernik is speaker for the companies Richard Wolf GmbH (D) and Boston Scientific (USA). Additionally, he performed expert activities for the Ludwig Boltzmann Gesellschaft, Wien (A). A. Miernik is involved in numerous patents and inventions in the field of medical technology. L. Kraft provided consulting services for Dornier MedTech Laser GmbH, Weßzling (D). C. Gratzke is advisor for Astellas Pharma GmbH, Munich (D), Ipsen Pharma GmbH, Munich (D), Steba Biotech S.A., Luxembourg (LUX), Bayer Pharma, Leverkusen (D), Olympus Winter & Ibe GmbH, Hamburg (D), Medi-Tate Ltd., Or Akiva (IL), MSD, Haar (D), Astra-Zeneca, Cambridge (UK) and Roche, Basel (CH). C. Gratzke receives speaker fees from Amgen, California (USA), Astellas Pharma GmbH, Munich (D), Ipsen Pharma GmbH, Munich (D), Janssen-Cilag GmbH, Neuss (D), Bayer Pharma, Leverkusen (D), Takeda Pharmaceuticals, Tokio (JPN) and medac GmbH, Wedel (D). D. Schlager,

R. S. Ibarrola, A. Schulte, M. Yilmaz declare to have no conflicts of interest.

The manuscript does not contain clinical studies or patient data. This article does not contain any studies with human subjects performed by any of the authors.

Authors' contribution

DS had full access to all the data in the study and takes responsibility for the integrity of the data and the accuracy of the data analysis. AM and DS conceived the study concept and design. DS, MY, RSI and LK interpreted the data and wrote the manuscript. AM and CG supervised the manuscript. All authors discussed the results and commented on the manuscript.

References

[1] M. Bultitude, *BJU Int.*, 2017, **120**, 601.
[2] G. Giusti *et al.*, *Eur. Urol.*, 2016, **70**, 188-194.
[3] D. Bagley, M. Erhard, *Tech. Urol.*, 1995, **1**, 25-30.
[4] A. Schulte, L. Kraft, T. Walther, R. Petzold, C. Gratzke, A. Miernik, *Urologe A*, 2021, **60**, 19-26.
[5] S. Hein, R. Petzold, M. Schoenthaler, U. Wetterauer, A. Miernik, *World J. Urol.*, 2018, **36**, 1469-1475.
[6] B. Lange, J. Cordes, R. Brinkmann, *Lasers Surg. Med.*, 2020, **52**, 456-471.
[7] S. Winfree *et al.*, *Urolithiasis*, 2021, **49**, 123-135.
[8] J. Schütz, A. Miernik, A. Brandenburg, D. Schlager, *J. Urol.*, 2019, **201**, 182-187.
[9] D. Schlager, A. Miernik, S. Lamrini, M. Vogel, H. O. Teichmann, A. Brandenburg, J. Schutz, *J. Urol.*, 2019, **202**, 1263-1269.
[10] D. Schlager, A. Schulte, J. Schutz, A. Brandenburg, C. Schell, S. Lamrini, M. Vogel, H. O. Teichmann, A. Miernik, *World J. Urol.*, 2020.
[11] B. Lange, J. Cordes, R. Brinkmann, *Lasers Surg. Med.*, 2015, **47**, 737-744.
[12] B. Lange, D. Jocham, R. Brinkmann, J. Cordes, *Lasers Surg. Med.*, 2017, **49**, 361-365.
[13] G. J. Vassar, K. F. Chan, J. M. Teichman, R. D. Glickman, S. T. Weintraub, T. J. Pfefer, A. J. Welch, *J. Endourol.*, 1999, **13**, 181-190.
[14] P. Kronenberg, B. Somani, *Curr. Urol. Rep.*, 2018, **19**, article no. 45.

Comptes Rendus
Chimie
2022, Vol. 25, Special Issue S1, p. 425-430
https://doi.org/10.5802/crchim.107

Microcrystalline pathologies: Clinical issues and nanochemistry

Characterization of deposits on double J stents

Paula Calvó [a], Jose Luis Bauza [b], Francisca Julià [a], Jordi Guimerá [b], Enrique C. Pieras [b], Antonia Costa-Bauzá [a] and Felix Grases [*, a]

[a] Laboratory of Renal Lithiasis Research, University Institute of Health Sciences Research (IUNICS-IdISBa), University of Balearic Islands, Palma de Mallorca 07122, Spain

[b] Urology Service, University Hospital Son Espases, Palma de Mallorca 07120, Spain

E-mails: paula.calvo@uib.es (P. Calvó), jose.bauza@ssib.es (J. L. Bauza), juliaf0910@gmail.com (F. Julià), jorge.guimera@ssib.es (J. Guimerá), enriquec.pieras@ssib.es (E. C. Pieras), antonia.costa@uib.es (A. Costa-Bauzá), fgrases@uib.es (F. Grases)

Abstract. We have characterized the types of encrustations that form on ureteral stents. The deposit that generates blocks is composed of hydroxyapatite/magnesium ammonium phosphate (44%). Calcium oxalate dihydrate was also detected at a high degree of encrustation (13%). Hydroxyapatite deposits, also of high degree of encrustation (13%) are generated due to their formation as a consequence of persistently high urinary pH values. The formation of large uric acid deposits (31%) must be attributed to the persistence of urinary pH < 5.5. To avoid development of encrustations of ureteral stents, urinary calcium levels and urinary pH control should be carried out, avoiding urinary infections.

Keywords. Ureteral stents, Ammonium magnesium phosphate, Hydroxyapatite, Calcium oxalate dihydrate, Uric acid.

Funding. Financial support from Agencia Estatal de Investigación (Spain) (PID2019-104331RB-I00/AEI/10.13039/501100011033), and Fundación para la Investigación en Urología are acknowledged. PC is grateful to the Conselleria d'Educació, Universitat i Recerca of the Government of the Balearic Islands for the fellowship FPI_003_2020.

Published online: 17 August 2021

1. Introduction

Double J catheters are one of the most commonly used indwelling ureteral devices to treat obstructive uropathy, to facilitate the drainage of urine through the urinary system. However, they can promote the appearance of urinary tract infections (UTIs) and the development of encrustations, which can hinder and even prevent its removal [1–3].

The introduction of a catheter into the urinary system implies the placement of a foreign body that facilitates the flow of urine between the renal pelvis and the urinary bladder. Therefore, the catheter will be permanently bathed in urine that will flow from the kidney to the urinary bladder. As it is a foreign solid in contact with urine, it is evident that it may act as a heterogeneous nucleant for those substances that are supersaturated in this medium. It is precisely for this reason that extensive research has been carried out to develop nonstick materials that avoid as much as possible the capacity that a catheter can

* Corresponding author.

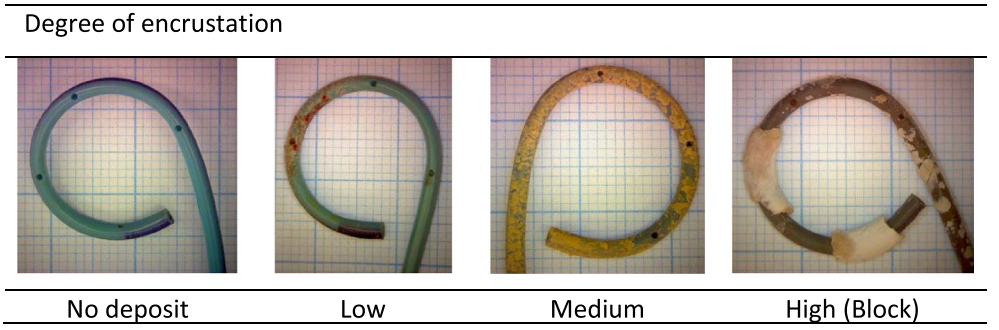

Figure 1. Degree of embedding of the catheters studied. Image obtained by stereoscopic microscopy.

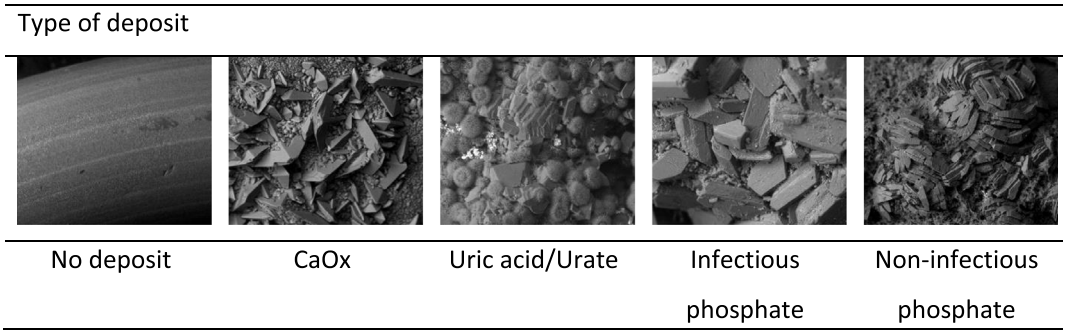

Figure 2. Types of deposits observed. Images obtained by Scanning Electron Microscopy (SEM).

present as a heterogeneous nucleant. In any case, urine is a medium rich in organic matter and proteins, mainly albumin and mucin in the absence of infections, which can adhere on the surface of the catheter covering it [4]. Once deposited, this material will act as an effective heterogeneous nucleant that will induce crystallization of those substances that are supersaturated in urine.

The main objective of this paper is to characterize and study the different types of encrustations that form on double J catheters, in order to be able to relate their characteristics to the urinary conditions that have induced them.

2. Material and methods

Ninety double J catheters (Angiomed, UROSOFT-ureteral-stent-set based on a soft-polyurethane compound, REF 57410030) of patients with an indwelling time approximately from 1 to 3 months were studied, processing the renal part and the bladder part separately. Thus each catheter is divided into two equal parts. This was an observational study, where 57.8% of the patients were males (age 57 ± 15) and 42.2% females (age 54 ± 13).

In all cases, the stent was placed as a consequence of ureteral obstruction due to benign pathology.

Each catheter was submitted to the following procedure: First, it was photographed with a stereoscopic microscope. By observational study, they were classified into four categories according to the degree of encrustation observed (0–3, 0 being no deposit and 3 high degree of encrustation or deposit block, as shown in Figure 1). Subsequently, each stent was weighed and the total weight of deposit present in each catheter was evaluated, by comparison with an unused catheter. Later, by Scanning Electron Microscopy (SEM) the type of embedded deposit was identified: no deposit, calcium oxalate (monohydrate, dihydrate), uric acid (anhydrous, dihydrate) and/or urate, infectious phosphate (magnesium ammonium phosphate + hydroxyapatite) and noninfectious phosphate (hydroxyapatite + brushite) (Figure 2).

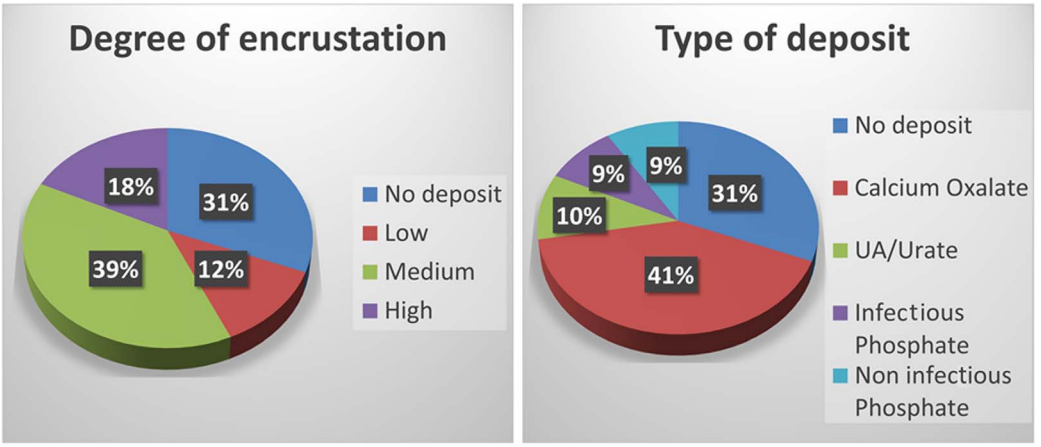

Figure 3. (A) Percentage of no deposit or low, medium and high degree of encrustation in the 90 stents. (B) Percentage of each type of deposit in the 90 stents.

Finally, the catheters were cut into several fragments to facilitate dissolution of the deposits with 2 M HCl (except for those with uric acid and/or urate) to determine the amount of calcium, phosphorus and magnesium by ICP-OES.

2.1. *Statistics*

Normality graphs and plots were used to assess the data distribution. Data were represented as median and interquartile range or percentages. Intergroup comparisons (between deposit types and deposit grades) were performed using Kruskal–Wallis test and the Mann–Whitney U as post hoc test for continuous variables. For categorical variables, the Chi-square or Fisher's exact test was performed. A two-tailed p-value less than 0.05 was considered statistically significant. Statistical analyses were performed using SPSS 25.0 (SPSS Inc., Chicago, IL, USA).

3. Results

Of the 90 catheters studied, most (39%) presented a medium degree of embedding (degree 2), and 41% had calcium oxalate (CaOx) deposits. 31% did not have any type of deposit on their surface (Figure 3).

Twenty patients (22%) were diagnosed with UTIs and 15% amongst them developed magnesium ammonium phosphate deposits.

Twenty four percent of the patients did not present deposits three months after catheter placement, while 68% formed medium/high deposits during this period.

Whereas magnesium ammonium phosphate + hydroxyapatite appeared in 9% of the catheters (Figure 3B), this composition corresponded more frequently to the high degree of encrustation group (43.8%, p value < 0.05; Figure 4), while in contrast CaOx was the most frequent composition of the low and medium degree of encrustation (63.3% and 80% respectively, p value < 0.05, Figure 4). Hydroxyapatite with no infection was also identified in 9% of catheters (Figure 3B) equally distributed at low, medium and high degree of encrustation (Figure 4), and uric acid was detected in 10% of catheters, mainly with high degree of encrustation (31%, Figure 4).

The qualitative classification was compared with the total weight of the stents (Figure 5). A positive and high correlation between the deposit weight of the 90 stents and the degree of deposit is observed ($rs = 0.777$, p value < 0.001), with greater the weight of the deposit on the stent, the higher the degree of encrustation (Figure 5).

In concordance with these findings, it is also seen that the higher the degree of encrustation, the greater the amount of calcium, phosphorus and magnesium quantified for each type of deposit (Table 1). Catheters with greater weight of deposited material (median = 393 mg, Figure 6) presented mostly an infectious phosphate-type deposit. When comparing the renal and bladder parts of the catheters, no

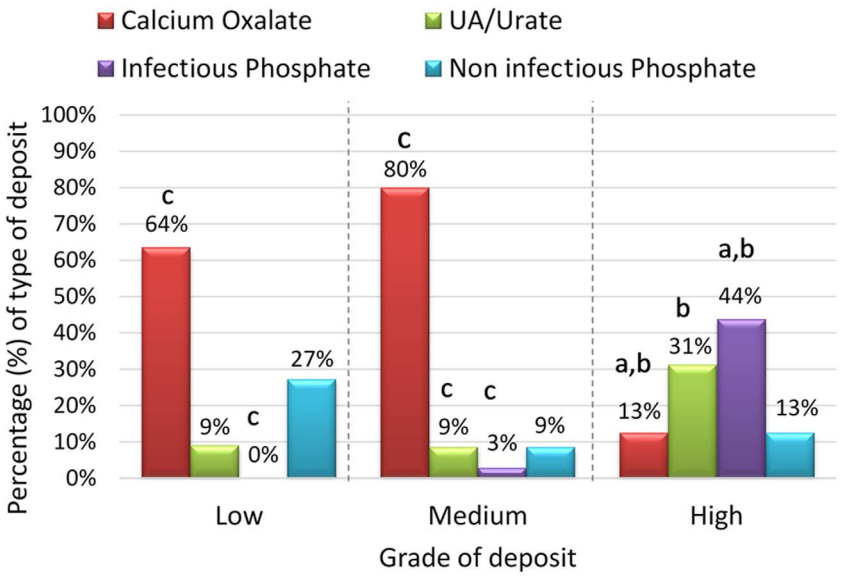

Figure 4. Percentage of type of deposit in each grade of deposit group. (a) Significant differences with the Low deposit group. (b) Significant differences with the Medium deposit group. (c) Significant differences with the High deposit group. Differences were considered significant if p value < 0.05 in the Chi-square or Fisher's exact test.

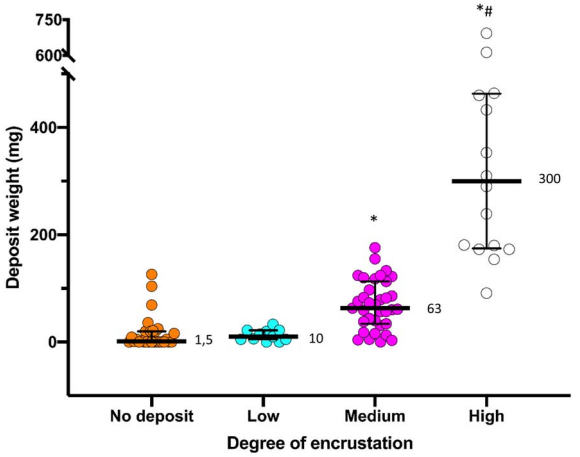

Figure 5. Deposit weight for each degree of encrustation group. Medians are represented in the figure. * Significant differences with the no deposit and low deposit group, p-value < 0.05 Kruskal–Wallis test and the Mann–Whitney U as post hoc test. # Significant differences with the medium group, p-value < 0.05 Kruskal–Wallis test and the Mann–Whitney U as post hoc test. Correlation between the two variables was assessed with the Spearman test, $rs = 0.777$, p value < 0.001.

difference between the degree of encrustation or the type of deposit was observed (Tables 2 and 3).

4. Discussion

The proposed sample processing method is effective when observing a good correlation between the degree of deposit and the weight obtained for each deposit (Figure 5).

From this study it is deduced that the deposit that generates the most trouble, due to its magnitude, is that of magnesium ammonium phosphate/hydroxyapatite. In the presence of ureolytic bacteria, large amounts of uromucoid and a significant increase in urinary pH (as a consequence of the formation of NH_3) are produced. Under these conditions, hydroxyapatite and magnesium ammonium phosphate precipitate on the catheter [5–8]. Therefore, the presence of urinary infection, which causes this type of deposits, should be controlled and avoided as far as possible. Precisely, as a very long treatment with antibiotics is not advisable, all those prophylactic measures to avoid urinary infection should be taken into account [9]. Among these measures, the most important are to avoid persistent

Table 1. Ca, P and Mg, expressed as median value, detected for each degree of deposit per type of deposit

	Degree of deposit								
	Ca (μmol)			P (μmol)			Mg (μmol)		
Type of deposit	L	M	H	L	M	H	L	M	H
Calcium oxalate	46.4	351	876	3.74	12.8	30.3	0.23	0.87	1.27
Infectious phosphate	—	486*	1687	—	784*	1202	—	366*	235
Noninfectious phosphate	4.99	390	3607	8.1	298	2674	0.43	10.4	112

Degree of deposit: L = Low, M = Medium, H = High.

* $n = 1$, value in μmol of the case.

Table 2. Percentage of each degree of encrustation in the renal and bladder parts

	Degree of encrustation (%)				
	No deposit	Low	Medium	High	Total
Renal	35.6%	21.1%	34.4%	8.9%	100.0%
Bladder	32.2%	13.3%	40.0%	14.4%	100.0%

Table 3. Percentage of each type of encrustation in the renal and bladder parts

	Type of deposit (in %)					
	No deposit	CaOx	Uric acid/urate	Infectious phosphate	Noninfectious phosphate	Total
Renal	33.3	40.0	10.0	7.8	8.9	100.0
Bladder	32.2	41.1	8.9	8.9	8.9	100.0%

high urinary pH which promotes bacterial infection, since acidic urinary pH values facilitate the transformation of nitrite generated by bacteria (from nitrate present in the urine) into NO, and this compound is toxic to bacteria [10,11]; it is advisable to drink large amounts of water and maintain strict hygienic conditions. It is interesting to observe that though 22% of the patients were diagnosed with UTIs, only 15% of them developed magnesium ammonium phosphate deposits. This is probably because these patients were initially treated with antibiotics.

It is important to observe how in a large number of patients (80%, Figure 4), calcium oxalate dihydrate was detected in medium degree of encrustation (degree 2) and even in a small percentage (13%, Figure 4) in the high encrustation (degree 3) group. This circumstance shows that in patients with hypercalciuria, control of calciuria should be carried out during the ureter implantation period, avoiding as far as possible high concentrations of urinary calcium, which should be maintained below 170 mg/L. In the absence of ureolytic bacteria, it is necessary to consider that, since it is advisable to keep double J catheters for short periods (maximum 2–3 months), only substances with very considerable supersaturations will crystallize massively [12,13].

It has also been observed that in the absence of infection, hydroxyapatite deposits in low degree of encrustation (27%) or medium/high grade of encrustation (9% and 13% respectively; Figure 4) are generated on the catheter in a certain group of patients, which could compromise its easy removal. In these cases, it is clear that the formation of these deposits is a consequence of the existence of persistently high urinary pH values. Therefore, as far as possible, attempts should be made to acidify these urines when it is possible and, in the presence of distal tubular acidosis, which precludes acidification, appropriate prophylactic measures should be taken [14].

The formation of large uric acid/urate deposits (31%) or medium and low grade of encrustation (9%, in both cases; Figure 5) has also been observed. These

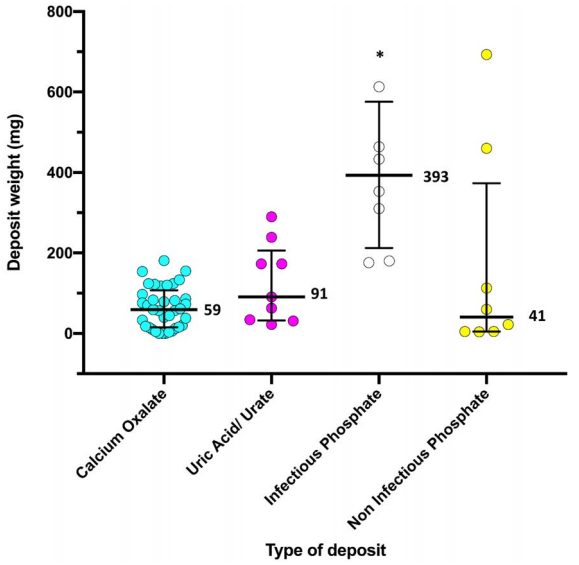

Figure 6. Deposit weight for each type of encrustation group. Medians are represented in the figure. * Significant differences with all the other groups, p-value < 0.05 Kruskal–Wallis test and the Mann–Whitney U as post hoc test.

deposits must be clearly attributed to the persistence of urinary pH values below 5.5 and also to the possibility of elevated urinary uric acid concentration, when uric acid dihydrate was observed. Therefore, excessively acidic urinary pH values below 5.5 should also be avoided.

As can be deduced, with the exception of high consumption of liquids, the other preventive measures must be adapted to the urinary composition of each patient, to avoid the implementation of contraindicated treatments.

The degree of encrustation on the stents is quite high, even for time periods shorter than one month, since 11% developed high grade deposits during this period. This shows that polyurethane, which is the material composing these stents, develops important deposits with relative ease, which is consistent with a recently published study that shows that this material generates deposits more easily than others such as hydrocoated silicone [15].

5. Conclusion

To prevent the development of large encrustations in the double J catheters, strict control should be carried out to prevent urinary infections, high urinary pH values (above 6.2) or too low values (below 5.5). In addition, control of excessive urinary calcium levels is also important.

References

[1] I. Scarneciu, O. G. Bratu, C. P. Cobelschi, C. D. Neculoiu, C. C. Scarneciu, S. Lupu, A. Brinza, D. Marcu, B. Socea, L. Maxim, *Rev. Chim.*, 2018, **69**, 3406-3409.
[2] D. J. Stickler, *Nat. Clin. Pract. Urol.*, 2008, **5**, 598-608.
[3] M. Beysens, T. O. Tailly, *Asian J. Urol.*, 2018, **5**, 274-286.
[4] M. Santin, A. Motta, S. P. Denyer, M. Cannas, *Biomaterials*, 1999, **20**, 1245-1251.
[5] T. Kawahara, H. Ito, H. Terao, M. Yoshida, J. Matsuzaki, *J. Endourol.*, 2012, **26**, 178-182.
[6] G. Bonkat, M. Rieken, G. Müller, A. Roosen, F. Siegel, R. Frei, S. Wyler, T. Gasser, A. Bachmann, A. F. Widmer, *World J. Urol.*, 2013, **31**, 541-546.
[7] S. Khoddami, B. H. Chew, D. Lange, *Turkish J. Urol.*, 2020, **46**, S11-S18.
[8] R. J. Broomfield, S. D. Morgan, A. Khan, D. J. Stickler, *J. Med. Microbiol.*, 2009, **58**, 1367-1375.
[9] D. J. Stickler, A. Evans, N. Morris, G. Hughes, *Int. J. Antimicrob. Agents*, 2002, **19**, 499-506.
[10] S. Carlsson, "Antibacterial effects of nitrite in urine", PhD Thesis, Karolinska Institutet, Stockholm, Sweden, 2005.
[11] J. Burns, C. P. McCoy, N. J. Irwin, *J. Hosp. Infect.*, 2021, **111**, 69-77.
[12] C. Torrecilla, J. Fernández-Concha, J. R. Cansino, J. A. Mainez, J. H. Amón, S. Costas, O. Angerri, E. Emiliani, M. A. Arrabal Martín, M. A. Arrabal Polo, A. Garciá, M. C. Reina, J. F. Sánchez, A. Budiá, D. Pérez-Fentes, F. Grases, A. Costa-Bauzá, J. Cuñé, *BMC Urol.*, 2020, **20**, article no. 65.
[13] H. Bouzidi, O. Traxer, B. Doré, J. Amiel, H. Hadjadj, P. Conort, M. Daudon, *Prog. Urol.*, 2008, **18**, 230-237.
[14] N. Mohebbi, C. A. Wagner, *J. Nephrol.*, 2018, **31**, 511-522.
[15] Y. Barghouthy, O. Wiseman, E. Ventimiglia, J. Letendre, J. Cloutier, M. Daudon, F. Kleinclauss, S. Doizi, M. Corrales, O. Traxer, *World J. Urol.*, 2021.

Comptes Rendus
Chimie
2022, Vol. 25, Special Issue S1, p. 431-444
https://doi.org/10.5802/crchim.143

Microcrystalline pathologies: Clinical issues and nanochemistry

SEM-EDX micro-analysis and FTIR infrared microscopy by ATR of a bladder stone from the IIIth millennium BC from the B1S passage-grave of the necropolis in Chenon (Charente, France)

Gérard R. Colmont[*,a], **Dominique Bazin**[b] **and Michel Daudon**[c]

[a] Honorary Professor of Biology, PhD of Archaeology from EHESS, Paris, France

[b] Université Paris-Saclay, CNRS, Institut de Chimie Physique, 91405, Orsay, France

[c] Laboratory of Physiology and INSERM Unit UMRS 1155, Tenon Hospital, Paris, France

Current address: 66 bis Rue des Saules F-33500 Libourne, France (G. R. Colmont)

E-mails: colmont.gerard@wanadoo.fr (G. R. Colmont), dominique.bazin@universite-paris-saclay.fr (D. Bazin), daudonmichel24@gmail.com (M. Daudon)

Abstract. Here is a case of bladder stone of average size dated to the Late Neolithic period, found in the multiple burial of the B1S passage-grave in Chenon (Charente, France). Chemical analysis showed a mixed composition. The core, intermediate and surface envelopes consist in calcium phosphate apatite associated with whitlockite and amorphous carbonated calcium phosphate, all clarified by Fourier Transform InfraRed spectroscopy. Calcium phosphatic stones are characteristic of communities, such as those of the Neolithic period, where the diet was rich in cereal carbohydrates and poor in animal proteins. The excavation of such extra-skeletal objects is an event that is particularly interesting as it provides documents on the history of diseases and diets in ancient populations. The complete set of data suggests that this bladder stone was formed during a urinary tract infection with a germ possessing a very active urease.

Keywords. Infectious stone, Carbapatite, Whitlockite, Amorphous carbonated calcium phosphate, FTIR spectroscopy, Microchemical analysis, Urease.

Published online: 14 January 2022

1. Introduction

The graves do not only contain skeletal remains and offerings accompanying the deceased. Calcified extra-skeletal objects can also be found there such as bladder stones or kidney stones, gallstones, prostatic and pancreatic stones, uterine and gastrointestinal leiomyomas, ovarian cysts, ovaries, fetus, lymph node, etc. [1–6].

* Corresponding author.

Urinary lithiasis (from the Greek *lithos*, stone) is one of the major pathologies in which environmental factors play a major role. It was widespread in ancient populations [7,8] and dates back at least to the Paleolithic Age, as evidenced by the discovery of a urinary stone dated to about 8500 years BC in a Mesolithic cave on the Sicilian coast [9,10]. As early as 1797, Wollaston described urinary stone components as magnesium and ammonium phosphate in his publication entitled "On gouty and urinary concretions" [11]. By the end of the 18th century, the chemical composition of urinary stones was identified by chemists and physicians of the time. In addition to ammonium and magnesium phosphate, calcium phosphate, calcium oxalate, uric acid, ammonium urate, cystine, xanthine and even silica were found in stones, with major epidemiological differences compared to what is now known. Uric acid was more frequent in adults from well-to-do backgrounds, whereas phosphates were more prevalent in poorer populations and in children who were more exposed to malnutrition and urinary tract infections. Nowadays, in almost all countries of the world, the most common composition of stones is calcium oxalate.

Archaeological evidence has revealed that humans knew about kidney stones and, more important, knew how to treat them [12]. In 1550 BC, during the reign of Amenhotep I of the XVIIIth Dynasty, the Ebers Papyrus, about twenty meters long, relates the various remedies used in Pharaonic Egypt in 877 prescriptions, in particular those concerning the bladder diseases. The calculi are named *Ourmyt* [13]: the prescription recommended for "hunting" them is based on cow-milk or beer [14] (Eb 20 (6, 10–16)). In ancient Greece, Hippocrates pointed out the dangers of bladder stones and advocated urinalysis. Indian Sanskrit documents mention the removal of stones via the supra-pubic route [15]. During the reigns of Augustus and Tiberius, the Roman encyclopedist and physicist Aulus Cornelius Celsus described in his book *De Medicina* the symptoms of "stone disease" as well as the surgery to be used to extract bladder stones [16].

Studies have shown that bladder stones were a disease of communities where the diet was high in cereal carbohydrates and low in animal protein [17]. And we know that Neolithic populations were agricultural, that they had domesticated wild cereals, but also that they practiced animal husbandry. Conversely, obesity due to a diet rich in animal proteins, nucleoproteins (offal, game) and fats may be the cause of the formation of other stones, including uric acid and calcium oxalate, a superinfection of the urinary tract by urease microorganisms that can transform uric acid into ammonium urate. This may explain rare observations in the literature such as the one reported in 2011 by Giuffra *et al.* [18] regarding a left kidney stone found in the mummy of an Italian nobleman in 15th century our era composed of ammonium urate with 5% weddellite. Several months before his death, the subject had developed an infection, presumably with a urinary tract origin. It led to sepsis that was responsible for his death [18]. It has even been considered that the risk of stone development may be related to seasonal changes in climate, increased ambient temperature [19] and the number of hours of sunlight per month [20], and therefore changes in body hydration and vitamin D metabolism.

The discoveries of biological calcifications dated to Prehistoric and early historical times are rare, which makes their analysis interesting. This was the case for a calcified tuberculous lymph node found under a dolmen near Carcassonne (Aube) in an archaeological layer from the Chalcolithic period [1, 21]. Likewise, a urinary bladder calculus with a diameter of 42 mm, composed of calcium phosphate, was discovered among the human bones of the Bertrandoune dolmen in Prayssac (Lot) dated 2200 years BC [21,22]. The sense of observation allowed Dr. E. Gauron in 1971–1972 to collect in the B1S passage-grave at Chenon (in its corridor?) a calcification, already reported [23], which will be considered below.[1] As urolithiasis can be due either to dietary errors [24–27] or to urinary tract infections [24,25,28,29], its study could possibly provide information on the diet of the populations of that time and their diseases as well as its history and its causes.

[1] Dr. E. Gauron (†) was the director of the excavation of this passage-grave and at the same time the only physician in the team. This bladder stone was collected by him alone without being recognised. Being for some time the custodian of the human bones of this excavation, the main author of this article (GRC) noticed this "stone", reported it in an article of a paper [23] and he had it analysed in order to know about its nature.

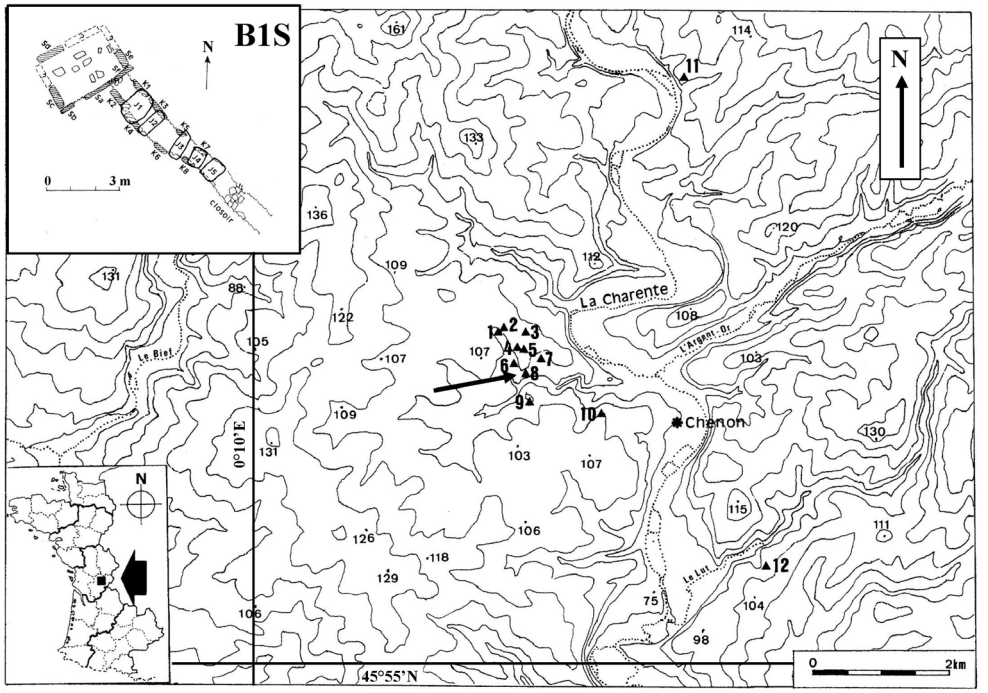

Figure 1. Monumental plan of the passage-grave B1S in Chenon (by Lotte [30]) with the topographic situation of the necropolis in Chenon (Charente, France) in its archaeological environment (on the IGN map of Ruffec in 1/50,000[e]).

2. The study area. The archaeological context

At the time of its excavation, cairn B1 at Chenon (which contained the two passage-graves named B1S and B1T) had a sagging and oval appearance [30]. It was made up of more or less flat limestone and stones. S-chamber lacked the cover table. Its corridor was covered with five disjointed slabs (Figure 1). The dental MNI (Minimum Number of Individuals) made it possible to count twenty-nine adults and seventeen subadults in the S-chamber (eight young child, four older child, five adolescents), and fourteen subadults in the S-corridor (one infant, seven young child, four older child, two adolescents). It is the bone MNI (with the axis) that has been used to claim that twenty-four adult skulls have passed through the S-corridor [23].

Two absolute dates were obtained on human bone fragments collected respectively on the north side of the S-chamber and in half of the S-corridor near the chamber giving the 3rd millennium BC (Ly-17044: 3081 to 2896 cal BC at 2σ and Ly-17045: 3012 to 2888 cal BC at 2σ) as the period of deposit, i.e. the Early Neolithic I period (according to Guilaine [31]) while bones of the deep layer of the T-chamber are related to an older period, the 5th millennium BC (Ly-1105: 4712 to 4040 BC at 2σ), i.e. the beginning of the Middle Neolithic (according to Guilaine, [31]) close to the period of construction of the monument.

The human skeleton has kept the marks of external aggressions, this during childhood and until adulthood. Thus, when the nutrient supply is not sufficient, it appears in the bones or teeth "biological stress" [32]. This stress can be seen by a more or less pronounced microporous aspect of the orbits [33] called *cribra orbitalia* (seen in the chamber of the B1T dolmen, [23]. In this specific case, some authors presently think about a vitamin B12 deficiency in the mother followed in childhood by a nutritional deficiency coupled with intestinal infections [34]. The other indicator of stress is dental enamel hypoplasia, which consists of a reduction in the thickness of the enamel appearing on the crown as parallel horizontal depressions but sometimes also as pits. There are a lot of causes of dental enamel hypoplasia:

genetic predisposition, nutritional deficiencies, infections, prematurity, high fever [35–38]. As with bladder or kidney stones, the study of linear enamel hypoplasia (LEH) is an essential tool for the reconstructing aspects of health in the past [39–42]. In these studies, the age at which this physiological stress occurred and its duration are still to be asserted [43], knowing that enamel grows nonlinearly [44]. As the skeletal remains of children are generally under-represented in the archaeological record, the study of LEHs will be carried out in adults and will provide a historical account of childhood stress episodes for a particular region and time period [38]. Such hypoplasias were observed on permanent adult teeth in the corridor of the B1S passage grave (20 cases), mainly on upper lateral incisors and lower canines, and on permanent subadult teeth found in the chamber (one lower incisor) and in the corridor (one lower canine and one lower first premolar) of the B1S passage-grave [23].

All these studies and observations point to a better knowledge of the living conditions of populations in the past. We can already observe that a bad diet as well as diseases contracted sometimes in childhood leave traces in the skeleton.

3. Methods

At present, the diagnosis of calcified biological masses such as bladder stones remains a procedure widely used in medicine and paleopathology. First there are the conventional techniques which are morphological, radiographic and microscopic analyzes. Advanced techniques, for their part, consist of elementary microanalysis by energy dispersive X-ray analysis (SEM-EDX) and X-ray fluorescence (XRF) as well as chemical analysis through Powder X-ray diffraction (XRD) and Fourier Transform InfraRed spectroscopy (FTIR) to obtain information on the elementary and chemical composition of the different envelopes of the calculus and of its nucleus [45].

The different methods we have used in this investigation are obviously nondestructive one. First, imaging at the micrometer scale has been performed with a micro-scanner (GE V/tome/XS). The samples have been observed with two SEM in environmental mode to preserve it [46–48]. Observations have been performed by backscattered electrons BSE (Zeiss EVO 50, SEM LaB6 at optimized variable pressure, 25 kV) and secondary electrons (field-emission "gun" Zeiss SUPRA 55-VP, at low voltage between 0.5 and 2 kV), on the surface, and in depth thanks to its section, with different magnifications (500× to 4500×), to detect crystals and identify them as well as to look for possible imprints of bacteria [28,29] that can be responsible for the formation of the calculus. X-ray microanalysis (EDX) done on the second electron microscope makes an elemental analysis by detecting the characteristic lines of the present chemical elements [29,46–48]. Finally, chemical analysis has been performed by attenuated total reflection ATR with the Spotlight 400 FTIR Imaging System from Perkin-Elmer. The spectral range adopted goes from 4000 to 520 cm^{-1} at a resolution of 16 cm^{-1} [49,50].

Such approach has been successfully applied to different kinds of concretions including kidney [51–53], prostatic [54,55] and pancreatic [56] stones and in the case of two giants bladder stones found in the pelvis of a sixteenth–seventeenth century adult as well [57].

Thus, these various observations and analyzes will make it possible to analyze and define, with the maximum of supporting evidence, the nature of this calculus and, if possible, its cause.

4. Analysis and results

The preliminary remarks of Gauron and Massaud [30] suggest the risks of pollution of the funeral deposit by the external environment with the consequence of a modification of its physicochemical characteristics of origin. Rather, if this bladder stone was collected in the archaeological layer of the S-corridor (and not outside) that is relatively thick of 54 cm, then these "pollutions" were very reduced, and that would be good news.

This calcification appears in a slightly flattened ovoid shape, 13.9 mm long, 10.2 mm wide and 8.5 mm thick (Figure 2A). Its mass is 0.94 grams, with a beige exterior color. Its surface is mostly smooth, with granulations in some places. Microscanner analysis (voxel of 8.25 μm, 120 kV acceleration voltage) shows a lighter eccentric nucleus (7.1 mm long) surrounded with several dark coarse-element thick layers, each bordered by a thin, lighter border (Figure 2C).

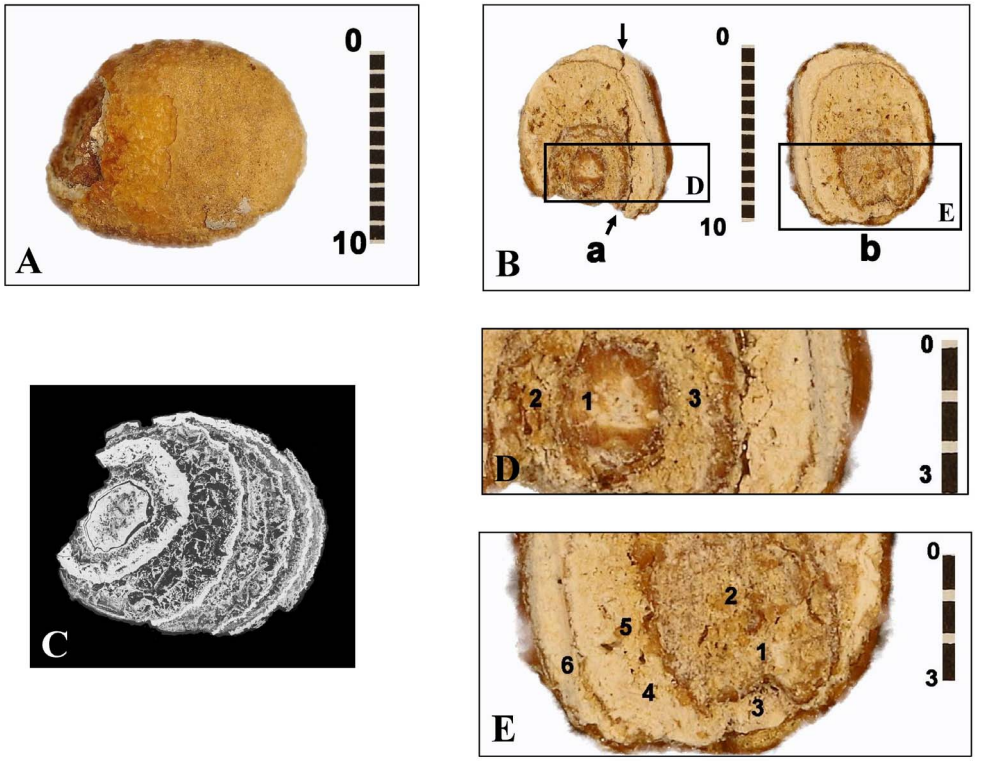

Figure 2. Different views of the bladder stone found in the B1S passage-grave in Chenon (Charente, France). (A) External appearance. (B) Views of the two sections of the bladder stone (section a and section b) showing its nucleus and its various layers. Arrows: break plane for section a. (C) Micro-tomography of the bladder stone finely pointing its different layers, some thin, others thick with coarse granulation. (D) Enlarged view of part of section a of the bladder stone with the marking of the three areas D1–D3 analyzed by EDX micro-analysis. (E) Enlarged view of part of section b of the bladder stone with the marking of the six areas E1–E6 analyzed by EDX micro-analysis. Scales in mm.

The microelementary analysis EDX study at SEM (25 kV, resolution of 125 eV) of the two intermediate zones, external and internal (Table 1), has revealed the following average concentrations of the main elements: (O) = 43.00%, (C) = 2.52%, (P) = 14.75%, (Ca) = 37.45%, (Al) = 1.30%, (Mg) = 0.71%. Other elements such as Na, Zn, Si, S are also present in smaller proportions, however with a high percentage of error. In the internal structure of the nucleus, a concentration of (O) = 39.14%, (C) = 2.21%, (P) = 15.21%, (Ca) = 41.42%, (Al) = 1.15%, (Mg) = 0.41% shows a little more calcium phosphate in the core than in the outer layers and less CO_3 substitution in the core than in the outer areas. EDX analysis confirms a significant proportion of magnesium in the internal intermediate zone of the stone (Table 1, E5; Figure 3) in proportions which, relative to calcium, are compatible with whitlockite. A Ca/P ratio has been found around 2.54 for the peripheral areas and around 2.73 for the nucleus (Table 1). Its high value can be explained by the presence of calcite due to a limestone environment. It is indeed a stone of calcium phosphates with as minor elements: sodium, zinc, silicon and sulfur.

FTIR infrared microscopy (Figure 4) is relatively easy to use when using the ATR technique. The υ_1 and υ_2 modes (absorption band at 474 cm^{-1}) of the phosphate anion (PO_4) are only weakly active in infrared. The shoulder, here present at 963–957 cm^{-1} (υ_1 de PO_4), is typical of phosphate components [58, 59]. The υ_3 and υ_4 of (PO_4) areas, much more intense, are located here (with a shift due to the technique used here) at peaks around 1013 cm^{-1} (υ_3 of PO_4), 599 cm^{-1} (υ_4 of PO_4) and 559 cm^{-1} [60]. The anion $(HPO_4)^{2-}$ shows an IR band at 871 cm^{-1}.

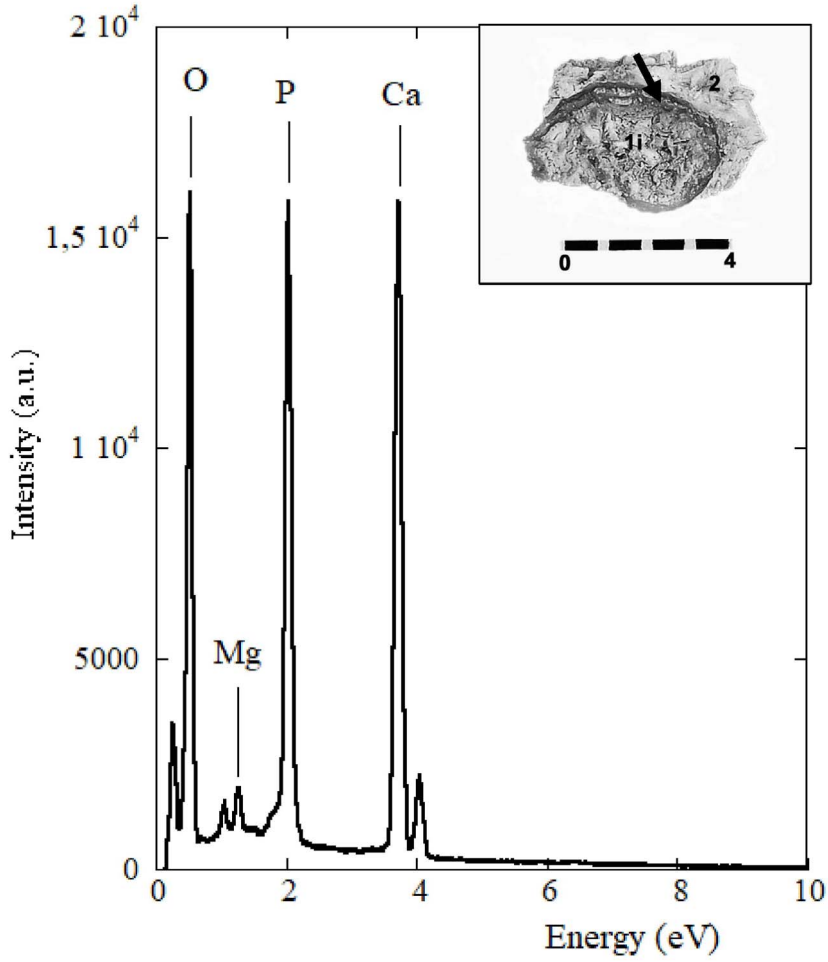

Figure 3. Spectrum of the microchemical EDX analysis of the internal intermediate zone 2 (arrow) close to the stone shell found in the B1S passage-grave in Chenon (Charente, France).

The shift of the peaks means that the peak of carbonates (substituted for hydroxyls in the apatitic structure) is around 1412–1413 cm^{-1} (υ_3 band of $(CO_3)^{2-}$) and not at 1419–1420 cm^{-1}, and at 871–872 cm^{-1} (bending band υ_4 of $(CO_3)^{2-}$). We know that proteins are mainly detected by their amide bands I and II around 1550 cm^{-1} and 1650 cm^{-1} (here 1640–1643 cm^{-1}). The absence of infrared vibrations in the 1300–1370 cm^{-1} and 700–800 cm^{-1} regions excludes the presence of calcium oxalates and purines [61].

These FTIR spectra (Figure 4) confirm the preponderant presence in this stone of carbapatite or carbonated apatite of Ca_{10} $(PO_4)_6$ (CO_3) $(OH)_2$ [62] general formula. Lateral inflections of the absorbance peak curve from 1011 cm^{-1} to 1136 and 1078 cm^{-1} (the latter corresponding to the stretching vibration band $HPO_4{}^{2-}$) indicate the presence of whitlockite or mixed phosphate of calcium and hydrated magnesium which has the formula Ca_9 Mg (HPO_4) $(PO_4)_6$ [63,64]. This rare phosphate found in kidney stones is stabilized by incorporating a little magnesium into its structure. Whitlockite has been identified in particular by its vibration at 992 cm^{-1}, on the shoulder of the peak at 1011 cm^{-1}. Another calcium phosphate, amorphous carbonated calcium phosphate ACCP, has been seen on several of the spectra shown here with vibrations at 1064 cm^{-1} and 543 cm^{-1}.

Different biochemical conditions therefore have caused several forms of crystallization during the

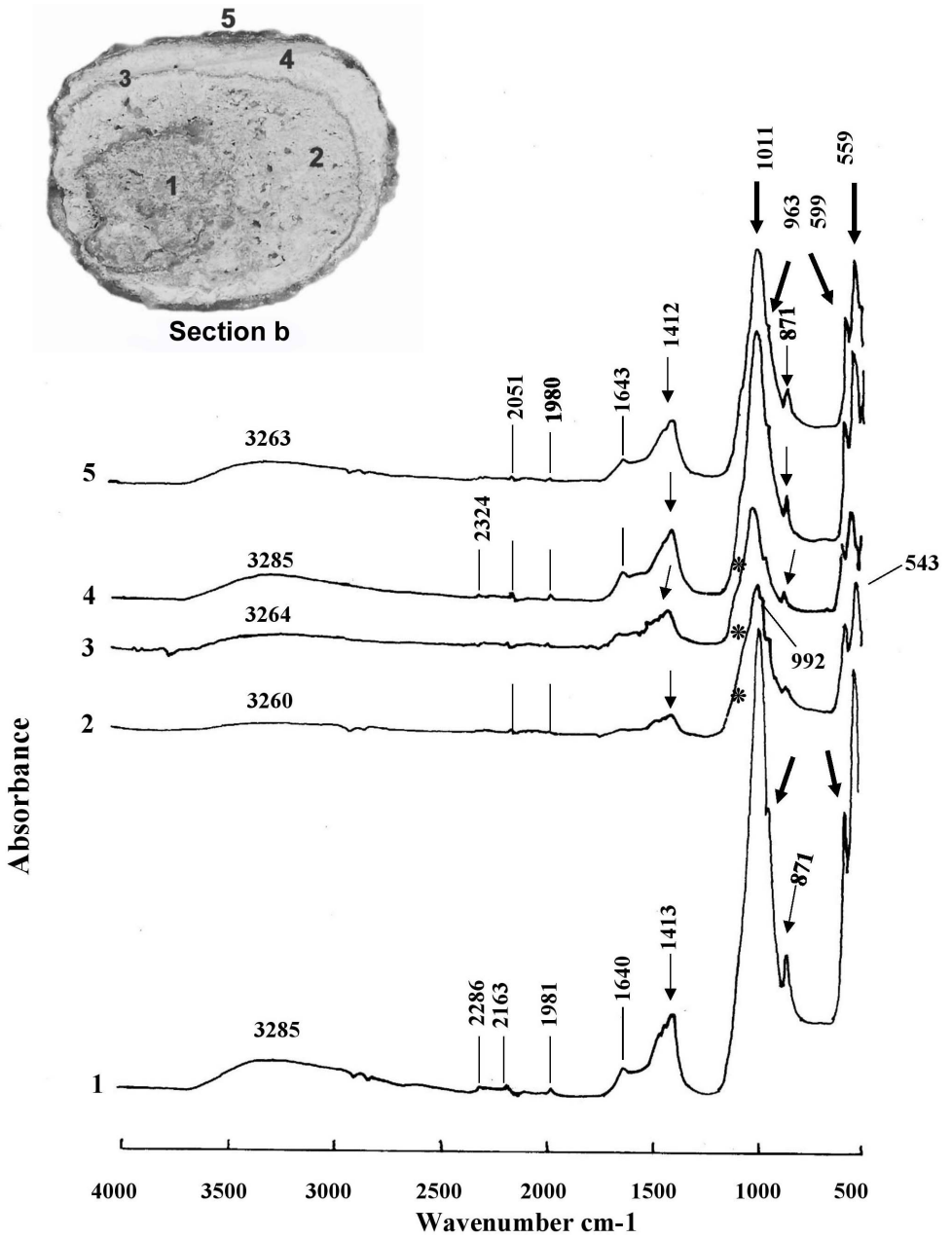

Figure 4. Infrared FT-IR spectra of the five areas analyzed in the section b of the bladder stone of the B1S passage-grave in Chenon (Charente, France) composed of calcium phosphate (carbapatite) mixed with whitlockite and amorphous carbonated calcium phosphate ACCP: 1, the nucleus; 2, the internal intermediate zone; 3, the external intermediate thin zone; 4, the external intermediate thick zone; 5, the external layer. Peaks at 1011, 963, 599 and 559 cm^{-1} correspond to phosphate absorptions (thick arrows). Peaks at 1412–1413 and 871 cm^{-1} denote carbonate ions (thin arrows). The stars on the shoulder of the peak at 1011 cm^{-1} indicate whitlockite as well the peak at 992 cm^{-1}. The peak at 543 cm^{-1} indicates the presence of ACCP.

Table 1. Quantitative results in mass percentages of the main chemical elements and secondary elements obtained by EDX analysis of the bladder stone found in the B1S passage-grave in Chenon (Charente, France)

% mass		O	C	P	Ca	Al	Mg	Na	Zn	Si	S	Ca/P
External interm. area	E6	41.21	3.77	14.79	37.02	2.30	0.54	0.43	0.25	0.14	0.07	2.50
Internal interm. area	E5	44.47	1.75	14.80	36.82	0.80	1.05	0.00	0.21	0.06	0.04	2.49
	E4	40.62	1.61	15.90	39.98	0.89	0.70	0.04	0.17	0.03	0.05	2.51
	E3	45.55	2.95	13.50	35.97	1.19	0.53	0.00	0.14	0.10	0.06	2.66
Central area	E1	42.10	2.22	15.36	37.38	1.74	0.78	0.11	0.16	0.07	0.09	2.43
	D2	34.11	1.65	14.36	47.85	0.95	0.25	0.04	0.52	0.14	0.13	3.33
	D3	38.01	2.26	15.55	42.86	0.75	0.24	0.04	0.14	0.08	0.07	2.76
Nucleus	E2	41.95	2.54	15.01	38.63	1.18	0.34	0.12	0.09	0.11	0.05	2.57
	D1	39.51	2.38	15.76	40.37	1.15	0.44	0.00	0.17	0.10	0.13	2.56

Refer to Figure 2 for the numbering of the different areas. The highest percentages are shown in red and the lowest in green.

formation of this calculus. It is therefore a mixed stone at least tertiary (with three components, all of a phosphatic nature).

A high carbonation rate CR = $(CO_3)^{2-}/(PO_4)^{3-}$ [28] is an important criterion to be taken into account to suspect the involvement of a urease germ infection in the formation of a stone [65]. Its value is obtained (also called R c/p) by making the ratio of the areas calculated on the IR graph (Figure 4, spectrum 4) located between the vibrations υ_3 of $(CO_3)^{2-}$ from 1530 to 1330 cm^{-1}—here 1412–1417 cm^{-1}—and υ_3 of $(PO_4)^{3-}$ from 1230 to ~900 cm^{-1}—here 1011–1017 cm^{-1}— [66]. The high content of carbonate ions (despite the absence of the υ_4 vibration at 712 cm^{-1}) suggests that the sample does not contain (or very little) calcium carbonate, but that the carbonate ions have been incorporated into the apatite during crystallization. This carbonate content reaches 25% in the carbapatite of the peripheral layers of the B1S dolmen calculus at Chenon and 17% in its core, which certainly makes it an infection stone.

SEM investigation may show carbapatite spherules associated with rhombohedral whitlockite crystals and granules of amorphous carbonate calcium phosphate. Pictures taken inside the peripheral layers of this stone (Figure 5) made it possible to identify these small spheres of agglomerated carbapatite filaments with an average diameter of 2.72 µm (range 1.76 µm to 3.57 µm). It appears that the carbapatite spherules have a smaller diameter in males (3.4 ± 1.8 µm) than in females (5.7 ± 3.9 µm), but the range of measurements prevents it from being asserted [28].

Bacterial imprints can be seen with SEM on the surface of carbapatite spherules [28], either in the form of rods (*Proteus sp.* or *Klebsiella sp.*) or in round prints indicating the ancient presence of *Cocci* such as *Staphylococcus sp.* [67,68]. The search for bacterial imprints in these spherules has been carried out in our case without convincing results (Figure 5).

5. Discussion

The diagnosis of bladder stones is immediately confirmed in our study by the concentric arrangement of the different layers [69–71] and by the alternation in these layers of crystalline and microcrystalline [72] that is typical of phosphate urinary lithiases, well observed on micro-scan (Figure 2C). A study of the chemical composition of kidney stones is important to understand how they formed. It is widely accepted that different areas of a stone should be analyzed separately. Laser Induced Breakdown Spectroscopy (LIBS) technology that is not used for our stone appears to be currently the most appropriate method to perform a rapid and simultaneous multi-elemental analysis of each part of a urinary stone, as it does not damage the sample, and, in addition, some of these analyzers are portable [45]. However, unlike infrared spectrophotometry, this technique does not give the

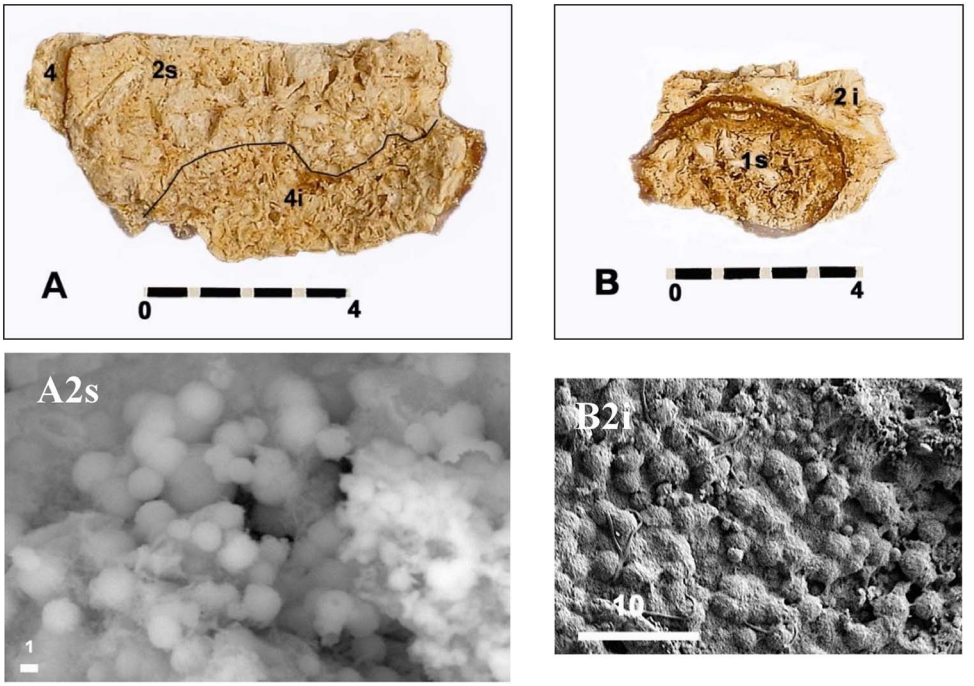

Figure 5. Internal views (A, B) of two fragments of the fracture plane of half a of Chenon's B1S bladder stone. (A2s) Spherules of carbapatite without any bacterial imprints magnified 4000× observed at the level of the upper part of the internal intermediate zone 2. (B2i) Spherules of carbapatite without any bacterial imprints magnified 1000× observed at the level of the lower part of the internal intermediate zone 2 located in contact with the surface of the core 1. Scales in mm (A, B) and in μm (A2s, B2i).

molecular and crystalline composition of the samples and therefore cannot replace infrared analysis (or X-ray diffraction) of the samples whose nature we want to identify precisely.

The presence of three calcium phosphates, two of which are highly carbonated, points to an infectious cause for the formation and growth of this stone. Usually, this lithogenesis results in the presence of a fourth phosphate, struvite (ammonium magnesium phosphate hexahydrate) which was not detected here. It should be noted that when stones have been stored for a long time in the air (which is our case), struvite tends to degrade and disappear [73]. The high carbonate content (between 17 and 25%) suggests lithogenesis into alkaline urine under the dependence of ureolysis by bacteria that possess urease. Elevation of urine pH above 6.8 (alkaline or weakly acidic urine) promotes oxidation of CO_2 to carbonate $(CO_3)^{2-}$ and then its precipitation as carbonate-apatite or carbapatite [74,75]. Carbapatite appears to be more abundant in the stones of women than in those of men, who more frequently produce stones composed mainly of calcium oxalate dihydrate [65].

Nowadays, seven major types of calculi are distinguished according to their crystalline composition [24,76]. The Chenon B1S stone studied here, falls into Daudon's type IVb [24] since it includes at least three phosphates : carbapatite, amorphous carbonate calcium phosphate PACC and whitlockite (calcium magnesium hydrogen phosphate of chemical formula $Ca_9Mg\ (HPO_4)\ (PO_4)_6$). The morphological details and chemical compositions of a number of ancient bladder stones have been surveyed by Steinbock [8]. His table has been repeated and expanded (Table 2; [7,9,10,15,22,23,77–91]).

EDX analysis established that the basic structure of our calculation was calcium and phosphorus. The high Ca/P value found for our example has been reported several times: for a predominantly calcium phosphate bladder stone (with calcium carbonate and some calcium oxalate) collected from a tomb in

Table 2. Some examples of kidney and bladder stones found in excavations in Africa, America and Europe (shaded) in burials dated to prehistoric and early historical times (after Steinbock, [8], completed)

Location	Sex/Age	Size-type	Composition	Date [reference]
Uzzo, Trapani, Sicily, Italy	F/20–25		Carbonate Phosphate	8500 BC [9,10]
El Amrah Egypt	M/16	65 mm Bladder	Urate	3500 BC [77,78]
Egypt	—	45 × 30 mm 40 × 25 mm, Bladder	Urate, Mg Ammon., Phosph.	3500 BC [79]
Indian Knoll Kentucky, USA	M/24	40 × 27 × 23 mm Bladder	Oxalate	3300 BC [80]
Helouan Egypt	—	35 × 30 mm (5 kidney stones) 30 × 20 mm, Renal?	—	3100 BC [81]
Chenon B1S Charente, France	M?	14× 10 × 8.5 mm Bladder	Carbapatite Whitlockite, CCPA	Ille millenium BC [23]
Naga-el-Dier Egypt	—	16 mm (4 kidney stones), Renal	Oxalate Phosphate	2800 BC [77]
Egypt	F/35	Renal pelvis Renal	Carbonate Phosphate	2650–2150 BC [82,83]
Prayssac, Lot France	Adult	41 × 35 × 30 mm Bladder	Phosphate	2200 BC [22]
Yorkshire England	Adult	40 × 30 × 30 mm Bladder	—	2000–700 BC [84]
Fulton County Illinois, USA	F/20–22	17 × 10 × 7 mm Renal	Apatite Struvite	1500 BC [15]
Csongréd-Felgyd Hungary	F/Adult	35 × 34 × 30 mm Bladder?	Oxalate, Sulfate Ammon. Mg	1800–500 BC [85]
Arizona USA	?/18	42 × 34 × 27 mm Bladder	Carbonate Phosphate, Urate	<1100 BC [86]
Egypt	M/Adult	Bladder	—	1000 BC [87]
Sudan	32 cases	30 × 39 mm Bladder	Calcite Apatite	1000 BC [88]
Schleswig Germany	M/40–50	11 × 11 mm 4 × 4 mm, Renal?	Apatite	500–250 BC [89]
Northeast Arizona USA	M/> 30	30 × 27 × 25 mm Bladder	Oxalate, Struvite Phosphate	500–750 AD [7]
Székkutas-Képolna Hungary	M/41–50	50 × 40 × 35 mm Bladder	Carbonate Apatite	700–800 AD [90]
Oluz Höyük Turquey	F/59–71	65 × 45 mm Bladder	Phosphate	11th Century [91]

the medieval cemetery of Gdańsk, Poland (2.23 for the outer layers and 1.99 for the inner layers) [4]; for the hydroxyapatite bladder stone of a 59–71 year old woman who lived in the XIth century in Olüz Höyük, Turkey (2.47 for the cortex and 2.54 for the core) [91].

Water infiltration into a non-hermetic grave can have several consequences on the chemical analysis of a stone, either enrichment in calcium carbonate or dissolution of phosphate ions if the water is acidic. This was reported for a bladder stone dated to 700–800 AD found in a 41–50 year old man in Székkutas-Képolna, Hungary [90]. The core was dissolved. It was the same for another adult female bladder stone dated to the 9th–7th millennia BC buried in an oval pit filled with soil and limestone blocks that was found in the Uzzo Cave in Italy. Chemical analysis yielded a significant amount of calcium carbonate with small amounts of phosphate components [10]. The consequence was a Ca/P ratio of more than 6 both at the periphery of the stone and in its core.

Many discoveries of oxalate stones have been made inside mummies—especially Egyptian—but also in pre-Columbian tombs, to mention the most frequent cases. The size of these stones can vary up to that of a golf ball [92]. Without contact with the outside world, these mummies perfectly preserve all the components of the stones. This is the case of a naturally dehydrated mummy, dated from 500 to 750 AD, discovered in Arizona wrapped in a fabric decorated with furs and feathers, which could be fully studied in 1979 [7]. The bladder stone was still in the contracted bladder. Its complete chemical composition was calcium oxalate monohydrate in monoclinic crystals (75%), magnesium oxalate (9%), struvite in orthorhombic crystals (6%), calcium phosphate (4%), ammonium acid urate (2%) and silicon dioxide (1%). This complete analysis shows an absence of pollution. Another mummy of an adult woman, dated to the beginning of the 19th century, found in a rough wooden coffin in the church of Borgo Cervato in Umbria (Italy), had a bladder stone of 7.5 cm in diameter, the outer layers of which were composed of crystallized struvite and the inner layers of acid ammonium urate. The Ca/P ratio was only 0.6 for the outer layers and 1.6 for the inner layers [92]. Fortunately the mummy was in a cool place away from light, which allowed the struvite not to disappear, when it is known that a poor storage condition (e.g., high temperature in summer in a warehouse) can lead to its disappearance [73].

The calculation of the carbonation rate for our stone and the observation of carbapatite spherules have allowed us to affirm that the stone found in the B1S passage-grave of Chenon had a bacterial origin without it being possible for us to observe impressions with certainty. Only a few structures with pores of about 2 μm, compatible with cocci, but not bacilli, were observed locally. The relationship between bacteria and urinary stones has been documented since the time of Hippocrates [93]. An important contribution to understanding the origin of infection stones was made by Brown [93]. He was the first to put forward the theory that bacteria split the urine and thus cause the formation of stones. At the same time, he isolated *Proteus vulgaris* from a stone nucleus, although the genus *Proteus* had first been described by Hauser as early as 1885 [94]. In 1925, Hager and Magath [95] suggested the enzyme "urease" as the cause of hydrolysis of urine into ammonia and carbonic acid. A year later, Sumner [96] succeeded in isolating the enzyme from *Canavalia ensiformis*. Nowadays, more than 200 species of bacteria show urease activity using urea as a nitrogen source [97].

The most important urease-producing pathogens are: *Proteus, Klebsiella, Pseudomonas* and several species of *Staphylococcus* [98]. However, the *Proteus* group is the main culprit in infection stones [99,100]. Over 90% of its strains possess a highly active urease. They are widespread saprophytic bacteria in soil and water. *Proteus* is known as an opportunistic bacterial pathogen. The essential characteristic of *Proteus* bacteria is a swarming phenomenon, a process of multicellular differentiation of short rods into elongated swarm cells [100].

A large number of trace elements have been quantitatively detected in kidney stones [45,101,102]. The first paper on trace elements in urine was published in 1963 [103]. Their influence on the crystallization process in stones was recognized in the following years [104,105]. Food intake, metabolism and the role of the environment explain their presence. Many of these trace elements are known to be essential in specific metabolic processes [106]. A few trace elements such as zinc and magnesium are thought to have an inhibitory effect on urinary lithiasis [107]. A high proportion of zinc and strontium has been found in calcium phosphate stones [108] and a correlation

between the two of them [109]. Authors believe that zinc may play a role in the formation of the stone core [106,110,111]. However, the role of zinc in lithogenesis remains unclear. The presence of whitlockite in our stone, which is very rare in the urinary system, can be explained by the traces of zinc found in the EDX analysis because zinc stabilizes this phosphate, and it should not be forgotten that zinc is found in significant amounts in the nearby prostate, if it is a male [112].

6. Conclusion

This investigation confirms once again that FTIR micro-spectrometry offers multiple advantages for the identification and quantification of the mineral phase of the constituents of bladder stones, and this in a non-destructive manner, which is an advantage in archaeology.

The combined use of FTIR spectroscopy by ATR with EDX chemical micro-analysis and SEM observation of crystalline constituents as well as bacterial fingerprints at the origin of urolithiasis, show their effectiveness in the analysis of bladder stones. The stone studied here, which is dated to the Final Neolithic period, was found in a multiple grave in the Chenon Necropolis and belonged to an individual (a man?) who had a possibly recurrent urinary tract infection due to a urease bacterium (probably not from the *Proteus sp.* group).

This study has also made it possible to draw the attention of any searcher to the possibility of discovering extra-skeletal objects accompanying the skeletal remains of prehistoric and ancient burials. Everyone must consider that there are several steps for an archaeologist or anthropologist researcher to make a diagnosis on a biological object recovered in excavation [91]. First, defining the location of the object among the exposed human body; second, determining the type of calcification if possible *in situ*; third, working to identify the mineralogy and elementary compositions of the object to define possible causes. Thus, discoveries of this type may multiply and provide new, well-documented evidence to the history of diseases in past populations.

And in the case of the discovery of a biological object resembling a urolithiasis, we have to make sure that it is put in a hermetic box, protected from light and cool [73]. In this way, discoveries of this type can be multiplied, analyzed in good conditions and bring new well documented evidence to the history of diseases in past populations.

Conflicts of interest

Authors have no conflict of interest to declare.

Acknowlegments

The main author (GRC) thanks Messrs Grégory Hauss and Philippe Legros, research engineers at PLACAMAT in Pessac (Gironde, France), for their competence and efficiency in handling the micro-scanner and the SEM-EDX.

References

[1] C. A. Baud, C. Kramar, *Bull. Mém. Soc. Anthropol. Paris*, 1990, **2**, 163-170.
[2] D. Komar, J. E. Buikstra, *Int. J. Osteaechaeol.*, 2003, **13**, 157-164.
[3] G. Fornaciari, V. Giufra, *Pathobiology*, 2012, **79**, 257-267.
[4] J. J. Gladykowska, D. Nowakowski, *PLoS One*, 2014, **9**, 1-6.
[5] G. Cole, C. Rando, L. Sibun, T. Waldron, *J. Paleopathol.*, 2015, **10**, 51-57.
[6] B. Kwiatkowska, A. Bisiecka, L. Pawelec, A. Witek, J. Witan, D. Nowakowski, *PLoS One*, 2021, **16**, 1-16.
[7] J. M. Streitz, A. C. Aufderheide, M. El Najjar, D. Ortner, *J. Urol.*, 1981, **126**, 452-453.
[8] R. T. Steinbock, *J. Paleopathol.*, 1989, **3**, 39-59.
[9] M. Piperno, *Kokalos*, 1976, **XXII–XXIII**, 798-816.
[10] A. d'Alessio, E. Bramanti, M. Piperno, G. Naccarato, P. Vergamini, *Archaeometry*, 2005, **47**, 127-136.
[11] W. H. Wollaston, *Philos. Trans.*, 1797, **87**, 386-401.
[12] M. López, B. Hoppe, *Pediatr. Nephrol.*, 2010, **25**, 49-59.
[13] M. E. Salem, G. Eknoyan, *Am. J. Nephrol.*, 1999, **19**, 140-147.
[14] T. Bardinet, *Les papyrus médicaux de L'Egypte Ancienne*, Fayard, Paris, 1995.
[15] C. W. Beck, W. P. Mulvaney, *JAMA*, 1966, **195**, 1044-1045.
[16] V. A. Master, M. V. Meng, M. L. Stoller, in *Urinary Stone Disease. The Practical Guide to Medical and Surgical Management* (M. L. Stoller, M. V. Meng, eds.), Wiley-Blackwell, 2007, 3-26.
[17] W. G. Robertson, *Br. J. Urol.*, 1978, **50**, 449-454.
[18] V. Giuffra, L. Ventura, S. Minozzi, A. Lunardini, R. Quaresina, *Am. J. Med.*, 2011, 1186-1187.
[19] Ch. L. Prince, P. L. Scardino, C. T. Wolan, *J. Urol.*, 1956, **75**, 209-215.
[20] W. G. Robertson, M. Peacock, P. J. Heyburn, F. A. Hanes, *Scand. J. Urol. Nephrol.*, 1980, **Suppl. 53**, 15-30.
[21] H. Duday, *The Archaeology of the Dead: Lectures in Archaeothanatology*, Oxbow Books, Oxford, UK, 2009, 85-88 pages.

[22] H. Duday, J. Clottes, H. Mercadier, F. Rouzaud, J. Zammit, "Un calcul urinaire provenant du dolmen de la Bertraundoune à Prayssac (Lot, France)", in *Actes du 3ème Congrès Européen de l'Association de Paléopathologie, Caen (France), Condé-sur-Noireau* (Collectif, ed.), 1980, 87-90.

[23] G. R. Colmont, *Ann. Soc. Sci. Nat. Charente-Marit.*, 2016, **X**, 791-824, Museum La Rochelle.

[24] M. Daudon, C. A. Bader, P. Jungers, *Scanning Microsc.*, 1993, **7**, 1081-1104.

[25] M. Daudon, *Arch. Pédiatr.*, 2000, **7**, 855-865.

[26] M. Daudon, H. Bouzidi, D. Bazin, *Urol. Res.*, 2010, **38**, 459-467.

[27] M. Daudon, A. Dessombz, V. Frochot, E. Letavernier, J.-Ph. Haymann, P. Jungers, D. Bazin, *C. R. Chim.*, 2016, **19**, 1470-1491.

[28] X. Carpentier, M. Daudon, O. Traxer, P. Jungers, A. Mazouyes, G. Matzen, E. Véron, D. Bazin, *Urology*, 2009, **73**, 968-975.

[29] D. Bazin, G. André, R. Weil, G. Matzen, E. Véron, X. Carpentier, M. Daudon, *Urology*, 2012, **79**, 786-790.

[30] E. Gauron, J. Massaud, *XVIIIe supplément à Gallia-Préhistoire*, Editions du CNRS, Paris, 1983, 85-119 pages.

[31] J. Guilaine, in *Archéologie de la France : le Néolithique* (J. Tarrête, Ch.-T. Le Roux, eds.), Editions A. et J. Picard, Paris, 2008, 9-30.

[32] E. Crubézy, P. Sellier, *Bull. Mém. Anthropol. Paris*, 1990, **2**, 171-177.

[33] S. Mays, *The Archaeology of Human Bones*, Routledge, London and New York, 1998, 143 pages.

[34] P. L. Walker, R. R. Bathurst, R. Richman, T. Gjerdrum, V. A. Andrushko, *Am. J. Phys. Anthropol.*, 2009, **139**, 109-125.

[35] A. H. Goodman, J. C. Rose, *Yearb. Phys. Anthropol.*, 1990, **33**, 59-110.

[36] M. Skinner, *J. Archaeol. Sci.*, 1996, **23**, 833-852.

[37] L. Alvesalo, *Hum. Genet.*, 1997, **101**, 1-5.

[38] E. MacLellan, *TOTEM*, 2005, **13**, 41-52.

[39] A. H. Goodman, G. J. Armelagos, J. C. Rose, *Hum. Biol.*, 1980, **52**, 515-528.

[40] K. M. Lamphear, *Am. J. Phys. Anthropol.*, 1990, **81**, 35-43.

[41] N. J. Malville, *Am. J. Phys. Anthropol.*, 1997, **102**, 351-367.

[42] M. Slaus, *Am. J. Phys. Anthropol.*, 2000, **111**, 193-209.

[43] D. H. Temple, M. Nakatsukasa, J. N. McGroarty, *J. Archaeol. Sci.*, 2012, **39**, 1634-1641.

[44] D. J. Reid, M. C. Dean, *Am. J. Phys. Anthropol.*, 2000, **113**, 135-139.

[45] V. K. Singh, P. K. Rai, *Biophys. Rev.*, 2014, **6**, 291-310.

[46] F. Brisset, M. Repoux, J. Ruste, F. Grillon, F. Robaut, *Microscopie électronique à balayage et microanalyses*, EDP Sciences, Paris, 2009.

[47] D. Bazin, M. Daudon, *Ann. Biol. Clin.*, 2015, **73**, 517-534.

[48] D. Bazin, E. Bouderlique, M. Daudon, V. Frochot, J.-Ph. Haymann, E. Letavernier, F. Tielens, R. Weil, *C. R. Chim.*, 2022, **25**, no. S1, 37-60.

[49] N. Quy Dao, M. Daudon, *Infrared and Raman Spectra of Calculi*, Elsevier, Paris, 1997.

[50] M. Daudon, D. Bazin, *C. R. Chim.*, 2016, **19**, 1416-1423.

[51] M. Daudon, D. Bazin, "New techniques to characterize kidney stones and Randall's plaque", in *Urolithiasis: Basic Science and Clinical Practice* (J. J. Talati, H. G. Tiselius, D. M. Albala, Z. Ye, eds.), Springer, 2012, 683-707.

[52] D. Bazin, E. Letavernier, J.-P. Haymann, P. Méria, M. Daudon, *Prog. Urol.*, 2016, **26**, 608-618.

[53] D. Bazin, M. Daudon, *J. Spect. Imaging*, 2019, **8**, article no. a16.

[54] A. Dessombz, P. Méria, D. Bazin, M. Daudon, *PLoS One*, 2012, **7**, article no. e51691.

[55] A. Dessombz, P. Méria, D. Bazin, E. Foy, S. Rouzière, R. Weil, M. Daudon, *Prog. Urol.*, 2011, **21**, 940-945.

[56] C. J. Cros, D. Bazin, A. Kellum, V. Rebours, M. Daudon, *C. R. Chim.*, 2016, **19**, 1642-1664.

[57] M. G. Baron, N. Benmoussa, D. Bazin, I. Abadie, M. Daudon, P. Charlier, *Urolithiasis*, 2018, **47**, 487-488.

[58] A. Hess, W. Hicking, W. Vahlensieck, *GIT-Labor-Medizin*, 1981, **1**, 19-25.

[59] A. Hess, G. Sanders, *Atlas of Infrared Spectra for the Analysis of Urinary Concrements*, Georg Thieme Verlag, Stuttgart, 1988.

[60] D. Bazin, M. Daudon, *Ann. Biol. Clin.*, 2015, **73**, 517-534, John Libbey Eurotext.

[61] I. Petit, G. D. Belletti, T. Debroise, M. J. Llansola-Portoles, I. T. Lucas, C. Leroy, C. Bonhomme, L. Bonhomme-Coury, D. Bazin, M. Daudon, E. Letavernier, J. Ph. Haymann, V. Frochot, F. Babonneau, P. Quaino, F. Tielens, *ChemistrySelect*, 2018, **3**, 8801-8812.

[62] T. White, C. Ferraris, J. Kim, S. Madhavi, *Rev. Mineral. Geochem.*, 2005, **57**, 307-401.

[63] P. Carmona, J. Bellanato, E. Escolar, *Biospectroscopy*, 1997, **3**, 331-346.

[64] D. Bazin, R. J. Papoular, E. Elkaim, R. Weil, D. Thiaudière, C. Pisapia, B. Ménez, N. S. Hwang, F. Tielens, M. Livrozet, E. Bouderlique, J.-Ph. Haymann, E. Letavernier, L. Hennet, V. Frochot, M. Daudon, *C. R. Chim.*, 2022, **25**, no. S1, 343-354.

[65] L. Maurice-Estepa, P. Levillain, B. Lacour, M. Daudon, *Scand. J. Urol. Nephrol.*, 1999, **33**, 299-305.

[66] A. Grunenwald, Ch. Keyser, A.-M. Sautereau, E. Crubézy, B. Ludes, *J. Archaeol. Sci.*, 2014, **49**, 134-141.

[67] L. Cifuentes Delatte, M. Santos, *Eur. Urol.*, 1977, **3**, 96-99.

[68] L. Cifuentes Delatte, *Composición y estructura de los cálculos renales*, Salvat Editores, Barcelona, 1984.

[69] H. J. Rodgers, R. G. Spector, J. R. Trounce, *A Textbook of Clinical Pharmacology*, Hodder and Stoughton, London, 1981.

[70] T. Anderson, *Br. J. Urol. Int.*, 2001, **88**, 351-354.

[71] T. Anderson, *Int. J. Osteoarchael.*, 2003, **13**, 165-167.

[72] M. G. Baron, N. Benmoussa, D. Bazin, I. Abadie, M. Daudon, P. Charlier, *Urolithiasis*, 2018, **47**, 487-488.

[73] J. C. Williams Jr, A. J. Sacks, K. Englert, R. Deal, T. L. Farmer, M. E. Jackson, J. E. Lingeman, J. A. Mc Ateer, *J. Endourol.*, 2012, **26**, 726-731.

[74] A. Hess, W. D. Miersch, *Int. Urol. Nephrol.*, 1989, **21**, 257-267.

[75] T. Deguchi, T. Yoshida, T. Miyazawa, M. Yasuda, M. Tamaki, H. Ishiko, S. Maeada, *Sex. Transm. Dis.*, 2004, **31**, 192-195.

[76] M. Daudon, O. Traxer, P. Jungers, *Médecine-Sciences*, Lavoisier, Paris, 2012.

[77] S. G. Shattock, *Transactions of the Pathological Society of London*, vol. 56, Adlard and Son, London, 1905, 275-290 pages.

[78] G. Elliot Smith, *The Ancient Egyptians and the Origin of Civilization*, Harper & Brother, London/New York, 1911.

[79] M. A. Ruffer, *Cairo Sci. J.*, 1910, **4**, 1-5.

[80] H. W. Smith, *Anthropology*, 1948, **4**, 511-513.
[81] J. Bitschai, *Am. J. Surg.*, 1952, **83**, 215-224.
[82] R. Boano, E. Fulcheri, R. Grilletto, E. Leospo, E. Rabino Massa, in *Egyptology at the Dawn of the Twenty-first Century, vol 3: Proceedings of the Eighth International Congress of Egyptologists, Il Cairo 2000, 138(4)* (Z. Hawass, ed.), The American University in Cairo Press, Cairo, New York, 2003, 138-144.
[83] E. Fulcheri, R. Grilletto, *Paléobios*, 1988, **5**, 61-63.
[84] J. R. Mortimer, *Forty Year's Researches in British and Saxon Burial Mounds of East Yorkshire*, A. Brown and Sons Limited, London, 1905.
[85] M. M. Boross, J. Nemeskeri, *Homo*, 1963, **14**, 149-150.
[86] G. D. Williams, *JAMA*, 1926, **87**, 941.
[87] G. E. Smith, W. R. Dawson, *Egyptian Mummies*, George Allen & Unwin, London, 1924.
[88] D. R. Brothwell, A. T. Sandison (eds.), *Diseases in Antiquity: A Survey of the Diseases, Injuries and Surgery of Early Populations*, Charles Thomas, Springfield, Illinois, 1967, 349-351 pages.
[89] H. Schutkowski, S. Hummel, S. Gegner, *Paleopathol. Newsl.*, 1986, **55**, 11-12.
[90] F. Szalai, E. Javor, *Int. Urol. Nephrol.*, 1987, **19**, 151-157.
[91] K. Özdemir, A. A. Akyolb, Y. S. Erdal, *Int. J. Osteoarchaeol.*, 2015, **25**, 827-837.
[92] V. Giuffra, L. Costantini, L. Costantini Biasini, D. Caramella, G. Fornaciari, *Urology*, 2008, **72**, 780-781.
[93] T. R. Brown, *JAMA*, 1901, **36**, 1395-1397.
[94] G. Hauser, *Über Fäulnissbacterien und deren beziehungen zur septicämie. Ein betrag zur morphologie der spaltpilze*, F.C.W. Vogel, Leipzig, 1885.
[95] B. H. Hager, T. B. Magath, *JAMA*, 1925, **85**, 1352-1355.
[96] J. B. Sumner, *J. Biol. Chem.*, 1926, **69**, 435-441.
[97] R. J. C. MacLean, J. C. Nickel, K.-J. Cheng, J. W. Costerton, *Crit. Rev. Microbiol.*, 1988, **16**, 37-79.
[98] D. P. Griffith, C. A. Osborne, *Miner. Electrolyte Metab.*, 1987, **13**, 278-285.
[99] D. P. Griffith, *Kidney Int.*, 1978, **13**, 372-382.
[100] A. Rózalski, A. Torzewska, M. Moryl, I. Kwil, A. Maszewka, K. Ostrowska, D. Drzewiecka, A. Zablotni, A. Palusiak, M. Siwinska, P. Staczek, *Folia Biologica Oecologica*, 2012, **8**, 1-17, Acta Universitatis Lodziensis.
[101] B. Hannache, A. Boutefnouchet, D. Bazin, M. Daudon, E. Foy, S. Rouzière, A. Dahdouh, *Prog. Urol.*, 2015, **25**, 22-26.
[102] S. Rouzière, D. Bazin, M. Daudon, *C. R. Chim.*, 2016, **19**, 1404-1415.
[103] Z. Nagy, E. Szabó, M. Kelenhegyi, *Z. Urol.*, 1963, **56**, 185-190.
[104] E. Eusebio, J. S. Elliot, *Invest. Urol.*, 1967, **4**, 431-435.
[105] D. J. Sutor, *Br. J. Urol.*, 1969, **41**, 171-178.
[106] A. Hesse, R. Siener, in *Urolithiasis* (J. J. Talati, F. Abbas, eds.), Springer, London, 2012, 227-230.
[107] I. H. Atakan, M. Kaplan, G. Seren, T. Aktoz, H. Gül, O. Inci, *Int. Urol. Nephrol.*, 2007, **39**, 351-356.
[108] D. Bazin, P. Chevallier, G. Matzen, P. Jungers, M. Daudon, *Urol. Res.*, 2007, **35**, 179-184.
[109] M. Słojewski, B. Czerny, K. Safranow, K. Jakubowska, M. Olszewska, A. Pawlik, A. Gołąb, M. Droździk, D. Chlubek, A. Sikorski, *Biol. Trace Elem. Res.*, 2010, **137**, 301-316.
[110] S. M. Lin, C. L. Tseng, M. H. Yang, *Int. J. Rad. Appl. Instrum. A*, 1987, **38**, 635-639.
[111] V. K. Singh, A. K. Rai, P. K. Rai, P. K. Jindal, *Lasers Med. Sci.*, 2009, **24**, 749-759.
[112] V. A. Master, M. V. Meng, M. L. Stoller, in *Urinary Stone Disease. The Practical Guide to Medical and Surgical Management* (M. L. Stoller, M. V. Meng, eds.), Humana Press Inc., San Francisco, 2007, 3-26.

Comptes Rendus
Chimie
2022, Vol. 25, Special Issue S1, p. 445-476
https://doi.org/10.5802/crchim.153

Microcrystalline pathologies: Clinical issues and nanochemistry

Pathologies related to abnormal deposits in dermatology: a physico-chemical approach

Hester Colboc [*, a], Philippe Moguelet [b], Emmanuel Letavernier [c, d], Vincent Frochot [c, d], Jean-François Bernaudin [e, f], Raphaël Weil [g], Stéphan Rouzière [g], Patricia Senet [h], Claude Bachmeyer [i], Naomi Laporte [a], Ivan Lucas [j], Vincent Descamps [k], Reyhan Amode [k], Florence Brunet-Possenti [k], Nicolas Kluger [k, l], Lydia Deschamps [m], Arnaud Dubois [n], Solenn Reguer [o], Andrea Somogyi [o], Kadda Medjoubi [o], Matthieu Refregiers [o], Michel Daudon [c, d] and Dominique Bazin [p]

[a] Sorbonne Université, AP-HP, Hôpital Rothschild, Service Plaies et Cicatrisation, Paris, France

[b] Sorbonne Université, AP-HP, Hôpital Tenon, Anatomie et Cytologie Pathologiques, Paris, France

[c] Sorbonne Université, AP-HP, Hôpital Tenon, Service d'explorations fonctionnelles, Paris, France

[d] INSERM, UMRS 1155, Sorbonne Université, Hôpital Tenon, Paris, France

[e] Faculté de médecine Sorbonne Université, Paris, France

[f] INSERM UMR 1272 Université Sorbonne Paris-Nord, Bobigny, France

[g] Université Paris-Saclay, CNRS, Laboratoire de Physique des Solides, 91405, Orsay, France

[h] Sorbonne Université, AP-HP, Hôpital Tenon, Service de Dermatologie, Paris, France

[i] Sorbonne Université, AP-HP, Hôpital Tenon, Service de Médecine Interne, Paris, France

[j] Sorbonne Université, UMR 8235, Paris, France

[k] Service de Dermatologie, AP-HP, Hôpital Bichat, Paris, France

[l] Department of Dermatology, Allergology and Venereology, Helsinki University Hospital, Helsinki, Finland

[m] Anatomie et Cytologie Pathologiques, AP-HP, Hôpital Bichat, Paris, France

[n] Laboratoire Charles Fabry, CNRS, Institut d'Optique Graduate School, Université Paris-Saclay, Palaiseau, France

[o] Synchrotron SOLEIL L'Orme des Merisiers Saint-Aubin, Synchrotron Soleil, Gif-sur-Yvette, France

[p] Université Paris-Saclay, CNRS, Institut de Chimie Physique, 91405, Orsay, France

E-mails: hestercolboc@gmail.com (H. Colboc), philippe.moguelet@aphp.fr (P. Moguelet), emmanuel.letavernier@aphp.fr (E. Letavernier),

[*] Corresponding author.

vincent.frochot@aphp.fr (V. Frochot), jf.bernaudin-univ@orange.fr (J.-F. Bernaudin), raphael.weil@u-psud.fr (R. Weil), stephan.rouziere@universite-paris-saclay.fr (S. Rouzière), patricia.senet@aphp.fr (P. Senet), claude.bachmeyer@aphp.fr (C. Bachmeyer), naomijylaporte@gmail.com (N. Laporte), ivan.lucas@upmc.fr (I. Lucas), vincent.descamps@aphp.fr (V. Descamps), reyhan_amode@hotmail.com (R. Amode), florence.brunet-possenti@aphp.fr (F. Brunet-Possenti), nicolaskluger@yahoo.fr (N. Kluger), lydia.deschamps@aphp.fr (L. Deschamps), arnaud.dubois@institutoptique.fr (A. Dubois), solenn.reguer@synchrotron-soleil.fr (S. Reguer), andrea.somogyi@synchrotron-soleil.fr (A. Somogyi), kadda.medjoubi@synchrotron-soleil.fr (K. Medjoubi), matthieu.refregiers@synchrotron-soleil.fr (M. Refregiers), daudonmichel24@gmail.com (M. Daudon), dominique.bazin@universite-paris-saclay.fr (D. Bazin)

Abstract. Although numerous pathologies are associated with abnormal skin deposits, these remain poorly described, as accurate characterization continues to present a challenge for dermatologists. Their submicrometer size as well as their diverse chemistry require various characterization tools. We aim to exemplify characterization of endogenous and exogenous skin deposits in some selected skin diseases using different physico-chemical techniques. We begin with a presentation of selected diseases associated with skin deposits. We then present those of our results which show their variety of structure, location and chemical composition, obtained with various tools: Field Emission Scanning Electron Microscopy coupled with Energy Dispersive X-ray Spectroscopy, X-ray fluorescence, vibrational spectroscopies, as well as techniques specific to synchrotron radiation. Our results constitute a real opportunity to improve diagnosis, and to understand the pathogenesis of many skin diseases, and opportunities for therapeutic intervention.

Keywords. Dermatology, Calcification, Vibrational spectroscopies, Electronic microscopy, Synchrotron radiation.

Published online: 24 February 2022

1. Introduction

A wide variety of diseases produces pathological deposits in tissues, including cancers, genetic disorders, infectious processes and environmental diseases. Such diversity explains the strong interest of the scientific and the medical community in these pathological deposits, as well as the difficulty of establishing a meaningful relationship between their physicochemistry and the underlying pathology [1–6].

In dermatology, the medical literature reveals the same complexity, and various skin diseases are associated with either endogenous (mineral or organic) or exogenous deposits [7,8]. Mineral endogenous deposits are generally composed of calcium phosphate apatite deposits, and are often considered to be provoked by the skin disease itself [9], while exogenous deposits can present various chemical phases, and are often considered as potential disease causes [10].

Due to their submicrometer size as well as their chemical diversity, characterization of pathological deposits in the dermis cannot be performed with conventional techniques routinely used in hospital laboratories. Some standard staining procedures such as von Kossa, Yasu or alizarin red, can demonstrate the phospho-calcic nature of the deposits, but they do not provide further information on their chemical composition [11]. It is therefore necessary to develop physico-chemical techniques able to describe their structural characteristics at a micrometre, or even nanometer, scale, as well as their chemical composition [12,13]. Such an approach has been applied successfully to various pathological calcifications in different organs, such as the kidney [14,15], prostate [16,17] or thyroid [18,19].

Various techniques can be used, including Field Emission Scanning Electron Microscopy coupled with Energy Dispersive X-ray Spectroscopy (FE-SEM/EDX) [20–22], μX-ray fluorescence (XRF) [23–25], μX-ray scattering [26–29], vibrational spectroscopies: μFourier Transform Infra-Red (FTIR) and μRaman spectroscopies [30–35] as well as techniques specific to synchrotron radiation [36–39] such as X-ray absorption near edge structure (XANES) [40–45]. These techniques allow the clinician a deeper un-

derstanding of the biophysical mechanisms related to the pathogenesis of an abnormal deposit [46], establish a medical diagnosis [47–50] and have a better idea of the effects of drugs on pathological calcifications [51].

The aim of this paper is to present structural and chemical characterisations of both endogenous and exogenous deposits seen in various skin diseases and to discuss the advantages and the limitations of different physico-chemical techniques.

2. Generalities regarding skin calcifications

We will first review definitions related to skin calcification with reference to the literature, after which we will present some recent results using physico-chemical techniques on various skin disease.

2.1. *Usual description of disease related to skin calcifications*

Skin calcification, also known as calcinosis cutis, has been described for decades, and linked to inflammatory, metabolic, tumoral, genetic and infectious skin diseases [52].

Various authors have proposed classifications of these diseases based on the physiological process leading to the pathological skin calcifications. Four categories are generally recognized: metastatic, dystrophic, idiopathic and iatrogenic calcifications [53], mainly distinguished based on their formation mechanism. The most commonly encountered skin calcifications are metastatic and dystrophic [52].

As Table 1 shows, skin calcifications are not always associated with abnormal calcium and phosphate serum levels. Dystrophic calcifications, for example, are induced by local tissue injury or abnormalities affecting collagen or elastic fibres specifically. Systemic sclerosis [54], lupus erythematosus [55], dermatomyositis [56], or mixed connective tissue diseases, are typical examples of skin pathologies that induce such tissue damage, leading to a calcification nidus. In contrast, metastatic calcifications result from skin calcifications that form on normal tissue adjacent to areas with abnormal calcium and/or phosphate metabolism [53].

Some diseases are not easily classified into these categories. Pseudoxanthoma elasticum, for example, is an inherited disease, associated with both a deficit in anti-mineralizing factor (pyrophosphate) and alterations of elastic fibres [57]. The initial phenomenon causing the disease is still disputed, making calcifications observed in pseudoxanthoma elasticum difficult to classify from dystrophic to metastatic calcifications.

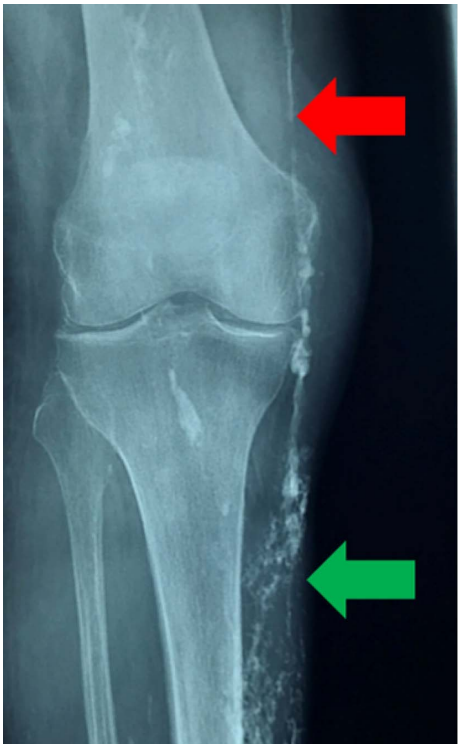

Figure 1. Vascular (red arrow) and subcutaneous (green arrow) skin calcifications of the lower limb, in the case of chronic venous insufficiency and leg ulcers.

Many skin structures can be calcified, especially in the dermis, including vessel walls and dermal interstitium. Figure 1 illustrates the radiological aspects of dystrophic calcifications in chronic venous insufficiency and leg ulcers. Presence of both vascular calcifications, shown by the linear aspect of the deposit, and dermal calcifications, illustrated by a more scattered aspect, are depicted.

While in mammalian epidermis a characteristic calcium gradient exists between lower and upper layers of the epidermis, little data exists regarding the calcium gradient within the dermis [58–60].

Table 1. Types of skin calcifications and related diseases with some of their mechanisms

Type of calcifications	Calcification mechanism	Related diseases
Metastatic	Systemic alteration of calcium phosphate metabolism	Chronic kidney disease Calciphylaxis Hyperparathyroidism Paraneoplastic syndrom Sarcoidosis
Dystrophic	Inflammation/cell death or mineral deposition at sites of tissue damage or alteration of collagen and elastin fibres Serum calcium and phosphate levels are within normal ranges	Connective tissue diseases Scleroderma Lupus erythematosus Dermatomyositis Cutaneous neoplasms Infection Trauma Chronic venous insufficiency Inherited disorders Werner Syndrome Pseudoxanthoma elasticum Ehlers–Danlos syndrome Familial tumoral calcinosis
Idiopathic	No underlying tissue damage or metabolic disorder	Subepidermal calcified nodules
Iatrogenic	Elevated tissue concentration of calcium and tissue damage at the site of extravasated calcium	Intravenous calcium or para-aminosalicylic acid

A dermis calcium gradient and its disruption consequent on disease remodelling of skin structures may play a role in skin calcification. However, not all patients with disrupted calcium-phosphate metabolism, nor all patients with local tissue injury, develop skin calcifications. It is probably the consequence of a complex interaction between metabolic disorders and genetic predispositions.

2.2. *Diversity of skin calcification localisation and morphology*

Latest generation FE-SEM allows a submicrometer scale structural description of these calcified deposits [20–22]. While optical microscopy is limited to a magnification of ca. 1000 (i.e. with a 100× objective and a 10× eyepiece), low voltage electrons can define skin surface topology at magnifications greater than 10,000, constituting a unique opportunity to describe micro calcifications undetected optically.

For our observations, we used a Zeiss SUPRA55-VP SEM, a field-emission "gun" microscope (FE-SEM) operating at 0.5–30 kV. High-resolution observations were obtained using an Everhart-Thornley SE detector. An in-lens SE detector is also available. All the measurements were taken at low voltage (between 0.5 and 2 kV) without the usual carbon deposits at the sample surface. Electron induced X-ray fluorescence experiments are also possible. Five micron tissue slices were deposited on low-e microscope slides (MirrIR, Kevley Technologies, Tienta Sciences, Indianapolis) to enable IR measurements to be performed on the very same sample [13]. Figure 2 shows five skin slices deposited on the low-e microscope slide and positioned in the FE-SEM.

Based on such FE-SEM observations, we identified three different locations where skin calcifications are typically observed: hypodermis, vessel, and dermal fibres (Figure 3). These micrometer scale descriptions constitute a significantly complementary

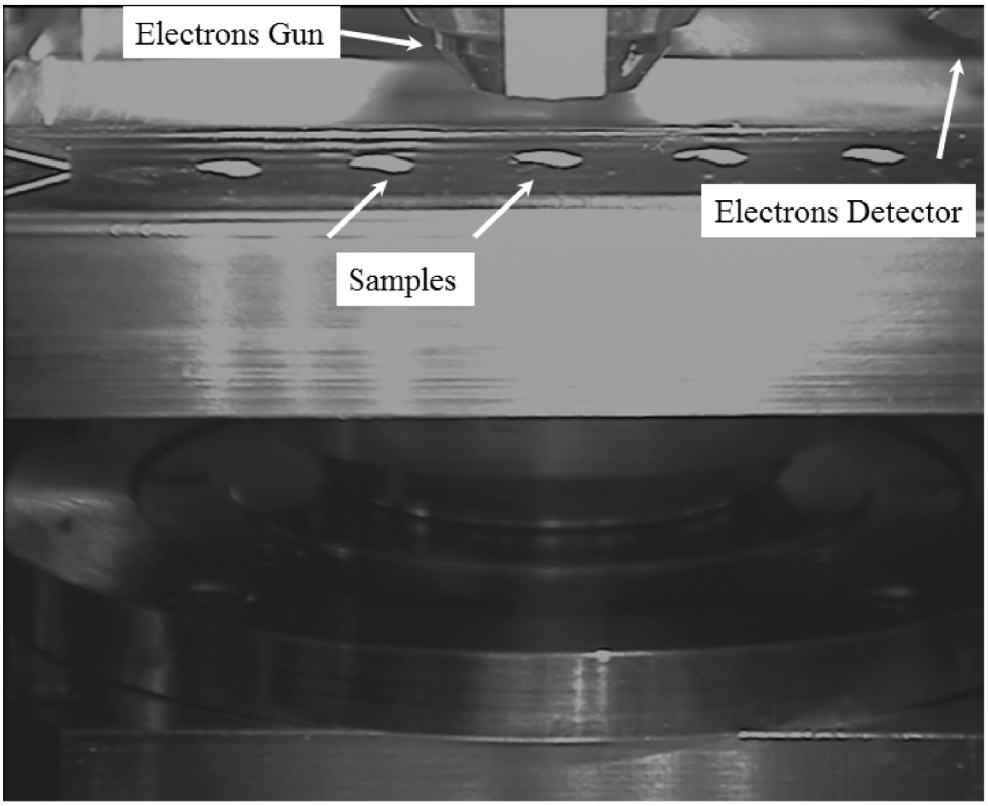

Figure 2. Skin biopsy slices are shown on the low-e microscope slide, positioned in the FE-SEM.

approach to the usual routine hospital radiologic observations shown in Figure 1. Indeed, the spatial resolution of radiological measurements is far inferior [61]; FE-SEM therefore provides unique information regarding the exact location of sub micrometer pathological skin deposits.

FE-SEM also provides information on the morphology of the pathological calcifications. Morphology of skin calcifications varies: in Figure 3A and B calcifications appear as voluminous plaques while on Figures 3C, 4 and 5, high magnification emphasizes sub-micrometre spherical entities.

Calcification size is also very variable. Some are nanometric, making them difficult to identify. For example, in Figure 5 we can see that the calcification size is less than 1 μm.

Regarding the formation mechanisms of the different morphologies of skin calcification, we can hypothesize that the agglomeration of small spherical bodies leads to the formation of a plaque (Figure 6A). A similar mechanism has been identified in ectopic breast calcifications [62] (Figure 6B). These similarities hightlight the fact that the pathogenesis of ectopic calcifications can be similar although the tissue and its function may be very different.

2.3. *Chemical diversity of skin calcifications*

Literature regarding the chemical composition of skin calcifications is scanty. What exists almost consistently reports carbapatite (calcium phosphate apatite) [63–65] as a unique chemical phase in the skin, which was usually the case in the samples we studied. However, our complete set of investigations reveals at least three chemical phases: namely calcite (one of the $CaCO_3$ polymorphs [66]), amorphous carbonated calcium phosphate (ACCP) and carbapatite (Table 2). More precisely, in both calciphylaxis and arteriosclerosis, we identified carbapatite, while calcium deposits observed in sarcoidosis were composed

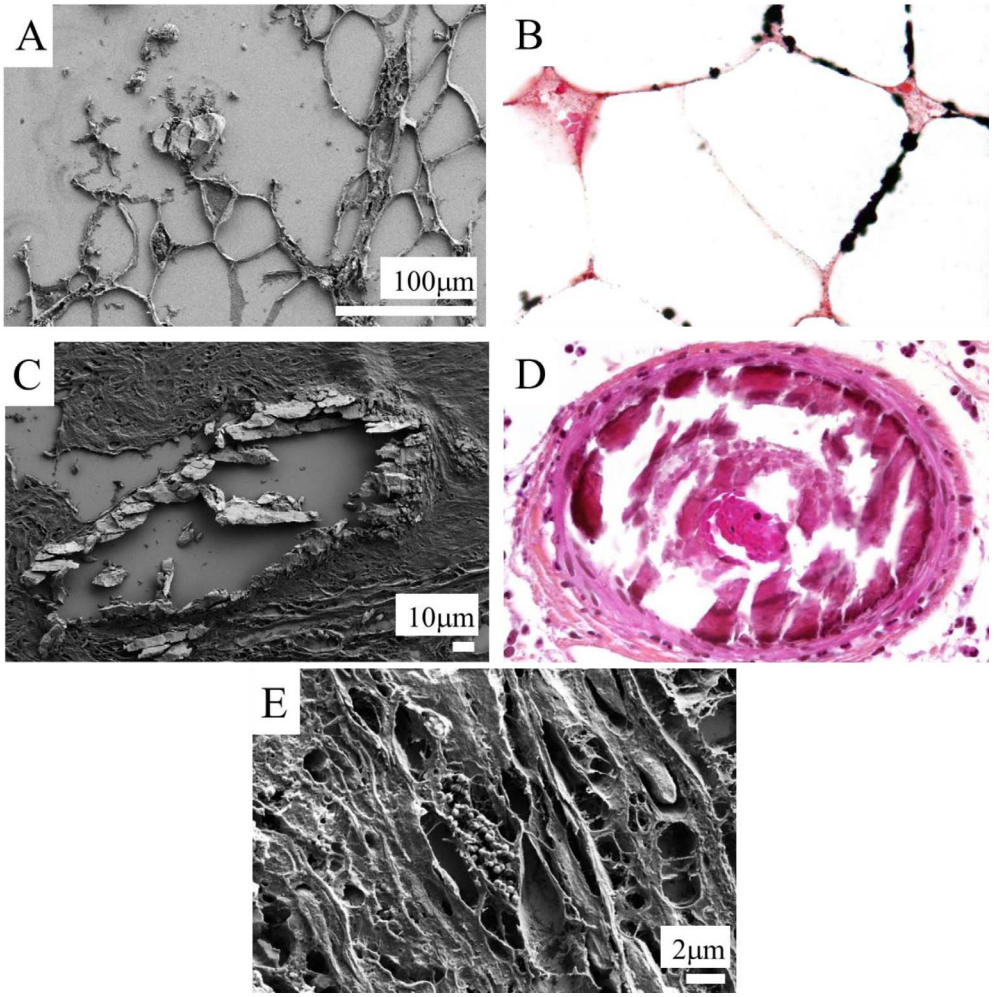

Figure 3. Different skin calcification localisation. Calcification in the hypodermis in cases of calciphylaxis; (A) FE-SEM, (B) Von Kossa-stained ×400. Massive circumferential calcifications of a dermal capillary in cases of calciphylaxis; (C) FE-SEM, (D) HES-stained ×400. (E) Nanometric spherical calcifications in dermal fibers in a case of sarcoidosis, not visible in optical miscroscopy. FE-SEM.

of calcite. The variety of dermal fibre structural modification associated with different skin diseases may lead to different modifications of skin functions and therefore the formation of different chemical types of calcifications.

Very few studies discuss the chemical diversity of skin calcifications. Among these, a report by Reid and Andersen [67] mentioned the presence of dolomite (not really a true calcium carbonate as its stoichiometric formula is $CaMg(CO_3)_2$). Yet, this chemical diversity has been well described in other organs: different calcium carbonate polymorphs have been identified in pancreatic stones, gallstones, salivary stones, and in the liver [68–71]. A better understanding of the chemical variety of skin calcifications would probably help in understanding the pathophysiology of these skin diseases, as well as the therapeutic options.

Carbapatite and its precursor ACCP represent compounds identified in pathological calcifications present in kidney, cartilage, thyroid, aortic valve, and breast [72–76]. At this point, it would be

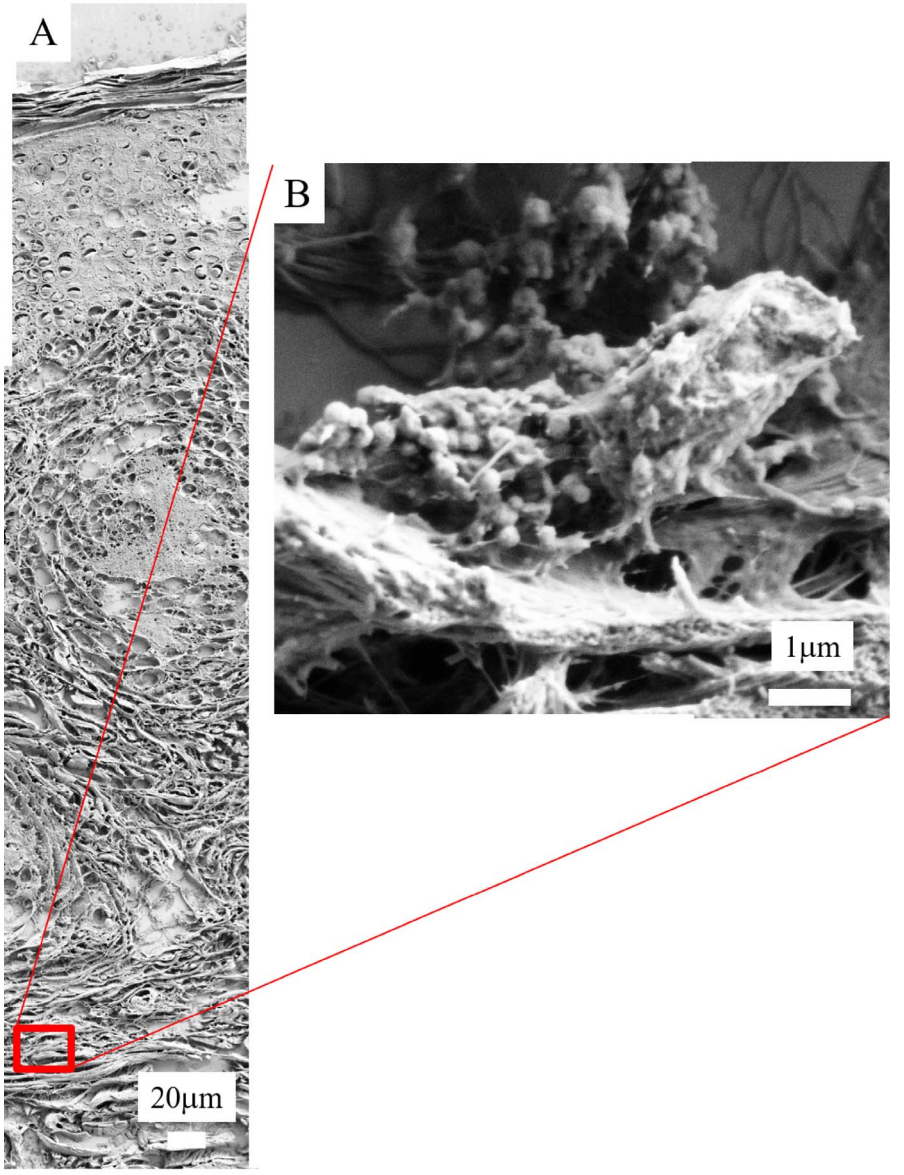

Figure 4. Calcified spherical bodies at the periphery of a granuloma in a sarcoidosis case, observed using FE-SEM.

useful to summarize some relevant chemical characteristics of carbapatite. Biological apatites correspond to substituted calcium hydroxyapatite (HAP, $Ca_{10}(PO_4)_6(OH)$) [77–81]. The fundamental structure can tolerate substitutions by other ions with the same or a different charge. Some cations which can replace Ca^{2+} are Pb^{2+}, Sr^{2+}, Co^{2+}, Zn^{2+}, Fe^{2+}, Cu^{2+} or Mg^{2+}. Investigations regarding a possible insertion of these cations in biological apatite have thus been performed [82–84]. Other substitutions involve replacement of the original PO_4^{3-} and OH^- anions which may have the same or a different electric charge (for example F^- substituted for OH^- or CO_3^{2-} substituted for PO_4^{3-} and/or OH^-). This wide range of ion substitutions can modify the physico-chemical and biological properties of apatites.

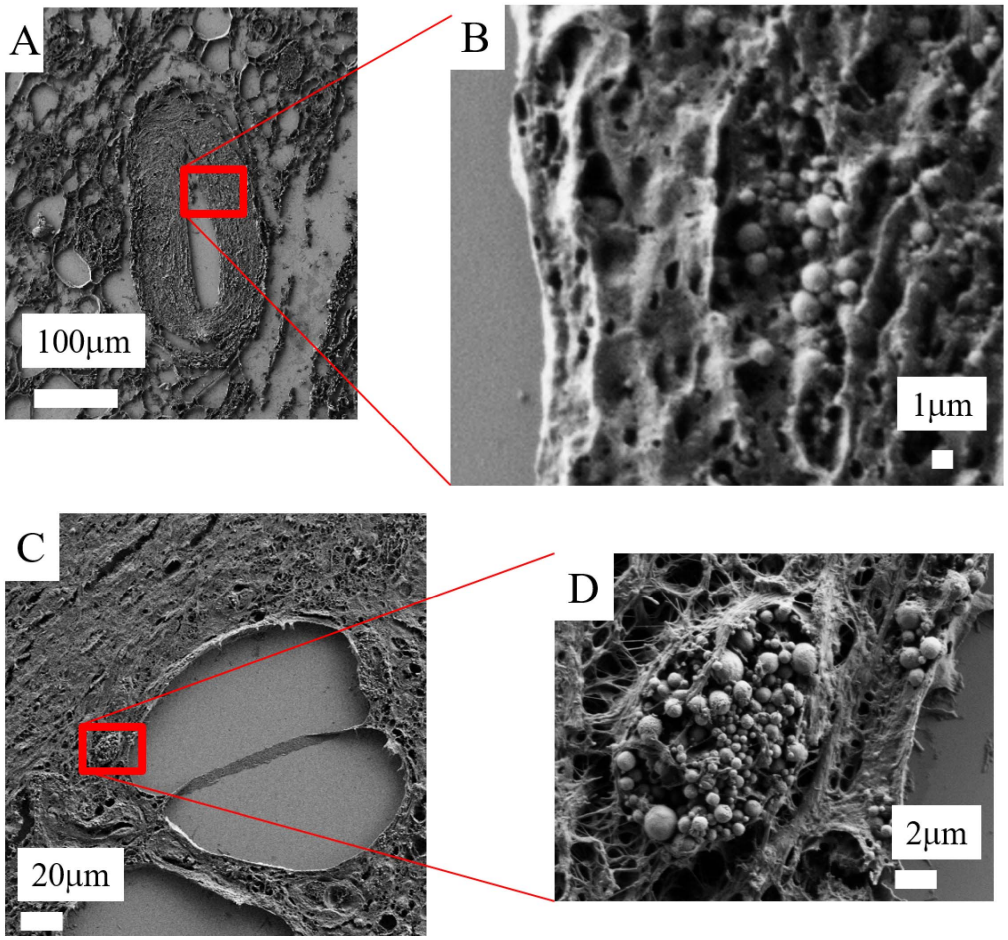

Figure 5. Calcified spherical bodies in a case of calciphylaxis, observed using FE-SEM in the vessel wall (A and B) and on the surface of an adipocyte (C and D).

Numerous studies have been devoted to apatites which are conventionally regarded as conforming to the $A_5(BO_4)_3X$ canonical chemical formula [85,86]. The crystallographic structure (Figure 7) of apatite is well known, the space group is $P6_3/m$ with $a = b = 9.41844$ Å, $c = 6.88374$ Å [87,88].

The framework of the stoichiometric calcium hydroxyapatite can be described as an assemblage of tetrahedral PO_4 groups [89,90]. An interesting aspect of this is the existence of two channels. The first has a diameter of 2.5 Å and is surrounded by Ca^{2+} cations while the second is wider (3–4.5 Å).

Finally, biological apatites display some specific features. One is the widely reported deficiency of OH^- [91–93]. Another, established more recently, is the presence of hydrogen phosphate (HPO_4^{2-}) ions in PO_4^{3-} sites [94]. Thus, as proposed by Combes *et al.* [80], we report in Table 2 the general formulae for biological apatites.

Regarding physicochemical investigations of biological apatites, it is of major importance to underline that the physicochemical characteristics of calcium phosphate apatite may significantly influence medical diagnostic. For example, in kidney stones, a high carbonate level in calcium phosphate apatite, as well as the presence of amorphous calcium phosphate apatite, indicate an infectious process implying the need for antibiotics [48,95]. The morphology of the kidney stones at the macroscopic scale as well as the morphology of calcium phosphate apatite crystallites at the micrometre scale may indicate an inherited distal renal tubular acidosis [49] or primary

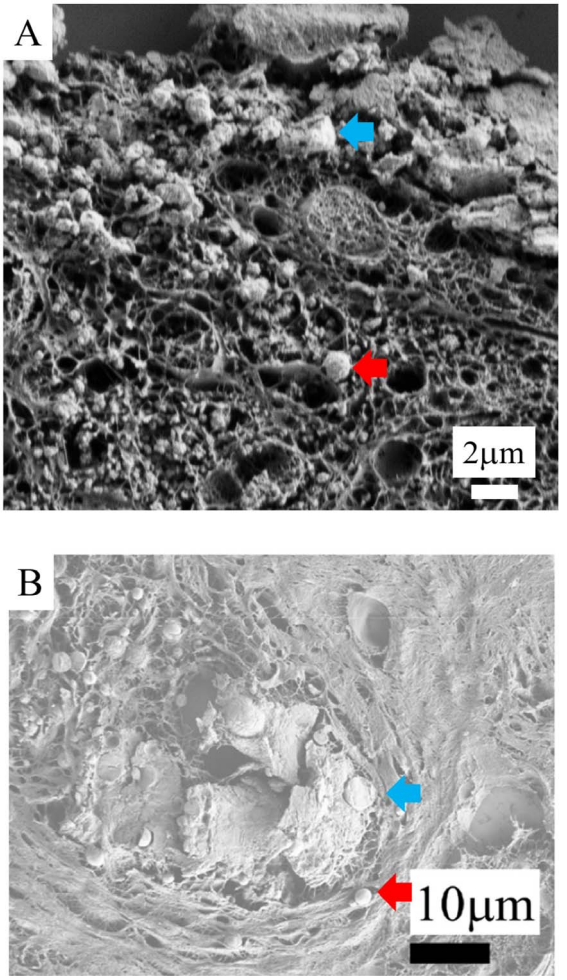

Figure 6. FE-SEM: (A) Agglomeration of spherical bodies (red arrow) leading to the formation of a plaque (blue arrow) in a case of calciphylaxis. (B) Comparison with calcification in a case of breast cancer: agglomeration of spherical bodies (red arrow) leading to the formation of a plaque (blue arrow).

hyperoxaluria [47,96]. Finally, its zinc content may indicate inflammatory processes [84,97,98].

Another interesting aspect is that calcification morphology at the micrometre scale is not predictive of its chemistry. Spherical calcifications, for example, could be composed of either calcite or carbapatite. The calcification localisation (vascular, dermal or hypodermal) within the skin tissue again does not correlate with chemical composition, suggesting a relatively modest contribution of the skin tissue environment to the calcifications chemistry.

3. Generalities regarding exogenous skin deposits

The exposome concept was conceived in 2005 to represent the environmental, i.e. non-genetic, drivers of health and disease [99]. The exposome concept takes into account exposure to particles present in food and air or directly in contact with the skin. Skin protects the body from the external environment and it is therefore directly impacted by the exposome.

Penetration of this exogenous material can occur after a trauma, an injection, or a tattoo puncture; they have also been shown to penetrate into the skin through follicular orifices, for example after cosmetic application [100].

There is an increasing interest in understanding the effects of exogenous materials, including nanoparticles, on living tissues, among them skin. Recent developments in nanotechnology have established a link between exogenous deposits and some inflammatory diseases, such as in sarcoidosis [101, 102], frontal fibrosing alopecia [103,104] and tattoos [105,106].

4. Physico-chemical characteristics of deposits in various skin diseases

4.1. *Calciphylaxis*

Calciphylaxis is a disease with high morbidity. It affects up to 4% of patients with end stage renal disease, and its incidence rate increases for those on chronic hemodialysis [107]. Calciphylaxis is unlikely for patients with normal renal function.

The significant morbidity and mortality of calciphylaxis results from extensive skin necrosis, septic complications, and organ failure, which are the direct consequences of these ectopic calcifications. Female sex, diabetes mellitus, high body mass index, elevated calcium, phosphorus, and parathyroid hormone serum levels, nutritional status, and cinacalcet or vitamin K antagonist treatments, are associated with an increased risk of developing the disease [108,109].

Treatments usually achieve poor outcomes. They include calcimimetics, surgical parathyroidectomy, sodium thiosulfate, and bisphosphonates [110–112].

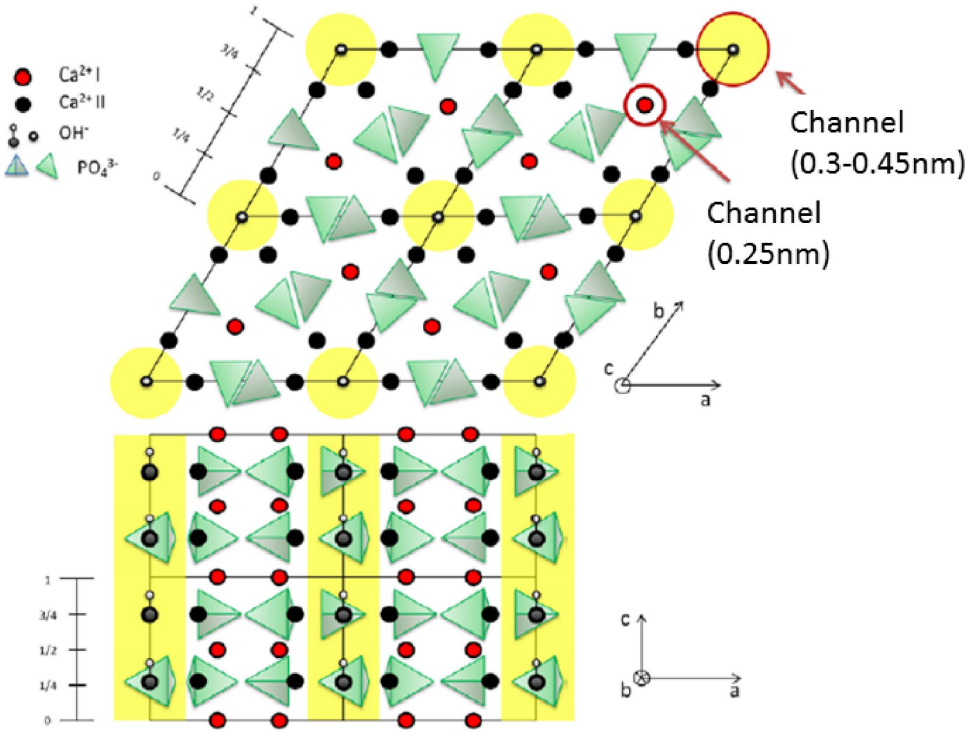

Figure 7. Crystallographic structure of the apatite 001 (top) and 010 (bottom) planes (from Ref. [77]).

Table 2. Different calcium phosphate compounds with their stoichiometry and their Ca/P ratio

Skin diseases	Serum calcium and phosphate levels	Calcifications' localisation	Chemical phase	Stoichiometry
Calciphylaxis	Usually elevated	Vessels, dermis, hypodermis	Amorphous carbonated calcium phosphate (ACCP)	$Ca_9(PO_4)_6\ nH_2O$
Calciphylaxis	Usually elevated	Vessels, dermis, hypodermis	Carbapatite	$Ca_{10-x}(PO_4)_{6-x}(HPO_4^{2-}$ or $CO_3^{2-})_x(OH)_{2-x}$ with $0 \leq x \leq 2$
Sarcoidosis	Usually normal	Dermis (surrounding granulomas)	Calcite	$CaCO_3$

Pathogenesis of the disease is still under debate. Calcifications observed in calciphylaxis are considered to be metastatic calcifications, as they occur in patients with a phospho-calcic metabolic disturbance [52,53]. However, some authors also suspect that metalloproteinase digestion of elastin might occur in calciphylaxis, enhancing deposition of calcium within these modified elastic fibres [113]. In this hypothesis, calcium deposits in calciphylaxis could also be considered as dystrophic calcifications. Other authors suspect that metal deposits in the skin tissue are a trigger for a phenotypic switch of vascular smooth muscle cells from a contractile to an osteogenic phenotype [114].

Recently, we have combined FE-SEM observations of calcic skin deposits in calciphylaxis with FT-IR and Raman spectroscopic chemical analysis, and compared these results to calcifications observed in

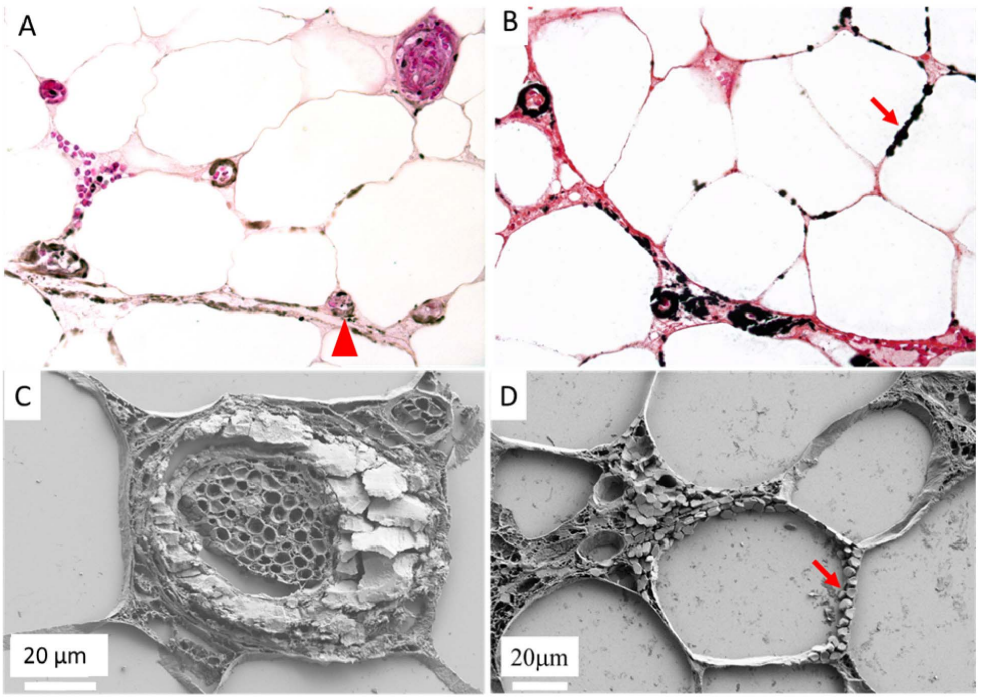

Figure 8. Optical microscopy and FE-SEM comparisons in calciphylaxis. Optical microscopy showing multiple calcifications along adipocytes and in vessels walls, (A) Hypodermis, arrow head: calcified vessel, HES ×400, (B) Hypodermis, arrow: calcifications along adipocytes, Von Kossa ×400. FE-SEM: (C) Massively calcified vessel, (D) Calcifications along adipocytes.

arteriosclerosis [63]. We showed that calcifications in calciphylaxis are composed of carbapatite, always located circumferentially, mostly in the intima of otherwise normal-looking vessels and often associated with interstitial deposits (Figure 8). Although vascular calcifications in arteriosclerosis were also composed of carbapatite, they are associated with medial hypertrophia, localized to parts of the vessel, and not associated with interstitial deposits. These results suggest a different pathogenesis and provide new insights into calciphylaxis pathogenesis that could explain the poor outcomes of vasodilators compared with the relative effectiveness of calcium-solubilising-drugs.

4.2. *Sarcoidosis: cases of exogeneous and endogenous abnormal deposits*

Sarcoidosis or Besnier–Boeck–Schaumann disease [115] is a chronic, multiorgan inflammatory disorder. The disease onset peaks during the third and fourth decades of life, and has a higher incidence among women and in Afro-American patients [116,117]. If the lungs are affected, in the vast majority of diagnosed patients other organ systems are often affected as well [118,119]. According to literature [120], skin is the second most affected organ, and may be involved in 25% to 30% of cases. Cutaneous sarcoidosis preferentially affects sites of prior injury such as tattoos [121,122] and scars [123].

Although clinical phenotypes, particularly of cutaneous lesions, are widely variable, the hallmarks of sarcoidosis are always noncaseating epithelioid and giant cell granulomas. The granulomatous inflammation (Figure 9) observed in sarcoidosis is considered to be caused by a complex interaction between genetic background, environmental agents, infectious antigens, and T lymphocyte driven immune reactions [124].

Sarcoidosis, as well as being observed in other granulomatous diseases, is associated with calcium metabolism disorders. High serum calcium levels

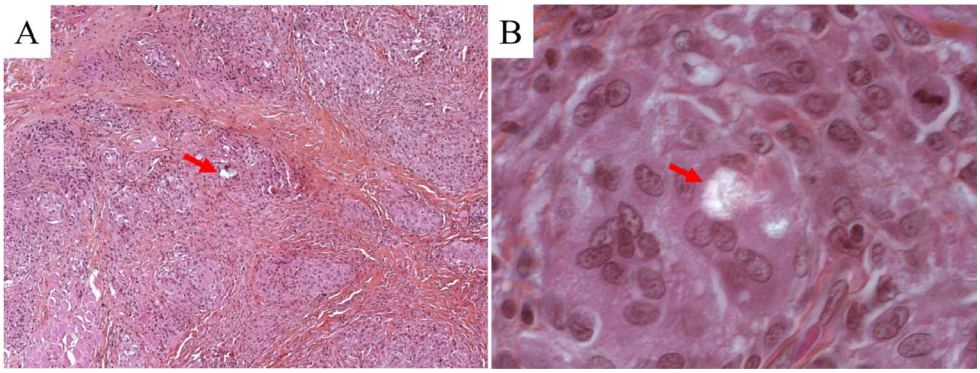

Figure 9. Optical microscopy and polarized light examination of granulomas in skin sarcoidosis, showing birefringent particles (arrow): (A) HES ×100, (B) HES ×400.

are seen in 5 to 10% of patients, mainly due to dysregulated production of calcitriol by activated macrophages which form the granulomatous lesions. These metabolic disturbances may lead to calcium deposits in various organs, including the skin, causing metastatic calcifications [125]. Reid and Andersen have indeed reported the presence of calcium oxalate and phosphate deposits in sarcoidosis involving lymph nodes and lungs [67]. Even though these chemical analyses have been done in different organs, they have never been performed in skin sarcoidosis.

Exact causes of the disease are still unknown; however the role of environmental mineral particles is highly suspected on epidemiological grounds [126]. There is a polarizable material in the centre of some granulomas, suggesting that foreign materials could be a nidus for granuloma formation and a potential trigger for the disease [127–130]. Using biopsy specimens of granulomatous lesions from 50 patients, Kim *et al.* [131] have estimated the frequency of polarizable foreign bodies in cutaneous lesions of sarcoidosis. These authors noticed that polarizable foreign bodies were present in the granulomatous skin lesions of 12 of 50 patients (24%) with cutaneous sarcoidosis. Using electron probe microanalysis, they identified the following elements: Calcium, phosphorus, silicon, and aluminium. Unfortunately, such a characterization technique is not able to identify the compounds in which these elements occur.

Electron microscopy has been used in several previous investigations [114–118]. For example, Takemura *et al.* [132] clearly demonstrated that ultrastructural examination improves the diagnostic utility of endomyocardial biopsy in cardiac sarcoidosis, by clearly identifying even only one epithelioid cell. More recently, Kuribayashi *et al.* [133] showed by electron microscopy that multinuclear giant cells were formed by epithelioid histiocytes and an aggregation of lymphocytes. Interesting FE-SEM results by Catinon *et al.* [134] indicate the presence of calcium phosphate particles in 7 out of 10 patients.

Recently, we have investigated 14 skin biopsies from cutaneous sarcoidosis patients by FE-SEM/EDX and FTIR spectroscopy [135,136]. FE-SEM allowed the identification in three patients of silica in the centre of skin granulomas (Figure 10). Some FE-SEM apparatus are able to acquire X-ray fluorescence spectra [20–22] so it is possible to know the elementary composition of specific materials in the tissue. Note that this selection can be performed at the submicrometer scale when electrons are employed as probes.

Figure 10E displays the X-ray fluorescence spectra induced by the primary electrons of the microscope on the foreign material we identified, and we can clearly see the contributions of Si (K_α = 1.740 keV) and the contributions of other elements in the support (Zn, $L_{\alpha 1}$ = 1011.7 keV; Ag, $L_{\alpha 1}$ = 2.984 keV).

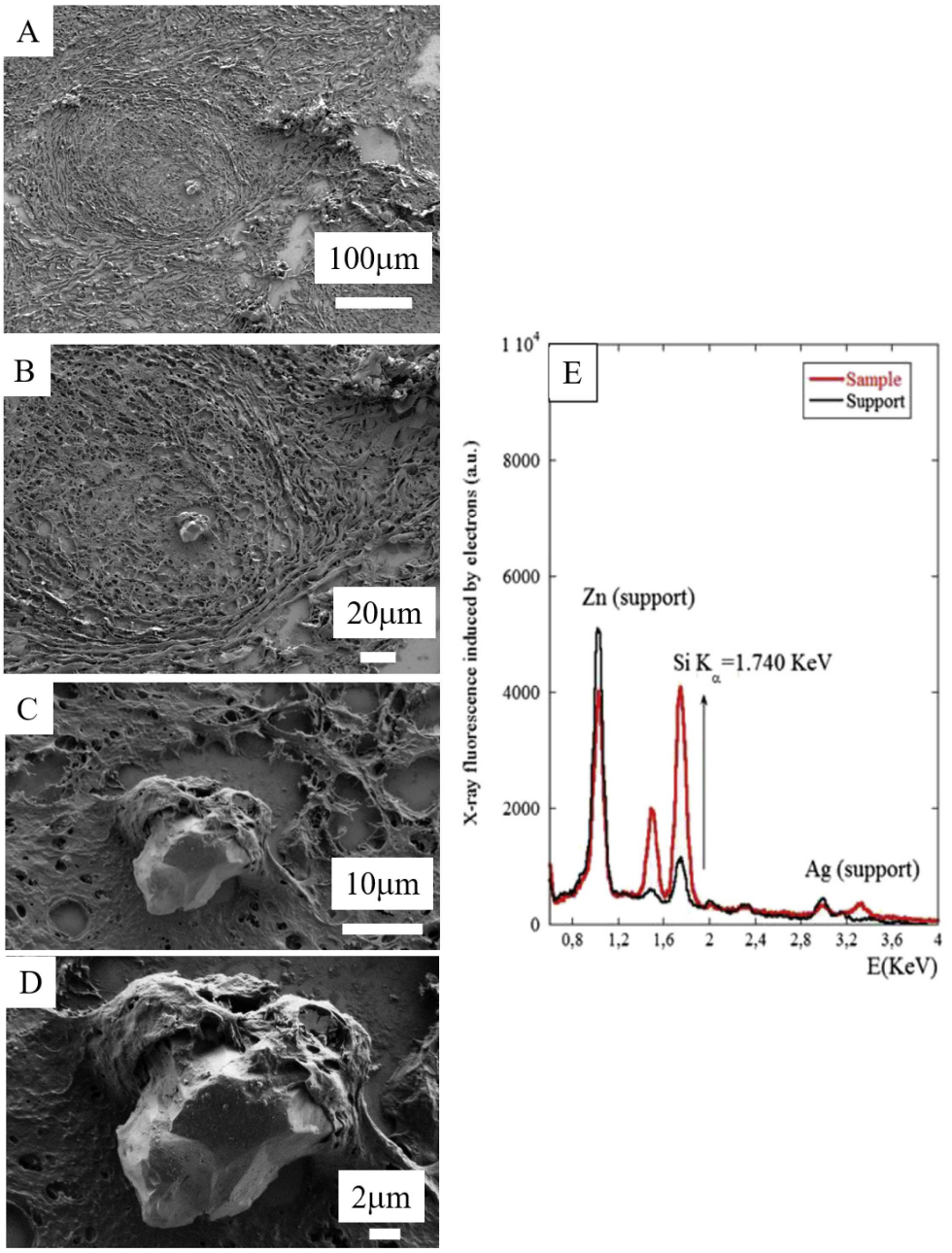

Figure 10. (A–D) FE-SEM photographs of foreign material in the skin biopsy of the arm of a patient with cutaneous sarcoidosis. (E) EDX spectrum identifies silica in the abnormal deposit at the centre of the granuloma.

To determine the chemical nature of the foreign material precisely, FTIR data have been collected on the same sample. Infrared spectroscopy is an advantageous, non-destructive, and label-free technique for chemical analysis of biological tissues (Figure 11) [137–139]. This spectroscopy detects vibrational energy levels and phonons of materials and leads to precise chemical and structural information

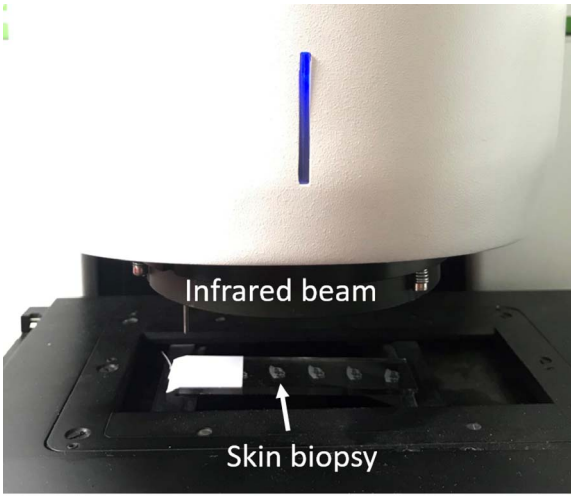

Figure 11. Slices from a skin biopsy are visible on the low-e microscope slide, which is positioned in the FTIR spectrometer.

by comparison with data bank reference spectra [30].

It is convenient to conceptualize an IR spectrum as two regions: 4000–1000 cm^{-1} known as the functional group region, and <1000 cm^{-1} known as the fingerprint region, even if for many chemists the dividing line is in fact 1450 cm^{-1}. The functional group region contains relatively few peaks, which are typically associated with the stretching vibrations of functional groups. In the fingerprint region, the spectra usually consist of bending vibrations within the molecule. This region is the key to the data analysis because it is here that each distinct compound produces its own unique pattern of peaks, effectively a fingerprint [140–143].

A large number of investigations are based on another vibrational spectroscopy, namely Raman [33–35]. As emphasized by Khulbe and Matsuura [144, 145], infrared and Raman spectra of a given molecule complement each other. The symmetrical stretching, n1 (normal vibration) of CO_2 is infrared inactive, but active in Raman. On the contrary, the bending, ν_2, and asymmetric stretching, ν_3, vibrations are Raman inactive and infrared active.

These differences arise from the fact that infrared spectroscopy exploits an absorption process dependent on the permanent dipolar moment of a molecular bond, while Raman spectroscopy is a scattering process related to a modification of the polarizability (induced change of the dipolar moment) of the molecule.

Recently, Krafft *et al.* [146] have compared these two spectroscopies in colon tissue applications. These authors note that the advantages of FTIR imaging are related to shorter acquisition times and higher spectral quality, while Raman imaging displays better spatial and spectral resolution. Also, significant differences also exist with respect to the preparation of biological tissue samples.

In Figure 12, the infrared bands show clearly that the foreign material is composed of crystalline silica [135], a chemical characteristic clearly indicating an exogenous origin of this abnormal deposit.

As we have seen previously, FE-SEM also offers the possibility of precisely describing skin deposits. For two of the samples, we have been able to pinpoint nanometer scale spherical bodies between the collagen fibres not detectable by classical optical microscopy. To determine their chemical composition (Figure 13A), we performed FTIR spectroscopy (Figure 13B) as well as EDX measurements (Figure 13C). Based on specific IR absorption bands, we can conclude that the spherical entities are calcite. On EDX analysis, we noticed the absence of a fluorescent P signal (2.01 keV) and the presence of a significant signal related to Ca (3.7 keV) in line with the FTIR spectrum showing the presence of calcite.

Another striking result of this investigation was the identification of spherical calcite entities in the periphery of the granuloma in 4 patients. This is in line with the fact that sarcoidosis, as well as observed

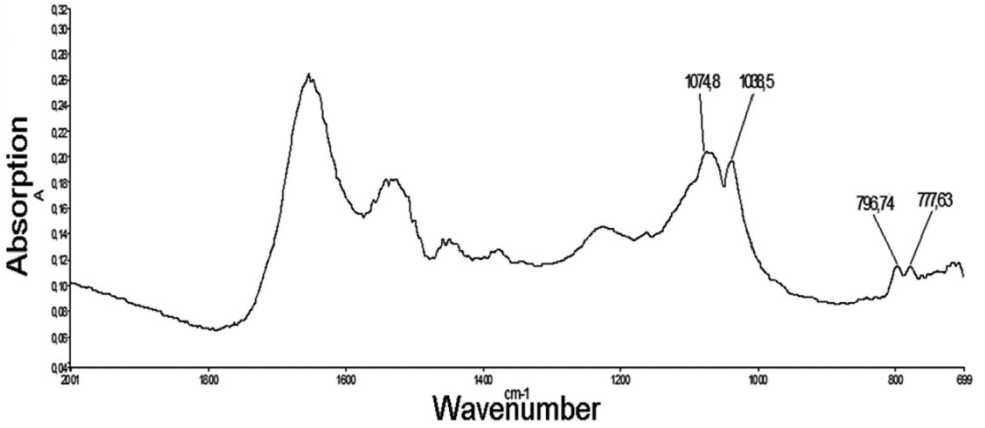

Figure 12. Infrared spectrum of the foreign material. The absorption bands at 1074 and 1038 cm^{-1} are associated with crystalline silica. Also, we can clearly see the α-quartz doublet (Silica) around 800 cm^{-1} in accordance with established infrared spectrometric data [30].

in other granulomatous diseases, is associated with calcium metabolism disorders [146,147].

Based on the entirety of our data, sarcoidosis exemplifies a case where both endogenous and an exogenous pathological deposit can be identified. Note that the presence of the nanometer scale endogenous calcifications cannot be discerned through classic staining procedures. This specific chemical composition observed only in sarcoidosis may be due to the significant dermal structure modification observed in the disease, which modifies the physiological spatial distribution of calcium through granuloma driven skin restructuring. A well-developed sarcoid granuloma consists of a tightly packed conglomerate of epithelioid- and multinucleated-giant cells encircled by lymphocytes, especially CD4+ T helper cells, but also rare CD8+ T cells and B cells [147–149]. Such reorganisation may lead to a specific calcification pathogenesis in sarcoidosis, explaining the presence of calcite and not carbapatite.

4.3. *Tattoo-associated keratoacanthoma*

Tattooing involves introducing pigmented material into the dermis by puncturing the skin, in order to obtain a permanent design. It is a very old practice, which has probably been performed since the Neolithic times [150]. Nowadays, tattoos are very widespread: in Europe, there are around 100 million people with tattoos [151,152]. Tattoo inks are made of almost insoluble pigments mixed with additives such as formulants, dispersants, and preservatives [153, 154]. Nowadays, natural pigments are very rarely used, and most tattoo inks are composed of synthetic substances [155–160], allowing cheaper mass production of inks with a large variety of shades. The composition of tattoo inks is poorly regulated worldwide, including in Europe, with few recent guidelines [161,162]. Various types of carcinogenic compounds occur in tattoo inks, including primary aromatic amines (PAA), cleavage products of organic azo colourants used in the inks [163]. Tattoos therefore effectively present permanent lifelong exposure to potentially carcinogenic compounds [164,165]. Many cases of skin cancers occurring within tattoos have been reported, including cases of keratoacanthoma (KA) on red ink, and the role of PAA is suspected [166,167]. Furthermore, cases of multiple or recurrent KA on tattoos have been reported, making the causality link between these skin tumours and tattoos even stronger [168].

Recently, we published an investigation regarding the chemical composition and distribution of tattoo inks within tattoo associated KA [169]. Clinical and histopathological data from three patients coming from Bichat Hospital diagnosed with tattoo associated KA in 2017 were selected (Figure 14). The medical file was completed by structural and chemical characterisation of tattoo inks within KA.

Regarding laboratory characterization techniques, we used X-ray fluorescence (XRF) [23–25] to identify the inorganic elements and Raman spec-

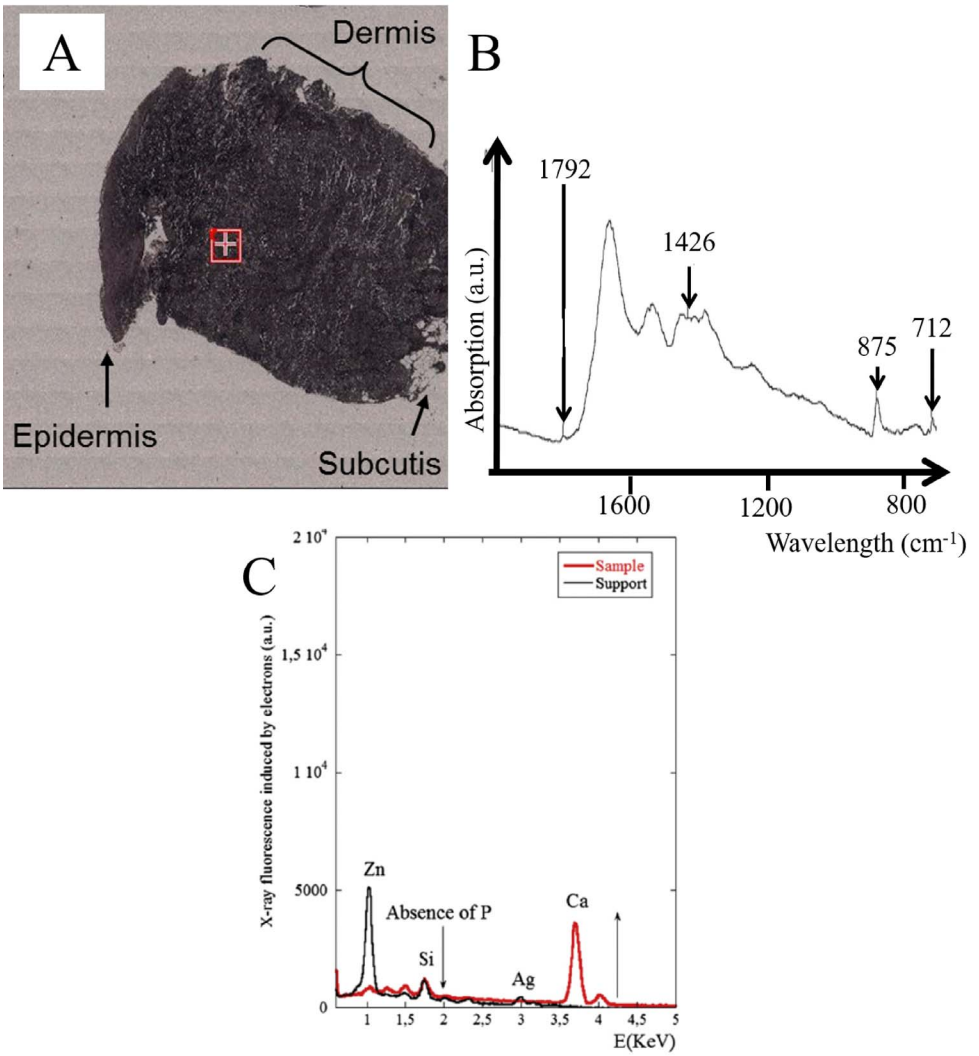

Figure 13. (A) Optical photograph of skin sarcoidosis; (B) Infrared spectrum of the peaks characteristic of calcite (1087 cm^{-1} (weak), 881 cm^{-1}, 1432 cm^{-1}, 712 cm^{-1}) in a protein matrix, from the area corresponding to the red square on the map, located in the dermis. (C) Electron induced X-ray fluorescence of the sample. The contributions of trace elements from the support, namely Zn (1.01 keV), Si (1.74 keV) and Ag (2.98 keV), are clearly visible.

troscopy to identify the organic compounds present in tattoo inks [170–173]. As we can see in Figure 15, the sensitivity of laboratory XRF is sufficient to show the presence of various elements in a skin biopsy. The micrometre resolution of Raman spectroscopy enabled the identification of an organic compound, namely the Pigment Red 170 (PR170) dye, as well as agglomerates of TiO_2 nanoparticles (Figure 16). Even though it is usually possible to define the chemical nature of iron oxide [174,175], this approach was not possible with our sample, probably due to a lack of sensitivity.

Like other researchers working on tattoos [176, 177], we also used synchrotron characterization techniques, specifically XANES spectroscopy where acquisition at the iron K edges (Figure 17) defines the iron environment.

While Ti always has an exogenous origin, iron and

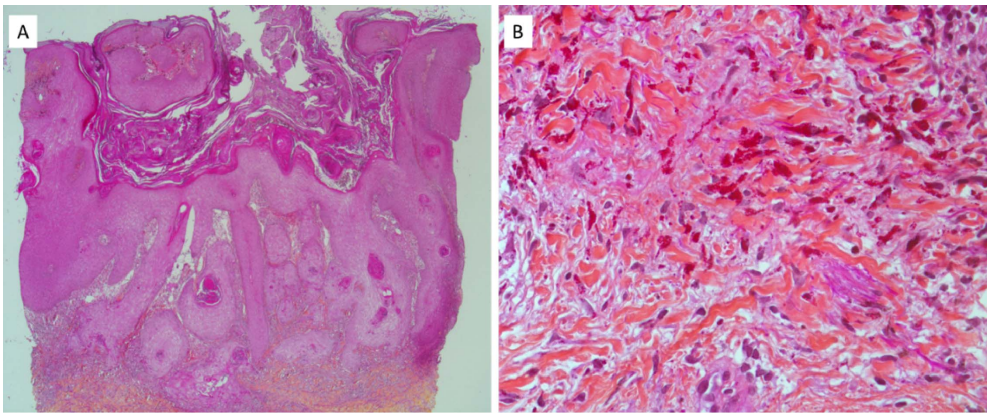

Figure 14. Optical microscopy of a KA developed on a tattoo made of red ink, from one of the three patients previsously described. (A) HES ×25. (B) Superficial dermis, HES ×400.

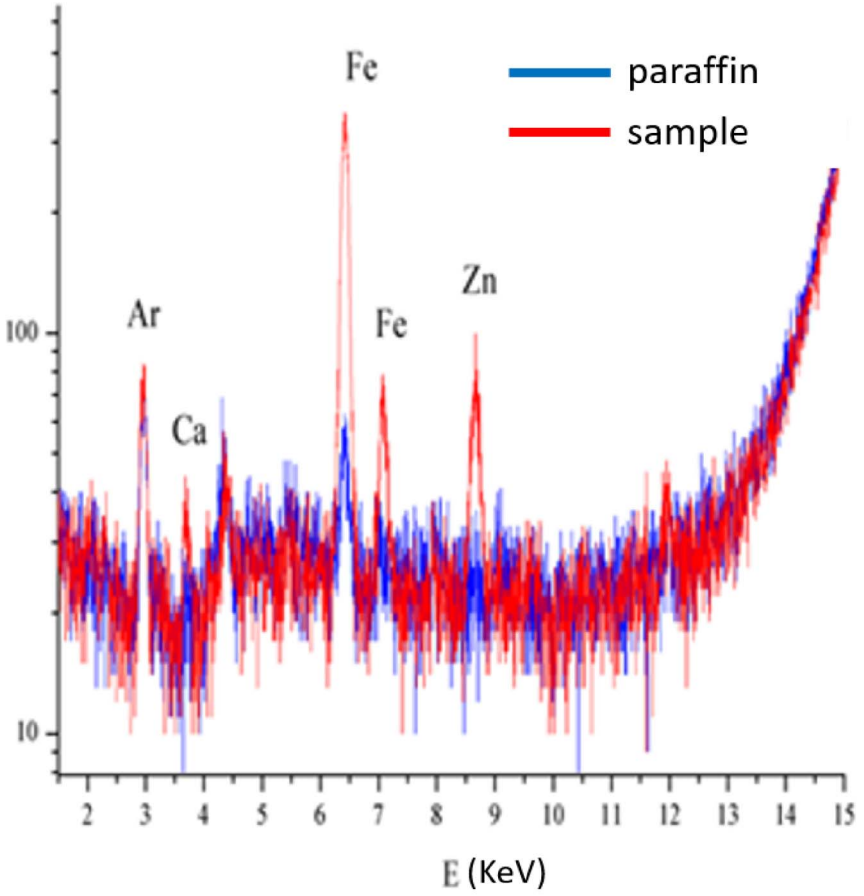

Figure 15. Laboratory XRF spectra of skin reaction to a tattoo. The sample contains high levels of iron and zinc which may be of exogenous or endogenous origin.

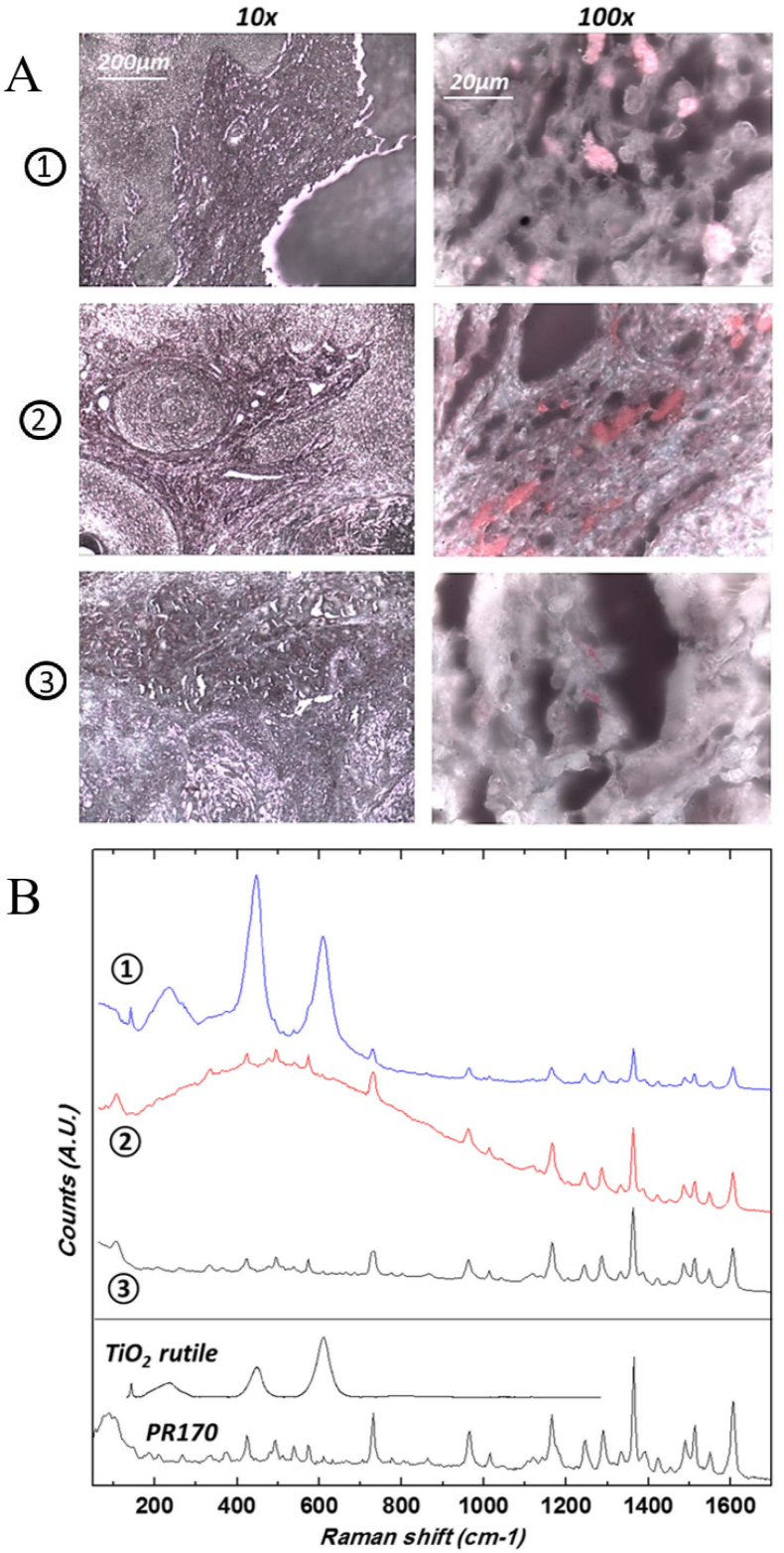

Figure 16. Caption continued on next page.

Figure 16 (cont.). (A) Optical micrographs of the samples of the three patients previously described, at two different magnifications (10× and 100×) revealing micron size red pigment clusters. In patient 1, note the heterogenous and lighter aspect of the red pigment, suggesting the presence of nanoparticles of TiO_2. (B) Corresponding Raman spectra. Reference spectra are also given as a comparison: PR170 dye sample (Kremer) and rutile (TiO_2) downloaded from the RRUFF database.

Table 3. Synthetic iron oxide (found in pigments)

Name	Formula	Colour
Hematite	Fe_2O_3	Red
Magnetite	Fe_3O_4	Black
Goethite	FeO(OH)	Yellow
Limonite	$Fe_2O_3\,H_2O$	Brown

Table 4. Synthetic compounds used as pigments

Colour	Ingredients
Black	Magnetite
Red	Iron oxide/common rust, ferric sulfate, hematite,
Green	Ferrocyanide and ferro-ferric cyanide,
Blue	Ferric ferrocyanide

zinc can be either exogenous or endogenous. XANES spectroscopy can be used to chemically characterize these elements; for example, in the case of iron, XANES spectra of human adult deoxyhaemoglobin and myoglobin have been measured [178]. For exogenous iron, among the different compounds which have been identified in pigments, H. Petersen and D. Lewe noticed the presence of the following oxides: Fe_2O_3, FeO(OH) and Fe_3O_4 [176]. Table 3 summarizes synthetic iron oxides used as pigments [179]. Islam *et al.* [180] reported other chemical compounds containing iron (Table 4). As we can see, ferric sulfate, ferric ferrocyanide (the anion $[Fe(CN)_6]^{4-}$) and ferricyanide (the anion $[Fe(CN)_6]^{-3}$) may be also present. Most of the particles used in pigments can be considered to be nanomaterials [181].

Other elements in tattoo ink are associated with the iron or titanium. For example, as underlined by Prior [153,154], all iron oxide pigments contain minor amounts of nickel impurities, even when iron oxide pigments are refined to a high degree of purity. The fact that nickel incorporates into the crystal structure constitutes a health risk of possible allergic reactions [153,154].

Figure 17 shows the spatial repartition of iron in a KA developed on tattoo ink. When we compare the experimental Xanes spectra of the selected POI with that ofv goethite, it is quite clear that this compound has been used.

4.4. *Frontal fibrosing alopecia*

Fibrosing frontal alopecia (FFA) was first described 20 years ago. It is characterized by scarring alopecia on the anterior area of the scalp and mainly affects women after menopause [182]. Its origin is unknown, but as the number of cases continues to increase, it is suspected that extraneous compounds found in leave-on facial skin care products are implicated [183]. TiO_2 is the most widely used white pigment. It is found in a very large number of products: paints, construction materials, food (candies, cookies, etc.), pharmaceuticals (capsule shell, toothpaste, etc.) but also in cosmetics: creams and sunscreens, due to the UV blocking properties of TiO_2. The potential toxicity of TiO_2 is currently a major public health concern—TiO_2 has been classified in group 2B ("possibly carcinogenic to humans") by the International Agency for Research on Cancer; the long-term dermatological impact of these particles is not yet well known in humans. It is still debated whether TiO_2 penetrates the stratum corneum, but it has been clearly demonstrated that it can be deposited in the follicular orifice [184].

In a previous publication, we reported finding titanium dioxide (TiO_2) nanoparticles along the hair follicles of a patient with FFA, who had been using daily sunscreens containing TiO_2 for years [104]. The analyses were carried out by electron microscopy, and by X-ray fluorescence spectroscopy at the Nanoscopium beamline (Figure 18). First, a search for nanoparticles was carried out by scanning electron microscopy coupled with energy dispersive X-ray absorption

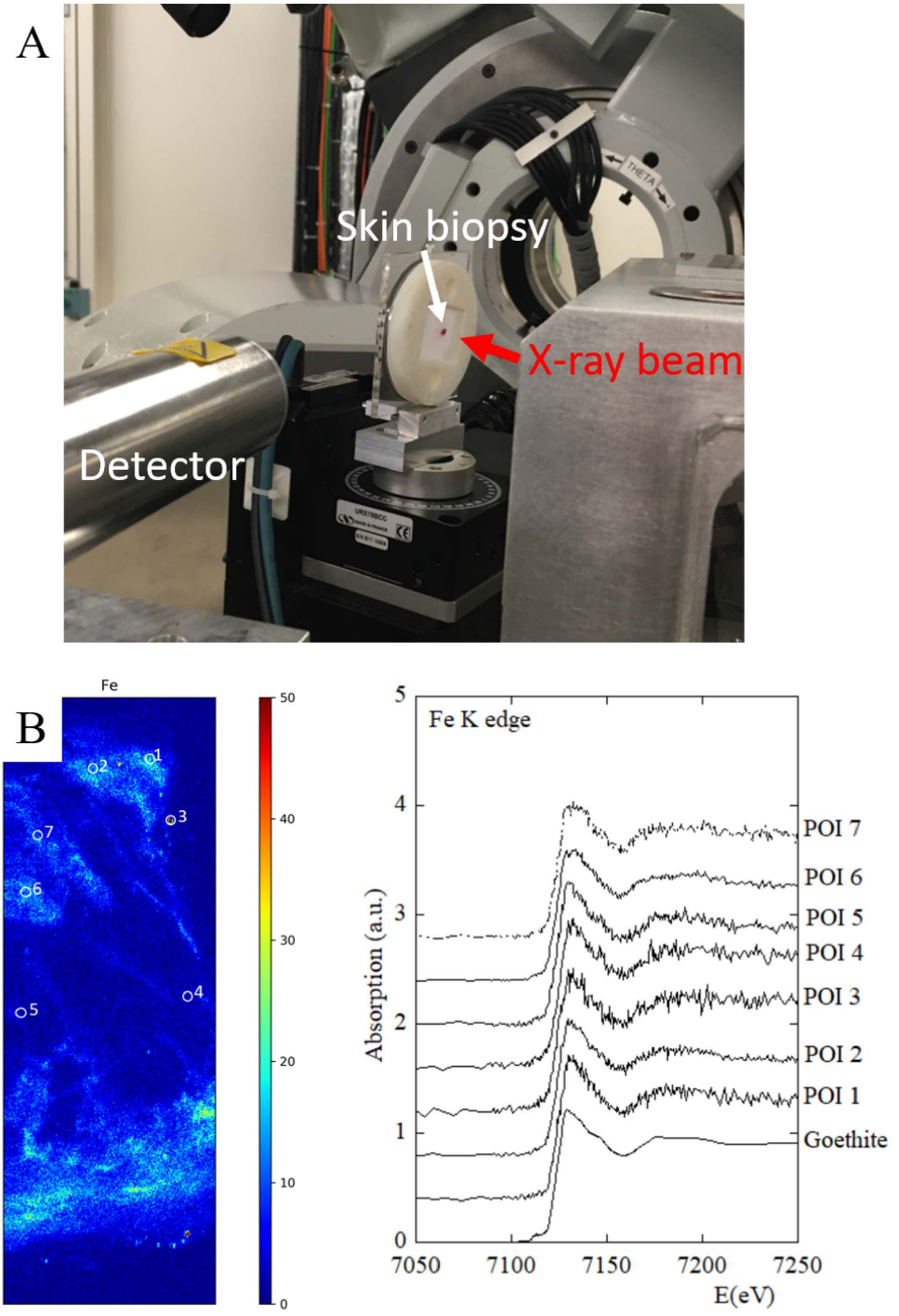

Figure 17. (A) Xanes spectroscopy set-up at Synchrotron Soleil, Diffabs beam line. (B) XANES spectroscopy at the Fe K-edge: XANES spectra at Fe K-edge were acquired at 7 points of interest (POI) in order to characterize the Fe environment.

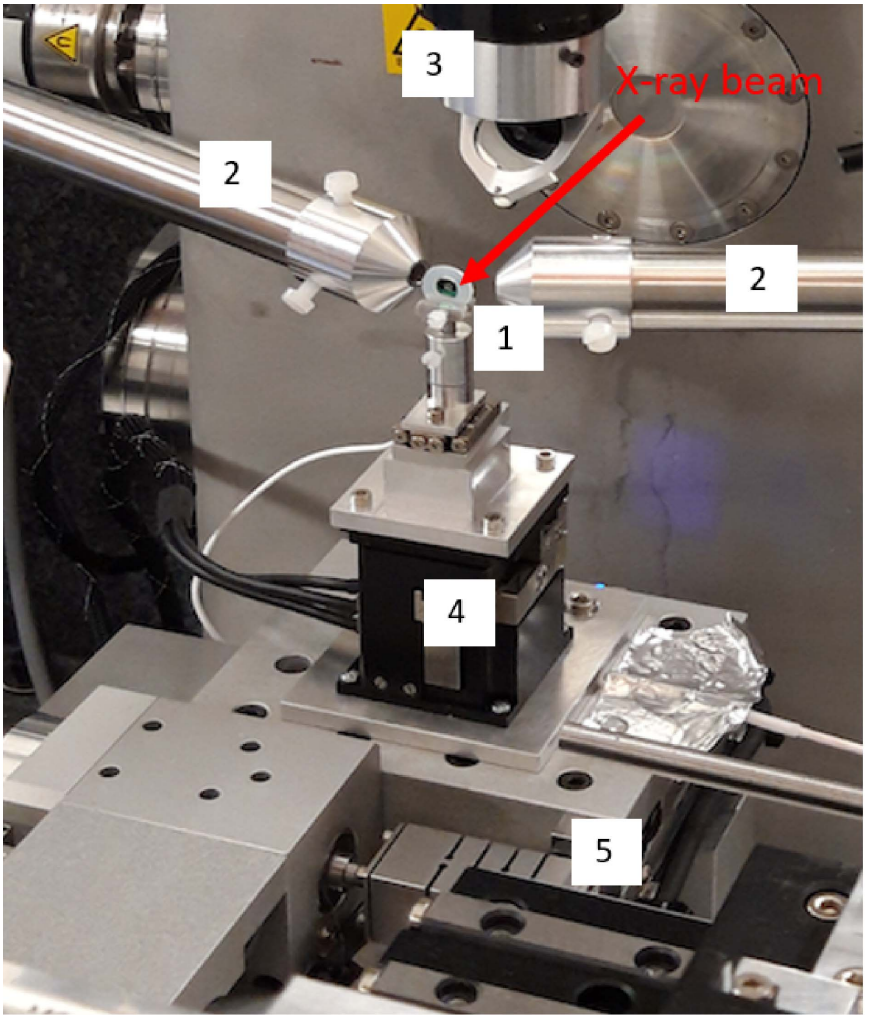

Figure 18. Nanoscopium set up. 1: Sample. 2: X-Ray fluorescence detectors. 3: Visible microscope for sample alignement. 4: Nanopositioning for high spatial resolution. 5: Stepper motors for large field of view.

spectroscopy. Abnormal deposits, micrometric in size, were observed along the hair and their analysis revealed that they contained titanium.

To refine these results, the deposits were studied on the Nanoscopium beamline of the Synchrotron Soleil by fluorescence spectroscopy using an X-ray nanobeam (300×300 nm^2), in order to obtain elemental maps of several areas of these deposits [185]. Figure 19 shows a typical X-ray fluorescence spectrum in which contributions of different elements appear, namely S, Ca, Ti, Fe, Zn and Br.

As we can see on Figure 19, XRF spectroscopy is able to detect different elements in biopsy [186,187] and thus can play a major role in metal intoxication [188]. Here we would like to consider three of them namely sulfur, zinc and titanium and thus discuss health problems not connected to pathological calcifications. X-ray Sulfur detection in human hair fibers (Figure 19) is due to the fact that hair is primarily composed of keratin proteins with a very high content of cysteine, a sulfur-containing amino acid, which commonly forms cystine via a disulfide bond [189,190]. The detection of sulfur in hair by XRF and XANES in dementia has been discussed, for example by Siritapetawee *et al.* [191] in the context of possible roles of calcium, chlorine, phosphorus and

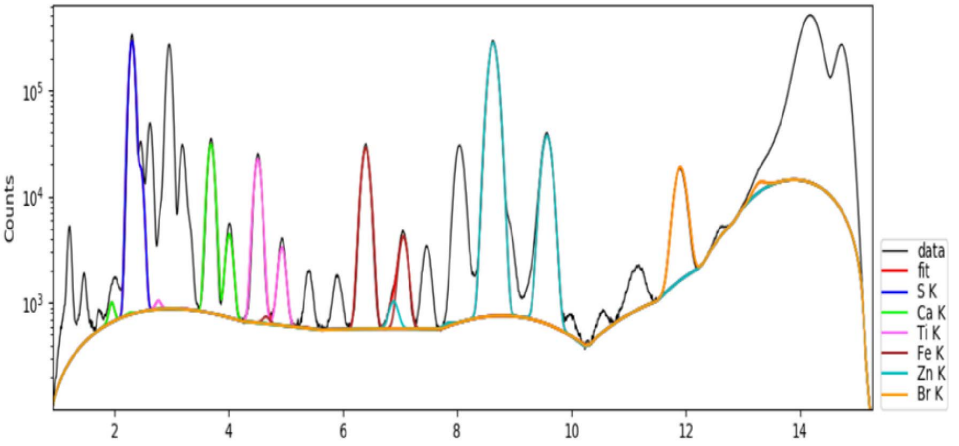

Figure 19. Typical X-ray fluorescence spectrum collected from a hair with the contributions of S (K_α at 2.31 keV, K_β at 2.46 keV), Ca (K_α at 3.69 keV, K_β at 4.01 keV) Ti (K_α at 4.51 keV, K_β at 4.93 keV), Fe (K_α at 6.40 keV, K_β at 7.06 keV), Zn (K_α at 8.638 keV, K_β at 9.572 keV) and Br (K_α at 11.92 keV, K_β at 13.29 keV).

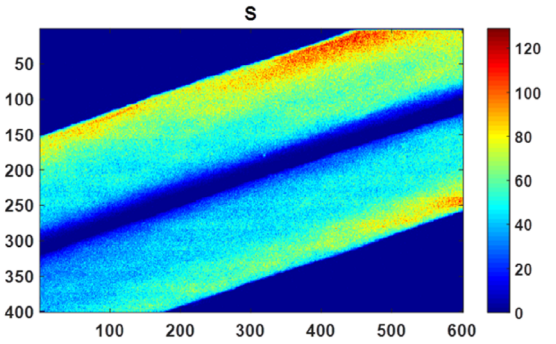

Figure 20. Micro X-ray fluorescence spectroscopy: high 500 nm resolution distribution maps of sulfur (S) within a hair shaft.

sulfur in the etiology of elderly patients' dementia. Also, Inoue *et al.* [189] showed that it is possible to map the oxidation state of cysteine in human hair through Xanes spectroscopy. In our experiment (Figure 20), it is quite clear that the nanometer scale resolution allows us to precisely define the distribution of sulfur in hair.

Numerous publications have discussed the presence of Zn in hairs. A first investigation performed by Bertazzo *et al.* [192] determined the Cu and Zn levels of both 607 men (1–85 y old) and 649 women (1–92 y old) by atomic absorption spectrometry. These authors noticed that sex does not influence Zn content (200.97 ± 9.68 μg/g for men and 209.81 ± 9.49 μg/g hair for women). Subsequently Dastgheib *et al.* [193] investigated the relationship between alopecia areata (AA) and iron, zinc, and copper levels in serum and hair. According to their data, there was no statistically significant difference between trace elements among AA patients and control patients. Such a conclusion is not in line with Ozaydin-Yavuz *et al.*'s publication [194]. These authors found that low levels of Zn and Mn are associated with AA while other metals were normal: Zn supplementation may therefore have some beneficial effect in AA. In our case, it is quite difficult to extract a conclusion regarding the spatial repartition of Zn in hairs (Figure 21). As underlined by Nicolis *et al.* [195], the usual techniques applied to human hair analysis yield a mean concentration, whilst the analysis of a single hair reveals important fluctuations in three levels: with time (along the hair), between the hairs of the same person, as well as between the hairs of different people.

Finally, it is worth noting that various shampoos contain zinc; clinical studies have established that Zn pyrithione is one of the most effective anti-dandruff ingredients in shampoo formulations [189–191,196].

We paid particular attention to Ti. TiO_2 microparticles (0.5–1 μm) were detected along the surface of follicles thanks to the high sensitivity of the Nanoscopium beamline (Figure 22).

As in tattoo associated KA, we have also used Ra-

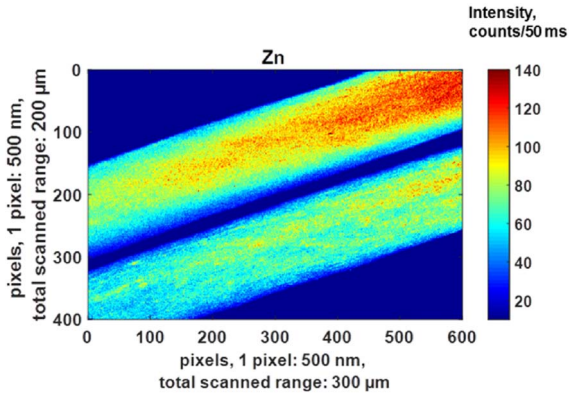

Figure 21. Micro X-ray fluorescence spectroscopy: high 500 nm resolution distribution maps of Zn within a hair shaft.

man spectroscopy in FFA, allowing us to both localize TiO_2 and identify its crystalline form i.e. whether anatase or rutile (Figure 23).

The hypothesis formulated by the researchers to explain FFA is that TiO_2 provokes an inflammatory reaction [192–194,197–199]. Up to now, there is no data available concerning the impact of TiO_2 exposure on hair. However, the detection of TiO_2 along the hair shafts of our patient raises the question of possible implication of TiO_2 in FFA pathogenesis: these inflammatory reactions, when occurring in the bulge of the hair follicle, could lead to the destruction of the stem cells located within the bulge. Dynamic studies on hair follicles extracted after application of cream containing TiO_2, with measurements of nanoparticles on different parts of the hair follicle, as well as more detailed analyses to characterize the exact location of the nanoparticles, are necessary to confirm the potential link between FFA and TiO_2 nanoparticles.

5. *In vivo* characterization

In vivo characterization is a promising approach for the clinican. Among those physiocochemical characterization techniques able to collect data on skin *in vivo* are Raman spectroscopy [195,200–203], FTIR spectroscopy [204,205], X-ray fluorescence [206,207] and Optical Coherence Tomography (OCT). We have used two of these: OCT in sarcoidosis and FTIR spectroscopy on tattoos.

OCT is a technology based on low-coherence optical interferometry to image biological tissues with a micrometer-scale spatial resolution [208,209]. It is commonly used in several medical fields [210], especially in ophthalmology to obtain images of the retina and the anterior segment of the eye [211]. Moreover, OCT has begun to be used in interventional cardiology [212], and in gastro-enterology for the detection and diagnosis of tumors [213,214]. OCT can be a useful tool for non-invasive imaging of brain tissues [215,216], and shows promise in dermatology to improve the diagnosis of skin lesions [217,218].

In this study, we used a commercially available swept-source OCT device (Thorlabs, OCS1300SS) operating in the near-infrared at a center wavelength of 1300 nm, producing images with a spatial resolution of 12 µm × 25 µm (axial × transverse). Figure 24 shows an example of an OCT image obtained from a biopsy of skin sarcoidosis embedded in paraffin. OCT is effective in identifying granulomas in the dermis, suggesting that this technique could also be used to diagnose cutaneous sarcoidosis *in vivo*, which would prevent the patient from having to undergo a biopsy.

Finally, we have recently tested the acquisition of *in vivo* FTIR spectra using an Agilent 4300 Handheld FTIR spectrometer. The experimental setup, routinely used for archeomaterials [219], allows the acquisition of infrared spectra in the range 5000–650 cm^{-1} with a spectral resolution of 4 cm^{-1}. The detector is thermal and the signal is related to a change in temperature caused by the absorption of the infrared radiation. Experiments were performed in attenuated total reflection mode (with a 2 µm typical penetration depth) using a diamond interface window on a patient with a tattoo. A set of infrared spectra were collected (Figure 25): it is clear that the signal to noise is excellent and thus it seems possible to extract spectral information regarding the chemical composition of the tattoos. Following these preliminary experiments, we have started an investigation in order to analyse quantitatively these IR spectra.

6. Conclusion and perspectives

This contribution exemplifies different physicochemical techniques, encompassing imaging at the submicrometer scale by FE-SEM, chemical identification by two vibrational spectroscopies namely

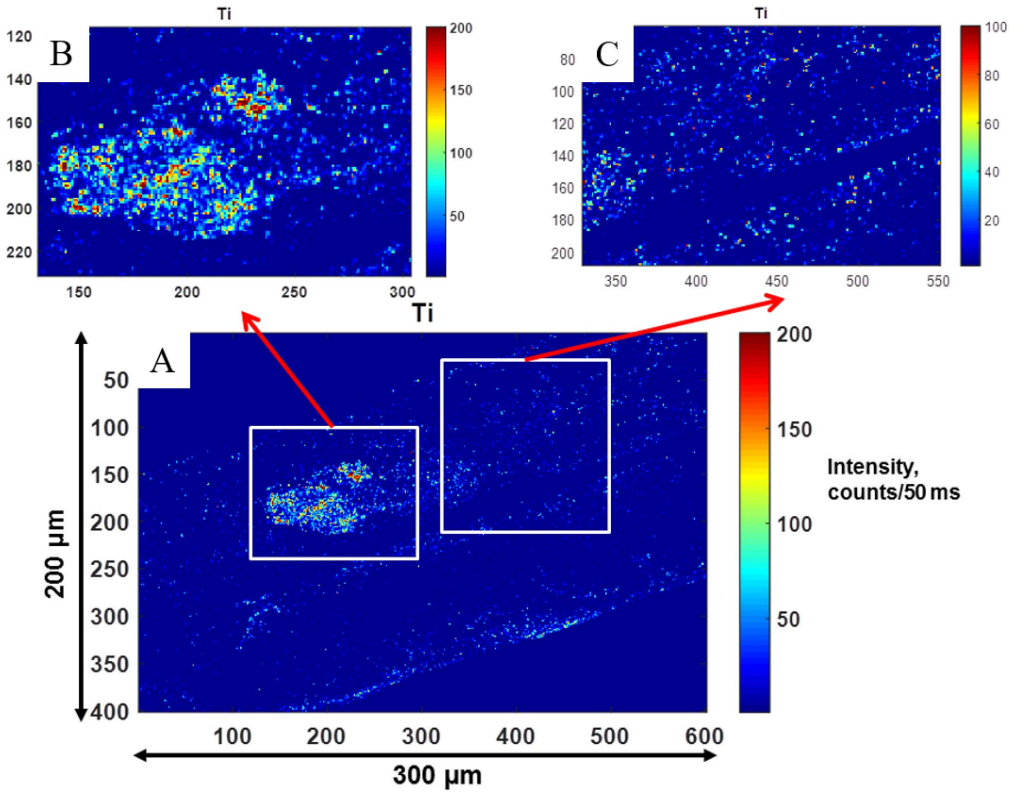

Figure 22. Nano X-ray fluorescence spectroscopy: high 500 nm resolution distribution maps of Ti within a hair sample. Red color areas correspond to a high concentration of Ti.

FTIR and Raman, as well as techniques specific to synchrotron radiation such as XRF and XANES, have been used to describe both endogenous and exogenous skin deposits.

The complete set of results demonstrates clearly that, although carbapatite is usually identified in endogenous deposits, various other chemical compounds can be identified. Such chemical diversity in skin calcifications suggests different biochemical mechanisms. We have also demonstrated the variety of structures and locations adopted by such skin deposits.

Regarding exogenous skin deposits, we identified PAA and metal oxides in KA, which were strongly correlated with the position of the tumour, and identified TiO_2 in FFA, which was closely located next to the area rich in stem cells of the hair follicle. This co-localization suggests a direct involvement of these compounds in these diseases.

In the near future, we would like to apply other tools in various skin diseases. Nowadays, it is possible to perform a description of the pathological calcifications at the nanometer scale. Transmission electron microscopy (TEM) has already been used and such description has led to different scientific breakthroughs [220–222]. Combining TEM and electron energy loss experiments tells the clinician the morphology and the elemental composition of abnormal tissue deposits at the nanometre scale [223,224]. There is also now the possibility of identifying chemical composition by the acquisition of NanoInfrared spectra [225–228].

Other tools, such as UV spectroscopy [229–231] or Second Harmonic Generation (SHG) [232–234] are also very interesting for the exploration of skin diseases. We have obtained promising preliminary results at the Disco beamline, Synchrotron Soleil, and we will proceed with more analyses in the future. Figure 26 shows as an example of spontaneous fluorescence within sweat glands (red arrow).

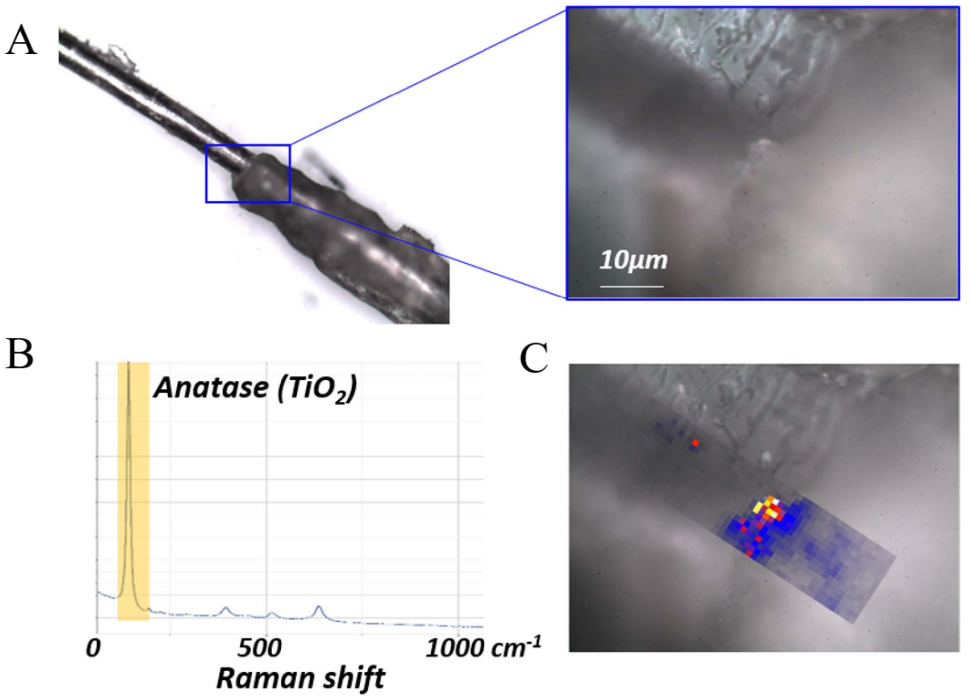

Figure 23. Raman characterization of a hair follicle from a patient with frontal fibrosing alopecia: (a) Optical micrograph at 10× and 100× magnification, (b) Raman spectrum (785 nm, laser power: 22.5 mW Acq. time = 0.5 s) revealing the presence of anatase and (c) Raman mapping by integration of the intensity of the 142 cm^{-1} band of anatase over the energy range 120–160 cm^{-1}, showing a high concentration of anatase at the hair/follicle junction.

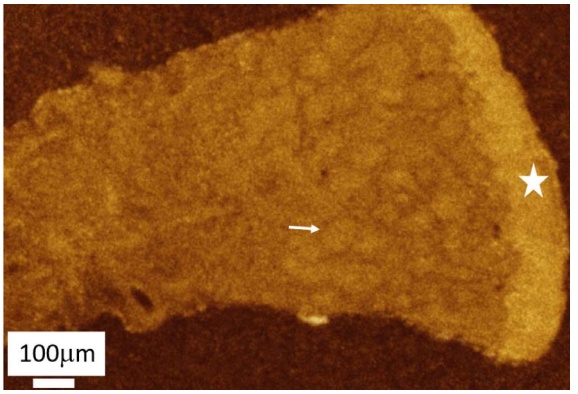

Figure 24. OCT analysis in skin sarcoidosis: epidermis (dot), dermis and clear visualisation of many granulomas (arrow).

Synchrotron radiation provides other opportunities for nanometer scale definition. For example, scanning transmission X-ray microscopy performed at the carbon K-edge and at the Ca $L_{2,3}$-edges can accurately assess the pathogenesis of calcifications inside bacteria [235].

Finally, all these nanometer scale experimental data have to be considered via a "bottom-up" approach based on DFT model chemistry [236–238]. Such a theoretical approach can model different kinds of apatite/biomolecule [239–241] and metal or metal oxide/small molecule interactions [242–244] which can have a major influence in the case of tattoos.

Further collaborations and studies are therefore projected, including multiphoton microscopy analyses, in order to provide a better understanding of skin diseases associated with endogenous and exogenous deposits, and hopefully improve their treatment.

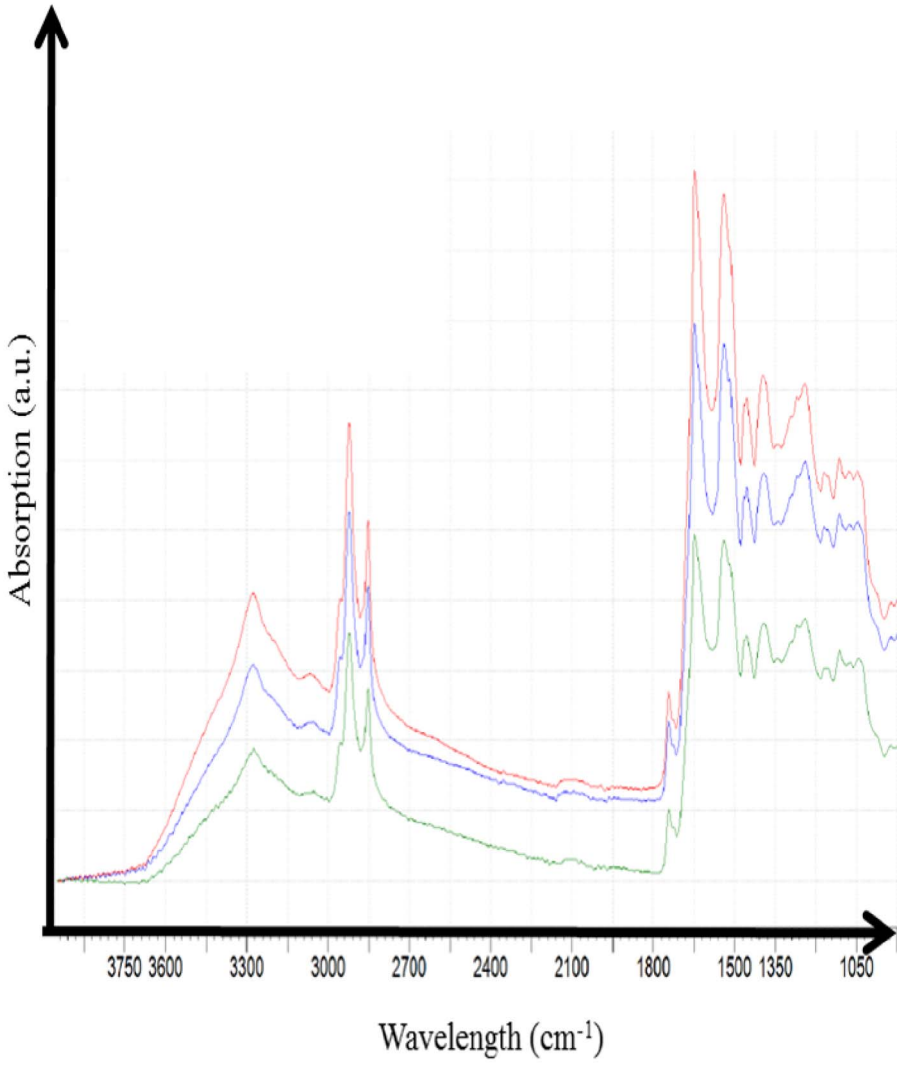

Figure 25. *In vivo* infrared spectra of a skin tattoo acquired with a portable infrared experimental setup.

Conflicts of interest

Authors have no conflict of interest to declare.

Acknowledgments

We acknowledge SOLEIL for providing access to their Synchrotron radiation facilities (proposals 20170374 and 2018362) and we would like to thank the DiffAbs, Nanoscopium and Disco beamlines teams for their assistance during experiments. We would like to thank the clusters of excellence MiChem and Matisse (ANR-11-IDEX-0004-02) led by Sorbonne Université. We would like to thank the "Fondation pour la Recherche Médicale" for their financial support of these studies.

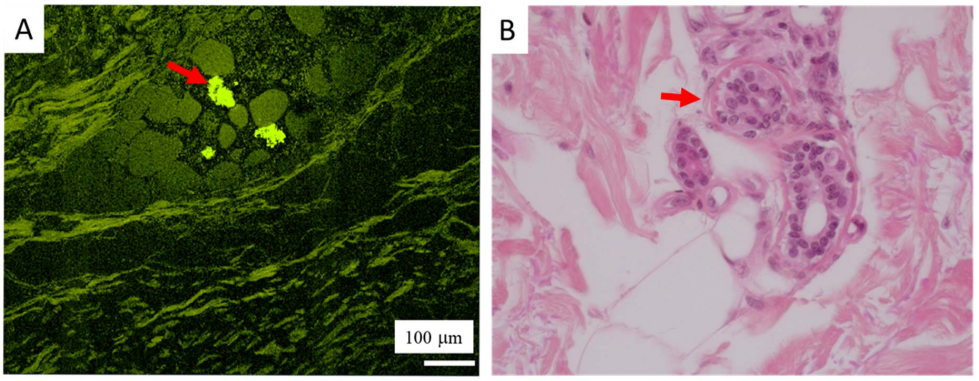

Figure 26. Comparison of SHG and optical microscopy. (A) Spontaneous fluorescence is observed within sweat glands (red arrow), here surrounded by adipocytes. (B) HES ×400, sweat glands (red arrow), also surrounded by adipocytes.

References

[1] D. Bazin, M. Daudon, C. Combes, C. Rey, *Chem. Rev.*, 2012, **112**, 5092-5120.

[2] D. Bazin, M. Daudon, *J. Phys. D: Appl. Phys.*, 2012, **45**, article no. 383001.

[3] L. N. Poloni, M. D. Ward, *Chem. Mater.*, 2014, **26**, 477-495.

[4] E. Tsolaki, S. Bertazzo, *Materials*, 2019, **12**, article no. 3126.

[5] D. Bazin, M. Daudon, *J. Spectral Imaging*, 2019, **8**, article no. a16.

[6] N. Vidavsky, J. A. M. R. Kunitake, L. A. Estroff, *Adv. Healthc. Mater.*, 2020, article no. e2001271.

[7] A. M. Molina-Ruiz, L. Cerroni, H. Kutzner, L. Requena, *Am. J. Dermatopathol.*, 2014, **36**, 1-48.

[8] F. Rongioletti, "Exogenous cutaneous deposits with special consideration to skin reactions to soft-tissue fillers", in *Clinical and Pathological Aspects of Skin Diseases in Endocrine, Metabolic, Nutritional and Deposition Disease* (B. Smoller, F. Rongioletti, eds.), Springer, New York, NY, 2010.

[9] M.-T. Liu, W.-T. Cheng, M.-J. Li, H.-N. Liu, D.-M. Yang, S.-Y. Lin, *Arch. Dermatol. Res.*, 2005, **297**, 231-234.

[10] V. Rafnsson, O. Ingimarsson, I. Hjalmarsson, H. Gunnarsdottir, *Occup. Environ. Med.*, 1998, **55**, 657-660.

[11] L. F. Bonewald, S. E. Harris, J. Rosser, M. R. Dallas, S. Dallas, N. P. Camacho, B. Boyan, A. Boskey, *Calcif. Tissue Int.*, 2003, **72**, 537-547.

[12] M. Daudon, D. Bazin, "New techniques to characterize kidney stones and Randall's plaque", in *Urolithiasis: Basic Science and Clinical Practice* (J. J. Talati, H. G. Tiselius, D. M. Albala, Z. Ye, eds.), Springer, London, 2012, 683-707.

[13] D. Bazin, Ch. Jouanneau, S. Bertazzo, Ch. Sandt, A. Dessombz, M. Réfrégiers, P. Dumas, J. Frederick, J.-Ph. Haymann, E. Letavernier, P. Ronco, M. Daudon, *C. R. Chim.*, 2016, **19**, 1439-1454.

[14] V. Frochot, D. Bazin, E. Letavernier, Ch. Jouanneau, J.-Ph. Haymann, M. Daudon, *C. R. Chim.*, 2016, **19**, 1565-1572.

[15] H. Bilbault, J. Perez, L. Huguet, S. Vandermeersch, S. Placier, N. Tabibzadeh, V. Frochot, E. Letavernier, D. Bazin, M. Daudon, J.-P. Haymann, *Sci. Rep.*, 2018, **8**, article no. 16319.

[16] A. Dessombz, P. Méria, D. Bazin, M. Daudon, *PLoS One*, 2012, **7**, article no. e51691.

[17] A. Dessombz, P. Méria, D. Bazin, E. Foy, S. Rouzière, R. Weil, M. Daudon, *Prog. Urol.*, 2011, **21**, 940-945.

[18] M. Mathonnet, A. Dessombz, D. Bazin, R. Weil, F. Triponez, M. Pusztaszeri, M. Daudon, *C. R. Chim.*, 2016, **19**, 1672-1678.

[19] J. Guerlain, S. Perie, M. Lefevre, J. Perez, S. Vandermeersch, Ch. Jouanneau, L. Huguet, V. Frochot, E. Letavernier, R. Weil, S. Rouziere, D. Bazin, M. Daudon, J. P. Haymann, *PLoS One*, 2019, **14**, article no. e0224138.

[20] F. Brisset, M. Repoux, J. Ruste, F. Grillon, F. Robaut, *Microscopie Electronique à Balayage et Microanalyses*, EDP Sciences, Les Ulis, 2009.

[21] D. Bazin, M. Daudon, *Ann. Biol. Clin.*, 2015, **73**, 517-534.

[22] D. Bazin, E. Bouderlique, M. Daudon, V. Frochot, J.-Ph. Haymann, E. Letavernier, F. Tielens, R. Weil, *C. R. Chim.*, 2022, **25**, no. S1, 37-60.

[23] A. Dessombz, C. Nguyen, H.-K. Ea, S. Rouzière, E. Foy, D. Hannouche, S. Réguer, F.-E. Picca, D. Thiaudière, F. Lioté, M. Daudon, D. Bazin, *J. Trace Elem. Med. Biol.*, 2013, **27**, 326-333.

[24] S. Rouzière, D. Bazin, M. Daudon, *C. R. Chim.*, 2016, **19**, 1404-1415.

[25] D. Bazin, E. Foy, S. Reguer, S. Rouzière, B. Fayard, H. Colboc, J.-Ph. Haymann, M. Daudon, C. Mocuta, *C. R. Chim.*, 2022, **25**, no. S1, 165-188.

[26] A. Guinier, *Théorie et technique de la radiocristallographie*, Dunod, Paris, 1964.

[27] D. Bazin, C. Chappard, C. Combes, X. Carpentier, S. Rouzière, G. André, G. Matzen, M. Allix, D. Thiaudière, S. Reguer, P. Jungers, M. Daudon, *Osteoporos. Int.*, 2009, **20**, 1065-1075.

[28] S. Reguer, C. Mocuta, D. Thiaudière, M. Daudon, D. Bazin, *C. R. Chim.*, 2016, **19**, 1424-1431.

[29] D. Bazin, V. Frochot, J.-Ph. Haymann, E. Letavernier, M. Daudon, *C. R. Chim.*, 2022, **25**, no. S1, 133-147.

[30] N. Quy Dao, M. Daudon, *Infrared and Raman Spectra of Calculi*, Elsevier, Paris, 1997.
[31] L. Estepa, M. Daudon, *Biospectroscopy*, 1997, **3**, 347-369.
[32] S. Y. Lin, *Expert Rev. Mol. Med.*, 2014, **16**, article no. e6.
[33] M. Daudon, D. Bazin, *C. R. Chim.*, 2016, **19**, 1416-1423.
[34] I. T. Lucas, D. Bazin, M. Daudon, *C. R. Chim.*, 2022, **25**, no. S1, 83-103.
[35] S. Tamosaityte, M. Pucetaite, A. Zelvys, S. Varvuolyte, V. Hendrixson, V. Sablinskas, *C. R. Chim.*, 2022, **25**, no. S1, 73-82.
[36] D. Bazin, M. Daudon, P. Chevallier, S. Rouzière, E. Elkaim, D. Thiaudière, B. Fayard, E. Foy, P. A. Albouy, G. André, G. Matzen, E. Véron, *Ann. Biol. Clin. (Paris)*, 2006, **64**, 125-139.
[37] D. Bazin, J.-Ph. Haymann, E. Letavernier, J. Rode, M. Daudon, *Presse Med.*, 2014, **43**, 135-148.
[38] M. Daudon, D. Bazin, *J. Phys.: Conf. Ser.*, 2013, **425**, article no. 022006.
[39] D. Bazin, E. Letavernier, J.-P. Haymann, P. Méria, M. Daudon, *Prog. Urol.*, 2016, **26**, 608-618.
[40] D. E. Sayers, F. W. Lytle, E. A. Stern, *Adv. X-ray Anal.*, 1970, **13**, 248-271.
[41] J. J. Rehr, A. L. Ankudinov, *Coord. Chem. Rev.*, 2005, **249**, 131-140.
[42] D. Bazin, D. Sayers, J. Rehr, *J. Phys. Chem. B*, 1997, **101**, 11040-11050.
[43] D. Bazin, D. Sayers, J. J. Rehr, C. Mottet, *J. Phys. Chem. B*, 1997, **101**, 5332-5336.
[44] D. Bazin, J. J. Rehr, *J. Phys. Chem. B*, 2003, **107**, 12398-12402.
[45] D. Bazin, S. Reguer, D. Vantelon, J.-Ph. Haymann, E. Letavernier, V. Frochot, M. Daudon, E. Esteve, H. Colboc, *C. R. Chim.*, 2022, **25**, no. S1, 189-208.
[46] D. Bazin, E. Letavernier, J. P. Haymann, V. Frochot, M. Daudon, *Ann. Biol. Clin.*, 2020, **78**, 349-362.
[47] M. Daudon, P. Jungers, D. Bazin, *New England J. Med.*, 2008, **359**, 100-102.
[48] D. Bazin, G. André, R. Weil, G. Matzen, E. Véron, X. Carpentier, M. Daudon, *Urology*, 2012, **79**, 786-790.
[49] A. Dessombz, E. Letavernier, J.-Ph. Haymann, D. Bazin, M. Daudon, *J. Urol.*, 2015, **193**, 1564-1569.
[50] S. Kaščáková, C. M. Kewish, S. Rouzière, F. Schmitt, R. Sobesky, J. Poupon, C. Sandt, B. Francou, A. Somogyi, D. Samuel, E. Jacquemin, A. Dubart-Kupperschmitt, T. H. Nguyen, D. Bazin, J.-C. DuclosVallée, C. Guettier, F. Le Naour, *J. Pathol. Clin. Res.*, 2016, **2**, 175-186.
[51] D. Bazin, M. Daudon, G. André, R. Weil, E. Véron, G. Matzen, *J. Appl. Crystallogr.*, 2014, **47**, 719-725.
[52] N. Reiter, L. El-Shabrawi, B. Leinweber, A. Berghold, E. Aberer, *J. Am. Acad. Dermatol.*, 2011, **65**, 14-15.
[53] J. S. Walsh, J. A. Fairley, *J. Am. Acad. Dermatol.*, 1995, **33**, 693-706.
[54] A. Valenzuela, L. Chung, *Curr. Treat Options Rheumatol.*, 2016, **2**, 85-96.
[55] A. G. Tristano, J. L. Villarroel, M. A. Rodríguez, A. Millan, *Clin. Rheumatol.*, 2006, **25**, 70-74.
[56] B. C. Presley, J. S. Bush, S. C. Watson, *West J. Emerg. Med.*, 2012, **13**, 136-138.
[57] O. Le Saux, Z. Urban, C. Tschuch, K. Csiszar, B. Bacchelli, D. Quaglino, I. Pasquali-Ronchetti, F. Michael Pope, A. Richards, S. Terry, L. Bercovitch, A. de Paepe, C. D. Boyd, *Nat. Genet.*, 2000, **25**, article no. 223.
[58] S. E. Lee, S. Hun, *Ann. Dermatol.*, 2018, **30**, 265-275.
[59] A. B. G. Lansdown, *Wound Rep. Reg.*, 2002, **10**, 271-285.
[60] M. P. Adams, D. G. Mallet, G. J. Pettet, *PLoS One*, 2015, **10**, article no. e0116751.
[61] P. Henrot, A. Leroux, C. Barlier, P. Génin, *Diagn. Interv. Imaging*, 2014, **95**, 141-152.
[62] A. B. Lakhdar, M. Daudon, M. C. Mathieu, A. Kellum, C. Balleyguier, D. Bazin, *C. R. Chim.*, 2016, **19**, 1610-1624.
[63] H. Colboc, Ph. Moguelet, D. Bazin, P. Carvalho, A.-S. Dillies, G. Chaby, H. Maillard, D. Kottler, E. Goujon, Ch. Jurus, M. Panaye, V. Frochot, E. Letavernier, M. Daudon, I. Lucas, R. Weil, Ph. Courville, J.-B. Monfort, F. Chasset, P. Senet, *JAMA Dermatol.*, 2019, **155**, 789-796.
[64] L. M. Pachman, A. Veis, S. Stock, K. Abbott, F. Vicari, P. Patel, D. Giczewski, C. Webb, L. Spevak, A. L. Boskey, *Arthritis Rheumatol.*, 2006, **54**, 3345-3350.
[65] R. Kramann, V. M. Brandenburg, L. J. Schurgers, M. Ketteler, S. Westphal, I. Leisten, M. Bovi, W. Jahnen-Dechent, R. Knüchel, J. Floege, R. K. Schneider, *Nephrol. Dial. Transplant.*, 2013, **28**, 856-868.
[66] T. Ogino, T. Suzuki, K. Sawada, *Geochim. Cosmochim. Acta*, 1987, **51**, 2757-2767.
[67] J. D. Reid, M. E. Andersen, *Am. J. Clin. Pathol.*, 1988, **90**, 545-585.
[68] C. J. Cros, D. Bazin, A. Kellum, V. Rebours, M. Daudon, *C. R. Chim.*, 2016, **19**, 1642-1664.
[69] J.-K. Yua, H. Pan, Sh.-M. Huang, N.-L. Huang, Ch.-Ch. Yao, K.-M. Hsiao, Ch.-W. Wu, *Asian J. Surg.*, 2013, **36**, 26-35.
[70] S. Kraaij, H. S. Brand, E. H. van der Meij, J.-G. de Visscher, *Med. Oral. Patol. Oral. Cir. Bucal*, 2018, **23**, article no. e540.
[71] J. A. Terzakis, W. J. Eisenmenger, J. J. Reidy, *Am. J. Clin. Pathol.*, 1984, **82**, 236-239.
[72] M. Daudon, H. Bouzidi, D. Bazin, *Urol. Res.*, 2010, **38**, 459-467.
[73] H.-K. Ea, Ch. Nguyen, D. Bazin, A. Bianchi, J. Guicheux, P. Reboul, M. Daudon, F. Lioté, *Arthritis Rheum.*, 2010, **63**, 10-18.
[74] S. De Santis, G. Sotgiu, A. Crescenzi, C. Taffon, A. C. Felici, M. Orsini, *J. Pharm. Biomed. Anal.*, 2020, **190**, article no. 113534.
[75] J. M. Richards, J. A. M. R. Kunitake, H. B. Hunt, A. N. Wnorowski, D. W. Lin, A. L. Boskey, E. Donnelly, L. A. Estroff, J. T. Butcher, *Acta Biomateri.*, 2018, **71**, 24-36.
[76] J. A. M. R. Kunitake, S. Choi, K. X. Nguyen, M. M. Lee, F. He, D. Sudilovsky, P. G. Morris, M. S. Jochelson, C. A. Hudis, D. A. Muller, P. Fratzl, C. Fischbach, A. Masic, L. A. Estroff, *J. Struct. Biol.*, 202, **2018**, 25-34.
[77] Ch. Rey, Ch. Combes, Ch. Drouet, H. Sfihi, A. Barroug, *Mater. Sci. Eng.*, 2007, **C27**, 198-205.
[78] S. Cazalbou, D. Eichert, Ch. Drouet, Ch. Combes, Ch. Rey, *C. R. Paleontol.*, 2004, **3**, 563-572.
[79] M. Iafisco, J. M. Delgado-Lopez, C. Drouet, in *Apatites: Synthesis, Structural Characterization and Biomedical Applications* (M. Iafisco, J. M. Delgado-Lopez, eds.), Nova Science Publishers, New York, 2014, Chapter 2, eBook.
[80] Ch. Combes, S. Cazalbou, Ch. Rey, *Minerals*, 2016, **6**, article no. 34.

[81] I. Russoni de Lima, G. Gomes Alves, C. A. Soriano, A. P. Campaneli, Th. H. Gasparoto, E. S. Ramos Jr., L. Á. de Sena, A. M. Rossi, J. M. Granjeiro, *J. Biomed. Mater. Res. A*, 2011, **98**, 351-358.
[82] D. Bazin, M. Daudon, Ch. Chappard, J. J. Rehr, D. Thiaudière, S. Reguer, *J. Synchrotron Radiat.*, 2011, **18**, 912-918.
[83] D. Bazin, A. Dessombz, Ch. Nguyen, H. K. Ea, F. Lioté, J. Rehr, Ch. Chappard, S. Rouzière, D. Thiaudière, S. Reguer, M. Daudon, *J. Synchrotron Radiat.*, 2014, **21**, 136-142.
[84] X. Carpentier, D. Bazin, Ch. Combes, A. Mazouyes, S. Rouzière, P. A. Albouy, E. Foy, M. Daudon, *J. Trace Elem. Med. Biol.*, 2011, **25**, 160-165.
[85] S. Naray-Szabo, *Z. Kristallogr Kristallgeom Kristallphys Kristallchem*, 1930, **75**, 387-398.
[86] T. J. White, D. Zhi Li, *Acta Crystallogr.*, 2003, **B 59**, 1-16.
[87] J. C. Elliott, *Structure and Chemistry of the Apatites and Other Calcium Orthophosphates*, Elsevier, Amsterdam, 1994.
[88] M. Vallet-Regi, M. J. Gonzalez-Calbet, *Prog. Solid State Chem.*, 2004, **32**, 1-31.
[89] S. Ouizat, A. Barroug, A. Legrouri, C. Rey, *Mater. Res. Bull.*, 2000, **34**, 2279-2289.
[90] Ch. Drouet, Ch. Rey, *Nanostructured Biomaterials for Regenerative Medicine*, Woodhead Publishing Series in Biomaterials, Woodhead Publishing, Cambridge, 2020, 223-254 pages.
[91] C. Rey, J. L. Miquel, L. Facchini, A. P. Legrand, M. J. Glimcher, *Bone*, 1995, **16**, 583-586.
[92] C. K. Loong, Ch. Rey, L. T. Kuhn, Ch. Combes, Y. Wu, S. H. Chen, M. J. Glimcher, *Bone*, 2000, **26**, 599-602.
[93] G. Cho, Y. Wu, J. L. Ackerman, *Science*, 2003, **300**, 1123-1127.
[94] R. Legros, N. Balmain, G. Bonel, *Calcif. Tissue Int.*, 1987, **41**, 137-144.
[95] X. Carpentier, M. Daudon, O. Traxer, P. Jungers, A. Mazouyes, G. Matzen, E. Véron, D. Bazin, *Urology*, 2009, **73**, 968-975.
[96] M. Daudon, D. Bazin, G. André, P. Jungers, A. Cousson, P. Chevallier, E. Véron, G. Matzen, *J. Appl. Crystallogr.*, 2009, **42**, 109-115.
[97] A. S. Prasad, *J. Trace Elem. Med. Biol.*, 2014, **28**, 364-371.
[98] N. Z. Gammoh, L. Rink, *Nutrients*, 2017, **9**, article no. 624.
[99] C. P. Wild, *Cancer Epidemiol. Biomarkers Prev.*, 2005, **14**, 1847-1850.
[100] J. Lademann, H. Weigmann, C. Rickmeyer, H. Barthelmes, H. Schaefer, G. Mueller, W. Sterry, *Skin Pharmacol. Appl. Skin Physiol.*, 1999, **12**, 247-256.
[101] R. G. M. Keijsers, D. A. F. van den Heuvel, J. C. Grutters, *Eur. Respir. J.*, 2013, **41**, 743-751.
[102] B. P. Barna, M. A. Judson, M. J. Thomassen, *Adv. Exp. Med. Biol.*, 2021, **1304**, 39-52.
[103] S. A. Ma, S. Imadojemu, K. Beer, J. T. Seykora, *J. Cutan. Pathol.*, 2017, **44**, 672-676.
[104] F. Brunet-Possenti, L. Deschamps, H. Colboc, A. Somogyi, K. Medjoubi, D. Bazin, V. Descamps, *J. Eur. Acad. Dermatol. Venereol.*, 2018, **32**, e442-e443.
[105] R. Ruiz-Villaverde, P. Fernandez-Crehuet, P. Aguayo-Carreras, J. L. Hernandez-Centeno, C. Cuenca-Barrales, *Sultan Qaboos Univ. Med. J.*, 2018, **18**, e215-e218.
[106] R. Bose, Ch. Sibley, S. Fahim, *SAGE Open Med. Case Rep.*, 2020, **8**, article no. 2050313X20936036.
[107] R. H. Weenig, L. D. Sewell, M. D. Davis, J. T. McCarthy, M. R. Pittelkow, *J. Am. Acad. Dermatol.*, 2007, **56**, 569-579.
[108] S. U. Nigwekar, S. Zhao, J. Wenger, J. L. Hymes, F. Maddux, R. I. Thadhani, K. E. Chan, *J. Am. Soc. Nephrol.*, 2016, **27**, 3421-3429.
[109] S. U. Nigwekar, R. Thadhani, V. M. Brandenburg, *N. Engl. J. Med.*, 2018, **378**, 1704-1714.
[110] Z. Yu, L. Gu, H. Pang, Y. Fang, H. Yan, W. Fang, *Case Rep. Nephrol. Dial.*, 2015, **5**, 77-82.
[111] H.-K. Sin, P.-N. Wong, K.-Y. Lo, M.-W. Lo, S.-F. Chan, K.-C. Lo, Y.-Y. Wong, L.-Y. Ho, W.-T. Kwok, K.-C. Chan, A. K.-M. Wong, S.-K. Mak, *Transplant. Rep.*, 2020, **5**, article no. 100068.
[112] E. A. Ross, *Am. J. Nephrol.*, 2011, **34**, 460-467.
[113] G. Munavalli, A. Reisenauer, M. Moses, S. Kilroy, J. L. Arbiser, *J. Dermatol.*, 2003, **30**, 915-919.
[114] L. Amuluru, W. High, K. M. Hiatt, J. Ranvill, S. V. Shah, B. Malik, S. Swaminathan, *J. Am. Acad. Dermatol.*, 2009, **61**, 73-79.
[115] W. T. Longcope, *J. Am. Med. Assoc.*, 1941, **117**, 1321-1327.
[116] N. Danbolt, *Postgrad. Med. J.*, 1958, **34**, 245-247.
[117] ATS Board of Directors and ERS Executive Committee, "Statement on Sarcoidosis. Joint statement of the American Thoracic Society (ATS), the European Respiratory Society (ERS) and the World Association of Sarcoidosis and Other Granulomatous Disorders (WASOG)", *Am. J. Respir. Crit. Care Med.*, 1999, **160**, no. 2, 736-755.
[118] E. A. Bresnitz, B. L. Strom, *Epidemiol. Rev.*, 1983, **5**, 124-156.
[119] L. S. Newman, C. S. Rose, L. A. Maier, *N. Engl. J. Med.*, 1997, **336**, 1224-1234.
[120] M. A. Hilal, J. Krotva, L. Chichierchio, N. Obeidat, M. Madanat, *G. Ital. Dermatol. Venereol.*, 2010, **145**, 733-745.
[121] A. Lyons, G. Brayman, S. Tahhan, *J. Gen. Intern. Med.*, 2018, **33**, 128-129.
[122] S. M. Ali, A. C. Gilliam, R. T. Brodell, *J. Cutan. Med. Surg.*, 2008, **12**, 43-48.
[123] S. Zhao, Q. Wang, B. Cheng, X.-F. Zhu, *Exp. Ther. Med.*, 2017, **13**, 1535-1537.
[124] J. Müller-Quernheim, M. Schürmann, S. Hofmann, K. I. Gaede, A. Fischer, A. Prasse, G. Zissel, S. Schreiber, *Clin. Chest Med.*, 2008, **29**, 391-414.
[125] J. L. Berlin, G. P. Shantha, H. Yeager, L. Thomas-Hemak, *BMJ Case Rep.*, 2014, **2014**, 1-4.
[126] R. P. Baughman, A. S. Teirstein, M. A. Judson, M. D. Rossman, H. Yeager Jr., E. A. Bresnitz, L. DePalo, G. Hunninghake, M. C. Iannuzzi, C. J. Johns, G. McLennan, D. R. Moller, L. S. Newman, D. L. Rabin, C. Rose, B. Rybicki, S. E. Weinberger, M. L. Terrin, G. L. Knatterud, R. Cherniak, *Am. J. Respir. Crit. Care Med.*, 2001, **164**, 1885-1889.
[127] K. A. Wanat, M. Rosenbach, *Clin. Chest Med.*, 2015, **36**, 685-702.
[128] J. P. Callen, *Arch. Dermatol.*, 2001, **137**, 485-486.
[129] J. Marcoval, A. Moreno, J. Mana, *J. Cutan. Pathol.*, 2004, **31**, 516-517.
[130] N. M. Walsh, J. G. Hanly, R. Tremaine, S. Murray, *Am. J. Dermatopathol.*, 1993, **15**, 203-207.
[131] Y. C. Kim, M. K. Triffet, L. E. Gibson, *Am. J. Dermatopathol.*, 2000, **22**, 408-412.
[132] G. Takemura, Y. Takatsu, K. Ono, T. Miyatake, M. Ono, T. Izumi, H. Fujiwara, *Heart Vessels*, 1995, **10**, 275-278.
[133] Y. Kuribayashi, K. Ohtani, T. Saito, T. Ide, *Eur. Heart J. Cardiovasc. Imaging*, 2017, **18**, 944-945.
[134] M. Catinon, C. Chemarin, F. Thivolet, M. Kambouchner, J.-F.

Bernaudin, C. Cavalin, A.-M. Sfarghiu, F. Arbib, O. Freynet, N. Freymond, J.-F. Mornex, P.-A. Rosental, M. Vincent, D. Valeyre, Ch. Pison, *Eur. Respir. J.*, 2017, **50**, article no. PA3263.

[135] H. Colboc, D. Bazin, Ph. Moguelet, V. Frochot, R. Weil, E. Letavernier, Ch. Jouanneau, C. Frances, C. Bachmeyer, J.-F. Bernaudin, M. Daudon, *C. R. Chim.*, 2016, **19**, 1631-1641.

[136] H. Colboc, P. Moguelet, D. Bazin, C. Bachmeyer, V. Frochot, R. Weil, E. Letavernier, C. Jouanneau, M. Daudon, J. F. Bernaudin, *J. Eur. Acad. Dermatol. Venereol.*, 2019, **33**, 198-203.

[137] L. M. Miller, P. Dumas, *Biochim. Biophys. Acta*, 2006, **1758**, 846-857.

[138] A. Dessombz, D. Bazin, P. Dumas, C. Sandt, J. Sule-Suso, M. Daudon, *PLoS One*, 2011, **6**, article no. e28007.

[139] D. Bazin, E. Letavernier, J.-Ph. Haymann, F. Tielens, A. Kellum, M. Daudon, *C. R. Chim.*, 2016, **19**, 1548-1557.

[140] W. Herschel, J. L. E. Dreyer, *The Scientific Papers of Sir William*, Herschel, Royal Society and Royal Astronomical Society, London, 1912.

[141] J. Chamberlain, *The Principles of Interferometric Spectroscopy*, Wiley, Chichester, UK, 1979.

[142] P. R. Griffiths, J. A. Haseth, *F.T.-IR Spectroscopy in Chemical Analysis: A Series of Monographs on Analytical Chemistry and its Applications*, Wiley, New York, 1986, 38 pages.

[143] D. C. Fernandez, R. Bhargava, S. M. Hewitt, I. W. Levin, *Nat. Biotechnol.*, 2005, **23**, 469-474.

[144] K. C. Khulbe, T. Matsuura, *Polymer*, 2000, **41**, 1917-1935.

[145] C. Krafft, D. Codrich, G. Pelizzo, V. Sergo, *J. Biophoton.*, 2008, **1**, 154-169.

[146] O. P. Sharma, *Curr. Opin. Pulm. Med.*, 2000, **6**, 442-447.

[147] M. Conron, C. Young, H. L. C. Beynon, *Rheumatology*, 2000, **39**, 707-713.

[148] G. W. Hunninghake, U. Costabel, M. Ando, R. Baughman, J. F. Cordier, R. du Bois, A. Eklund, M. Kitaichi, J. Lynch, G. Rizzato, C. Rose, O. Selroos, G. Semenzato, O. P. Sharma, *Sarcoidosis Vasc. Diffuse Lung Dis.*, 1999, **16**, 149-173.

[149] C. E. Broos, M. Van Nimwegen, H. C. Hoogsteden, R. W. Hendriks, M. Kool, B. van den Blink, *Front Immunol.*, 2013, **4**, article no. 437.

[150] A. Deter-Wolf, B. Robitaille, L. Krutak, S. Galliot, *J. Archaeol. Sci. Rep.*, 2016, **5**, 19-24.

[151] N. Kluger, S. Seité, C. Taieb, *J. Eur. Acad. Dermatol. Venereol.*, 2019, **33**, e484-e486.

[152] N. Kluger, L. Misery, S. Seité, C. Taieb, *J. Am. Acad. Dermatol.*, 2019, **81**, 607-610.

[153] G. Prior, *Curr. Probl. Dermatol. Basel, Karger*, 2015, **48**, 152-157.

[154] G. Prior, *Tattoo Inks: Analysis, Pigments, Legislation*, epubli, Berlin, 2014.

[155] M. Manso, S. Pessanha, M. Guerra, U. Reinholz, C. Afonso, M. Radtke, H. Lourenço, M. L. Carvalho, A. G. Buzanich, *Biol. Trace Elem. Res.*, 2019, **187**, 596-601.

[156] H. Petersen, D. Lewe, *Curr. Probl. Dermatol.*, 2015, **48**, 136-141.

[157] A. L. Timko, C. H. Miller, F. B. Johnson, E. Ross, *Arch Dermatol.*, 2001, **137**, 143-147.

[158] S. Gaudron, M.-C. Ferrier-Le Bouëdec, F. Franck, M. D'Incan, *Contact Derm.*, 2014, **72**, 97-105.

[159] J. Serup, K. Hutton Carlsen, N. Dommershausen, M. Sepehri, B. Hesse, C. Seim, A. Luch, I. Schreiver, *Contact Dermatitis*, 2020, **82**, 73-82.

[160] I. Schreiver, C. Hutzler, S. Andree, P. Laux, A. Luch, *Arch. Toxicol.*, 2016, **90**, 1639-1650.

[161] P. Piccinini, S. Pakalin, L. Contor, I. Bianchi, C. Senaldi, 2016, Final Report, EUR27947.

[162] C. of Europe Strasbourg, "Europe C of. Resolution ResAP (2008) 1 on requirements and criteria for the safety of tattoos and permanent make-up (superseding Resolution ResAP (2003) 2 on tattoos and permanent make-up): adopted by the Committee of Ministers on 20 February 2008 at the 1018th meeting of The Ministers' Deputies", 2008.

[163] P. Laux, T. Tralau, J. Tentschert, A. Blume, S. Al Dahouk, W. Bäumler, E. Bernstein, B. Bocca, A. Alimonti, H. Colebrook, Ch. de Cuyper, L. Dähne, U. Hauri, P. C. Howard, P. Janssen, L. Katz, B. Klitzman, N. Kluger, L. Krutak, Th. Platzek, V. Scott-Lang, J. Serup, W. Teubner, I. Schreiver, E. Wilkniß, A. Luch, *Lancet*, 2016, **387**, 395-402.

[164] M. Arl, D. J. Nogueira, J. Schveitzer Köerich, N. Mottim Justino, D. Schulz Vicentini, W. Gerson Matias, *J. Hazard Mater.*, 2019, **364**, 548-561.

[165] E. Maxim, H. Higgins, L. D'Souza, *Int. J. Womens Dermatol.*, 2017, **3**, 228-230.

[166] N. Kluger, D. Douvin, F. Dupuis-Fourdan, J. M. Doumecq-Lacoste, V. Descamps, *Ann. Dermatol. Venereol.*, 2017, **144**, 776-783.

[167] N. Kluger, V. Koljonen, *Lancet Oncol.*, 2012, **13**, e161-e168.

[168] N. Kluger, D. Douvin, F. Dupuis-Fourdan, J.-M. Doumecq-Lacoste, V. Descamps, *Ann. Dermatol. Vénéréol.*, 2017, **144**, 776-783.

[169] H. Colboc, D. Bazin, P. Moguelet, S. Reguer, R. Amode, C. Jouanneau, I. Lucas, L. Deschamps, V. Descamps, N. Kluger, *J. Eur. Acad. Dermatol. Venereol.*, 2020, **34**, e313-e315.

[170] N. C. Scherrer, Z. Stefan, D. Francoise, F. Annette, K. Renate, *Spectrochim. Acta A Mol. Biomol. Spectrosc.*, 2009, **73**, 505-524.

[171] K. H. Carlsen, M. Køcks, M. Sepehri, J. Serup, *Skin Res. Technol.*, 2016, **22**, 460-469.

[172] M. E. Darvin, J. Schleusener, F. Parenz, O. Seidel, C. Krafft, J. Popp, J. Lademann, *Analyst*, 2018, **143**, 4990-4999.

[173] S. L. Schneider, I. Kohli, I. H. Hamzavi, M. L. Council, A. M. Rossi, D. M. Ozog, *J. Am. Acad. Dermatol.*, 2019, **80**, 1121-1131.

[174] D. Bersani, P. P. Lottici, A. Montenero, *J. Raman Spectrosc.*, 1999, **30**, 355-360.

[175] I. Chourpa, L. Douziech-Eyrolles, L. Ngaboni-Okassa, J.-F. Fouquenet, S. Cohen-Jonathan, M. Soucé, H. Marchais, P. Dubois, *Analyst*, 2005, **130**, 1395-1403.

[176] I. Schreiver, B. Hesse, Ch. Seim, H. Castillo-Michel, J. Villanova, P. Laux, N. Dreiack, R. Penning, R. Tucoulou, M. Cotte, A. Luch, *Sci. Rep.*, 2017, **7**, article no. 11395.

[177] I. Schreiver, B. Hesse, Ch. Seim, H. Castillo-Michel, L. Anklamm, J. Villanova, N. Dreiack, A. Lagrange, R. Penning, Ch. De Cuyper, R. Tucoulou, W. Bäumler, M. Cotte, A. Luch, *Part. Fibre Toxicol.*, 2019, **16**, article no. 33.

[178] A. Bianconi, A. Congiu-Castellano, M. Dell'Ariccia, A. Giovannelli, P. J. Durham, E. Burattini, M. Barteri, *FEBS Lett.*, 1984, **178**, 165-170.

[179] *The MAK Collection for Occupational Health and Safety*, vol. 1, Wiley-VCH, Verlag GmbH & Co. KGaA, 2016.
[180] P. S. Islam, Ch. Chang, C. Selmi, E. Generali, A. Huntley, S. S. Teuber, M. E. Gershwin, *Clin. Rev. Allergy Immunol.*, 2016, **50**, 273-286.
[181] T. Høgsberg, K. Loeschner, D. Löf, J. Serup, *Br. J. Dermatol.*, 2011, **165**, 1210-1218.
[182] K. T. Tan, A. G. Messenger, *Br. J. Dermatol.*, 2009, **160**, 75-79.
[183] A. Debroy Kidambi, K. Dobson, S. Holmes, D. Carauna, V. Del Marmol, A. Vujovic, M. R. Kaur, A. Takwale, P. Farrant, C. Champagne, M. Harries, A. G. Messenger, *Br. J. Dermatol.*, 2017, **177**, 260-261.
[184] J. Lademann, H. Weigmann, C. Rickmeyer, H. Barthelmes, H. Schaefer, G. Mueller, W. Sterry, *Skin Pharmacol. Appl. Skin Physiol.*, 1999, **12**, 247-256.
[185] A. Somogyi, K. Medjoubi, G. Baranton, V. Le Roux, M. Ribbens, F. Polack, P. Philippot, J. P. Samama, *J. Synchrotron Radiat.*, 2015, **22**, 1118-1129.
[186] E. Esteve, D. Bazin, Ch. Jouanneau, S. Rouzière, A. Bataille, A. Kellum, K. Provost, Ch. Mocuta, S. Reguer, D. Thiaudiere, K. Jorissen, J. J. Rehr, A. Hertig, E. Rondeau, E. Letavernier, M. Daudon, P. Ronco, *C. R. Chim.*, 2016, **19**, 1580-1585.
[187] E. Esteve, D. Bazin, Ch. Jouanneau, S. Rouzière, A. Bataille, A. Kellum, K. Provost, Ch. Mocuta, S. Reguer, D. Thiaudiere, K. Jorissen, J. J. Rehr, A. Hertig, E. Rondeau, E. Letavernier, M. Daudon, P. Ronco, *C. R. Chim.*, 2016, **19**, 1586-1589.
[188] E. Esteve, S. Reguer, C. Boissiere, C. Chanéac, G. Lugo, Ch. Jouanneau, C. Mocuta, D. Thiaudière, N. Leclercq, B. Leyh, J.-F. Greisch, J. Berthault, M. Daudon, P. Ronco, D. Bazin, *J. Synchrotron Radiat.*, 2017, **24**, 991-999.
[189] T. Inoue, K. Takehara, N. Shimizu, Y. Kitajima, K. Shinohara, A. Ito, *J. X-ray Sci. Technol.*, 2011, **19**, 313-320.
[190] C. Couteau, H. Diarra, Z. Schmitt, L. Coiffard, *Eur. J. Dermatol.*, 2019, **29**, 141-159.
[191] J. Siritapetawee, W. Pattanasiriwisawa, U. Sirithepthawee, *J. Synchrotron Radiat.*, 2010, **17**, 268-272.
[192] A. Bertazzo, C. Costa, M. Biasiolo, G. Allegri, G. Cirrincione, G. Presti, *Biol. Trace Element Res.*, 1996, **52**, 37-53.
[193] L. Dastgheib, Z. Mostafavi-pour, A. A. Abdorazagh, Z. Khoshdel, M. S. Sadati, I. Ahrari, S. Ahrari, M. Ghavipisheh, *Dermatol. Res. Pract.*, 2014, **2014**, article no. 784863.
[194] G. Ozaydin-Yavuz, I. Halil Yavuz, H. Demir, C. Demir, S. G. Bilgili, *Indian J. Dermatol.*, 2019, **64**, 7-11.
[195] I. Nicolis, P. Deschamps, E. Curis, P. Chevallier, O. Corriol, V. Colomb, S. Bénazeth, *J. Trace Microprobe Techn.*, 2000, **18**, 511-516, Informa UK (Marcel Dekker).
[196] E. Y. Bonnist, P. D. Pudney, L. A. Weddell, J. Campbell, F. L. Baines, S. E. Paterson, J. R. Matheson, *Int. J. Cosmet. Sci.*, 2014, **36**, 347-354.
[197] K. Müller, E. Valentine-Thon, *Neuro Endocrinol. Lett.*, 2006, **27**, 31-35.
[198] S. G. Han, B. Newsome, B. Hennig, *Toxicology*, 2013, **306**, 1-8.
[199] T. Wu, M. Tang, *Nanomedicine (Lond).*, 2018, **13**, 233-249.
[200] P. J. Caspers, G. W. Lucassen, R. Wolthuis, H. A. Bruining, G. J. Puppels, *Biospectroscopy*, 1998, **4**, S31-S39.
[201] H. Lui, J. Zhao, D. McLean, H. Zeng, *Cancer Res.*, 2012, **72**, 2491-2500.
[202] C. A. Lieber, S. K. Majumder, D. L. Ellis, D. D. Billheimer, A. Mahadevan-Jansen, *Lasers Surg. Med.*, 2008, **40**, 461-467.
[203] P. J. Caspers, G. W. Lucassen, G. J. Puppels, *Biophys. J.*, 2003, **85**, 572-580.
[204] A. P. M. Michel, S. Liakat, K. Bors, C. F. Gmach, *Biomed. Opt. Express*, 2013, **4**, 520-530.
[205] A. Bauer, O. Hertzberg, A. Küderle, D. Strobel, M. A. Pleitez, W. Mäntele, *J. Biophoton.*, 2018, **11**, article no. e201600261.
[206] D. A. Bradley, M. J. Farquharson, *J. Radioanal. Nucl. Chem.*, 2000, **244**, 213-217.
[207] H. Shehab, E. D. Desouza, J. O'Meara, A. Pejović-Milić, D. R. Chettle, D. E. B. Fleming, F. E. McNeill, *Physiol. Meas.*, 2016, **37**, 145-161.
[208] F. Fercher, *J. Biomed. Opt.*, 1996, **1**, 157-173.
[209] Gh. Podoleanu, *J. Microsc.*, 2012, **247**, 209-219.
[210] M. Zysk, F. T. Nguyen, A. L. Oldenburg, D. L. Marks, S. A. Boppart, *J. Biomed. Opt.*, 2007, **12**, article no. 051403.
[211] J. S. Schuman, C. A. Puliafito, J. G. Fujimoto, J. S. Duker, *Optical Coherence Tomography of Ocular Diseases*, 3rd ed., Slack Inc., Thorofare, NJ, 2013.
[212] H. G. Bezerra, M. A. Costa, G. Guagliumi, A. M. Rollins, D. I. Simon, *JACC Cardiovasc. Interv.*, 2009, **2**, 1035-1046.
[213] D. C. Adler, Y. Chen, R. Huber, J. Schmitt, J. Connolly, J. G. Fujimoto, *Nat. Photon.*, 2007, **1**, 709-716.
[214] X. Yu, Q. Ding, C. Hu, G. Mu, Y. Deng, Y. Luo, Z. Yuan, H. Yu, L. Liu, *IEEE J. Sel. Top. Quantum Electron*, 2019, **25**, 1-8.
[215] J. Men, Y. Huang, J. Solanki, X. Zeng, A. Alex, J. Jerwick, Z. Zhan, R. E. Tanzi, A. Li, C. Zhou, *IEEE J. Sel. Top. Quantum Electron*, 2016, **22**, article no. 6803213.
[216] Y. Fan, Y. Xia, X. Zhang, Y. Sun, J. Tang, L. Zhang, H. Liao, *Biosci. Trends*, 2018, **18**, 12-23.
[217] A. Levine, K. Wang, O. Markowitz, *Dermatol. Clin.*, 2017, **35**, 465-488.
[218] A. Dubois, O. Levecq, H. Azimani, D. Siret, A. Barut, M. Suppa, V. Del Marmol, J. Malvehy, E. Cinotti, J. L. Perrot, *J. Biomed. Opt.*, 2018, **23**, article no. 106007.
[219] G. Pothier Bouchard, S. M. Mentzer, J. Riel-Salvatore, J. Hodgkins, Ch. E. Miller, F. Negrino, R. Wogelius, M. Buckley, *J. Archaeol. Sci. Rep.*, 2019, **26**, article no. 101862.
[220] S. Bertazzo, E. Gentleman, *Eur. Heart J.*, 2017, **38**, 1189-1193.
[221] J. D. Hutcheson, C. Goettsch, S. Bertazzo, N. Maldonado, J. L. Ruiz, W. Goh, K. Yabusaki, T. Faits, C. Bouten, G. Franck, Th. Quillard, P. Libby, M. Aikawa, S. Weinbaum, E. Aikawa, *Nat. Mater.*, 2016, **15**, 335-343.
[222] C. Verrier, D. Bazin, L. Huguet, O. Stéphan, A. Gloter, M.-Ch. Verpont, V. Frochot, J.-Ph. Haymann, I. Brocheriou, O. Traxer, M. Daudon, E. Letavernier, *J. Urol.*, 2016, **196**, 1566-1574.
[223] M. A. Aronova, R. D. Leapman, *MRS Bull.*, 2012, **37**, 53-62.
[224] C. Gay, E. Letavernier, M.-Ch. Verpont, M. Walls, D. Bazin, M. Daudon, N. Nassif, O. Stephan, M. de Frutos, *ACS Nano.*, 2020, **14**, 1823-1836.
[225] A. Dazzi, F. Glotin, R. Carminati, *J. Appl. Phys.*, 2010, **107**, article no. 124519.
[226] A. Dazzi, C. B. Prater, *Chem. Rev.*, 2017, **17**, 5146-5173.
[227] E. Esteve, Y. Luque, J. Waeytens, D. Bazin, L. Mesnard, Ch. Jouanneau, P. Ronco, A. Dazzi, M. Daudon, A. Deniset-Besseau, *Anal. Chem.*, 2020, **92**, 7388-7392.
[228] D. Bazin, M. Rabant, J. Mathurin, M. Petay, A. Deniset-Besseau, A. Dazzi, Y. Su, E. P. Hessou, F. Tielens, F. Borondics,

M. Livrozet, E. Boudelicque, J.-Ph. Haymann, E. Letavernier, V. Frochot, M. Daudon, *C. R. Chim.*, 2022, **25**, no. S1, 489-502.
[229] F. Jamme, S. Villette, A. Giuliani, V. Rouam, F. Wien, B. Lagarde, M. Réfrégiers, *Microsc. Microanal.*, 2010, **16**, 507-514.
[230] E. Batard, F. Jamme, S. Villette, C. Jacqueline, M.-F. de la Cochetière, J. Caillon, M. Réfrégiers, *PLoS One*, 2011, **6**, article no. 19440.
[231] F. Jamme, S. Kascakova, S. Villette, F. Allouche, S. Pallu, V. Rouam, M. Réfrégiers, *Biol. Cell*, 2013, **105**, 277-288.
[232] M. Strupler, M. Hernest, C. Fligny, J.-L. Martin, P.-L. Tharaux, M.-C. Schanne-Klein, *J. Biomed. Opt.*, 2008, **13**, article no. 054041.
[233] N. Vuillemin, P. Mahou, D. Débarre, Th. Gacoin, P.-L. Tharaux, M.-C. Schanne-Klein, W. Supatto, E. Beaurepaire, *Sci. Rep.*, 2016, **6**, article no. 29863.
[234] A.-M. Pena, Th. Boulesteix, Th. Dartigalongue, M.-C. Schanne-Klein, *J. Am. Chem. Soc.*, 2005, **127**, 10314-10322.
[235] K. Benzerara, F. Skouri-Panet, J. Li, C. Férard, M. Gugger, Th. Laurent, E. Couradeau, M. Ragon, J. Cosmidis, N. Menguy, I. Margaret-Oliver, R. Taver, P. López-Garcíac, D. Moreira, *Proc. Natl. Acad. Sci. USA*, 2014, **111**, 10933-10938.
[236] P. Hohenberg, W. Kohn, *Phys. Rev. B*, 1964, **136**, 864-871.
[237] R. O. Jones, *Rev. Mod. Phys.*, 2015, **87**, 897-923.
[238] N. Mardirossian, M. Head-Gordon, *Mol. Phys.*, 2017, **115**, 2315-2372.
[239] M. Cutini, M. Corno, D. Costa, P. Ugliengo, *J. Phys. Chem. C*, 2019, **123**, 7540-7550.
[240] M. Corno, C. Busco, V. Bolis, S. Tosoni, P. Ugliengo, *Langmuir*, 2009, **25**, 2188-2198.
[241] A. Rimola, M. Aschi, R. Orlando, P. Ugliengo, *J. Am. Chem. Soc.*, 2012, **134**, 10899-10910.
[242] D. Bazin, F. Tielens, *Appl. Catal.*, 2015, **504**, 631-641.
[243] F. Tielens, D. Bazin, *C. R. Chim.*, 2018, **21**, 174-181.
[244] I. C. Oğuz, H. Guesmi, D. Bazin, F. Tielens, *J. Phys. Chem. C*, 2019, **123**, 20314-20318.

Comptes Rendus
Chimie
2022, Vol. 25, Special Issue S1, p. 477-487
https://doi.org/10.5802/crchim.202

Microcrystalline pathologies: Clinical issues and nanochemistry

Relationship between calcinosis cutis in epidermal necrolysis and caspofungin, a physicochemical investigation

Hester Colboc [a,*,#,b], Thomas Bettuzzi [a,#,c,d,e], Marine Badrignans [f], Dominique Bazin [g,*], Antoine Boury [g], Emmanuel Letavernier [b,h], Vincent Frochot [b,h], Ellie Tang [a,b], Philippe Moguelet [i], Nicolas Ortonne [a,e], Nicolas de Prost [j], Saskia Ingen-Housz-Oro [c,d,e] and Michel Daudon [b,h]

[a] Sorbonne Université, Hôpital Rothschild, Service Plaies et Cicatrisation, Paris, France

[b] UMR_S 1155, Sorbonne Université-UPMC Paris VI, F-75020 Paris, France

[c] Service de Dermatologie, Hôpital Henri Mondor, Assistance Publique Hôpitaux de Paris, 94000 Créteil, France

[d] Univ Paris Est Créteil, EpiDermE, Créteil, France

[e] Reference center for toxic bullous dermatoses and severe drug reactions TOXIBUL, Créteil, France

[f] Service de Pathologie, Hôpital Henri Mondor, Assistance Publique Hôpitaux de Paris, 94000 Créteil, France

[g] Université Paris-Saclay, CNRS, Institut de Chimie Physique, 310 rue Michel Magat, 91400 Orsay, France

[h] Sorbonne Université, Hôpital Tenon, Service des Explorations Fonctionnelles Multidisciplinaires, Paris, France

[i] Sorbonne Université, Hôpital Tenon, Service de Pathologie, Paris, France

[j] Service de Réanimation médicale, Hôpital Henri Mondor, Assistance Publique Hôpitaux de Paris, 94000 Créteil, France

Current address: APHP, Service Plaies et Cicatrisation, Hôpital Rothschild, 5, Rue Santerre, 75012 Paris, France (H. Colboc)

E-mails: hester.colboc@aphp.fr (H. Colboc), thomas.bettuzzi@aphp.fr (T. Bettuzzi), marine.badrignans@aphp.fr (M. Badrignans), dominique.bazin@universite-paris-saclay.fr (D. Bazin), antoine.boury@universite-paris-saclay.fr (A. Boury), emmanuel.letavernier@tnn.aphp.fr (E. Letavernier), vincent.frochot@aphp.fr (V. Frochot), Ellieyali.tang@hotmail.com (E. Tang), philippe.moguelet@aphp.fr (P. Moguelet), nicolas.ortonne@aphp.fr (N. Ortonne), nicolas.de-prost@aphp.fr

[*] Corresponding authors.

[#] Contributed equally.

(N. de Prost), saskia.oro@aphp.fr (S. Ingen-Housz-Oro), daudonmichel24@gmail.com
(M. Daudon)

Abstract. Epidermal necrolysis (EN) is a rare life-threatening condition, usually drug-induced and characterised by a diffuse epidermal and mucosal detachment. Calcinosis cutis is reported in various skin diseases, occurring preferentially with tissue damage, but has never been described in EN. Clinical, biological and histopathological characteristics of three patients were retrospectively obtained from medical charts. Immunohistochemistry of classical osteogenic markers was used to explore the pathogenesis of the calcifications; their chemical composition was determined by μFourier transform infra-red (μFTIR) spectroscopy and their localization and morphology by field-emission scanning electron microscopy (FE-SEM). In a recent letter, part of the results of this investigation has been already presented. In this contribution, we have added original data to this previous letter. We have investigated a set of biopsies corresponding to patients who presented atypical healing retardation due to calcinosis cutis. Through FE-SEM observations at the nanometre scale, we describe different areas where are present voluminous calcifications at the surface, submicrometre spherical entities within the papillary dermis and then large "normal" fibres. FE-SEM observations show clearly that "large" calcifications are the result of an agglomeration of small spherical entities. Moreover, micrometre scale spherical entities are the results of an agglomeration of nanometer scale spherical entities. Finally, the last set of data seems to show that the starting point of the calcifications process is "distant" from the epidermis in part of the dermis which appears undamaged. Regarding the chemical composition of large calcifications, different μFTIR maps which underlined the presence of calcium-phosphate apatite have been gathered. Moreover, histopathology indicates that these pathological calcifications are not induced following a trans-differentiation of the skin cells into an osteochondrogenic phenotype. The association of caspofungin administration, known to induce in vitro intracellular calcium influx, and inflammation, induced by EN, known to favor dystrophic calcifications in various inflammatory skin diseases, could explain this never-before reported occurrence of calcinosis cutis.

Keywords. Epidermal necrolysis, Caspofungin, Pathological calcifications, Scanning electron microscopy, Fourier Transform Infrared Spectroscopy.

Published online: 20 July 2022

1. Introduction

Epidermal necrolysis (EN) (i.e., Stevens Johnson syndrome and toxic epidermal necrolysis (TEN) according to the extent of detached body surface area) is a rare life-threatening condition, usually drug-induced, characterised by a diffuse epidermal and mucosal detachment. Skin histology reveals pan epidermal necrolysis. Mucocutaneous healing usually lasts 2 to 3 weeks [1]. Bacterial or fungal infections, with skin as a portal of entry, are a main complication of the disease, especially in TEN [2,3].

As recalled by Le and Bedocs [4], calcinosis cutis is classified into five main types: dystrophic, metastatic, idiopathic, iatrogenic, and calciphylaxis. Dystrophic calcification is the most common cause and occurs preferentially with tissue damage. Little is known regarding the chemical composition of calcium salts associated to calcinosis cutis which are deposited in the skin and subcutaneous tissue.

From a chemical point of view, the chemical diversity of abnormal deposit in skin [5] with an exogenous origin has been investigated in several papers dedicated for example to tattoo [6–9] or to sarcoidosis [10,11]. The chemical diversity of abnormal deposits in skin with an endogenous origin is less documented but has been underlined. In our case, for calcification of endogenous origin, we give evidence through physicochemical characterization techniques of the presence of calcium carbonate in the case of sarcoidosis [12,13] or of calcium phosphate apatite in the case of calcific uremic arteriolopathy [14].

Such chemical diversity of pathological calcifications [15–21] calls for a characterization through physicochemical techniques such vibrational spectroscopies namely Fourier Transform Infra-Red (FTIR) or Raman spectroscopies [18,22–26] which are able to describe precisely their chemistry. Imaging through field-emission scanning electron microscopy (FE-SEM) coupled with an energy-dispersive X-ray (EDX) spectrometer have also to be performed to describe and localize precisely at the submicrometre scale such abnormal deposits [18,27–29].

Here we describe three patients who presented atypical healing retardation due to calcinosis cutis, a finding not previously described in EN. Part of the results presented in this investigation has been already published in a letter [30]. Here, a completely new set of unpublished data encompassing FE-SEM observations, EDX and μFTIR measurements is presented in order to discuss more precisely the pathogenesis process related to calcinosis cutis.

2. Methods

The main characteristics of the three patients, admitted to the intensive care unit of our SJS/TEN reference centre between October, 2017 and February 2021, were retrospectively obtained from medical charts.

To investigate the origin and the composition of the epidermal calcifications, we conducted several experiments. For the hypothesis of calcium deposition induced by a trans-differentiation of fibroblasts or keratinocytes to an osteochondrogenic phenotype, immunohistochemistry was used to investigate classical osteogenic markers. Sections of paraffin-embedded skin biopsy, 4 μm thick, were dewaxed, heated in citric acid solution (Target Retrieval Solution pH6, Dako), then incubated with antibodies. After blockade of endogenous peroxidase (peroxidase blocking solution, Dako), sections were immunostained with antibodies specific for the following osteogenic markers: bone morphogenic protein 2 (BMP-2, polyclonal, 1:300; Abcam), runt-related transcription factor 2 (Runx2, polyclonal, 1:200; GeneTex), alkaline phosphatase (monoclonal, 1:200; Abcam) and sclerostin (polyclonal, 1:100; Santa Cruz Biotechnology). Immunostaining was revealed by specific Histofin (Nichirei Biosciences) and AEC (k34769, Dako) staining.

Additional 4 μm thick sections of paraffin-embedded skin biopsies were deposited on low-e microscope slides (MirrIR, Kevley Technologies, Tienta Sciences, Indianapolis, IN, USA) for μFTIR spectroscopy, FE-SEM observations and EDX measurements.

μFTIR spectra have been collected by using a Spectrum Spotlight 400 imaging system (Perkin-Elmer Life Sciences), with 6.25 μm spatial resolution and 8 cm^{-1} spectral resolution [22,23,30–32]. The concise description of the topology at the submicrometer scale of the sample is obtained using a FE-SEM (Zeiss SUPRA55-VP) microscope. High-resolution images were obtained with an Everhart-Thornley secondary electron detector. Measurements were taken at low voltage (less than 1 kV generally), without the usual carbon-coating of the sample surface. Finally, EDX spectroscopy was also used to identify the different elements present in the sample. Special attention has been taken to calcium and phosphor in tissue [18,27–29].

3. Results and discussion

3.1. *Clinical data*

Regarding epidemiology, calcinosis cutis commonly occurs in patients with systemic sclerosis, especially the limited form (CREST syndrome). Twenty-five to fourty percent of patients with limited systemic sclerosis will develop calcinosis cutis ten years after the onset of disease. Calcinosis cutis is seen in 30% of adults and up to 70% of children and adolescents with dermatomyositis. Patients with systemic lupus erythematosus can present with periarticular calcification in 33% of cases and soft tissue calcification in 17%.

Here we report three patients with severe TEN in whom secondary epidermal detachment with calcinosis cutis developed that was not previously described in this condition. This event was observed in the three cases a few days after caspofungin administration. One patient died and the two other patients presented an unusual, prolonged cutaneous healing. Clinical characteristics and histological results for the three patients are presented in Table 1.

Patient 1 was a 57 year-old woman, with TEN induced by pantoprazole. At day 6 after admission in our dermatology department, she was referred to ICU for a first septic shock to *P. aeruginosa* and *P. mirabilis*. On day 12 after admission, cutaneous healing was almost complete (Figure 1A). On day 18, she presented septic shock with *Candida parapsilosis* bloodstream infection and received caspofungin for 14 days. On day 29, dermatological examination revealed a diffuse epidermal detachment associated with atone fibrinous plaques (Figure 1B). Thereafter, the evolution was slowly favourable and the patient

Table 1. Clinical and demographic data of three patients admitted to the intensive care unit for toxic epidermal necrolysis

	Patient 1	Patient 2	Patient 3
Age	57	49	59
Sex	Female	Male	Male
Drug culprit of the TEN	Pantoprazole	Ibuprofen	Allopurinol
SCORTEN[a] at admission	2	4	3
Maximal body surface area involved	100%	100%	80%
Cutaneous biopsy at admission	Epidermal necrolysis	Epidermal necrolysis	Epidermal necrolysis
Time between caspofungin administration and abnormal epidermal detachment[b]	8 days	1 day	3 days
Cutaneous biopsy at epidermal detachment	Necrosis of the corneal layer associated with calcium deposition in the superficial dermis and epidermis	Necrosis of the corneal layer associated with calcium deposition in the superficial dermis	Necrosis of the corneal layer associated with calcium deposition in the superficial dermis
Type of delayed cutaneous healing	Relapse of fibrinous erosions 17 days after complete healing	Extension of fibrinous erosions 3 days after the beginning of healing	Relapse of cutaneous erosions 22 days after complete healing
Topography of detachment	Anterior trunk and limbs	Limbs, trunk	Upper trunk, shoulders, back
Time to complete healing	166 days	Not available (died at day 33)	Not obtained at day 156

[a] SCORTEN is a specific severity-of-illness score for TEN, ranging from O to ≥5. A high SCORTEN is associated to a higher mortality rate.

[b] As defined by the day it was evidenced by the dermatologist.

was discharged from the ICU. Complete healing occurred 166 days after the second epidermal detachment.

Patient 2 was a 49 year-old man TEN with ibuprofen suspected. He was transferred to ICU because of respiratory distress. At day 3 after admission in ICU, he showed places of beginning of healing. On day 5, he presented non-documented septic shock and received vancomycin, piperacillin-tazobactam and caspofungin. On day 6, diffuse epidermal detachment was noted, together with extended fibrinous areas. He died on day 33 of multiple organ failure, without healing of fibrinous plaques.

Patient 3 was a 59 year-old male with TEN induced by allopurinol. He was transferred in the ICU and was rapidly treated with piperacilline-tazobactam for *Klebsiella aerogenes* pneumonia. On day 12 after admission, cutaneous healing was almost complete. The same day, caspofungin was administered for *Candida lusitaniae* catheter infection, with fluconazole relay 2 days later. On day 26, the patient presented a septic shock to *Candida parapsilosis*. Caspofungin was reintroduced for 2 days, followed by fluconazole for 12 more days. On day 34, dermatological examination revealed a diffuse epidermal detachment with extended atone fibrinous areas. On day 156, complete mucocutaneous healing still had not occurred.

In the three cases, skin biopsy performed at diagnosis revealed epidermal necrosis typical of EN [33].

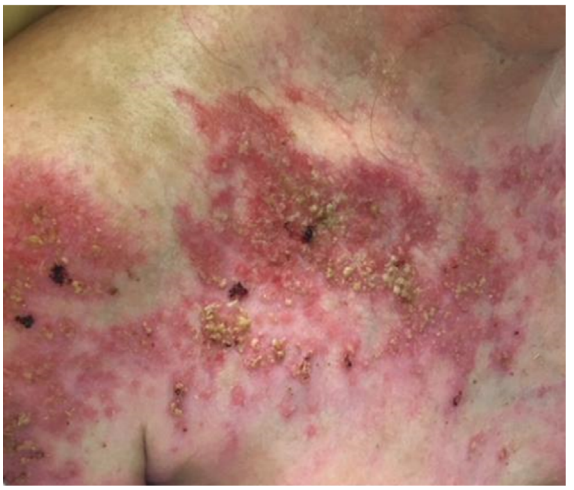

Figure 1. Clinical presentation of patient 1, showing delayed healing with prolonged erosions covered with yellowish crusts.

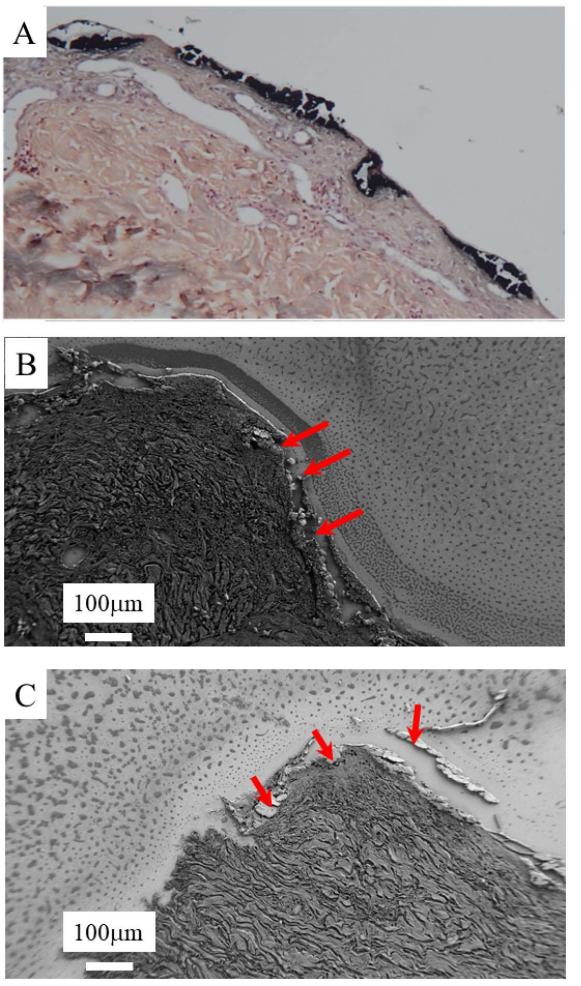

Figure 2. Skin biopsy sections. Diffuse necrosis of the corneal layer associated with calcium deposition in the superficial dermis. A, Von Kossa staining (×100). B and C, FE-SEM observations at low magnification. Red arrows indicate the voluminous calcifications.

In light of healing retardation, a new biopsy revealed diffuse necrosis of the corneal layer associated with calcium deposition in the superficial dermis and in the epidermis, which was confirmed by Von Kossa staining (Figure 2A). Median ionized calcemia was 1.19 (0.97–1.25) mmol/L (normally 1.15–1.33). No patient had received calcium supplementation. Median phosphoremia was 0.89 mmol/L (normally 0.61–1.11 mmol/L). Phosphate supplementation was administered in routine care [1]. The three patients received caspofungin for fungal sepsis, a rare infectious event in EN.

On retrospectively reviewing all patients ($n = 115$) in our centre between January, 2015 and December, 2020, four other patients with TEN had also received caspofungin: three had died in the following days without any dermatological examination. In the fourth case, new fibrinous plaques were described in the medical chart 4 days after caspofungin administration (no imaging or histology performed).

Caspofungin is an inhibitor of the β-D glucan synthesis of fungal pathogens [34]. Nonetheless, caspofungin is also a proven agonist of ryanodine receptor (RyR), found on cardiomyocytes and on pulmonary epithelial cells, inducing intracellular calcium influx from endoplasmic reticulum to cytosol [35,36]. Although the effect of caspofungin on keratinocytes has not been studied, Denda *et al.* [37] reported that RyR is strongly expressed in keratinocytes and that the application of another RyR agonist induced intracellular calcium flux, leading to a precocious keratinocyte differentiation in an *in vitro* model and a delayed cutaneous healing in a mouse model. All osteogenic markers were negative on keratinocytes as on fibroblasts, excluding a trans-differentiation to an osteochondrogenic phenotype.

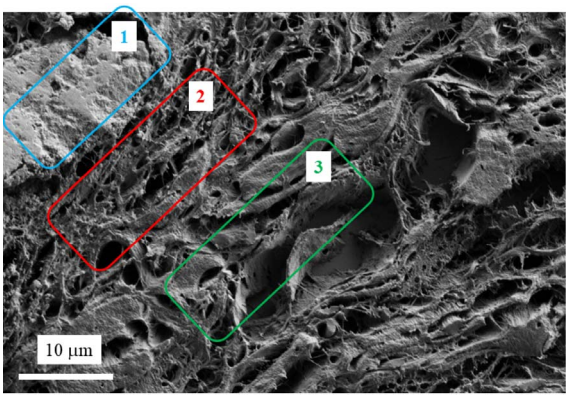

Figure 3. Skin biopsy sections as seen with a FE-SEM at higher magnification. A and B voluminous calcification (inside the blue rectangle) and spherical calcifications within the papillary dermis.

3.2. *The three different areas as defined by SEM observations*

FE-SEM revealed that these deposits consisted of voluminous plaques (Figures 2B and C). FE-SEM observations at higher magnification (Figure 3) underline the presence of the voluminous plaques (area 1 in Figure 3). Just below, we can see spherical entities within the papillary dermis (area 2 in Figure 3). Finally, an area which seems to be free of calcification can be defined (area 3 in Figure 3).

In order to gather information regarding the chemistry of the abnormal deposits, we have performed EDX and µFTIR. Figure 4 shows three EDX spectra. In the first one corresponding to the support, different elements are identified, namely O ($K_{\alpha 1}$ = 0.524 KeV), Zn ($K_{\alpha 1}$ = 8.638 KeV, K_{L1} = 1.011 KeV), Si ($K_{\alpha 1}$ = 1.740 KeV), P ($K_{\alpha 1}$ = 2.013 KeV), Ag ($L_{\alpha 1}$ = 2.985 KeV, $L_{\beta 1}$ = 3.150 KeV), K ($K_{\alpha 1}$ = 3.310 KeV) and Ca ($K_{\alpha 1}$ = 3.690 KeV, $K_{\beta 1}$ = 4.010 KeV) [38,39]. In EDX spectra (red line in Figure 4) related to the large calcification (area 1 in Figure 3), contribution coming from some elements present in the support namely Si, Ag, K and Zn are no more visible. Instead, contributions of Ca and P are associated with a strong amplitude. Note that the X-ray fluorescence peak at 1.0 KeV corresponds to a sum peak (star in Figure 4) due to the coincidence of two O $K_{\alpha 1}$ photons. Finally, in EDX spectra (blue line in Figure 4) related to the spherical calcifications (area 2 in Figure 3), contributions of Ca and P related to the calcifications and of other elements present in the support are measured.

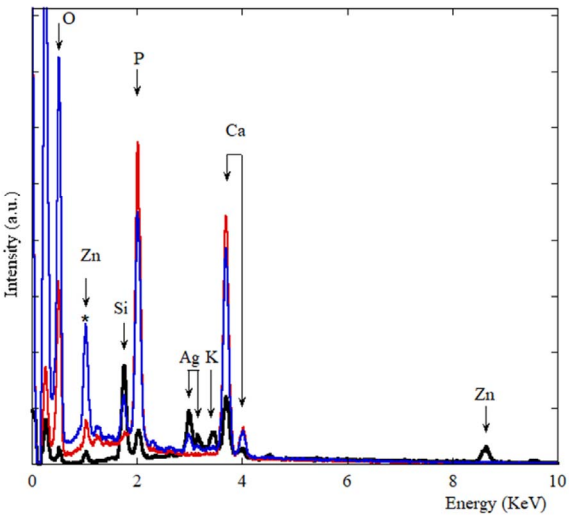

Figure 4. EDX spectra of the support (black line), calcification 1 (red line) and spherical entities which belong to calcification 2 (blue line). We can see the different contributions coming from the support namely O ($K_{\alpha 1}$ = 0.524 KeV), Zn ($K_{\alpha 1}$ = 8.638 KeV, K_{L1} = 1.011 KeV), Si ($K_{\alpha 1}$ = 1.740 KeV), P ($K_{\alpha 1}$ = 2.013 KeV), Ag ($L_{\alpha 1}$ = 2.985 KeV, $L_{\beta 1}$ = 3.150 KeV), K ($K_{\alpha 1}$ = 3.310 KeV) and Ca ($K_{\alpha 1}$ = 3.690 KeV, $K_{\beta 1}$ = 4.010 KeV).

On Figure 5, µFTIR spectra corresponding to large calcifications (red line in Figure 5) and tissue (black line in Figure 5) are visualized. µFTIR spectroscopy revealed that calcifications consisted of amorphous calcium phosphate and calcium-phosphate apatite which is consistent with the composition of most dystrophic skin calcifications [40–43].

3.3. *The pathogenesis of large calcifications*

On Figure 6, we can see that "large" submillimeter scale calcifications are the result of an agglomeration of micrometer scale spherical entities. Such fusion process of spherical entities leading to "large" submillimeter scale calcifications has been also observed in other organs such breast [44].

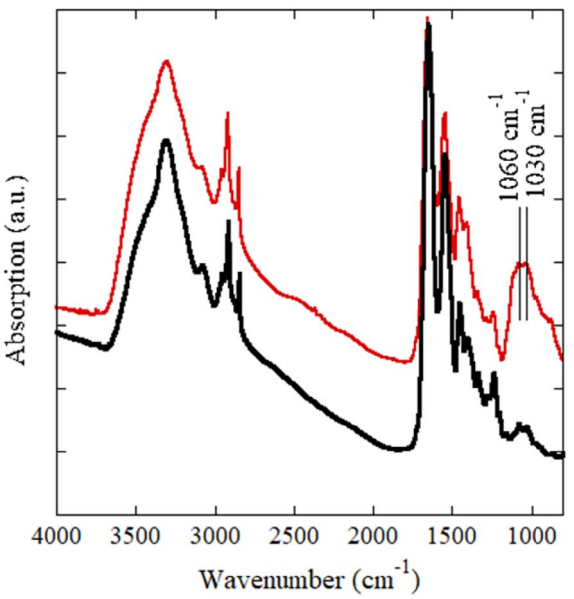

Figure 5. μFourier transform infra-red spectroscopy of calcium deposition. The presence of amorphous calcium phosphate and calcium phosphate apatite spectrum with characteristic peaks (1060 cm^{-1} and 1030 cm^{-1}) in a protein matrix (skin tissue) is detected.

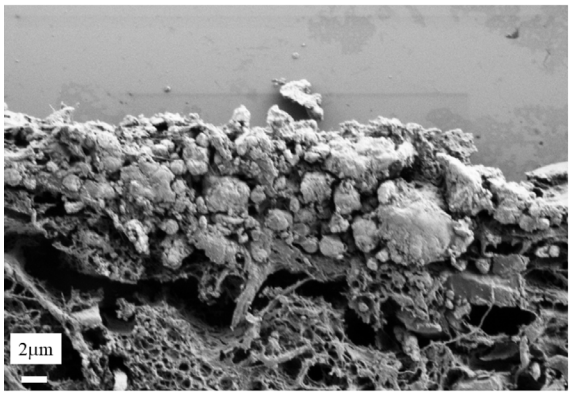

Figure 6. Area 1 is made of "large" calcifications (area 1 in Figure 3) which are the result of an agglomeration of small spherical entities (area 2 in Figure 3).

3.4. *The pathogenesis of micrometer spherical entities*

It is worth to underline that the internal structure of spherical entities may display different configuration as we have shown previously in the case of an investigation dedicated to breast calcifications (Figure 7) [44].

3.5. *The very first steps of the pathogenesis of micrometer spherical entities*

Finally, we have tried to localize precisely the very first steps of the calcification process. In Figure 8, we can see a set of nanometre scale spherical entities without micrometre spherical ones. It seems that the organisation of the skin is altered by the presence of the nanospherical calcifications. Intermingled tiny fibres are clearly visible around these calcifications and might be reticulin. Note that ectopic presence of reticulin has been found in pseudoxanthoma elasticum, a genetic calcifying skin disorders, suggesting the existence of a tropism of the calcification for such kind of fibres [45].

3.6. *Physiological and biochemical considerations*

The presence of spherical calcified entities within the upper but not deeper dermis suggests that these calcifications formed in the upper part of the skin tissue, contiguous to the epidermal necrolysis. Such co-location suggests a link between inflammation induced by the EN and calcifications, as in other dystrophic calcified skin diseases such as dermatomyositis [46,47].

Regarding the pathogenesis of these calcifications, caspofungin administration might have disrupted the extracellular/intracellular gradient of calcium in keratinocytes, causing an extracellular calcium deposit, associated with secondary epithelial detachment in these patients with previous skin fragility (ongoing TEN healing) and prolonged inflammation. Because of the negativity of osteogenic markers in all three patients, the hypothetical mechanism of trans-differentiation of fibroblasts or keratinocytes to an osteochondrogenic phenotype, as suspected with vascular smooth muscle cells of dermal arterioles in calciphylaxis, seems unlikely [48]. We acknowledge

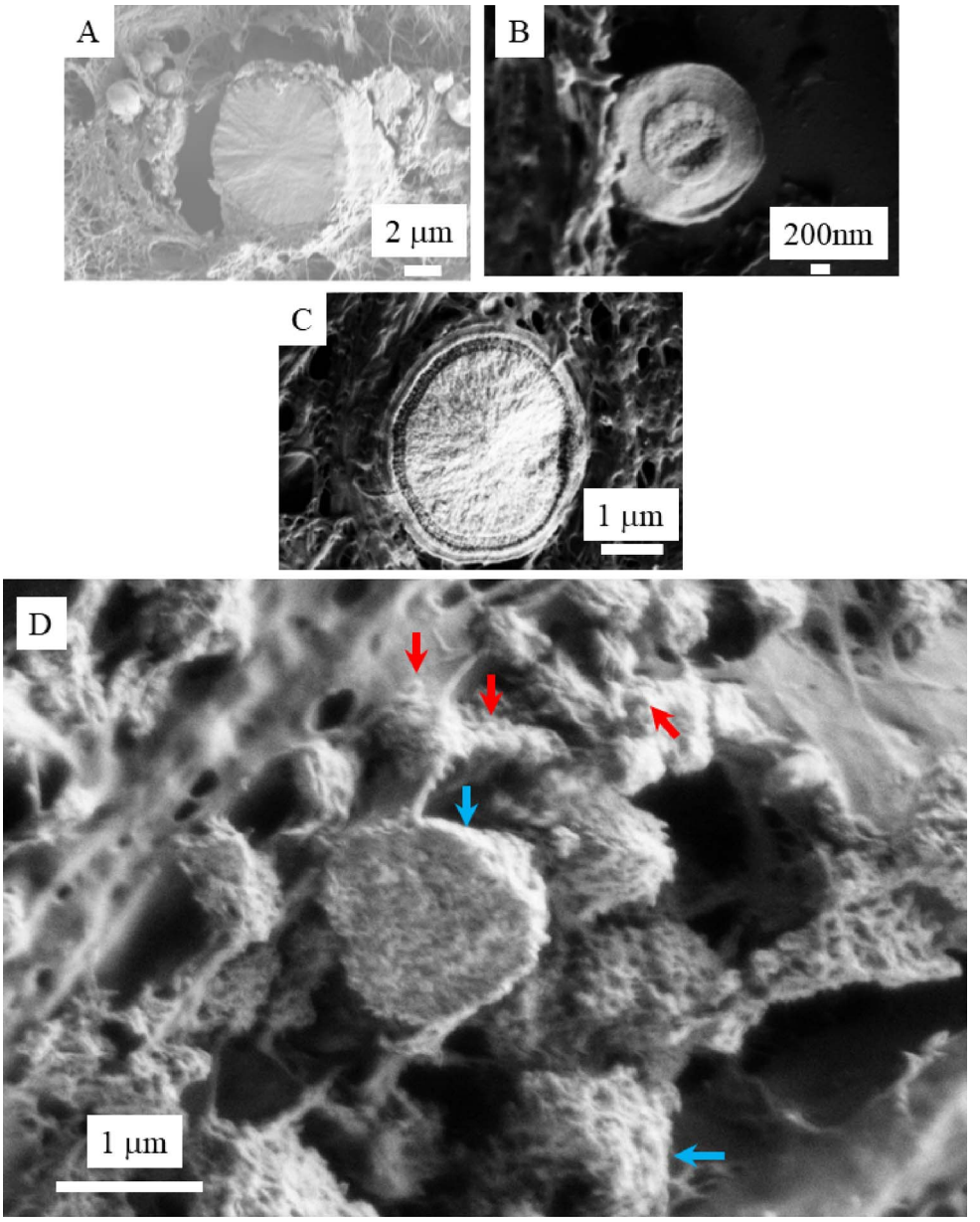

Figure 7. Spherical entities may display different internal structures: (A) Radial structures; (B): Concentric layers; (C): Both radial and concentric structure (A to C images are breast calcifications). In the case of calcinosis cutis (D), microspherical entities (blue arrows) result of an agglomeration of nano-spherules (red arrows).

some limitations of the study. The first is the retrospective design associated with a limited number of patients and the absence of a control arm. Moreover, we did not use an *in vitro* model of the possible pathogenesis link between calcification and caspofungin. Nonetheless, the occurrence of the same situation in three similar patients after caspofungin administration associated with a possible pathogenesis

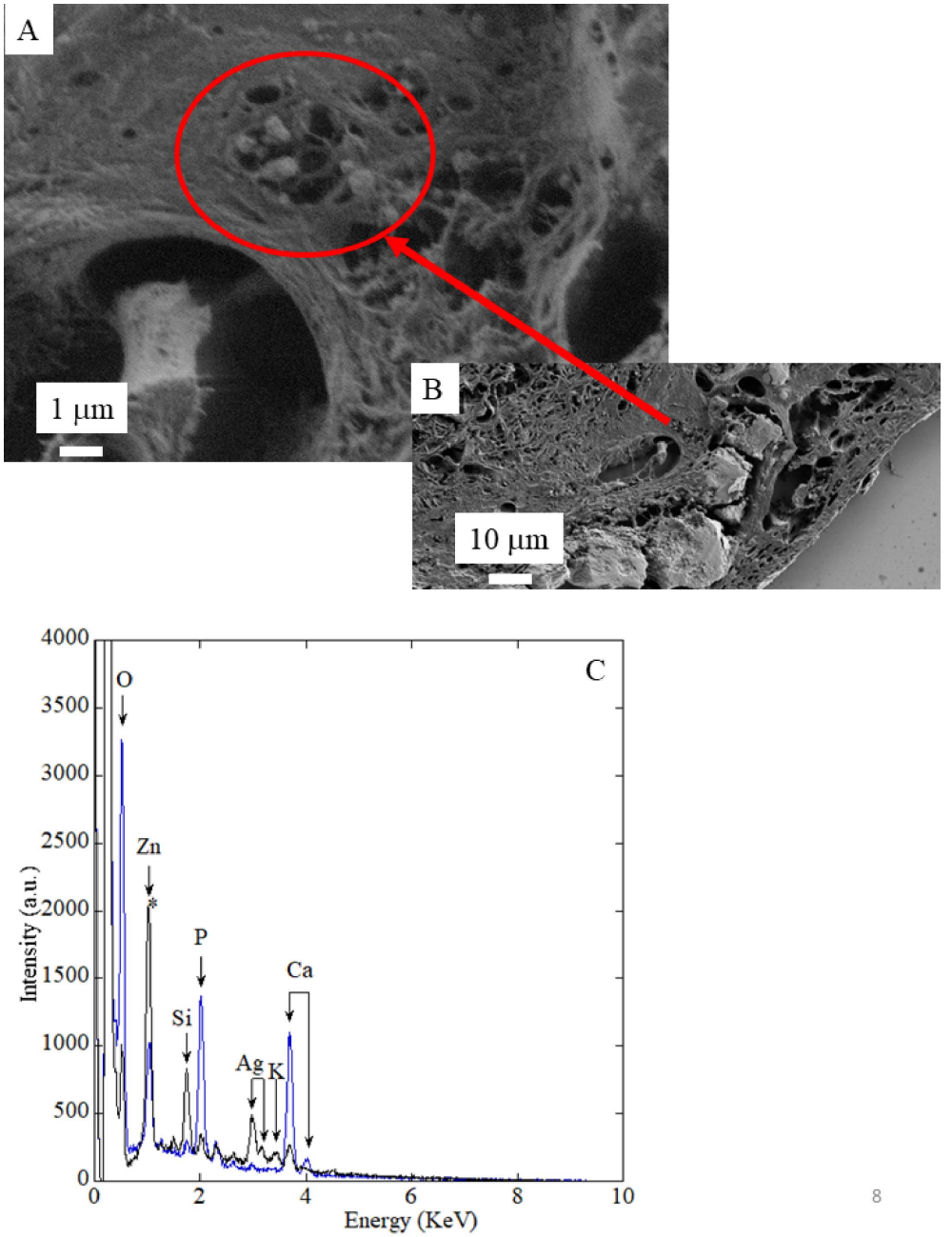

Figure 8. (A, B) Spherical entities as seen at two magnifications; (C) black line corresponds to the EDX spectra of the support and blue line corresponds to spherical entities visible in (A).

hypothesis raises the possible causality of caspofungin. Liposomal amphotericin B or fluconazole might therefore be preferred for patients with TEN in case of invasive fungal infection.

4. Conclusion

We have investigated a set of biopsies corresponding to patients who presented atypical healing retardation due to calcinosis cutis. Through SEM observations at the nanometer scale, we describe different areas: voluminous calcifications present at the surface of the skin tissue, submicrometer spherical entities within the papillary dermis and then normally structured dermal fibers. FE-SEM observations show clearly that "large" calcification are the result of an agglomeration of micrometer spherical entities. Moreover, micrometer scale spherical entities are the results of an agglomeration of nanometer scale spherical entities. Finally, the last set of data seems to show that the starting point of the calcifications process is "distant" from the epidermis in part of the dermis which appears undamaged.

From a medical point of view, our cases alert to the administration of caspofungin in patients presenting diffuse epidermal detachment and pave the way for further studies regarding dermatological adverse events induced by caspofungin, especially on mucocutaneous healing.

Conflicts of interest

Authors have no conflict of interest to declare.

Acknowledgment

The patients in this manuscript have given written informed consent to publication of their case details.

References

[1] S. Ingen-Housz-Oro, T.-A. Duong, B. Bensaid, N. Bellon, N. de Prost, D. Lu, B. Lebrun-Vignes, J. Gueudry, E. Bequignon, K. Zaghbib, G. Royer, A. Colin, G. Do-Pham, Ch. Bodemer, N. Ortonne, A. Barbaud, L. Fardet, O. Chosidow, P. Wolkenstein, *Orphanet J. Rare Dis.*, 2018, **13**, article no. 56.

[2] T. A. Duong, L. Valeyrie-Allanore, P. Wolkenstein, O. Chosidow, *The Lancet*, 2017, **390**, 1996-2011.

[3] A. Lecadet, P.-L. Woerther, C. Hua, A. Colin, C. Gomart, J.-W. Decousser, A. MekontsoDessap, P. Wolkenstein, O. Chosidow, N. de Prost, S. Ingen-Housz-Oro, *J. Am. Acad. Dermatol.*, 2019, **81**, 342-347.

[4] C. Le, P. M. Bedocs, "Calcinosis cutis", in *StatPearls [Internet]*, StatPearls Publishing, Treasure Island, FL, 2021, [Updated 2021 Jul 17]. Available from: https://www.ncbi.nlm.nih.gov/books/NBK448127/.

[5] H. Colboc, Ph. Moguelet, E. Letavernier, V. Frochot, J.-F. Bernaudin, R. Weil, S. Rouzière, P. Senet, C. Bachmeyer, N. Laporte, I. Lucas, V. Descamps, R. Amode, F. Brunet-Possenti, N. Kluger, L. Deschamps, A. Dubois, S. Reguer, A. Somogyi, K. Medjoubi, M. Refregiers, M. Daudon, D. Bazin, *C. R. Chim.*, 2022, **25**, no. S1, 445-476.

[6] H. Colboc, D. Bazin, P. Moguelet, S. Reguer, R. Amode, C. Jouanneau, I. Lucas, L. Deschamps, V. Descamps, N. Kluger, *J. Eur. Acad. Dermatol. Venereol.*, 2020, **34**, e313-e315.

[7] G. Forte, F. Petrucci, A. Cristaudo, B. Bocca, *Sci. Total Environ.*, 2009, **407**, 5997-6002.

[8] M. Arl, D. J. Nogueira, J. Sch. Köerich, N. M. Justino, D. S. Vicentini, W. G. Matias, *J. Hazard. Mater.*, 2019, **364**, 548-561.

[9] H. Colboc, D. Bazin, P. Moguelet, S. Reguer, R. Amode, C. Jouanneau, I. Lucas, L. Deschamps, V. Descamps, N. Kluger, *J. Synchrotron Radiat.*, submitted.

[10] L. Ch. Oliver, A. M. Zarnke, *Chest*, 160, **2021**, 1360-1367.

[11] L. S. Newman, C. S. Rose, E. A. Bresnitz, M. D. Rossman, J. Barnard, M. Frederick, M. L. Terrin, S. E. Weinberger, D. R. Moller, G. McLennan, G. Hunninghake, L. DePalo, R. P. Baughman, M. C. Iannuzzi, M. A. Judson, G. L. Knatterud, B. W. Thompson, A. S. Teirstein, H. Yeager Jr., C. J. Johns, D. L. Rabin, B. A. Rybicki, R. Cherniack, *Am. J. Respir. Crit. Care Med*, 170, **2004**, 1324-1330, ACCESS Research Group.

[12] H. Colboc, D. Bazin, Ph. Moguelet, V. Frochot, R. Weil, E. Letavernier, Ch. Jouanneau, C. Frances, C. Bachmeyer, J.-F. Bernaudin, M. Daudon, *C. R. Chim.*, 2016, **19**, 1631-1641.

[13] H. Colboc, P. Moguelet, D. Bazin, C. Bachmeyer, V. Frochot, R. Weil, E. Letavernier, C. Jouanneau, M. Daudon, J.-F. Bernaudin, *J. Eur. Acad. Dermatol. Venereol.*, 2019, **33**, 198-203.

[14] H. Colboc, Ph. Moguelet, D. Bazin, P. Carvalho, A.-S. Dillies, G. Chaby, H. Maillard, D. Kottler, E. Goujon, Ch. Jurus, M. Panaye, V. Frochot, E. Letavernier, M. Daudon, I. Lucas, R. Weil, Ph. Courville, J.-B. Monfort, F. Chasset, P. Senet, *JAMA Dermatol.*, 2019, **155**, 789-796.

[15] D. Bazin, M. Daudon, C. Combes, C. Rey, *Chem. Rev.*, 2012, **112**, 5092-5120.

[16] D. Bazin, M. Daudon, *J. Phys. D: Appl. Phys.*, 2012, **45**, article no. 383001.

[17] L. N. Poloni, M. D. Ward, *Chem. Mater.*, 2014, **26**, 477-495.

[18] D. Bazin, M. Daudon, *Ann. Biol. Clin.*, 2015, **73**, 517-534.

[19] S. R. Mulay, H.-J. Anders, *N. Engl. J. Med.*, 2016, **374**, 2465-2476.

[20] M. Li, J. Zhang, L. Wang, B. Wang, Ch. V. Putnis, *J. Phys. Chem. B*, 2018, **122**, 1580-1587.

[21] E. Tsolaki, S. Bertazzo, *Materials*, 2019, **12**, article no. 3126.

[22] M. Daudon, D. Bazin, *C. R. Chim.*, 2016, **19**, 1416-1423.

[23] D. Bazin, Ch. Jouanneau, S. Bertazzo, Ch. Sandt, A. Dessombz, M. Réfrégiers, P. Dumas, J. Frederick, J.-Ph. Haymann,

E. Letavernier, P. Ronco, M. Daudon, *C. R. Chim.*, 2016, **19**, 1439-1454.

[24] D. Bazin, E. Letavernier, J. P. Haymann, V. Frochot, M. Daudon, *Ann. Biol. Clin.*, 2020, **78**, 349-362.

[25] I. T. Lucas, D. Bazin, M. Daudon, *C. R. Chim.*, 2022, **25**, no. S1, 83-103.

[26] S. Tamosaityte, M. Pucetaite, A. Zelvys, S. Varvuolyte, V. Hendrixson, V. Sablinskas, *C. R. Chim.*, 2022, **25**, no. S1, 73-72.

[27] F. Brisset, *Microscopie Électronique à Balayage et Microanalyses*, EDP Sciences, Paris, France, 2012.

[28] M. Racek, J. Racek, I. Hupáková, *Scand. J. Clin. Lab. Invest.*, 2019, **79**, 208-217.

[29] D. Bazin, E. Bouderlique, M. Daudon, V. Frochot, J.-Ph. Haymann, E. Letavernier, F. Tielens, R. Weil, *C. R. Chim.*, 2022, **25**, no. S1, 37-60.

[30] H. Colboc, T. Bettuzzi, M. Badrignans, D. Bazin, A. Boury, E. Letavernier, V. Frochot, E. Tang, P. Moguelet, N. Ortonne, N. de Prost, S. Ingen-Housz-Oro, *J. Eur. Acad. Dermatol. Venereol.*, 2022, **36**, e313-e315.

[31] D. Bazin, M. Daudon, *J. Spectr. Imaging*, 2019, **8**, article no. a16.

[32] D. Bazin, J.-Ph. Haymann, E. Letavernier, J. Rode, M. Daudon, *Presse Med.*, 2014, **43**, 135-148.

[33] L. Valeyrie-Allanore, S. Bastuji-Garin, S. Guégan, N. Ortonne, M. Bagot, J.-C. Roujeau, J. E. Revuz, J. Wechsler, P. Wolkenstein, *J. Am. Acad. Dermatol.*, 2013, **68**, e29-e35.

[34] P. L. McCormack, C. M. Perry, *Drugs*, 2005, **65**, 2049-2068.

[35] S. Müller, C. Koch, S. Weiterer, M. A. Weigand, M. Sander, M. Henrich, *Sci. Rep.*, 2020, **10**, article no. 11723.

[36] C. Koch, J. Jersch, E. Schneck, F. Edinger, H. Maxeiner, F. Uhle, M. A. Weigand, M. Markmann, M. Sander, M. Henrich, *Antimicrob. Agents Chemother.*, 2018, **62**, e01114-e01118.

[37] S. Denda, J. Kumamoto, K. Takei, M. Tsutsumi, H. Aoki, M. Denda, *J. Invest. Dermatol.*, 2012, **132**, 69-75.

[38] S. Rouzière, D. Bazin, M. Daudon, *C. R. Chim.*, 2016, **19**, 1404-1415.

[39] D. Bazin, E. Foy, S. Reguer, S. Rouzière, B. Fayard, H. Colboc, J.-Ph. Haymann, M. Daudon, C. Mocuta, *C. R. Chim.*, 2022, **25**, no. S1, 165-188.

[40] J. C. Elliott, *Structure and Chemistry of the Apatites and other Calcium Orthophosphates*, Elsevier, Amsterdam, 1994.

[41] C. Combes, C. Rey, *Minerals*, 2016, **6**, article no. 34.

[42] D. Eichert, C. Drouet, H. Sfihia, C. Rey, C. Combes, "Nanocrystalline apatite-based biomaterials: synthesis, processing and characterization", in *Trends in Biomaterials Research* (J. Patrick, ed.), Nova Science Publishers Inc., Pannone, 2007.

[43] N. Reiter, L. El-Shabrawi, B. Leinweber, A. Berghold, E. Aberer, *J. Am. Acad. Dermatol.*, 2011, **65**, 1-12.

[44] A. Ben Lakhdar, M. Daudon, M. C. Matthieu, A. Kellum, C. Balleyguier, D. Bazin, *C. R. Chim.*, 2016, **19**, 1610-1624.

[45] L. Danielsen, T. Kobayasi, H. W. Larsen, K. Midtgaard, H. E. Christensen, *Acta Derm. Venereol.*, 1970, **50**, 355-373.

[46] H. Colboc, Ph. Moguelet, D. Bazin, A. Croué, V. Frochot, M. Daudon, R. Weil, E. Letavernier, L. Martin, *Annales de Dermatologie et de Vénéréologie*, 2019, **146**, article no. A202.

[47] G. Munavalli, A. Reisenauer, M. Moses, S. Kilroy, J. L. Arbiser, *J. Dermatol.*, 2003, **30**, 915-919.

[48] S. U. Nigwekar, R. Thadhani, V. M. Brandenburg, *N. Engl. J. Med.*, 2018, **378**, 1704-1714.

Comptes Rendus
Chimie
2022, Vol. 25, Special Issue S1, p. 489-502
https://doi.org/10.5802/crchim.135

Microcrystalline pathologies: Clinical issues and nanochemistry / *Pathologies microcristallines : questions cliniques et nanochimie*

Cystinuria and cystinosis are usually related to L-cystine: is this really the case for cystinosis? A physicochemical investigation at micrometre and nanometre scale

Dominique Bazin [*, a], **Marion Rabant** [b], **Jérémie Mathurin** [a], **Margaux Petay** [a], **Ariane Deniset-Besseau** [a], **Alexandre Dazzi** [a], **Yangyang Su** [c], **Etienne P. Hessou** [c], **Frederik Tielens** [c], **Ferenc Borondics** [d], **Marine Livrozet** [e, f], **Elise Bouderlique** [e, f], **Jean-Philippe Haymann** [e, f], **Emmanuel Letavernier** [e, f], **Vincent Frochot** [e, f] **and Michel Daudon** [e, f]

[a] Institut de Chimie Physique, Université Paris-Saclay, 310, rue Michel Magat, 91400, Orsay, France

[b] Pathology Department, Necker-Enfants Malades Hospital, 75015 Paris, France

[c] General Chemistry (ALGC) – Materials Modelling Group, Vrije Universiteit Brussel (Free University Brussels-VUB), Pleinlaan 2, 1050 Brussel, Belgium

[d] Synchrotron SOLEIL, L'Orme des Merisiers, Saint-Aubin, BP 48, 91192 Gif-sur-Yvette Cedex, France

[e] INSERM, UMRS 1155, UPMC, Hôpital Tenon, 75970 Paris, France

[f] Service d'Explorations Fonctionnelles, Hôpital Tenon, AP-HP, 4, rue de la Chine, 75970 Paris Cedex 20, France

E-mails: Dominique.bazin@u-psud.fr (D. Bazin), marion.rabant@aphp.fr (M. Rabant), jeremie.mathurin@u-psud.fr (J. Mathurin), margaux.petay@universite-paris-saclay.fr (M. Petay), ariane.deniset@u-psud.fr (A. Deniset-Besseau), alexandre.dazzi@u-psud.fr (A. Dazzi), Yangyang.Su@vub.be (Y. Su), Etienne.Paul.Hessou@vub.be (E. P. Hessou), frederik.tielens@vub.be (F. Tielens), ferenc.borondics@synchrotron-soleil.fr (F. Borondics), marine.livrozet@aphp.fr (M. Livrozet), Eliseboud@aol.com (E. Bouderlique), jean-philippe.haymann@tnn.aphp.fr (J.-P. Haymann), Emmanuel.letavernier@aphp.fr (E. Letavernier), vincent.frochot@aphp.fr (V. Frochot), daudonmichel24@gmail.com (M. Daudon)

Abstract. Medical literature indicates clearly that cystinuria and cystinosis, two severe genetic pathologies, are related to the presence of abnormal L-cystine deposits. While L-cystine adopts a hexagonal crystal morphology consistent with its crystallographic structure (hexagonal, $P6_122$ space

* Corresponding author.

group), abnormal deposits related to cystinosis display a rectangular shape. Because this is unexpected from the hexagonal crystallographic structure of L-cystine, we have investigated this inconsistency using SEM (scanning electron microscopy) and IR (infrared) spectroscopy at micrometre and nanometre scales. Our data clearly indicate the presence of both L-cysteine and L-cystine. Considering that L-cysteine crystals display a rectangular shape, and that a transition phase between L-cysteine and L-cystine is well known, we propose the following model for deposit evolution in cystinosis. The initial abnormal deposit consists of L-cysteine, with a rectangular crystal morphology. The micrometre scale rectangular crystallite shape is retained after the phase transition equilibrium between L-cysteine and L-cystine is established, with some crystalline L-cysteine still remaining.

Keywords. Cystinuria, Cystinosis, FTIR, SEM, AFM-IR, OPTIR.
Published online: 30 November 2021

1. Introduction

Several genetic pathologies lead to the formation of abnormal deposits in the human body [1–4]. Some induce kidney stone formation and/or crystalline nephropathy [5,6] such as primary hyperoxaluria [7–10], adenine phosphoribosyltransferase deficiency [11–15] or distal renal tubular acidosis [16]. In the case of cystinuria and cystinosis, a precise determination of the chemical composition of the abnormal deposits can be a considerable aid to diagnosis.

Cystinuria is an autosomal recessive disorder arising from a mutation in renal epithelial cell transporters [17–21], which induces a significant reduction in dibasic amino acids and L-cystine (cystine—$C_6H_{12}N_2O_4S_2$) reabsorption by the proximal tubule. The poor solubility of cystine in urine leads to a high risk of cystine precipitation and the formation of cystine crystallites (Figure 1a), and eventually of kidney stones (Figure 1b) [22–25].

Cystinosis [26] is a rare autosomal recessive lysosomal storage disorder, the treatment of which has advanced in recent years [27]. In cystinosis patients, cystine accumulates in the lysosomes of cells [28]. The presence of cystine has been reported in many organs and tissues namely kidneys, eyes, muscles, thyroid and pancreas [29]. A small number of publications have reported physicochemical investigation of abnormal deposits in these tissues. Frazier and Wong [30] have characterised the rectangular extracellular crystalline forms observed in ocular tissue in two childhood and two adult cases by X-ray diffraction (XRD), leading to the identification of cystine crystals. More recently, Centeno *et al.* [31] have confirmed this chemical composition based on Raman spectroscopy analysis of abnormal deposits present in liver and spleen. Note that various extracellular matrices and proteins may affect the initial crystal structure.

Based on our previous investigation on kidney stones composed of cystine [24], such results are quite surprising. The crystallographic structure of cystine reported by Dahaoui *et al.* [32], displays the space group $P6_122$, predicting that cystine crystallites should exhibit hexagonal morphology in kidney stones; however in cystinosis cases cystine crystallites with a rectangular morphology are observed.

This unusual cystine crystal habit in cystinosis pathology requires investigation using a panel of physicochemical analytical tools able to decipher their morphology and chemistry at the micrometre and then the nanometre scale [33–38]. To do this, we undertook a structural and spectroscopic analysis of such abnormal deposits using scanning electron microscopy (SEM) [14,39,40], μFTIR (Fourier Transform InfraRed) [14,41,42], AFM-IR (atomic force microscopy coupled with IR) spectroscopy [43,44] and OPTIR (Optical Photothermal IR) spectroscopy [45,46].

SEM offers the opportunity to directly observe the morphology and size of crystallites at the micrometre scale and contributes significantly to the structural description of cystine crystals (see for examples [47–54]). μFTIR spectroscopy constitutes the gold standard for precisely determining the chemical composition of kidney stones [41,42,55,56]. AFM-IR [43,44] and OPTIR [45,46] are able to collect IR spectra beyond the diffraction limit i.e. around 50 nm and 500 nm, respectively. The complete set of techniques can precisely describe the morphology and chemical nature of the abnormal deposits in tissues or cells in cystinuria and cystinosis at the submicrometre scale.

2. Materials and methods

The biological samples analysed in the present investigation were provided by the Necker and Tenon

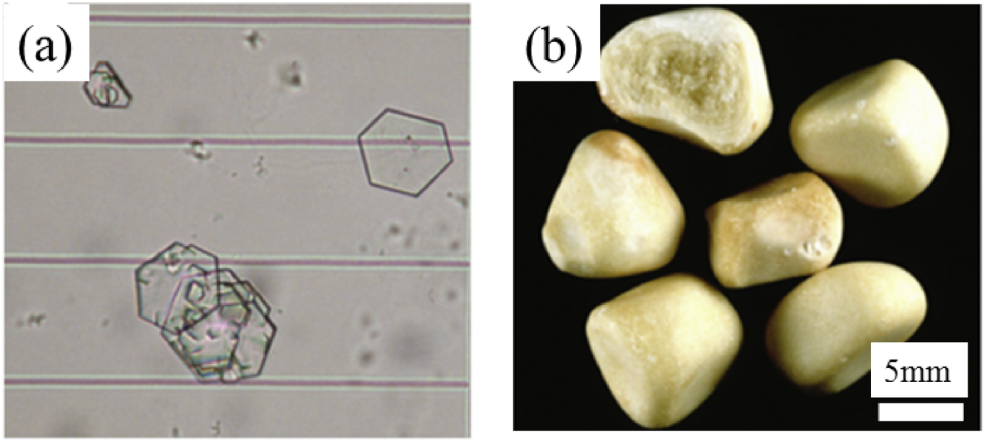

Figure 1. Optical images of (a) cystine crystallites in urine and (b) of cystine kidney stones (from Letavernier *et al.* [19]).

hospitals, following the usual ethics procedures strictly [13]. All participants (adults or parents of children participating in the study) gave their verbal consent, documented by the researchers, for use of the material. Samples were examined without knowledge of the name of the patient or other identifying data. Ethical approval for the study was obtained from the ethics committee of Tenon Hospital. The investigation conformed to the principles of the Declaration of Helsinki.

Regarding cystinuria, SEM observations have been performed on cystine crystals present in urine. This investigation is also based on SEM observations, FTIR and neutron diffraction data on twenty-five cystine kidney stones which has already been published [24] and on the kidney stone data bank in which 1216 kidney stones have been studied through FTIR spectroscopy. Regarding cystinosis, only one kidney biopsy has been considered in this investigation.

For precise characterisation of the surface of an abnormal biological sample, observations at the micrometre scale were performed using a FEI/Philips XL40 environmental scanning electron microscope [39,40]. Compared to a conventional scanning electron microscope this device does not need a conductive coating and thus permits direct observation with no damage to the sample. Imaging was performed with a low accelerating voltage (around 1 kV).

At the micrometre scale, the pathological calcifications were first characterised using FTIR spectroscopy (Vector 22, Bruker Spectrospin, Wissembourg, France) as previously described [41,42]. Data were collected in absorption mode between 4000 and 400 cm^{-1}, with 4 cm^{-1} spectral resolution.

Chemical characterisations of the pathological calcifications in kidney biopsies at the nanometre scale were performed by two techniques which use mid-infrared photons, namely AFM-IR and OPTIR.

The AFM-IR system used for this study is a NanoIR2 (Bruker Nano, Santa Barbara). It couples an AFM system with a quantum cascade laser focus on the AFM tip for top-down illumination. The laser covers the wavenumber range from 900 cm^{-1} to 1945 cm^{-1} with a tuneable repetition rate which allows enhanced mode acquisition [57] which is more sensitive than the setup we have already used to study abnormal deposits in the kidney [58]. AFM acquisitions were made in contact mode with a gold-coated silicon cantilever (Budget Sensors, contact mode, 13 kHz, 0.2 N/m). For this study, only AFM topographies were acquired and all local IR spectra were collected with 1 cm^{-1} spectral resolution and an average of 20 acquisitions.

OPTIR measurements (spectra and images) were done on a mIRage™ Infrared Microscope (Photothermal Spectroscopy Corp., Santa Barbara, CA, USA). Samples were placed on low-e microscope slides (MirrIR, Kevley Technologies, Tienta Sciences, Indianapolis). To generate data high signal-to-noise ratio, 20–50 spectra were collected in reflection mode, at 2 cm^{-1} spectral data points spac-

ing, through a 40×, 0.78 NA, 8 mm working distance Schwarzschild objective. The pump IR source was a pulsed, tunable four-stage QCL device, scanning from 800 to 1900 cm^{-1}, and we used a CW 532 nm visible variable power probe laser.

A Density Functional Theory-Dispersion corrected (DFT-D) IR spectrum was calculated. The computational procedures are similar to those described in our earlier studies [59–63].

3. Results and discussion

3.1. *The case of cystinuria*

The structural characterisation of cystine kidney stones has been discussed in several publications. Consistent with its crystallographic structure (hexagonal crystal system, $P6_122$ space group), all the papers on synthetic [47–54] or biological [18–21,24,55,56,64–66] cystine have reported a hexagonal morphology. On SEM observations, at the micrometre scale, we can clearly see the hexagonal shape of the cystine deposits in kidney stones from mice and humans affected by cystinuria (Figure 2).

For a complete classification of kidney stones [5, 6], the determination of the morphology of these concretions is complemented by chemical composition determined by FTIR spectroscopy [41,42,67]. In Figure 3, we plot the FTIR spectrum of biological cystine (in this case from a human kidney stone). It is compared with a theoretical (DFT-D) spectrum in the IR spectral range from 700 to 1800 cm^{-1} on which the present study focuses.

The IR spectrum of zwitterionic cystine was calculated between 500 and 3500 cm^{-1}. In the experimental IR spectrum (Figure 3, Table 1), the 1035 cm^{-1} absorption peak corresponds to the C–N stretching vibration. The bands at 1372, 1197 and 1125 cm^{-1} are the C–C stretching vibrations, and that at 1406 cm^{-1} is due to CH_2–CO deformation. Finally, the band at 1490 cm^{-1} is due to COO– stretching while bands at 1584 and 845 cm^{-1} are due to the asymmetric deformation and rocking vibrations of NH^{3+}, supporting the zwitterionic nature of cystine in the solid state. These results are consistent with previous publications [68–70].

Comparing the experimental with the DFT-D spectrum, a global shift in wavenumbers can be observed. Van der Waals interactions, which are difficult to evaluate even with the inclusion of the dispersion corrections we used, can explain this well-known discrepancy. Besides, the DFT-D calculations were performed at 0 K whereas the experimental spectrum was recorded at 300 K. Both effects are known to af-

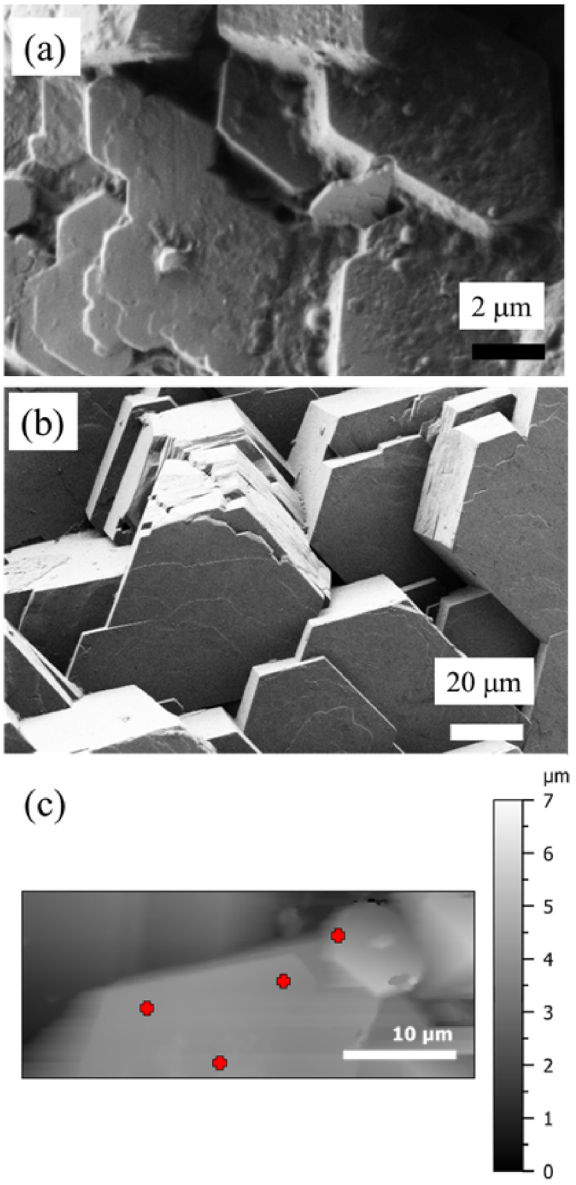

Figure 2. (a) SEM observation of cystine crystallites in kidney stones from mice; cystine crystallites present in human urine (b) by SEM and (c) by AFM. The red crosses on (c) indicate the different points selected for acquisition of IR spectrum using the 50 nm probe.

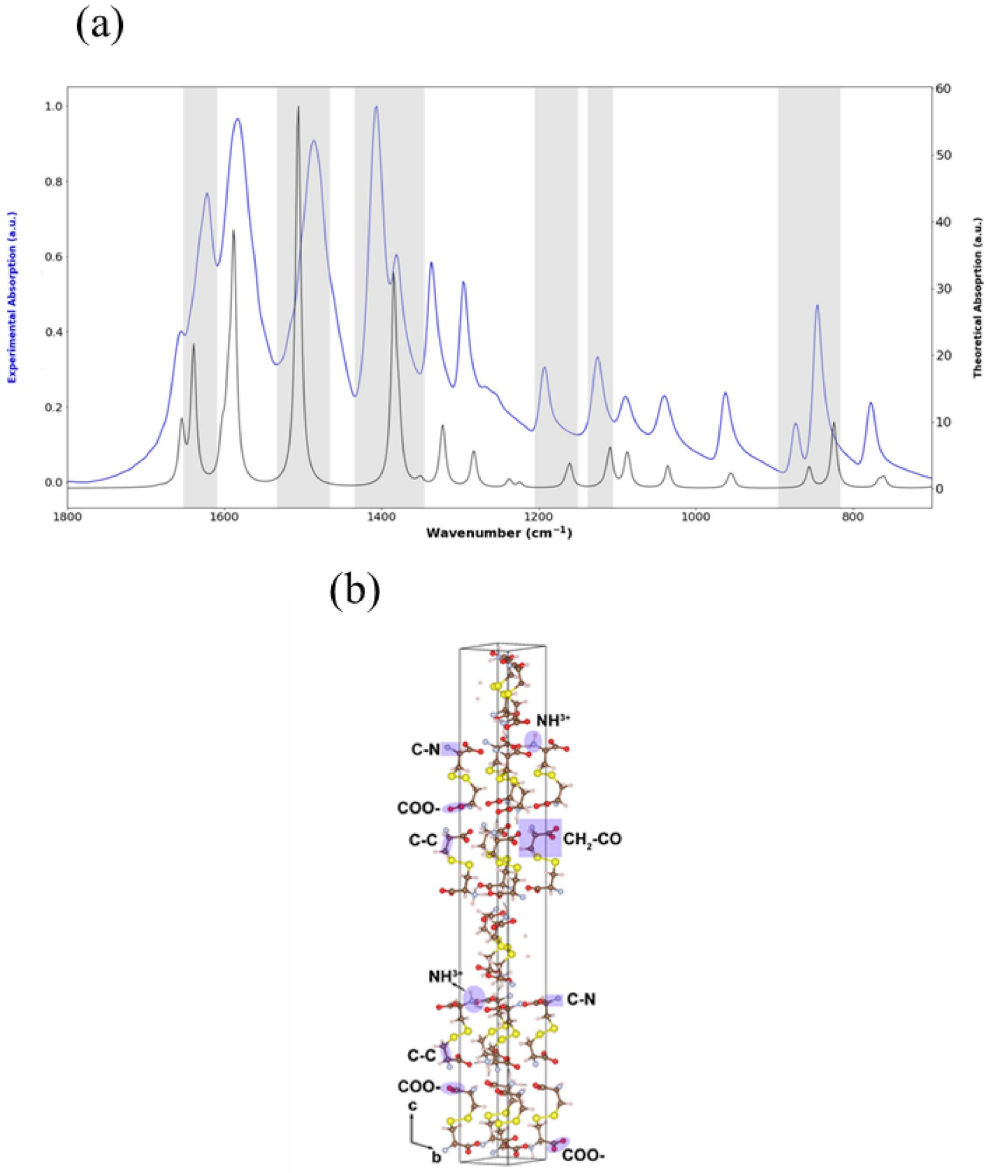

Figure 3. (a) DFT-D theoretical (black) and experimental (blue) IR spectra between 1800 cm^{-1} and 800 cm^{-1}. For the experimental data, a μFTIR spectrometer was used. The most significant wavenumber shifts between theoretical and experimental absorption bands are highlighted in grey. (b) Crystallographic structure of cystine.

fect the harmonic oscillator approximation negatively. Moreover, the cystine crystal structure is modelled as a periodic defect-free lattice, whereas the experimental sample consists of crystallites of finite sizes; this difference also affects the correspondence between theory and experiment. This small disagreement confirms that the real sample is composed of finite crystallites that probably contain different types of atomic level crystal defects.

In the human kidney stone case, we have compared the IR spectrum of cystine obtained by μFTIR and the ones obtained by AFM-IR and OPTIR (Figure 4). Although we can see extensive similarity between all the three spectra, some differences exist.

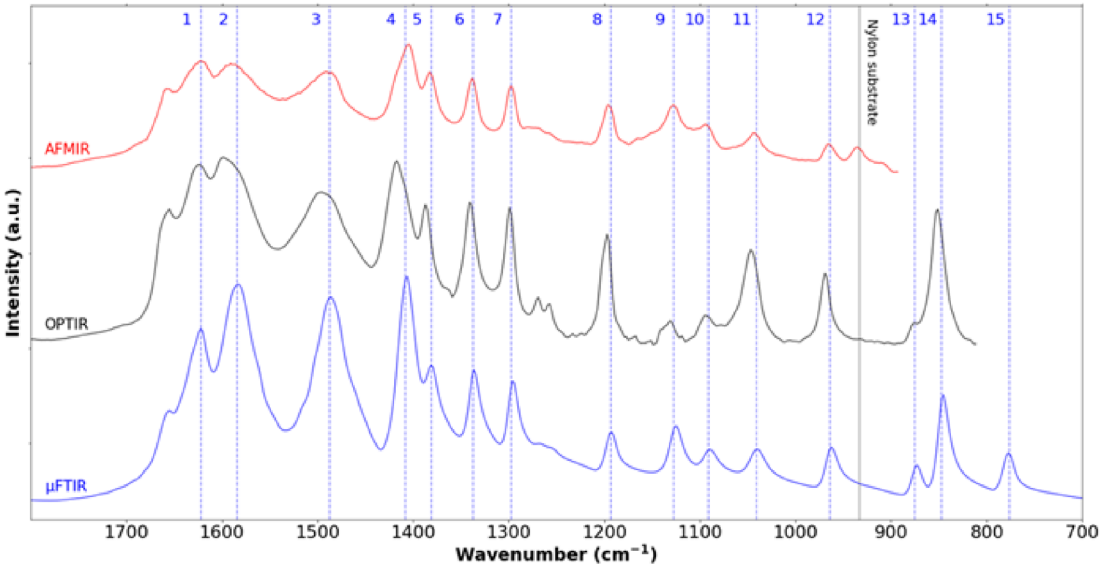

Figure 4. Cystine crystallites in cystinuria. IR spectra collected between 1800 cm^{-1} and 800 cm^{-1} using three different experimental setups namely μFTIR (blue—cystine kidney stone), OPTIR (black—cystine crystallite in human urine) and AFM-IR (red—cystine crystallite in human urine). We can see the different characteristic IR bands 1622 cm^{-1} (1), 1584 cm^{-1} (2), 1487 cm^{-1} (3), 1408 cm^{-1}(4), 1381 cm^{-1} (5), 1337 cm^{-1} (6), 1297 cm^{-1} (7), 1193 cm^{-1} (8), 1127 cm^{-1} (9), 1091 cm^{-1} (10), 1041 cm^{-1} (11), 964 cm^{-1} (12), 875 cm^{-1} (13), 847 cm^{-1} (14) and 776 cm^{-1} (15). IR absorption band at 933 cm^{-1} corresponds to the nylon support.

Table 1. Infrared bands of cystine and their assignments

1035 cm^{-1}	C–N stretching
1372, 1197 and 1125 cm^{-1}	C–C stretching
1406 cm^{-1}	CH_2–CO deformation
1490 cm^{-1}	COO^- stretching
1584 and 845 cm^{-1}	NH^{3+} asymmetric deformation and rocking vibrations

We observe a supplementary IR absorption band in the AFM-IR spectrum due to the support material (black vertical line at 933 cm^{-1} in Figure 4). Also, note some small spectral shifts between the spectrum obtained by μFTIR and those obtained with the two photothermic techniques. These discrepancies seem to be optical in origin but work to understand this fully is still in progress. A point which can already be highlighted is a possible polarisation effect on the observed spectra. Unlike μFTIR measurement, the light from quantum cascade lasers used in OPTIR and AFM-IR has an intrinsic polarisation which can induce changes in band intensity in spectra of highly oriented objects such as crystals compared to those from μFTIR. As a consequence, for each technique it may be possible to have different band intensities from the same sample depending on the orientation of the object. Furthermore, the angle of incident illumination is different from OPTIR and AFM-IR, inducing different polarisation effects even for a sample with the same orientation. AFM-based techniques such as AFM-IR also produces a micrometre scale image of the sample (Figure 2c) which can be compared to SEM observation of the same sample (Figure 2b). This is not the case for OPTIR which is associated with an optical microscope. The red crosses

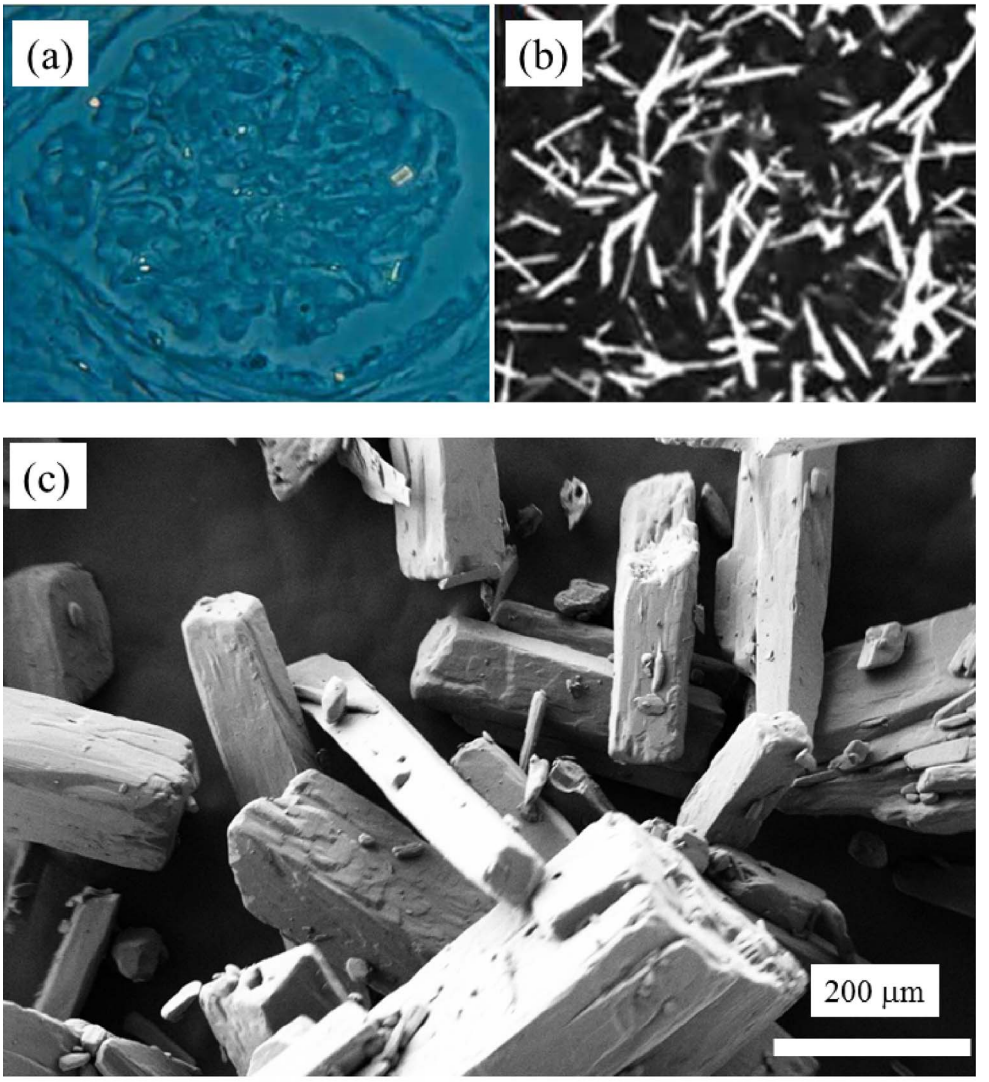

Figure 5. Crystallites in cystinosis. (a) Rectangular morphologies of abnormal deposits observed in kidney (according to [24]). (b) Rectangular morphologies of abnormal deposits observed by slit lamp in the cornea (according to [60]). (c) Synthetic cysteine crystals observed by SEM (Figure 5a from Nesterova *et al.* [29] and Figure 5b from Elmonem *et al.* [71]).

in Figure 2c indicate different points on which the 50 nm probe has been positioned to acquire an IR spectrum.

3.2. *The case of cystinosis*

3.2.1. *Observations of abnormal deposits through optical microscope*

The cystinosis situation is quite different from cystinuria. An analysis of the literature [29–31,71,72] indicates that cystine is the only compound represented in the abnormal deposits and that such crystals (Figures 5 and 6) do not exhibit a hexagonal morphology. Optical microscopy in contrast shows a rectangular crystal morphology in both the kidney (Figure 5a, according to Nesterova *et al.* [29]) and the cornea (Figure 5b, according to Elmonem *et al.* [71]).

A kidney biopsy from a patient (B1742) reveals rectangular crystal morphology in the abnormal deposits (Figure 6). However, such an examination

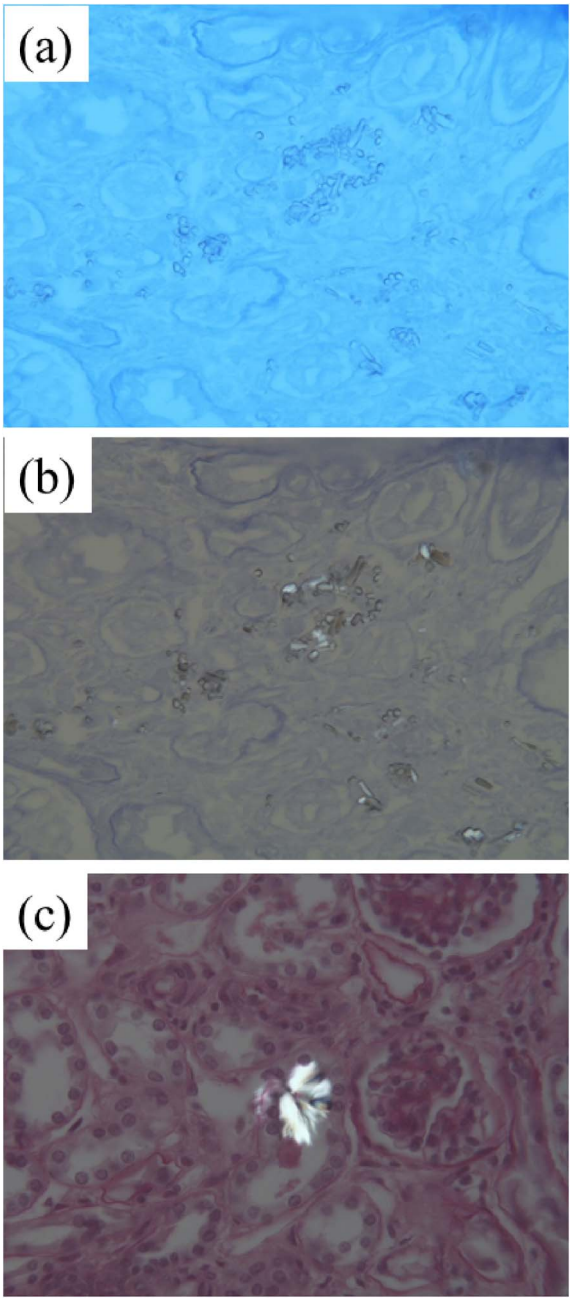

Figure 6. Light microscopy images from the kidney biopsy of a patient with cystinosis. (a) Toluidine Blue (×400). (b) Small isolated or aggregated crystals. (c) Birefringent aggregated rectangular crystals seen under polarised light.

is not a characterisation of the chemistry of these structures.

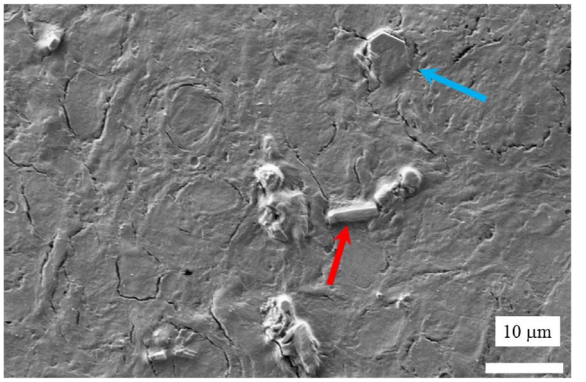

Figure 7. SEM observation of abnormal deposits in the kidney biopsy of a cystinosis patient (kidney biopsy deposited on a low-e microscope slide).

3.2.2. *Characterisation at the micrometre scale*

We start by locating the abnormal deposits in the kidney biopsy (B1742) by SEM. At the micrometre scale, Figure 7 shows the presence of two kinds of morphologies, the usual cystine hexagonal one (blue arrow), and the morphology typical in a cystinosis patient i.e. a rectangular one (red arrow). Note that with dimensions of 4–5 µm, such hexagonal crystals can be detected by optical microscopy if isolated, but this is difficult if they are embedded in tissue, as in this example.

We then performed a range of µFTIR experiments (Figure 8, Table 2). In the top panel of the figure, we have indicated the IR bands associated with cystine by blue numbers, and in the bottom panel those of cysteine by red. The three IR spectra of the sample (black in Figure 8 corresponding to the abnormal deposits displayed in Figure 7) in fact arise from a combination of IR bands associated with tissue (black lines in Figure 8) and those associated with cystine (blue line in Figure 8). The first three IR bands (1, 2, 3 in blue in Table 2) are obscured by signal from the tissue. This is consistent with the literature on physicochemical characterisation of crystals present in the tissue of patients with cystinosis. We now present results from nanometre scale IR spectroscopy.

3.2.3. *Characterisation at the nanometre scale*

We chose the same sample for OPTIR experiments as the one we used for µFTIR. Figure 9 shows IR

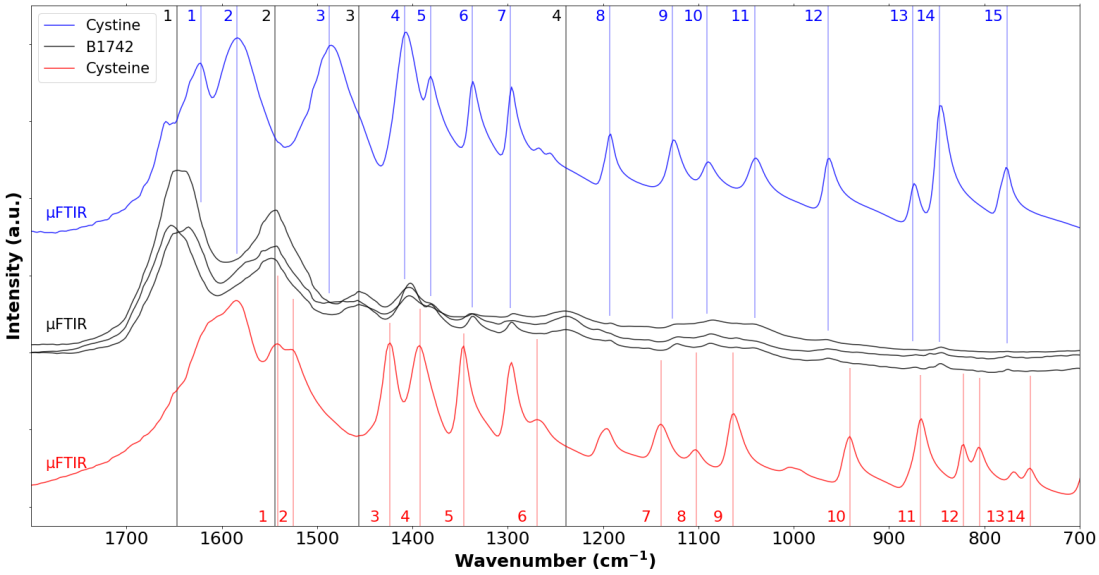

Figure 8. FTIR spectra of the B1742 sample (black) compared to the IR spectra of cystine (blue) and cysteine (red), coloured dashed lines indicate the specific positions for each species, respectively, B1742 sample (black), cystine (blue) and cysteine (red).

spectra from the sample (black spectra) collected by OPTIR with a device yielding a spatial resolution of ≈500 nm. This explains why tissue IR bands can still be observed but with lower relative intensity (black lines 1, 2, 3 and 4). This new set of experimental data shows cystine IR bands (Table 2). However the striking point of these OPTIR measurement is the observation of IR peaks related to cysteine at 1541 cm^{-1} (IR band number 1 of cysteine; all subsequent band numbers also correspond to those of cysteine), 1521 cm^{-1} (band 2), 1424 cm^{-1} (band 3 of cysteine), 1392 cm^{-1} (band 4), 1345 cm^{-1} (band 5), 1060 cm^{-1} (band 9) and 867 cm^{-1} (band 11); those at 1060 cm^{-1} (band 9) and 867 cm^{-1} (band 11) are quite intense.

To perform structural and chemical characterisation at the nanometre scale with the AFM-IR experimental setup, part of the kidney biopsy was deposited on a CaF_2 slide. SEM (Figure 10) was performed prior to AFM-IR and led to similar conclusions regarding the morphology of the biopsy crystallites.

Figure 11 plots a localised IR spectrum collected with the ≈50 nm spatial resolution AFM-IR experimental setup; the tissue bands are not apparent because the high spatial resolution confines the IR signal to the crystals in the biopsy only. At first sight, the IR bands of the sample are similar to the IR bands of cystine. Nevertheless, it seems that various shoulders are observed in the AFM-IR spectrum which likely correspond to cysteine (1424 cm^{-1}, band 3; 1392 cm^{-1}, band 4; 1345 cm^{-1}, band 5; 1269 cm^{-1} band 6; 1137 cm^{-1}, band 7; and 1060 cm^{-1}, band 9).

In conclusion, from the results obtained at the nanoscale with both techniques, OPTIR and AFM-IR, it seems that the sample can be understood as a mixing of cystine and cysteine instead of pure cystine as observed in μFTIR.

3.3. *Discussion*

As previously reported, cystinosis affects all ocular structures [73]. The most frequently described ocular manifestation is cystine crystal deposition in the cornea [74]. As underlined by Csorba *et al.* [65], in vivo confocal microscopy (IVCM) constitutes the best imaging technique to characterise corneal cystine crystals in vivo [72–81]. This literature indicates that IVCM enables quantification and identification of the

Table 2. Position of the IR bands obtained for the reference compounds (cystine and cysteine) and for the samples in μFTIR, OPTIR and AFM-IR

Sample	Reference compounds		Patient		
	Cystine	Cysteine	μFTIR	OPTIR	AFM-IR
1–1647 cm^{-1}			1	1	
	1–1622 cm^{-1}			1	1
	2–1584 cm^{-1}			2	2
2–1544 cm^{-1}			2	2	
		1–1541 cm^{-1}		1	
		2–1521 cm^{-1}		2	
	3–1487 cm^{-1}				3
3–1456 cm^{-1}			3	3	
		3–1424 cm^{-1}		3	3
	4–1408 cm^{-1}		4	4	4
		4–1392 cm^{-1}		4	
	5–1381 cm^{-1}		5	5	5
		5–1345 cm^{-1}		5	5
	6–1337 cm^{-1}		6	6	6
	7–1297 cm^{-1}		7	7	7
		6–1269 cm^{-1}			6
4–1239 cm^{-1}			4	4	
	8–1193 cm^{-1}		8	8	8
		7–1137 cm^{-1}			7
	9–1127 cm^{-1}		9	9	9
		8–1101 cm^{-1}			
	10–1091 cm^{-1}		10	10	10
		9–1060 cm^{-1}		9	9
	11–1041 cm^{-1}		11	11	11
	12–964 cm^{-1}		12	12	12
		10–937 cm^{-1}			
	13–875 cm^{-1}		13		
	14–847 cm^{-1}		14		
		11–867 cm^{-1}		11	
		12 – 817 cm^{-1}			
		13–805 cm^{-1}			
	15–776 cm^{-1}		15		
		14–750 cm^{-1}			

deposits at the cellular level, and is thus considered as the gold standard for ophthalmological follow-up of patients with cystinosis [73–81]. Nevertheless, it is worth mentioning that a detailed description of crystal morphology is not equivalent to chemical identification.

The physicochemistry of cystinosis seems to be quite inconsistent. The literature clearly indicates the

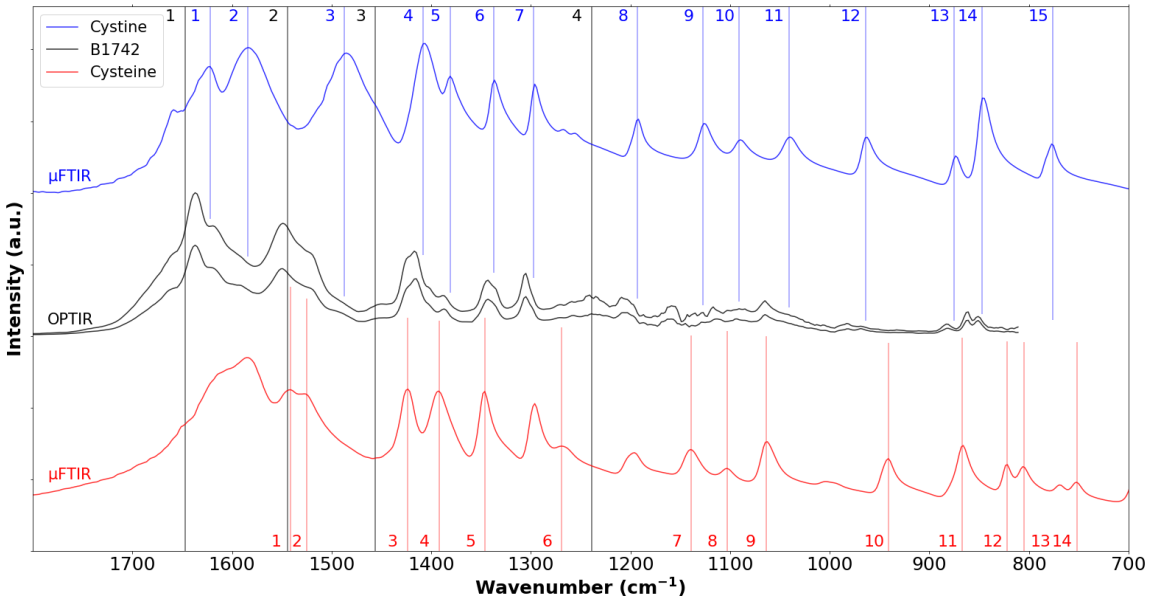

Figure 9. OPTIR spectra of the B1742 sample (black line) compared to the IR spectra of cystine (blue) and cysteine (red).

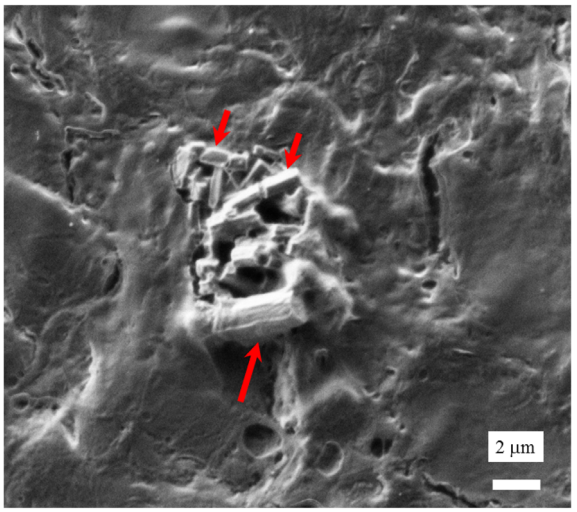

Figure 10. SEM observation of abnormal deposits (red arrows) in the kidney biopsy of a nephropathic cystinosis patient.

presence of rectangular crystals made of cystine [29–31,71–79,81]. Such morphology is not expected for cystine crystals which are typically hexagonal for synthetic [47–54] as well as for biological [18–21,24,55,56, 64–66] samples. Rectangular-like crystallites are observed in the case of synthetic cysteine (Figure 5c). This observation is complemented by our IR data collected at the nanometre scale using OPTIR (Figure 9) and AFM-IR (Figure 11) which clearly suggest the presence of domains of cysteine and of cystine. Such chemical heterogeneity may explain why the signals measured by AFM-IR and OPTIR are not exactly the same. In our study, we have also identified the presence of hexagonal crystals (Figure 7). Such mixing is consistent with the chemistry of these two compounds, namely that cysteine is spontaneously oxidised to cystine at neutral pH [82–84]. All these data seem to show that in fact cystinosis is linked to the pathogenesis of cysteine crystallites associated with a rectangular morphology, and to the pathogenesis of cystine, as evidenced by our observation of hexagonal cystine crystals.

It is worth pointing out that there is an analogous crystalline conversion which occurs in kidney stones, from weddellite (unstable) to whewellite (stable). In this case, the conversion also results in contradictory FTIR spectra indicating whewellite whereas bipyramidal crystallites, a morphology specific to weddellite, can be observed [85]. In fact, the

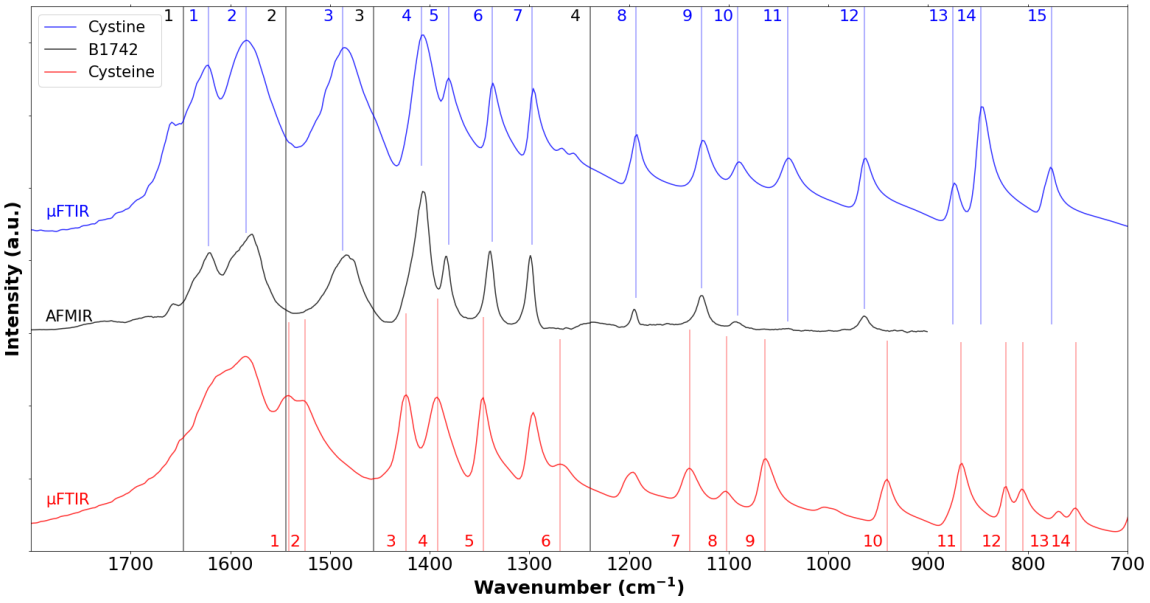

Figure 11. AFM-IR spectrum of the B1742 sample (black line) compared to the IR spectra of cystine (blue line) and cysteine (red line).

IR spectra corresponding to such kidney stones (undergoing the weddellite to whewellite phase transition) exhibit IR spectra which do not correspond exactly to whewellite. Some subtle differences exist which indicate the presence of amorphous calcium oxalate monohydrate which constitutes an intermediate state reflecting the dissolution–recrystallisation process. In our case it seems that a phase transition also occurs but probably without a dissolution–recrystallisation process and thus a similar situation is observed i.e. a lack of intensity for the IR band at 1584 cm^{-1}. It may be due to the fact that the final chemical composition comprising cystine and cysteine associated with acicular crystallites may alter the intensity of IR bands. Work is in progress to better understand this experimental observation.

Finally, we have to mention a possible weak point of this investigation which is related to the low number of samples considered in this investigation. Although the section of this study dedicated to cystinuria is based on a large number of publications, only one patient has been considered in this research. Despite this fact, we believe that the existence of crystallites of pure cystine as well as the well-known phase transition between cysteine and cystine constitute strong arguments supporting the idea that cystinosis leads to pathogenic cysteine crystallites.

4. Conclusion

A comprehensive set of SEM micrometre scale and IR micrometre and nanometre scale data suggests that cystinosis is related to the pathogenesis of rectangular crystals of cysteine and not cystine. This is probably due to the well-known phase transition between cysteine and cystine which occurs at room temperature.

Acknowledgements

Computational resources and services were also provided by the Shared ICT Services Centre funded by the Vrije Universiteit Brussel, the Flemish Supercomputer Center (VSC) and FWO. FT wishes to acknowledge the VUB for support, including a Strategic Research Program awarded to his group.

References

[1] J. A. Sayer, *Nephron Exp. Nephrol.*, 2008, **110**, e37-e43.

[2] L. Beara-Lasic, V. O. Edvardsson, R. Palsson, J. C. Lieske, D. S. Goldfarb, D. S. Milliner, *Clin. Rev. Bone Miner. Metab.*, 2012, **10**, 2-18.

[3] P. M. Ferraro, A. D'Addessi, G. Gambaro, *Nephrol. Dial. Transplant.*, 2013, **28**, 811-820.

[4] G. Rumsby, *Int. J. Surg.*, 2016, **36**, 590-595.

[5] M. Daudon, C. A. Bader, P. Jungers, *Scanning Microsc.*, 1993, **7**, 1081-1104.

[6] M. Daudon, A. Dessombz, V. Frochot, E. Letavernier, J. P. Haymann, P. Jungers, D. Bazin, *C. R. Chim.*, 2016, **19**, 1470-1491.

[7] P. Cochat, *Kidney Int.*, 1999, **55**, 2533-2547.

[8] E. Leumann, B. Hoppe, *J. Am. Soc. Nephrol.*, 2001, **12**, 1986-1993.

[9] M. Daudon, P. Junger, D. Bazin, *N. Engl. J. Med.*, 2008, **359**, 100-102.

[10] M. Daudon, D. Bazin, G. André, P. Jungers, A. Cousson, P. Chevallier, E. Véron, G. Matzen, *J. Appl. Cryst.*, 2009, **42**, 109-115.

[11] G. Bollée, C. Dollinger, L. Boutaud, D. Guillemot, A. Bensman, J. Harambat, P. Deteix, M. Daudon, B. Knebelmann, I. Ceballos-Picot, *J. Am. Soc. Nephrol.*, 2010, **21**, 679-688.

[12] G. Bollée, J. Harambat, A. Bensman, B. Knebelmann, M. Daudon, I. Ceballos-Picot, *Clin. J. Am. Soc. Nephrol.*, 2012, **7**, 1521-1527.

[13] A. Dessombz, D. Bazin, P. Dumas, C. Sandt, J. Sule-Suso, M. Daudon, *PLoS One*, 2011, **6**, article no. e28007.

[14] D. Bazin, M. Daudon, *Ann. Biol. Clin.*, 2015, **73**, 517-534.

[15] P. Eriksson, T. Denneberg, H. G. Tiselius, *Urol. Res.*, 1996, **24**, 39-43.

[16] A. Dessombz, E. Letavernier, J.-P. Haymann, D. Bazin, M. Daudon, *J. Urol.*, 2015, **193**, 1564-1569.

[17] E. Pras, N. Arber, I. Aksentijevich, G. Katz, J. M. Schapiro, L. Prosen, L. Gruberg, D. Harel, U. Liberman, J. Weissenbach, M. Pras, D. L. Kastner, *Nat. Genet.*, 1994, **6**, 415-419.

[18] H. Bouzidi, M. Daudon, *Annal. Biol. Clin.*, 2007, **65**, 473-481.

[19] E. Letavernier, O. Traxer, J.-P. Haymann, D. Bazin, M. Daudon, *Prog. Urol. – FMC*, 2012, **22**, F119-F123.

[20] J. P. Haymann, M. Livrozet, J. Rode, S. Doizi, O. Traxer, V. Frochot, E. Letavernier, D. Bazin, M. Daudon, *Prog. Urol. – FMC*, 2021, **31**, F1-F7.

[21] M. Livrozet, S. Vandermeersch, L. Mesnard, E. Thioulouse, J. Jaubert, J.-J. Boffa, J.-P. Haymann, L. Baud, D. Bazin, M. Daudon, E. Letavernier, *PLoS One*, 2014, **9**, article no. e102700.

[22] M. Daudon, F. Cohen-Solal, F. Barbey, M.-F. Gagnadoux, B. Knebelmann, P. Jungers, *Urol. Res.*, 2003, **31**, 207-211.

[23] A. P. Evan, F. L. Coe, J. E. Lingeman, Y. Shao, B. R. Matlaga, S. C. Kim, S. B. Bledsoe, A. J. Sommer, M. Grynpas, C. L. Phillips, E. M. Worcester, *Kidney Int.*, 2006, **69**, 2227-2235.

[24] D. Bazin, M. Daudon, G. André, R. Weil, E. Véron, G. Matzen, *J. Appl. Cryst.*, 2014, **47**, 719-725.

[25] K. H. Andreassen, K. V. Pedersen, S. S. Osther, H. U. Jung, S. K. Lilda, P. J. S. Osther, *Urolithiasis*, 2016, **44**, 65-76.

[26] W. A. Gahl, J. G. Thoene, J. A. Schneider, *N. Engl. J. Med.*, 2002, **347**, 111-121.

[27] A. Jamalpoor, C. AGH van Gelder, F. A. Yousef Yengej, E. A. Zaal, S. P. Berlingerio, K. R. Veys, C. P. Casellas, K. Voskuil, K. Essa, C. M. E. Ammerlaan, L. R. Rega, R. van der Welle, M. R. Lilien, M. B. Rookmaaker, H. Clevers, J. Klumperman, E. Levtchenko, C. R. Berkers, M. C. Verhaar, M. Altelaar, R. Masereeuw, M. J. Janssen, *EMBO Mol. Med.*, 2021, **13**, article no. e13067.

[28] A. Servais, C. Goizet, A. Bertholet-Thomas, S. Decramer, B. Llanas, G. Choukroun, R. Novo, *Néphrol. Thérapeut.*, 2015, **11**, 152-159.

[29] G. Nesterova, W. Gahl, *Pediatr. Nephrol.*, 2008, **23**, 863-878.

[30] P. D. Frazier, V. G. Wong, *Arch. Ophthalmol.*, 1968, **80**, 87-91.

[31] J. A. Centeno, K. G. Ishak, F. G. Mullick, W. A. Gahl, T. J. O'Leary, *Appl. Spectrosc.*, 1994, **48**, 569-572.

[32] S. Dahaoui, V. Pichon-Pesme, J. A. K. Howard, C. Lecomte, *J. Phys. Chem. A*, 1999, **103**, 6240-6250.

[33] D. Bazin, M. Daudon, C. Combes, C. Rey, *Chem. Rev.*, 2012, **112**, 5092-5120.

[34] D. Bazin, M. Daudon, *J. Phys. D: Appl. Phys.*, 2012, **45**, article no. 383001.

[35] D. Bazin, J.-P. Haymann, E. Letavernier, J. Rode, M. Daudon, *Presse Med.*, 2014, **43**, 135-148.

[36] D. Bazin, E. Letavernier, J.-P. Haymann, P. Méria, M. Daudon, *Prog. Urol.*, 2016, **26**, 608-618.

[37] E. Tsolaki, S. Bertazzo, *Materials*, 2019, **12**, article no. 3126.

[38] N. Vidavsky, J. A. M. R. Kunitake, L. A. Estroff, *Adv. Healthc. Mater.*, 2020, article no. e2001271.

[39] F. Brisset, M. Repoux, J. Ruste, F. Grillon, F. Robaut, *Microscopie Électronique à Balayage et Microanalyses*, EDP Sciences, Les Ulis, France, 2009.

[40] R. F. Egerton, *Physical Principles of Electron Microscopy, An Introduction to TEM, SEM, and AEM*, Springer-Verlag, US, 2005.

[41] N. Quy Dao, M. Daudon, *Infrared and Raman Spectra of Calculi*, Elsevier, Paris, 1997.

[42] L. Estepa, M. Daudon, *Biospectroscopy*, 1997, **3**, 347-369.

[43] A. Dazzi, F. Glotin, R. Carminati, *J. Appl. Phys.*, 2010, **107**, article no. 124519.

[44] A. Dazzi, C. B. Prater, *Chem. Rev.*, 2017, **117**, 5146-5173.

[45] D. Zhang, C. Li, C. Zhang, M. N. Slipchenko, G. Eakins, J.-X. Cheng, *Sci. Adv.*, 2016, **2**, article no. e1600521.

[46] O. Klementieva, C. Sandt, I. Martinsson, M. Kansiz, G. K. Gouras, F. Borondics, *Adv. Sci.*, 2020, **7**, article no. 1903004.

[47] M. Ejgenberg, Y. Mastai, *Cryst. Growth Des.*, 2012, **12**, 4995-5001.

[48] L. N. Poloni, Z. Zhu, N. Garcia-Vázquez, A. C. Yu, D. M. Connors, L. Hu, A. Sahota, M. D. Ward, A. G. Shtukenberg, *Cryst. Growth Des.*, 2017, **17**, 2767-2781.

[49] J. D. Rimer, Z. An, Z. Zhu, M. H. Lee, D. S. Goldfarb, J. Wesson, M. D. Ward, *Science*, 2010, **330**, 337-341.

[50] D. Heimbach, D. Jacobs, S. C. Müller, A. Hesse, *Urology*, 2000, **55**, 17-21.

[51] T. Mandal, A. G. Shtukenberg, A. C. Yu, X. Zhong, M. D. Ward, *Cryst. Growth Des.*, 2016, **16**, 423-431.

[52] M. Adobes-Vidal, A. G. Shtukenberg, M. D. Ward, P. R. Unwin, *Cryst. Growth Des.*, 2017, **17**, 1766-1774.

[53] M. Song, W. Li, X. Zhang, J. Liu, K. Li, H. Zhang, *ACS Earth Space Chem.*, 2021, **5**, 1525-1534.

[54] A. G. Shtukenberg, L. N. Poloni, Z. Zhu, Z. An, M. Bhandari, P. Song, A. L. Rohl, B. Kahr, M. D. Ward, *Cryst. Growth Des.*, 2015, **15**, 921-934.

[55] G. H. Noehden, *Ann. Philos.*, 1824, **7**, article no. 146.
[56] S. R. Khan, R. L. Hackettm, *J. Urol.*, 1986, **135**, 818-825.
[57] F. Lu, M. Belkin, *Opt. Express*, 2011, **19**, 19942-19947.
[58] E. Esteve, Y. Luque, J. Waeytens, D. Bazin, L. Mesnard, C. Jouanneau, P. Ronco, A. Dazzi, M. Daudon, A. Deniset-Besseau, *Anal. Chem.*, 2020, **92**, 7388-7392.
[59] J. Vekeman, F. Tielens, *Nanomaterials*, 2020, **10**, article no. 540.
[60] I. Petit, G. D. Belletti, T. Debroise, M. Llansola, I. T. Lucas, C. Leroy, C. Bonhomme, L. Bonhomme-Coury, D. Bazin, M. Daudon, E. Letavernier, J. P. Haymann, V. Frochot, F. Babonneau, P. Quaino, F. Tielens, *Chem. Select.*, 2018, **3**, 8801-8812.
[61] T. Debroise, E. Colombo, G. Belletti, J. Vekeman, Y. Su, R. Papoular, N. S. Hwang, D. Bazin, M. Daudon, P. Quaino, F. Tielens, *Cryst. Growth Des.*, 2020, **20**, 2553-2561.
[62] I. Can Oğuz, H. Guesmi, D. Bazin, F. Tielens, *J. Phys. Chem. C*, 2019, **123**, 20314-20318.
[63] F. Tielens, J. Vekeman, D. Bazin, M. Daudon, *C. R. Chim.*, 2022, **25**, no. S1, 209-218.
[64] A. Hesse, G. Sanders, D. B. Leusman, *Scan. Electron. Microsc.*, 1986, **1986**, 1705-1712.
[65] M. Racek, J. Racek, I. Hupáková, *Scand. J. Clin. Lab. Investig.*, 2019, **79**, 208-217.
[66] T. Qiao, R.-H. Ma, X.-B. Luo, Y.-Y. Feng, X.-Q. Wang, P.-M. Zheng, Z.-L. Luo, *Eur. J. Med. Res.*, 2012, **17**, article no. 6.
[67] M. Daudon, D. Bazin, *C. R. Chim.*, 2016, **19**, 1416-1423.
[68] S. K. Chandran, R. Paulraj, P. Ramasamy, *Spectrochim. Acta A: Mol. Biomol. Spectr.*, 2015, **151**, 432-437.
[69] T. U. Devi, N. Lawrence, R. Rameshbabu, S. Selvanayagam, H. Stoeckli-Evans, G. Bhagavannarayana, K. Ramamurthi, *J. Miner. Mater. Charact. Eng.*, 2010, **9**, 495-507.
[70] Y. Su, E. P. Hessou, P. Quiano, E. Colombo, A. Moussadik, I. Lucas, V. Frochot, M. Daudon, D. Bazin, F. Tielens, submitted, to be published in the *Journal of Crystal Growth*.
[71] M. A. Elmonem, K. R. Veys, N. A. Soliman, M. van Dyck, L. P. van den Heuvel, E. Levtchenko, *Orphanet J. Rare Dis.*, 2016, **11**, article no. 47.
[72] H. Liang, C. Baudouin, R. T. J. Hassani, F. Brignole-Baudouin, A. Labbe, *Investig. Ophthalmol. Vis. Sci.*, 2015, **56**, 3218-3225.
[73] A. Csorba, E. Maka, O. A. Maneschg, A. Szabó, N. Szentmáry, M. Csidey, M. Resch, L. Imre, K. Knézy, Z. Z. Nagy, *BMC Ophthalmol.*, 2020, **20**, article no. 73.
[74] H. Liang, C. Baudouin, R. Tahiri Joutei Hassani, F. Brignole-Baudouin, A. Labbe, *Investig. Ophthalmol. Vis. Sci.*, 2015, **56**, 3218-3225.
[75] A. H. Alsuhaibani, A. O. Khan, M. D. Wagoner, *Br. J. Ophthalmol.*, 2005, **89**, 1530-1531.
[76] F. Shams, I. Livingstone, D. Oladiwura, K. Ramaesh, *Clin. Ophthalmol.*, 2014, **8**, 2077-2084.
[77] A. Labbe, P. Niaudet, C. Loirat, M. Charbit, G. Guest, C. Baudouin, *Ophthalmology*, 2009, **116**, 870-876.
[78] C. N. Grupcheva, S. E. Ormonde, C. McGhee, *Arch Ophthalmol.*, 2002, **120**, 1742-1745.
[79] A. M. Pinxten, M. T. Hua, J. Simpson, K. Hohenfellner, E. Levtchenko, I. Casteels, *Ophthalmol. Ther.*, 2017, **6**, 93-104.
[80] H. Liang, A. Labbe, J. Le Mouhaer, C. Plisson, C. Baudouin, *Investig. Ophthalmol. Vis. Sci.*, 2017, **58**, 2275-2283.
[81] A. Labbe, C. Baudouin, G. Deschenes, C. Loirat, M. Charbit, G. Guest, P. Niaudet, *Mol. Genet. Metab.*, 2014, **111**, 314-320.
[82] O. Warburg, *Biochem. Z.*, 1927, **187**, article no. 255.
[83] L. H. Gray, *Progress in Radiobiology*, vol. 267, Oliver and Boyd, Ltd, Edinburgh, UK, 1956.
[84] D. L. Dewey, J. Beecher, *Nature*, 1965, **206**, 1369-1370.
[85] D. Bazin, C. Leroy, F. Tielens, C. Bonhomme, L. Bonhomme-Coury, F. Damay, D. Le Denmat, J. Sadoine, J. Rode, V. Frochot, E. Letavernier, J.-P. Haymann, M. Daudon, *C. R. Chim.*, 2016, **19**, 1492-1503.

Comptes Rendus
Chimie
2022, Vol. 25, Special Issue S1, p. 503-515
https://doi.org/10.5802/crchim.187

Microcrystalline pathologies: Clinical issues and nanochemistry / *Pathologies microcristallines : questions cliniques et nanochimie*

Characterization through scanning electron microscopy and μFourier transform infrared spectroscopy of microcalcifications present in fine needle aspiration smears

Caractérisation par microscopie électronique à balayage et microspectroscopie infrarouge de dépôts anormaux présents dans des ponctions thyroïdiennes

Lucas Henry [a], Dominique Bazin [*, b, c], Clotilde Policar [a], Jean-Philippe Haymann [d, e], Michel Daudon [d, e], Vincent Frochot [d, e] and Muriel Mathonnet [f]

[a] Laboratoire des BioMolécules, LBM, Département de chimie, École normale supérieure, PSL University, Sorbonne Université, CNRS, F-75005 Paris, France

[b] Laboratoire de Chimie Physique, Université Paris Saclay, 310, rue Michel Magat, 91400 Orsay, France

[c] Laboratoire de Physique des Solides, Université Paris Saclay, 91400 Orsay, France

[d] INSERM, UMRS 1155, UPMC, Hôpital Tenon, 75970 Paris, France

[e] Service d'explorations fonctionnelles, Hôpital Tenon, AP-HP, 4, rue de la Chine, 75970 Paris Cedex 20, France

[f] Service de chirurgie digestive, générale et endocrinienne, CHU Dupuytren, Limoges, France

E-mails: lucas.henry@ens.fr (L. Henry), dominique.bazin@universite-paris-saclay.fr (D. Bazin), clotilde.policar@ens.psl.eu (C. Policar), jean-philippe.haymann@tnn.aphp.fr (J.-P. Haymann), daudonmichel24@gmail.com (M. Daudon), vincent.frochot@aphp.fr (V. Frochot), muriel.mathonnet@unilim.fr (M. Mathonnet)

Abstract. In this contribution, we have characterized for the first time (to the best of our knowledge), microcalcifications present in fine needle aspiration (FNA) smears of thyroid nodules. Abnormal deposits were analysed through μFourier Transform Infrared Spectroscopy (μFTIR) and Field Emission

* Corresponding author.

Scanning Electron Microscopy (FE-SEM) in order to obtain their chemical composition as well as their morphology at the micrometer scale. Thirty-one samples coming from 13 patients were investigated comprising five cases of papillary carcinoma, two of Graves' disease, and six of adenomatous goitre. The smears were also stained for analysis of the cellular characteristics of these lesions for classifying according to the Bethesda classification. Two mineral species, amorphous and nanocrystallised apatite calcium phosphate, have been identified with very different morphologies. Moreover, FE-SEM observations at the micrometer scale underline the presence of different kinds of abnormal deposits.

Résumé. Dans cette contribution, nous avons caractérisé pour la première fois à notre connaissance, les microcalcifications présentes dans les ponctions thyroïdiennes. Les dépôts anormaux ont été analysés par micro spectroscopie infrarouge à transformée de Fourier et par microscopie électronique à balayage à émission de champ (FE-SEM) afin d'obtenir leur composition chimique ainsi que leur morphologie à l'échelle micrométrique. Trente et un échantillons provenant de 13 patients ont été étudiés, dont 5 cas de carcinome papillaire, 2 de maladie de Basedow et 6 de goitre adénomateux. Les ponctions ont également été colorées pour analyser les caractéristiques cellulaires de ces lésions afin de les classer selon la classification de Bethesda. Deux espèces minérales, le phosphate de calcium apatite amorphe et nanocristallisé, ont été identifiées avec des morphologies très différentes. De plus, les observations FE-SEM à l'échelle micrométrique soulignent la présence de différents types de dépôts anormaux.

Keywords. Thyroid, Nodule, Smears, Infrared spectroscopy, Scanning electron microscopy.

Mots-clés. Thyroïde, Nodule, Ponctions, Spectroscopie infrarouge, Microscopie électronique à balayage.

Published online: 27 July 2022

1. Introduction

The most common thyroid disease in the community is simple (diffuse) physiological goitre [1]. While the prevalence of diffuse goitre declines with age, different investigations underline an increase in frequency of thyroid nodules and thyroid antibodies with age. More precisely, epidemiologic investigations suggest that nodular thyroid disease is a common clinical problem, with a prevalence of nodules in 4%–7% of the adult population.

Thyroid nodules [2–7] as well as thyroid calcifications [8–14] are observed for different thyroid pathologies. Recently, we have conducted two physicochemical investigations on thyroid macrocalcifications for patients corresponding to Grave's disease, papillary carcinoma, benign nodules, multinodular goitre [15,16]. Two characterization techniques, namely μFourier Transform Infrared Spectroscopy (μFTIR) [17–20] and Field Emission Scanning Electron Microscopy (FE-SEM) [18–21] were used in order to assess a possible relationship between the pathology and the physicochemical characteristics of the macrocalcifications. Such approaches have been already developed for microcalcifications in organs such as the kidney showing that the morphology of the crystallites of which the agglomeration gives the macrocalcifications as well as their chemical identification are of major importance [22–25]. Such complexity calls for physicochemical techniques to characterize such deposits which may exist also at the micrometer and at the nanometer scales [26–31].

At this point, we have to recall that a careful analysis of the IR absorption spectra of thyroid tissue revealed the presence of amorphous and nanocrystallized calcium phosphate apatite, calcium oxalate monohydrate and/or dihydrate as well as triglycerides and cholesterol [15,16]. The complete set of data we have obtained on these macrocalcifications seems to indicate that there is no clear relationship between their chemical composition and the disease. Nevertheless, from a biochemical point of view, the presence of the various types of crystals is a marker of very different biological conditions, and as such, of different pathologies [22–25].

Though the presence of microcalcifications in smears has already been attested, very little information exists on their chemical composition. The aim of our work was to analyze the composition of thyroid microcalcifications from smears obtained by ultrasound-guided fine needle puncture. Such an approach is a first step to establish a possible relationship between the physico-chemistry of abnormal deposits in thyroid smears and the disease which induces their formation.

Table 1. Clinical data and chemical compounds identified in smears of thyroid biopsies for patients with sclerosing variant of papillary thyroid carcinoma stage 3 or papillary thyroid carcinoma

Samples	Sex and age	FTIR analysis	Bethesda classification	Pathology
Patient 1 Biopsy 1	M, 14	Presence of lipids without calcifications	5	Sclerosing variant of papillary thyroid carcinoma stage 3
Patient 1 Biopsy 2	M, 14	Presence of CA	5	Sclerosing variant of papillary thyroid carcinoma stage 3
Patient 1 Biopsy 3	M, 14	Presence of CA and glycoprotein	5	Sclerosing variant of papillary thyroid carcinoma stage 3
Patient 1 Biopsy 4	M, 14	Sample without apatite but note the presence of polysaccharides	5	Sclerosing variant of papillary thyroid carcinoma stage 3
Patient 2 Biopsy 1	M, 75	Some calcifications made of CA have been detected. Presence of acicular calcifications	5	Papillary thyroid carcinoma stage 3
Patient 2 Biopsy 2	M, 75	Some calcifications made of CA have been detected	5	Papillary thyroid carcinoma stage 3
Patient 3 Biopsy 1	F, 34	Some calcifications made of CA have been detected	1	Papillary thyroid carcinoma stage 1
Patient 3 Biopsy 2	F, 34	Some spherical calcifications made of CA have been detected	1	Papillary thyroid carcinoma stage 1
Patient 4 Biopsy 1	F, 51	The deposit was too thick	1	Papillary thyroid carcinoma stage 2
Patient 4 Biopsy 2	F, 51	Sample without apatite but note the presence of polysaccharides	1	Papillary thyroid carcinoma stage 2
Patient 5 Biopsy 1	M, 42	Some calcifications made of CA have been detected	1	Papillary thyroid carcinoma stage 2
Patient 5 Biopsy 2	M, 42	Some calcifications made of CA have been detected	1	Papillary thyroid carcinoma stage 2
Patient 5 Biopsy 3	M, 42	Some calcifications made of ACCP have been detected as well as lipids	1	Papillary thyroid carcinoma stage 2
Patient 5 Biopsy 4	M, 42	CA calcifications have been detected	1	Papillary thyroid carcinoma stage 2

CA = carbapatite or calcium phosphate apatite; ACCP = amorphous carbonated calcium phosphate.

2. Experimental

A set of 31 thyroid smears corresponding to 13 patients, coming from the Service de Chirurgie digestive, Générale et Endocrinienne, CHU Dupuytren (Limoges, France) and the Department of Thoracic Surgery of Geneva have been considered (Tables 1 and 2). Of the 13 patients, five (Patient number 1–5) had papillary cancer, two (Patient number 6 and 7) had Graves' disease, six had benign nodules (Nodular goitre Patient number 8–12 and Patient 13 Thyroid adenoma). For one patient (Patient number 9), the thyroid disease was associated with primary hyperparathyroidism (HPT). The smears were ob-

Table 2. Clinical data and chemical compounds identified in smears of thyroid biopsies for patients with Graves' disease, nodular goitre or thyroid adenoma

Samples	Sex and age	FTIR analysis	Bethesda classification	Pathology
Patient 6 Biopsy 1	F, 35	Some calcifications made of CA have been detected	2	Graves' disease
Patient 6 Biopsy 2	F, 35	Some lipids have been detected	2	Graves' disease
Patient 6 Biopsy 3	F, 35	Some calcifications made of CA and lipids have been detected	1	Graves' disease
Patient 7 Biopsy 1	F, 55	No calcification	1	Graves' disease
Patient 8 Biopsy 1	M, 72	Some calcifications made of CA and/or ACCP have been detected	4	Nodular goitre
Patient 8 Biopsy 2	M, 72	Sample without apatite but note the presence of polysaccharides	4	Nodular goitre
Patient 9 Biopsy 1	F, 75	Some calcifications made of CA and/or ACCP have been detected	3	Nodular goitre
Patient 9 Biopsy 2	F, 75	Some calcifications made of CA and/or ACCP have been detected	3	Nodular goitre
P. No 10 Biopsy 1	M, 67	The deposit was too thick	1	Nodular goitre
P. No 10 Biopsy 2	M, 67	The deposit was too thick	1	Nodular goitre
P. No 10 Biopsy 3	M, 67	Some calcifications made of CA and/or ACCP have been detected	1	Nodular goitre
P. No 11 Biopsy 1	F, 31	The deposit was too thick	4	Nodular goitre
P. No 11 Biopsy 2	F, 31	Glycoproteins. No visible calcification	4	Nodular goitre
P. No 12 Biopsy 1	F, 70	Spherical calcifications made of CA and/or ACCP have been detected	1	Nodular goitre
P. No 12 Biopsy 2	F, 70	Spherical calcifications made of CA and/or ACCP have been detected	1	Nodular goitre
P. No 13 Biopsy 1	F, 45	No deposit	2	Thyroid adenoma
P. No 13 Biopsy 2	F, 45	Some calcifications made of CA have been detected	2	Thyroid adenoma

CA = carbapatite; ACCP = amorphous carbonated calcium phosphate.

tained through aspiration, with a fine needle, performed under ultrasound guidance to ensure accurate placement of the needle within the thyroid nodule [32–34]. Calcifications were visualized in 17 of 31 samples taken (55%) (Table 2). Histopathological analysis of the specimens was performed by a senior pathologist. The specimens from patients 1–5 and 11 were re-read by a second pathologist to confirm the

diagnosis.

All patient-derived tissues were collected and archived at the Tumorotheque of Limoges University Hospital, under protocols approved by the Institutional Review Board (AC N 2007-34, DC 2008-604 and 72-201118). Written informed consent was obtained from all subjects of this study. Each sample was only named by a study number, without indication of the name of the patient or potential identification data.

All the calcifications were investigated with a Zeiss SUPRA55-VPFE-SEM in order to describe their morphology at the micrometer scale. To maintain the integrity of the samples, measurements were performed at low voltage (1.0 keV) and without the usual deposits of carbon at the surface of the sample [18,21]. All calcifications were characterized using μFTIR spectrometry (Cary 620 infrared microscope equipped with a 64 × 64 pixels Stingray MCT detector coupled to a Cary 660 spectrometer equipped with a KBr beamsplitter and a Michelson interferometer, LBM, ENS-PSL). Data were collected in the reflexion mode between 4000 and 700 cm^{-1}, with a resolution of 8 cm^{-1}. The different compounds were identified by comparing their IR spectrum to the IR spectrum of reference compounds [35].

3. Results and discussion

3.1. *The point of view of the clinician: the state of the art*

Ultrasonography (US) is the main tool to explore thyroid diseases, especially for detecting nodules, measuring their dimensions, and evaluating any associated changes in the thyroid glands [36]. The use of a standardized US reporting system to analyze US imaging reporting reduces the inconsistency of US descriptive reports and ease the management of thyroid nodules. The most used system is the thyroid imaging reporting and data system (TIRADS) recently updated [37,38]. It has the best correlation with cytologic findings. Suspicious US lesions such as a solid hypoechoic nodule, with a spiculated or lobulated margin or a hypoechoic halo, or the presence of intra nodular calcifications, need fine needle aspiration (FNA). The average malignancy risk of such nodules is around 56% but increases with the number of suspicious features [39–41]. Microcalcifications are a good predictor of malignancy especially in partially cystic nodules [42]. Microcalcifications appear as tiny hyperechoic spots, <1 mm. They correspond to psammomas bodies and are highly suggestive of the most frequent type of thyroid carcinoma, papillary thyroid carcinoma [16,43]. A recent meta-analysis including 41 studies for a total of 29,678 patients demonstrated that microcalcifications were associated with a high risk of malignancy with a 676 odds ratio (OR) [44]. However, if their specificity for malignancy is elevated (85–95%), their sensitivity is low, particularly in nodules under 1 cm diameter [45]. However, the risk of carcinoma does not decrease with nodule size. This risk depends on the ultrasonographic criteria placing the risk at 19.7% vs 7.8% for nodules sized 1 cm or more without suspicious sonographic findings [46].

Such results are in line with a recent investigation performed by Yin *et al.* [47]. These authors found that thyroid microcalcifications and partial macrocalcifications, such as eggshell discontinuous calcifications, and multilayer-like calcifications were associated with thyroid carcinoma (41.4% vs 21%). Eggshell discontinuous macrocalcifications and multilayer-like macrocalcifications also occurred mainly in malignant nodules, while eggshell calcifications in a row are more often seen in benign nodules [47]. The type of calcification is therefore an important predictor of cancer.

The FNA allows to withdraw cells from a suspicious nodule such as a nodule containing microcalcifications or nodule of size >1 cm. FNA under US guidance is recommended because it reduces false-negative cytology, established at around 1% [48]. The three classification systems rank the cytology diagnosis in five major classes and the widely used is the Bethesda System [49] (Table 3).

Classifications depend on cell features. Suspicion of malignancy or malignant results force the patient to be referred to an endocrine surgeon. The risk of malignancy in benign lesion (named Bethesda 2) is about 1% and a clinical or US follow-up is recommended. Two categories are less consistent, Bethesda 3 and Bethesda 1. The first one is the indeterminate category that imposes surgery or careful follow-up because the risk of malignancy is around 15% [50]. The second one is nondiagnostic specimens due to insufficient number of thyroid cells, or virtually acel-

Table 3. The 2017 Bethesda system for reporting thyroid cytopathology, implied risk of malignancy and recommended clinical management [49]

Rank	Diagnostic category	Risk of malignancy	Usual management
Bethesda 1	Non-diagnostic or unsatisfactory	5–10%	Repeat FNA
Bethesda 2	Benign	0–3%	Clinical and sonographic follow-up
Bethesda 3	Atypia or undetermined significance or follicular lesion	10–30%	Repeat FNA or lobectomy
Bethesda 4	Follicular neoplasm or suspicious for a follicular neoplasm	25–40%	Lobectomy
Bethesda 5	Suspicious for malignancy	50–75%	Total thyroidectomy or lobectomy
Bethesda 6	Malignant	97–99%	Total thyroidectomy or lobectomy

lular specimen. In this category, the risk of malignancy is estimated to be 16% [51] and a real evaluation of the need for surgery is necessary. The balance between the risks of a potentially delayed diagnosis of carcinoma that imposes surgery, and those of superfluous surgery should be considered.

In 2015, ATA recommended basing management of thyroid nodules on their risk of malignancy assessed on ultrasound coupled with FNA if the nodules are supra-centimetric. Only Bethesda 2 nodules, i.e. benign, do not require FNA [52]. This risk varies from 10 to 30% for Bethesda 3. Ultrasound, even coupled with cytology, does not therefore make it possible to accurately determine the risk of cancer in a nodule. The development of new methods, like automated machine learning for identifying nodules with high-risk mutations on molecular testing, promises to facilitate the identification of suspicious nodules but is not yet routine practice [53]. The risk is to wrongly operate on benign nodules, and to ignore the cancer in a centimetric or supracentimetric nodule.

3.2. *The point of view of the physico-chemist: more new questions*

In all the above literature dedicated to calcifications present in thyroid, the chemical phases present in the calcifications are not identified through physicochemical techniques. The only parameter which is discussed is the size of the calcifications and two cases are distinguished: micro and macrocalcifications. In an attempt to establish a significant correlation between the pathological calcifications and the pathology, the morphologic characteristics of the pathological calcification as well as their chemical composition must be considered.

For example, whewellite kidney stones, depending on their morphologic features at both macroscopic and mesoscopic scales, can be associated with an alimentation disorder or a genetic abnormality, namely primary hyperoxaluria, each pathology being related to a specific morphology [22,25,54–56]. It is based on the fact that pathologies correspond to very different biochemical conditions leading to the formation of different chemical compounds with different crystallite morphologies [22,24].

Here, we start by a selected presentation of FE-SEM observations. In Figure 1, we have reported the observations performed on the sample B399 (Patient 1, Biopsy 1). We can see micrometer-sized acicular objects. Unfortunately, due to the small thickness of these biological objects we were not able to obtain valuable FTIR spectra.

Other usual morphologies have been obtained on the sample B400 (Patient 1, Biopsy 2, Figure 2). In that case, observation at large magnification (Figure 2C) indicates an agglomeration of crystals. Their morphologies seem to be close to the ones of both weddellite (or COD for calcium oxalate dihydrate) and whewellite (or COM for calcium oxalate monohydrate) [57]. These two crystalline phases of calcium oxalate have been already identified in thyroid calcifications [15,16].

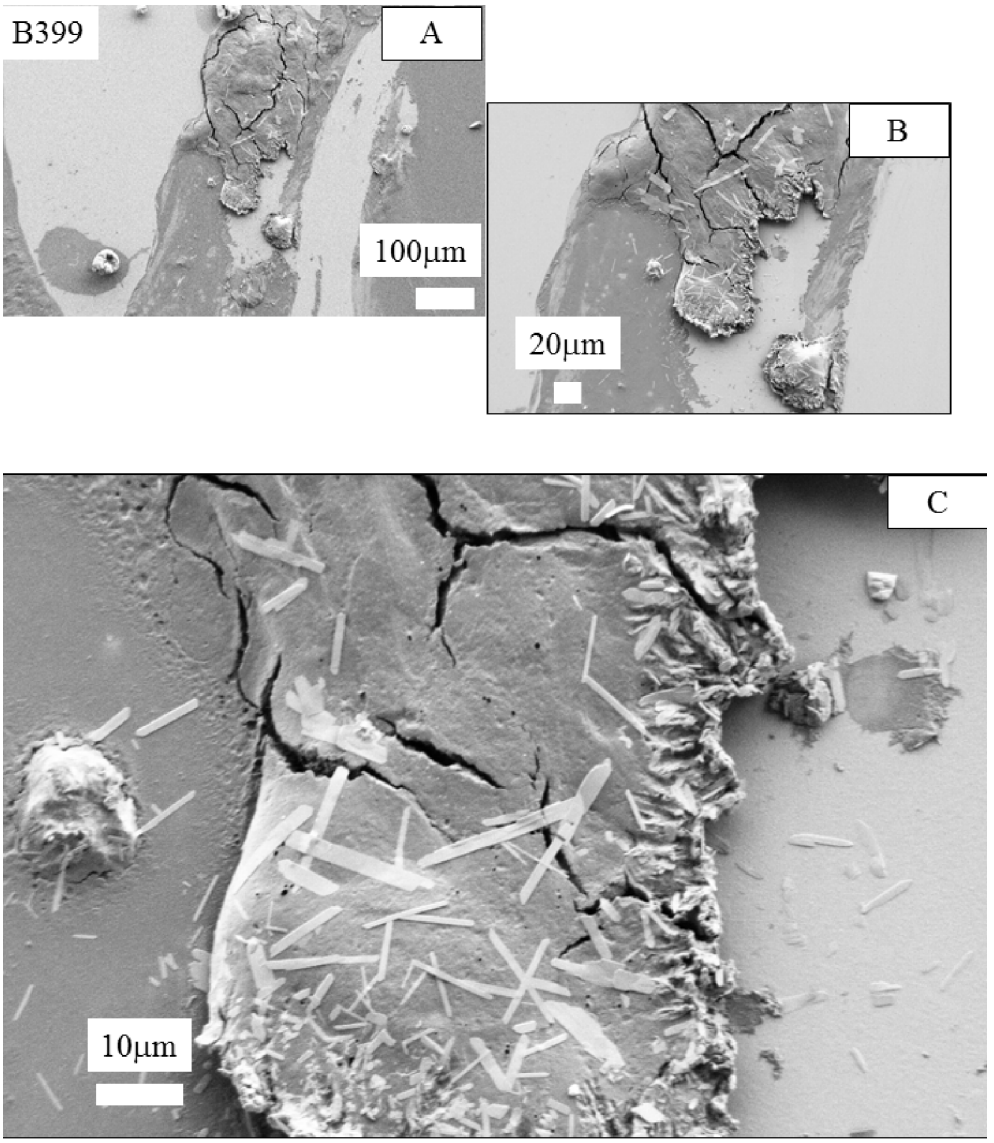

Figure 1. FE-SEM observations at different magnifications obtained for the sample B399. We can note the presence of 10 µm acicular objects which display a very small thickness.

In Figure 3, we have compared this morphology to the ones observed for whewellite (A) and for weddellite (B) in the case of kidney stones to (C,D) weddellite crystals present in thyroid biopsies as shown by Guerlain *et al.* [16].

In Figure 4A (sample B403, Patient 3 Biopsy 2), we have superimposed an optical image as collected by the FTIR spectrometer and a FE-SEM observation at low magnification. Then, we selected an area of interest and increased the magnifications (Figures 4B–D). Figure 4D shows the presence of spherical entities (black arrows), a typical morphology for biological calcium phosphate apatite corresponding to two chemical phases namely either carbonated calcium phosphate apatite (CA) or amorphous carbonated calcium phosphate (ACCP) [59–61]. We have

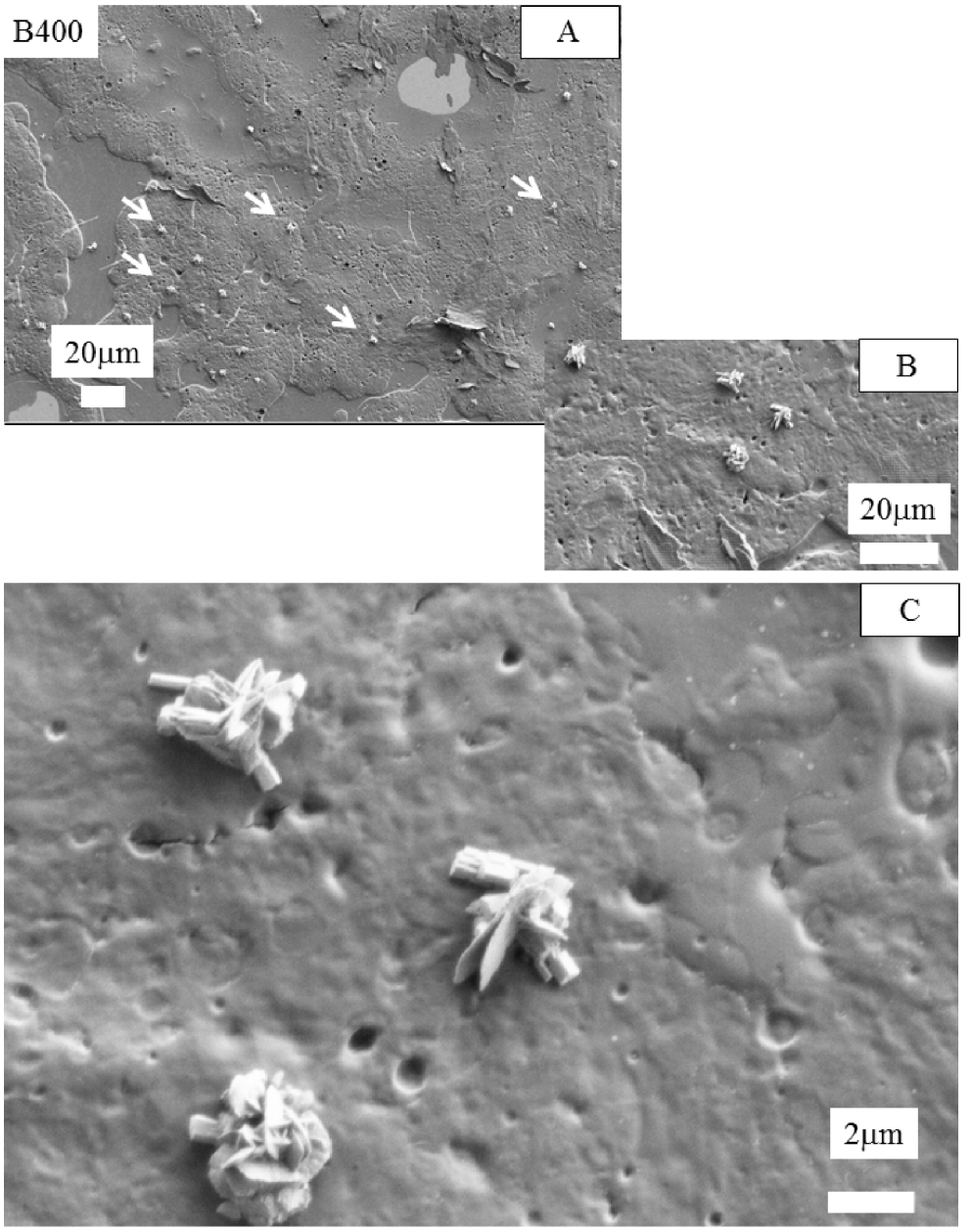

Figure 2. FE-SEM observations at different magnifications obtained for the sample B400 (Patient 1, Biopsy 2). We can note the presence of several aggregates of crystals which have a similar morphology to weddellite and whewellite crystals [57,58].

already found for these two chemical phases such spherical morphology in different parts of the human body, namely kidney [62–68], breast [69–72], skin [73,74], cartilage [75,76] or prostate [77]. At this point, it is worth underlining that spherical entities can be made of calcium carbonate [78]. Note the presence of a crystal (white arrow) probably made of cholesterol.

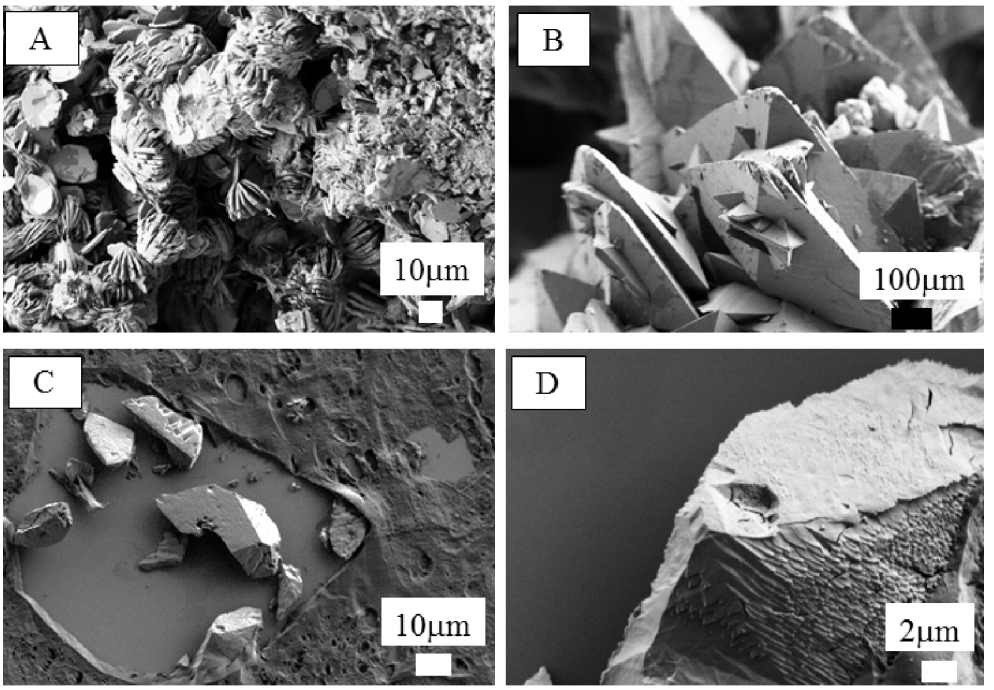

Figure 3. (A) Morphology observed for whewellite (or COM for calcium oxalate monohydrate) and (B) for weddellite (or COD for calcium oxalate dihydrate) in the case of kidney stones. (C,D) Weddellite crystals present in thyroid biopsies as shown by Guerlain *et al.* [16].

In Figure 5A, the optical image present on Figure 4A corresponds to the area where IR spectra have been collected. To build Figure 5B, we have considered the intensity of the IR band at 1000 cm^{-1}, the red part corresponding to high intensity, while the blue one corresponds to low intensity. The B403 (Patient 3 Biopsy 2) sample is shown and compared to FTIR data (Figures 5C and D) which are displayed along with SEM observations (Figure 5D). Significant IR absorption bands underline the presence of ACCP and CA corresponding to the spherical entities (red arrows on Figures 5C and D).

4. Conclusion and perspectives

In this contribution, microcalcifications present in FNA smears of thyroid nodules have been characterized through two different physicochemical techniques namely µFTIR spectroscopy and FE-SEM. Such an approach allows us to obtain their chemical composition as well as morphology at the micrometer scale. The smears were also stained for analysis of the cellular characteristics of these lesions for classifying according to Bethesda classification.

Even if the number of samples is quite low, such an investigation underlines the chemical diversity of the mineral species. Also, FE-SEM observations underline the presence of crystals with unusual morphology which were too small for an accurate identification by µFTIR spectroscopy. We will soon start an investigation using other physicochemical techniques which are able to characterize nanometer scale abnormal deposits, namely a combination of atomic force microscopy and IR spectroscopy [79,80] and optical photothermal IR (OPTIR) spectroscopy [81]. Different publications clearly show that such characterization brings out valuable information in the case of abnormal deposits in biological tissues [72,82–84].

Finally, regarding the relationship between the physico-chemistry of abnormal deposits in thyroid smears and the disease which induces their formation, such a relationship is complex and may depend also on the amount of the compound. In the case of infection, whatever the amount of struvite, this

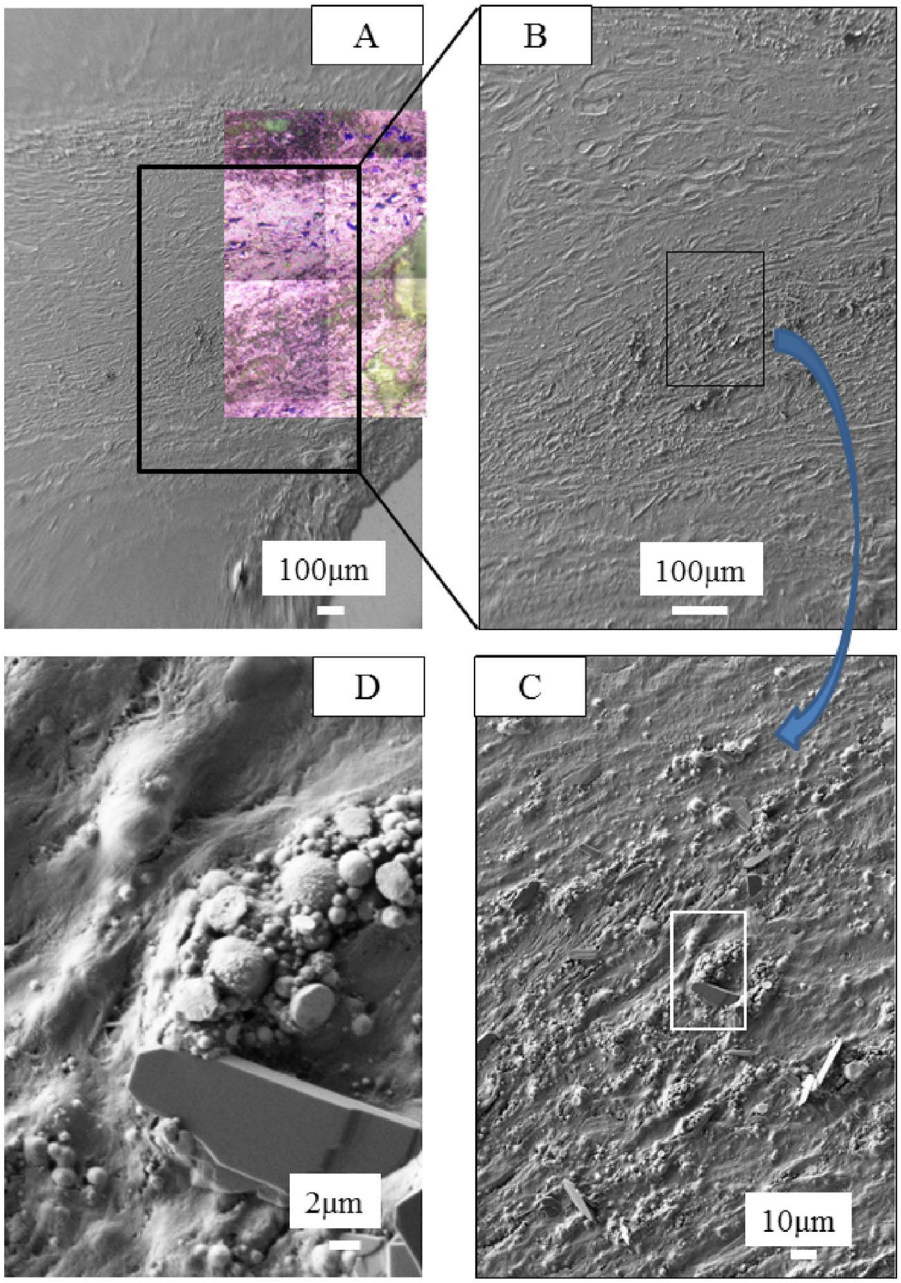

Figure 4. (A) Optical image collected by the FTIR spectrometer with FE-SEM observations at different magnifications (B–D) obtained for the sample B403. Numerous spherical entities (black arrows) are present at the surface and in the smears. Also, a large crystal is also present (white arrow in Figure 4D). Its morphology seems to indicate that it is made of cholesterol.

chemical compound is related to urinary tract infection [85–87]. In the case of whitlockite, its amount in kidney stones has to be greater than 20% (estimated by FTIR) to be related to infection [88,89]. We have thus to define an approach which will be able to identify the different chemical compounds present

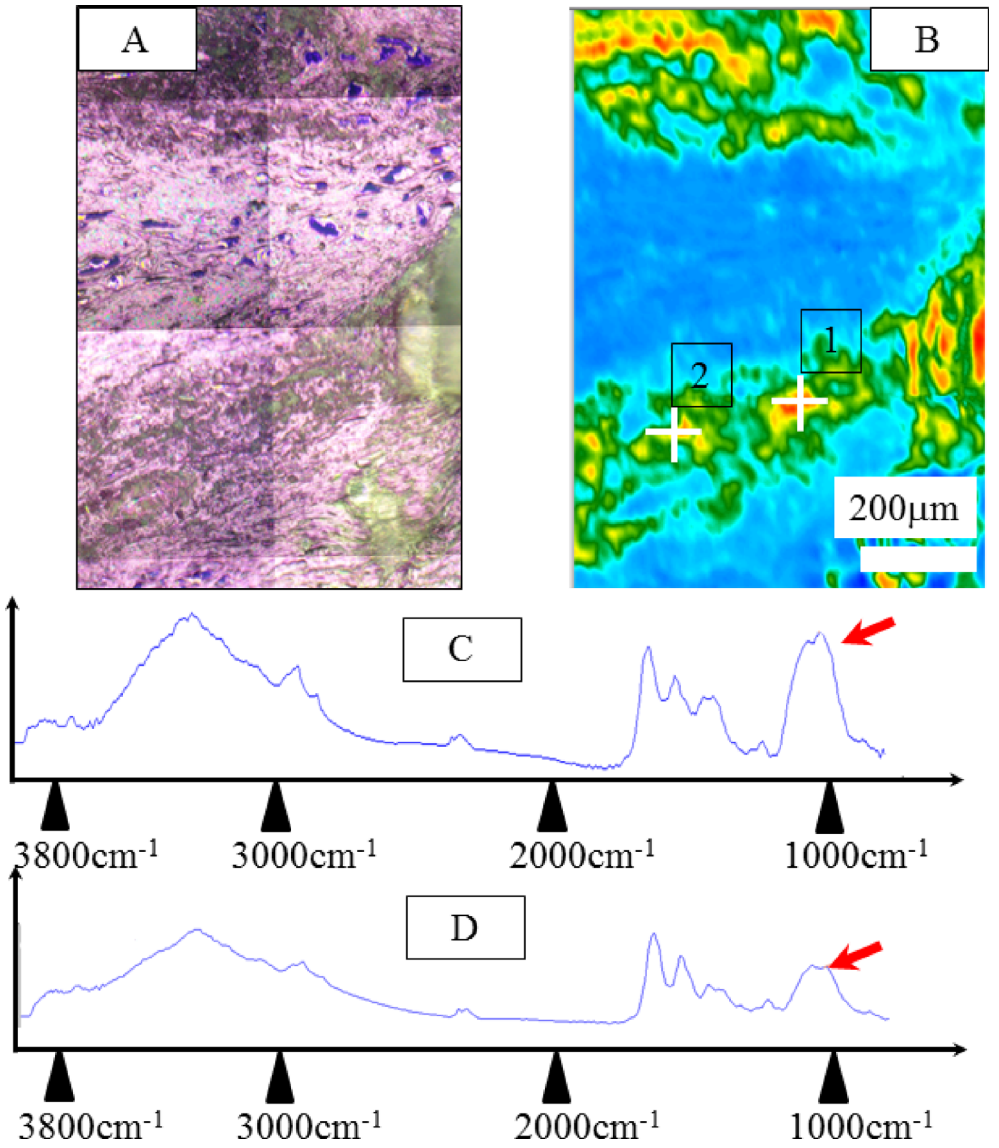

Figure 5. Sample B403. (A) Optical image collected by the FTIR spectrometer (same to Figure 4A). (B) Typical infrared spectrum: ν_3 P-O stretching vibration modes are measured at 1035–1045 cm^{-1}, particular attention has to be paid to the presence of a feature in the ν_3 absorption band, which can be used as a fingerprint for the presence of a mixture of ACCP and CA. (C) and (D) correspond to IR spectra collected respectively to point of interest 1 and 2 of Figure 5B.

in smears, to evaluate their amount and finally to describe the morphology of the abnormal deposits.

Conflicts of interest

Authors have no conflict of interest to declare.

Acknowledgements

We thank ENS-PSL for LH's PhD fellowship, and *Fondation pour la Recherche Biomédicale* (project DEI20151234413) for financial support.

References

[1] A. Maniakas, L. Davies, M. E. Zafereo, *Clin. North Am.*, 2018, **51**, 631-642.

[2] N. Azar, C. Lance, D. Nakamoto, C. Michael, J. Wasman, L. Pantanowitz, *Diagn. Cytopathol.*, 2013, **41**, 1107-1114.

[3] L. Davies, G. Randolph, *Otolaryngol. Clin. North Am.*, 2014, **47**, 461-474.

[4] S. Tamhane, H. Gharib, *Clin. Diabet. Endocrinol.*, 2016, **2**, article no. 17.

[5] J. Luo, C. Zhang, F. Huang, J. Chen, Y. Sun, K. Xu, P. Huang, *Sci. Rep.*, 2017, **7**, article no. 13109.

[6] H. S. Mo, Z. X. Li, S.-D. Wang, X.-H. Liao, M. Liang, X.-Y. Hao, *Int. J. Clin. Exp. Med.*, 2017, **10**, 13473-13481.

[7] R. Wong, S. G. Farrell, M. Grossmann, *Med. J. Aust.*, 2018, **206**, 92-98.

[8] S. Taki, S. Terahata, R. Yamashita, K. Kinuya, K. Nobata, K. Kakuda, Y. Kodama, I. Yamamoto, *Clin. Imag.*, 2004, **28**, 368-371.

[9] J. Jiang, X. Shang, H. Wang, Y.-B. Xu, Y. Gao, Q. Zhou, *Kaohsiung J. Med. Sci.*, 2015, **31**, 138-144.

[10] Q. A. Hassan, A. A. Asghar, M. A. Had, *Int. J. Med. Res. Health Sci.*, 2016, **5**, 148-158.

[11] Y.-J. Tsai, S.-M. Huang, *Ultrasound Med. Biol.*, 2017, **43**, s115-s116.

[12] G. Shandilya, R. K. Sinha, N. Ekka, V. Kumar, *J. Clin. Diagn. Res.*, 2017, **11**, PD01-PD03.

[13] D. Bianchi, U. Morandi, A. Stefani, B. Aramini, *Int. J. Surg. Case Rep.*, 2019, **60**, 46-48.

[14] L. Yin, W. Zhang, W. Bai, W. He, *Ultrasound Med. Biol.*, 2020, **46**, 20-25.

[15] M. Mathonnet, A. Dessombz, D. Bazin, R. Weil, F. Triponez, M. Pusztaszeri, M. Daudon, *C. R. Chim.*, 2016, **19**, 1672-1678.

[16] J. Guerlain, S. Perie, M. Lefevre, J. Perez, S. Vandermeersch, Ch. Jouanneau, L. Huguet, V. Frochot, E. Letavernier, R. Weil, S. Rouzière, D. Bazin, M. Daudon, J.-Ph. Haymann, *PLoS One*, 2019, **14**, article no. e0224138.

[17] D. Bazin, J.-Ph. Haymann, E. Letavernier, J. Rode, M. Daudon, *Presse Med.*, 2014, **43**, 135-148.

[18] D. Bazin, M. Daudon, *Ann. Biol. Clin.*, 2015, **73**, 517-534.

[19] M. Daudon, D. Bazin, *C. R. Chim.*, 2016, **19**, 1416-1423.

[20] D. Bazin, E. Letavernier, J.-P. Haymann, P. Méria, M. Daudon, *Prog. Urol.*, 2016, **26**, 608-618.

[21] D. Bazin, E. Bouderlique, M. Daudon, V. Frochot, J.-Ph. Haymann, E. Letavernier, F. Tielens, R. Weil, *C. R. Chim.*, 2022, **25**, no. S1, 37-60.

[22] M. Daudon, C. A. Bader, P. Jungers, *Scan. Microsc.*, 1993, **7**, 1081-1104.

[23] M. Daudon, P. Jungers, D. Bazin, *AIP Conf. Proc.*, 2008, **1049**, 199-215.

[24] M. Daudon, A. Dessombz, V. Frochot, E. Letavernier, J. P. Haymann, P. Jungers, D. Bazin, *C. R. Chim.*, 2016, **19**, 1470-1491.

[25] M. Daudon, P. Jungers, D. Bazin, *New Engl. J. Med.*, 2008, **359**, 100-102.

[26] D. Bazin, M. Daudon, C. Combes, C. Rey, *Chem. Rev.*, 2012, **112**, 5092-5120.

[27] D. Bazin, M. Daudon, *J. Phys. D: Appl. Phys.*, 2012, **45**, article no. 383001.

[28] A. Dessombz, E. Letavernier, J.-Ph. Haymann, D. Bazin, M. Daudon, *J. Urol.*, 2015, **193**, 1564-1569.

[29] D. Bazin, Ch. Jouanneau, S. Bertazzo, Ch. Sandt, A. Dessombz, M. Réfrégiers, P. Dumas, J. Frederick, J.-Ph. Haymann, E. Letavernier, P. Ronco, M. Daudon, *C. R. Chim.*, 2016, **19**, 1439-1454.

[30] E. Tsolaki, S. Bertazzo, *Materials*, 2019, **12**, article no. 3126.

[31] D. Bazin, E. Letavernier, J. P. Haymann, V. Frochot, M. Daudon, *Ann. Biol. Clin.*, 2020, **78**, 349-362.

[32] P. D. Gutman, M. Henry, *Clin. Lab. Med.*, 1998, **18**, 461-482.

[33] N. Hayashi, M. Kitaoka, *Nihon Rinsho.*, 2007, **65**, 2003-2007.

[34] E. M. Khan, R. Pandey, *Acta Cytol.*, 1996, **40**, 959-962.

[35] N. Quy Dao, M. Daudon, *Infrared and Raman Spectra of Calculi*, Elsevier, Paris, 1997.

[36] L. Solbiati, V. Osti, L. Cova, M. Tonolini, *Eur. Radiol.*, 2001, **11**, 2411-2424.

[37] P. Trimboli, R. Ngu, B. Royer, L. Giovanella, C. Bigorgne, R. Simo, P. Caroll, G. Russ, *Clin. Endocrinol.*, 2019, **91**, 340-347.

[38] F. N. Tessler, W. D. Middleton, E. G. Grant, J. K. Hoang, L. L. Berland, S. A. Teefey, J. J. Cronan, M. D. Beland, T. S. Desser, M. C. Frates, L. W. Hammers, U. M. Hamper, J. E. Langer, C. C. Reading, L. M. Scoutt, A. T. Stavros, *J. Am. Coll. Radiol.*, 2017, **14**, 587-595.

[39] G. Russ, B. Royer, C. Bigorgne, A. Rouxel, M. Bienvenu-Perrard, L. Leenhardt, *Eur. J. Endocrinol.*, 2013, **15**, 649-655.

[40] P. Seifert, R. Görges, M. Zimny, M. C. Kreissl, S. Schenke, *Endocrine*, 2020, **67**, 143-155.

[41] G. Russ, S. J. Bonnema, M. F. Erdogan, C. Durante, R. Ngu, L. Leenhardt, *Eur. Thyroid*, 2017, **6**, 225-237.

[42] D. G. Na, D. S. Kim, S. J. Kim, J. W. Ryoo, S. L. Jung, *Ultrasonography*, 2016, **35**, 212-219.

[43] Y. J. Hong, E. J. Son, E. K. Kim, J. Y. Kwak, S. W. Hong, H. S. Chang, *Clin. Imag.*, 2010, **34**, 127-133.

[44] F. Ianni, P. Campanella, C. A. Rota, A. Prete, L. Castellino, A. Pontecorvi, S. M. Corsello, *Endocrine*, 2016, **51**, 313-321.

[45] M. C. Chammas, V. J. de Araujo Filho, R. A. Moysés, M. D. Brescia, G. C. Mulatti, L. G. Brandao, G. G. Cerri, A. R. Ferraz, *Head Neck*, 2008, **30**, 1206-1210.

[46] Y. H. Bo, H. Y. Ahn, Y. H. Lee, Y. J. Lee, J. H. Kim, J. H. Ohn, E. S. Hong, K. W. Kim, I. K. Jeong, S. H. Choi, S. Lim, D. J. Park, H. C. Jang, B. H. Oh, B. Y. Cho, Y. J. Park, *J. Korean Med. Sci.*, 2011, **26**, 237-242.

[47] L. Yin, W. Zhang, W. Bai, W. He, *Ultrasound Med. Biol.*, 2020, **46**, 20-25.

[48] H. Gharib, E. Papini, J. R. Garber, D. S. Duicks, R. M. Harrell, L. Hegedüs, R. Paschke, R. Valcavi, P. Vitti, *Endocr. Pract.*, 2016, **22**, 622-639.

[49] E. S. Cibas, S. Z. Ali, *Thyroid*, 2017, **27**, 1341-1346.

[50] P. A. Vanderlaan, J. F. Krane, E. S. Cibas, *Acta Cytol.*, 2011, **55**, 512-517.

[51] M. Bongiovanni, C. Bellevicine, G. Troncone, G. P. Sykiotis, *Gland Surg.*, 2019, **8**, S98-S104.

[52] B. R. Haugen, E. K. Alexander, G. M. Doherty, S. J. Mandel, Y. E. Nikiforov, F. Pacini, G. W. Randolph, A. M. Sawka, M. Schlumberger, K. G. Schuff, S. I. Sherman, J. A. Sosa, D. L. Steward, R. M. Tuttle, L. Wartofsky, *Thyroid*, 2016, **26**, 1-133.

[53] K. Daniels, S. Gummadi, Z. Zhu, S. Wang, J. Patel, B. Swendseid, A. Lyshchik, J. Curry, E. Cottrill, J. Eisenbrey, *JAMA Otolaryngol. Head Neck Surg.*, 2020, **146**, 36-41.

[54] M. Daudon, D. Bazin, G. André, P. Jungers, A. Cousson, P. Chevallier, E. Véron, G. Matzen, *J. Appl. Cryst.*, 2009, **42**, 109-115.

[55] D. Bazin, C. Leroy, F. Tielens, Ch. Bonhomme, L. Bonhomme-Coury, F. Damay, D. Le Denmat, J. Sadoine, J. Rode, V. Frochot, E. Letavernier, J. Ph. Haymann, M. Daudon, *C. R. Chim.*, 2016, **19**, 1492-1503.

[56] F. Meiouet, S. El Kabbaj, J. M. Daudon, *C. R. Chim.*, 2022, **25**, no. S1, 281-293.

[57] I. Petit, G. D. Belletti, T. Debroise, M. J. Llansola-Portoles, I. T. Lucas, C. Leroy, Ch. Bonhomme, L. Bonhomme-Coury, D. Bazin, M. Daudon, E. Letavernier, J. Ph. Haymann, V. Frochot, F. Babonneau, P. Quaino, F. Tielens, *Chem. Select*, 2018, **3**, 8801-8812.

[58] X. Sheng, M. D. Ward, J. A. Wesson, *J. Am. Soc. Nephrol.*, 2005, **16**, 1904-1908.

[59] C. Rey, C. Combes, C. Drouet, A. Lebugle, H. Sfihi, A. Barroug, *Mater. Sci. Eng. Technol. C*, 2007, **38**, 996-1002.

[60] C. Rey, C. Combes, C. Drouet, H. Sfihi, A. Barroug, *Mater. Sci. Eng.: C*, 2007, **27**, 198-205.

[61] C. Drouet, C. Rey, "Nanostructured calcium phosphates for hard tissue engineering and nanomedicine", in *Nanostructured Biomaterials for Regenerative Medicine* (V. Guarino, M. Iafisco, S. Spriano, eds.), Woodhead Publishing Series in Biomaterials, Woodhead Publishing, Sawston, UK, 2020, 223-254.

[62] D. Bazin, V. Frochot, J.-Ph. Haymann, E. Letavernier, M. Daudon, *C. R. Chim.*, 2022, **25**, no. S1, 133-147.

[63] N. Çiftçioğlu, K. Vejdani, O. Lee, G. Mathew, K. M. Aho, E. O. Kajander, D. S. McKay, J. A. Jones, M. L. Stoller, *Int. J. Nanomed.*, 2008, **3**, 105-115.

[64] X. Carpentier, M. Daudon, O. Traxer, P. Jungers, A. Mazouyes, G. Matzen, E. Véron, D. Bazin, *Urology*, 2009, **73**, 968-975.

[65] S. R. Khan, B. K. Canales, *Urolithiasis*, 2015, **43**, 109-123.

[66] C. Verrier, D. Bazin, L. Huguet, O. Stéphan, A. Gloter, M.-Ch. Verpont, V. Frochot, J.-Ph. Haymann, I. Brocheriou, O. Traxer, M. Daudon, E. Letavernier, *J. Urol.*, 2016, **196**, 1566-1574.

[67] E. Letavernier, G. Kauffenstein, L. Huguet, N. Navasiolava, E. Bouderlique, E. Tang, L. Delaitre, D. Bazin, M. de Frutos, C. Gay, J. Perez, M. C. Verpont, J.-Ph. Haymann, V. Pomozi, J. Zoll, O. Le Saux, M. Daudon, G. Leftheriotis, L. Martin, *J. Am. Soc. Nephrol.*, 2018, **29**, 2337-2347.

[68] C. Gay, E. Letavernier, M.-Ch. Verpont, M. Walls, D. Bazin, M. Daudon, N. Nassif, O. Stephan, M. de Fruto, *ACS Nano*, 2020, **14**, 1823-1836.

[69] A. Ben Lakhdar, M. Daudon, M.-Ch. Mathieu, A. Kellum, C. Balleyguier, D. Bazin, *C. R. Chim.*, 2016, **19**, 1610-1624.

[70] J. A. M. R. Kunitake, S. Choi, K. X. Nguyen, M. M. Lee, F. He, D. Sudilovsky, P. G. Morris, M. S. Jochelson, C. A. Hudis, D. A. Muller, P. Fratzl, C. Fischbach, A. Masi, L. A. Estroff, *J. Struct. Biol.*, 2018, **202**, 25-34.

[71] K. S. Shin, M. Laohajaratsang, S. Men, B. Figueroa, S. M. Dintzis, D. Fu, *Theranostics*, 2020, **10**, 5865-5878.

[72] M. Petay, M. Cherfan, E. Bouderlique, S. Reguer, J. Mathurin, A. Dazzi, M. l'Heron, M. Daudon, V. Frochot, J.-Ph. Haymann, E. Letavernier, A. Deniset-Besseau, D. Bazin, *C. R. Chim.*, 2022, **25**, no. S1, 553-576.

[73] H. Colboc, J. Fontaine, D. Bazin, V. Frochot, E. Letavernier, M. Daudon, N. Laporte, S. Rouzière, M. Reby, A. Galezowski, Ch. Forasassi, S. Meaume, *J. Gerontol. A: Biol. Sci. Med. Sci.*, 2022, **77**, 27-32.

[74] H. Colboc, Ph. Moguelet, E. Letavernier, V. Frochot, J.-F. Bernaudin, R. Weil, S. Rouzière, P. Seneth, C. Bachmeyeri, N. Laporte, I. Lucas, V. Descamps, R. Amodek, F. Brunet-Possentik, N. Kluger, L. Deschamps, A. Dubois, S. Reguer, A. Somogyi, K. Medjoubi, M. Refregiers, M. Daudon, D. Bazin, *C. R. Chim.*, 2022, **25**, no. S1, 445-476.

[75] Ch. Nguyen, D. Bazin, M. Daudon, A. Chatron-Colliet, D. Hannouche, A. Bianchi, D. Côme, A. So, N. Busso, F. Lioté, H.-K. Ea, *Arthritis Res. Therapy*, 2013, **15**, article no. R103.

[76] A. Gauffenic, D. Bazin, Ch. Combes, M. Daudon, H.-K. Ea, *C. R. Chim.*, 2022, **25**, no. S1, 517-534.

[77] A. Dessombz, P. Méria, D. Bazin, M. Daudon, *PLoS One*, 2021, **7**, article no. e5169.

[78] H. Colboc, D. Bazin, Ph. Moguelet, V. Frochot, R. Weil, E. Letavernier, Ch. Jouanneau, C. Frances, C. Bachmeyer, J.-F. Bernaudin, M. Daudon, *C. R. Chim.*, 2016, **19**, 1631-1641.

[79] A. Dazzi, C. B. Prater, *Chem. Rev.*, 2017, **17**, 5146-5173.

[80] J. Mathurin, A. Deniset-Besseau, D. Bazin, E. Dartois, M. Wagner, A. Dazzi, *J. Appl. Phys.*, 2022, **131**, article no. 010901.

[81] D. Fournier, F. Lepoutre, A. Boccara, *J. Phys.*, 1983, **44**, 479-482.

[82] E. Esteve, Y. Luque, J. Waeytens, D. Bazin, L. Mesnard, Ch. Jouanneau, P. Ronco, A. Dazzi, M. Daudon, A. Deniset-Besseau, *Anal. Chem.*, 2020, **92**, 7388-7392.

[83] D. Bazin, M. Rabant, J. Mathurin, M. Petay, A. Deniset-Besseau, A. Dazzi, Y. Su, E. P. Hessou, F. Tielens, F. Borondics, M. Livrozet, E. Bouderlique, J.-Ph. Haymann, E. Letavernier, V. Frochot, M. Daudon, *C. R. Chim.*, 2022, **25**, no. S1, 489-502.

[84] D. Bazin, E. Bouderlique, E. Tang, M. Daudon, J.-Ph. Haymann, V. Frochot, E. Letavernier, E. Van de Perre, J. C. Williams, Jr., J. E. Lingeman, F. Borondics, *C. R. Chim.*, 2022, **25**, no. S1, 105-131.

[85] X. Carpentier, M. Daudon, O. Traxer, P. Jungers, A. Mazouyes, G. Matzen, E. Véron, D. Bazin, *Urology*, 2009, **73**, 968-975.

[86] D. Bazin, G. André, R. Weil, G. Matzen, E. Véron, X. Carpentier, M. Daudon, *Urology*, 2012, **79**, 786-790.

[87] M. Daudon, M. Petay, S. Vimont, A. Deniset, F. Tielens, J.-Ph. Haymann, E. Letavernier, V. Frochot, D. Bazin, *C. R. Chim.*, 2022, **25**, no. S1, 315-334.

[88] L. Maurice-Estepa, P. Levillain, B. Lacour, M. Daudon, *Scand. J. Urol. Nephrol.*, 1999, **33**, 299-305.

[89] D. Bazin, R. J. Papoular, E. Elkaim, R. Weil, D. Thiaudière, C. Pisapia, B. Ménez, N. S. Hwang, F. Tielens, M. Livrozet, E. Bouderlique, J.-P. Haymann, E. Letavernier, L. Hennet, V. Frochot, M. Daudon, *C. R. Chim.*, 2022, **25**, no. S1, 343-354.

Comptes Rendus
Chimie
2022, Vol. 25, Special Issue S1, p. 517-534
https://doi.org/10.5802/crchim.193

Microcrystalline pathologies: Clinical issues and nanochemistry / *Pathologies microcristallines : questions cliniques et nanochimie*

Pathological calcifications in the human joint

Alan Gauffenic [a], Dominique Bazin [*, b, c], Christèle Combes [d], Michel Daudon [e, f] and Hang-Korng Ea [a]

[a] Université de Paris, INSERM UMR 1132, BIOSCAR, Hôpital Lariboisière, Service de rhumatologie, DMU locomotion, APHP, Paris, France

[b] Université Paris-Saclay, CNRS, Institut de Chimie Physique, 91405 Orsay cedex, France

[c] Université Paris-Saclay, CNRS, Laboratoire de Physique des Solides, 91405, Orsay, France

[d] CIRIMAT, Université de Toulouse, CNRS, Toulouse INP – ENSIACET, 4 allée Emile Monso, 31030 Toulouse cedex 4, France

[e] INSERM, UMRS 1155, Sorbonne Université, Hôpital Tenon, 75020 Paris, France

[f] Service d'explorations fonctionnelles, Hôpital Tenon, AP-HP, 4, rue de la Chine, 75020 Paris Cedex 20, France

E-mails: alan.gauffenic@gmail.com (A. Gauffenic), dominique.bazin@universite-paris-saclay.fr (D. Bazin), christele.combes@ensiacet.fr (C. Combes), daudonmichel24@gmail.com (M. Daudon), korngea@yahoo.fr (H.-K. Ea)

Abstract. This contribution emphasizes the chemical complexity of abnormal cartilaginous deposits. First, we briefly describe some key techniques used to precisely describe their physicochemical characteristics. Then, we present the main chemical and structural characteristics of these two chemical phases, of either biological or synthetic origins. Finally, we discuss selected examples of calcification characterization.

Keywords. Cartilage, Human joint, Pathological calcifications, Scanning electron microscopy, Synchrotron radiation.

Published online: 20 July 2022

1. Introduction

Various epidemiological studies [1,2] rank osteoarthritis (OA), a rheumatic musculoskeletal disorder, as the most common joint disorder in the world. Thus the economic burden of OA on patients as well as on society is considerable. OA not only causes pain, but loss of function and consequent disability in adults. The American Joint Replacement Registry (AJRR) and the American Academy of Orthopedic Surgeons (AAOS), reported 1.2 million patients with over 1.7 million hip and knee replacement procedures in America in May 2020 [3,4].

OA affects the entire joint [5]. More precisely, the pathological modifications seen in OA encompass degradation of the articular cartilage, thicken-

* Corresponding author.

ing of the subchondral bone, osteophyte formation, variable degrees of synovial inflammation, degeneration of ligaments and menisci in the knee, and hypertrophy of the joint capsule [6].

Regarding cartilage, some investigators consider articular calcium phosphate crystals as "innocent bystanders" or the natural consequence of the joint damage [7]. Recent studies present evidence that intra-articular calcium phosphate crystals can elicit synovial inflammation and cartilage degradation, suggesting that these crystals play a direct pathogenic role in OA [8,9]. As stated by Murphy *et al.* [10] even if the presence of intra-articular calcium phosphate crystals is a consequence of joint damage, these crystals participate actively in aggravating the symptoms and signs of OA, especially via their effects on the synovium. Finally, Liu *et al.* [11] have extracted crystals from human osteoarthritic knee cartilage: they noticed that such crystals induce the production of proinflammatory and catabolic mediators (NO, MMP-13 and PGE2) in human primary chondrocytes and synoviocytes.

Cartilage calcifications can comprise different crystalline calcium phosphate phases: a calcium orthophosphate phase, i.e. carbonated apatite (CA), and two calcium pyrophosphate (CPP) phases, particularly monoclinic, and triclinic, CPP dihydrate phases (m-CPPD) and (t-CPPD) [12,13]. Carbonated apatite (CA) crystals are observed in 90%–100% of OA cartilage and associated with m- or t-CPPD crystals in 20%. The inflammatory mechanisms triggered by these different calcium phosphate crystal types are similar. However, m-CPPD has been reported to induce a more potent pro-inflammatory response via NF-κB pathway activation leading to the production of interleukin (IL)1β, IL6 and IL8 [14].

In this contribution, we present some recent investigations focused on the relationship between OA and calcifications. Accordingly we will present some selected physicochemical results based either on in-lab techniques or those available on large scale synchrotron radiation facilities, and discuss the advantages and limitations of these techniques. We will start with some general considerations on the relationship between disease and calcification, and a short review of the different techniques which have already been used to characterize pathological calcifications. Then some physico-chemical characteristics of calcium phosphate phases (CA and CPPD) involved in joint calcifications will be presented, and finally the detailed elemental, structural and morphological characterization of calcified cartilage will be described.

2. Brief summary of analytical methods for characterization of physiological and pathological calcifications

Following the example of Yavorskyy *et al.* [15], we consider several different families of techniques which can be classified as either imaging or spectroscopic.

2.1. *Imaging techniques*

Firstly, ultrasonography (US) [16], conventional radiography (CR) [16] and computed tomography (CT) [17,18], are routine imaging techniques typically available in hospitals. Recently, Cipolletta *et al.* [19] have evaluated and compared the accuracy of conventional radiography and musculoskeletal ultrasonography in the diagnosis of calcium pyrophosphate crystal deposition disease showing that these two techniques are complementary and aid diagnosis. US appeared helpful, and more sensitive than CR, in revealing CPPD-based calcification.

In clinical routine, polarized light microscopy is useful for identifying CPP crystals, and discriminates them from crystalline monosodium urate (MSU), but is insufficient for CA crystals which are too small. The spatial resolution of these three imaging techniques is currently sufficient for medical diagnosis but not particularly applicable in clinical research.

MicroCT, and contrast-enhanced CTs (CE-CT), can provide images of cartilage samples and calcifications but application at the *in vivo* scale (under 6 micrometers resolution) appears challenging. Dual-energy computed tomography (DECT) has recently emerged as a promising tool for chemical discrimination of cartilage calcifications. Pascart *et al.* [20] published a first proof of concept study on the potential of DECT for differentiating CPPD from apatite on subchondral and trabecular bone. Subsequently, the DECT approach has been used to effectively distinguish calcium orthophosphate (such as CA) and CPP crystal deposition in human joints *in vivo*. DECT can differentiate intra-articular CPP deposits from bone apatite [21].

Multi-energy spectral photon-counting CT (SPCCT) is a novel imaging technique which has potential advantages over DECT in characterizing MSU crystal deposits but needs to be further evaluated in the assessment of calcification pathologies *in vivo* [22,23].

Among conventional techniques, only ultrasonography is able to detect calcium phosphate crystal deposition, while advanced techniques, micro-CT and SPCCT, are both able to detect the crystals at micrometre spatial resolution (0.018 × 0.018 × 0.018 mm^3 and 0.090 × 0.090 × 0.090 mm^3 respectively). However, only SPCCT has been reported to be able to discriminate between CPPD and HA crystal deposits [24].

Field emission scanning electron microscopy (FE-SEM) plays a key role in OA research and achieves submicrometre spatial resolution [25,26]. Since the emergence of such technology (which replaces a single tungsten filament with a sharp pointed tip as the electron source), observations of calcifications on the surface of cartilage can be performed at low voltage (between 0.5 and 2 kV) without the need for conventional sample preparation such as surface deposition of carbon. As Figure 1 shows, micrometre scale FE-SEM images can distinguish between CA and CPPD crystals by their morphology [12].

In pathological calcifications, CA deposits generally manifest as spherical structures constituted of nanocrystal agglomerates [9,27,28], while CPPD crystals are larger and display an acicular morphology [29], as can be seen in Figure 1. More generally, the well understood relationship between crystal morphology, crystal symmetry, and chemical identity, constitutes a solid basis of crystallo-chemical analysis [30,31]. The spherical morphology of CA results from an agglomeration of nanocrystals of dimensions typically less than one hundred nanometres [32] and with a platelet morphology [33,34].

On an FE-SEM apparatus, an X-ray detector is usually positioned to gather information on the elemental composition of the calcification through X-ray fluorescence induced by the primary electrons [25,26]. This can give the Ca/P atomic ratio, which may be informative regarding the nature of the calcium orthophosphate phase (especially for dicalcium phosphate dihydrate (DCPD: Ca/P = 1) or octacalcium phosphate (OCP: Ca/P = 1.33), which are known as CA precursor phases) [35] except for biological CA which is a non-stoichiometric apatite with a Ca/P ratio lower than 1.67 (stoichiometric hydroxyapatite (HA)) [36,37] and which can reach Ca/P values as low as that of OCP.

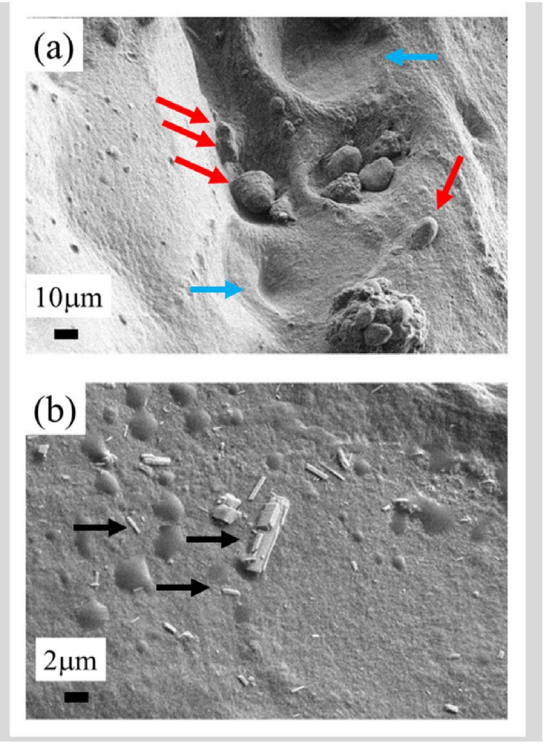

Figure 1. Examples of cartilage calcifications: (a) Agglomerates of several apatite crystallites (red arrows) localized in structures suggestive of chondrons (blue arrows). (b) Typical rod-shaped m- or t-calcium pyrophosphate dihydrate crystals (black arrows).

Nanometer scale imaging informs the clinician about the very first steps of pathogenic calcification [38]. There is a wide diversity of pathological calcification nucleation mechanisms, which may be homogeneous [39] or heterogeneous [40]. In the latter case, the role of vesicles [41,42], DNA [43], or proteins like elastin [44,45], as pathological calcification nuclei have been discussed. At this point, we emphasize that to determine the chemical nature of intravesicular calcifications, and more general nanometer scale deposits, various techniques such as electron energy loss micro-spectroscopy [42,46] are available. Several papers discuss the presence of vesicles in car-

tilage [47–49]. For instance Anderson [47] has identified vesicles of very different size (~300 Å–1 μm) within the cartilage matrix of the upper tibial epiphyseal plate of normal mice.

Finally, it is worth noting that 3D images can be obtained through classical tomography [50,51] in a typical hospital environment with a spatial resolution around 100 μm [52]. Using synchrotron radiation as a probe, Marenzana *et al.* [53] demonstrate that it is moreover possible to collect microCT data with an effective resolution of approximately 9 μm.

2.2. *Vibrational spectroscopies*

As emphasized previously, the various calcium phosphate phases in OA calcified cartilage (CA, m-CPPD and t-CPPD) require physico-chemical techniques, more specifically vibrational spectroscopies such as Raman [54–56] or Fourier transform infra-red (FT-IR) [57–61], which are advantageously non-destructive and label-free, for chemical analysis of biological tissues [54–61]. They detect vibrational energy levels and phonons of materials, and comparison with data bank reference spectra yields precise chemical and structural information [62]. These two spectroscopies are complementary, and both techniques are usually required to comprehensively measure the vibrational modes of a solid or dissolved molecule. In the case of pathological calcifications, advantages and limitations of these two spectroscopies with respect to sample preparation and data acquisition have been discussed by Daudon *et al.* [58]. At this point, let's recall that a Raman spectrum depicts the optical transitions between the various rotational–vibrational energy states of molecules, or ionic groupments and therefore enables precise characterization of material chemical composition [54–56,63,64]. The "Raman active" energy transitions observed in Raman spectra originate from a change in the polarizability of a molecular entity, i.e. the distortion of its electron cloud upon interaction with the incident light (i.e. a strong oscillating electromagnetic field in the UV, visible, or infrared energy domain) [56]. Raman spectroscopy has been applied to several kinds of biological samples encompassing fluids [65], cells [66], minerals as physiological [67] and pathological calcifications [68] and tissues [69].

Regarding FT-IR spectroscopy, or mid-FTIR region spectroscopy (wavenumber between 400–4000 cm^{-1}), the classical FTIR microscope experimental set–up which utilizes conventional sources (globar) can collect chemical images with a spatial resolution of approximately 5–10 μm depending on wavelength [70]. This spatial resolution can be significantly improved by combining atomic force microscopy and IR lasers [71–76], in which case spatial resolution is determined by the tip dimension and thus not diffraction limit constrained, and can be around 10 nm. Note that Optical PhotoThermal IR spectroscopy represents another opportunity, based on a pump–probe architecture using two laser sources, one for mid-infrared excitation (the pump) and the other for measuring the photothermal effect (the probe). With this geometry, it is possible to acquire IR spectra with a lateral resolution around 500 nm [75,77–84].

Numerous investigations (see review [85]) have been performed on cartilage following the pioneering work of Camacho *et al.* [86] and Potter *et al.* [87]. In terms of the preparation protocol, Spencer *et al.* [88] have clearly shown that the spectrum of fresh cartilage displays an altered amide I (1590–1720 cm^{-1})/amide II (1480–1590 cm^{-1}) peak ratio after 24 h, which corresponds to a significant alteration of the cartilage tissue, the amide I being correlated with the amount of collagen. In the case of CA, the ν_1 and ν_3 PO_4 stretching vibration modes occur at 960–962 cm^{-1} and 1035–1045 cm^{-1} respectively, while the ν_4PO_4 bending mode corresponds to the bands at 602–563 cm^{-1}. Finally, note the absence of the bands at 3570 and 633 cm^{-1}, which correspond to the stretching and vibrational modes of the OH^- groups characteristic of hydroxyapatite [62]. We will show that other techniques such as X-ray absorption spectroscopy when applied to nanometer scale materials [89–91] may also give essential information regarding pathological cartilage calcifications [92–96].

3. Some physicochemical aspects of the calcium phosphate phases in pathological joint calcifications

Two distinct calcium phosphate crystalline families are prominent in synovial fluids and cartilage, namely calcium pyrophosphate dihydrates and calcium orthophosphate [97]. In terms of the former,

both t-CPPD and m-CPPD phases occur in joint calcifications. Among the latter family, CA is the main phase encountered; it corresponds to a non-stoichiometric nanocrystalline carbonated apatite family (CA: $Ca_{10-x}(PO_4)_{6-x}(HPO_4,CO_3)_x(OH)_{2-x}$) [98,99]. Other crystalline calcium phosphate phases have been occasionally identified in synovial fluids and cartilage: octacalcium phosphate (OCP; $Ca_8(HPO_4)_2(PO_4)_4 \cdot 5H_2O$), tricalcium phosphate ($Ca_3(PO_4)_2$) [100], dicalcium phosphate dihydrate (DCPD) [101], and whitlockite ($Ca_9Mg(HPO_4)(PO_4)_6$) [60,102], based essentially on crystal morphology and size, and elemental composition [103]. As pointed out by Yavorskyy *et al.* [14], such diversity of calcium phosphate phases calls for physicochemical characterization techniques, and even a combination of several techniques, in addition to standard staining procedures which may help to detect pathological calcifications [27,28,104] but are not able to distinguish among these different calcium phosphate phases. Later we present some physicochemical aspects relevant to the main calcium phosphates identified in OA cartilage calcifications: CA and m-/t-CPPD phases.

3.1. *Biological and synthetic nanocrystalline carbonated apatites*

There are several excellent publications and reviews on the structural characteristics of phosphocalcic apatites [105–107]. Stoichiometric hydroxyapatite (HA: $Ca_{10}(PO_4)_6(OH)_2$) which crystallizes in the monoclinic $P2_1/b$ group (Figure 2) has generally been used as a model for biological apatites (bone mineral and tooth enamel). Unlike stoichiometric HA, biological apatites crystallize in the hexagonal $P6_3/m$ space group with the following unit cell parameters $a = b =$ 9.41844 Å and $c = 6.88374$ Å [105,106].

The presence of significant amounts of carbonate ions located in the PO_4^{3-} sites (type B carbonated apatite) and the OH^- sites (type A carbonated apatite) in apatites from pathological calcifications or normal hard tissues constitutes one of the main differences from the HA stoichiometric model [108]. Long a topic of debate, non-stoichiometric carbonated apatite is widely accepted as a model for biological hard tissue apatites, and described by the general chemical formula: $Ca_{10-x}\square_x(PO_4)_{6-x}(CO_3)_x(OH)_{2-x}\square_x$ with $0 \leq x \leq 2$ ($\square$ is a vacancy) [109–111]. The presence of hydrogen phosphate (HPO_4^{2-}) ions in PO_4^{3-} sites has also been reported in biological apatites [112,113]. Both divalent ions (carbonate and hydrogen phosphate) substituting for PO_4^{3-} are associated with a charge compensation mechanism involving the formation of one vacancy on a cationic site and one on a monovalent anionic site. Each divalent ion replacing PO_4^{3-} is thus associated with a missing OH^-, which explains why bone apatite is depleted in hydroxide ions.

In addition to large substitution capacity, tolerance of defects (mainly calcium and hydroxyl deficient non-stoichiometric apatites), nanocrystalline apatites present specific physicochemical and structural characteristics including exceptional surface reactivity, making this compound adaptable to various biological conditions and functions [114,115]. This reactivity is related to the existence on the nanocrystal surface of an hydrated layer containing mainly loosely bound divalent ions which can be easily exchanged in solution with cations, anions or proteins [116]. The carbonate content may be a clinical marker of alkaline medium. Thus, it is high in CA crystals identified in OA and bone. By contrast, it is low in kidney stones, except in the case of urinary tract infection by urease-splitting bacteriae [117,118].

The hydrated surface layer responsible for the strong surface reactivity of nanocrystalline apatites (ageing/maturation, ionic exchange, adsorption) is the most interesting structural feature but also the most complex to characterize. The latter can often be achieved with a combination of methods including chemical titrations and spectroscopic techniques such as vibrational spectroscopies (FTIR and Raman) and solid state nuclear magnetic resonance (NMR) [119,120]. The model of apatite nanocrystals based on an apatitic core and a more or less structured surface hydrated layer including non-apatitic domains is accepted but the precise description of the organization within this hydrated layer is still discussed. The reader will find illustrations of the apatite nanocrystal model in several papers [111,116].

Biomimetic nanocrystalline carbonated apatites can be synthesized by double decomposition between a soluble calcium salt solution and a soluble phosphate salt solution with a large excess of phosphate and carbonate ensuring pH buffering around physiological pH [116]. Precipitation of apatite is achieved by rapidly pouring the calcium solution into

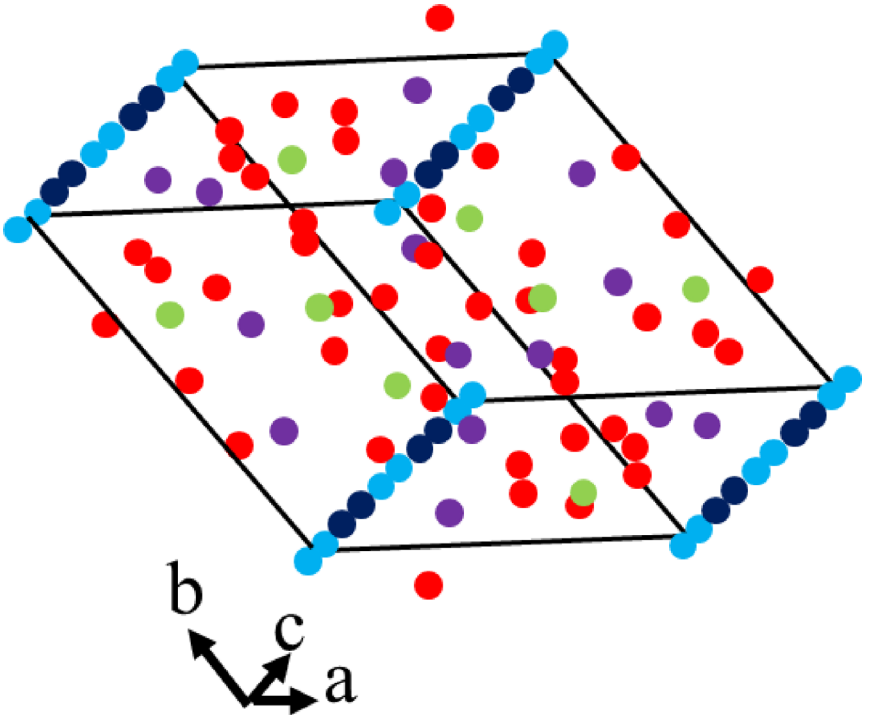

Figure 2. Spatial repartition of the different atoms in the case of stoichiometric hydroxyapatite (HA: $Ca_{10}(PO_4)_6(OH)_2$). Hydrogen and oxygen atoms of the hydroxyl groups represented in blue and dark blue respectively are located on the *c*-axis.

the phosphate/carbonate solution at room temperature and ageing the precipitate in the mother solution for variable periods of time. It is then filtered, washed, freeze-dried, and kept dry in a freezer to prevent from any transformations. This method yields plate-like apatite nanocrystals with a size and morphology analogous to bone apatite crystals (Figure 3).

Biological and synthetic apatite nanocrystals show a thin platelet morphology elongated toward the *c* axis with crystal dimensions of less than 100 nm, and even 50 nm, in length and a few nanometers in thickness [121]. TEM and SEM images of biological and synthetic nanocrystalline carbonated apatites are presented in Figure 3.

Finally, it is worth pointing out the presence of essential biological trace elements namely Mg, Fe, Sr, Se and Zn. In the cartilage examples we will show that the Zn content may be related to inflammation (Section 3.2) [122–124].

3.2. *Biological and synthetic calcium pyrophosphate phases*

As opposed to calcium orthophosphates, and especially apatites which have been extensively studied over many decades, the physicochemistry of calcium pyrophosphate phases of biological interest are not well documented although they were identified more than 60 years ago in menisci and synovial fluids [125, 126]. One of the main reasons is certainly related to the difficulty of obtaining pure synthetic CPPD compounds in large enough amounts to be able to thoroughly study the formation of those phases involved in biological processes and their detailed characterization.

Calcium pyrophosphate hydrated phases ($Ca_2P_2O_7 \cdot nH_2O$) have been studied in several excellent investigations [127–131]. Several forms of pure crystalline and amorphous calcium pyrophosphate hydrates have also been synthesized [131] including the two phases detected in joints of OA patients, m-CPPD and t-CPPD both of chemical

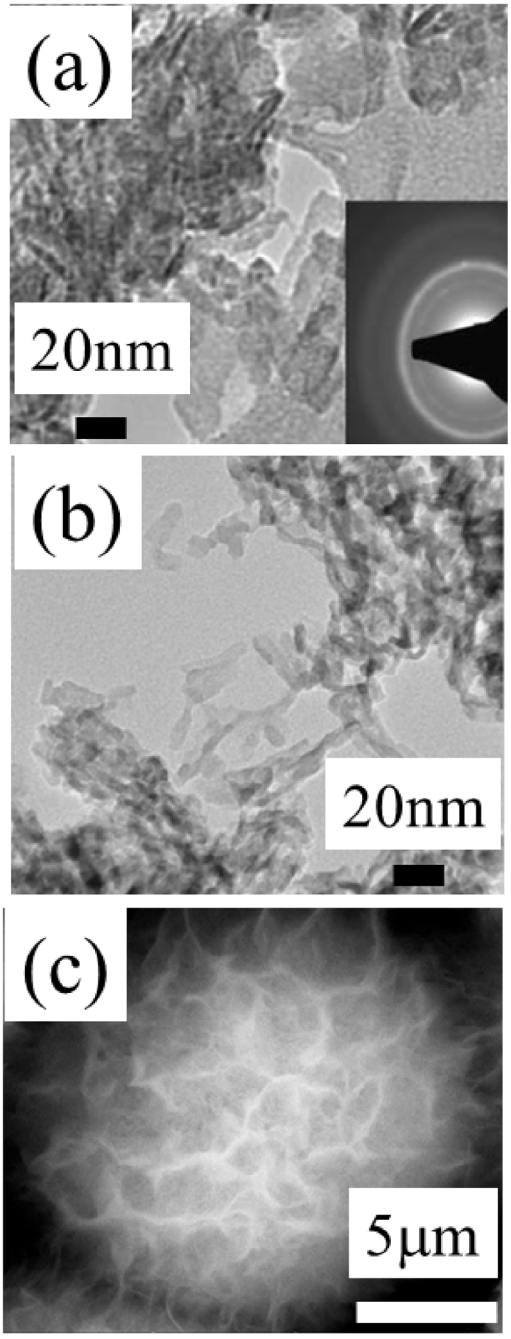

Figure 3. (a) TEM observation of bone tissue cross-section. (b) TEM observation of synthetic carbonated apatite (from Ref. [121]). (c) SEM observation of a pathological calcification composed of apatite (kidney stone).

formula $Ca_2P_2O_7 \cdot 2H_2O$. The existence of four other forms, namely one calcium pyrophosphate monohydrate phase ($Ca_2P_2O_7 \cdot H_2O$) [132], two monoclinic calcium pyrophosphate tetrahydrates (CPPT: $Ca_2P_2O_7 \cdot 4H_2O$) denoted m-CPPT-α and m-CPPT-β, and an amorphous phase, denoted a-CPP ($Ca_2P_2O_7 \cdot nH_2O$ with n around 4) [131,133–135] must also be mentioned. m-CPPT β and a-CPP phases are *in vitro* precursor phases of m/t-CPPD phases [126,136]. In acidic medium t-CPPD is the thermodynamically most stable crystalline phase of the CPP hydrates, followed by m-CPPD and then m-CPPT β phases.

Hydrolysis of some pyrophosphate ions ($P_2O_7^{4-}$) into orthophosphates (HPO_4^{2-}) can occur in the solid or in solution according to (1); this reaction is favored by acidic pH and/or increase of temperature in solution, and also at high temperature as a solid state reaction (internal hydrolysis) [130,137]. The presence of orthophosphate ions may stabilize some CPP hydrated phases and/or explain the co-existence of calcium orthophosphate (CA) and calcium pyrophosphate (m-CPPD and/or t-CPPD) phases in joint calcifications.

$$P_2O_7^{4-} + H_2O \rightarrow 2HPO_4^{2-} \quad (1)$$

A one-step fast protocol allowed the synthesis of the four CPP hydrated phases of biological interest (m-CPPD, t-CPPD, m-CPPT β and a-CPP) by controlling the pH and temperature during their precipitation by a double decomposition reaction between potassium pyrophosphate and calcium nitrate salt solutions [131]. With this method, we obtained pure m-CPPD powder and fully solved the m-CPPD structure including precise determination of hydrogen atom positions using Rietveld refinement of complementary data from synchrotron powder X-ray, and neutron, diffraction (Figure 4) [135]. Its unit-cell corresponds to the monoclinic system $P2_1/n$ and its parameters are: a = 12.60842(4) Å, b = 9.24278(4) Å, c = 6.74885(2) Å and β = 104.9916(3)°. The m-CPPD cell includes four formula units. The volume per formula unit is 189.93(1) Å^3; it is almost equal to that of the t-CPPD structure, 189.32(9) Å^3, the other CPPD phase found in OA joints, which presents a high inflammatory potential but lower than that of m-CPPD [138,139]. These new structural data on this pathological phase, with the highest inflammatory potential among the crystalline CPPD forms [140]

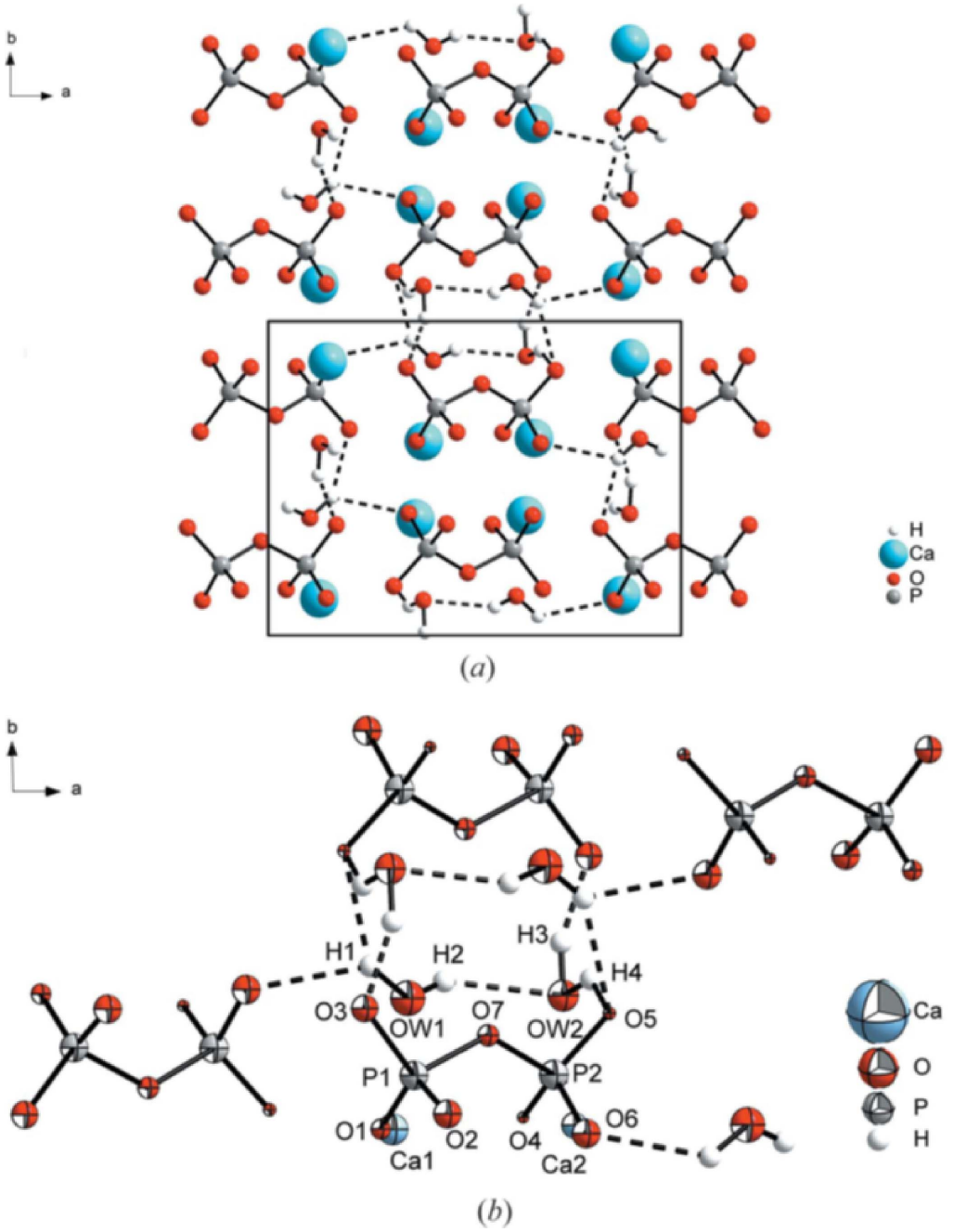

Figure 4. (a) Crystal structure of the m-CPPD phase and (b) representation of m-CPPD crystal structure showing the hydrogen bond network. Displacement ellipsoids are drawn at the 50% probability level. (Reprinted from Ref. [135].)

are of particular importance to further understand *in vivo* phenomena related to crystal structure-inflammatory response relationships in OA.

Detailed structural aspects of the biogenic CPPD phases have also been investigated by ^{1}H, ^{31}P and ^{43}Ca MAS solid state NMR spectroscopy leading to

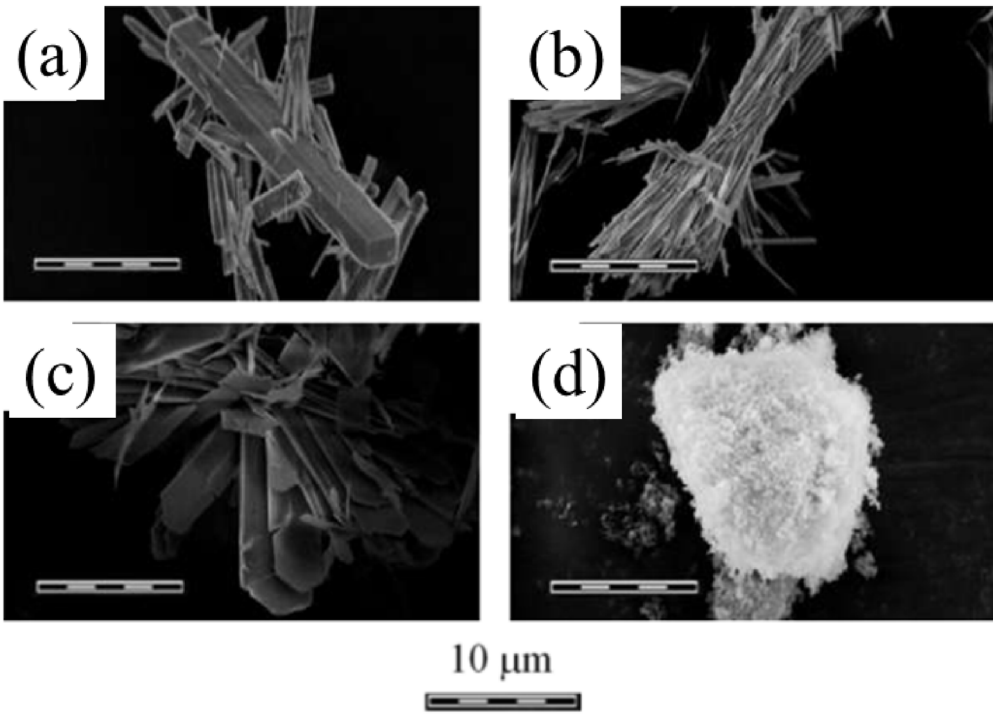

Figure 5. Morphologies of the different synthetic crystalline and amorphous phases of the calcium pyrophosphate hydrates of biological interest: (a) t-CPPD, (b) m-CPPD, (c) m-CPPT β and (d) *a*-CPP. (Reprinted from Ref. [131].)

informative fingerprints characterizing each phase [129]. Vibrational spectroscopies (FTIR and Raman) allow the different CPPD phases to be identified and provide valuable information on the conformations of the $P_2O_7^{4-}$ ions [131]. Indeed the flexibility of the pyrophosphate anion in the structure leads to different P–O–P bridge vibrations, and variation of the P–O–P angle, resulting in an effective means of clearly identifying the four calcium pyrophosphate hydrated phases (m-CPPD, t-CPPD, m-CPPT β and *a*-CPP). Gras *et al.* [131] have published a full description of the characteristic Raman and FTIR spectroscopy bands using reference synthetic phases.

The four main synthetic crystalline and amorphous phases of calcium pyrophosphate hydrates display very different morphologies (Figure 5) [131, 139]. The two CPPD polymorphs showed different acicular crystal habits: thin needles for m-CPPD (Figure 5b) and rods for t-CPPD (Figure 5a). Figure 5a shows t-CPPD synthetic crystal morphology, which appears analogous to that of biological crystals observed at the surface of calcified cartilage (Figure 1b). m-CPPT β (Figure 5c) has a faceted plate morphology related to the layered structure of this compound [126] and *a*-CPP appears as agglomerates of round nanoparticles of about 100 nm (Figure 5d). In addition to the different morphology of these four hydrated CPP phases, the distribution of pyrophosphate groups on the surface planes could explain the difference in inflammatory potential reported during *in vitro* and *in vivo* tests [139,140].

McCarty *et al.* [126] have proposed a scheme which establishes some structural evolution between all the calcium pyrophosphate forms.

4. Selected results on characterization of cartilage calcifications

4.1. *X-ray absorption spectroscopy*

Nguyen *et al.* [92] have characterized the chemical composition of medial and lateral cartilage from femoral condyles and tibial plateau (Figure 6) by

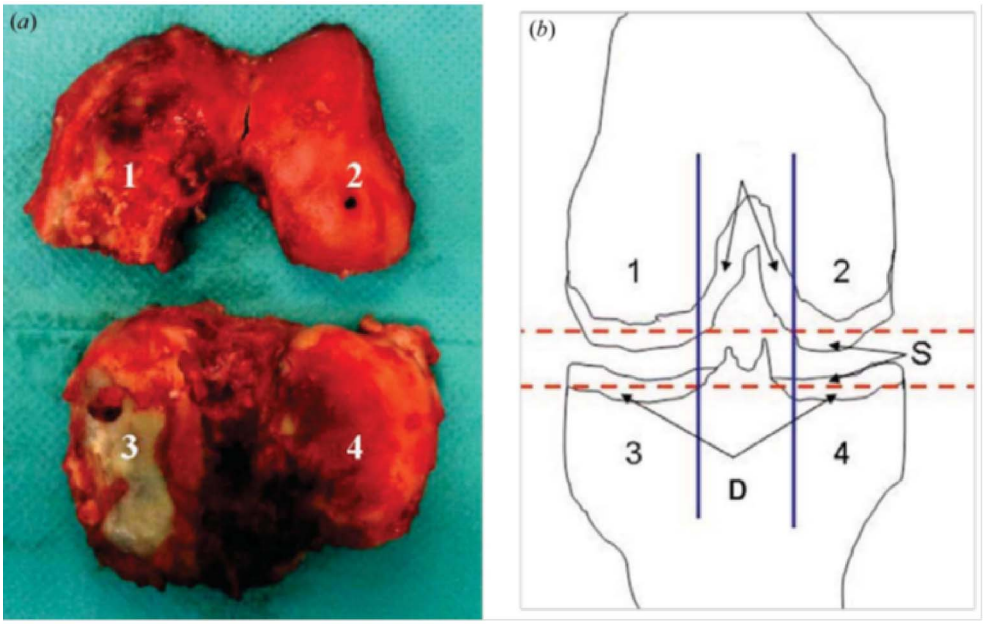

Figure 6. Knee joint specimen obtained during arthroplasty (a), and a schematic of the sample collection protocol (b). The specimen included femoral condyle and tibial plateau cartilage from both the medial and the lateral compartments (a). Cartilage areas are labelled as follows: 1—medial condyle; 2—lateral condyle; 3—medial tibial plateau; 4—lateral tibial plateau; S—superficial layer; D—deep layer (b) (from Ref. [92]).

FT-IR spectroscopy (Figure 7), and X-ray absorption spectroscopy (XAS) at the Ca K-absorption edge. The different regions of interest investigated are shown in Figure 6.

Figure 7 shows FTIR absorption spectra of cartilage samples. The absorption bands of carbonated apatite (CA) and calcium pyrophosphate dihydrate (CPPD) are well documented. Regarding CA, the ν_1 and ν_3 P–O stretching vibration modes occur at 960–962 cm^{-1} and 1035–1045 cm^{-1}, respectively, while the ν_4 O–P–O bending mode corresponds to the doublet at 602–563 cm^{-1}. The bands at 3570 and 633 cm^{-1}, corresponding to the stretching and vibrational modes of the OH^- groups characteristic of hydroxyapatite, are absent from CA. Regarding m-CPPD, O–P–O bending is observed at 535 cm^{-1} and 508 cm^{-1}. P–O stretching vibrations correspond to absorption bands at 923 cm^{-1} and 991 cm^{-1}, whereas asymmetric stretching vibrations give rise to absorption bands at 1037 cm^{-1} and 1089 cm^{-1}.

Synchrotron generated XAS is a sensitive technique which has been used to characterize the local environment of specific elements [137,141] such as S [95], Ca [92,142–145], Zn [94,146,147], Se [96], Pb [93], and Sr [148,149], in pathological calcifications. While for FTIR spectroscopy samples must be ground in a mortar to reduce the average particle size to 1 or 2 μm, XAS experiments can be performed directly on the biological sample with minimal preparation [92,142]. Note that many medically important substances such as anticancer molecules [150,151] and nanometer scale materials [152,153] can also be characterized with XAS spectroscopy [154–156].

Eichert *et al.* [157] demonstrate that XAS at the Ca K edge distinguishes between different non-apatitic calcium phosphates, namely dicalcium phosphate dihydrate, anhydrous dicalcium phosphate, octacalcium phosphate, amorphous calcium phosphate, beta tri-calcium phosphate and alpha tri-calcium phosphate (Figure 8).

The XAS spectra have been rationalized by Eichert *et al.* [157]. With increasing energy, we encounter the most intense resonance, known as the "white line", corresponding to the main 1s→np transition (Figure 9), exhibiting a characteristic three peak

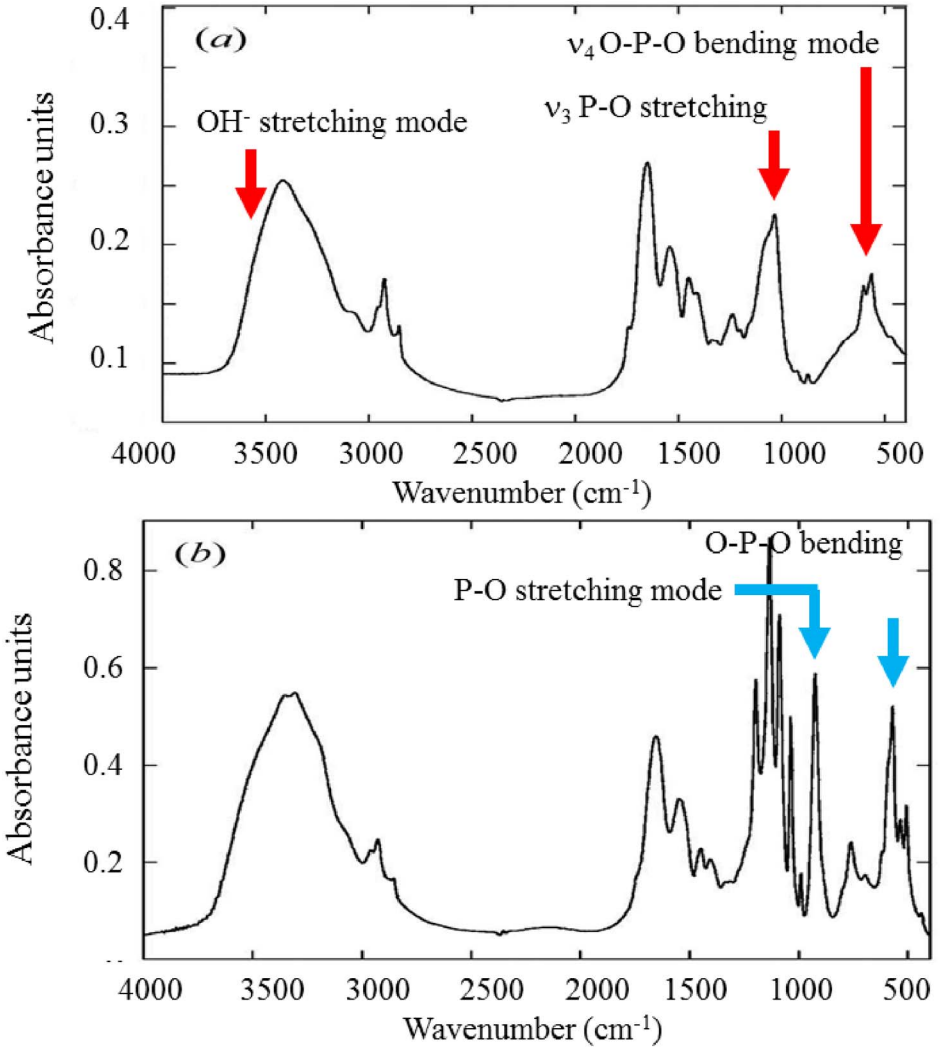

Figure 7. FT-IR absorption spectra of cartilage samples exhibiting pathological calcifications, namely, CA (a) and m-CPPD (b) (from Ref. [75]). Regarding m-CPPD, other IR bands are visible such as those related to νPO_3 (990–1200 cm^{-1}) and νOH (3100–3600 cm^{-1}) (see Ref. [131]).

structure: a shoulder (labelled B, 4047 eV) on the low energy side that remains unaltered across the series, assigned to the 1s→4s transition, a principal peak (C) corresponding to the allowed 1s→4p transition comprising two components (C1 and C2), whose relative intensities depend on Ca type (I or II) and may reflect deviation from stoichiometry in the samples [158]. D peak (4058.6 eV) corresponds to transitions to unoccupied states, mainly 5s states [159]. In addition, more XANES structures (labelled from E to H), mainly due to multiple scattering contributions, are resolved at higher energies for all compounds.

Nguyen *et al.* [92] investigated 12 cartilage samples by FTIR and X-ray absorption spectroscopy. FTIR spectroscopy detected CA and CPPD crystals in four, and three, out of 12 samples respectively. Three reference compounds were used, biological m-CPPD, CA, and amorphous carbonated calcium phosphate (ACCP).

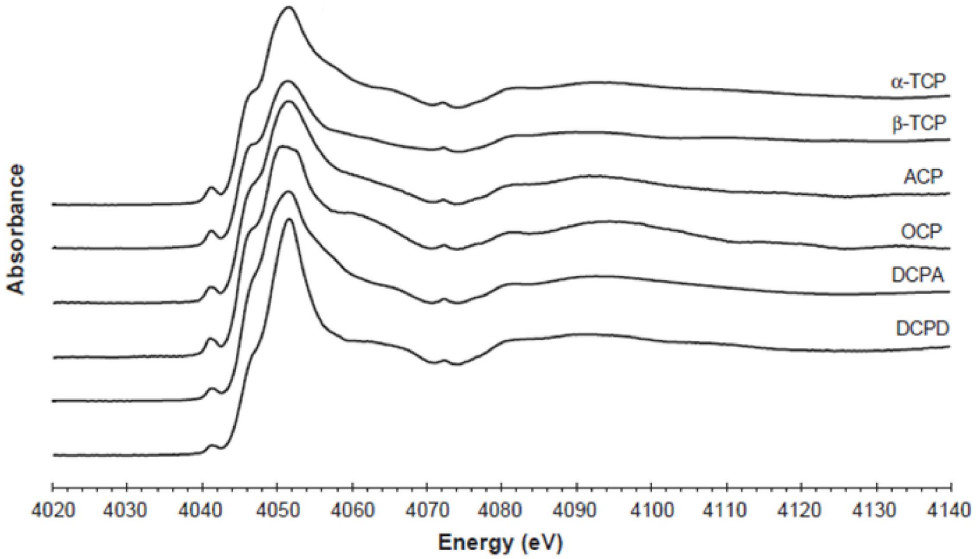

Figure 8. XANES spectra at the Ca K-edge of different non-apatitic calcium phosphate compounds. (DCPD: dicalcium phosphate dihydrate, DCPA: anhydrous dicalcium phosphate, OCP: octacalcium phosphate, ACP: amorphous calcium phosphate, β-TCP: beta tri-calcium phosphate, α-TCP: alpha tri-calcium phosphate). Reprinted from Ref. [157].

A striking result arises from the fact that calcium XAS spectra differ between calcified and non-calcified cartilage areas. In calcified areas calcium appears to be mainly associated with crystalline phase(s). In a more recent investigation, Nguyen *et al.* [12] demonstrate that mineralization involved several compartments, and processes associated with an increase in the expression of genes regulating inorganic phosphate and pyrophosphate homeostasis, which suggests a switch toward a promineralizing chondrocyte phenotype in OA.

4.2. *Heavy elements in cartilage*

Techniques specific to synchrotron radiation such as μX-ray fluorescence or μXAS can also be used to detect heavy elements in cartilage. Jarup [160], for example, has pointed out that the main threats to human health are associated with exposure to lead, cadmium, mercury, and arsenic. Lead is predominantly stored in the skeleton [161]. This localization may be due to the capacity of CA to accumulate heavy elements [162]. Using synchrotron radiation-based micro-X-ray fluorescence analysis, Zoeger *et al.* [163, 164] have shown a highly selective accumulation of Pb in the transition zone between calcified and non-calcified articular cartilage, the so-called "tidemark". This tidemark transition zone is an active calcification front and is thus of great clinical importance. More recently, using XAS, Meirer *et al.* [93] have determined the state of Pb in this tidemark zone.

The same approach can be applied to calcified cartilage. For example, Bradley *et al.* [165] have explored the changes in mineralization associated with osteoarthrosis development by X-ray diffraction and Ca and Sr Kα X-ray fluorescence microscopy. To achieve this, they analyzed lesions showing cartilage thinning and changes in the trabecular organization and density of the underlying bone. The complete set of data indicates that at the centre of the lesion the ratio of strontium to calcium was much lower than that in normal tissue, although the calcified cartilage still showed a higher ratio than the underlying bone. Moreover, in the superficially normal tissue around the lesion the calcified cartilage returned to a normal ratio much more rapidly than the underlying bone.

The presence of Zn in calcified cartilage has also been established, using a beamline able to collect XRD patterns and XAS spectra from the same sample (Figure 10) [166,167]. For this study, human carti-

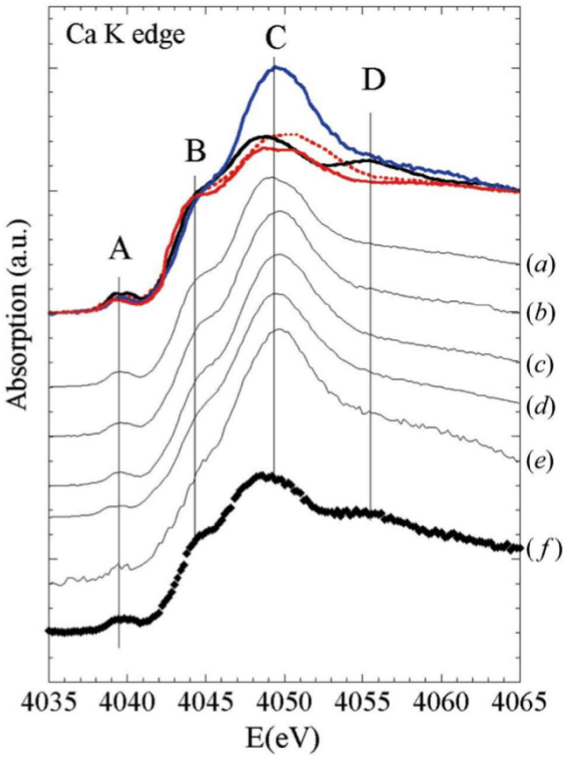

Figure 9. XANES spectra at Ca K-edge of human osteoarthritic cartilage, and reference synthetic calcium phosphate phases previously characterized by FTIR spectroscopy. Red solid line: synthetic nanocrystalline carbonated apatite (CA); red dotted line: amorphous carbonated calcium phosphate (ACCP); black solid line: m-CPPD; blue solid line: calcified tissue. (a) Patient 1, (b) Patient 3, (c) Patient 4, (d) Patient 5, (e) Patient 6 and (f) Patient 2 (from Ref. [92]).

lage (HC) and medial meniscus (MEM) samples were assigned a number.

Thus it was possible to characterize calcification by X-ray diffraction [168–175] while the environment of Zn was determined by XAS spectroscopy [94]. The complete set of data indicates that at least two Zn species were present: one may correspond to Zn metalloproteins (various Zn metalloproteins are known to inhibit biological calcification), and the other may be associated with a Zn "trap" in or on the surface of the calcification. Calcification in OA cartilage may significantly modify the spatial distribution of Zn, a fraction of which may be trapped in the calcification, altering the associated biological function of Zn metalloproteins.

5. Conclusion

The presence of apatite crystals has been reported to be associated with OA severity and cartilage degradation, whereas CPP is rather associated with chondrocyte senescence and aging [176]. While the contribution of the different types of calcium phosphate crystals to the clinical phenotype has been described, non-invasive imaging approaches to discriminate these calcifications are yet to be standardized.

In this article, we have described some of the physicochemical characteristics of various calcium phosphate phases identified in cartilage. Also, using a set of appropriate publications, we showed that it is possible to precisely describe not only the chemical composition and the spatial distribution of pathological calcifications in cartilage at the molecular and elemental level but also to detect trace elements

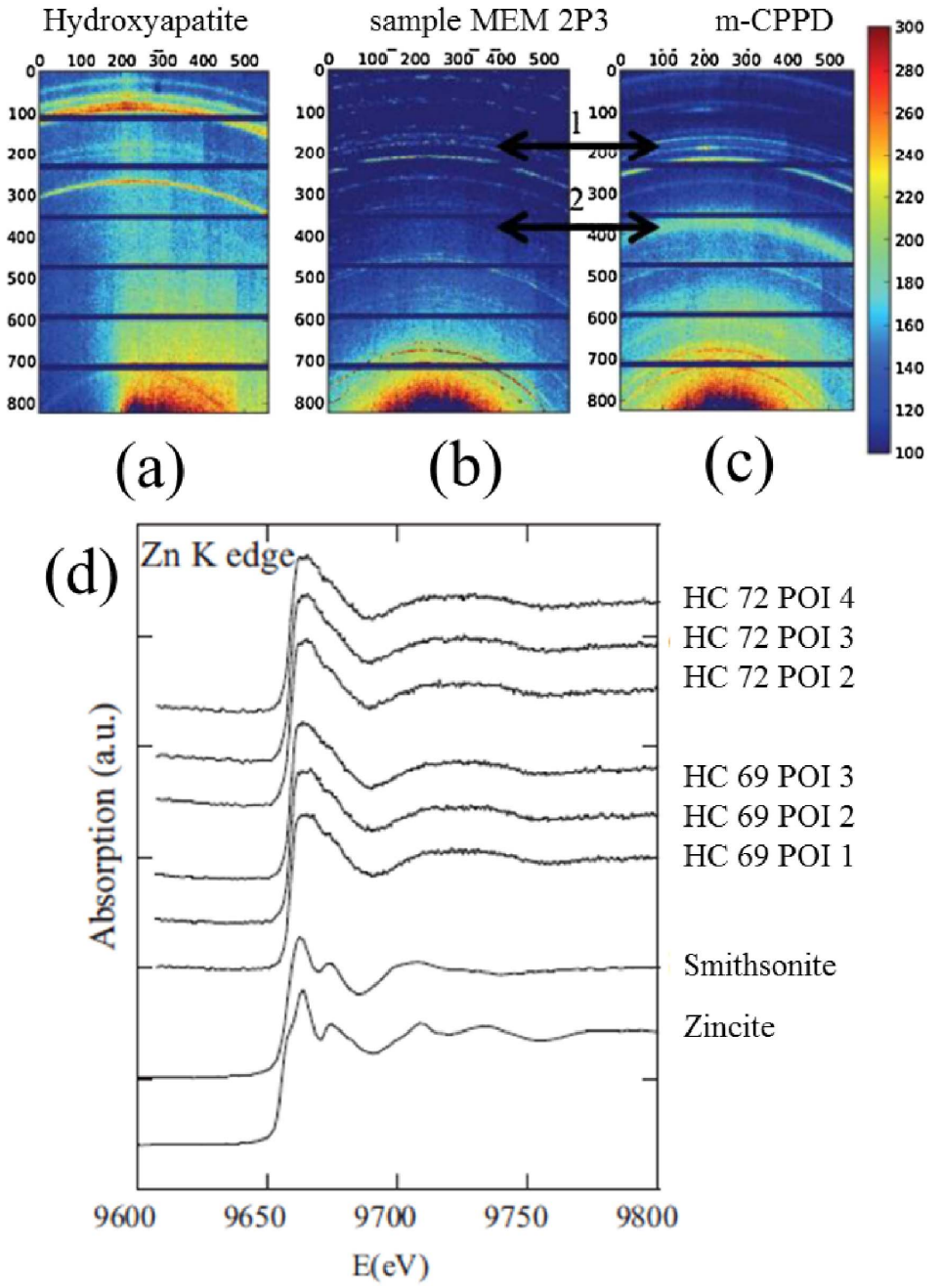

Figure 10. Micro-XRD analysis diagrams for the synthetic reference compounds and a biological specimen: (a) synthetic stoichiometric hydroxyapatite (HA), (b) biological sample MEM 2 P3, and (c) synthetic m-CPPD analyzed with the XPAD detector; (d) μXAS spectra recorded at the Zn K edge for biological samples (two calcified cartilage samples are considered namely HC69 and HC72 and for each of them, different points of interest (POI) have been considered in the study corresponding to Dessombz *et al.* [94]) and two reference compounds (smithsonite and zincite).

such as Zn which may be related to inflammatory processes.

Obviously, synchrotron radiation techniques offer further opportunities as shown by various excellent publications on cartilage as well as bone [177–181]. We hope that this contribution will reinforce collaboration between the medical and the physicochemical scientific communities.

Conflicts of interest

Authors have no conflict of interest to declare.

Acknowledgements

The authors thank the Centre National de la Recherche Scientifique (CalArthros project—"Longévité et Vieillissement 2010" CNRS interdisciplinary program) and the Agence Nationale de la Recherche (CAPYROSIS project—ANR-12-BS08-0022-01) for supporting part of this research work.

References

[1] Y. Zhang, J. M. Jordan, *Clin. Geriatr. Med.*, 2010, **26**, 355-369.
[2] E. R. Vina, C. K. Kwoh, *Curr. Opin. Rheumatol.*, 2018, **30**, 160-167.
[3] *American Joint Replacement Registry (AJRR): 2020 Annual Report*, American Academy of Orthopaedic Surgeons (AAOS), Rosemont, IL, 2020.
[4] L. Murphy, Ch. G. Helmick, *Am. J. Nurs.*, 2012, **112**, S13-S19.
[5] D. J. Hunter, D. T. Felson, *Br. Med. J.*, 2006, **332**, 639-642.
[6] R. F. Loeser, S. R. Goldring, C. R. Scanzello, M. B. Goldring, *Arthritis Rheum.*, 2012, **64**, 1697-1707.
[7] H. Mitsuyama, R. M. Healey, R. A. Terkeltaub, R. D. Coutts, D. Amiel, *Osteoarth. Cart.*, 2007, **15**, 559-565.
[8] B. Pazár, H. K. Ea, S. Narayan, L. Kolly, N. Bagnoud, V. Chobaz, T. Roger, F. Lioté, A. So, N. Busso, *J. Immunol.*, 2011, **186**, 2495-2502.
[9] H.-K. Ea, V. Chobaz, C. Nguyen, S. Nasi, P. van Lent, M. Daudon, A. Dessombz, D. Bazin, G. McCarthy, B. Jolles-Haeberli, A. Ives, D. Van Linthoudt, A. So, F. Lioté, N. Busso, *PLoS One*, 2013, **8**, article no. e57352.
[10] C.-L. Murphy, G. M. McCarthy, *EMJ Rheumatol.*, 2014, **1**, 96-102.
[11] Y. Z. Liu, A. P. Jackson, S. D. Cosgrove, *Osteoarth. Cart.*, 2009, **17**, 1333-1340.
[12] Ch. Nguyen, D. Bazin, M. Daudon, A. Chatron-Colliet, D. Hannouche, A. Bianchi, D. Côme, A. So, N. Busso, F. Lioté, H.-K. Ea, *Arthritis Res. Therapy*, 2013, **15**, article no. R103.
[13] M. Fuerst, J. Bertrand, L. Lammers, R. Dreier, F. Echtermeyer, Y. Nitschke, F. Rutsch, F. K. W. Schäfer, O. Niggemeyer, J. Steinhagen, C. H. Lohmann, T. Pap, W. Rüther, *Arthritis Rheum.*, 2009, **60**, 2694-2703.
[14] L. Campillo-Gimenez, F. Renaudin, M. Jalabert, P. Gras, M. Gosset, Ch. Rey, S. Sarda, C. Collet, M. Cohen-Solal, Ch. Combes, F. Lioté, H.-K. Ea, *Front Immunol.*, 2018, **9**, article no. 2248.
[15] A. Yavorskyy, A. Hernandez-Santana, G. McCarthy, G. McMahon, *The Analyst*, 2008, **133**, 302-318.
[16] G. Devrimsel, M. S. Beyazal, A. K. Turkyilmaz, S. B. Sahin, *J. Phys. Therm. Sci.*, 2016, **28**, 2249-2252.
[17] F. Eckstein, A. Guermazi, G. Gold, J. Duryea, M.-P. H. Le Graverand, W. Wirth, C. G. Miller, *Osteoarth. Cart.*, 2014, **22**, 1516-1532.
[18] J. Sullivan, M. H. Pillinger, M. Toprover, *Curr. Rheumatol. Rep.*, 2021, **23**, article no. 77.
[19] E. Cipolletta, G. Filippou, C. A. Scirè, A. Di Matteo, J. Di Battista, F. Salaffi, W. Grassi, E. Filippucci, *Osteoarth. Cart.*, 2021, **29**, 619-632.
[20] T. Pascart, L. Norberciak, J. Legrand, F. Becce, J.-F. Budzik, *Osteoarth. Cart.*, 2019, **27**, 1309-1314.
[21] T. Pascart, G. Falgayrac, L. Norberciak, C. Lalanne, J. Legrand, E. Houvenagel, H.-K. Ea, F. Becce, J. F. Budzik, *Therm. Adv. Musculoskelet. Dis.*, 2020, **24**, article no. 1759720X20936060.
[22] L. K. Stamp, N. G. Anderson, F. Becce, M. Rajeswari, M. Polson, O. Guyen, A. Viry, Ch. Choi, T. E. Kirkbride, A. Y. Raja, *Arthritis Rheum.*, 2019, **71**, 1158-1162.
[23] T. E. Kirkbride, A. Y. Raja, K. Müller, Ch. J. Bateman, F. Becce, N. G. Anderson, *AJR Am. J. Roentgenol.*, 2017, **209**, 1088-1092.
[24] I. Bernabei, Y. Sayous, A. Y. Raja, M. R. Amma, A. Viry, S. Steinmetz, G. Falgayrac, R. van Heeswijk, P. Omoumi, T. Pascart, L. K. Stamp, S. Nasi, Th. Hügle, N. Busso, A. K. So, F. Becce, *Rheumatology (Oxford)*, 2021, **60**, 2483-2485, MARS Collaboration.
[25] D. Bazin, M. Daudon, *Ann. Biol. Clin.*, 2015, **73**, 517-534.
[26] D. Bazin, E. Bouderlique, M. Daudon, V. Frochot, J.-Ph. Haymann, E. Letavernier, F. Tielens, R. Weil, *C. R. Chim.*, 2022, **25**, no. S1, 37-60.
[27] D. Bazin, M. Daudon, C. Combes, C. Rey, *Chem. Rev.*, 2012, **112**, 5092-5120.
[28] D. Bazin, M. Daudon, *J. Phys. D: Appl. Phys.*, 2012, **45**, article no. 383001.
[29] X. Cheng, D. G. Haggins, R. H. York, Y. N. Yeni, O. Akkus, *Appl. Spectrosc.*, 2009, **63**, 381-386.
[30] J. N. Lalena, *Crystallogr. Rev.*, 2006, **12**, 125-180.
[31] H. Kubbinga, *Z. Kristallogr.*, 2012, **227**, 1-26.
[32] M. Van Meerssche, J. Feneau-Dupont, *Introduction à la Cristallographie et à la Chimie Structurale*, Vander, Louvain-Cesson, Belgium, 1973.
[33] M. Vallet-Regı, M. J. Gonzalez-Calbet, *Prog. Solid. State. Chem.*, 2004, **32**, 1-31.
[34] D. Bazin, C. Chappard, C. Combes, X. Carpentier, S. Rouzière, G. André, G. Matzen, M. Allix, D. Thiaudière, S. Reguer, P. Jungers, M. Daudon, *Osteoporos. Int.*, 2009, **20**, 1065-1075.
[35] M. Banu, PhD Thesis, Polytechnic National Institute of Toulouse, 2005.
[36] C. Rey, C. Combes, C. Drouet, A. Lebugle, H. Sfihi, A. Barroug, *Mater. Sci. Eng. Technol.*, 2007, **38**, 996-1002.
[37] C. Drouet, C. Rey, *Nanostructured Biomaterials for Regener-*

ative Medicine, Woodhead Publishing Series in Biomaterials, Elsevier, Amsterdam, Netherlands, 2020, 223-254 pages.
[38] D. Bazin, E. Letavernier, J. P. Haymann, V. Frochot, M. Daudon, *Ann. Biol. Clin.*, 2020, **78**, 349-362.
[39] M. Daudon, V. Frochot, D. Bazin, P. Jungers, *C. R. Chim.*, 2016, **19**, 1514-1526.
[40] J. R. Espinosa, C. Vega, Ch. Valeriani, D. Frenkel, E. Sanz, *Soft Matt.*, 2019, **15**, 9625-9631.
[41] S. R. Khan, D. E. Rodriguez, L. B. Gower, M. Monga, *J. Urol.*, 2012, **187**, 1094-1100.
[42] C. Gay, E. Letavernier, M.-Ch. Verpont, M. Walls, D. Bazin, M. Daudon, N. Nassif, O. Stephan, M. de Fruto, *ACS Nano.*, 2020, **14**, 1823-1836.
[43] R. Coscas, M. Bensussan, M.-P. Jacob, L. Louedec, Z. Massy, J. Sadoine, M. Daudon, C. Chaussain, D. Bazin, J.-B. Michel, *Atherosclerosis*, 2017, **259**, 60-67.
[44] H. Colboc, Ph. Moguelet, D. Bazin, P. Carvalho, A.-S. Dillies, G. Chaby, H. Maillard, D. Kottler, E. Goujon, Ch. Jurus, M. Panaye, V. Frochot, E. Letavernier, M. Daudon, I. Lucas, R. Weil, Ph. Courville, J.-B. Monfort, F. Chasset, P. Senet, *JAMA Dermatol.*, 2019, **155**, 789-796.
[45] H. Colboc, Ph. Moguelet, E. Letavernier, V. Frochot, J.-F. Bernaudin, R. Weil, S. Rouzière, P. Seneth, C. Bachmeyeri, N. Laporte, I. Lucas, V. Descamps, R. Amodek, F. Brunet-Possentik, N. Kluger, L. Deschamps, A. Dubois, S. Reguer, A. Somogyi, K. Medjoubi, M. Refregiers, M. Daudon, D. Bazin, *C. R. Chim.*, 2022, **25**, no. S1, 445-476.
[46] K. Nitiputri, Q. M. Ramasse, H. Autefage, C. M. McGilvery, S. Boonrungsiman, N. D. Evans, M. M. Stevens, A. E. Porter, *ACS Nano.*, 2016, **10**, 6826-6835.
[47] H. C. Anderson, *J. Cell. Biol.*, 1969, **41**, 59-72.
[48] S. Miyaki, M. K. Lotz, *Curr. Opin. Rheumatol.*, 2018, **30**, 129-135.
[49] A. K. Rosenthal, *Curr. Opin. Rheumatol.*, 2016, **28**, 127-132.
[50] J. C. Williams, J. E. Lingeman, M. Daudon, D. Bazin, *C. R. Chim.*, 2022, **25**, no. S1, 61-72.
[51] C. Delecourt, M. Relier, S. Touraine, H. Bouhadoun, K. Engelke, J. D. Laredo, C. Chappard, *Osteoarth. Cart.*, 2016, **24**, 567-571.
[52] M. U. Ghani, Z. Zhou, L. Ren, Y. Li, B. Zheng, K. Yang, H. Liu, *NIM A.*, 2016, **807**, 129-136.
[53] M. Marenzana, Ch. K. Hagen, P. Das Neves Borges, M. Endrizzi, M. B. Szafraniec, T. L. Vincent, L. Rigon, F. Arfelli, R.-H. Menk, A. Olivo, *Phil. Trans. R. Soc. Lond. A*, 2014, **372**, article no. 20130127.
[54] M. Daudon, M. F. Protat, R. J. Reveillaud, H. Jaeschke-Boyer, *Kidney Int.*, 1983, **23**, 842-850.
[55] S. Tamosaityte, M. Pucetaite, A. Zelvys, S. Varvuolyte, V. Hendrixson, V. Sablinskas, *C. R. Chim.*, 2022, **25**, no. S1, 73-82.
[56] I. T. Lucas, D. Bazin, M. Daudon, *C. R. Chim.*, 2022, **25**, no. S1, 83-103.
[57] L. Estepa, M. Daudon, *Biospectroscopy*, 1997, **3**, 347-369.
[58] M. Daudon, D. Bazin, *C. R. Chim.*, 2016, **19**, 1416-1423.
[59] A. K. Rosenthal, E. Mattson, C. M. Gohr, C. J. Hirschmugl, *Osteoarth. Cart.*, 2008, **16**, 1395-1402.
[60] Th. Debroise, E. Colombo, G. Belletti, J. Vekeman, Y. Su, R. Papoular, N. S. Hwang, D. Bazin, M. Daudon, P. Quaino, F. Tielens, *Cryst. Growth Des.*, 2020, **20**, 2553-2561.
[61] A. Dessombz, D. Bazin, P. Dumas, C. Sandt, J. Sule-Suso, M. Daudon, *PLoS One*, 2011, **6**, article no. e28007.
[62] N. Quy Dao, M. Daudon, *Infrared and Raman Spectra of Calculi*, Elsevier, Paris, 1997.
[63] Z. Xu, Z. He, Y. Song, X. Fu, M. Rommel, X. Luo, A. Hartmaier, J. Zhang, F. Fang, *Micromachines (Basel)*, 2018, **9**, article no. 361.
[64] R. S. Das, Y. K. Agrawal, *Vib. Spectrosc.*, 2011, **57**, 163-176.
[65] A. Bonifacio, S. Cervo, V. Sergo, *Anal. Bioanal. Chem.*, 2015, **407**, 8265-8277.
[66] J. M. Surmacki, B. J. Woodhams, A. Haslehurst, B. A. J. Ponder, S. E. Bohndiek, *Sci. Rep.*, 2018, **8**, article no. 12604.
[67] G. S. Mandair, M. D. Morrisa, *Bonekey Rep.*, 2015, **4**, 1-8.
[68] V. Frochot, V. Castiglione, I. T. Lucas, J.-P. Haymann, E. Letavernier, D. Bazin, G. B. Fogazzi, M. Daudon, *Clin. Chim. Acta*, 2021, **515**, 1-4.
[69] H. Colboc, D. Bazin, P. Moguelet, S. Reguer, R. Amode, C. Jouanneau, I. Lucas, L. Deschamps, V. Descamps, N. Kluger, *J. Eur. Acad. Dermatol. Venereol.*, 2020, **34**, e313-e315.
[70] P. Lasch, D. Naumann, *Biochim. Biophys. Acta*, 2006, **1758**, 814-829.
[71] A. Dazzi, F. Glotin, R. Carminati, *J. Appl. Phys.*, 2010, **107**, article no. 124519.
[72] A. Dazzi, C. B. Prater, *Chem. Rev.*, 2017, **17**, 5146-5173.
[73] J. Mathurin, "Nanospectroscopie infrarouge avancée : développements instrumentaux et applications", PhD Thesis, Université Paris-Saclay, 2019.
[74] E. Esteve, Y. Luque, J. Waeytens, D. Bazin, L. Mesnard, Ch. Jouanneau, P. Ronco, A. Dazzi, M. Daudon, A. Deniset-Besseau, *Anal. Chem.*, 2020, **92**, 7388-7392.
[75] D. Bazin, M. Rabant, J. Mathurin, M. Petay, A. Deniset-Besseau, A. Dazzi, Y. Su, E. P. Hessou, F. Tielens, F. Borondics, M. Livrozet, E. Bouderlique, J.-Ph. Haymann, E. Letavernier, V. Frochot, M. Daudon, *C. R. Chim.*, 2022, **25**, no. S1, 489-502.
[76] J. Mathurin, A. Deniset-Besseau, D. Bazin, E. Dartois, M. Wagner, A. Dazzi, *J. Appl. Phys.*, 2022, **131**, article no. 010901.
[77] M. Kansiz, C. Prater, E. Dillon, M. Lo, J. Anderson, C. Marcott, A. Demissie, Y. Chen, G. Kunkel, *Microsc. Today*, 2020, **28**, 26-36.
[78] C. Lima, H. Muhamadali, Y. Xu, M. Kansiz, R. Goodacre, *Anal. Chem.*, 2021, **93**, 3082-3088.
[79] A. Spadea, J. Denbigh, M. J. Lawrence, M. Kansiz, P. Gardner, *Anal. Chem.*, 2021, **93**, 3938-3950.
[80] P. Zhao, Y. Zhao, L. Cui, Y. Tian, Z. Zhang, Q. Zhu, W. Zhao, *Sci. Total Environ.*, 2021, **775**, article no. 145846.
[81] D. Khanal, J. Zhang, W.-R. Ke, M. M. Banaszak Holl, H.-K. Chan, *Anal. Chem.*, 2020, **92**, 8323-8332.
[82] D. Zhang, C. Li, C. Zhang, M. N. Slipchenko, G. Eakins, J.-X. Cheng, *Sci. Adv.*, 2016, **2**, article no. e1600521.
[83] O. Klementieva, Ch. Sandt, I. Martinsson, M. Kansiz, G. K. Gouras, F. Borodics, *Adv. Sci.*, 2020, **7**, article no. 1903004.
[84] D. Bazin, E. Bouderlique, E. Tang, M. Daudon, J.-Ph. Haymann, V. Frochot, E. Letavernier, E. Van de Perre, J. C. Williams Jr., J. E. Lingeman, F. Borondics, *C. R. Chim.*, 2022, **25**, no. S1, 105-131.
[85] L. Rieppo, J. Töyräs, S. Saarakkala, *Appl. Spectrosc. Rev.*, 2017, **52**, 249-266.

[86] N. P. Camacho, P. West, P. A. Torzilli, R. Mendelsohn, *Biopolymers*, 2001, **62**, 1-8.

[87] K. Potter, L. H. Kidder, I. W. Levin, E. N. Lewis, R. G. Spencer, *Arthritis Rheum.*, 2001, **44**, 846-855.

[88] R. G. Spencer, E. F. Calton, N. P. Camacho, *J. Biomed. Opt.*, 2006, **11**, article no. 064023.

[89] D. E. Sayers, E. A. Stern, F. W. Lytle, *Phys. Rev. Lett.*, 1971, **27**, 1204-1207.

[90] D. Bazin, D. Sayers, J. Rehr, *J. Phys. Chem. B*, 1997, **101**, 11040-11050.

[91] D. Bazin, D. Sayers, J. J. Rehr, C. Mottet, *J. Phys. Chem.*, 1997, **101**, 5332-5336.

[92] Ch. Nguyen, H. K. Ea, D. Thiaudiere, S. Reguer, D. Hannouche, M. Daudon, F. Lioté, D. Bazin, *J. Syn. Rad.*, 2011, **18**, 475-480.

[93] F. Meirer, B. Pemmer, G. Pepponi, N. Zoeger, P. Wobrauschek, S. Sprio, A. Tampieri, J. Goettlicher, R. Steininger, S. Mangold, P. Roschger, A. Berzlanovich, J. G. Hofstaettere, Ch. Streli, *J. Synchrotron Rad.*, 2011, **18**, 238-244.

[94] A. Dessombz, C. Nguyen, H.-K. Ea, S. Rouzière, E. Foy, D. Hannouche, S. Réguer, F.-E. Picca, D. Thiaudière, F. Lioté, M. Daudon, D. Bazin, *J. Trace Elem. Med. Biol.*, 2013, **27**, 326-333.

[95] D. Brown, "Understanding the role of sulfur in cartilage development: How structural Proteoglycans are implicated in cartilage maturation", PhD Thesis, University of Saskatchewan, Saskatoon, 2017.

[96] C. Bissardon, O. Proux, S. Bureau, E. Suess, L. H. E. Winkel, R. S. Conlan, L. W. Francis, I. M. Khan, L. Charlet, J. L. Hazemann, S. Bohic, *Analyst*, 2019, **144**, 3488-3493.

[97] N. Mandel, G. Mandel, *Rheum. Dis. Clin. North Am.*, 1988, **14**, 321-340.

[98] R. Legros, N. Balmain, G. Bonel, *Calcif. Tissue Int.*, 1987, **41**, 137-144.

[99] G. M. Mccarthy, H. S. Cheung, *Curr. Rheumatol. Rep.*, 2009, **11**, 141-147.

[100] D. J. McCarty, J. R. Lehr, P. B. Halverson, *Arthritis Rheum.*, 1983, **26**, 1220-1224.

[101] D. McCarty, *Ann. Rheum. Dis.*, 1983, **42**, 243-253.

[102] D. Bazin, R. J. Papoular, E. Elkaim, R. Weil, D. Thiaudière, C. Pisapia, B. Ménez, N. S. Hwang, F. Tielens, M. Livrozet, E. Bouderlique, J.-Ph. Haymann, E. Letavernier, L. Hennet, V. Frochot, M. Daudon, *C. R. Chim.*, 2022, **25**, no. S1, 343-354.

[103] C. A. Scotchford, S. Y. Ali, *Ann. Rheum. Dis.*, 1995, **54**, 339-344.

[104] D. Bazin, Ch. Jouanneau, S. Bertazzo, Ch. Sandt, A. Dessombz, M. Réfrégiers, P. Dumas, J. Frederick, J.-Ph. Haymann, E. Letavernier, P. Ronco, M. Daudon, *C. R. Chim.*, 2016, **19**, 1439-1454.

[105] J. C. Elliott, *Structure and Chemistry of the Apatites and Other Calcium Orthophosphates*, Elsevier, Amsterdam, 1994.

[106] T. J. White, D. Zhi Li, *Acta Crystallogr. B*, 2003, **59**, 1-16.

[107] C. Rey, C. Combes, C. Drouet, H. Sfihi, A. Barroug, *Mater. Sci. Eng. C*, 2007, **27**, 198-205.

[108] C. Rey, B. Collins, T. Goehl, I. R. Dickson, M. J. Glimcher, *Calcif. Tissue Int.*, 1989, **45**, 157-164.

[109] R. Z. Legeros, *Monogr. Oral Sci.*, 1991, **15**, 1-201.

[110] M. E. Fleet, X. Liu, *Biomaterials*, 2007, **28**, 916-926.

[111] C. Combes, C. Rey, *Minerals*, 2016, **6**, article no. 34.

[112] Y. Wu, M. J. Glimcher, C. Rey, J. L. Ackerman, *J. Mol. Biol.*, 1994, **244**, 423-435.

[113] C. Rey, M. Shimizu, B. Collins, M. J. Glimcher, *Calcif. Tissue Int.*, 1990, **46**, 384-394.

[114] S. Cazalbou, D. Eichert, X. Ranz, C. Drouet, C. Combes, M. F. Harmand, C. Rey, *J. Mater. Sci. Mater. Med.*, 2005, **16**, 405-409.

[115] S. Cazalbou, C. Combes, D. Eichert, C. Rey, *J. Mater. Chem.*, 2004, **14**, 2148-2153.

[116] D. Eichert, C. Drouet, H. Sfihi, C. Rey, C. Combes, "Nanocrystalline apatite-based biomaterials: synthesis, processing and characterization", in *Trends in Biomaterials Research* (P. J. Pannone, ed.), Nova Science Publishers, Inc., 2007, ISBN1-978-1-60021-361-8.

[117] X. Carpentier, M. Daudon, O. Traxer, P. Jungers, A. Mazouyes, G. Matzen, E. Véron, D. Bazin, *Urology*, 2009, **73**, 968-975.

[118] D. Bazin, G. André, R. Weil, G. Matzen, E. Véron, X. Carpentier, M. Daudon, *Urology*, 2012, **79**, 786-790.

[119] C. Gervais, C. Bonhomme, D. Laurencin, *Solid State Nucl. Magn. Reson.*, 2020, **107**, article no. 101663.

[120] S. Von Euw, W. Ajili, T.-H. C. Chan-Chang, A. Delices, G. Laurent, F. Babonneau, N. Nassif, T. Azaïs, *Acta Biomater.*, 2017, **59**, 351-360.

[121] P. Pascaud, "Apatites nanocristallines biomimétiques comme modèles de la réactivité osseuse : Etude des propriétés d'adsorption et de l'activité cellulaire d'un bisphosphonate, le tiludronate", PhD Thesis, Université de Toulouse, 2012.

[122] M. Foster, S. Samman, *Nutrients*, 2012, **4**, article no. 676.

[123] N. Z. Gammoh, L. Rink, *Nutrients*, 2017, **9**, article no. 624.

[124] J. Olechnowicz, A. Tinkov, A. Skalny, J. Suliburska, *J. Phys. Sci.*, 2018, **68**, 19-31.

[125] N. N. Kohn, R. E. Hughes, D. J. McCarty Jr., J. S. Faires, *Ann. Intern. Med.*, 1962, **56**, 738-745.

[126] D. J. McCarty Jr., J. M. Hogan, R. A. Gatter, M. Grossman, *J. Bone Joint Surg. Am.*, 1966, **48**, 309-325.

[127] T. Balić-Žunić, M. R. Christoffersen, J. Christoffersen, *Acta Crystallogr. B*, 2000, **56**, 953-958.

[128] C. I. R. De Oliveira, L. F. C. de Oliveira, F. A. Dias Filho, Y. Messaddeq, S. J. L. Ribeiro, *Spectrochim. Acta. A*, 2005, **61**, 2023-2028.

[129] C. Roiland, F. Fayon, P. Simon, D. Massiot, *J. Non. Cryst. Solids*, 2011, **357**, 1636-1646.

[130] P. Gras, "Physico-chemical and structural study of hydrated calcium pyrophosphates: application to microcalcifications associated with arthritis", PhD Thesis, Toulouse University, 2014.

[131] P. Gras, C. Rey, O. Marsan, S. Sarda, C. Combes, *Eur. J. Inorg. Chem.*, 2013, **34**, 5886-5895.

[132] P. Gras, N. Ratel-Ramond, S. Teychené, C. Rey, E. Elkaim, B. Biscans, S. Sarda, C. Combes, *Acta Crystallogr. C*, 2014, **70**, 862-866.

[133] E. H. Brown, J. R. Lehr, J. P. Smith, A. W. Frazier, *J. Agric. Food. Chem.*, 1963, **11**, 214-222.

[134] C. Slater, D. Laurencin, V. Burnell, M. E. Smith, L. M. Grover, J. A. Hriljac, A. J. Wright, *J. Mater. Chem.*, 2011, **21**, 18783-18791.

[135] P. Gras, C. Rey, G. André, C. Charvillat, S. Sarda, C. Combes, *Acta Crystallogr. B*, 2016, **72**, 96-101.

[136] R. B. Stockbridge, R. Wolfende, *J. Biol. Chem.*, 2011, **286**, 18538-18546.
[137] O. Proux, E. Lahera, W. Del Net, I. Kieffer, M. Rovezzi, D. Testemale, M. Irar, S. Thomas, A. Aguilar-Tapia, E. F. Bazarkina, A. Prat, M. Tella, M. Auffan, J. Rose, J. L. Hazemann, *J. Environ Qual.*, 2017, **46**, 1146-1157.
[138] N. S. Mandel, *Acta Crystallogr. B—Struct. Sci.*, 1975, **31**, 1730-1734.
[139] L. Campillo-Gimenez, F. Renaudin, M. Jalabert, P. Gras, M. Gosset, C. Rey, S. Sarda, C. Collet, M. Cohen-Solal, C. Combes, F. Lioté, H.-K. Ea, *Front Immunol.*, 2018, **9**, article no. 2248.
[140] M. Roch-Arveiller, R. Legros, B. Chanaud, O. Muntaner, S. Strzalko, A. Thuret, D. A. Willoughby, J. P. Giroud, *Biomed. Pharmacother.*, 1990, **44**, 467-474.
[141] F. Porcaro, S. Roudeau, A. Carmona, R. Ortega, *Trends Anal. Chem.*, 2018, **104**, 22-41.
[142] X. Carpentier, D. Bazin, P. Jungers, S. Reguer, D. Thiaudière, M. Daudon, *J. Synchrotron Rad.*, 2010, **17**, 374-379.
[143] R. F. Weska, C. G. Aimoli, G. M. Nogueira, A. A. Leirner, M. J. S. Maizato, O. Z. Higa, B. Polakievicz, R. N. M. Pitombo, M. M. Beppu, *Artif. Organs*, 2010, **34**, 311-318.
[144] L. Pascolo, A. Gianoncelli, C. Rizzardi, V. Tisato, M. Salomé, C. Calligaro, F. Salvi, D. Paterson, P. Zamboni, *Sci. Rep.*, 2014, **4**, article no. 6540.
[145] V. Martin-Diaconescu, M. Gennari, B. Gerey, E. Tsui, J. Kanady, R. Tran, J. Pécaut, D. Maganas, V. Krewald, E. Gouré, C. Duboc, J. Yano, Th. Agapie, M.-N. Collomb, S. DeBeer, *Inorg. Chem.*, 2015, **54**, 1283-1292.
[146] D. Bazin, X. Carpentier, O. Traxer, D. Thiaudière, A. Somogyi, S. Reguer, G. Waychunas, P. Jungers, M. Daudon, *J. Synchrotron Rad.*, 2008, **15**, 506-509.
[147] D. Bazin, X. Carpentier, I. Brocheriou, P. Dorfmuller, S. Aubert, Ch. Chappard, D. Thiaudière, S. Reguer, G. Waychunas, P. Jungers, M. Daudon, *Biochimie*, 2009, **91**, 1294-1300.
[148] D. Bazin, A. Dessombz, Ch. Nguyen, H. K. Ea, F. Lioté, J. Rehr, Ch. Chappard, S. Rouzière, D. Thiaudière, S. Reguer, M. Daudon, *J. Synchrotron Rad.*, 2014, **21**, 136-142.
[149] D. Bazin, M. Daudon, Ch. Chappard, J. J. Rehr, D. Thiaudière, S. Reguer, *J. Synchrotron Rad.*, 2011, **18**, 912-918.
[150] E. Esteve, D. Bazin, Ch. Jouanneau, S. Rouzière, A. Bataille, A. Kellum, K. Provost, Ch. Mocuta, S. Reguer, D. Thiaudiere, K. Jorissen, J. J. Rehr, A. Hertig, E. Rondeau, E. Letavernier, M. Daudon, P. Ronco, *C. R. Chim.*, 2016, **19**, 1580-1585.
[151] E. Esteve, D. Bazin, Ch. Jouanneau, S. Rouzière, A. Bataille, A. Kellum, K. Provost, Ch. Mocuta, S. Reguer, D. Thiaudiere, K. Jorissen, J. J. Rehr, A. Hertig, E. Rondeau, E. Letavernier, M. Daudon, P. Ronco, *C. R. Chim.*, 2016, **19**, 1586-1589.
[152] E. Esteve, S. Reguer, C. Boissiere, C. Chanéac, G. Lugo, Ch. Jouanneau, C. Mocuta, D. Thiaudière, N. Leclercq, B. Leyh, J.-F. Greisch, J. Berthault, M. Daudon, P. Ronco, D. Bazin, *J. Synchrotron Rad.*, 2017, **24**, 991-999.
[153] D. Bazin, *C. R. Chim.*, 2022, **25**, no. S3, Forthcoming.
[154] J. Moonen, J. Slot, L. Lefferts, D. Bazin, H. Dexpert, *Physica B*, 1995, **208–209**, 689-690.
[155] D. Bazin, J. Rehr, *J. Phys. Chem. B*, 2003, **107**, 12398-12402.
[156] D. Bazin, J. Rehr, *J. Phys. Chem. C*, 2011, **115**, 23233-23236.
[157] D. Eichert, M. Salome, M. Banu, J. Susini, C. Rey, *Spectrochim. Acta B*, 2005, **60**, 850-858.
[158] K. Asokan, J. C. Jan, J. W. Chiou, W. F. Pong, P. K. Tseng, I. N. Lin, *J. Synchrotron Radiat.*, 2001, **8**, 839-841.
[159] J. Chaboy, S. Quartieri, *Phys. Rev. B*, 1995, **52**, 6349-6357.
[160] L. Jarup, *Br. Med. Bull.*, 2003, **68**, 167-182.
[161] L. E. Wittmers, J. Wallgren, A. Alich, A. C. Aufderheide, G. Rapp, *Arch. Environ. Health*, 1988, **43**, 381-391.
[162] J. Boisson, A. Ruttens, M. Mench, J. Vangronsvel, *Environ. Pollut.*, 1999, **104**, 225-233.
[163] N. Zoeger, P. Roschger, J. Hofstaetter, C. Jokubonis, G. Pepponi, G. Falkenberg, P. Fratzl, A. Berzlanovich, W. Osterode, C. Streli, P. Wobrauschek, *Osteoarth. Cart.*, 2006, **14**, 906-913.
[164] N. Zoeger, C. Streli, P. Wobrauschek, C. Jokubonis, G. Pepponi, P. Roschger, J. Hofstaetter, A. Berzlanovich, D. Wegrzynek, E. Chinea-Cano, A. Markowicz, R. Simon, G. Falkenberg, *X-ray Spectrom.*, 2008, **37**, 3-11.
[165] D. A. Bradley, P. Muthuvelu, R. E. Ellis, E. M. Green, D. Attenburrow, R. Barrett, K. Arkill, D. B. Colridge, C. P. Winlove, *NIM B*, 2007, **263**, 1-6.
[166] S. Reguer, C. Mocuta, D. Thiaudière, M. Daudon, D. Bazin, *C. R. Chim.*, 2016, **19**, 1424-1431.
[167] D. Bazin, S. Reguer, D. Vantelon, J.-Ph. Haymann, E. Letavernier, V. Frochot, M. Daudon, E. Esteve, H. Colboc, *C. R. Chim.*, 2022, **25**, no. S1, 189-208.
[168] A. Guinier, *Théorie et Technique de la Radiocristallographie*, Dunod, Paris, 1964.
[169] A. Le Bail, *Mater. Sci. Forum*, 2001, **378–381**, 65-70.
[170] D. Bazin, L. Guczi, J. Lynch, *Appl. Catal. A*, 2002, **226**, 87-113.
[171] A. Le Bail, D. Bazin, M. Daudon, A. Brochot, V. Robbez-Masson, V. Maisonneuve, *Acta Crystallogr. B*, 2009, **65**, 350-354.
[172] M. Daudon, D. Bazin, K. Adil, A. Le Bail, *Acta Crystallogr. E*, 2011, **67**, article no. o1458.
[173] A. Le Bail, M. Daudon, D. Bazin, *Acta Crystallogr. C*, 2013, **69**, 734-737.
[174] S. Rouzière, D. Bazin, M. Daudon, *C. R. Chim.*, 2016, **19**, 1404-1415.
[175] D. Bazin, V. Frochot, J.-Ph. Haymann, E. Letavernier, M. Daudon, *C. R. Chim.*, 2022, **25**, no. S1, 133-147.
[176] S. Stücker, M. Bollmann, Ch. Garbers, J. Bertrand, *Best Pract. Res. Clin. Rheumatol.*, 2021, **35**, article no. 101722.
[177] R. Cancedda, A. Cedola, A. Giuliani, V. Komlev, S. Lagomarsino, M. Mastrogiacomo, F. Peyrin, F. Rustichelli, *Biomaterials*, 2007, **28**, 2505-2524.
[178] A. D. Olubamiji, Z. Izadifar, D. Xiongbiao Chen, *Tissue Eng. Part B Rev.*, 2014, **20**, 503-522.
[179] Z. Izadifar, L. D. Chapman, X. Chen, *Tissue Eng. Part C Meth.*, 2014, **20**, 140-148.
[180] A. Horng, E. Brun, A. Mittone, S. Gasilov, L. Weber, T. Geith, S. Adam-Neumair, S. D. Auweter, A. Bravin, M. F. Reiser, P. Coan, *Invest. Radiol.*, 2014, **49**, 627-634.
[181] A. Horng, J. Stroebel, T. Geith, S. Milz, A. Pacureanu, Y. Yang, P. Cloetens, G. Lovric, A. Mittone, A. Bravin, P. Coan, *J. Biomed. Sci.*, 2021, **28**, article no. 42.

Comptes Rendus
Chimie
2022, Vol. 25, Special Issue S1, p. 535-552
https://doi.org/10.5802/crchim.203

Microcrystalline pathologies: Clinical issues and nanochemistry / *Pathologies microcristallines : questions cliniques et nanochimie*

Features of gallstones in adult sickle cell patients

Michel Daudon *, [a, b], **François Lionnet** [c], **Valéria Loi** [d], **Xavier Amiot** [e], **Antoine Boury** [f], **Jean-Philippe Haymann** [a, b, g] **and Dominique Bazin** [f, h]

[a] Sorbonne Universités, UPMC Univ Paris 06, UMR S 1155, Paris, France

[b] INSERM, UMR S 1155, Hôpital Tenon, Paris, France

[c] Centre de la Drépanocytose, Service de Médecine interne, AP-HP, Hôpital Tenon, Paris, France

[d] Service de Chirurgie Générale et Digestive, AP-HP, Hôpital Saint-Antoine, Paris, France

[e] Service de Gastro-Entérologie et d'Hépatologie, AP-HP, Hôpital Tenon, Paris, France

[f] Laboratoire de physique des solides, UMR CNRS 8502, Bâtiment 510, Université Paris-Sud, 91405 Orsay cedex, France

[g] Explorations fonctionnelles multidisciplinaires, AP-HP, Hôpital Tenon, Paris, France

[h] Institut de Chimie Physique, UMR CNRS 8000, Bâtiment 350, Université Paris Saclay, 91405 Orsay cedex, France

E-mails: daudonmichel24@gmail.com (M. Daudon), francois.lionnet@aphp.fr (F. Lionnet), valeria.loi@aphp.fr (V. Loi), xavier.amiot@aphp.fr (X. Amiot), antoine.boury@universite-paris-saclay.fr (A. Boury), jean-philippe.haymann.aphp.fr (J.-P. Haymann), dominique.bazin@universite-paris-saclay.fr (D. Bazin)

Abstract. Morpho-constitutional analysis of gallstones revealed significant differences between sickle cell patients and other gallbladder stone formers. As expected, pigment stones, mainly composed of calcium bilirubinates, were the most common type of stones in the former (74.7 versus 22.5%, $p < 10^{-6}$), which could be explained by haemolysis. However, if we consider that only 25% of sickle cell patients form stones in the bile ducts, this suggests that other factors could be involved such as mutations in the UGT1A1 gene. While calcium phosphates were found with the same frequency as the main component of gallstones in both groups, a high proportion of gallstones that had nucleated from carbapatite were observed in sickle cell patients in comparison to patients without sickle cell disease (23.5% versus 5.5%, $p < 0.0001$). In addition, among sickle cell patients, those who were homozygous were more prone than heterozygous subjects to form pigment gallstones from calcium phosphate (31.4 versus 5.9%, $p < 0.01$).

Keywords. Sickle cell disease, Gallstones, FTIR spectroscopy, FE-SEM, Calcium bilirubinates, Calcium phosphates.

Published online: 4 August 2022

* Corresponding author.

1. Introduction

Gallbladder lithiasis is a common pathology, but its prevalence varies greatly in different regions of the world. It can affect 5–20% of the general population in Western countries, with women being 1.5 to twice as often affected as men of the same age [1–3]. Glambek *et al.* found that 41.3% of women aged more than 60 years presented with gallstones [3]. Most studies have observed a correlation with the age of patients, with the prevalence of cholelithiasis reaching up to 25% in subjects over 60 years old [4–6]. It appears to be less common in Asia [7,8]. Differences by ethnic groups have been observed [9,10], as in the USA where cholelithiasis seems very common (60–70%) in Indian populations, and less common in Black Americans than in Caucasian adults who are affected in 10–15% of cases [5]. Similarly, in China, cholelithiasis is twice as prevalent in the Uighur population (22.9%) than the Han population (11.6%) [11]. It very often remains asymptomatic (65–80% of cases), especially in young adults [4,6,12,13]. Gallstones are more prevalent in obese and hypertriglyceridemic subjects and in multiparous women [2]. Assumed in Western populations to be mainly composed of cholesterol [5,6], this lithiasis has, however, like its renal counterpart, a number of components actually suggesting not only diverse etiological factors of metabolic, genetic, dietary, but also infectious, origin. Basically, however, two compounds dominate the profile of cholelithiasis, on the one hand cholesterol, on the other pigment stones such as calcium bilirubinate [14–18]. Three main types of stones have been described: cholesterol stones, brown pigment stones and black pigment stones [6,19]. The first are related to lipid imbalances, the second mainly to infectious contexts, and the third to haemolytic phenomena. Concerning stone analysis, this distinction is not always so clear cut because many mixed stones contain significant proportions of cholesterol and bile pigments, or even other calcium-rich compounds such as carbonated calcium phosphate apatite (carbapatite) or calcium carbonates [14,15].

In sickle cell disease, vesicular lithiasis is a common complication of the disease [20–23]. The nature of the stones is essentially related to haemolysis but the analysis of the calculi again shows a diversity of components that suggests the contribution of other factors to this lithogenesis. In addition, while all patients are exposed to haemolysis due to their haemoglobin abnormalities, not all develop stones suggesting that other factors than repeated haemolysis may contribute to lithogenic activity in these patients. The purpose of the study was to compare the morphological and compositional characteristics of sickle cell stones from adult patients with those of common gallstones.

2. Materials and methods

We had the opportunity to analyze 408 gallstones from adult patients, 75 of which came from patients with sickle cell disease. Among the latter, 56 were homozygous (ss) and 19 were heterozygous (sc). The analysis included morphological examination with a binocular magnifying glass (Stereomicroscope Olympus SZ51) and, for some calculi, Field Emission Scanning Electron Microscopy (FE-SEM) to specify the structural characteristics of the stones [24]. Samples were examined without coating through FE-SEM.

Then, the calculi were subjected to a sequential analysis by Fourier Transform Infrared (FTIR) spectroscopy from the core to the periphery to precisely define the composition and possible variations between the nucleation zone and the surface of the stone [25]. Infrared spectra were collected in the transmission mode on a Vector 22 FTIR spectrophotometer from Bruker Optics using the KBr pellet technique as described elsewhere [26,27]. Statistical comparisons were made on the NCSS software using the Fisher's exact test.

Ethical approval was obtained by the CPP of Tenon Hospital for this non-interventional patient study. Each sample was named only by a study number, without indicating the name of the patient or other potential identification data. The study was carried out as part of routine patient care without any specific sampling apart from the stone transferred to the laboratory for compositional analysis.

3. Results

The average age of sickle cell patients who underwent cholecystectomy is 14 years younger than that of patients operated on cholelithiasis of other causes (32.7 ± 13.5 years (extreme limits: 18.9 and 64.4 years) versus 46.8 ± 25.5 years (extreme limits: 17.8 and 95.7 years), $p < 0.0001$). Women with common bladder

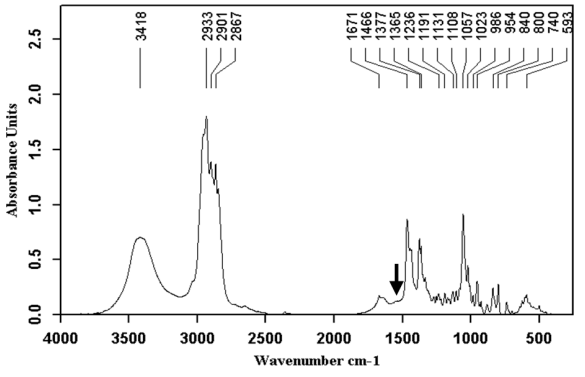

Figure 1. Cholesterol anhydrous and monohydrate with small proportions of proteins (black arrow).

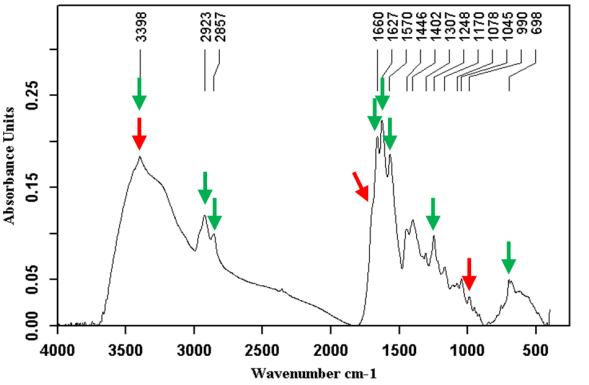

Figure 2. Calcium bilirubinates (green arrows) and free bilirubin (peaks at 3407, 1693 and 991 cm^{-1}, red arrows). Two forms of calcium bilirubinate are often present in gallstones. The preponderant form is neutral calcium bilirubinate with its characteristic bands at 1664, 1627 and 1570 cm^{-1}. The second form, more or less frequent and always less abundant than neutral bilirubinate resembles free bilirubin with peaks moved to 3395 and 1703 cm^{-1} that correspond to hydrogen bond and free carboxyl groups respectively. In the common cases where acid calcium bilirubinate and free bilirubin are mixed in the same stone, the peaks are slightly shifted to the intermediate position as shown at 3398 cm^{-1} in Figure 2.

stones (n = 198) were more frequent than men (n = 135) but not in the case of sickle cell stones (women = 37, men = 38). The difference between groups was not significant (p = 0.1).

3.1. *FTIR analysis*

Of all 408 gallstones included in this series, FTIR analysis highlighted the preponderance of cholesterol and bile pigments as the most common and abundant constituents, but also the fact that many stones are mixed and have three or four components, or even more. In patients with sickle cell disease, the most common and abundant component was calcium bilirubinate. In addition, FTIR analysis revealed a great diversity of compounds in gallstones with more than 30 different components identified (Table 1).

The spectra presented below illustrate this diversity. Even when a stone is composed of a single chemical species, it can contain several crystalline forms such as anhydrous cholesterol and monohydrate for cholesterol stones, neutral and acid calcium bilirubinate for pigment stones, or calcite and vaterite for calcium carbonate stones. In addition, sequential analysis from the core to the surface can reveal a change in composition suggesting the successive involvement of several factors in the formation of the stone. Finally, some components such as free bilirubin, which are abundant in gallbladder, can be incorporated into the stone without necessarily playing an active part in the lithogenic process. By contrast, polymers of bilirubin can be involved in stone formation [28]. Figures 1–16 illustrate the diversity of stone components and mixtures found in gallstones by FTIR analysis. Commonly, gallbladder stones are made of cholesterol (Figure 1), calcium bilirubinate (Figure 2) and/or calcium carbonate (Figure 3) and/or calcium phosphates (Figure 4) with various proportions of proteins (Figure 5). Calcium palmitate (Figure 6) or calcium stearate can also be frequently found. Exogenous compounds have also been identified such as drugs or surgical ligatures: they were found in 2% of stones in our series. Glafenine, dipyridamole, sulindac or indinavir were described more than 20 years ago [29–32]. More recently calcium ceftriaxonate (Figure 7) and atazanavir (Figure 8) have been also reported in gallstones with a high frequency in patients receiving these treatments [33–39]. Gallstones can contain multiple components as shown in Figures 9–16. More than 43% of the stones contain at least five components and often more (Table 2).

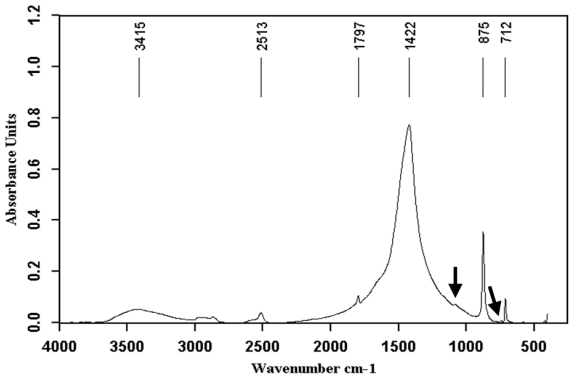

Figure 3. Calcite (calcium carbonate anhydrous crystallized in the rhombohedral system) + vaterite (also calcium carbonate anhydrous but crystallized in the hexagonal system) (black arrows).

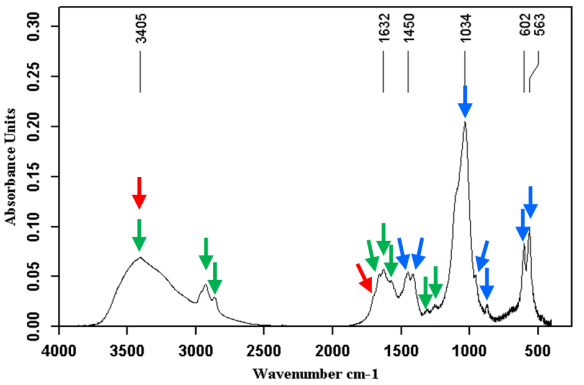

Figure 4. Calcium phosphate stone (carbapatite, blue arrows) also containing calcium bilirubinates (green arrows) and bilirubin (peak at 3405 cm^{-1}, shoulder at 1698 cm^{-1}, red arrows).

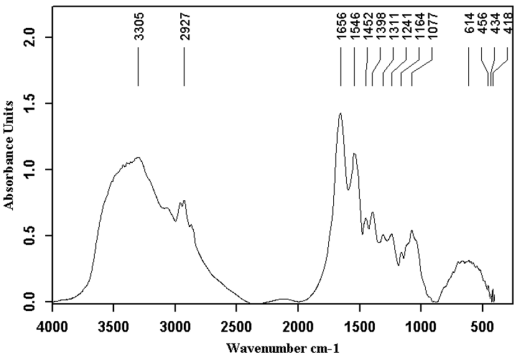

Figure 5. Proteins stone.

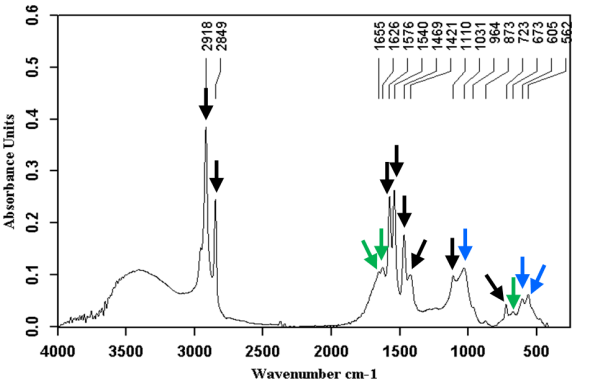

Figure 6. Calcium palmitate (black arrows) mixed with calcium bilirubinates (green arrows) and carbapatite (blue arrows).

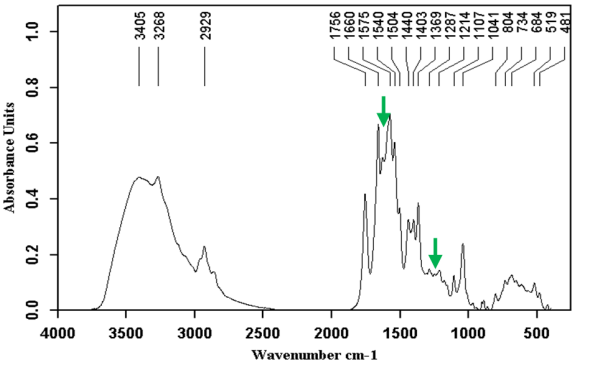

Figure 7. Calcium ceftriaxonate with small proportions of calcium bilirubinates (green arrows).

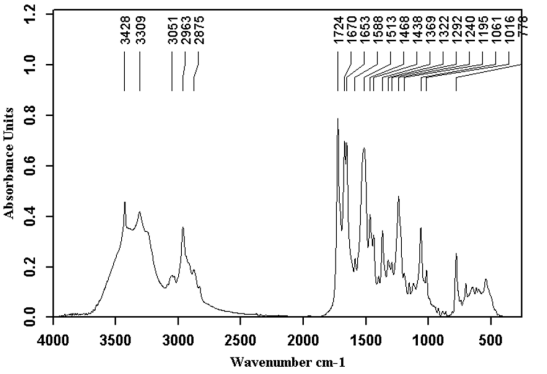

Figure 8. Atazanavir.

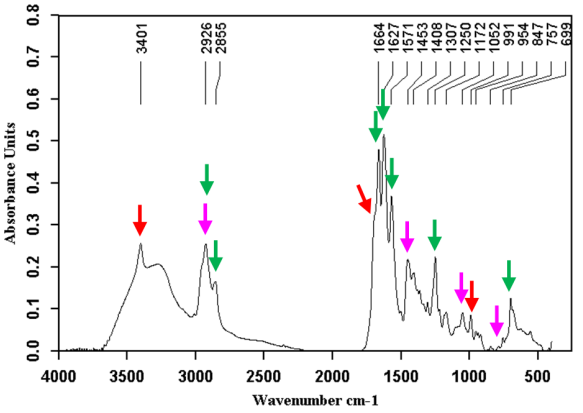

Figure 9. Calcium bilirubinates (green arrows) + cholesterol (pink arrows) + bilirubin (red arrows).

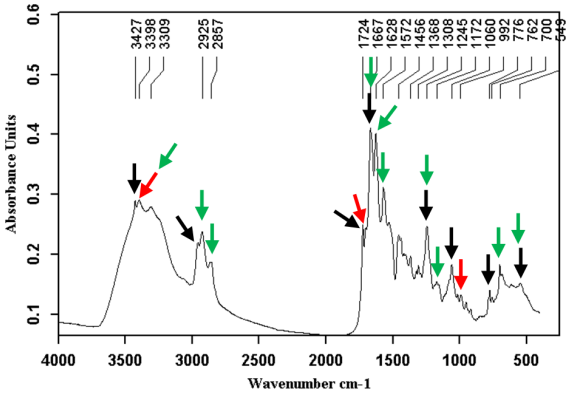

Figure 10. Pigment stone made of a mixture of calcium bilirubinates (green arrows), bilirubin (red arrows) and atazanavir (black arrows).

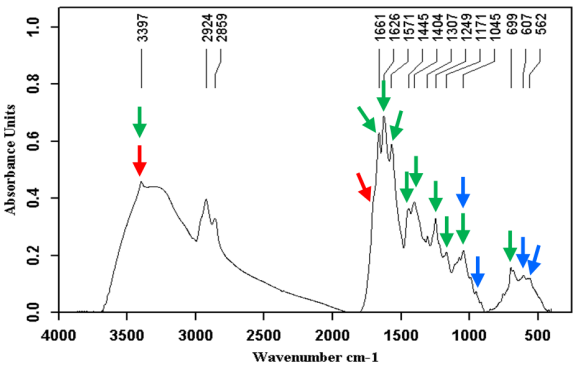

Figure 11. Calcium bilirubinates (green arrows) + bilirubin (red arrows) + carbapatite (blue arrows).

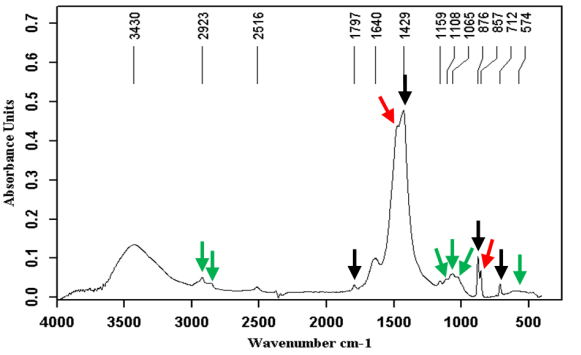

Figure 12. Calcite (black arrows) + aragonite (red arrows) + mucopolysaccharides (green arrows).

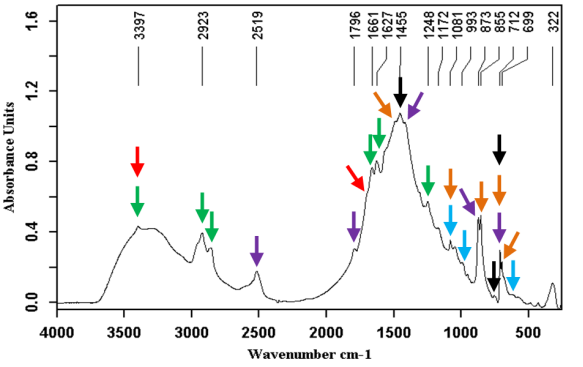

Figure 13. Calcite (▼) + aragonite (▼) + vaterite (▼) + calcium bilirubinates (▼) + bilirubin (▼) + calcium cholate (▼).

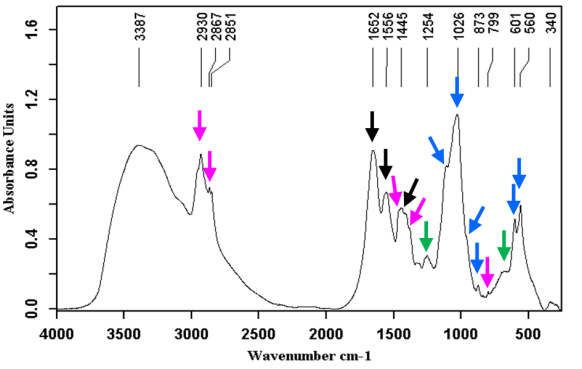

Figure 14. Carbapatite (blue arrows) + proteins (black arrows) + cholesterol (pink arrows) + calcium bilirubinates (green arrows).

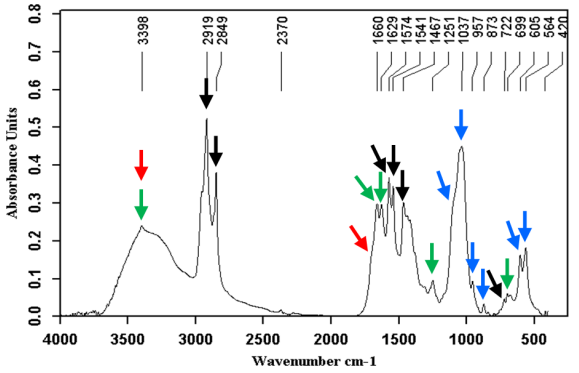

Figure 15. Carbapatite (blue arrows) + calcium bilirubinates (green arrows) + calcium palmitate (black arrows) + bilirubin (red arrows).

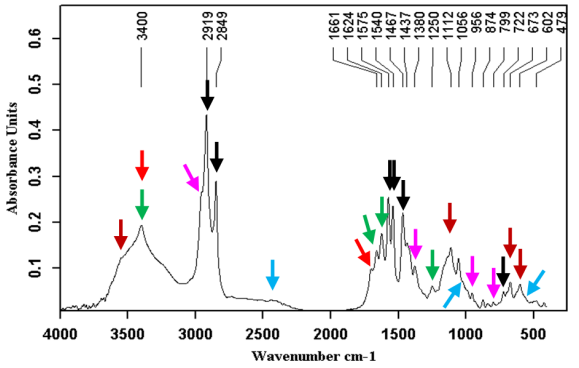

Figure 16. Calcium palmitate (↓) + calcium bilirubinates (↓) + bilirubin (↓) + gypsum (↓) + struvite (↓).

3.2. *Stone morphology*

As with urinary stones, morphology can help classify stones according to their main component. However, morphological criteria based on the texture, internal organization, and colour of the calculi are much less relevant. Indeed, if a light colour on the surface or section suggests a predominance of cholesterol (Figures 17A–C and 18A,B), a dark brown or brown-black suggests pigment stones (or portions of stones), that is to say containing bilirubin derivatives (Figures 17D,E and 18D,E). Actually, as shown in the images below, the stones can be highly pigmented and yet be composed mainly of calcium carbonates, especially aragonite, or of calcium phosphates such as carbapatite (Figure 17F). Calcium carbonate-rich stones can be poorly organized or, by contrast, reveal a more or less compact concentric structure of different colours ranging from greyish to brown-black or, sometimes, light yellow-brown or red-brown. In some cases, a pure calcium carbonate shell can cover stones of a different type. In Figure 17H, the smooth surface of the stone was pure aragonite. The colour was dark grey with bluish reflections. In the case of calcium phosphate-rich stones containing various proportions of calcium bilirubinates as well, the inner structure is often poorly organized and the colour ranges from dark brown to black. When gallstones contain other compounds such as drugs, the morphology and colour are often unusual as in Figure 17G where the stones were made of nearly pure calcium ceftriaxonate. As seen in Figure 18, stone sections can reveal a succession of different structures, sometimes unorganized, sometimes concentric or radial, with different colours suggesting both a different composition and an evolution of lithogenic factors. For example, in Figure 18C the dark brown stone core is mainly composed of calcium bilirubinates with a small proportion of calcium palmitate while the surrounding yellowish layers are nearly pure cholesterol. Such a structure is highly suggestive of a lithogenic process related to infection with a secondary coating of cholesterol crystals as a consequence of lipid anomalies. Figure 18F shows a stone initiated by strands of non-absorbable ligations related to previous bile duct surgery. Calcium bilirubinate encrustations followed by accumulation of calcium bilirubinate deposits and finally calcium carbonate coating resulted in an obstruction of the bile duct requiring further intervention. Figure 18G illustrates a case of pigment stones mainly composed of calcium bilirubinates with a whitish core of calcium palmitate aggregates.

When examined under FE-SEM, the characteristics of the crystals and their organization within the stone can be ascertained at the mesoscopic scale. Figure 19 presents various images of gallstones from patients without sickle cell disease. In Figures 19A and B, two different cholesterol stone organisations can be seen, the first of lamellar crystals stacked on top of each other and the second of crystals organized in perpendicular spans. Figures 19C and D illustrate the appearance of the surface of the pigment stones, one smooth and cracked, the other rough

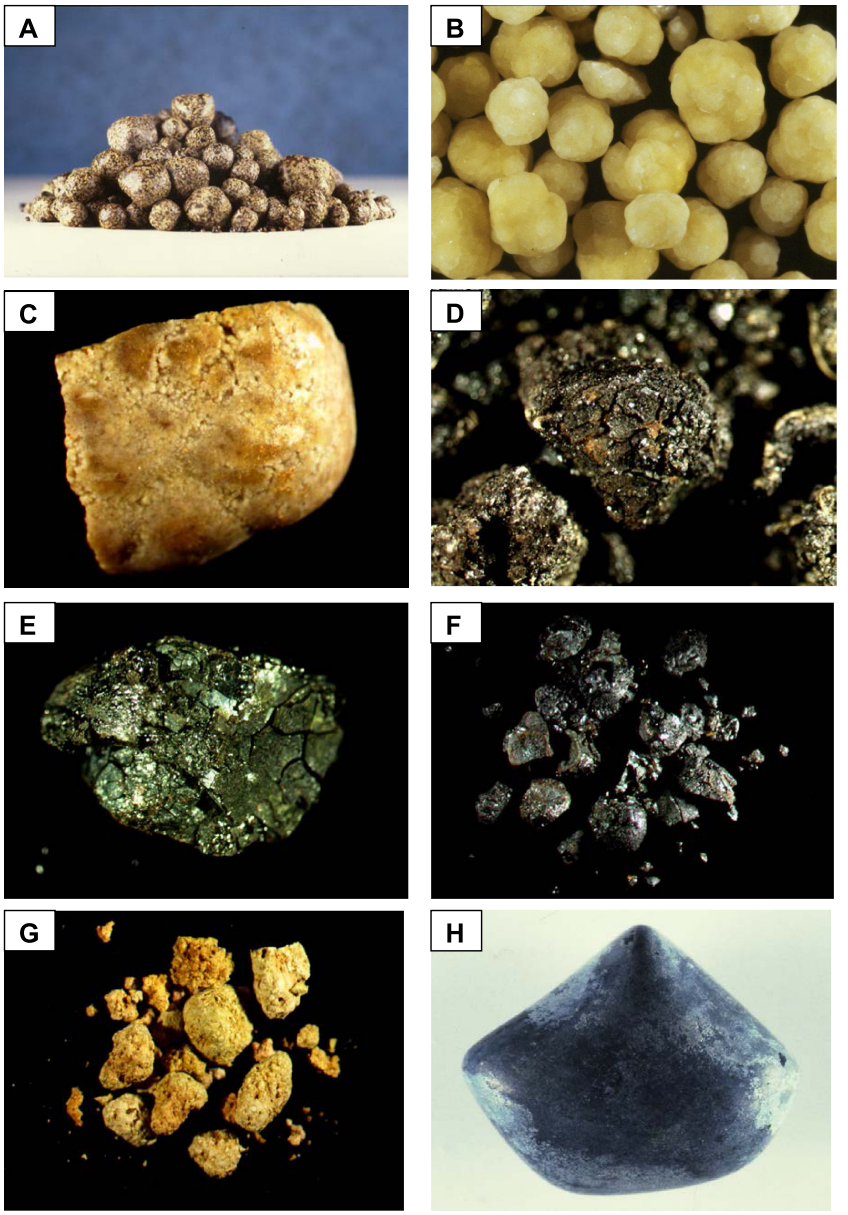

Figure 17. (A) Multiple cholesterol stones. (B) Another example of multiple cholesterol stones. (C) Large gallbladder stone made of a mixture of cholesterol monohydrate and anhydrous. (D) Black pigment gallstone in a patient with sickle cell disease. (E) Another example of black-greenish pigment gallstone in a patient with sickle cell disease. One explanation for greenish-coloured reflections could be the abundant presence of calcium carbonate (calcite) mixed with calcium bilirubinates. (F) Multiple small black gallstones in a patient with sickle cell disease. Unexpectedly, the predominant crystalline phase is not calcium bilirubinate but carbapatite mixed with amorphous carbonated calcium phosphate. (G) Multiple gallstones mainly made of calcium ceftriaxonate. (H) Calcium carbonate gallbladder stone made of a mixture of calcium carbonates and calcium bilirubinates. The stone shell is made of nearly pure aragonite.

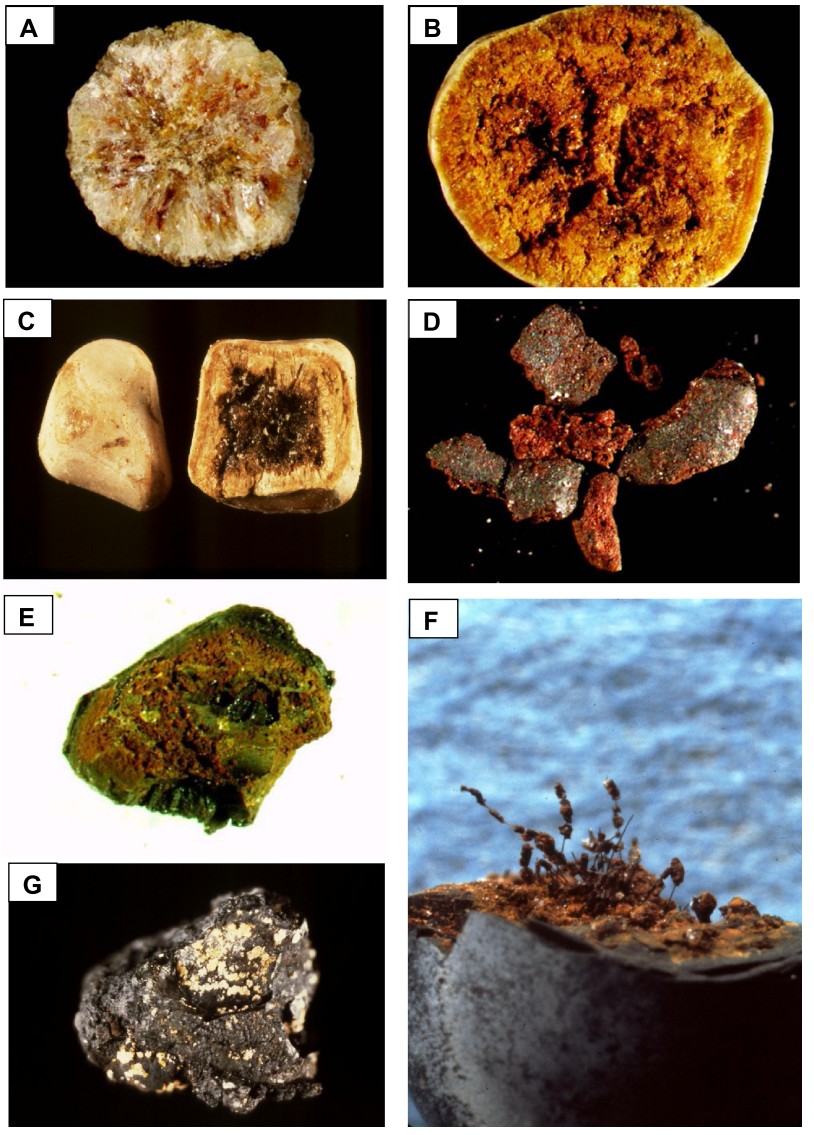

Figure 18. (A) Section of a pure cholesterol gallstone. Colour is very light. The inner structure shows a diffuse radiating organization of the crystals. (B) Poorly organized section of a cholesterol gallstone containing a mixture of cholesterol anhydrous and monohydrate. The red colour is due to the presence of small proportion of calcium bilirubinate randomly distributed within the stone. (C) Another section of a cholesterol stone. Note that the core is dark brown because the stone was initiated from calcium bilirubinate crystals. (D) Dark brown stone made of calcium bilirubinates in a patient with sickle cell disease. The surface is rough and the section red-brown is unorganized. (E) Another example of poorly organized section of a pigment stone in a patient with sickle cell disease. Colour is dark brown to brown-greenish. Photograph E corresponds to the section of the stone shown in Figure 17E. (F) Example of a pigment gallstone initiated from the threads of a surgical ligation. The inner part of the stone is mainly composed of calcium bilirubinates while the peripheral layers are made of calcium carbonates (aragonite and calcite). (G) Gallbladder black pigment stone initiated from whitish lamellar crystals of calcium palmitate.

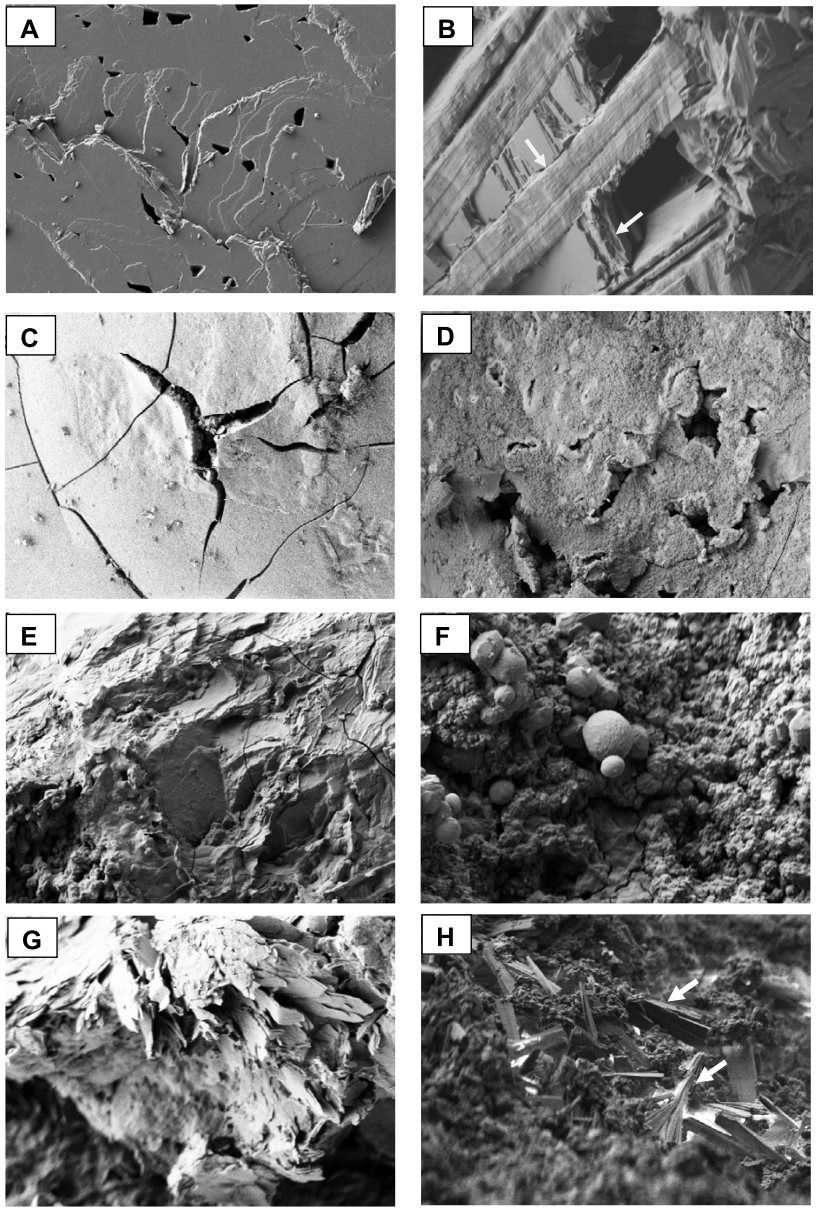

Figure 19. Scanning electron microscopic (SEM) images of gallstones. (A) Peripheral layers of a cholesterol gallstone. Note that large cholesterol plaques are stacked on top of each other. (B) Another gallstone made of a mixture of cholesterol anhydrous and cholesterol monohydrate. The inner organization shows that the cholesterol plaques stacked on top of each other are organized alternately in two orthogonal directions (arrows). (C) Smooth, cracked surface of a black pigment stone mainly composed of calcium bilirubinates. (D) Rough and lacunar surface of another pigment stone mainly composed of calcium bilirubinates. (E) Unorganized section of a black pigment gallstone, made of nearly pure calcium bilirubinate. (F) Spheres of calcite in a pigment stone predominantly composed of calcium bilirubinates. (G) Core of a pigment gallstone with lamellar crystals of calcium palmitate. (H) Unorganized section of a pigment gallstone made of a mixture of calcium bilirubinates and atazanavir. Atazanavir rod crystals are grouped into small asymmetric aggregates (white arrows).

with irregularly arranged holes. Figure 19E shows the poorly organized interior of another pigment stone. Figure 19F reveals calcium carbonate spheres mixed with an unorganized and rough structure made of calcium bilirubinate. In Figure 19G, lamellar crystals of calcium palmitate are observed in the core of a pigment stone; in Figure 19H, aggregated rod atazanavir crystals are mingled with calcium bilirubinate.

Figures 20A–H illustrate microscopic aspects of gallstones from patients suffering sickle cell disease. In Figures 20A and B, two different pigment gallstones surface types can be observed, with cracks in Figure 20A and a smooth aspect in Figure 20B. Figure 20C illustrates the rough structure of a pigment stone similar to that in Figure 19E for patients without sickle cell disease. In Figures 20D and E, needle-shaped bilirubin crystals organized as asymmetric aggregates can be seen. Figure 20F illustrates the association of a rough and cracked structure composed of calcium bilirubinate with multiple calcite spheres. Figure 20G shows a less common "crossed rod" calcite crystal morphology. Finally, in Figure 20H, another type of spheres can be seen, this time made of carbapatite.

Excluding sickle cell disease, the morpho-constitutional analysis of gallstones occurring in France shows essentially four categories: cholesterol stones (60.1%), pigment stones (32.1%), calcium carbonate stones (4.7%) and atypical stones (3.1%). The latter group can include various compounds: bile pigments, cholesterol, calcium carbonates, calcium phosphate, but also drugs such as calcium ceftriaxonate or antiproteases such as indinavir or atazanavir. Of 75 sickle cell patient stones, we found the following distribution: cholesterol stones: 6.7%; bile pigments: 74.7%; calcium carbonates: 14.6%; atypical: 4%. Of note, no sickle cell stones contained any drug deposits.

3.3. *Stone composition*

The composition of gallstones shows a great diversity of mineral and/or organic phases: more than 30 different species have been identified (Table 1). In addition, gallstones are rarely pure in a single crystalline species (1.3%). Up to nine different compounds have been identified within a single stone. As shown in Table 2, a quarter of the stones in our series contained four different compounds and 43% had at least five components belonging to several chemical families.

Many of the compounds described above have been identified in minor proportions within a limited number of calculi. If we look at the main components of gallstones (Table 3), we note, as might be expected, a significant difference in the distribution of the main phases detected within the stones associated with sickle cell disease compared to other groups of cholelithiasis. For example, calcium bilirubinates accounted for 74.7% of cases in sickle cell patients versus 22.5% in other conditions ($p < 10^{-6}$). Similarly, calcium carbonates (mainly calcite) were more frequent in sickle cell patients (14.6% versus 3.9%, $p < 0.001$). By contrast, cholesterol stones accounted only for 6.7% of gallstones in the case of sickle cell disease while they accounted for 67.6% of stones in other patients ($p < 10^{-6}$). Of note, calcium phosphate stones were found with a similar occurrence in both groups.

Of the 408 stones, 30 cores were lost due to significant fragmentation during extraction. Of the remaining 378 calculi, infrared analysis of the selectively collected nucleation zone shows that 118 nuclei (31.2%) have a different composition than that observed later on the entire stone. The proportion was similar (41.1%) for stones associated with sickle cell disease and for those from other aetiologies (29%, NS). Thus, about 1/3 of the calculi are initiated by a mechanism other than the one responsible for their subsequent growth. In sickle cell patients, 60% of the stones were initiated by calcium bilirubinate and only 1.5% by cholesterol. On the contrary, in other situations, cholesterol was the component of the nucleus of stones in 51.6% of cases and calcium bilirubinate in 31.6% of cases.

Table 4 shows the distribution of the stones according to the main component and the component of the nucleus that initiated the calculus. It shows that, for cholesterol stones and those composed mainly of bile pigments, about 70% had a nucleus of the same nature. This was even clearer for calcium phosphate stones, since 100% of them were formed from a calcium phosphate nucleus. On the other hand, calcium carbonate calculi were initiated in 69.2% of cases from another chemical phase. However, it still seemed to be a calcium salt, mainly calcium bilirubinate. An interesting point was an unusual prevalence of calcium phosphates in the nuclei

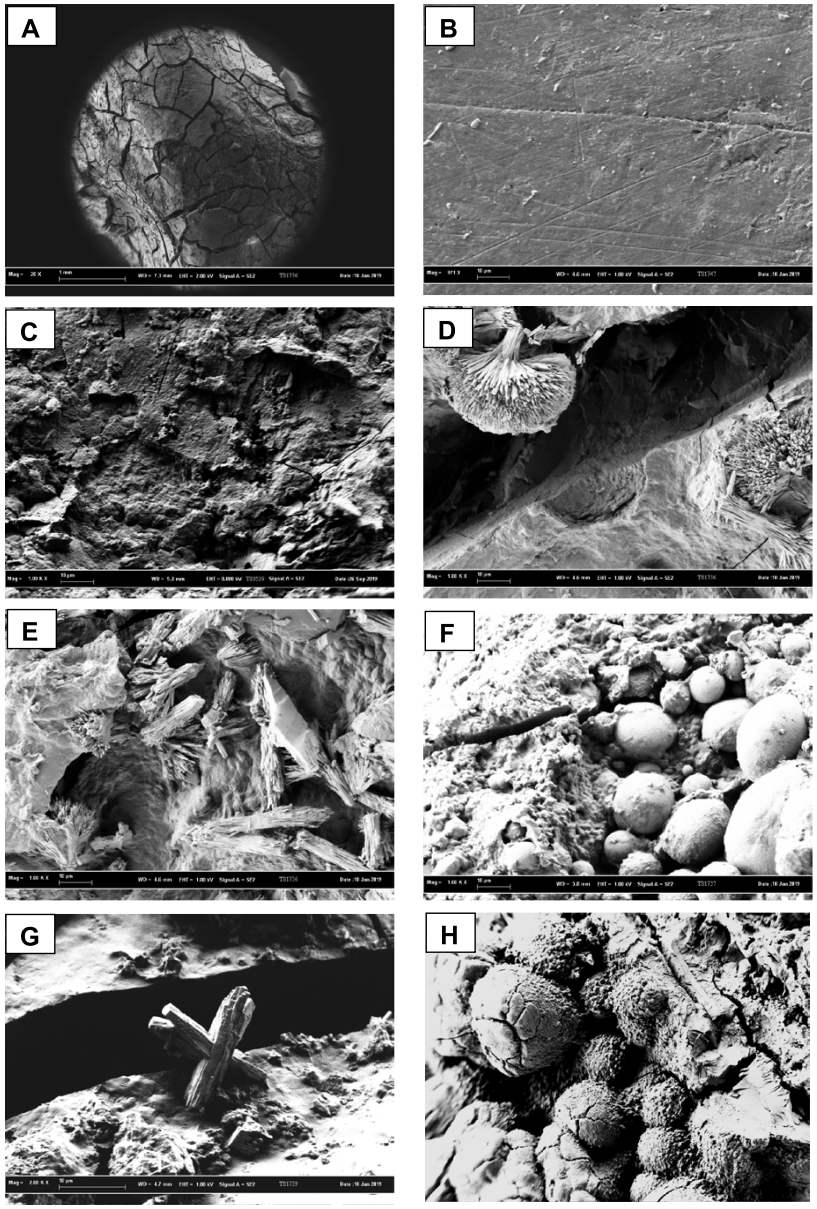

Figure 20. SEM photographs of stones from patients with sickle cell disease. (A) Cracked surface of a black pigment stone that contains 75% calcium bilirubinates, 20% cholesterol and 5% free bilirubin. (B) Smooth surface of a black-brown pigment stone made of 85% calcium bilirubinates, 12% carbapatite and 3% of free bilirubin. (C) Rough unorganized section of a black pigment stone composed of 55% calcium bilirubinates, 30% calcite, 7% carbapatite, 4–5% proteins and 3–4% cholesterol. (D) Asymmetric aggregates of free bilirubin within the black pigment stone of A. (E) Other aggregates of bilirubin crystals inside the same pigment stone as in D. (F) Numerous spheres of calcite crystals within a pigment gallstone mainly made of calcium bilirubinates (55%) + calcite (20%) + vaterite (10%) + aragonite (10%) + free bilirubin (5%). (G) Other morphology of calcite crystals as aggregated rods in another pigment stone shown in C. (H) Spheres of carbapatite in the core of a black pigment stone made of calcium bilirubinates (≥65%) + carbapatite (25%) + calcite (5%) + bilirubin (≤5%).

Table 1. Components identified in gallstones

Components	Frequency (%)
Biliary pigments	
Calcium neutral bilirubinate	83.6
Calcium acid bilirubinate	58.2
Bilirubin	14.3
Steroids	
Cholesterol anhydrous	69.9
Cholesterol monohydrate	13.3
Cholesterol palmitate and/or stearate	7.0
Calcium desoxycholate	0.8
Calcium taurocholate	0.5
Calcium glycocholate	0.5
Sodium cholate	0.3
Calcium chenodesoxycholate	0.3
Fatty acids and triglycerides	
Calcium palmitate and/or stearate	28.0
Triglycerides (tripalmitine, tristearine ...)	13.5
Calcium carbonates	
Calcite	25.7
Aragonite	12.2
Vaterite	3.4
Calcium phosphates	
Carbapatite	21.8
Amorphous carbonated calcium phosphate	3.6
Whitlockite	0.8
Octacalcium phosphate pentahydrate	0.3
Magnesium phosphates	
Struvite	0.3
Calcium sulfates	
Gypsum	0.3
Proteins	64.7
Drugs	
Atazanavir	0.8
Calcium ceftriaxonate	0.5
Indinavir	0.3
Glafenic acids	0.3
Others	
Ligatures	0.8
Metal staples	0.5
Monosodium urate monohydrate	0.3
Phospholipids	0.3

Table 2. Number of components/stone

	Frequency (%)
Pure stones (only one component)	1.3
Two-component stones	9.7
Three-component stones	20.0
Four-component stones	25.8
Five-component stones	20.2
Six-component stones	13.4
Seven-component stones	7.5
Eight-component stones	1.3
Nine-component stones	0.7

of stones from sickle cell patients which appeared significantly higher than that observed in other conditions (23.5% versus 5.5%, $p < 0.0001$). Moreover, when a distinction was made between homozygous and compound heterozygous subjects, it appeared that the prevalence of phosphate nuclei was very high in the first group (31.4%) and not different from other bile stone contexts in the second group (5.9%, $p < 0.01$). No other significant difference was found in stone composition among homozygous and heterozygous sickle cell patients.

4. Discussion

The varied nature of gallstones must, as with urinary stones, point to different aetiologies. However, several crystalline species can signal the same etiological process. For example, the presence of anhydrous cholesterol and cholesterol monohydrate points to lipid disorders. Conversely, the presence of neutral calcium bilirubinate, calcium hydrogen bilirubinate, or even free bilirubin, points to a very different lithogenic mechanism related to overproduction of bilirubin or a lack of conjugation thereof. Similarly, calcium carbonate stones, whether calcite, aragonite or vaterite, can point to local metabolic imbalances involving pH, calcium, and carbonate homeostasis.

As expected, the gallstones of sickle cell patients were composed mainly of bile pigments resulting from increased haemolysis in these patients (74.7% versus 22.5% for all gallstones excluding sickle cell disease, $p < 10^{-6}$). However, a quarter of the stones were composed mainly of another crystalline species, in particular calcium salts (18.6%), such as calcium carbonate (14.6%) or carbapatite (4%). Despite the haemolytic background, about 7% of stones were mainly made of cholesterol, suggesting that abnormalities in lipid balance were also present in some patients and might actively participate in lithogenesis, even if cholesterol was rarely the cause of the stone (1.5%). In addition, analysis of the stones by SEM suggests that some of them might be related to a bile duct infection. These stones, few in number ($n = 4/75$, or 5.3%), were pigment stones and black in colour on the periphery with a lighter brown-rust center, in which imprints of bacteria have been observed.

Not all sickle cell patients are susceptible to lithiasis. The lithogenic risk mainly arises from unconjugated forms of bilirubin which can then precipitate in the form of calcium salts. It is therefore necessary to question the participation of factors other than haemolysis in lithogenesis, in particular an alteration of glucuronoconjugation which can significantly increase the proportion of free bilirubin. Mutations of the hepatic UGT1A1 gene, which is able to ensure glucuronidation of bilirubin, could be an important factor in pigment gallstone formation. UGT1A1 gene polymorphisms with mutations in the TATA box promoter region were associated with serum level of unconjugated bilirubin and the risk of cholelithiasis in various populations, including sickle cell patients [40–47]. It was shown that the TATA box region of the UGT1A1 gene contains a group of TA repeats, with four alleles that differ in the number (from 5 to 8) repeats [42]. As reported for thalassemia patients, homozygous mutations TA(7)/TA(7) of the UGT1A1 gene were associated with a high probability of the prevalence of gallstones, in comparison with thalassemia patients exhibiting TA(6)/TA(6) UGT1A1 gene: OR = 3.88 (95% CI: 1.31–11.55) versus 1.68 (95% CI: 0.7–4.03) [48]. Chaouch *et al.* [49] have compared the variants of the UGT1A1 gene in sickle cell and thalassemia patients and they have shown a significant association between heterogeneous TA(6)/TA(7) or homogenous TA(7)/TA(7) mutations and the risk of cholelithiasis among these patients. The Gilbert syndrome-associated UGT1A1 mutation is a common finding affecting about 10% of the general population, and can be involved in hyperbilirubinemia states, intermittent episodes of jaundice and black pigment gallstones [50–53]. In cystic fibrosis patients, it was reported that those with UGT1A1 allele muta-

Table 3. Main components identified in gallstones related to sickle cell disease or to other etiological situations

Main component	Sickle cells disease Number (%)	Other contexts Number (%)	*p*
Biliary pigments	***56 (74.7)***	***75 (22.5)***	$<10^{-6}$
Calcium bilirubinates	56 (74.7)	75 (22.5)	$<10^{-6}$
Calcium carbonates	***11 (14.6)***	***13 (3.9)***	***<0.001***
Calcite	10 (13.3)	8 (2.4)	<0.001
Aragonite	1 (1.3)	5 (1.5)	NS
Cholesterol	***5 (6.7)***	***225 (67.6)***	$<10^{-6}$
Cholesterol anhydrous	5 (6.7)	220 (66.1)	$<10^{-6}$
Cholesterol monohydrate	0	5 (1.5)	—
Calcium phosphates	***3 (4.0)***	***8 (2.4)***	***NS***
Carbapatite	3 (4.0)	7 (2.1)	NS
Amorphous carbonated calcium phosphate	0	1 (0.3)	—
Proteins	***0***	***8 (2.4)***	***NS***
Drugs	***0***	***4 (1.2)***	—
Calcium ceftriaxonate	0	2 (0.6)	—
Atazanavir	0	1 (0.3)	—
Indinavir monohydrate	0	1 (0.3)	—
Total	75	333	

tions were susceptible to gallstones (OR = 7.3 versus normal UGT1A1 gene) and higher serum levels of unconjugated bilirubin [54]. In a recent meta-analysis of 34 studies, it was reported that the overall prevalence of cholelithiasis among sickle cell patients was 25.3% and that the frequencies of (TA)7 and (TA)8 were significantly higher in patients with cholelithiasis [23].

Note that other types of gallbladder stones may be related to a defect in the UGT1A1 gene. In our series of stones we found three cases of calculi that contained atazanavir, a protease inhibitor extensively used in the past decade in therapy of HIV+ patients. One stone was almost pure atazanavir and the two others were pigment stones with a high content of both calcium bilirubinates and atazanavir. Indeed, it has been reported that serum bilirubin level was correlated to the plasma concentration of atazanavir and that atazanavir is able to inhibit the hepatic UGT1A1 metabolic pathway [55]. Moreover, it has been shown that atazanavir-treated patients carrying a variant of the UGT1A1 gene had a higher baseline bilirubin level and a slower atazanavir hepatic clearance [56], favouring the drug crystallization.

Several studies have reported that crystallization of calcium salts could be reduced by proteins such as mucin [57–59], and that imbalance of bile composition with respect to calcium, carbonate, and macromolecules, could favour calcium carbonate crystallization. Gleeson *et al.* [60] and more recently Yu *et al.* [61] provided convincing arguments that bile pH, calcium concentration and CO_3^{2-} concentrations were significantly increased in patients who formed calcium carbonate gallstones compared with control subjects.

Other predisposing factors such as chronic inflammation and reactive oxygen species production may be involved in gallstones as well as in other clinical complications of sickle cell disease [58,61–63].

It has been known for some time that bile infection is another possible cause of gallstones [64–66]. Bilirubin deconjugation by bacterial glucuronidases could explain why brown pigment stones are more frequent in Asia than in western countries [67,68]. These are often located in the bile ducts and associated with obstruction [68,69]; calcium palmitate is often identified within such infected stones. Its pres-

Table 4. Composition of stone nucleus according to the main component of the stone

Main component (number)	Component of the nucleus	Number (%)
Sickle cell disease		
Calcium bilirubinate (***n* = *49***)	**Calcium bilirubinate**	**33 (67.4)**
	Carbapatite	11 (22.4)
	Calcium palmitate/stearate	3 (6.1)
	Calcium carbonate	1 (2.0)
	Unknown component	1 (2.0)
Calcium carbonate (***n* = *11***)	**Calcium carbonate**	**3 (27.3)**
	Calcium bilirubinate	4 (36.3)
	Carbapatite	2 (18.2)
	Calcium palmitate/stearate	2 (18.2)
Cholesterol (***n* = *5***)	**Cholesterol**	**1 (20.0)**
	Calcium bilirubinate	4 (80.0)
Carbapatite (***n* = *3***)	**Carbapatite**	**3 (100)**
Sickle cell disease excluded		
Cholesterol (***n* = *215***)	**Cholesterol**	**158 (73.5)**
	Calcium bilirubinate	36 (16.7)
	Calcium palmitate/stearate	11 (5.1)
	Carbapatite	7 (3.3)
	Calcium carbonate	2 (0.9)
	Ligature	1 (0.5)
Calcium bilirubinate (***n* = *76***)	**Calcium bilirubinate**	**53 (69.7)**
	Calcium palmitate/stearate	11 (14.5)
	Carbapatite	6 (7.9)
	Foreign material (ligature, staple)	3 (3.9)
	Cholesterol	2 (2.6)
	Proteins	1 (1.3)
Calcium carbonate (***n* = *15***)	**Calcium carbonate**	**5 (33.3)**
	Calcium bilirubinate	9 (60.0)
	Calcium palmitate/stearate	1 (6.7)
Carbapatite (***n* = *4***)	**Carbapatite**	**4 (100)**

ence could be linked to increased activity of bacterial phospholipases increasing the generation of free fatty acids which can precipitate as calcium salts [70]. In sickle cell patients, such a mechanism cannot be excluded but seems of limited importance in stone formation. We note that in our series of 75 stones, only five (6.7%) contained calcium palmitate and SEM images of four of them suggested the presence of bacterial imprints.

An unexpected finding from stone analysis was the high proportion of gallstones from sickle cell patients that were nucleated from calcium phosphate (23.5% versus 5.5% in other conditions, $p < 0.0001$). It has been reported that serum phosphate is increased in sickle cell disease [71–73]. However, phosphate content was determined in bile of patients who formed pigment stones and no difference was found in comparison with patients producing cholesterol

stones. We have shown in Table 4 that calcium phosphate is not frequent in pigment stones from patients without sickle cell disease. In addition, the frequency of phosphate nuclei was very high in homozygous patients (31.4%), but was not different from other bile stone contexts in the heterozygous subjects (5.9%, $p < 0.01$). A possible explanation could be a more frequent and severe haemolysis in homozygous than heterozygous sickle cell patients. However, biochemical data to demonstrate this link with stone formation are lacking. It would be of interest to determine the phosphate content in bile of sickle cell patients with stones nucleated from calcium phosphate, and to correlate the data with their homozygous or heterozygous status, and also compare with the bile phosphate of sickle cell patients without stones.

All these observations suggest that several factors may contribute to the formation of stones in patients with sickle cell disease. Given the diversity of aetiologies and the number of identifiable components in gallstones, it would certainly be interesting to refine the composition studies of these stones by improving the phenotyping of patients, as we have shown over several years with respect to urinary tract stones [74–78]. This would improve correlation between clinical history, etiopathogenic factors, and the composition of calculi. Admittedly, unlike renal lithiasis, cholelithiasis leads to clinically symptomatic recurrences of stones in only a small proportion of cases, which limits the clinical interest in these stones and their cause(s). However, the chronic metabolic context that characterizes sickle cell disease predisposes to recurrence of bile duct lithiasis more than other pathological conditions [22]. This justifies improving understanding of the individual lithogenic risk factors in order to mitigate them with more selective protective measures.

5. Conclusion

Gallstones of sickle cell patients appear significantly different from those from the general population. As expected, chronic haemolysis favours the formation of pigment stones. However other factors may be involved and this should prompt more studies. For instance, an accurate examination of stone composition, especially of the stone nucleus, has revealed that a high proportion of stones are initiated from carbapatite. An increase in serum phosphate could be indicated, but, as shown for calcium carbonate crystallization in bile, the phosphate content of bile in sickle cell patients remains to be assessed in the future.

Conflicts of interest

Authors have no conflict of interest to declare.

References

[1] D. Bainton, G. T. Davies, K. T. Evans, I. H. Gravelle, *New Eng. J. Med.*, 1976, **294**, 1147-1149.
[2] L. Barbara, C. Sama, A. M. Morselli Labate, F. Taroni, A. G. Rusticali, D. Festi, C. Sapio, E. Roda, C. Banterle, A. Puci, F. Formentini, S. Colasanti, F. Nardin, *Hepatology*, 1987, **7**, 913-917.
[3] I. Glambek, G. Kvaale, B. Arnesjö, O. Soreide, *Scand. J. Gastroenterol.*, 1987, **22**, 1089-1094.
[4] Rome group for the epidemiology and prevention of cholelithiasis (GREPCO), *Am. J. Epidemiol.*, 1984, **119**, 796-805.
[5] E. A. Shaffer, *Best Pract. Res. Clin. Gastroenterol.*, 2006, **20**, 981-996.
[6] F. Lammert, K. Gurusamy, C. W. Ko, J. F. Miquel, N. Méndez-Sánchez, P. Portincasa, K. J. van Erpecum, C. J. van Laarhoven, D. Q. Wang, *Nat. Rev. Dis. Primers*, 2016, **2**, article no. 16024.
[7] N. B. Satheesha, K. V. Soumya, *Kathmandu Univ. Med. J.*, 2020, **18**, 340-343, PMID: 34165088.
[8] S. T. Song, J. Shi, X. H. Wang, Y. B. Guo, P. F. Hu, F. Zhu, X. Zeng, W. F. Xie, *J. Dig. Dis.*, 2020, **21**, 237-245.
[9] C. N. Williams, J. L. Johnston, K. L. M. Weldon, *Can. Med. Assoc. J.*, 1977, **117**, 758-760, PMID: 907946.
[10] A. K. Diehl, *Gastroenterol. Clin. North Am.*, 1991, **20**, 1-19, PMID: 2022415.
[11] L. Zhu, A. Aili, C. Zhang, A. Saiding, K. Abudureyimu, *World J. Gastroenterol.*, 2014, **28**, 14942-14949.
[12] T. Jorgensen, *Am. J. Epidemiol.*, 1987, **126**, 912-921.
[13] Rome group for the epidemiology and prevention of cholelithiasis (GREPCO), *Hepatology*, 1988, **8**, 904-906.
[14] D. J. Sutor, S. E. Wooley, *Gut*, 1969, **10**, 681-683.
[15] B. W. Trotman, T. A. Morris III, H. M. Sanchez, R. D. Soloway, J. D. Ostrow, *Gastroenterology*, 1977, **72**, 495-498.
[16] E. Wentrup-Byrne, L. Rintoul, J. L. Smith, P. M. Fredericks, *Appl. Spectrosc.*, 1995, **49**, 1028-1036.
[17] A. K. Diehl, W. H. Schwesinger, D. R. Holleman Jr, J. B. Chapman, W. E. Kurtin, *Am. J. Gastroenterol.*, 1995, **90**, 967-972.
[18] R. Sharma, S. Soy, C. Kumar, S. G. Sachan, S. R. Sharma, *Indian J. Gastroenterol.*, 2015, **34**, 29-37.
[19] P. F. Malet, A. Takabayashi, B. W. Trotman, R. D. Soloway, N. E. Weston, *Hepatology*, 1984, **4**, 227-234.
[20] T. M. Walker, I. R. Hambleton, G. R. Serjeant, *J. Pediatr.*, 2000, **136**, 80-85.
[21] E. C. Ebert, M. Nagar, K. D. Hagspiel, *Clin. Gastroenterol. Hepatol.*, 2010, **8**, 483-489.
[22] M. O. Amoako, J. F. Casella, J. J. Strouse, *Pediatr. Blood Cancer*, 2013, **60**, 650-652.

[23] S. O. O. Mohamed, O. A. O. Ibrahim, D. A. A. Mohammad, A. H. M. Ali, *J. Gastroenterol. Hepatol. Open*, 2021, **5**, 997-1003.
[24] D. Bazin, M. Daudon, *Ann. Biol. Clin.*, 2015, **73**, 517-534.
[25] D. Bazin, E. Bouderlique, M. Daudon, V. Frochot, J.-Ph. Haymann, E. Letavernier, F. Tielens, R. Weil, *C. R. Chim.*, 2022, **25**, no. S1, 37-60.
[26] M. Daudon, D. Bazin, *C. R. Chim.*, 2016, **19**, 1416-1423.
[27] F. Meiouet, S. El Kabbaj, M. Daudon, *C. R. Chim.*, 2022, **25**, no. S1, 281-293.
[28] H. Ohkubo, J. Donald Ostrow, S. H. Car, R. V. Rege, *Gastroenterology*, 1984, **87**, 805-814.
[29] C. Moesch, M. Daudon, J. Leymarie, C. Raby, *Eur. J. Clin. Chem. Clin. Biochem.*, 1993, **31**, 329-333.
[30] C. Moesch, C. Lorgue, D. Sautereau, *Ann. Biol. Clin.*, 1994, **52**, 293-294.
[31] F. Tokumine, T. Sunagawa, Y. Shiohira, T. Nakamoto, F. Miyazato, Y. Muto, *Am. J. Gastroenterol.*, 1999, **94**, 2285-2288.
[32] R. Verdon, M. Daudon, F. Albessard, J. L. Brefort, C. Bazin, *Clin. Infect. Dis.*, 2002, **35**, e57-e59.
[33] A. J. Lopez, P. O'Keefe, M. Morrissey, J. Pickleman, *Ann. Int. Med.*, 1991, **115**, 712-714.
[34] C. W. Ko, J. H. Sekijima, S. P. Lee, *Ann Intern. Med.*, 1999, **130**, 301-311.
[35] F. Papadopoulou, S. Efremidis, S. Karyda, M. Badouraki, E. Karatza, C. Panteliadis, K. Malaka, *Acta Paediatr.*, 1999, **88**, 1352-1355.
[36] D. A. Rodríguez Rangel, A. P. Pinilla Orejarena, M. Bustacara Diaz, L. Henao García, A. López Cadena, R. Montoya Camargo, L. A. Moreno, *Ann. Pediatr. (Barc).*, 2014, **80**, 77-80.
[37] L. Ustyol, M. D. Bulut, K. Agengin, K. A. Bala, A. Yavuz, A. Bora, K. Demiroren, M. Dogan, *Hum. Exp. Toxicol.*, 2017, **36**, 547-553.
[38] A. C. Jacques, P. Giguère, G. Zhang, C. Touchie, C. J. la Porte, *Ann. Pharmacother.*, 2010, **44**, 202-206.
[39] T. Nishijima, T. Shimbo, H. Komatsu, Y. Hamada, H. Gatanaga, Y. Kikuchi, S. Oka, *J. Antimicrob. Chemother.*, 2014, **69**, 1385-1389.
[40] E. J. Benjamin, J. Dupuis, M. G. Larson, K. L. Lunetta, S. L. Booth, D. R. Govindaraju, S. Kathiresan, J. F. Keaney Jr, M. J. Keyes, J. P. Lin, J. B. Meigs, S. J. Robins, J. Rong, R. Schnabel, J. A. Vita, T. J. Wang, P. W. Wilson, P. A. Wolf, R. S. Vasan, *BMC Med. Genet.*, 2007, **8**, S1-S11.
[41] M. M. Heeney, T. A. Howard, S. A. Zimmerman, R. E. Ware, *J. Lab. Clin. Med.*, 2003, **141**, 279-282.
[42] V. Chaar, L. Kéclard, J. P. Diara, C. Leturdu, J. Elion, R. Krishnamoorthy, J. Clayton, M. Romana, *Haematologica*, 2005, **90**, 188-199.
[43] R. G. Passon, T. A. Howard, S. A. Zimmerman, W. H. Schultz, R. E. Ware, *J. Pediatr. Hematol. Oncol.*, 2001, **23**, 448-451.
[44] E. V. Haverfield, C. A. McKenzie, T. Forrester, N. Bouzekri, R. Harding, G. Serjeant, T. Walker, T. E. A. Peto, R. Ward, D. J. Weatherall, *Blood*, 2005, **105**, 968-972.
[45] S. L. Carpenter, S. Lieff, T. A. Howard, B. Eggleston, R. E. Ware, *Am. J. Hematol.*, 2008, **83**, 800-803.
[46] R. Martins, A. Morais, A. Dias, I. Soares, C. Rolão, J. L. Ducla-Soares, L. Braga, T. Seixas, B. Nunes, G. Olim, L. Romão, J. Lavinha, P. Faustino, *J. Hum. Genet.*, 2008, **53**, 524-528.
[47] J. N. Milton, P. Sebastiani, N. Solovieff, S. W. Hartley, P. Bhatnagar, D. E. Arking, D. A. Dworkis, J. F. Casella, E. Barron-Casella, C. J. Bean, W. C. Hooper, M. R. DeBaun, M. E. Garrett, K. Soldano, M. J. Telen, A. Ashley-Koch, M. T. Gladwin, C. T. Baldwin, M. H. Steinberg, E. S. Klings, *PLoS One*, 2012, **7**, article no. e34741.
[48] C. Borgna-Pignatti, F. Rigon, L. Merlo, R. Chakrok, R. Micciolo, L. Perseu, R. Galanello, *Haematologica*, 2003, **88**, 1106-1109.
[49] L. Chaouch, M. Kalai, D. Chaouachi, F. Mallouli, R. Hafsia, S. Ben Ammar, S. Abbes, *Tunis Med.*, 2015, **93**, 237-241.
[50] P. J. Bosma, J. R. Chowdhury, C. Bakker, S. Gantla, A. de Boer, B. A. Oostra, D. Lindhout, G. N. J. Tytgat, P. L. M. Jansen, R. P. J. Oude Elferink, N. R. Chowdhury, *New Eng. J. Med*, 1995, **333**, 1171-1175.
[51] G. Bale, U. S. Avanthi, N. R. Padaki, M. Sharma, N. R. Duvvur, V. R. Kanth Vishnubhotla, *J. Clin. Exp. Hepatol.*, 2018, **8**, 362-366.
[52] M. Persico, E. Persico, C. T. Bakker, I. Rigato, A. Amoroso, R. Torella, P. J. Bosma, C. Tiribelli, J. D. Ostrow, *Hepatology*, 2001, **33**, 627-632.
[53] H. C. Teng, M. J. Huang, K. S. Tang, S. S. Yang, C. S. Tseng, C. S. Huang, *Clin. Genet.*, 2007, **72**, 321-328.
[54] H. E. Wasmuth, H. Keppeler, U. Herrmann, R. Schirin-Sokhan, M. Barker, F. Lammert, *Hepatology*, 2006, **43**, 738-741.
[55] D. E. Smith, S. Jeganathan, J. Ray, *HIV Clin. Trials*, 2006, **7**, 34-38.
[56] D. H. Johnson, C. Venuto, M. D. Ritchie, G. D. Morse, E. S. Daar, P. J. McLaren, D. W. Haas, *Pharmacogenet. Genom.*, 2014, **24**, 195-203.
[57] T. Yamasaki, K. Chijiiwa, M. Endo, *Dig. Dis. Sci.*, 1993, **38**, 909-915.
[58] H. M. Burt, J. K. Jackson, D. R. Taylor, R. S. Crowther, *Dig. Dis. Sci.*, 1997, **42**, 1283-1289.
[59] C. Sayers, J. Wyatt, R. D. Soloway, D. R. Taylor, M. D. Stringer, *Pediatr. Surg. Int.*, 2007, **23**, 219-223.
[60] D. Gleeson, K. A. Hood, G. M. Murphy, R. H. Dowling, *Gastroenterology*, 1992, **102**, 1707-1716.
[61] J.-K. Yu, H. Pan, S.-M. Huang, N.-L. Huang, C.-C. Yao, K.-M. Hsiao, C.-W. Wu, *Asian J. Surg.*, 2013, **36**, 26-35.
[62] L. E. Muñoz, S. Boeltz, R. Bilyy, C. Schauer, A. Mahajan, N. Widulin, A. Grüneboom, I. Herrmann, E. Boada, M. Rauh, V. Krenn, M. H. C. Biermann, M. J. Podolska, J. Hahn, J. Knopf, C. Maueröder, S. Paryzhak, T. Dumych, Y. Zhao, M. F. Neurath, M. H. Hoffmann, T. A. Fuchs, M. Leppkes, G. Schett, M. Herrmann, *Immunity*, 2019, **51**, 443-450.
[63] K. Tozatto-Maio, R. Girot, I. D. Ly, A. C. Silva Pinto, V. Rocha, F. Fernandes, I. Diagne, Y. Benzerara, C. L. Dinardo, J. Pavan Soler, S. Kashima, I. Leston Araujo, C. Kenzey, G. H. H. Fonseca, E. S. Rodrigues, F. Volt, L. Jarduli, A. Ruggeri, C. Mariaselvam, S. F. M. Gualandro, H. Rafii, B. Cappelli, F. Melo Nogueira, G. M. Scigliuolo, R. L. Guerino-Cunha, K. C. Ribeiro Malmegrim, B. P. Simões, E. Gluckman, R. Tamouza, *Front. Immunol.*, 2020, **11**, article no. 2041.
[64] T. Maki, *Ann. Surg.*, 1966, **164**, 90-100.
[65] M. Tabata, F. Nakayama, *Dig. Dis. Sci.*, 1981, **26**, 218-224.
[66] B. W. Trotman, *Gastroenterol. Clin. North Am.*, 1991, **20**, 111-126.
[67] C. Y. Chen, S. C. Shiesh, H. C. Tsao, X. Z. Lin, *J. Gastroenterol. Hepatol.*, 2000, **15**, 1071-1075.

[68] J. Shoda, N. Tanaka, T. Osuga, *Front. Biosci.*, 2003, **8**, e398-e409.
[69] F. Cetta, *Ann. Surg.*, 1991, **213**, 315-326.
[70] T. Nakano, J. Yanagisawa, F. Nakayama, *Hepatology*, 1988, **8**, 1560-1564.
[71] P. E. De Jong, L. T. de Jong-van Den Berg, L. W. Statius van Eps, *Clin. Sci. Mol. Med.*, 1978, **55**, 429-434.
[72] N. Al-Harbi, S. H. Annobil, F. Abbag, F. Adzaku, W. Bassuni, *Am. J. Nephrol.*, 1999, **19**, 552-554.
[73] V. M. S. Raj, M. Freundlich, D. Hamideh, O. Alvarez, W. Seeherunvong, C. Abitbol, C. Katsoufis, J. Chandar, P. Ruiz, G. Zilleruelo, *Pediatr. Blood Cancer*, 2014, **61**, 2267-2270.
[74] M. Daudon, O. Traxer, P. Conort, B. Lacour, P. Jungers, *J. Am. Soc. Nephrol.*, 2006, **17**, 2026-2033.
[75] M. Daudon, P. Jungers, D. Bazin, *New Eng. J. Med.*, 2008, **359**, 100-102.
[76] A. Dessombz, E. Letavernier, J.-Ph. Haymann, D. Bazin, M. Daudon, *J. Urol.*, 2015, **193**, 1564-1569.
[77] J. Cloutier, L. Villa, O. Traxer, M. Daudon, *World J. Urol.*, 2015, **33**, 157-169.
[78] M. Daudon, A. Dessombz, V. Frochot, E. Letavernier, J.-Ph. Haymann, P. Jungers, D. Bazin, *C. R. Chim.*, 2016, **19**, 1470-1491.

Comptes Rendus
Chimie
2022, Vol. 25, Special Issue S1, p. 553-576
https://doi.org/10.5802/crchim.210

Microcrystalline pathologies: Clinical issues and nanochemistry / *Pathologies microcristallines : questions cliniques et nanochimie*

Multiscale approach to provide a better physicochemical description of women breast microcalcifications

Margaux Petay [a], Maguy Cherfan [b], Elise Bouderlique [c, d, e], Solenn Reguer [f], Jérémie Mathurin [a], Alexandre Dazzi [a], Maëva L'Heronde [g], Michel Daudon [c, d, e], Emmanuel Letavernier [c, d, e], Ariane Deniset-Besseau [*, a] and Dominique Bazin [*, a]

[a] Institut de Chimie Physique, UMR 8000, CNRS, Université Paris Saclay, 91405 Orsay, France

[b] Service Anatomie et Cytologie Pathologiques, Centre Hospitalier René Dubos/GHT NOVO, 95300 Pontoise, France

[c] Sorbonne Universités, UPMC Université Paris 06, UMR S 702, Paris, France

[d] INSERM, UMR S 702, Paris, France

[e] Explorations fonctionnelles multidisciplinaires, AP-HP, Hôpital Tenon, Paris, France

[f] Synchrotron Soleil, L'Orme des Merisiers, Saint-Aubin, BP 48, 91192 Gif-sur-Yvette, France

[g] Ipanema, Ancient Materials Research Platform, USR 3461 CNRS/MC/UVSQ/MNHN, BP48 Saint-Aubin, 91192 Gif-sur-Yvette, France

E-mails: margaux.petay@universite-paris-saclay.fr (M. Petay), maguy.cherfan@ght-novo.fr (M. Cherfan), elise.bouderlique@inserm.fr (E. Bouderlique), solenn.reguer@synchrotron-soleil.fr (S. Reguer), jeremie.mathurin@universite-paris-saclay.fr (J. Mathurin), alexandre.dazzi@universite-paris-saclay.fr (A. Dazzi), maeva.lheronde@synchrotron-soleil.fr (M. L'Heronde), daudonmichel24@gmail.com (M. Daudon), emmanuel.letavernier@aphp.fr (E. Letavernier), ariane.deniset@universite-paris-saclay.fr (A. Deniset-Besseau), dominique.bazin@universite-paris-saclay.fr (D. Bazin)

Abstract. Despite the incidence of breast cancer among women, mammography and anatomopathology investigations are still the gold standard method for preventive screening and diagnosis. Several criteria are used to diagnose precisely the severity of the pathology like the distribution and shape of breast microcalcifications (BMCs). However, the link between the different chemical phases of BMCs and the cancer stage remains unclear. As BMCs physicochemical speciation has the potential to help clinicians during their diagnosis, this study aims to propose a methodology using advanced spectroscopical analysis techniques to finely characterize BMCs and uncover the relationship between

* Corresponding authors.

mineralization processes and breast cancer. A state of the art in the domain is first proposed to highlight the role of BMCs and the importance of extensive analytical analysis using electron microscopy and vibrational techniques. Secondly, a detailed methodology for BMCs multiscale analysis is proposed and the relevance of each technique illustrated through the study of a biopsy from a patient suffering of an infiltrating low-grade ductal carcinoma: scanning electron microscopy analysis was used for the morphological description of BMCs, infrared micro and nanospectroscopy techniques for their chemical speciation at the micrometric and sub-micrometric scales.

Keywords. Breast cancer, Microcalcification, Scanning electron microscopy, Infrared microspectroscopy, Infrared nanospectroscopy, AFM-IR.

1. Introduction

In industrial countries, cancer alongside circulatory system disorders (cerebrovascular and heart diseases) are the two most common causes of death [1,2]. In particular, breast cancer constitutes a major public health concern, as it is the most frequent cancer in women [3–7]: with more than two million new cases reported worldwide in 2020 and a mortality rate accounting for 16% of all female related deaths [8]. As of now, mammography is considered the gold standard for breast cancer preventive screening [9–11]. This medical examination enables the observation of a broad range of breast tissue abnormalities, including abnormal mass and microcalcifications. However, mammography is an X-ray based imaging technique of the breast and does not provide histological or chemical information of these abnormalities.

Breast microcalcifications (BMCs) refer to up to one-millimeter diameter calcium-based mineral deposits within the breast tissue, that appear as white spots or blemishes on mammograms [12]. Despite being an indicator of breast lesions and routinely used for the diagnosis of non-palpable cancer [13], a lack of knowledge remains regarding the correlation between BMCs physical and chemical properties and the pathology. A BMC chemical classification exists and discriminates BMCs based on the basis of their chemical composition [14]. Two types of BMCs are distinguished: type I made of calcium oxalate dihydrate (COD), also called weddellite [15–20], and type II composed of carbonated calcium phosphate apatite (CA) [21–28]. Microcalcifications of type I are acknowledged to be associated with benign lesions, whereas type II with either benign or malignant lesions. However, this chemical classification is incomplete. Other chemical phases, such as whitlockite (Wk) and amorphous carbonated calcium phosphate (ACCP) have been observed in breast [13,29–32]. Recent studies suggested that physicochemical characteristics of BMCs may be related to the nature of the cancer and its severity [33–35]. Hence, BMCs physico-chemical speciation has potential to be relevant for clinicians.

This article draws an overview of the current information provided by BMCs, as well as the gaps that remain regarding their pathological role and aims to emphasize the need for further research to understand BMCs properties in regards to breast pathology. As shown in Figure 1, the article is divided into two main parts. First, Section 2 describes the existing clinical examination used in routine at the hospital for breast cancer diagnosis, and successively addresses mammography examination (Section 2.1) and histological analysis (Section 2.2). The role of BMCs in these processes will be emphasized. Then, Section 3 proposes an extensive description of the techniques for BMCs characterization. First, we will discuss field emission scanning electron microscopy (FE-SEM) analysis for the morphological description of BMCs (Section 3.1), then we will address vibrational spectroscopy techniques for the chemical speciation from the micrometric to the sub-micrometric scales (Section 3.2). The end of this section is dedicated to the thorough characterization of BMCs and describes methods that are mostly implemented in research laboratories like super-resolution vibrational technique. During this study, a multiscale approach was developed and tested on one specific clinical example to demonstrate its medical relevance and its suitability with standard sample preparation protocols routinely used in hospital anatomopathological departments.

2. BMCs as a contingent marker of breast cancer: clinical considerations

2.1. *Mammography as the diagnosis starting point*

Mammography is a procedure that consists of radiography of the breast. This technique, first described

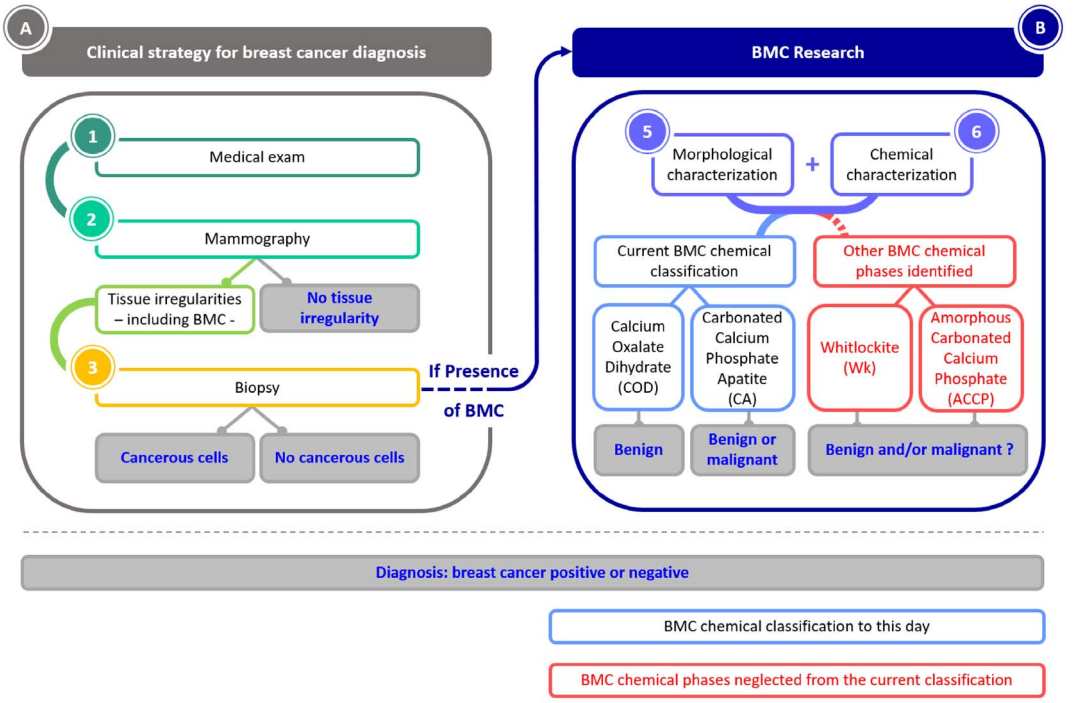

Figure 1. Schematic organization of the article. First the clinical strategy for breast cancer diagnosis, and then the ongoing research on BMCs that aims to understand their role in breast cancer.

by the surgeon A. Salomon in 1913 in Berlin, is the medical examination of reference for breast cancer screening and constitutes the main strategy for early diagnosis. Standard medical systems have a spatial resolution of between a few dozen and a hundred microns [36,37]. The presence of BMCs on mammograms is very valuable information as they are considered a benchmark of breast cancer early signs [38]. Some specific BMC features discernible on mammograms can be indicative of malignancy and raise concerns about the presence of cancerous cells. Several studies focused on fostering an understanding of the link between BMCs and breast cancer [13,29,39–48] to clarify those concerning characteristics. They are five main BMC distributions: grouped (or clustered), linear, segmental, regional, and diffuse (Figure 2). In particular, grouped, regional and segmental distributions are considered as suspect BMC distributions and are associated with high risks of ductal carcinoma [11,47,49–51].

In addition to BMCs distribution, their morphological aspects are also used to suspect malignancies. Many BMCs morphologies have been described in the literature. Studies investigating the link between microcalcifications and cancer, have emphasized that fine pleomorphic and fine linear microcalcifications have a greater risk to be associated with malignancies (Figure 3), as reported in BI-RADS [49] (the acronym for Breast Imaging-Reporting and Data System: a classification system used worldwide by radiologists to evaluate breast lesions and the associated pathology).

Those criteria—BMCs morphologies and distribution—help evaluate the risk of malignancies but do not allow to diagnose malignancy through the presence of BMCs.

2.2. *Histological analysis: the utmost assessment for cancer diagnosis*

Since mammograms do not enable to distinguish calcifications associated with benign from malignant pathologies, if any anomalies and suspect BMCs are observed on mammograms, histological analyses [53] will be performed to confirm or rule out the presence of cancerous cells (Figure 4). To this end,

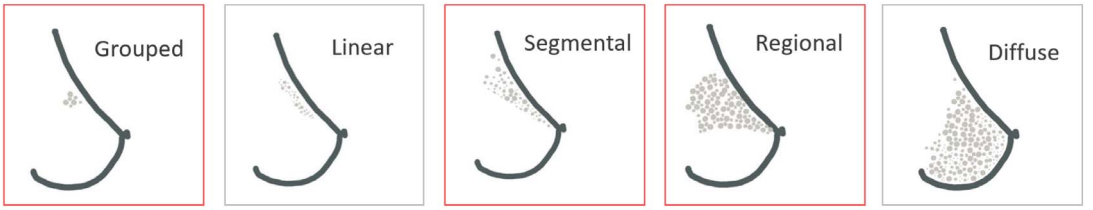

Figure 2. Main distributions of microcalcifications in the breast. Distributions highlighted in red are distribution associated with higher risks of breast cancer.

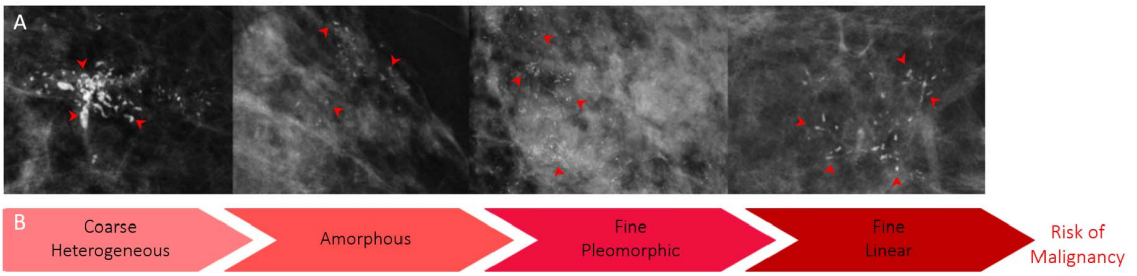

Figure 3. (A) BMCs suspect morphological features. Digital zoom mammographic projection images show calcifications with increasing risk for malignancy, Rao *et al.* [52]. From left to right: coarse heterogeneous, amorphous, fine pleomorphic, and fine linear. Red arrows were added to highlight BMCs on the images. (B) Their relative risk for malignancy.

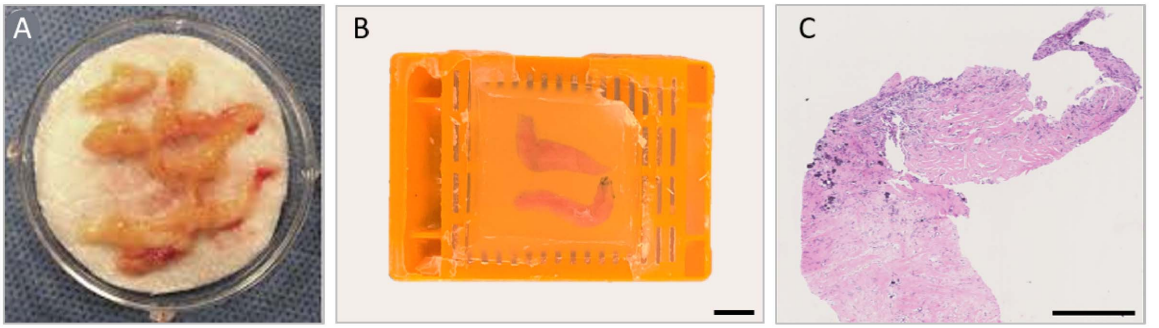

Figure 4. Breast tissue preparation for histopathological analyses. (A) Breast biopsy, (B) paraffin embedded breast tissue, 5 mm scale bar, and (C) H&E stained breast biopsy, ×10 optical image, 500 µm scale bar.

a fraction of suspect tissue has to be collected. Samples, for which the risk of cancer cells' presence lies, can be harvested either through needle biopsy (fine needle aspiration biopsy or core needle biopsy) or surgical excision (lumpectomy or mastectomy) [54]. Thereupon, BMCs are used to make sure the sample was collected in the suspicious area of the breast but are not further used for the diagnosis. Thereafter resection (Figure 4A), samples are usually fixed using formalin and embedded in paraffin (Figure 4B, C). To this end, a 4 to 6 µm thick slice of the sample is cut from the paraffin block using a microtome and deposited on a glass microscope slide. Hematoxylin and Eosin (H&E) staining is performed after paraffin removal using xylene. H&E staining is the most largely used method for histopathological analysis. Hematoxylin complex with nucleic acids which takes a purple color, whereas eosin stains non-specifically

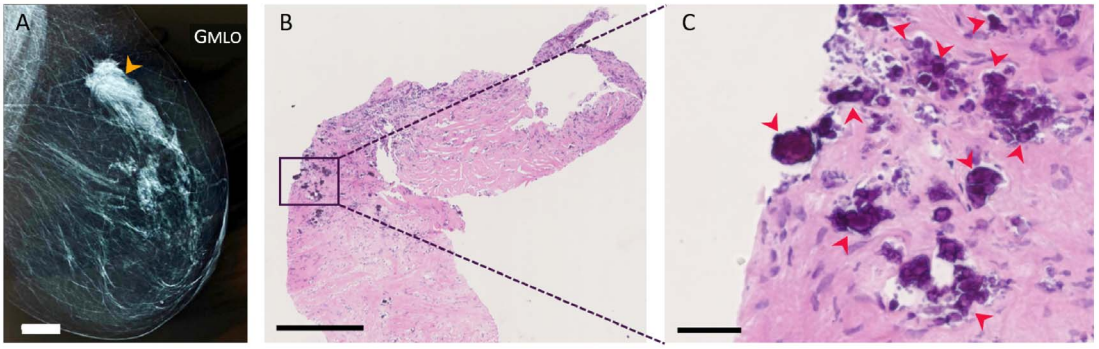

Figure 5. BMCs observation during the histopathological analyses of an abnormal mass in a 75 years old woman diagnosed with infiltrating low-grade ductal carcinoma (75-IDC patient) in the upper-outer quadrant of her right breast. (A) Mammogram of the patient's right breast. The orange arrow indicates the estimated position where tissue resection was performed, 20 mm white scale bar. (B,C) Histopathological analyses of the patient's biopsy at two different magnifications. H&E slide with 500 μm and 50 μm black scale bar respectively. Red arrows indicate the presence of BMCs.

proteins in pink [55] (Figure 4C). Thus, based on the morphology of the cell nucleus and cytoplasm, cancerous cells can be distinguished from healthy ones. If cancerous cells are observed, the stage of the cancer is accordingly evaluated on three criteria: nuclear polymorphism, glandular differentiation and mitotic count [56–58].

If BMCs are observed on the histopathological slide, it confirms that the biopsy was harvested within the region with suspect lesions and gives indications where cancerous cells may be present; but BMCs are not further investigated clinically. Yet studies investigating the correlation between BMCs [33–35] and cancer suggest that BMCs physicochemical properties can be correlated to the pathology and its severity. The following section focuses on analytical strategy for physical and chemical characterization of BMCs, that could provide a better understanding of the possible relationship between BMCs physicochemical properties and the pathology.

Figure 5 displays a mammogram of a 75-years old woman right breast with lesions suspicious of malignancy. A biopsy was performed on the breast lesions, and histopathological analyses (Figure 5B, C), conclude to an infiltrating low-grade ductal carcinoma diagnosis. This patient (75-IDC patient) presented BMCs as shown in Figure 5C, and was used to illustrate the capabilities of BMCs characterization techniques not classically used for breast cancer investigation: FE-SEM (Section 3.1) and vibrational spectromicroscopy (Section 3.2), including Fourier transform infrared spectroscopy (FT-IR), Fourier transform infrared spectromicroscopy (μFT-IR) and atomic force microscopy coupled with infrared spectroscopy (AFM-IR), and to evaluate their relevance.

3. Characterization of BMCs to uncover the relationship between mineralization processes and breast cancer

3.1. *SEM: sub-micrometer scale morphological description*

Mammography and histology examinations are the agreed clinical protocol for breast cancer diagnosis, but techniques enabling morphological description and chemical speciation of BMCs at the micrometric and sub-micrometric scale are necessary to understand their role and implication with breast cancer. Investigating the correlations between BMCs morphological and chemical features with the pathology could provide valuable information to apprehend the molecular changes occurring in breast tissues.

In this context, SEM is a relevant tool to study BMCs morphology at the sub-micrometer scale [59–61] without any specific sample preparation except those already implemented in most anatomopathological laboratories and used for medical diagnosis [62,63].

From tissue resection embedded in paraffin, FE-SEM analysis can be performed by depositing a few micrometer thick slice of tissue on a classical glass microscope slide or on specific Infrared-Raman compatible substrate (such as low-e microscope slides [64–66]) in case of correlative measurements using vibrational microspectroscopies. Then, paraffin is removed with xylene without any further treatment. Since tissue block radiography is a valuable adjunctive method to ensure that SEM analyzed samples contain BMCs and are interpreted within their histopathological context, an H&E serial section is prepared. Usually, for samples with low conductivity properties, such as biological samples, SEM analyses are performed on carbon-coated samples. However, using FE-SEM that enables less electrostatic distortion of images compared to SEM, and if low tension is used during the experiment (between 0.5 and 3 keV), analyses can be performed directly on the sample without carbon coating [67] allowing complementary spectroscopical analysis on the same sample. Resulting FE-SEM images provide structural descriptions of both BMC and their surrounding native environment (Figure 6).

In tissue biopsy, BMCs can have diversified shapes and forms (Figure 6). In breast tissue sections, four chemical phases were observed: COD (BMCs of type I), CA (BMCs of type II), and more recently BMCs containing Wk and ACCP were reported [32,68,69]. Noteworthy, ACCP is an amorphous mineral without characteristic morphology, in contrast with COD, CA and Wk that can have highly specific shapes.

First, COD ($CaC_2O_4{\cdot}2{,}2H_2O$) BMCs: they have been identified in pathologies affecting various organs like the thyroid [70,71], kidney [72–74], and prostate [75,76]. Nevertheless, in the breast, the type of BMC is always associated with benign lesions. They can be easily identified by FE-SEM due to their characteristic bipyramidal or dodecahedral shapes (Figure 7A–C) that depends on the calcification calcium rate [74].

Secondly, CA BMCs ($Ca_{10-x}\square_x(PO_4)_{6-x}(CO_3)_x(OH)_{2-x}$, where $\square$ corresponds to vacancy, and $0 \leq x \leq 2$ [68,78–80]) were observed in breast, kidney and thyroids. In the breast tissue, CA BMCs have been observed for both benign or malignant lesions. They can be recognized thanks to their spherical shapes (Figure 7D–F). Furthermore, it was highlighted that those spherical BMCs can have diversified internal structures, from radial to concentric internal organizations (Figure 8) [81]. These observations are consistent with Frappart *et al.* study [77], which distinguishes three subtypes of spherical calcifications using transmission electron microscopy. These three subtypes are characterized by respectively, a succession of concentric layers, randomly arranged feltings of fibers, and finally granular materials linked by organic matter. In addition, CA BMCs can present as porous surfaces [81].

Eventually, another mineral phase observed in breast and with specific morphology is Wk. Wk ($Ca_{18}Mg_2(HPO_4)_2(PO_4)_{12}$) is a mineral close to synthetic CA. The difference lies in the presence of HPO_4^{2-} ions, as well as Ca^{2+} vacancies and Mg^{2+} substitutions [82,83]. Abnormal deposits of Wk were observed in gallstones [84], aorta [85], cartilage [86], salivary glands [87] and kidney [88]. In the breast, a few studies suggest that the percentage of Mg, associated with Wk BMC, increases with the cancer malignancy [89]. Nevertheless, the possible correlation between Mg and cancer severity is not substantiated and remains poorly understood [34]. Wk BMCs can be identified by SEM due to their specific pseudo cubical shapes (Figure 7G–I) [64]. Thus, BMCs with distinctive form as shown in Figure 7 are associated with specific chemistry, but the reciprocal implication is false. CA, COD, and Wk calcifications can be observed without, respectively, spherical, dodecahedral, and pseudo cubical morphologies.

Since BMCs chemical composition can be associated with specific morphology, SEM is a valuable tool for an initial characterization of BMCs. Indeed, without further preparation than those routinely used for anatomopathological analysis, it's easier to evaluate their size and morphology (their shapes as well as the porosity of the surface) using SEM images than mammography.

To illustrate the relevance of SEM, a thin section of the 75-IDC patient resection, whose mammography section is presented in Figure 5, was investigated. Both mammography and histological analyses highlighted the presence of microcalcifications. On the exact same region given in Figures 5B and C, we performed FE-SEM analysis (Figure 9). Many BMCs can be observed on those images at low magnification (Figure 9A). They appear as white materials on the darker breast tissue. At higher magnification

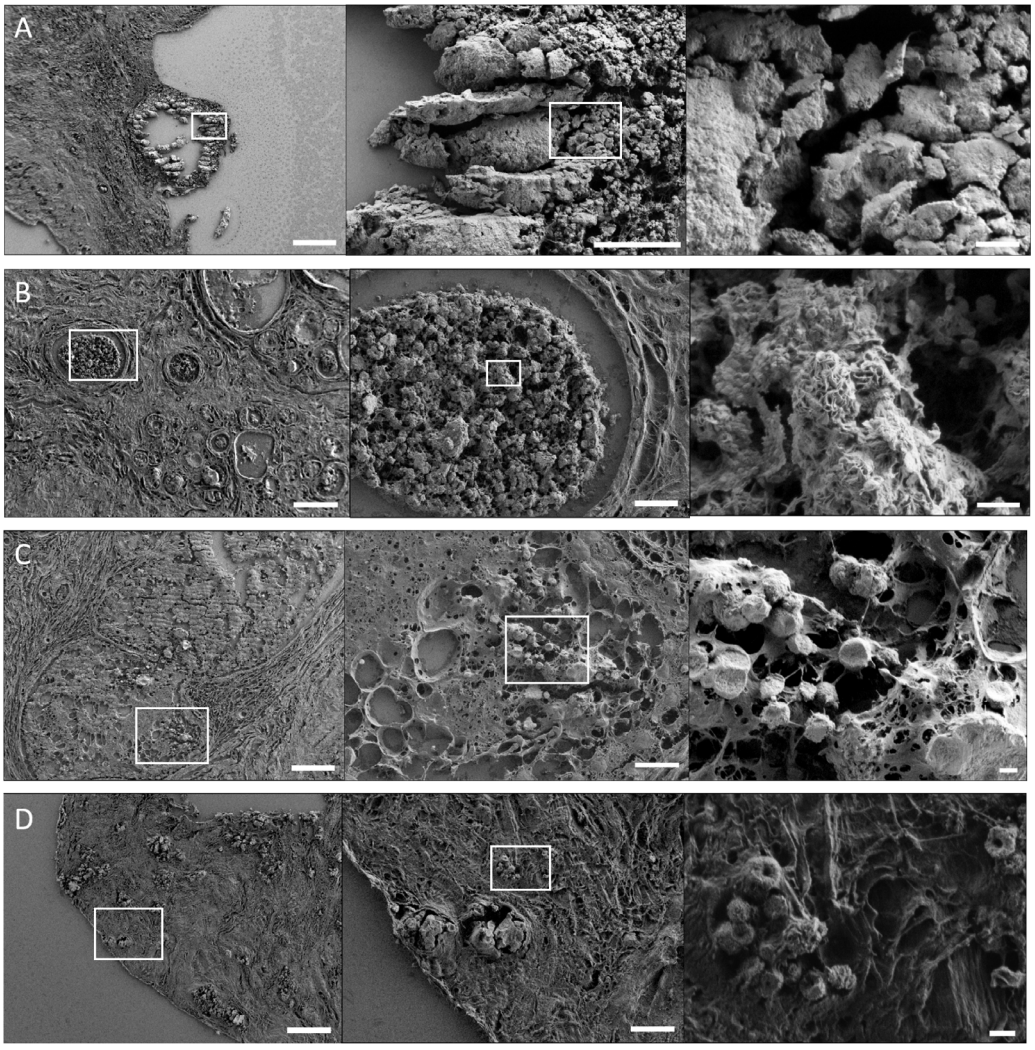

Figure 6. FE-SEM images of breast microcalcifications. BMCs in the breast of patients diagnosed with (A) infiltrating ductal carcinoma, (B) mastopathy, (C) in-situ ductal carcinoma, and (D) infiltrating ductal carcinoma. (A–D) From left to right, increasing magnification of the area indicated with a white square. The left, middle and right images have a 100 μm, 20 μm and 2 μm scale bar respectively. Breast biopsy slices were deposited on MirrIR low-e microscope slides (MirrIR, Kevley Technologies, Tienta Sciences, Indianapolis), and FE-SEM (field emission scanning electron microscopy) images were acquired using a Zeiss SUPRA 55-VP at low-voltage (1–2 kV), and an Everhart–Thornley SE detector.

(Figure 9B, C), we can notice that some BMCs display spherical structures with porous surfaces. This may indicate that, in this area, a few BMCs are like type II calcification composed of CA. CA BMCs need particular attention as they have been observed in both benign and malignant pathologies, and might suggest the presence of cancerous cells, as it was the case for this patient.

Even if SEM does not allow direct chemical speciation of a BMC, it can provide information regarding their elemental constitution through energy dispersive X-ray (EDX) analysis. EDX measurements consist of the analysis of photons emitted by materials when exposed to a primary electron beam. Indeed, the energy of the emitted photons will depend on the elements present in the sample. Hence, by looking

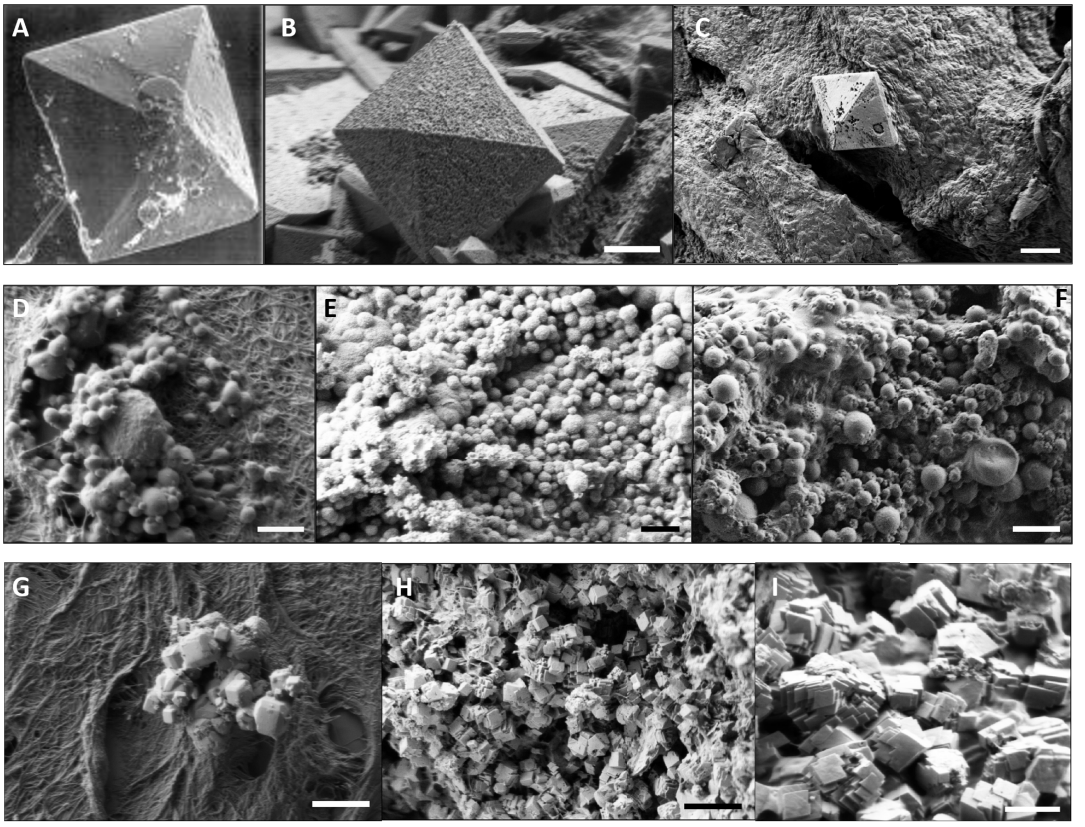

Figure 7. SEM images of BMCs composed of COD (A–C), CA (D–F), and Wk (G–I). (A–C) COD in (A) breast, magnification ×980, from Frappart *et al.* [77], (B) kidney—5 μm scale bar, and (C) thyroid—2 μm scale bar. (D–F) CA observed in (D) breast—2 μm scale bar, (E) kidney—5 μm scale bar and (F) thyroid—5 μm scale bar. (G–I) Wk in (G) breast—5 μm scale bar, (H) and (I) in kidney—5 μm and 2 μm scale bar respectively.

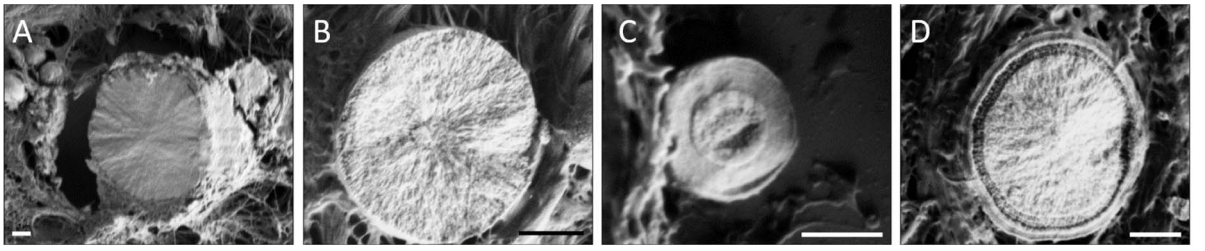

Figure 8. FE-SEM images of the internal structure of spherical CA calcifications, 1 μm scale bar. (A,B) Radial structure and (C,D) concentric layer. Adapted from Bazin *et al.* [62].

at the energy of those photons one can evaluate which elements constitute the sample. This technique is widely used for the elemental analysis of biological calcifications [89–91]. EDX analysis was also performed on the 75-IDC patient section (Figure 10), in the same region of interest (see Figure 9). Calcium, phosphorus, and oxygen were observed in major amounts, which is consistent with CA-based BMCs.

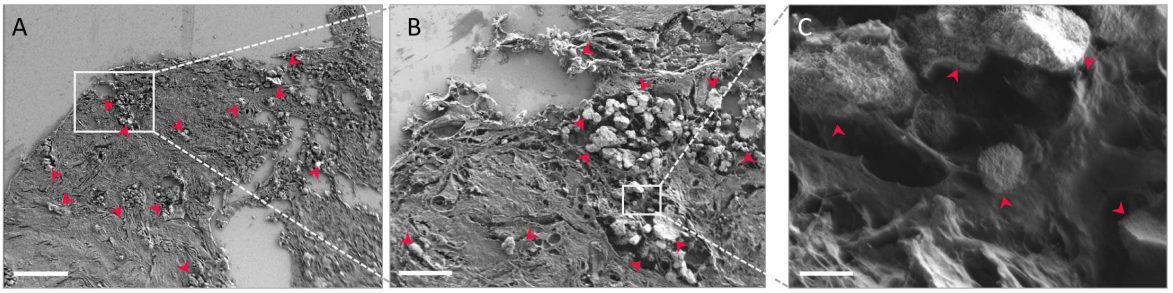

Figure 9. Observation of BMCs, using FE-SEM at different magnifications in the 75-IDC patient biopsy. The same region has shown in Figures 5B and C was investigated. FE-SEM images were acquired with a Zeiss SUPRA55-VP scanning electron microscope, using an Everhart–Thornley SE detector and the electron beam energy set to 1 keV. (A) 100 µm, (B) 20 µm, and (C) 2 µm scale bar. Red arrows indicate the presence of BMCs.

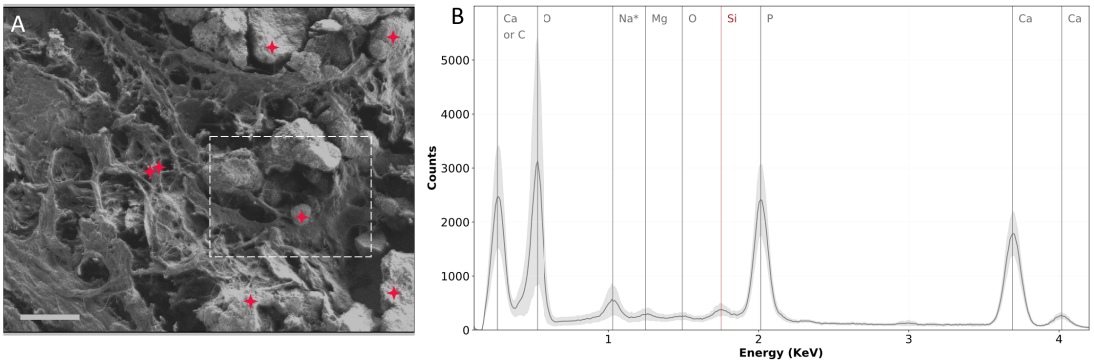

Figure 10. SEM and EDX experiments performed on the biopsy of the 75-IDC patient. (A) SEM image of the region analyzed. Red crosses indicate locations at which EDX spectra were recorded. The dashed white line delimits the region shown in Figure 9C. (B) EDX spectra. The gray curve represents the mean spectrum of all 7 spectra recorded in the region analyzed. The light gray contour indicates the standard deviation. Silicon observed on the EDX spectra (red vertical line) comes from the substrate (Low-e microscope slide). * The attribution of the 1 keV peak should be carefully done: it could be due to Na or O as its concentration is high in tissue sections.

EDX allows access to the elemental composition of BMCs but does not provide any information about the chemical bonds. To this end, additional characterization techniques, such as IR spectroscopy, have to be used to accurately characterize BMC chemical composition. It is important to note that EDX measurements may be destructive for the proteins constitutive of the tissue since it needs to be performed at higher voltage (at least 13 kV for Ca identification), and is very likely to locally deteriorate the sample. Therefore, if other characterization techniques are required on the same region, EDX analysis has to be performed last.

3.2. *Vibrational spectroscopy*

3.2.1. *IR spectroscopy and BMC chemical speciation*

IR absorption spectroscopy (including FT-IR and µFT-IR) is an advantageous, non-destructive and label-free technique for chemical speciation. IR spectroscopy directly probes vibrational energy levels of materials, providing chemical composition of organic and inorganic matter. The IR absorption spectrum of species depends on the chemical bonds present. As a consequence, each chemical compound possesses its specific response in the mid-IR region (4000–400 cm^{-1}). Calcification, based on

its chemical composition will thus exhibit a specific and characteristic IR absorption spectrum. For unknown complex samples, the chemical composition can be deduced by comparison with reference spectra data bank. In the medical field, IR microscopy, when combined with morphological description, has already demonstrated that it is possible to obtain significant clinical information regarding microcrystalline pathologies through the analysis of concretions as well as of ectopic calcifications in different human tissues [92,93].

Figure 11 displays IR spectra of the four calcium-based mineral phases reported in the breast, e.g., CA, COD, Wk and ACCP. All these four compounds have specific and characteristic IR signatures as shown in Figure 11B. The 1100–950 cm^{-1} spectral range is mainly associated with absorption bands of phosphate groups (PO_3^{4-}), and in particular O–P–O bonds. In inorganic compounds, the number of phosphate absorption bands depends on the symmetry of phosphate ions within the crystalline structure. For phosphate with tetrahedral symmetry—which is the case for both CA and Wk [94,95]—two vibration modes, one stretching mode and one bending mode, are active in the mid-IR range. The antisymmetric stretching of phosphate bonds is observed between 1150 and 1020 cm^{-1}, whereas symmetric stretching is observed between 1000 and 960 cm^{-1} (Figure 11) [96,97]. Phosphate bending modes appear in the 560–500 cm^{-1} region. On Wk FT-IR absorption spectrum (Figure 11A, brown curve), we can notice the presence of several shoulders in the phosphate region compared to CA spectrum (Figure 11A, red curve). This complex structure of the absorption band can be explained by the presence of both Ca and Mg atoms in Wk, compared to CA. Indeed, since IR spectroscopy probes bonds vibration of chemical compound, the energy of each vibration will be affected by the local chemical environment. For phosphate, the frequency of the absorption band will decrease inversely to the mass of the atom it is coordinated. Hence, in Wk, phosphate groups are surrounded by either Ca or Mg, which multiplies the number of absorption bands of the phosphate groups in comparison with CA or ACCP (where phosphate groups are surrounded by only Ca atoms). In addition, we can notice the presence of tribasic and dibasic phosphate ions, which have different response in IR and create additional bands. In particular, the absorption band at 1141 cm^{-1} corresponds to the antisymmetric stretching of dibasic phosphate (HPO_4^{2-}). Furthermore, FT-IR spectroscopy can be used to evidence the crystallinity level of a compound. For instance, between the amorphous ACCP and its crystalline species CA, a shift of the maximum of absorption is observed from respectively 1032 cm^{-1} to 1078 cm^{-1}.

In addition to phosphate groups absorption bands, other absorption bands can be observed (spectra Figure 11) between 1600 and 1400 cm^{-1} corresponding to carbonates (CO_3^-) in inorganic calcium carbonated compounds, and more specifically to their asymmetric stretching mode. Depending on the crystalline structure of the calcification, a doublet of (CO_3^-) asymmetric stretching can be observed (resulting from lifting of degeneracy), as for CA spectrum and the two bands at 1414 and 1456 cm^{-1}. Carbonates present also absorption bands in the 1100–1000 cm^{-1} region, but a lot weaker in intensity. Hence, the absorption describes in this spectral range will be dominated by the contribution of phosphate groups.

For hydrated materials, such as COD (Figure 11 orange curve), the presence on the IR spectrum of an absorption band at 1647 cm^{-1} can be associated to the absorption of oxalate group, as well as the deformation vibration mode of water molecules. Finally, we can notice on CA, COD, Wk and ACCP, the presence of a broad absorption band centered near 3400 cm^{-1}. This can be associated to residual water molecules, and more specifically H–O–H stretching modes.

ACCP and Wk BMCs aren't very well described in the breast yet. Nevertheless, they both can be identified and investigated through FT-IR spectroscopy. ACCP was recently, reported in breast calcifications [98] and is observed alongside CA, as it is considered as its precursor. This association of ACCP and CA in BMCs is revealed by the presence of a shoulder at 1032 cm^{-1} in the phosphate absorption band [99]. The link between the presence of ACCP in BMCs and breast cancer is yet to be discovered, but in other pathologies, its implication has been demonstrated. In kidney tissues, Carpentier *et al.* [100] showed that ACCP can be considered as a precursor of Randall's Plaque: an ectopic calcification present at the tip of the kidney papilla responsible for a significant increase of the prevalence of urolithiasis in the last decades. Regarding Wk, only a few publications

A

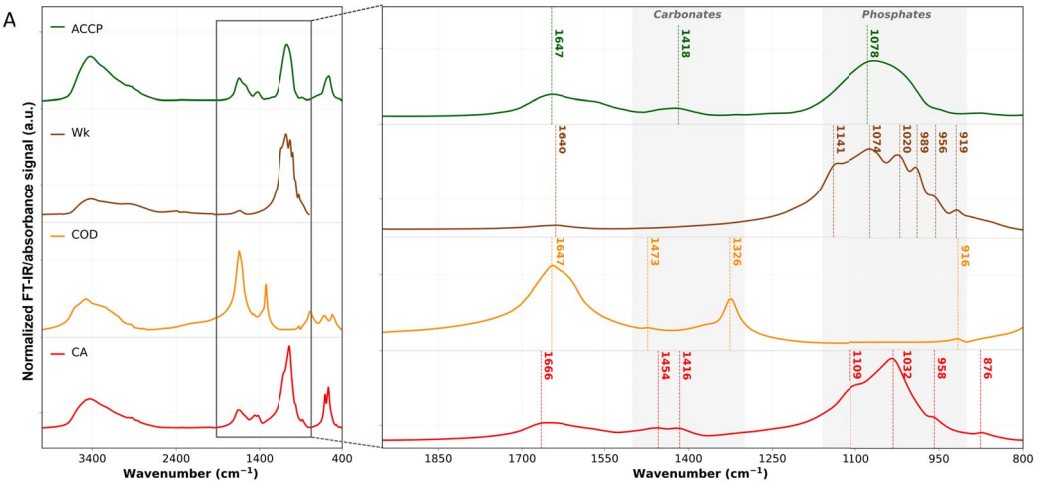

B

Carbonated Calcium Phosphate Apatite (CA) $Ca_{10-x}\square_x(PO_4)_{6-x}(CO_3)_x(OH)_{2-x}$	Calcium Oxalate Dihydrate (COD) $Ca(C_2O_4).2.2(H_2O)$	Whitlockite (Wk) $Ca_9Mg(HPO_4)(PO_4)_6$	Amorphous Carbonated Calcium Phosphate (ACCP) $Ca_6(PO_4)_\beta(CO_3)_\gamma(OH)_\delta$
876 cm^{-1}	-	-	-
-	916 cm^{-1}	919 cm^{-1}	-
958 cm^{-1}	-	956 cm^{-1}	947 cm^{-1}
-	-	989 cm^{-1}	-
1032 cm^{-1}	-	1020 cm^{-1}	1003 cm^{-1}
-	-	1074 cm^{-1}	1078 cm^{-1}
1109 cm^{-1}	-	1141 cm^{-1}	-
-	1326 cm^{-1}	-	-
1416 cm^{-1}	-	-	1418 cm^{-1}
1454 cm^{-1}	1473 cm^{-1}	-	-
-	-	-	1562 cm^{-1}
-	1619 cm^{-1}	-	-
1666 cm^{-1}	1647 cm^{-1}	1640 cm^{-1}	1647 cm^{-1}

Figure 11. FT-IR analyses of the standard calcification chemical phases reported in the breast. (A) Normalized FT-IR spectra of carbonated calcium phosphate apatite (CA) in red, calcium oxalate dihydrate (COD) in orange, whitlockite (Wk) in brown and amorphous carbonated calcium phosphate (ACCP) in green. Main absorption bands and shoulders are outlined with dashed vertical lines with the associated wavenumber as caption. KBr pellets were prepared from chemically high purity (at least 95%) kidney stones, and spectra were acquired in transmission mode using a Vector 22 spectrometer from Bruker Spectrospin (Wissembourg, France), collected between 4000 cm^{-1} and 400 cm^{-1} with a spectral resolution of 4 cm^{-1}. (B) Summary of CA, COD, Wk, and ACCP main absorption bands and shoulders on the 1900–800 cm^{-1} spectral range. Absorption bands and shoulders wavenumbers were determined using spectra second derivative. For the chemical formula of CA: $0 \leq x \leq 2$, and $\square$ represents vacancy.

mentioned its presence in the breast [29,34]. Scimeca *et al.* [101] may have been the first to report Wk in the breast through FT-IR spectrum and the observation of an absorption band at 990 cm^{-1}. Besides, Scott *et al.* [89] discovered that the proportion of Wk seemed to increase from benign to invasive cancer. However, this correlation between Wk with cancer malignancy needs further investigation as contradictory observation have been made and no consensus has been reached yet [34,89]. Noteworthy, like ACCP, Wk is known to be associated with pathological calcification in other organs. For example, the weight fraction of Wk, estimated by FT-IR, in kidney stones is highly related to infection if greater than 20% (80% of statistical significance) [64]. On the other hand, Tsolaki *et al.* [102] recently reported the presence of nano to micrometer sized spherical particles made of highly crystalline Wk in malignant breast tumors.

Nanometric Wk crystallites are challenging to detect using IR techniques, especially if they are present in low quantity. The spatial resolution of FT-IR spectromicroscopy is wavelength dependent, limited by the diffraction limit and is, at the best, around 5 to 10 μm. Although the resolution is limited, μFT-IR is a powerful tool for clinician as it can easily give insight on BMCs chemical composition without additional sample preparation. To highlight that, we performed hyperspectral analyses of a BMC-rich region of the 75-IDC patient previously introduced (Figure 12). FT-IR hyperspectral imaging [103] consists in segmenting an area into pixels and measure, for each one of them, an IR absorption spectrum on the whole spectral range. A multidimensional data block is then obtained: two dimensions for the spatial coordinates and one dimension for each wavelength of the spectral range of interest (Figure 12B). μFT-IR spectrum depends among others on the concentration of molecule that absorbs and the thickness of the sample (Beer–Lambert's law). That is why to compare spectrum between one another, spectra must be normalized to remove any scaling effect that can be observed on chemically and structurally heterogeneous samples. Thereafter, the data can be easily interpreted by creating IR mapping (here called heatmap): representing the absorption intensity at a fixed wavenumber for each pixel, which enables to study the distribution of chemical compounds over the whole region of interest (Figure 13).

To locate BMCs within the tissue matrix of the 75-IDC patient's biopsy, two heatmaps were generated using normalized spectra by dividing the absorbance at 1036 cm^{-1} by the absorbance at 1655 cm^{-1} (Figure 13C), and the absorbance at 1420 cm^{-1} by the absorbance at 1655 cm^{-1} (Figure 13D). 1036 cm^{-1} and 1420 cm^{-1} being respectively associated to the absorption of phosphates and carbonates in BMCs and 1655 cm^{-1} corresponding to the Amide I band (the stretching mode of amide C=O bonds) [104,105] characteristic of the total protein content of the tissue. These ratios provide information about regions rich in BMCs (higher ratio value in light green on the maps in Figure 13) compared to region mainly composed of tissue (lower ratio value in dark blue on the maps). Pixels with high ratio in Figures 13C and D, correlate with the presence of BMCs on the associated FE-SEM image of the region (Figure 13A, red arrows). Finally, a third heatmap was generating by dividing the absorption intensity at 1420 cm^{-1} by the absorption at 1036 cm^{-1} (Figure 13E), to evaluate if all BMCs are chemically homogenous in terms of carbonate contents. On this representation, location at which BMCs were detected on FE-SEM and other IR heatmaps (Figure 13C, D) are associated with low and medium 1420 cm^{-1}/1036 cm^{-1} ratio value, suggesting different levels of carbonate substitution in BMCs. Besides, strong signal was also observed at location without BMC, at least as far as we can observe on the FE-SEM images. Indeed, other molecular species in the breast tissue absorb in the 1450–1400 cm^{-1} region, as well as in the 1200–1000 cm^{-1} region, including carbohydrates, glycoproteins, residues of paraffin, lipids, sugar, or DNA, as can be seen on the IR absorption spectrum of pure tissue (Figure 13B, blue dashed line). Hence, the overlapping absorption bands may lead to misinterpretation of the data.

μFT-IR can enable localizing BMCs in a sample (Figure 13) but is first and foremost a technique of choice to elucidate their chemical speciation (Figure 14). Figure 14C displays local spectra measured at location showing strong calcification signal (Figure 14, grey square) on the heatmap of the 1036 cm^{-1}/1655 cm^{-1} ratio (Figures 13C and 14A). These spectra present intense absorption bands at 1650 cm^{-1}, 1550 cm^{-1} and a weaker band at 1260 cm^{-1}, corresponding respectively to the Amide I, II and III vibration band of proteins, e.g.,

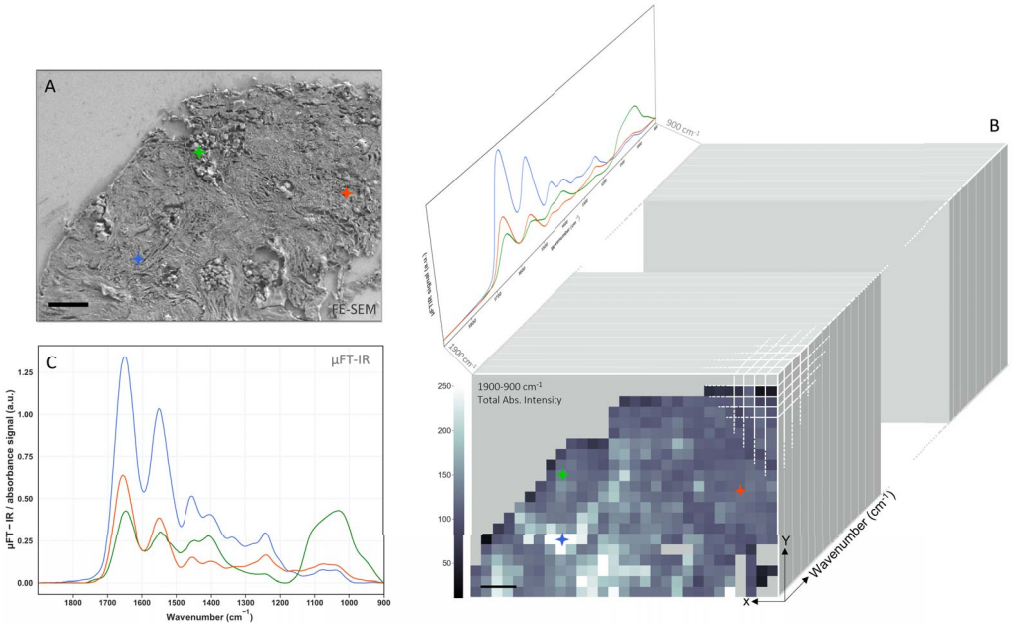

Figure 12. µFT-IR analysis of the 75-IDC patient. (A) FE-SEM image of the whole region analyzed, 50 µm scale bar. (B) Schematic representation of the multidimensional data block resulting from the hyperspectral analysis. The heatmap represents the total absorption intensity for each point over the 1900–900 cm^{-1} spectral. A baseline correction was applied to the spectra and a Savitzky–Golay filter (order 1, 13 points), without normalization, 50 µm scale bar. (D) Spectra measured at position indicated by the color-coded crosses on (A) and (C), and presenting low (orange), medium (green), and high (blue) total absorption intensity over the spectral range of interest. Spectra were recorded every 15 µm with a diaphragm of 30 µm × 30 µm and a 4 cm^{-1} spectral resolution, using Lumos infrared microscope from Bruker. 24 spectra were measured per point and averaged.

the tissue [97,106]. Besides, these spectra present a broad absorption band between 1100 cm^{-1} and 1030 cm^{-1}, suggesting the presence of BMCs made of CA and a small proportion of ACCP as highlighted by the shoulder of the band. The shape of the phosphate bands varies from a spectrum to another (Figure 14C). To further investigate the structure of this absorption band, the second derivative of the experimental spectra, as well as CA and ACCP reference spectra were calculated. A shoulder at 1114 cm^{-1} is present for all four spectra acquired on BMC rich area of the 75-IDC patient biopsy and also observed in ACCP second derivative. On the other hand, we can notice a shift of the maximum of the phosphate absorption band between 1032 cm^{-1} and 1003 cm^{-1}. A similar observation can be made for the shoulder near 950 cm^{-1}. These results might suggest that BMCs in this sample might be composed of mixture of CA and ACCP, with chemical heterogeneities between and/or within BMCs.

In the literature, a few hypotheses have been raised regarding the correlation between BMCs chemical composition, the pathology and its degree of malignancy. These hypotheses rely on vibrational spectroscopic studies, either FT-IR or Raman spectroscopy. For example, through Raman spectroscopy, Haka *et al.* [105] found that the proportion of carbonates in BMCs was greater in benign breast tissue compared to malignant breast tumors. Likewise, Baker *et al.* [33], investigated the relationship between the carbonate content of BMCs in regards to the pathology through FT-IR analyses. They collected FT-IR spectra of synthetic apatite containing 0, 0.5, 1.4, 2.3, and 3.5% of carbonates (Figure 15A), creating a calibration data base to establish a link between BMCs carbonate content and the grade of the pathology (Figure 15B). Similarly, to Haka *et al.* [105],

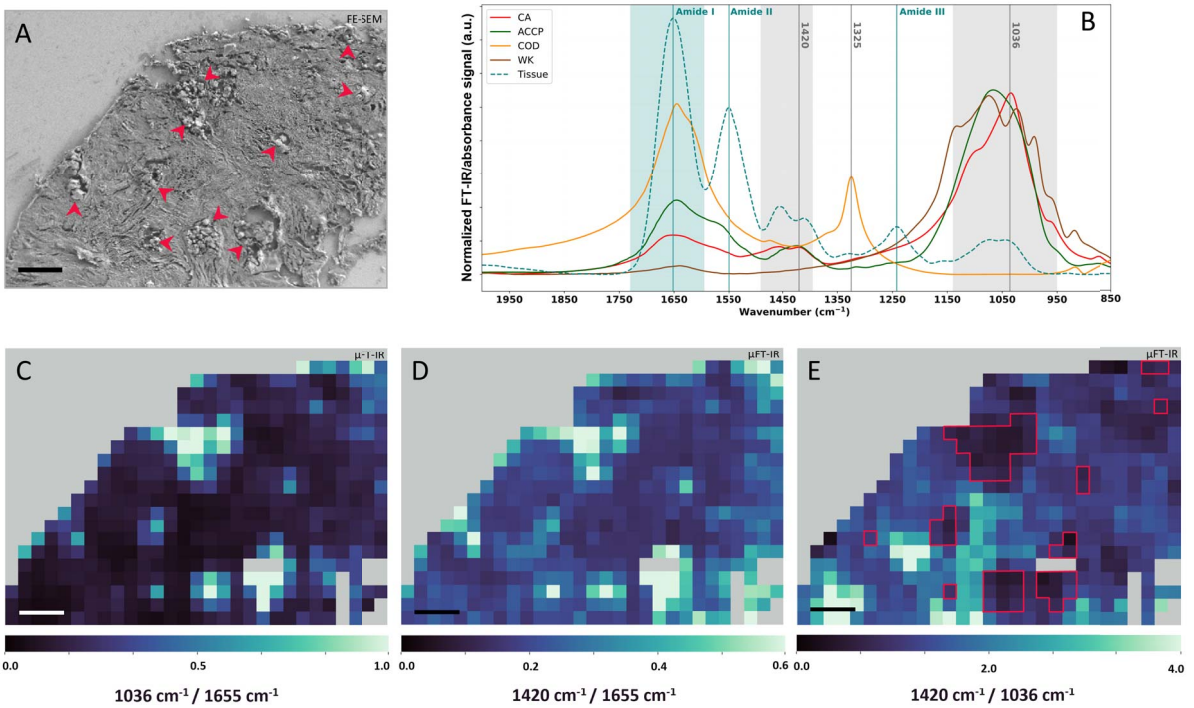

Figure 13. μFT-IR analyses of the 75-IDC patient biopsy. (A) FE-SEM image of the biopsy region analyzed through μFT-IR. Red arrows indicate the presence of BMCs. (B) Calcification normalized reference FT-IR spectra: CA (red), COD (orange), Wk (brown), and ACCP (dark green), as well as tissue μFT-IR reference spectrum (blue–green curve) measured on areas without BMC, based on FE-SEM images. Spectral range highlighted in light blue is the IR region associated with absorption contribution of the tissue Amide I and spectral range highlighted in light grey are regions associated with absorption contribution of BMCs carbonate and phosphate absorption bands. (C–E) μFT-IR heatmaps of absorption intensity ratio calculated using normalized spectra. (C) 1036 cm^{-1}/1655 cm^{-1} heatmap, (D) 1420 cm^{-1}/1655 cm^{-1} heatmap, and (E) 1420 cm^{-1}/1036 cm^{-1} heatmap with red solid lines indicating BMC identified through μFT-IR analyses on (C) and (D). (A, C, D, and E): 50 μm scale bar.

they observe a decreasing carbonate percentage with increasing grade of the breast lesion. Based on equivalent data, Gosling *et al.* [35] have proposed a model that rationalizes mineralization in the breast and the proportion of carbonate in BMCs with the severity of the pathology (Figure 15C).

Besides, Ben Lakhdar *et al.* [68] have shown that the carbonate percentage is inhomogeneous within BMC themselves. This work, investigating BMCs through μFT-IR spectroscopy emphasized that, in the case of ductal carcinoma in situ, the carbonates content is greater in the core of the BMC compared to its surface, as the CO_3^{2-}/PO_4^{3-} ratio is decreasing from the center of the microcalcification to its surface.

Those different studies illustrate the complex organization of BMCs and raise the following question: is global analysis sufficient to characterize BMCs and reach a final diagnosis that links their chemical composition to malignancy level? Or, is the submicrometric scale exploration crucial to precise eventual local gradient for the diagnosis?

Unfortunately, μFT-IR system has a wavenumber-dependent spatial resolution that varies roughly from a few microns to dozens of microns [106], and close to a micron for Raman microscope, which could be a limitation to individually characterize sub-micrometric objects. Figure 14 presents IR spectrum of a few BMCs identified in the 75-IDC patient. On the FE-SEM image of this region (Figure 14B),

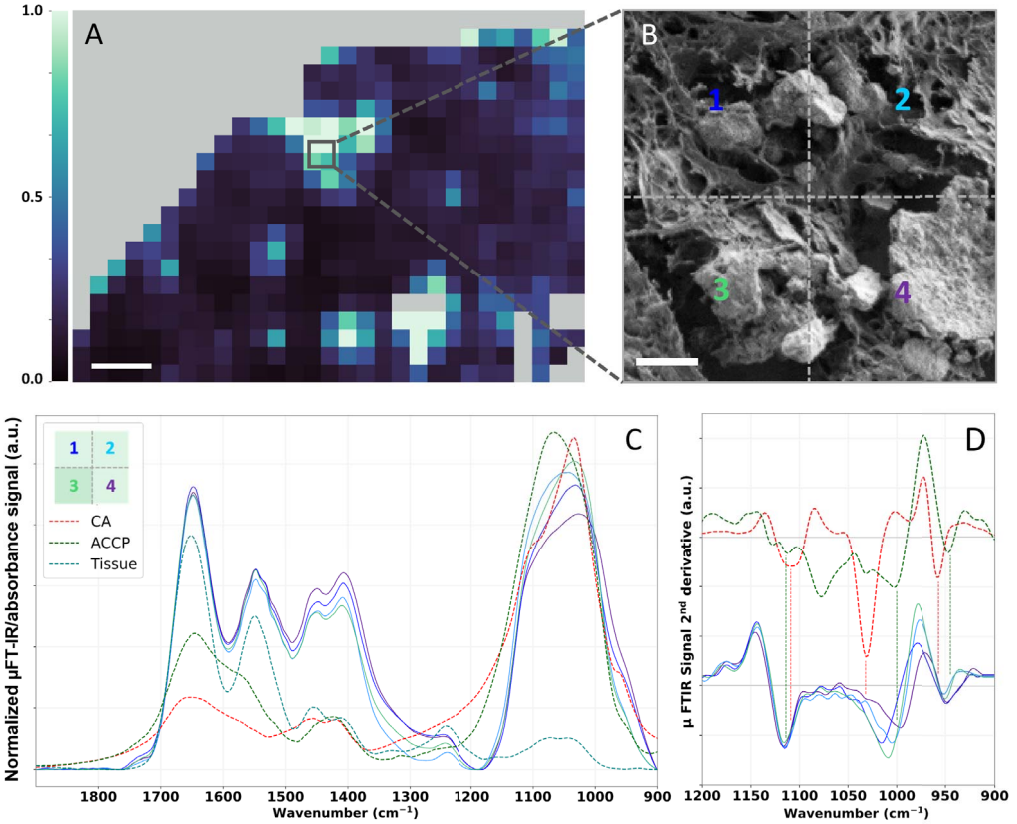

Figure 14. µFT-IR analyses of BMC in the 75-IDC patient. (A) Heatmap of the absorption intensity ratio: 1036 cm^{-1}/1655 cm^{-1} (as shown Figure 13C), 50 µm scale bar. (B) FE-SEM image of a small region of the biopsy presenting multiple BMCs with different sizes and shapes, 5 µm scale bar. (C) Associated normalized µFT-IR spectra recorded in this area and FT-IR reference spectra of CA (red curve) and ACCP (dark green curve). Positions, at which spectra were recorded, are indicated by the color-coded numeration (B and C). (D) Second derivatives spectra of reference CA and ACCP over the 1200–900 cm^{-1} spectral range. Second derivatives were calculated using Savitzky–Golay algorithm (order 2, 11 points). For better visualization, an offset was applied to CA and ACCP second derivatives spectra.

several BMCs can be observed: BMCs of different shapes and sizes, including BMCs of a few hundred nanometers only. Due to the spatial resolution of classical IR characterization system, the resulting signal is a superposition of both contribution of BMCs and the surrounding tissue. Hence, weak signal, originating from nanometric BMCs or BMCs with chemical properties in very little proportion may be missed. Therefore, due to the complexity of BMCs organization within the tissue µFT-IR fails to characterize BMCs individually, and nanometric calcifications can't be properly described by classical vibrational techniques. This might be overcome by the use of super-resolved IR techniques, also called IR nanospectroscopy techniques.

3.2.2. *IR nanospectroscopy to characterize BMCs at the nanoscale*

AFM-IR is an AFM based technique that provides IR analysis at nanometer scale. It combines the high spatial resolution of the AFM and the chemical identification capability of the IR spectroscopy [107]. This system assesses topographic images as well as chemical speciation through its nanometric tip apex. To that end, the sample surface is highlighted with a tunable IR laser which will produce—if

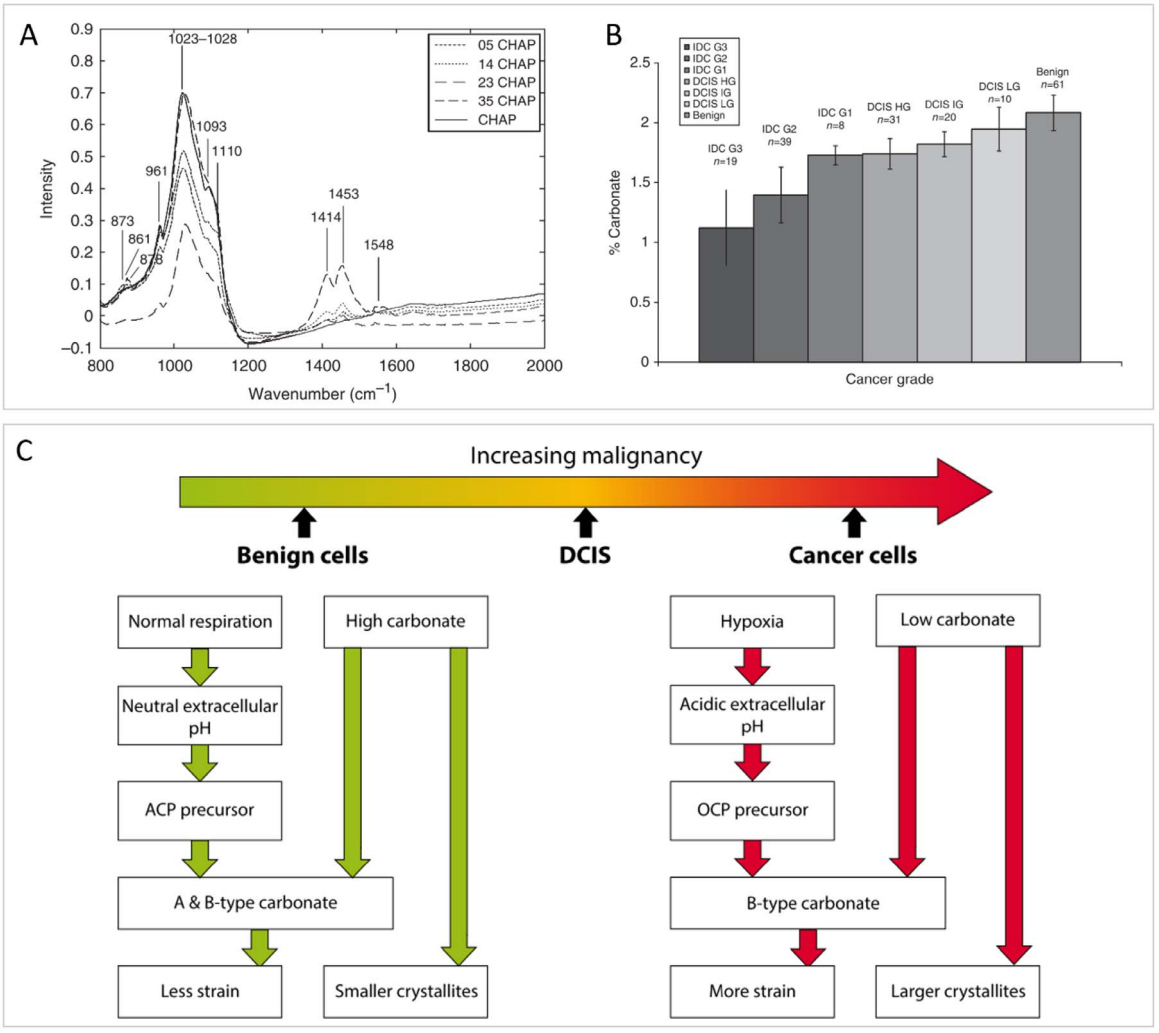

Figure 15. Investigation of the carbonated content of BMCs with breast pathology severity. (A) IR spectra of synthetic calcium phosphate hydroxyapatite (CHAP) with different proportion of carbonate substitution (0%, 0.5%, 1.4%, 2.3%, and 3.5%) use as calibration curves to quantify carbonate content in biological BMCs. (B) Mean carbonate content in calcifications from all invasive, in-situ, and benign breast tissue, quantified using (A). (A, B) from Baker *et al.* [33]. (C) Summary of the microenvironmental factors affecting the carbonate substitution in calcium phosphate hydroxyapatite in BMCs associated with benign, ductal carcinoma in-situ and invasive breast tissue cells. From Gosling *et al.* [35].

the sample absorbs at the laser's wavenumber—rapid picometer expansion [108] of the surface due to conversion of the absorbed light into heat (photothermal process [109]). This expansion is probed by the AFM tip in contact (contact mode) or intermittent-contact (tapping mode) with the surface: the energy collected is transferred to the cantilever that will oscillate on its eigenmode. The oscillation amplitude is directly proportional to the absorption of the sample, which enables direct comparison with conventional absorption IR spectra. Unlike μFT-IR, AFM-IR technique does not acquire systematically a spectral data cube, but can record local IR spectra by fixing the tip position and scanning the laser spectral range, or IR chemical maps by fixing the wavenumber of the laser and scanning

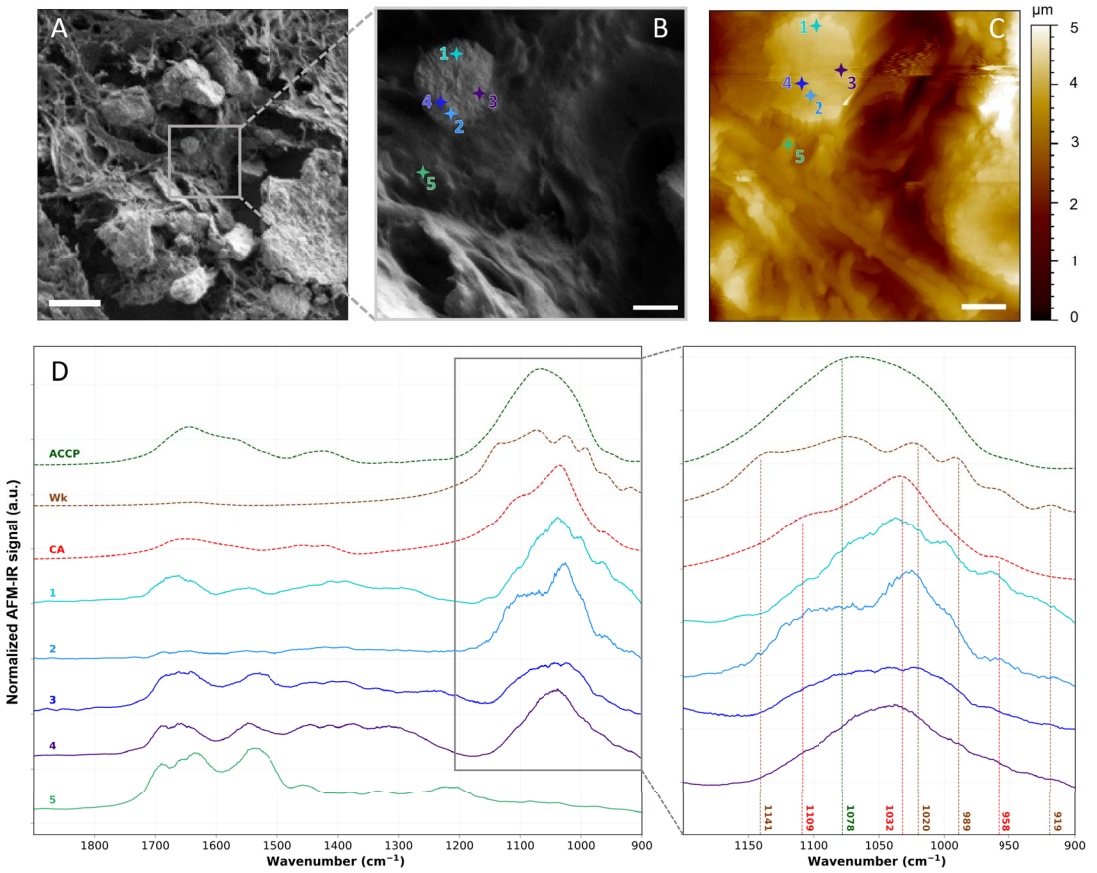

Figure 16. AFM-IR analyses of the 75-IDC patient. (A, B), FE-SEM images of the analyzed region. 5 μm and 1 μm scale bar respectively. (C) AFM topography of the same region shown in (B). 1 μm scale bar. (D) Local AFM-IR spectra measured at location indicated by the crosses on (B, C), and FT-IR reference spectra of CA, Wk, and ACCP (dashed lines). Baseline correction, Savitzky–Golay smoothing (order 1, 15 points) and vector normalization were applied to AFM-IR spectra presented in (D). AFM-IR measurements were performed using NanoIR2 from Bruker Nano coupled with a QCL laser covering the 1900–900 cm^{-1} spectral range. Imaging was performed in tapping mode and spectra were recorded in contact mode using gold coated cantilever (Budget Sensors, Multi75GB-G, 3 N/m) from 1900 to 900 cm^{-1} with a 1 cm^{-1} spectral resolution, at 335 kHz and with 160 ns laser pulse width.

the surface. The resulting chemical information has a lateral spatial resolution close to 20 nm, limited by the AFM tip radius [110–112]. AFM-IR is, therefore, a promising technique to precise BMCs topography and their composition at the nanoscale. However, since the IR source is a laser, AFM-IR spectral range (1900–900 cm^{-1}) is usually less extended than μFT-IR systems that possess globar sources with working range from 4000 cm^{-1} to 400 cm^{-1}.

Figure 16 compares AFM-IR analyses performed on the 75-IDC patient breast biopsy with reference FT-IR spectra. A calcification structure surrounded by tissue can be identified in the upper left corner of both the FE-SEM image and the AFM topography of the studied region (Figure 16B, C). The AFM topography represents the morphology of the surface in false color. The color scale outlines the height of the surface: zero being the deepest point probed on the surface and the light-yellow the highest point of the surface analyzed. Based on the AFM topography, this rounded-shape calcification has a diameter of about 2.5 μm, lower than the spatial resolution of μFT-IR.

Using AFM-IR four local spectra were acquired at different points on top of the BMC (spectra 1 to 4 in Figure 16D), and shape and sub-structure variations of the phosphate bands (1150 and 960 cm^{-1}—Figure 16D) can be observed. This band was not observed in the spectrum acquired within the tissue which only presents a strong protein signal at 1655 cm^{-1} (Amide I), 1535 cm^{-1} (Amide II), and 1260 cm^{-1} (Amide III) (spectrum 5 in Figure 16C). Spectrum 1 acquired near the upper edge of the BMC (Figure 16C) presents maxima of absorption at 1109 cm^{-1}, 1032 cm^{-1}, and 958 cm^{-1} characteristics of CA, as well as two shoulders at 1074 and 991 cm^{-1} also observed on reference Wk spectrum; while spectrum 2 measured on the opposite side of the BMC presents an absorption band that might be associated to CA. On the other hand, spectrum 3 and 4 present less structured absorption bands that might be explained by the coexistence of either Wk and ACCP or CA and ACCP, respectively. These results highlight a possible chemical and/or physico-chemical heterogeneity at the nanometric scale. Thus, we suppose that BMCs might not be composed of a single chemical phase but rather a mix of different chemical phases. Due to spatial resolution limitation, these heterogeneities would not be observed with μFT-IR analyses (Figure 14C), thus AFM-IR opens new opportunities for characterizing BMC at the nanometer scale, thus enabling to investigate early-stage BMCs formation during mineralization processes in the breast.

In a recent study, Bouzy *et al.* [113] proposed monitoring by Raman microspectroscopy the early stages of the mineralization processes in breast cancer cell lines. They investigated two different pathways of cell mineralization to demonstrate that cells' microenvironments affect the mineralization, as well as BMC physicochemical features. They evaluated the cellular proliferation and adhesion to the surface (i.e. cancer progression) as well as the location of mineral deposits within the cell culture but they did not observe significant chemical changes in the extracellular matrix, i.e. the collagen. In their conclusion, they pointed out that Raman microscopy lacks resolution to be really precise about the location of the deposits and probably to investigate subtle chemical changes within the extracellular matrix.

Using AFM-IR, these changes could be monitored throughout the mineralization maturation and help decipher the link between BMC and breast pathologies.

Our study is the first step to reach a better understanding of the mineralization process at the nanometer scale. One of the next steps could be to perform in parallel with studies done on biopsies, an *in-vitro* study using a model cancer cell line like the one proposed by Bouzy *et al.*

4. Conclusion and perspectives

Compared to other pathologies, breast cancer, in routine diagnosis and preventive procedure, mostly relies on classical medical examination like mammography as well as anatomopathological analysis. Unfortunately, it doesn't really benefit from the advances of more specific techniques like electron microscopy or vibrational spectroscopy commonly used in medical research or for the diagnosis of pathological calcifications, even though, breast medical examination is partially based on the spatial repartition and morphological aspects of microcalcifications. The goal of our study was to evaluate the relevance of FE-SEM, μFT-IR, advanced IR super-resolution technique, such as AFM-IR, to study BMCs in breast biopsy and to propose a multiscale approach, in order to investigate the link between microcalcifications and malignancy.

As a result, FE-SEM confirmed its efficiency to provide accurate morphological diagnosis of BMCs. Four different types of BMCs can be easily distinguished thanks to their typical 3D shape: bipyramidal or dodecahedral for COD (recognized as BMCs of type I), spherical for CA (recognized as BMCs of type II), pseudo cubical for Wk and amorphous mineral for ACCP. COD seems to be linked to benign lesions whereas CA and Wk might be related to malignant lesions. As an example, tissue section from a 75-years old woman suffering with an infiltrating low-grade ductal carcinoma was explored and exhibited BMCs with a characteristic spherical shape of CA. Then a question was raised: were we able to measure the exact chemical composition of such BMCs and its micro-environment? To go deeper into the chemical characterization of tissue section, we proposed to use μFT-IR as it is a widely used, non-destructive and label-free technique, and which is routinely used in hospitals in cases of kidney stones. Like FE-SEM analysis, it is possible to

perform IR measurements on tissue sections obtained from embedded paraffin biopsy without any further treatment, except the removal of paraffin just after micro-sectioning. It provides information on the chemical bonds present within a sample by probing molecular vibrations. It might precisely describe the environment and even the crystallinity of a probed species. In the case of BMCs, each type presents a specific IR absorption signature, which is easily recognizable. Their IR absorption spectra present some similarities: an intense absorption band in the 1100–950 cm^{-1} spectral range mainly associated to phosphate groups (PO_3^{4-}). But the number of phosphate absorption bands depends on the symmetry of phosphate ions within the crystalline structure. As a consequence, the shape, the width, the position of the maximum absorption and the number of shoulders differ from one type of BMCs to another. For example, on Wk FT-IR absorption spectrum, several shoulders in the phosphate region are present compared to CA or ACCP spectrum. The tissue IR response exhibits intense absorption bands at 1650 cm^{-1}, 1550 cm^{-1} and a weaker band at 1260 cm^{-1}, characteristic of the peptide bond vibration band of proteins. Surprisingly, the μFT-IR study of 75-IDC patient BMCs revealed the presence of micrometer heterogeneities not visible on FE-SEM clichés. The IR spectra of different regions of interest presented the characteristic absorption bands of carbonate and phosphate but without the shape nor width of the absorption band of pure CA or ACCP compounds. This suggested that BMCs in this sample might be a mixture of CA and ACCP. Moreover, by looking at the other absorption bands, we can even evaluate if the BMCs are linked to other tissue compounds and even their interaction with the extracellular matrix. The main drawback of this technique is its poor lateral resolution, dependent of the wavelength and thus ranging from around 2.5 μm in the 4000 cm^{-1} region to at least 25 μm in the 400 cm^{-1} region. To overcome this optical limitation of μFT-IR and assess if those heterogeneities are still present at a nanometer scale, the exact same region of interest of the 75-IDC patient section was explored using a IR super-resolution technique called AFM-IR. AFM-IR is widely used in material sciences and microbiology [112,114–116], and applications for the characterization of tissue deposits and organic minerals have been growing in recent years [117,118]. Nonetheless, complex biological samples characterization, such as breast biopsies, using AFM-IR remain challenging because of, among others, the tissue deposits thickness and important height variation of the sample surface due to the presence of BMC. However, the very local IR spectra acquired on our BMCs of interest confirmed the spatial heterogeneity of those objects and revealed a more complex structure than excepted. Based on these preliminary results, AFM-IR has the potential to decipher the fine chemical composition of breast calcifications with very high resolution (nanometer), improving our understanding of the chemical changes that occur during the biomineralization process in breast, and the entailment of BMCs with the pathology.

Moreover, it will be of great interest to go beyond chemical speciation and investigate further the microenvironment of BMCs through trace elements analysis to obtain a more complete picture of the entanglement between pathology, presence of microcalcification and immune response of the body. Indeed, trace elements are essential for the equilibrium of cell metabolism by taking part, among other, to the activation/inhibition of enzymes [119]. In addition, to being essential to the regulation of the cellular activity, trace elements have been highlighted to play a role with carcinogenesis [120–122]. Physiological elementary composition changes may dysregulate cell activities, resulting in immunological breakdown [123] and accelerate tumor growth [124]. Several studies have already reported and highlighted that trace elements are tightly linked with breast cancer and cancer in general. For example, using in-vitro neutron activation analysis (NAA), Ng *et al.* [125] showed that many trace elements were significantly higher in cancerous breast tissues compared to the adjacent normal tissues (e.g., within the same sample), this includes: Al, Br, Ca, Cl, Co, Cs, Fe, K, Mn, Na, Rb, and Zn. Especially, as Zn is involved, among other, in carcinogenesis processes and tumor growth [126–128], some studies have investigated the relationship between Zn and cancer, showing the dysregulation of Zn seems to be organ dependent [129,130]. In this context, some of them highlight an increase of Zn content in breast cancerous tissues compared to healthy breast tissue [131,132]. But, the correlation between Zn concentration, the cancer malignancy

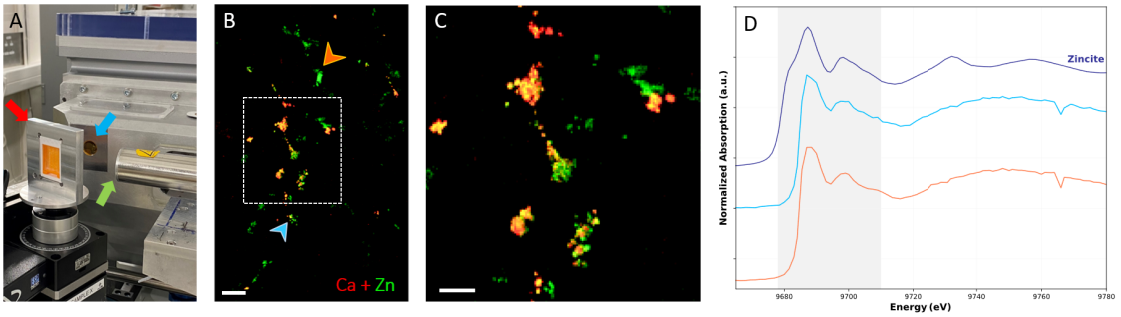

Figure 17. X-ray spectroscopy analyses on paraffin-embedded breast resection using synchrotron radiation. (A) DiffAbs beamline setup at Soleil Synchrotron (Saint-Aubin, France). The arrows indicate: the sample older (red arrow), the beam output (blue arrow) and the detector (green arrow). (B) Composite images of XRF maps of Zn (in green) and Ca (in red); 500 μm scale bar. (C) Zoom of the overlay XRF maps (white rectangle on B composite image) showing partial Ca and Zn colocalization; 200 μm scale bar, and (D) XAS spectra at position indicated by the color-coded arrows on (B). The spectral region highlighted in grey corresponds to the spectral region where differences are observed between experimental spectra. Blue spectra measured at a position with both Ca and Zn signal while the orange spectrum was acquired at a position with only Zn XRF signal. The dark blue spectrum is the Zincite (ZnO): reference spectrum of tetra-coordinated Zn.

and the presence of microcalcification, is poorly documented. To explore this relation, one can propose to use X-ray fluorescence (XRF) and X-ray absorption spectroscopy (XAS). Those techniques can determine the distribution of Zn within the tissue depending on the pathology and the presence/absence of BMC. Compared to other trace element characterization techniques, XRF presents the advantage to be compatible with classical fixed tissue section or paraffin embedded biopsies [133,134] (Figure 17). As a consequence, no additional preparation than those already performed for biopsies analyses and storage in hospital anatomopathological departments, is required.

Furthermore, XRF has proven to be clinically relevant, providing trace elements analyses without heavy complex and time-consuming protocol. In particular, using synchrotron radiation trace elements can be detected and described, in biological samples, at the micrometer scale, thanks to the high brightness of synchrotron radiation compared to XRF lab benchtop setup [135]. Therefore, Ca (mainly link to BMC) and Zn XRF maps (distribution within the tissue resection) of the breast biopsy can be obtained to study the presence/absence of Zn with the presence/absence of BMCs (e.g., Ca). Figure 17B and C, present XRF maps acquired on a patient diagnosed with in infiltrating ductal carcinoma. Ca and Zn distribution in the region of the resection are very localized and a partial colocalization of Ca and Zn can be observed (Figure 17C), suggesting Zn with different physical–chemical environment and thus biological role. To confirm that hypothesis, Zn can be further analyzed through Zn K-edge X-ray absorption near edge structure (XANES) spectroscopy to identify Zn electronic and coordination state (Figure 17D). This kind of spectroscopical analysis has already been reported on calcifications [100,133,134]. X-ray fluorescence and X-ray spectroscopy are promising techniques to highlight the role of Zn in breast cancer and obtain a better description of the BMC micro-environment. Moreover, this technique allows to follow other trace elements like Mg. As a study suggested that the percentage of Mg, associated with Wk BMC, increases with the cancer malignancy, it could be interesting to precise this kind of hypothesis and investigate by XRF and XANES measurements the possible correlation between Mg and cancer severity. In the future, we propose to perform a systematic multiscale analysis of BMCs, using electron, vibrational and X-ray spectroscopy techniques on benign, non-invasive, and invasive breast samples. It would provide better insight into the relationship between Zn and BMC,

as well as the local environment modifications that occur in malignant cancer. We hope that in the future, women will benefit from a better physico-chemical characterization of their BMCs for lesion diagnosis purposes.

Conflicts of interest

Authors have no conflict of interest to declare.

Acknowledgments

The authors acknowledge the Synchrotron SOLEIL for provision of synchrotron radiation facilities and XRF-XANES equipment. The authors also acknowledge the department of pathological anatomy and cytology of René Dubos Hospital, and in particular L. Moumi and L. Durupt for the sample preparation.

Author contributions

Margaux Petay performed infrared microspectroscopy, XRF-XANES, SEM and AFM-IR measurements, implemented data treatment, prepared figures and wrote the manuscript.

Maguy Cherfan provided human sample, their anatomopathological study, designed the research and corrected the manuscript.

Elise Bouderlique corrected the manuscript.

Solenn Reguer performed XRF and XANES measurements.

Jérémie Mathurin corrected the manuscript.

Alexandre Dazzi corrected the manuscript.

Maëva l'Heronde performed part of SEM measurements.

Michel Daudon performed FT-IR study, initiated the study, participated in the study design.

Emmanuel Letavernier initiated the study, participated in the study design and corrected the manuscript.

Ariane Deniset-Besseau participated in the study design, participated in the writing and in the correction of the manuscript.

Dominique Bazin performed SEM measurements, initiated the study, participated in the study design, prepared figures and participated in the writing of the manuscript.

References

[1] T. F. Lüscher, *Eur. Heart J.*, 2018, **39**, 489-492.
[2] L. A. Torre, R. L. Siegel, E. M. Ward, A. Jemal, *Cancer Epidemiol. Biomarkers Prev.*, 2016, **25**, 16-27.
[3] T. J. Key, P. K. Verkasalo, E. Banks, *Lancet Oncol.*, 2001, **2**, 133-140.
[4] G. O. Abdulrahman, G. A. Rahman, *J. Cancer Epidemiol.*, 2012, **2012**, article no. 915610.
[5] Z. Q. Tao, A. Shi, C. Lu, T. Song, Z. Zhang, J. Zhao, *Cell Biochem. Biophys.*, 2015, **72**, 333-338.
[6] A. Balekouzou, P. Yin, C. M. Pamatika, G. Bishwajit, S. W. Nambei, M. Djeintote, B. E. Ouansaba, C. Shu, M. Yin, Z. Fu, T. Qing, M. Yan, Y. Chen, H. Li, Z. Xu, B. Koffi, *BMC Public Health*, 2016, **16**, 1-10.
[7] Z. Momenimovahed, H. Salehiniya, *Breast Cancer (London)*, 2019, **11**, 151-164.
[8] H. Sung, J. Ferlay, R. L. Siegel, M. Laversanne, I. Soerjomataram, A. Jemal, F. Bray, *Cancer J. Clin.*, 2021, **71**, 209-249.
[9] M. Eriksson, K. Czene, Y. Pawitan, K. Leifland, H. Darabi, P. Hall, *Breast Cancer Res.*, 2017, **19**, 1-8.
[10] Breast Screening Programme, England - 2014–15 - NHS Digital, (n.d.)., https://digital.nhs.uk/data-and-information/publications/statistical/breast-screening-programme/breast-screening-programme-england-2014-15.
[11] S. Hofvind, B. F. Iversen, L. Eriksen, B. M. Styr, K. Kjellevold, K. D. Kurz, *Acta Radiol.*, 2011, **52**, 481-487.
[12] P. Henrot, A. Leroux, C. Barlier, P. Génin, *Diagn. Interv. Imaging*, 2014, **95**, 141-152.
[13] M. Gülsün, F. B. Demirkazik, M. Ariyürek, *Eur. J. Radiol.*, 2003, **47**, 227-231.
[14] L. Frappart, I. Remy, H. C. Lin, A. Bremond, D. Raudrant, B. Grousson, J. L. Vauzelle, *Virchows Arch. A. Pathol. Anat. Histopathol.*, 1986, **410**, 179-187.
[15] C. Sterling, *Science*, 1964, **146**, 518-519.
[16] C. Sterling, *Acta Crystallogr.*, 1965, **18**, 917-921, Urn:Issn:0365-110X.
[17] W. Drexler, Y. Chen, A. D. Aguirre, B. Považay, A. Unterhuber, J. G. Fujimoto, "Ultrahigh resolution optical coherence tomography", in *Optical Coherence Tomography: Technology and Applications*, Springer, Cham, 2nd ed., 2015, 277-318.
[18] A. R. Izatulina, V. Y. Yelnikov, "Structure, chemistry and crystallization conditions of calcium oxalates — The Main components of kidney stones", in *Minerals as Advanced Materials I*, Springer, Berlin, Heidelberg, 2008, 231-239.
[19] C. Conti, L. Brambilla, C. Colombo, D. Dellasega, G. D. Gatta, M. Realini, G. Zerbi, *Phys. Chem. Chem. Phys.*, 2010, **12**, 14560-14566.
[20] V. Tazzoli, C. Domeneghetti, *Am. Mineral.*, 1980, **65**, 327-334.
[21] S. Naray-Szabi, *Z. Kristallogr. Cryst. Mater.*, 1930, **75**, 387-398.
[22] J. C. Elliott, *Phosphates Geochem. Geobiol. Mater. Importance.*, 2019, **48**, 427-454.
[23] J. C. Elliot, *Structure and Chemistry of the Apatites and Other Calcium Orthophosphates*, Elsevier, Amsterdam, 1994, 63-230 pages.
[24] C. Combes, C. Rey, *Biomaterials*, 2002, **23**, 2817-2823.
[25] T. J. White, D. ZhiLi, *Acta Crystallogr.*, 2003, **59**, 1-16, Urn:Issn:0108-7681.
[26] C. Drouet, *BioMed Res. Int.*, 2013, **2013**, 1-12.

[27] S. Cazalbou, D. Eichert, C. Drouet, C. Combes, C. Rey, *C. R. Palevol.*, 2004, **3**, 563-572.
[28] L. Wang, G. H. Nancollas, *Chem. Rev.*, 2008, **108**, 4628-4669.
[29] S. O'Grady, M. P. Morgan, *Biochim. Biophys. Acta - Rev. Cancer.*, 2018, **1869**, 310-320.
[30] M. S. Soo, E. L. Rosen, J. Q. Xia, S. Ghate, J. A. Baker, *Am. J. Roentgenol.*, 2005, **184**, 887-892.
[31] J. A. M. R. Kunitake, S. Choi, K. X. Nguyen, M. M. Lee, F. He, D. Sudilovsky, P. G. Morris, M. S. Jochelson, C. A. Hudis, D. A. Muller, P. Fratzl, C. Fischbach, A. Masic, L. A. Estroff, *J. Struct. Biol.*, 2018, **202**, 25-34.
[32] R. Vanna, C. Morasso, B. Marcinno, F. Piccotti, E. Torti, D. Altamura, S. Albasini, M. Agozzino, L. Villani, L. Sorrentino, O. Bunk, F. Leporati, C. Giannini, F. Corsi, *Cancer Res.*, 2020, **80**, 1762-1772.
[33] R. Baker, K. D. Rogers, N. Shepherd, N. Stone, *Br. J. Cancer.*, 2010, **103**, 1034-1039.
[34] R. Scott, C. Kendall, N. Stone, K. Rogers, *Sci. Rep.*, 2017, **7**, 1-9.
[35] S. Gosling, R. Scott, C. Greenwood, P. Bouzy, J. Nallala, I. D. Lyburn, N. Stone, K. Rogers, *J. Mammary Gland Biol. Neoplasia*, 2019, **24**, 333-342.
[36] E. D. Pisano, M. J. Yaffe, *Radiology*, 2005, **234**, 353-362.
[37] N. Karssemeijer, J. T. M. Frieling, J. H. C. L. Hendriks, *Invest. Radiol.*, 1993, **28**, 413-419.
[38] J. M. Johnson, R. R. Dalton, S. M. Wester, J. Landercasper, P. J. Lambert, *Arch. Surg.*, 1999, **134**, 712-716.
[39] R. Leborgne, *Am. J. Roentgenol Radium Ther.*, 1951, **65**, 1-11, https://pubmed.ncbi.nlm.nih.gov/14799661/.
[40] S. Ciatto, S. Bianchi, S. Vezzosi, *Eur. Radiol.*, 1994, **4**, 23-26.
[41] B. S. Monsees, *Radiol. Clin. North Am.*, 1995, **33**, 1109-1121, https://pubmed.ncbi.nlm.nih.gov/7480659/.
[42] M. P. Morgan, M. M. Cooke, G. M. McCarthy, *J. Mammary Gland Biol. Neoplasia*, 2005, **10**, 181-187.
[43] Y. V. Nalawade, *Indian J. Radiol. Imaging*, 2009, **19**, 282-286.
[44] R. Nishimura, N. Taira, S. Sugata, D. Takabatake, S. Ohsumi, S. Takashima, *Breast Cancer*, 2010, **18**, 33-36.
[45] P. Tabrizian, M. Moezzi, T. S. Menes, *Breast Cancer*, 2010, **18**, 314-318.
[46] M. Rominger, C. Wisgickl, N. Timmesfeld, *Rofo*, 2012, **184**, 1144-1152.
[47] S. Y. Kim, H. Y. Kim, E. K. Kim, M. J. Kim, H. J. Moon, J. H. Yoon, *Ann. Surg. Oncol.*, 2015, **22**, 2895-2901.
[48] C. M. Kuzmiak, R. Dancel, E. Pisano, D. Zeng, E. Cole, M. A. Koomen, R. McLelland, *Acad. Radiol.*, 2006, **13**, 621-629.
[49] C. J. D'Orsi, E. A. Sickles, E. B. Mendelson, E. A. Morris, *ACR BI-RADS ATLAS*, 5th ed., American College of Radiology, Reston, VA, 2013.
[50] E. S. Burnside, J. E. Ochsner, K. J. Fowler, J. P. Fine, L. R. Salkowski, D. L. Rubin, G. A. Sisney, *Radiology*, 2007, **242**, 388-395.
[51] P. L. Arancibia Hernández, T. Taub Estrada, A. López Pizarro, M. L. Díaz Cisternas, C. Sáez Tapia, *Rev. Chil. Radiol.*, 2016, **22**, 80-91.
[52] A. A. Rao, J. Feneis, C. Lalonde, H. Ojeda-Fournier, *Radiographics*, 2016, **36**, 623-639.
[53] R. Rashmi, K. Prasad, C. B. K. Udupa, *J. Med. Syst.*, 2022, **46**, article no. 7.
[54] *Breast Biopsy*, Johns Hopkins Medicine, (n.d.), https://www.hopkinsmedicine.org/health/treatment-tests-and-therapies/breast-biopsy.
[55] A. H. Fischer, K. A. Jacobson, J. Rose, R. Zeller, *Cold Spring Harb. Protoc.*, 2008, **3**, 4986-4988.
[56] World Health Organization, International Agency for Research on Cancer, *Breast Tumours*, 5th ed., IARC, France, 2019.
[57] C. I. Li, D. J. Uribe, J. R. Daling, *Br. J. Cancer*, 2005, **93**, 1046-1052.
[58] J. Kollias, C. W. Elston, I. O. Ellis, J. F. R. Robertson, R. W. Blamey, *Br. J. Cancer*, 1997, **75**, 1318-1323.
[59] K. de Haan, Z. S. Ballard, Y. Rivenson, Y. Wu, A. Ozcan, *Sci. Rep.*, 2019, **9**, 1-7.
[60] A. E. Vladár, M. T. Postek, B. Ming, *Micros. Today*, 2009, **17**, 6-13.
[61] D. C. Joy, "The aberration-corrected SEM", in *Biological Low-Voltage Scanning Electron Microscopy*, Springer, Cham, 2008, 107-127.
[62] D. Bazin, E. Bouderlique, M. Daudon, V. Frochot, J. P. Haymann, E. Letavernier, F. Tielens, R. Weil, *C. R. Chim.*, 2022, **25**, no. S1, 37-60.
[63] J. Goldstein, D. E. Newbury, P. Echlin, D. C. Joy, A. D. Romig Jr, C. E. Lyman, C. Fiori, E. Lifshin, *Scanning Electron Microscopy and X-Ray Microanalysis*, 2nd ed., Springer, Boston, MA, 1992.
[64] D. Bazin, R. J. Papoular, E. Elkaim, R. Weil, D. Thiaudière, C. Pisapia, B. Ménez, N. S. Hwang, F. Tielens, M. Livrozet, E. Bouderlique, J. P. Haymann, E. Letavernier, L. Hennet, V. Frochot, M. Daudon, *C. R. Chim.*, 2022, **25**, no. S1, 343-354.
[65] S. Catherine, *Am. Mineral.*, 1998, **83**, 1122-1126.
[66] J. Cros, D. Bazin, A. Kellum, V. Rebours, M. Daudon, *C. R. Chim.*, 2016, **19**, 1642-1655.
[67] H. Schatten, J. Pawley (eds.), *Biological Low-Voltage Scanning Electron Microscopy*, Springer, Cham, 2008, https://link.springer.com/book/10.1007/978-0-387-72972-5.
[68] A. Ben Lakhdar, M. Daudon, M. C. Mathieu, A. Kellum, C. Balleyguier, D. Bazin, *C. R. Chim.*, 2016, **19**, 1610-1624.
[69] S. Gosling, D. Calabrese, J. Nallala, C. Greenwood, S. Pinder, L. King, J. Marks, D. Pinto, T. Lynch, I. D. Lyburn, E. S. Hwang, K. Rogers, N. Stone, *Analyst*, 2022, **147**, 1641-1654.
[70] M. Mathonnet, A. Dessombz, D. Bazin, R. Weil, T. Frédéric, M. Pusztaszeri, M. Daudon, *C. R. Chim.*, 2016, **19**, 1672-1678.
[71] J. Guerlain, S. Perie, M. Lefevre, J. Perez, S. Vandermeersch, C. Jouanneau, L. Huguet, V. Frochot, E. Letavernier, R. Weil, S. Rouziere, D. Bazin, M. Daudon, J. P. Haymann, *PLoS One*, 2019, **14**, article no. e0224138.
[72] M. Daudon, C. A. Bader, P. Jungers, W. G. Robertson, H. G. Tiselius, B. Hess, J. R. Asplin, *Scanning Microsc.*, 1993, **7**, 1081-1106.
[73] M. Daudon, *Arch. Pédiatrie*, 2000, **7**, 855-865.
[74] M. Daudon, P. Jungers, D. Bazin, *AIP Conf. Proc.*, 2008, **1049**, 199-215.
[75] A. Dessombz, P. Méria, D. Bazin, M. Daudon, *PLoS One*, 2012, **7**, 1-5.
[76] A. Dessombz, P. Méria, D. Bazin, E. Foy, S. Rouzière, R. Weil, M. Daudon, *Prog. Urol.*, 2011, **21**, 940-945.
[77] L. Frappart, M. Boudeulle, J. Boumendil, H. C. Lin, I. Martinon, C. Palayer, Y. Mallet-Guy, D. Raudrant, A. Bremond, Y. Rochet, J. Feroldi, *Hum. Pathol.*, 1984, **15**, 880-889.

[78] M. Daudon, V. Frochot, D. Bazin, P. Jungers, *C. R. Chim.*, 2016, **19**, 1514-1526.
[79] I. Petit, G. D. Belletti, T. Debroise, M. J. Llansola-Portoles, I. T. Lucas, C. Leroy, C. Bonhomme, L. Bonhomme-Coury, D. Bazin, M. Daudon, E. Letavernier, J. P. Haymann, V. Frochot, F. Babonneau, P. Quaino, F. Tielens, *ChemistrySelect.*, 2018, **3**, 8801-8812.
[80] D. Bazin, C. Leroy, F. Tielens, C. Bonhomme, L. Bonhomme-Coury, F. Damay, D. Le Denmat, J. Sadoine, J. Rode, V. Frochot, E. Letavernier, J. P. Haymann, M. Daudon, *C. R. Chim.*, 2016, **19**, 1492-1503.
[81] J. A. Terzakis, *Ultrastruct. Pathol.*, 2009, **22**, 181-184.
[82] R. Z. LeGeros, *Monogr. Oral Sci.*, 1991, **15**, 1-201.
[83] M. E. Fleet, X. Liu, *Biomaterials*, 2007, **28**, 916-926.
[84] A. Cariati, *Clin. Res. Hepatol. Gastroenterol.*, 2013, **37**, e69-e72.
[85] J. D. Reid, M. E. Andersen, *Atherosclerosis*, 1993, **101**, 213-224.
[86] C. A. Scotchford, S. Y. Ali, *Ann. Rheum. Dis.*, 1995, **54**, 339-344.
[87] L. S. Burstein, A. L. Boskey, P. J. Tannenbaum, A. S. Posner, I. D. Mandel, *J. Oral Pathol.*, 1979, **8**, 284-291.
[88] L. Maurice-Estepa, P. Levillain, B. Lacour, M. Daudon, *J. Urol. Nephrol.*, 1999, **33**, 299-305.
[89] R. Scott, N. Stone, C. Kendall, K. Geraki, K. Rogers, *NPJ Breast Cancer*, 2016, **2**, 1-6.
[90] M. Scimeca, S. Bischetti, H. K. Lamsira, R. Bonfiglio, E. Bonanno, *Eur. J. Histochem.*, 2018, **62**, 89-99.
[91] T. Kodaka, R. Mori, T. Sano, K. Debari, *J. Electron Microsc. (Tokyo)*, 1995, **44**, 289-294.
[92] L. Louvet, D. Bazin, J. Büchel, S. Steppan, J. Passlick-Deetjen, Z. A. Massy, *PLoS One*, 2015, **10**, 1-17.
[93] M. Daudon, D. Bazin, *C. R. Chim.*, 2016, **19**, 1416-1423.
[94] M. E. Fleet, *Biomaterials*, 2009, **30**, 1473-1481.
[95] R. Gopal, C. Calvo, J. Ito, W. K. Sabine, *Can. J. Chem.*, 1974, **52**, 1155-1164.
[96] W. Jastrzbski, M. Sitarz, M. Rokita, K. Bułat, *Spectrochim. Acta - A Mol. Biomol. Spectrosc.*, 2011, **79**, 722-727.
[97] G. Socrates, *Infrared and Raman Characteristic Group Frequencies. Tables and Charts*, John Wiley & Sons, Hoboken, NJ, 2001 (accessed 10 March 2022), 347 pages.
[98] I. T. Lucas, D. Bazin, M. Daudon, *C. R. Chim.*, 2022, **25**, no. S1, 83-103.
[99] N. Quy Daon, M. Daudon, *Infrared and Raman Spectra of Calculi*, Elsevier, Amsterdam, 1997.
[100] X. Carpentier, D. Bazin, P. Jungers, S. Reguer, D. Thiaudire, M. Daudon, *J. Synchrotron Radiat.*, 2010, **17**, 374-379.
[101] M. Scimeca, E. Giannini, C. Antonacci, C. A. Pistolese, L. G. Spagnoli, E. Bonanno, *BMC Cancer*, 2014, **14**, 1-10.
[102] E. Tsolaki, S. Bertazzo, *Materials*, 2019, **12**, article no. 3126.
[103] M. Hermes, R. B. Morrish, L. Huot, L. Meng, S. Junaid, J. Tomko, G. R. Lloyd, W. T. Masselink, P. Tidemand-Lichtenberg, C. Pedersen, F. Palombo, N. Stone, *J. Opt.*, 2018, **20**, article no. 023002.
[104] Z. Movasaghi, S. Rehman, I. U. Rehman, *Appl. Spectrosc. Rev.*, 2008, **43**, 134-179.
[105] A. S. Haka, K. E. Shafer-Peltier, M. Fitzmaurice, J. Crowe, R. R. Dasari, M. S. Feld, *Cancer Res.*, 2002, **62**, 5375-5380.
[106] P. Lasch, D. Naumann, *Biochim. Biophys. Acta - Biomembr.*, 2006, **1758**, 814-829.
[107] A. Dazzi, C. B. Prater, Q. Hu, D. B. Chase, J. F. Rabolt, C. Marcott, *Appl. Spectrosc.*, 2012, **66**, 1365-1384.
[108] J. Chae, S. An, G. Ramer, V. Stavila, G. Holland, Y. Yoon, A. A. Talin, M. Allendorf, V. A. Aksyuk, A. Centrone, *Nano Lett.*, 2017, **17**, 5587-5594.
[109] J. Sell, *Photothermal Investigations of Solids and Fluids*, 1st ed., Elsevier, Amsterdam, 1989.
[110] A. Dazzi, F. Glotin, J. M. Ortega, R. Prazeres, *Opt. Lett.*, 2005, **30**, 2388-2390.
[111] A. Dazzi, C. B. Prater, *Chem. Rev.*, 2017, **117**, 5146-5173.
[112] J. Mathurin, A. Deniset-Besseau, D. Bazin, E. Dartois, M. Wagner, A. Dazzi, *J. Appl. Phys.*, 2022, **131**, article no. 010901.
[113] P. Bouzy, S. O'Grady, H. Madupalli, M. Tecklenburg, K. Rogers, F. Palombo, M. P. Morgan, N. Stone, *Lab. Invest.*, 2021, **101**, 1267-1280.
[114] A. Dazzi, J. Saunier, K. Kjoller, N. Yagoubi, *Int. J. Pharm.*, 2015, **484**, 109-114.
[115] C. Mayet, A. Dazzi, R. Prazeres, J. M. Ortega, D. Jaillard, *Analyst*, 2010, **135**, 2540-2545.
[116] K. Kochan, D. Perez-Guaita, J. Pissang, J. H. Jiang, A. Y. Peleg, D. McNaughton, P. Heraud, B. R. Wood, *J. R. Soc. Interface*, 2018, **15**, article no. 20180115.
[117] E. Esteve, Y. Luque, J. Waeytens, D. Bazin, L. Mesnard, C. Jouanneau, P. Ronco, A. Dazzi, M. Daudon, A. Deniset-Besseau, *Anal. Chem.*, 2020, **92**, 7388-7392.
[118] D. Bazin, M. Rabant, J. Mathurin, M. Petay, A. Deniset-Besseau, A. Dazzi, Y. Su, E. P. Hessou, F. Tielens, F. Borondics, M. Livrozet, E. Bouderlique, J.-P. Haymann, E. Letavernier, V. Frochot, M. Daudon, *C. R. Chim.*, 2022, **25**, no. S1, 489-502.
[119] B. L. Vallee, *Sci. Mon.*, 1957, **72**, 368-376.
[120] K. Schwartz, *Cancer Res.*, 1975, **35**, 3481-3487.
[121] S. J. Mulware, *J. Biophys.*, 2013, **2013**, article no. 192026.
[122] S. J. Mulware, *3 Biotech.*, 2012, **3**, 85-96.
[123] A. N. Garg, V. Singh, R. G. Weginwar, V. N. Sagdeo, *Biol. Trace Elem. Res.*, 1994, **46**, 185-202.
[124] A. N. Garg, R. G. Weginwar, V. Sagdeo, *Biol. Trace Elem. Res.*, 1990, **26–27**, 485-496.
[125] K. H. Ng, D. A. Bradley, L. M. Looi, *Br. J. Radiol.*, 1997, **70**, 375-382.
[126] R. B. Franklin, L. C. Costello, *J. Cell. Biochem.*, 2009, **106**, 750-757.
[127] A. S. Prasad, F. W. J. Beck, L. Endre, W. Handschu, M. Kukuruga, G. Kumar, *J. Lab. Clin. Med.*, 1996, **128**, 51-60.
[128] B. J. Grattan, H. C. Freake, *Nutrients*, 2012, **4**, 648-675.
[129] P. Rusch, A. V. Hirner, O. Schmitz, R. Kimmig, O. Hoffmann, M. Diel, *Arch. Gynecol. Obstet.*, 2021, **303**, 195-205.
[130] E. J. Margalioth, J. G. Schenker, M. Chevion, *Cancer*, 1983, **52**, 868-872.
[131] S. Alam, S. L. Kelleher, *Nutrients*, 2012, **4**, 875-903.
[132] M. P. Silva, A. Tomal, C. A. Pérez, A. Ribeiro-Silva, M. E. Poletti, *X-Ray Spectrom.*, 2009, **38**, 103-111.
[133] D. Bazin, S. Reguer, D. Vantelon, J. P. Haymann, E. Letavernier, V. Frochot, M. Daudon, E. Esteve, H. Colboc, *C. R. Chim.*, 2022, **25**, no. S1, 189-208.
[134] A. Dessombz, C. Nguyen, H. K. Ea, S. Rouzière, E. Foy, D. Hannouche, S. Réguer, F. E. Picca, D. Thiaudière, F. Lioté,

M. Daudon, D. Bazin, *J. Trace Elem. Med. Biol.*, 2013, **27**, 326-333.

[135] M. R. Gherase, D. E. B. Fleming, *Crystals*, 2020, **10**, article no. 12.

Comptes Rendus
Chimie
2022, Vol. 25, Special Issue S1, p. 577-595
https://doi.org/10.5802/crchim.125

Microcrystalline pathologies: Clinical issues and nanochemistry / *Pathologies microcristallines : questions cliniques et nanochimie*

From visible light to X-ray microscopy: major steps in the evolution of developmental models for calcification of invertebrate skeletons

Jean-Pierre Cuif *, [a], **Kadda Medjoubi** [b], **Andrea Somogyi** [b], **Yannicke Dauphin** [c] and **Dominique Bazin** [d]

[a] CR2P Centre de Recherche sur la Paléodiversité et les Paléoenvironnements, UMR 7207, Muséum National d'Histoire Naturelle CNRS Sorbonne-Université, 75005 Paris, France

[b] Nanoscopium Beamline, Synchrotron Soleil, 91190 Saint Aubin, France

[c] ISYEB Institut de Systématique, Evolution, Biodiversité, UMR 7205 CNRS Sorbonne-Université EPHE Muséum National d'Histoire Naturelle, 75005 Paris, France

[d] Université Paris-Saclay, CNRS, Institut de Chimie Physique, 91405 Orsay cedex, France

E-mails: jean-pierre.cuif@orange.fr (J.-P. Cuif), kadda.medjoubi@synchrotron-soleil.fr (K. Medjoubi), andrea.somogyi@synchrotron-soleil.fr (A. Somogyi), yannicke.dauphin@upmc.fr (Y. Dauphin), dominique.bazin@universite-paris-saclay.fr (D. Bazin)

Abstract. The calcareous skeletons built by invertebrate organisms share a paradoxical property. Although growing outside the mineralizing cell layers the crystal-like skeleton units exhibit morphologies and three-dimensional arrangements that imply an efficient link between crystallization process and taxonomy. Almost two centuries of investigation led to a series of developmental models in which biological and physical or chemical influences are variously balanced. Recent innovative methods allow for their re-examination. From control of the overall shape of the shell to photo-spectroscopic evidence at the atomic level, influence of the biological processes on mineral properties may be a widely shared specificity of the calcareous biomineralization mechanism.

Keywords. Calcareous skeletons, Biomineralization models, Hierarchical structures, Biological control, Microscopy.

Published online: 6 October 2021

* Corresponding author.

1. The paradox of calcareous biominerals

In the study of the widely distributed calcareous shells (mostly produced by marine organisms) a major breakthrough occurred in the middle of the 19th century. At that time, the main lines of the zoological classification in which morphology of the calcareous skeletons play a major role were already established. A first synthesis had been produced by Linné [1] and value of shell morphology as taxonomic criteria was also made obvious through development of palaeontological research in the earliest decades of the 19th century. Investigating tertiary fauna from the Paris basin, Lamarck [2], for instance, created many invertebrate genera (mostly molluscs and corals) whose representatives were later found alive in the tropical seas. This point was important at the beginning of geological investigations because the ratio between still living and exclusively fossil genera was the key point to separate the periods in Cenozoic era. When progress of the microscopes and development of appropriate preparative methods allowed for observation of thin sections of these calcareous shells, a wealth of additional information became available. The origin of this innovative step is well known and provides a remarkable example of unexpected results and correlated interrogations.

The Microscopical Society of London (founded 1839) was dedicated to the study of cellular organization of living organisms, a theory whose universality had just been suggested [3,4]. Among the seventeen founders of the Society, the figure of Bowerbank is of particular interest because he focused his investigation on the shells and other biological mineralized structures. In his first results (published in the first issue of the Transactions of the Microscopical Society [5]), followed by more extended works by Carpenter [6,7], conclusion was that, in contrast to the other organs of the molluscs, their shells were not made of cells. This key point was extended to any calcified structure built by invertebrates. Even for unicellular organisms (e.g., Foraminifera or the Haptophyte algae Coccoliths), formation and growth of the mineral units occur in specific spaces inside the cell, but carefully isolated from the biologically active compartment.

Not only are the calcareous structures of the invertebrates *non-cellular*, but between cross-nicols the mineralized units exhibit crystalline appearances regardless of their shapes (Figure 1a–c). Conclusively, specialized cell layers (e.g., the outer epithelium of the mollusc mantles) produce the chemical components, but crystallization of the shell-building units always occurs outside the mineralizing cell layers, following a process that Huxley assimilated to a secretion [8]. Almost two hundred years later, the mechanism enabling a given species to keep so precise control over construction of its shell that microscopic observation allows for its taxonomic identification remains an unsolved enigma.

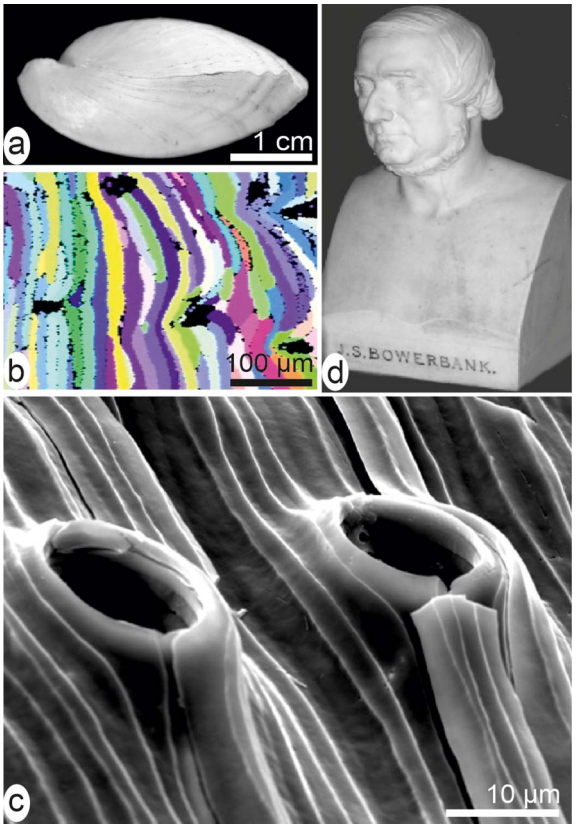

Figure 1. Species-specific morphology of the shell-building units exemplified by fibres in a brachiopod shell (a). Each fibre is a continuous single crystal of calcite ((b) EBSD diagram) whose shape has been adapted to animal anatomy during growth (c) without changing its individual crystallographic orientation. (d) Bowerbank bust.

From an applied viewpoint, however, the Bowerbank and Carpenter's results were immediately appreciated in another then rapidly evolving research area: the geology of sedimentary rocks, in which the fossilized shells could be now more precisely identified by studying small fragments. Therefore, at Burlington Hall (home of the Geological Society of London) the Bowerbank bust (among very few others) is an expression of the durable impact of his innovative approach (Figure 1d).

Eighty years later, the Schmidt's exhaustive synthesis of microscopic organization of the mineralized structures among living organisms [9] may be considered as an achievement of the Bowerbank and Carpenter's investigations [5–7]. In this milestone study the major patterns and respective importance of the three main types of biogenic mineralized categories were precisely described. Calcium carbonate is by far the most used [10]. It is distributed among most of invertebrate phyla and, accordingly, a remarkable diversity of taxonomy-linked crystal-like building units is generated. Their shapes always differ from the typical forms of the non-biogenic calcite and aragonite. In most cases, a given species can produce two distinct microstructural types simultaneously, with sometimes mineralogical change between the two distinct areas of the mantle as shown by this bivalve (Figure 2a–e).

To emphasize specificity of the calcareous biocrystallization, mention must be made of silica as the second biomineral from a quantitative point of view. Its geological importance was recognized since the beginning of scientific oceanography. First data were collected during Ross explorations of the Antarctic oceans (1839 to 1842) and popularized by the spectacular drawings made by Haeckel [11]. In contrast to Ca-carbonates of the shells, silica is always deposited as amorphous material. However, deposition of this silica is precisely controlled (Figure 3a–d) assessing for the presence of an extremely effective biological process that allows for creation of a precise morphology-based classification for thousands of species.

A third of the major chemical types of biominerals (although of lesser quantitative importance), calcium phosphate, is used in the vertebrate phylum, but also contribute to shell formation in some brachiopods and crustacea [9,12]. Bones (of mesodermal origin) and teeth (mesodermal by the dentine and ectodermal by their enamel) are crystallized materials characterized by the very small sizes of the mineral units (Figure 3e, f) [13]. It is worthwhile to note that when a vertebrate produces calcareous structures (e.g., fish otoliths or eggshells), the mineralization mode closely resembles the invertebrate microstructural growth patterns [10].

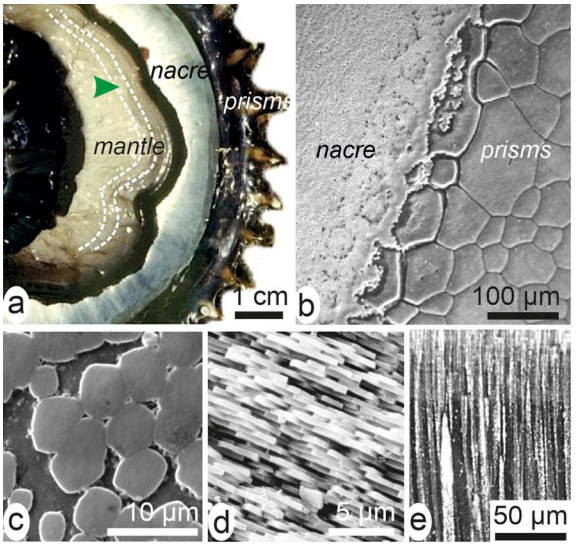

Figure 2. Shell of *Pinctada margaritifera*, the Polynesian pearl oyster. (a) On the inner side of the valve, the mantle is visible but the physical link between the mantle and the shell growing edge has been disrupted. The mantle produces calcite prisms at its periphery (black area of the mantle and shell). The internal light reflective area is the nacre. (b) Enlarged view (SEM) of the contact between prism and nacre areas. (c, d) Nacre built by thin densely packed aragonite tablets parallel to shell surface: (c) front view, (d) lateral view. (e) Prisms are large calcitic polygonal units perpendicular to the internal surface of the shell.

In the third decade of the last century, association of biochemical compounds to the mineral phases in the biogenic mineral structures was recognized (or at least hypothesized) in the three major biomineralization mechanisms. Nevertheless, even in the calcareous units whose sizes make observation easily accessible, obtaining precise data regarding relationships between the organic components and the mineral phases was subject to the oc-

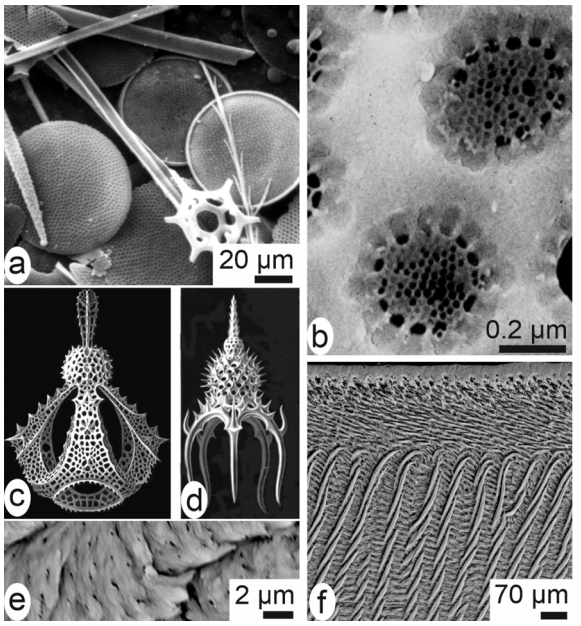

Figure 3. Siliceous and phosphate structures. (a) Diatoms, sponge spicules and silicoflagellid skeletons are typical siliceous materials in the world ocean. (b) Each of the about 1 µm wide holes in a diatom skeleton contains a delicate siliceous grid very precisely controlled. (c, d) Radiolaria drawings by Haeckel [11]. (e) Bone phosphate crystalline units are not visible at the enlargement of the optical microscope. (f) SEM view showing the complex arrangement of enamel microstructure of a rodent incisor, but not the very small crystallite units.

currence of innovative observational and analytical methods. Synchronous with the publication of the Schmidt's synthesis, the famous de Broglie's paper paved the way to electron microscopy [14], but complexity of the calcareous structures and associated biochemical compounds were still far from being deciphered.

2. Attempts to reconciliate the crystal-like patterns and taxonomy-linked diversity of the calcareous skeletal units

Once the permanent association between their organic and mineral phases was recognized, the calcareous biominerals, owing to the frequently large size of their crystal-like units, offer diversified case studies to investigate the respective roles of the two components. The most immediate questionable points were the origin of their obviously controlled crystallographic orientation and in parallel the relationship between this physical pattern and the biological growth mode.

2.1. *Biologically induced and matrix-mediated crystallizations*

Lowenstam coined these two terms [15] to formally separate the biologically produced calcareous structures depending on the degree of control exerted over their morphology and the three-dimensional arrangements of the mineral units. This distinction appears efficient when comparing the highly organized skeletons produced by the major invertebrate phyla such as molluscs, brachiopods, echinoderms to the disordered arrangement of mineral particles in the green algae, for instance (Figure 4a). Here the small aragonite acicular units are growing without any spatial organization within the organic mucus between the last-order branching structures of the Udoteacea *Halimeda* (Figure 4b–e) or the Dasycladacea.

Position of the coral skeletons exemplifies how uncertain could be the limit between the two branches of the Lowenstam's scheme. Up to 2005, finding statements placing coral skeletons among the weakly controlled structures was possible: "*In "biologically induced" mineralization—for example in corals—the minerals adopt crystal shapes similar to those formed by inorganic processes and have essentially random crystal orientations*" [16]. Actually, such a commonly shared view was based on previous papers emphasizing the similarity of coral skeletal structures with spherulitic crystallization, a chemical precipitation process frequently observed in sedimentary rocks. In corals "*each fibre is a single orthorhombic crystal of aragonite ... we have concluded that these organisms [Hexacoralla] have adopted spherulitic crystallization as an essential mechanism of skeletal development*" [17]. In addition the Barnes's statement that "*three-dimensional arrangement of fibres is due to "crystal growth competition"*" [18] largely contributes to the

interpretation of coral skeletons as weakly controlled materials.

Multiple structural and biochemical evidences have unambiguously placed corals among the "matrix-mediated" calcifying organisms. Most significant is the layered growth mode of the septa and walls, the existence of two distinct mineralizing areas in the basal epithelium synchronically producing specific microstructures with different isotopic fractionations, and the presence of organically coated nanometre-sized grains in both calcitic and aragonitic skeletons [19–21]. All these patterns show that these diploblastic animals also exert a full biological control on their skeletogenesis, equivalent to those of the triploblastic phyla.

2.2. *Control of orientation for the crystal-like units: template model and crystal growth competition*

Growth of oriented crystals on the surface of organic polymers has been emphasized by Mann [22] as a possible mechanism generating the specific orientation of the skeletal units in the calcareous biocrystallization process. Recent investigation of shell development in the Polynesian pearl oyster *Pinctada margaritifera* exemplifies template process in the early developmental phase of the prisms. But here, in contrast to the classical scheme of direct growth of the oriented crystals onto the polymer surface, a complex developmental process has to be followed at the growing edge of shell to transfer the structural properties of the initial organic grain to each of the distinct individual prisms (see below Section 3.2).

For molluscs and corals as major case study, the long-dominant view was that crystallization of the skeleton units occurs within dedicated spaces between the mineralizing cellular layer and the calcareous structure, e.g. the sub-ectodermal space between the polyp and the underlying coral skeleton (Figure 5a, b) or the hypothesized extrapallial space in molluscs (Figure 5c, d). These spaces were admittedly filled in by liquids in which secretions of the epithelial cells provide the appropriate organic molecules and mineral ions up to fulfilling conditions for precipitation of the calcareous material [23–26]. Accordingly, the specific shapes

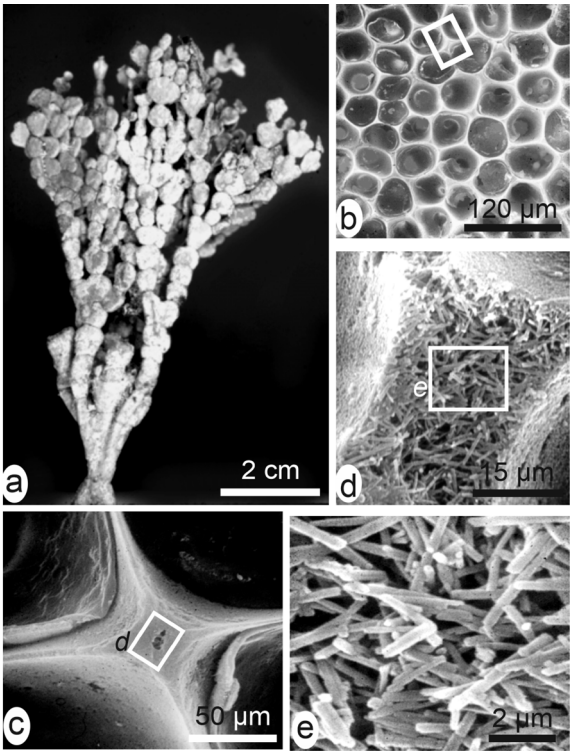

Figure 4. Example of biologically induced mineralization. (a) Dendroid green algae *Halimeda*. (b–e) At the periphery of this algae, disordered aragonite needles crystallize within an organic mucus between the last-order branches.

and three-dimensional arrangements of the skeleton units were considered depending on a "crystal growth competition" process [27,28], based on adequacy between direction of the crystallographic axes and the limited available space between the neighbouring and simultaneously growing units. The diverging fibrous fan systems common in the coral skeletons (Figure 5e) illustrate this apparently competing contact between growing fibres. New preparative methods revealing the micrometric control over growth of these crystal-like units led to modify this purely physical interpretation (Figure 5f, g).

From the classical ionic crystallization mechanism, authors also recognized that taxonomy-linked structural patterns could be due to various additional processes such as development of crystals onto specific organic substrates acting as "template" (e.g., [22]). For instance, when Grégoire and cowork-

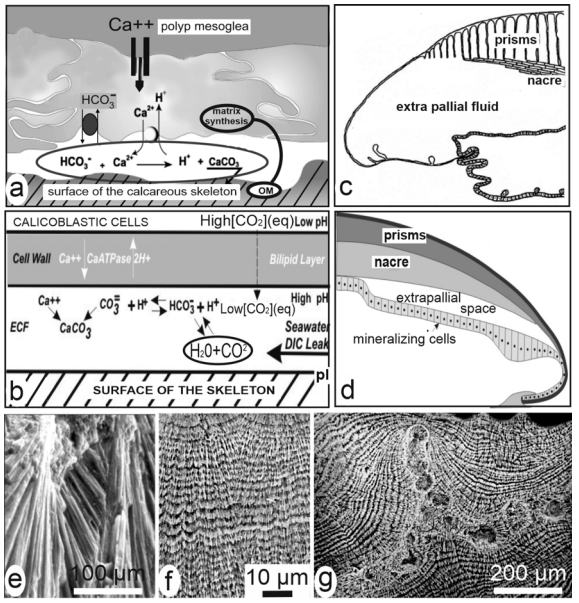

Figure 5. Models of crystallization in liquid-filled chambers. (a) In corals [23], (b) in corals [24], (c) in molluscs [25], (d) in molluscs [26]. (e, f) Biological evidence that growth of coral fibres is not an individual and competitive process but a series of synchronic and biologically controlled mineralization layers. (e) Two neighbouring fibrous fan systems (SEM view of a fractured septa without any preparation). (f) The same area after etching: the two distinct fibrous areas are built by synchronically produced growth layers whose similar thickness variations do not support interpretation by conflictual growth. (g) In the septa of coral skeletons an early mineralization area is built by distinct granular patches later covered by superposed layers of fibrous structures (both aragonite). This double microstructure is a permanent pattern whose three-dimensional variations are linked to taxonomy.

ers carried out a series of investigations about mollusc shells from 1955 to 1977 [29–32], they could observe (using transmission electron microscopy) the alternating organic and mineral layers within the calcareous prismatic structures. The leading role of organic compounds in the formation of the overlying mineral layer was an admitted paradigm.

An alternative mechanism was later suggested in which morphology of the normally growing crystals could be continuously modified by adsorption of species-specific sets of organic molecules onto their lateral faces. This model: "shaping crystals with biomolecules" [33] was followed by emergence of the "non-classical crystallization" theory [34], a collaborative attempt to gather several research areas into a common crystallization mechanism: the "particle attachment" model [35]. The main change is that crystallization is viewed as a two-step process in which tiny initial crystals are admittedly forming larger units by mutual accretion due to interactions between their lateral faces.

Regarding biogenic calcareous structures (also included in this proposed model), the main objection to the hypothesized lateral accretion mechanism was already known: it is that the nanometre-sized building units of the biogenic skeletal units are always lacking crystal faces (see below Section 3.3).

Finally a long series of microstructural observations and chemical measurements have contributed to reduce recognition of the "crystallization chamber model". It was first disproved by Crenshaw [36] following a biological approach that led him to conclusion that between the mineralizing epithelium and the growing mineral surface "the transfer of material is essentially direct". The most significant data disproving the existence of a common liquid-filled chamber for crystallization of the skeletal unit were due to occurrence of physical instruments allowing for precisely located measurements of the isotopic fractionation or chemical partitioning. Taking into account the distinct calcareous microstructures, important differences were found *within a given specimen* between the isotopic ratio or trace element concentrations measured in the simultaneously produced minerals of the distinct areas (e.g., [24,37]). As long as measurements were carried out on powders drilled from skeletons without consideration to local microstructure, Urey's "vital effect" (i.e. the distinct fractionation between species living in the same water pool) was considered as depending on species. As distinct records can be obtained *from a given specimen* depending on the type of skeleton microstructure on which measurements are made, the "vital effect" is not only a matter of species, but is also linked to the distinct biocrystallization processes that may occur within a given specimen.

2.3. *A "radical change" in the model of the secretion mechanism for calcareous skeletons: an intracellular phase predating the extracellular crystallization*

As crystallization is obviously extracellular, the "direct transfer" process hypothesized by Crenshaw [36] implies that the components secreted by the mineralizing cell layer can directly produce the mineral phase of the growing units. It was about thirty years later that additional information was forthcoming, basically modifying the initial working framework on which previous modelling attempts were relying on.

Intracellular granules found in *Helix* were amorphous Ca carbonate (ACC), and mineralization can occur in vacuoles or vesicles [38]. Then, it was shown that in the growth of a larval spicule of the echinoderms the initially deposited material was made of ACC [39]. Moreover, ACC was shown to be present within cultivated mantle cells of *Pinctada* [40]. Thus, a few years later, to extend these findings to the main calcifying groups, its generalization was considered as a "tantalizing possibility" [41]. In this new view, formation of the calcareous materials involves two distinct phases: the first one produces an accumulation of Ca-carbonate *in amorphous status* within the cells of the mineralizing epithelium. This preparative phase is followed by exocytosis of the amorphous material and its external crystallization.

In elaboration of a developmental model for biogenic calcium carbonate, this two-phased mineralization concept made irrelevant an unsolved key question: the transit through the crystallization chambers of the sea-water volume needed to continuously produce a compact calcareous structure taking into account the low calcium concentration of sea water. This had sometimes led authors to hypothesize some ionic "leaks" that had no anatomical support [24] (Figure 5b). Now the origin of mineral components, far from elucidated yet, is attributed to internal physiological processes [42,43].

In contrast, a very positive result of this "two-phase" calcification model was that an understandable link was made possible with previous approaches developed since the late 70's, investigations that have made obvious the existence of a layered growth mode of the skeletal units in a wide diversity of calcareous skeletons.

3. Evidence of a generalized layered growth mode for the calcareous crystal-like units and their common granular ultrastructure at the nanometre range

Presence of an organic phase whose distribution was inaccessible to optical observation or X-ray diffraction method led H. Mutvei to develop an etching approach to display the internal structure of the calcareous biominerals. By carefully dissolving the outer organic film surrounding the tablets of nacre (using oxidative–fixative solutions) the respective distributions of organic and mineral phases become visible up to certain extent. Taking advantage of scanning electron microscopy it was thus possible to reveal the internal organization and growth mode even for the few micrometre-sized aragonite of the nacre, usually described as a uniform "brick and mortar" assemblage (Figure 6a, b). This approach deeply modified the common view about the nacre tablets by showing their taxonomy-linked internal diversity [44–47]. Similarly, the inner nano structure of the calcite laths of the foliated layer of oysters was revealed by enzymatic or bacterial etchings [48] (Figure 6c–f).

Applying this method to a wide diversity of calcareous biostructures [49] and focusing attention to the anatomical areas where development of the skeleton units was starting resulted in conceptual change by revealing the unsuspected architectural organization of some reference materials.

3.1. *The* Pinna *prism internal substructures reveal a three-dimensional stepping growth mode of the shell*

Since the beginning of biomineralization studies, *Pinna* prisms are the reference owing to their geometrical simplicity and perfect calcite crystal-like behaviour (Figure 7a–c). However, etching reveals that within the organic envelopes, two cyclic mineralization systems exist, clearly related to the overall growth of the shell.

The first one is parallel to the internal surface of the shell (Figure 7d: *gl*). It shows that the prisms whose elongation is produced by addition of superposed growth layers (Figure 7e) are synchronically growing through a coordinated stepping mode. This synchronic growth mode of the whole prismatic surface is clearly demonstrated by electron microprobe

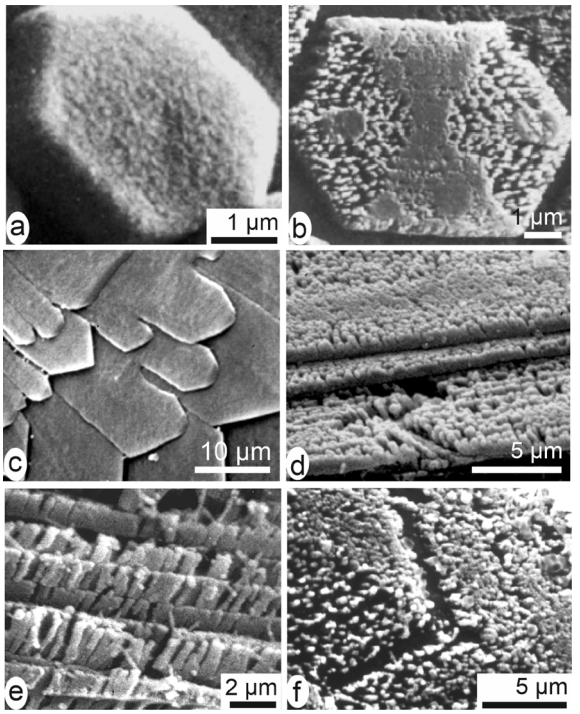

Figure 6. Layered growth mode of calcareous biocrystals. Nacreous tablets of *Unio* before (a) and after (b) etching (from [43]). (c) Foliated microstructure of the internal layer of *Crassostrea gigas* before etching. (d–f) Linear arrangement of the calcified units. Note that (a, b) pictures are from an aragonite biocrystal, pictures (c–f) are from a calcite one.

mapping of the polished surface (Figure 7f, g). This shows that traces of environmental chemical or isotopic variations can be inserted into the shell through the pulsed growth mode of the skeletal units. Each growth layer appears as a crystallization unit whose composition varies from layer to layer [50].

In addition, a second crest-and-grove system is visible on the etched surface: it is slightly oblique with respect to overall geometry of the prisms (Figure 7d: *or*). It is linked to lateral extension of the shell (Figure 8a). In contrast to their apparently distinct geometry (emphasized by crystallography) a remarkable correspondence exists between neighbouring prisms. The second crests-and-groves system is well coordinated (Figure 8b, c) through the organic envelopes surrounding each prism. This shows that the lateral extension of the shell is also a stepping process [51]. It is obtained by synchronic deposition of elongation layers coordinated between neighbouring prisms a process that is also visible on their lateral faces (Figure 8d).

Applying the "two-phases" mineralization model to the layered structure of the *Pinna* prisms offers an understandable solution to their paradoxical properties. For each growth layer, deposition of amorphous material is followed by crystallization driven by the previously crystallized substrate (i.e. the internal surfaces of the prisms that play a template role). As a result, individual crystallographic patterns are maintained from a common amorphous mineral deposition. So, the outer shell layer of *Pinna* is not a simple juxtaposition of independent crystal-like units as suggested by polarization microscopy. It is a wholly integrated three-dimensional structure in which the stepping secretion process of the mantle simultaneously increases thickness and lateral dimensions.

3.2. *Prisms from their early beginning: origin of the distinct crystallographic orientations in the prisms of* Pinctada margaritifera

In contrast to investigations that deal with well-established prisms, the microstructural approach applied to the growing edge of the shells provides information about the complex ontogenetic process that drives their initial stages.

A fully open shell (e.g., Figure 2a) displays a wrong picture of the relationships between mantle and shell. In the natural status of any pelecypod mollusc a physical continuity exists between the animal and its shell valves: this continuity is ensured by the periostracum [52–54]. This is an organic membrane secreted by a specialized group of cells located in the outer mantle groove (Figure 9a). In *Pinctada* it directly contributes to shell formation [55,56] because it acts as a conveyor belt and transports on its internal side the earliest calcified materials of the shell.

The mineralizing cells of the mantle grove produce organic grains deposited onto the internal side of the periostracal membrane (Figure 9a, b: arrows). Calcification occurs around these initial mineralization centres (Figure 9b–d) following a concentric stepping process (Figure 9e). These disks have a crystal-like behaviour, each of them with slightly distinct orientation [57]. Thus, numerous flat disks

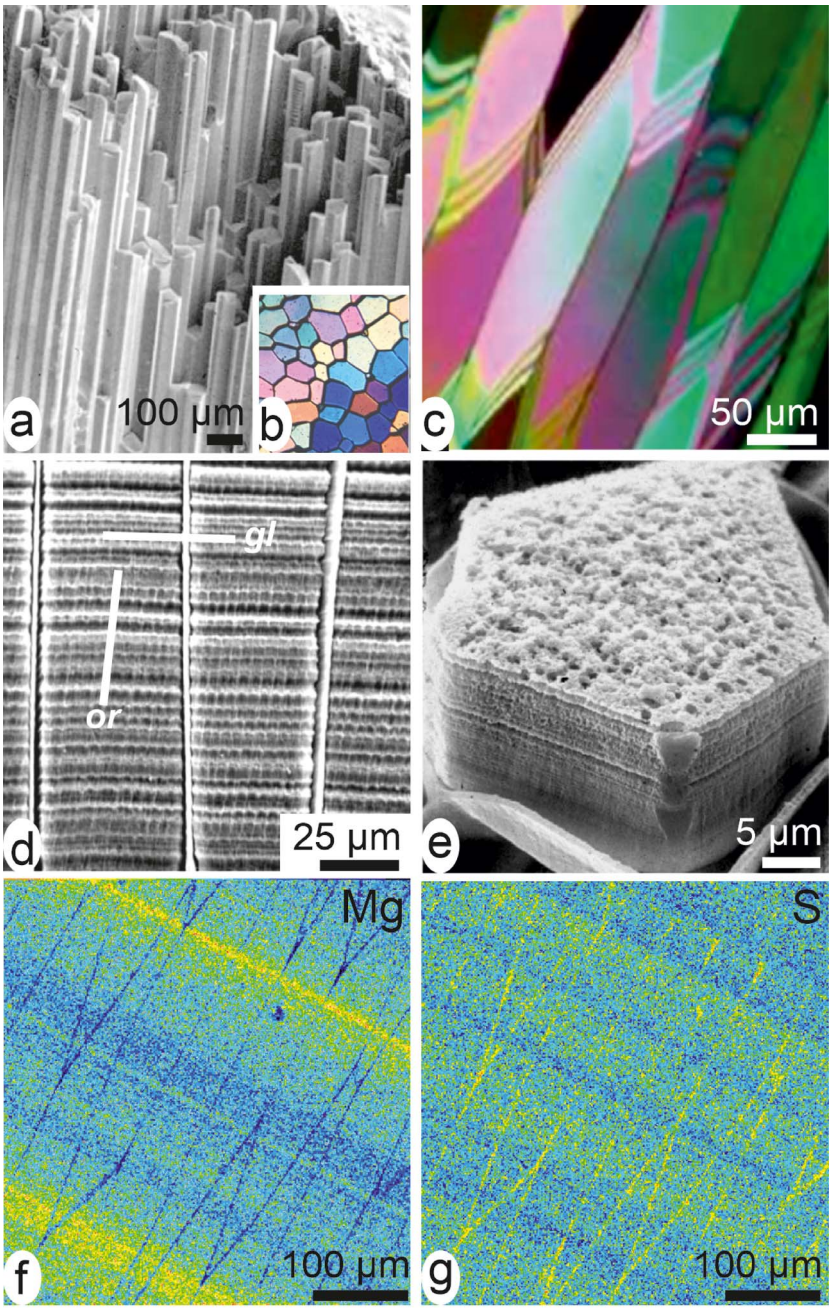

Figure 7. From crystal-like to layered structure of a *Pinna* calcite simple prism. Rectilinear polygonal prisms (a) appear as single crystal units in both transversal (b) and slightly oblique longitudinal (c) sections between cross-nicols. (d) Etched longitudinal sections reveal the superposed growth layers synchronic through the whole mineralizing surface of the shell (*gl* = growth lines) and the series of shell elongation units (*or*) (see also Figure 8). (e) Sides of a young prism show its layered growth mode; note the "non-ionic" growth pattern of the upper surface. (f, g) Distribution of sulphur and magnesium emphasizes the layered growth mode and the distinct absorption of chemical elements within each superposed layer: each growth layer is an independent crystallization unit.

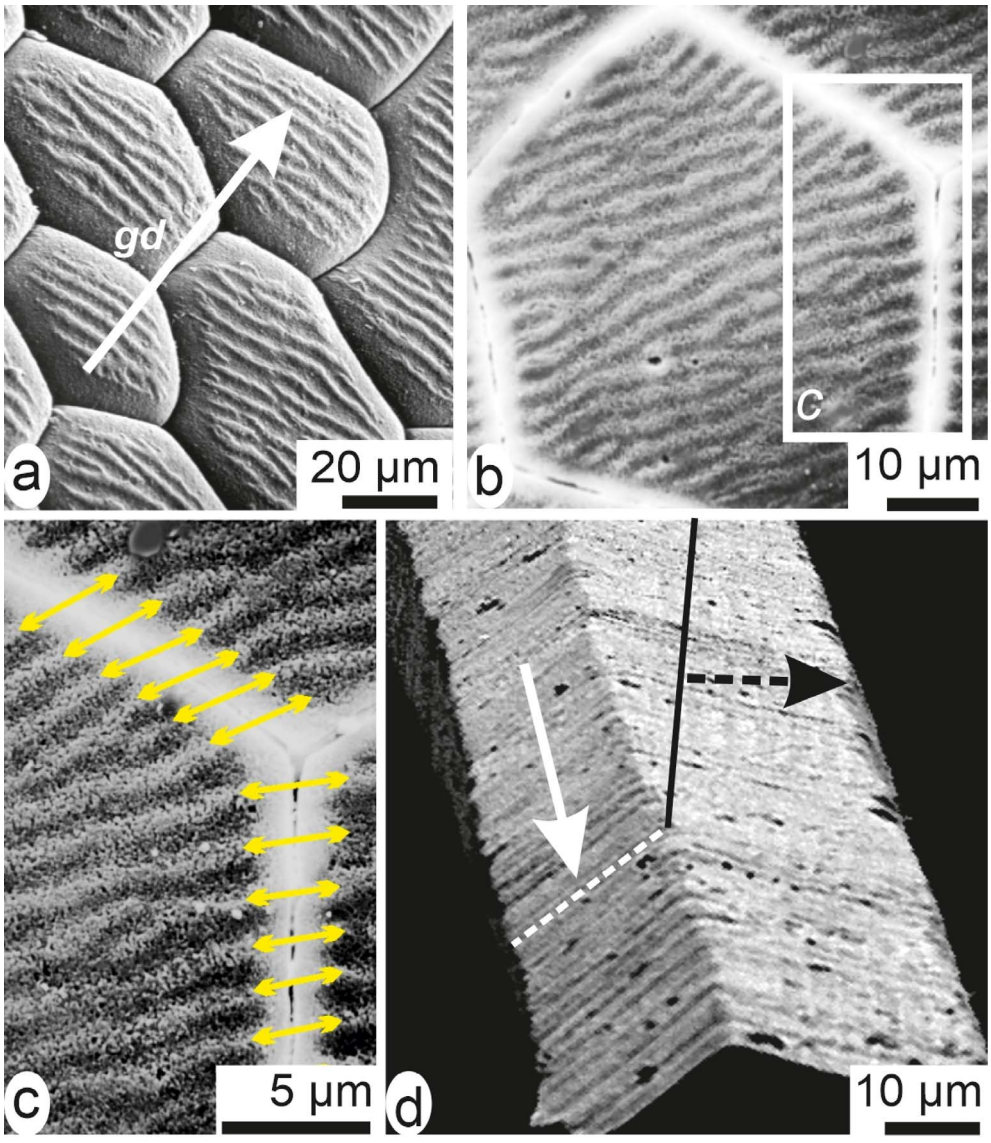

Figure 8. Two-dimensional stepping growth mode of the *Pinna* prisms. (a) On the actively growing internal surface of the Pinna shell a crest-and-grove system is visible, perpendicular to growth direction of the shell (*gd* arrow). (b, c) SEM view of a polished surface in the same area: note the correspondence of the lateral growth layers between neighbouring prisms, showing that elongation of the whole shell is a coordinated process. (d) Lateral faces of an isolated prism showing traces of the stepping elongation: orientation of the traces depends on orientation of the prism faces with respect to growth direction of the shell.

are formed with thickness never exceeding 3–4 µm with diameter reaching 20–25 µm. This is the "flexible shell", in which disks are growing independently as crystallographically distinct units [57–59].

Reaching the growing edge of the shell, the periostracal disks are used as substrates for prism formation (Figure 9f). As in the *Pinna* shell (Figure 7b) prisms of the *Pinctada* are distinctly oriented as shown by polarized light (Figure 9g) in spite of the synchronic production of the growth layers. Secretion of the shell growth layers as amorphous material explains the distinct crystallization

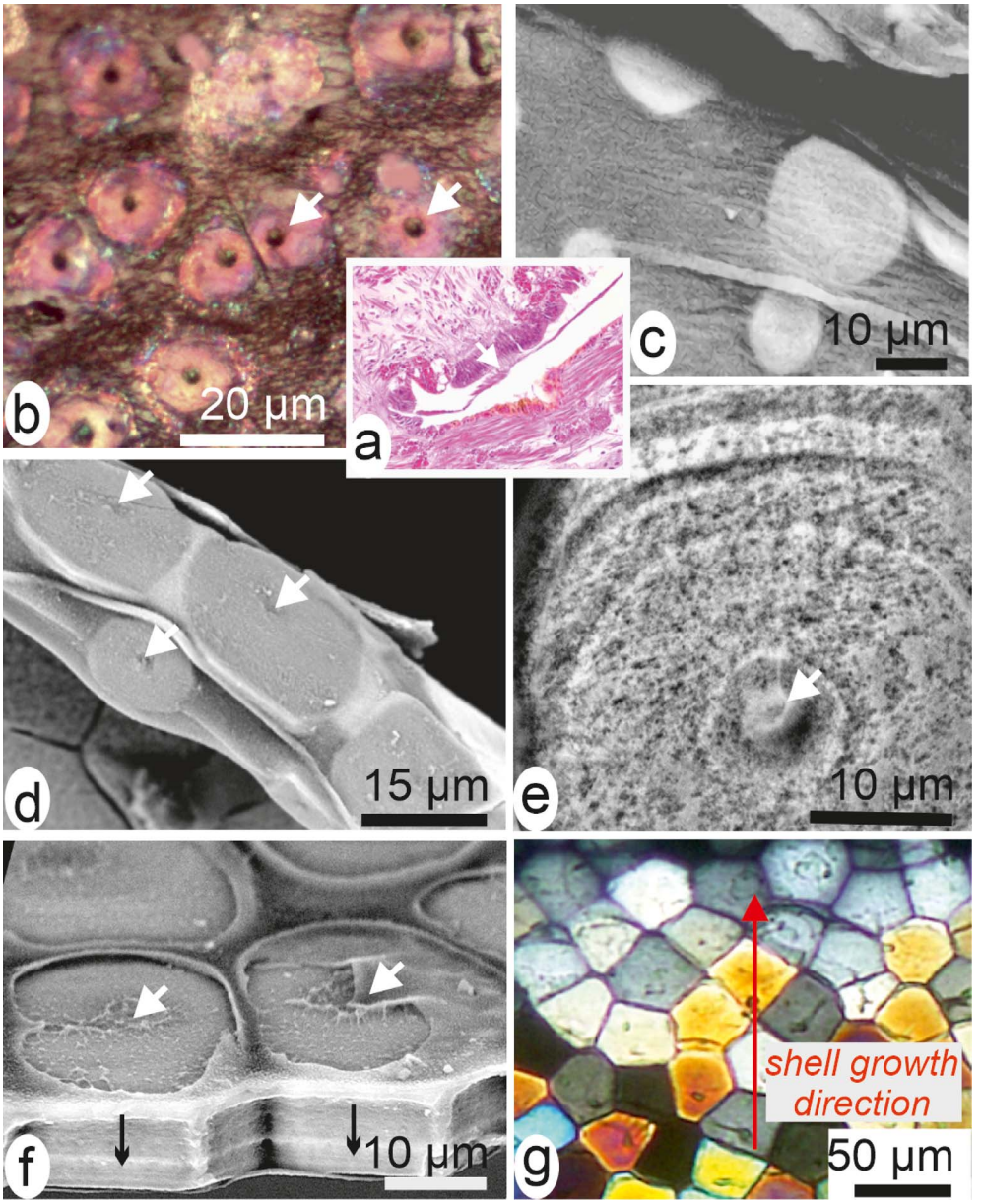

Figure 9. Example of a double transfer of substrate orientation in the development of the prisms in *Pinctada margaritifera*. (a, b) Close to the formation of the periostracum in the outer mantle grove small patches of organic material are deposited on its internal surface (arrows). (c–e) Repeated concentric depositions of calcite results in formation of flat disks. (f, g) At the shell growth edge, disks are shown forming the top of the prisms; (f) distinct crystallographic orientations of the prisms is visible between cross-nicols; (g) emphasizing the initial differences between the initial disks.

of the prisms. The amorphous layer synchronically secreted by the mantle crystallizes according to crystallographic orientation of the disk it is facing. Polarization colours passing from first-order grey to the end of first order (Figure 9g) show that once established the initial crystallographic differences between neighbouring prisms are maintained [57–59].

Therefore early development of the *Pinna* and *Pinctada* prism layers exemplifies how the concept of "template model" must be carefully examined, taking into account the series of ontogenic events that occurs not only at the shell growing edge but also in the deeper part of the outer mantle grove. A first template process occurs when crystallization of the periostracal disks is based on the organic grains secreted onto the internal side of the periostracum, a second one occurs when the resulting disks provide support to the early stages of disk growth.

In conclusion, these two admittedly "simple" prisms revealing distinct development processes, but in both cases the two-phase mineralization mechanism contributes to explain their respective specificity.

3.3. *The common granular ultrastructure of the calcareous units observed at the nanometre scales*

In parallel to evidence that the calcareous shell-building units may exhibit distinct internal architectures a surprising similarity of their structural pattern at the nanometre range was made obvious by using atomic force microscopy (AFM).

Owing to its capability to simultaneously capture distinct signals corresponding to different material properties, this method provides us with information about organization of the calcareous biominerals with an unprecedented resolution. It has shown that calcareous growth layers were built by round-shaped nanometre-sized mineral grains (Figure 10a–f) surrounded by organic material. The densely packed spheroidal grains are illustrated by Figures 10a, b and 10c, d, in aragonite of cephalopod nacre [60], coral fibre [61] and brachiopod fibre (calcite) [62]. They have been observed in materials biologically distant like fish otoliths [63], eggshells [64], calcareous sponges, foraminifera, etc. Everywhere the typical AFM phase-contrast imaging indicates the presence of a highly interactive phase (strongly adherent to the AFM cantilever tip) at the periphery of the grains (Figure 10e, f).

In the concept of an intracellular preparative phase predating exocytosis, crystallization of ACC within the mineralizing cells must be prevented by organic compounds [65]. After exocytosis, crystallization occurs and reticular structures are now visible

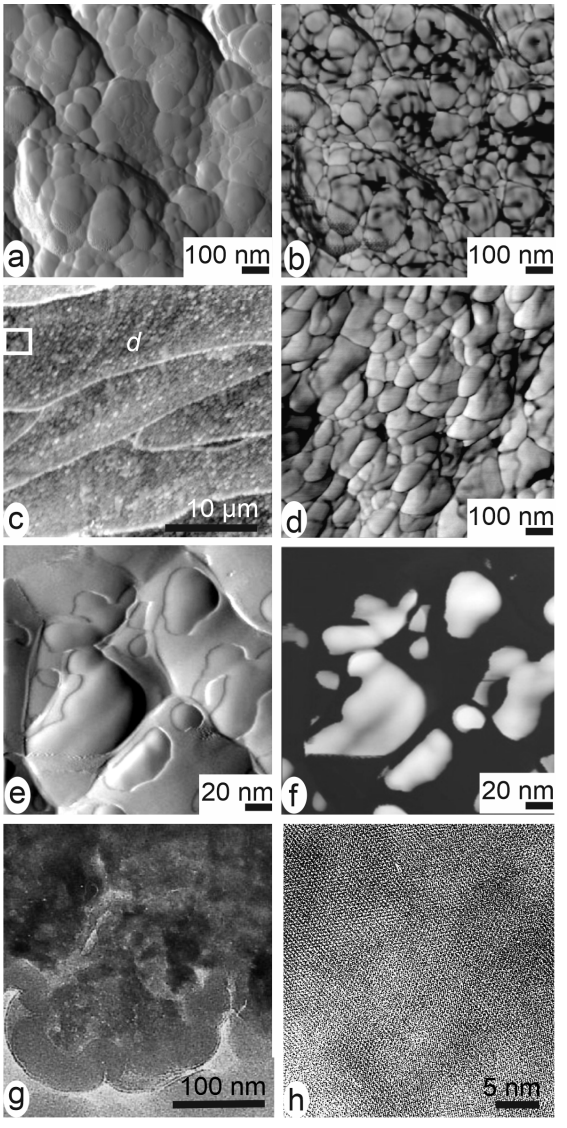

Figure 10. Coated-mineral grains common to biogenic calcareous structures. Independently of the producing phylum, the layered growth units in calcareous structures are built by infra-micrometre-sized grains (in the range of the 50–150 nanometres). (a, b) Coral fibres. (c, d) Brachiopod fibres. (e, f) *Pinctada margaritifera*, amplitude (e) and phase-contrast (f) images of the calcareous grains showing the correspondence between the peripheral envelopes (e) and their strong interaction with the AFM tip (f). (g, h) Transmitted electron images of the grains: below the organic coating, grains are well crystallized.

in the nanometre-sized units (Figure 10g, h). The organic compounds that have prevented amorphous crystallization inside the cells are now squeezed between the crystallizing grains preventing formation of faceted surfaces.

That similar nanometre-sized spheroidal structure was found in every calcareous biocrystal, whatever their taxonomic origin, indicates that an equivalent process is running in every calcareous biomineralization [66]. From an evolutionary view point, this remarkable consistency of the infra-micrometric structural organization suggests that any biological system having developed a calcification process was submitted to common requirements linked to basic chemical properties of the Ca-carbonates.

With respect to molecular diversity of the intraskeletal organic materials, the "two-phases" mineralization concept opens a plausible explanation to the biochemical complexity of the organic matrices. Over several decades, attempts to establish a structural relationship between organic and mineral components were almost exclusively based on proteins [67,68], owing to technical improvements that allows for protein sequencing and amino-acid analysis [69]. In contrast, no role was attributed to the polysaccharides although their presence was established and sometimes emphasized specifically in the sulphated form [70–72]. Evidence now emerges that taxonomy-related chemistry involved in the formation of amorphous material during the intracellular phase of the mineralizing process is a prerequisite to understand the crystallization process of the structural units.

4. Abnormal mineralization in pearls: evidence for a recovery process leading to nacre deposition

Among the diversity of the calcareous materials produced in the living world, nacre has long attracted attention. Built by densely packed flat aragonite tablets (Figure 2c, d), nacre reflects visible light at the tablet surfaces (in contrast to other calcium carbonate structures). This property becomes of particular interest in the mollusc class Pelecypods because, inside their bivalved shells, some families can produce rare round-shaped bodies whose ornamental power has long been noticed: the pearls.

In the first decade of the last century Mise and Nishikawa elaborated the pearl cultivation method which essentially remains unchanged up to now. It involves two "pearl oysters" and comprises a surgical operation. A small fragment of the nacre producing mantle tissue—the "graft"—is first cut from one of these oysters (the "donor"). It is then transported into a "recipient" oyster and deposited onto a spherical body (the "nucleus") previously introduced into the "pearl pocket" (a part of the pelecypod gonad). Inside this pocket the graft spreads by cellular multiplication up to a complete wrapping of the nucleus, producing the "pearl sac" in which pearl grows during about two years and is then collected.

Over decades it has been admitted that onto the nucleus surface the graft was producing the same nacre as it was doing just before being cut from the animal mantle. Therefore the observation by Kawakami [73,74] that *calcite deposition* may occur during early development of pearls can be considered as a major step in biomineralization studies. It is important from a practical view point (calcite deposition is a major cause of morphological irregularity in pearls); moreover calcite deposition reveals in-depth alteration of the well-established process that was running in the graft cells when it was a part of the mantle. Comparison between Figure 2c, d (*Pinctada* nacre) and Figures 11–12 (early pearl mineralization) reveals how important perturbation of the mineralizing process can be. Therefore, exploring the early stages of pearl formation was a thoroughly investigated topic in Japan during the second half of the last century [75–77]. More recently deposition of calcite was integrated in a general concept of the pearls viewed as a "reversed sequence of layers" of the shell [78].

Investigations using standard X-ray characterization and XANES mapping have shown that the reversed shell hypothesis does not account for the sequence of structural events that can be observed during early stages of pearl formation [79]. Recent developments in X-ray microscopy [80] provided high-resolution evidence suggesting that the long and somewhat erratic recovery pathway by which nacreous secretion is finally restored in the cultivated pearls could be informative about the control of the biomineralization process [81,82].

In place of nacre the mineralized units produced by the newly formed pearl sac frequently appear as

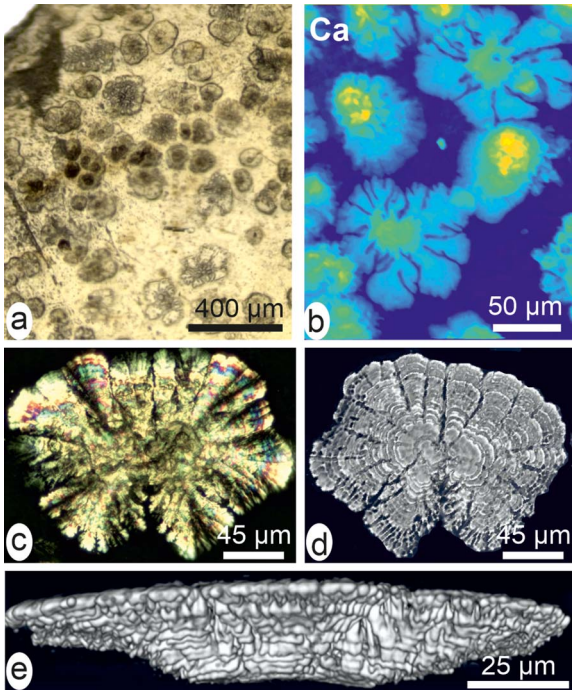

Figure 11. Early mineral deposition after a 20-day post-grafting cultivation (compare to nacre in Figure 2c, d). (a) Distinct patches in a detached fragment. (b) High-resolution X-ray fluorescence showing the radial expansion of the mineralization. (c) Radiating unit between cross-nicols. (d) Full field tomography showing the inferior face of the unit. (e) Reconstructed lateral view showing its mode of growth by superposed layers with increasing diameters.

distinct patches ranging in size from 50–100 µm (Figure 11a, b). Their irregularly radiating growth is well evidenced by high-resolution X-ray Ca fluorescence. Polarization shows their radiating crystallization (Figure 11c) but phase-contrast imaging reveals their layered structure. Figure 11d (lower surface of the unit) and Figure 11e (lateral view) show that these units are not simple mineral spherulites. They are built by repeated superposition of micrometre-thick calcified layers whose diameters are regularly increasing. This shows that in spite of the strong degradation of the mineralizing process the fundamental layered growth mode has been preserved in the pearl sac.

A 30-day post-grafting sample illustrates important changes in mineralization as the early stages are now covered by continuously mineralized surfaces (Figure 12a–c). Previous investigations using standard X-ray diffraction had shown that components of the neighbouring areas were heterogeneous with respect to mineralogy [81,82]. High-Resolution X-ray fluorescence mapping allows for fine scale microstructural patterns and elemental distribution (Figure 12d–g).

It is important to emphasize that, in contrast to the regularity of the mineralization in shells, these early developmental stages of the pearls reveal a high structural and compositional diversity. As the grafting process requires time consuming operations, it may generate various levels of disturbance in gene expressions in the pearl-sac cells. Abnormal structures made of calcite and non-nacreous aragonite exemplify such perturbations as they can be simultaneously produced, each of them with different organic contents (Figure 13a–d) and [79, Figures 4–5], [82]. Remarkably, recovery of the nacre production process generally occurs after times varying from days to weeks and sometimes months. Structural examination of the transitional areas (Figure 13a–d) and variation in the corresponding XANES maps (Figure 13e, f) show that in the superposed growth layers the boundary between abnormal mineralization and true nacre secretion is not straightforward. In the Polynesian pearls a progressive return to nacre is made visible by the spreading of the black pigment (Figure 13b). From a biochemical view point replacement of calcite by nacre is correlated to the end of polysaccharide secretion (Figure 13e).

From an overall viewpoint, what appears more significant is the surprising ability of the pearl sac to reproduce nacre deposition through various transitional pathways. This makes it obvious that some biological control over pearl-sac secretion related to initial production of nacre by the graft has persisted through the abnormal mineralization period.

5. Conclusion: converging evidences of a multi-scale biological control over developmental process in the matrix-mediated biomineralizations

Investigations dealing with pearls provided evidence of a multiscaled biological control over developmental process in the matrix-mediated biomineralizations.

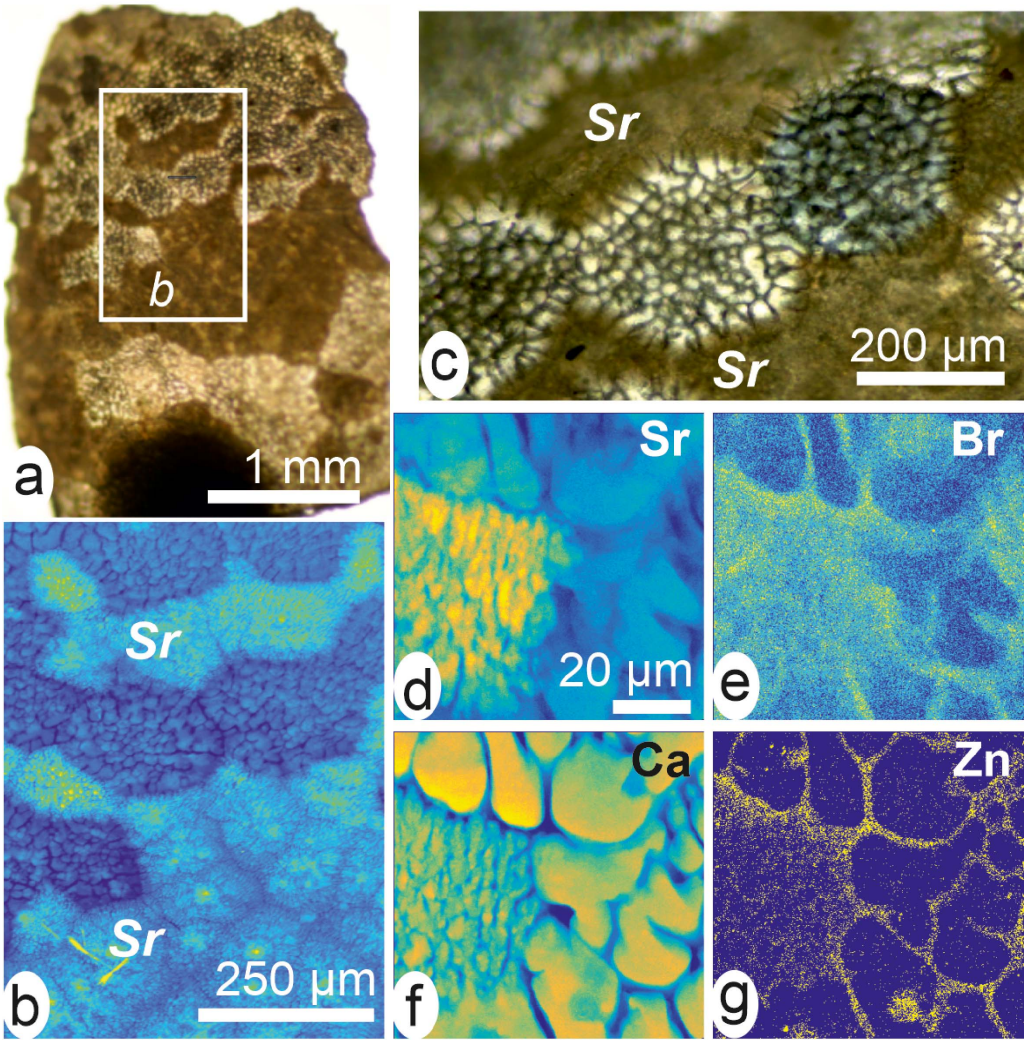

Figure 12. High-resolution X-ray fluorescence maps of the early mineralization stage in a cultivated pearl of *Pinctada margaritifera*. (a, b) Optical views of a fragment showing distinct mineralization patterns. (b) Between Sr-rich areas, crystallization occurs by forming distinct grains consistently polarizing within polygonal areas. (e–g) Distribution maps of Sr (d), Br (e), Ca (f) and Zn (g) in the same fragment. Note the clearly distinct morphologies of the mineral units between high and low Sr contents areas.

Nowhere are the relationships between biology and crystallization more apparent than in this several decade-old figure by Wada [76] in which a close correspondence is shown between crystallographic orientations of the nacreous tablets and growth directions in the shell of *Pinctada martensi* (Figure 14a, b). This obviously implies that nucleation and growth of the tablets are related to an oriented organic framework whose directional changes during ontogeny induce correlative modifications in orientation of the mineral units. Note that overall tablet orientation is not the only biologically influenced feature: crystallization of the nacreous tablets also depends on biological control. In sedimentary aragonite, the main growth direction for aragonite is the *c*-axis, leading sometimes to production of acicular crystals in the *c*-direction. In contrast, in the nacre aragonite tablets the *c*-axis is perpendicular to the flat surface,

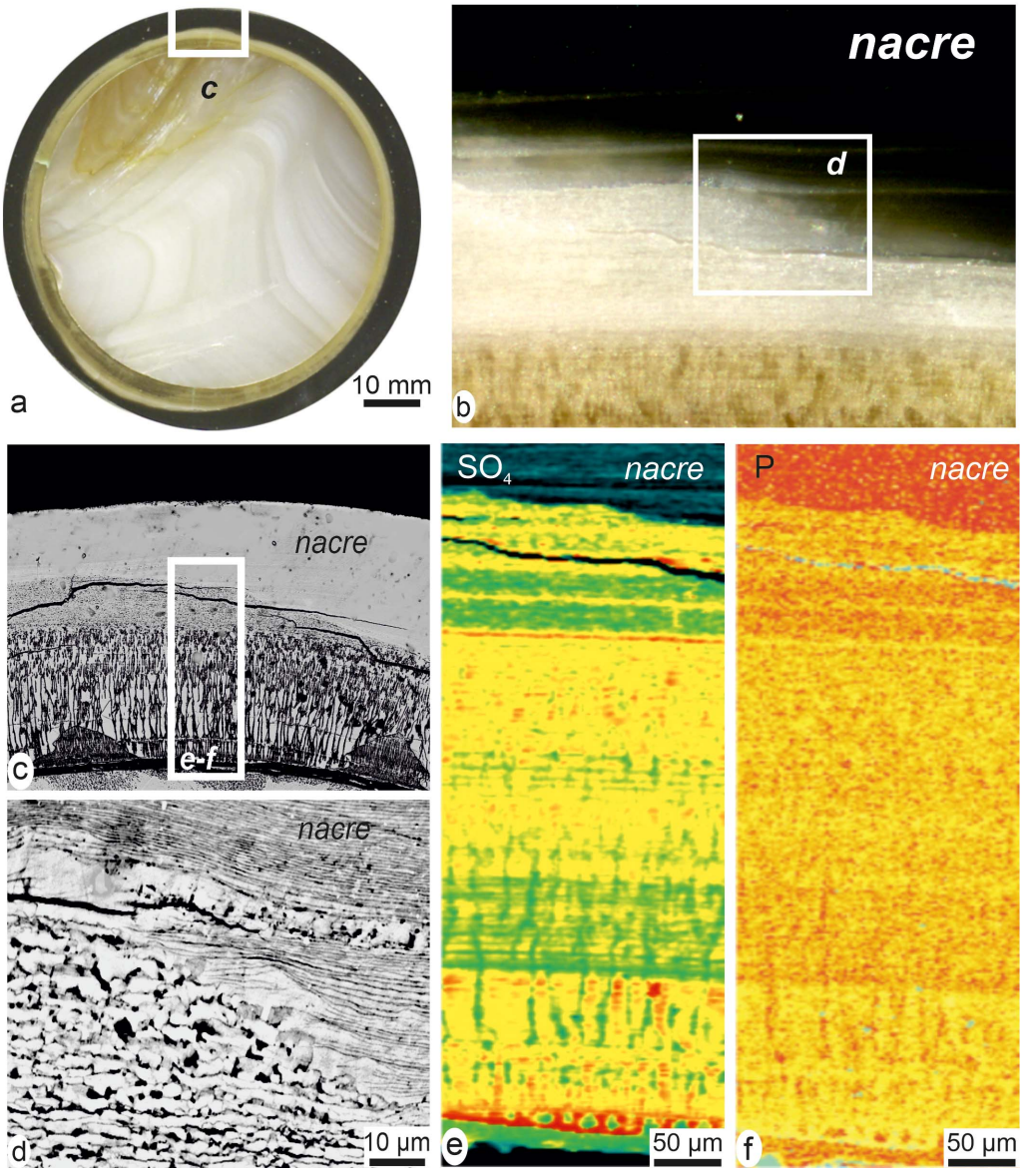

Figure 13. The stepping return to nacre production in cultivated pearls. (a) The external black nacreous layer makes the abnormal mineralization phase well visible. (b) Enlarged view of the extension of the nacre, progressively replacing the complex lower layer. (c) The radial envelopes (perpendicular to nucleus surface) may contain calcite or non-nacreous aragonite. (d) Enlarged view of the contact line between true nacre (note the specific layering) and abnormal mineralization. (e, f) XANES distribution of sulphated polysaccharides (e) and phosphorus (f) during the abnormal mineralization period. Note the progressive metabolic changes in the upper layers of the field, corresponding to nacre expansion.

showing that in this direction growth is restricted at about 1/10 ratio, resulting in the optical property of the nacre [76].

Biological influence on crystal growth is also obvious in the prisms of the *Pinctada* shell. Not only is the *c*-axis *perpendicular to the main growth direction*

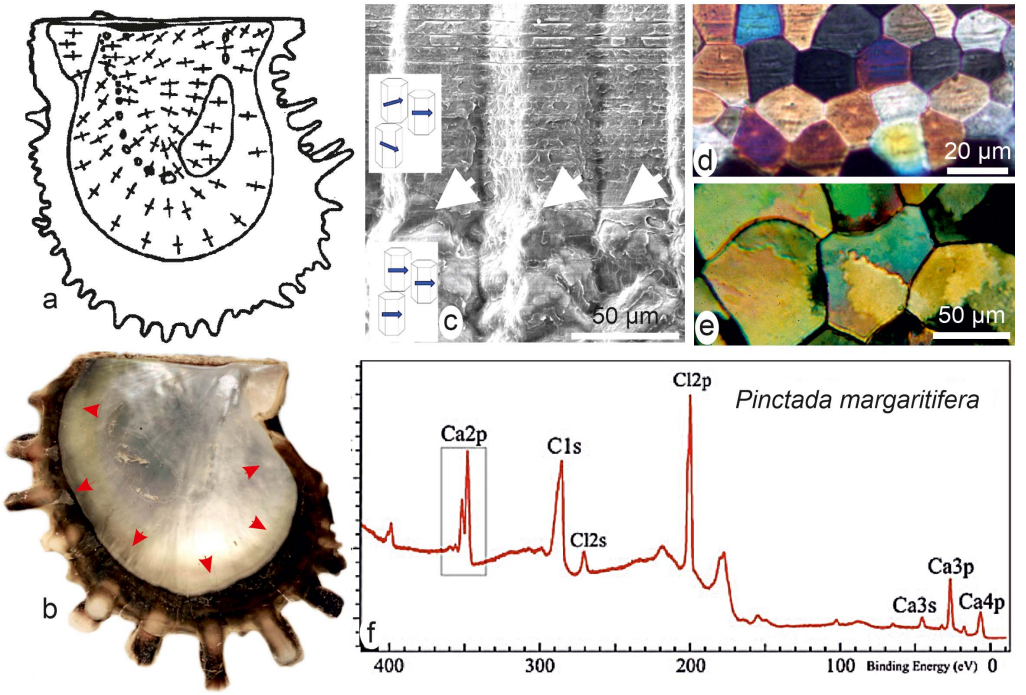

Figure 14. Multi-scaled evidences of organic–mineral interactions during shell formation from overall growth up to atomic level. (a, b) Tablets of nacre have their *a*- and *b*-axes consistently oriented with respect to direction of shell expansion ((a) original figure in [76]). (c–e) Modification of crystallization patterns during growth of the prisms of a Pinctada shell. (f) Taxonomy-linked shifted values of the Ca2p binding energies suggest interaction with the species-specific mineralization matrices and origin of abnormal crystalline parameters of the resulting mineral phases [83].

of the prism [84], but a microstructural change regularly occurs in the prisms after about 150 to 200 µm of thickness increase (Figure 14c, arrows) [85,86]. This has unexpected crystallographic consequences (Figure 14g, h). In the initial growth stages (single-crystal like), the *c*-axes are differently oriented whereas in the second growth phase, much more disordered with respect to microstructural arrangement, the *c*-axes are more consistently oriented perpendicular to growth direction [84].

Thus, in the *Pinctada* shell, growth of both calcite and aragonite units demonstrate opposite behaviour with respect to the common views regarding crystal growth. It shows that influence of the biochemical compounds that drive mineralization of the shell-building unit is predominant over admitted rules for chemical crystallization.

Looking at the lowest structural levels, the organic coating of spheroidal nanometre-sized units has suggested that these components may play a key role in preventing the development of faceted nanocrystals (no particle attachment model). Interestingly, synchrotron-based photo-emission spectroscopy carried out on the soluble part of the organic compounds extracted from calcite or aragonite skeletons have shown that the binding energies of Ca orbitals were significantly distinct from the corresponding values in pure calcite or aragonite (Figure 14f). Distinct values have been observed depending on the taxonomy of the organism from which organic compounds are coming from [83]. This establishes that organic compounds extracted from Ca-carbonate nanograins have preserved their binding capabilities to the calcium atoms. This could be the reason why crystallization of the growth layers results in rounded grains and not the faceted crystals occurring in non-biogenic crystallization [87].

Conclusively, comparative investigations now possible for each of the structural levels allow for

in-depth examination of materials produced by abnormal or pathological mineralization processes in both animal and human biology. Animal mineralization disturbances (such as deficiency in formation of coral skeletons) may result in global consequences at the world-wide oceanic level. Conversely deciphering ultrastructure and growth mode of the abnormally mineralized materials may contribute to the understanding of biological/environmental imbalance in human pathologies.

Acknowledgements

This study was supported in part by SOLEIL Grants 201770784 and 20180995 to J-PC and YD.

References

[1] C. Linné, *Systema naturæ per regna tria naturæ, secundum classes, ordines, genera, species, cum characteribus, differentiis, synonymis, locis*, Impensis L. Salvii, Holmiæ, 1758.
[2] J.-B. Lamarck, *Mémoire sur les fossiles des environs de Paris*, Annales du Muséum d'histoire naturelle, 1802–1806, vol. 1–8, Muséum d'histoire naturelle, Paris, 1802.
[3] M. Schleiden, *Archiv für Anatomie, Physiologie und wissenschaftliche Medicin*, Verlag von Veit et comp., Berlin, 1838.
[4] T. Schwann, *Mikroskopische Untersuchungen über die Uebereinstimmung in der Struktur und dem Wachsthum der Thiere und Pflanzen*, Sander, Berlin, 1839, 268 pages.
[5] J. S. Bowerbank, *Trans. Microsc. Soc. Lond.*, 1844, **1**, 123-152.
[6] W. Carpenter, *Br. Assoc. Adv. Sci.*, 1844, **14**, 1-24.
[7] W. Carpenter, *Br. Assoc. Adv. Sci.*, 1847, **17**, 93-134.
[8] T. H. Huxley, *Proc. Zool. Soc. Lond.*, 1879, **46**, 751-788.
[9] W. J. Schmidt, *Die Bausteine des Tierkörpers in Polarisiertem Lichte*, F. Cohen, Bonn, 1924.
[10] H. Lowenstam, S. Weiner, *On biomineralization*, Oxford University Press, New York, 1989, 324 pages.
[11] E. Haeckel, *Die Radiolarian (rhizopoda Radiara). Eine Monographie*, Reimer, Berlin, 1862.
[12] N. Watabe, C. M. Pan, *Am. Zool.*, 1984, 977-985.
[13] S. Weiner, W. Traub, *Connect. Tissue Res.*, 1989, **21**, 259-265.
[14] M. de Broglie, *J. Phys. Radium*, 1924, **5**, 1-19.
[15] H. A. Lowenstam, *Science*, 1981, **211**, 1126-1131.
[16] A. Veis, *Science*, 2005, **307**, 1419-1420.
[17] W. H. Bryan, D. Hill, *Proc. R. Soc. Queensland*, 1941, **52**, 78-91.
[18] D. J. Barnes, *Science*, 1970, **170**, 1305-1308.
[19] J. P. Cuif, Y. Dauphin, *Paläont. Zeit.*, 1998, **72**, 257-270.
[20] J. P. Cuif, Y. Dauphin, *Biogeosciences*, 2005a, **2**, 61-73.
[21] J. P. Cuif, Y. Dauphin, *J. Struct. Biol.*, 2005b, **150**, 319-331.
[22] S. Mann, *Biomineralization: Principles and Concepts in Bioinorganic Materials Chemistry*, Oxford University Press, Oxford, 2001.
[23] P. Furla, I. Galgani, I. Durand, D. Allemand, *J. Exp. Biol.*, 2000, **203**, 3445-3457.
[24] J. F. Adkins, E. A. Boyle, W. B. Curry, A. Lutringer, *Geochim. Cosmochim. Acta*, 2003, **67**, 1129-1143.
[25] H. Petit, "Recherches sur des séquences d'événements périostracaux lors de L'élaboration de la coquille d'*Amblema plicata* Conrad, 1834", PhD Thesis, Lab. Zoologie, Université de Bretagne occidentale, France, 1978, Thèse doc. Lab. Zoologie, 276 pages.
[26] D. Volkmer, "Biologically Inspired Crystallization of Calcium Carbonate beneath Monolayers: A Critical Overview", in *Handbook of Biomineralization. Biomimetic and Bioinspired Chemistry* (P. Behrens, E. Bauerlein, eds.), Wiley VCH, Weinheim, Germany, 2007, 65-87.
[27] J. D. Taylor, W. J. Kennedy, A. Hall, *Bull. Br. Mus. Nat. Hist. Zool.*, 1969, **63**, 1-125.
[28] A. G. Checa, T. Okamoto, J. Ramirez, *Proc. R. Soc. Lond. B*, 2006, **273**, 1329-1337.
[29] C. Grégoire, G. Duchateau, M. Florkin, *Ann. Inst. Océanogr.*, 1955, **31**, 1-36.
[30] C. Grégoire, *Biol. Rev.*, 1967, **42**, 653-687.
[31] C. Grégoire, *Bull. Inst. R. Sci. Nat. Belg.*, 1960, **36**, 1-22.
[32] G. Goffinet, C. Grégoire, M. F. Voss-Foucart, *Arch. Intern. Physiol. Biochem.*, 1977, **85**, 849-863.
[33] J. J. De Yoreo, P. M. Dove, *Science*, 2004, **306**, 1301-1302.
[34] H. Cölfen, M. Antonietti, *Mesocrystals and Nonclassical Crystallization*, John Wiley & Sons, Chichester, UK, 2008.
[35] J. J. De Yoreo, P. U. P. A. Gilbert, N. A. J. M. Sommerdijk, R. L. Penn, S. Whitelam, D. Joester, H. Zhang, J. D. Rimer, A. Navrotsky, J. F. Banfield, A. F. Wallace, F. M. Michel, F. C. Meldrum, H. Cölfen, P. M. Dove, *Science*, 2015, **349**, article no. aaa6760.
[36] M. A. Crenshaw, in *Skeletal Growth of Aquatic Organisms* (D. C. Rhoads, R. A. Lutz, eds.), Plenum Press, New York, 1980, 115-132.
[37] C. Rollion-Bard, D. Blamart, J. P. Cuif, A. Juillet-Leclerc, *Coral Reefs*, 2003, **22**, 405-415.
[38] K. Simkiss, *Am. Zool.*, 1984, **24**, 847-856.
[39] E. Beniash, J. Aizenberg, L. Addadi, S. Weiner, *Proc. R. Soc. Lond. B*, 1997, **264**, 461-465.
[40] L. Xiang, W. Kong, J. Su, J. Liang, G. Zhang, L. Xie, R. Zhang, *PLoS One*, 2014, **9**, article no. e113150.
[41] L. Addadi, S. Raz, S. Weiner, *Adv. Mater.*, 2003, **15**, 959-970.
[42] A. S. Mount, A. P. Wheeler, R. P. Paradkar, D. Snider, *Science*, 2004, **304**, 297-300.
[43] A. V. Ivanina, H. I. Falfushynska, E. Beniash, H. Piontkivska, I. M. Sokolova, *J. Exp. Biol.*, 2017, **220**, 3209-3221.
[44] H. Mutvei, "Biomineralization", in *Int. Symp. on Problems of Biomineralization*, vol. 6, Schattauer Verlag, Stuttgart, New York, 1972, 96-100.
[45] H. Mutvei, *Calcif. Tiss. Res.*, 1977, **24**, 11-18.
[46] H. Mutvei, *Zool. Scr.*, 1978, **7**, 287-296.
[47] H. Mutvei, in *Scanning Electron Microscopy II* (O. Johari, ed.), SEM Inc., Chicago Press, Chicago, 1979, 451-462.
[48] B. Frérotte, A. Raguideau, J. P. Cuif, *C. R. Acad. Sci. Paris*, 1983, **297**, 383-388.
[49] J. P. Cuif, Y. Dauphin, J. E. Sorauf, *Biominerals and Fossils through Time*, Cambridge University Press, Cambridge, UK, 2011, 490 pages.
[50] Y. Dauphin, J. P. Cuif, J. Doucet, M. Salomé, J. Susini, C. T. Williams, *Mar. Biol.*, 2003, **142**, 299-304.

[51] J. P. Cuif, O. Belhadj, S. Borensztajn, M. Geze, S. Trigos-Santos, P. Prado, Y. Dauphin, *Heliyon*, 2020, **6**, article no. e04513.
[52] J. D. Taylor, W. J. Kennedy, *Calc. Tis. Res.*, 1969, **3**, 274-283.
[53] J. H. Waite, in *The Mollusca, Vol. 1, Metabolic Biochemistry and Molecular Biomechanics* (P. W. Hochachka, ed.), Academic Press, New York, 1983, 467-504.
[54] E. M. Harper, *Palaeontology*, 1997, **40**, 71-97.
[55] H. Nakahara, G. Bevelander, *Calcif. Tissue Res.*, 1971, **7**, 31-45.
[56] M. Suzuki, S. Nakayama, H. Nagasawa, T. Kogure, *Micron*, 2013, **45**, 136-139.
[57] J. P. Cuif, M. Burghammer, V. Chamard, Y. Dauphin, P. Godard, G. Le Moullac, G. Nehrke, A. Perez-Huerta, *Minerals*, 2014, **4**, 815-834.
[58] J. P. Cuif, Y. Dauphin, G. Luquet, K. Medjoubi, A. Somogyi, A. Perez-Huerta, *Minerals*, 2018, **8**, article no. 370.
[59] J. P. Cuif, Y. Dauphin, in *Biomineralization, from Molecular and Nano-structural Analyses to Environmental Science* (K. Endo, T. Kogure, H. Nagasawa, eds.), Springer, Singapore, 2018, 349-357.
[60] Y. Dauphin, *Palaont. Zeit*, 2001, **75**, 113-122.
[61] J. P. Cuif, Y. Dauphin, P. Berthet, J. Jegoudez, *Geochem. Geophys. Geosys.*, 2004, **5**, 1-9.
[62] M. Cusack, P. Chung, Y. Dauphin, A. Perez-Huerta, *Palaeontology*, 2010, **84**, 99-105.
[63] Y. Dauphin, E. Dufour, *Micron*, 2008, **39**, 891-896.
[64] Y. Dauphin, G. Luquet, A. Perez-Huerta, M. Salomé, *Connect. Tissue Res.*, 2018, **59**, 67-73.
[65] J. Aizenberg, G. Lambert, L. Addadi, S. Weiner, *Adv. Mater.*, 1996, **8**, 222-226.
[66] J. P. Cuif, Y. Dauphin, B. Farre, G. Nehrke, J. Nouet, M. Salomé, *Mineral. Mag.*, 2008, **72**, 233-237.
[67] Q. Cheng, W. Hu, Z. Bai, *Front. Mar. Sci.*, 2021, **8**, article no. 657263.
[68] M. Suzuki, H. Nagasawa, *Can. J. Zool.*, 2013, **91**, 349-399.
[69] E. T. Degens, D. W. Spencer, *Comp. Biochem. Physiol.*, 1967, **25**, 553-579.
[70] K. Simkiss, *Comp. Biochem. Physiol.*, 1965, **16**, 427-435.
[71] M. A. Crenshaw, H. Ristedt, in *The Mechanisms of Mineralization in the Invertebrates and Plants* (N. Watabe, K. M. Wilbur, eds.), vol. 5, University of South Carolina Press, Columbia, 1976, 355-367.
[72] F. Nudelman, B. A. Gotliv, L. Addadi, S. Weiner, *J. Struct. Biol.*, 2006, **153**, 176-187.
[73] I. K. Kawakami, *Mem. Fac. Sci., Kyushu Univ.*, 1952a, **1**, 83-89.
[74] I. K. Kawakami, *J. Fuji Pearl Institute*, 1952b, **2**, 1-4.
[75] K. Wada, *Bull. Natl. Pearl Res. Lab.*, 1957, **3**, 167-174.
[76] K. Wada, *Bull. Natl. Pearl Res. Lab.*, 1961, **36**, 703-828.
[77] K. Wada, *Bull. Gemmol. Soc. Japan*, 1999, **20**, 47-62.
[78] J. Taylor, E. Strack, "Pearl production", in *The Pearl Oyster* (P. C. Southgate, J. S. Lucas, eds.), Elsevier, Amsterdam, The Netherlands, 2008, 273-302.
[79] J. P. Cuif, Y. Dauphin, L. Howard, J. Nouet, S. Rouzière, M. Salomé, *Aquat. Living Resour.*, 2011, **23**, 277-284.
[80] A. Somogyi, K. Medjoubi, G. Baranton, V. Le Roux, M. Ribbens, F. Polack, P. Philippot, J. P. Samama, *J. Synchrotron Radiat.*, 2015, **22**, 1118-1129.
[81] J. P. Cuif, Y. Dauphin, G. Luquet, O. Belhadj, S. Rouzière, M. Salomé, M. Cotte, A. Somogyi, K. Medjoubi, C. Lo, D. Saulnier, *Aquac. Res.*, 2019, **51**, 506-522.
[82] Y. Dauphin, O. Belhadj, L. Bellot-Gurlet, M. Cotte, C. Lo, K. Medjoubi, A. Somogyi, M. Salomé, D. Saulnier, J. P. Cuif, *Mater. Charact.*, 2020, **163**, article no. 110276.
[83] J. P. Cuif, A. Bendounan, Y. Dauphin, J. Nouet, F. Sirotti, *Anal. Bioanal. Chem.*, 2013, **405**, 8739-8748.
[84] Y. Dauphin, E. Zolotoyabko, A. Berner, E. Lakin, C. Rollion-Bard, J. P. Cuif, P. Fratzl, *J. Struct. Biol.*, 2019, **205**, 121-132.
[85] Y. Dauphin, *J. Biol. Chem.*, 2003, **278**, 15168-15177.
[86] A. G. Checa, A. B. Rodriguez-Navarro, F. J. Esteban-Delgado, *Biomaterials*, 2005, **26**, 6404-6414.
[87] B. Pokroy, J. P. Quintana, E. N. Caspi, A. Berner, E. Zolotoyabko, *Nat. Mater.*, 2004, **3**, 900-902.

Comptes Rendus

Chimie

Objet de la revue

Les *Comptes Rendus Chimie* sont une revue électronique évaluée par les pairs de niveau international, qui couvre l'ensemble des domaines de la discipline. Ils publient principalement des numéros spéciaux, mais également des articles originaux de recherche, des annonces préliminaires, des articles de revue, des mises en perspective historiques, des textes à visée pédagogique ou encore des actes de colloque, sans limite de longueur, en anglais ou en français. Les *Comptes Rendus Chimie* sont diffusés selon une politique vertueuse de libre accès diamant, gratuit pour les auteurs (pas de frais de publications) comme pour les lecteurs (libre accès immédiat et pérenne).

À propos de la revue

Toutes les informations concernant la revue, y compris le texte des articles publiés qui est en accès libre intégral, figurent sur le site https://comptes-rendus.academie-sciences.fr/chimie/.

Informations à l'attention des auteurs

Pour toute question relative à la soumission des articles, les auteurs peuvent consulter le site https://comptes-rendus.academie-sciences.fr/chimie/.

Contact

Académie des sciences
23, quai de Conti, 75006 Paris, France
CR-Chimie@academie-sciences.fr

Comptes Rendus
de l'Académie des sciences

Chimie

Volume 25, nº S1, 2022

Special issue / *Numéro thématique*

Microcrystalline pathologies: Clinical issues and nanochemistry / *Pathologies microcristallines : questions cliniques et nanochimie*

Guest editors / *Rédacteurs en chef invités*

Dominique Bazin (Université Paris-Saclay, CNRS, ICP, France), Michel Daudon, Vincent Frochot, Emmanuel Letavernier Jean-Philippe Haymann (Sorbonne Université, INSERM, AP-HP, Hôpital Tenon, France)

Cover illustration / *Illustration de couverture*

Michel Daudon. 1.3 kg bladder stone with a cross-section showing the internal structure and change in composition over time as a record of the patient's history / *Calcul vésical de 1,3 kg dont la section montre la structure interne et le changement de composition au cours du temps comme un enregistrement de l'histoire du patient*

Contents

1878-1543 (electronic)

Académie des sciences — Paris

COMPTES RENDUS
DE L'ACADÉMIE DES SCIENCES

Chimie

Volume 25, nº S1, 2022